ENERGY ASPECTS OF ACOUSTIC CAVITATION AND SONOCHEMISTRY

Fundamentals and Engineering

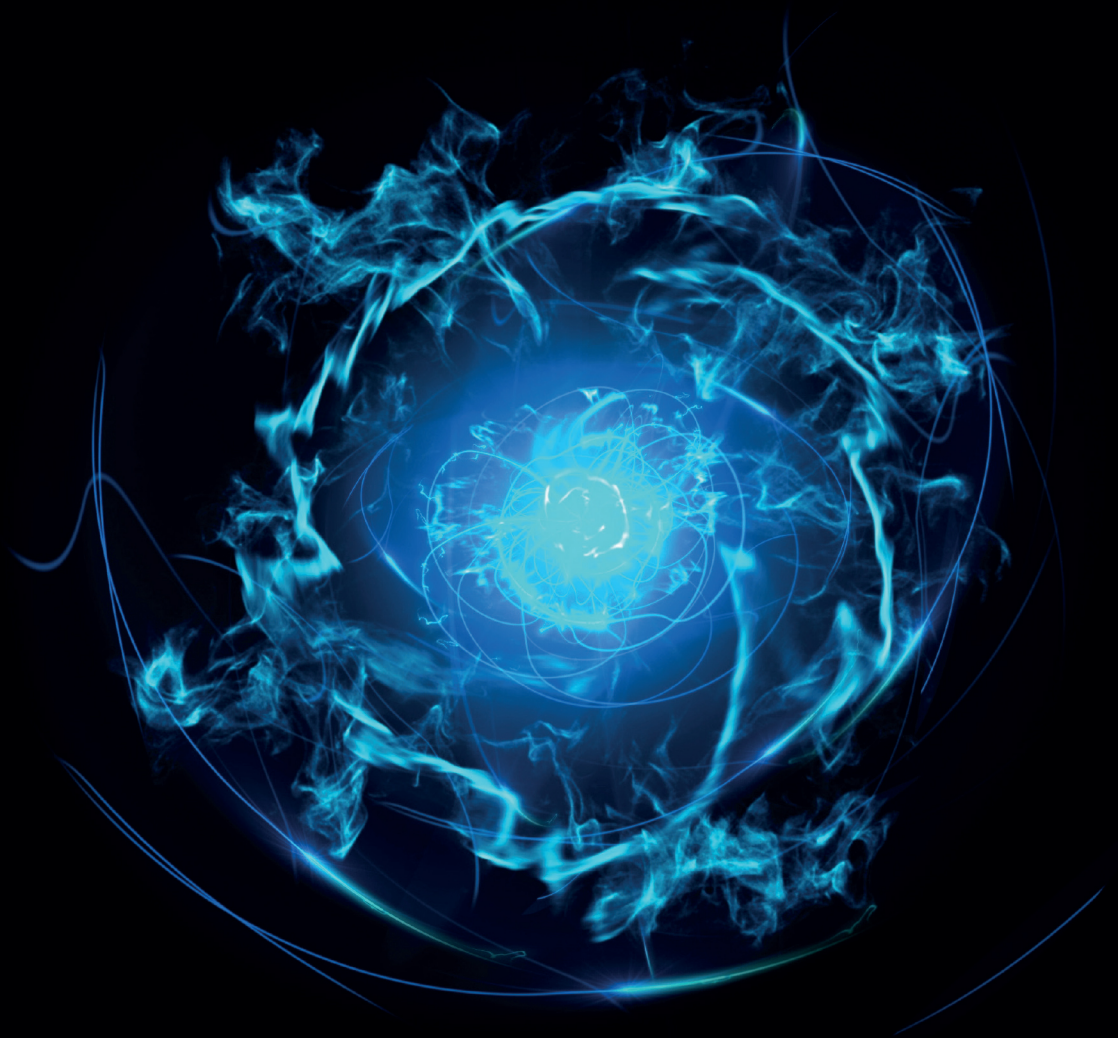

Edited by
Oualid Hamdaoui
Kaouther Kerboua

ELSEVIER

Energy Aspects of Acoustic Cavitation and Sonochemistry

Energy Aspects of Acoustic Cavitation and Sonochemistry

Fundamentals and Engineering

Edited by

Oualid Hamdaoui
Chemical Engineering Department, College of Engineering, King Saud University, Riyadh, Saudi Arabia

Kaouther Kerboua
Higher School of Industrial Technologies, Department of Engineering, Annaba, Algeria

ELSEVIER

Elsevier

Radarweg 29, PO Box 211, 1000 AE Amsterdam, Netherlands
The Boulevard, Langford Lane, Kidlington, Oxford OX5 1GB, United Kingdom
50 Hampshire Street, 5th Floor, Cambridge, MA 02139, United States

Copyright © 2022 Elsevier Inc. All rights reserved.

No part of this publication may be reproduced or transmitted in any form or by any means, electronic or mechanical, including photocopying, recording, or any information storage and retrieval system, without permission in writing from the publisher. Details on how to seek permission, further information about the Publisher's permissions policies and our arrangements with organizations such as the Copyright Clearance Center and the Copyright Licensing Agency, can be found at our website: www.elsevier.com/permissions.

This book and the individual contributions contained in it are protected under copyright by the Publisher (other than as may be noted herein).

Notices
Knowledge and best practice in this field are constantly changing. As new research and experience broaden our understanding, changes in research methods, professional practices, or medical treatment may become necessary.

Practitioners and researchers must always rely on their own experience and knowledge in evaluating and using any information, methods, compounds, or experiments described herein. In using such information or methods they should be mindful of their own safety and the safety of others, including parties for whom they have a professional responsibility.

To the fullest extent of the law, neither the Publisher nor the authors, contributors, or editors, assume any liability for any injury and/or damage to persons or property as a matter of products liability, negligence or otherwise, or from any use or operation of any methods, products, instructions, or ideas contained in the material herein.

ISBN: 978-0-323-91937-1

For Information on all Elsevier publications visit our website at
https://www.elsevier.com/books-and-journals

Publisher: Susan Dennis
Acquisitions Editor: Anita Koch
Editorial Project Manager: Kyle Gravel
Production Project Manager: Kumar Anbazhagan
Cover Designer: Miles Hitchen

Typeset by Aptara, New Delhi, India

Contents

Contributors xi

Part I
The single acoustic cavitation bubble as an energetic system: qualitative and quantitative assessments 1

1. Single acoustic cavitation bubble and energy concentration concept 3

Kaouther Kerboua, Djihane Mazouz, Imen Hasaounia

1.1 Introduction 3
1.2 Single acoustic cavitation bubble: Thermodynamic aspects of inception and growth, and dynamics of bubble oscillation 4
1.2.1 Bubble inception, growth and dynamics of oscillation 4
1.2.2 Thresholds 7
1.2.3 Dynamics of bubble oscillation 9
1.3 The hot spot theory 10
1.4 Thermodynamics of acoustic cavitation bubble and energy balance 11
1.4.1 Polytropic model 12
1.4.2 Energetics of sonochemistry 12
1.4.3 Mass diffusion 12
1.4.4 Nonequilibrium of evaporation and condensation 13
1.4.5 Conduction 14
1.4.6 Convection 14
1.5 Energy concentration concept 15
1.5.1 Acoustic energy 15
1.5.2 Acoustic radiation as a source of cavitation 16
1.5.3 Acoustic radiation from collapsing bubble 16
1.5.4 Energy concentration 18
1.6 Engineering outcomes 20
References 21

2. The energy forms and energy conversion 23

Aissa Dehane, Slimane Merouani and Oualid Hamdaoui

2.1 Introduction 23
2.2 Theoretical background 24
2.3 Energetic evolution of an oscillating bubble 25
2.4 Influence of acoustical conditions 27
2.5 Energy analysis as function of initial bubble size 30
2.6 Conclusion 31
Acknowledgments 31
References 31

3. Physical effects and associated energy release 35

Imen Hasaounia, Djihane Mazouz and Kaouther Kerboua

3.1 Introduction 35
3.2 The theoretical approach of the propagation of an acoustic wave in a liquid medium and acoustic streaming 36
3.2.1 Propagation of an ultrasonic wave in a liquid medium 36
3.2.2 Acoustic streaming 37
3.3 The theoretical approach of the oscillation of acoustic cavitation bubbles and its associated physical effects 38
3.3.1 The energetic mechanism of bubble inception, oscillation, and collapse 38
3.3.2 The physical effects associated with acoustic cavitation bubbles 43
3.4 Energetic outcomes: Macroscopic dissipation of acoustic energy 45
3.5 Conclusion 45
References 46

4. Sonochemical reactions, when, where and how: Modelling approach 49

Ferenc Hegedűs, Csanád Kalmár, Tamás Turányi, István Gy. Zsély and Máté Papp

4.1 Introduction 49
4.2 The governing equations 50
4.2.1 State-of-the-art reaction mechanism of an oxygen bubble 50
4.2.2 The complete bubble model 54
4.3 Numerical technique and the investigated parameter space 60
4.4 Chemical yield of a single bubble 61
4.5 Energy efficiency considerations 68
4.6 Discussion and summary 71
References 73

5. Sonochemical reactions, when, where and how: Experimental approach 77

Xingaoyuan Xiong and Zongsu Wei

5.1 When do the sonochemical reactions take place? 77
5.2 Where and how do sonochemical reactions take place? 78
5.2.1 In the gas phase of collapsing bubbles 78
5.2.2 At the interfacial region surrounding collapsing bubbles 79
5.2.3 In the bulk solution 81
5.3 Techniques for ultrasonic cavitation observation and measurement 82
5.3.1 Sonoluminescence (SL) 82
5.3.2 Tube arrest method 83
5.3.3 Color Doppler ultrasound imaging 84
5.3.4 Quantify acoustic bulk cavitation in multiple bubble system 85
5.3.5 Micro-PIV method 86
5.4 Application of sonochemical reactions 86
5.4.1 US/persulfate system 87
5.4.2 US/permanganate system 88
5.4.3 US/Fenton system 88
5.4.4 US/O_3 system 89
5.4.5 US/electrochemistry system 89
5.4.6 US/UV system 90
5.5 Conclusions and perspective 91
References 92

Part II
The bubble population: an analytic view into mutual forces and allied energy exchange 97

6. The Bjerknes forces and acoustic radiation energy 99

Ke-ming Quan

6.1 Acoustic radiation force in a plane traveling wave field 99
6.2 Bjerknes forces 100
6.2.1 Primary Bjerknes force 100
6.2.2 Secondary Bjerknes force 101
6.3 Experimental aspects of determining acoustic radiation energy 102
6.3.1 Acoustic dosimetry based on radiation force measurement 102
6.3.2 Acoustic radiation force in the near field 103
6.3.3 Measurement of acoustic radiation energy from a liquid of multibubbles 103
6.3.4 Interpretation of acoustic energy spectra from multibubble cavitation 103
6.4 Conclusion 106
References 107

7. Nonlinear oscillations and resonances of the acoustic bubble and the mechanisms of energy dissipation 109

Amin Jafari Sojahrood and Michael C. Kolio

7.1 Introduction 109
7.2 The bubble model 110
7.2.1 Thermal effects 110
7.3 Scattered pressure by bubbles 111
7.4 Various regimes of complex bubble oscillations 111
7.5 Damping constants for the linear regime of oscillations 114
7.6 Nonlinear resonances of the bubble oscillator 116
7.7 Nonlinear bubble behavior analysis 118
7.7.1 Poincaré section 118
7.7.2 Method of maxima 118
7.7.3 Final construction 118
7.8 Nonlinear dissipation terms 118
7.8.1 Nonlinear dissipation terms of the uncoated free bubble 119

7.9 Bifurcation structure and the nonlinear dissipations of the bubble 119
7.10 Summarizing points and discussion 124
7.11 Concluding remarks 126
References 127

8. Damping mechanisms of oscillating gas/vapor bubbles in liquids 131

Yuning Zhang, Xiaoxiao Zheng, Xuan Du and Yuning Zhang

8.1 Introduction 131
8.2 Bubble wall motion equation 131
8.2.1 Prosperetti-Lezzi equation 132
8.2.2 Gilmore equation 132
8.2.3 Keller-Miksis equation 132
8.2.4 Herring equation 132
8.2.5 Rayleigh-Plesset equation 133
8.3 Linear oscillations of gas bubbles 133
8.3.1 Bubble wall motion equation with thermal effects 133
8.3.2 Linearization process 133
8.3.3 Damping constants 134
8.4 Thermal effects and thermal damping 134
8.4.1 Basic equations 134
8.4.2 Solutions for the nonuniform pressure inside bubble 135
8.4.3 Solutions for the uniform pressure inside bubble 136
8.5 Effects of liquid compressibility and acoustic damping 136
8.6 Total damping constants and comparisons of damping mechanisms 137
8.7 Damping mechanisms of vapor bubbles 137
8.7.1 Basic equations 137
8.7.2 Linear oscillations 138
8.7.3 Effects of mass transfer 139
8.8 Wave propagation in the liquids containing bubbles 139
8.8.1 Basic equations 139
8.8.2 Wave speed and attenuation 141
8.9 Nonlinear oscillations of bubbles 141
8.9.1 Comparisons of the viscous and acoustic damping mechanisms 141
8.9.2 Comparisons of predictions by different bubble wall motion equations 143
8.10 Conclusions 143
Acknowledgment 143
References 143

9. Energy controlling mechanisms: Relationship with operational conditions 145

Aissa Dehane, Slimane Merouani and Oualid Hamdaoui

9.1 Introduction 145
9.2 Model description 146
9.3 Chemical activity in single bubble and multibubble systems 148
9.4 Energy variation of a multibubble system 149
9.5 Conclusion 151
Acknowledgments 152
References 152

Part III
Ultrasound assisted processes, sonochemical reactors and energy efficiency 155

10. Efficiency assessment and mapping of cavitational activities in sonochemical reactors 157

Vinayak S. Sutkar, Amit V. Mahulkar and Aniruddha B. Pandit

10.1 Introduction 157
10.2 Types, classification and working principle of the sonochemical reactors 158
10.3 Overview of cavitational activities in the sonochemical reactors 161
10.3.1 Spatial and temporal distribution (mapping activities and bubble dynamics studies) 161
10.3.2 Active and passive cavitational zones 161
10.3.3 Effect of operating parameters on distribution of cavitational activities 162
10.3.4 Challenges in efficient design and operation of sonochemical reactors 162
10.4 Efficiency assessment and mapping of cavitational activities in sonochemical reactors 164
10.4.1 Efficiency assessment 164
10.4.2 Overview of techniques for quantifying cavitational activity distribution 166

10.4.3 Experimental techniques 167
10.4.4 Numerical investigations 172
10.5 Case study 176
10.5.1 Experimental setup 176
10.5.2 Measurements of Iodine liberated in reactor 176
10.5.3 Quantification of local pressure field by wave equation 178
10.5.4 Bubble dynamics studies 178
10.5.5 Observations 178
10.6 Outlook and path forward 180
References 180

11. Sources of dissipation: An outlook into the effects of operational conditions 183

Rana Kıdak

11.1 Introduction 183
11.2 Theoretical approaches 183
11.3 Formation of extreme conditions in reactions 184
11.3.1 Sonochemical reaction sites 185
11.3.2 Definition of "cavitation treshold" 185
11.4 Transducers 185
11.5 Signals 186
11.6 Effects of operational parameters 186
11.6.1 The primary parameters 186
11.6.2 Secondary parameters 188
11.7 Conclusion 189
References 189

12. Mechanistic issues of energy efficiency of an ultrasonic process: Role of free and dissolved gas 193

Vijayanand Suryakant Moholkar, T. Sivasankar, Bhaskar Jyoti Choudhury and Kuldeep Roy

12.1 Introduction 193
12.2 Experimental summary 194
12.3 The mathematical model 196
12.3.1 Determining the acoustic impedance 196
12.3.2 Acoustic wave propagation in bubbly liquids 197
12.3.3 Cavitation nucleation and bubble dynamics 198
12.3.4 Rectified diffusion 199
12.4 Results and reasoning 200
12.4.1 Interpretation of the spectral characteristics 201
12.4.2 Radial motion of the bubbles 203
12.4.3 Analysis of the spectral characteristics of acoustic emission 204
12.5 Overview 206
12.6 Case studies of ultrasonic processes based on energy transformation analysis 207
12.7 Intensification of wet textile treatment 207
12.8 Case study 2: Weissler reaction 210
References 216

13. Simulation of sonoreators accounting for dissipated power 219

Olivier Louisnard and Igor Garcia-Vargas

13.1 Introduction 219
13.2 Linear acoustics 220
13.2.1 Energetics of nondissipative linear acoustics 220
13.2.2 Energetics of dissipative linear acoustics 223
13.3 Sound propagation accounting for cavitation 224
13.3.1 The Caflisch model 224
13.3.2 Linear case 225
13.3.3 Energy formulation 225
13.3.4 Energy dissipation functions 227
13.3.5 A reduced model 228
13.3.6 Summary of the cavitating liquid model 229
13.4 Acoustics of solid parts and piezo-electrics 230
13.4.1 Elastic materials 230
13.4.2 Boundary conditions 230
13.4.3 Energy conservation for solids 231
13.4.4 Piezo-electric materials 233
13.4.5 Energy conservation for piezo-electrics 233
13.4.6 Dissipation in solids 235
13.5 Simulation examples 235
13.5.1 Known transducer 235
13.5.2 A nondocumented tip-transducer 240
13.5.3 A radial probe transducer 242
13.6 Conclusion 244
Acknowledgment 245
References 245

14. Technological designs and energy efficiency: The optimal paths 249

Kaouther Kerboua and Oualid Hamdaoui

14.1 Introduction 249
14.2 Ultrasound source 250
14.2.1 Gas-driven transducers 250
14.2.2 Liquid-driven transducers 250
14.2.3 Electromechanical transducers 250
14.3 Electric-acoustic energy conversion 254

14.4 Performance of power transducers 255
14.5 Mapping acoustic wave propagation 256
14.6 Overall energy efficiency 257
14.7 Designs and energy efficiency 257
14.8 Conclusion 259
References 259

Part IV
Green, sustainable and benign by design process? The place and perspective of ultrasound assisted processes and sonochemistry in industrial applications based on energy efficiency 263

15. Acoustic cavitation and sonochemistry in industry: State of the art 265

Md Hujjatul Islam and Bruno G. Pollet

15.1 Introduction 265
15.2 Power ultrasound and acoustic cavitation 265
15.3 Sonochemistry 266
15.4 Physical and chemical impact of power ultrasound 265
15.5 Industrial applications 268
15.5.1 Cavitation in the food industry 268
15.5.2 Cavitation in the biofuel industry 269
15.5.3 Cavitation in the petroleum industry 272
15.5.4 Cavitation in the metal industry 273
15.6 Conclusion 275
References 275

16. Crystallization of pharmaceutical compounds: Process Intensification using ultrasonic irradiations - Experimental approach 279

Hamza Ferkous and Oualid Hamdaoui

16.1 Introduction 279
16.2 Theorical approach 279
16.3 Physical effect of cavitation bubble on crystallization 280
16.3.1 Supersaturation 280
16.3.2 Nucleation 281
16.3.3 Crystal growth 282
16.4 Sonocrystallization of pharmaceutical compounds: Effect of operating parameters 282
16.4.1 Effect of US frequency 282
16.4.2 Effect of acoustic power 283
16.5 Conclusion 285
References 285

17. Sonochemical degradation of fluoroquinolone and β-lactam antibiotics – A view on transformations, degradation efficiency, and consumed energy 287

Efraím A. Serna-Galvis, Jazmín Porras and Ricardo A. Torres-Palma

17.1 Principles of sonochemical treatment of organic pollutants in water 287
17.2 Sonochemical degradation of β-lactam antibiotics 288
17.3 Degradation of fluoroquinolone antibiotics using ultrasound 292
17.4 Relationship between degradation efficiency and consumed power/energy 294
17.5 Concluding remarks 296
Acknowledgments 297
References 297

18. The use of ultrasonic treatment in technological processes of complex processing of industrial waste: Energetic insights 299

Yarusova S.B., Gordienko P.S., Buravlev I.Yu., Bulanova S.B. and Sushkov Yu.V.

18.1 Introduction 299
18.2 Characteristics of technogenic waste 300
18.3 Experimental part 301
18.3.1 Ultrasonic synthesis of calcium hydrosilicate 301
18.3.2 Methods of analysis 301
18.4 Analysis of the kinetics of the reaction of alkaline treatment of borogypsum under conditions of ultrasonic exposure 302
18.5 Application of the product of UST of borogypsum as a sorbent 309
18.6 Conclusions 310
Acknowledgments 311
References 311

19. The sonochemical and ultrasound-assisted production of hydrogen: energy efficiency for the generation of an energy carrier 313

Nour Hane Merabet and Kaouther Kerboua

19.1 Introduction: hydrogen and ultrasound 313
19.1.1 State of the art 313
19.1.2 Role of ultrasound 315
19.2 The ultrasound-assisted pathway for hydrogen production: theoretical approach and outcomes 318
19.2.1 Proposed mechanisms and comprehensive findings 318
19.2.2 Experimental findings 323
19.3 Analysis and orientations on the future of the sonochemical hydrogen: insights into the main challenges 323
19.3.1 Energy-yields balance 323
19.3.2 Adapting the technology 325
19.4 Conclusion 326
References 326

20. Future trends and promising applications of industrial sonochemical processes 329

Gaurav G. Dastane, Vinayak S. Sutkar, Amit V. Mahulkar and Aniruddha B. Pandit

20.1 Intensification of chemical process via cavitation 329
20.2 Demonstrated applications in various fields 329
20.2.1 Water/wastewater treatment and biotechnology applications 329
20.2.2 Nanomaterials 330
20.2.3 Food and beverage 331
20.2.4 Petroleum industry 335
20.2.5 Textile processing 336
20.2.6 Azeotropic distillation 339
20.3 Outlook and path forward 340
References 341

21. Raising challenges of ultrasound-assisted processes and sonochemistry in industrial applications based on energy efficiency 349

Mohit Singla and Nandan Sit

21.1 Introduction 349
21.2 Theoretical aspects of ultrasound energy 350
21.3 Industrial uses of ultrasound power 351
21.3.1 Cleaning and decontamination 351
21.3.2 Extraction and impregnation 352
21.3.3 Crystallization and precipitation 352
21.3.4 Filtration and separation 353
21.3.5 Textile industry 353
21.3.6 Electrochemistry 355
21.4 Energy efficiency of ultrasound-assisted processes 355
21.4.1 Acoustic cavitation based methods 355
21.4.2 Energy or flow velocity method 355
21.4.3 Physical properties measurement methods 355
21.5 Factors affecting the application of ultrasound 356
21.5.1 Effect of solution 356
21.5.2 Effect of frequency 356
21.5.3 Effect of power 357
21.5.4 Effect of sonication time 357
21.5.5 Effect of substrate 357
21.5.6 Physical effect of ultrasound 358
21.5.7 Bulk liquid temperature 358
21.6 Energy efficiency and scale up issue for industrial application of ultrasound 359
21.6.1 Challenges in ultrasound in food processing 360
21.6.2 Challenges in sonochemical processes for pollutant degradation 360
21.6.3 Challenges for sonohydrogen reactor design 361
21.7 Recent developments in design and scale-up of sonoreactors for industrial processes 362
21.7.1 Reactor design 363
21.7.2 Frequency of sonication 364
21.7.3 Large-size sonochemical reactor 365
21.8 Future prospects for the scale-up of sonochemistry 366
21.9 Conclusion 366
References 366

Index 373

Contributors

Bhaskar Jyoti Choudhury, Department of Chemical Engineering, Indian Institute of Technology Guwahati, Guwahati, Assam, India

Gaurav G. Dastane, Department of Chemical Engineering, Institute of Chemical Technology, Mumbai, India

Aissa Dehane, Laboratory of Environmental Process Engineering, Department of Chemical Engineering, Faculty of Process Engineering, University Salah Boubnider-Constantine 3, Constantine, Algeria

Xuan Du, Key Laboratory of Power Station Energy Transfer Conversion and System, Ministry of Education, North China Electric Power University, Beijing, China

Hamza Ferkous, Department of Process Engineering, Faculty of Tehnology, Badji Mokhtar - Annaba University, Algeria

Igor Garcia-Vargas, Centre RAPSODEE, IMT Mines-Albi, UMR CNRS 5302, Université de Toulouse, Albi CT, France; SinapTec, Lezennes, France; Laboratoire de Génie Chimique, Université de Toulouse, CNRS, INP, UPS, Toulouse, France

Oualid Hamdaoui, Chemical Engineering Department, College of Engineering, King Saud University, Riyadh, Saudi Arabia

Imen Hasaounia, Higher School of Industrial Technologies, Department of Engineering, Annaba, Algeria

Ferenc Hegedűs, Department of Hydrodynamic Systems, Budapest University of Technology and Economics, Budapest, Hungary

Buravlev I.Yu., Institute of Chemistry, Far Eastern Branch of Russian Academy of Sciences, Vladivostok, Russia

Md Hujjatul Islam, Department of Chemical Engineering and Applied Chemistry, University of Toronto, Toronto, Canada

Amin Jafari Sojahrood, Institute for Biomedical Engineering, Science and Technology (IBEST) a partnership between Ryerson University and St. Mike's Hospital, Toronto, Ontario, Canada

Csanád Kalmár, Department of Hydrodynamic Systems, Budapest University of Technology and Economics, Budapest, Hungary

Kaouther Kerboua, Higher School of Industrial Technologies, Department of Engineering, Annaba, Algeria

Rana Kıdak, Cyprus International University, Nicosia, Turkey

Michael C. Kolios, Institute for Biomedical Engineering, Science and Technology (IBEST) a partnership between Ryerson University and St. Mike's Hospital, Toronto, Ontario, Canada

Olivier Louisnard, Centre RAPSODEE, IMT Mines-Albi, UMR CNRS 5302, Université de Toulouse, Albi CT, France

Amit V. Mahulkar, Department of Chemical Engineering, Institute of Chemical Technology, Mumbai, India

Djihane Mazouz, Higher School of Industrial Technologies, Department of Engineering, Annaba, Algeria

Nour Hane Merabet, Higher School of Industrial Technologies, Department of Engineering, Annaba, Algeria

Slimane Merouani, Laboratory of Environmental Process Engineering, Department of Chemical Engineering, Faculty of Process Engineering, University Salah Boubnider-Constantine 3, Algeria

Vijayanand Suryakant Moholkar, Department of Chemical Engineering, Indian Institute of Technology Guwahati, Guwahati, Assam, India

Gordienko P.S., Institute of Chemistry, Far Eastern Branch of Russian Academy of Sciences, Vladivostok, Russia

Máté Papp, Chemical Kinetics Laboratory, Institute of Chemistry, ELTE Eötvös Loránd University, Budapest, Hungary

Aniruddha B. Pandit, Department of Chemical Engineering, Institute of Chemical Technology, Mumbai, India

Bruno G. Pollet, Hydrogen Research Institute (HRI), Université du Québec à Trois-Rivières (UQTR), Trois-Rivières, Canada

Jazmín Porras, Grupo de Investigaciones Biomédicas Uniremington, Facultad de Ciencias de la Salud, Corporación Universitaria Remington (Uniremington), Medellín, Colombia

Ke-ming Quan, Procter & Gamble Company, West Chester, Ohio, United States

Kuldeep Roy, Department of Chemical Engineering, National Institute of Technology Trichy, Tiruchirapalli, India

Bulanova S.B., Institute of Chemistry, Far Eastern Branch of Russian Academy of Sciences, Vladivostok, Russia

Yarusova S.B., Institute of Chemistry, Far Eastern Branch of Russian Academy of Sciences, Vladivostok, Russia; Vladivostok State University of Economics and Service, Vladivostok, Russia

Efraím A. Serna-Galvis, Grupo de Investigaciones Biomédicas Uniremington, Facultad de Ciencias de la Salud, Corporación Universitaria Remington (Uniremington), Medellín, Colombia; Grupo de Investigación en Remediación Ambiental y Biocatálisis (GIRAB), Instituto de Química, Facultad de Ciencias Exactas y Naturales, Universidad de Antioquia UdeA, Medellín, Colombia

Mohit Singla, Department of Food Engineering and Technology, Tezpur University, Tezpur, Assam, India

Nandan Sit, Department of Food Engineering and Technology, Tezpur University, Tezpur, Assam, India

T. Sivasankar, Department of Chemical Engineering, National Institute of Technology Trichy, Tiruchirapalli, India

Vinayak S. Sutkar, Department of Chemical Engineering, Institute of Chemical Technology, Mumbai, India

Ricardo A. Torres-Palma, Grupo de Investigación en Remediación Ambiental y Biocatálisis (GIRAB), Instituto de Química, Facultad de Ciencias Exactas y Naturales, Universidad de Antioquia UdeA, Medellín, Colombia

Tamás Turányi, Chemical Kinetics Laboratory, Institute of Chemistry, ELTE Eötvös Loránd University, Budapest, Hungary

Zongsu Wei, Department of Biological and Chemical Engineering, Centre for Water Technology (WATEC), Aarhus University, Aarhus, Denmark

Xingaoyuan Xiong, Department of Biological and Chemical Engineering, Centre for Water Technology (WATEC), Aarhus University, Aarhus, Denmark

Sushkov Yu.V., Institute of Chemistry, Far Eastern Branch of Russian Academy of Sciences, Vladivostok, Russia

Yuning Zhang, Key Laboratory of Power Station Energy Transfer Conversion and System, Ministry of Education, North China Electric Power University, Beijing, China

Yuning Zhang, College of Mechanical and Transportation Engineering, China University of Petroleum-Beijing, Beijing, China; Beijing Key Laboratory of Process Fluid Filtration and Separation, China University of Petroleum-Beijing, Beijing, China

Xiaoxiao Zheng, Key Laboratory of Power Station Energy Transfer Conversion and System, Ministry of Education, North China Electric Power University, Beijing, China

István Gy. Zsély, Chemical Kinetics Laboratory, Institute of Chemistry, ELTE Eötvös Loránd University, Budapest, Hungary

Part I

The single acoustic cavitation bubble as an energetic system: qualitative and quantitative assessments

1. Single acoustic cavitation bubble and energy concentration concept 3
2. The energy forms and energy conversion 23
3. Physical effects and associated energy release 35
4. Sonochemical reactions, when, where and how: Modelling approach 49
5. Sonochemical reactions, when, where and how: Experimental approach 77

Chapter 1

Single acoustic cavitation bubble and energy concentration concept

Kaouther Kerboua, Djihane Mazouz and Imen Hasaounia
Higher School of Industrial Technologies, Department of Engineering, Annaba, Algeria

1.1 Introduction

In the last two decades, a great deal of interest has been focused on the phenomena that occur within the acoustic cavitation bubble created under the effect of ultrasonic waves. Acoustic cavitation, defined as the formation, growth, and collapse of microbubbles within a liquid medium, results from pressure oscillations that occur in the liquid medium irradiated by an acoustic field in the range of ultrasounds, with the appropriate acoustic conditions. The formed cavities drain and accumulate ultrasonic energy, and explosively release their energy at their collapse (Luo et al., 2015). The event of a collapsing bubble, illustrated in Fig. 1.1, is a microscopic implosion accompanied by a significant increase of temperature and pressure of up to thousands of Kelvin and hundreds of Bar (Leong et al., 2011).

As a first approximation, the dynamics of the bubble is a consequence of the competing inertial forces, that is, the cohesion resulting from the surface tension and the pressure of the oscillation applied to the liquid medium in which the cavitation bubbles appear. This results in a variation of several parameters in the bubble, which are described by numerous numerical models that estimate this variation, especially with respect to bubble volume, pressure and temperature (Kerboua & Hamdaoui, 2017).

The ultrasonic wave is emitted from ultrasonic generator, transducer, horn, and radiation rod to the liquid, causing medium molecules vibration. The average distance between molecules decreases in the acoustic compression phase, while increases in the rarefaction phase. In pure liquid, cavitation will occur when the liquid additional negative pressure reaches a critical value, whose magnitude is called cavitation threshold (Carrillo-Lopez et al., 2017).

Ultrasonic waves are acoustic pressure waves oscillating over a frequency range of 15 kHz–10 MHz. When ultrasonic waves pierce and pass through a liquid with sufficient amplitude, the vacuum exceeds the local tensile strength of the liquid and bubbles are created. Bubbles are typically generated near pre-existing impurities (e.g., cracks filled with gas dust particles) that oscillate and grow during compression and expansion cycles. As the bubbles reach an increasingly specific resonance size, they effectively absorb ultrasonic wave energy during a single compression-expansion cycle. The resonance size depends on the frequency of the irradiated ultrasound. At the resonance size, the bubbles grow rapidly during a single acoustic cycle due to the effective absorption of energetic waves. Since the bubbles cannot be sustained without energy absorption, they collapse implosively after reaching the resonance size. This process is called acoustic cavitation.

The bubble collapse produces hot spots, which have temperatures in the vicinity of 5000 K and pressures of 1000 atm, with an intense local heating rate and rapid cooling greater than 10^{10} K/s. Acoustic cavitation phenomenon has both chemical and physical effects which can be described from an energetic point of view as the release of the concentrated thermal energy into various forms of energies such as shockwaves with velocities as high as 4000 m/s and high-pressure amplitudes of 10^6 kPa (Kim & Suslick, 2018).

In the present chapter, the thermodynamics of bubble inception, growth and collapse is first presented in order to establish a rational for the existence of acoustic cavitation bubble from an energetic point of view. The dynamics of bubble oscillation is described according to the so called “thresholds," which refer to the minimum conditions, generally the minimum value of the acoustic pressure by the variation of the ambient radius, necessary to cause a cavitation (whether stable or transient), allow

Energy Aspects of Acoustic Cavitation and Sonochemistry: Fundamentals and Engineering. DOI: https://doi.org/10.1016/B978-0-323-91937-1.00020-7
Copyright © 2022 Elsevier Inc. All rights reserved.

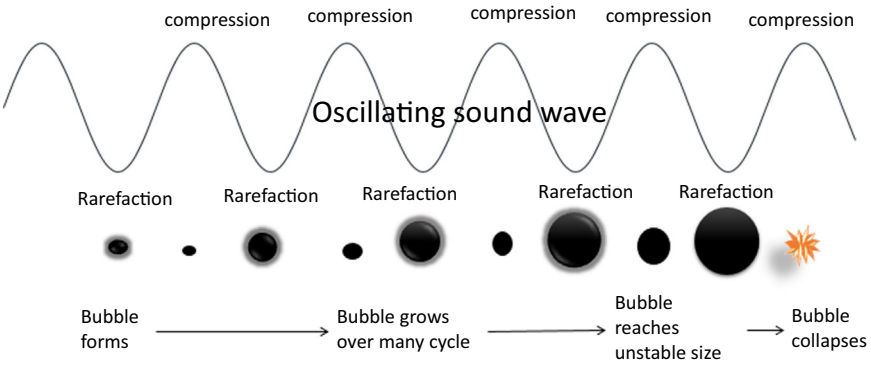

FIGURE 1.1 Graphical summary of the event of bubble formation, bubble growth and subsequent collapse over several acoustic cycles. A bubble oscillates in phase with the applied sound wave, contracting during compression and expanding during rarefactions. *Reproduced from (Leong et al., 2011).*

it to grow by rectified diffusion, and induce it into transient state. The energy balance is then elaborated at the single acoustic bubble scale according to different scenarios. The conversion of the acoustic energy is then discussed at the bubble cloud level, considering the different forms of energies associated with the oscillation and the collapse of acoustic bubbles. Next, the "hot spot" model is then explained and the variations of temperature and pressure during both phases of expansion and collapse are modelled accordingly. The accumulated thermal energy by the end of the collapse phase is modelled to introduce the energy concentration concept. This concept is discussed qualitatively, in terms of the volume energy accumulation and its conversion into various forms of energies associated with the chemical and physical effects at the collapse. It is also discussed quantitatively, particularly by focusing on the acoustic energy radiation from the acoustic cavitation bubbles at collapse.

1.2 Single acoustic cavitation bubble: Thermodynamic aspects of inception and growth, and dynamics of bubble oscillation

1.2.1 Bubble inception, growth and dynamics of oscillation

Typically, weaknesses in liquid medium occur in two forms. (1) Homogeneous nucleation, induced by the thermal motions within the liquid, which form temporary microscopic voids that constitute nuclei, and (2) heterogeneous nucleation that explains the major weaknesses occurring in liquid medium, and manifesting at the boundary between two different phases, such as the liquid and a solid phase or the liquid and small particles suspended in the liquid (Jena, 1965).

1.2.1.1 Homogeneous nucleation theory

In the case of pure liquid, the relation between the exterior pressure P exerted on the bubble wall of radius R and the interior pressure P_B is given in Eq. 1.1 (Brennen, 1995).

$$P_B - P = 2\sigma/R \tag{1.1}$$

With the condition of temperature uniformity, and if the bubble contains only vapor, the interior pressure will equal the saturated vapor pressure P_v (T). Nonetheless, the exterior liquid pressure given by Eq. 1.2 must be less than the vapor pressure so that the equilibrium condition is verified.

$$P = P_v - 2\sigma/R \tag{1.2}$$

Thus, if the exterior liquid pressure is decreased below $P_v - 2\sigma/R$, the radius of the bubble will increase, and the excess pressure will arise leading to rupture. Accordingly, if the maximum size of the vacancy is R_c, then the tensile strength of the liquid is expressed as shown in Eq. 1.3.

$$\Delta P_c = 2\sigma/R_c \tag{1.3}$$

The second expression that makes up the homogeneous nucleation theory is related to the excess of energy that must be deposited in the body of pure liquid in order to create a nucleus or microbubble of critical size R_c. Assuming that the critical nucleus is in thermal equilibrium with its surroundings after its creation, then the increased energy that must be brought to

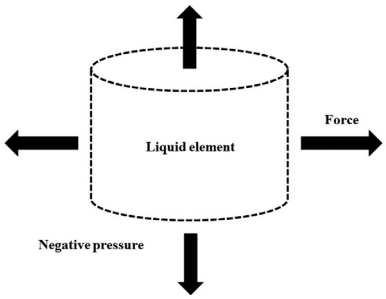

FIGURE 1.2 Negative pressure. Reproduced from Yasui (2017).

the medium consists of two parts. Firstly, the required energy to maintain the surface of the bubble $4\pi\ R_c^2\,\sigma$. Secondly, the work of pressure forces exerted by the fluid to create the bubble $\frac{-4\pi R_c^3 \Delta P_c}{3}$. Thus, the net energy W_{CR} that must be deposited to form a bubble (C. Brennen, 1995) is given in Eq. 1.4.

$$W_{CR} = 4\pi\ R_C^2\sigma - \frac{4}{3}\pi\ R_C^3 \Delta P_C \tag{1.4}$$

In the case of pure liquid, cavities are formed when adequately large negative pressure is applied to the liquid so that the average distance between the molecules exceeds the critical molecular distance required to hold the liquid intact. However, considering a surface tension of 0.05 $\frac{kg}{s^2}$, and an R_c comparable to the inter-molecular distance estimated at 10^{-10} m, the resulting ΔP_c will be in the order of 10,000 bar according to Eq. 1.3, and hence, an enormous energy would be required according to Eq. 1.4.

In the case of acoustic cavitation, the presence of gaseous impurities considerably decreases the necessary energy for bubble's formation since the tensile strength is dramatically reduced, lowering consequently the required negative pressure. This has been proved by experiments on tensile strength. These experiments demonstrated that the tensile strength is a function of the contamination of the liquid and the nature of the surface in contact (Brennen, 1995).

Summing up, ultrasonic waves passing through a pure liquid can hardly, if at all, give rise to cavitating bonds in homogenous conditions. Acoustic cavitation then belongs to the second category of nucleation, namely heterogeneous cavitation. This occurs if dissolved substances, gaseous germs or impurities are present in the liquid volume. In practice, this is always the case. The ultrasonic cavitation that forms is due to the existence of dissolved gases that decrease the cohesion of the liquid or, in other words, reduce the surface tension.

1.2.1.2 Heterogeneous nucleation theory

Heterogenous nucleation occurs in a heterogenous phase, for instance at a solid-liquid interface. It is important to note that, at the microscopic level, the surfaces of solids are not flat, so we must consider the implications of other local surface geometries (Brennen, 1995). Some specific sites on a solid surface will have the optimal geometry to enhance the growth and the macroscopic appearance of vapor bubbles. These sites are called the nucleation sites. Moreover, it is clear that the lower the pressure, the sites become able to generate and release bubbles in the body of the liquid (C. Brennen, 1995).

During the rarefaction phase of the acoustic wave travelling across the liquid, instantaneous local pressures in liquid become negative when the acoustic pressure amplitude is larger than the ambient pressure, that is, 1 atm. Negative pressure is possible only in liquids or solids, and impossible in gases. This is the "force" to expand a liquid element as shown in Fig. 1.2. Consequently, gases dissolved in the liquid appear as gas bubbles because gases can no longer be dissolved in the liquid under negative pressures (Yasui, 1997). During the negative pressure cycle, the liquid is pulled apart at sites containing such gaseous impurities, which are known as "weak spots" in the fluid (Leong et al., 2011).

1.2.1.3 Thermodynamics of formation of a gaseous nucleus

Moholkar et al. (2000) measured the spatial distribution of the acoustic cavitation intensity with partially degassed demineralized water (less than 2 ppm concentration) sonicated in an ultrasound bath at 35 kHz and 110 kPa. They demonstrated using numerical simulations a proportional relationship between the measured cavitation intensity and the calculated spatial variation of the amplitude of shock wave emitted by gas bubbles. This proved that the lower the gas concentration in the sonicated liquid, the less important the cavitation phenomenon, which evidenced the heterogeneous pathway for the nucleation of acoustic cavitation bubbles.

From a thermodynamic point of view, let's consider a gas–liquid system in which two phases are separated by a plane surface. The saturation concentration x, expressed in mole fraction, of the dissolved gas at the gas pressure P_g is given by the Henry's law using the Henry's law constant H [17] as indicated in Eq. (1.5) (Zijlstra, 2011).

$$x = \frac{P_g}{H} \tag{1.5}$$

With the propagation of the acoustic wave characterized by a frequency f and a pressure amplitude P_A, and an initial liquid pressure P_{I0}, the instantaneous local pressure $P_I(t)$ in the liquid bulk changes as a sinusoidal function of time t, and is as follows:

$$P_I(t) = P_{I0} - P_A \cdot \sin(2\pi f t) \tag{1.6}$$

When the local liquid pressure falls below the vapor pressure P_{vap}^T, the liquid molecules transform into gas through a boiling mechanism and the saturation solubility of the gas becomes null. Thus the saturation solubility of the gas x_l is expressed in function of the instantaneous pressure of the liquid when it varies between P_{I0} and P_{vap}^T as:

$$x_I = \frac{x}{P_{I0} - P_{vap}^T}\left(P_I\ (t) - P_{vap}^T\right) \tag{1.7}$$

When the gas is dissolved in the liquid with a solubility c, below the saturation, expressed in mole fraction as:

$$c = z \times x_I = \frac{z \times x}{P_{I0} - P_{vap}^T}\left(P_I(t) - P_{vap}^T\right) \tag{1.8}$$

According to this equation, during the rarefaction phase, the decrease in the local liquid pressure $P_I\ (t)$ induces a linear decrease in solubility of the gas.

The required local pressure at which the solubility c would equal the saturation solubility x, or in other words, the liquid would become saturated in gas, is given as:

$$P_I(t) = z \times P_{I0} + P_{vap}^T(1 - z) \tag{1.9}$$

This liquid pressure is attained at the instant:

$$t_A = \frac{\sin^{-1}\left(\frac{P_{I0} - \left(z \times P_{I0} + P_{vap}^T(1-z)\right)}{P_A}\right)}{2\pi f} \tag{1.10}$$

After the instant t_A, the dissolved gas would start desorbing, which creates a spatial unbalance in the gas concentration. The created gradient in the gas concentration within the liquid will induce a diffusion of the gas molecules toward the desorbed gas phase, that is, the nucleus. Through this process, the gas phase would grow in the liquid, forming the acoustic cavitation bubble.

It is also worthy to note that if the average pressure is below the vapor pressure, then the average saturation concentration of the gas is taken as zero, meaning that the gas cannot be dissolved any longer in the liquid during the corresponding time slot, starting at t_A and ending at t_C, which is the instant corresponding to the minimum pressure applied on the liquid phase, it is given as:

$$t_C = \frac{1}{4f} \tag{1.11}$$

The characteristic length l in the liquid medium through which the desorption will take place is expressed as

$$l = \sqrt{D(t_C - t_A)} \tag{1.12}$$

With D being the diffusivity of the dissolved gas.

The total number of gas molecules n_g desorbed from a hypothetical sphere of radius l during the time interval between t_A and t_C in the given time interval of the rarefaction region can be calculated as follows:

$$n_g = x\left(z - \frac{P^{t_A - t_c} - P_{vap}}{P_{I0} - P_{vap}}\right)\frac{4}{3}\pi\ l^3 \times \rho_L \times N_A \tag{1.13}$$

Where N_A is the Avogadro's number and $P^{t_A-t_c}$ is the average liquid pressure between the instants t_A and t_C expressed as:

$$P^{t_A-t_c} = \frac{\int_{t_A}^{t_c} (P_{I0} - P_A.\sin(2\pi f t))dt}{t_C - t_A} = \frac{P_{I0}2\pi f(t_C - t_A) + P_A(\cos(2\pi f t_c) - \cos(2\pi f t_A))}{2\pi f(t_C - t_A)} \tag{1.14}$$

The gaseous nucleus radius corresponding to P_{vap} is expressed as:

$$R_g = \sqrt[3]{\frac{3nRT}{4\pi P_{vap}}} \tag{1.15}$$

1.2.1.4 Thermodynamics of coalescence

The thermodynamics of the bubbles' coalescence, identified as one of the pathways of the growth of acoustic cavitation bubbles, relies on the diminution of the surface tension force, and the hydrodynamics of the rupture of thin liquid films at the gas-liquid interfaces. In fact, two or more gaseous nuclei may undergo a coalescence process, considering the effect of surface tension (Lee et al., 2005a). In order to reduce the surface tension force, two or more nuclei separated by a single layer of water molecules would merge and result in one nucleus. Lee et al. (Lee et al., 2005a) proved using a capillary system that the undissolved gas volume within a sonicated liquid tends to increase with the augmentation of the concentration of the dissolved gas in liquid. Pandit and Davidson (Pandit & Davidson, 1990) studied the hydrodynamics of the rupture of thin liquid films and demonstrated that below the critical film thickness of 0.07 μm, the liquid film undergoes a natural rupture without any external puncturing force. Accordingly, it is very likely that such two or more nuclei formed in adjacent spherical volumes may coalesce spontaneously to produce relatively larger stable nucleus that grow to form acoustic cavitation bubbles.

1.2.2 Thresholds

The "cavitation threshold" term has been employed in a various way to describe the minimum conditions, usually the minimum acoustic pressure, required to induce cavitation either stable or transient cavity. Below this limit, the acoustic cavitation bubble is not susceptible to form, and the excitation field is judged insufficient to bring about any significant growth of the so called "bubble".

It is worthy to mention that the threshold for a specific type of cavitation is not usually a measure of a pure liquid property, but most likely a measure of the impurities (including undissolved ones) that exist in the liquid, and the liquid's history (i.e., the method of preparing the liquid) (Apfel, 1981). This is numerically translated into an initial bubble radius describing the size of the bubble formed around in the liquid impurities at mechanical equilibrium. The oscillation of the bubble starts theoretically from this size, also known as "ambient size".

1.2.2.1 Blake nucleation threshold

By supposing that the gas bubbles are slowly dissolving in the liquid, we can consider which minimal value of the acoustic pressure P_A is responsible for the growth of a gas-filled bubble of radius R_B. Following Blake (1988) and Neppiras and Noltingk, it becomes clear that if the bubble is in mechanical equilibrium, then the pressure inside it P_i needs to be equal to $P_0 + {}^{2\sigma}/_{R_B}$.

If the size of the bubble changes afterward as a result of a diminution of the absolute external pressure (applying a sound field), the condition of mechanical equilibrium is given by:

$$\left(P_0 + {}^{2\sigma}/_{R_B}\right)\left({}^{R_B}/_{R}\right)^3 = P_0 - P_A + {}^{2\sigma}/_{R} \tag{1.16}$$

The left term is the pressure of the gas in the bubble related to an isothermal expansion. The right term, P_A, represents the maximum negative value of the acoustic pressure. To find the minimum value of $P_A - P_0$ for the growth, we assume that

$$\frac{\partial\,(P_0 - P_A)}{\partial R} = 0 \tag{1.17}$$

This results in

$$P_A - P_0 = {}^{4\sigma}/_{3R^*} \tag{1.18}$$

Where

$$R^* = \left[3\left(P_0 + {}^{2\sigma}/_{R_B}\right){}^{R_B^3}/_{2\sigma}\right]^{1/2} \tag{1.19}$$

By resolving P_A as a function of the bubble's initial size, we come up with the P_B Blake threshold pressure for a bubble of radius R_B (Apfel, 1981).

$$\frac{P_B}{P_0} = 1 + \frac{4}{9}X_B \frac{3X_B}{4(1+X_B)}^{1/2} \tag{1.20}$$

Where

$$X_B = \frac{2\sigma}{P_0 R_B} \tag{1.21}$$

1.2.2.2 Rectified diffusion threshold

The "rectification of mass" toward the growing acoustic cavitation bubble is a direct consequence of the applied acoustic field (Lee et al., 2005b). This process becomes significant whenever a sufficiently intense ultrasound field exists in a liquid containing dissolved gas (Crum, 1984). The concept of rectified diffusion consists in the slow growth of a pulsating gas bubble due to an average flow of mass into the bubble as a function of time.

Because the bubbles are unstable mechanically in the liquid, they will slowly change equilibrium size at a rate defined by the diffusion of gas through the interface. However, this diffusion is being accelerated by the existence of the sound field. In a process, which was first discussed by Harvey and later reviewed and referred to as "rectified diffusion" by Blake, in the negative part of the acoustic cycle, there is more gas that diffuses into the bubble than exits it in the positive part, as a result of the slightly larger surface area during the half-cycle of expanded size. This means that the gas is being "pumped" into the bubble acoustically. Safar gave a general result for the rectified scattering acoustic pressure threshold P_D, for a bubble of radius R_D and relative gas saturation C, as shown in Eq. 1.22.

$$\frac{P_D}{P_0} = \frac{[3_k\,(1+X_D) - X_D]\left[1 - \left({}^{f}/_{f_D}\right)^2\right]}{[6(1+X_D)]^{1/2}[1 - C + X_D]^{-1/2}} \tag{1.22}$$

Where

$$X_D = \frac{2\sigma}{P_0 R_D} \tag{1.23}$$

There is an uncertainty in the rectified diffusion threshold prediction regarding the adiabatic or isothermal behavior of the bubble (Apfel, 1981).

1.2.2.3 Transient cavitation threshold

A transient cavitation threshold $P_T = P_A$ could be well defined by $R_M = 2.3\,R_0$ the condition that guarantees that a bubble will attain just a supersonic collapse velocity in water.

The transient threshold P_T, inversely proportional to the radius of the threshold bubble, R_T as a function of P, as indicated in Eq. 1.24.

$$R_T = \left\{ \begin{array}{c} \dfrac{0.13}{f}\left(\dfrac{P_0}{\rho}\right)^{1/2}\left[\dfrac{p-1}{\sqrt{p}}\left[1 + \dfrac{2}{3}(p-1)\right]^{1/3}\right];\ p \le 11 \\ \dfrac{0.3}{f}\left(\dfrac{P_0}{\rho}\right)^{1/2}\left(\dfrac{2}{3}(p-1)\right)^{1/2};\ p \ge 11 \end{array} \right\} \tag{1.24}$$

Where $p = \frac{P_T}{P_0}$.

The physical meaning of the transient cavitation threshold may correspond to the conditions of surface instability and consequently of bubble rupture in low viscosity fluids.

Eq. 1.24 proposes that even if each individual bubble will be only transient, by the previous definition, the larger one will store much more energy in the expanded bubble and give back much more energy in the kinetic energy of the collapse.

As such, the "violence" of a transient event is most appropriately related to the maximum size reached by the bubble, corresponding to the energy stored in the liquid. Under the previous assumptions, this maximum size is independent of the initial size and depends only on the acoustic pressure and the frequency. Thus, for a given frequency, a given degree of violence will occur for a given acoustic pressure (Apfel, 1981).

1.2.3 Dynamics of bubble oscillation

The dynamics of a single acoustic cavitation bubble immersed in a sonicated liquid can be described by the Navier-Stokes equations applied to the gas inside the bubble, initially at rest, and to the incompressible liquid adjacent to the bubble wall. The Navier-Stokes equations can be solved analytically in spherical coordinates or numerically using a radial formulation (Patel et al., 2019). The effect of the compressibility of the liquid is accounted for in the bubble dynamics equation through the continuity equation Eq. 1.25, expressing the conservation of the mass, and the Euler equation Eq. 1.26, or the equation of motion, expressing the conservation of the momentum.

$$\frac{\partial \rho}{\partial t} + \nabla \cdot \left(\rho \vec{u}\right) = \frac{\partial \rho}{\partial t} + \vec{u} \cdot \nabla \rho + \rho \nabla \cdot \vec{u} = 0 \tag{1.25}$$

$$\rho \frac{D\vec{u}}{Dt} = \rho \left(\frac{\partial \vec{u}}{\partial t} + \left(\vec{u}.\nabla\right)\vec{u} \right) = -\nabla p \tag{1.26}$$

Where $\nabla = \left(\frac{\partial}{\partial x}, \frac{\partial}{\partial y}, \frac{\partial}{\partial z}\right)$ and $\nabla \cdot \left(\rho \vec{u}\right) = \frac{\partial}{\partial x}\left(\rho u_x\right) + \frac{\partial}{\partial y}\left(\rho u_y\right) + \frac{\partial}{\partial z}\left(\rho u_z\right)$, ρ is the instantaneous local density of liquid, $\vec{u}$ is the instantaneous local velocity of liquid $\vec{u} = \left(u_x, u_y, u_z\right)$, and $\nabla \rho = \left(\frac{\partial \rho}{\partial x}, \frac{\partial \rho}{\partial y}, \frac{\partial \rho}{\partial z}\right)$.

$\frac{D}{Dt}$ is the material time derivative, $\left(\frac{D}{Dt} = \frac{\partial}{\partial t} + \vec{u}.\nabla\right)$, with $\vec{u} \cdot \nabla = u_x \frac{\partial}{\partial x} + u_y \frac{\partial}{\partial y} + u_z \frac{\partial}{\partial z}$, and p in Eq. 1.26 is the instantaneous local pressure of the liquid. The effects of gravitational force and liquid viscosity are neglected.

Here, it is assumed that the velocity field of the liquid around a pulsating bubble has only a radial component. In this case, the liquid flow is irrotational, and the velocity field is expressed by using a velocity potential ϕ.

$$\vec{u} = \nabla \phi = \frac{\partial \phi}{\partial r} \overrightarrow{e_r} \tag{1.27}$$

where r is the radial distance from the center of a bubble, and $\vec{e_r}$ is a radial unit vector. Then, Eq. 1.26 and Eq. 1.27 are respectively expressed by Eq. 1.28 and 1.29.

$$\frac{\partial \rho}{\partial t} + \left(\frac{\partial \phi}{\partial r}\right)\left(\frac{\partial \rho}{\partial r}\right) + \rho \Delta \phi = 0 \tag{1.28}$$

$$\rho \left[\frac{\partial^2 \phi}{\partial t \partial r} + \left(\frac{\partial \phi}{\partial r}\right)\left(\frac{\partial^2 \phi}{\partial^2 r^2}\right) \right] = -\frac{\partial \rho}{\partial r} \tag{1.29}$$

From Eqs 1.28 and Eqs 1.29 the following modified wave equation is derived.

$$\Delta \phi - \frac{1}{c^2}\frac{\partial^2 \phi}{\partial t^2} = \frac{1}{c^2}\left(\frac{\partial \phi}{\partial r}\right)\left(\frac{\partial^2 \phi}{\partial t \partial r}\right) - \frac{1}{\rho}\left(\frac{\partial \rho}{\partial r}\right)\left(\frac{\partial \phi}{\partial r}\right) \tag{1.30}$$

where c represents the instantaneous local sound velocity. In the derivation of the Keller equation of bubble dynamics, the right-hand side of Eq. 1.30 is ignored and Eq. 1.31 may be used. Thus, the Keller equation is an equation, that is, approximate and only valid when:

$$\frac{\left|\dot{R}\right|}{c_\infty} \ll 1$$

where e_∞ is the sound velocity at ambient condition.

$$\Delta \phi - \frac{1}{c_\infty^2}\frac{\partial^2 \phi}{\partial t^2} = 0 \tag{1.31}$$

By integrating Eq. 1.31 with respect to r, the following approximate equation may be derived:

$$\frac{\partial \phi}{\partial t} + \frac{1}{2}u^2 + \frac{p - p_\infty}{\rho_{L,\infty}} = 0 \tag{1.32}$$

Where p_∞ is the ambient pressure, and the density of the liquid is considered to be constant at ambient conditions $\rho = \rho_{L,\infty} = const$. The condition at the boundaries is shown as below:

$$\left(\frac{\partial \phi}{\partial r}\right)_{r=R} = \dot{R} \tag{1.33}$$

The general solution of the wave Eq. 1.31 under spherical symmetry is given as follows.

$$\phi = -\frac{f\left(t - \frac{r}{c_\infty}\right)}{r} - \frac{g\left(t + \frac{r}{c_\infty}\right)}{r} \tag{1.34}$$

where f and g are arbitrary functions. From Eqs.1.33 and 1.34., Eq. 1.35 is obtained.

$$\frac{f'}{R} = c_\infty \left[\dot{R} + \frac{\phi(R)}{R}\right] + \frac{g'}{R} \tag{1.35}$$

where $'$ means derivative. From Eqs.1.34 and 1.35, Eq. 1.36 is obtained.

$$\left(\frac{\partial \phi}{\partial t}\right)_{r=R} = -c_\infty \left[\dot{R} + \frac{\phi(R)}{R}\right] - \frac{2g'}{R} \tag{1.36}$$

Inserting Eq. 1.33 and Eq. 1.34 into Eq. 1.32 yields in Eq. 1.37.

$$-c_\infty \left[\dot{R} + \frac{\phi(R)}{R}\right] - \frac{2g'}{R} + \frac{1}{2}\dot{R}^2 + \frac{p_B - p_\infty}{\rho_{L,\infty}} = 0 \tag{1.37}$$

where p_B is the liquid pressure at the bubble. Thus, multiplying Eq. 1.23 by R and differentiating by t yields in Eq. 1.38.

$$0 = -c_\infty \left[\dot{R}^2 + +R\ddot{R} + \left(\frac{\partial \phi}{\partial t}\right)_{r=R}\right] - 2\frac{dg'}{dt} + \frac{1}{2}\dot{R}^3 + R\dot{R}\ddot{R} + \frac{R}{\rho_{L,\infty}}\frac{dp_B}{dt} + \frac{1}{\rho_{L,\infty}}\dot{R}(p_B - p_\infty) \tag{1.38}$$

where $''$ means the second derivative. From Eqs.1.33 and 1.34, Eq. 1.39 is obtained.

$$\left(\frac{\partial \phi}{\partial t}\right)_{r=R} = \frac{\partial \phi}{\partial t} + \frac{\partial \phi}{\partial r}\frac{dr}{dt} = -\frac{1}{2}\dot{R}^2 - \frac{p_B - p_\infty}{\rho_{L,\infty}} + \dot{R}^2 \tag{1.39}$$

When the incident field is a plane acoustic wave having an angular frequency ω and a pressure amplitude P_A, the undermentioned relationship applies.

$$2\, g'' = -\frac{c_\infty}{\rho_{L,\infty}} P_A \sin \omega t \tag{1.40}$$

Inserting Eq. 1.40 and Eq. 1.39 into Eq. 1.38 yields the equation of bubble dynamics called the Keller-Miksis equation and shown in Eq. 1.41.

$$\left(1 - \frac{\dot{R}}{c_\infty}\right)R\ddot{R} + \frac{3}{2}\dot{R}^2\left(1 - \frac{\dot{R}}{3c_\infty}\right) = \frac{1}{\rho_{L,\infty}}\left(1 + \frac{\dot{R}}{c_\infty}\right)[p_B - p_s(t) - p_\infty] + \frac{R}{c_\infty \rho_{L,\infty}}\frac{dp_B}{dt} \tag{1.41}$$

where $P_A \sin \omega t$ is replaced by $p_s(t)$.

1.3 The hot spot theory

When ultrasounds propagate through a liquid medium via a series of compressions and rarefactions, at sufficiently high power, the rarefaction cycle may exceed the attractive forces of the molecules of the liquid, and cavitation bubbles will consequently form (Oladokun et al., 2019; Suslick et al., 1986). The collapse of the formed cavitation during compression cycles generates high-energy 'hot spots' throughout the system (Mason & Cintas, 2002). This energy can for instance enhance chemical reactivity in a liquid medium. chemical and mechanical effects. The "hot sport" theory refers to intense local heating and high pressures, with very short lifetimes. The high local temperature may exceed 5000 K, and the corresponding pressure exceeds the order of 1000 bar created within the bubble volume at collapse.

In addition to the chemical effects of ultrasound, light is often emitted (Lee et al., 2006; Yasui, 1999), this phenomenon is known as "sonoluminescence". The hot spot conditions can be indirectly revealed by the intensity of the light emitted at collapse. The sonoluminescence provides indeed an extremely useful spectroscopic probe of the cavitation bubble conditions during the collapse.

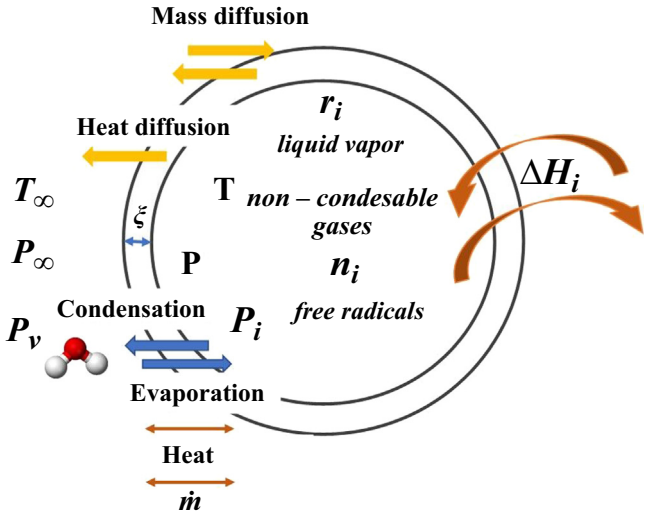

FIGURE 1.3 Schematic view of mass and heat flow around a single acoustic cavitation bubble (Kerboua et al., 2021; Royer et al., 2017).

The formed hot spots in bubble clouds have extreme pressures and temperatures, but also rapid heating and cooling rates above 10^{10} K/s. In single bubble cavitation, conditions may be even more extreme (Bhangu & Ashokkumar, 2016; Grieser et al., 2015; Suslick, 2003). Thus, cavitation can create extraordinary physical and chemical conditions in otherwise cold liquids (Suslick et al., 1999).

The hot spot is explained by the volume concentration of acoustic energy in form of thermal energy, that is, heat. Actually, the oscillating acoustic cavitation bubble serves as an effective means of concentrating the diffuse energy of sound into a microscopic volume. The compression of the gas inside the bubble volume generates heat. When the compression of bubbles occurs, heating is more rapid than thermal transport (almost by diffusion), which creates a short-lived, localized hot spot.

One of the earliest mathematical models is that of Rayleigh for the collapse of acoustic cavitation bubbles in incompressible liquids, this model predicted enormous local temperatures and pressures (Fuster et al., 2011). Richards and Loomis were the first to report the observable chemical effects of ultrasound (Loomis, 1927). Nowadays, more complex models based on the hot spot theory have been developed. These models rely on the thermodynamics of acoustic cavitation bubbles and the chemical mechanisms related to the sonochemistry within and around the bubbles.

Alternatively, some mechanisms involving electrical microdischarge have been proposed (Lepoint & Mullie, 1994), and have been referred to as the "electrical microdischarge theory." However, this theory, developed in the late thirties, was gradually substituted by the hot spot theory after a bank of knowledge had been accumulated about the behavior of cavitation bubbles in sonic fields, and proved that it lacks several arguments and remains weak as compared to the hot spot theory.

Hence, there is a nearly universal consensus that the hot spot is the source of homogeneous sonochemistry and sonoluminescence, which holds that the acoustic energy given the bubble as it expands to its maximum size is concentrated into a heated gas core during the bubble's implosion, that is, converted into a huge amount of thermal energy within a microscopic volume.

Probing the conditions present in the cavitation hot spot has proved to be a difficult problem in practice. Although some protocols are proposed to assess them indirectly, such as the tracking of competing unimolecular chemical reactions with known temperature dependency (Suslick et al., 1986) or the measurement of light emission, that is, sonoluminescence. The transient nature of cavitation, especially in bubble clouds, precludes any conventional measurement of the temperature and pressure conditions generated during bubble collapse. Numerical modeling, however, suggests several methodologies to describe the hot spot conditions and kinetics, this will be detailed in Section 1.4.

1.4 Thermodynamics of acoustic cavitation bubble and energy balance

The energy balance in a bubble evolving under an ultrasonic field irradiating a liquid can be described by several modeling approaches. The first law of thermodynamics applied to the bubble as a thermodynamic system, illustrated in Fig. 1.3, gives:

$$\frac{dU}{dt} = \frac{\partial W}{\partial t} + \frac{\partial Q}{\partial t} \tag{1.42}$$

According to the adopted approach, the variation of the internal energy, and hence the variation of the temperature of the gas phase within the bubble volume is determined.

1.4.1 Polytropic model

The polytropic model assuming a polytropic transformation during the bubble oscillation is usually adopted with different gas models (Ideal gas, VDW, SRK, and PR).

As a first approach, the expansion phase of the bubble is considered isothermal, while during the collapse phase, the thermal process is considered adiabatic (Colussi et al., 1998). The heat absorption and release due to the endothermal and exothermal reactions within the bubble and the variation of the molar amounts of the chemical species inside the bubble are neglected. This results in the following expression of the time variation of the internal energy:

$$\frac{\mathrm{dU}}{\mathrm{dt}} = \frac{\mathrm{d}}{\mathrm{dt}}\left(\sum_{\mathrm{i}} \mathrm{u_i n_i}\right) = \sum_{\mathrm{i}} \mathrm{n_i}\frac{\mathrm{du_i}}{\mathrm{dt}} = \sum_{\mathrm{i}} \mathrm{n_i c_{vi}}\frac{\mathrm{dT}}{\mathrm{dt}} \tag{1.43}$$

With $\mathrm{h_i}$ the molar enthalpy of the $\mathrm{i^{th}}$ species, $\mathrm{n_i}$ the molar yield of the ith species, and $\mathrm{P_i}$ its partial pressure.

Hence, the first law of thermodynamics is expressed during the collapse as:

$$\sum_{\mathrm{i}} \mathrm{n_i c_{vi}}\frac{\mathrm{dT}}{\mathrm{dt}} = -PdV \tag{1.44}$$

The differential equation giving the variation of the temperature during the collapse takes the following form when using the ideal gas law:

$$\frac{dT}{dt} = \frac{-1.2\mathrm{T_\infty R_{max}}^{1.2}\,\dot{\mathrm{R}}}{R^{2.2}} \tag{1.45}$$

while it is expressed by Eq. 1.46 when using the Van der Waals equation.

$$\frac{dT}{dt} = -(\gamma - 1)\,T_0\,(V_0 - n_0 b)^{\gamma-1}\,(V - nb)^{-\gamma}\,4\pi\,\dot{R}\,R^2 \tag{1.46}$$

where b is the Van der Waals constant corresponding to the measure of the volume excluded by a mole of particles.

1.4.2 Energetics of sonochemistry

In this second approach, an energy balance is applied to the single acoustic cavitation bubble as a closed thermodynamic system with a spherical geometry and a variable volume, housing a chemical mechanism which evolves around the strong collapse. The thermal intakes of the exothermal and endothermal elementary reactions are then considered in the variation of the internal energy of the bubble, and consequently its temperature and pressure. With this approach, the time variation of the internal energy would be (Kerboua & Hamdaoui, 2018):

$$\frac{\mathrm{dU}}{\mathrm{dt}} = \frac{\mathrm{d}}{\mathrm{dt}}\left(\sum_{\mathrm{i}} \mathrm{u_i n_i}\right) = \sum_{\mathrm{i}} \mathrm{n_i}\frac{\mathrm{du_i}}{\mathrm{dt}} + \sum_{\mathrm{i}} \mathrm{u_i}\frac{\mathrm{dn_i}}{\mathrm{dt}} = \sum_{\mathrm{i}} \mathrm{n_i c_{vi}}\frac{\mathrm{dT}}{\mathrm{dt}} + \sum_{\mathrm{i}} \mathrm{h_i}\frac{\mathrm{dn_i}}{\mathrm{dt}} - \frac{\mathrm{PV}}{\mathrm{n}}\sum_{\mathrm{i}} \mathrm{n_i}\frac{\mathrm{dn_i}}{\mathrm{dt}} \tag{1.47}$$

Neglecting the term $\frac{\mathrm{PV}}{\mathrm{n}}\sum_{\mathrm{i}} \mathrm{n_i}\frac{\mathrm{dn_i}}{\mathrm{dt}}$ as compared to $\sum_{\mathrm{i}} \mathrm{h_i}\frac{\mathrm{dn_i}}{\mathrm{dt}}$, the energy balanced expressed by the first law of thermodynamics becomes:

$$\mathrm{n\,C_V}\frac{\mathrm{dT}}{\mathrm{dt}} = -\mathrm{P_g}\,\frac{\mathrm{dV}}{\mathrm{dt}} - \sum_{\mathrm{i=1}}^{\mathrm{n}} \Delta\mathrm{H_i}\;\mathrm{r_i V} \tag{1.48}$$

1.4.3 Mass diffusion

With the inclusion of mass transfer across the bubble interface by a diffusive process, the single bubble becomes an opened thermodynamic system. The principle of energy conservation within this system is governed by the first law of thermodynamics, accounting for the mass variation induced by the mass diffusion, as well as the heat exchange due to the gain and loss of mass toward and from the bulk volume of the bubble. The mass diffusion is described by the Fick's law which

expresses the surface flow J_i of the i^{th} species travelling across the bubble interface according to the linear relationship:

$$J_i = -D_{ij}\nabla c_j \tag{1.49}$$

Let's consider the positive flow in the entering direction to the bulk volume of the bubble, there exists a mass diffusion layer of width δ through which the gas molecules are transferred. Fick's law is written considering a radial distribution:

$$\frac{dn_i}{dt} = -D_{Li} \times 4\pi R^2 \times \frac{C_i(\delta) - C_i(0)}{\delta} \tag{1.50}$$

C_i (0) constitutes the concentration of the i^{th} gaseous species at the liquid side of the bubble interface, C_i (δ) its concentration inside the bubble volume, and D_{Li} the binary diffusion coefficient of the i^{th} species in the liquid, calculated using the below correlation (Poling et al., 2004).

$$D_{ji} = \frac{0,00143\, T^{1.75}}{P\left[M_i^{-1} + M_j^{-1}\right]^{-1/2}\left[\left(\sum_v\right)_i^{1/3} + \left(\sum_v\right)_j^{1/3}\right]^2} \tag{1.51}$$

M_i and M_j being the molecular masses of both species (here, the liquid and the gas i), while v represents the diffusion volume related to the molecule. The width of the mass diffusion layer is defined by Tögel (Tögel, 2002) as:

$$\delta = \min\left(\sqrt{D_{H_2O\,O_2}\frac{R}{|\dot{R}|}},\ \frac{R}{\pi}\right)$$

Consequently, the energy balance applied to the bubble becomes:

$$n\,C_V\frac{dT}{dt} = -P_g\frac{dV}{dt} - \sum_i u_i\frac{dn_i}{dt} \tag{1.52}$$

Furthermore, if the chemical mechanism is considered, the previous equation becomes:

$$n\,C_V\frac{dT}{dt} = -P_g\frac{dV}{dt} - \sum_{i=1}^{n}\Delta H_i\, r_i V - \sum_i u_i\frac{dn_i}{dt} \tag{1.53}$$

In both Eqs.1.52 And 1.53, $\frac{dn_i}{dt}$ represents the molar flow of species undergoing the mass diffusion process.

1.4.4 Nonequilibrium of evaporation and condensation

The gaseous phase inside the bubble volume is composed of noncondensable gases, initially dissolved in the liquid, and liquid vapor. The liquid vapor is subjected to a nonequilibrium process of evaporation and condensation at the bubble interface, due to the partial pressure gradient at both sides of the interface. The existence of the nonequilibrium of evaporation and condensation would affect the boundary condition applied to the velocity potential of the bubble wall φ. It is expressed as:

$$\frac{d\varphi}{dr} = \dot{R} - \frac{\dot{m}}{\rho_L} \tag{1.54}$$

$\dot{m}$ represents the mass flow of liquid molecules transferred per surface unit between the bubble and the surrounding liquid medium. This flow is submitted to the Hertz-Knudsen equation given as (Yasui, 1997):

$$\dot{m} = \frac{M}{\sqrt{2\pi M R_g}}\alpha\left(\frac{P_V}{\sqrt{T_{Li}}} - \frac{P_L}{\sqrt{T}}\right) \tag{1.55}$$

In this equation, the determination of the incident and emitted mass flow toward and from the bubble at the gas-liquid interface follows the Maxwell law, while the probability of liquid gas collision, conducting to the adhesion of liquid molecules to the bubble interface is defined using the accommodation coefficient a (Yasui, 1996).

Considering the nonequilibrium of evaporation and condensation, the energy balance becomes:

$$nC_V\frac{dT}{dt} = -P_g\frac{dV}{dt} + 4\pi R^2\frac{\dot{m}}{M}C_{V_L}T \tag{1.56}$$

Besides, if the chemical mechanism and the mass diffusion of gases are taken into account, the energy balance is written (Sivasankar & Moholkar, 2009):

$$\mathrm{nC_V}\frac{dT}{dt} = -\mathrm{P_g}\frac{dV}{dt} + 4\pi R^2\frac{\dot{m}}{M}\mathrm{C_{V_L}T} - \sum_{i=1}^{n}\Delta\mathrm{H_i}\,\mathrm{r_i V} - \sum_{i}\mathrm{u_i}\frac{\mathrm{dn_i}}{\mathrm{dt}} \tag{1.57}$$

1.4.5 Conduction

In the simple conductive model, the bubble is assumed static in the fluid with a uniform surface temperature. The heat flow traveling across the bubble wall is expressed through Fourrier's law as:

$$\tilde{\theta} = -\lambda\,\overrightarrow{\mathrm{grad}}\,(\mathrm{T}) \tag{1.58}$$

$\tilde{\theta}$ represents the heat flow density, while λ is the thermal conductivity of the thermal layer of the bubble. Assuming the spatial uniformity of the temperature within the bubble volume, we consider a hypothetical thermal layer of small width ξ, separating the bulk of the bubble from the external liquid medium of temperature T_∞. The thermal layer width is defined as a function of the mean free path MFP (Yasui, 1997):

$$\xi = 3\ \times\ \mathrm{MFP} \tag{1.59}$$

Which results in:

$$\mathrm{nC_V}\frac{dT}{dt} = -\mathrm{P_g}\frac{dV}{dt} - \frac{\lambda}{\xi}4\pi\,\mathrm{R}^2(\mathrm{T}-\mathrm{T}_\infty) \tag{1.60}$$

Including the effect of the chemical mechanism, the mass diffusion of gases, and the nonequilibrium of evaporation and condensation at the bubble interface, the energy balance becomes:

$$\mathrm{nC_V}\frac{dT}{dt} = -\mathrm{P_g}\frac{dV}{dt} + 4\pi R^2\frac{\dot{m}}{M}\mathrm{C_{V_L}T} - \sum_{i=1}^{n}\Delta\mathrm{H_i}\,\mathrm{r_i}\,\mathrm{V} - \sum_{i}\mathrm{u_i}\frac{\mathrm{dn_i}}{\mathrm{dt}} - \frac{\lambda}{\xi}4\pi\,\mathrm{R}^2(\mathrm{T}-\mathrm{T}_\infty) \tag{1.61}$$

The rationale for the conductive approach based on the Fourrier's law is based on certain considerations of orders of magnitude. The studied system would be assimilated to a semi-infinite liquid and gaseous phases abruptly put in contact. In fact, at the instant of collapse, the variation of the temperature is very rapid and the width of the thermal layer, at both liquid and gaseous sides, is very small, which justifies the previous assimilation. The analytical solution of this classic problem demonstrates that the ratio of temperature differences very far from the interface and at the interface in both phases is inversely proportional to the ratio of their respective thermal effusivities. Taking into account the thermo-physical properties of water and usual dissolved gases, the gradient of temperature at the liquid side would be by far lower than the temperature gradient at the gas side. The temperature at the liquid side of the bubble interface can then be assimilated to the bulk liquid temperature. This results in a conductive problem within a homogeneous gaseous medium.

1.4.6 Convection

The convective approach considers the motion of the bubble creating a convective component for the heat transfer within water. The bubble surface is supposed isothermal, the analytical method for laminar free convective heat transfer from an isothermal sphere result in the following expression of the convective heat flow (Royer et al., 2017).

$$\frac{\partial Q}{\partial t} = \lambda\left(\frac{1}{R} + \frac{1}{\sqrt{\mu\pi t}}\right)(T - T_\infty) \tag{1.62}$$

μ represents the thermal diffusivity. The previous equation is inserted in the energy balance derived from the first law of thermodynamics, with the terms corresponding to the adopted assumptions.

1.5 Energy concentration concept

1.5.1 Acoustic energy

1.5.1.1 The acoustic energy parameters

Ultrasound is defined as sound wave of a frequency beyond the limit of human hearing. The normal range of human hearing is between 16 Hz and about 18 kHz. For younger people 20 kHz is audible but the frequency response limit reduces with age. Conventionally, the ultrasound range is considered to lie between 20 kHz and 500 MHz.

Let's consider the energy density w, which constitutes the energy of fluid motion per unit volume associated with the wave disturbance. When there is no ambient velocity (macroscopic motion) and when the viscosity and thermal conduction are neglected, the energy density w carried by an acoustic wave is expressed as:

$$w = \frac{1}{2}\rho\, v^2 + \frac{1}{2}\frac{1}{\rho c^2}\, p^2 \tag{1.63}$$

The first term in the expression for w corresponds to the acoustic kinetic energy per unit volume, and the second term is identified as the potential energy per unit volume due to compression of the fluid.

Let's consider another physical parameter, the vector quantity $\vec{I}$ known as the acoustic intensity vector (or energy flux vector). The dot product of $\vec{I}$ with any surface unit vector $\vec{S}$ characterized by a normal vector $\vec{n}$, represents the energy flowing per unit area and time across a normal surface. In the ideal case, it is assumed that there is no ambient velocity, and both viscosity and thermal conduction are neglected. The acoustic intensity is then expressed as:

$$I = p.v \tag{1.64}$$

For this ideal case, there is no dissipative term, the energy density and the acoustic intensity verify:

$$\frac{\partial w}{\partial t} + \nabla \vec{I} = 0 \tag{1.65}$$

Another interesting case is that of the plane wave, for which the kinetic and potential energies are the same. The energy density associated with a plane wave is then given by:

$$w = \rho\, v^2 = \frac{1}{\rho c^2} p^2 \tag{1.66}$$

The acoustic intensity becomes:

$$\vec{I} = \vec{n}\frac{1}{\rho c} p^2 \tag{1.67}$$

The energy density and the acoustic intensity of the plane wave are related by the equation:

$$\vec{I} = c \cdot w \cdot \vec{n} \tag{1.68}$$

Consequently, the sound speed can be regarded as an energy propagation velocity, hence, the group and phase velocities are the same. Consequently, the plane wave is considered nondispersive.

1.5.1.2 The propagation across a liquid medium

The propagation of ultrasonic waves in liquids is associated to the propagation of acoustic energy. The energy conservation principle applied to an elementary volume of liquid subjected to the propagation of an ultrasonic wave usually yields the corollary:

$$\frac{\partial w}{\partial t} + \nabla \vec{I} = -D \tag{1.69}$$

The term w constitutes, as already mentioned, the kinetic and potential energies of the fluid motion per unit volume associated with the wave disturbance, and the quantity D represents the energy that is dissipated per unit time and volume, it is either zero or positive. The vector quantity $\vec{I}$ is the intensity vector or energy flux vector defined previously, as shown in Fig. 1.4. The integration of the previous equation of energy conservation over an arbitrary volume V_L of the liquid results in:

$$\frac{\partial}{\partial t}\int\int\int_{v_L} w\, dV_L + \iint_s \vec{I}\cdot\vec{n}\, dS = -\int\int\int_v D dV_L \tag{1.70}$$

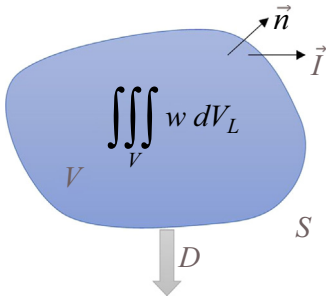

FIGURE 1.4 A schematic view of the energy conservation applied to an elementary volume irradiated by ultrasounds.

This conservative equation states that the net rate of variation of acoustical energy within the volume must equal the acoustic power flowing into the volume across its confining surface, minus the energy that is being dissipated per unit time within the volume (Rossing, 2009).

1.5.2 Acoustic radiation as a source of cavitation

When a liquid is submitted to the action of ultrasounds, the only rationale for the formation of acoustic cavitation remains the existence of gas pockets in the liquid, forming weaknesses that may evolve to an acoustic cavitation bubble. Bapat and Pandit (Bapat & Pandit, 2008) presented a very interesting demonstration for the acoustic energy threshold required to form cavities in a degassed water. The question was treated from an energetic point of view and can serve as an absurdum for the impossibility of creating cavities in a degassed water.

One can investigate the possibility for an acoustic wave to induce the inception of cavitation within a degassed water. The maximum threshold pressure for the stable cavity inception reported by Briggs (Briggs, 1950) in the degassed water is about 295×10^5 Pa. Accordingly, the required intensity I of the acoustic source at this threshold pressure can be calculated as follows:

$$I = \frac{{P_A}^2}{2\rho c} = 30\, kW/cm^2 \tag{1.71}$$

Let's consider a source irradiating a simple harmonic plane wave of $30 kW/cm^2$ of acoustic intensity at 20 kHz frequency. The studied receiving point in the liquid medium is deemed to be a spherical nucleus adjacent to the vibrating surface of the ultrasounds source. This assumption allows neglecting the damping effect of the liquid medium. The nucleus is spatially located in a hypothetical cylinder which is parallel to the direction of propagation of the acoustic wave. The hypothetical cylinder would have a diameter and a length equal to the spherical nucleus diameter.

Bapat and Pandit (Bapat & Pandit, 2008) suggested a simple technique for the estimation of the diameter of the initial vaporous nuclei created by the vaporization of liquid water at 303 K. The authors considered the molar volume of steam at 303 K and deduced the volume of one molecule of steam. This latter has been considered as the volume of a spherical initial vaporous nucleus. Simple calculations would demonstrate that it corresponds to a sphere of 12.34 nm of diameter. This sphere is delimited by a hypothetical cylinder, as stated previously and shown in Fig. 1.5, which receives and transmits the acoustic energy through its flat side S_{cyl}, that is, 1.19×10^{-16} m^2.

Based on this dimension, the volume of the hypothetical cylinder is determined, and consequently, the potential energy it can store. Considering the acoustic intensity calculated earlier, the stored potential energy during the rarefaction phase, that is, from 0 to 25 µs, is equal to 1.65×10^{-22} J. This amount of energy is by far less than the required yield to create a vaporous nucleus. The demonstration is quite easy, taking into account the latent enthalpy of vaporization per mole of water at 303 K, the required energy to create an initial vaporous nucleus (one molecule) is estimated at 7.27×10^{-20} J. The impossibility to form vaporous nuclei using ultrasound irradiation of degassed water is then established.

1.5.3 Acoustic radiation from collapsing bubble

During the bubble oscillation, energy is accumulated inside the bubble volume and is subjected to a sequence of energy conversion. However, it is believed that by the end of the strong collapse, all the energy forms are dissipated around the bubble as a thermal energy. The bubble collapse is accompanied of an acoustic radiation of the bubble. The acoustic radiation reveals a strong pressure release from the interior to the exterior of the bubble, known as the shockwave

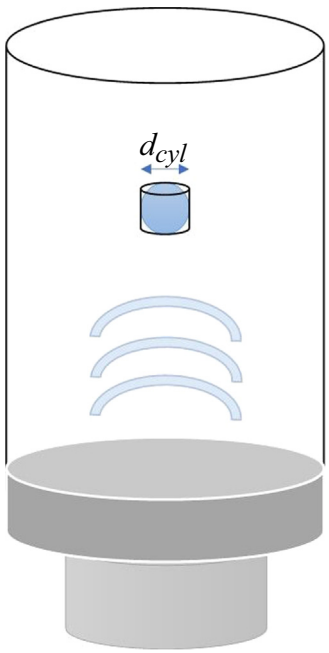

FIGURE 1.5 Schematic view of the initial nucleus and the hypothetical cylinder receiving the acoustic energy.

(Yusof et al., 2016), and believed to be one of the most powerful physical manifestations of the energy release during the bubble collapse (Bermúdez-aguirre et al., 2011; Kim & Suslick, 2018).

The radiation forces on a bubble in liquid under ultrasound originate in pressure inhomogeneity around the bubble. If the pressure inhomogeneity originates from an external acoustic field (driving ultrasound), the radiation force is called primary Bjerknes force. If it originates from an acoustic wave radiated by a neighboring bubble, it is called secondary Bjerknes force. For most combinations of ambient radii, the secondary Bjerknes force is attractive. However, when one of the bubbles has a relatively small ambient radius (1–2 um), the secondary Bjerknes force is repulsive if the ambient radius of the other bubble is larger (Yasui, 2017).

When a liquid in which gas is dissolved is irradiated by strong ultrasound, many tiny gas bubbles are generated. Bubbles expand during the rarefaction phase of ultrasound and collapse during the compression phase. When the bubble expansion is large enough during the rarefaction phase of ultrasound, the bubble violently collapses due to the inertia of the surrounding liquid as well as the spherically shrinking geometry (Rayleigh collapse). The speed of the bubble collapse often reaches the sound velocity of the liquid. At the end of the violent collapse, the inward liquid flow suddenly stops as the internal pressure of the bubble dramatically increases when the density inside the bubble nearly reaches that of the condensed phase.

The existence of the secondary Bjerknes force could influence the effect of cavitation in sonochemical reactors through increasing the fraction of energy transfer of the combined collapsing bubbles. After agglomeration due to the secondary Bjerknes force, bubbles may deform at the early stage of collapse, which decreases the efficiency of energy conversion of the cavitation as well as the efficiency of the sonochemical reactions. The direction of the secondary Bjerknes force (i.e., the bubbles whether attracting or repulsing each other) is a paramount topic of cavitation systems (Zhang et al., 2016). The secondary Bjerknes force is described by Eq. 1.72.

$$\overrightarrow{F_B} = \left\langle \overrightarrow{F_P} \right\rangle = -\left\langle V \vec{\nabla} p \right\rangle \tag{1.72}$$

Noting that $\vec{\nabla} = \left(\frac{\partial}{\partial x}, \frac{\partial}{\partial y}, \frac{\partial}{\partial z}\right)$.

The pulsating bubble, particularly at the strong collapse, radiates acoustic wave into the surrounding liquid. Let's consider the Euler equation (equation of motion) in fluid dynamics:

$$\frac{\partial \vec{u}}{\partial t} + (\vec{u}.\nabla)\vec{u} = -\frac{1}{\rho}\nabla P \tag{1.73}$$

According to the condition of liquid incompressibility, the fluid velocity u around a pulsating bubble is given by Eq. 1.74.

$$\vec{u} = \frac{R^2\dot{R}}{r^2}\overrightarrow{e_r} \tag{1.74}$$

Then, the second term on the left-hand side of Eq. 1.73 is proportional to r^{-5} and negligible compared to the first term. Inserting Eq. 1.74 into Eq. 1.73 yields Eq. 1.75.

$$\frac{\partial P}{\partial r} = -\frac{\rho}{r^2}\frac{d}{dt}\left(R^2\dot{R}\right) \tag{1.75}$$

where P is the acoustic pressure radiated from a bubble. Integrating Eq. 1.75 with r yields Eq. 1.76.

$$P = \frac{\rho}{r}\frac{d}{dt}\left(R^2\,\dot{R}\right) = \frac{\rho}{4\pi r}\frac{d^2V}{dt^2} \tag{1.76}$$

Where $V = \frac{4}{3}\,\pi\,R^3$ is the instantaneous volume of a bubble. Eq. 1.72 becomes:

$$\overrightarrow{F_{1\to 2}} = -V_2\vec{\nabla}P_1 \tag{1.77}$$

Inserting Eq. 1.76 into Eq. 1.77 yields Eq. 1.78.

$$\overrightarrow{F_{1\to 2}} = \frac{\rho}{4\pi d^2}\ddot{V}_1V_2\,\overrightarrow{e_{1\to 2}} \tag{1.78}$$

noting that $\ddot{V}_1 = \frac{d^2V_1}{dt^2}$.

When the sign of $\overrightarrow{e_{1\to 2}}$ in Eq. 1.78 is negative, the secondary Bjerknes force is attractive.

The energy related to the force radiated by a bubble is described by:

$$E = \frac{4\pi r^2}{\rho c}\int P^2dt \tag{1.79}$$

The pressure of acoustic waves radiated by a pulsating bubble is estimated by:

$$P = \frac{\rho}{r}\left(R^2\ddot{R} + 2R\dot{R}^2\right) \tag{1.80}$$

the dot denotes the time derivative. From Eqs.1.79 and 1.80, the acoustic energy radiated by a pulsating bubble is as indicated in Eq. 1.81.

$$E = \frac{4\pi\rho}{c}\int\left(R^2\ddot{R} + 2R\dot{R}^2\right)^2dt \tag{1.81}$$

Thus, the acoustic power is expressed as shown in Eq. 1.82 (Yasui et al., 2011).

$$\dot{E} = \frac{4\pi\rho}{c}\left(R^2\ddot{R} + 2R\dot{R}^2\right)^2 \tag{1.82}$$

The acoustic energy radiation can be used to probe the energy concentration inside the bubble volume, by reporting the radiated power at the instant of collapse to the minimum volume achieved by the bubble during this phase. This approach yields to the equation:

$$\dot{E}_V = \frac{3\rho}{cR_{min}{}^3}\left(R_{min}{}^2\ddot{R}_{max} + 2R_{min}\dot{R}^2_{max}\right)^2 \tag{1.83}$$

1.5.4 Energy concentration

1.5.4.1 The volume energy concentration concept

The effects of ultrasound derive primarily from cavitation, where bubble collapse results in an enormous concentration of energy from the conversion of the surface energy and kinetic energy of liquid motion into heat and chemical energy. The feasibility of converting sound into chemistry has been demonstrated more than eighty years ago after Lord Rayleigh had postulated the existence of cavitation bubbles (Shchukin et al., 2011)

The inertial collapse of a bubble in a liquid can create quite remarkable physicochemical conditions in a fluid system. Although the effects are quite short lived, their result could be dramatical with the repetition in space and time. The bubbles

needed for this remarkable concentration of energy can be rapidly and readily generated by the exposure of a liquid to ultrasound, and this has been increasingly harnessed in several sonophysical and sonochemical applications (Dharmarathne et al., 2012). During a typical bubble collapse, kinetic and potential energy of the acoustic wave serve to the compression of the bubble content. The content of the bubble can be compressed by many orders of magnitude on a time scale of microseconds. The process happens so fast that there is no time for heat exchange with the surrounding liquid hence the volume change practically occurs adiabatically. This creates extreme thermal and mass concentration gradients at the bubble surface that drive heat and mass transfer processes between the bubble interior and the surrounding liquid (Calvisi et al., 2007).

One common pathway for the release of concentrated energy concerns shockwaves created by cavity collapse in the liquid as explained earlier in Section 1.5.3. Oscillating bubbles are very effective in redistributing and dissipating acoustic energy. Stable and transient cavities behave differently in this respect. With transient cavities, great concentration of energy occurs towards the end of the last contraction before the bubble breaks up (Rosselló et al., 2013). In effect, energy is extracted from the sound beam and rapidly concentrated into small volumes. Energy from progressive waves is converted after a sequence of events into spherical shock waves emanating from the hot spot (Kuna et al., 2017).

However, in heterogeneous systems, the solid particles dispersed in the liquid and the trapped gas in the crevices act as nuclei for the concentration of the acoustic energy (Penconi et al., 2015). When cavitation occurs near extended liquid—solid interface, the concentrated energy is usually released in the form of microjet impacts. Such energy concentration can result in severe mechanical damage to the boundary surface. Energetically speaking, the induced physical effects in heterogeneous systems are explained by the conversion of the potential energy of the expanded bubble into kinetic energy of a liquid jet that extends through the bubble's interior and penetrates the opposite bubble wall. Most of the available energy is transferred to the accelerating jet, rather than the bubble wall itself. Consequently, this jet can reach velocities of hundreds of meters per second (Guo, 2018; Yuan and Prosperetti, 1997). The jet often impacts the local boundary and can deposit enormous energy densities at the site of impact resulting in spectacular erosion, especially for larger bubbles formed at lower frequencies (Kuna et al., 2017). The energy conversion pathways within a control volume of the liquid under the effect of ultrasounds will be particularly discussed in the absence of solid interface in the following paragraph.

1.5.4.2 Macroscopic energy conversion

Let's consider a volume of control dV_L which knows during an infinitesimal time interval dt a variation of its total energy accounting for the acoustic energy, the internal energy, the macroscopic kinetic energy, and the macroscopic potential energy. The passage of the wave through the volume dV_L generates a variation of the acoustic energy which is expressed as the sum of potential and kinetical energies acquired by the fluid and expressed in Eq. 1.84 (Rienstra & Hirschberg, 2018).

$$\frac{dw}{dt} = \frac{d}{dt}\left(\frac{\rho_L\, v^2}{2} dV_L + \frac{P^2}{2\,\rho_L\, c^2} dV_L\right) \tag{1.84}$$

v, which represents the vibrational velocity of the fluid as stated earlier in Section 1.5.1.1, is related to the acoustic pressure through its acoustic impedance.

The variation of the total energy of the control volume dV_L is the sum of the variations of the internal energy, the macroscopic kinetic energy and the macroscopic potential energy. This variation constitutes the accumulation of energy within the volume dV_L.

The internal energy of the control volume would vary due to the conversion of energy to work and heat as indicated by the first principle of thermodynamics. Hence, the variation of the internal energy during the time interval dt is the result of the variations of:

(i) The pressure forces work exerted on liquid and gaseous phases located on both sides of the walls of bubbles contained in the volume dV_L as indicated below.

$$\frac{dW_p(t)}{dt} = -(P_\infty - P_a \sin(\omega t))\frac{d}{dt}\left(\frac{4}{3}\pi\, R^3 N dV_L\right) + P_g \frac{d}{dt}\left(\frac{4}{3}\pi\, R^3 N dV_L\right) \tag{1.85}$$

(ii) The energy of surface tension that maintains the bubbles (Shu-tang & Yi-xin, 1983) as indicated in Eq. 1.86.

$$\frac{dE_i(t)}{dt} = \frac{d}{dt}\left(\sigma 4\pi\, R^3\, N d\, V_L\right) \tag{1.86}$$

(iii) The heat dissipated within the liquid in the volume dV_L due to absorption phenomenon (Destaillats et al., 2001) according to Eq. 1.87.

$$\frac{dQ(t)}{dt} = \frac{d}{dt}\left(\frac{\rho_L}{M} C_{VL}\, T_\infty\, d\, V_L\right) \tag{1.87}$$

The macroscopic kinetic energy of the control volume is due to the motion of the bubble walls from and toward the bubble centers, which streams the surrounding liquid particles. The liquid particles acquire consequently a kinetic energy, the variation of this kinetic energy during dt can be estimated within the volume dV_L through Eq. 1.88 (Vokurka, 2017). Though gas particles are in motion as well, their kinetic energy is relatively very low, taking into account the neglected ratio ρ_G/ρ_L, it is then ignored.

$$\frac{dE_k(t)}{dt} = \frac{d}{dt}\left(2\pi\ \rho_L\ R^3\ \dot{R}^2\ Nd\ V_L\right) \tag{1.88}$$

The variation of the macroscopic potential energy is actually the result of both physical and chemical transformations that induce a variation of the molar yields in liquid and gaseous phases, which generates a variation in the chemical potential energy in the control volume dV_L. However, as the proportion of liquid in the control volume dV_L is strictly predominant, the variation of the chemical potential energy of liquid phase is neglected as compared to that of the gaseous phase. The variation of the macroscopic chemical potential energy within the volume of control is then expressed by the contribution of all the bubbles contained in the control volume dV_L as reported below (Shu-tang & Yi-xin, 1985).

$$\frac{dE_p(t)}{dt} = \frac{d}{dt}\left(NdV\sum_{i=1}^{k} n_i u_i\right) \tag{1.89}$$

Besides, the control volume dV_L knows a creation of energy due to the chemical kinetics, which results in the release and absorption of energy according to the reaction enthalpies. The flow of the created energy is expressed in the below equation (Kerboua & Hamdaoui, 2018).

$$\frac{dC(t)}{dt} = -\sum_{j=1}^{n}\frac{4}{3}\pi\,\Delta H_i r_i R^3 NdV \tag{1.90}$$

To sum up, a typical black box energy analysis applied to the infinitesimal volume dV_L receiving an acoustic intensity $I(x)$ on a surface dS and transmitting an acoustic intensity $I(x+dx)$ by the same surface, would result in (Kerboua & Hamdaoui, 2019):

$$I(x)dS + \frac{dC(t)}{dt} = I(x+dx)dS + \frac{dw(t)}{dt} + \frac{dW_p(t)}{dt} + \frac{dE_i(t)}{dt} + \frac{dQ}{dt} + \frac{dE_k(t)}{dt} + \frac{dE_p(t)}{dt} \tag{1.91}$$

It is noticeable that if the sonochemical activity is ignored, this balance simplifies to Eq. 1.92 (Louisnard, 2012).

$$\frac{d}{dt}\left(\frac{P^2}{2\ \rho_L\ c^2} + \frac{\rho_L\ v^2}{2}\right) + \frac{dI}{dx} = (P_\infty + P)\frac{d}{dt}\left(\frac{4}{3}\pi\ R^3 N\right) \tag{1.92}$$

This equation is known as the corollary of acoustic wave propagation (Rossing, 2009).

1.6 Engineering outcomes

The energy concentration concept, which explains the harsh physical and chemical effects associated with the acoustic cavitation bubble, has several interesting applications in Engineering. During the violent spherical bubble collapse, the extreme compression leads to gas pressures of several hundreds of megapascals and temperatures rising to thousands of Kelvin. The so-called "hot spots" created within the cold liquid are the sites of molecular excitation and dissociation, chemical reaction catalysis, and emission of photons. These intriguing high energetic effects brought forth by an acoustic field are referred to as sonochemistry (Mettin et al., 2015), sonoluminescence (Brenner et al., 2002), shockwaves (Loske, 2010), and microjets in the presence of solid interfaces (Brujan, 2004; Peters et al., 2015). When cavitation arises in the neighborhood of a solid interface, the impingement of microjets and shock waves on the surface creates the localized erosion responsible for ultrasonic cleaning and many of the sonochemical effects on heterogeneous reactions (Mohamed, 2019), particularly at low frequencies.

This energy concentration is less violent at higher frequencies in the order of MHz, simply because the cavitation bubbles are much smaller. Yet, the physical effects induced by the release of the concentrated energy of the acoustic bubbles at high frequencies do have an interesting application in the cleaning for microelectronics (Kenneth S. Suslick, 2003), requiring soft physical attack.

References

Apfel, R.E., 1981. Acoustic cavitation. Methods in Experimental Physics 19 (C), 355–411. https://doi.org/10.1016/S0076-695X(08)60338-5.

ASME (1933) Steam tables. (n.d.).

Bapat, P.S., Pandit, A.B., 2008. Thermodynamic and kinetic considerations of nucleation and stabilization of acoustic cavitation bubbles in water. Ultrason. Sonochem. 15 (1), 65–77. https://doi.org/10.1016/j.ultsonch.2007.01.005.

Bermúdez-aguirre, D., Mobbs, T., & V, B.G. (2011). Ultrasound Technologies for Food and Bioprocessing.

Bhangu, S.K., Ashokkumar, M., 2016. Theory of Sonochemistry. Top. Curr. Chem. 374 (4). https://doi.org/10.1007/s41061-016-0054-y.

Blake, J.R., 1988. The Kelvin impulse: application to cavitation bubble dynamics. J. Aust. Math. Soc. Ser. B Appl. Math. 30, 127–146. https://doi.org/10.1017/s0334270000006111.

Brennen, C.E., 1995. Spherical Bubble Dynamics. Cavitation and Bubble Dynamics. Oxford University Press, United Kingdom, pp. 48–78. https://doi.org/10.1017/CBO9781107338760.

Brenner, M.P., Hilgenfeldt, S., Lohse, D., 2002. Single-bubble sonoluminescence. Rev. Mod. Phys. 74 (2), 425–484. https://doi.org/10.1103/RevModPhys.74.425.

Briggs, L.J., 1950. Limiting negative pressure of water [2]. J. Appl. Phys. 21 (7), 721–722. https://doi.org/10.1063/1.1699741.

Brujan, E.A., 2004. The role of cavitation microjets in the therapeutic applications of ultrasound. Ultrasound Med. Biol. 30 (3), 381–387. https://doi.org/10.1016/j.ultrasmedbio.2003.10.019.

Calvisi, M.L., Lindau, O., Blake, J.R., Szeri, A.J., 2007. Shape stability and violent collapse of microbubbles in acoustic traveling waves. Phys. Fluids 19, 1–16. https://doi.org/10.1063/1.2716633.

Carrillo-Lopez, L.M., Alarcon-Rojo, A.D., Luna-Rodriguez, L., Reyes-Villagrana, R., 2017. Modification of food systems by ultrasound. J. Food Qual. 2017. https://doi.org/10.1155/2017/5794931.

Colussi, A.J., Weavers, L.K., Hoffmann, M.R., 1998. Chemical bubble dynamics and quantitative sonochemistry. J. Phys. Chem. A 102 (35), 6927–6934. https://doi.org/10.1021/jp980930t.

Crum, L., 1984. Rectified diffusion. Ultrasonics 215.

Destaillats, H., Lesko, T.M., Knowlton, M., Wallace, H., Hoffmann, M.R., 2001. Scale-up of sonochemical reactors for water treatment. Ind. Eng. Chem. Res. 40 (18), 3855–3860. https://doi.org/10.1021/ie010110u.

Dharmarathne, L., Ashokkumar, M., Grieser, F., 2012. Photocatalytic generation of hydrogen using sonoluminescence and sonochemiluminescence. J. Phys. Chem. C 116 (1), 1056–1060. https://doi.org/10.1021/jp209946s.

Fuster, D., Dopazo, C., Hauke, G., 2011. Liquid compressibility effects during the collapse of a single cavitating bubble. J. Acoust. Soc. Am. 129 (1), 122–131. https://doi.org/10.1121/1.3502464.

Grieser, F., Choi, P.K., Enomoto, N., Harada, H., Okitsu, K., Yasui, K., 2015. Sonochemistry and the acoustic bubble. Sonochemistry and the Acoustic Bubble. Elsevier, Netherlands, pp. 1–282. https://www.sciencedirect.com/book/978012801530.

Guo, C., 2018. The relationship between the collapsing cavitation bubble and its microjet near a rigid wall under an ultrasound field. Cavitation - Selected Issues. IntechOpen, London, United Kingdom, pp. 73–88.

Jena, F., 1965. Sonochemistry of selected hydrocarbons, sulfur-containing and nitrogen-containing organic compounds in aqueous solutions and nonaqueous liquids dissertation.

Kerboua, K., Hamdaoui, O., 2017. Computational study of state equation effect on single acoustic cavitation bubble's phenomenon. Ultrason. Sonochem. 38, 174–188. https://doi.org/10.1016/j.ultsonch.2017.03.005.

Kerboua, K., Hamdaoui, O., 2018. Influence of reactions heats on variation of radius, temperature, pressure and chemical species amounts within a single acoustic cavitation bubble. Ultrason. Sonochem. 41, 449–457. https://doi.org/10.1016/j.ultsonch.2017.10.001.

Kerboua, K., Hamdaoui, O., 2019. Void fraction, number density of acoustic cavitation bubbles, and acoustic frequency: a numerical investigation. J. Acoust. Soc. Am. 146 (4), 2240–2252. https://doi.org/10.1121/1.5126865.

Kerboua, K., Hamdaoui, O., Alghyamah, A., 2021. Acoustic frequency and optimum sonochemical production at single and multi-bubble scales: A modeling answer to the scaling dilemma. Ultrason. Sonochem. 70, 105341. https://doi.org/10.1016/j.ultsonch.2020.105341.

Kim, H.N., Suslick, K.S., 2018. The effects of ultrasound on crystals: sonocrystallization and sonofragmentation. cryst. 8 (7). https://doi.org/10.3390/cryst8070280.

Kuna, E., Behling, R., Valange, S., Chatel, G., Colmenares, J.C., 2017. Sonocatalysis: A Potential Sustainable Pathway for the Valorization of Lignocellulosic Biomass and Derivatives. Top. Curr. Chem. 375 (2). https://doi.org/10.1007/s41061-017-0122-y.

Lee, J., Ashokkumar, M., Kentish, S., Grieser, F., 2006. Effect of alcohols on the initial growth of multibubble sonoluminescence. J. Phys. Chem. B 110 (34), 17282–17285. https://doi.org/10.1021/jp063320z.

Lee, J., Kentish, S., Ashokkumar, M., 2005a. Effect of surfactants on the rate of growth of an air bubble by rectified diffusion. J. Phys. Chem. B 109 (30), 14595–14598. https://doi.org/10.1021/jp051758d.

Lee, J., Kentish, S.E., Ashokkumar, M., 2005b. The effect of surface-active solutes on bubble coalescence in the presence of ultrasound. J. Phys. Chem. B 109 (11), 5095–5099. https://doi.org/10.1021/jp0476444.

Leong, T., Ashokkumar, M., Sandra, K., 2011. The fundamentals of power ultrasound - a review. Acoustics Australia 39 (2), 54–63.

Lepoint, T., Mullie, F., 1994. What exactly is cavitation chemistry? Ultrasonics - Sonochemistry 1 (1), S13–S22. https://doi.org/10.1016/1350-4177(94)90020-5.

Loomis, A.L., 1927. The chemical effects of high frequency sound waves i. a preliminary survey 49, 3086–3100.

Loske, A.M., 2010. The role of energy density and acoustic cavitation in shock wave lithotripsy. Ultrasonics 50 (2), 300–305. https://doi.org/10.1016/j.ultras.2009.09.012.

Louisnard, O., 2012. A simple model of ultrasound propagation in a cavitating liquid. Part I: Theory, nonlinear attenuation and traveling wave generation. Ultrason. Sonochem. 19 (1), 66–76. https://doi.org/10.1016/j.ultsonch.2011.06.008.

Luo, J., Fang, Z., Smith, R., & Qi, X. (2015). Fundamentals of acoustic cavitation in sonochemistry.

Mason, T., Cintas, 2002. Sonochemistry. Handbook of Green Chemistry and Technology. Wiley, USA, pp. 372–396.

Mettin, R., Cairós, C., Troia, A., 2015. Sonochemistry and bubble dynamics. Ultrason. Sonochem. 25 (1), 24–30. https://doi.org/10.1016/j.ultsonch.2014.08.015.

Mohamed, M.A., 2019. Sonochemistry (Applications of Ultrasound in Chemical Synthesis and Reactions): a Review Part III. J Pharmaceutical Res Int 1–19. https://doi.org/10.9734/jpri/2019/v31i630363.

Moholkar, V.S., Sable, S.P., Pandit, A.B., 2000. Mapping the cavitation intensity in an ultrasonic bath using the acoustic emission. AIChE J. 46, 684–694. https://doi.org/10.1002/aic.690460404.

Oladokun, O., Ahmad, A., Ripin, A., Abdullah, T.A.T., Nyakuma, B.B., Hadi, N.A., Al-Shatri, A.H., Ahmed, M., Alkali, H., Bello, A.A., 2019. Modelling ultrasound waves bubble formation in ethanol/ethyl acetate azeotrope mixture. E3S Web of Conferences, 90. EDP Sciences Vol. https://doi.org/10.1051/e3sconf/20199002005 .

Pandit, A.B., Davidson, J.F., 1990. Hydrodynamics of the rupture of thin liquid films. J. Fluid Mech. 212, 11–24. https://doi.org/10.1017/S0022112090001823.

Patel, T., Patel, D., Thakkar, N., Lakdawala, A., 2019. A numerical study on bubble dynamics in sinusoidal channels. Phys. Fluids 31 (5). https://doi.org/10.1063/1.5092870.

Penconi, M., Rossi, F., Ortica, F., Elisei, F., Gentili, P.L., 2015. Hydrogen production from water by photolysis, sonolysis and sonophotolysis with solid solutions of rare earth, gallium and indium oxides as heterogeneous catalysts. Sustainability (Switzerland) 7 (7), 9310–9325. https://doi.org/10.3390/su7079310.

Peters, A., Sagar, H., Lantermann, U., el Moctar, O., 2015. Numerical modelling and prediction of cavitation erosion. Wear 338–339, 189–201. https://doi.org/10.1016/j.wear.2015.06.009.

Poling, B., Prausnitz, J., Connel, O., P, J., 2004. The properties of gases and liquids.

Rienstra, S., Hirschberg, A., 2018. An introduction to acoustics.

Rosselló, J.M., Dellavale, D., Bonetto, F.J., 2013. Energy concentration and positional stability of sonoluminescent bubbles in sulfuric acid for different static pressures. Phys. Rev. E - Stat. Nonlinear, Soft Matter. Phys. 88, 1–9. https://doi.org/10.1103/PhysRevE.88.033026.

Rossing, T., 2009. Handbook of acoustics.

Royer, J.J., Monnin, N., Pailot-Bonnetat, N., Filippov, L.O., Filippova, I.V., Lyubimova, T., 2017. Thermodynamics of ultra-sonic cavitation bubbles in flotation ore processes. Journal of Physics: Conference Series. Institute of Physics Publishing (Vol. 879, Issue 1) https://doi.org/10.1088/1742-6596/879/1/012024 .

Shchukin, D.G., Skorb, E., Belova, V., Möhwald, H., 2011. Ultrasonic cavitation at solid surfaces. Adv. Mater. 23 (17), 1922–1934. https://doi.org/10.1002/adma.201004494.

Shu-tang, T., Yi-xin, L., 1985. Similarity problem of inceptive cavitation. Applied Mathematics and Mechanics 6 (11), 1045–1051. https://doi.org/10.1007/BF03250503.

Shu-tang, T., Yi-xin, L., 1983. Thermodynamics on cavitation. Applied Mathematics and Mechanics 4 (6), 825–831. https://doi.org/10.1007/BF01896169.

Sivasankar, T., Moholkar, V.S., 2009. Physical insights into the sonochemical degradation of recalcitrant organic pollutants with cavitation bubble dynamics. Ultrason. Sonochem. 16 (6), 769–781. https://doi.org/10.1016/j.ultsonch.2009.02.009.

Suslick, K.S., McNamara, W.B., Didenko, Y., 1999. Hot Spot Conditions During Multi-Bubble Cavitation. Springer Science and Business Media LLC, pp. 191–204.

Suslick, KS., 2003. Sonoluminescence and Sonochemistry. Elsevier BV, pp. 363–376.

Suslick, KS., Hammerton, D.A., Cline, R.E., 1986. Sonochemical hot spot. J. Am. Chem. Soc. 108 (18), 5641–5642. https://doi.org/10.1021/ja00278a055.

Tögel, R. (2002). Reaction-diffusion kinetics of a single sonoluminescing bubble.

Vokurka, K., 2017. Significant intervals of energy transforms in bubbles freely oscillating in liquids. J. Hydrodyn. Ser. B (English Ed.) 29 (2), 217–225. https://doi.org/10.1016/S1001-6058(16)60731-X.

Yasui, K., 1996. Variation of liquid temperature at bubble wall near the sonoluminescence threshold. J. Phys. Soc. Japan 65, 2830–2840. https://doi.org/10.1143/JPSJ.65.2830.

Yasui, K., 1997. Alternative model of single-bubble sonoluminescence. Physical Review E - Statistical Physics, Plasmas, Fluids, and Related Interdisciplinary Topics 56 (6), 6750–6760. https://doi.org/10.1103/PhysRevE.56.6750.

Yasui, K., 1999. Single-bubble sonoluminescence from hydrogen. J. Chem. Phys. 111 (12), 5384–5389. https://doi.org/10.1063/1.479798.

Yasui, K., Towata, A., Tuziuti, T., Kozuka, T., Kato, K., 2011. Effect of static pressure on acoustic energy radiated by cavitation bubbles in viscous liquids under ultrasound. J. Acoust. Soc. Am. 130 (5), 3233–3242. https://doi.org/10.1121/1.3626130.

Yasui, K., 2017. Acoustic cavitation. In: B. G. Pollet & M. Ashokkumar (Eds.), *Acoustic Cavitation and Bubble Dynamics* (pp. 1–31). Nagoya: Springer Briefs in Molecular Science. Retrieved from http://www.springer.com/series/15634.

Yuan, H., Prosperetti, A., 1997. Gas-liquid heat transfer in a bubble collapsing near a wall. Phys. Fluids 9, 127–142. https://doi.org/10.1063/1.869153.

Yusof, N.S.M., Babgi, B., Alghamdi, Y., Aksu, M., Madhavan, J., Ashokkumar, M., 2016. Physical and chemical effects of acoustic cavitation in selected ultrasonic cleaning applications. Ultrason. Sonochem. 29, 568–576. https://doi.org/10.1016/j.ultsonch.2015.06.013.

Zhang, Y., Zhang, Y., Li, S., 2016. The secondary Bjerknes force between two gas bubbles under dual-frequency acoustic excitation. Ultrason. Sonochem. 29, 129–145. https://doi.org/10.1016/j.ultsonch.2015.08.022.

Zijlstra, A., 2011. Acoustic surface cavitation. PhD Thesis.

Chapter 2

The energy forms and energy conversion

Aissa Dehane[a], **Slimane Merouani**[a] **and Oualid Hamdaoui**[b]

[a] *Laboratory of Environmental Process Engineering, Department of Chemical Engineering, Faculty of Process Engineering, University Salah Boubnider-Constantine 3, Constantine, Algeria,* [b] *Chemical Engineering Department, College of Engineering, King Saud University, Riyadh, Saudi Arabia*

2.1 Introduction

Over the last two decades, ultrasonic irradiation of a solution has attracted the attention of several researchers as one of the promising AOPs (Adewuyi, 2001; Sathishkumar et al., 2016). The main advantages of this technique is its ability to generate radicals species, that is •OH, HO_2•, …, that promote the degradation of refractory substances present in water (Henglein, 1995; Merouani et al., 2015; Pokhrel et al., 2016; Thompson & Doraiswamy, 1999; Yasui et al., 2007). Unfortunately, this technique is not largely used in large-scale chemical process because it requires costly equipment and consumes high amount of energy while not all of the cavitational energy can transform into chemical and physical effects (Kerabchi et al., 2018a, 2018b, 2019; Pang et al., 2011; Wood et al., 2017). Therefore, several theoretical (Chadi et al., 2018; K. Kerboua & Hamdaoui, 2017; Ono et al., 2019) and experimental (Gondrexon et al., 1997; Mark et al., 1998; Petrier & Francony, 1997; Wei et al., 2018) studies have been focused on the improvement of this method through a deep analysis of the different operational conditions affecting the energetic efficiency of this method. On the other hand, many experimental works were deduced for the measurement of the energetic efficiency of a sonochemical reactor (Asakura et al., 2008; Koda et al., 2003; Merouani et al., 2010; Son et al., 2011, 2008; Toma et al., 2011; Verhaagen et al., 2016). For example, *Loning et al.* (Löning et al., 2002) investigated the energy transformation in a sonochemical process using electrical power measurement techniques and calorimetry, where it has been demonstrated that the increase of liquid temperature and its viscosity causes the power transferred in the system to be decreased, therefore, the energetic efficiency of the sonoprocess is reduced. Similarly, *Kuijpers et al.* (Kuijpers et al., 2002) indicate that the energy conversion, that is, estimated by comparison of the ultrasound power transferred to the liquid and the radical's formation kinetics, is highest at low acoustic amplitude and liquid temperatures. Additionally, *Son et al.* (Son et al., 2009) analyzed the effect of ultrasound frequency on the energetic efficiency of a sonoreactor by using a 3D cavitation energy analysis. It was concluded that the highest cavitation energy distribution is obtained when wave frequency is decreased. Son's team (Son et al., 2011, 2008) also analyzed the ultrasonic cavitation energy in a pilot-scale sonoreactor working at 72, 110, and 170 kHz as well as the characteristics of the ultrasound field at various liquid heights in pilot-scale sonochemical reactor.

On the other hand, it was observed that microscopic analysis of the energetic efficiency of the sonochemical process are very scarce. Recently, *Kerboua et al.* (Kaouther Kerboua et al., 2021) have used an energetic analysis in order to identify the major forms of energy influencing the internal energy and the activity of a stable acoustic cavitation. It was concluded that the pressure forces work is the major energetic input during bubble oscillation, whilst the main energetic loss results from heat transfer and enthalpy loss accompanying water condensation. In other study, *Kerboua and Hamdaoui* (K. Kerboua & Hamdaoui, 2019) performed a theoretical analysis of the accumulated energy for a one acoustic cavitation in the purpose to understand the manner of conversion of the acoustic energy within a control volume. It was observed an increase of the energy required to maintain the oscillation of bubble proportionally with the decrease of ultrasound frequency. This observation was used to clarify the minimization of number density with the decrease of ultrasound frequency. Furthermore, *Merouani et al.* (Merouani et al., 2014) and *Vichare et al.* (Vichare et al., 2000) investigated the impact of different operational conditions on the microscopic energy balance of an acoustic bubble; however, only the PV work is considered to express the internal

Energy Aspects of Acoustic Cavitation and Sonochemistry: Fundamentals and Engineering. DOI: https://doi.org/10.1016/B978-0-323-91937-1.00012-8
Copyright © 2022 Elsevier Inc. All rights reserved.

TABLE 1.1 Instantaneous evolutions of Energies due to PV work, heat exchange, mass transfer and reaction heats, respectively.

Equation		Description
$\frac{dE_{PV}}{dt} = -P\left(4\pi \dot{R} R^2\right)$	(2.9)	Energy variation resulting from the exerted pressure forces on the bubble wall "PV work."
$\frac{dE_{\dot{Q}}}{dt} = 4\pi R^2 \lambda \frac{(T_{liq} - T)}{L_{th}}$	(2.10)	Energy variation resulting from the heat transferred through thermal conduction outside and inside the bubble.
$\frac{dE_{\dot{m}}}{dt} = 4\pi R^2 \frac{\dot{m}}{M_{H_2O}} C_{v,H_2O}$	(2.11)	Energy flow due to the nonequilibrium evaporation and condensation of water molecules at the bubble interface.
$\frac{dE_{\Delta H}}{dt} = -\frac{4}{3}\pi R^3 \sum_{i=1}^{n} H_i r_i$	(2.12)	Energy flow resulting from the absorbed or released reactions heat.

bubble energy in the *Merouani* and *Vichare* works (Merouani et al., 2014; Vichare et al., 2000) because they used an adiabatic model for bubble collapse.

The present chapter aims principally to give a special focus on the energetic analysis of the bubble internal energy balance with respect to the variation of acoustical conditions, that is, ultrasound frequency and acoustic intensity. The contribution of each of the different terms of the internal bubble energy balance, that is, PV work, heat transfer, mass transport and reaction heat, was analyzed with respect to frequency, acoustic amplitude and initial bubble size.

2.2 Theoretical background

The single bubble model adopted herein has been fully described previously (A. Dehane et al., 2021; Aissa Dehane, Merouani, & Hamdaoui, 2021b; Aissa Dehane, Merouani, Hamdaoui, et al., 2021a, 2021b). Briefly, the physical situation is as a gas (argon) and water vapor-filled bubble isolated in water and oscillating under the action of sinusoidal acoustic wave of a fixed frequency and amplitude. The temperature and pressure inside bubble are spatially uniform. The chemical reaction inside the bubbles is described through a reaction scheme consisting in 25 reversible reactions involving nine species (i.e., $H^{\bullet}$, O, $^{\bullet}OH$, H_2O, $HO_2{}^{\bullet}$, H_2O_2, H_2, O_2 and O_3), as shown in Table 2.1 of (Aissa Dehane, Merouani, Hamdaoui, et al., 2021a). The radial motion of the bubble is described by the modified Keller-Miksis equation (Yasui, 1995):

$$\left(1 - \frac{\dot{R}}{C} + \frac{\dot{m}}{C\rho_L}\right) R\ddot{R} + \frac{3}{2}\dot{R}^2\left(1 - \frac{\dot{R}}{3C} + \frac{2\dot{m}}{3C\rho_L}\right) = \frac{1}{\rho_L}\left(1 + \frac{\dot{R}}{C}\right)\left[P_B(t) - P_A sin\left(2\pi f\left(t + \frac{R}{C}\right)\right) - P_\infty\right] + \frac{\dot{m}R}{\rho_L}\left(1 - \frac{\dot{R}}{C} + \frac{\dot{m}}{C\rho_L}\right) + \frac{\dot{m}}{\rho_L}\left(\dot{R} + \frac{\dot{m}}{2\rho_L} + \frac{\dot{R}\dot{m}}{2C\rho_L}\right) + \frac{R}{C\rho_L}\frac{dP_B(t)}{dt} \tag{2.1}$$

where $R(t)$ is the bubble radius-versus time, $\dot{m}$ is the net rate of evaporation per unit area and unit time, C is the sound speed in the medium (water), P_∞ is the ambient static pressure and ρ_L is the liquid density. PA, the acoustic amplitude, is proportional to the acoustic intensity Ia as follows: $P_A = (2I_n\rho_L C)^{1/2}$. The exterior liquid pressure $P_B(t)$ on the bubble wall is linked to the interior pressure $P(t)$ by the equation below (Aissa Dehane, Merouani, Hamdaoui, et al., 2021a):

$$P_B(t) = P(t) - \frac{2\sigma}{R} - \frac{4\mu}{R}\left(\dot{R} + \frac{\dot{m}}{\rho_L}\right) - \dot{m}^2\left(\frac{1}{\rho_L} - \frac{1}{\rho_g}\right) \tag{2.2}$$

where and μ are the liquid surface tension and viscosity, respectively. The van der Waals equation (Eq. 2.3) is used to compute $P(t)$ as (Aissa Dehane, Merouani, & Hamdaoui, 2021a):

$$P(t) = \frac{nR_gT}{V - nb} + \frac{an^2}{V^2} \tag{2.3}$$

where a and b are the Van de Waals constants, R_g is the universal gas constant, $V=4/3(\pi R^3)$ is the bubble volume and T is the temperature within the bubble. The Van der Waals constants, a and b, are given in (Yasui et al., 2016).

The Hertz-Knudsen model (Eq. 2.4) was used for expressing the mass flux $\dot{m}$ of water evaporation and condensation at the bubble interface (Holzfuss, 2005):

$$\dot{m} = \alpha \bar{C}(T_s) \frac{\left[\rho^{sat}_{g,H_2O} - \rho_{g,H_2O}(R)\right]}{4} \tag{2.4}$$

α is the evaporation coefficient, that is, considered constant $\alpha = 0.4$, $\bar{C}$ (T_s)= $\sqrt{8T_sR_g/\pi M_{H_2O}}$ is the average velocity of molecules, $\rho_{g,H_2O}(R)$ is the density of water vapor in the bubble and = 0.0173 Kg m^{-3} is the saturated vapor density. The temperature of the external bubble surface is $Ts = Tliq$.

The heat exchange between the interior and outside of the bubble is estimated by (Toegel & Lohse, 2003):

$$\dot{Q} = 4\pi R^2 \lambda_{mix} \frac{(T_{liq} - T)}{L_{th}} \tag{2.5}$$

$$L_{th} = min\left\{\frac{R}{\pi}, \sqrt{\frac{R\chi}{\dot{R}}}\right\} \tag{2.6}$$

χ and λ_{mix} are the thermal diffusivity and the heat conductivity of the gas mixture, *Lth* is the thickness of the thermal boundary layer. The calculation of these parameters (λmix, χ and *Lth*) is given in (A. Dehane et al., 2021). The temperature (T) inside bubble is calculated by solving the following equation (Yasui, 1995):

$$E = n_{H_2O} \int_0^T C_{v,H_2O}(T)dT + n_{Ar} \int_0^T C_{v,Ar}(T)dT - \frac{an^2}{V} \tag{2.7}$$

where E is the internal energy of the bubble and *C V,H2O (T) (C v,Ar (T))* is the isochoric heat capacity of vapor (Argon) at temperature T, given as a polynomial approximation (expressions are available in (A. Dehane et al., 2021)). The variation of bubble internal energy (ΔE) in time (Δt), due to the pressure work, heat of chemical reactions within the bubble, energy carried by water molecules by evaporation and condensation and heat exchange by diffusion at the interface, is expressed by (Shen et al., 2017; Yasui, 1995):

$$\Delta E = -P(t)\Delta V(t) + 4\pi R^2 \Delta t \frac{\dot{m}}{M_{H_2O}} C_{v,H_2O} + 4\pi R^2 \Delta t \lambda \frac{(T_{liq} - T)}{L_{th}} - \frac{4}{3}\pi R^3 \Delta t \sum_{i=1}^{n} \Delta H_i r_i \tag{2.8}$$

The first term in the right-hand side of Eq. 2.8 is the PV work. The second term is the energy carried by evaporating water molecules from the surrounding liquid into the bubble and by condensing vapor from the bubble into the liquid in Δt. The third term is the energy change due to the thermal conduction. The last term is the heat of chemical reactions taking place inside the bubble during the collapse, where $\Delta H\ i$ and $r\ i$ are the enthalpy change and the rate of the i *th* reaction respectively, that is, their mathematical expressions are given in (A. Dehane et al., 2021).

The outputs of the present model are the bubble wall velocity, evolution of the bubble radius, variation of bubble temperature, pressure and energy all along the bubble oscillation and the variation in time of number of moles of each species housed within the bubble, respectively. The amount of argon remains unchanged during the bubble oscillation (that is, chemically inert). More details are given in (A. Dehane et al., 2021).

The contribution of each of the terms of the internal bubble energy (Eq. 2.8), was calculated for different bubble dynamics model, namely:

1. Model with all energetic terms included, that is, denoted as *normal model*,
2. Model without heat transfer, that is, denoted as $\dot{Q} = 0$
3. Model without mass transfer, that is, denoted as $\dot{m} = 0$
4. Model without reaction heats, that is, denoted as $\Delta H = 0$.

2.3 Energetic evolution of an oscillating bubble

Fig. 2.1 show the contribution of each of the energy parameters (PV work, heat exchange, mass transport and reactions heat) into the global energy balance of the bubble (Eq. 2.8). Simulations data are given for a bubble of $R_0 = 3.2$ µm oscillates in Ar-saturated water under an ultrasound frequency of 355 kHz and an acoustic intensity of 1 W/cm^2. The instantaneous evolutions of these energy parameters are obtained by resolving equations of Table 2.1, whereas the overall internal bubble energy is computed via Eq. 2.8. According to Fig. 2.1, two regimes are observed:

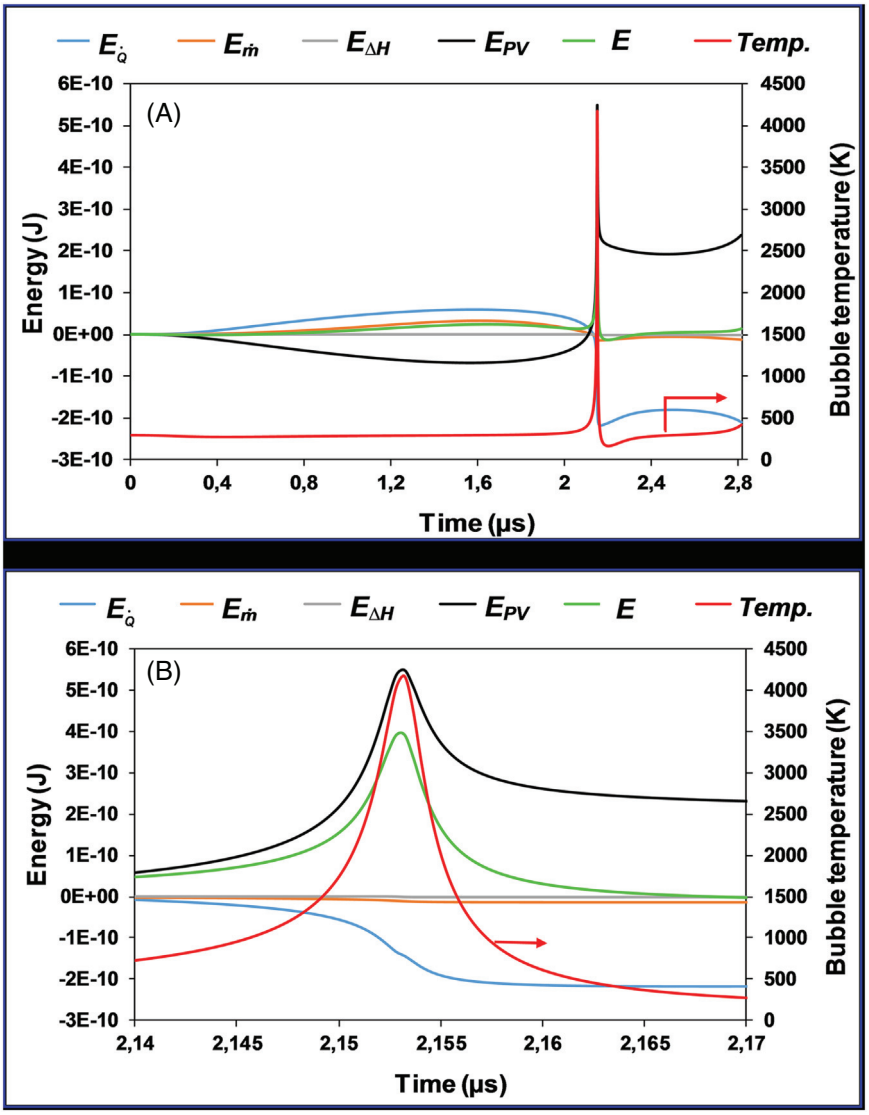

FIGURE 2.1 Instantaneous contribution of each of the energetic parameters (PV work, heat exchange, mass transport and reactions heat) into the internal bubble energy balance. Fig. (B) is an enlarged view of Fig. (A) at around the end of the bubble collapse (t∼2.14-2.14 µs). The ultrasound frequency, the acoustic intensity and the ambient bubble radius are 355 kHz, 1 W/cm^2 and 3.2 µm [53], respectively. The solution temperature and the ambient static pressure are 20°C and 1 atm. The gas atmosphere is argon.: Energy due to heat exchange, $E_{\dot{m}}$: Energy due to mass transport by evaporation/condensation, $E_{\Delta H}$: Energy due to reaction heats, E_{PV}: Energy due to PV work and E: overall internal bubble energy (Eq. 2.8).

Rarefaction phase for t = 0–1.66 µs, during which the internal energy of the bubble goes up due to the carried energy (into the bubble) of the evaporating vapor molecules in addition to the heat flows from the surrounding liquid (T_{liq}) into the bubble ($T<T_{liq}$) by thermal conduction. Some energy is lost through the PV work (expansion of bubble), however, the internal bubble energy is positively affected by the total contribution of each of these energy parameters (mass transport, heat exchange and PV work). No chemical reaction is considered during this phase because the bubble temperature is very low, around 293.15 K. It can be seen that, during the rarefaction phase, the contribution of PV work and heat exchange into the bubble internal energy is greater than that of mass transport.

Collapse phase for t = 1.66–2.153 µs: at this stage, the predominance of PV work, that is, liquid pressure forces applied on the bubble, and heat transfer outside to the bubble on the global evolution of the internal bubble energy is clearly observed compared to the energetical contribution of mass transport via vapor condensation at the bubble wall and endothermal reactions heat. During this phase of compression, the internal energy of the bubble as well as its temperature increase rapidly, due especially to the PV work, where a maximum of 3.91×10^{-10} J and 4167 K are attained at the end of bubble

collapse, that is, t∼2.153 μs. It should be noted that the observed energetical evolutions in Fig. 2.1 are in accordance with those obtained by Yasui (Yasui, 1995), whereas in our case we have added the impact of reactions heat. The observed behaviors during the bubble rarefaction and compression phases (Fig. 2.1) indicate the necessity of more investigations about the impacts of the different energy parameters (*i.e.,* mass transport, heat exchange, PV work, and reactions heat) as functions of acoustical conditions and ambient bubble radii.

2.4 Influence of acoustical conditions

Fig. 2.2 show the power evolutions of the bubble, via the effects of PV work, heat exchange, mass transport and reactions heat, during the expansion and compression phases. These effects are given for model without heat exchange ($\dot{Q} = 0$), model without mass transport ($\dot{m} = 0$) model without reaction heat ($\Delta H = 0$) and normal model (all phenomenon's accounted). The power variations due to each of the energy parameters, in addition to the total power of the bubble, over the expansion (t_e) and compression periods (t_c) are simply calculated as follows:

$$W_i\left(\frac{J}{s}\text{or}\,W\right) = \frac{\Delta E_i\ (J)}{t_e\ \text{or}\ t_c\ (s)} \tag{2.9}$$

where $i = \dot{Q}$, $\dot{m}$, ΔH, PV or 'tot' symbolizes heat transfer, mass transport, reactions heat, PV work or the total power (or energy) of the bubble, respectively. It should be noted that ΔEi is calculated over the whole period of expansion (t_e) or collapse (t_c) phases. The energetic power evolutions are simulated for various ultrasound frequencies (213 to 1000 kHz) under an acoustic intensity of 1 W/cm^2.

Firstly, as it can be seen in Fig. 2.2, for a normal and without reactions heat models, an important contribution of power is observed for heat exchange (positive effect), mass transport (positive effect) and PV work (negative effect) during the rarefaction phase for all ultrasound frequencies (213–1000 kHz). However, it is found that the energetic power participation of mass transport is rapidly decreased with the increase of ultrasound frequency (213 to 1000 kHz) compared to the cases of PV work and heat exchange. For example, for a normal model, the increase of wave frequency from 213 to 1000 kHz decreases the impact of mass transport, heat transfer and PV work from 4.29×10^{-5}, 4.84×10^{-5} and -5.86×10^{-5} W to 4.6×10^{-6}, 2.01×10^{-5} and -2.16×10^{-5} W, respectively. This observation is confirmed even when one of the transfer mechanisms, that is, mass transport or heat exchange, is eliminated for all wave frequencies. This behavior is clearly due to the decrease of the maximum bubble radius due to the increase of the wave frequency, which means that less amount of vapor molecules (and energy) is encapsulated within the bubble during the expansion phase. Interestingly, it is observed that the elimination of mass transport mechanism highly disrupts the energetic power of the bubble compared to heat exchange, whereas this effect is decreased proportionally with the increase of ultrasound frequency. This observation indicates the importance of an accurate choice of the mathematical model simulating mass transfer mechanism, particularly at low frequencies where an important quantity of evaporating water molecules is found at the end of the expansion phase.

Secondly, it is found that during the compression regime (Fig. 2.2), the effects of PV work (positive effect) and heat exchange (negative effect) on the bubble internal energy are clearly dominant compared to those obtained by reactions heat (negative effect) and mass transport (negative effect) for all the used ultrasound frequencies (213–1000 kHz). In addition, the positive impact of PV work on the overall bubble energy balance is very important especially with the gradual decrease of ultrasound frequency from 1000 to 213 kHz. For example, for a normal model, the decrease of ultrasound frequency from 1000 to 213 kHz increases the energy flow of the external pressure forces from 2.81×10^{-4} to 1.81×10^{-3} W (6.44 fold of increase). On the other hand, an important flow of energy is dissipated through thermal conduction (outside the bubble) mechanism compared to mass transport (vapor condensation at the bubble interface) and reactions heat (endothermal character) during the collapse phase. This is corroborated for a model without heat exchange (Fig. 2.2), where the internal energy of the bubble is clearly enhanced by the ignorance of thermal conduction mechanism. Moreover, for all models, the increase of ultrasound frequency reduces the energy variation of the bubble. Therefore, the energy consumption for one cycle is reduced with the increase of ultrasound frequency. For example, for a normal model, the global power of the bubble goes down from 1.05×10^{-3} to 1.32×10^{-4} W, as the wave frequency is increased from 213 to 1000 kHz.

Through analyzing the two phases of bubble lifetime, *i.e.* rarefaction and collapse regimes [Fig. 2.1 and Fig. 2.2], it appears that PV work of the external liquid pressures represents the important energy source contributing to the increase of bubble internal energy, whilst a great part of the bubble internal energy is lost through thermal conduction (outside the bubble) and mass transport (condensation at the bubble wall), where the energy dissipation via thermal conduction is greater than that of vapor condensation. Our findings are in good agreement with those found recently by *Kerboua et al.* (Kaouther Kerboua et al., 2021) for the study of the effect of dual frequency on the stable bubble energy balance. On the other hand,

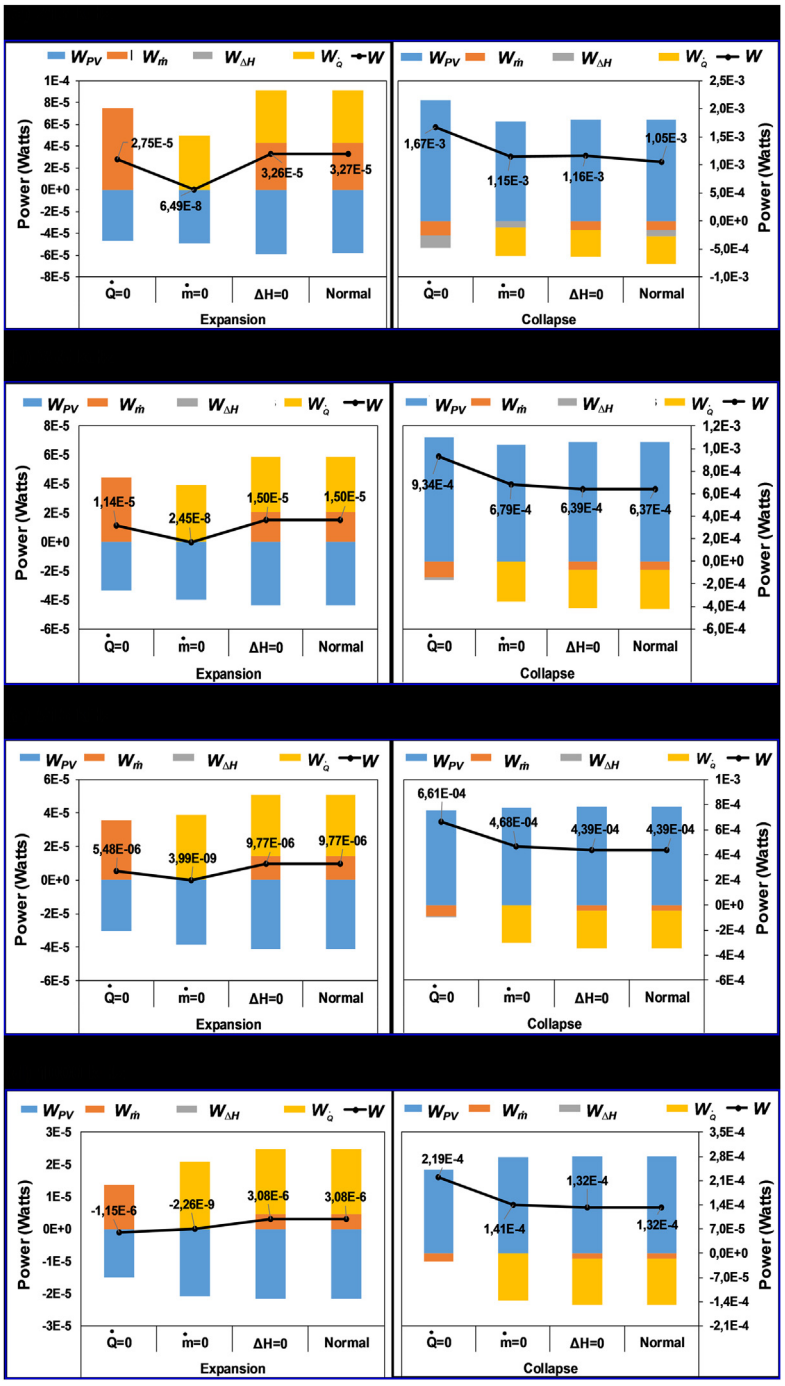

FIGURE 2.2 Power contribution of each of the energy parameters (PV work, heat transfer, mass transport, and reactions heat) into the global bubble energetic power. The contributions are given for various models (normal, without mass transport, without heat exchange, and without reactions heat). The range of ultrasound frequency is from 213 to 1000 kHz. Acoustic intensity is 1 W/cm^2. Ambient bubble radii are 3.9 μm for 213 kHz, 3.2 μm for 355 kHz, 3 μm for 515 kHz, and 2 μm for 1000 kHz.

it has been found that the effects of the different energy parameters (PV work, heat transfer, mass transport and reactions heat) are decreased with the increase of ultrasound frequency. This result is in line with that obtained by *Merouani et al.* (Merouani et al., 2014) through the analyzation of the bubble internal energy under different operational conditions. In contrast, *Vichare et al.* (Vichare et al., 2000) found that in an incompressible medium, the efficiency of cavity is increased with the rise of ultrasound frequency.

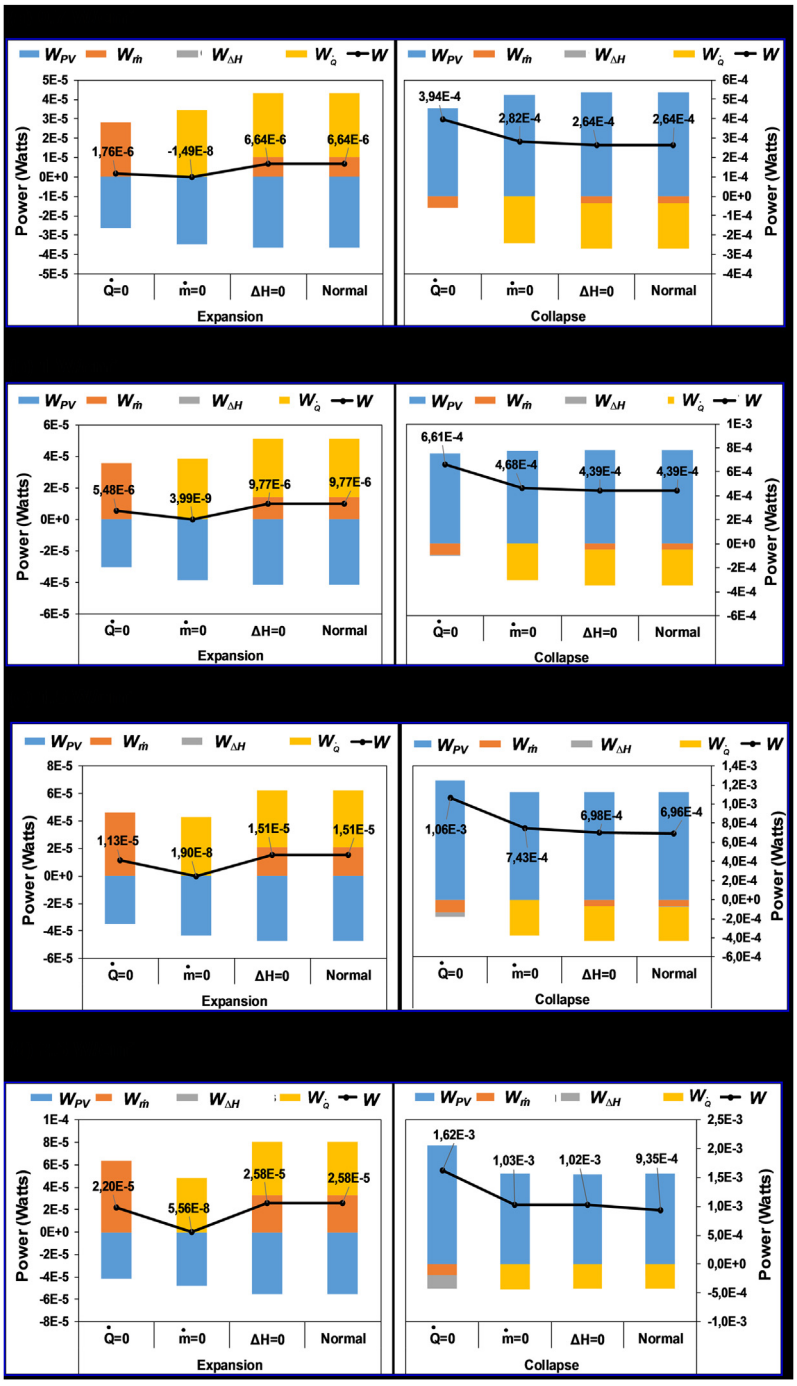

FIGURE 2.3 Power contribution of each of the energy parameters (PV work, heat transfer, mass transport and reactions heat) into the global bubble energetic power. The contributions are given for various models (normal, without mass transport, without heat exchange and without reactions heat). The acoustic intensity ranges from 0.7 to 2.5 W/cm^2 for an ultrasound frequency of 515 kHz ($R_0 = 3$ μm).

The same trends retrieved for the ultrasound frequency case were observed with the increase of acoustic intensity (0.7–2.5 W/cm^2) for a wave frequency of 515 kHz, as stated in Fig. 2.3, where the effects of the different energy parameters (mass transport, heat exchange, reactions heat and PV work) are increased proportionally with the rise of acoustic intensity. Similarly to the case of ultrasound frequency (Fig. 2.2), it can be seen through Fig. 2.3 that the major energetic input during bubble lifetime is the PV work received by acoustic bubble from the surrounding liquid. On the other hand, an important

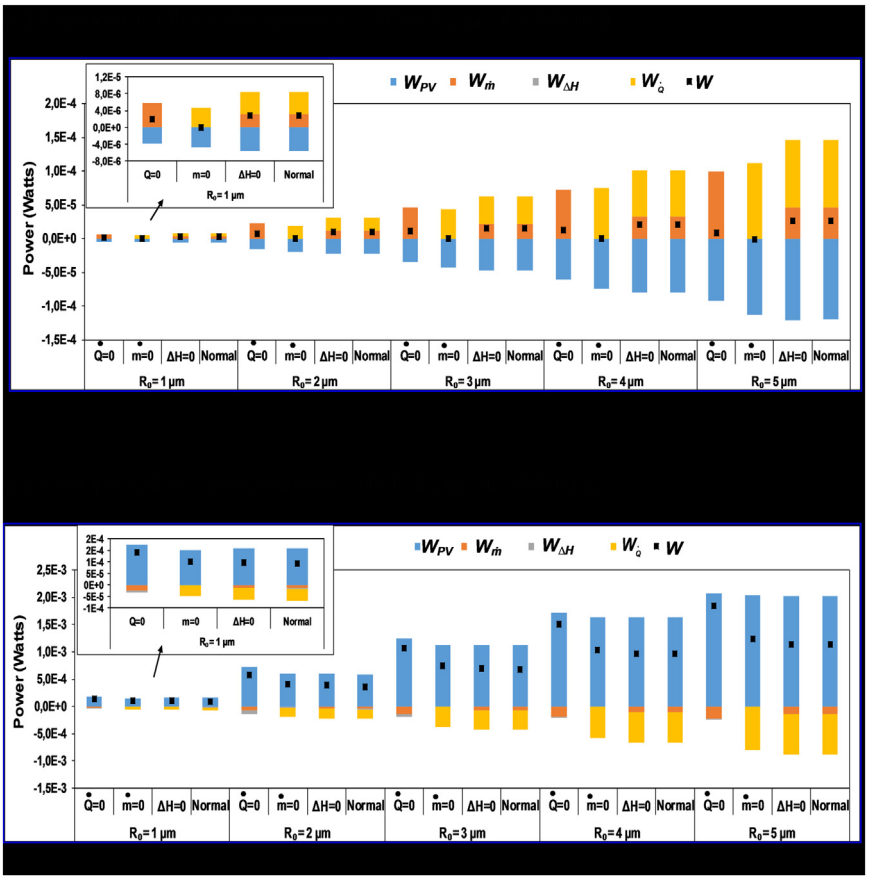

FIGURE 2.4 Power contribution of each of the energy parameters (PV work, heat transfer, mass transport and reactions heat) into the global bubble energetic power. The contributions are given for various models (normal, without mass transport, without heat exchange and without reactions heat) over a range of ambient bubble radii (from 1 to 5 µm) for (A) the expansion and (B) the compression regimes. The ultrasound frequency and acoustic intensity are 515 kHz and 1.5 W/cm^2, respectively ($R_0 = 3$ µm).

amount of energy is lost by thermal conduction (outside the bubble) and mass transport (condensation of vapor at the bubble interface), whereas the effect of thermal conduction is greater than that of mass transport.

2.5 Energy analysis as function of initial bubble size

This section aims to show the energy evolutions of the different energetic parameters for a range of initial bubble radii. All the previous analyses were done for single values of ambient bubble radius (R_0) representing the mean radii of the bubbles population, retrieved experimentally by *Brotchie et al.* (Brotchie et al., 2009) for different frequencies. However, in reality this is not the true situation, because, bubbles population in acoustic field is an interval rather than a single value; the statement which is well proven experimentally through several technics (Brotchie et al., 2009, 2010; Burdin et al., 1999; Labouret & Frohly, 2002; Thiemann et al., 2011; Tsochatzidis et al., 2001) and theoretically through different models (Brotchie et al., 2009, 2010; Burdin et al., 1999; Labouret & Frohly, 2002; Merouani et al., 2013, 2016; Thiemann et al., 2011; Tsochatzidis et al., 2001; Yasui et al., 2008). Therefore, it is of great important to state the impact of the initial ambient bubble radius on the contribution of PV work, heat transfer, mass transport and reaction heat in the overall internal bubble energy throughout the rarefaction and the collapse of bubble.

In Fig. 2.4, the energy flow of PV work, heat transfer, mass transport and reactions heat (in addition to the bubble power variation) are shown for various ambient bubble radii for an ultrasound frequency of 515 kHz and an acoustic intensity $I_n = 1.5$ W/cm^2. These evolutions are shown for a range of R_0 from 1 to 5 µm for which the molar production of the bubble is greater than the threshold limit of 3.22×10^{-22} mol (Merouani et al., 2013; Yasui et al., 2008).

As it can be seen, during the expansion phase (Fig. 2.4A), the energy variation due to the PV work (negative effect) and heat exchange (positive effect) is greater than that of mass transport (positive effect) with the exception of the model

without heat transfer in which energy flow due to the mass transport is ≈ PV work. During this rarefaction phase, it is clearly observed that the overall bubble power is not highly influenced, that is, compared to the compression phase (Fig. 2.4B), by the energy flows resulting from the different energetic parameters. The important point that can be inferred from Fig. 2.4A is the increase of energy consumption (over the expansion phase) with the increase of the ambient bubble radius. During the collapse regime, Fig. 2.4B, the positive effect of PV work on the overall bubble energy balance is clearly dominant compared to that of heat exchange (negative impact), whereas, the negative effect of reactions heat (endothermic character) is the lowest. On the other hand, it is observed from Fig. 2.4B that the global energy of the bubble is highly affected by the evolution of the different energy parameters, where the energy consumption per collapse is increased proportionally with the increase of ambient bubble radius.

2.6 Conclusion

In this chapter, a theoretical analysis is conducted for an energetical assessment of the effects of the different energy parameters, that is, are PV work, heat transfer, mass transport and chemical reactions heat, influencing the maximal bubble temperature as well as the cavity sonoactivity. In general, it has been demonstrated that the effect of these energetic parameters is decreased proportionally with the increase of ultrasound frequency or if acoustic intensity or ambient bubble radius are reduced. Therefore, the energy consumption, per expansion or collapse, of the bubble is increased proportionally with the decrease of ultrasound frequency or if the acoustic intensity or ambient bubble radius are increased. In addition, it has been corroborated that for all cases of ultrasound frequency, acoustic intensity or ambient bubble radius variation, the effects of PV work and thermal conduction are greater than those of mass transport and reactions heat during expansion and compression phases. On the other hand, it was found that during the bubble lifetime, the PV work of the surrounding liquid represents the major energetic input for the overall bubble energy balance, whereas, an important energy is dissipated through thermal conduction outside the bubble and mass transport via vapor condensation at the bubble wall. However, the effect of thermal exchange outside the bubble is greater than that of mass transport.

Acknowledgments

This research. was funded by Algeria's Ministry of Education. and Science Research, as well as the General. Directorate for Scientific. Research and Technological. Development (GD-SRTD) (project No. A16N01UN250320220002).

References

Adewuyi, Y.G., 2001. Sonochemistry: environmental science and engineering applications. Ind. Eng. Chem. Res. 40 (22), 4681–4715. https://doi.org/10.1021/ie010096l.

Asakura, Y., Nishida, T., Matsuoka, T., Koda, S., 2008. Effects of ultrasonic frequency and liquid height on sonochemical efficiency of large-scale sonochemical reactors. Ultrason. Sonochem. 15 (3), 244–250. https://doi.org/10.1016/j.ultsonch.2007.03.012.

Brotchie, A., Grieser, F., Ashokkumar, M., 2009. Effect of power and frequency on bubble-size distributions in acoustic cavitation. Phys. Rev. Lett. 102 (8). https://doi.org/10.1103/PhysRevLett.102.084302.

Brotchie, A., Statham, T., Zhou, M., Dharmarathne, L., Grieser, F., Ashokkumar, M., 2010. Acoustic bubble sizes, coalescence, and sonochemical activity in aqueous electrolyte solutions saturated with different gases. Langmuir 26 (15), 12690–12695. https://doi.org/10.1021/la1017104.

Burdin, F., Tsochatzidis, N.A., Guiraud, P., Wilhelm, A.M., Delmas, H., 1999. Characterisation of the acoustic cavitation cloud by two laser techniques. Ultrasonics Sonochemistry, 6, pp. 43–51. https://doi.org/10.1016/S1350-4177(98)00035-2.

Chadi, N.E., Merouani, S., Hamdaoui, O., Bouhelassa, M., 2018. New aspect of the effect of liquid temperature on sonochemical degradation of nonvolatile organic pollutants in aqueous media. Sep. Purif. Technol. 200, 68–74. https://doi.org/10.1016/j.seppur.2018.01.047.

Dehane, A., Merouani, S., Hamdaoui, O., Alghyamah, A., 2021. A complete analysis of the effects of transfer phenomenons and reaction heats on sono-hydrogen production from reacting bubbles: Impact of ambient bubble size. Int. J. Hydrogen Energy 46 (36), 18767–18779. https://doi.org/10.1016/j.ijhydene.2021.03.069.

Dehane, A., Merouani, S., Hamdaoui, O., 2021a. Carbon tetrachloride (CCl4) sonochemistry: a comprehensive mechanistic and kinetics analysis elucidating how CCl4 pyrolysis improves the sonolytic degradation of nonvolatile organic contaminants. Sep. Purif. Technol. 275, 118614. https://doi.org/10.1016/j.seppur.2021.118614.

Dehane, A., Merouani, S., Hamdaoui, O., 2021b. Theoretical investigation of the effect of ambient pressure on bubble sonochemistry: special focus on hydrogen and reactive radicals production. Chem. Phys. 547, 111171. https://doi.org/10.1016/j.chemphys.2021.111171.

Dehane, A., Merouani, S., Hamdaoui, O., Alghyamah, A., 2021a. A comprehensive numerical analysis of heat and mass transfer phenomenons during cavitation sono-process. Ultrason. Sonochem. 73, 105498. https://doi.org/10.1016/j.ultsonch.2021.105498.

Dehane, A., Merouani, S., Hamdaoui, O., Alghyamah, A., 2021b. Insight into the impact of excluding mass transport, heat exchange and chemical reactions heat on the sonochemical bubble yield: Bubble size-dependency. Ultrason. Sonochem. 73, 105511. https://doi.org/10.1016/j.ultsonch.2021.105511.

Gondrexon, N., Renaudin, V., Boldo, P., Gonthier, Y., Bernis, A., Pettier, C., 1997. Degassing effect and gas-liquid transfer in a high frequency sonochemical reactor. Chem. Eng. J. 66 (1), 21–26. https://doi.org/10.1016/s1385-8947(96)03124-5.

Henglein, A., 1995. Chemical effects of continuous and pulsed ultrasound in aqueous solutions. Ultrasonics - Sonochemistry 2 (2), S115–S121. https://doi.org/10.1016/1350-4177(95)00022-X.

Holzfuss, J., 2005. Unstable diffusion and chemical dissociation of a single sonoluminescing bubble. Physical Review E - Statistical, Nonlinear, and Soft Matter Physics 71 (2). https://doi.org/10.1103/PhysRevE.71.026304.

Kerabchi, N., Merouani, S., Hamdaoui, O., 2018a. Depth effect on the inertial collapse of cavitation bubble under ultrasound: special emphasis on the role of the wave attenuation. Ultrason. Sonochem. 48, 136–150. https://doi.org/10.1016/j.ultsonch.2018.05.004.

Kerabchi, N., Merouani, S., Hamdaoui, O., 2018b. Liquid depth effect on the acoustic generation of hydroxyl radical for large scale sonochemical reactors. Sep. Purif. Technol. 206, 118–130. https://doi.org/10.1016/j.seppur.2018.05.039.

Kerabchi, N., Merouani, S., Hamdaoui, O., 2019. Relationship between liquid depth and the acoustic generation of hydrogen: design aspect for large cavitational reactors with special focus on the role of the wave attenuation. Int. J. Green Energy 16 (6), 423–434. https://doi.org/10.1080/15435075.2019.1577741.

Kerboua, K., Hamdaoui, O., 2017. Computational study of state equation effect on single acoustic cavitation bubble's phenomenon. Ultrason. Sonochem. 38, 174–188. https://doi.org/10.1016/j.ultsonch.2017.03.005.

Kerboua, K., Hamdaoui, O., 2019. Void fraction, number density of acoustic cavitation bubbles, and acoustic frequency: a numerical investigation. J. Acoust. Soc. Am. 146 (4), 2240–2252. https://doi.org/10.1121/1.5126865.

Kerboua, K., Hamdaoui, O., Alghyamah, A., 2021. Energy balance of high-energy stable acoustic cavitation within dual-frequency sonochemical reactor. Ultrason. Sonochem. 73, 105471. https://doi.org/10.1016/j.ultsonch.2021.105471.

Koda, S., Kimura, T., Kondo, T., Mitome, H., 2003. A standard method to calibrate sonochemical efficiency of an individual reaction system. Ultrason. Sonochem. 10 (3), 149–156. https://doi.org/10.1016/S1350-4177(03)00084-1.

Kuijpers, M.W.A., Kemmere, M.F., Keurentjes, J.T.F., 2002. Calorimetric study of the energy efficiency for ultrasound-induced radical formation. In Ultrasonics 40 (1–8), 675–678. Vol.Issues https://doi.org/10.1016/S0041-624X(02)00197-X .

Labouret, S., Frohly, J., 2002. Bubble size distribution estimation via void rate dissipation in gas saturated liquid. Application to ultrasonic cavitation bubble fields. EPJ Applied Physics 19 (1), 39–54. https://doi.org/10.1051/epjap:2002047.

Löning, J.M., Horst, C., Hoffmann, U., 2002. Investigations on the energy conversion in sonochemical processes. Ultrason. Sonochem. 9 (3), 169–179. https://doi.org/10.1016/S1350-4177(01)00113-4.

Mark, G., Tauber, A., Laupert, R., Schuchmann, H.-P., Dorothea, S., Mues, A., Von Sonntaga, C., 1998. OH-radical formation by ultrasound in aqueous solution-Part II: Terephthalate and Fricke dosimetry and the influence of various conditions on the sonolytic yield. Ultrason. Sonochem 5, 41–52. https://doi.org/10.1016/S1350-4177(98)00012-1.

Merouani, S., Hamdaoui, O., Rezgui, Y., Guemini, M., 2016. Computational engineering study of hydrogen production via ultrasonic cavitation in water. Int. J. Hydrogen Energy 41 (2), 832–844. https://doi.org/10.1016/j.ijhydene.2015.11.058.

Merouani, S., Hamdaoui, O., Rezgui, Y., Guemini, M., 2015. Computer simulation of chemical reactions occurring in collapsing acoustical bubble: dependence of free radicals production on operational conditions. Res. Chem. Intermed. 41 (2), 881–897. https://doi.org/10.1007/s11164-013-1240-y.

Merouani, S., Hamdaoui, O., Rezgui, Y., Guemini, M., 2013. Effects of ultrasound frequency and acoustic amplitude on the size of sonochemically active bubbles-Theoretical study. Ultrason. Sonochem. 20 (3), 815–819. https://doi.org/10.1016/j.ultsonch.2012.10.015.

Merouani, S., Hamdaoui, O., Rezgui, Y., Guemini, M., 2014. Energy analysis during acoustic bubble oscillations: relationship between bubble energy and sonochemical parameters. Ultrasonics 54 (1), 227–232. https://doi.org/10.1016/j.ultras.2013.04.014.

Merouani, S., Hamdaoui, O., Saoudi, F., Chiha, M., 2010. Influence of experimental parameters on sonochemistry dosimetries: KI oxidation, Fricke reaction and H_2O_2 production. J. Hazard. Mater. 178 (1–3), 1007–1014. https://doi.org/10.1016/j.jhazmat.2010.02.039.

Ono, Y., Shinashi, K., Tanaka, H., Harada, H., 2019. Mechanism of improving the rate of sono-oxidation of a KI solution by introduction of CO_2 into an Ar atmosphere. Ultrason. Sonochem. 51, 145–150. https://doi.org/10.1016/j.ultsonch.2018.10.033.

Pang, Y.L., Abdullah, A.Z., Bhatia, S., 2011. Review on sonochemical methods in the presence of catalysts and chemical additives for treatment of organic pollutants in wastewater. Desalination 277 (1–3), 1–14. https://doi.org/10.1016/j.desal.2011.04.049.

Petrier, C., Francony, A., 1997. Incidence of wave-frequency on the reaction rates during ultrasonic wastewater treatment. Water Sci. Technol. 35, 17–180. https://doi.org/10.1016/S0273-1223(97)00023-1.

Pokhrel, N., Vabbina, P.K., Pala, N., 2016. Sonochemistry: science and Engineering. Ultrasonics Sonochemistry, 29, 104–128. https://doi.org/10.1016/j.ultsonch.2015.07.023.

Sathishkumar, P., Mangalaraja, R.V., Anandan, S., 2016. Review on the recent improvements in sonochemical and combined sonochemical oxidation processes - a powerful tool for destruction of environmental contaminants. Renewable Sustainable Energy Rev. 55, 426–454. https://doi.org/10.1016/j.rser.2015.10.139.

Shen, Y., Yasui, K., Zhu, T., Ashokkumar, M., 2017. A model for the effect of bulk liquid viscosity on cavitation bubble dynamics. Phys. Chem. Chem. Phys. 19 (31), 20635–20640. https://doi.org/10.1039/c7cp03194g.

Son, Y., Lim, M., Ashokkumar, M., Khim, J., 2011. Geometric optimization of sonoreactors for the enhancement of sonochemical activity. J. Phys. Chem. C 115 (10), 4096–4103. https://doi.org/10.1021/jp110319y.

Son, Y., Lim, M., Khim, J., 2009. Investigation of acoustic cavitation energy in a large-scale sonoreactor. Ultrason. Sonochem. 16 (4), 552–556. https://doi.org/10.1016/j.ultsonch.2008.12.004.

Son, Y., Lim, M., Park, I.B., Khim, J., 2008. Analysis of the ultrasonic cavitation energy in a pilot-scale sonoreactor. Japan. J. Appl. Phys. 47 (5), 4119–4122. https://doi.org/10.1143/JJAP.47.4119.

Thiemann, A., Nowak, T., Mettin, R., Holsteyns, F., Lippert, A., 2011. Characterization of an acoustic cavitation bubble structure at 230 kHz. Ultrason. Sonochem. 18 (2), 595–600. https://doi.org/10.1016/j.ultsonch.2010.10.004.

Thompson, L.H., Doraiswamy, L.K., 1999. Sonochemistry: science and engineering. Ind. Eng. Chem. Res. 38 (4), 1215–1249. https://doi.org/10.1021/ie9804172.

Toegel, R., Lohse, D., 2003. Phase diagrams for sonoluminescing bubbles: a comparison between experiment and theory. J. Chem. Phys. 118 (4), 1863–1875. https://doi.org/10.1063/1.1531610.

Toma, M., Fukutomi, S., Asakura, Y., Koda, S., 2011. A calorimetric study of energy conversion efficiency of a sonochemical reactor at 500 kHz for organic solvents. Ultrason. Sonochem. 18 (1), 197–208. https://doi.org/10.1016/j.ultsonch.2010.05.005.

Tsochatzidis, N.A., Guiraud, P., Wilhelm, A.M., Delmas, H., 2001. Determination of velocity, size and concentration of ultrasonic cavitation bubbles by the phase-Doppler technique. Chem. Eng. Sci. 56 (5), 1831–1840. https://doi.org/10.1016/S0009-2509(00)00460-7.

Verhaagen, B., Liu, Y., Pérez, A.G., Castro-Hernandez, E., Fernandez Rivas, D., 2016. Scaled–up sonochemical microreactor with increased efficiency and reproducibility. ChemistrySelect 1 (2), 136–139. https://doi.org/10.1002/slct.201600023.

Vichare, N.P., Senthilkumar, P., Moholkar, V.S., Gogate, P.R., Pandit, A.B., 2000. Energy analysis in acoustic cavitation. Ind. Eng. Chem. Res. 39 (5), 1480–1486. https://doi.org/10.1021/ie9906159.

Wei, H., Shi, J., Yang, X., Wang, J., Li, K., He, Q., 2018. CCl_4-Enhanced ultrasonic irradiation for ciprofloxacin degradation and antibiotic activity. Water Environ. Res. 90 (7), 579–588. https://doi.org/10.2175/106143017X15131012153077.

Wood, R.J., Lee, J., Bussemaker, M.J., 2017. A parametric review of sonochemistry: control and augmentation of sonochemical activity in aqueous solutions. Ultrason. Sonochem. 38, 351–370. https://doi.org/10.1016/j.ultsonch.2017.03.030.

Yasui, K., 1995. Effects of thermal conduction on bubble dynamics near the sonoluminescence threshold. J. Acoust. Soc. Am. 98 (5), 2772–2782. https://doi.org/10.1121/1.413242.

Yasui, K., Tuziuti, T., Kanematsu, W., 2016. Extreme conditions in a dissolving air nanobubble. Phys. Rev. E 94 (1). https://doi.org/10.1103/PhysRevE.94.013106.

Yasui, K., Tuziuti, T., Kozuka, T., Towata, A., Iida, Y., 2007. Relationship between the bubble temperature and main oxidant created inside an air bubble under ultrasound. J. Chem. Phys. 127 (15). https://doi.org/10.1063/1.2790420.

Yasui, K., Tuziuti, T., Lee, J., Kozuka, T., Towata, A., Iida, Y., 2008. The range of ambient radius for an active bubble in sonoluminescence and sonochemical reactions. J. Chem. Phys. 128 (18). https://doi.org/10.1063/1.2919119.

Chapter 3

Physical effects and associated energy release

Imen Hasaounia, Djihane Mazouz and Kaouther Kerboua
Higher School of Industrial Technologies, Department of Engineering, Annaba, Algeria

3.1 Introduction

Acoustic cavitation is the result of precursor studies that dealt first with the hydraulic or hydrodynamic cavitation (Shah et al., 1999), that is, cavitation provoked by local depression in a liquid flow. Hydrodynamic cavitation was first mentioned by Leonhard Euler in 1754. This was 150 years before it became important in ship propellers, turbines, pumps, and hydrofoils. In 1895, Thornycroft and Barnaby observed that the propeller of their submarine became pitted and eroded over a relatively short operation period. The observed erosion was the result of intense pressure and temperature gradients in the local vicinity, generated during the collapse of hydrodynamic cavitation bubbles. In 1917, Lord Rayleigh published the first mathematical model describing a cavitation event in an incompressible fluid. Acoustic cavitation showed up in connection with high-intensity underwater sound projectors in the late 1920s (Shah et al., 1999), specifically in 1927, when Loomis reported the first chemical and biological effects of ultrasound, and since then, Scientifics recognized that acoustic cavitation can be a useful tool in chemical reaction processes. One of the first applications reported in the literature was the use of ultrasound induced cavitation to degrade a biological polymer. In this context, Brohult first described the ultrasonic degradation of a biological polymer in 1937, which initiated the studies of Schmid, who carried out the first experiments of ultrasonic degradation with synthetic polymers (Henglein, 1987).

With the advancement of the applications of ultrasound, the interest in the modelling of the acoustic cavitation evolved. After the first mathematical model published by Lord Rayleigh in 1917, further numerical integrations have been carried out by several investigators, namely Gilmore, Hunter, Hickling, and Plesset. In 1949, Plesset first applied the equation to the problem of traveling cavitation bubbles. However, when the bubble contains some noncondensable gas or when thermal effects become important, the solution becomes more complex since the pressure in the bubble is no longer constant. Under these circumstances, it was necessary to find some way of incorporating the effects of liquid compressibility in a modified version of the Rayleigh-Plesset equation. The first modifications were proposed by Noltingk and Prostsky, followed by Keller and Kolodner, who included the effects of acoustic radiation by treating the surrounding liquid as slightly compressible (Keller & Miksis, 1980). The oscillations of a bubble in a compressible liquid have concisely been studied by Keller and Miksis in 1980 (Shah et al., 1999). Keller and Miksis proposed a radial equation suitable for describing large-amplitude forced oscillations, incorporating the effects of acoustic radiation by the bubble and using the approximation of a linear polytropic index (Leighton & Apfel, 1994). Keller-Miksis equation is currently the most used equation to fairly represent all the effects existing during the cavitation. The Keller-Miksis equation has been further modified to include the dynamics of a thin flexible shell encapsulating the bubble, to model an ultrasound contrast agent, and to include the effects of multiple bubbles (Pandey, 2019).

The increasing scientific interest in sonoprocessing opened the doors to several applications of acoustic cavitation bubble and presented them as promising solutions, particularly as novel alternatives for the production of polymer, enhancement of chemical reactions, emulsification of oils and degradation of chemical or biological pollutants. The advantage of using acoustic cavitation for these applications is that much more mild operating conditions are utilized in comparison to conventional techniques and many reactions which may require toxic reagents or solvents are not necessary (Leong et al., 2011). The oscillation and collapse of cavitation bubbles, particularly driven at low ultrasonic frequencies, can also generate strong shear forces, microjets, microstreaming and shockwaves.

Energy Aspects of Acoustic Cavitation and Sonochemistry: Fundamentals and Engineering. DOI: https://doi.org/10.1016/B978-0-323-91937-1.00018-9
Copyright © 2022 Elsevier Inc. All rights reserved.

In terms of the physical and chemical involved phenomena, strong collapse is the most interesting but also the most challenging aspect of bubble dynamics. It is the key to many (if not all) acoustic cavitation applications. When the spherical bubble is more and more excited, the accelerated movement of the bubble wall almost instantly reverses from the expansion movement to the collapse peak, radiating a highly concentrated energy to the surrounding (M. R. Luo, 2020).

The physical effects of ultrasound can be generally summarized as increased turbulence throughout the medium, with the strongest effects occuring in the vicinity of the system's boundaries and interfaces (Bermúdez-aguirre et al., 2011). The physical effects of cavitation have been found useful in the generation of highly viscoelastic micelles, deactivating pathogens in wastewater, cleaning of surfaces by ultrasonics or with cavitating jets, dispersing particles in a liquid medium, producing emulsions, and limitating flowrates in confined flows due to the development of supercavities (Yusof et al., 2016).

Acoustic cavitation leads to different physical effects. If a bubble develops in the vicinity of a solid particle larger than the resonance size of the bubble, the bubble will be deformed from its sphericity at the last instant of collapse due to the deflected environment. This asymmetry causes the bubbles to burst unevenly and form a fast-moving fluid stream, that is, microjets. The micro-jet moves towards the solid particles and causes deformation of the surface or changes in the chemical composition of the surface.

When the solid particles in the mixture are smaller than the resonance size of the bubbles, the shockwave generated by the acoustic cavitation can cause collisions between the particles. In addition, the shockwaves directly interact with the solid particles, which results in their fragmentation. Particle collisions and acoustic fragmentation affect the average particle size and particle size distribution by reducing the size of the existing crystals and creating secondary nucleation sites (Kim & Suslick, 2018).

Viscous stress in the boundary layer of the bubble near a wall or an object, regardless of the position of the standing wave, causes vortex flow. When the length scale of the flow caused by viscous stress in the vicinity of an object such as a bubble is much smaller than the acoustic wavelength, it is called microstreaming. This phenomenon occurs not only around a bubble, but also around a solid particle, but it is much larger around a bubble (Yasui, 2017).

Overall, at the instant of the strong collapse, the high pressure inside the collapsing bubbles is suddenly released into the liquid medium, producing shockwaves that are needed, for instance, to enhance mass transfer and shear-induced processes, as well as microjets of impressive impacts on solid surfaces. Besides, the sonication of the liquid is accompanied of an instantaneous mechanical effect on liquid particles known as the acoustic streaming, while the oscillation of the walls of acoustic cavitation bubbles generates in the surrounding liquid a microscopic vibration known as microstreaming (Yusoft et al., 2016).

The present chapter presents the fundamentals of the propagation of acoustic wave in the liquid and the formation, growth and collapse of acoustic cavitation bubbles. It then discusses qualitatively the physical effects accompanying sonication and acoustic cavitation, either during oscillation or harsh collapse, and describes numerically the acoustic streaming, microstreaming, microjets and shockwave considering the distance from the bubble wall and the variation of the acoustic intensity and frequency. The physical effects are quantitatively described based on the pressures and forces they exert, their velocities and their associated energies and powers.

3.2 The theoretical approach of the propagation of an acoustic wave in a liquid medium, and acoustic streaming

3.2.1 Propagation of an ultrasonic wave in a liquid medium

An acoustic wave is a propagation of pressure oscillation with sound velocity in a medium such as liquid, gas, or solid.

Ultrasounds are longitudinal acoustic waves with frequencies falling below the limit of human hearing, that is, beyond 20 kHz. The ultrasonic wave can be fairly modelled as a sinusoidal wave inducing successive positive and negative pressures into the liquid medium as shown in Eq. 3.1.

$$P_w(t) = -P_A \sin(2\pi f t) \tag{3.1}$$

During the rarefaction phase of the ultrasonic wave, instantaneous local pressures in the liquid become negative when the acoustic pressure amplitude is larger than the ambient pressure. In contrast, the compression phase of the wave creates over-pressure in the liquid medium.

3.2.2 Acoustic streaming

3.2.2.1 Mechanism of acoustic streaming

When a liquid medium is irradiated with ultrasound, the immediate consequence is acoustic streaming. This large-scale streaming refers to the regular oscillatory motion of the fluid volume elements with a time independent flow velocity due to the second-order of the nonlinear acoustic wave propagation occurring when the acoustic wave propagates through the liquid medium. Acoustic streaming can be viewed as time-independant physical forces of the sound waves that provide a driving force capable of displacing ions and small molecules (Marshall & Wu, 2015). Acoustic streaming can have an extremely complex pattern, with linear and nonlinear interactions between the cavitation bubbles and with the microstreaming associated with the microbubbles occurring at the small scale. Junru Wu (Wu, 2018) exposed in a recent review of acoustic streaming and its applications the detailed theoretical background behind the acoustic streaming.

There are mainly two types of acoustic streaming, namely, Eckart streaming and Rayleigh streaming (X. Luo et al., 2018). One is accelerating direct current fluid flow in the direction of the acoustic traveling wave propagation. This is caused by the attenuation of the acoustic traveling wave mainly resulting of the viscosity of the fluid. Due to attenuation, an unbalance of radiation forces is created since the radiation pressure pushing a fluid parcel becomes stronger than that pulling it. This causes the accelerating fluid flow which is called Eckart streaming (Bjørnø, 2017). The second type of acoustic streaming is a vortex-like streaming caused by viscous stress at the boundary layer near a wall or an object regardless of the situation of a traveling or standing wave. This type is known as Rayleigh streaming (Yasui, 2017).

Large scale acoustic streaming plays a significant role in enhancing heat and mass transfer processes in the liquid but also around solid surfaces. Indeed, the acoustic streaming patterns around solid objects are believed to be the strongest within a few millimeters distance from the solid surface. This boundary layer effect around a solid surface is important and quite interesting in several applications, because it is usually such boundary layers that offer the greatest resistance to both heat and mass transfers. The surface effects of large-scale acoustic streaming are also important in emulsification, where interfacial turbulence is associated with droplet formation and nebulization. The acoustic streaming effects cause a fountain structure to form at the air/water interface from which microdroplets are ejected (M. R. Luo, 2020).

3.2.2.2 Numerical modeling of the acoustic streaming

acoustic streaming is the direct consequence of the passage of an ultrasonic wave across the water. Acoustic streaming is represented as a steady oscillatory motion of the fluid volume elements with time-independent flow velocity, due to the second-order of nonlinear acoustic wave propagation. In a recent paper by Junru Wu (Wu, 2018), the author described the detailed theoretical background of the formation of acoustic streaming. In the acoustic streaming, the environment receives the kinetic energy from the acoustic waves, the particles in the receiving medium are then carried away by the acoustical radiation pressure from the acoustic wave (Sato & Fujii, 1998). As an illustrative application, by employing acoustic flow in a convenient pattern, liquids in a covered bottle can be thoroughly mixed in a highly efficient manner. The application and development of this kind of mixer would minimize the potential risks linked to the processing of dangerous chemical or biological materials and radioactive isotopes (Suri et al., 2002).

At microscopic scale, Markham (Markham, 1952) proved between 1951 and 1952 that streaming is caused by the absorption and relaxation processes of sound. In principle, steady streaming happens in all the fields of acoustic radiation, as a function of the shape of the field and the characteristics of the medium, and grows till it decreases in intensity through beam divergence or through relaxation of the medium (Nowicki et al., 1997). In the case of a sinusoidal acoustic wave travelling across a liquid medium, the liquid particles undergo a local displacement under the effect of the oscillating wave, the maximum velocity of the liquid particles is given by Eq. 3.2 (Nowicki et al., 1997).

$$v = \left(8\,\alpha_0\, I_0\, a^2\right)/\mu c \tag{3.2}$$

In this equation, a_0 represent the absorption or attenuation coefficient, it is expressed in the travelled medium by Eq. 3.3.

$$\alpha_0 = \left(b\,\omega^2\right)/\left(2\rho\, c^3\right) \tag{3.3}$$

a represents the radius of the ultrasonic projector, and ω is the angular frequency, given in Eq. 3.4.

$$\omega = 2\pi f \tag{3.4}$$

The acoustic intensity is related to the acoustic amplitude through Eq. 3.5 (Kerboua et al., 2021).

$$I_0 = {P_A}^2/2\rho c \tag{3.5}$$

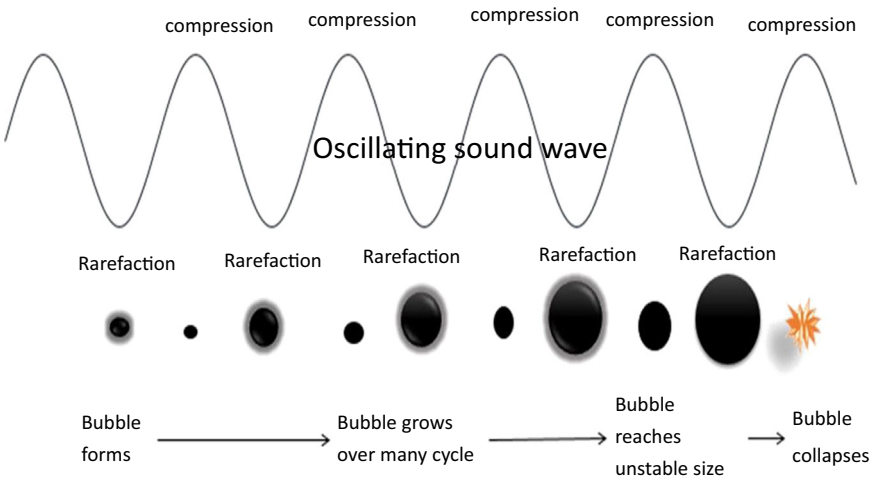

FIGURE 3.1 Graphical summary of the event of bubble formation, bubble growth, and subsequent collapse over several acoustic cycles. A bubble oscillates in phase with the applied sound wave, contracting during compression and expanding during rarefactions. Reproduced from (Leong et al., 2011).

b is a function of the dilatational and shear viscosities; it is given by Eq. 3.6 (Zarembo, 1971).

$$b = \frac{4}{3}\eta + \eta^{\circ} \tag{3.6}$$

$\eta\circ$ represents the dilatational viscosity, it equals for water at 298 K almost 2.4×10^{-3} kg.m^{-1}.s^{-1} while η represents the shear viscosity, which equals 1×10^{-3} kg.m^{-1}.s^{-1} at the same conditions.

The maximum kinetic energy acquired by the liquid particles due to acoustic streaming is then expressed by Eq. 3.7.

$$E = \frac{1}{2} m_p v^2 \tag{3.7}$$

3.3 The theoretical approach of the oscillation of acoustic cavitation bubbles and its associated physical effects

Owing to the high oscillating frequency of liquid molecules in an ultrasonic field and the high viscosity of the liquid medium compared with a gas, liquid molecules absorb a large amount of energy from the propagation of the ultrasonic waves. The high energy absorption of liquid molecules and high acoustic pressure make it possible for the ultrasonic field to overcome intermolecular interactions in a solvent, and produce numerous cavities starting from existing gaseous germs, which is referred to as acoustic cavitation.

3.3.1 The energetic mechanism of bubble inception, oscillation, and collapse

In practice, weaknesses in a liquid medium can typically occur in two forms. (1) Homogeneous nucleation, induced by the thermal motions within the liquid, which form temporary microscopic voids that constitute nuclei. (2) Heterogeneous nucleation that explains the major weaknesses occurring in a liquid medium, and manifesting at the boundary between the liquid and a solid phase or between the liquid and small particles suspended in the liquid (Jena, 1965).

3.3.1.1 Homogeneous nucleation theory

We present here a brief and simplified version of homogeneous nucleation theory. Acoustic cavitation, concisely defined as the formation, growth, and collapse of microbubbles within an aqueous solution, results from pressure fluctuations that occur in the liquid medium irradiated by an acoustic field in the range of ultrasounds, with the appropriate value of frequency and amplitude. The formed cavities drain and accumulate ultrasonic energy, and explosively release their energy by the collapse of cavities (J. Luo et al., 2014). The event of a collapsing bubble, illustrated in Fig. 3.1, is a microscopic implosion accompanied of a significant increase of temperature and pressure of up to thousand Kelvin and hundred Bar (Leong et al., 2011).

The ultrasonic wave propagates from ultrasonic generator, transducer, horn and radiation rod to liquid, causing medium molecules vibration. The average distance between molecules decreases in the acoustic compression phase, while it increases in the rarefaction phase. In pure liquid, cavitation occurs when the liquid additional negative pressure reaches a critical value, whose magnitude is called the cavitation threshold (Carrillo-Lopez et al., 2017).

In the case of pure liquid, the relation between the exterior pressure P exerted on the bubble wall of radius R and the interior pressure P_B is given in Eq. 3.8.

$$P_B - P = 2\sigma/R \tag{3.8}$$

The concept of surface energy can be prolonged to bubbles or gaps of some intermolecular distances. This approximation was demonstrated to be of good accuracy by Skripov (Brennen, 2013).

With the condition of temperature uniformity, and if the bubble contains only vapor, the interior pressure will equal the saturated vapor pressure P_v (T). Nonetheless, the exterior liquid pressure must be less than the vapor pressure so that the equilibrium condition is verified. This leads to Eq. 3.9.

$$P = P_v - 2\sigma/R \tag{3.9}$$

Thus, if the exterior liquid pressure is decreased below $P_v - 2\sigma/R$, the radius of the bubble increases, and the excess pressure arises leading to rupture. Accordingly, if the maximum size of the vacancy is R_c, then the tensile strength of the liquid is expressed as shown in Eq 3.10.

$$\Delta P_c = 2\sigma/R_c \tag{3.10}$$

Eq. 3.10 is the first basic relation that makes up the homogeneous nucleation theory. The second expression we need to mention relates to the excess of energy that must be deposited in the body of pure liquid in order to create a nucleus or microbubble of critical size R_c. Assuming that the critical nucleus is in thermal equilibrium with its surroundings after its creation, then the energy that must be brought to the medium consists of two parts. Firstly, the required energy to maintain the surface of the bubble. Secondly, the work of pressure forces exerted by the fluid to create the bubble. Thus, the net energy that must be deposited to form a bubble (Brennen, 1995a) is given in Eq. 3.11.

$$W_{CR} = 4\pi R_C^2 \sigma - 4/3\pi R_C^3 \Delta P_C \tag{3.11}$$

In fact, cavities are formed when adequately large negative pressure is applied to the liquid so that the average distance between the molecules exceeds the critical molecular distance required to hold the liquid intact. However, considering a surface tension of 0.05 $\frac{kg}{s^2}$ and an comparable to the intermolecular distance estimated at 10^{-10} m, the resulting negative pressure to apply will be in the order of 10000 bar according to Eq. 3.10. Another example is that of the creation of a microscopic cavity-void with a radius of barely 0.4 nm in water, the minimum required negative pressure is estimated at 1400 atm. In both previous cases, in order to attain the critical distance, a huge energy is needed according to Eq. 3.11.

Nonetheless, what makes it easier in the case of acoustic cavitation is the presence of gaseous impurities, which dramatically reduces the tensile strength and consequently the required negative pressure. This has been proved by experiments on tensile strength. These experiments consist of degassing a very pure liquid in a freshly formed capillary tube under vacuum conditions. Heating the tube causes the liquid to expand, filling the tube to a certain high temperature and pressure. Using steel tubes, it was not possible to cope with the increased stress observed in glass tubes. Thus, it was clear from the data that the tensile strength is a function of the contamination of the liquid and the nature of the surface it contains (Brennen, 2013).

3.3.1.2 Heterogeneous nucleation theory

In the case of homogeneous nucleation, microscopic voids of radius R grow causing a rupture in the fluid as soon as the pressure in the liquid is reduced below the critical value.

However, heterogeneous nucleation occurs in a heterogenous phase, for instance at a solid-liquid interface. It is important to note that, at the microscopic level, the surfaces of solids are not flat, so we must consider the implications of the local surface geometries. Thus, considering the range of microscopic surface geometries, it is not at all surprising that vapor pockets develop in some surface cavities at near vapor pressures, especially when the surface is hydrophobic (Brennen, 2013). Some specific sites on a solid surface will have the optimal geometry to enhance the growth and the apparition of vapor bubbles at the macroscopic scale. These sites are called nucleation sites. Moreover, it is clear that the lower the pressure, the more the sites become able to generate and release bubbles in the body of the liquid (Brennen, 1995b).

Thus, the acoustic cavitation event is explained by a sound wave imposing a sinusoidally varying pressure upon existing cavities in solution, namely gaseous impurities. In the rarefaction phase of the ultrasonic wave, instantaneous local pressures

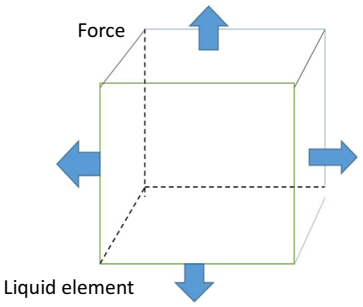

FIGURE 3.2 Negative pressure. Reproduced from (Yasui, 2017).

in liquid become negative when the acoustic pressure amplitude is larger than the ambient pressure, that is, 101325 Pa. Negative pressure is possible only in liquids or solids, and impossible in gases. This is the "force" to expand a liquid element as shown in Fig. 3.2. Consequently, gases dissolved in the liquid appear as gas bubbles because gases can no longer be dissolved in the liquid under negative pressures (Yasui, 2017). During the negative pressure cycle, the liquid is pulled apart at sites containing such a gaseous impurity, which are known as "weak spots" in the fluid. The number of bubbles that are produced during this rarefaction cycle is proportional to the density of such weak spots present in the fluid (Leong et al., 2011).

3.3.1.3 Bubble Nuclei and Blake threshold

At ambient temperature, the theoretical tensile strength is about 1000 atm. This indicates that a sound wave utilized to provoke cavitation should have a pressure amplitude in the order of 1000 atm. However, cavitation is observed with a pressure amplitude of about 1 atm, implying that pre-existing nuclei or sites for nucleation and the growth of bubbles assist cavitation. The most evident nucleus to take into account is the spherical bubble saturated with a mix of liquid-vapor or any gas dissolved in the liquid. Notwithstanding the physical fact that the bubble never reaches stability, we progress with a hypothesis of equilibrium. Neglecting vapor pressure, we obtain Eq. 3.12.

$$P_g = P_0 + 2\sigma/R_0 \tag{3.12}$$

Now rearranging Eq. 3.12 we obtain Eq. 3.13.

$$R_0 = 2\sigma/\left(P_g - P_0\right) \tag{3.13}$$

Let us call this value of R the critical radius R_c for stability, this leads to Eq. 3.14.

$$R_c = 2\sigma/\left(P_g - P_0\right) \tag{3.14}$$

This condition becomes unstable for $R \neq R_c$. The surface tension term predominates and the bubble contracts if $R < R_c$, and the gas pressure predominates and the bubble expands indefinitely if $R > R_c$. A bubble may be destabilized through several processes, such as rise due to buoyancy, dissolution due to diffusion of gas outside the bubble, contraction due to surface tension and growth due to gas pressure.

For the growth of the bubble of the radius R_B, a minimum pressure amplitude of the acoustic wave denoted as P_A is necessary, it can be reached with the following assumptions:

(1) the bubble is in a state of unstable equilibrium.
(2) The bubble is rising slowly and dissolving.

Following Neppiras (Neppiras, 1980), Neppiras and Noltingk (Neppiras & Noltingk, 1951) and Blake (Shah et al., 1999), we note that if the bubble is in equilibrium, then the pressure inside it must be ($P_0 + 2\sigma\ R_B$) at $t = 0$. At $t>0$, the change in the size of the bubble can be assumed to be the result of the application of ultrasound and the new equilibrium condition is given in Eq. 3.15.

$$(P_0 + 2\sigma/R_B)(R_B/R)^3 = P_0 - P_A + 2\sigma/R \tag{3.15}$$

On the right, P_A represents the maximum negative acoustic pressure. The term on the left describes the gas pressure in the bubble due to isothermal expansion. The minimum value of the acoustic pressure required to achieve steady bubble

growth can be obtained by differentiating the pressure compared to the bubble radius as shown in Eq. 3.16.

$$\partial(P_A - P_0)/\partial R = 0 \tag{3.16}$$

This leads to Eq. 3.17.

$$P_A - P_0 = \frac{4\sigma}{3R^*} \tag{3.17}$$

Where R^* is given in Eq. 3.18

$$R^* = \sqrt{\left(3R_B^3(P_0 + 2\sigma/R_B)\right)/2\sigma} \tag{3.18}$$

R^* is named the critical radius. By solving Eq. 3.18 for P_A as a function of the initial bubble size, we find out P_B which is called the Blake's threshold pressure (Leighton & Apfel, 1994), and given in Eq. 3.19.

$$P_B = P_0 + \frac{8\sigma}{9}\left[\frac{3\sigma}{2(P_0 + 2\sigma/R_B)R_B^3}\right]^{1/2} \tag{3.19}$$

On approximation, when $\left(\frac{2\sigma}{R_B}\right) \gg P_0$ this gives Eq. 3.20.

$$P_B = P_0 + 0.77(\sigma/R_B) \tag{3.20}$$

And when $P_0 \gg \left(\frac{2\sigma}{R_B}\right)$, Eq. 3.21 is retrieved.

$$P_B = P_0 + \frac{8\sigma}{9}\left[3\sigma/\left(2P_0R_B^3\right)\right]^{0.5} \tag{3.21}$$

R_B is the minimum radius of the bubble expected to grow. A major limitation to the application of this equation is that it can only be applied to quasi-static processes since it has neglected inertial and viscous effects. Still, it can be used on systems where the frequency of the applied sound field is much lower than the natural oscillation frequency of the bubble. The earlier procedure is the basic procedure for determining the pressure threshold required for the steady growth of the bubble. We then retain the following general form of the Blake threshold, presented in Eq. 3.22, that should be respected when selecting the acoustic and equilibrium conditions in order to deal with acoustic cavitation bubbles (Ye & Zhu, 2017).

$$P_B = P_0 - P_v + \frac{2}{3}\left[\frac{(2\sigma/R_0)^3}{3((P_0 - P_v + 2\sigma)/R_0)}\right]^{0.5} \tag{3.22}$$

3.3.1.4 Cavitation types and expected effects

Two principal types of cavitation exist: vaporous and gaseous. The first type, vaporous cavitation, refers to a boiling process that happens when the bubble grows in an explosive way and without limit, including that the liquid turns to vapor quickly. This occurs in the case that the pressure level is less than the vapor pressure of the liquid. The second type is gaseous cavitation. This type appears when a liquid contains noncondensable gas, so as gas cavitation occurs through diffusion process. Gas cavitation is much slower than vapor cavitation that occurs in microseconds, this time depends on the degree of convection (fluid flow). Speaking about the expected effects, cavitation wears only occur under vaporous cavitation conditions favored by the low frequency as shown in Fig. 3.3, the surface could be eroded because of shockwaves and microjet. Cavitation wear is also known as cavitation erosion, vapor cavitation, cavitation pitting, cavitation fatigue, liquid impact erosion, and wire drawing. At the opposite, gaseous cavitation does not cause erosion, however, it creates noise, generates high temperatures (even cracking at the molecular level), and degrades the chemical composition of the fluid through oxidation.

Table 3.1 shows the types of cavitation and their main effects, specifying the frequency range of each type.

3.3.1.5 Growth of the bubble

The bubbles created by cavitation will begin to expand and collapse under the influence of the acoustic field. The expansion/collapse cycle imitating the acoustic wave can thus be sinusoidal. However, for certain bubble sizes and acoustic pressures, the expansion phase is prolonged and accompanied by a violent collapse that reduces the bubbles to a smaller size. This is called inertial cavitation. This mode of bubble oscillation can continue for up to a hundred acoustic cycles, which is called stable or repetitive transient cavitation. On the other hand, bubbles grow and collapse dramatically within a

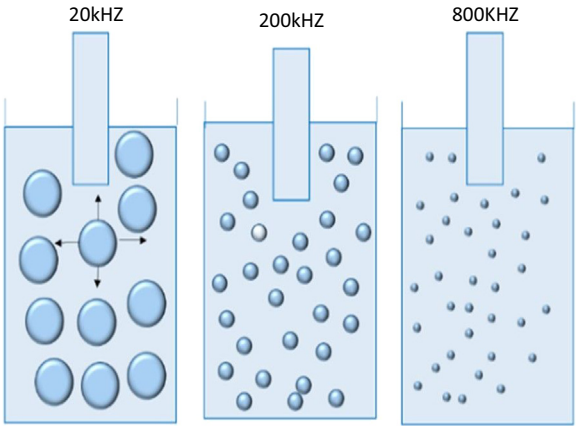

FIGURE 3.3 Influence of frequency on the number of diameters of the cavitation bubbles reproduced from (Carrillo-Lopez et al., 2017).

TABLE 3.1 Broad classification of ultrasound frequencies and their major effect, defining the nature of the formed acoustic cavitation bubble (Bhaskaracharya et al., 2009).

Classification	Frequency range	Major effects	Nature of bubble
Low frequency high power	20–100 kHz	Physical effect (e.g.: shear; streamers; etc.)	Vaporous bubble
Intermediate frequency medium power	100 kHz–1 MHz	Free radical formation and sonochemistry	Gaseous bubble
High frequency low power	1–10 MHz	Diagnostic applications	Gaseous bubble

few acoustic cycles, and the collapsed bubble then disintegrates into a mass of smaller bubbles when the acoustic amplitude is higher (Bermúdez-aguirre et al., 2011). These daughter bubbles are often small and collapse rapidly so that the original bubble is annihilated (Bermúdez-aguirre et al., 2011). This phenomenon is called unstable or transient cavitation and is usually observed at low frequencies (20–100 kHz). Besides, the mass transfer boundary layer is thinner and the interfacial area is larger during bubble expansion than during bubble collapse. This means that the amount of air transferred into the bubble during the expansion phase is greater than the amount of air that exits during the collapse. This leads to the growth of larger bubbles over a very large number of acoustic cycles in a process called rectified diffusion (Bermúdez-aguirre et al., 2011).

That's said, the rectified diffusion and the coalescence of bubbles are the two mechanisms of bubble growth in acoustic cavitation. There are two mechanisms that drive the coalescence of bubbles, the first one is the attractive radiation force between the bubbles called secondary Bjerknes force. The other consists of pushing the active bubbles toward the pressure antinode of a standing wave field, called the primary Bjerknes force. The rate of bubble growth depends strongly on acoustic amplitude and frequency. For instance, with a very weak driving amplitude such as 0.2 bar at 20 kHz, the bubble growth rate is in the order of a few mm per 100 s for the initial radius of 35 mm (Crum, 1980). For a much more powerful driving amplitude, such as 2 bars at 30 kHz, it varies from 10 to a few hundred mm per second depending on the initial radius (Louisnard & Gomez, 2003). In addition, the growth speed decreases when the ultrasonic frequency increases for the same sound pressure amplitude. Among the both mechanisms, bubble coalescence may be the main mechanism for bubble growth, after the full onset of acoustic cavitation, however, during the initial development of acoustic cavitation, rectified scattering may be the main mechanism because the coalescence rate is proportional to the square of the bubble number density, which is expected to be low in the initial stage of acoustic cavitation (Pankaj & Ashokkumar, 2011). The thresholds for Blake nucleation, rectified diffusion, and transient cavitation are shown in Table 3.2.

3.3.1.6 Dynamics of bubble oscillation

As sound travels through a gas, regions will be compressed, and others undergo rarefaction. The gas in such regions will tend to be heated and cooled respectively (Leighton & Apfel, 1994). The average distance between molecules decreases in the acoustic compression phase, while it increases in the rarefaction phase. In pure liquid, cavitation will occur when

TABLE 3.2 Summary of cavitation thresholds (Apfel, 1981).

Thresholds	Expression
"Blake" nucleation threshold, P_B for bubble of radius R_B	$P_B/P_0 = 1 + \frac{4}{9}X_B[(3X_B)/(4(1+X_B))]^{0.5}$ Where $X_B = \frac{2}{p_{oR_B}}$
Threshold for rectified diffusion, P_D for bubble of radius R_D	$P_D/P_0 = \frac{[3\gamma(1+X_D) - X_D]\left[1-(f/f_D)^2\right]}{[6(1+X_D)]^{0.5}[1-C+X_D]^{-0.5}}$ Where $X_D = \frac{2\sigma}{p_{0\,R_D}}$
Transient threshold P_T, inversely as threshold bubble radius, R_T as a function of P	$R_T = \frac{0.13}{f}\left(\frac{P_0}{\rho}\right)^{1/2}\left[\frac{p-1}{\sqrt{p}}\left(1+\frac{2}{3}(p-1)\right)^{1/3}\right]$ for $p \le 11$ $R_T = \frac{0.3}{f}\left(\frac{P_0}{\rho}\right)^{1/2}\left(\frac{2}{3}(p-1)\right)^{1/2}$ for $p \ge 11$ Where $p = \frac{P_T}{P_0}$

the liquid additional negative pressure reaches a critical value, whose magnitude is called cavitation threshold (Carrillo-Lopez et al., 2017). The tiny nuclei in the liquid undergo growth, expansion, compression and collapse under the alternating action of ultrasonic positive and negative pressure phases (Ye & Zhu, 2017). The expansion of the bubble is assumed as quasi-isothermal and its compression is considered as quasi-adiabatic (Ferkous et al., 2017).

In the rarefaction phase of the ultrasonic wave, the local instantaneous pressures in the liquid become negative as the amplitude of the acoustic pressure is higher than ambient pressure. Many small bubbles expand during this phase as the pressure applied on the bubble wall is greater than the pressure of the liquid at a distance from the bubble. During the compression phase of the ultrasonic wave, some of the bubbles violently collapse generating extreme conditions of temperature and pressure of up to thousand Kelvin, and hundred Bar (Leong et al., 2011), a release of heat energy and a high local turbulence (Tuziuti et al., 2018). The elevated temperatures in the vicinity of the collapsing bubble, known as "hot spots", can activate chemical mechanisms particularly characterized by the formation of free radicals (Leong et al., 2011), while the local turbulence and the abrupt release of concentrated localized energy induce several physical effects (K. Kerboua & Hamdaoui, 2021) of mechanical nature such as mass transfer and surface erosion (Bermúdez-aguirre et al., 2011).

3.3.2 The physical effects associated with acoustic cavitation bubbles

Overall, at the instant of the strong collapse, the high pressure inside the collapsing bubbles is suddenly released into the liquid medium, producing shockwaves that are needed for instance to enhance mass transfer and shear-induced processes, as well as microjets of impressive impacts on solid surfaces. Besides, the sonication of the liquid is accompanied by an instantaneous mechanical effect on liquid particles known as acoustic streaming, while the oscillation of the walls of acoustic cavitation bubbles generates in the surrounding liquid a microscopic vibration known as microstreaming (Yusof et al., 2016).

The present section deals with all the aforementioned physical effects accompanying sonication and acoustic cavitation bubble oscillation and collapse. The chapter presents the numerical modeling of the acoustic streaming, microstreaming, microjets, and shockwaves considering the distance from the bubble wall and the variation of the acoustic intensity and frequency. The physical effects are quantitatively described in terms of the pressures and forces they exert, their velocities, and their associated energies and powers. The expected results are interpreted from a mechanistic point of view and the chapter is finalized with a conclusion that summarizes the most important results.

3.3.2.1 Microjet

Small nuclei in the liquid are subjected to growth, expansion, compression and collapse under the action of alternating positive and negative phases of ultrasonic pressure. By the end of the collapse phase, bubble collapsing near a solid wall loses its sphericity. This instant knows the apparition of micro-jets directed towards the side of the bubble away from the wall. A change of the shape of the bubble occurs, from the original approximate sphere to a slender shape and then flattened. Finally, the microjet breaks the bubble wall near the solid and impacts towards it, which results in cavitation damage of the solid wall. Since the collapse of the bubble process is extremely complex and random, micro-jet crash speed is difficult to

calculate. Plesset and Chapmann (Ye & Zhu, 2017) obtained the following micro-jet velocity estimation formula.

$$v = 8.97\left(\frac{R+d}{R}\right)^2\sqrt{\frac{P_0 - P_v}{\rho}} \tag{3.23}$$

where d is the distance between the bubble wall and the solid wall, and P_0 is the pressure in the liquid medium. Due to the additional ultrasound pressure in the liquid, $P_0 = P_\infty + P_A \sin(\omega t)$.

The pressure due to microjet and applied on the wall of a fictive sphere surrounding the bubble at a distance d from the bubble wall is given in Eq. 3.24.

$$P = \frac{\rho v^2}{2} \tag{3.24}$$

3.3.2.2 Microstreaming

The "microstreaming" term is usually used for streaming liquid around a pulsating bubble. The microstreaming occurs not only around a bubble but also around a solid particle. However, it is much more significant around a bubble because its speed is proportional to the square of the speed of vibration of the object. The speed of microstreaming around a pulsating bubble is 10^2–10^6 times larger than that around a solid particle, because it is of the order of $\frac{u^2}{\omega\alpha}$.

The radial speed of microstreaming at each instant of the collapse phase at a distance d from the bubble wall, also known as the microstreaming velocity, is given in Eq. 3.25.

$$U = {R^2\dot{R}}/{(R+d)}^2 \tag{3.25}$$

The maximum value of the shear pressure the microstreaming applies on an abject at the distance d from the bubble wall is expressed in Eq. 3.26.

$$P = \frac{1}{27}\rho\left({\mu}/{\pi\rho f}\right)^{1/2}\frac{1}{(R+d)^4}\left(2R^3\dot{R}^2 + R^4\ddot{R}\right) \tag{3.26}$$

Energy engaged instantaneously in the process of shearing of a surface located at a fictive sphere surrounding the bubble at a distance d from the bubble wall is written in Eq. 3.27.

$$E = \int_R^{R+d} -PdV \tag{3.27}$$

Eq. 3.28 represents the mathematical formula to calculate the power engaged instantaneously in the process of shearing of a surface located at a distance d from the bubble wall.

$$\dot{E} = \frac{dE}{dt} \tag{3.28}$$

3.3.2.3 Shockwave

At the end of the violent collapse, the inwardly liquid flow stops when the internal pressure inside the bubble increases dramatically as the density within the bubble almost reaches that of the condensed phase. Therefore, a spherical shockwave is emitted from the bubble in the liquid. When the shockwave hits agglomerates of nanoparticles, they can be disintegrated by the transmitted energy. This is one of the main mechanisms of the nanoparticle dispersion by the ultrasonic irradiation. Shockwaves radiated by cavitation bubbles were observed through both optical and acoustic methods (Bermúdez-aguirre et al., 2011).

The Mach number M is described as the fluid velocity divided by the speed of sound. As the shockwave is defined as the propagation of a discontinuous pressure in a medium, when a shockwave is propagating in homogeneous medium in steady state, the upstream velocity of the fluid is typically superior to the speed of sound according to the Rankine-Hugoniot relations. Nevertheless, generally, a shockwave might be emitted even when the Mach number is lower than 1, this is the case when a shockwave is emitted by a bubble during its collapse (M. R. Luo, 2020). Therefore, we suggest estimating the evolution of the Mach number and the forces resulting from the emitted shockwave. The Mach number is expressed as shown in Eq. 3.29:

$$M = \frac{\dot{R}}{c} \tag{3.29}$$

The energy of a spherical shockwave E is estimated by Eqs.3.30:

$$E = \frac{4\pi r^2}{\rho c} \int P^2 dt \tag{3.30}$$

The radiated pressure accompanying the emission of the shockwave is estimated by Eqs.3.31:

$$P = \frac{\rho}{r}\left(R^2\ddot{R} + 2\dot{R}^2 R\right) \tag{3.31}$$

By replacing Eq. 3.31 in Eq. 3.30 and derivating it, the power associated with the emission of the shockwave is expressed as follows (Yasui et al., 2011).

$$\dot{E} = \frac{4\pi\rho}{c}\left(R^2\ddot{R} + 2\dot{R}^2 R\right)^2 \tag{3.32}$$

3.4 Energetic outcomes: Macroscopic dissipation of acoustic energy

Regardless of the mechanism for dissipation of acoustic energy, be it steady streaming, cavitation microstreaming, micro jetting, shockwaves, or sonochemical activity, the energy is ultimately converted into heat.

The measurement of the acoustic power absorbed in a volume of liquid is a current and important problem that has not been solved yet. To determine the efficiency of erosion, emulsification, sonochemical processes, etc... under the action of ultrasound, the acoustic energy introduced and absorbed in the liquid volume is required. The measurement of the radiation pressure in a small volume of liquid (Henglein, 1987) may give erroneous results under the action of multiple refractions of the ultrasonic waves. All these drawbacks are absent using the calorimetric method. The main assumption of this method is that all the absorbed acoustic energy is transformed into heat. Therefore, it is not necessary to know the value of the acoustic resistance of the bubbling liquid, the conversion coefficient of the transducer, etc (Suslick et al., 1984). Nonetheless, the use of the calorimetric technique may lead to underestimated values due to heat loss to the environment, including reactor walls, transducers, and air. In general, the calorimetric method of measuring the energy supplied to a medium is based on the assumption that acoustic energy is converted to thermal energy and that the temperature in the bulk liquid is uniform (Toma et al., 2011). It is well known that heat generation by ultrasonic irradiation is due mainly to the attenuation/absorption of sound in the medium (Cheeke & Zagzebski, 2004), (Sanderson, 2004). However, it has been shown that calorimetric data are compromised by high viscosity media and insufficient convection (Löning et al., 2002; Toma et al., 2011).

Researchers have suggested a modified calorimetric method, cavitation energy measurement, to understand the contribution of cavitational heat generation to total heat generation using air-saturated (cavitation) and degassed (noncavitation) liquids (Son et al., 2012).

It is also known that the intensity of the cavitation field is under the strong influence of the physical and chemical properties of the host solvent, the processing conditions, and the characteristics of the ultrasonic irradiation (Hua & Hoffmann, 1997). Vapor pressure is an important property that controls cavitational activity in solvents (Suslick et al., 1984; Toma et al., 2011). The intensity of cavitation is obviously related to the acoustic power, and the increase in ultrasonic power entering the reaction is associated with an increase in the cavitational effect in the system (Toma et al., 2011).

3.5 Conclusion

The present work explored the fundamentals of sonication and acoustic cavitation bubble and their related physical effects, as well as their implication in the energetic characteristics of the acoustic cavitation bubble, particularly at the collapse, through the dynamics of bubble oscillation, the velocity of the bubble wall, the acoustic conditions and the vaporous/gaseous nature of the bubble at the beginning of the collapse.

Theoretically, several studies proposed numerical models to simulate the cavitation bubble growth based on various assumptions and different approaches. The inclusion of the nonequilibrium of evaporation and condensation at the bubble interface plays a significant role in the study of the physical effects related to the acoustic cavitation bubble and is primordial for a consistent link between the nature of the collapsing bubble and the expected effect.

Throughout the present chapter, the modelling of the physical effects related to sonication and acoustic cavitation bubble was presented in terms of velocities, forces, pressures, powers and energies.

The velocity of the liquid particles driven by the acoustic streaming is in proportional relationship with the increasing intensity and frequency. Energetically speaking, the acoustic energy conversion into effective cavitational energy is increased by the decrease of the frequency, which is equivalent to harsher physical effects observed at low frequencies.

The energy due to the microstreaming is equivalent to the kinetic energy acquired by the liquid particles around the oscillating bubble. This energy remains in the order of the nanojoules per cycle and per bubble.

The microjet is characterized by a very high pressure exerted on the solid wall it hits, this pressure is of the order of hundreds of bars, that's why this effect is often associated with the deformation observed on solid materials in sonicated liquids.

The modeling of the shockwave demonstrates that it irradiates a pressure that increases when the frequency decreases and the intensity increases. This energy is of the order of 10^{-5} J per cycle and per bubble. According to the value of the Mach number at the instant of the collapse, the shockwave would be able to reach a certain distance from the bubble wall, beyond which its effect will be considered as completely attenuated.

References

Apfel, R.E., 1981. Acoustic cavitation. https://doi.org/10.1016/S0076-695X(08)60338-5 Methods Exp. Phys. 19, 355–411.

Bermúdez-aguirre, D., Mobbs, T., & Barbosa-cánovas, G.V. (2011). Ultrasound technologies for food and bioprocessing 65–105. https://doi.org/10.1007/978-1-4419-7472-3.

Bhaskaracharya, R.K., Kentish, S., Ashokkumar, M., 2009. Selected applications of ultrasonics in food processing. Food Eng. Rev. 1, 31–49. doi:https://doi.org/10.1007/s12393-009-9003-7.

Bjørnø, Leif, 2017. Finite-amplitude waves. Applied Underwater Acoustics. Elsevier, Taastrup, Denmark, pp. 857–888. https://doi.org/10.1016/B978-0-12-811240-3.00013-8.

Brennen, C.E., 2013. Cavitation and bubble dynamics. Cavitation and Bubble Dynamics. Cambridge University Press, Cambridge, pp. 1–249. https://doi.org/10.1017/CBO9781107338760.

Brennen, C.E. (1995a). Cavitation and bubble dynamics.

Brennen, C.E. (1995b). Cavitation and bubble dynamics.

Carrillo-Lopez, L.M., Alarcon-Rojo, A.D., Luna-Rodriguez, L., Reyes-Villagrana, R., 2017. Modification of food systems by ultrasound. J. Food Qual. 2017. https://doi.org/10.1155/2017/5794931.

Cheeke, J.D., Zagzebski, J., 2004. Fundamentals and applications of ultrasonic waves. Am. J. Phys. 719. https://doi.org/10.1119/1.1645288.

Crum, L.A., 1980. Measurements of the growth of air bubbles by rectified diffusion. J. Acoust. Soc. Am. 68 (1), 203–211. https://doi.org/10.1121/1.384624.

Ferkous, H., Merouani, S., Hamdaoui, O., Pétrier, C., 2017. Persulfate-enhanced sonochemical degradation of naphthol blue black in water: evidence of sulfate radical formation. Ultrason. Sonochem. 34, 580–587. https://doi.org/10.1016/j.ultsonch.2016.06.027.

Henglein, A., 1987. Sonochemistry: Historical developments and modern aspects. Ultrasonics 25 (1), 6–16. https://doi.org/10.1016/0041-624X(87)90003-5.

Hua, I., Hoffmann, M.R., 1997. Optimization of ultrasonic irradiation as an advanced oxidation technology. Environ. Sci. Technol. 31 (8), 2237–2243. https://doi.org/10.1021/es960717f.

Introduction the Main Features of Cavitating Flows (Vol. 76, pp. 1–14). (n.d.). Springer Science and Business Media LLC. https://doi.org/10.1007/1-4020-2233-6_1.

Jena, F. (1965). Sonochemistry of selected hydrocarbons, sulfur-containing and nitrogen-containing organic compounds in aqueous solutions and nonaqueous liquids dissertation.

Keller, J.B., Miksis, M., 1980. Bubble oscillations of large amplitude. J. Acoust. Soc. Am. 68 (2), 628–633. https://doi.org/10.1121/1.384720.

Kerboua, K., Hamdaoui, O., 2021. Sonochemistry for water remediation: toward an up-scaled continuous technology. Remediation Technologies, Vol. 2. Scrivener Publishing LLC, Massachusetts, USA, pp. 437–468.

Kerboua, K., Hamdaoui, O., Alghyamah, A., 2021. Acoustic frequency and optimum sonochemical production at single and multi-bubble scales: a modeling answer to the scaling dilemma. Ultrason. Sonochem. 70, 105341. https://doi.org/10.1016/j.ultsonch.2020.105341.

Kim, H.N., Suslick, K.S., 2018. The effects of ultrasound on crystals: sonocrystallization and sonofragmentation. cryst. 8 (7). https://doi.org/10.3390/cryst8070280.

Leighton, T.G., Apfel, R.E., 1994. The Acoustic Bubble. J. Acoust. Soc. Am. 2616. https://doi.org/10.1121/1.410082.

Leong, T., Ashokkumar, M., Sandra, K., 2011. The fundamentals of power ultrasound - a review. Acoust. Aust. 39 (2), 54–63.

Löning, J.M., Horst, C., Hoffmann, U., 2002. Investigations on the energy conversion in sonochemical processes. Ultrason. Sonochem. 9 (3), 169–179. https://doi.org/10.1016/S1350-4177(01)00113-4.

Louisnard, O., Gomez, F., 2003. Growth by rectified diffusion of strongly acoustically forced gas bubbles in nearly saturated liquids. Physical Review E - Statistical Physics, Plasmas, Fluids, and Related Interdisciplinary Topics 67 (3), 12. https://doi.org/10.1103/PhysRevE.67.036610.

Luo, J., Fang, Z., Smith, R.L., 2014. Ultrasound-enhanced conversion of biomass to biofuels. Prog. Energy Combust. Sci. 41, 56–93. https://doi.org/10.1016/j.pecs.2013.11.001.

Luo, M.R. (n.d.). Color science and technology. 1.

Luo, M.R. (2020). Encyclopedia of color science and technology, encyclopedia of color science and technology. https://doi.org/10.1007/978-3-642-27851-8

Luo, X., Cao, J., Gong, H., Yan, H., He, L., 2018. Phase separation technology based on ultrasonic standing waves: a review. Ultrason. Sonochem. 48, 287–298. https://doi.org/10.1016/j.ultsonch.2018.06.006.

Markham, J.J., 1952. Second-order acoustic fields: Streaming with viscosity and relaxation. Phys. Rev. 86 (4), 497–502. https://doi.org/10.1103/PhysRev.86.497.

Marshall, J.S., Wu, J., 2015. Acoustic streaming, fluid mixing, and particle transport by a Gaussian ultrasound beam in a cylindrical container. Phys. Fluids 27 (10). https://doi.org/10.1063/1.4932232.

Neppiras, E.A., 1980. Acoustic cavitation. Phys. Rep. 159–251. https://doi.org/10.1016/0370-1573(80)90115-5.

Neppiras, E.A., Noltingk, B.E., 1951. Cavitation produced by ultrasonics: theoretical conditions for the onset of cavitation. Proc. Phys. Soc. London Sect. B 64 (12), 1032–1038. https://doi.org/10.1088/0370-1301/64/12/302.

Nowicki, A., Secomski, W., Wójcik, J., 1997. Acoustic streaming: comparison of low-amplitude linear model with streaming velocities measured by 32-MHz Doppler. Ultrasound Med. Biol. 23 (5), 783–791. https://doi.org/10.1016/S0301-5629(97)00005-7.

Pandey, V., 2019. Asymmetricity and sign reversal of secondary Bjerknes force from strong nonlinear coupling in cavitation bubble pairs. Phys. Rev. E 99 (4). https://doi.org/10.1103/PhysRevE.99.042209.

Pankaj, Ashokkumar, M., 2011. Theoretical and experimental sonochemistry involving inorganic systems. Theoretical and Experimental Sonochemistry Involving Inorganic Systems. Springer, Netherlands, pp. 1–404.

Sanderson, B., 2004. Applied sonochemistry– the uses of power ultrasound in chemistry and processing. By Timothy J Mason and John P Lorimer, Wiley-VCH Verlag, Weinheim, 2002, 303 pp, ISBN 3-527-30205-0. J. Chem. Technol. Biotechnol. 79 (2), 207–208. https://doi.org/10.1002/jctb.957.

Sato, M., Fujii, T., 1998. Redshift of the ultrasonic wave frequency in acoustic streaming. Proceedings of the IEEE Ultrasonics Symposium 2, 1187–1192.

Shah, Y.T., Pandit, A.B., & Moholkar, V.S. (1999). Cavitation reaction engineering.

Son, Y., Lim, M., Khim, J., Kim, L.H., Ashokkumar, M., 2012. Comparison of calorimetric energy and cavitation energy for the removal of bisphenol-A: the effects of frequency and liquid height. Chem. Eng. J. 183, 39–45. https://doi.org/10.1016/j.cej.2011.12.016.

Suri, C., Takenaka, K., Yanagida, H., Kojima, Y., Koyama, K., 2002. Chaotic mixing generated by acoustic streaming. Ultrasonics 40, 393–396. https://doi.org/10.1016/S0041-624X(02)00150-6.

Suslick, K.S., Gawienowski, J.J., Schubert, P.F., Wang, H.H., 1984. Sonochemistry in non-aqueous liquids. Ultrasonics 22 (1), 33–36. https://doi.org/10.1016/0041-624X(84)90059-3.

Toma, M., Fukutomi, S., Asakura, Y., Koda, S., 2011. A calorimetric study of energy conversion efficiency of a sonochemical reactor at 500kHz for organic solvents. Ultrason. Sonochem. 18 (1), 197–208. https://doi.org/10.1016/j.ultsonch.2010.05.005.

Tuziuti, T., Yasui, K., Kanematsu, W., 2018. Influence of addition of degassed water on bulk nanobubbles. Ultrason. Sonochem. 43, 272–274. https://doi.org/10.1016/j.ultsonch.2018.01.015.

Wu, J., 2018. Acoustic streaming and its applications. Fluids 3 (4). https://doi.org/10.3390/fluids3040108.

Yasui, K., 2017. Acoustic cavitation. Acoustic Cavitation and Bubble Dynamics. Springer Briefs in Molecular Science Ultrasound and Sonochemistry. Springer, Nogaya, Japan, pp. 1–31.

Yasui, K., Towata, A., Tuziuti, T., Kozuka, T., Kato, K., 2011. Effect of static pressure on acoustic energy radiated by cavitation bubbles in viscous liquids under ultrasound. J. Acoust. Soc. Am. 130 (5), 3233–3242. https://doi.org/10.1121/1.3626130.

Ye, L., Zhu, X., 2017. Analysis of the effect of impact of near-wall acoustic bubble collapse micro-jet on Al 1060. Ultrason. Sonochem. 36, 507–516. https://doi.org/10.1016/j.ultsonch.2016.12.030.

Yusof, N.S.M., Babgi, B., Alghamdi, Y., Aksu, M., Madhavan, J., Ashokkumar, M., 2016. Physical and chemical effects of acoustic cavitation in selected ultrasonic cleaning applications. Ultrason. Sonochem. 29, 568–576. https://doi.org/10.1016/j.ultsonch.2015.06.013.

Zarembo, L.K., 1971. Acoustic Streaming. High Intensity Ultrasonic Fields, pp. 139–196.

Chapter 4

Sonochemical reactions, when, where and how: Modelling approach

Ferenc Hegedűs[a], **Csanád Kalmár**[a], **Tamás Turányi**[b], **István Gy. Zsély**[b] **and Máté Papp**[b]

[a] *Department of Hydrodynamic Systems, Budapest University of Technology and Economics, Budapest, Hungary,*

[b] *Chemical Kinetics Laboratory, Institute of Chemistry, ELTE Eötvös Loránd University, Budapest, Hungary*

4.1 Introduction

A unique way of creating bubbles is the irradiation of a liquid domain with high-intensity and high-frequency ultrasound. The phenomenon is called acoustic cavitation (Leighton, 2012). The generated bubbles are aggregated into clusters having various forms depending on the acoustic field (Mettin, 2007). Due to the periodically varying nature of the pressure field, the individual bubbles in the cluster exhibit radial pulsation. As the size of the bubbles is in the order of micrometre, spherical symmetry is often a reasonable assumption. A typical bubble dynamics scenario is the growth during the rarefaction phase of the pressure signal, which is followed by a rapid contraction in the compression phase. Due to the highly nonlinear nature of the oscillation (Klapcsik et al., 2018; Lauterborn & Holzfuss, 1991; Lauterborn & Parlitz, 1988; A.J. Sojahrood et al., 2019; Amin Jafari Sojahrood et al., 2017), the growth of the bubble is relatively slow, while the compression can be so fast and the compression ratio can be so high that approaching the minimum size of the bubble, chemical reactions can take place (Yasui, 2001; Yasui et al., 2004, 2007). This ultrasound-induced chemistry is called sonochemistry (Cavalieri et al., 2016). The application possibilities are various. For instance, the produced highly reactive radicals are used in wastewater treatment to degrade hazardous and toxic pollutants (Gole et al., 2018). The synthesis of various organic compounds and pharmaceuticals can be done using fewer toxic (or even toxic-free) solvents (Green Chemistry) (Draye & Kardos, 2016). Recent research directions focus on the production of hydrogen (Islam et al., 2019; Rashwan et al., 2019), or the production of hydrocarbons by the hydrogenation of CO_2 (Islam et al., 2021). These approaches are regarded as alternative fuel production technologies.

To address the issues in sonochemistry, for example, the challenge of scaling up by magnitudes making feasible for commercial applications (Gogate & Patil, 2016; Kanthale et al., 2007; Prabhu et al., 2004), experimental investigations have a vital role to play. However, a sonochemical reactor has many control parameters that makes the optimization of reactors purely via experiments essentially a trial-and-error approach. The problem is demonstrated in a recent publication of the authors (Hegedűs et al., 2020), where numerical simulations of the dynamics of a single spherical bubble were carried out in a six-dimensional parameter space. Although the resolution of each parameter was moderate (21 or 101), the total number of parameter combinations were nearly 2 billion. Therefore, high-performance numerical approaches are mandatory for optimization processes. In this regard, one of the main aims of the present study is to demonstrate the benefit of GPU programming in sonochemistry via the computation of the chemical output of acoustic cavitation bubbles.

Numerical approaches have their own difficulties. Even in the case of a single spherical bubble, one encounters a complex multiphase physics with evaporation, condensation, heat transfer, and diffusion (Brenner et al., 2002). In addition, to obtain the exact information on the chemical production of the various species, the solution of the differential equations of chemical kinetics inside the bubbles is necessary (Colussi et al., 1998; Sochard et al., 1997). Keep in mind again that the number of parameter combinations is still high for a proper optimization procedure, and in real sonochemical reactors, there are hundreds or thousands of bubbles. With finite computational resources, the reasons mentioned above are leading to a compromise between model complexity (including the number of the investigated bubbles) and the

Energy Aspects of Acoustic Cavitation and Sonochemistry: Fundamentals and Engineering. DOI: https://doi.org/10.1016/B978-0-323-91937-1.00013-X
Copyright © 2022 Elsevier Inc. All rights reserved.

number of parameter combinations (optimization complexity). A perfect example is the pioneering work of Storey & Szeri (Storey & Szeri, 2000), who computed the chemical reactions inside a spherically oscillating vapor/gas bubble together with the conservation equations (partial differential equations) of the n-component system; however, they employed only a few parameter combinations.

One of the main focuses of this study is the modelling aspect of chemical reactions inside a single spherical bubble with a spatially homogeneous interior. Building up a proper reaction mechanism is a nontrivial task (Turányi & Tomlin, 2014). For instance, due to the extreme compression ratio at the collapse phase of a bubble, the modelling of the pressure dependence of the reactions is essential. The third body efficiency has to be taken into account as well. It is advisable to compute the backward reaction rates via thermodynamic equilibrium conditions. Some reactions have non-Arrhenius temperature dependence. In this case, the corresponding reaction is duplicated, and two sets of Arrhenius constants are used to describe the nonexponential temperature dependence. Finally, the determination of the Arrhenius constants alone is a nontrivial procedure. Chemical reactions are complicated processes where intermediate products appear. Therefore, simulation results based on complete reactions mechanisms have to be compared with experimental data. As the measurement techniques have been continuously improved, the up-to-date Arrhenius constants have been changed even by orders of magnitudes over the past years/decades. Consequently, it is always advisable to work with the latest available combustion mechanisms instead of adopting a former one from previous sonochemical publications. In the present study, the reaction mechanism to describe the chemical reaction in the bubble (initial content is water vapor and oxygen) is based on publications by Varga et al. (2016); Zhao et al. (2016).

The calculation of the chemical production of a single bubble has a long history in sonochemistry. Although the pioneering works of many research groups (Kyuichi Yasui, 2001; Kyuichi Yasui et al., 2004, 2007) have significant contributions to the understanding of sonochemical processes on a single bubble basis, the available models in the literature lack one or more of the previously introduced modelling criteria. For instance, the only paper the authors have found in the literature that takes into account the pressure dependency of the reaction steps is written by Storey & Szeri (Storey & Szeri, 2000) in 2000. However, they employed an outdated set of Arrhenius constants taken from (Gardiner, 1984) (written in 1984). The primary objective of this Chapter is to provide a description of a state-of-the-art reaction mechanism of an oxygen bubble placed in liquid water.

The secondary objective is to implement our bubble model into the general-purpose, in-house ordinary differential equation solver MPGOS (Hegedűs, 2021) that can exploit the high processing power of professional graphics cards (GPUs). In this way, high-performance computation and single bubble sonochemistry are connected, and large parameter scans (in the order of a few hundred thousand's) can be carried out within a reasonable time (i.e., within a day). The complex parameter dependencies of the high-resolution scans revealed that the optimal production of different chemical species (e.g., hydrogen or free radicals) have different optimal operation setups (irradiation frequency and intensity). Furthermore, the dissipated energy during the oscillation of the bubble is computed based on the work of Jamshidi & Brenner (Jamshidi & Brenner, 2013); thus, the results are also discussed in terms of the chemical yield per unit dissipated power/energy. Such results provide estimations for upper theoretical energy efficiency limits of specific sonochemical processes.

4.2 The governing equations

To keep the model complexity simple enough to perform a large parameter study, the two major assumptions applied here are spherical symmetry and homogeneous bubble interior. That is, no three-dimensional hydrodynamic computation is necessary, and the physics inside the bubble can be described by a set of ordinary differential equations (ODEs).

The description of the mathematical model of the chemically active bubble is separated into two parts: physical and chemical modelling. The chemical part describes the main ingredients of the proper build-up of a reaction mechanism through the example of an oxygen bubble (initial composition is water vapor and oxygen). The physical part describes all the other effects: inertia of the liquid domain, nonequilibrium evaporation/condensation and the thermal equilibrium of the bubble interior.

4.2.1 State-of-the-art reaction mechanism of an oxygen bubble

Several studies have been published during the last decades that describe the chemical reactions in bubbles (K Kerboua, Hamdaoui, et al., 2021; K Kerboua, Merouani, et al., 2021; K Kerboua & Hamdaoui, 2020; Merouani et al., 2015; Rivas et al., 2013; Stricker & Lohse, 2014; K. Yasui et al., 2008; Kyuichi Yasui & Kato, 2012). However,

most of them employed out-of-date reaction mechanisms that lack important features mentioned already in the Introduction. The usual reason is the adoption-chain of reaction mechanisms leading to an old source. A detailed description of state-of-the-art modelling principles is introduced in this section based on the excellent overview published in (Turányi & Tomlin, 2014). In addition, a specific reaction mechanism is defined used for simulating the chemical processes inside a bubble initially containing pure oxygen and vapor.

First, let us consider the following reversible chemical reactions involving K chemical species in the general form of

$$\sum_{k=1}^{K} \nu_{ki}^{f} \chi_k \Leftrightarrow \sum_{k=1}^{K} \nu_{ki}^{b} \chi_k \quad (i = 1, ..., I) \tag{4.1}$$

where ν_{ki} are the stoichiometric coefficients, X_k is the chemical symbol for the kth species, and I is the total number of reactions. The superscripts f and b indicate forward and backward directions, respectively. It is worth mentioning that most chemical reactions involve two or three species on each side of the chemical equation; hence, the matrices ν_{ki}^{f} and ν_{ki}^{b} are relatively sparse, especially with increasing K.

Reaction kinetics mostly focuses on the rate of chemical reactions. The net rate of reaction i (q_i) is calculated as the difference of forward and backward rates as

$$q_i = k_{f_i} \prod_{k=1}^{K} c_k^{\nu_{ki}^{f}} - k_{b_i} \prod_{k=1}^{K} c_k^{\nu_{ki}^{b}} \tag{4.2}$$

where k_{f_i} and k_{b_i} are the forward and backward reaction rate constants of reaction i (see later). The quantity c_k is the molar concentration of species k in the examined volume. With the reaction rates (q_i), the production rate of each species can be written as

$$\dot{\omega}_k = \sum_{i=1}^{I} \nu_{ki} q_i \tag{4.3}$$

where $\nu_{ki} = \nu_{ki}^{b} - \nu_{ki}^{f}$. The production rate represents how fast the amount of species k changes in time in a unit volume.

The forward rate k_{f_i} in Eq. (4.2) is generally described by the extended Arrhenius-equation written as

$$k_{f_i} = A_i T^{b_i} \exp\left(\frac{-E_i}{R_g T}\right) \tag{4.4}$$

where R_g is the universal gas constant, T is the temperature, A_i is the pre-exponential factor, b_i is the temperature exponent and E_i is the activation energy. The three constants (A_i, b_i and E_i) are different for each reaction, and they are fundamental inputs of a reaction mechanism. The backward rate constants k_{b_i}— unlike in most other sonochemical articles—are calculated as follows. They are related to the forward rates through the equilibrium constants defined by

$$K_{c_i} = \frac{k_{f_i}}{k_{b_i}} \tag{4.5}$$

The equilibrium constants K_{c_i} (given in concentration unit) can be determined as

$$K_{c_i} = K_{p_i} \left(\frac{P_{atm}}{R_g T}\right)^{\sum_{k=1}^{K} \nu_{ki}} \tag{4.6}$$

where P_{atm} is the atmospheric pressure and K_{p_i} is obtained from

$$K_{p_i} = \exp\left(\frac{\Delta S_i}{R_g} - \frac{\Delta H_i}{R_g T}\right) \tag{4.7}$$

Here, S_k and H_k are the entropy and enthalpy of species k at temperature T, respectively. The notation Δ means the total change in a reaction (from reactants to products):

$$\frac{\Delta S_i}{R_g} = \sum_{k=1}^{K} \nu_{ki} \frac{S_k}{R_g} \tag{4.8}$$

$$\frac{\Delta H_i}{R_g T} = \sum_{k=1}^{K} \nu_{ki} \frac{H_k}{R_g T} \tag{4.9}$$

The Arrhenius-equation is a general approach for describing reaction rates; however, some chemical reactions behave in a more complex manner and their rate constants cannot be defined with this function. In the following, the three most important alternative definitions are presented that are included in our modelling technique.

4.2.1.1 Three-body reactions

Several reactions—often dissociation or recombination reactions—need a third molecule to remove the excess energy of the energetically excited reaction intermediately. Generally, any molecule or radical present can act as a third body, but the collision of larger molecules is more effective. This factor is taken into account in the third-body *collision efficiency factor*. This factor is of unit value for N_2, smaller than 1 for O_2, and larger for H_2O or H_2O_2. The third-body efficiency factor is very large for H_2O; $\alpha_{H_2O} = 12$ is assumed for several reactions. This means that considering the third-body efficiency factor of water is essential for this modelling of chemical systems where large number of water vapour is present. It is worth to mention that these collision efficiency factors of each species are different for the various reaction sets.

In the reaction equation, a third-body reaction is marked with an additional M species on both sides, suggesting that the third-body does not take part in the reaction itself, for example

$$\mathrm{OH + H + M \Leftrightarrow H_2O + M} \tag{4.10}$$

In the case of these type of third-body reactions, the reaction rate q_i obtained from Eq. (4.10) is modified as

$$q_i{}' = q_i\,[M] \tag{4.11}$$

$$[M] = \sum_{k=1}^{K} \alpha_{ki}\, c_k$$

where $q_i{}'$ is the modified reaction rate, $[M]$ is the effective total concentration of the third-body species and a_{ki} is the matrix of the third-body efficiencies. Usually, most a_{ki} is assumed to be 1 and only those that differ from 1 are highlighted.

4.2.1.2 Pressure-dependent reactions

Some reaction rate constants were found to be pressure-dependent, as well (besides temperature). It was first interpreted by Lindemann et al. (1922) for the model reaction of cyclopropane isomerization. Several later researches confirmed the idea and extended the method for other areas in reaction kinetics (Atkins & De Paula, 2014; Gilbert et al., 1983; Pilling & Seakins, 1995). Here, only a brief description of *unimolecular fall-off* reactions is presented; the curious reader is referred to the papers mentioned above.

A pressure-dependent reaction is marked with an M in brackets in the reaction equations, for example

$$\mathrm{H + O_2\,(+M) \Leftrightarrow HO_2\,(+M)} \tag{4.12}$$

First of all, a high-pressure limit (k_∞) and a low-pressure limit (k_0) has to be defined as

$$k_\infty = A_\infty\, T^{b_\infty} \exp\left(\frac{-E_\infty}{R_g T}\right) \tag{4.13}$$

$$k_0 = A_0\, T^{b_0} \exp\left(\frac{-E_0}{R_g T}\right) \tag{4.14}$$

Consequently, two different sets of Arrhenius constants have to be used. These two limiting rate constants together yield an overall rate constant written as

$$k_{f_i}{}' = k_\infty \frac{P_r}{1 + P_r} F \tag{4.15}$$

where the reduced pressure P_r is given by

$$P_r = \frac{k_0}{k_\infty}[M] \tag{4.16}$$

Here, $[M]$ is the total concentration of the mixture enhanced by possible third-body efficiencies (see Eq. 4.11). In Eq. (4.15), there are several approaches for the computation of F; here, only the *Troe* formalism (Gilbert et al., 1983) is

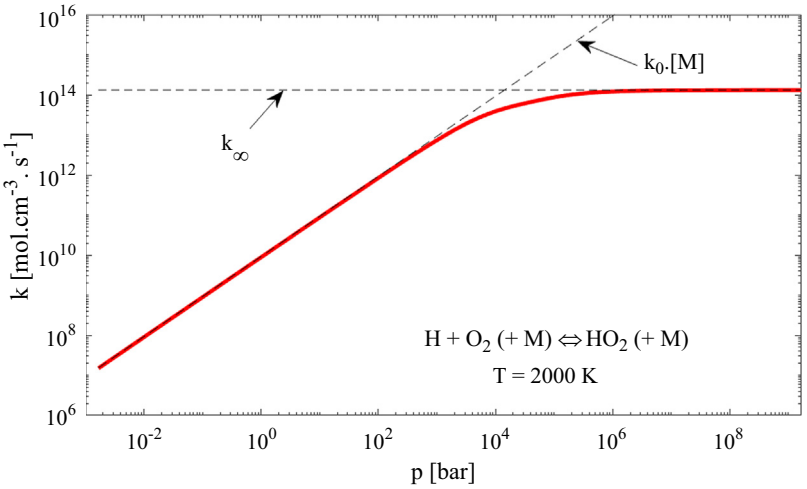

FIGURE 4.1 The rate constant of the reaction $H + O_2 (+ M) \Leftrightarrow HO_2 (+ M)$ as a function of pressure at T = 2000 K.

introduced:

$$\log F = \left[1 + \left[\frac{\log P_r + c}{n - d(\log P_r + c)}\right]^2\right]^{-1} \log F_{\text{cent}} \tag{4.17}$$

with

$$c = -0.4 - 0.67 \log F_{\text{cent}} \tag{4.18}$$

$$n = 0.75 - 1.27 \log F_{\text{cent}} \tag{4.19}$$

$$d = 0.14 \tag{4.20}$$

and

$$F_{\text{cent}} = (1 - \alpha) \exp\left(\frac{-T}{T^{***}}\right) + \alpha \exp\left(\frac{-T}{T^{*}}\right) + \exp\left(\frac{-T^{**}}{T}\right) \tag{4.21}$$

From the equations above it follows that $k_{f_i}' \to k_\infty$ if $p \to \infty$ and $k_{f_i}' \to k_0 [M]$ if $p \to 0$ (for a fall-off reaction).

The four parameters α, T^{***}, T^{*} and T^{**} are different parameters for each Troe-form reaction. In some cases, T^{**} is not used and the last term in Eq. (4.21) is neglected. In summary, ten parameters have to be defined for each pressure dependent reaction using Troe-formalism: Six Arrhenius and the four Troe coefficients. In most cases, these are extended with the corresponding third-body efficiency factors. As an example, the rate constant of the pressure-dependent reaction $H + O_2 (+ M) = HO_2 (+ M)$ is depicted in Fig. 4.1 as a function of pressure at $T = 2000$ K. Observe that the rate constant can vary by several orders of magnitude.

As a result of this procedure, the (modified) forward rate constant k_{f_i}' can be determined. The backward reaction rate is calculated in the same way as in the case of the non-pressure-dependent reactions, see Eqs. (4.5)-(4.9).

4.2.1.3 Duplicated reactions

Most elementary reactions occur via a single molecular mechanism and the temperature dependence of the rate constants of these reactions can be defined by a single set of Arrhenius parameters. In some rare cases the reactants and products of an elementary reaction are identical, but the reaction proceeds via two different ways. The rate constants of these two channels have different temperature dependence, therefore can be characterized by two different sets of Arrhenius parameters. These reactions are given in the mechanisms as two separate reactions, like in the reaction $2HO_2 \Leftrightarrow O_2 + H_2O_2$ with the sets of $A_1 = 1.3 \cdot 10^{11}$ cm^3/mol/s, $b_1 = 0$, $E_1 = -1.9983 \cdot 10^3$ cal/mol^1 and $A_2 = 1.6048 \cdot 10^{15}$ cm^3/mol/s, $b_2 = 0$, $E_2 = 1.9063 \cdot 10^4$ cal/mol.

At the calculation of the reaction rates, the sum of the rates of the two channels is used as the rate of the reaction step. In Fig. 4.2, the rate constant of the above reaction is shown, on normal scale on the left side, and logarithmic scale on the

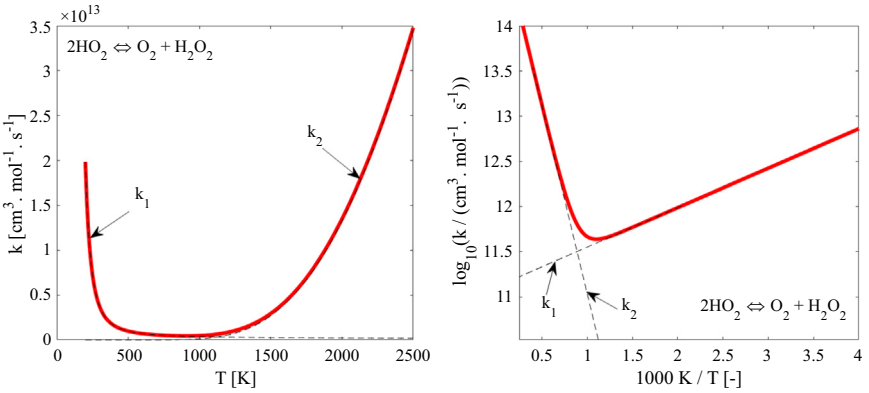

FIGURE 4.2 The overall rate constant as a function of temperature for the duplicated reaction $2HO_2 \Leftrightarrow O_2 + H_2O_2$. Left panel: k versus T, right panel: $\log(k)$ versus $1000/T$.

right side. It can be seen that for this reaction, the rate constant of one channel (k_2) is dominant above 1500 K, those of the other channel (k_1) is dominant below 500 K, while both channels have to be taken into account in the temperature range of 500–1500 K.

4.2.1.4 *The applied chemical mechanism for a pure oxygen/water vapor bubble*

In this section, the details of the employed reaction mechanism is given for an initially pure oxygen/water vapor bubble. The various constants and coefficients are summarized through several tables in the followings. Table 4.1 presents the reaction equations with their corresponding Arrhenius coefficients. This chemical mechanism is developed by (Varga et al., 2016), extended with the O_3 reactions from (Zhao et al., 2016). In the case of pressure-dependent reactions (with (+M) on both sides), these values represent the constants A_∞, b_∞, and E_∞. The third-body efficiencies are shown in Table 4.2. For every other non-mentioned component, $\alpha_{ki} = 1$. The mandatory parameters for the pressure-dependent reactions are given in Table 4.3 and Table 4.4. For more detailed discussions of state-of-the-art reaction mechanisms, the interested reader is referred to studies (Olm et al., 2015; Varga et al., 2015).

4.2.2 The complete bubble model

The reaction mechanism described in the previous section needs the temperature and pressure to compute the reaction rates. Assuming ideal gas mixture inside the bubble, the enthalpy and the entropy are purely temperature dependent. The temperature and pressure are governed by the dynamics of the volume oscillation and the heat transfer between the bubble interior and the bulk liquid. In what follows is the closure of the mathematical model and the derivation of the governing equations (a set of ODEs) that describes the behavior of the chemically active bubble.

The inertia of the liquid domain has the most important effect on the radial dynamics of a bubble. This is the main reason for the developed high compression ratio during the collapse phase: to stop the liquid moving toward the center of the bubble, a high internal pressure has to build-up (even hundreds of atmospheres (Leighton, 2012). Due to such an extreme dynamic, the liquid compressibility has to be taken into account. The modified Keller-Miksis equation (Klapcsik et al., 2018; W. Lauterborn & Holzfuss, 1991; W. Lauterborn & Parlitz, 1988; A.J. Sojahrood et al., 2019; Sojahrood et al., 2017) (and its various forms) is a widely used equation in sonochemistry to model the inertial effect, its form is given as

$$\left(1-\frac{\dot{R}}{c_L}\right)R\ddot{R}+\left(1-\frac{\dot{R}}{3c_L}\right)\frac{3}{2}\dot{R}^2=\left(1+\frac{\dot{R}}{c_L}+\frac{R}{c_L}\frac{d}{dt}\right)\frac{(p_L-p_\infty(t))}{\rho_L} \tag{4.22}$$

where $R(t)$ is the radius of the bubble, t is the time, c_L is the sound speed in the liquid, and ρ_L is the density of the liquid. The liquid pressure at the bubble wall is p_L, which is related to the internal pressure (p) via the boundary condition

$$p=p_L+\frac{2\sigma}{R}+4\mu_L\frac{\dot{R}}{R} \tag{4.23}$$

Here, σ is the surface tension, and μ_L is the dynamic viscosity of the liquid. The dots stand for derivatives with respect to time. The far-field pressure p_∞ is composed by a static ambient pressure P_0 and a harmonic component according to the

TABLE 4.1 The applied chemical mechanism with their Arrhenius constants. For pressure dependent reactions marked with (+M), the values represent the high-pressure limit values, respectively.

No.	Reaction	A_i [cm^3/mol/.s]	b_i [-]	E_i [cal/mol[1]]
1.	H + OH + M ⇔ H2O + M	$1.4818 \cdot 10^{24}$	−2.5379	$1.4808 \cdot 10^{2}$
2.	2O + M ⇔ O2 + M	$6.165 \cdot 10^{15}$	−0.5	0
3.	O + H + M ⇔ OH + M	$4.714 \cdot 10^{18}$	−1	0
4.	$H + O_2 \Leftrightarrow O + OH$	$5.0712 \cdot 10^{15}$	−0.48596	$1.9771 \cdot 10^{4}$
5.	H + O2 (+ M) ⇔ HO2 (+ M)	$4.65 \cdot 10^{12}$	0.44	0
6.	$2OH \Leftrightarrow O + H_2O$	$8.4999 \cdot 10^{4}$	2.2642	$-2.1881 \cdot 10^{3}$
7.	$H + HO_2 \Leftrightarrow H_2 + O2$	$2.1231 \cdot 10^{6}$	2.1133	$-1.9919 \cdot 10^{3}$
8.	$H + HO_2 \Leftrightarrow 2OH$	$5.7734 \cdot 10^{13}$	0	$2.0967 \cdot 10^{2}$
9.	$O + HO_2 \Leftrightarrow OH + O_2$	$3.25 \cdot 10^{13}$	0	0
10.	$OH + HO_2 \Leftrightarrow O_2 + H_2O$	$9.584 \cdot 10^{11}$	0.42008	$-1.1629 \cdot 10^{3}$
11.	2H + M ⇔ H2 + M	$4.9806 \cdot 10^{18}$	−1.2127	$7.5034 \cdot 10^{2}$
12.	$O + H_2 \Leftrightarrow H + OH$	$1.2554 \cdot 10^{6}$	2.2704	$8.5289 \cdot 10^{3}$
13.	$H_2 + OH \Leftrightarrow H + H_2O$	$1.3193 \cdot 10^{7}$	1.878	$3.863 \cdot 10^{3}$
14.	2OH (+ M) ⇔ H2O2 (+ M)	$2.148 \cdot 10^{5}$	2.3219	$-4.1712 \cdot 10^{3}$
15.	$H + H_2O_2 \Leftrightarrow OH + H_2O$	$2.41 \cdot 10^{13}$	0	$4.8671 \cdot 10^{3}$
16.	$H + H_2O_2 \Leftrightarrow H_2 + HO_2$	$9.7543 \cdot 10^{19}$	−1.9249	$1.1555 \cdot 10^{4}$
17.	$O + H2O2 \Leftrightarrow OH + HO_2$	$9.55 \cdot 10^{6}$	2	$4.8671 \cdot 10^{3}$
18.	$OH + H_2O_2 \Leftrightarrow H_2O + HO_2$ (dupl.)	$1.74 \cdot 10^{12}$	0	$3.8986 \cdot 10^{2}$
19.		$7.59 \cdot 10^{13}$	0	$8.9116 \cdot 10^{3}$
20.	$2HO_2 \Leftrightarrow O_2 + H_2O_2$ (dupl.)	$1.3 \cdot 10^{11}$	0	$-1.9983 \cdot 10^{3}$
21.		$1.6048 \cdot 10^{15}$	0	$1.9063 \cdot 10^{4}$
22.	O3 (+ M) ⇔ O + O2 (+ M)	$1.37 \cdot 10^{15}$	−0.67	$2.599 \cdot 10^{4}$
23.	$H + O_3 \Leftrightarrow OH + O_2$	$8.43 \cdot 10^{13}$	0	$9.34 \cdot 10^{2}$
24.	$H + O_3 \Leftrightarrow O + HO_2$	$4.52 \cdot 10^{11}$	0	0
25.	$OH + O_3 \Leftrightarrow O_2 + HO_2$	$1.85 \cdot 10^{11}$	0	$8.31 \cdot 10^{2}$
26.	$HO_2 + O_3 \Leftrightarrow OH + 2O_2$	$6.62 \cdot 10^{9}$	0	$9.94 \cdot 10^{2}$
27.	$O + O_3 \Leftrightarrow 2O_2$	$4.82 \cdot 10^{12}$	0	$4.094 \cdot 10^{3}$
28.	$H_2O + O_3 \Leftrightarrow O_2 + H_2O_2$	66.2	0	0
29.	O + H + M ⇔ OHex + M	$1.5 \cdot 10^{13}$	0	$7.3252 \cdot 10^{3}$
30.	$H_2O + OH_{ex} \Leftrightarrow OH + H_2O$	$5.93 \cdot 10^{12}$	0.5	$-1.0543 \cdot 10^{3}$
31.	$H_2 + OH_{ex} \Leftrightarrow H_2 + OH$	$2.95 \cdot 10^{12}$	0.5	$-5.4432 \cdot 10^{2}$
32.	$OH + OH_{ex} \Leftrightarrow 2OH$	$6.01 \cdot 10^{12}$	0.5	$-9.3664 \cdot 10^{2}$
33.	$H + OH_{ex} \Leftrightarrow H + OH$	$1.31 \cdot 10^{12}$	0.5	$-2.0475 \cdot 10^{2}$
34.	$O_2 + OH_{ex} \Leftrightarrow OH + O_2$	$2.1 \cdot 10^{12}$	0.5	$-5.86 \cdot 10^{2}$

ultrasonic irradiation:

$$p_\infty(t) = P_0 + p_A \sin(2\pi f t) \tag{4.24}$$

where p_A and f are the ultrasound pressure amplitude and frequency, respectively. To be able to calculate p in Eq. (4.23), an equation of state (EoS) has to be applied. Assuming ideal gas mixture, the EoS is written as

$$p = MR_gT \tag{4.25}$$

TABLE 4.2 The enhanced third-body efficiencies. For every other non-mentioned component, the value is assumed to be 1.

No.	Reaction	Enhanced third-body efficiencies ($\alpha_{k,i}$)
1.	$H + OH + M \Leftrightarrow H_2O + M$	H_2: 2.5 H_2O: 12
2.	$2O + M \Leftrightarrow O_2 + M$	H_2: 2.5 H_2O: 12
3.	$O + H + M \Leftrightarrow OH + M$	H_2: 2.5 H_2O: 12
5.	$H + O2 (+ M) \Leftrightarrow HO_2 (+ M)$	H_2: 1.511 H_2O: 11.372
11.	$2H + M \Leftrightarrow H_2 + M$	H_2: 2.5 H_2O: 12
14.	$2OH (+ M) \Leftrightarrow H_2O_2 (+ M)$	H_2: 2.47 O_2: 0.8 H_2O: 5 H_2O_2: 5.13
22.	$O_3 (+ M) \Leftrightarrow O + O_2 (+ M)$	O: 6 H_2: 3 O_2: 1.5 O_3: 3.75
29.	$O + H + M \Leftrightarrow OH_{ex} + M$	O_2: 0.4 H_2O: 6.5

TABLE 4.3 The low-pressure limit Arrhenius parameters of the pressure-dependent reactions.

No.	Reaction	A_0 [$cm^3 .mol^{-1}.s^{-1}$]	b_0 [-]	E_0 [cal. mol^{-1}]
5.	$H + O_2 (+ M) \Leftrightarrow HO_2 (+ M)$	$5.2669 \bullet 10^{19}$	−1.3737	0
14.	$2OH (+ M) \Leftrightarrow H_2O_2 (+ M)$	$1.9928 \bullet 10^{18}$	−1.178	$-5.2382 \bullet 10^3$
22.	$O_3 (+ M) \Leftrightarrow O + O_2 (+ M)$	$2.275 \bullet 10^{28}$	−4.37	$2.7297 \bullet 10^4$

TABLE 4.4 The Troe-parameters of the pressure-dependent reactions.

No.	Reaction	α [-]	T^{***} [K]	T^{*} [K]	T^{**} [K]
5.	$H + O2 (+ M) \Leftrightarrow HO2 (+ M)$	0.67	10^{-30}	10^{30}	10^{30}
14.	$2OH (+ M) \Leftrightarrow H2O2 (+ M)$	0.43	10^{-30}	10^{30}	10^{30}
22.	$O3 (+ M) \Leftrightarrow O + O2 (+ M)$	0.6417	$3.91 \bullet 10^{-4}$	$8.6807 \bullet 10^3$	$6.0607 \bullet 10^3$

where M is the total concentration of the mixture. The temperature is calculated by solving the first law of thermodynamics in the time-dependent form of

$$\dot{T} = \frac{-p\dot{V} + \sum \dot{Q}}{n_t \bar{C}_v} \tag{4.26}$$

where $V = 4R^3\pi/3$ is the volume of the bubble, $\sum \dot{Q}$ is the heat production term originated from the sum of heat diffusion and reaction heats (their exact formulae are presented later), n_t is the total amount of substance of the mixture and $\bar{C}_v$ is the average molar heat capacity of the mixture at constant volume.

The various thermodynamic quantities (heat capacities, enthalpies, and entropies) are calculated using the NASA chemical equilibrium code (Gordon, 1976). This assumes that these properties are the functions of temperature only and they are given in the terms of polynomial fits as

$$\frac{C_{p,k}}{R_g} = \sum_{n=1}^{N} a_{n,k} T^{n-1} \tag{4.27}$$

$$\frac{H_k}{R_g T} = \sum_{n=1}^{N} \frac{a_{n,k} T^{n-1}}{n} + \frac{a_{N+1,k}}{T} \tag{4.28}$$

$$\frac{S_k}{R_g} = a_{1,k} \ln T + \sum_{n=2}^{N} \frac{a_{n,k} T^{n-1}}{n-1} + a_{N+2,k} \tag{4.29}$$

Here, $C_{p,k}$ stands for the molar heat capacity at constant pressure, H_k is the molar enthalpy of formation and S_k is the entropy of component k, $N = 5$ (for NASA polynomials) and $a_{n,k}$ are the polynomial coefficients for component k. It is worth noting that NASA polynomials have different set of $a_{n,k}$ coefficients for intervals $[T_{low}, T_{mid}]$ and $[T_{mid}, T_{high}]$. If $T <$

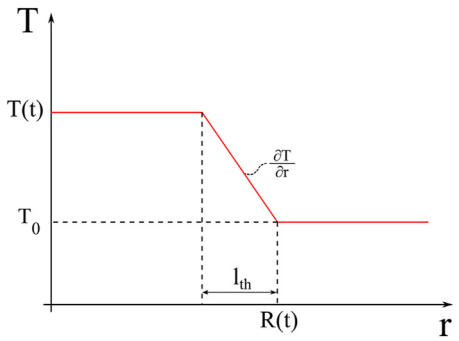

FIGURE 4.3 The simplified temperature distribution. The temperature changes linearly from T to T_0 in the thermal boundary layer.

T_{low} or $T > T_{high}$, the values for the low or high bound are used, respectively. Consequently, $(N + 2)\bullet\ 2 = 14$ coefficients belong to each chemical component. T_{low}, T_{mid}, and T_{high} can also be different for each component. The applied values of $a_{n,k}$ and other parameters are shown below, see Table 4.5, Table 4.6, and Table 4.7.

The molar heat capacities on constant volume are calculated as

$$C_{v,k} = C_{p,k} - R_g \tag{4.30}$$

Some average values of the mixture are calculated as follows. The mole fraction of component k is defined as

$$X_k = \frac{c_k}{M} \tag{4.31}$$

where M is the sum of each concentration ($M = \Sigma c_k$). Most of the average values of the mixture are the weighted average of the components with respect to the mole fraction, such as

$$\bar{W} = \sum_{k=1}^{K} X_k W_k \tag{4.32}$$

$$\bar{\rho} = \sum_{k=1}^{K} c_k W_k \tag{4.33}$$

$$\bar{C}_p = \sum_{k=1}^{K} X_k C_{p,k} \tag{4.34}$$

$$\bar{C}_v = \sum_{k=1}^{K} X_k C_{v,k} \tag{4.35}$$

where W is the molecular weight, ρ is the density of the gas mixture, and the bars mean the averaged values for the mixture.

Heat conduction between the fluid and the bubble interior is modelled with the approach recommended by (Toegel et al., 2000). That is, a thin thermal boundary layer is introduced at the bubble wall where the temperature changes linearly from the bubble mean temperature T to the ambient liquid temperature T_0, which is kept constant. A sketch about the simplified temperature distribution is shown in Fig. 4.3. In this approach, the amount of heat transfer is approximated as

$$\dot{Q}_{th} = A\,\bar{\lambda}\,\frac{\partial T}{\partial r}\bigg|_{r=R} \approx A\,\bar{\lambda}\,\frac{T_0 - T}{l_{\text{th}}} \tag{4.36}$$

where A is the area of the bubble surface, $\bar{\lambda}$ is the averaged thermal conductivity of the mixture and l_{th} is the thickness of the thermal boundary layer calculated as

$$l_{\text{th}} = \min\left(\sqrt{\frac{R\bar{\chi}}{\dot{R}}},\ \frac{R}{\pi}\right) \tag{4.37}$$

where $\bar{\chi}$ is the averaged thermal diffusivity of the mixture. Heat diffusion is a rather important phenomenon that damps temperature peaks during violent collapses. Since the temperature is one of the most influential variables regarding the chemical processes, a proper estimation of heat transfer is essential.

TABLE 4.5 NASA coefficients. The applied NASA coefficients of each species. The units are so that the values are in CGS unit system.

Component		NASA coefficients						
		a_1	a_2	a_3	a_4	a_5	a_6	a_7
O	low	3.1683	$-3.2793 \cdot 10^{-3}$	$6.6431 \cdot 10^{-6}$	$-6.1281 \cdot 10^{-9}$	$2.1127 \cdot 10^{-12}$	$2.9122 \cdot 10^{4}$	2.0519
	high	2.5436	$-2.7316 \cdot 10^{-5}$	$-4.1903 \cdot 10^{-9}$	$4.9548 \cdot 10^{-12}$	$-4.7955 \cdot 10^{-16}$	$2.9226 \cdot 10^{4}$	4.9223
H	low	2.5	0	0	0	0	$2.5474 \cdot 10^{4}$	$-4.4668 \cdot 10^{-1}$
	high	2.5	0	0	0	0	$2.5474 \cdot 10^{4}$	$-4.4668 \cdot 10^{-1}$
H_2	low	2.3443	$7.9805 \cdot 10^{-3}$	$-1.9478 \cdot 10^{-5}$	$2.0157 \cdot 10^{-8}$	$-7.3761 \cdot 10^{-12}$	$-9.1794 \cdot 10^{2}$	$6.8301 \cdot 10^{-1}$
	high	2.9329	$8.2661 \cdot 10^{-4}$	$-1.464 \cdot 10^{-7}$	$1.541 \cdot 10^{-11}$	$-6.888 \cdot 10^{-16}$	$-8.1307 \cdot 10^{2}$	−1.0243
OH	low	3.992	$-2.4011 \cdot 10^{-3}$	$4.6166 \cdot 10^{-6}$	$-3.8792 \cdot 10^{-9}$	$1.3632 \cdot 10^{-12}$	$3.3689 \cdot 10^{3}$	$-1.04 \cdot 10^{-1}$
	high	2.8385	$1.1074 \cdot 10^{-3}$	$-2.94 \cdot 10^{-7}$	$4.207 \cdot 10^{-11}$	$-2.4229 \cdot 10^{-15}$	$3.6978 \cdot 10^{3}$	5.8449
O2	low	3.7825	$-2.9967 \cdot 10^{-3}$	$9.8473 \cdot 10^{-6}$	$-9.6813 \cdot 10^{-9}$	$3.2437 \cdot 10^{-12}$	$-1.0639 \cdot 10^{3}$	3.6577
	high	3.661	$6.5637 \cdot 10^{-4}$	$-1.4115 \cdot 10^{-7}$	$2.058 \cdot 10^{-11}$	$-1.2991 \cdot 10^{-15}$	$-1.216 \cdot 10^{3}$	3.4154
H_2O	low	4.1986	$-2.0364 \cdot 10^{-3}$	$6.5203 \cdot 10^{-6}$	$-5.4879 \cdot 10^{-9}$	$1.772 \cdot 10^{-12}$	$-3.0294 \cdot 10^{4}$	$-8.4901 \cdot 10^{-1}$
	high	2.677	$2.9732 \cdot 10^{-3}$	$-7.7377 \cdot 10^{-7}$	$9.4434 \cdot 10^{-11}$	$-4.269 \cdot 10^{-15}$	$-2.9886 \cdot 10^{4}$	6.8826
HO_2	low	4.3018	$-4.7491 \cdot 10^{-3}$	$2.1158 \cdot 10^{-5}$	$-2.4276 \cdot 10^{-8}$	$9.2923 \cdot 10^{-12}$	$2.6402 \cdot 10^{2}$	3.7167
	high	4.1723	$1.8812 \cdot 10^{-3}$	$-3.4628 \cdot 10^{-7}$	$1.9466 \cdot 10^{-11}$	$1.7626 \cdot 10^{-16}$	31.0207	2.9577
H_2O_2	low	4.3152	$-8.4739 \cdot 10^{-4}$	$1.764 \cdot 10^{-5}$	$-2.2676 \cdot 10^{-8}$	$9.0895 \cdot 10^{-12}$	$-1.7707 \cdot 10^{4}$	3.2737
	high	4.5798	$4.0533 \cdot 10^{-3}$	$-1.2984 \cdot 10^{-6}$	$1.9821 \cdot 10^{-10}$	$-1.1397 \cdot 10^{-14}$	$-1.8007 \cdot 10^{4}$	$6.6497 \cdot 10^{-1}$
O_3	low	3.4074	$2.0538 \cdot 10^{-3}$	$1.3849 \cdot 10^{-5}$	$-2.2331 \cdot 10^{-8}$	$9.7607 \cdot 10^{-12}$	$1.5864 \cdot 10^{4}$	8.2825
	high	12.3303	$-1.1932 \cdot 10^{-2}$	$7.9874 \cdot 10^{-6}$	$-1.7719 \cdot 10^{-9}$	$1.2608 \cdot 10^{-13}$	$1.2676 \cdot 10^{4}$	−40.8823
OH_{ex}	low	3.6373	$1.8509 \cdot 10^{-4}$	$-1.6762 \cdot 10^{-6}$	$2.3872 \cdot 10^{-9}$	$-8.4314 \cdot 10^{-13}$	$5.0021 \cdot 10^{4}$	1.3589
	high	2.8827	$1.014 \cdot 10^{-3}$	$-2.2769 \cdot 10^{-7}$	$2.1747 \cdot 10^{-11}$	$-5.1263 \cdot 10^{-16}$	$5.0265 \cdot 10^{4}$	5.5957

TABLE 4.6 Thermodynamic properties. The thermodynamic properties of each species.

Component	W [g/mol]	T_{low} [K]	T_{mid} [K]	T_{high} [K]
O	16	200	1000	6000
H	1	200	1000	6000
H_2	2	200	1000	6000
OH	17	200	1000	6000
O_2	32	200	1000	6000
H_2O	18	200	1000	6000
HO_2	33	200	1000	5000
H_2O_2	34	200	1000	6000
O_3	48	200	1000	6000
OH_{ex}	17	300	1000	5000

TABLE 4.7 Physical properties. The applied physical constants during the simulations.

Name	Abbrev.	Value	Unit
Liquid sound speed	C_L	1483	m/s
Liquid density	ρ_L	998.2	kg/m^3
Surface tension	σ	$71.97 \bullet 10^{-3}$	N/m
Dynamic viscosity	μ_L	0.001	Pa • s
Ambient pressure	P_0	1	bar
Ambient temperature	T_0	300	K
Universal gas constant	R_g	8.31446	J/mol • K
Accommodation coefficient for evaporation	a_M	0.35	–
Saturated vapor pressure	p_v^*	2338.1	Pa

The other part in the first law of thermodynamics defined via Eq. (4.26) is the reaction heats that are produced during chemical reactions. It is calculated as

$$\dot{Q}_r = -\sum_{k=1}^{K} H_k \dot{\omega}_k \tag{4.38}$$

where $\dot{Q}_r$ is the total net reaction heat. With these two terms, the total heat transfer $\sum \dot{Q}$ through the bubble interface is

$$\sum \dot{Q} = \dot{Q}_{th} + \dot{Q}_r \tag{4.39}$$

The evaporation and condensation of water are considered as a net substance flow rate into the fluid. The rate of evaporation and condensation are expressed as (Fujikawa & Akamatsu, 1980)

$$\dot{n}_{eva} = \frac{\alpha_M p_v^*}{W_{H_2O}\sqrt{2\pi R_v T_0}} \tag{4.40}$$

and

$$\dot{n}_{con} = \frac{\alpha_M p_{H_2O}}{W_{H_2O}\sqrt{2\pi R_v T}} \tag{4.41}$$

respectively. Here, a_M is the accommodation coefficient for the evaporation (assuming non-equilibrium phase change), p_v^* is the saturated vapour pressure, W_{H_2O} is the molecular weight of water, R_v is the specific gas constant of water and p_{H_2O} is

the partial pressure of the vapour inside the bubble:

$$p_{H_2O} = X_{H_2O} \cdot p \tag{4.42}$$

The quantities $\dot{n}_{\text{eva}}$ and $\dot{n}_{\text{con}}$ are representing the amount of evaporating and condensing moles of water in unit area and unit time, respectively. The difference of the two is the net evaporation rate, denoted simply by $\dot{n}_{\text{net}} (= \dot{n}_{\text{eva}} - \dot{n}_{\text{con}})$. The evaporation and condensation processes have a significant effect on the sonochemical behavior since they considerably modify the amount of vapor trapped inside the bubble that can dissociate during the collapse phase and act as an effective third-body (see the corresponding section again for details).

Finally, the complete system of ODEs that has to be solved simultaneously consists of the following equations. The Keller-Miksis equation (second order ODE) for the radial dynamics, see Eq. (4.22). The temperature is calculated from the equation of the first law of thermodynamics given by Eq. (4.26). The pressure is obtained from the algebraic equation of the ideal gas law. For the temporal evolution of the concentration of each chemical component an ODE has to be solved:

$$\dot{c}_k = \dot{\omega}_k - c_k \frac{\dot{V}}{V} \tag{4.43}$$

The concentration of water vapour is adjusted with the net evaporation rate as

$$\dot{c}_{H_2O} = \dot{\omega}_{H_2O} - c_{H_2O} \frac{\dot{V}}{V} + \dot{n}_{\text{net}} \frac{A}{V} \tag{4.44}$$

Practically speaking, the dimension of the ODE system is $K + 3$. Two for the Keller-Miksis equation (since it is of second order), one for the temperature equation, and K for the concentration of each chemical species. Both the size of the system and the complexity of the equations can lead to strong stiffness that requires special numerical treatment.

4.3 Numerical technique and the investigated parameter space

The governing equations introduced in the previous section are simple in the sense that these are composed only of a relatively low number of ODEs. However, the efficient implementation is far from straightforward for the following reasons. First, due to the complicated form of the system, its implementation is error-prone. Second, for the same reason, the efficient implementation of the right-hand side is far from obvious, especially by employing GPUs (see the forthcoming discussion). Third, the governing equations contain many expensive operations, for example, divisions and various kinds of transcendental functions. Regardless of the hardware architecture (CPU or GPU), the peak performance is measured in terms of additions/subtractions and multiplications (elementary operations). Although the division operation has a dedicated compute unit inside the hardware, it is approximately 50–70 times slower than the elementary operations. All transcendental functions are implemented as approximations (e.g., as Taylor series) and compiled into microcode having only elementary operations and division, and use an excessive amount of fast register memory. Finally, in some parameter combinations, the ODE system is stiff that require specialized implicit solution techniques.

After building up the governing equations, the next step is to choose a suitable hardware and software environment. As for the hardware, our choice is the massively parallel architecture of professional graphics cards (GPUs). The reason is their excellent computing power/price ratio. Nowadays, they are a solid part of any high performance computing cluster. In addition, as GPU programming is not straightforward and for many physical problems specialized codes are necessary to achieve reasonable performance, it is very likely to find free compute resources compared to CPUs. The massively parallel architecture of GPUs is also suitable for our purpose: performing extensive parameter studies. The replicated ODE systems having a different set of parameters are independent, and thus they can easily be parallelized. The ODE system is implemented in the general-purpose solver called MPGOS (Hegedűs, 2021) developed by the authors at the Department of Hydrodynamic Systems at the Budapest University of Technology and Economics. It is written in C++ and CUDA C software environment; therefore, low-level optimizations are possible during the implementation of the right-hand side of the ODEs. The program package is designed to overcome the various difficulties arising during the applications of GPUs (Hegedűs, 2021). Currently, only explicit Runge-Kutta schemes are implemented, which is the only drawback of the package. Nevertheless, the high processing power of the GPUs can usually compensate the requirements for the short time steps, and still, it is a better option than CPUs.

The details of the difficulties using GPUs can be summarized briefly as follows. The most important task is the proper exploitation of the memory hierarchy as the global memory bandwidth is not enough to feed the compute units with enough data and keep them busy. The main goal is to keep the frequently used data in the fast memory subsystem of the hardware. In CPUs, the problem is not severe as a low number of ODE systems are assigned to each CPU core (e.g., one ODE system

to a single core). Consequently, all the variables, parameters and coefficients comfortably fit into the fastest level-1 cache (for example, 64 kb cache means 8192 double-precision floating-point numbers) of the core, and extensive data reuse can be achieved, easing the pressure on the slow system memory. In addition, the data flow in the caches are managed by the hardware; thus, the user does not need extra effort.

In contrast, GPUs have thousands of threads residing on a main computational core (streaming multiprocessor) but still have roughly the same amount of level-1 cache. Therefore, the level-1 cache has much less importance. The strategy here is the efficient exploitation of the registers and the shared memory. Registers are the fastest memories in a GPU, and the user can easily define variables and even arrays in the registers, and load important and frequently used data from the slow global memory. However, it is a scarce resource, and in case of overuse, the compiler automatically spills data back to the slow global memory. Therefore, it needs special care by the user to prevent as much spilling as possible and use the available number of registers as efficiently as possible. This is a highly nontrivial task. The other available option is the exploitation of shared memory that is a user-manageable cache. It is shared as the content is visible for all the GPU threads in a block. In our specific application, shared memory can typically be used to store solver constants (e.g., the Butcher's tableau of Runge-Kutta algorithms), the Arrhenius constants or the third-body efficiency matrix and other coefficients common to all the threads. In summary, in the case of a complex system like our chemically active bubble model, extensive and explicit memory management is required by the user for efficient coding. This is the real pitfall (and art) of GPU programming.

The implemented ODE system is used for large parameter studies to reveal the complex dependency of the chemical yield on the driving parameters. In this sense, the pressure amplitude p_A and frequency f of the irradiation are the main control parameters. The pressure amplitude is varied between 0 and 2 bar with a linear distribution. The frequency range is 20 kHz–1 MHz, and its values are distributed logarithmically. The resolutions of both control parameters are 256; thus, a single bi-parametric simulation contains approximately 65 thousand parameter combinations (replication of independent ODE systems). In a sonochemical reactor, bubbles are presented with a variety of sizes; thus, the computations are repeated at four different bubble sizes: $R_E = 2$, 4, 6, and 8 μm, which covers typical bubble size distributions in experiments (Lee et al., 2005; R. Mettin et al., 1999). The total number of parameter combinations is 256 thousand.

4.4 Chemical yield of a single bubble

A good way of visualizing the chemical output of a bubble is to create high-resolution contour plots in the frequency-amplitude parameter space at different bubble sizes for each chemical species. In a contour plot, only a single value (amount of substance in mol) can be presented for a given parameter set, and information of the complete time series is lost. Therefore, special care has to be taken for the proper extraction of the plotted molar values. In Fig. 4.4, a typical numerical simulation is presented for a bubble size of $R_E = 8$ μm at pressure amplitude $p_A = 1.7$ bar and at frequency $f = 90$ kHz. The first eight acoustic cycles are regarded as a transient and discarded; the next four acoustic cycles are plotted. Keep in mind that a single acoustic cycle is defined as $\Delta\tau = 1$. In our experience, in situations of chemically highly active bubbles, such a short transient is enough due to the high energy loss (dissipation rate) of the bubble at the strong collapse. For chemically inactive bubbles, a much longer transient is necessary; however, these cases have a marginal influence on the plotted results. In the top panel of Fig. 4.4, the dimensionless bubble radius and the internal temperature are plotted as a function of the time. During the slow growth phase, the bubble radius (blue curve) reaches a local maximum; meanwhile, the temperature remains near the ambient temperature of the liquid (red curve). This process is followed by rapid contraction culminating in a highly compressed bubble and several thousands of degrees of Kelvin internal temperature. Due to the extreme conditions, chemical reactions take place. The temporal evolution of the ten chemical species is depicted in the bottom panel of Fig. 4.4. Their rapid change near the bubble collapse is clearly visible. These temporal fluctuations vanish during the bubble growth phase, and after some short time, the steady molecular composition of the bubble interior is reached by the following local maximum of the radius, see the vertical dashed lines. As the initial transient is dropped, all the chemical species are immediately presented in Fig. 4.4 at $\tau = 0$. For further use in the high-resolution contour plots, the chemical yield at a parameter combination is determined as the average of the amount (in mol) of a chemical species taken at four local maxima of the bubble radius (steady chemical composition) of four subsequent acoustic cycles. The values of the steady composition are used as the chemical yields near the collapse phase cannot be realized/extracted in a sonochemical reactor.

Fig. 4.5 shows the *average yield* (in mol) of different chemical species as a function of the excitation frequency and pressure amplitude with a bubble size of $R_E = 2$ μm. In order to avoid an overcrowded figure, out of the ten chemical species, only six is depicted. The resolution 256×256 mentioned previously is enough to reveal all the essential details. It is evident that each species requires specialised operation strategy (frequency-amplitude combination) to maximize their production. Roughly speaking, three types of optimal parameter domain can be distinguished altogether. For species H_2 and O_3, the optimal setup is organized along a band-shaped region in the parameter plane. This means that a definite optimum

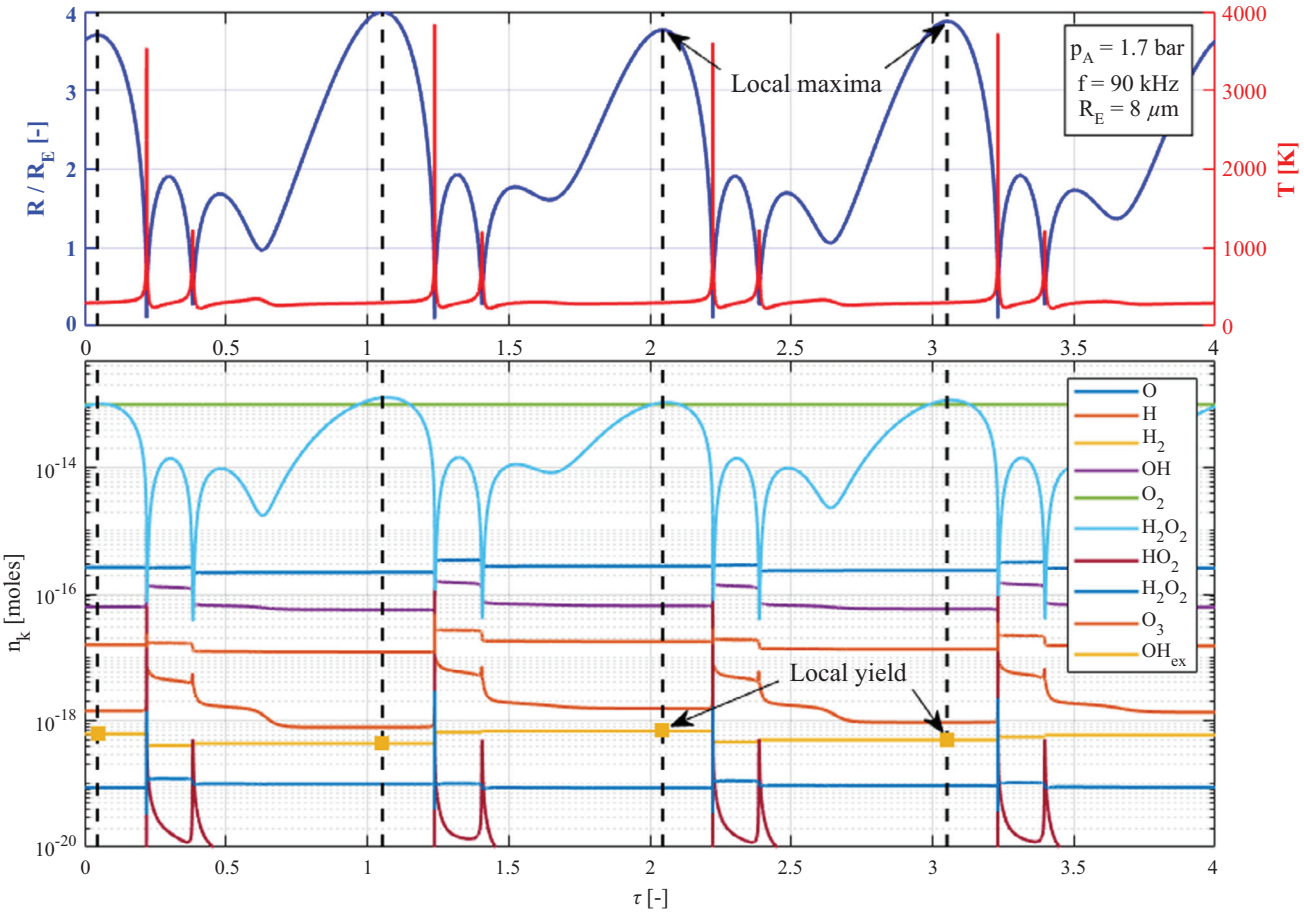

FIGURE 4.4 Top panel: Typical example of a bubble radius and temperature time series. Bottom panel: Temporal evolution of the corresponding chemical species inside a bubble.

operation frequency does not exist; however, for a given frequency value, there is an optimum operation pressure amplitude. Due to efficiency reasons, the frequency during a measurement cannot be tuned arbitrarily, it must be adjusted according to the resonance properties of the ultrasonic transducer and the geometry of the reactor. Therefore, this behavior can be advantageous from experimental point of view because of the wide range of applicable frequency values. The pressure amplitude can be easily fine-tuned via the irradiation intensity. The second type of domain is when the optimal operation conditions are organized around an optimal frequency value (in the applied parameter ranges). The chemical species O (≈65 kHz) and OH (≈300 kHz) fit into this category, where the employed pressure amplitude should be as high as possible. In this case, special care has to be taken during the design of the setup for an energy efficient ultrasonic irradiation at the desired frequency value. The third type of domain is the combination of the band-like and the optimum frequency-like behavior. In the case of the species H, an optimum frequency region (≈40 kHz) dominates the parameter space. In the case of H_2O_2, the band-type structure characterizes the pressure amplitude-frequency plane; however, the band itself is more dominant at higher frequency regions (≈300 kHz).

Comparing the contour plots of the chemical yields with the corresponding peak temperature and achieved maximum bubble expansion (indicator of the collapse strength) presented in Fig. 4.6, it is clear that reaching as high a temperature as possible must not be the primary objective. In terms of operation parameters, the optimal setup is *not* the lowest frequency with the highest-pressure amplitude. In terms of the state of the bubble dynamics, for some chemical species, there is an optimal internal temperature and collapse strength, see for example, the correlation of the isoline between the peak temperature values and the chemical yield of H_2 and O_3. A similar phenomenon is already demonstrated by (Kyuichi Yasui et al., 2004), who proved the existence of optimal internal temperature for the maximum production of oxidants (OH, O, H_2O_2, and O_3) in case of an air bubble. This seems to be a good qualitative agreement with the present results; however, in their study, the existence of an optimal temperature is vanished for an oxygen bubble (our case). The contradiction in the

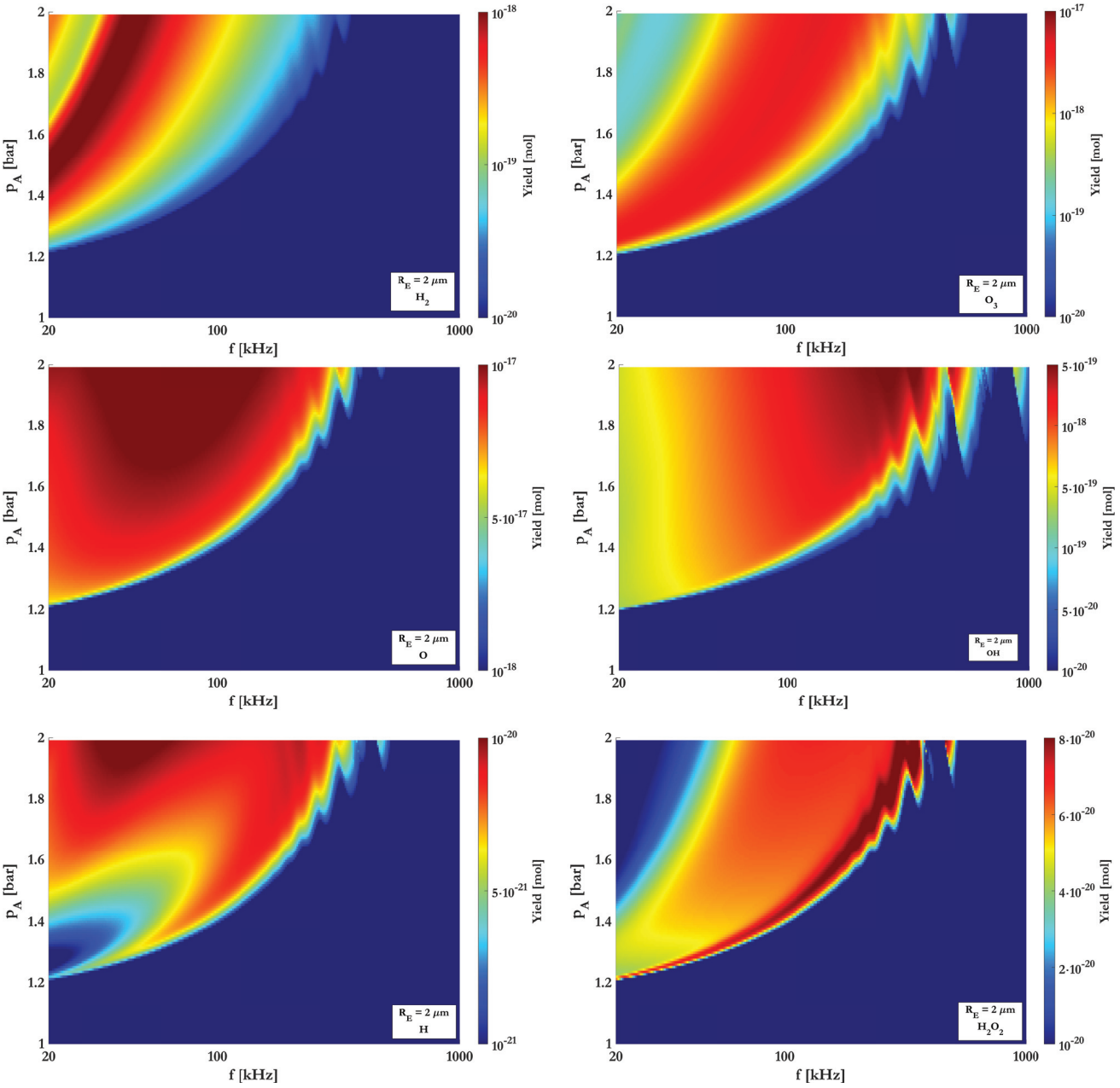

FIGURE 4.5 Average yield in mole of different chemical species as a function of the excitation frequency and pressure amplitude. The bubble equilibrium size is 2 microns.

qualitative behavior is driven by two main reasons. First, the employed parameters and their limits are slightly different: 0.5 μm bubble size and 3 bar maximum pressure amplitude. Second, the reaction mechanism is outdated.

The authors of the present study believe that there is no simple theoretical explanation for the existence of optimal parameter setups. Moreover, the region(s) of the high chemical yield can have a relatively complicated structure (which also differs from species to species); see, for instance, the contour plots of O and OH in Fig. 4.5. To demonstrate the problem, Fig. 4.7 presents simulations at 20 kHz excitation frequency and at two different pressure amplitude values: 1.5 bar (optimal for hydrogen molecule production) and 1.75 bar (next local minimum). In both cases, the initial time is shifted to the peak temperature value. The left-hand side of the figure shows that the after bounces can play a significant role in the steady composition at the maximum bubble radius. After the first collapse, the total amount of hydrogen molecules is larger at the higher-pressure amplitude (higher peak temperature, see the red curves). However, the impact of the molecular recombination of the first after bounce at $p_A = 1.75$ bar significantly reduces the amount of H_2 molecules compared to the

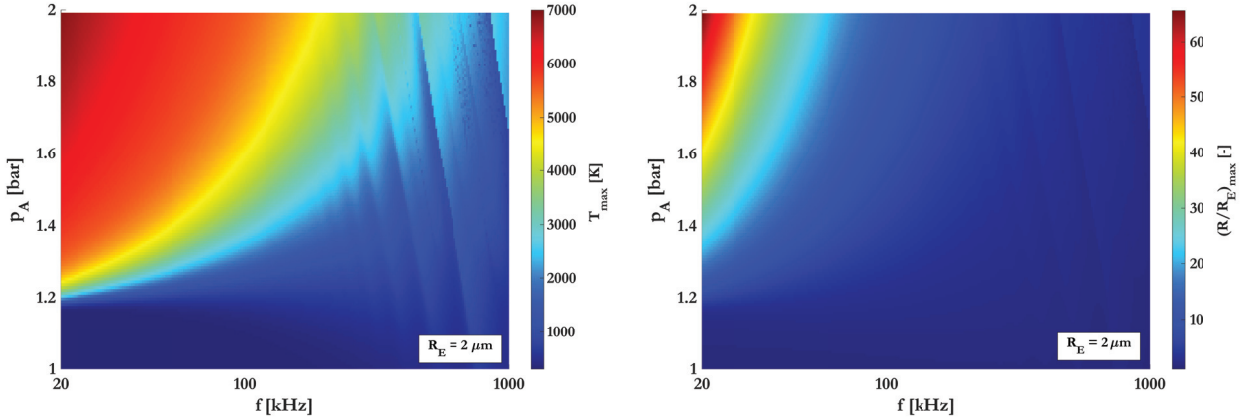

FIGURE 4.6 Peak temperature and maximum bubble expansion contour plots as a function of the frequency and pressure amplitude for an equilibrium bubble size of two micron.

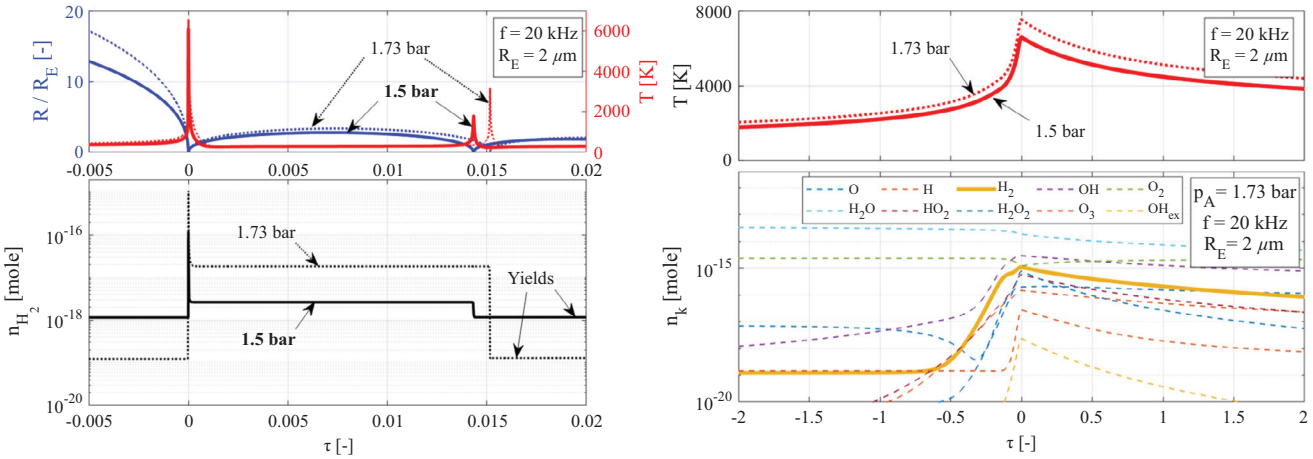

FIGURE 4.7 Left: dynamics of the bubble radius (blue curve), internal temperature (red curve) and the amount of H2 (black curve) near the main collapse and the after the first rebound. Right: Evolution of the temperature and all the chemical species near the main collapse.

$p_A = 1.5$ bar case. Thus, the overall amount of H_2 is higher for the lower pressure amplitude case. The right-hand side of the figure illustrates the dynamics of the whole system near the main collapse. It is clearly visible that at the peak temperature state, the temporal evolution of the chemical species is in the middle of a fast transient. Therefore, the actual composition at the peak temperature can vary significantly and can have a notable influence on the recombination process in the growth phase and thus on the equilibrium concentrations at the maximum bubble radius. Consequently, the nontrivial optimal parameter domains and their shapes can be the feature of the complex dynamical system of the chemically active bubble.

Despite the discrepancy with (Kyuichi Yasui et al., 2004) (optimal temperature issue), our optimal operation parameter domains show good qualitative agreements with experiments. For instance, (Gogate & Patil, 2016; P.M. Kanthale et al., 2007; Prabhu et al., 2004) showed that the production of H_2O_2 has a maximum at 355 kHz excitation frequency. The employed frequencies during the experiment were 213 kHz, 355 kHz, 647 kHz, and 1056 kHz. The equilibrium size of the bubble was around 4 μm; however, we shall see at the end of this section that the approximately 300 kHz optimum frequency for the production of H_2O_2 is nearly independent of the bubble size. A similar observation is reported by (Brotchie, Ashokkumar, et al., 2008; Brotchie, Grieser, et al., 2008); namely, higher production of H_2O_2 at 355 kHz than at 20 kHz excitation frequency. The experimental results of (Jiang et al., 2006) and (Pétrier & Francony, 1997) demonstrated that the degradation of 4-chlorophenol and carbon tetrachloride was maximal at 200 kHz out of the frequency values of 20 kHz, 200 kHz, 500 kHz, and 800 kHz. They attribute the degradation to the production of OH radicals and hydrogen peroxide (H_2O_2). This is also consistent with our numerical findings, especially for larger bubble sizes where the optimal frequency domain for these species is shifted from around 300 kHz to approximately around 200 kHz, see Fig. 4.8, Fig. 4.9 and Fig. 4.10. Because of the good qualitative agreement with experimental findings, we consider our bubble model, including the reaction mechanism, qualitatively validated.

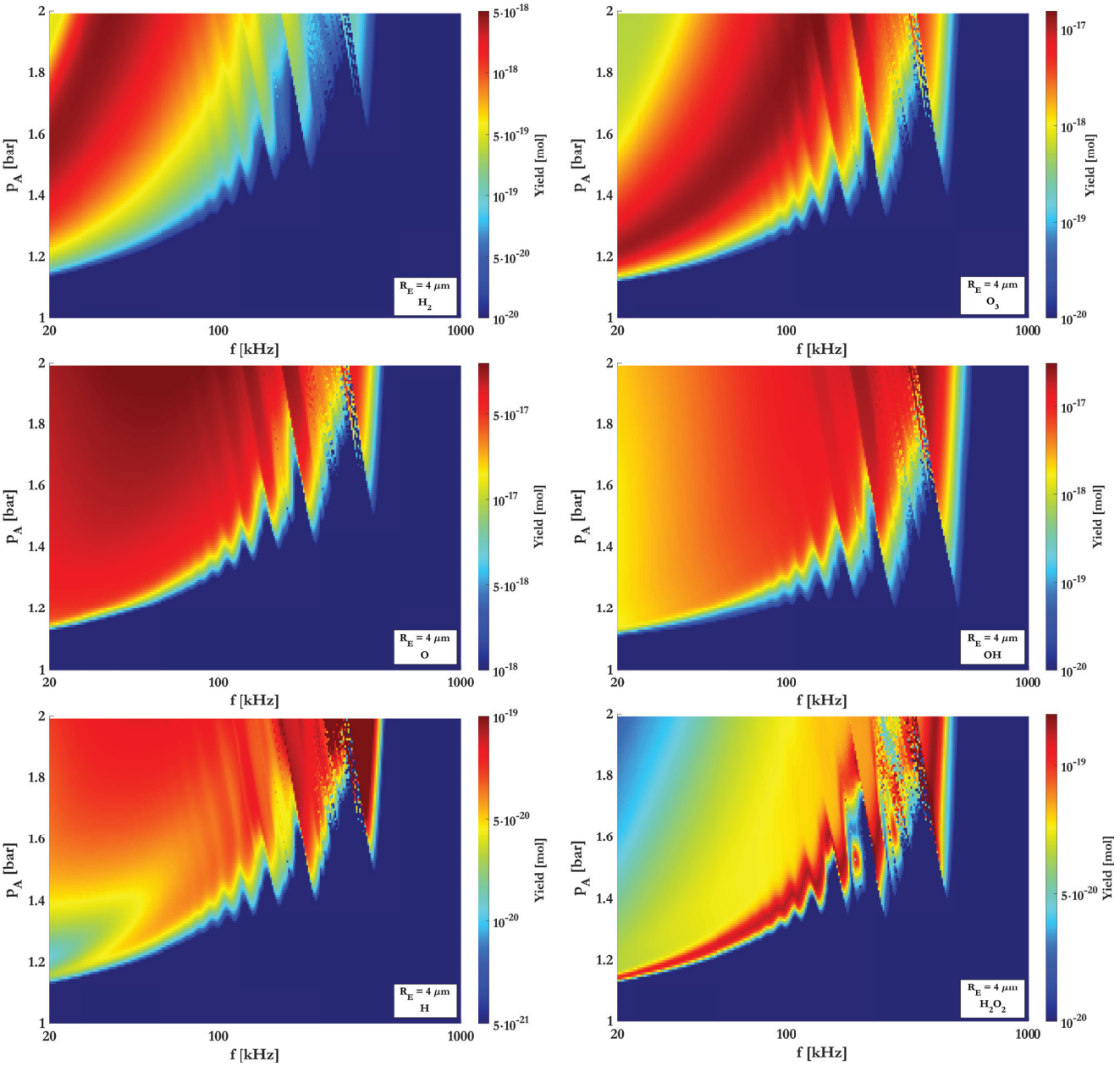

FIGURE 4.8 Average yield in mole of different chemical species as a function of the excitation frequency and amplitude. The bubble equilibrium size is 4 micron.

In a sonochemical reactor, the presented bubble clusters consist of bubbles having specific size distributions (Lee et al., 2005; R. Mettin et al., 1999). To reveal the effect of the equilibrium bubble size on the chemical yield, another series of figures are created and plotted using 4 μm (Fig. 4.8), 6 μm (Fig. 4.9), and 8 μm bubble sizes (Fig. 4.10). The parameter resolution and their ranges are the same as in the case of Fig. 4.5. Also, the same chemical species are investigated.

The comparison of the domains of optimal operation parameters shows that the identified three types of structures (band, optimal frequency value, mixed) are still present at all the studied bubble sizes. In fact, these domains do not change significantly with the bubble size except for the slight shift towards the lower frequency regions, compare, for instance, the subplots of OH and H_2O_2. This observation can explain the good qualitative agreement with the experimental results discussed previously (Brotchie, Ashokkumar, et al., 2008; Brotchie, Grieser, et al., 2008; Jiang et al., 2006; P. Kanthale et al., 2008; Pétrier & Francony, 1997): all the bubbles (having different equilibrium sizes) in the sonochemical reactor have approximately the same optimal operation conditions for producing a chemical species. The only notable difference that

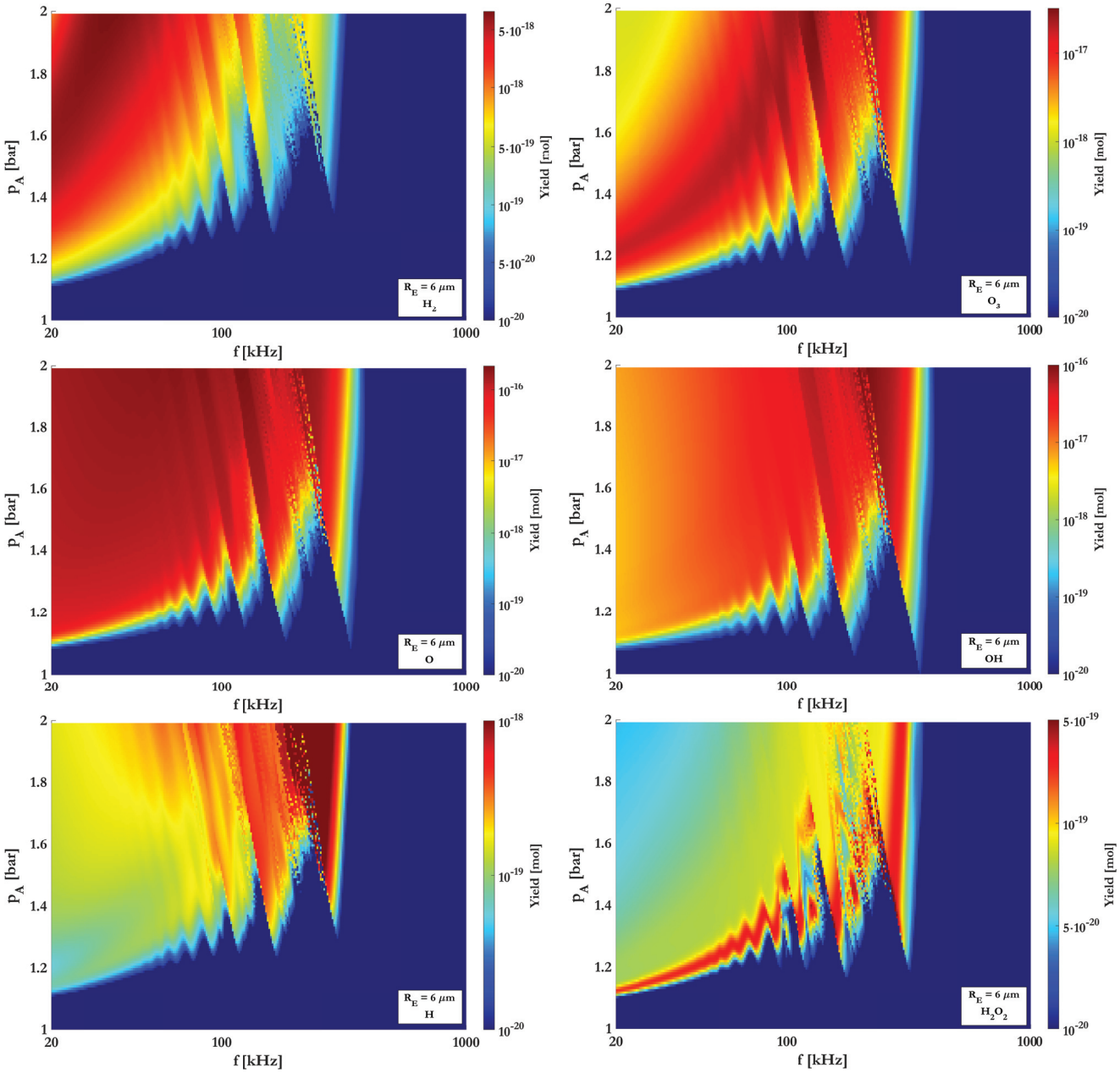

FIGURE 4.9 Average yield in mole of different chemical species as a function of the excitation frequency and amplitude. The bubble equilibrium size is 6 micron.

appears with growing bubble size is the increasing influence of the resonance behavior of the bubble. This phenomenon appears as parallel stripes in the red regions of the contour plots, see especially Fig. 4.10. In order to illustrate that the stripes are indeed caused by the main and harmonic resonances of the system, the maximum bubble expansion is plotted in the frequency-pressure amplitude parameter plane in Fig. 4.11. The resonance horns (local peaks in the bubble expansion) appear as light-blue wedges. The main resonance frequency of an 8 μm bubble is approximately 430 kHz represented by the biggest wedge. The smaller wedges accumulated towards the lower frequency ranges are the harmonics of the main resonance caused by the non-linearity of the system (Klapcsik et al., 2018; W. Lauterborn, 1976; W. Lauterborn & Holzfuss, 1991). For the details of the resonance properties of a single bubble, the reader is referred to publications (Klapcsik & Hegedűs, 2017; W. Lauterborn, 1976; A.J. Sojahrood et al., 2019; A. J. Sojahrood et al., 2015). Observe that the left-hand sides of the resonance horns in Fig. 4.11 match with the left-hand sides of the stripes in Fig. 4.10. This sudden change in the amplitude of the oscillation and the chemical yield is due to the hysteric behavior of the resonances. Although the appearance

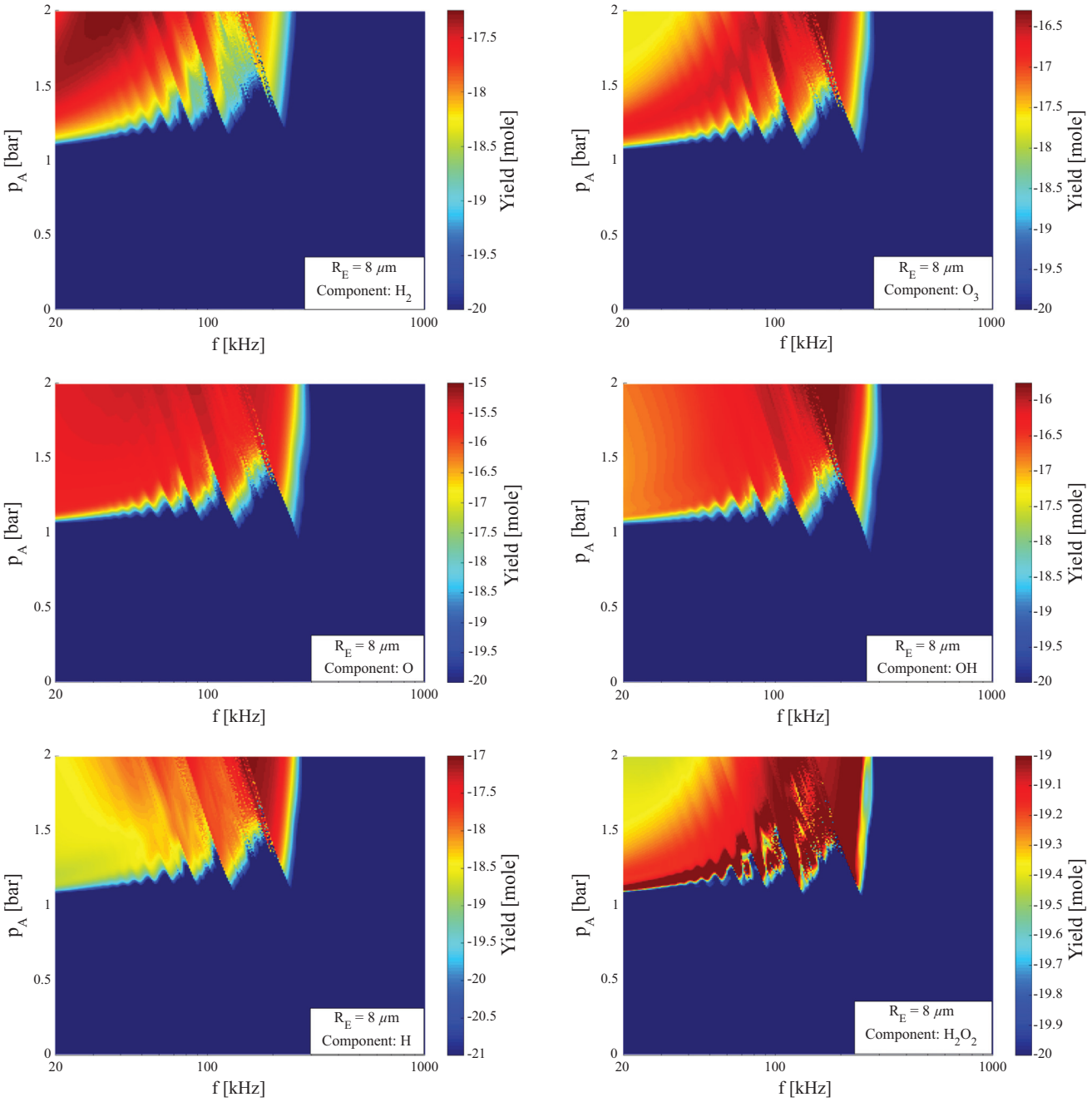

FIGURE 4.10 Average yield in mole of different chemical species as a function of the excitation frequency and amplitude. The bubble equilibrium size is 8 micron.

of the resonance properties complicates the structure of optimal operation conditions, it does not alter significantly the location and extent of these domains.

As a final remark of this section, let us highlight the importance and strength of high-resolution parameter scans (thus, high-performance computing). In the study of (K. Kerboua, Hamdaoui, & Alghyamah, 2021; K. Kerboua, Merouani, et al., 2021; K. Kerboua & Hamdaoui, 2018, 2020; Kaouther Kerboua & Hamdaoui, 2018, 2019; Rashwan et al., 2020, 2019; Rivas et al., 2013; Stricker & Lohse, 2014; Toegel & Lohse, 2003; K. Yasui et al., 2008; Kyuichi Yasui et al., 2007; Kyuichi Yasui, 2001; Kyuichi Yasui et al., 2004; Kyuichi Yasui & Kato, 2012), the effect of the saturating gas on the production of hydrogen by a single bubble is investigated. The employed saturating gases were oxygen, air, nitrogen, and argon. Based on

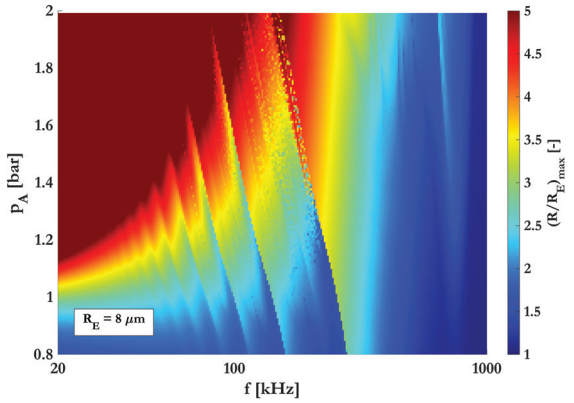

FIGURE 4.11 Maximum bubble expansion as a function of the frequency and pressure amplitude for an equilibrium bubble size of 8 micron.

a single parameter combination (20 kHz frequency, 0.403 W/cm^2 irradiation intensity), the amount of hydrogen production (in mole) was in the order of 10^{-27} (oxygen bubble) and 10^{-17} (argon bubble). The other saturating gases performed in between these two values. Due to the many orders of magnitude difference, the authors correctly concluded that employing argon is superior to all the other gases. However, our results show that with an oxygen bubble, the production of hydrogen can also be in the order of 10^{-17} mole with the proper choice of the frequency—amplitude combinations, see the main red domains in the top-left panels of Fig. 4.5-Fig. 4.10. This implies that a) other gases can also be as efficient as argon with the proper selection of the driving parameters, or b) argon is still superior, and its hydrogen production capability can still be improved by optimizing the excitation parameters. This question can be easily resolved by performing similar high-resolution scans with other gases. This is beyond the scope of the present study.

4.5 Energy efficiency considerations

In the previous section, the net yield of sonochemical bubbles was examined. However, from an engineering point of view, it could become essential to find optimal operation areas also in terms of energy consumption. This means that an efficiency metric has to be defined that compares the chemical yield to the amount of power or energy dissipated by the oscillating bubble. For the input power, some important considerations have to be made.

In sonochemical experiments, a common approach is to calculate the emitted power by the employed ultrasonic transducers and measure the concentration of a chemical species after some sonication time (Son et al., 2012). This provides an overall energy efficiency estimate for the production of a chemical species. Many numerical studies try to mimic this approach (K. Kerboua, Hamdaoui, & Alghyamah, 2021; K. Kerboua, Merouani, et al., 2021; K. Kerboua & Hamdaoui, 2018, 2020; Kaouther Kerboua & Hamdaoui, 2018, 2019; Rashwan et al., 2020a, 2019; Rivas et al., 2013; Stricker & Lohse, 2014; Toegel & Lohse, 2003; K. Yasui et al., 2008; Kyuichi Yasui et al., 2007; Kyuichi Yasui, 2001; Kyuichi Yasui et al., 2004; Kyuichi Yasui & Kato, 2012): (1) the required input power can be estimated from the employed pressure amplitude; (2) the computation of the overall chemical yield is based on the calculation of the chemical yield of a single bubble multiplied by the estimated average number of the bubbles present in the sonochemical reactor. However, the determination of the number of bubbles can be inaccurate as it is based on empirical correlations between the bubble population density and the irradiation parameters (K. Kerboua, Hamdaoui, & Alghyamah, 2021; K. Kerboua, Merouani, et al., 2021; K. Kerboua & Hamdaoui, 2020; Merouani et al., 2015; Rashwan et al., 2020a, 2019; Rivas et al., 2013; Stricker & Lohse, 2014; K. Yasui et al., 2008; Kyuichi Yasui & Kato, 2012). Such a numerical approach cannot estimate the theoretical energy efficiency as there is no direct connection between the chemical production and the dissipated power.

The primary source of energy dissipation comes from the oscillation of the individual bubbles. There are three main mechanisms identified (Jamshidi & Brenner, 2013; Louisnard, 2010, 2012; Trujillo, 2018, 2020). First, the liquid viscosity itself causes damping on the bubble oscillation. Second, the elevated temperature during the compression phase induces heat transfer from the bubble interior to the bulk liquid resulting in thermal damping. Third, in strong collapses, the bubbles themselves emit pressure waves (or even shock waves), representing a considerable loss of kinetic energy. Assuming spherical bubble behavior and calculating the dissipated power/energy based on the aforementioned mechanisms,

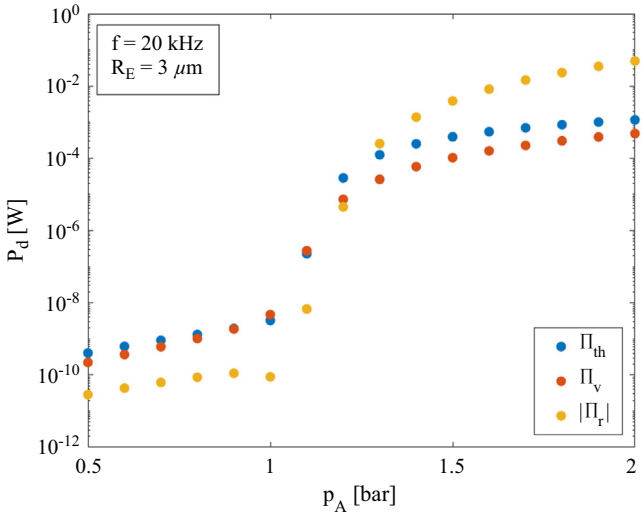

FIGURE 4.12 The three dissipated power terms for various pressure amplitudes at 20 kHz driving frequency and a bubble size of 3 micron.

a theoretical upper limit for the energy efficiency of the chemical production can be estimated. This approach uses consistent data related to the dynamics of a single bubble.

Naturally, in an actual sonochemical reactor, the thousands of bubbles have complicated interactions that might lead to non-spherical collapse (K. Klapcsik et al., 2018; W. Lauterborn & Holzfuss, 1991; W. Lauterborn & Parlitz, 1988; A.J. Sojahrood et al., 2019; A.J. Sojahrood et al., 2017) or acoustic shielding of the ultrasonic irradiation (van Iersel et al., 2008). These phenomena have negative effect on energy efficiency (less chemical production and/or increased dissipation rate). With a clever operation strategy, these negative effects can be minimized or controlled, see, for example, a simple ON-OFF technique to decrease the effect of acoustic shielding (Lee et al., 2011). This is the other reason why the single bubble-based approach is employed in this study. That is, even if we estimate the number of bubbles in a reactor correctly, the overall energy dissipation highly depends on the bubble cluster structure (and on its temporal evolution), which cannot be determined merely from the irradiation parameters accurately.

The estimation of the power dissipation of a single bubble is an extensive research area in sonochemistry (Jamshidi & Brenner, 2013; Louisnard, 2010, 2012; Trujillo, 2018, 2020). The technique employed in this study is adopted from (Jamshidi & Brenner, 2013). The effect of the three main dissipation mechanisms can be calculated as

$$\Pi_{th} = \frac{1}{T_p} \int_0^{T_p} -\left(p\left(1 + \frac{\dot{R}}{c_L}\right)\frac{R}{c_L}\dot{p}\right)\dot{V}\, dt \tag{4.45}$$

$$\Pi_{v} = \frac{1}{T_p} \int_0^{T_p} 16\pi\, \mu_L \left(R\dot{R}^2 + \frac{R^2\dot{R}\ddot{R}}{c_L}\right) dt \tag{4.46}$$

$$\Pi_{r} = \frac{4\pi}{T_p c_L} \int_0^{T_p} R^2\, \dot{R}\left(\dot{R}p + \dot{p}R - \frac{1}{2}\rho_L\dot{R}^3 - \rho_L R\dot{R}\ddot{R}\right) dt \tag{4.47}$$

where $T_p = 1/f$ is the period of the excitation, Π_v, Π_v and Π_r are the thermal, viscous and radiation dissipations in units of Watt, respectively. Note that all these three quantities can be calculated from the time curves presented in the section about the governing equations. The sum of them is the total dissipated power Π_w of a single bubble is

$$\Pi_w = \Pi_{th} + \Pi_v + \Pi_r \tag{4.48}$$

where the subscript w indicates the unit of Watt. It is worth noting that Π_w is an average value for a complete acoustic cycle. The three dissipation quantities are depicted in Fig. 4.12 for several values of p_A at $f = 20$ kHz and $R_E = 3\ \mu m$.

Similarly, the total dissipated *energy* can be estimated with Π_w as

$$\Pi_{J,i} = \sum_{j=1}^{i} T_p\, \Pi_{w,j} \tag{4.49}$$

where $\Pi_{J,i}$ the total (accumulated) dissipated energy after the ith cycle, and $\Pi_{w,j}$ is the dissipated power in the jth cycle. With these two dissipation quantities, it is possible to define efficiency metrics in terms of a single bubble.

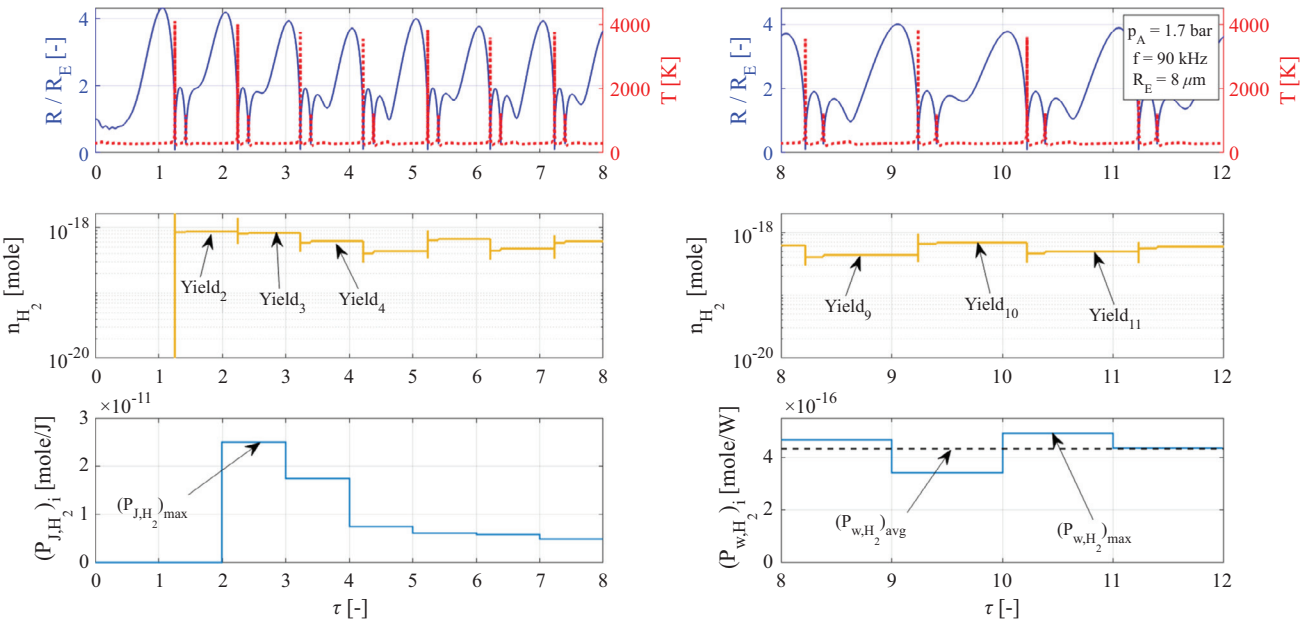

FIGURE 4.13 An example for the calculation of the energy efficiency metrics. The parameter values are pA = 1.7 bar, f = 90 kHz and RE = 8 micron.

The first metric is obtained from the Π_w values: the local yield of chemical species k is divided by the local value of $\Pi_{w,j}$ in the actual (jth) cycle as

$$P^k_{w,j} = \frac{\text{Yield}^k_j}{\Pi_{w,j}} \tag{4.50}$$

Note that the unit of $P^k_{w,j}$ is mole/Watt. It is calculated only in the convergent phase of the simulations (after 8 acoustic cycles). An average and a maximum value of $P^k_{w,j}$ can be determined from the convergent period as

$$P^k_{w,avg} = \frac{1}{J}\sum_{j=1}^{J} P^k_{w,j} \tag{4.51}$$

and

$$P^k_{w,max} = \max_j \left(P^k_{w,j}\right) \tag{4.52}$$

where J is the total number of convergent cycles. These quantities provide information on how much power is continuously dissipated without further increase of the chemical yield (convergent bubble oscillations).

In order to take into account, the lifetime of the bubble, a second metric is defined from the Π_J values: the local yield of a chemical component k is divided by the accumulated dissipated energy $\Pi_{J,i}$ in the ith transient cycle as

$$P^k_{J,i} = \frac{\text{Yield}^k_i}{\Pi_{J,i}} \tag{4.53}$$

Note that the unit of $P^k_{J,i}$ is mole/Joule and that the accumulated dissipated energy grows gradually from cycle to cycle. Therefore, $P^k_{J,i}$ has a rapid increase in the first few cycles followed by slow decreasing as time passes. The maximum value of $P^k_{J,i}$ defined as

$$P^k_{J,max} = \max_i \left(P^k_{J,i}\right) \tag{4.54}$$

can provide an estimation for the upper theoretical limit of the energy efficiency of a sonochemical process: *maximum* chemical yield with the *least number* of acoustic cycles.

For demonstration purposes, Fig. 4.13 shows an example for the calculation of the energy efficiency metrics. On the left panel, the time curves in the transient phase are shown for the molecule H_2 at the same parameter combination as in the

case of Fig. 4.4. It is clearly seen that after two acoustic cycles, the total amount of hydrogen molecule does not change significantly (middle chart). Such a short period is enough to obtain a relatively stable chemical composition of the bubble interior. Naturally, at each collapse phase, high fluctuations (peaks) still exist. Since the diffusion from the bubble interior into the liquid domain is a slow process, the long lifetime of a highly spherical bubble is energetically disadvantageous. One way to overcome this issue is to adjust the driving parameters so that the bubble loses its spherical stability. The non-spherical collapse enhances the mixing between the bubble interior and the liquid domain. This phenomenon has been demonstrated in a single-bubble experiment (a levitated bubble) (Mettin et al., 2015), where the fragmented bubble collapse caused high chemical activity (even visible by the naked eye) in contrast to the case of a spherically stable bubble. Naturally, the non-spherical oscillation increases the energy dissipation rate; for instance, it increases the turbulence around a bubble (called micromixing (Jordens et al., 2016)) and thus the viscous dissipation. In a sonochemical reactor, the generated bubble clusters have complicated dynamics via translation, merging, and splitting (Mettin, 2007); thus, bubble fragmentation is only a matter of time in the long term. Still, a proper optimization strategy has to take into account the useful bubble lifetime. This is also demonstrated by the bottom-left panel of Fig. 4.13, where the value of $P_{J,i}^{H_2}$ shows a decreasing trend after the third transient cycle.

The right panel of Fig. 4.13 presents the same time series curves as the left-hand side but for the convergent phase of the simulation (cycles 8–12). On the bottom chart, the local $P_{w,i}^{H_2}$ values are drawn for each convergent cycle. Since the solution is not purely periodic, the values have an oscillating behaviour. Their global maximum and their average (dashed line) are shown in the figure as well.

To reveal the optimal operation conditions in terms of energy efficiency, Fig. 4.14 and Fig. 4.15 plot the values of $P_{w,max}^{k}$ (middle rows) and $P_{J,max}^{k}$ (bottom rows), and compare them with the average yields (top rows) discussed already in the previous section. To avoid the overuse of the panels, only results of $RE = 6\ \mu m$ is shown for some selected chemical species (H_2, H_2O_2, O_3 and H). The comparison of the different subplots reveals that the optimal domains of the driving parameters are not altered significantly by taking into account the energy dissipation mechanisms. The chemical species H_2 and O_3 have the only noticeable difference: the shift of the optimal parameter domain towards the lower frequency values (if energy efficiency is considered). This observation implies that no compromise has to be made between the maximum chemical yield and the energy-efficient operation. However, keep in mind that the driving parameters significantly influence the bubble structure and its temporal evolution in a sonochemical reactor. Therefore, the presented diagrams have to be considered as results of fundamental research instead of a direct guidance of operation strategies. As a final remark, the same conclusions can be drawn for the rest of the bubble sizes and chemical species (not shown here).

Finally, let us compare energy efficiency metrics of hydrogen production with the literature. In the present study, the production of hydrogen (theoretical peak) by a single bubble is approximately 10^{-10} mole/J. In the paper of (Rashwan et al., 2020b), this number is orders of magnitudes lower (approx. 10^{-15} mole/J). The authors employed energy efficiency calculations based on single bubble chemical yield and the total input energy of a reactor. The chemical computation and the energy dissipation are decoupled (see our previous discussion about the topic). This indicates that with a clever control of the acoustic bubble structure to minimize additional dissipation mechanisms, the sonochemical hydrogen production has a much larger potential.

4.6 Discussion and summary

Modelling the chemical reactions inside sonochemical bubbles has been in large interest of researchers in the last decades. Many studies were made with different chemical mechanisms in order to maximize or optimize the operation of sonochemical reactors. They focused on net chemical output and energetic approaches, as well. However, chemical modelling of these works turned out to be outdated, and several specific effect (such as third-body efficiencies, pressure-dependency, etc.) were barely taken into account.

In this chapter, an up-to-date, precisely validated chemical mechanism is presented for bubbles containing pure oxygen and water vapor. Specific third-body efficiencies are used, pressure-dependency of several reactions are taken into account, and duplicated reactions are included as well. The backward reaction constants are calculated via thermodynamic equilibrium conditions. Various thermodynamical quantities are obtained from the NASA chemical equilibrium code, as the polynomial fits of temperature. The complete bubble model is finalized with first law of thermodynamics and the Keller-Miksis equation.

High-resolution parameters studies were carried out regarding the ultrasound parameters (pressure amplitude and frequency) on 4 different bubble sizes. It was shown that each species requires different operation strategy in order to maximize the chemical output. Three types of optimal parameter domains were distinguished (band-shaped, optimal

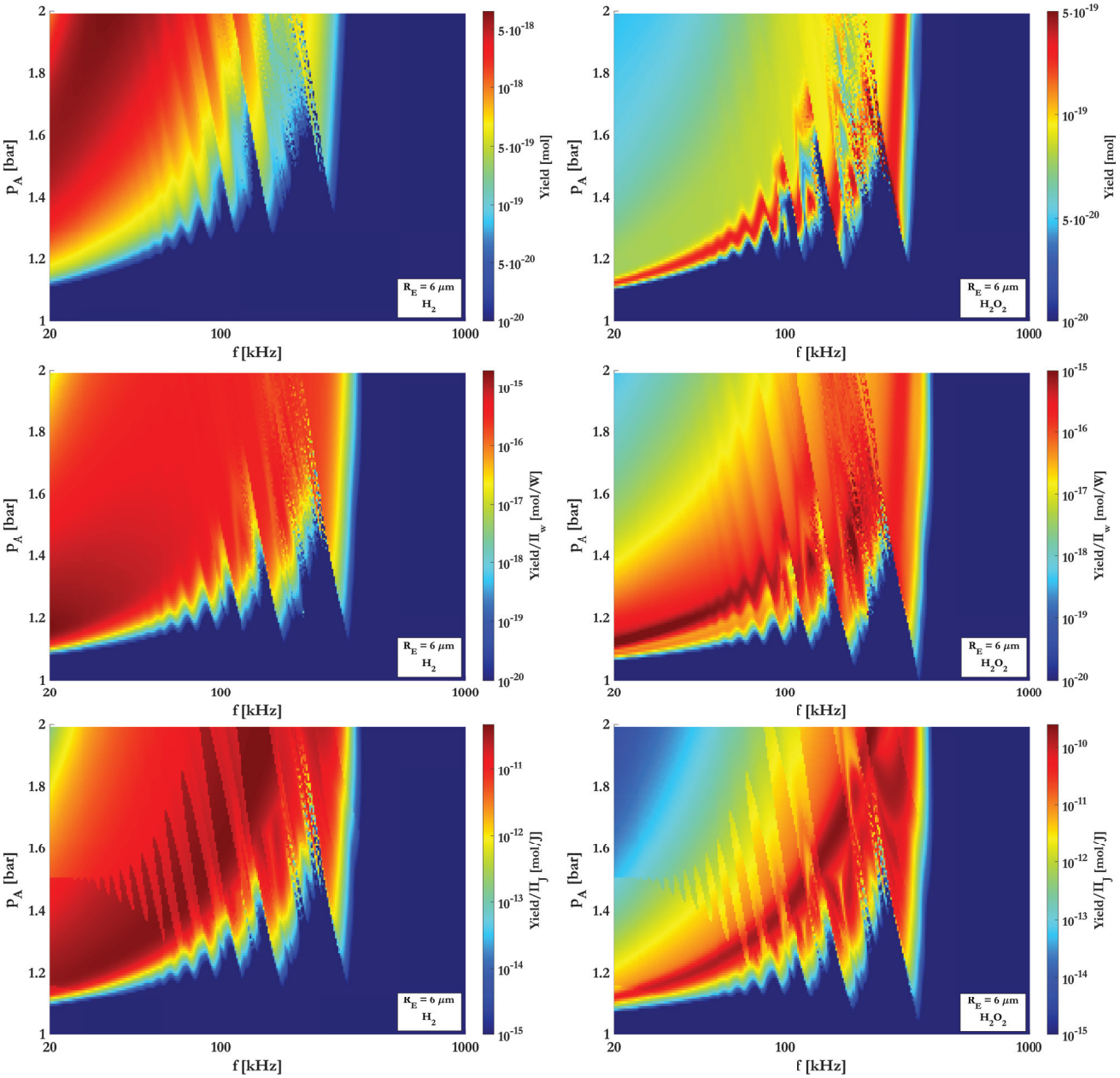

FIGURE 4.14 Average yield in mole and energy efficiency charts as a function of the excitation frequency and amplitude for chemical species H_2 and H_2O_2. The bubble equilibrium size is 6 micron.

frequency, and combined). It was identified that reaching as high temperature as possible not necessarily induce the highest chemical output. It was also hypothesized that there is simple theoretical explanation for the existence of optimal setups. The best operational domains can vary from species to species and can have a fairly complex structure. The findings were compared to several numerical and experimental results, with reasonably good agreement being found.

In the other part of the chapter, some energy efficiency conclusions were taken. Two different efficiency metrics were introduced using the dissipated energy by a single sonochemcial bubble. It was shown that only a slight shift can be observed between the maximum chemical output and the energy-efficient operation. However, these results are rather fundamental behavior then direct guidelines for operation strategies. The energy-efficiency of H_2 was compared to the assumptions of (Rashwan et al., 2020). It was revealed that even several magnitudes higher efficiency can be achieved applying proper driving strategy.

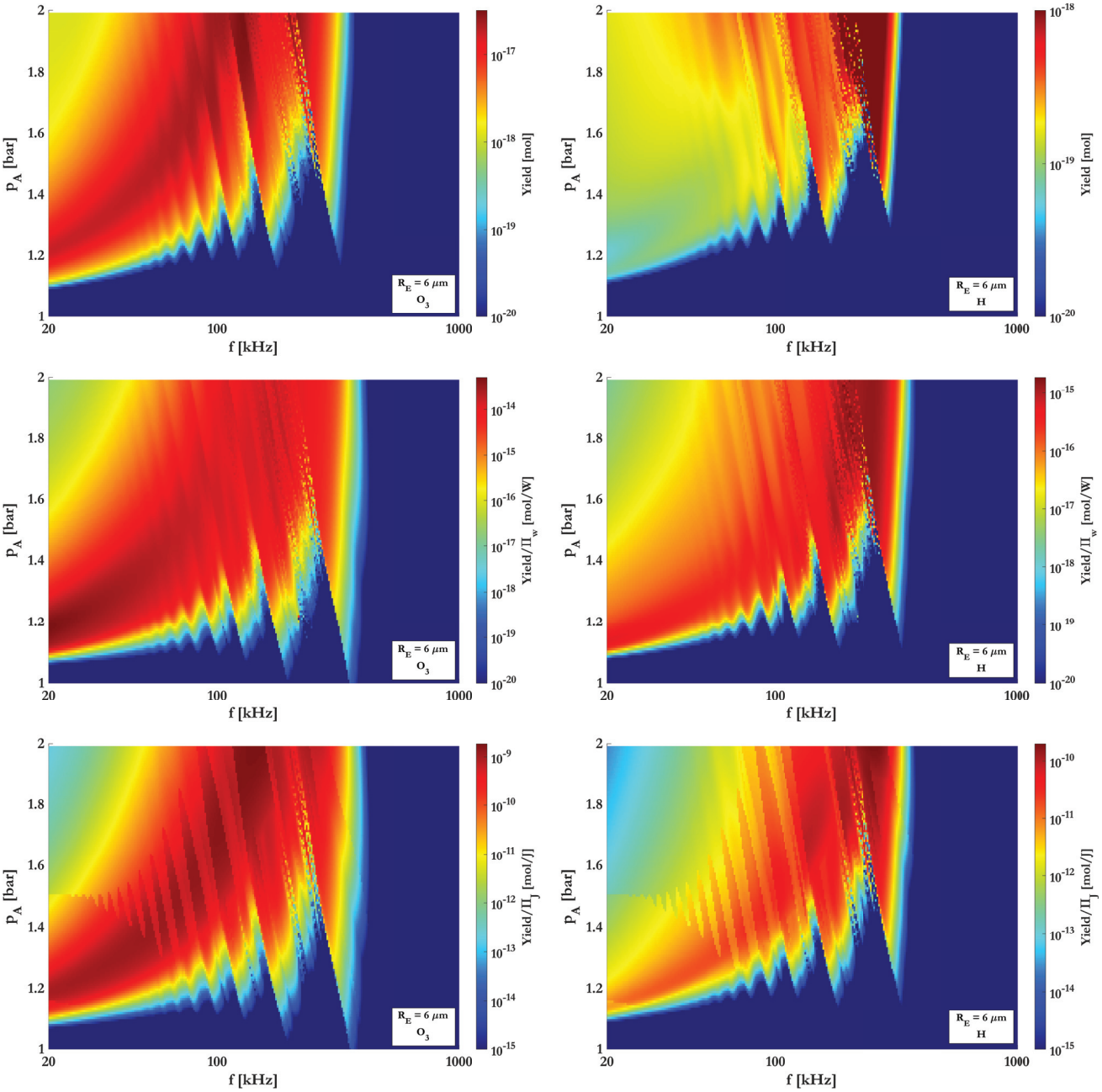

FIGURE 4.15 Average yield in mole and energy efficiency charts as a function of the excitation frequency and amplitude for chemical species O_3 and H. The bubble equilibrium size is 6 micron.

References

Atkins, P., De Paula, J., 2014. Atkins' Physical Chemistry. OUP, Oxford.

Brenner, M.P., Hilgenfeldt, S., Lohse, D., 2002. Single-bubble sonoluminescence. Rev. Mod. Phys. 74 (2), 425–484.

Brotchie, A., Ashokkumar, M., Grieser, F., 2008. Sonochemistry and sonoluminescence under simultaneous high- and low-frequency irradiation. J. Phys. Chem. C 112 (22), 8343–8348.

Brotchie, A., Grieser, F., Ashokkumar, M., 2008. Sonochemistry and sonoluminescence under dual-frequency ultrasound irradiation in the presence of water-soluble solutes. J. Phys. Chem. C 112 (27), 10247–10250.

Cavalieri, F., Chemat, F., Okitsu, K., Sambandam, A., Yasui, K., Zisu, B., 2016. Handbook of Ultrasonics and Sonochemistry, 1st ed. Springer Nature, Singapore. https://doi.org/10.1007/978-981-287-278-4.

Colussi, A.J., Weavers, L.K., Hoffmann, M.R., 1998. Chemical bubble dynamics and quantitative sonochemistry. J. Phys. Chem. A 102 (35), 6927–6934.
Draye, M., Kardos, N., 2016. Advances in green organic sonochemistry. Top. Curr. Chem. (Z) 374 (74), 1–29.
Fujikawa, S., Akamatsu, T., 1980. Effects of the non-equilibrium condensation of vapour on the pressure wave produced by the collapse of a bubble in a liquid. J. Fluid Mech. 97 (3), 481–512. https://doi.org/10.1017/S0022112080002662.
Gardiner Jr., W.C., 1984. Combustion Chemistry. Springer-Verlag, New York, NY.
Gilbert, R.G., Luther, K., Troe, J., 1983. Theory of thermal unimolecular reactions in the fall-off range. II. Weak collision rate constants. Ber. Bunsenges. Phys. Chem. 87 (2), 169–177.
Gogate, P.R., Patil, P.N., 2016. Sonochemical Reactors. Top. Curr. Chem. (Z) 374 (61), 1–27.
Gole, V.L., Fishgold, A., Sierra-Alvarez, R., Deymier, P., Keswani, M., 2018. Treatment of perfluorooctane sulfonic acid (PFOS) using a large-scale sonochemical reactor. Sep. Purif. Technol. 194, 104–110.
Gordon, S., 1976. Computer Program for Calculation of Complex Chemical Equilibrium Compositions, Rocket Performance, Incident and Reflected Shocks, and Chapman-Jouguet Detonations, Vol. 273. Scientific and Technical Information Office, National Aeronautics and Space Administration, Houston, TX.
Hegedűs, F., 2021. Program package MPGOS: challenges and solutions during the integration of a large number of independent ODE systems using GPUs. Commun. Nonlinear Sci. Numer. Simul. 97, 105732.
Hegedűs, F., Klapcsik, K., Lauterborn, W., Parlitz, U., Mettin, R., 2020. GPU accelerated study of a dual-frequency driven single bubble in a 6-dimensional parameter space: The active cavitation threshold. Ultrason. Sonochem. 67, 105067.
Islam, M.H., Burheim, O.S., Hihn, J.-Y., Pollet, B.G., 2021. Sonochemical conversion of CO2 into hydrocarbons: The Sabatier reaction at ambient conditions. Ultrason. Sonochem. 73, 105474.
Islam, M.H., Burheim, O.S., Pollet, B.G., 2019. Sonochemical and sonoelectrochemical production of hydrogen. Ultrason. Sonochem. 51, 533–555.
Jamshidi, R., Brenner, G., 2013. Dissipation of ultrasonic wave propagation in bubbly liquids considering the effect of compressibility to the first order of acoustical Mach number. Ultrasonics 53 (4), 842–848.
Jiang, Y., Pétrier, C., Waite, T.D., 2006. Sonolysis of 4-chlorophenol in aqueous solution: Effects of substrate concentration, aqueous temperature and ultrasonic frequency. Ultrason. Sonochem. 13 (5), 415–422.
Jordens, J., Bamps, B., Gielen, B., Braeken, L., van Gerven, T., 2016. The effects of ultrasound on micromixing. Ultrason. Sonochem. 32, 68–78.
Kanthale, P., Ashokkumar, M., Grieser, F., 2008. Sonoluminescence, sonochemistry (H2O2 yield) and bubble dynamics: frequency and power effects. Ultrason. Sonochem. 15 (2), 143–150.
Kanthale, P.M., Gogate, P.R., Pandit, A.B., 2007. Modeling aspects of dual frequency sonochemical reactors. Chem. Eng. J. 127 (1–3), 71–79. https://doi.org/10.1016/j.cej.2006.09.023.
Kerboua, K., Hamdaoui, O., 2018. Influence of reactions heats on variation of radius, temperature, pressure and chemical species amounts within a single acoustic cavitation bubble. Ultrason. Sonochem. 41, 449–457.
Kerboua, K., Hamdaoui, O., 2020. Oxygen-argon acoustic cavitation bubble in a water-methanol mixture: effects of medium composition on sonochemical activity. Ultrason. Sonochem. 61, 104811.
Kerboua, K., Hamdaoui, O., Alghyamah, A., 2021. Energy balance of high-energy stable acoustic cavitation within dual-frequency sonochemical reactor. Ultrason. Sonochem. 73, 105471.
Kerboua, K., Hamdaoui, O., Islam, M.H., Alghyamah, A., Hansen, H.E., Pollet, B.G., 2021. Low carbon ultrasonic production of alternate fuel: Operational and mechanistic concerns of the sonochemical process of hydrogen generation under various scenarios. Int. J. Hydrog. Energy.
Kerboua, K., Merouani, S., Hamdaoui, O., Alghyamah, A., Islam, Md.H., Hansen, H.E., Pollet, B.G., 2021. How do dissolved gases affect the sonochemical process of hydrogen production? An overview of thermodynamic and mechanistic effects – on the "hot spot theory. Ultrason. Sonochem. 72, 105422.
Kerboua, K., Hamdaoui, O., 2018. Numerical investigation of the effect of dual frequency sonication on stable bubble dynamics. Ultrason. Sonochem. 49 (March), 325–332. https://doi.org/10.1016/j.ultsonch.2018.08.025.
Kerboua, K., Hamdaoui, O., 2019. Sonochemical production of hydrogen: Enhancement by summed harmonics excitation. Chem. Phys. 519 (November), 27–37. https://doi.org/10.1016/j.chemphys.2018.11.019.
Klapcsik, K., Hegedűs, F., 2017. The effect of high viscosity on the evolution of the bifurcation set of a periodically excited gas bubble. Chaos Solitons Fract 104 (17), 198–208.
Klapcsik, K., Varga, R., Hegedűs, F., 2018. Bi-parametric topology of subharmonics of an asymmetric bubble oscillator at high dissipation rate. Nonlinear Dyn 94 (4), 2373–2389.
Klapcsik, K., Hegedűs, F., 2019. Study of non-spherical bubble oscillations under acoustic irradiation in viscous liquid. Ultrason. Sonochem. 54, 256–273. https://doi.org/10.1016/j.ultsonch.2019.01.031.
Lauterborn, W., 1976. Numerical investigation of nonlinear oscillations of gas bubbles in liquids. J. Acoust. Soc. Am. 59 (2), 283–293.
Lauterborn, W., Holzfuss, J., 1991. Acoustic chaos. Int. J. Bifurcat. Chaos 01 (01), 13–26.
Lauterborn, W., Parlitz, U., 1988. Methods of chaos physics and their application to acoustics. J. Acoust. Soc. Am. 84 (6), 1975–1993.
Lauterborn, W., Kurz, T., 2010. Physics of bubble oscillations. Rep. Prog. Phys. 73 (10). https://doi.org/10.1088/0034-4885/73/10/106501.
Lee, J., Ashokkumar, M., Kentish, S., Grieser, F., 2005. Determination of the size distribution of sonoluminescence bubbles in a pulsed acoustic field. J. Am. Chem. Soc. 127 (48), 16810–16811.
Lee, J., Ashokkumar, M., Yasui, K., Tuziuti, T., Kozuka, T., Towata, A., Iida, Y., 2011. Development and optimization of acoustic bubble structures at high frequencies. Ultrason. Sonochem. 18 (1), 92–98.
Leighton, T.G., 2012. The Acoustic Bubble. Academic Press, San Diego, CA.

Lindemann, F.A., Arrhenius, S., Langmuir, I., Dhar, N.R., Perrin, J., Lewis, W.C.M., 1922. Discussion on "the radiation theory of chemical action. Trans. Faraday Soc. 17, 598–606.

Louisnard, O., 2012. A simple model of ultrasound propagation in a cavitating liquid. Part I: theory, nonlinear attenuation and traveling wave generation. Ultrason. Sonochem. 19 (1), 56–65.

Louisnard, O., 2010. Nonlinear attenuation of sound waves by inertial cavitation bubbles. Phys. Procedia 3 (1), 735–742.

Merouani, S., Ferkous, H., Hamdaoui, O., Rezgui, Y., Guemini, M., 2015. A method for predicting the number of active bubbles in sonochemical reactors. Ultrason. Sonochem. 22, 51–58.

Merouani, S., Hamdaoui, O., Rezgui, Y., Guemini, M., 2015. Ultrasonics Sonochemistry Sensitivity of free radicals production in acoustically driven bubble to the ultrasonic frequency and nature of dissolved gases. Ultrasonics Sonochemistry 22, 41–50. https://doi.org/10.1016/j.ultsonch.2014.07.011.

Mettin, R., Luther, S., Ohl, C.-D., Lauterborn, W., 1999. Bubble size distribution near a pressure antinode. J. Acoust. Soc. Am. 105 (2), 1075.

Mettin, R. (2007). From a single bubble to bubble structures in acoustic cavitation. Oscillations, Waves and Interactions. https://doi.org/10.1016/j.ultsonch.2004.05.010.

Mettin, R., Cairós, C., Troia, A., 2015. Sonochemistry and bubble dynamics. Ultrason. Sonochem. 25 (1), 24–30. https://doi.org/10.1016/j.ultsonch.2014.08.015.

Olm, C., Zsély, I.G., Varga, T., Curran, H.J., Turányi, T., 2015. Comparison of the performance of several recent syngas combustion mechanisms. Combust. Flame 162 (5), 1793–1812.

Pétrier, C., Francony, A., 1997. Ultrasonic waste-water treatment: incidence of ultrasonic frequency on the rate of phenol and carbon tetrachloride degradation. Ultrason. Sonochem. 4 (4), 295–300.

Pilling, M.J., Seakins, P.W., 1995. Reaction kinetics. Oxford University Press, Oxford.

Prabhu, A.V., Gogate, P.R., Pandit, A.B., 2004. Optimization of multiple-frequency sonochemical reactors. Chem. Eng. Sci. 59 (22–23), 4991–4998.

Rashwan, S.S., Dincer, I., Mohany, A., 2020a. A unique study on the effect of dissolved gases and bubble temperatures on the ultrasonic hydrogen (sonohydrogen) production. Int. J. Hydrog. Energy. 45 (41), 20808–20819.

Rashwan, S.S., Dincer, I., Mohany, A., 2020b. An investigation of ultrasonic based hydrogen production. Energy 205, 118006.

Rashwan, S.S., Dincer, I., Mohany, A., Pollet, B.G., 2019. The Sono-Hydro-Gen process (Ultrasound induced hydrogen production): challenges and opportunities. Int. J. Hydrog. Energy. 44 (29), 14500–14526.

Rivas, D.F., Stricker, L., Zijlstra, A.G., Gardeniers, H.J.G.E., Lohse, D., Prosperetti, A., 2013. Ultrasound artificially nucleated bubbles and their sonochemical radical production. Ultrason. Sonochem. 20 (1), 510–524.

Sochard, S., Wilhelm, A.M., Delmas, H., 1997. Modelling of free radicals production in a collapsing gas-vapour bubble. Ultrason. Sonochem. 4 (2), 77–84.

Sojahrood, A.J., Wegierak, D., Haghi, H., Karshfian, R., Kolios, M.C., 2019. A simple method to analyze the super-harmonic and ultra-harmonic behavior of the acoustically excited bubble oscillator. Ultrason. Sonochem. 54, 99–109. https://doi.org/10.1016/j.ultsonch.2019.02.010.

Sojahrood, A.J., Falou, O., Earl, R., Karshafian, R., Kolios, M.C., 2015. Influence of the pressure-dependent resonance frequency on the bifurcation structure and backscattered pressure of ultrasound contrast agents: a numerical investigation. Nonlinear Dyn 80 (1–2), 889–904.

Sojahrood, A.J., Li, Q., Haghi, H., Karshafian, R., Porter, T.M., Kolios, M.C, 2017. Towards the accurate characterization of the shell parameters of microbubbles based on attenuation and sound speed measurements. J. Acoust. Soc. Am. 141 (5), 3493. https://doi.org/10.1121/1.4987297.

Son, Y., Lim, M., Khim, J., Kim, L.-H., Ashokkumar, M., 2012. Comparison of calorimetric energy and cavitation energy for the removal of bisphenol-A: the effects of frequency and liquid height. Chem. Eng. J. 183, 39–45.

Storey, B.D., Szeri, A.J., 2000. Water vapour, sonoluminescence and sonochemistry. Proc. R. Soc. Lond. 456 (1999), 1685–1709. https://doi.org/10.1098/rspa.2000.0582.

Stricker, L., Lohse, D., 2014. Radical production inside an acoustically driven microbubble. Ultrason. Sonochem. 21 (1), 336–345. https://doi.org/10.1016/j.ultsonch.2013.07.004.

Toegel, R., Gompf, B., Pecha, R., Lohse, D., 2000. Does water vapor prevent upscaling sonoluminescence? Phys. Rev. Lett. 85 (15), 3165.

Toegel, R., Lohse, D., 2003. Phase diagrams for sonoluminescing bubbles: a comparison between experiment and theory. J. Chem. Phys. 118 (4), 1863–1875. https://doi.org/10.1063/1.1531610.

Trujillo, F.J., 2018. A strict formulation of a nonlinear Helmholtz equation for the propagation of sound in bubbly liquids. Part I: theory and validation at low acoustic pressure amplitudes. Ultrason. Sonochem. 47, 75–98.

Trujillo, F.J., 2020. A strict formulation of a nonlinear Helmholtz equation for the propagation of sound in bubbly liquids. Part II: application to ultrasonic cavitation. Ultrason. Sonochem. 65, 105056.

Turányi, T., Tomlin, A.S., 2014. Analysis of kinetic reaction mechanisms. Springer, Berlin.

van Iersel, M.M., Benes, N.E., Keurentjes, J.T.F., 2008. Importance of acoustic shielding in sonochemistry. Ultrason. Sonochem. 15 (4), 294–300.

Varga, T., Nagy, T., Olm, C., Zsély, I.G., Pálvölgyi, R., Valkó, É., Vincze, G., Cserháti, M., Curran, H.J., Turányi, T., 2015. Optimization of a hydrogen combustion mechanism using both direct and indirect measurements. Proc. Combust. Inst. 35 (1), 589–596.

Varga, T., Olm, C., Nagy, T., Zsély, I.G., Valkó, É., Pálvölgyi, R., Curran, H.J., Turányi, T., 2016. Development of a joint hydrogen and syngas combustion mechanism based on an optimization approach. Int. J. Chem. Kinet. 48 (8), 407–422.

Yasui, K., Tuziuti, T., Lee, J., Kozuka, T., Towata, A., Iida, Y., 2008. The range of ambient radius for an active bubble in sonoluminescence and sonochemical reactions. J. Chem. Phys. 128 (18), 184705.

Yasui, K. (2001). Effect of liquid temperature on sonoluminescence. 64(March), 1–10. https://doi.org/10.1103/PhysRevE.64.016310.

Yasui, K., Kato, K., 2012. Bubble dynamics and sonoluminescence from helium or xenon in mercury and water. Phys. Rev. E 86 (3), 36320.

Yasui, K., Tuziuti, T., Iida, Y., 2004. Optimum bubble temperature for the sonochemical production of oxidants. Ultrasonics - Sonochemistry 42 (1–9), 579–584. https://doi.org/10.1016/j.ultras.2003.12.005.

Yasui, K., Tuziuti, T., Kozuka, T., Towata, A., & Iida, Y. (2007). Relationship between the bubble temperature and main oxidant created inside an air bubble under ultrasound. 1–10. https://doi.org/10.1063/1.2790420.

Zhao, H., Yang, X., Ju, Y., 2016. Kinetic studies of ozone assisted low temperature oxidation of dimethyl ether in a flow reactor using molecular-beam mass spectrometry. Combust. Flame 173, 187–194.

Chapter 5

Sonochemical reactions, when, where and how: Experimental approach

Xingaoyuan Xiong and Zongsu Wei

Department of Biological and Chemical Engineering, Centre for Water Technology (WATEC), Aarhus University, Aarhus, Denmark

5.1 When do the sonochemical reactions take place?

The concept of "sonochemistry" refers to ultrasound–assisted chemistry (Suslick et al., 1990), this is, applying high-intensity (ultra)sound to cause, enhance, or influence chemical reactions in a liquid–gas system (Wu, 2005). The chemistry research in this area is termed sonochemistry (Mason & Theory, 1988; Suslick, 1988), which mainly concerns the reactions rendering increased reaction rates, product yields, and surfaces erosion (Suslick, 1988).

Because of the difference in scales between the acoustic wavelengths (0.01 to 10 cm) and molecules, ultrasound can not directly couple with the chemical species; hence, sonochemistry as well as sonochemical reactions are not attributed to the interaction between acoustic field and substances in liquid phase (Suslick et al., 1990). Cavitation phenomenon is recognized as the main reason for most of the observed sonochemical reactions (Kıdak & Doğan, 2018; Pollet, 2010; Suslick & Nyborg, 1990). It stems from the compression and rarefaction generated when an ultrasound wave propagates in an aqueous solution (Kıdak & Doğan, 2018). The compression causes a positive pressure by squeezing the molecules together while the rarefaction exerts a negative pressure by tearing the molecules apart (Cao et al., 2020). When the amplitude of ultrasound is larger than thecavitation threshold of a specific liquid, the "weak link" connecting the liquid molecules would be torn apart, which attributes to the formation of massive gas nuclei (Ye et al., 2019). The nucleation sites may be found throughout the solution or at crevices on solid impurities or surface. The periodic vibration of ultrasonic pressure renders – the nucleation, growth, and implosive collapse of bubble in a liquid phase (Suslick et al., 1990), and this process is cavitation [Fig. 5.1 (Abdurahman and Abdullah, 2020)]. During this loop, the cavitation bubble is able to absorb energy from the soundwaves and release it with a localized high energy density in a short time interval (Pollet, 2010). The rapid collapse of cavitation bubble is a nearly adiabatic heating process due to the comparatively slow thermal transport speed (Suslick et al., 1990). In this instantaneous process which occurs within 100 ns (Hoffmann et al., 1996), the localized hot–spot is formed, which is currently the most accepted theory to explain the mechanism of cavitation phenomena (Suslick et al., 1990). Simultaneously, shockwaves, shearing stress, and microjets are also generated in the liquid medium (Yasuda, 2021). These chemical and physical effects (Yasuda, 2021) offer effective approaches of driving chemical reactions under extreme conditions, which is account for the increase in stoichiometric chemical reactions (Suslick et al., 1997).

Note that sonochemistry and bubble behavior are correlated. However, it is hard to describe a single bubble behavior in the acoustic field where the microscopic dynamics of bubbles are highly related to the parameters and details of their environment, e.g., frequency and pressure of ultrasound, properties of liquid and dissolved gas, neighboring bubbles, and boundaries. In multibubble environments, "bubble population" refers to a group of similar bubbles (Leighton, 2012). In this case, cavitation isa combination of many individual events occurred in isolated space and time, through a smoothly varying or potentially homogeneous primary sound field (Mettin et al., 2015). The "sonochemical reaction" and "cavitation" in this chapter all occur in one of the similar bubbles in the multibubble system.

Energy Aspects of Acoustic Cavitation and Sonochemistry: Fundamentals and Engineering. DOI: https://doi.org/10.1016/B978-0-323-91937-1.00019-0
Copyright © 2022 Elsevier Inc. All rights reserved.

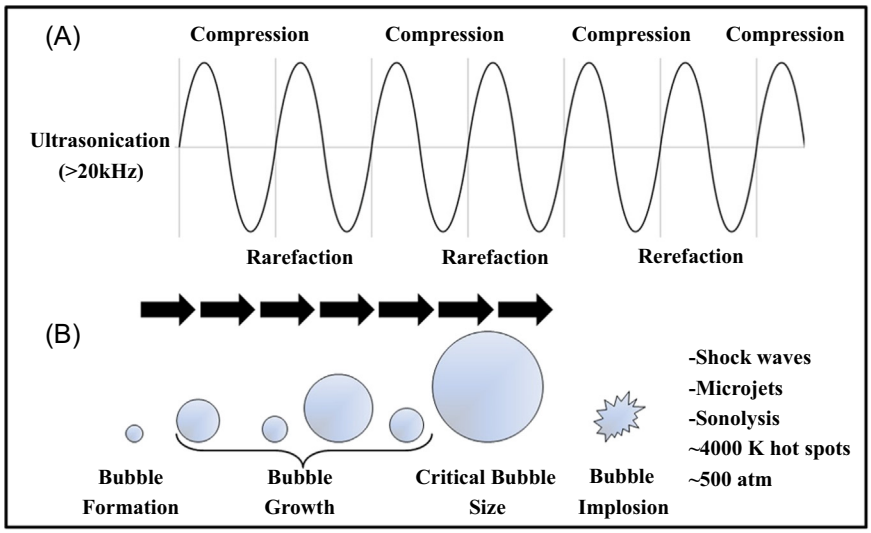

FIGURE 5.1 Cavitation bubble formation at various stages during alternating compression and rarefaction cycles of the ultrasonic wave. *Reprinted from Abdurahman, M. H. and Abdullah, A. Z. (2020). Mechanism and reaction kinetic of hybrid ozonation-ultrasonication treatment for intensified degradation of emerging organic contaminants in water: A critical review. Chemical Engineering and Processing – Process Intensification. Copyright (2020), with permission from Elsevier.*

5.2 Where and how do sonochemical reactions take place?

Based on the hot–spot theory, sonochemical reactions can take place in three regions (Henglein, 1987; Ince et al., 2001): the gas phase inside of bubble, the interface of bubble–liquid (i.e., the thin shell surrounding the bubble), and the bulk solution. This section will discuss the mechanism of sonochemical reactions at different sites, and specific examples will also be given.

5.2.1 In the gas phase of collapsing bubbles

The vapor undergoes pyrolysis in the gas phase of collapsing cavitation bubble; thus, the properties of both liquid solvent and dissolved gas can affect the collapsing temperature, as well as the radical types and yields generated in this process. In the gas phase of the cavitation bubble, the maximum temperature can be calculated by Eq. (5.1) (Kojima et al., 2005; Nagata et al., 2000):

$$T_{max} = T_{in}\left[\frac{P_a(\gamma - 1)}{P_{in}}\right] \tag{5.1}$$

where T_{in} and P_{in} are the initial temperatures and pressure in the bubble at the end of the expansion, respectively; P_a is the acoustic pressure; γ is the specific ratio of C_p (the specific heat at constant pressure) and C_v (the specific heat at constant volume), which depends on the gas type (Riesz & Kondo, 1992). Generally, the temperature and the pressure of the "instantaneous hot–spot" can up to 5000–6000 K (Suslick et al., 1990) and 1000–2000 atms (Pollet, 2010), respectively. This localized high temperature and pressure, combined with extraordinarily rapid cooling rates of 10^{9-10} K/s, provide a special way to drive chemical reactions under extreme conditions (Kıdak & Doğan, 2018). Here, water vapor sonolysis occurs resulting in the cleavage of water molecules into hydroxyl radicals (•OH) and hydrogen radicals (•H) (Eq. 5.2) (Kıdak & Doğan, 2018; Wu, 2005):

$$H_2O+))) \rightarrow {}^{\bullet}OH + {}^{\bullet}H \tag{5.2}$$

The primary free radical •OH can be demonstrated using the spin trap 5,5–dimethyl–pyrroline N–oxide (DMPO), while •H can be detected by α–(4–pyridyl–1–oxide)–N–t–butylnitrone (POBN) (Riesz et al., 1985). Because of the extremely reactive •OH, the sonochemical treatment is regarded as an effective advanced oxidation process (AOP) (Pétrier et al., 2010) possessing significant advantages such as higher reaction rates, lower process cost, and more feasible conditions (Cao et al., 2020; Wang et al., 2019). Likewise, self–combining reactions of •H (Eq. 5.3) and •OH (Eq. 5.4) can undergo both in the gas phase and at the interfacial region around cavitation bubble under noble gas atmosphere, resulting

in the formation of H_2 and H_2O_2, respectively (Lippitt et al., 1972):

$$2^{\bullet}H \rightarrow H_2 \tag{5.3}$$

$$2^{\bullet}OH \rightarrow H_2O_2 \tag{5.4}$$

This situation also brings the entrapped molecules of dissolved gases (e.g., O_2) to an excited state and dissociate, and subsequently generate hydroperoxyl radicals ($^{\bullet}$OOH) (Eqs. 5.5 and 5.6) and $^{\bullet}$OH (Eqs. 5.7 and 5.8) (Torres et al., 2008):

$$O_2 +))) \rightarrow 2O \tag{5.5}$$

$$H + O_2 \rightarrow {}^{\bullet}OOH \tag{5.6}$$

$$O + H_2O \rightarrow 2^{\bullet}OH \tag{5.7}$$

$$H + O_2 \rightarrow {}^{\bullet}OH + O \tag{5.8}$$

Oxygen atoms (O, Eq. 5.3) has never been directly detected but has been confirmed by the detection of O_2 during sonolysis of oxygen–free solutions (Henglein, 1987). In addition, the formation of superoxide radicals ($O_2^{\bullet-}$) was initially discovered during sonolysis of oxygen–saturated aqueous solution (Lippitt et al., 1972). Later, the $O_2^{\bullet-}$ formation has been extended in the oxygen–free argon solution (Kondo et al., 1996).

Compounds with high Henry's constant, hydrophobicity and vapor pressure are attracted towards the bubble cavity (Shende et al., 2019), which is the most effective site for their destruction. The volatile compounds, such as chlorinated methanes, ethanes, and ethenes, evaporate during the expansion cycle and decompose via pyrolysis within the collapsing cavitation bubble (Colussi et al., 1999). A typical example of pyrolysis reactions (Eqs. 5.9–5.12) is carbon tetrachloride (CCl_4), and the mechanism in the interior of the cavitation bubble is shown as below (Hoffmann et al., 1996; Hua & Hoffmann, 1996):

$$CCl_4 \xrightarrow{\Delta} {}^{\bullet}CCl_3 + {}^{\bullet}Cl \tag{5.9}$$

$$CCl_4 \xrightarrow{\Delta} {}^{\bullet\bullet}CCl_2 + Cl_2 \tag{5.10}$$

$${}^{\bullet}CCl_3 \xrightarrow{\Delta} {}^{\bullet\bullet}CCl_2 + {}^{\bullet}Cl \tag{5.11}$$

$${}^{\bullet}CCl_3 + {}^{\bullet}CCl_3 \xrightarrow{\Delta} CCl_4 + {}^{\bullet\bullet}CCl_2 \tag{5.12}$$

Besides, the incineration of hydrophobic molecules is also feasible inside the cavitation bubble (Nam et al., 2003; Nanzai et al., 2008). The repulsive interactions between hydrophobic pollutants (e.g., with $–NO_2$ and –Cl groups (Sivasankar & Moholkar, 2009)) and water molecules can "drive" the hydrophobic molecules towards the bubble–water interface, which leads to an enhanced concentration of these molecules in the bubble–water interface region (Sivasankar & Moholkar, 2009). This would raise the partial pressure of the hydrophobic molecule, resulting in higher evaporation and subsequent entrapment of the hydrophobic molecules into the cavitation bubble (Sivasankar & Moholkar, 2009).

The pyrolysis reaction in the gas phase of cavitation bubble is also critical to the synthesis of nanostructured materials. For instance, the bond of volatile organometallic compounds could dissociate in the gas phase of cavitation bubble which produces free metal atoms that then diffuses into the bulk solution followed by the nucleation with appropriate templates (Hangxun et al., 2013).

5.2.2 At the interfacial region surrounding collapsing bubbles

High Henry's constant and vapor pressure allow diffusion of the volatile compounds into the cavity. With low Henry's constant and rectifying diffusion resistance at the bubble–water interface, the diffusion of non–volatile compounds is thus limited (Chiha et al., 2010; Shende et al., 2019; Tronson et al., 2003), Fig. 5.2 shows the schematic diagram of the degradation behavior of non–volatile compounds during sonolysis (Lu et al., 2021). For the degradation of hydrophobic non–volatile pollutants under ultrasonic radiation, the initial degradation of pollutants happens at bubble–water interface.

The adiabatical collapse of the cavitation bubble generates temperatures in the range of 1000–1500 K at the bubble–water interface (Gole et al., 2018), which is adequate for pyrolytic degradation of most compounds. The hydrophobicity of non–volatile compounds reveals their ability to accumulate on the bubble surface, which thus positively affect their pyrolysis efficiency in this region (Riesz & Kondo, 1992). Vecitis et al. (Vecitis et al., 2008) described the schematic diagram

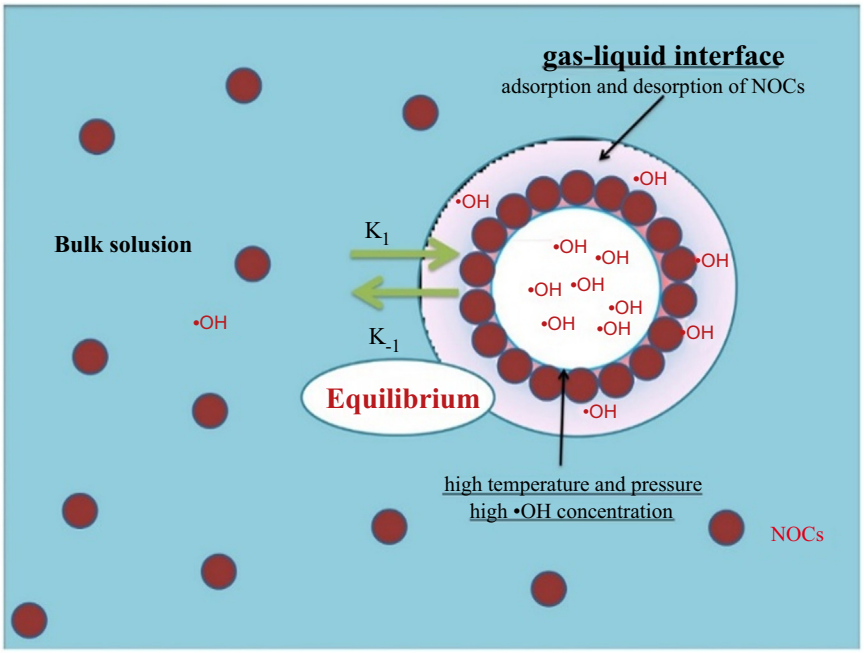

FIGURE 5.2 Diagrammatic representation of the degradation behavior of non–volatile compounds during sonolysis. *Reprinted from Lu, X., Qiu, W., Peng, J., Xu, H., Wang, D., Cao, Y., Zhang, W. and (Ma, J. 2021). A Review on Additives-assisted Ultrasound for Organic Pollutants Degradation. Journal of Hazardous Materials, 403, 123915. https://doi.org/10.1016/j.jhazmat.2020.123915. Copyright (2020), with permission from Elsevier.*

of sonochemical degradation of perfluorooctanesulfonic acid (PFOS), which involves the PFOS adsorption (step 1) and pyrolytic cleavage of C–S bond (step 2) at the bubble–water interface. The volatile fluorochemical intermediates undergo further pyrolytic reactions in the bubble vapor contributing to C1 fluoro–radicals (step 4), and thereafter CO, CO_2, and HF (step 5) [Fig. 5.3 (Vecitis et al., 2008)].

The atomic and radical species like O, $^{\bullet}H$, $^{\bullet}OOH$, and $^{\bullet}OH$ formed by hemolysis/pyrolysis reaction of gaseous contents are responsible for attacking non–volatile compounds along with polar compounds at the bubble–water interface and/or in the bulk phase (Nam et al., 2003), e.g., the ultrasonic degradation of Rhodamine B (RhB), a non–volatile basic dye (Merouani et al., 2010). Serpone et al. (Serpone et al., 1994) investigated three chlorophenols under ultrasonic irradiation, and the kinetics shows the degradation rate at low concentration is zero–order while at high concentration displays saturation–type kinetics, which can be associated with Langmuirian type behavior. The two different degradation kinetics indicate the ultrasonic degradation of chlorophenols at low concentrations proceeds in the bulk solution, while at the high concentration occurs at the bubble–water interface. Without pollutants, free radicals can recombine at the bubble–water interface (Eqs. 5.4, 5.13–5.15) (Kıdak & Doğan, 2018):

$$^{\bullet}OH + {}^{\bullet}H \rightarrow H_2O \tag{5.13}$$

$$2^{\bullet}OH \rightarrow H_2O + O \tag{5.14}$$

$$2^{\bullet}OOH \rightarrow H_2O_2 + O_2 \tag{5.15}$$

The extreme condition at the bubble–water interface makes the water in a supercritical state, i.e., the water is supercritical water with properties of the same diffusion coefficient as gas, the same density as the liquid, and lower viscosity (Wang et al., 2019). Example of an organic compound decomposition in supercritical water is shown as below (Eqs. 5.16–5.19) (Wang et al., 2019):

$$RH + O_2 \rightarrow {}^{\bullet}R + {}^{\bullet}OOH \tag{5.16}$$

$$RH + {}^{\bullet}OOH \rightarrow {}^{\bullet}R + H_2O_2 \tag{5.17}$$

$$^{\bullet}R + O_2 \rightarrow {}^{\bullet}OOR \tag{5.18}$$

$$^{\bullet}OOR + RH \rightarrow ROOH + {}^{\bullet}R \tag{5.19}$$

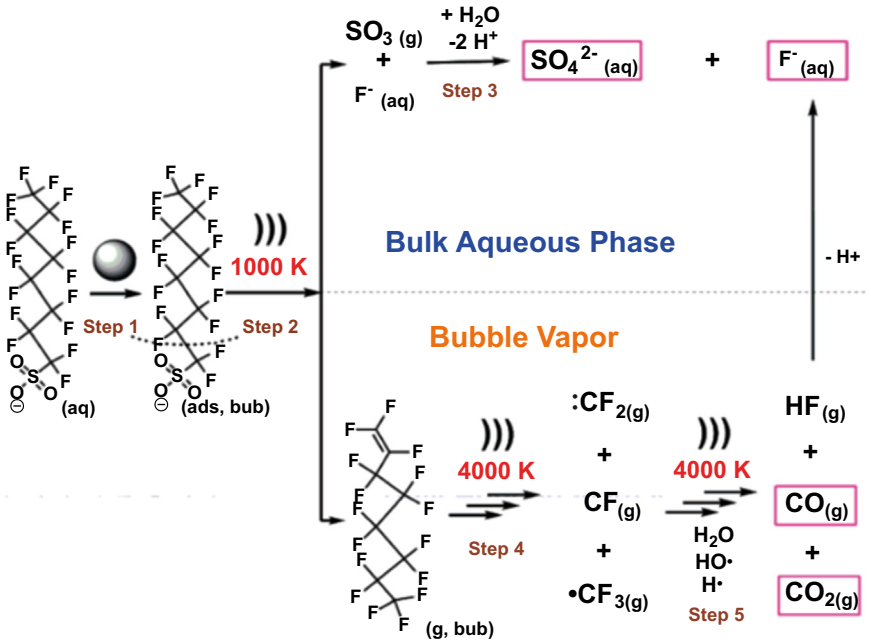

FIGURE 5.3 Diagram of the sonochemical degradation of PFOS. *Reprinted from Vecitis, C. D., Park, H., Cheng, J., Mader, B. T. and Hoffmann, M. R. (2008). Kinetics and Mechanism of the Sonolytic Conversion of the Aqueous Perfluorinated Surfactants, Perfluorooctanoate (PFOA), and Perfluorooctane Sulfonate (PFOS) into Inorganic Products. Journal of Physical Chemistry A, 112(18), 4261–4270. https://doi.org/10.1021/jp801081y. Copyright (2008) by the American Physical Society.*

TABLE 5.1 Summary of sonochemical reactions sites and corresponding mechanisms.

Sonochemical reactions site	Mechanism
Inside the bubble	Pyrolysis reaction at high temperature
At/around the bubble–water interface	Pyrolysis reaction at high temperature, free radical oxidation/reduction, supercritical water oxidation reaction
In the bulk solution	Free radical oxidation/reduction

5.2.3 In the bulk solution

5.2.3.1 Homogeneous system

In contrast to volatile and hydrophobic compounds, the non–volatile, hydrophilic compounds with low vapor pressure have the tendency to remain in the bulk solution (Ince et al., 2001) where the reactive species, especially •OH, are responsible for the degradation reactions (Kıdak & Doğan, 2018; Merouani et al., 2010; Torres et al., 2008; Wu, 2005). Since the cavitation bubble is extremely unstable and short-lived, reactive species only exist in a small region in the vicinity of the bubble collapse (Sivasankar & Moholkar, 2009). Likewise, the bulk solution is at ambient temperature, so the extent of sonochemical reactions of compounds within bulk solution is restrained by the quantity of oxidizing species (Merouani et al., 2010). For example, during materials synthesis from non–volatile precursor under ultrasonic radiation, the precursor needs to react with radicals that diffuse into the liquid phase to trigger subsequent reactions (Hangxun et al., 2013).

In short, the sonolysis of compounds proceeds by two major pathways/mechanisms (Merouani et al., 2010): pyrolysis of the volatile molecules inside the bubble and the non–volatile and hydrophobic compounds at the bubble–water interface (Weavers & Hoffmann, 1998); and the radical reactions involving substances attached at the bubble–water interface and in the bulk (Hoffmann et al., 1996) (Table 5.1). The pyrolysis at the bubble core and bubble–water interface is effective for non–polar as well as volatile and semi–volatile compounds, while the radicals predominantly attack the polar, non–volatile compounds (Panda et al., 2019).

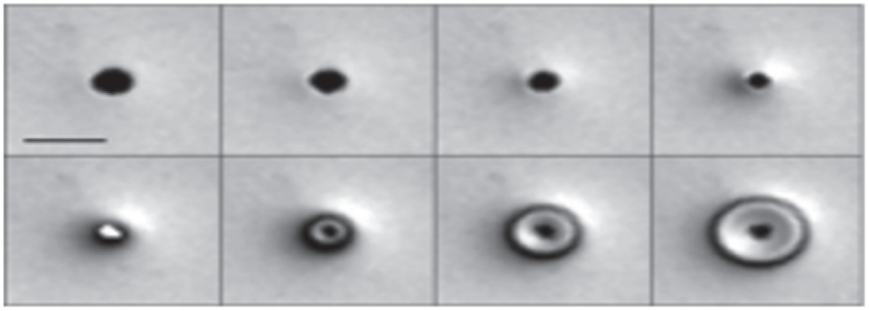

FIGURE 5.4 A spherical shockwave launched from a laser–induced collapsing bubble. *Reprinted from Supponen, O., Obreschkow, D., Kobel, P., Tinguely, M., Dorsaz, N. and Farhat, M. (2017). Shockwaves from nonspherical cavitation bubbles. Physical Review Fluids, 2(9). https://doi.org/10.1103/PhysRevFluids.2.093601. Copyright (2017) American Chemical Society.*

5.2.3.2 Heterogenous system

Heterogenous system refers to liquid–liquid or liquid–solid system, and sonocatalytic system usually includes the two. Besides chemical reactions, unique physical effects are also generated in the presence of solids. The presence of a boundary near the bubble can make the collapse asymmetric, resulting in a bubble deformation (Leighton, 2012). During this process, most of the energy from the expanded bubble can be transformed and consumed by accelerating a liquid jet that can pass through the inside of the bubble to the opposite bubble wall with a high speed (hundreds of meters per second). Consequently, this high-speed jet hits the surface of boundary with a deposition of huge energy densities (Blake & Gibson, 1987). Another mechanism is shockwave, which arises from the symmetric collapse of cavitation bubble in the liquid [Fig. 5.4 (Supponen et al., 2017)]. Both microjet and shockwave in the heterogeneous system contribute to the emulsion at the interfaces between two liquids, the erosion and cleaning at the interface between liquid and solid, the damage and deformation of solid surfaces, the increase in surface area, and the enhancement of mass transfer efficiency.

For example, ultrasonic irradiation is often applied in liquid–powder suspensions. The cavitation can speed up solid particles, which leads to the collision of the high-velocity particles (Doktycz & Suslick, 1990). Hence, it is possible to changes morphology, composition, and reactivity of solids via sonication (Crum et al., 1999).

5.3 Techniques for ultrasonic cavitation observation and measurement

Many techniques have been developed to study the occurrence and performance of sonochemical reactions. While the EPR technique with radical spin trapping agent can verify the free radicals generated under ultrasonic irradiation, the techniques that can directly observe the cavitation bubble behavior or measure the corresponding conditions are more appealing for more intuitive and credible evidence. This section briefly introduces 5 typical techniques with applicable scope and measurable parameters for cavitation characterization.

5.3.1 Sonoluminescence (SL)

Sonoluminescence (SL) is light emission due to cavitation, and is an important and useful tool for sonochemistry research to ascertain the condition of the cavitation bubble (Matula & Roy, 1997). Spectroscopic analysis of the light emission can infer the maximum pressure and temperature inside of the cavitation bubble (Flint & Suslick, 1991), while the measurement of the light intensity can deduce the sonochemical reaction rates (Matula & Roy, 1997). It is a visual and photographic method that can be applied to observe both single and multiple bubble systems, i.e., single bubble sonoluminescence (SBSL) and multiple bubble sonoluminescence (MBSL). Unfortunately, it is difficult to conduct strict scientific studies (Matula & Roy, 1997) because the complexity of cavitation fields and the operation conditions cannot be precisely controlled, especially in MBSL (Matula & Roy, 1997). The SBSL is hence more suitable for studying the dynamics of cavitation bubble in a highly controllable and repeatable manner (Matula & Roy, 1997).

However, the SBSL from pure water lacks spectral features which present a problem in sonochemistry research (H. Xu & Suslick, 2010). Fortunately, SL in acids, such as concentrated sulfuric acid (H_2SO_4) and phosphoric acid (H_3PO_4), can give a dramatic increase in SBSL intensity which makes the measurement of the single bubble system possible (Matula & Roy, 1997; Thiemann et al., 2017). Noble gases (e.g., argon and xenon) (Thiemann et al., 2017) in acids idealize the sonoluminescence study because even at daylight the naked eye can observe the very bright light emission [as shown in

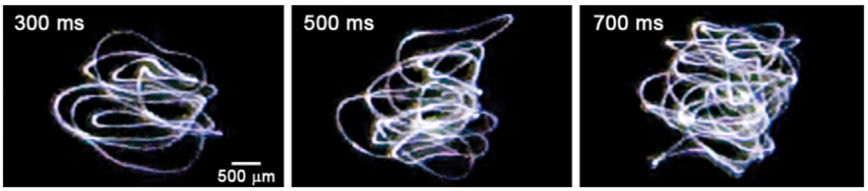

FIGURE 5.5 Photographs of a moving sonoluminescing bubble with different exposure times (in H_3PO_4 (65%) regassed with Ar). *Reprinted from Xu, H. and Suslick, K. S. (2010). Molecular emission and temperature measurements from single-bubble sonoluminescence. Physical Review Letters, 104(24). https://doi.org/10.1103/PhysRevLett.104.244301. Copyright (2010) by the American Physical Society.*

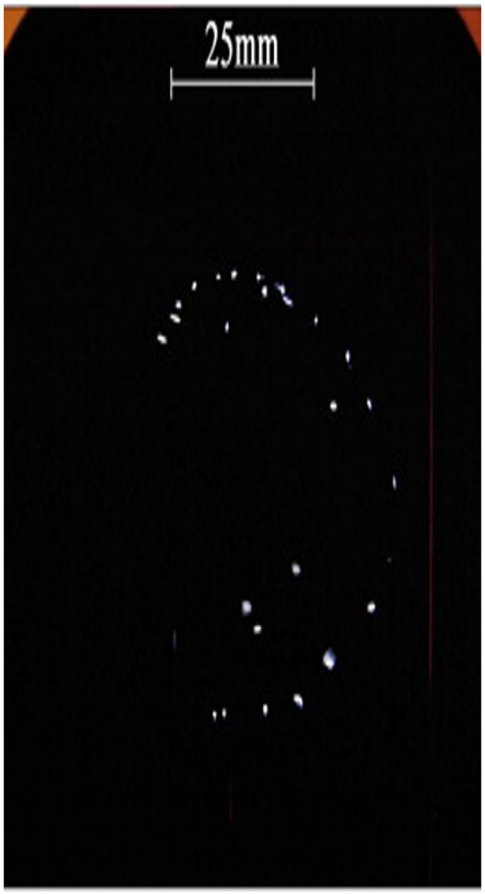

FIGURE 5.6 Photographs of ellipsoidal bubble cluster (in H_2SO_4 (85%) regassed with Ar). *Reprineted from Rosselló, J. M., Dellavale, D. and Bonetto, (F. J. 2015). Stable tridimensional bubble clusters in multi-bubble sonoluminescence (MBSL). Ultrasonics Sonochemistry, 22, 59–69. https://doi.org/10.1016/j.ultsonch.2014.06.003. Copyright (2014), with permission from Elsevier.*

Fig. 5.5 (H. Xu & Suslick, 2010)]. Similarly, the multiple bubble system can also be observed by SL in H_2SO_4 (85%) with argon gas dissolved, as depicted in Fig. 5.6 (Rosselló et al., 2015).

5.3.2 Tube arrest method

In configuration of cloud cavitation, the "instantaneous hot–spot" is probably up to 5000–6000 K (Suslick et al., 1990). However, in case of single bubble configuration, the temperature can reach 15,000 K (Suslick et al., 1990), because the bubble collapse is spherical, giving a greater compression of the gas (Hamdi et al., 2018). In addition, the plasma formation at such extreme conditions makes an optically opaque area at the center of the bubble (Hamdi et al., 2018). The detection of the high-frequency temperature variations in the flow presents a challenge to the precision of instrumentation.

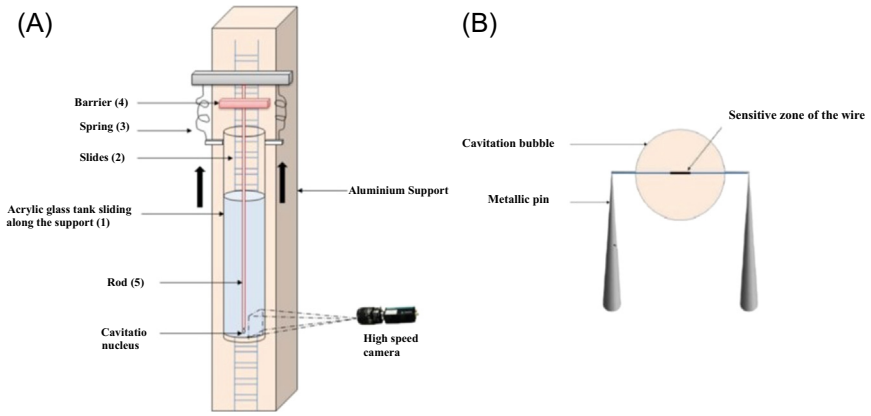

FIGURE 5.7 Schematic of the experimental setup employing the tube arrest method: (A) single bubble growth and collapse, and (B) temperature measurement with a cold wire. *Reprinted from Hamdi, M., Coutier-Delgosha, O. and Baudoin, M. (Hamdi et al., 2018). Measurements of the temperature variations during the growth and collapse of cavitation bubbles. Copyright (2018) by the 10th International Symposium on Cavitation (CAV2018).*

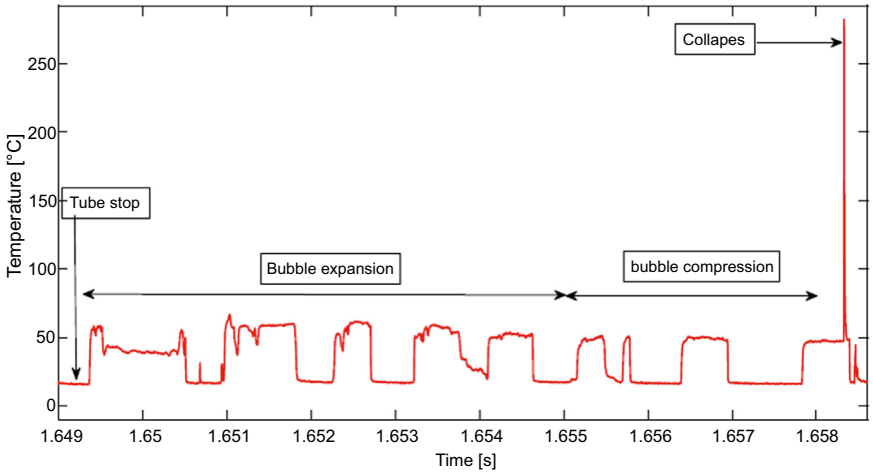

FIGURE 5.8 The temperature signal during bubble lifetime obtained by the tube arrest method. *Reprinted from Hamdi, M., Coutier-Delgosha, O. and Baudoin, M. (Hamdi et al., 2018). Measurements of the temperature variations during the growth and collapse of cavitation bubbles. Copyright (2018) by the 10th International Symposium on Cavitation (CAV2018).*

Hamdi et al. (Hamdi et al., 2018) proposed a tube arrest method on the basis of cold wires to measure the temperature variation during the growth and collapse of the single cavitation bubble, which is characterized by a very small–time response. As shown in Fig. 5.7 (Hamdi et al., 2018), the sensor for high frequency temperature measurements is a specific thin (15 μm diameter) cold wire decorated by Nickel metallic coating, which should be located very close to the cavitation nucleus such that the sensitive zone can be included inside the bubble during the cavitation. The temperature peak given by the test result [Fig. 5.8 (Hamdi et al., 2018)] was about 280 °C, appeared at 10–30 μs; the temperature peak is varying between 300 and 600 °C in most cases. All these results were obtained from the nonspherical bubble. Therefore, it is possible that higher temperatures can be measured in the gas phase of the spherical bubble, but this study did not discuss the sensitivity and accuracy of the thin cold wire sensor at high temperatures.

5.3.3 Color Doppler ultrasound imaging

A method proposed by Koda et al. (Koda et al., 2019) can visualize the real–time instantaneous frequency from bubble cavitation by a color Doppler imaging method, which utilizes the phase differences between tested US sytem and an external reference signal. The establish of this system resolved the problem of post–processing and achieved real–time observation (time resolution: sub–microseconds) of the cavitation bubble dynamics.

The schematic diagram of this system is depicted in Fig. 5.9 (Koda et al., 2019). The US imaging unit is in charge of controlling and detecting the irradiation time of the imaged pulse wave; the electrical circuit provides a fixed interval

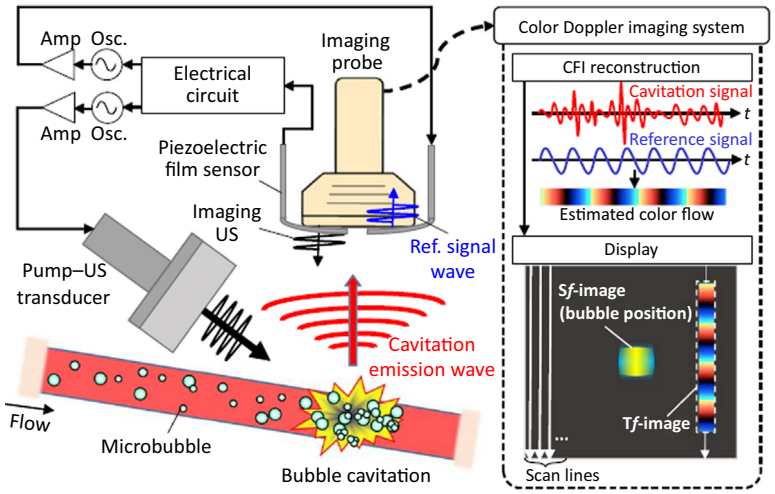

FIGURE 5.9 Schematic of the experimental setup employing the color Doppler method. *From Koda, R., Nakajima, T., Horiuchi, H. and (Yamakoshi, Y. 2019). Real-time visualization of instantaneous frequency from bubble cavitation using color Doppler ultrasound imaging. Japanese Journal of Applied Physics, 58(11). https://doi.org/10.7567/1347-4065/ab4eb1. Copyright (2019) The Japan Society of Applied Physics.*

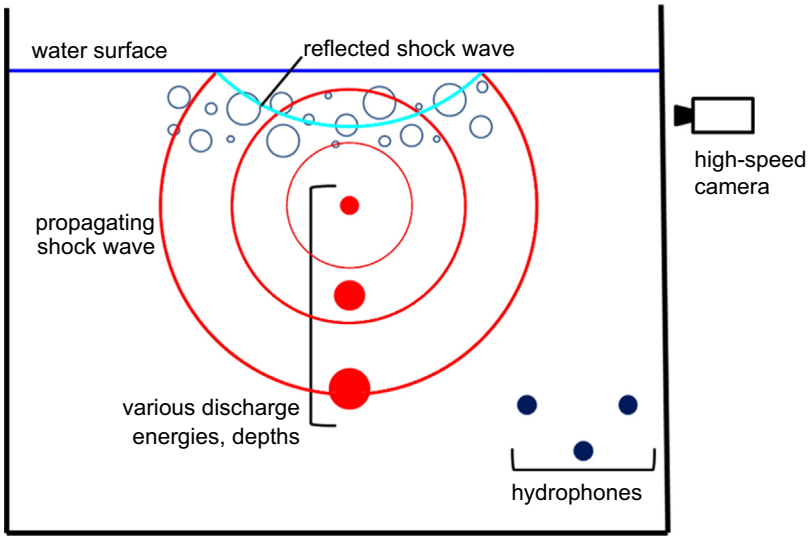

FIGURE 5.10 Schematic showing the experimental setup. *Reprinted from Esplin, J. J., Kim, B. J., Kinzel, M. P. and Culver, R. L. (2021). Measurement and quantification of acoustic bulk cavitation extent. Experiments in Fluids, 62(8). https://doi.org/10.1007/s00348-021-03249-w. Copyright (2021) by the Springer Nature.*

between the irradiation of the imaged pulse wave and US; the pump–US transducer produces cavitation, which is converted into an acoustic cavitation emission (ACE) signal; the piezoelectric film sensor attached on the front of the image US probe inputs the reference signal; finally, the color flow image (CFI) can be reconstructed (T*f*–image, a vertical line image) by the these accepted signals. Additionally, research group checked the accuracy of this system and it was estimated to be 8.59%. Despite the superiority of this method, authors considered that the development of a wide band probe and a feedback system will be able to expand the range of the frequency measurement.

5.3.4 Quantify acoustic bulk cavitation in multiple bubble system

Esplin et al. (Esplin et al., 2021) provided a simple, repeatable experimental apparatus and procedures to quantify the acoustic bulk cavitation. As illustrated in Fig. 5.10 (Esplin et al., 2021), a sparker generates a large, spherical symmetry bubble near the water surface. The collapse of this bubble produces a bulk cavitation region, which is manifested as a bubble cloud.

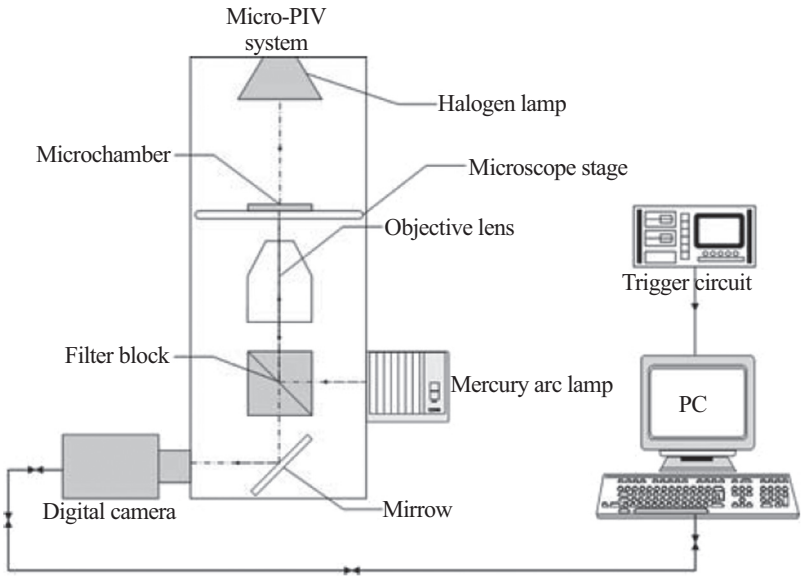

FIGURE 5.11 Schematic diagram of the micro–PIV system. *From Tho, P., Manasseh, R. and Ioo, A. (2007). Cavitation microstreaming patterns in single and multiple bubble systems. Journal of Fluid Mechanics, 576, 191–233. https://doi.org/10.1017/S0022112006004393. Copyright (2007) by the Cambridge University Press.*

This process is recorded by a high-speed photography and Müller–Platte needle hydrophones (high-pressure waveform). The collected images are processed by a Gaussians model to distinguish the bubble cloud from the static background, and the data recorded by hydrophones is first fitted by a double–exponential function to reduce the noise, and then is processed by the Anderson finite-amplitude propagation model. The formation and collapse of cavitation bubbles by this method shows advantages of the high-pressure waves propagating spherically. This avoid the nonlinear process associated with shockwaves, thereby reducing the number of external variables. However, this method still has limitations. The electrode near the cavitation region can affect the dynamics of the cavitation bubble, while the spark discharge generates interferences from light or electromagnetic fields for camera and hydrophone, respectively.

5.3.5 Micro–PIV method

Studies have proven that the micro–PIV (particle image velocimetry) method coupled with photography can be used to investigate the cavitation microstreaming surrounding a single and two oscillating bubbles lean upon solid boundary (Tho et al., 2007), as well as a single cavitation bubble on the leastic boundary (Yu et al., 2020). Fig. 5.11 (Tho et al., 2007) depicts the schematic diagram of a micro–PIV system, and the core units include a camera, light sources, a circuit, and an acoustic excitation unit. Once the cavitation bubble is generated, the region around the cavitation bubble is illuminated by the light source, and then is recorded by a high-speed camera. The images can directly provide the physical properties of the cavitation field, offering an approach to study the behavior of bubble or estimate the related parameters. Then, the streaming flow field and the oscillatory motion of bubble is mapped through the changes of bubble's radius and the movement of bubble. Therefore, it is crucial to obtain a clearly frozen image in the oscillating field. Tho's group (Tho et al., 2007) chose a streak photography method to ensure a sufficient contrast between the target region and the background, and the example images of streaming patterns are shown in Fig. 5.12. However, no research has shown that this method can be applied to observe the multiple cavitation bubble systems.

5.4 Application of sonochemical reactions

Ultrasound has been widely used in the fields of water treatment (Al-Bsoul, 2020; Goncharuk et al., 2008), nanomaterial synthesis (Hangxun et al., 2013), food processing (Bhargava, 2021; Rastogi, 2011), pharmaceuticals (Castillo-Peinado & Luque de Castro, 2016), etc., where ultrasonic energy can represent a clean and efficient tool because of its unique chemical and physical properties. Currently, the implementation of environmental–friendly and energy–saving technologies is one of the main objectives in improving green transition and life quality (Yao et al., 2020). Ultrasound can be considered to belong

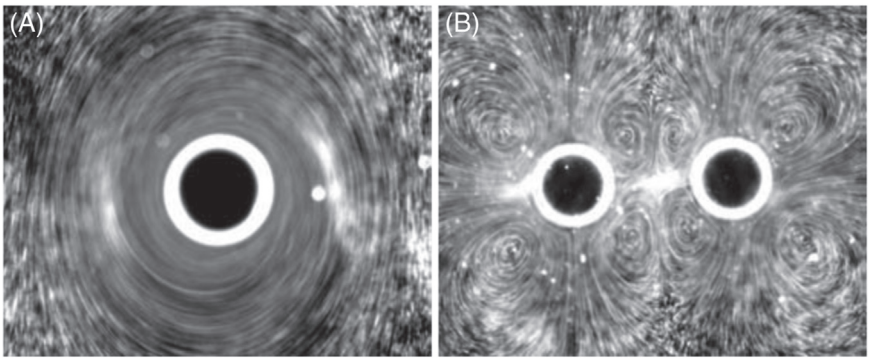

FIGURE 5.12 Example of streaming patterns around (A) a single bubble (acoustic frequency: 1 kHz, radius: 272 μm); (B) two bubbles undergoing translating oscillations along single axes (acoustic frequency: 1.381 kHz, radius: 207 and 215 μm). *From Tho, P., Manasseh, R. and Ioo, A. (2007). Cavitation microstreaming patterns in single and multiple bubble systems. Journal of Fluid Mechanics, 576, 191–233. https://doi.org/10.1017/S0022112006004393. Copyright (2007) by the Cambridge University Press.*

to this category of technologies. This section takes the pollutants degradation under ultrasound radiation as examples to discuss the sonochemical reactions and corresponding mechanisms. The focus herein is the sonohybrid process that has been proven to efficiently accelerate the removal of persistent pollutants. The potential to save chemical consumption and reduce toxic intermediates yields makes the ultrasound technology a more environmental–friendly approach to remediation.

5.4.1 US/persulfate system

The attention on the US/persulfate process has been accumulating rapidly due to its potential of in–situ chemical oxidation (ISCO) and water/wastewater decontamination in large scale (Lee et al., 2020). The sulfate radicals ($SO_4^{\bullet-}$) with similar redox potential and relatively longer lifetimes ($t_{1/2}$=30–40 μs) (Kermani et al., 2020) compared to $^{\bullet}OH$ are expected to be generated at the bubble–water interface where peroxydisulfate (PDS) (Eq. 5.20) (Gu et al., 2019) or peroxymonosulfate (PMS) (Eq. 5.21) (Gu et al., 2019) is activated. The produced radicals will however be quenched when overdosing (Eqs. 5.22 and 5.23) (Gu et al., 2019):

$$S_2O_8^{2-} +))) \rightarrow 2SO_4^{\bullet-} \tag{5.20}$$

$$HSO_5^- +))) \rightarrow {}^{\bullet}OH + SO_4^{\bullet-} \tag{5.21}$$

$$S_2O_8^{2-} + SO_4^{\bullet-} \rightarrow SO_4^{2-} + S_2O_8^- \tag{5.22}$$

$$SO_4^{\bullet-} + HSO_5^- \rightarrow SO_5^{\bullet-} + HSO_4^- \tag{5.23}$$

Fagan et al. (Fagan et al., 2020) proved the combination of US and PDS has significant synergetic effects over a large temperature range (20–50 °C) and the PAH degradation in US/PDS system undergoes pyrolysis in bubble/at bubble–water interface, whereas the radical oxidation by $^{\bullet}OH$ and $SO_4^{\bullet-}$ is dominant in the bulk phase. The study conducted by Kermani et al. (Kermani et al., 2020) shows 95.3% and 58.4% furfural ($C_5H_4O_2$) degradation can be obtained in 90 min in PDS/US and PMS/US systems, respectively, while only 39.3% in the US alone process revealing that radical oxidation in the bulk was significantly improved by adding PDS/PMS. The radical scavenging results indicate that the $SO_4^{\bullet-}$ generated at bubble–water interface in both US/PDS and US/PMS systems are the major radicals responsible for furfural degradation (Kermani et al., 2020). The PFOA degradation pathway in US/PDS system investigated by Lei et al. (Lei et al., 2020) verifies the rate controlling step of PFOA degradation via pyrolysis at the bubble water–interface. Perfluoroalkyl radicals ($C_7F_{15}^{\bullet}$) and $^{\bullet}COOH$ were produced by breaking the C—C bond between the perfluoroalkyl tail and the carboxylate head. The excess radicals (both $^{\bullet}OH$ and $SO_4^{\bullet-}$) generated in the presence of PDS under ultrasonic radiation can accelerate the oxidation of $C_7F_{15}^{\bullet}$ to form unstable $C_6F_{13}COF$ that later lose one F atom to complete the defluorination step. Given the step–by–step defluorination, the PFOA is finally mineralized into CO_2, H_2O, and F^- ions.

5.4.2 US/permanganate system

The oxidant permanganate (PM, $KMnO_4$) is featured by relatively high stability, strong pH adaptability, and high standard redox potential (0.558–1.692 V). Ultrasonic radiation can reduce PM to colloidal MnO_2 particles (Eqs. 5.24 and 5.25) (Abulizi et al., 2014; Okitsu et al., 2009), which can either act as a catalyst promoting permanganate oxidation of the target compounds or serve as a cavitation nucleus decreasing the cavitation nucleation threshold (Zhao et al., 2014).

$$2MnO_4^- + 6H^\bullet \rightarrow 2MnO_2 + 2OH^- + 2H_2O \tag{5.24}$$

$$2MnO_4^- + 3H_2O_2 \rightarrow 2MnO_2 + 3O_2 + 2OH^- + 2H_2O \tag{5.25}$$

Hu et al. (Hu et al., 2018) studied the US/PM process and selected PFOA as the target compound. The diameter range of the MnO_2 particles generated in PFOA degradation process was from 0.09 to 6.15 μm. The energy dispersive spectrum (EDS) indicates Mn(III) might also be generated, which can undergo complexation reaction with the carboxyl groups (–COOH) of PFOA, while the perfluoroalkyl chain of the adsorbed PFOA can reduce the aggregation of MnO_2 particles (Hu et al., 2018). In general, PFOA degradation in US/PM system primarily underwent via pyrolytic decomposition on the surface of cavitation bubble near MnO_2 particles, and the radical oxidation may also contribute to some extent (Hu et al., 2018).

5.4.3 US/Fenton system

Fenton oxidation process based on the reaction between Fe(II) and H_2O_2 under acidic conditions (Eq. 5.26) is limited by the uneasy regeneration of Fe(II) (Eqs. 5.27 and 5.28), which causes the insufficient use of H_2O_2 and the formation of excessive Fe(III) hydroxide sludge (Adityosulindro et al., 2017). Theoretically, the combination of the US and Fenton process is expected to promote faster pollutant degradation owing to: 1) the higher radicals yield (Neppolian et al., 2002), 2) enhanced compounds and radicals contact (Bagal & Gogate, 2014) and 3) efficient Fe(II) regeneration (Lin & Ma, 2000) (Eqs. 5.29 and 5.30).

$$Fe^{2+} + H_2O_2 \rightarrow Fe^{3+} + {}^\bullet OH + OH^- \tag{5.26}$$

$$Fe^{2+} + {}^\bullet OH \rightarrow Fe^{3+} + OH^- \tag{5.27}$$

$$Fe^{3+} + H_2O_2 \rightarrow Fe - OOH^{2+} + H^+ \tag{5.28}$$

$$Fe - OOH^{2+} \rightarrow Fe^{2+} + {}^\bullet OOH \tag{5.29}$$

$$Fe^{3+} + {}^\bullet OOH \rightarrow Fe^{2+} + O_2 + H^+ \tag{5.30}$$

The synergetic effect of the US/Fenton process was confirmed by Adityosulindro et al. (Adityosulindro et al., 2017) where they compared the ibuprofen (IBP) degradation in US and US/Fenton processes. They found the IBP degradation occurred at the bubble–water interface via pyrolysis and $^\bullet$OH oxidation, and regeneration of Fe(II) under ultrasonic irradiation contributes to the synergy of the US/Fenton process (Adityosulindro et al., 2017).

Replacing Fe(II) with Fe(0), a process called advanced Fenton reaction (Bagal & Gogate, 2014), will induce additional reaction mechanisms as follows (Eqs. 5.31 and 5.32):

$$Fe^0 + 2H^+ \rightarrow Fe^{2+} + H_2 \tag{5.31}$$

$$Fe^0 + 2Fe^{3+} \rightarrow 3Fe^{2+} \tag{5.32}$$

In acidic environment and in the presence of H_2O_2, the Fe(0) converts to Fe(II) (Eq. 5.31) and then reacts with H_2O_2. In an advanced Fenton process, the formed Fe(III) can be reduced back to Fe(II) by Fe(0) (Eq. 5.32). The combination of ultrasound technology favors the dispersion of iron particles in liquid phase, which is beneficial to Fe(II) regeneration (Bagal & Gogate, 2014) and thus the Fe(III) sludge reduction (Bagal & Gogate, 2012). Bagal & Gogate (2012) investigated the alachlor degradation in the US, US/Fenton, and US/advanced Fenton processes, and results show alachlor degradation in Fenton involved processes followed second–order kinetics while in US alone process was first–order degradation (Bagal & Gogate, 2012). Only 55.80% degradation was obtained in the US-alone system but the sonohybrid processes achieved 100% degradation; Fe(0) system showed a larger rate constant than Fe(II) system (Bagal & Gogate, 2012). The enhanced mass transfer of pollutant–radical interaction and Fe cycle due to US is ascribed to the synergistic effect in US/Fenton systems.

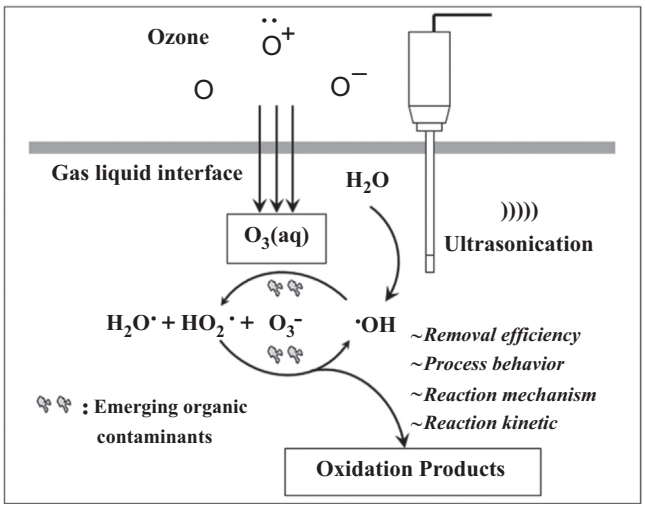

FIGURE 5.13 Diagrammatic representation of the US/O_3 system. *Reprinted from Thokchom, B., Kim, K., Park, J. & Khim, J. (2015). Ultrasonically enhanced electrochemical oxidation of ibuprofen. Ultrasonics Sonochemistry, 22, 429–436. https://doi.org/10.1016/j.ultsonch.2014.04.019. Copyright (2014), with permission from Elsevier.*

5.4.4 US/O_3 system

The prerequisite of ozonation is the transfer of ozone gas into the bulk solution. To improve the ozone-liquid mass transfer efficiency, numerous studies demonstrated the US/O_3 process had promising synergistic effects in dyes (Zhang et al., 2008), pesticides (Fan et al., 2015), and antibiotics (Guo et al., 2015) degradation. In addition, the US/O_3 system is more energy effective than either US alone or O_3 alone (Abdurahman and Abdullah, 2020).

The schematic of US/O_3 process is shown in Fig. 5.13 (Abdurahman and Abdullah, 2020). The physical effect caused by ultrasound irradiation leads to the local turbulence thus reduces the mass transfer resistance by decreasing the liquid film thickness and enlarges the ozone-liquid contact area by smashing the ozone bubble into smaller ones. Then the pyrolysis of dissolved ozone in cavitation bubble (Eqs. 5.4, 5.33 and 5.34) (Lu et al., 2021) produces a large amount of $^{\bullet}OH$ which leads to further mineralization of compounds by attacking ozone resistant oxidation intermediates such as aldehydes and carboxylic acids from parent compounds (Nawrocki & Kasprzyk-Hordern, 2010).

$$O_3 +))) \rightarrow O_2(g) + O\left(^3P\right)(g) \tag{5.33}$$

$$O\left(^3P\right)(g) + H_2O(g) \rightarrow 2^{\bullet}OH \tag{5.34}$$

The hybrid US/O_3 technology also has notable effects on aniline degradation. An increment of approximately 64% degradation and 110% mineralization were observed concerning the addition of either O_3 or US system after 5 min oxidation (Song et al., 2007). A similar result was reported by Barik et al. (Lei et al., 2020) that 2,4–dichlorophenol degradation can reach 93.42% while in US alone system it is only 28.85%. Moreover, the rate constant increased from 3.1×10^{-3} 1/min to 2.23×10^{-2} 1/min. Kidak et al. (Kıdak & Doğan, 2018) found that only 10 % and 32% of amoxicillin mineralization were detected when US and O_3 were applied individually (Kıdak & Doğan, 2018), while the combined system showed improvement with a 45% mineralization. Likewise, the US/O_3 process remarkably reduced the toxicity from 10% to 14% $EC_{50\%}$ (half maximal effective concentration) to almost 70% (Kıdak & Doğan, 2018).

Although the US/O_3 effectively improves the pollutants degradation efficiency, unfortunately most studies have not focused on the strengthening mechanism. The exploration and discussion on whether the generation of additional radicals or enhanced ozone mass transfer dominates the degradation are necessary.

5.4.5 US/electrochemistry system

In the electrochemical oxidation (EC) process, pollutants can be destroyed by either direct oxidation on the electrode (anode) surface or indirect radical oxidation near the electrode (cathode) or in the bulk solution (Sirés et al., 2014). The quantity of reactive radicals, especially $^{\bullet}OH$ (Eqs. 5.35 and 5.36), produced on the electrode surface is critical to the indirect

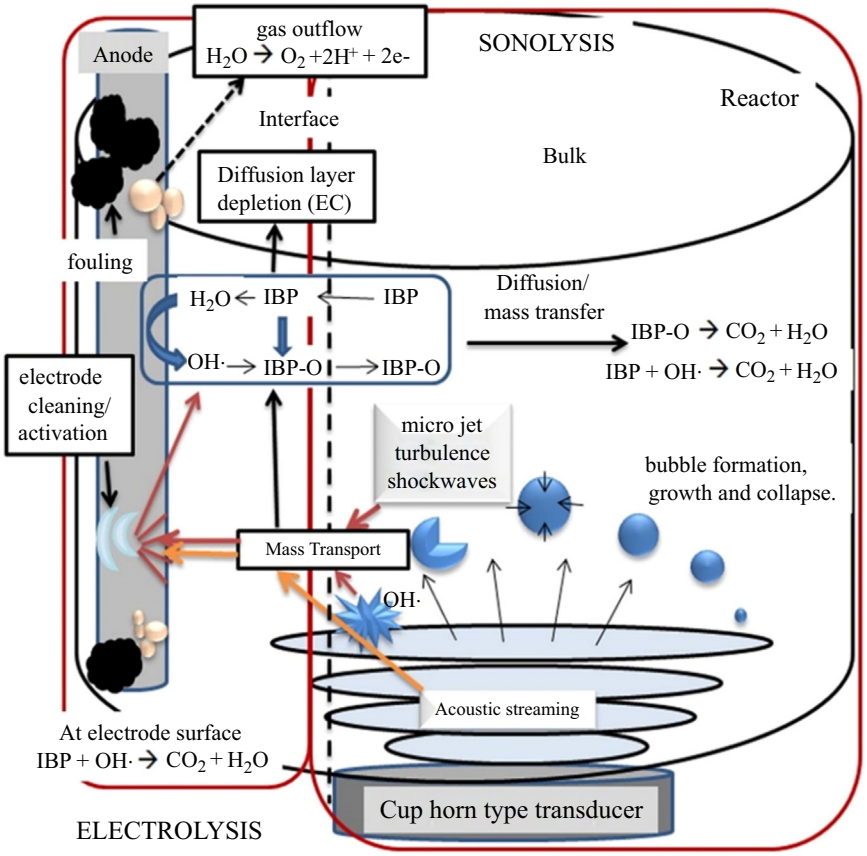

FIGURE 5.14 Diagrammatic representation of the US/EC system. *Reprinted from Thokchom, B., Kim, K., Park, J. & Khim, J. (2015). Ultrasonically enhanced electrochemical oxidation of ibuprofen. Ultrasonics Sonochemistry, 22, 429–436. https://doi.org/10.1016/j.ultsonch.2014.04.019. Copyright (2014), with permission from Elsevier.*

oxidation (Chaplin, 2014). The synergism between the US and EC processes can be achieved by: 1) the in–situ activation of the electrode surface as the cavitation-induced microjets and shockwaves can remove the corrosion on the electrode surface; 2) the excellent transfer rates of compounds/intermediates/radicals between the bulk solution, electrode area, and electrode surface due to reduced diffusion–layer thickness; and 3) the generation of additional oxidizing radicals that can accelerate the pollutants degradation rates. The schematic of the US/EC process is depicted in Fig. 5.14 (Thokchom et al., 2015).

$$H_2O \rightarrow {}^{\bullet}OH + H^+ + e^- \tag{5.35}$$

$$OH^- \rightarrow {}^{\bullet}OH + e^- \tag{5.36}$$

A 37% synergy index of chlorpyrifos degradation was measured in the combined US/EC reaction system by Ren et al. (Ren et al., 2019), but they did not clearly explain the enhancement mechanism. Finkbeiner et al. (Finkbeiner et al., 2015) evaluated the diclofenac degradation in US, EC, and US/EC processes which used ultrasound at 850 kHz and boron–doped diamond (BDD) electrode. A 90% degradation was achieved in the US/EC process while only 38% in the US alone process; the pseudo first–order rate constants increased from 0.121 1/min for US to 0.505 1/min for US/EC (Finkbeiner et al., 2015). These results show this combined US/EC process is an effective method for pollutants removal and has great potential for large–scale application given its unique advantages, such as mild reaction conditions, excellent mass transfer, wild range of pollutant concentrations, and free of chemicals (Yaqub & Ajab, 2013).

5.4.6 US/UV system

Although US process is favorable for degrading hydrophobic compounds (Henglein & Kormann, 1985), its degradation efficiency can be restricted because of the accumulation of relatively hydrophilic intermediates in bulk solution without

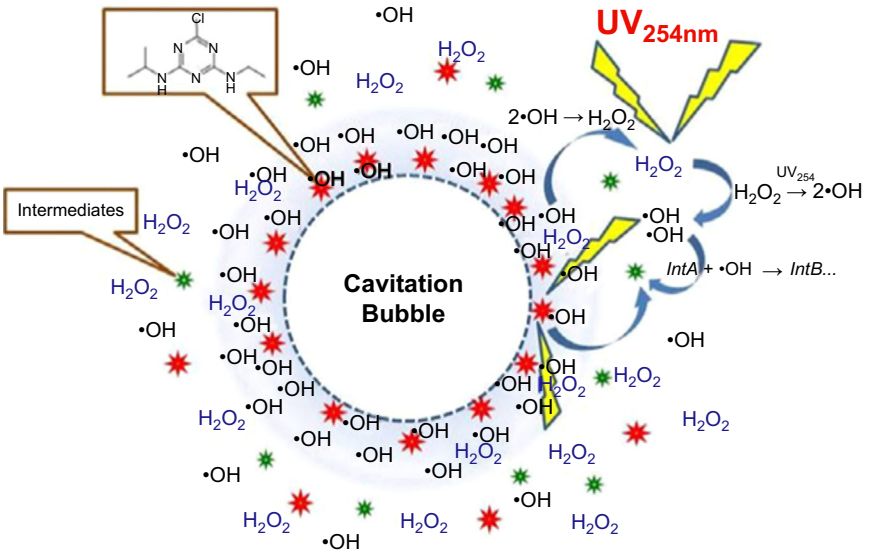

FIGURE 5.15 Diagrammatic representation of the US/UV system. *Reprinted from Xu, L. J., Chu, W. & Graham, N. (2014). Atrazine degradation using chemical-free process of USUV: Analysis of the micro-heterogeneous environments and the degradation mechanisms. Journal of Hazardous Materials, 275, 166–174. https://doi.org/10.1016/j.jhazmat.2014.05.007. Copyright (2014), with permission from Elsevier.*

being oxidized immediately (Patidar and Srivastava, 2021). The combination of US and UV is a chemical–free process with attractive features of 1) direct photolysis of the hydrophilic intermediates; and 2) production of additional •OH in the bulk solution via hemolysis of the H_2O_2 generated by ultrasound irradiation (schematic shown in Fig. 5.15 (L. J. Xu et al., 2014)), which allow the US/UV process to be a possible candidate for efficiently removing pollutants (L. J. Xu et al., 2014).

Patidar and Srivastava (2021) reported a 4.7% ofloxacin (OFLX) degradation in the US alone process, while the US/UV can give a 10.1% degradation, with TOC removal increased from 2.7% to 5.1%. Such enhancement has been confirmed and explained by Xu et al. (L. J. Xu et al., 2014) in the atrazine (ATZ) degradation process. The US/UV is able to degrade the 2–hydroxyatrazine (OIET), which is the main intermediate of ATZ in photolytic degradation process that was insensitive to UV irradiation. Based on the intermediates of US, UV, and US/UV identified by LC/ESI–MS^2, they speculate that the high efficiency of the US/UV process for ATZ degradation could be attributed to the generation of •OH from US-produced H_2O_2 (L. J. Xu et al., 2013).

5.5 Conclusions and perspective

Ultrasonic radiation in the liquid phase triggers cavitation including nucleation, growth, and implosive collapse of gas and vapor filled bubbles (When), which is responsible for sonochemical reactions. Sonochemical reactions occur at three different sites (bubble core, bubble–water interface, and bulk phase; Where) and proceeds through pyrolysis, radicals oxidation or driven by microjets/shockwaves (How). The mechanism is often complicated and highly dependent on the reaction conditions in applications, making the techniques available to investigate the sonochemical reactions particularly important. This chapter exemplifies several methods that can observe bubble behavior or measure the actual values of different parameters of the ultrasonic field. The last section discusses the application of sonochemical reactions, in terms of sonohybrid processes, in pollutant removal from waters.

Despite the enormous efforts, it is still challenging to reach clear and reasonable explanation of sonochemical reactions processes and mechanisms in application. First, most of the techniques have harsh requirements on operation conditions. In addition, it is difficult to use a single technique to simultaneously measure multiple parameters, which are not conductive to elaborate the sonochemical reaction mechanism. The innovation and improvement of detection methods is necessary and urgently needed. Modifying ultrasound device or introducing other technologies/chemicals as sonohybrid processes is another measure to improve the sonochemical reactions. However, the possible issues related to toxic adding chemicals or intermediates should be further evaluated before scaling up any sono–hybrid processes.

References

Abdurahman, M.H., Abdullah, A.Z., 2020. Mechanism and reaction kinetic of hybrid ozonation-ultrasonication treatment for intensified degradation of emerging organic contaminants in water: a critical review. Chemical Engineering and Processing - Process Intensification 154, 108047. https://doi.org/10.1016/j.cep.2020.108047.

Abulizi, A., Yang, G.H., Okitsu, K., Zhu, J.J., 2014. Synthesis of MnO2 nanoparticles from sonochemical reduction of MnO4O in water under different pH conditions. Ultrason. Sonochem. 21 (5), 1629–1634. https://doi.org/10.1016/j.ultsonch.2014.03.030.

Adityosulindro, S., Barthe, L., González-Labrada, K., Jáuregui Haza, U.J., Delmas, H., Julcour, C., 2017. Sonolysis and sono-Fenton oxidation for removal of ibuprofen in (waste)water. Ultrason. Sonochem. 39, 889–896. https://doi.org/10.1016/j.ultsonch.2017.06.008.

Al-Bsoul, A., 2020. Optimal conditions for olive mill wastewater treatment using ultrasound and advanced oxidation processes. Sci. Total Environ. 700, 134567. https://doi.org/10.1016/j.scitotenv.2019.134576.

Bagal, M.V., Gogate, P.R., 2012. Sonochemical degradation of alachlor in the presence of process intensifying additives. Sep. Purif. Technol. 90, 92–100. https://doi.org/10.1016/j.seppur.2012.02.019.

Bagal, M.V., Gogate, P.R., 2014. Wastewater treatment using hybrid treatment schemes based on cavitation and Fenton chemistry: a review. Ultrason. Sonochem. 21 (1), 1–14. https://doi.org/10.1016/j.ultsonch.2013.07.009.

Bhargava, N., 2021. Advances in application of ultrasound in food processing: a review. Ultrason. Sonochem. 70, 105293. https://doi.org/10.1016/j.ultsonch.2020.105293.

Blake, J.R., Gibson, D.C., 1987. Cavitation bubbles near boundaries. Annual Review of Fluid Mechanics, Vol. 19. Annual Reviews Inc, U.S., pp. 99–123.

Cao, H., Zhang, W., Wang, C., Liang, Y., 2020. Sonochemical degradation of poly- and perfluoroalkyl substances – a review. Ultrason. Sonochem. 69, 105245. https://doi.org/10.1016/j.ultsonch.2020.105245.

Castillo-Peinado, L., de los, S., Luque de Castro, M.D., 2016. The role of ultrasound in pharmaceutical production: sonocrystallization. J. Pharm. Pharmacol. 68 (10), 1249–1267. https://doi.org/10.1111/jphp.12614.

Chaplin, B.P., 2014. Critical review of electrochemical advanced oxidation processes for water treatment applications. Environmental Sciences: Processes and Impacts 16 (6), 1182–1203. https://doi.org/10.1039/c3em00679d.

Chiha, M., Merouani, S., Hamdaoui, O., Baup, S., Gondrexon, N., Pétrier, C., 2010. Modeling of ultrasonic degradation of non-volatile organic compounds by Langmuir-type kinetics. Ultrason. Sonochem. 17 (5), 773–782. https://doi.org/10.1016/j.ultsonch.2010.03.007.

Colussi, A.J., Hung, H.M., Hoffmann, M.R., 1999. Sonochemical degradation rates of volatile solutes. J. Phys. Chem. A 103 (15), 2696–2699. https://doi.org/10.1021/jp984272o.

Doktycz, S.J., Suslick, K.S., 1990. Interparticle collisions driven by ultrasound. Science 247 (4946), 1067–1069. https://doi.org/10.1126/science.2309118.

Esplin, J.J., Kim, B.J., Kinzel, M.P., Culver, R.L., 2021. Measurement and quantification of acoustic bulk cavitation extent. Exp. Fluids 62 (8). https://doi.org/10.1007/s00348-021-03249-w.

Fagan, W.P., Zhao, J., Villamena, F.A., Zweier, J.L., Weavers, L.K., 2020. Synergistic, aqueous PAH degradation by ultrasonically-activated persulfate depends on bulk temperature and physicochemical parameters. Ultrason. Sonochem. 67. https://doi.org/10.1016/j.ultsonch.2020.105172.

Fan, X.D., Zhang, W.L., Xiao, H.Y., Qiu, T.Q., Jiang, J.G., 2015. Effects of ultrasound combined with ozone on the degradation of organophosphorus pesticide residues on lettuce. RSC Advances, 5 (57), 45622–45630. https://doi.org/10.1039/c5ra03024b.

Finkbeiner, P., Franke, M., Anschuetz, F., Ignaszak, A., Stelter, M., Braeutigam, P., 2015. Sonoelectrochemical degradation of the anti-inflammatory drug diclofenac in water. Chem. Eng. J. 273, 214–222. https://doi.org/10.1016/j.cej.2015.03.070.

Flint, E.B., Suslick, K.S., 1991. The temperature of cavitation. Science 253 (5026), 1397–1399. https://doi.org/10.1126/science.253.5026.1397.

Gole, V.L., Sierra-Alvarez, R., Peng, H., Giesy, J.P., Deymier, P., Keswani, M., 2018. Sono-chemical treatment of per- and poly-fluoroalkyl compounds in aqueous film-forming foams by use of a large-scale multi-transducer dual-frequency based acoustic reactor. Ultrason. Sonochem. 45, 213–222. https://doi.org/10.1016/j.ultsonch.2018.02.014.

Goncharuk, V.V., Malyarenko, V.V., Yaremenko, V.A., 2008. Use of ultrasound in water treatment. J. Water Chem. Technol. 30 (3), 137–150. https://doi.org/10.3103/S1063455X08030028.

Gu, D., Guo, C., Lv, J., Hou, S., Zhang, Y., Feng, Q., Zhang, Y., Xu, J., 2019. Removal of methamphetamine by UV-activated persulfate: Kinetics and mechanisms. J. Photochem. Photobiol. A 379, 32–38. https://doi.org/10.1016/j.jphotochem.2019.05.009.

Guo, W.Q., Yin, R.L., Zhou, X.J., Du, J.S., Cao, H.O., Yang, S.S., Ren, N.Q., 2015. Sulfamethoxazole degradation by ultrasound/ozone oxidation process in water: Kinetics, mechanisms, and pathways. Ultrason. Sonochem. 22, 182–187. https://doi.org/10.1016/j.ultsonch.2014.07.008.

Hamdi, M., Coutier-Delgosha, O., Baudoin, M., 2018. Measurements of the temperature variations during the growth and collapse of cavitation bubbles. ASME. https://doi.org/10.1115/1.861851_ch134.

Hangxun, X., Zeiger, B.W., Suslick, K.S., 2013. Sonochemical synthesis of nanomaterials. Chem. Soc. Rev. 42 (7), 2555–2567. https://doi.org/10.1039/c2cs35282f.

Henglein, A., 1987. Sonochemistry: Historical developments and modern aspects. Ultrasonics 25 (1), 6–16. https://doi.org/10.1016/0041-624X(87)90003-5.

Henglein, A., Kormann, C., 1985. Scavenging of OH radicals produced in the sonolysis of water. Int. J. Radiat. Biol. 48 (2), 251–258. https://doi.org/10.1080/09553008514551241.

Hoffmann, M.R., Hua, I., Höchemer, R., 1996. Application of ultrasonic irradiation for the degradation of chemical contaminants in water. Ultrason. Sonochem. 3 (3), S163–S172. https://doi.org/10.1016/S1350-4177(96)00022-3.

Hu, Y.b., Lo, S.L., Li, Y.F., Lee, Y.C., Chen, M.J., Lin, J.C., 2018. Autocatalytic degradation of perfluorooctanoic acid in a permanganate-ultrasonic system. Water Res. 140, 148–157. https://doi.org/10.1016/j.watres.2018.04.044.

Hua, I., Hoffmann, M.R., 1996. Kinetics and mechanism of the sonolytic degradation of CCL4: intermediates and byproducts. Environ. Sci. Technol. 30 (3), 864–871. https://doi.org/10.1021/es9502942.

Ince, N.H., Tezcanli, G., Belen, R.K., Apikyan, G., 2001. Ultrasound as a catalyzer of aqueous reaction systems: the state of the art and environmental applications. Appl. Catal. B 29 (3), 167–176. https://doi.org/10.1016/S0926-3373(00)00224-1.

Kermani, M., Farzadkia, M., Morovati, M., Taghavi, M., Fallahizadeh, S., Khaksefidi, R., Norzaee, S., 2020. Degradation of furfural in aqueous solution using activated persulfate and peroxymonosulfate by ultrasound irradiation. J. Environ. Manage. 266, 110616. https://doi.org/10.1016/j.jenvman.2020.110616.

Kıdak, R., Doğan, Ş., 2018. Medium-high frequency ultrasound and ozone based advanced oxidation for amoxicillin removal in water. Ultrason. Sonochem. 40, 131–139. https://doi.org/10.1016/j.ultsonch.2017.01.033.

Koda, R., Nakajima, T., Horiuchi, H., Yamakoshi, Y., 2019. Real-time visualization of instantaneous frequency from bubble cavitation using color Doppler ultrasound imaging. Japan. J. Appl. Phys. 58 (11). https://doi.org/10.7567/1347-4065/ab4eb1.

Kojima, Y., Fujita, T., Ona, E.P., Matsuda, H., Koda, S., Tanahashi, N., Asakura, Y., 2005. Effects of dissolved gas species on ultrasonic degradation of (4-chloro-2-methylphenoxy) acetic acid (MCPA) in aqueous solution. Ultrason. Sonochem. 12 (5), 359–365. https://doi.org/10.1016/j.ultsonch.2004.04.002.

Kondo, T., Mišík, V., Riesz, P., 1996. Sonochemistry of cytochrome c. Evidence for superoxide formation by ultrasound in argon-saturated aqueous solution. Ultrason. Sonochem. 3 (3), S193–S199. https://doi.org/10.1016/S1350-4177(96)00025-9.

Lee, J., Von Gunten, U., Kim, J.H., 2020. Persulfate-based advanced oxidation: critical assessment of opportunities and roadblocks. Environ. Sci. Technol. 54 (6), 3064–3081. https://doi.org/10.1021/acs.est.9b07082.

Lei, Y.J., Tian, Y., Sobhani, Z., Naidu, R., Fang, C., 2020. Synergistic degradation of PFAS in water and soil by dual-frequency ultrasonic activated persulfate. Chem. Eng. J. 388. https://doi.org/10.1016/j.cej.2020.124215.

Leighton, T. (2012). The acoustic bubble.

Lin, J.G., Ma, Y.S., 2000. Oxidation of 2-chlorophenol in water by ultrasound/fenton method. J. Environ. Eng. 126 (2), 130–137. https://doi.org/10.1061/(ASCE)0733-9372(2000)126:2(130).

Lippitt, B., McCord, J.M., Fridovich, I., 1972. The sonochemical reduction of cytochrome c and its inhibition by superoxide dismutase. J. Biol. Chem. 247 (14), 4688–4690. doi:10.1016/S0021-9258(19)45041-2.

Lu, X., Qiu, W., Peng, J., Xu, H., Wang, D., Cao, Y., Zhang, W., Ma, J., 2021. A review on additives-assisted ultrasound for organic pollutants degradation. J. Hazard. Mater. 403, 123915. https://doi.org/10.1016/j.jhazmat.2020.123915.

Mason, T.J., Theory, 1988. Applications and uses of ultrasound in chemistry. SONOCHEMISTRY.

Matula, T.J., Roy, R.A., 1997. Comparisons of sonoluminescence from single-bubbles and cavitation fields: Bridging the gap. Ultrason. Sonochem. 4 (2), 61–64. https://doi.org/10.1016/S1350-4177(97)00005-9.

Merouani, S., Hamdaoui, O., Saoudi, F., Chiha, M., 2010. Sonochemical degradation of Rhodamine B in aqueous phase: Effects of additives. Chem. Eng. J. 158 (3), 550–557. https://doi.org/10.1016/j.cej.2010.01.048.

Mettin, R., Cairós, C., Troia, A., 2015. Sonochemistry and bubble dynamics. Ultrason. Sonochem. 25 (1), 24–30. https://doi.org/10.1016/j.ultsonch.2014.08.015.

Nagata, Y., Nakagawa, M., Okuno, H., Mizukoshi, Y., Yim, B., Maeda, Y., 2000. Sonochemical degradation of chlorophenols in water. Ultrason. Sonochem. 7 (3), 115–120. https://doi.org/10.1016/S1350-4177(99)00039-5.

Nam, S.N., Han, S.K., Kang, J.W., Choi, H., 2003. Kinetics and mechanisms of the sonolytic destruction of non-volatile organic compounds: Investigation of the sonochemical reaction zone using several OH • monitoring techniques. Ultrason. Sonochem. 10 (3), 139–147. https://doi.org/10.1016/S1350-4177(03)00085-3.

Nanzai, B., Okitsu, K., Takenaka, N., Bandow, H., Maeda, Y., 2008. Sonochemical degradation of various monocyclic aromatic compounds: Relation between hydrophobicities of organic compounds and the decomposition rates. Ultrason. Sonochem. 15 (4), 478–483. https://doi.org/10.1016/j.ultsonch.2007.06.010.

Nawrocki, J., Kasprzyk-Hordern, B., 2010. The efficiency and mechanisms of catalytic ozonation. Appl. Catal. B 99 (1–2), 27–42. https://doi.org/10.1016/j.apcatb.2010.06.033.

Neppolian, B., Jung, H., Choi, H., Lee, J.H., Kang, J.W., 2002. Sonolytic degradation of methyl tert-butyl ether: The role of coupled fenton process and persulphate ion. Water Res. 36 (19), 4699–4708. https://doi.org/10.1016/S0043-1354(02)00211-7.

Okitsu, K., Iwatani, M., Nanzai, B., Nishimura, R., Maeda, Y., 2009. Sonochemical reduction of permanganate to manganese dioxide: The effects of H2O2 formed in the sonolysis of water on the rates of reduction. Ultrason. Sonochem. 16 (3), 387–391. https://doi.org/10.1016/j.ultsonch.2008.10.009.

Panda, D., Sethu, V., Manickam, S., 2019. Kinetics and mechanism of low-frequency ultrasound driven elimination of trace level aqueous perfluorooctanesulfonic acid and perfluorooctanoic acid. Chemical Engineering and Processing – Process Intensification 142, 107542. https://doi.org/10.1016/j.cep.2019.107542.

Patidar, R., Srivastava, V.C., 2021. Mechanistic and kinetic insights of synergistic mineralization of ofloxacin using a sono-photo hybrid process. Chem. Eng. J. 403, 125736. https://doi.org/10.1016/j.cej.2020.125736.

Pétrier, C., Torres-Palma, R., Combet, E., Sarantakos, G., Baup, S., Pulgarin, C., 2010. Enhanced sonochemical degradation of bisphenol-A by bicarbonate ions. Ultrason. Sonochem. 17 (1), 111–115. https://doi.org/10.1016/j.ultsonch.2009.05.010.

Pollet, B.G., 2010. The use of ultrasound for the fabrication of fuel cell materials. Int. J. Hydrogen Energy 35 (21), 11986–12004. https://doi.org/10.1016/j.ijhydene.2010.08.021.

Rastogi, N.K., 2011. Opportunities and challenges in application of ultrasound in food processing. Crit. Rev. Food Sci. Nutr. 51 (8), 705–722. https://doi.org/10.1080/10408391003770583.

Ren, Q., Yin, C., Chen, Z., Cheng, M., Ren, Y., Xie, X., Li, Y., Zhao, X., Xu, L., Yang, H., Li, W., 2019. Efficient sonoelectrochemical decomposition of chlorpyrifos in aqueous solution. Microchem. J. 145, 146–153. https://doi.org/10.1016/j.microc.2018.10.032.

Riesz, P., Berdahl, D., Christman, C.L., 1985. Free radical generation by ultrasound in aqueous and nonaqueous solutions. Environ. Health Perspect. 64, 233–252. https://doi.org/10.1289/ehp.8564233.

Riesz, P., Kondo, T., 1992. Free radical formation induced by ultrasound and its biological implications. Free Radical Biol. Med. 13 (3), 247–270. https://doi.org/10.1016/0891-5849(92)90021-8.

Rosselló, J.M., Dellavale, D., Bonetto, F.J., 2015. Stable tridimensional bubble clusters in multi-bubble sonoluminescence (MBSL). Ultrason. Sonochem. 22, 59–69. https://doi.org/10.1016/j.ultsonch.2014.06.003.

Serpone, N., Terzian, R., Hidaka, H., Pelizzetti, E., 1994. Ultrasonic induced dehalogenation and oxidation of 2-, 3-, and 4-chlorophenol in air-equilibrated aqueous media. Similarities with irradiated semiconductor particulates. J. Phys. Chem. 98 (10), 2634–2640. https://doi.org/10.1021/j100061a021.

Shende, T., Andaluri, G., Suri, R.P.S., 2019. Kinetic model for sonolytic degradation of non-volatile surfactants: perfluoroalkyl substances. Ultrason. Sonochem. 51, 359–368. https://doi.org/10.1016/j.ultsonch.2018.08.028.

Sirés, I., Brillas, E., Oturan, M.A., Rodrigo, M.A., Panizza, M., 2014. Electrochemical advanced oxidation processes: today and tomorrow. A review. Env. Sci. Pollut. Res. 21 (14), 8336–8367. https://doi.org/10.1007/s11356-014-2783-1.

Sivasankar, T., Moholkar, V.S., 2009. Physical insights into the sonochemical degradation of recalcitrant organic pollutants with cavitation bubble dynamics. Ultrason. Sonochem. 16 (6), 769–781. https://doi.org/10.1016/j.ultsonch.2009.02.009.

Song, S., He, Z., Chen, J., 2007. US/O3 combination degradation of aniline in aqueous solution. Ultrason. Sonochem. 14 (1), 84–88. https://doi.org/10.1016/j.ultsonch.2005.11.010.

Supponen, O., Obreschkow, D., Kobel, P., Tinguely, M., Dorsaz, N., Farhat, M., 2017. Shockwaves from nonspherical cavitation bubbles. Phys. Rev. Fluids 2 (9). https://doi.org/10.1103/PhysRevFluids.2.093601.

Suslick, K.S., Nyborg, W.L., 1990. Ultrasound: its chemical, physical, and biological effects.

Suslick, K.S., Doktycz, S.J., Flint, E.B., 1990. On the origin of sonoluminescence and sonochemistry. Ultrasonics 28 (5), 280–290. https://doi.org/10.1016/0041-624X(90)90033-K.

Suslick, K.S., & Nyborg, W.L. 1990. Ultrasound: its chemical, physical and biological effects.

Suslick, K.S., Fang, M.M., Hyeon, T., Mdleleni, M.M., 1999. Applications of sonochemistry to materials synthesis. Part of the NATO ASI Series book series (ASIC, vol. 524), In: L.A. Crum et al. (eds.), Sonochemistry and Sonoluminescence, Springer, Dordrecht, pp. 291–320. https://doi.org/10.1007/978-94-015-9215-4_24.

Suslick, K.S., Sonoluminescence, sonochemistry, 1997. IEEE Ultrasonics Symposium Proceedings. An International Symposium (Cat. No. 97CH36118.

Thiemann, A., Holsteyns, F., Cairós, C., Mettin, R., 2017. Sonoluminescence and dynamics of cavitation bubble populations in sulfuric acid. Ultrason. Sonochem. 34, 663–676. https://doi.org/10.1016/j.ultsonch.2016.06.013.

Tho, P., Manasseh, R., Ioo, A., 2007. Cavitation microstreaming patterns in single and multiple bubble systems. J. Fluid Mech. 576, 191–233. https://doi.org/10.1017/S0022112006004393.

Thokchom, B., Kim, K., Park, J., Khim, J., 2015. Ultrasonically enhanced electrochemical oxidation of ibuprofen. Ultrason. Sonochem. 22, 429–436. https://doi.org/10.1016/j.ultsonch.2014.04.019.

Torres, R.A., Pétrier, C., Combet, E., Carrier, M., Pulgarin, C., 2008. Ultrasonic cavitation applied to the treatment of bisphenol A. Effect of sonochemical parameters and analysis of BPA by-products. Ultrason. Sonochem. 15 (4), 605–611. https://doi.org/10.1016/j.ultsonch.2007.07.003.

Tronson, R., Ashokkumar, M., Grieser, F., 2003. Multibubble sonoluminescence from aqueous solutions containing mixtures of surface active solutes. J. Phys. Chem. B 107 (30), 7307–7311. https://doi.org/10.1021/jp034360v.

Vecitis, C.D., Park, H., Cheng, J., Mader, B.T., Hoffmann, M.R., 2008. Kinetics and Mechanism of the Sonolytic Conversion of the Aqueous Perfluorinated Surfactants, Perfiuorooctanoate (PFOA), and Perfluorooctane Sulfonate (PFOS) into Inorganic Products. J. Phys. Chem. A 112 (18), 4261–4270. https://doi.org/10.1021/jp801081y.

Wang, J., Wang, Z., Vieira, C.L.Z., Wolfson, J.M., Pingtian, G., Huang, S., 2019. Review on the treatment of organic pollutants in water by ultrasonic technology. Ultrason. Sonochem. 55, 273–278. https://doi.org/10.1016/j.ultsonch.2019.01.017.

Weavers, L.K., Hoffmann, M.R., 1998. Sonolytic decomposition of ozone in aqueous solution: mass transfer effects. Environ. Sci. Technol. 32 (24), 3941–3947. https://doi.org/10.1021/es980620o.

Wu, Z.L., 2005. Sonochemistry of selected hydrocarbons, sulfur-containing and nitrogen-containing organic compounds in aqueous solutions and nonaqueous liquids.

Xu, H., Suslick, K.S., 2010. Molecular emission and temperature measurements from single-bubble sonoluminescence. Phys. Rev. Lett. 104 (24). https://doi.org/10.1103/PhysRevLett.104.244301.

Xu, L.J., Chu, W., Graham, N., 2014. Atrazine degradation using chemical-free process of USUV: analysis of the micro-heterogeneous environments and the degradation mechanisms. J. Hazard. Mater. 275, 166–174. https://doi.org/10.1016/j.jhazmat.2014.05.007.

Xu, L.J., Chu, W., Graham, N., 2013. Sonophotolytic degradation of dimethyl phthalate without catalyst: analysis of the synergistic effect and modeling. Water Res. 47 (6), 1996–2004. https://doi.org/10.1016/j.watres.2013.01.015.

Yao, Y., Pan, Y., Liu, S.Q., 2020. Power ultrasound and its applications: a state-of-the-art review. Ultrason. Sonochem. 104722 (62). https://doi.org/10.1016/j.ultsonch.2019.104722.

Yaqub, A., Ajab, H., 2013. Applications of sonoelectrochemistry in wastewater treatment system. Rev. Chem. Eng. 29 (2), 123–130. https://doi.org/10.1515/revce-2012-0017.

Yasuda, K., 2021. Sonochemical green technology using active bubbles: degradation of organic substances in water. Current Opinion in Green and Sustainable Chemistry 27. https://doi.org/10.1016/j.cogsc.2020.100411.

Ye, L., Zhu, X., Liu, Y., 2019. Numerical study on dual-frequency ultrasonic enhancing cavitation effect based on bubble dynamic evolution. Ultrason. Sonochem. 59. https://doi.org/10.1016/j.ultsonch.2019.104744.

Yu, Q., Xu, Z., Zhao, J., Zhang, M., Ma, X., 2020. PIV-based acoustic pressure measurements of a single bubble near the elastic boundary. Micromachines 11 (7). https://doi.org/10.3390/MI11070637.

Zhang, H., Lv, Y., Liu, F., Zhang, D., 2008. Degradation of C.I. Acid Orange 7 by ultrasound enhanced ozonation in a rectangular air-lift reactor. Chem. Eng. J. 138 (1–3), 231–238. https://doi.org/10.1016/j.cej.2007.06.031.

Zhao, H., Zhang, G., Zhang, Q., 2014. MnO2/CeO2 for catalytic ultrasonic degradation of methyl orange. Ultrason. Sonochem. 21 (3), 991–996. https://doi.org/10.1016/j.ultsonch.2013.12.002.

Part II

The bubble population: an analytic view into mutual forces and allied energy exchange

6. The Bjerknes forces and acoustic radiation energy 99
7. Nonlinear oscillations and resonances of the acoustic bubble and the mechanisms of energy dissipation 109
8. Damping mechanisms of oscillating gas/vapor bubbles in liquids 131
9. Energy controlling mechanisms: relationship with operational conditions 145

Chapter 6

The Bjerknes forces and acoustic radiation energy

Ke-ming Quan

Procter & Gamble Company, West Chester, Ohio, United States

Acoustic cavitation has been applied for chemical and biological applications (Mason & Peters, 2002; Feng et al., 2010) due to the unique conditions generated by cavitation (Suslick et al., 1999). Bubble oscillation and movement in an acoustic field are subjected to external as well as mutual radiation forces. Over the past few decades, sonoluminescence and dynamics of single bubbles under irradiation of ultrasound have been widely investigated (Matula, 1999; Putterman and Weninger, 2000). However, in almost all sonochemical reactors, cavitation field consists of a large population of bubbles aggregate into clusters or "bubble clouds"; hence, studies of multibubble systems are required.

Particles and bubbles in a liquid in an acoustic field are subjected to various acoustic radiation forces. The acoustic wave generated by an ultrasound transducer exerts a radiation force which influences bubble movement and distribution in the acoustic field. In a standing wave field, dispersed bubbles can be concentrated at pressure nodes or antinodes, owing to primary Bjerknes forces. When bubbles oscillate in acoustic field, the radiation pressure generated by other cavitation bubbles can cause mutual attraction or repulsion between bubbles. This phenomenon is caused by the secondary Bjerknes force. In the following sections, the different types of radiation forces are presented, which are essential for understanding the dynamics of bubble clouds and their applications in sonochemistry.

6.1 Acoustic radiation force in a plane traveling wave field

The acoustic radiation force is the time-averaged force acting on reflecting and/or absorbing bodies and particles in a sound field. Lord Rayleigh was credited for making it a well-defined scientific subject after his classical work in 1902 (Rayleigh, 1902), and many studies followed since.

One of such theoretical analysis was given by Nyborg (Nyborg, 1965), valid for a plane-traveling wave, where acoustic pressure p, liquid density ρ and oscillating velocity u, in equations of fluid dynamics are expanded in series

$$\begin{pmatrix} p(x,t) \\ \rho(x,t) \\ u(x,t) \end{pmatrix} = \begin{pmatrix} p_0 \\ \rho_0 \\ u_0 \end{pmatrix} + \begin{pmatrix} p_1(x,t) \\ \rho_1(x,t) \\ u_1(x,t) \end{pmatrix} + \begin{pmatrix} p_2(x,t) \\ \rho_2(x,t) \\ u_2(x,t) \end{pmatrix} + \cdots \tag{6.1}$$

Each term of a series in Eqs. (6.1) is assumed to be much smaller than the preceding term, for example $| p_2 | \ll | p_1 | \ll | p_0 |$. When the fluid is motionless, $p = p_0 = const, \rho = \rho_0 = const, u = u_0 = 0$. Terms p_1, ρ_1, u_1 are 1st order approximation for a time-oscillating acoustic field.

Considering a simple situation where the first order terms describe a decaying traveling plane wave of small amplitude:

$$u_1 = u_0 \, exp(-\alpha x) \cos(wt - kx) \tag{6.2}$$

where α is the absorption coefficient, $\omega = 2\pi f$ and f the frequency, and $k = \omega/c_0$, c_0 the sound velocity. If averaging each of the first terms over a full period, for example, u_1, it is evident that $\langle u_1 \rangle = 0$. However, the time average of momentum is nonzero because of the nonlinear term in the equation of motion. Thus, the mean change in the momentum in a unit of volume is:

$$\left\langle \rho \frac{du}{dt} \right\rangle = \left\langle \rho \left(\frac{\partial u}{\partial t} + u \frac{\partial u}{\partial x} \right) \right\rangle = \left\langle (\rho_0 + \rho_1 + \ldots) \times \left(\frac{\partial (u_1 + u_2 + \ldots)}{\partial t} + \frac{1}{2} \frac{\partial (u_1 + u_2 + \ldots)^2}{\partial x} \right) \right\rangle \tag{6.3}$$

Energy Aspects of Acoustic Cavitation and Sonochemistry: Fundamentals and Engineering. DOI: https://doi.org/10.1016/B978-0-323-91937-1.00003-7
Copyright © 2022 Elsevier Inc. All rights reserved.

Keeping terms no smaller than the second order of magnitude, Eq. (6.3) reduces to the form:

$$\left\langle \rho \frac{du}{dt} \right\rangle = \left\langle \rho_1 \frac{\partial u_1}{\partial t} + \frac{1}{2}\rho_0 \frac{\partial u_1^2}{\partial x} \right\rangle \tag{6.4}$$

Consider now the equation of continuity with accuracy as given by the first-order terms:

$$\frac{\partial \rho_1}{\partial t} = -\rho_0 \frac{\partial u_1}{\partial x} \tag{6.5}$$

One can rewrite the first term of the right-hand side of Eq. (6.4) in another form:

$$\left\langle \rho_1 \frac{\partial u_1}{\partial t} \right\rangle = \left\langle \frac{\partial}{\partial t}(\rho_1 u_1) - u_1 \frac{\partial \rho_1}{\partial t} \right\rangle = \left\langle \frac{1}{2}\rho_0 \frac{\partial u_1^2}{\partial x} \right\rangle \tag{6.6}$$

Referring to Eq. (6.4), one can calculate the mean change in linear momentum of a decaying plane wave:

$$\left\langle \rho \frac{du}{dt} \right\rangle = \left\langle \rho_0 \frac{\partial u_1^2}{\partial x} \right\rangle = \frac{\partial}{\partial x}\left(\frac{1}{2}\rho_0 u_0^2 \, exp(-2\alpha x) \right) \tag{6.7}$$

In a plane wave, acoustic pressure p_1 is

$$p_1 = \rho_0 c_0 u_1 = \rho_0 c_0 u_0 \, exp(-\alpha x) \cos\,(wt - kx) \tag{6.8}$$

And the acoustic intensity is given by

$$I = \rho_0 c_0 \langle u_1^2 \rangle = \frac{1}{2}(\rho_0 c_0 u)^2 \, exp(-2\alpha x) \tag{6.9}$$

Combined Eq. (6.9) with Eq. (6.7), the volume radiation force arises from viscous absorption of plane wave can be expressed as

$$F^{rad} = -\left\langle \rho \frac{du}{dt} \right\rangle = -\frac{\partial}{\partial x}\left(\frac{I}{c_0} \right) = 2\alpha \frac{I}{c_0} \tag{6.10}$$

Acoustic radiation force, F^{rad} is in unit of N/m^3. Acoustic radiation pressure arising from the acoustic force is typically orders of magnitude smaller than the oscillating pressure.

6.2 Bjerknes forces

There are two types of Bjerknes forces. The primary Bjerknes forces are caused by an external sound field on bubbles, in particular, in a standing wave field; the secondary Bjerknes forces are between pairs of bubbles. They were first described by Vilhelm Bjerknes in his 1906 book "Fields of Force" (Bjerknes, 1906).

6.2.1 Primary Bjerknes force

The force acts on a bubble arises from an instantaneous pressure gradient due to the finite wavelength of the sound field. Using the same denotations as in a plane wave radiation force analysis, primary Bjerknes forces (F^{PB}) can be expressed as

$$F^{PB} = -\frac{4}{3}\pi R^3 \frac{\partial p}{\partial x} \tag{6.11}$$

where p and R are instantaneous local pressure and bubble radius. If using the same notation as before, $p = p_0 + p_1 = p_0 + |p_1| cos(wt\text{-}kx)$ and $R = R_0 + R_1 = R_0\,(1+\varepsilon)$, substituting p and R in the Rayleigh-Plesset equation and neglecting second order terms, one (Valentin & Cancelos, 2012) can show that

$$\varepsilon = \frac{|p_1|\left(\omega^2 - \omega_0^2\right)\sin(kx)}{\rho R_0^2\left[\left(\omega^2 - \omega_0^2\right)^2 + \left(\frac{4\mu}{\rho R_0^2}\omega\right)^2\right]} \tag{6.12}$$

where

$$\omega_0 = \left(\frac{1}{\rho R_0^2}\right)^{\frac{1}{2}}\left(3\kappa p_0 - \frac{2\sigma}{R_0}\right)^{\frac{1}{2}} \tag{6.13}$$

is the resonant frequency of the bubble at the equilibrium radius. Here κ and σ are the polytropic gas constant and interfacial tension.

If ω is not close to ω_0, Eq. (6.12) can be simplified as

$$\varepsilon = \frac{|p_1|\sin(kx)}{\rho R_0^2(\omega^2 - \omega_0^2)} \tag{6.14}$$

For a linear response of bubble, Eq. (6.11) can be rewritten as

$$F^{PB} = -2\pi R_0^3 \varepsilon \frac{\partial p_1}{\partial x} = -\frac{\pi k R_0 |p_1|^2 sin(2kx)}{\rho(\omega^2 - \omega_0^2)} \tag{6.15}$$

This is known as the primary Bjerknes force which can produce some interesting bubble migration patterns in a standing wave field. Note from Eq. (6.15) that if the ultrasound frequency, ω, is less than the bubble natural frequency, ω_0, then the primary Bjerknes force will cause migration of the bubbles away from the nodes in the pressure field and toward the antinodes. On the opposite end where $\omega > \omega_0$ the bubbles will tend to migrate from the antinodes to the nodes. A number of investigators, e.g., Crum & Eller (1970) have observed the process by which small bubbles in a standing wave field first migrate to the antinodes, where they grow by rectified diffusion until they are larger than the resonant radius. They then migrate back to the nodes. Crum and Eller (1970) have shown that the translational velocities of migrating bubbles are compatible with the Bjerknes force estimates given above.

6.2.2 Secondary Bjerknes force

When bubbles oscillate in an acoustic field, the radiation pressure generated by other cavitation bubbles can cause mutual attraction or repulsion between bubbles. This phenomenon is termed as the secondary Bjerknes force (Crum, 1975). The mutual interaction between bubbles can affect bubble agglomeration, cavitation intensity, and consequently sonochemical reactions (Zhang et al., 2016).

Consider two bubbles of radius R_1 and R_2 separated by a distance of d. The radiation pressure generated by one oscillating bubble can be expressed as

$$p_i = \frac{\rho}{r}\frac{d}{dt}\left(R_i^2 \dot{R}_i\right) \qquad i = 1, 2 \tag{6.16}$$

where r is the radial coordinate. Applying Eq. (6.15), bubble of radius R_2 in a liquid under pressure gradient $\partial p_1/\partial r$ experiences a force

$$F_{12} = -\frac{4}{3}\pi R_2^3 \left.\frac{\partial p_1}{\partial r}\right|_{r=d} \hat{r} = \frac{4}{3}\pi R_2^3 \frac{\rho}{d^2}\frac{d}{dt}\left(R_1^2 \dot{R}_1\right)\hat{r} = \frac{\rho}{4\pi d^2} V_2 \frac{d^2 V_1}{dt^2}\hat{r} \tag{6.17}$$

V_1 and V_2 are bubble volumes, $\hat{r}$ denotes the radial unit vector. For bubbles oscillating periodically in time, the net force on the second bubble, time averaged F_{12} over a period, is the secondary Bjerknes force F^{SB}.

$$F^{SB} = \langle F_{12} \rangle = -\frac{\rho}{4\pi d^2}\langle \dot{V}_1 \dot{V}_2 \rangle \hat{r} \tag{6.18}$$

Note that expression of the secondary Bjerknes force between two bubbles are symmetric, so that $\langle F_{12} \rangle = -\langle F_{21} \rangle$.

The secondary Bjerknes force can be attractive or repulsive force depending on the sign of $\dot{V}_1 \dot{V}_2$. To calculate the bubble oscillations, the model of (Keller & Miksis, 1980) has been applied, where interaction between bubbles is considered by including the radiation pressure from one bubble on another.

In the original analysis by Vilhelm Bjerknes (1906), the theoretical expression for this force was derived with the following assumptions: (1) The surrounding medium is incompressible; (2) the gas behaves adiabatically; (3) the bubble size is smaller than their distance of separation and the bubbles remain spherical; (4) the driving pressure is low and the bubbles oscillate linearly with the driving frequency. Under these conditions, the secondary Bjerknes force is repulsive if the driving frequency lies between the resonance frequencies of the two bubbles, otherwise the force is attractive.

The linear theory has been extended by many researchers. When nonlinear oscillation is considered, the direction of the force may change. For example, several authors have found that the distance between the bubbles could affect the direction of the secondary Bjerknes force (Doinikov and Zavtrak, 1995; Harkin et al., 2001; Ida, 2002). This phenomenon was explained by (Zabolotskaya, 1984) that the resonance frequencies of bubbles increase when two bubbles get closer. Mettin et al. (Mettin et al., 1997) found that the sign of the secondary Bjerknes force changes with the amplitude of acoustic field pressure.

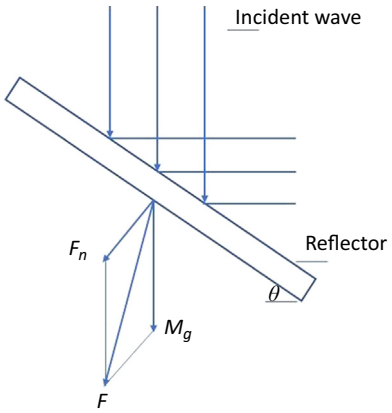

FIGURE 6.1 Plane reflector for radiation force measurement. Schematic diagram of the forces acting on a plane reflector subjected to a plane ultrasound beam.

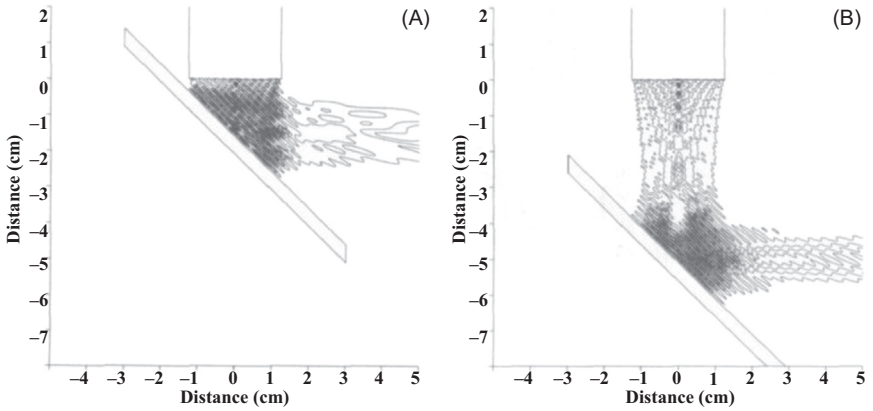

FIGURE 6.2 Acoustic energy density distribution in the near field. Contour plots showing the relative energy density distribution in the field with the reflector inclined at 45° and at distance of 15 mm and 50 mm from the center of the transducer. Complex diffraction pattern and wave interference caused by reflection at reflector can be seen from the contour maps.

6.3 Experimental aspects of determining acoustic radiation energy

6.3.1 Acoustic dosimetry based on radiation force measurement

One of the most prominent methods to evaluate ultrasonic power output was introduced by Kossoff (Kossoff, 1965), utilizing a sensitive analytical balance from which a reflecting target is suspended. A modified version of this technique was described by Hill (Hill, 1970), in which a rectangular aluminium plate inclined at an angle of 45° to the vertical is suspended in a water bath, being attached to the balance by fine threads. Fig. 6.1 schematically illustrates the setup developed by Hill (Hill, 1970).

In this case, a totally reflecting plane target suspended at an angle to the horizontal, situated in a water bath. When a plane wave travels vertically downwards, the normal and tangential components of the radiation force on the reflector are given by

$$F_n = \frac{IA}{c_0} \cos(\theta) \, and \, F_t = 0 \tag{6.19}$$

where A is the total surface area of the reflector, I the acoustic intensity.

$$F^2 = Mg^2 + F_n^2 - 2MgF_n \cos(\theta) \tag{6.20}$$

Here F is not directed along the vertical direction but inclined at an angle γ to it, given by

$$sin(\gamma) = \frac{F_n sin(\theta)}{F} \tag{6.21}$$

However, when the power output is small, i.e. $Fn \ll Mg$, angle γ is very small and the contribution of radiation force F measured by the balance can be approximated by

$$\Delta F \approx F - Mg \approx F_n \cos(\theta) = \frac{2IA}{c_0} cos^2\theta \tag{6.22}$$

which was given by Kossoff (Kossoff, 1965) to calculate the power ($W = IA$) output. This approach has been used by many authors to determine acoustic power from transducers.

6.3.2 Acoustic radiation force in the near field

Most analysis of acoustic radiation force has assumed plane traveling waves. In reality a non-plane wave is the rule and not the exception. This is particularly relevant for acoustic radiation force measurement in the near field, where complex wave diffraction occurs. After deriving the radiation force in a three-dimensional sound field, (Beissner, 1984) raised questions about the validity of applying the formula derived from plane wave to calculate the power output from a transducer in the near field.

Using the balance method, Quan et al. (Quan et al., 1992) observed that the radiation force varied depending on the position of a 45° angled plane reflector. At the same acoustic power output, the further the reflector is positioned away from the transducer, the smaller the radiation force it measures. The measurement starts to converge when the reflector moves out of the near field, where the wave approximates to a plane field. More studies are needed to determine how best to conduct radiation force measurement for ultrasound power output.

6.3.3 Measurement of acoustic radiation energy from a liquid of multibubbles

A number of experimental techniques have been developed to measure acoustic radiation from multibubble systems. A hydrophone, a passive acoustic detection system, is often the sensor of choice to study cavitation. For example, a hydrophone was used to detect subharmonic emission from cavitation generated by an ultrasound wave (Crum et al., 1992). Collapsing bubbles can induce weakly light emission, a phenomenon termed sonoluminescence (Suslick & Flannigan, 2008), which has been captured to characterize cavitation distribution and intensity (Lee et al., 2018). Other techniques to explore cavitation include using X-ray image (Izadifar et al., 2015) and an optical technique called Schlieren image (Carnell & Emmony, 1995).

Knowledge of bubble size distribution and the intensity of cavitation activity in a cavitation reactor is important in assessing and scaling the performance of the reactor. All micro scale mixing and mass transfer occurring in the cavitating medium is related to the size distribution of the oscillating bubbles. Several attempts have been reported to assess cavitation size and number density generated by ultrasound reactors (Delebarre et al., 1993; Tsochatzidis et al., 2001; Judy et al., 2005).

6.3.4 Interpretation of acoustic energy spectra from multibubble cavitation

The violent and catastrophic collapse of cavitation bubbles results in the production of acoustic radiation signal. The acoustic spectrum produced by a cavity during its collapse is closely related to its size. Large cavities generate low-frequency noise, whereas small cavities generate high-frequency noise. This can be seen from Eq. 6.23 that the collapse time for big cavity is longer than that of small ones. Assuming that the bubble collapses from a maximum radius of R_0 to a minimum (critical) radius of R_c, the collapse time may be approximated by the Rayleigh time,

$$\tau = 0.915 R_0 \sqrt{\frac{\rho}{P_\infty - P_V}} \tag{6.23}$$

The cavity may rebound back a number of cycles. As it takes about the same time to rebound to the next maximum radius, the oscillating frequency of a cavity as it collapses and rebounds can be obtained by rewriting Eqs. (6.23) (Yan et al., 1998) as

$$f_c = \frac{1}{2} \frac{1}{0.915 R_0} \sqrt{\frac{P_\infty - P_V}{\rho}} \tag{6.24}$$

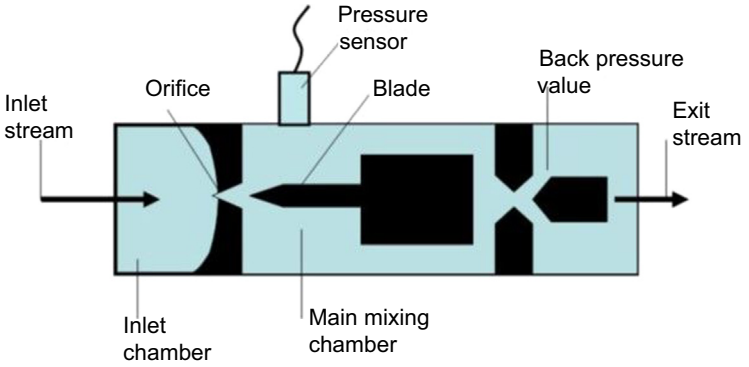

FIGURE 6.3 Sonolator. Schematic diagram of a Sonolator manufactured by Sonic Corp.

The factor 1/2 refers to rebound, which takes about the same time to reach the next maximum radius. It is important to point out that as energy dissipates into heat and sound, the rebound radius is reduced after each collapse, and therefore, the oscillating frequency changes over the whole period of oscillation.

Under the linear theory of small oscillation of a gas bubble, Avvaru and Pandit (Avvaru & Pandit, 2009) shows that f_c can be approximated by the resonance frequency of a gas bubble defined by

$$f_0 = \frac{1}{2\pi R_0}\sqrt{\frac{3P_\infty}{\rho}} \tag{6.25}$$

They derived a simple expression for the pressure radiated by the oscillating bubble of radius of R_0 at distance r from the center of the bubble as

$$p_r = 2\left(\frac{\rho}{r}\right)R_0 = \frac{(3\kappa P_\infty \rho)^{\frac{1}{2}}}{\pi f_0 r} \tag{6.26}$$

When a group of bubbles of radius R_0 oscillate, the resultant pressure of n bubbles, p_{res}, at frequency f_0 is given by the following equation:

$$p_{res}{}^2 = np_r^2 \tag{6.27}$$

Thus, the total number of bubbles of radius R_0, n, at a particular location with measured resultant pressure p_{res} can be calculated as:

$$n = \frac{p_{res}^2}{(3\kappa P_\infty \rho)}(\pi f_0 r)^2 \tag{6.28}$$

Avvaru and Pandit successfully applied this approach to obtain cavitation size and number density distribution generated in a 20kHz ultrasonic bath.

6.3.4.1 Sonolator as a hydrodynamic cavitation reactor

At industrial scales, cavitation can be generated acoustically or hydrodynamically. Each can introduce the energy to bring about the desired chemical and physical change. A crucial hindrance in the application of acoustic (ultrasonic) sonochemical reactors on an industrial scale has been the lack of suitable large-scale design strategies, coupled with the fact that intense cavitation activity is obtained very close to the transducers (device used for generating ultrasound) (Mason, 2000). Hydrodynamic cavitation, an alternative means of cavitation production, can simply be generated by the passage of the liquid through a constriction such as throttling valve, orifice plate, venturi, etc. (Gogate & Pandit, 2001). A careful design of the system allows generating cavity collapse conditions similar to acoustic cavitation, with much increased energy efficiency (Senthilkumar & Pandit, 1999).

An example of a hydrodynamic cavitation reactor is Sonolator, manufactured by Sonic Corp, based on a liquid whistle design originally proposed by Janovsky and Pohlman (Janovsky & Pohlman, 1948; Fig. 6.3). Although the commercial unit has been available since 60's, there is renewed interest in this technology in the last decade as evident by a number of recent publications (Tang and Sivakumar, 2013; Ryan et al., 2018; John et al., 2020).

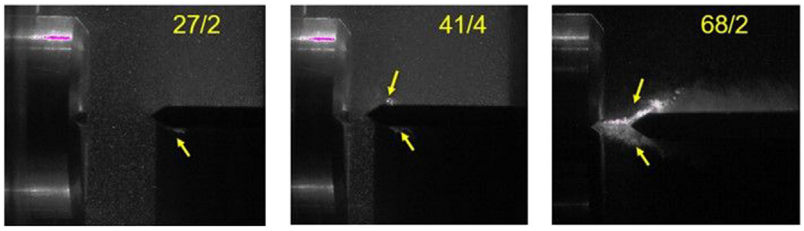

FIGURE 6.4 Cavitation in a Sonolator. Bright field optical image showing multibubble cavitation (arrowed) between orifice and the leading edge of the blade when operating pressure and back pressure were set at 27 and 2 bar, 41 and 4 bar, 68 and 2 bar.

FIGURE 6.5 Cavitation in a Sonolator. Bright field image and the corresponding sonoluminescence (SL) image from the Sonolator. It shows that SL emission is positioned behind the bubble cloud, where cavitation is expected to implode due to recovery of hydrodynamic pressure.

The system is essentially an orifice reactor, where the jet of liquid flow from the orifice is directed at a blade. The blade, which is clamped from behind by the blade holder, is expected to vibrate at its resonant frequency upon impingement of the jet. The vibration of the blade is believed to further enhance the cavitation intensity. The operating variables of the resonating blade include inlet pressure, back pressure, and the distance gap between the blade tip and orifice. All of these operating variables are expected to have an impact on cavitation occurring within the cavitating chamber.

The operating pressure of a Sonolator can be as high as 350 bar. When the inlet stream is fed through the orifice, a high velocity jet is formed with cavitation generated between the orifice and around the leading edge of the blade (Fig. 6.4).

The cavitation field formed within the Sonolator can be further interrogated with corresponding sonoluminescence to confirm the intensity of cavitation activity. In this case, the liquid jet is moving at a high speed and cavitation is generated by the kinetic energy of the fluid. The presence of blade boundary has an impact on decelerating the jet, which in turn, elevates the hydrodynamic pressure. Cavitation, conceived initially by liquid acceleration as it leaves the orifice, will subsequently implode as hydrodynamic pressure recovers. Because the liquid is moving at such a high velocity, there is a clear displacement between the region where the cloud of bubbles is initially formed and the location of sonoluminescence.

6.3.4.2 *Acoustic radiation from cavitation generated by a Sonolator*

Quan et al. (Quan et al., 2011) studies acoustic radiation from cavitation generated by a Sonolator, using a hydrophone (PCB Piezotronics, Model-111A21). The transducer measures the dynamic pressure only and has a rise time 2 μ s and sensitivity of 5.8 mV/kPa. The signal is acquired and analyzed using Quattro DSP centric signal processing hardware (DATA Physics), which has two 24-bit inputs, one 24-bit Output, and 94 kHz analysis bandwidth. The acoustic emission from cavitation in the time domain has been captured and is then converted into frequency spectra (FFT) using Auto-Signal 1.7, (SYSTAT), a commercial signal processing software. Tap water at room temperature as the liquid medium is used in this study. The orifice used in this study is supplied by Sonic Corporation, which takes a cat eye shape and has a cross sectional area of 0.645 mm^2.

Fig. 6.6 shows the measured energy spectra from cavitation generated in a Sonolator. For a given liquid, cavitation activity inside the Sonolator varies depending on the inlet pressure, back pressure and the position of the blade. For a sonochemical process that critically depends on cavitation, it is important to be able to control the number and size distribution of cavitation for process optimization and scalability.

Applying the approach described by Avvaru and Pandit (Avvaru & Pandit, 2009), Quan et al. (Quan et al., 2011) evaluated cavitation signal obtained from the Sonolator. An example of such analysis is shown in Figs. 6.7 and 6.8.

In this case, the number density (total number) of the bubbles is increasing from 11 to 6401 as inlet pressure changes from 34.5 bar-344.5 bar (Note that there is uncertainty about the absolute number of the bubbles, given the arbitrary dampening factor). At the same time, bubble size distribution changes significantly, even though the averaged size remains about the same. At low pressure, bubble size is broadly distributed up to 200 μm. As the inlet pressure increases, the bubble size

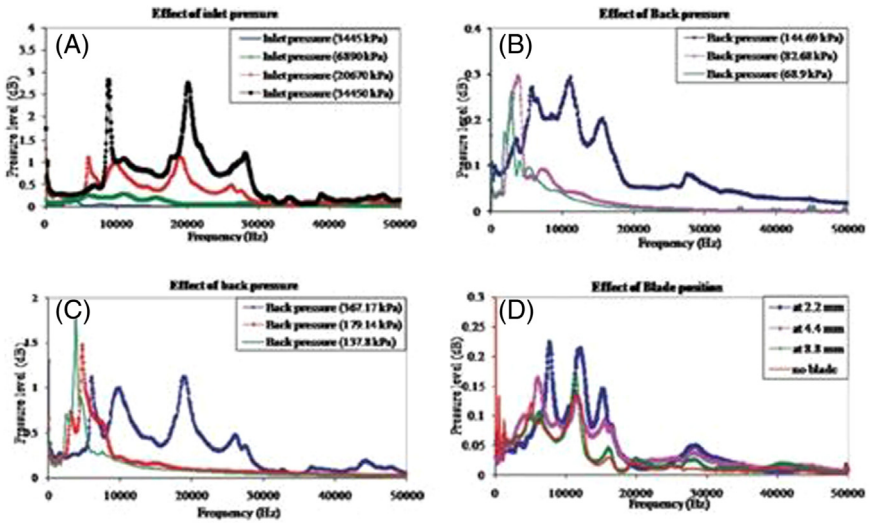

FIGURE 6.6 Acoustic radiation energy spectra from a Sonolator.

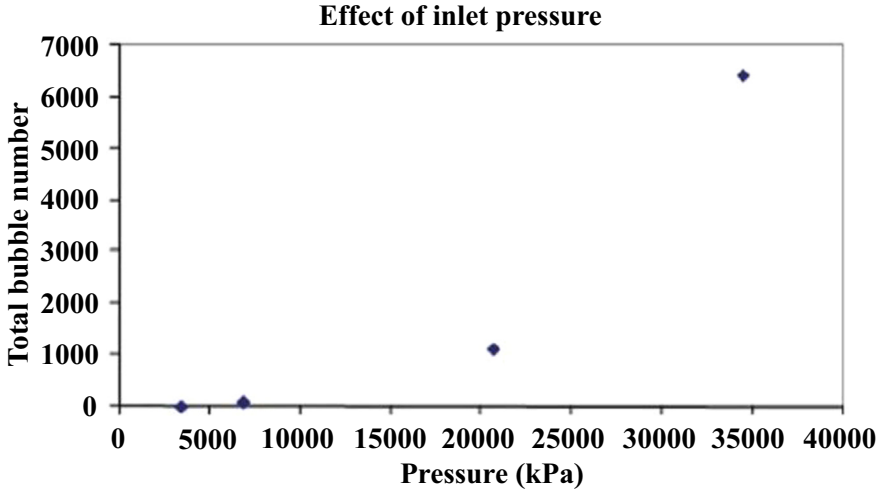

FIGURE 6.7 Number of cavitation in Sonolator as function of inlet pressure. The total number of cavitation bubbles generated in the Sonolator at different inlet pressure.

distribution becomes increasingly narrower. The same analysis was extended other operating parameters of the Sonolator, including back pressure and the blade position.

6.4 Conclusion

In a cavitation field, there are different types of acoustic radiation forces acting on the bubbles. If cavitation is generated ultrasonically, the ultrasound wave exerts a radiation force on all particles and bubbles, the magnitude of the force being proportional to the acoustic intensity. Measuring the radiation force can be a way to calibrate the acoustic power output from the reactor.

In a standing wave field, bubbles may be separated at pressure node and antinode planes according to the bubble size, driven by the primary Bjerknes force. Small bubbles of resonant frequency greater than the ultrasound frequency move towards a pressure antinode plane, large bubbles of resonant frequency lower than the ultrasound frequency to a node plane. The small bubbles may grow through rectified diffision and/or coalescence to large sizes, and start to move to a node plane once their resonant frequency goes below the ultrasound frequency.

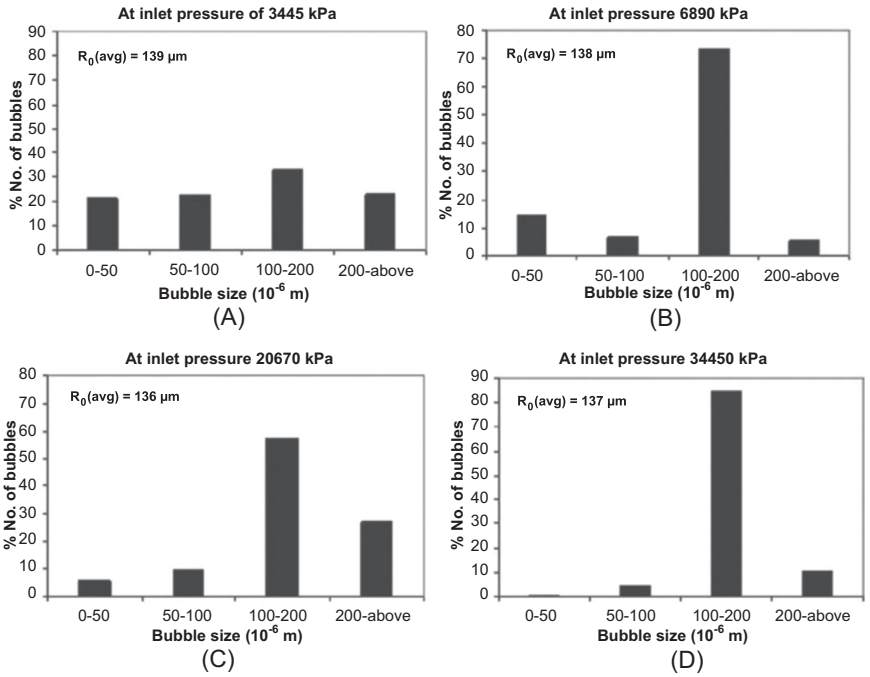

FIGURE 6.8 Cavitation size distribution in a Sonolator. The size distribution and the averaged size of cavitation bubble in the Sonolator as function of inlet pressure.

An oscillating bubble exerts radiation pressure on other bubbles nearby. This inter-bubble force is termed the secondary Bjerkens forces, which can be attractive or repulsive in nature between bubbles.

The radiation forces may work spontaneously in a multibubble cavitation field, influencing spatial distribution of bubbles and the kinetics of bubble clustering and coalescence. For a cavitation reactor, changes in bubble spatial and size distribution are important as they determine the rates of energy and mass transfer, mixing homogeneity, and, ultimately, the scalability and energy efficiency of the reactor.

For either an acoustic or a hydrodynamic cavitation reactor, the exact knowledge of the bubble size distribution and concentration is important for process optimization, energy efficiency and scalability. Avvaru and Pandit's approach represents a novel attempt to analyze cavitation quantitatively within a reactor by measuring the acoustic radiation energy. Although the example described in this chapter is for a case of hydrodynamic cavitation, the same approach has been applied elsewhere to characterize ultrasonically induced cavitation. Whilst further development is required, the method described here has tremendous potential to be adapted for future reactor design, process scalability and inline feedback for operation control of a cavitation reactor.

References

Avvaru, B., Pandit, A.B., 2009. Oscillating bubble concentration and its size distribution using acoustic emission spectra. Ultrason. Sonochem. 16 (1), 105–115. https://doi.org/10.1016/j.ultsonch.2008.07.003.

Beissner, K., 1984. Acoustic radiation pressure in the near field. J. Sound Vib. 93 (4), 537–548. https://doi.org/10.1016/0022-460X(84)90422-X.

Bjerknes, V. (1906). Fields of force.

Carnell, M.T., Emmony, D.C., 1995. Optical distortion in the field of a lithotripter shock wave. Appl. Opt. 34 (28), 6465–6470. https://doi.org/10.1364/AO.34.006465.

Crum, L.A., 1975. Bjerknes forces on bubbles in a stationary sound field. J. Acoust. Soc. Am. 57 (6), 1363–1370. https://doi.org/10.1121/1.380614.

Crum, L.A., Eller, A.I., 1970. Motion of bubbles in a stationary sound field. J. Acoust. Soc. Am. 48 (1B), 181–189. https://doi.org/10.1121/1.1912115.

Crum, L.A., Roy, R.A., Dinno, M.A., Church, C.C., Apfel, R.E., Holland, C.K., Madanshetty, S.I., 1992. Acoustic cavitation produced by microsecond pulses of ultrasound: a discussion of some selected results. J. Acoust. Soc. Am. 91 (2), 1113–1119. https://doi.org/10.1121/1.402638.

Delebarre, C., Frohly, J., Baquet, I., Derouiche, Z., Bruneel, C., 1993. Acoustic signature estimation of the cavitation noise. In: Proceedings of the Ultrasonics International Conference. Publ by Butterworth-Heinemann Ltd, pp. 719–722. https://doi.org/10.1016/b978-0-7506-1877-9.50178-5.

Feng, H., Barbosa-Canovas, G., Weiss, J., 2010. Ultrasound technologies for food and bioprocessing.

Doinikov, A.A., Zavtrak, S.T., 1995. On the mutual interaction of two gas bubbles in a sound field. Phys. Fluids 7, 1923–1930.

Gogate, P.R., Pandit, A.B., 2001. Hydrodynamic cavitation reactors: a state of the art review. Rev. Chem. Eng. 17 (1), 1–85. https://doi.org/10.1515/REVCE.2001.17.1.1.

Harkin, A., Kaper, T.J., Nadim, A.L.I., 2001. Coupled pulsation and translation of two gas bubbles in a liquid. J. Fluid Mech. 445, 377–411. https://doi.org/10.1017/s0022112001005857.

Hill, C.R., 1970. Calibration of ultrasonic beams for bio-medical applications. Phys. Med. Biol. 15 (2), 241–248. https://doi.org/10.1088/0031-9155/15/2/001.

Ida, M., 2002. A characteristic frequency of two mutually interacting gas bubbles in an acoustic field. Physics Letters, Section A: General, Atomic and Solid State Physics 297 (3–4), 210–217. https://doi.org/10.1016/S0375-9601(02)00422-X.

Izadifar, Z., Belev, G., Babyn, P., Chapman, D., 2015. Application of analyzer based X-ray imaging technique for detection of ultrasound induced cavitation bubbles from a physical therapy unit. BioMedical Engineering Online 14 (1). https://doi.org/10.1186/s12938-015-0085-6.

Janovsky, W., Pohlman, R., 1948. Z. Angew. Rhys. 1.

John, T.P., Carrillo De Hert, S., Ren, Z., Kowalski, A., Rodgers, T.L., 2020. Predicting droplet size distributions of emulsions produced in a sonolator. Ind. Eng. Chem. Res. 59 (14), 6681–6695. https://doi.org/10.1021/acs.iecr.9b05596.

Judy, A.M., Sandra, K., Franz, G., 2005. Determination of the size distribution of sonoluminescence bubbles in a pulsed acoustic field. J. Am. Chem. Soc 127.

Keller, J.B., Miksis, M., 1980. Bubble oscillations of large amplitude. J. Acoust. Soc. Am. 68 (2), 628–633. https://doi.org/10.1121/1.384720.

Kossoff, G., 1965. Balance technique for the measurement of very low ultrasonic power outputs. J. Acoust. Soc. Am. 38 (5), 880–881. https://doi.org/10.1121/1.1909822.

Lee, J., Yasui, K., Ashokkumar, M., Kentish, S.E., 2018. Quantification of cavitation activity by sonoluminescence to study the sonocrystallization process under different ultrasound parameters. Cryst. Growth Des. 18 (9), 5108–5115. https://doi.org/10.1021/acs.cgd.8b00547.

Mason, T., Peters, D., 2002. Practical Sonochemistry: uses and applications of ultrasound.

Mason, T.J., 2000. Large scale sonochemical processing: aspiration and actuality Ultrason. Sonochem. 7, 145–149.

Matula, 1999. Single-bubble sonoluminescence: some recent experiments. Sonochemistry and Sonoluminescence. Springer, pp. 145–158.

Mettin, R., Akhatov, I., Parlitz, U., Ohl, C., Lauterborn, W., 1997. Bjerknes forces between small cavitation bubbles in a strong acoustic field. Phys. Rev. E 56 (3), 2924–2931. https://doi.org/10.1103/physreve.56.2924.

Nyborg, W. L. (1965). Acoustic streaming, Physical acoustics 2B edited by.

Putterman, S.J., Weninger, K.R., 2000. Sonoluminescence: how bubbles turn sound into light. Annu Rev Fluid Mech 32, 445–476. https://doi.org/10.1146/annurev.fluid.32.1.445.

Quan, K.M., Shrian, M., Watmough, D, 1992. Effect of wave diffraction on the measurement of ultrasonic power output using the radiation force method with a plane reflecting target angled at 45°. Meas. Sci. Technol. 3, 338–346.

Quan, K.M., Avvaru, B., Pandit, A.B., 2011. Measurement and interpretation of cavitation noise in a hybrid hydrodynamic cavitating device. AlChE J. 57 (4), 861–871. https://doi.org/10.1002/aic.12323.

Rayleigh, 1902. On the pressure of vibrations. Phyl Mag 3, 338–346.

Ryan, D.J., Baker, M.R., Kowalski, A.J., Simmons, M.J.H., 2018. Emulsification using a "Sonolator" liquid whistle: a new correlation for droplet size from pilot-scale experiments. Chem. Eng. Sci. 189, 369–379. https://doi.org/10.1016/j.ces.2018.06.004.

Senthilkumar, P., Pandit, A.B., 1999. Modelling of hydrodynamic cavitation. Chem. Eng. Technol. 22, 1017–1027.

Suslick, K.S., Didenko, Y., Fang, M.M., Hyeon, T., Kolbeck, K.J., McNamara, W.B., Mdleleni, M.M., Wong, M., 1999. Acoustic cavitation and its chemical consequences. Philos. Trans. R. Soc., A 357 (1751), 335–353. https://doi.org/10.1098/rsta.1999.0330.

Suslick, K.S., Flannigan, D.J., 2008. Inside a collapsing bubble: sonoluminescence and the conditions during cavitation. Annu. Rev. Phys. Chem. 59, 659–683. https://doi.org/10.1146/annurev.physchem.59.032607.093739.

Tang, S.Y., Sivakumar, M., 2013. A novel and facile liquid whistle hydrodynamic cavitation reactor to produce submicron multiple emulsions. AlChE J. 59 (1), 155–167. https://doi.org/10.1002/aic.13800.

Tsochatzidis, N.A., Guiraud, P., Wilhelm, A.M., Delmas, H., 2001. Determination of velocity size and concentration of ultrasonic cavitation bubbles by the Phase-Doppler technique. Chem. Eng. Sci 56, 1831–1840.

Valentin, F.I., Cancelos, S., 2012. Predicting bubble migration due to Bjerknes force in a complex 3D geometry: numerical and experimental results. American Society of Mechanical Engineers. Fluids Engineering Division (Publication) FEDSM (Vol. 2), Rio Grande, Puerto Rico, USA, pp. 223–232. https://doi.org/10.1115/FEDSM2012-72322.

Yan, Y., Thorpe, R.B., Pandit, A.B., 1998. Cavitation noise and its suppression by air in orifice flow. In: Symposium on Flow Induced Vibration and Noise, pp. 25–40.

Zabolotskaya, E.A., 1984. Interaction of gas bubbles in a sound wave field, Akust. Zh. 30, 618. English translation: Zabolotskaya E.A., Interaction of gas bubbles in a sound field. Soviet Physics Acoustics-USSR 30, 365–368.

Zhang, Y., Zhang, Y., Li, S., 2016. The secondary Bjerknes force between two gas bubbles under dual-frequency acoustic excitation. Ultrason. Sonochem. 29, 129–145. https://doi.org/10.1016/j.ultsonch.2015.08.022.

Chapter 7

Nonlinear oscillations and resonances of the acoustic bubble and the mechanisms of energy dissipation

Amin Jafari Sojahrood and Michael C. Kolio

Institute for Biomedical Engineering, Science and Technology (IBEST) a partnership between Ryerson University and St. Mike's Hospital, Toronto, Ontario, Canada

7.1 Introduction

An ultrasonically driven bubble is a nonlinear oscillator that is the building block of a wide range of applications from underwater acoustics to medicine and sonochemistry (Werner Lauterborn & Kurz, 2010). When high intensity ultrasound is applied to an aqueous solution, the pressure achieved in the rarefaction cycle can become so strong that bubbles (cavities) are formed within the liquid. Bubbles oscillate and collapse in response to the sound field and acoustic cavitation is generated (W. Lauterborn & Suchla, 1984; Werner Lauterborn, 1976). The bubble response to the sound filled is nonlinear which can be accompanied by intense noise emission which is called the acoustic cavitation noise (W. Lauterborn & Suchla, 1984).

The enhanced chemical effects by ultrasound is called sonochemistry which is an indirect consequence of the ultrasonic waves, that harnesses the acoustic cavitation (Yasui, 2011). The repeating pattern of compression and rarefaction by the ultrasound wave exerts positive and negative pressures on the bubble resulting in the compression and expansion of the bubble. The strong collapse of the bubble causes extremes of temperatures and pressures which results in high-energy micro-reactors that create chemical reactions within collapsing cavities.

In medicine, bubbles are encapsulated with a shell (e.g., phospholipids) and are injected intravenously with many potential clinical applications ranging from contrast enhanced imaging (Fischer et al., 1986; Versluis et al., 2020) to delivering drugs with submitter precision in brain (Arif et al., 2020). In all the mentioned applications the frequency and pressure amplitude of the ultrasonic wave determines the oscillation properties of the bubbles.

Bubble response to ultrasound however, is complex and nonlinear (Behnia et al., 2009; Hegedus et al., 2013; Werner Lauterborn & Kurz, 2010; Parlitz et al., 1990). Moreover, the presence of the bubbles in a medium changes the medium's attenuation and sound speed (Commander & Prosperetti, 1989; Dogan et al., 2017; Louisnard, 2012; A.J. Sojahrood et al., 2015; A.J. Sojahrood et al., 2018). The changes are nonlinear and depend on the bubble behavior (Jamshidi & Brenner, 2013; Louisnard, 2012; Segers et al., 2016; A.J. Sojahrood et al., 2015; A.J. Sojahrood et al., 2018). Achieving the full potential of bubbles in applications requires not only understanding the bubble dynamics, but also a detailed knowledge on the effect of the bubble oscillations on the acoustical properties of the host medium. As an example, increased attenuation due to the presence of the bubbles in the ultrasound beam path limits the ultrasound energy that can reach the target location (Doinikov & Bouakaz, 2010).

The first step to understand and optimize the ultrasound exposure parameters to harness the maximum potential of bubbles is to have a comprehensive understanding of the nonlinear bubble behavior and its resonances. The second step is to gain insight on the frequency and pressure dependent dissipation mechanisms in the bubble oscillations. In this chapter, we will first introduce the nonlinear bubble resonances as a function of applied acoustic pressure. We then drive the linear and pressure dependent dissipation mechanisms in the bubble oscillations. The evolution of the dissipation mechanisms are studied at each bubble resonance. At the end we present a comprehensive insight on the pressure dependent bubble

Energy Aspects of Acoustic Cavitation and Sonochemistry: Fundamentals and Engineering. DOI: https://doi.org/10.1016/B978-0-323-91937-1.00006-2
Copyright © 2022 Elsevier Inc. All rights reserved.

oscillations and the related dissipation effects using the bifurcation diagrams of the bubble oscillations in tandem with the corresponding dissipation powers at various nonlinear oscillation regimes. Using this information, the nonlinear bubble behavior and the corresponding dissipation mechanisms are classified.

7.2 The bubble model

The dynamics of the uncoated bubble including the compressibility effects to the first order of Mach number can be modeled using Keller-Miksis (KM) equation:

$$\rho\left[\left(1-\frac{\dot{R}}{c}\right)R\ddot{R}+\frac{3}{2}\dot{R}^2\left(1-\frac{\dot{R}}{3c}\right)\right]=\left(1+\frac{\dot{R}}{c}+\frac{R}{c}\frac{d}{dt}\right)\left(P_g-\frac{4\mu_L\dot{R}}{R}-\frac{2\sigma}{R}-P_0-P_A\sin(2\pi ft)\right) \tag{7.1}$$

In this equation, R is radius at time t, R_0 is the initial bubble radius, $\dot{R}$ is the wall velocity of the bubble, $\ddot{R}$ is the wall acceleration, ρ is the liquid density (998 kg/m^3), c is the sound speed (1481 m/s), where σ is the surface tension (0.0725 N/m), μ_{L} is the liquid viscosity (0.001 Pa.s), P_A and f are the amplitude and frequency of the applied acoustic pressure, and P_g is the gas pressure.

In the absence of thermal effects, P_g is given by:

$$P_g=\left(P_0+\frac{2\sigma}{R_0}\right)\left(\frac{R_0}{R}\right)^{3\gamma} \tag{7.2}$$

In this chapter the gas inside the bubble is air, and water is the host medium.

7.2.1 Thermal effects

7.2.1.1 Full ODE thermal model

If thermal effects are considered, P_g is given by Eq. (7.3) (Stricker et al., 2011; Toegel et al., 2006):

$$P_g=\frac{N_gKT}{\frac{4}{3}\pi R(t)^3-N_gB} \tag{7.3}$$

where N_g is the total number of the gas molecules, K is the Boltzman constant and B is the molecular co-volume of the gas inside the bubble. The average temperature inside the gas can be calculated using Eq. (7.4) (Stricker et al., 2011; Toegel et al., 2006):

$$\dot{T}=\frac{4\pi R(t)^2}{C_v}\left(\frac{L(T_0-T)}{L_{th}}-\dot{R}P_g\right) \tag{7.4}$$

where C_v is the heat capacity at constant volume, $T_0=293$ K is the initial gas temperature, L_{th} is the thickness of the thermal boundary layer. L_{th} is given by $L_{th}=\min\left(\sqrt{DR(t)/\left|\dot{R}(t)\right|},R(t)/\pi\right)$, where D is the thermal diffusivity of the gas which can be calculated using $a=L/c_p\rho_g$, where L is the gas thermal conductivity and c_p is specific heat capacity at constant pressure and ρ_g is the gas density.

We refer to this model as the full ODE thermal model (FTM). Predictions of the FTM have been shown to be in good agreement with predictions of the models that incorporate the thermal effects using the partial differential equations (PDEs) (Stricker et al., 2011) that incorporate the temperature gradients within the bubble. To calculate the radial oscillations of the uncoated bubble while including the thermal effects, Eq. (7.1) is coupled with Eqs. (7.3) and (7.4) and is then solved using the ode45 solver of Matlab. The two Matlab solvers of ode45 and ode15s (used for stiff equations) return identical solutions for the parameter ranges that used in this chapter.

7.2.1.2 Linear thermal model

The linear thermal model (LTM) (Commander & Prosperetti, 1989) has been widely used in studies related to oceanography (Dogan et al., 2017) and the modeling and characterization of coated bubble oscillations (Raymond et al., 2014; Shekhar et al., 2016). In this model thermal damping is approximated through linearization by adding an artificial viscosity term to the liquid viscosity. Furthermore, a variable isoentropic index is used instead of the polytropic exponent of the gas.

In this model P_g is given by:

$$P_g = P_{g_0}\left(\frac{R_0}{R}\right)^{3k} \tag{7.5}$$

where the polytropic exponent γ is replaced by isoentropic indice (k):

$$k = \frac{1}{3}\Re(\phi) \tag{7.6}$$

where $\Re$ denotes the real part and the complex term ϕ is calculated from

$$\phi = \frac{3\gamma}{1 - 3(\gamma - 1)i\chi\left[\left(\frac{i}{\chi}\right)^{\frac{1}{2}}\coth\left(\frac{i}{\chi}\right)^{\frac{1}{2}} - 1\right]} \tag{7.7}$$

where γ is the polytropic exponent and $\chi = D/\omega R_0^2$ represents the thermal diffusion length. D is the thermal diffusivity of the gas. $D = L/c_p\,\rho_g$ where c_p, ρ_g, and L are the specific heat capacity at constant pressure, density and thermal conductivity of the gas inside the bubble. The liquid viscosity is artificially increased by adding a thermal viscosity (μ_{th}) to the liquid viscosity. The thermal viscosity (μ_{th}) is given by:

$$\mu_{th} = \frac{P_{g_0}\Im(\phi)}{\omega} \tag{7.8}$$

In the above equations $\Im$ denotes the imaginary part. To calculate the radial oscillations of the bubble while including the linear thermal effects, Eq. (7.1) is coupled with Eq. (7.5) and liquid viscosity is increased by μ_{th} (Eq. (7.8)). In this chapter for air (Toegel et al., 2006) the following thermal properties are used: $L = 0.001165 + 5.528 \times 10^{25} \times T^2$ W/mK, $C_p = 1.0049$ kJ/kgK, $C_v = 0.7187$ kJ/kgK, and $\rho_g = 1.025$ kg/m^3.

7.3 Scattered pressure by bubbles

Oscillations of the bubbles generate a scattered pressure (P_{sc}) which can be calculated by (Hilgenfeldt et al., 1998; Vokurka, 1985).

$$P_{sc} = \rho\left(\frac{R}{d}\right)\left(R\ddot{R} + 2\dot{R}^2\right) \tag{7.9}$$

where d is the distance from the center of the bubble (and for simplicity is considered as 1 m in this chapter). Calculation of the scattered pressure is of crucial importance since in several applications the scattered pressure (P_{sc}) resulting from bubble oscillations plays a critical role. For example, in imaging applications P_{sc} is detected and analyzed to create images. In the majority of the applications and phenomena involving bubble dynamics, monitoring the behavior of the bubbles is through saving the P_{sc} signal and analyzing its frequency components.

7.4 Various regimes of complex bubble oscillations

In this section some of the main nonlinear regimes of the oscillations of a bubble are introduced. Eq. (7.1) is coupled to Eqs. (7.3) and (7.4) and the radial oscillations of an air bubble with $R_0 = 8$ μm are simulated at different pressures and frequencies. The simulations are performed using the ode45 solver of Matlab with relative and absolute tolerances of 1×10^{-10} and 1×10^{-11} with time steps of $0.001/f$ where f is the driving acoustic frequency.

Fig. 7.1A shows the radial oscillations of the bubble as a function of driving periods for the steady state regime of oscillations when $f = 382$ kHz and $P_A = 1$ kPa. The radial oscillations have one maxima (denoted by the red circle) with very small expansion ration (<1.5%). The maxima occur at the end of each period and the wall velocity is in phase with the driving acoustic filed. In phase wall velocity occurs when the bubble is oscillating in the resonance mode (Leighton, 2012). The scattered pressure (P_{sc}) by the bubble (Fig. 7.1B) have one maxima and is in phase with the driving acoustic field. The corresponding frequency spectrum of the bubble (f_b) consists of the frequency of the driving filed (fundamental frequency) and it's harmonics at ($2f$, $3f$, $4f$ and etc). The scattered frequency at the fundamental has the highest power compared to other frequency components.

When $f = 191$ kHz and $P_A = 20$ kPa, the radial oscillations (Fig. 7.1D) and P_{sc} (Fig. 7.1E) have two maxima. Within each period the bubble collapses twice. The frequency spectrum consists of the fundamental and its harmonics, however, the second harmonic at $2f$ has the highest power (Fig. 7.1F).

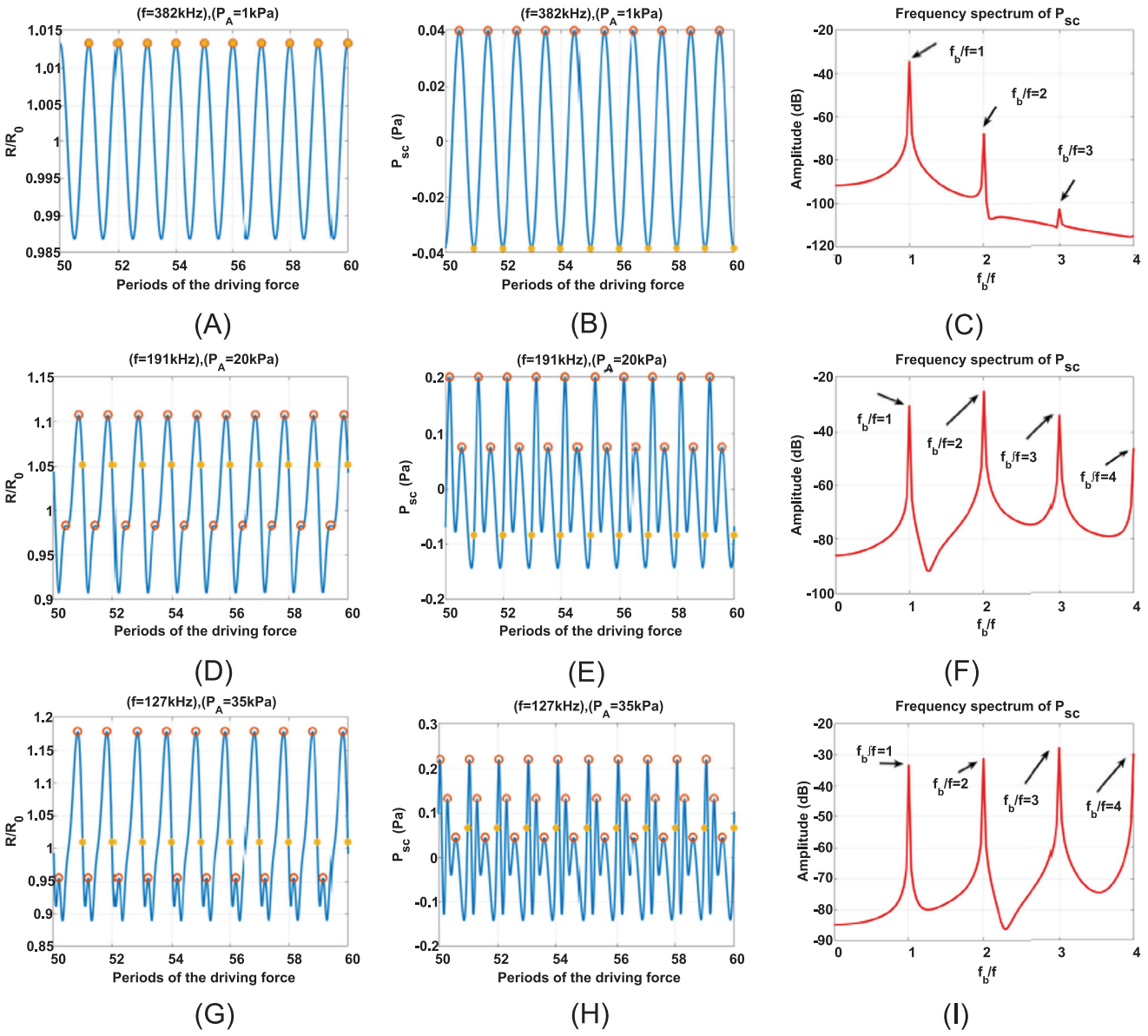

FIGURE 7.1 Radial oscillations, the corresponding scattered pressure (P_{sc}) and the frequency spectrum of the P_{sc} for an air bubble with $R_0 = 8$ μm. First row is for $f = 382$ kHz and $P_A = 1$ kPa, second row is for $f = 191$ kHz and $P_A = 20$ kPa, and third row is for $f = 127$ kHz and $P_A = 35$ kPa. The yellow dots represent the bubble radius after every acoustic period and red circles represent the maxima of the radial oscillations.

Fig. 7.1G shows the radial oscillations of the bubble when $f = 127$ kHz and $P_A = 35$ kPa. Radial oscillations have two maxima and one inflection point. The corresponding frequency spectrum of the bubble (f_b) consists of the frequency of the driving filed (fundamental frequency) and it's harmonics. P_{sc} in Fig. 7.1H has three maxima within each driving period. The frequency spectrum consists of the fundamental frequency and its harmonics with the 3rd harmonic at $3f$ with the maximum power.

When $f = 237$ kHz and $P_A = 95$ kPa, the radial oscillations (Fig. 7.2A) and P_{sc} (Fig. 7.2B) have four maxima, and within each period two maxima occur and this pattern repeats itself for all the driving periods. The wall velocity becomes in phase with the driving sound field at the end of each period. In addition to the fundamental frequency and its harmonics, the frequency spectrum consists of the 1/2 order subharmonic (SH) at $f/2$ and ultraharmonics (UH) at $3f/2$, $5f/2$, $7f/2$, with the UHs components exhibiting higher power than the sub-harmonic (SH) component.

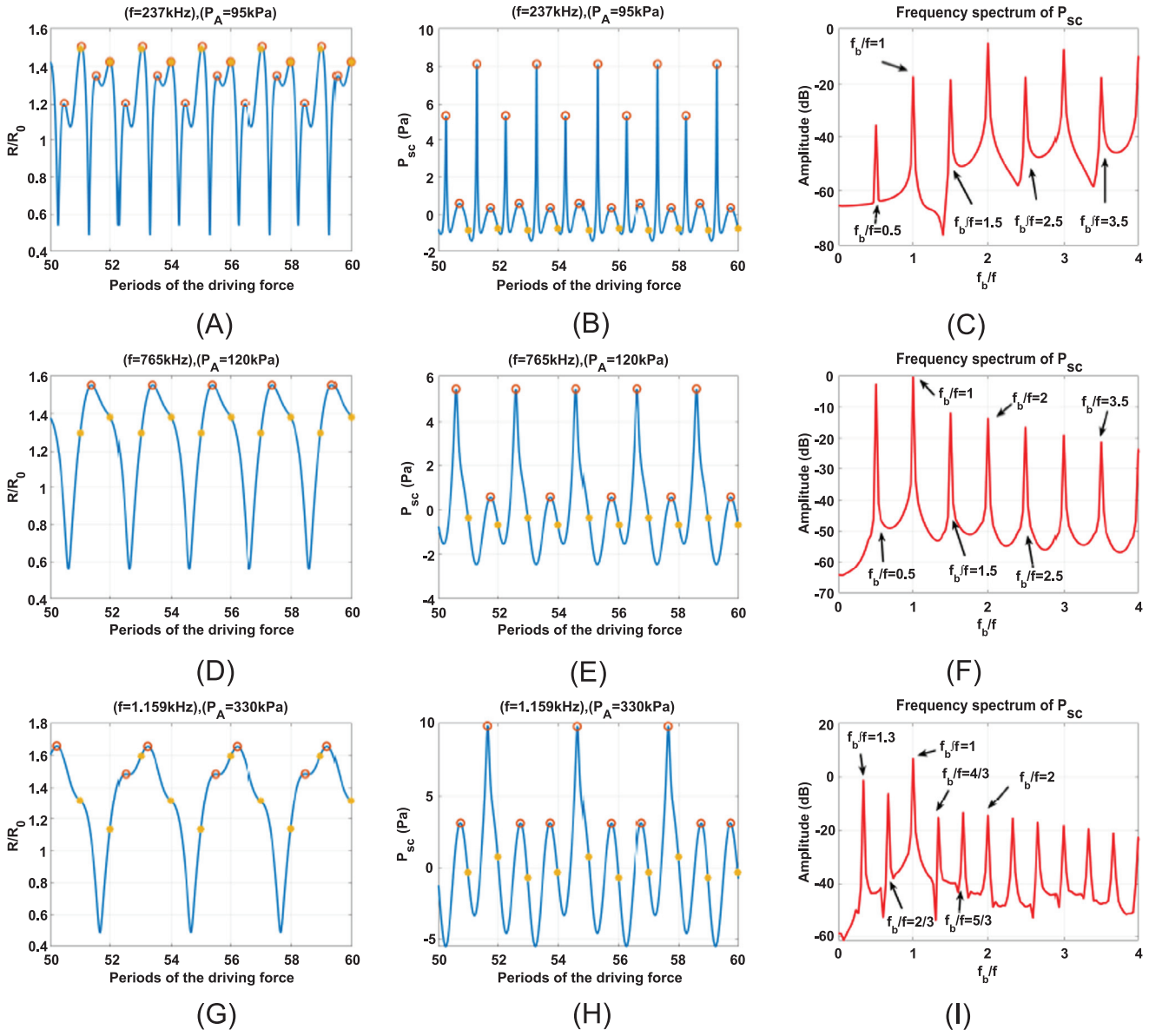

FIGURE 7.2 Radial oscillations, the corresponding scattered pressure (P_{sc}) and the frequency spectrum of the P_{sc} for an air bubble with $R_0 = 8$ μm. First row is for $f = 237$ kHz and $P_A = 95$ kPa, second row is for $f = 765$ kHz and $P_A = 120$ kPa, and third row is for $f = 1.159$ MHz and $P_A = 330$ kPa. The yellow dots represent the bubble radius after every acoustic period and red circles represent the maxima of the radial oscillations.

Fig 7.2D shows the radial oscillations when $f = 765$ kHz and $P_A = 120$ kPa. The bubble collapses once every two acoustic cycles and the corresponding P_{sc} has two maxima each occurring in a separate cycle. The corresponding frequency spectrum has a strong 1/2 order SH which is stronger than the UH and harmonic components of the scattered signal.

When $f = 1.159$ MHz and $P_A = 330$ kPa, the bubble collapses strongly once every three acoustic cycles (Fig. 7.2G). The corresponding P_{sc} (Fig. 7.2H) has three maxima, and each maximum occur in a separate acoustic cycle. The frequency spectrum has a 1/3 order SH at (f/3), 2/3 order SH at (2f/3) and their corresponding UHs (e.g., at 4f/3). Compared to the SHs, UHs and the harmonic components, the 1/3 order SHs has the strongest power.

Case of $f = 382$ kHz and $P_A = 270$ kPa, is shown in Fig. 7.3. The radial oscillations and the corresponding P_{sc} (Figs. 7.3A–B) have many maxima but with no particular order. This case is referred to as chaotic oscillations (Holt et al., 1994; Werner Lauterborn & Kurz, 2010; Parlitz et al., 1990). The frequency spectrum no longer has distinct harmonics or SH peaks and the signal energy is broadband and is distributed over a wide range of frequencies (Fig. 7.3C).

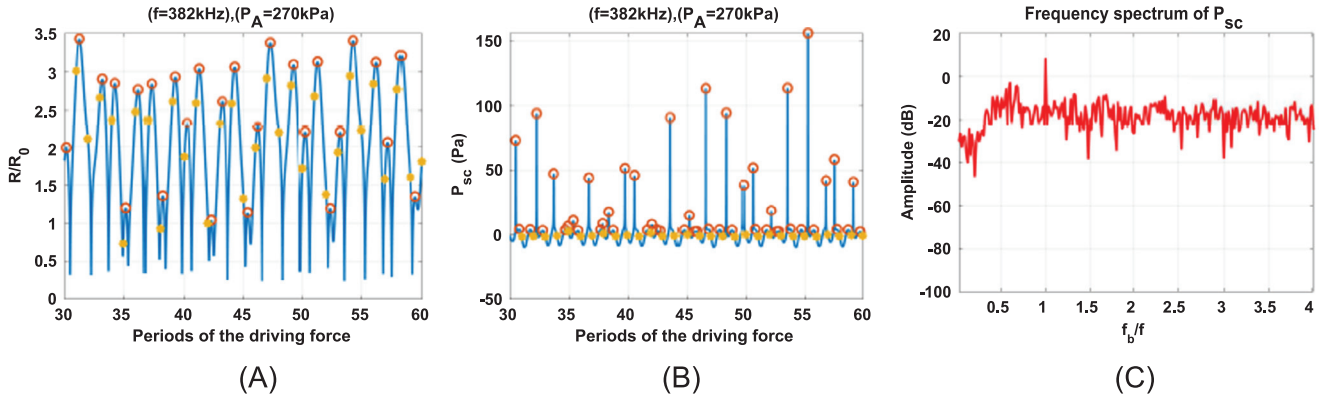

FIGURE 7.3 Radial oscillations, corresponding scattered pressure (P_{sc}) and the frequency spectrum of the P_{sc} for an air bubble with $R_0 = 8\ \mu$m during a case of chaotic oscillations where $f = 382$ kHz and $P_A = 270$ kPa.

It is observed in Fig. 7.3 that the bubble oscillator is a complex nonlinear oscillator and has many different regimes of oscillations. Each of these regimes dissipates the acoustic energy in its unique way. Optimization and understanding bubble related phenomena thus, requires detailed information of the nonlinear oscillatory regimes and the corresponding associated energy loss. In the following sections we will classify these regimes using the bubble resonance curves and bifurcation diagrams in a simple and easy to understand way. Using the classification scheme, different regimes of power dissipation are investigated and classified.

7.5 Damping constants for the linear regime of oscillations

To understand the nonlinear regimes of oscillations and the corresponding power dissipation associated with them, it useful to first focus on the linear regime of the oscillations and derive the linear resonance frequency and the linear damping constants. To drive the linear damping constants, the linear thermal \ Eqs. (7.5)–(7.8) are coupled to the bubble model in Eq. (7.1). For the linear regime, radial oscillations can be considered as $R = R_0\ (1 + x)$ where x is a small displacement amplitude (Commander & Prosperetti, 1989; Dogan et al., 2017; Hoff et al., 2000). Thus, $\dot{R} = R_0\dot{x}$ and $R^{-n} = R_0\ (1 - nx)$ (higher order small terms are neglected in the Taylor series expansion of R^{-n}). A function $g(t) = e^{i\omega t}$ is also defined (Commander & Prosperetti, 1989; Dogan et al., 2017; Hoff et al., 2000). The incident pressure can be linearized as (Dogan et al., 2017; Mantouka et al., 2016):

$$P_A g(t) = \frac{\rho \ddot{R} R_0}{\left(1 - \frac{i\omega R_0}{C_l}\right)} \tag{7.10}$$

Using these linear approximations, a linear analytical solution to Eqs. (7.1) can be provided. The linear solution can be written in the following general form of forced damped oscillations:

$$\alpha\ddot{x} + 2\beta\dot{x} + \gamma x = -P_A e^{i\omega t} \tag{7.11}$$

where constants α, β and γ can be defined by solving the appropriate equations. We can transfer Eq. (7.11) to the frequency domain by setting $x(t) = x(\omega)\ e^{i\omega t}$:

$$-\alpha\omega^2 x(\omega)e^{i\omega t} + 2i\beta\omega x(\omega)e^{i\omega t} + \gamma x(\omega)e^{i\omega t} = -P_A e^{i\omega t} \tag{7.12}$$

Eq. (7.12) can be simplified by dividing both sides by $\alpha\ e^{i\omega t}$ and inputting $\omega_0 = \frac{\gamma}{\alpha}$ (ω_0 is angular resonance frequency). Thus:

$$x(\omega)\left[\omega_0^2 - \omega^2 + \frac{2i\beta}{\alpha}\omega\right] = -\frac{P_A}{\alpha} \tag{7.13}$$

The constants α, β and γ of Eq. (7.12) can be derived using an approach similar to (Dogan et al., 2017; Mantouka et al., 2016):

$$\begin{cases} \alpha = \rho R_0^2 + \dfrac{4\mu R_0}{C_l} \\ \beta = 2\mu_{th} - \dfrac{\sigma}{C_l} + 2\mu + \dfrac{\left(\dfrac{\omega R_0}{C_l}\right)}{1+\left(\dfrac{\omega R_0}{C_l}\right)^2}\dfrac{\omega}{2}\left(\rho R_0^2\right) \\ \gamma = P_{g_0} R(\phi) - \dfrac{2\sigma}{R_0} + \dfrac{\omega^2 \rho R_0^2}{1+\left(\dfrac{\omega R_0}{C_l}\right)^2} \end{cases} \tag{7.14}$$

and the angular resonance frequency $\omega_0 = 2\pi f_r$ (f_r is the linear resonance frequency) is given by:

$$\omega_0 = \sqrt{\frac{P_{g_0}\Re(\phi) - \frac{2\sigma}{R_0} + \frac{\omega^2 \rho R_0^2}{1+\left(\frac{\omega R_0}{C_l}\right)^2}}{\rho R_0^2 + \frac{4\mu R_0}{C_l}}} \tag{7.15}$$

The constant δ_{total} is the total damping and is defined as $\delta_{\text{total}} = \delta_{\text{L}} + \delta_{\text{R}} + \delta_{\text{T}} = \frac{\beta}{\alpha}$ (in the last term in the left hand side of Eq. (7.13)). Thus:

$$\delta_{\text{total}} = \frac{\beta}{\alpha} = \frac{2\mu_{th} - \frac{\sigma}{C_l} + 2\mu + \frac{\left(\frac{\omega R_0}{C_l}\right)}{1+\left(\frac{\omega R_0}{C_l}\right)^2}\frac{\omega}{2}\left(\rho R_0^2\right)}{\rho R_0^2 + \frac{4\mu R_0}{C_l}} \tag{7.16}$$

and

$$\begin{cases} \delta_L = \dfrac{2\mu}{\rho R_0^2 + \dfrac{4\mu R_0}{C_l}} \\ \delta_T = \dfrac{2\mu_{th}}{\rho R_0^2 + \dfrac{4\mu R_0}{C_l}} \\ \delta_R = \dfrac{\dfrac{\left(\frac{\omega R_0}{C_l}\right)}{1+\left(\frac{\omega R_0}{C_l}\right)^2}\dfrac{\omega}{2}\left(\rho R_0^2\right)}{\rho R_0^2 + \dfrac{4\mu R_0}{C_l}} \\ \delta_{int} = \dfrac{-\sigma}{\rho C_l R_0^2 + 4\mu R_0} \end{cases} \tag{7.17}$$

where δ_L, δ_T, δ_R, and δ_{int} are damping constants due to liquid viscosity, thermal loss, reradiation and interfacial effects.

The linear damping constants are limited to very low excitation amplitudes (e.g., $P_A = 1$ kPa) and very small bubble expansion radii (e.g., $< 2\%$ expansion ratio in Fig. 7.1A). Fig. 7.4A shows the linear resonance curve of an air bubble with $R_0 = 8\mu$m at $P_A = 1$ kPa displayed as the maximum of the steady state radial oscillations plotted at each driving frequency. The corresponding damping constants in Eq. (7.17) are plotted in Fig. 7.4B. The bubble's resonance frequency f_r is at 385.6 kHz when P_A is 1 kPa. For frequencies $\approx < 2f_r$ thermal damping is the dominant damping mechanism while radiation damping is the weakest. δ_R increases with increasing frequency while δ_T decreases with frequency increase. Above $f = 1.4$ f_r, δ_R becomes stronger than δ_L and above $f = 3f_r$ becomes the dominant damping mechanism.

The linear damping constants depend on the bubble size and the gas content of the bubble (Leighton, 2012; A. Prosperetti, 1984; A.J. Sojahrood et al., 2020; A.J. Sojahrood et al., 2020; Zhang et al., 2018). At resonance δ_L and δ_R increase with decreasing R_0 while δ_T decreases. Gas types like C3F8 that are used in ultrasound contrast agents typically have much lower δ_T compared to gases like Air or Argon and even for big C3F8 bubbles ($R_0 = 10$ μm) δ_T at resonance can be smaller than δ_L and δ_R (A.J. Sojahrood et al., 2020). Throughout this book chapter, however, we only consider the case of an Air bubble with $R_0 = 8\mu$m for simplicity. For more information on the relative magnitude of the damping constants one can refer to (Leighton, 2012; Prosperetti, 1984; Sojahrood et al., 2021d; A.J. Sojahrood et al., 2020; Zhang et al., 2018).

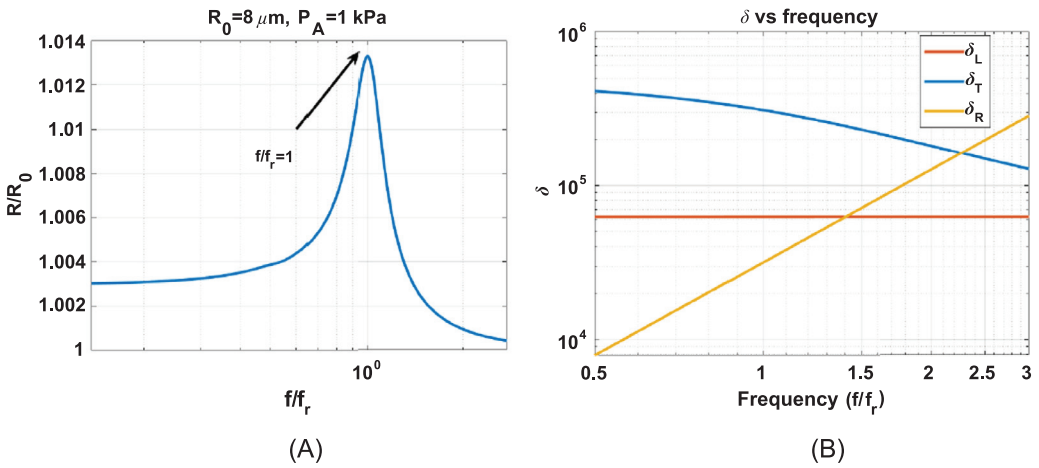

FIGURE 7.4 (A) Linear resonance curve of an air bubble with $R_0 = 8\ \mu$m in the form of R_{max}/R_0 as a function of normalized frequency where $f_r = 385.6$ kHz is the linear resonance frequency ($f_r = \omega_0/2\pi$). (B) The corresponding damping constants as a function of normalized frequency.

7.6 Nonlinear resonances of the bubble oscillator

As the pressure increases, however, the linear approximations are no longer valid. Radial oscillation amplitude increases and the bubble does not anymore exhibit only one resonance. Depending on the pressure amplitude, the bubble resonance curve may exhibit multiple harmonics and SH resonance peaks (Werner Lauterborn, 1976; Werner Lauterborn & Kurz, 2010; A.J. Sojahrood, Haghi, Li, et al., 2020). In this section different resonance frequencies of a bubble oscillator is studied.

Fig. 7.5A shows the resonance curve of an air bubble with $R_0 = 8\mu$m. Compared to Fig. 7.4A, the maximum radial amplitude at $f \approx f_r$ is higher by about 10%. At $f = 0.5f_r$ there is a new peak that is generated. This is called the 2nd harmonic resonance and the oscillation properties at this exposure parameter are similar to the second row of Fig. 7.1.

Increasing the pressure amplitude to 40 kPa results in further increase in the maximum bubble radius; however, the frequency at which maximum bubble radius occurs shifts to $0.87f_r$. This called the pressure dependent resonance frequency (PDf_r) and is studied in detail in (Werner Lauterborn, 1976; MacDonald et al., 2004; A.J. Sojahrood et al., 2015; A.J. Sojahrood, et al., 2020). (A.J. Sojahrood et al., 2015) showed that the maximum nondestructive P_{sc} [when $R_{max}/R_0 \leq 2$ (Flynn & Church, 1988)] can increase up to 9 folds when the bubble is sonicated with its PDf_r. The radial oscillations at 2nd harmonic resonance grow and 3rd harmonic resonance (3rd SuH) occurs at $f \approx 0.33f_r$. Oscillation properties at $f \approx 0.33\, f_r$ are similar to the ones shown in the third row of Fig. 7.1.

Further pressure amplitude increase to 80kPa (Fig. 7.5C) results in further shift of the fundamental resonance from f_r to $0.74\, f_r$; however, since the oscillation amplitude is higher than the threshold of $R_{max}/R_0 \leq 2$, the bubble may no longer be stable (Flynn & Church, 1988). The 2nd and 3rd SuH shift to $0.42f_r$ and $0.3\, f_r$ with possible bubble destruction at 2nd SuH. Two new resonance peaks occur at $f_r/4$ and $f_r/5$ corresponding to 4th and 5th SuH resonance. In these regimes the 4th and 5th harmonic component of the frequency spectrum are stronger than the rest of the components respectively. Sonication of bubbles with their 3rd–5th SuH resonance frequencies have particular advantage in increasing the contrast in super harmonic imaging applications (Cherin et al., 2019) in diagnostic ultrasound.

At $P_A = 90$ kPa new harmonic resonances occur and the fundamental resonance frequency, and harmonic resonances in Fig. 7.5D decrease further. At $f \approx 0.6f_r$, 3/2 UH resonance appears. The oscillation properties are similar to the first row of Fig. 7.2 where the 3/2 UH frequency component of the P_{sc} is higher in amplitude compared to other SH and UH components. SH and UH components of the P_{sc} have particular applications in monitoring and controlling the cavitation in therapeutic ultrasound applications (Haworth et al., 2017; O'Reilly & Hynynen, 2012).

At $P_A = 100$ kPa (Fig. 7.5E) a new peak appears at $f = 2f_r$. This frequency is called the 1/2 order SH resonance frequency (f_{sh}). It was long believed that when the bubble is sonicated with $f = 2f_r$ the 1/2 order SHs occur at the lowest possible pressure amplitude (Eller & Flynn, 1969; Andrea Prosperetti, 1974, 1977, 2013). However, these conclusions were based on linear approximations. Using extensive numerical simulations (Katiyar & Sarkar, 2011, 2012) showed that increased viscous damping shifts the f_{sh} to near f_r. However, their model did not incorporate the thermal effects. Recently (Sojahrood et al., 2021) incorporated a more accurate model of thermal dissipation [Eqs. (7.3) and (7.4)] and showed that depending on the gas, the pressure threshold for 1/2 order SHs can be minimum at a frequency between $0.5f_r \leq f \leq 0.6f_r$ due to the occurrence of 3/2 or 5/2 UH resonance. Sonication with f_{sh} however leads to the generation of more stable 1/2 SHs over

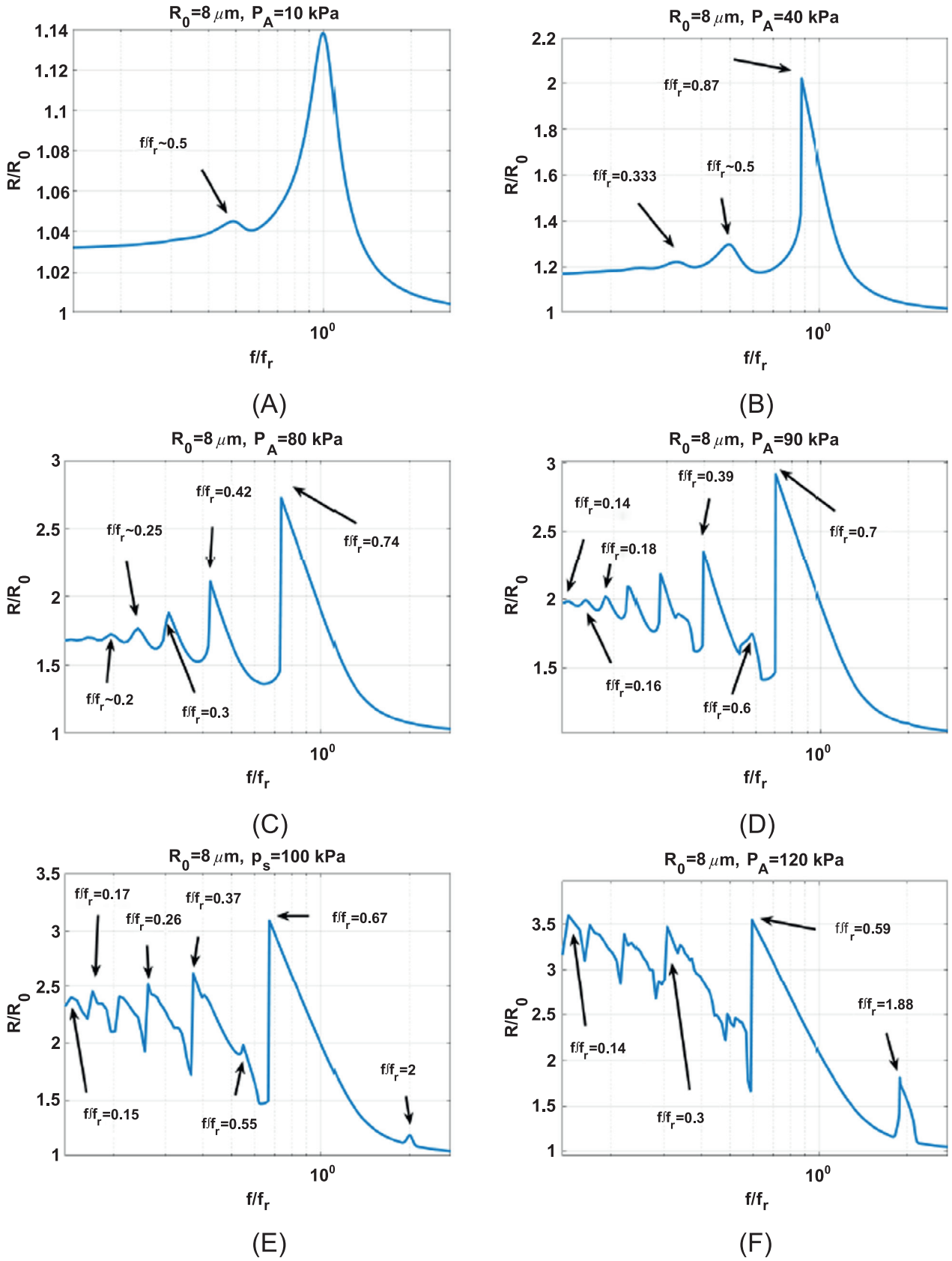

FIGURE 7.5 Resonance curves of an air bubble with $R_0 = 8\ \mu$m at various pressure amplitudes when: (A) $P_A = 10$ kPa, (B) $P_A = 40$ kPa, (C) $P_A = 80$ kPa, (D) $P_A = 90$ kPa, (E) $P_A = 100$ kPa and (F) $P_A = 120$ kPa.

a wider pressure region (A.J. Sojahrood et al., 2020). Thus, f_{sh} found particular interest in contrast enhanced applications of ultrasound (Forsberg et al., 2000; Goertz et al., 2005) where non-destructive bubble oscillations with strong 1/2 SH component are desired. In this regime oscillation properties are similar to the case shown in the second row of Fig. 7.2.

Further pressure increases to $P_A = 120$kPa (Fig. 7.5F) shifts the f_{sh} from $2f_r$ to $1.88f_r$. This frequency is called pressure dependent SH resonance (PDf_{sh}) (A.J. Sojahrood et al., 2021a). Sonication with PDf_{sh} can result in the enhancement of the stable upper limit of the 1/2 SH power in the scattered pressure with applications in increasing the signal to noise ratio in SH imaging (Sojahrood et al., 2021a, 2021c). At this pressure, the rest of the resonance frequencies exceed the threshold of $R_{max}/R_0 = 2$ in amplitude, thus, this bubble may no longer sustain stable oscillations.

7.7 Nonlinear bubble behavior analysis

In the previous section, it was shown that the bubble oscillator exhibits many resonances at different frequencies. However, the resonance graphs only provide information regarding the frequencies where the oscillation peaks occur. We need more accurate methods to analyze the bubble behavior capable of simultaneously revealing the nature and amplitude of the nonlinear oscillations. In this chapter, bifurcation diagrams are used to investigate the nonlinear bubble behavior over a wide range of acoustic exposure parameters (frequency and pressure) where the qualitative and quantitative changes of the bubble behavior can be investigated efficiently. We employ a comprehensive method of bifurcation analysis introduced by Sojahrood et al. in (A.J. Sojahrood et al., 2019) to investigate the nonlinear dynamics of the bubble. This method employs the Poincaré section analysis and the maxima of the bubble radial oscillations in tandem.

7.7.1 Poincaré section

Poincaré section method samples the *R(t)* curves using a specific time point for each driving period. This approach can be summarized as:

$$P \equiv (R(\Theta))\left\{\left(R(t), \dot{R}(t)\right) : \Theta = \frac{n}{f}\right\} \tag{7.18}$$

where P denotes the points in the bifurcation diagram, R and $\dot{R}$ are the time dependent radius and wall velocity of the bubble at a given set of control parameters of (R_0, P_A and f), Θ is given by n/f and n = 1, 2, ….440. Points on the bifurcation diagram are constructed by plotting the solution of $R(t)$ at time points that are multiples of the driving acoustic period. These points are highlighted with yellow points in Fig. 7.1 and 7.2. The results are plotted for $n = 400 - 440$ to ensure the initial transient regime of oscillations passed. This method has been used to investigate the bubble dynamics in the pioneering work of Parlitz et al. (Parlitz et al., 1990).

7.7.2 Method of maxima

A less common way for constructing bifurcation diagrams is by setting one of the phase space coordinates to zero:

$$Q \equiv m(R)\left\{\left(R, \dot{R}\right) : \dot{R} = 0\right\} \tag{7.19}$$

The maxima of the radial peaks (determined within $400 - 440$ cycles of the stable oscillations) ($\dot{R} = 0$ and $\ddot{R} > 0$) are identified and are plotted versus the given control parameter in the bifurcation diagrams. These points are denoted by red circles in Figs. 7.1 and 7.2.

7.7.3 Final construction

The bifurcation diagrams of the normalized bubble oscillations (R/R_0) are calculated using both methods (a) and (b). At each control parameter (here pressure amplitude) these points are plotted on the bifurcation diagram. Pressure amplitude is increased and the same procedure is repeated until the whole desired parameter region is covered. When the two results are plotted alongside each other, it is possible to reveal more important details about the super-harmonic (SuH) and UH oscillations, as well as the SH and chaotic oscillations (A.J. Sojahrood et al., 2019).

7.8 Nonlinear dissipation terms

The damping constants in Eq. (7.17) do not depend on pressure. Linear approximations are not valid at large bubble oscillation amplitudes due to the pressure dependent nonlinear bubble oscillations. In the majority of applications bubbles are not in the linear regimes, thus, for accurate modeling and understanding of the bubble behavior we need to develop an understanding of the pressure dependent dissipation mechanisms of the bubble oscillator. Louisnard (Louisnard, 2012)

derived the pressure dependent dissipation terms of Eq. (7.1) in the absence of impressibility effects. The Louisnard model was modified by Jamshidi & Brenner (Jamshidi & Brenner, 2013) to include the compressibility effects to the first order of Mach number. Using this approach, the nonlinear terms that describe the power loss due to radiation, thermal and viscous effects were presented. In (A.J. Sojahrood et al., 2020), critical corrections to the derived terms in (Jamshidi & Brenner, 2013) were provided. In Louisnard's approach, the terms for the nonlinear power dissipation are derived accounting for large bubble oscillation amplitude. One starts with the mass and momentum conservation equations in a bubbly media (Caflisch et al., 1985):

$$\begin{cases} \dfrac{1}{\rho C_l^2}\dfrac{\partial P}{\partial t} + \nabla \cdot v = \dfrac{\partial \beta}{\partial t} \\ \rho \dfrac{\partial v}{\partial t} = -\nabla P \end{cases} \tag{7.20}$$

here $P(r, t)$ *and* $v(r, t)$ are the pressure and velocity field. The above equation can be written as:

$$\frac{\partial}{\partial t}\left(\frac{1}{2}\frac{P^2}{\rho C_l^2} + \frac{1}{2}\rho v^2\right) + \nabla \cdot (P_v) = NP\frac{\partial V}{\partial t} \tag{7.21}$$

Where $V(r, t)$ is the instantaneous volume of the bubbles at time t and N is the number of bubbles per unit volume. V can be calculated by solving the bubble model Eq. (7.1) at any given pressure. In order to get an energetic interpretation of the bubble radial motion, both sides of the bubble model Eq. (7.1) can be multiplied by the time derivative of the bubble volume $\partial V/\partial t$. Afterwards, using the equation of the kinetic energy of the liquid (Louisnard, 2012) $K_l = 2\pi\rho R^3\dot{R}^2$ and Eq. (7.21) one can arrive at:

$$\tfrac{\partial}{\partial t}\left(\tfrac{1}{2}\tfrac{P^2}{\rho C_l^2} + \tfrac{1}{2}\rho v^2 + NK_l + 4N\pi R^2\sigma\right) + \nabla \cdot (Pv) = -N(\pi_{\text{total}}) \tag{7.22}$$

where π_{total} is the total dissipated energy term. By taking a time average of both sides of Eq. (7.22) and eliminating terms that are zero one arrives at:

$$\nabla \cdot \langle Pv \rangle = -N(\Pi_{\text{Total}}) \tag{7.23}$$

Where Π_{Total} is the total dissipated power. Eq. (7.22) expresses the conservation of mechanical energy averaged over one or many periods of oscillations. The physical interpretation of this equation is that the acoustic energy leaving a volume of bubbly liquid is always smaller than the one incident on it (Louisnard, 2012). This is due to the losses during the bubble oscillations. The detailed derivation of the nonlinear dissipation terms of the Keller-Miksis equation [Eq. (7.1)] can be found in (A.J. Sojahrood et al., 2020).

7.8.1 Nonlinear dissipation terms of the uncoated free bubble

Π_{Total} is the sum of the following dissipated powers (A.J. Sojahrood et al., 2020):

$$\begin{cases} T_d = \dfrac{-4\pi}{T}\displaystyle\int_0^T R^2\dot{R}P_g dt \\ L_d = \dfrac{16\pi\mu_L}{T}\displaystyle\int_0^T R\dot{R}^2 dt \\ R_d = \dfrac{1}{T}\displaystyle\int_0^T \left[\frac{4\pi}{C_l}\left(R^2\dot{R}\left(\dot{R}P + R\dot{P} - \frac{1}{2}\rho\dot{R}^3 - \rho R\dot{R}\ddot{R}\right)\right) - \left(\frac{\dot{R}}{C_l}P_g + \frac{R}{C_l}\dot{P}_g\right)\frac{\partial V}{\partial t} + \frac{16\pi\mu_L R^2\dot{R}\ddot{R}}{C_l}\right]dt \end{cases} \tag{7.24}$$

where T_d, L_d and R_d are the corresponding power dissipation due to thermal loss, liquid viscosity and radiation and T is the integration time interval.

7.9 Bifurcation structure and the nonlinear dissipations of the bubble

In this section we introduce various pressure dependent nonlinear regimes of the bubble oscillator and build a link with their corresponding power dissipation. This is done by analyzing the bifurcation structure of the R/R_0 of an air bubble

with $R_0 = 8\mu$m as a function of acoustic pressure amplitude for $0.25f_r \leq f \leq 3f_r$. Dissipated powers are calculated using Eq. (7.24) for the last 40 cycles of a 440 cycles driving acoustic force. Throughout this chapter, the blue diagram is constructed using the method of maxima (7.2) and the red diagram is constructed through Poincaré analysis (7.1).

When $f = 0.25\, f_r$, Fig. 7.6A, an increase in pressure results in the generation of third order SuH oscillations at $P_A \approx 40$ kPa [the blue curve shows three maxima for a period 1 oscillation (1 solution in the red graph)]. The red curve undergoes a period doubling (PD) bifurcation concomitant with a PD in the blue graph at $P_A \approx 80$ kPa. This results in 7/2 UH oscillations (P2 with six maxima). The period 2 (P2) oscillations undergo reverse PD to period 1(P1) oscillations with three maxima at $P_A \approx 100$ kPa. With a slight pressure increase, a saddle node (SN) bifurcation takes place to P1 oscillations with three maxima of higher amplitude. At this point, the bubble may not sustain stable oscillations as $R/R_0 > 2$ (for further discussion on the minimum threshold for bubble destruction, refer to (A.J. Sojahrood et al., 2020; A.J. Sojahrood et al., 2015). A further pressure increase results in period doubling cascades to chaos. Above 160 kPa, a P1 giant 2nd SuH resonance emerges out of the chaotic oscillations and undergoes PD cascades to chaos. At $P_A \approx 280$ kPa another P1 giant resonance emerges out of the chaotic window. The corresponding power losses are presented in Fig. 7.6B. For $P_A \approx \leq 40$ kPa, Rd is the weakest damping mechanism with Td being the strongest mechanism (≈2 orders of magnitude larger). Rd grows faster than other damping mechanisms with increasing pressure, and at $P_A \approx 80$ kPa, concomitant with the appearance of 7/2 UH oscillations, Rd becomes equal to Ld. Rd becomes stronger than Ld when UH oscillations occur; later, simultaneous with the saddle node bifurcation, Rd undergoes a large increase and becomes the strongest damping mechanism. Td is the dominant mechanism for pressures below 100 kPa (the saddle node bifurcation), and at ≈ 110 kPa, Rd > Td > Ld.

When $f = 0.5\, f_r$ (Fig. 7.6C), second order SuH oscillations are generated at $P_A \approx 20$ kPa; this manifests itself as a P1 oscillation (one red line) with two maxima (two maxima for the blue curve). Radial oscillations grow with increasing pressure, and at $P_A \approx 95$ kPa, the red curve undergoes a PD, which is coincident with a PD for the blue curve; this results in 5/2 order UH oscillations (P2 with four maxima). Oscillations become chaotic (through a cascade of PDs at $P_A \approx 115$ kPa; further at $P_A \approx 130$ kPa, a giant P1 resonance emerges out of chaos. Possible bubble destruction occurs at $P_A \approx 110$ kPa ($R/R_0 > 2$). For pressures below 60 kPa, Td > Ld > Rd. Later, concomitant with the saturation of second order SuH oscillations at ≈ 70 kPa (red line becomes equal to one of the maxima, indicating that the wall velocity becomes in phase with the driving acoustic pressure), Rd becomes equal to Ld and gets stronger than Ld during UH oscillations. Td is the dominant mechanism at $P_A < 100$ kPa; however, when UH oscillations are saturated, Rd supersedes Td and stays higher during the chaotic oscillation regime. The occurrence of the giant resonance is concomitant with a large increase in Rd as it becomes approximately two orders of magnitude stronger above the SN.

When $f = 0.9f_r$ (Fig. 7.6E), P1 oscillations (with one maximum) undergo a SN at 185 kPa; P2 oscillations undergo a cascade of PDs to chaos at 215 kPa. Chaotic oscillations region stretches to 400 kPa with a small window of P3 oscillations with 3 maxima. At $P_A \approx 400$ kPa a P2 giant f_r emerges out of the chaotic window. The corresponding dissipated power is presented in Fig. 7.6F. For pressure amplitudes below the saddle node (SN) bifurcation, Td is the strongest damping mechanism (an order of magnitude larger) with Rd the weakest damping mechanism. Concomitant with the SN (note that at this pressure, the wall velocity becomes in phase with the driving pressure), Rd becomes stronger than Ld and, at 95 kPa, surpasses the initially larger Td. A further increase in the pressure amplitude results in the fastest growth rate in Rd and the slow oscillation regime, Rd, Ld, and Td stay approximately constant (this can be due to the decrease in wall velocity concomitant with PD when the bubble is sonicated with a frequency near its resonance frequency (A.J. Sojahrood et al., 2015)). For the chaotic regime, Rd>Td>Ld. For the small P3 oscillation window, Rd undergoes a slight increase while Td experiences a slight decrease. Occurrence of the giant resonance at ≈400kPa is concomitant with an increase in Td and Ld and decrease in Td. This is due to the increase in the wall velocity which increases the radiation and viscous damping; at the same time due to the faster collapse and rebound, there is decreased time for the conduction of temperature at the collapse point which reduces the Td.

For $f = f_r$ *(Fig. 7.6G),* at lower pressures <25kPa (see the figure subset for better visualization), oscillations are P1 and the wall velocity is in phase with the driving acoustic force (blue and red curves are on top of each other). Further pressure increase results in possible bubble destruction at 105kPa (R/R_0 >2). At ≈180kPa, PD occurs. P2 oscillations become chaotic for 205kPa < P_A <305kPa followed by the emergence of a giant P2 resonance which later undergoes PD at ≈460kPa. The corresponding dissipation graph is presented in Fig. 7.6H. For P_A <25kPa where wall velocity is in phase with the driving pressure, Td >Rd≥Ld and there is a very sharp growth for all the damping factors (possibly due to the resonant nature of oscillations). Rd becomes bigger than Ld above 25kPa and grows faster than both Ld and Td until it becomes equal to Td at ≈165kPa. Rd becomes slightly higher than Td when PD occurs; however, the occurrence of PD decreases the rate of the growth of Rd and leads to a slight decline in Ld during P2 oscillations (due to possibly the decrease in the wall velocity during P2 oscillations when $f = f_r$ (A.J. Sojahrood et al., 2020; A.J. Sojahrood et al., 2015). Chaotic oscillations result in a slight decrease in Td, but Rd keeps growing, and at the giant resonance, Rd undergoes a large increase and becomes

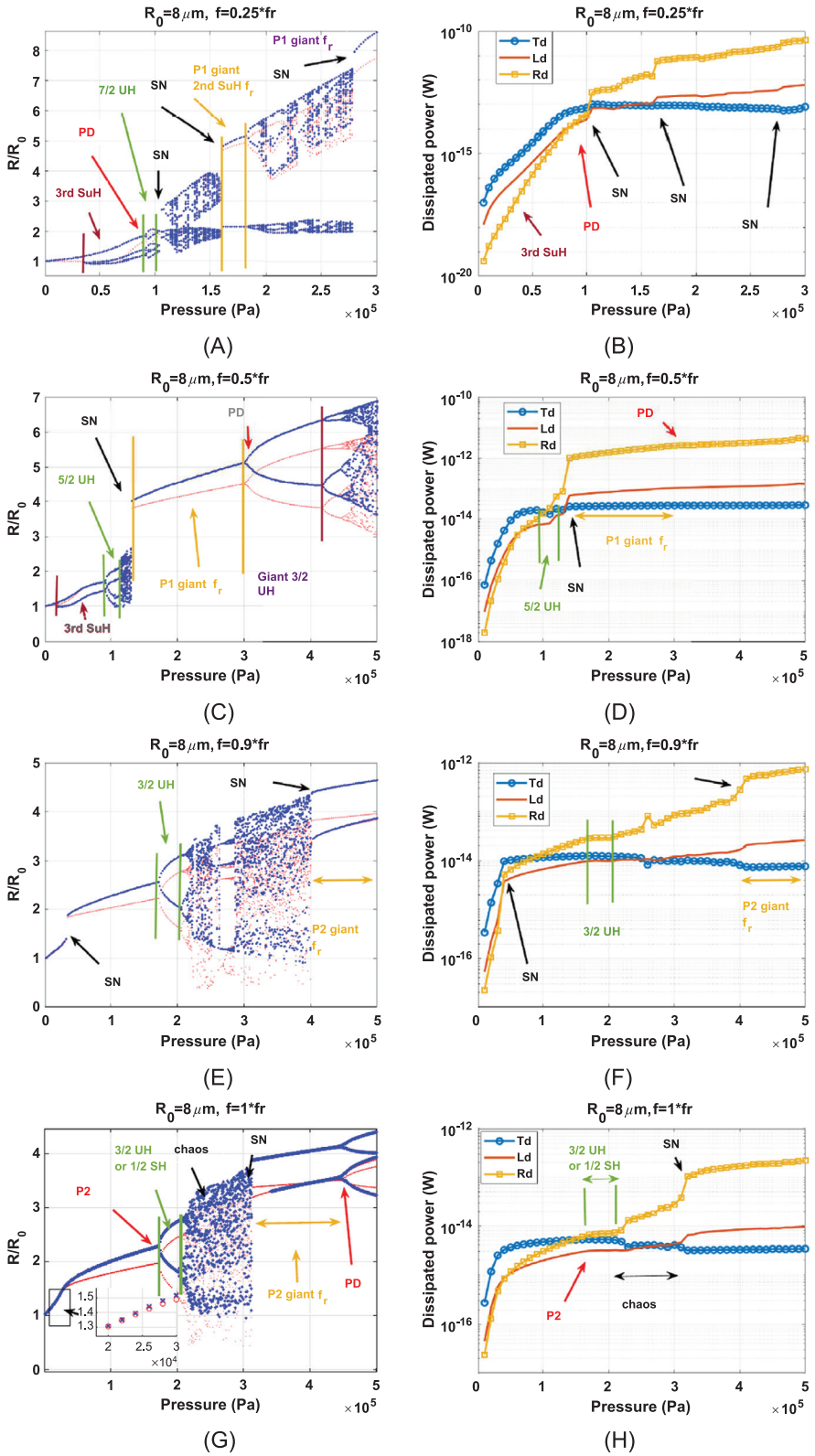

FIGURE 7.6 Bifurcation structure (left column) and the dissipated powers (right column) of the R/R_0 of an air bubble with $R_0 = 8$ μm as a function of pressure (The red curves are generated through the Poincaré method and the blue curves are generated via the method of maxima). (A–B) $f = 0.25f_r$, (C–D) $f = 0.5f_r$, (E–F) $f = 0.9f_r$ and G–H) $f = f_r$.

approximately two orders of magnitude larger than the other damping factors. The occurrence of the P2 giant resonance is concomitant with a decrease in Td. The reduction in Td may lead to better sonochemical efficacy as higher temperatures are created, while at the same time, thermal conduction becomes more limited.

Fig. 7.7A shows the case of sonication with $f = 1.2\, f_r$. The bubble is able to undergo nondestructive PD ($R/R_0 < 2$) at this frequency. It is previously shown (Sojahrood et al., 2020, 2021) that for uncoated bubbles, sonication with $f = f_r$ most likely results in bubble destruction before the development of any P2 oscillations. This was also seen in Fig. 7.6G where $f = f_r$. Fig. 7.7A shows that when $f = 1.2fr$, radial oscillations are initially of P1 and monotonically increase in amplitude as excitation pressure increases. At $\approx$ 190 kPa, PD takes place; with increasing pressure amplitude, oscillations become P3 (properties of this P3 oscillation have been studied in (A.J. Sojahrood et al., 2020), which can be concomitant with the bubble destruction as $R/R_0 > 2$. The bubble oscillations return to P2 after a very small window of chaos. Another chaotic window appears through a successive PD. A giant P2 resonance emerges out of the chaotic window when $P_A > 240$ kPa, which later undergoes successive PDs to chaos. The dissipated powers are shown in Fig. 7.7B. Td is the strongest damping factor for pressures below 190 kPa. For P_A <80 kPa, $Td \rangle Rd \geq Ld$. Rd becomes stronger than Ld with increasing pressure above 80 kPa. At $P_A = 195$ kPa, Rd becomes stronger than Td simultaneous with the occurrence of P3 oscillations; however, as soon as P3 converts to P2, Td becomes larger than Rd. The emergence of the P2 giant resonance is simultaneous with a large increase in Rd and Ld and a subsequent decrease in Td. This can be due to the faster bubble collapse with higher wall velocity and acceleration, resulting in an increase in Rd and Ld; however, due to the fast collapse, there is very little time for temperature conduction; thus, Td decreases. In this region, Rd is an order of magnitude larger than Ld and Td, and it is the only region in this pressure range where Ld is stronger than Td.

Fig. 7.7C displays the case of sonication with $f = 1.75\, f_r$, which is the pressure dependent SH resonance frequency of the bubble (PDf_{sh}) (A.J. Sojahrood et al., 2021a). This frequency is chosen as the SN bifurcation leads to non-destructive oscillations. Oscillations are of P1 initially; the pressure increase results in PD at $\approx$ 115 kPa. P2 oscillations (with two maxima) undergo a SN bifurcation to P2 oscillations (with one maximum) of higher amplitude at $\approx$ 140 kPa. At 195 kPa, the second maximum re-emerges with the same amplitude of the smaller solution in the red curve (indicating that wall velocity is in phase with the excitation pressure once every two acoustic cycles). At $\approx$ 220 kPa, $R/R_0 = 2$; beyond this pressure, the bubble may not sustain nondestructive oscillations. P2 oscillations undergo PDs to a P4 solution, which later undergoes successive PDs to chaos at $P_A = 300$kPa. A giant P3 (with two maxima) resonance emerges out of the chaotic window at 395 kPa. After a small sudden chaotic window in between, giant P3 *oscillations* undergoe cascades of PDs to chaos. Fig. 7.7D shows that for $P_A \langle 140$ kPa, Td > Rd > Ld. The occurrence of the SN bifurcation (over-saturation of the 1/2 order SH component of the scattered (Sojahrood et al., 2021a, 2021c)) results in a fast increase in Rd and enhancement in the scattering to dissipation ratio (STDR). Rd grows with the increase in pressure during the P2 oscillations; however, Td and Ld undergo small changes. The emergence of the giant resonance results in a sharp increase in Rd and Ld and a small decrease in Td. Rd > Ld > Td for the P3 giant resonance oscillation regime. The decrease in Td and the faster and larger radial collapses indicate that higher temperatures are generated, while the heat conduction becomes limited. The higher temperatures and lower thermal dissipation may have consequences in enhancing chemical reactions within the bubble. When sonicated with $f = 2fr$ (f_{sh} (A.J. Sojahrood et al., 2020), oscillations undergo a PD at $\approx$ 95 kPa; P2 oscillations increase in amplitude and evolve in a shape of a bow-tie (A.J. Sojahrood et al., 2020). Consistent with previous observations (A.J. Sojahrood et al., 2020), sonication with f_{sh} results in the largest pressure range with stable ($R/R_0 < 2$) P2 oscillations. At $P_A \approx 280$ kPa, a small window of P6 oscillations appear through a SN bifurcation with each solution undergoing PDs to P12 (the properties of this oscillation regime are investigated in detail in (A.J. Sojahrood et al., 2020). Oscillations return to P2, which then undergoe multiple PDs,where at $\approx$ 315 kPa, chaos appears. For $P_A < 210$ kPa, Td > Rd > Ld. After the occurrence of PD, Td remains relatively constant with increasing pressure, while Rd grows faster than Ld as pressure increases. Eventually, at $P_A = 220$ kPa, Rd becomes equal to Td. The occurrence of giant resonance results in a sharp increase in Rd and Ld, and Rd becomes the strongest damping factor with Rd > Ld > Td. Regeneration of chaos results in a decrease in Rd and Ld with Rd $\approx$ Td > Ld.

When $f = 3f_r$ (Fig. 7.7G), radial oscillations grow very slowly and monotonically with pressure; at $P_A = 300$ kPa, a SN bifurcation occurs and oscillations become P3 (three solutions for the red curve with two maxima). Properties of these oscillations have been investigated in (Hegedus et al., 2013; Hegedűs, 2016; Parlitz et al., 1990; Sojahrood et al., 2021a, 2021b, 2021e; Amin Jafari Sojahrood & Kolios, 2012; Varga et al., 2020). At 420 kPa, oscillations undergo a SN bifurcation to P6 oscillations for a small excitation pressure window, which then transition to P12 and then back to P3 oscillations. P12 oscillations then switch to P1 oscillations with increasing pressure. Power dissipation curves are shown in Fig. 7.7H. Here, Rd is the strongest damping mechanism for all the studied pressure amplitudes with Rd > Td > Ld. The SN bifurcation results in a sharp increase in the dissipated powers at 300 kPa with Td exhibiting the largest increase. Interestingly, Td

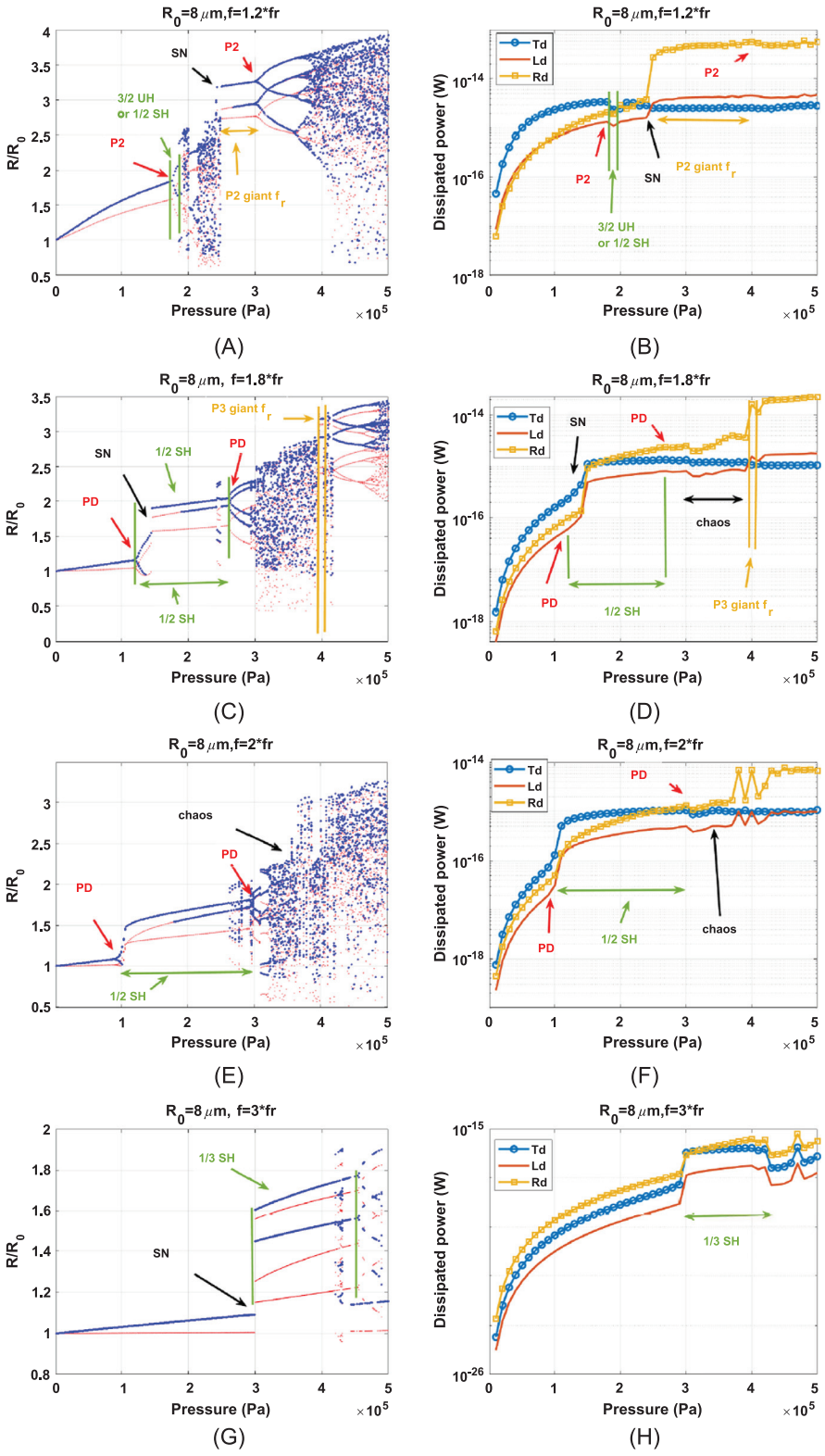

FIGURE 7.7 Bifurcation structure (left column) and the dissipated powers (right column) of the R/R_0 of an air bubble with $R_0 = 8$ μm as a function of pressure (The red curves are generated through the Poincaré method and the blue curves are generated via the method of maxima). (A–B) $f = 1.2f_r$, (C–D) $f = 1.8f_r$, (E–F) $f = 2f_r$, and (G–H) $f = 3f_r$.

becomes stronger than Rd for a short pressure range around 300 kPa, but soon Rd exceeds Td and stays the strongest damping mechanism with Rd > Td > Ld.

7.10 Summarizing points and discussion

Despite the complex bubble behavior and nonlinear characteristics of the dissipation mechanisms in the oscillations of acoustic bubbles, until recently majority of the studies were limited by linear approximations (Commander & Prosperetti, 1989; A. Prosperetti, 1984). As it was shown in Section 7.5, linear approximations are only valid for very small amplitude ($R_{max}/R_0 \approx 1.02$) regimes of oscillations. This leads to inaccurate calculation of the dissipation phenomenon in the majority of applications as bubble oscillations are above linear approximations. Moreover, it was shown in Section 7.6 that as pressure increases (as small as 10 kPa) bubble oscillator exhibits resonance peaks at frequencies below and above resonance and the frequency of maximum response at each peak is pressure dependent. The nonlinear resonance of the bubble oscillator is not captured by the linear models. In order to optimize and understand the bubble related phenomena thus, we need to have detailed knowledge not only on the nonlinear bubble behavior but also on the nature of the dissipation at each nonlinear regime. In this chapter, we introduced the bubble resonances and classified the main nonlinear regimes of radial oscillations and the corresponding dissipation mechanisms. The main points can be summarized as follows:

(1) Regardless of the insonation frequency, bubble oscillations at low pressure amplitudes (e.g., $P_A = 1$ kPa) are of period 1(P1) with one maxima. The power dissipation due to thermal loss (Td), liquid viscosity dissipation (Ld) and dissipation due to the re-radiation by the bubble (Rd) are in the same order as it is predicted by the linear model. Sojahrood et al. (A.J. Sojahrood et al., 2020) calculated the ratio of the dissipation powers (e.g., Rd/Td) and showed that these ratios are equal to the ratios of the linear damping constants (e.g., δ_R/δ_T).

(2) When the bubble is sonicated with a frequency that is approximately between $f_r/4$ and $f_r/3$, above a pressure threshold, three maxima occur in the P1 oscillations (oscillations properties can be seen in Fig. 7.1G–I). In this regime, the third harmonic component of the scattered pressure (P_{sc}) is the strongest frequency component. This regime is suitable for applications such as SuH imaging (Bouakaz et al., 2002; Cherin et al., 2019). Further pressure increase above a second threshold results in a period doubling (PD) and oscillations become P2 with six maxima. In this regime, the 7/2UH component of the P_{sc} is larger than the 1/2SH and other UH components of the signal. This regime is suitable for high resolution UH imaging (Maresca et al., 2014; Shekhar et al., 2016) and passive cavitation mapping techniques (Haworth et al., 2017; O'Reilly & Hynynen, 2012). Rd which was the weakest dissipation mechanism below the threshold for PD, grows faster than Td and Ld and becomes equal to Ld. Further increase in pressure amplitude results in a saddle node (SN) bifurcation to higher amplitude 3rd harmonic oscillations with a high probability in bubble destruction as R/R_0 exceeds 2. Concomitant with SN, Rd becomes the strongest dissipation mechanism. Increasing the sonication pressure also results in the generation of chaos and periodic oscillations of higher amplitudes. At higher pressures, a giant resonance (second order SuH) emerges out of the chaotic window.

Giant resonance is simultaneous with a large increase in Rd, making Rd an order of magnitude stronger than damping mechanisms. At this point Ld exceeds Td and dissipation mechanisms exhibit an opposite trend in magnitude (Rd > Ld > Td) compared to the linear predictions ($\delta_T > \delta_L > \delta_T$).

(3) When $f \approx 0.4 f_r - 0.6 f_r$, above an acoustic pressure threshold, a second maximum appears in the P1 oscillations. This is simultaneous with a rapid increase in the second harmonic component of the P_{sc} where the second harmonic component becomes the strongest frequency component in the frequency spectrum of the scattered pressure (oscillations properties of this regime are depicted in Figs. 7.1D–F). This regime is desired for second harmonic contrast enhanced ultrasound (Bouakaz et al., 2002; Cherin et al., 2019). Above a second pressure threshold, PD occurs and oscillations become P2 with four maxima. In this regime, the 5/2UH component of the P_{sc} is the strongest component in between the 1/2 order SH and other UHs (for oscillation properties refer to Figs. 7.2A–C). During the UH regime of oscillations, Rd which was initially the weakest dissipation mechanism surpasses Ld and Td. This regime can be used to enhance signal to noise (SNR) and contrast in UH imaging applications of ultrasound and passive cavitation mapping techniques or high resolution treatment monitoring using UH emissions. Stronger Rd in this regime, results in a higher scattering to dissipation ratio (A.J. Sojahrood et al., 2020) that can lead to a higher SNR. At a higher-pressure chaos appears, while R/R_0 exceeds 2. With pressure increase a P1 giant resonance emerges out of the chaotic window. Similar to the previous case, the occurrence of the giant resonance is concomitant with a large increase in Rd. In this regime, opposite to linear predictions, Rd > Ld > Td with Rd two orders of magnitude stronger than Td.

(4) When $f = 0.7$–$0.95 f_r$ (the pressure dependent resonance frequency (PDf_r) (A.J. Sojahrood et al., 2015), above a pressure threshold, a SN bifurcation takes place and P1 oscillations undergo a large increase in amplitude to another P1 oscillation with one maximum. The occurrence of the SN has advantages in contrast enhanced imaging techniques based

on amplitude modulation (Phillips, 2001) due to the sudden change in the P_{sc} before and after the SN (A.J. Sojahrood et al., 2015). SN occurrence is concomitant with a larger increase in Rd where Rd becomes stronger than Td. Increasing the pressure amplitude above the SN, leads to a monotonic increase in oscillation amplitude, and above a second pressure threshold, PD transforms the P1 oscillations to P2 with two maxima with possible destruction as R/R_0 exceeds 2. At this point Rd is stronger than Td and Ld. In this regime 3/2 UH component of the P_{sc} is stronger than the 1/2 order SHs and other UH components. Further pressure increase leads to successive PDs to chaos. At higher pressures, a P2 giant resonance may emerge out of the chaotic window. Emergence of the giant resonance is concomitant with an increase in Rd and Ld while Td undergoes a decrease. Sonocehmical applications may take advantage of this regime due to smaller thermal loss. In this regime Rd>Ld>Td.

(5) When $f = f_r$ (linear resonance frequency of the bubbles (Fig. 7.4A), P1 oscillations increase in amplitude monotonically with pressure increase. Above a pressure threshold, bubbles undergo PD to P2 oscillations with two maxima. In case of uncoated bubbles (A.J. Sojahrood et al., 2020; A.J. Sojahrood et al., 2021a; A.J. Sojahrood, et al., 2021) the bubble may no longer sustain stable P2 oscillations ($R/R_0 > 2$) and may undergo destruction. Thus, P2 oscillations may not be possible for uncoated bubbles sonicated with $f = f_r$. P2 oscillations undergo successive PD to chaos. When PD occurs, Rd becomes stronger than Td. During chaotic oscillations Td decreases and Ld becomes approximately equal to Td. At higher pressures, a P2 (with two maxima) giant resonance may emerge out of the chaotic window. Emergence of the giant resonance results in a large increase in Rd and Ld and further decrease in Td. In this regime Rd > Ld > Td. The giant resonance oscillations undergo successive PDs to chaotic oscillations of higher amplitude.

(6) When $f = 1.2\, f_r$, increasing pressure leads to PD, and oscillations becomes P2 with two maxima. Unlike the case of $f = f_r$, P2 oscillations can be nondestructive when $f = 1.2\, f_r$ (also seen for other sizes (A.J. Sojahrood et al., 2021a; A.J. Sojahrood et al., 2021)). P2 oscillations may lead to 3/2 order UH resonant oscillations (3/2 order UH amplitude of the scattered pressure may be stronger than the 1/2 order SH). Further increase in pressure amplitude, results in successive PDs to chaos. At higher pressures, a P2 giant resonance emerges out of the chaotic window, which later undergoes successive PDs to chaotic oscillations of higher amplitude. During P2 giant resonance, Rd > Ld > Td which is opposite to the predictions of the linear models.

(7) When $f = 1.6 - 1.8 f_r$ which is the pressure dependent subharmonic (SH) resonance frequency PD f_{sh} (A.J. Sojahrood et al., 2021a), increasing the pressure leads to the generation of PD above a pressure threshold and then a SN bifurcation from P2 oscillations of lower amplitude to P2 oscillations of higher amplitude. SN bifurcation can also happen from P1 oscillations to P2 oscillations (A.J. Sojahrood et al., 2021a; Sojahrood et al., 2021c). In this regime $R_{\max}/R_0 < 2$, and therefore, the bubbles may sustain non-destructive P2 oscillations in this frequency range. The occurrence of the SN can be beneficial in amplitude modulation techniques (Phillips, 2001) at frequencies above resonance. In his frequency range, the occurrence of SN leads to oversaturation of the 1/2 SH and 3/2UH frequency content of the P_{sc} (A.J. Sojahrood et al., 2021a; Sojahrood et al., 2021c) leading to possible higher contrast to tissue and SNR in SH imaging techniques (Goertz et al., 2005). In line with the predictions of the linear model (Fig. 7.4B), at lower pressures Td > Rd > Ld. When SN occurs, Rd undergoes the largest increase and becomes the strongest dissipation mechanism with Rd > Td > Ld. With increasing pressure, oscillations undergo successive PDs to chaos. A further pressure increase may lead to the emergence of a P3 giant resonance, which will undergo successive PDs to chaotic oscillations with further pressure increase. The giant resonance is concomitant with a large increase in Rd and Ld and a decrease in Td with Rd > Ld > Td.

(8) $f = 2 f_r$ is called the linear SH resonance frequency (f_{sh}) of the bubble (A.J. Sojahrood et al., 2020) Oscillations become P2 with two maxima above a relatively small pressure threshold. As pressure increases, one of the maxima disappears with increasing pressure and the P2 oscillations may evolve in the form of a bow-tie (A.J. Sojahrood et al., 2020; A.J. Sojahrood et al., 2021a). With increasing pressure, the second maximum re-appears with an amplitude equal to the higher amplitude branch of the Poincaré section (section and yellow lines in Figs. 7.1–7.2). Later, oscillations undergo successive PDs to chaos. When $f = 2\, f_r$, P2 oscillations occur over the widest range of the acoustic pressure amplitude with $R_{\max}/R_0 < 1.5$ (A.J. Sojahrood et al., 2020); thus, bubbles have the highest probability of sustaining non-destructive P2 oscillations. In line with the predictions of the linear model (Fig. 7.4B), at lower-pressures Td > Rd > Ld. Contrary to the previous cases, when PD occurs, Td undergoes the largest increase but stays relatively the same during the P2 oscillation regime. After PD, Rd grows faster with pressure increase and becomes equal to Td. Chaotic oscillations are concomitant with a larger growth in Rd and Rd becomes the strongest dissipation mechanism. Analytical solutions (Eller & Flynn, 1969; Andrea Prosperetti, 1974, 1977, 2013) predict that P2 oscillations are generated at the lowest pressure threshold when the bubble is sonicated with $f = 2f_r$. Numerical simulations at higher pressures however (Katiyar & Sarkar, 2011, 2012), showed that in the case of smaller bubbles (e.g., $R_0 = 0.6\mu$m) the lowest pressure threshold occurs when bubble is sonicated with a frequency near f_r. Increased damping was concluded as the responsible physical reason for the shift of the lowest frequency threshold. However, none of the previous studies included both of the pressure dependent thermal and radiation damping effects.

(A.J. Sojahrood et al., 2021) included both of these effects with their full nonlinearity and observed that depending on the gas, the lowest pressure threshold of $P2$ oscillations occur at neither $f = f_r$ or $f = 2f_r$, but it occurs at frequencies below $0.7f_r$. This is also seen in Figs. 7.6A and 7.6C ($f = 0.25f_r$ and $0.5f_r$) where the pressure threshold is smaller than that of Fig. 7.7E ($f = 2f_r$). The physical reason behind this is discussed in detail in (A.J. Sojahrood et al., 2021).

(9) When $f = 3f_r$, at lower pressures, Rd > Td > Ld which is line with the predictions of the linear model in Fig. 7.4B. Oscillation amplitude grows very slowly with increasing pressure amplitude, and above a pressure threshold, a SN bifurcation occurs and oscillations undergo a large increase in amplitude and become P3. Later, P3 oscillations undergo PD to P12 followed by successive PDs to a small chaotic window before the oscillations convert to P1 with lower amplitude. When SN occurs, Td undergoes the largest increase and becomes stronger than Rd for a short pressure range. With increasing pressure, however, Rd grows faster and becomes the dominant dissipation mechanism. When P3 occurs, P_{sc} undergoes a sharp increase concomitant with the SN bifurcation. This has advantages for amplitude modulation imaging techniques (Phillips, 2001) at higher frequencies for better resolution. The pressure amplitudes for the pulses should be chosen below and above the SN pressure.

7.11 Concluding remarks

In this chapter the major nonlinear oscillations and the corresponding dissipation mechanisms of an air bubble with $R_0 = 8\mu$m were studied. The major nonlinear regimes of the oscillations and the dissipation mechanisms due to thermal loss, acoustic re-radiation and liquid viscosity at each regime were classified as a function of the bubble resonance frequency and the driving pressure amplitude. For simplicity we focused only on one size of uncoated bubbles. However, it has recently been shown (A.J. Sojahrood et al., 2021a) that when the dynamics of bubble oscillators are studied as multiples of their resonance frequency, the classification scheme that is used in this chapter is universal. The dissipation mechanisms and their strength however depend on the bubble size (e.g., for very small bubbles and frequencies below resonance thermal damping is no longer the dominant dissipation mechanism (A.J. Sojahrood et al., 2021a; A.J. Sojahrood et al., 2020; Zhang et al., 2018), however, the pressure dependent evolution of the dissipation mechanisms follows the same trend presented in this chapter. Detailed size and pressure dependent dissipation mechanisms are investigated in (A.J. Sojahrood et al., 2021a; A.J. Sojahrood et al., 2020). In this paper, effects of mass transfer due to bubble oscillations were neglected. The bubble may grow due to rectified diffusion (Holt & Gaitan, 1996; Yang et al., 2004) or it may dissolve during oscillations (Viti et al., 2012). Mass conservation that was one of the assumptions in deriving the power dissipation terms may no longer be valid, and its effect must be considered. Using linear approximations, (A. Prosperetti, 2015; Zhang et al., 2018) studied the mass transfer effects on the damping mechanisms and showed that mass transfer can significantly alter the damping mechanisms of vapor bubbles. In vapor bubbles, mass transfer may become the dominant damping phenomenon (A. Prosperetti, 2015). Several recent studies investigated the nonlinear radial oscillations of the bubble while including the mass transfer effects and chemical reactions inside bubbles (Hegedűs et al., 2020; Kalmár et al., 2020; Kerboua & Hamdaoui, 2017, 2018a, 2018b). For a more accurate representation of bubble dynamics, and especially in the case of vapor bubbles, mass transfer effects should be considered.

In this chapter the nonlinear energy dissipation effects were only investigated for low Mach numbers and using a linear model of wave propagation (Caflisch et al., 1985; Louisnard, 2012; A.J. Sojahrood, Haghi, Karshafian, et al., 2020). The influence of nonlinear wave propagation (Daeichin et al., 2015; Holt & Roy, 2005; Huang et al., 2004) on the bubble dynamics and the dissipation mechanisms were neglected. Especially at higher pressure amplitudes, the shape of the pulse changes due to the nonlinear propagation which consequently influences the radial oscillations of the bubbles. Nonlinear propagation results in the generation of the harmonics of the sonication frequency, thus the distorted wave that drives the bubbles is no longer a pure sinusoidal wave and has multifrequency components. Many recent studies showed the strong influence of the frequency components of multi frequency acoustic forces on the nonlinear behavior of the bubble. In the context of nonlinear wave propagation, the linear bubble dissipation mechanisms and influence of the drag forces have been investigated with extensive details in (Kamei et al., 2021; Kanagawa & Kamei, 2021; Kikuchi & Kanagawa, 2021; Yatabe et al., 2021). For higher pressures amplitudes and high Mach numbers, future studies should investigate the dissipation mechanisms of the nonlinear bubble oscillations accounting for nonlinear propagation of ultrasound in the medium. For simplicity, this chapter focused only on the dynamics of a single bubble. In applications, however, bubbles are in polydisprse interacting clouds and the oscillation of each bubble impacts the oscillations of the neighboring bubbles (Chong et al., 2010; Dzaharudin et al., 2013; Guédra et al., 2017; A.J. Sojahrood et al., 2021a). Kerboua and Hamdaoui (Kerboua & Hamdaoui, 2019) incorporated the bubble number density and void fraction and performed an energy analysis both at the microscopic and macroscopic scales and characterized the bubble populations inside sonochemical reactors. For more

accurate representation of the power dissipation inside sonochemical reactors, bubble-bubble interaction effects should be incorporated with their full nonlinearity.

The nonlinear bubble oscillations and the corresponding dissipation mechanisms were only considered for a case of an uncoated bubble. In many applications, however, the bubble is coated with a shell for more stability (Versluis et al., 2020). The shell influences the bubble dynamics and especially in case of the lipid coated bubbles, due to the nonlinear viscoelastic behavior of the shell, it can dramatically influence the resonance frequency (Overvelde et al., 2010), bubble oscillation shapes (e.g., compression only behavior (de Jong et al., 2007)) and enhance the generation of subharnonics at low excitation levels (Frinking et al., 2010; Sojahrood et al., 2021b, 2021e). In case of bubbles encapsulated with shells exhibiting linear viscoelastic properties, Hoff et al. (Hoff et al., 2000) derived the linear damping constants. Later Sojahrood et al. (A.J. Sojahrood et al., 2020) derived the nonlinear terms for the dissipation mechanisms. Kikuchi and Kanagawa (Kikuchi & Kanagawa, 2021) derived the linear damping constants for encapsulated bubbles accounting for the nonlinear propagation of ultrasonic waves in bubbly media. However, nonlinear dissipation mechanisms have not studied in case of the lipid coated bubbles. In summary, this book chapter provided fundamental relationships between the acoustic exposure parameters (frequency and pressure amplitude) and the nonlinear dynamics of the bubbles. This relationship seems to be universal and independent of the bubble size within the size range studied in (A.J. Sojahrood et al., 2021a). It is shown that the linear damping constants are only valid for the very small amplitude oscillations and low pressure amplitude sonications. With pressure increase, dissipation mechanisms evolve in a nonlinear but universal manner and linear approximations are no longer valid. The fundamental information provided here forms the basis for better understanding of the bubble related phenomena and optimization of bubble oscillations in related applications.

References

Arif, W.M., Elsinga, P.H., Gasca-Salas, C., Versluis, M., Martínez-Fernández, R., Dierckx, R.A.J.O., Borra, R.J.H., Luurtsema, G., 2020. Focused ultrasound for opening blood-brain barrier and drug delivery monitored with positron emission tomography. J. Controlled Release 324, 303–316. https://doi.org/10.1016/j.jconrel.2020.05.020.

Behnia, S., Sojahrood, A.J., Soltanpoor, W., Jahanbakhsh, O., 2009. Suppressing chaotic oscillations of a spherical cavitation bubble through applying a periodic perturbation. Ultrason. Sonochem. 16 (4), 502–511. https://doi.org/10.1016/j.ultsonch.2008.12.016.

Bouakaz, A., Frigstad, S., Ten Cate, F.J., de Jong, N., 2002. Super harmonic imaging: a new imaging technique for improved contrast detection. Ultrasound Med. Biol. 28 (1), 59–68. https://doi.org/10.1016/S0301-5629(01)00460-4.

Caflisch, R.E., Miksis, M.J., Papanicolaou, G.C., Ting, L., 1985. Effective equations for wave propagation in bubbly liquids. J. Fluid Mech. 153, 259–273. https://doi.org/10.1017/S0022112085001252.

Cherin, E., Yin, J., Forbrich, A., White, C., Dayton, P.A., Foster, F.S., Démoré, C.E.M., 2019. In vitro superharmonic contrast imaging using a hybrid dual-frequency probe. Ultrasound Med. Biol. 45 (9), 2525–2539. https://doi.org/10.1016/j.ultrasmedbio.2019.05.012.

Chong, K.J.Y., Quek, C.Y., Dzaharudin, F., Ooi, A., Manasseh, R., 2010. The effects of coupling and bubble size on the dynamical-systems behaviour of a small cluster of microbubbles. J. Sound Vib. 329 (6), 687–699. https://doi.org/10.1016/j.jsv.2009.09.037.

Commander, K.W., Prosperetti, A., 1989. Linear pressure waves in bubbly liquids: comparison between theory and experiments. J. Acoust. Soc. Am. 85 (2), 732–746. https://doi.org/10.1121/1.397599.

Daeichin, V., Bosch, J.G., Needles, A., Foster, F.S., van der Steen, A., de Jong, N., 2015. Subharmonic, non-linear fundamental and ultraharmonic imaging of microbubble contrast at high frequencies. Ultrasound Med. Biol. 41 (2), 486–497. https://doi.org/10.1016/j.ultrasmedbio.2014.10.003.

de Jong, N., Emmer, M., Chin, C.T., Bouakaz, A., Mastik, F., Lohse, D., Versluis, M., 2007. Compression-Only" behavior of phospholipid-coated contrast bubbles. Ultrasound Med. Biol. 33 (4), 653–656. https://doi.org/10.1016/j.ultrasmedbio.2006.09.016.

Dogan, H., White, P.R., Leighton, T.G., 2017. Acoustic wave propagation in gassy porous marine sediments: the rheological and the elastic effects. J. Acoust. Soc. Am. 141 (3), 2277–2288. https://doi.org/10.1121/1.4978926.

Doinikov, A.A., Bouakaz, A., 2010. Theoretical investigation of shear stress generated by a contrast microbubble on the cell membrane as a mechanism for sonoporation. J. Acoust. Soc. Am. 128 (1), 11–19. https://doi.org/10.1121/1.3419775.

Dzaharudin, F., Suslov, S.A., Manasseh, R., Ooi, A., 2013. Effects of coupling, bubble size, and spatial arrangement on chaotic dynamics of microbubble cluster in ultrasonic fields. J. Acoust. Soc. Am. 134 (5), 3425–3434. https://doi.org/10.1121/1.4821202.

Eller, A., Flynn, H.G., 1969. Generation of subharmonics of order one-half by bubbles in a sound field. J. Acoust. Soc. Am. 46 (3B), 722–727. https://doi.org/10.1121/1.1911753.

Fischer, C.H., Hart, E.J., Henglein, A., 1986. Ultrasonic irradiation of water in the presence of oxygen 18,18O2: isotope exchange and isotopic distribution of hydrogen peroxide. J. Phys. Chem. 90 (9), 1954–1956. https://doi.org/10.1021/j100400a043.

Flynn, H.G., Church, C.C., 1988. Transient pulsations of small gas bubbles in water. J. Acoust. Soc. Am. 84 (3), 985–998. https://doi.org/10.1121/1.396614.

Forsberg, F., Shi, W.T., Goldberg, B.B., 2000. Subharmonic imaging of contrast agents. Ultrasonics 38 (1–8), 93–98. https://doi.org/10.1016/s0041-624x(99)00148-1.

Frinking, P.J.A., Gaud, E., Brochot, J., Arditi, M., 2010. Subharmonic scattering of phospholipid-shell microbubbles at low acoustic pressure amplitudes. IEEE Trans. Ultrason. Ferroelectr. Freq. Control 57 (8), 1762–1771. https://doi.org/10.1109/TUFFC.2010.1614.

Goertz, D.E., Cherin, E., Needles, A., Karshafian, R., Brown, A.S., Burns, P.N., Foster, F.S., 2005. High frequency nonlinear B-scan imaging of microbubble contrast agents. IEEE Trans. Ultrason. Ferroelectr. Freq. Control 52 (1), 65–79. https://doi.org/10.1109/TUFFC.2005.1397351.

Guédra, M., Cornu, C., Inserra, C., 2017. A derivation of the stable cavitation threshold accounting for bubble-bubble interactions. Ultrason. Sonochem. 38, 168–173. https://doi.org/10.1016/j.ultsonch.2017.03.010.

Haworth, K.J., Bader, K.B., Rich, K.T., Holland, C.K., Mast, T.D., 2017. Quantitative frequency-domain passive cavitation imaging. IEEE Trans. Ultrason. Ferroelectr. Freq. Control 64 (1), 177–191. https://doi.org/10.1109/TUFFC.2016.2620492.

Hegedűs, F., 2016. Topological analysis of the periodic structures in a harmonically driven bubble oscillator near Blake's critical threshold: infinite sequence of two-sided Farey ordering trees. Phys. Lett. A 380 (9–10), 1012–1022. https://doi.org/10.1016/j.physleta.2016.01.022.

Hegedus, F., Hos, C., Kullmann, L., 2013. Stable period 1, 2 and 3 structures of the harmonically excited Rayleigh-Plesset equation applying low ambient pressure. IMA J. Appl. Math. 78 (6), 1179–1195. https://doi.org/10.1093/imamat/hxs016.

Hegedűs, F., Klapcsik, K., Lauterborn, W., Parlitz, U., Mettin, R., 2020. GPU accelerated study of a dual-frequency driven single bubble in a 6-dimensional parameter space: The active cavitation threshold. Ultrason. Sonochem. 67, 105067. https://doi.org/10.1016/j.ultsonch.2020.105067.

Hilgenfeldt, S., Lohse, D., Zomack, M., 1998. Response of bubbles to diagnostic ultrasound: a unifying theoretical approach. The European Physical Journal B 4 (2), 247–255. https://doi.org/10.1007/s100510050375.

Hoff, L., Sontum, P.C., Hovem, J.M., 2000. Oscillations of polymeric microbubbles: effect of the encapsulating shell. J. Acoust. Soc. Am. 107 (4), 2272–2280. https://doi.org/10.1121/1.428557.

Holt, R.G., Gaitan, D.F., 1996. Observation of stability boundaries in the parameter space of single bubble sonoluminescence. Phys. Rev. Lett. 77 (18), 3791–3794. https://doi.org/10.1103/PhysRevLett.77.3791.

Holt, R.G., Gaitan, D.F., Atchley, A.A., Holzfuss, J., 1994. Chaotic sonoluminescence. Phys. Rev. Lett. 72, 1376.

Holt, R.G., Roy, R.A., 2005. Bubble dynamics in therapeutic ultrasound. Bubble and Particle Dynamics in Acoustic Fileds: Modern Trends and Applications. Research Signpost, Kerala, India, pp. 183–229.

Huang, J., Holt, R.G., Cleveland, R.O., Roy, R.A., 2004. Experimental validation of a tractable numerical model for focused ultrasound heating in flow-through tissue phantoms. J. Acoust. Soc. Am. 116 (4 I), 2451–2458. https://doi.org/10.1121/1.1787124.

Jamshidi, R., Brenner, G., 2013. Dissipation of ultrasonic wave propagation in bubbly liquids considering the effect of compressibility to the first order of acoustical Mach number. Ultrasonics 53 (4), 842–848. https://doi.org/10.1016/j.ultras.2012.12.004.

Kalmár, C., Klapcsik, K., Hegedűs, F., 2020. Relationship between the radial dynamics and the chemical production of a harmonically driven spherical bubble. Ultrason. Sonochem. 64, 104989. https://doi.org/10.1016/j.ultsonch.2020.104989.

Kamei, T., Kanagawa, T., Ayukai, T., 2021. An exhaustive theoretical analysis of thermal effect inside bubbles for weakly nonlinear pressure waves in bubbly liquids. Phys. Fluids 33 (5), 053302. https://doi.org/10.1063/5.0028655.

Kanagawa, T., Kamei, T., 2021. Thermal effect inside bubbles for weakly nonlinear pressure waves in bubbly liquids: theory on short waves. Phys. Fluids 33 (6).

Katiyar, A., Sarkar, K., 2012. Effects of encapsulation damping on the excitation threshold for subharmonic generation from contrast microbubbles. J. Acoust. Soc. Am. 132 (5), 3576–3585. https://doi.org/10.1121/1.4757099.

Katiyar, A., Sarkar, K., 2011. Excitation threshold for subharmonic generation from contrast microbubbles. J. Acoust. Soc. Am. 130 (5), 3137–3147. https://doi.org/10.1121/1.3641455.

Kerboua, K., Hamdaoui, O., 2017. Computational study of state equation effect on single acoustic cavitation bubble's phenomenon. Ultrason. Sonochem. 38, 174–188. https://doi.org/10.1016/j.ultsonch.2017.03.005.

Kerboua, K., Hamdaoui, O., 2018a. Influence of reactions heats on variation of radius, temperature, pressure and chemical species amounts within a single acoustic cavitation bubble. Ultrason. Sonochem. 41, 449–457. https://doi.org/10.1016/j.ultsonch.2017.10.001.

Kerboua, K., Hamdaoui, O., 2018b. Ultrasonic waveform upshot on mass variation within single cavitation bubble: investigation of physical and chemical transformations. Ultrason. Sonochem. 42, 508–516. https://doi.org/10.1016/j.ultsonch.2017.12.015.

Kerboua, K., Hamdaoui, O., 2019. Void fraction, number density of acoustic cavitation bubbles, and acoustic frequency: a numerical investigation. J. Acoust. Soc. Am. 146 (4), 2240–2252. https://doi.org/10.1121/1.5126865.

Kikuchi, Y., Kanagawa, T., 2021. Weakly nonlinear theory on ultrasound propagation in liquids containing many microbubbles encapsulated by visco-elastic shell. Japan. J. Appl. Phys. 60 (SD), SDDD14. https://doi.org/10.35848/1347-4065/abebba.

Lauterborn, W., Suchla, E., 1984. Bifurcation superstructure in a model of acoustic turbulence. Phys. Rev. Lett. 53 (24), 2304–2307. https://doi.org/10.1103/PhysRevLett.53.2304.

Lauterborn, Werner., 1976. Numerical investigation of nonlinear oscillations of gas bubbles in liquids. J. Acoust. Soc. Am. 59 (2), 283–293. https://doi.org/10.1121/1.380884.

Lauterborn, Werner, Kurz, T., 2010. Physics of bubble oscillations. Rep. Prog. Phys. 73 (10), 106501. https://doi.org/10.1088/0034-4885/73/10/106501.

Leighton, T. G. (2012). The Acoustic Bubble.

Louisnard, O., 2012. A simple model of ultrasound propagation in a cavitating liquid. Part I: theory, nonlinear attenuation and traveling wave generation. Ultrason. Sonochem. 19 (1), 56–65. https://doi.org/10.1016/j.ultsonch.2011.06.007.

MacDonald, C.A., Sboros, V., Gomatam, J., Pye, S.D., Moran, C.M., McDicken, W.N., 2004. A numerical investigation of the resonance of gas-filled microbubbles: resonance dependence on acoustic pressure amplitude. Ultrasonics 43 (2), 113–122. https://doi.org/10.1016/j.ultras.2004.04.001.

Mantouka, A., Dogan, H., White, P.R., Leighton, T.G., 2016. Modelling acoustic scattering, sound speed, and attenuation in gassy soft marine sediments. J. Acoust. Soc. Am. 140 (1), 274–282. https://doi.org/10.1121/1.4954753.

Maresca, D., Skachkov, I., Renaud, G., Jansen, K., Van Soest, G., De Jong, N., Van der Steen, A.F.W., 2014. Imaging microvasculature with contrast-enhanced ultraharmonic ultrasound. Ultrasound Med. Biol. 40 (6), 1318–1328. https://doi.org/10.1016/j.ultrasmedbio.2013.12.029.

O'Reilly, M.A., Hynynen, K., 2012. Blood-brain barrier: Real-time feedback-controlled focused ultrasound disruption by using an acoustic emissions-based controller. Radiology 263 (1), 96–106. https://doi.org/10.1148/radiol.11111417.

Overvelde, M., Garbin, V., Sijl, J., Dollet, B., de Jong, N., Lohse, D., Versluis, M., 2010. Nonlinear shell behavior of phospholipid-coated microbubbles. Ultrasound Med. Biol. 36 (12), 2080–2092. https://doi.org/10.1016/j.ultrasmedbio.2010.08.015.

Parlitz, U., Englisch, V., Scheffczyk, C., Lauterborn, W., 1990. Bifurcation structure of bubble oscillators. J. Acoust. Soc. Am. 88 (2), 1061–1077. https://doi.org/10.1121/1.399855.

Phillips, P.J., 2001. Contrast pulse sequences (CPS): Imaging nonlinear microbubbles. In: Proceedings of the IEEE Ultrasonics Symposium, pp. 1739–1745 Vol. 2.

Prosperetti, A., 1984. Bubble phenomena in sound fields: part one. Ultrasonics 22 (2), 69–77. https://doi.org/10.1016/0041-624X(84)90024-6.

Prosperetti, A., 2015. The speed of sound in a gas–vapour bubbly liquid. Interface focus 5, 20150024. doi:10.1098/rsfs.2015.0024.

Prosperetti, Andrea., 2013. A general derivation of the subharmonic threshold for non-linear bubble oscillations. J. Acoust. Soc. Am. 133 (6), 3719–3726. https://doi.org/10.1121/1.4802742.

Prosperetti, Andrea., 1977. Application of the subharmonic threshold to the measurement of the damping of oscillating gas bubbles. J. Acoust. Soc. Am. 61 (1), 11–16. https://doi.org/10.1121/1.381273.

Prosperetti, Andrea., 1974. Nonlinear oscillations of gas bubbles in liquids: steady-state solutions. J. Acoust. Soc. Am. 56 (3), 878–885. https://doi.org/10.1121/1.1903341.

Raymond, J.L., Haworth, K.J., Bader, K.B., Radhakrishnan, K., Griffin, J.K., Huang, S.L., McPherson, D.D., Holland, C.K., 2014. Broadband attenuation measurements of phospholipid-shelled ultrasound contrast agents. Ultrasound Med. Biol. 40 (2), 410–421. https://doi.org/10.1016/j.ultrasmedbio.2013.09.018.

Segers, T., De Jong, N., Versluis, M., 2016. Uniform scattering and attenuation of acoustically sorted ultrasound contrast agents: modeling and experiments. J. Acoust. Soc. Am. 140 (4), 2506–2517. https://doi.org/10.1121/1.4964270.

Shekhar, H., Huntzicker, S., Awuor, I., Doyley, M.M., 2016. Chirp-coded ultraharmonic imaging with a modified clinical intravascular ultrasound system. Ultrason. Imaging 38 (6), 403–419. https://doi.org/10.1177/0161734615618639.

Sojahrood, A.J., Haghi, H., Karshafian, R., Kolios, M.C., 2021a. Classification of the major nonlinear regimes of oscillations, oscillation properties, and mechanisms of wave energy dissipation in the nonlinear oscillations of coated and uncoated bubbles. Phys. Fluids 33 (1), 016105. https://doi.org/10.1063/5.0032766.

Sojahrood, A.J., Haghi, H., Porter, T.M., Karshafian, R., Kolios, M.C., 2021b. Experimental and numerical evidence of intensified non-linearity at the microscale: The lipid coated acoustic bubble. Phys. Fluids 33 (7), 072006. https://doi.org/10.1063/5.0051463.

Sojahrood, A.J., Earl, R., Haghi, H., Li, Q., Porter, T.M., Kolios, M.C., Karshafian, R., 2021c. Nonlinear dynamics of acoustic bubbles excited by their pressure-dependent subharmonic resonance frequency: influence of the pressure amplitude, frequency, encapsulation and multiple bubble interactions on oversaturation and enhancement of the subharmonic signal. Nonlinear Dyn. 103 (1), 429–466. https://doi.org/10.1007/s11071-020-06163-8.

Sojahrood, A.J., Earl, R., Kolios, M.C., Karshafian, R., 2020. Investigation of the 1/2 order subharmonic emissions of the period-2 oscillations of an ultrasonically excited bubble. Phys. Lett. A 384 (23), 126446. https://doi.org/10.1016/j.physleta.2020.126446.

Sojahrood, A.J., Falou, O., Earl, R., Karshafian, R., Kolios, M.C., 2015. Influence of the pressure-dependent resonance frequency on the bifurcation structure and backscattered pressure of ultrasound contrast agents: a numerical investigation. Nonlinear Dyn. 80 (1–2), 889–904. https://doi.org/10.1007/s11071-015-1914-7.

Sojahrood, A.J., Haghi, H., Karshafian, R., Kolios, M.C., 2021d. Classification of the major nonlinear regimes of oscillations, oscillation properties, and mechanisms of wave energy dissipation in the nonlinear oscillations of coated and uncoated bubbles. Phys. Fluids 33 (1). https://doi.org/10.1063/5.0032766.

Sojahrood, A.J., Haghi, H., Karshafian, R., Kolios, M.C., 2020. Critical corrections to models of nonlinear power dissipation of ultrasonically excited bubbles. Ultrason. Sonochem. 66, 105089. https://doi.org/10.1016/j.ultsonch.2020.105089.

Sojahrood, A.J., Haghi, H., Karshafian, R., Kolios, M.C., 2021e. Nonlinear dynamics and bifurcation structure of ultrasonically excited lipid coated microbubbles. Ultrason. Sonochem. 72, 105405. https://doi.org/10.1016/j.ultsonch.2020.105405.

Sojahrood, A.J., Haghi, H., Karshafian, R., Kolios, M.C., 2015. Nonlinear model of acoustical attenuation and speed of sound in a bubbly medium. In: 2015 IEEE International Ultrasonics Symposium, IUS 2015. Institute of Electrical and Electronics Engineers Inc.

Sojahrood, A.J., Haghi, H., Li, Q., Porter, T.M., Karshafian, R., Kolios, M.C., 2020. Nonlinear power loss in the oscillations of coated and uncoated bubbles: Role of thermal, radiation and encapsulating shell damping at various excitation pressures. Ultrason. Sonochem. 66, 105070. https://doi.org/10.1016/j.ultsonch.2020.105070.

Sojahrood, A.J., Haghi, H., Shirazi, N.R., Karshafian, R., Kolios, M.C., 2021. On the threshold of 1/2 order subharmonic emissions in the oscillations of ultrasonically excited bubbles. Ultrasonics 112, 106363. https://doi.org/10.1016/j.ultras.2021.106363.

Sojahrood, A.J., Li, Q., Haghi, H., Karshafian, R., Porter, T. M., & Kolios, M. C. (2018). Pressure dependence of the ultrasound attenuation and speed in bubbly media: Theory and experiment. arXiv. https://arxiv.org

Sojahrood, A.J., Wegierak, D., Haghi, H., Karshfian, R., Kolios, M.C., 2019. A simple method to analyze the super-harmonic and ultra-harmonic behavior of the acoustically excited bubble oscillator. Ultrason. Sonochem. 54, 99–109. https://doi.org/10.1016/j.ultsonch.2019.02.010.

Sojahrood, Amin Jafari, Kolios, M.C, 2012. Classification of the nonlinear dynamics and bifurcation structure of ultrasound contrast agents excited at higher multiples of their resonance frequency. Phys. Lett. A 376 (33), 2222–2229. https://doi.org/10.1016/j.physleta.2012.05.045.

Stricker, L., Prosperetti, A., Lohse, D., 2011. Validation of an approximate model for the thermal behavior in acoustically driven bubbles. J. Acoust. Soc. Am. 130 (5), 3243–3251. https://doi.org/10.1121/1.3626132.

Toegel, R., Luther, S., Lohse, D., 2006. Viscosity destabilizes sonoluminescing bubbles. Phys. Rev. Lett. 96 (11). https://doi.org/10.1103/PhysRevLett.96.114301.

Varga, R., Klapcsik, K., Hegedűs, F., 2020. Route to shrimps: dissipation driven formation of shrimp-shaped domains. Chaos Solitons Fractals 130, 109424. https://doi.org/10.1016/j.chaos.2019.109424.

Versluis, M., Stride, E., Lajoinie, G., Dollet, B., Segers, T., 2020. Ultrasound contrast agent modeling: a review. Ultrasound Med. Biol. 46 (9), 2117–2144. https://doi.org/10.1016/j.ultrasmedbio.2020.04.014.

Viti, J., Mori, R., Guidi, F., Versluis, M., Jong, N., Tortoli, P., 2012. Correspondence-nonlinear oscillations of deflating bubbles. IEEE Trans. Ultrason. Ferroelectr. Freq. Control 59 (12), 2818–2824. https://doi.org/10.1109/TUFFC.2012.2524.

Vokurka, K., 1985. On Rayleigh's model of a freely oscillating bubble. I. Basic relations. Czech. J. Phys. 35 (1), 28–40. https://doi.org/10.1007/BF01590273.

Yang, X., Roy, R.A., Holt, R.G., 2004. Bubble dynamics and size distributions during focused ultrasound insonation. J. Acoust. Soc. Am. 116 (6), 3423–3431. https://doi.org/10.1121/1.1823251.

Yasui, K., 2011. Fundamentals of acoustic cavitation and sonochemistry. Theoretical and Experimental Sonochemistry Involving Inorganic Systems. Springer, Netherlands, pp. 1–29.

Yatabe, T., Kanagawa, T., Ayukai, T., 2021. Theoretical elucidation of effect of drag force and translation of bubble on weakly nonlinear pressure waves in bubbly flows. Phys. Fluids 33 (3), 053314. doi:10.1063/5.0042625.

Zhang, Y., Gao, Y., Guo, Z., Du, X., 2018. Effects of mass transfer on damping mechanisms of vapor bubbles oscillating in liquids. Ultrason. Sonochem. 40, 120–127. https://doi.org/10.1016/j.ultsonch.2017.07.004.

Chapter 8

Damping mechanisms of oscillating gas/vapor bubbles in liquids

Yuning Zhang[a], **Xiaoxiao Zheng**[a], **Xuan Du**[a] **and Yuning Zhang**[b,c]

[a] *Key Laboratory of Power Station Energy Transfer Conversion and System, Ministry of Education, North China Electric Power University, Beijing, China,* [b] *College of Mechanical and Transportation Engineering, China University of Petroleum-Beijing, Beijing, China,* [c] *Beijing Key Laboratory of Process Fluid Filtration and Separation, China University of Petroleum-Beijing, Beijing, China*

8.1 Introduction

Damping mechanisms are essential for the cavitation and bubble dynamics (Zhang, 2013; Zhang et al., 2018a,b; Zhang, 2012). For example, for an underwater explosive bubble, if the damping mechanisms are ignored, the bubble will continue the oscillations forever. In fact, this is not true for the reality because of the presence of strong damping. During the motion of the bubble wall, the presence of the viscosity always tends to decrease the motion, working as a well-known damping mechanism. During the quick shrinkage/expansion of the bubble, waves with energy will be emitted and further travel around the bubbles (named as "acoustic damping mechanism"). As a result, the magnitude of the underwater explosive bubble will drop dramatically after the initial collapse and the subsequent collapses afterwards.

Except the viscous and the acoustic damping mechanisms, thermal effects could also make significant contributions. During the gas bubble shrinkage, the gas inside the bubble will be compressed with the increase of the temperature. Hence, there will be a temperature gradient across the bubble interface and the energy will be transferred from the bubble to the surrounding liquids. As a result, some energy will be lost during the bubble motion through heat transfer (termed as "thermal damping mechanism"). For the vapor bubbles, mass transfer plays an important role on the bubble oscillation process (Zhang et al., 2018a,b).

In this chapter, the damping mechanisms of gas and vapor bubbles will be discussed respectively. In section 8.2, the bubble wall motion equations will be introduced. In section 8.3, the linearization process of bubble wall motion equation will be shown. In section 8.4, the thermal effects will be introduced together with the thermal damping mechanism. In section 8.5, the effects of liquid compressibility on the bubble oscillations will be discussed. In section 8.6, the predictions of the total damping constant will be given together with the contributions of each mechanism. In section 8.7, damping mechanisms of vapor bubbles oscillating in liquids will be shown. In section 8.8, the acoustic wave propagation in the liquids containing gas bubbles will be introduced. In section 8.9, nonlinear bubble oscillations will be considered with comparisons of predictions given by different bubble wall motion equations. In section 8.10, some concluding remarks are given with perspectives.

8.2 Bubble wall motion equation

In this section, the bubble wall motion equation will be introduced. Firstly, a complex second-order (in terms of bubble wall Mach number) equation is introduced. Then, three different bubble wall motion equations will be derived based on the simplifications of the above second-order equation. Finally, the well-known Rayleigh-Plesset equation without considering liquid compressibility will be given.

Energy Aspects of Acoustic Cavitation and Sonochemistry: Fundamentals and Engineering. DOI: https://doi.org/10.1016/B978-0-323-91937-1.00010-4
Copyright © 2022 Elsevier Inc. All rights reserved.

8.2.1 Prosperetti-Lezzi equation

The bubble wall motion equation with the second-order accuracy is given as follows (Lezzi & Prosperetti, 1987; Prosperetti & Lezzi, 1986):

$$\left[1-(1+\lambda)\frac{\dot{R}}{c_l}+\left(\frac{14}{5}+2\lambda+\theta\right)\frac{\dot{R}^2}{c_l^2}\right]R\ddot{R}+\frac{3}{2}\left[1-\left(\frac{1}{3}+\lambda\right)\frac{\dot{R}}{c_l}+\left(\frac{16}{15}+\frac{4}{3}\lambda+\theta\right)\frac{\dot{R}^2}{c_l^2}\right]\dot{R}^2 + \left(\frac{R\ddot{R}}{c_l}\right)^2=\left[1+(1-\lambda)\frac{\dot{R}}{c_l}+\theta\frac{\dot{R}^2}{c_l^2}\right]H+\left[1-(1+\lambda)\frac{\dot{R}}{c_l}\right]\frac{R}{c_l}\frac{dH}{dt}^2 \tag{8.1}$$

where

$$H=\frac{c_l^2}{n-1}\left[\left(\frac{p_B+B}{P_0+B}\right)^{\frac{n-1}{n}}-1\right], n=7.15; B=3.049\times 1\,0^5 Pa \tag{8.2}$$

$$p_B=\left(P_0+\frac{2\sigma}{R_0}\right)\left(\frac{R_0}{R}\right)^{3\kappa}-\frac{2\sigma}{R}-\frac{4\mu_l\dot{R}}{R} \tag{8.3}$$

Here, λ and θ are arbitrary parameters which are of smaller order of $1/Ma$ (Ma is the bubble wall Mach number); R is the instantaneous bubble radius; the overdot denotes the time derivatives; c_l is the undisturbed speed of sound in the liquid; P_0 is the ambient pressure; σ is the surface tension coefficient; R_0 is the equilibrium bubble radius; κ is the polytropic exponent; μ_l is the viscosity of the liquid. Here, a polytropic process is assumed for the gas bubble oscillations.

Let $\lambda=0.5,\ \theta=0$, Eq. (8.1) becomes:

$$\left[1-\frac{\dot{R}}{c_l}\left(\frac{3}{2}-\frac{19}{5}\frac{\dot{R}}{c_l}\right)\right]R\ddot{R}+\frac{3}{2}\left[1-\frac{\dot{R}}{3c_l}\left(\frac{5}{2}-\frac{26}{5}\frac{\dot{R}}{c_l}\right)\right]\dot{R}^2+\left(\frac{R\ddot{R}}{c_l}\right)^2=\left[1+\frac{1}{2}\frac{\dot{R}}{c_l}\right]H+\left[1-\frac{3}{2}\frac{\dot{R}}{c_l}\right]\frac{R}{c_l}\frac{dH}{dt} \tag{8.4}$$

8.2.2 Gilmore equation

Substituting $\lambda=0,\ \theta=0$ into Eq. (8.1), only considering the second-order term $\left[1-(1+\lambda)\frac{\dot{R}}{c_l}\right]\frac{R}{c_l}\frac{dH}{dt}$ on the right side of the equation in Eq. (8.1) but ignoring other second-order terms, the Eq. (8.1) becomes (Gilmore, 1952):

$$\left(1-\frac{\dot{R}}{c_l}\right)R\ddot{R}+\frac{3}{2}\left(1-\frac{\dot{R}}{3c_l}\right)\dot{R}^2=\left(1+\frac{\dot{R}}{c_l}\right)H+\left(1-\frac{\dot{R}}{c_l}\right)\frac{R}{c_l}\frac{dH}{dt} \tag{8.5}$$

Here, the expression of H is shown in Eqs. (8.2) and (8.3). This equation is firstly obtained by Gilmore.

8.2.3 Keller-Miksis equation

Substituting $\lambda=0,\ \theta=0$ into Eq. (8.1), expressing enthalpy as pressure and keeping only the terms up to the first-order Mach number, the Keller-Miksis equation will be obtained (Keller & Miksis, 1980):

$$\left(1-\frac{\dot{R}}{c_l}\right)R\ddot{R}+\frac{3}{2}\left(1-\frac{\dot{R}}{3c_l}\right)\dot{R}^2=\left(1+\frac{\dot{R}}{c_l}\right)\frac{p_{ext}(R,t)-p_s(t)}{\rho_l}+\frac{R}{\rho_l c_l}\frac{d[p_{ext}(R,t)-p_s(t)]}{dt} \tag{8.6}$$

$$p_{ext}\,(R,t)=\left(P_0+\frac{2\sigma}{R_0}\right)\left(\frac{R_0}{R}\right)^{3\kappa}-\frac{2\sigma}{R}-\frac{4\mu_l\dot{R}}{R} \tag{8.7}$$

$$p_s\,(t)=P_0 \tag{8.8}$$

Here, ρ_l is the density of the liquid; t is the time.

8.2.4 Herring equation

Substituting $\lambda=1$ and keeping other settings as Keller-Miksis, the Herring's equation will be obtained as follows (Herring, 1941):

$$\left(1-\frac{2\dot{R}}{c_l}\right)R\ddot{R}+\frac{3}{2}\left(1-\frac{4\dot{R}}{3c_l}\right)\dot{R}^2=\frac{p_{ext}(R,t)-p_s(t)}{\rho_l}+\frac{R}{\rho_l c_l}\frac{d[p_{ext}(R,t)-p_s(t)]}{dt} \tag{8.9}$$

The expressions of $p_{ext}\,(R,t)$ and $p_s\,(t)$ are shown in Eqs. (8.7) and (8.8).

8.2.5 Rayleigh-Plesset equation

Ignoring the viscosity and compressibility of liquid in the Keller-Miksis equation, the Rayleigh-Plesset equation will be obtained as follows (Plesset, 1949):

$$R\,\ddot{R} + \frac{3}{2}\,\dot{R}^2 = \frac{p_{ext}(R,t) - p_s(t)}{\rho_l} \tag{8.10}$$

The expressions of p_{ext} (R,t) and p_s (t) could be still expressed as those shown in Eqs. (8.7) and (8.8) for the gas bubbles.

8.3 Linear oscillations of gas bubbles

In this section, the linearization process of Keller-Miksis equation mentioned in section 8.2.3 will be discussed. Different with the previous ones, the acoustic excitation will be further considered for the completeness. Based on the derivation, the damping constants will be derived and discussed.

8.3.1 Bubble wall motion equation with thermal effects

For the bubble wall motions equation, the Keller-Miksis equation shown in section 8.2.3 will be chosen. In the section 8.5, we will further demonstrate that for other choices (e.g. Herring equation in section 8.2.4), the resulting equations will be purely identical.

For the completeness, thermal effects will be considered and hence the thermal damping mechanisms could be included in our further discussions. To treat this, one of the convenient methods is to draw an analogy between thermal damping and viscous damping. To achieve this, effective thermal damping viscosity (μ_{th}) will be introduced. Then, Eq. (8.7) becomes:

$$p_{ext}\,(R,t) = \left(P_0 + \frac{2\sigma}{R_0}\right)(R_0/R)^{3\kappa} \;-\; \frac{4(\mu_l + \mu_{th})}{R}\,\dot{R} \;-\; \frac{2\sigma}{R} \tag{8.11}$$

For the completeness, the driving sound field is considered and the Eq. (8.8) can be expressed as,

$$p_s(t) = P_0 + P_A \cos\omega t = P_0\left[1 + \varepsilon e^{i\omega t}\right] \tag{8.12}$$

Here, P_A is the amplitude of external acoustic excitation; ω is the angular frequency of driving sound field; $\varepsilon = \frac{P_A}{P_0}$ is the non-dimensional amplitude of driving sound field. Hence, Eq. (8.6) combining Eqs. (8.11) and (8.12) will be the bubble wall motion equation for the further treatment.

8.3.2 Linearization process

When the bubble oscillation amplitude is small, the process could be assumed as a linear oscillation and the instantaneous bubble radius can be expressed as

$$R = R_0\,(1 + x) \tag{8.13}$$

Here, x is the non-dimensional perturbation of the instantaneous bubble radius, which is of the order of ε .

Substituting Eq. (8.13) into Eqs. (8.6), (8.11) and (8.12) and ignoring the quadratic and other higher order terms of x, the linearized equation could be obtained as follows (Zhang, 2012),

$$\ddot{x} \;+ 2\,\beta_{tot}\,\dot{x} + \omega_0^2\,x = -\,\alpha_0\,\varepsilon\,(1 + i\omega R_0/c_l)\,e^{i\omega t}/M \tag{8.14}$$

where

$$\alpha_0 = \frac{P_0}{\rho_l R_0^2} \tag{8.15}$$

$$M = 1 + \frac{R_0}{c_l}\frac{4(\mu_l + \mu_{th})}{\rho_l R_0^2} \tag{8.16}$$

$$\omega_0^2 = \frac{1}{M}\left(\frac{3\kappa P_{in,eq}}{\rho_l R_0^2} - \frac{2\sigma}{\rho_l R_0^3}\right) \tag{8.17}$$

$$P_{in,eq} = P_0 + \frac{2\sigma}{R_0} \tag{8.18}$$

Here, ω_0 is the natural frequency of the harmonic oscillator.

8.3.3 Damping constants

In Eq. (8.14), β_{tot} is the total damping constant. The total damping constant consists of three terms (Zhang, 2012),

$$\beta_{tot} = \beta_{vis} + \beta_{th} + \beta_{ac} \tag{8.19}$$

where

$$\beta_{vis} = 2\,\mu_l \,/\, \rho_l\, R_0^2\, M \tag{8.20}$$

$$\beta_{th} = 2\,\mu_{th} \,/\, \rho_l\, R_0^2\, M \tag{8.21}$$

$$\beta_{ac} = \frac{R_0}{2c_l}\,\omega_0^2 \tag{8.22}$$

representing the viscous, thermal and acoustic damping constants respectively. As shown in Eq. (8.20), the viscous damping constant is directly proportional to the dynamic viscosity. Similarly, the thermal damping constant is directly proportional to the effective thermal viscosity, which will be given in section 8.4 together with the polytropic exponent. As shown in Eq. (8.22), the acoustic damping constant is directly proportional to the square of the natural frequency of the bubble oscillator. Hence, for an incompressible liquids (i.e. with the infinite sound speed in the liquid), there will be no acoustic damping shown.

8.4 Thermal effects and thermal damping

In this section, the expressions of μ_{th} and κ in Eq. (8.21) and (8.17) relating to the thermal effects will be given for the closure of the model. For the bubble oscillations driven by the sound field, μ_{th} in Eq. (8.21) and κ in Eq. (8.17) can be determined by solving the bubble interior (Prosperetti, 1977),

$$\mu_{th} = \frac{1}{4}\,\omega\,\rho_g\,R_0^2\,\mathrm{Im}\,\varphi \tag{8.23}$$

$$\kappa = \frac{1}{3}\left(\omega^2\rho_g R_0^2/P_{in,eq}\right)\mathrm{Re}\,\varphi \tag{8.24}$$

Here, ρ_g is the gas density; ϕ is a function relating to the solution of bubble interior problem. In this section, the basic equations of the bubble oscillation problem will be introduced together with two typical solutions (with and without considerations of the pressure inside bubble respectively).

8.4.1 Basic equations

Here, the problem is still assumed as a linear one, supposing the deviations of quantities (e.g. density, pressure and temperature) are small away from their equilibrium values. Firstly, we define these quantities as (Prosperetti, 1977)

$$\rho = \rho_g\,(1+\eta) \tag{8.25}$$

$$P = P_0\,(1 + 2\sigma/R_0P_0 + p) \tag{8.26}$$

$$T_g = T_\infty\left(1+\theta_g\right) \tag{8.27}$$

$$T_l = T_\infty\,(1+\theta_l) \tag{8.28}$$

Here, ρ, P and T_g are the density, pressure and temperature inside the gas bubble respectively, being functions of both the time and the radial coordinate; η, p and θ_g are the non-dimensional deviations from the equilibrium values of density, pressure and temperature in the gas respectively; T_∞ is the ambient equilibirum temperature; T_l is the temperature in the liquid; θ_l is the non-dimensional deviation from the equilibrium liquid temperature.

Hence, the ideal gas law could be expressed as (Prosperetti, 1977)

$$P = \left(R_g/M_g\right)\,\rho\,T_g \tag{8.29}$$

Here, R_g is the universal constant; M_g is the molecular weight of the given type of the gas inside the bubble. Using Eqs. (8.25)–(8.27), Eq. (8.29) could be expressed using the nondimensional deviations such as (Prosperetti, 1977):

$$p = (1 + 2\sigma/R_0P_0)\left(\theta_g + \eta\right) \tag{8.30}$$

According the conservation law (mass, momentum and energy in the gas phase), the following equations could be given (Prosperetti, 1977).

$$\frac{\partial \eta}{\partial t} + \frac{1}{r^2}\frac{\partial\left(r^2 u\right)}{\partial r} = 0 \tag{8.31}$$

$$\frac{\partial u}{\partial t} + \frac{P_0}{\rho_g}\frac{\partial p}{\partial r} = 0 \tag{8.32}$$

$$\frac{1}{r^2}\frac{\partial}{\partial r}\left(r^2\frac{\partial \theta_g}{\partial r}\right) + \frac{(P_0 + 2\sigma/R_0)}{k_g T_\infty}\frac{\partial \eta}{\partial t} = \frac{1}{D_{g,v}}\frac{\partial \theta_g}{\partial t} \tag{8.33}$$

Here, u is the gas velocity; r is the radial coordinate. Similarly, the equation of conservation of energy in the liquid phase is (Prosperetti, 1977)

$$\frac{1}{r^2}\frac{\partial}{\partial r}\left(r^2\frac{\partial \theta_l}{\partial r}\right) = \frac{1}{D_l}\frac{\partial \theta_l}{\partial t} \tag{8.34}$$

Here, k_g is the thermal conductivity of the given gas; $D_{g,v}$ is the thermal diffusivity of the gas with a constant volume; D_l is the thermal diffusivity of the liquid.

The continuity must be satisfied at the gas-liquid interface in terms of temperature, heat flux and velocity. The relating equations are (Prosperetti, 1977)

$$\theta_l\big|_{(r=R_0,t)} = \theta_g\big|_{(r=R_0,t)} \tag{8.35}$$

$$-k_l\frac{\partial \theta_l}{\partial t}\big|_{(r=R_0,t)} = -k_g\frac{\partial \theta_g}{\partial t}\big|_{(r=R_0,t)} \tag{8.36}$$

$$u\big|_{(r=R_0,t)} = dR/dt \tag{8.37}$$

Here, k_l is the thermal conductivity of the liquid.

8.4.2 Solutions for the nonuniform pressure inside bubble

This section will give the solution of ϕ in Eqs. (8.23) and (8.24) to close the model. For the detailed procedure for solving the Eqs. (8.31)-(8.34), readers are referred to the given references (Prosperetti, 1977).

Firstly, three non-dimensional parameters are defined as follows (Prosperetti, 1977):

$$G_1 = M_g D_{g,v}\frac{\omega}{\gamma}R_g T_\infty \tag{8.38}$$

$$G_2 = \omega R_0^2/D_{g,v} \tag{8.39}$$

$$G_3 = \omega R_0^2/D_l \tag{8.40}$$

Here, γ is the ratio of specific heat of the gas. G_1 reflects the ratio between mean free path and the wavelength in the gas; G_2 reflects the ratio between bubble radius and thermal penetration depth. The expression of ϕ in Eqs. (8.23) and (8.24) could be written as (Prosperetti, 1977)

$$\varphi = \frac{kf(\Gamma_2 - \Gamma_1) + \lambda_2\Gamma_2 - \lambda_1\Gamma_1}{kf(\lambda_2\Gamma_1 - \lambda_1\Gamma_2) - \lambda_1\lambda_2(\Gamma_2 - \Gamma_1)} \tag{8.41}$$

where

$\beta_{1,2} = \left(\frac{1}{2}\gamma G_2\left\{i - G_1 \pm \left[(i - G_1)^2 + 4iG_1/\gamma\right]^{1/2}\right\}\right)^{1/2}; \lambda_i = \beta_i \coth\beta_i - 1\, i = 1, 2; \Gamma_{1,2} = i + G_1 \pm \left[(i - G_1)^2 + 4iG_1/\gamma\right]^{1/2}; f = 1 + (1 + i)\left(\frac{1}{2}G_3\right)^{1/2}; k = k_l / k_g.$

Using the definition of G_1 in Eq. (8.38), G_2 in Eq. (8.39), μ_{th} and κ can also be expressed as

$$\mu_{th} = \frac{P_{in,eq}\gamma G_1 G_2}{4\omega} \operatorname{Im}\varphi \tag{8.42}$$

$$\kappa = \frac{1}{3}\,\gamma\, G_1\, G_2 \operatorname{Re}\varphi \tag{8.43}$$

8.4.3 Solutions for the uniform pressure inside bubble

For the bubble with uniform pressure inside, the pressure will be only function of time rather than the radial coordinate. For this scenario, the equations relating with the thermal effects could be simplified as follows (Devin & Taylor, 1959):

$$\gamma G_1 G_2 \varphi \approx \Phi = 3\gamma/\left\{1 - 3(\gamma-1)i\chi\left[(i/\chi)^{1/2}\coth\,(i/\chi)^{1/2} - 1\right]\right\} \tag{8.44}$$

where

$$\chi = D_{g,p}\,/\omega\, R_0^2$$

$$D_{g,p} = D_{g,v}\,/\gamma$$

Here, $D_{g,p}$ is the thermal diffusivity of the gas at constant pressure. Hence, the expressions of μ_{th} and κ can be simplified as follows (Devin & Taylor, 1959),

$$\mu_{th} = \frac{P_{in,eq}}{4\omega} \operatorname{Im}\Phi \tag{8.45}$$

$$\kappa = \frac{1}{3} \operatorname{Re}\Phi \tag{8.46}$$

8.5 Effects of liquid compressibility and acoustic damping

In this section, the effects of liquid compressibility will be discussed together with their influences on the acoustic damping. In Eq. (8.1), if all the terms up to the second-order of bubble wall Mach number (term with c_l^{-2}) are ignored, the following one-parameter family equation (the "General Keller-Herring equation") could be obtained (Prosperetti & Lezzi, 1986):

$$\left[1 - (\lambda+1)\frac{\dot{R}}{c_l}\right] R\,\ddot{R} + \frac{3}{2}\left[1 - (3\lambda+1)\frac{\dot{R}}{3c_l}\right]\dot{R}^2 = \left[1 + (1-\lambda)\frac{\dot{R}}{c_l}\right]\frac{p_{ext}(R,t) - p_s(t)}{\rho_l} + \frac{R}{\rho_l c_l}\,\frac{d[p_{ext}(R,t) - p_s(t)]}{dt} \tag{8.47}$$

Here, $p_{ext}\,(R,t)$ and $p_s\,(t)$ are given by Eqs. (8.11) and (8.12) respectively in terms of pressure. If $\lambda = 0$, Eq. (8.47) reduces to Keller-Miksis equation (Eq. (8.7)). If $\lambda = 1$, Eq. (8.47) reduces to the equation derived by Herring (Eq. (8.9)).

Here, the linearization of Eq. (8.47) will be made as shown in our previous work (Zhang, 2012) and we will only keep terms up to the second order of ε (or x). Substituting $R = R_0\,(1 + x)$ into terms involving λ in Eq. (8.47), we obtain the following expressions term by term

$$\left[1 - (\lambda+1)\frac{\dot{R}}{c_l}\right] R\,\ddot{R} = \left[1 - (\lambda+1)\frac{R_0\dot{x}}{c_l}\right] R_0^2\,(1+x)\,\ddot{x} \;\approx\; R_0^2\,(1+x)\,\ddot{x} \;-\; (\lambda+1)\,\frac{R_0^3\dot{x}\ddot{x}}{c_l} \tag{8.48}$$

$$\frac{3}{2}\left[1 - (3\lambda+1)\frac{\dot{R}}{3c_l}\right]\dot{R}^2 \;\approx\; \frac{3}{2}\,R_0^2\,\dot{x}^2 \tag{8.49}$$

$$\begin{aligned}
&\left[1 + (1-\lambda)\frac{\dot{R}}{c_l}\right]\frac{p_{ext}(R,t) - p_s(t)}{\rho_l} = \frac{1}{\rho_l}\left[1 + (1-\lambda)\frac{\dot{R}}{c_l}\right]\left[\left(P_0 + \frac{2\sigma}{R_0}\right)(R_0/R)^{3\kappa} - \frac{2\sigma}{R} - \frac{4(\mu_l+\mu_{th})}{R}\dot{R} - P_0\left(1 + \varepsilon e^{i\omega t}\right)\right] \\
&\approx \frac{1}{\rho_l}\left[1 + (1-\lambda)\frac{R_0\dot{x}}{c_l}\right]\left\{\left[(-3\kappa)\left(P_0 + \frac{2\sigma}{R_0}\right) + \frac{2\sigma}{R_0}\right]x - 4(\mu_l+\mu_{th})\dot{x} - P_0\varepsilon e^{i\omega t} + \left[\frac{3\kappa(3\kappa+1)}{2}\left(P_0 + \frac{2\sigma}{R_0}\right) - \frac{2\sigma}{R_0}\right]x^2 + 4(\mu_l+\mu_{th})x\dot{x}\right\} \\
&\approx \frac{1}{\rho_l}\left\{\left[(-3\kappa)\left(P_0 + \frac{2\sigma}{R_0}\right) + \frac{2\sigma}{R_0}\right]x - 4(\mu_l+\mu_{th})\dot{x} - P_0\varepsilon e^{i\omega t} + \left[\frac{3\kappa(3\kappa+1)}{2}\left(P_0 + \frac{2\sigma}{R_0}\right) - \frac{2\sigma}{R_0}\right]x^2 + 4(\mu_l+\mu_{th})x\dot{x}\right\} \\
&\quad + \frac{1}{\rho_l}(1-\lambda)\,\frac{R_0\dot{x}}{c_l}\left\{\left[(-3\kappa)\left(P_0 + \frac{2\sigma}{R_0}\right) + \frac{2\sigma}{R_0}\right]x - 4(\mu_l+\mu_{th})\dot{x} - P_0\varepsilon e^{i\omega t}\right\}
\end{aligned} \tag{8.50}$$

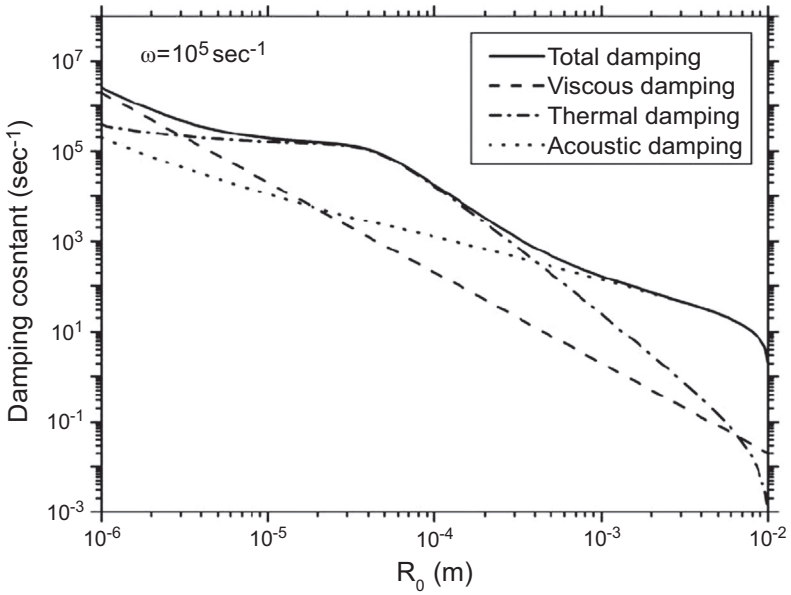

FIGURE 8.1 The predictions of the total, viscous, thermal and acoustic damping constants for the air bubble oscillating in the water. The angular frequency of the acoustic excitation is 10^5/sec.

Based on Eqs. (8.48–8.50), one could easily find that terms involving the λ in Eq. (8.47) are of the second or higher order of ε or x. Therefore, for linear oscillations, all the equations of the bubble wall motion belonging to the one-parameter family will give the same expressions for the damping and the natural frequency as those shown in Eqs. (8.14– 8.22).

8.6 Total damping constants and comparisons of damping mechanisms

In this section, the predictions of the total damping constants are given together with the contributions of each mechanism (viscous, thermal and acoustic damping mechanisms).

Fig. 8.1 predicts the total, viscous, thermal and acoustic damping constants for the air bubble oscillating in water (Zhang, 2013). For the detailed constants employed for the calculations, readers are referred to our previous work (Zhang, 2013). As shown in Fig. 8.1, the equilibrium bubble radius strongly affects the total damping constant. Generally speaking, the total damping constant will decrease with the increase of the bubble radius. However, the decreasing rate is quite different for different bubble sizes. For the small bubbles, the viscous damping constant is dominant and for the large bubbles, the acoustic damping constant is dominant. For the medium size of bubbles, the thermal damping constant is dominant. Hence, the damping mechanisms and the dominant ones are strongly depending on the bubble sizes. Furthermore, the external acoustic excitation could also alter the damping mechanisms in some extent (Zhang, 2013).

8.7 Damping mechanisms of vapor bubbles

In this section, the basic equations of the vapor bubbles will be discussed together with the linearization processes. Different with the gas bubbles, mass transfer strongly affects the damping mechanisms of the vapor bubbles.

8.7.1 Basic equations

The equation of bubble wall motion of the vapor bubble with the mass transfer and the liquid compressibility included could be given as follows (Zhang et al., 2018a,b),

$$\left(1-\frac{\dot{R}-\frac{J}{\rho_l}}{c_l}\right)R\left(\ddot{R}-\frac{\dot{J}}{\rho_l}\right)+2\dot{R}\left(\dot{R}-\frac{J}{\rho_l}\right)-\frac{1}{2}\left(1+\frac{\dot{R}}{c_l}\right)\left(\dot{R}-\frac{J}{\rho_l}\right)^2=\left(1+\frac{\dot{R}}{c_l}+\frac{R}{c_l}\frac{d}{dt}\right)\tilde{\chi} \tag{8.51}$$

with

$$\tilde{\chi} = \frac{1}{\rho_l}\left[P_{in} - \frac{2\sigma}{R} - 4\mu_l\frac{1}{R}\left(\dot{R} - \frac{J}{\rho_l}\right) - J^2\left(\frac{1}{\rho_b} - \frac{1}{\rho_l}\right) - P_0 - P_s\right] \tag{8.52}$$

where

$$P_{in}\,(R,t) = P_{in,eq}\left(\frac{R_0}{R}\right)^{3\kappa} - 4\,\mu_{th}\,\frac{1}{R}\left(\dot{R} - \frac{J}{\rho_l}\right)$$

$$P_s = P_A\,e^{i\omega t}$$

$$J = \rho_l\left(\dot{R} - U_l\right)$$

Here, J is total evaporation mass flux per unit area across the vapor bubble interface; ρ_b is the density of the gas phase of the vapor bubble; U_l is the speed in the liquid at the location of the bubble interface.

8.7.2 Linear oscillations

For the convenience of further derivation, Eq. (8.13) in section 8.3.2 is employed together with the following expression (Fuster & Montel, 2015)

$$J = J_0\,R_0\,x \tag{8.53}$$

$$J_0^* = \frac{J_0}{\rho_{b,0}R_0\omega} \tag{8.54}$$

Here, J_0 is the coefficient of mass flux variation; $\rho_{b,0}$ is the initial bubble density. The following equations could be obtained by the linearization of Eq. (8.51) (Zhang et al., 2018a,b),

$$\ddot{x} + 2\,\beta_{tot}\,\dot{x} + \omega_0^2\,x = -\,\alpha_0\,\varepsilon\,e^{i\omega t} \tag{8.55}$$

where

$$\beta_{tot} = \frac{2(\mu_l + \mu_{th})\varphi}{M\rho_l R_0^2} + \frac{R_0}{2c_l}\,\tilde{\omega}_0^2 - \frac{1}{2}\mathrm{Re}\left(J_0^*\right)\frac{\rho_b}{\rho_l}\omega \tag{8.56}$$

$$\omega_0^2 = \frac{P_{in,eq}}{M\rho_l R_0^2}\left(3\kappa - \frac{2\sigma}{P_{in,eq}R_0}\right) + \mathrm{Im}\left(J_0^*\right)\frac{\rho_b}{\rho_l}\omega^2 \tag{8.57}$$

with

$$\kappa = \frac{1}{3}\,\mathrm{Re}\,(\Phi)$$

$$\mu_{th} = \frac{4P_{in,eq}}{\omega}\,\mathrm{Im}(\Phi)$$

$$\varphi = 1 - \frac{\rho_b}{\rho_l}\,\mathrm{Im}(\,J_0^*)$$

$$\tilde{\omega}_0^2 = \frac{P_{in,eq}}{M\rho_l R_0^2}\left(3\kappa - \frac{2\sigma}{P_{in,eq}R_0}\right)$$

Here, Φ is the transfer function between the pressure inside bubbles and the oscillations of bubble radius. To close the model, J_0^* and Φ in Eqs. (8.56) and (8.57) are given as follows (Fuster & Montel, 2015)

$$J_0^* = J_c^*\left(1 - \Delta H_{vap}^*\Delta T_c^I\right)\Phi \tag{8.58}$$

$$\Phi = \frac{3\gamma}{1 - 3(\gamma-1)iPe_b^{-1}\left[\sqrt{Pe_b i}\,\coth\left(\sqrt{Pe_b i}\right) - 1\right]\left(1 - \Delta T_c^I\right) + 3\gamma i J_c^*\left(\Delta H_{vap}^*\Delta T_c^I - 1\right)} \tag{8.59}$$

where

$$P\,e_b = \omega\,R_0^2\,/\,D_b^T \tag{8.60}$$

$$\Delta\,H_{vap}^* = \Delta\,H_{vap}\,/\,c_{p,b}\,T_0 \tag{8.61}$$

$$\Delta\,T_c^I = \frac{k_b}{k_l}\,\frac{\sqrt{Pe_b i}\,\coth\left(\sqrt{Pe_b i}\right) - 1 + J_c^* Pe_b \Delta H_{vap}^* \left(\frac{\gamma}{\gamma-1}\right)}{1 + \sqrt{Pe_l i} + \frac{k_b}{k_l}\left[\sqrt{Pe_b i}\,\coth\left(\sqrt{Pe_b i}\right) - 1 + J_c^* Pe_b (\Delta H_{vap}^*)^2 \left(\frac{\gamma}{\gamma-1}\right)\right]} \tag{8.62}$$

$$J_c^* = \frac{J_{max}^*}{1 + J_{max}^* \left(J_{c,eq}^*\right)^{-1}} \tag{8.63}$$

with

$$J_{c,eq}^* = \frac{\sqrt{iSh_D}\,\coth\left(\sqrt{iSh_D}\right) - 1}{Sh_D}\,\frac{Y_0}{1 - Y_0} \tag{8.64}$$

$$S\,h_D = \omega\,R_0^2\,/\,D_{w/b} \tag{8.65}$$

$$J_{max}^* = \alpha_{evap}\,\frac{p_{in,eq}}{\rho_{b,0} R_0 \omega \sqrt{2\pi\,r_w T_0}} \tag{8.66}$$

$$P\,e_l = \omega\,R_0^2\,/\,D_l^T \tag{8.67}$$

Here, $J^*{}_c$ is the characteristic non-dimensional mass transfer flux; $\Delta\,T_c^I$ is the non-dimensional temperature variation at the bubble interface; γ is the specific heat ratio; D_b^T is the bubble thermal diffusivity; $\Delta\,H_{vap}$ is the enthalpy of vaporization of the liquid; $c_{p,b}$ is the specific heat inside the bubble; T_0 is the ambient temperature; k_b and k_l are the thermal conductivity of bubble and liquid respectively; $D_{w/b}$ is the diffusion coefficient of the vapor inside bubble; α_{evap} is the accommodation coefficient; r_w is the vapor's gas constant; D_l^T is the liquid thermal diffusivity; Y_0 is the fractions of the vapor inside the bubble.

8.7.3 Effects of mass transfer

The total damping constants shown in Eq. (8.56) are divided into four parts: the viscous damping constant, the thermal damping constant, the acoustic damping constant, and the mass-transfer damping constant. In fact, the mass transfer effects could affect all terms shown in Eq. (8.56) noticing that the expression of Φ is strongly related with the mass transfer.

Fig. 8.2 shows the predictions of the total damping constant for the vapor bubble oscillating in water with and without mass transfer effects (Zhang et al., 2018a). Without mass transfer, the total damping constant will drop especially in the regions with small Péclet number (e.g., small bubbles).

8.8 Wave propagation in the liquids containing bubbles

In this section, the approach for predictions of the propagation of acoustic waves in the liquids containing bubbles is introduced by considering the non-uniform pressure field outside the bubbles.

8.8.1 Basic equations

For propagation of linear acoustic waves in bubbly liquids, the equation is (Commander & Prosperetti, 1989)

$$\frac{1}{c_l^2}\,\frac{\partial^2 P}{\partial t^2} - \nabla^2\,P = 4\pi\,\rho_l\,n\,\int_0^\infty R_0^2 \ddot{R} f(R_0) dR_0 \tag{8.68}$$

with

$$\int_0^\infty f(R_0) dR_0 = 1$$

Here, P is the average pressure in the liquid; n is the total number of bubbles per unit volume; $f(R_0)$ is the density function of bubble size distribution in the bubbly liquid.

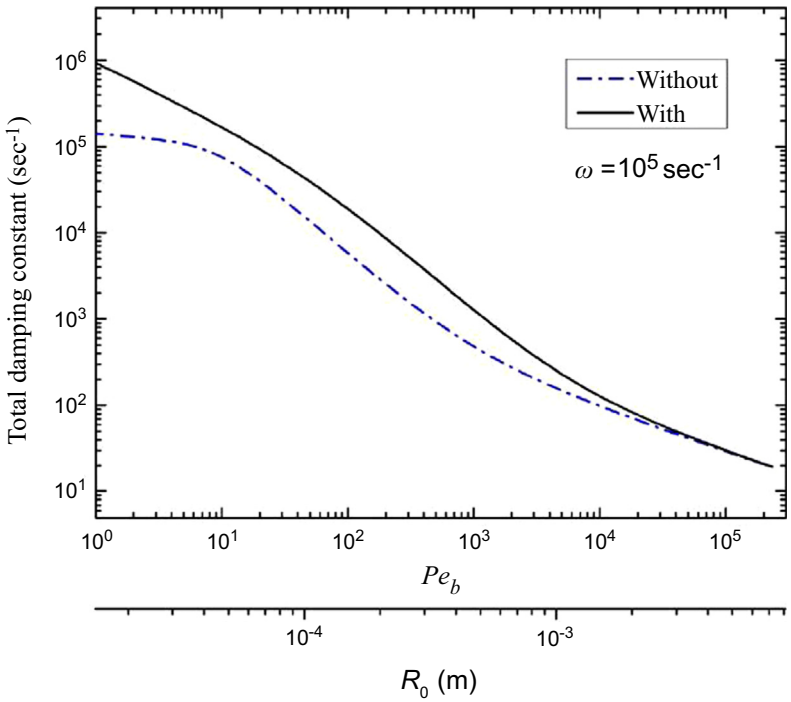

FIGURE 8.2 The predictions of the total damping constant for the vapor bubble oscillating in the water with and without mass transfer effects. The angular frequency of the acoustic excitation is 10^5/sec.

In order to close Eq. (8.68), Keller-Miksis equation of bubble motion (Eq. (8.6)) in section 8.2.3 will be employed. Here, considering non-uniform pressure induced by the acoustic wave, P_S in Eq. (8.6) can be expressed as follows (Gradshteyn et al., 1981; Thuraisingham, 1997),

$$P_S = P_A\, e^{i\omega t} \int_0^{\pi} e^{ikR\cos\phi}\, 2\pi R\, \sin\phi\, R d\phi \tag{8.69}$$

To close Eq. (8.69), the following expression could be employed (Gradshteyn et al., 1981)

$$\int_0^{\pi} e^{ikR\cos\phi} \sin\phi d\phi = \sqrt{\frac{2\pi}{kR}}\, \Gamma\,(1)\, J_{0.5}\,(kR) \tag{8.70}$$

$$J_{0.5}\,(kR) = \sqrt{\frac{2\pi}{kR}} \sin\,(kR) \tag{8.71}$$

Here Γ is the gamma function; $J_{0.5}$ is the Bessel function of order of 0.5. Substituting Eqs. (8.70) and (8.71) into Eq. (8.9), one can obtain (Thuraisingham, 1997)

$$P_S = P_A\, e^{i\omega t}\, \frac{\sin\,(kR)}{kR} \tag{8.72}$$

Through linearization of the Keller-Miksis's equation [Eq. (8.6)] with Eq. (8.72), one can obtain (Zhang & Du, 2015)

$$\ddot{x} + 2\,\beta_{tot}\,\dot{x} + \omega_0^2\, x = -\frac{P_A}{\rho_l R_0^2 M}\,(1 + i\omega R_0/c_l)\,\frac{\sin\,(kR_0)}{kR_0}\, e^{i\omega t} \tag{8.73}$$

The parameters shown in Eq. (8.73) are the same as those in Eq. (8.14) shown in section 8.3. Comparing with Eq. (8.4), the right side shows a correction term relating with the non-uniform pressure outside of the bubble.

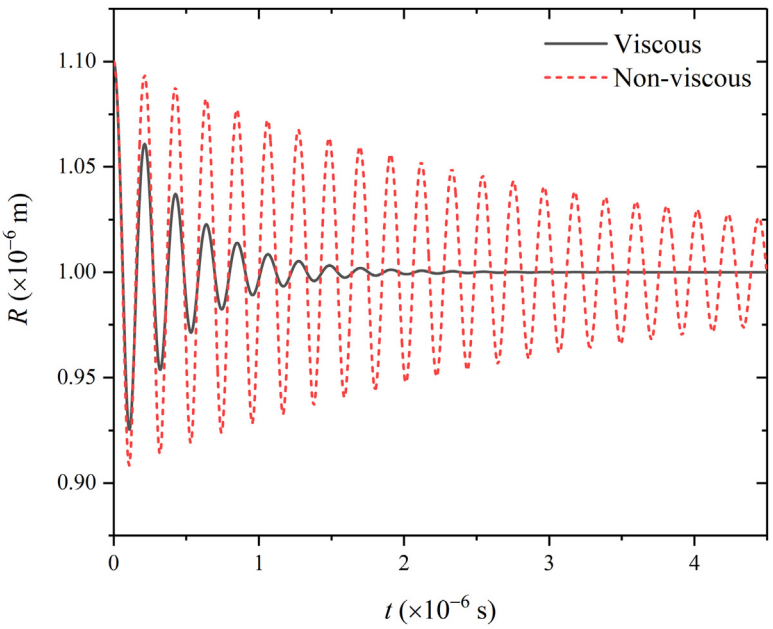

FIGURE 8.3 Predicted bubble radius as a function of time for the free oscillations of bubbles with the initial conditions $R\,(0) = 1.1\times10^{-6}$ m and $\dot{R}(0) = 0$ m/s. The solid and the dashed lines refer to the predictions with and without the viscous effects.

8.8.2 Wave speed and attenuation

Combining Eqs. (8.68) and (8.73), the complex wave speed (c_m) of acoustic wave in the bubbly liquid could be expressed as (Zhang & Du, 2015)

$$\frac{1}{c_m^2} = \frac{1}{c_l^2} + 4\pi n \int_0^\infty \frac{R_0 f(R_0) dR_0}{\psi} \tag{8.74}$$

with

$$\psi = \frac{kR_0}{\sin(kR_0)} \left\{ -\frac{\omega^2}{1+(\omega R_0/c_l)^2} + M\omega_0^2 + i\omega \left[\frac{4(\mu_l+\mu_{th})}{\rho_l R_0^2} + \frac{R_0}{c_l} \frac{\omega^2}{1+(\omega R_0/c_l)^2} \right] \right\} \tag{8.75}$$

The phase velocity (V) and attenuation (A) of acoustic waves in liquids containing gas bubbles can be described as (Commander & Prosperetti, 1989)

$$V = \{\mathrm{Re}(1/c_m)\}^{-1} \tag{8.76}$$

$$A = -20\left(\log_{10} e\right)\omega\,\mathrm{Im}(1/c_m) \tag{8.77}$$

Hence, as shown in Eq. (8.77), one can find that the wave attenuation is strongly related with the damping mechanisms. For the waves propagation in the mixture bubbles containing both vapor and gas bubbles, the waves speed will be greatly altered (Zhang et al., 2018a,b).

8.9 Nonlinear oscillations of bubbles

8.9.1 Comparisons of the viscous and acoustic damping mechanisms

In this section, Prosperetti-Lezzi equation will be employed for the comparisons of the viscous and acoustic damping mechanisms during gas bubble oscillations. Here, for the convenience, the thermal damping mechanisms will be ignored. Hence, through comparisons the cases with and without viscous effects, we could identify the contributions among the two damping mechanisms.

Fig. 8.3 shows the predicted bubble radius as a function of time for the free oscillations of bubbles with the initial conditions $R\,(0) = 1.1 \times 10^{-6}$ m and $\dot{R}\,(0) = 0$ m/s. The solid and the dashed lines refer to the predictions with and without the viscous effects. For this case, the viscous damping is very important and greatly affect the bubble oscillations.

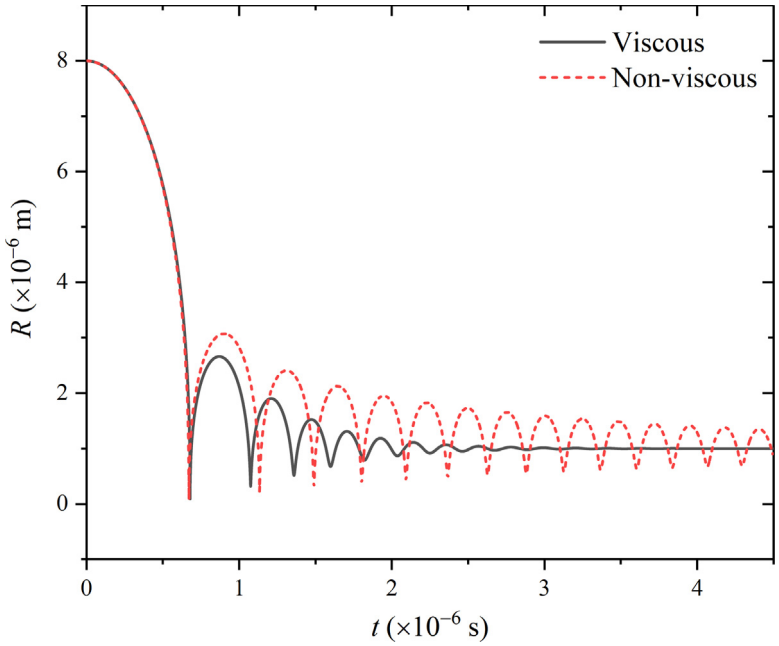

FIGURE 8.4 Predicted bubble radius as a function of time for the free oscillations of bubbles with the initial conditions $R(0) = 8 \times 10^{-6}$ m and $\dot{R}(0) = 0$ m/s. The solid and the dashed lines refer to the predictions with and without the viscous effects.

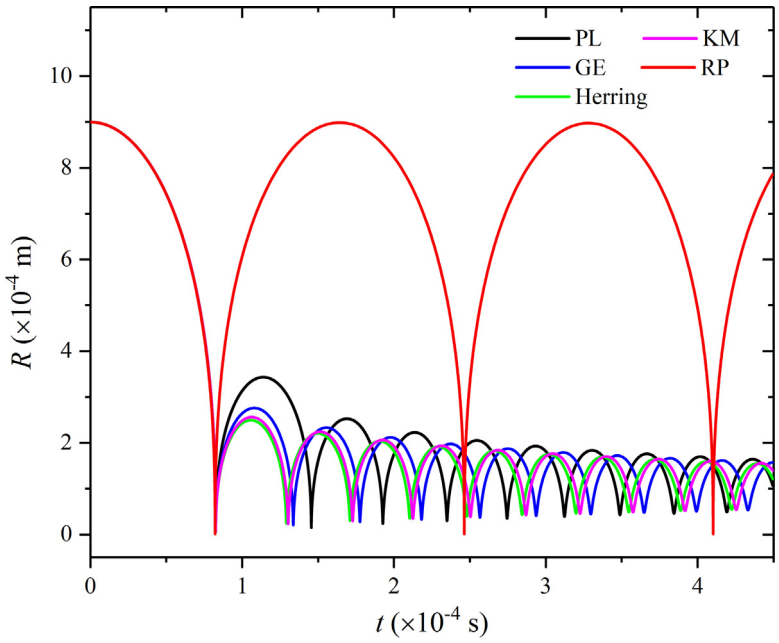

FIGURE 8.5 Predicted bubble radius as a function of time for the free oscillations of bubbles with the initial conditions $R(0) = 9 \times 10^{-4}$ m and $\dot{R}(0) = 0$ m/s based on five different bubble wall equations. The black line refers to Prosperetti-Lezzi equation. The blue line refers to Gilmore equation. The green line refers to Herring equation. The pink line refers to Keller-Miksis equation. The red line refers to Rayleigh-Plesset equation.

Fig. 8.4 further shows the predictions with the same settings of Fig. 8.3 but different initial condition ($R(0) = 8 \times 10^{-6}$ m). For this case, the nonlinearity will be much stronger because the bubble is far away from its equilibrium. As shown in Fig. 8.4, the viscous damping shows no influences on the initial collapse of the bubble. For the subsequent collapses, the viscous shows a little influences on the oscillation magnitude and frequencies. As shown before Eq. (8.20), for larger bubbles, the effects of viscosity will shrink.

8.9.2 Comparisons of predictions by different bubble wall motion equations

Fig. 8.5 shows the predicted bubble radius as a function of time for the free oscillations of bubbles with the initial conditions $R(0) = 9 \times 10^{-4}$ m and $\dot{R}(0) = 0$ m/s based on five different bubble wall equations. The black line refers to Prosperetti-Lezzi equation. The blue line refers to Gilmore equation. The green line refers to Herring equation. The pink line refers to Keller-Miksis equation. The red line refers to Rayleigh-Plesset equation. As shown in the Fig. 8.5, Rayleigh-Plesset equation shows nearly no damping, demonstrating that the influences of the viscosity could be ignored. Comparing with the predictions by the Prosperetti-Lezzi equation, the predictions by Gilmore equation, Keller-Miksis equation and Herring equation all over-predict the damping effects, leading to the smaller oscillation amplitude after the first collapse. Hence, the second-order correction is necessary especially for the nonlinear bubble oscillations.

8.10 Conclusions

In this chapter, the damping mechanisms of the oscillating gas/vapor bubbles are investigated in detail. For the gas bubbles, the damping is dominated by the viscous damping for the small bubble, by the thermal damping for the medium-sized bubble and by the acoustic damping for the large bubble. For the vapor bubble, the effects of mass transfer make significant contributions to the damping mechanisms. For the nonlinear oscillations of the bubbles, the second-order corrections are necessary otherwise the damping mechanisms will be over-predicted. However, the detailed investigations of the nonlinear damping mechanisms are still absent and should be further explored.

Acknowledgement

This work was financially supported by the National Natural Science Foundation of China (Project Nos.: 51976056, U1965106, and 52076215) and the Science Foundation of China University of Petroleum, Beijing (No.: 2462020XKJS01).

References

Commander, K.W., Prosperetti, A., 1989. Linear pressure waves in bubbly liquids: comparison between theory and experiments. J. Acoust. Soc. Am. 85 (2), 732–746. https://doi.org/10.1121/1.397599.

Devin, C., Taylor, D., 1959. Survey of thermal, radiation, and viscous damping of pulsating air bubbles in water. J. Acoust. Soc. Am. 31 (12), 1654–1667. https://doi.org/10.1121/1.1907675.

Fuster, D., Montel, F., 2015. Mass transfer effects on linear wave propagation in diluted bubbly liquids. J. Fluid Mech. 779, 598–621. https://doi.org/10.1017/jfm.2015.436.

Gilmore, F. R., 1952. The growth or collapse of a spherical bubble in a viscous compressible (Vol. 26, pp. 117–125).

Gradshteyn, I.S., Ryzhik, I.M., Jeffrey, A., Geronimus, Y.V., Tseytlin, M.Y., Fung, Y.C., 1981. Table of integrals, series, and products. J. Biomech. Eng. 58–58. https://doi.org/10.1115/1.3138251.

Herring, C., 1941. Theory of the pulsations of the gas bubble produced by an underwater explosion.

Keller, J.B., Miksis, M., 1980. Bubble oscillations of large amplitude. J. Acoust. Soc. Am. 68 (2), 628–633. https://doi.org/10.1121/1.384720.

Lezzi, A., Prosperetti, A., 1987. Bubble dynamics in a compressible liquid. part 2. second-order theory. J. Fluid Mech. 185, 289–321. https://doi.org/10.1017/s0022112087003185.

Plesset, M.S., 1949. The dynamics of cavitation bubbles. J. Appl. Mech. 16 (3), 277–282. https://doi.org/10.1115/1.4009975.

Prosperetti, A., 1977. Thermal effects and damping mechanisms in the forced radial oscillations of gas bubbles in liquids. J. Acoust. Soc. Am. 61 (1), 17–27. https://doi.org/10.1121/1.381252.

Prosperetti, A., Lezzi, A., 1986. Bubble dynamics in a compressible liquid. part 1. first-order theory. J. Fluid Mech. 168, 457. https://doi.org/10.1017/S0022112086000460.

Thuraisingham, R.A., 1997. New expressions of acoustic cross-sections of a single bubble in the monopole bubble theory. Ultrasonics 35 (5), 407–409. https://doi.org/10.1016/S0041-624X(97)00021-8.

Zhang, Y., 2012. Analysis of radial oscillations of gas bubbles in newtonian or viscoelastic mediums under acoustic excitation.

Zhang, Y., 2013. Heat transfer across interfaces of oscillating gas bubbles in liquids under acoustic excitation. international communications in heat and mass transfer, 43, 1–7. https://doi.org/10.1016/j.icheatmasstransfer.2013.01.007

Zhang, Y., Du, X., 2015. Influences of non-uniform pressure field outside bubbles on the propagation of acoustic waves in dilute bubbly liquids. Ultrason. Sonochem. 26, 119–127. https://doi.org/10.1016/j.ultsonch.2015.02.016.

Zhang, Y., Gao, Y., Guo, Z., Du, X., 2018a. Effects of mass transfer on damping mechanisms of vapor bubbles oscillating in liquids. Ultrason. Sonochem. 40, 120–127. https://doi.org/10.1016/j.ultsonch.2017.07.004.

Zhang, Y., Guo, Z., Gao, Y., Du, X., 2018b. Acoustic wave propagation in bubbly flow with gas, vapor or their mixtures. Ultrason. Sonochem. 40, 40–45. https://doi.org/10.1016/j.ultsonch.2017.03.048.

Chapter 9

Energy controlling mechanisms: Relationship with operational conditions

Aissa Dehane[a], Slimane Merouani[a] and Oualid Hamdaoui[b]

[a] *Laboratory of Environmental Process Engineering, Department of Chemical Engineering, Faculty of Process Engineering, University Salah Boubnider-Constantine 3, Constantine, Algeria,* [b] *Chemical Engineering Department, College of Engineering, King Saud University, Riyadh, Saudi Arabia*

9.1 Introduction

The propagation of ultrasonic waves through liquid induces vibrational motions in this medium, consequently, a series of expansions and compressions phases initiates the nucleation of micro-bubbles (acoustic cavitation). These tiny bubbles can grow and then collapse violently, where severe conditions of temperature and pressure (Tmax∼5000K, Pmax∼1000atm (Didenko et al., 1999)) are created at the end of compression phase, which favor the generation (Sonochemistry) of multiple active species (e.g., H_2O_2) and radicals (e.g.$^{\bullet}$OH, $HO_2^{\bullet}$, and $H^{\bullet}$) (Kamath et al., 1993; Toegel and Lohse, 2003; Yasui et al., 2004). These radicals are capable of initiating or promoting many fast reduction-oxidation reactions (Adewuyi, 2001). Therefore, these radicals have been employed in many chemical reactions such as the creation of nanomaterials, polymers, organic pollutant degradation… etc. (Ashokkumar, 2011; Matyjaszewski et al., 1995; Wang et al., 2011; Yang et al., 2008; Zhu et al., 2003). As a result, the increase of sonochemical process efficiency has attracted the attention of several researchers for a future scaling up to plant size of the different techniques applied in laboratory.

Over the last two decades, a huge number of theoretical and experimental works has been conducted in order to improve our understanding toward the different interactions between the acoustical cavitation (central event of sonochemistry) and operational conditions affecting the efficiency of these micro reactors (Lu et al., 2003; Moshaii et al., 2011; Nazari-Mahroo et al., 2018; Storey and Szeri, 1999; Wall et al., 1999). Practically, multibubble cavitation is a complicated system in which millions of bubbles interact with each other and with the sonic environment. The study of such a system is highly complex in comparison to the situation of single bubble cavitation, which is simple to analyze despite the fact that its production is a difficult process. Several numerical studies have attempted to examine the energy aspect of cavitation bubbles, although the majority of them concentrated on a single bubble system. Son et al. (2009) used a 3D cavitation energy analysis to investigate the influence of ultrasound frequency on the energetic efficiency of a sonoreactor. When the wave frequency is reduced, the greatest cavitation energy distribution is achieved. *Son*'s group (Son et al., 2011, 2008) also investigated the ultrasonic cavitation energy in a pilot-scale sonoreactor operating at 72, 110, and 170 kHz, as well as the properties of the ultrasound field at different liquid heights in a pilot-scale sonochemical reactor. also investigated the ultrasonic cavitation energy in a pilot-scale sonoreactor operating at 72, 110, and 170 kHz, as well as the properties of the ultrasound field at different liquid heights in a pilot-scale sonochemical reactor. Similarly, (Kuijpers et al., 2002) show that at low acoustic amplitudes and liquid temperatures, the energy conversion, as calculated by comparing the ultrasonic power delivered to the liquid and the radical production kinetics, is greatest.

Merouani et al. (2014a) and Vichare et al. (2000) investigated the impact of different operational conditions on the microscopic energy balance of an acoustic bubble; however, only the PV work is considered to express the internal bubble energy in the *Merouani* and *Vichare* works because they used an adiabatic model for the bubble collapse. Kerboua et al. (2021) have recently performed an energetic analysis to determine the primary types of energy that influence the internal energy and activity of a stable acoustic cavitation. It was determined that pressure forces work is the dominant

Energy Aspects of Acoustic Cavitation and Sonochemistry: Fundamentals and Engineering. DOI: https://doi.org/10.1016/B978-0-323-91937-1.00007-4
Copyright © 2022 Elsevier Inc. All rights reserved.

energy input during bubble oscillation, whereas heat transfer and enthalpy loss accompanying water condensation are the significant energetic losses. The same research group has conducted a theoretical analysis of the collected energy for a single acoustic cavitation in order to comprehend the method of acoustic energy conversion inside a control volume (Kerboua and Hamdaoui, 2019). The energy required to sustain the oscillation of the bubble increased proportionately to the reduction in ultrasonic frequency.

The present chapter tries to give an energetic analysis of a multibubble system under the action of sinusoidal ultrasonic irradiation. This analysis was conducted over a range of wave frequency from 204 to 613 kHz. The number density of bubbles was determined by using a semi-empirical method developed by Merouani et al. (2015a).

9.2 Model description

This chapter aims principally to evaluate the impacts of the different energy parameters, namely PV work, mass transport at the bubble wall (ṁ), heat exchange inside and outside the bubble ($\dot{Q}$) and the chemical reactions heat (ΔH), on the global energy of a multibubble system (MBS). The effects of energetic parameters are visualized for a range of ultrasound frequency, that is, 204, 362, and 613 kHz, where approximately the same acoustic intensity is adopted for this wave frequency range, that is, 1.64 W/cm^2 for 204 kHz, 1.72 W/cm^2 for 362 kHz, and 1.72 W/cm^2 for 613 kHz (Pflieger et al., 2015). The saturated gas is argon.

The global energy recovered from a MBS, that is, described as *power density E MB, is* calculated through multiplying the single bubble energy (*E SB*) by the number density of the bubbles (N):

$$EMB\left(J\,L^{-1}\,s^{-1}\right) = ESB\,(J)\,x\,N\left(L^{-1}\,s^{-1}\right) \tag{9.1}$$

Energetic contributions of each one of the mentioned energy parameters (*i.e.*, work, mass transport (ṁ), heat exchange ($\dot{Q}$) and the chemical reactions heat (ΔH)) in the global energy of an MBS is also calculated by Eq. 9.1 after determining their contributions for a single bubble system.

The variation of the internal bubble energy (ΔE) in time (Δt) for single bubble oscillating in argon-saturated water is given by (Dehane et al., 2021a,b,c,e):

$$\Delta E = -P\,(t)\,\Delta V\,(t) + 4\pi\,R^2\,\Delta t\,\frac{\dot{m}}{M_{H_2O}}\,C_{v,H_2O} + 4\pi\,R^2\Delta t\lambda\,\frac{\left(T_{liq}-T\right)}{L_{th}} - \frac{4}{3}\,\pi\,R^3\,\Delta t\,\sum_{i=1}^{n}\Delta H_i\,r_i \tag{9.2}$$

The first term in the right-hand side of Eq. 9.1 is the PV work. The second term is the energy carried by evaporating water molecules from the surrounding liquid into the bubble and by condensing vapor from the bubble into the liquid in Δt. The third term is the energy change due to the thermal conduction. The last term is the heat of chemical reactions taking place inside the bubble during the collapse, where ΔH_i and r_i are the enthalpy change and the rate of the i^{th} reaction respectively, that is, their mathematical expressions are given in (Dehane et al., 2021a). The chemical reaction inside the bubbles is described through a reaction scheme consisting in 25 reversible reactions involving nine species (*i.e.,* H$^\bullet$, O,$^\bullet$OH, H_2O, $HO_2^\bullet$, H_2O_2, H_2, O_2, and O_3), as shown in Table 1 of *Ref.* (Dehane et al., 2021d).

The instantaneous evolutions of the forth energy parameters of Eq. (9.1) are:

$$\frac{dE_{PV}}{dt} = -P\left(4\pi\dot{R}R^2\right) \tag{9.3}$$

$$\frac{dE_{\dot{Q}}}{dt} = 4\pi\,R^2\,\lambda\,\frac{\left(T_{liq}-T\right)}{L_{th}} \tag{9.4}$$

$$\frac{dE_{\dot{m}}}{dt} = 4\pi\,R^2\,\frac{\dot{m}}{M_{H_2O}}\,C_{v,H_2O} \tag{9.5}$$

$$\frac{dE_{\Delta H}}{dt} = -\frac{4}{3}\,\pi\,R^3\sum_{i=1}^{n}\Delta H_i\,r_i \tag{9.6}$$

In Eq. (9.1), the gas pressure inside the bubble *P(t)* is calculated using the Van der Waals:

$$P\,(t) = \frac{nR_gT}{V-nb} + \frac{an^2}{V^2} \tag{9.7}$$

where *a* and *b* are the Van de Waals constants, R_g is the universal gas constant, T is the temperature within the bubble and *V=4/3(πR^3)* is the bubble volume. The Van der Waals constants, *a* and *b*, are given in (Yasui et al., 2016). The variation of

the radial motion of the bubble $R(t)$ is defined by the modified Keller-Miksis equation (Yasui, 1995):

$$\left(1-\frac{\dot{R}}{C}+\frac{\dot{m}}{C\rho_L}\right)R\ddot{R}\ +\ \frac{3}{2}\dot{R}^2\left(1-\frac{\dot{R}}{3C}+\frac{2\dot{m}}{3C\rho_L}\right)\ =\ \frac{1}{\rho_L}\left(1+\frac{\dot{R}}{C}\right)\left[P_B(t)-P_A\sin\left(2\pi f\left(t+\frac{R}{C}\right)\right)-P_\infty\right]$$
$$+\ \frac{\ddot{m}R}{\rho_L}\left(1-\frac{\dot{R}}{C}+\frac{\dot{m}}{C\rho_L}\right)\ +\ \frac{\dot{m}}{\rho_L}\left(\dot{R}+\frac{\dot{m}}{2\rho_L}+\frac{\dot{R}\dot{m}}{2C\rho_L}\right)\ +\ \frac{R}{C\rho_L}\frac{dP_B(t)}{dt} \tag{9.8}$$

where ṁ is the net rate of evaporation per unit area and unit time, C is the sound speed in the medium (water), P_∞ is the ambient static pressureand ρ L is the liquid density. P A, the acoustic amplitude, is proportional to the acoustic intensity I_a as follows: $P\,A = (2I_a\ \rho\ L\mathrm{l}\ C)^{1/2}$. The exterior liquid pressure $PB(t)$ on the bubble wall is linked to the interior pressure $P(t)$ by (Yasui, 1995):

$$P_B\ (t)\ = P\ (t)\ -\ \frac{2\sigma}{R}\ -\ \frac{4\mu}{R}\left(\dot{R}+\frac{\dot{m}}{\rho_L}\right)\ -\ \dot{m}^{\,2}\left(\frac{\dot{1}}{\rho_L}-\frac{1}{\rho_g}\right) \tag{9.9}$$

where and μ are the liquid surface tension and viscosity, respectively.

The Hertz-Knudsen model (Eq. 9.5) was used for expressing the mass flux $\dot{m}$ of water evaporation and condensation at the bubble interface (Holzfuss, 2005):

$$\dot{m}\ =\alpha\ \bar{C}\ (T_s)\ \frac{\left[\rho^{sat}_{g,H_2O}-\rho_{g,H_2O}(R)\right]}{4} \tag{9.10}$$

α is the evaporation coefficient, that is, considered constant $\alpha = 0.4$, $\bar{\mathrm{C}}\ (\mathrm{T_s}) = \sqrt{8\mathrm{T_sR_g}/\pi\mathrm{M}_{H_2\mathrm{O}}})$ is the average velocity of molecules, $\rho_{g,\mathrm{H_2O}\,(R)}$ is the density of water vapor in the bubble and $\rho^{\mathrm{sat}}_{g,\mathrm{H_2O}} = 0.0173\ \mathrm{Kg\ m^{-3}}$ is the saturated vapor density. The temperature of the external bubble surface is T_s=T_{liq} .

The heat exchange between the interior and outside of the bubble is estimated by (Toegel and Lohse, 2003):

$$\dot{Q}\ =4\pi R^2\ \lambda_{mix}\ \frac{(T_{liq}-T)}{L_{th}} \tag{9.11}$$

$$L_{th}\ =\min\ \left\{\frac{R}{\pi},\sqrt{\frac{R\chi}{\dot{R}}}\right\} \tag{9.12}$$

χ and λ_{mix} are the thermal diffusivity and the heat conductivity of the gas mixture, L_{th} is the thickness of the thermal boundary layer. The calculation of these parameters (λ_{mix}, χ and L_{th}) is given in (Dehane et al., 2021a). The temperature (T) inside bubble is calculated by solving the following equation (Yasui, 1995):

$$E = n_{H_2O}\int_0^T C_{v,H_2O}(T)dT + n_{Ar}\int_0^T C_{v,Ar}\ (T)\ dT\ -\ \frac{an^2}{V} \tag{9.13}$$

where E is the internal energy of the bubble and $C_{V,H_2O}\ (T)$ ($C_{v,\mathrm{Ar}}\ (T)$) $C_{v,H_2O}\ (T)$ is the isochoric heat capacity of vapor (Argon) at temperature T, given as a polynomial approximation [expressions are available in (Dehane et al., 2021a)].

For the calculation of the number of bubbles "N", the semi-empirical method developed by Merouani et al. (2015a) is adopted (Eq. 9.14). The final form of this equation is given as function of the molar yield of H_2O_2,$^{\bullet}$OH and $HO_2^{\bullet}$ of a single bubble in addition to the production rate of H_2O_2 measured experimentally:

$$N\ \left(L^{-1}s^{-1}\right) = \frac{r_{H_2O_2}}{n_{H_2O_2}\ +0.5\left(n_{\bullet_{OH}}+n_{HO_2^{\bullet}}\right)} \tag{9.14}$$

where $r_{H_2O_2}$ $(mol\,L^{-1}\,s^{-1})$ is the production rate of H_2O_2, measured experimentally at each ultrasound frequency, $n_{H_2O_2}$,$n_{\bullet_{OH}}$ and $n_{HO_2^{\bullet}}$ are the molar yield of H_2O_2,$^{\bullet}$OH and $HO_2^{\bullet}$, respectively, obtained at the end of a single bubble collapse. It should be noted that the following assumptions have been adopted by Merouani et al. (2015a) for the development of their method:

- The cavitation is transient and the bubble breaks apart at the first collapse (when R_{min} is reached). This hypothesis is generally used in sonochemistry (Gireesan and Pandit, 2017; Sadighi-Bonabi et al., 2016; Yasui, 2001).
- At the end of bubble collapse, the acoustic cavitation breaks apart and we assume that the bubble content mix directly with the liquid phase surrounding the bubble.

By adopting *Merouani*'s assumptions, all energetic data simulated in our current study are given for inertial cavitation. This kind of bubbles are responsible all chemical aspects of ultrasound in aqueous media (Merouani et al., 2014b;

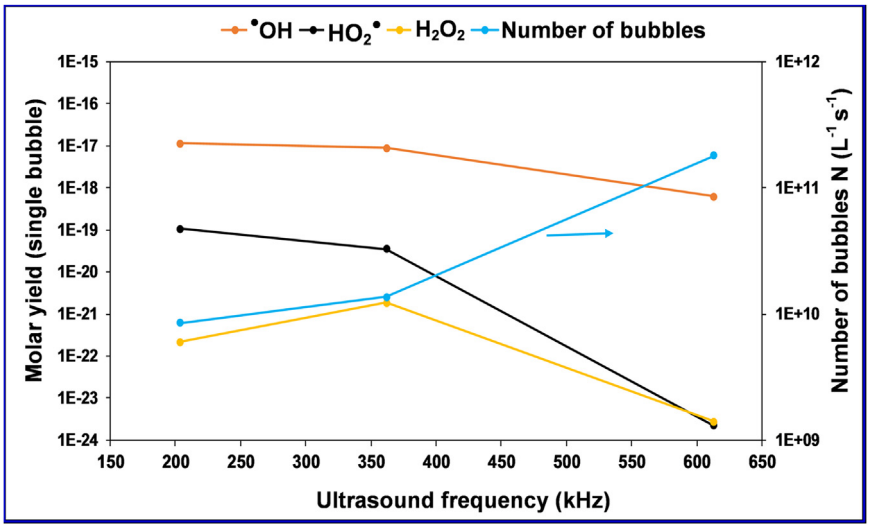

FIGURE 9.1 Molar production of $^{\bullet}OH$, $HO_2^{\bullet}$, and H_2O_2 molecules (mol) for a single bubble and the number of bubbles (L/s) for an ultrasound frequency range from 204 to 613 kHz. $I_{n,204kHz}$ =1.64 W/cm^2, $I_{n,363\ and\ 613\ kHz}$ = 1.72 W/cm^2, liquid temperature: 20°C and ambient static pressure: 1 atm.

Yasui, 2011). The second kind, that is, known as stable cavitation, cannot develop high temperature and pressure to be efficiently energetic. They oscillate about their average or equilibrium size for many acoustic cycles, in contrary to the inertial bubbles which grow to a certain size in one or at less than one acoustic cycles and violently collapse during the compression part of the sound wave (Merouani et al., 2015a). Stable cavitation bubbles are inactive in sonoluminescence and chemicals reactions (Merouani et al., 2015a).

For all single bubble calculations, the ambient bubble radius was taken as $R_0 = 3.9$ μm for 204 kHz, $R_0 = 3.2$ μm for 362 kHz and $R_0 = 2.9$ μm for 613 kHz (Brotchie et al., 2009; Merouani et al., 2015b). According to the experimental results of *Pflieger et al.* (Pflieger et al., 2015), rates of H_2O_2 production for an argon-saturated water are 4.92×10^{-8}, 6.02×10^{-8}, and 5.67×10^{-8} M/ s for the wave frequencies of 204, 362, and 613 kHz, respectively. The technique for resolving the set of differential equations that characterizes the single bubble system is available in (Dehane et al., 2021d,e). Detailed calculation of "N" can be found in (Merouani et al., 2015a; Merouani et al., 2016).

9.3 Chemical activity in single bubble and multibubble systems

Before undertaking multibubble energy analysis, we must verify the effect of ultrasound frequency on bubble population and sonoactivity. Fig. 9.1 shows the molar production of a single bubble, that is, $^{\bullet}OH$, $HO_2^{\bullet}$ and H_2O_2 quantities, in addition to the number of bubbles (N) over a range of ultrasound frequency (204, 362, and 613 kHz). As it can be seen, the increase of the wave frequency results in an increase of the number of acoustic cavities, that is, 8.55×10^9/L/s at 204 kHz, 1.37×10^{10}/L/s at 362 kHz and 1.81×10^{11}/L/s at 613 kHz. This trend is in good concordance with those found by *Merouani et al.* for air bubbles and frequency range of 300–1140 kHz (Merouani et al., 2015a)or oxygen bubbles under the experimental conditions of *Pétrier and Francony* (Petrier and Francony, 1997) and *Jiang et al.* (Jiang et al., 2006), that is, frequency: 20–800 kHz. The increase of number density of bubbles with the rise of ultrasound frequency is owing to the fact that when wave frequency goes up, the expansion and compression of bubble occur rapidly due to the short acoustic period. This leads to a faster yield of bubbles, because the number of cycles per second is increased proportionally with the increase of ultrasound frequency (Merouani et al., 2015a). On the other hand, for a single bubble case, molar yields of the different oxidants, that is,$^{\bullet}OH$, $HO_2^{\bullet}$, and H_2O_2, are observed to be decreased proportionally with the increase of ultrasound frequency, with an optimum of 1.86×10^{-21} mol for H_2O_2 at 362 kHz. The decrease of the molar yield is obviously explained by the reduction of collapse intensity of bubbles as the wave frequency is increased [40,44], consequently, bubble temperature (Fig. 9.2) is reduced as wells as the molar production of the different species. In contrast, for a multibubble system (Fig. 9.2), a slight optimum of 1.2×10^{-7} mol L/s is observed for the molar yield of $^{\bullet}OH$ radicals at 362 kHz. This result is in good agreement with the different experimental findings indicating the existence of frequency optimum at around 300 kHz with regard to the production rate of oxidants by bubbles (Beckett and Hua, 2001; Kang et al., 1999; Koda et al., 2003; Torres et al., 2008).

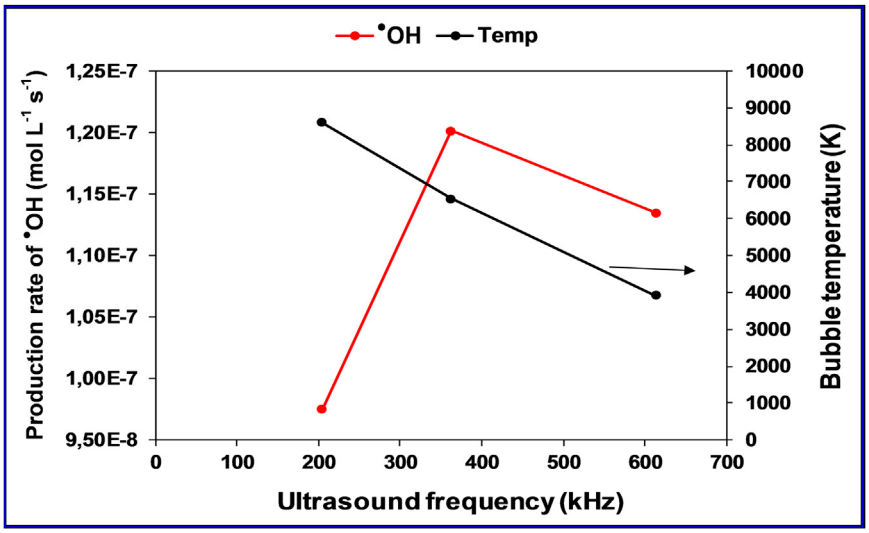

FIGURE 9.2 Production rate of •OH radicals for a multibubble system and the maximal bubble temperature (K) under the same conditions as in Fig. 9.1.

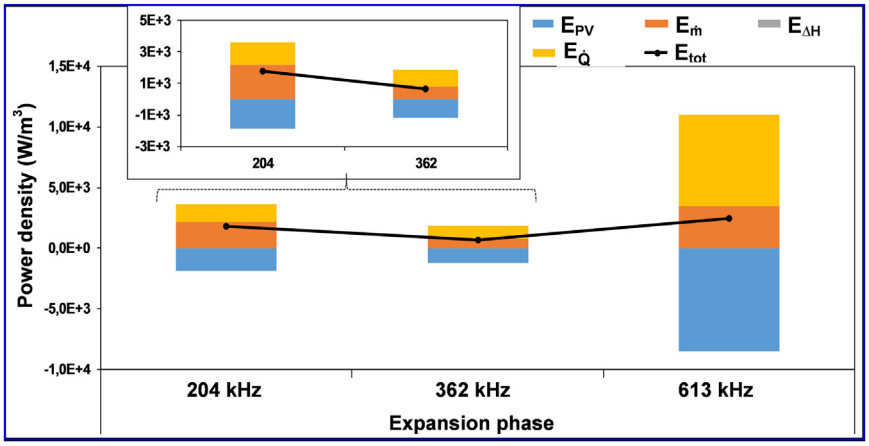

FIGURE 9.3 Energy flow per unit volume resulting from the effects of energy parameters, that is, PV work E_{PV}, heat exchange E_{PV}, reactions heat and mass transport, for a multibubble system during the expansion phase. Same conditions as in Fig. 9.1.

9.4 Energy variation of a multibubble system

In this section, energy analysis of the different energy parameters, that is, PV work, mass transport, heat exchange and reactions heat, in addition to the global bubble energy is performed according to the energy flow, either positive or negative effect, per unit volume (W/m^3). Additionally, the evolution of each energy parameter will be followed during expansion, collapse and the whole lifetime phases. From Figs. 9.3–9.5, it is observed that the effect of each of the energy parameters in the multibubble system is not ultrasound frequency dependent, conversely to the case of a single bubble case (K. Kerboua and Hamdaoui, 2019; Merouani et al., 2014a; Vichare et al., 2000). This means that other factors are influencing the different energetic parameters impacts.

Firstly, during the expansion phase (Fig. 9.3), it is seen that for ultrasound frequencies of 204 and 362 kHz, a comparable energy density, that is, energy flow per 1 m^3, is obtained through the PV work (negative effect), heat exchange (positive effect) and mass transport (positive effect). A similar trend is obtained by *Yasui* (Yasui, 1995) for a single air-bubble under a frequency of 26.5 kHz. In contrast, at 613 kHz, energy densities due to the PV work (-8.54×10^3 W/m^3) and heat transfer (7.57×10^3 W/m^3) are greater than that of mass transport (3.46×10^3 W/m^3). An accurate explanation of these behaviors is difficult; however, it seems that at 613 kHz there is no much time for vapor molecules to enter bubbles during the rarefaction phase (*i.e.,* short acoustic period), consequently, less energy is gained during this phase through mass transport compared to

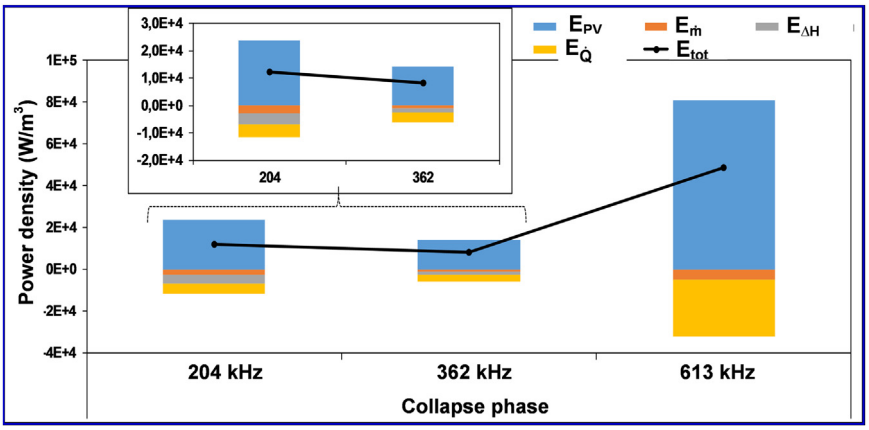

FIGURE 9.4 Internal energy variation of a multibubble system resulting from the effects of energy parameters (PV work, heat exchange, reactions heat, and mass transport) during the collapse phase. Same conditions as in Fig. 9.1.

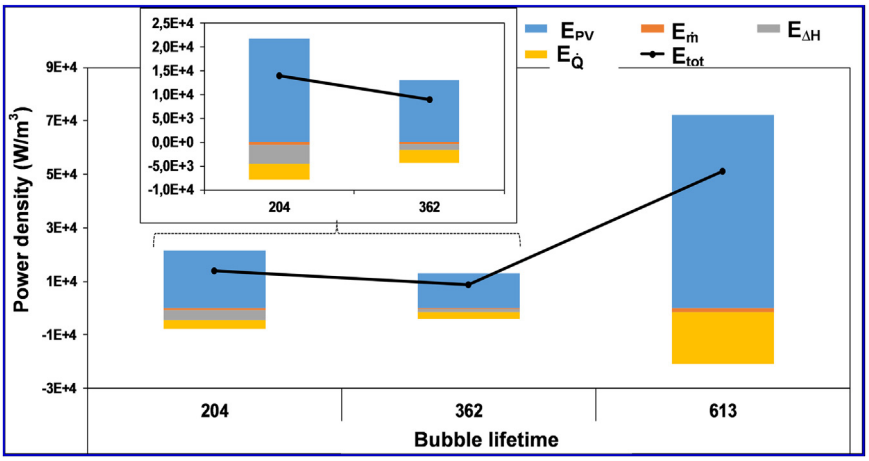

FIGURE 9.5 Internal energy variation of a multibubble system resulting from the effects of energy parameters (PV work, heat exchange, reactions heat and mass transport) during the whole lifetime period of the bubble. Same conditions as in Fig. 9.1.

that received by heat transfer or loosed via PV work. By observing Figs. 9.1 and 9.3, it appears that over the range from 204 to 362 kHz, the controlling key of power density for each energy parameter or the bubbles population is the single bubble system. Because it is found that in spite of the increase of bubbles number from 8.55×10^9/L/s at 204 kHz to 1.37×10^{10}/L/s at 362 kHz, more energy is injected into multibubble system at 204 kHz (1.79×10^3 W/m^3) compared to that at 362 kHz (6.55×10^2 W/m^3), as revealed in Fig. 9.3. This is corroborated by a single bubble case, where the total energy gained during the expansion phase is 2.09×10^{-10} and 4.78×10^{-11} J for ultrasound frequencies of 204 and 362 kHz, respectively. The same explanation is adopted for all the energy parameters.

At 613 kHz (Fig. 9.3), it is found that higher energies are consumed by the multibubble system via mass transport (3.46×10^3 W/m^3, positive impact), heat exchange (7.57×10^3 W/m^3, positive effect) and PV work (-8.54×10^3 W/m^3, negative impact) compared to the case of 204 and 362 kHz. On the contrary, at 613 kHz, it appears that the number of acoustic cavities generated at this frequency is the controlling parameter for the global power density of the multibubble system and for all energy parameters. This is due to the fact that in spite of the lower energy gained by a single bubble at 613 kHz (1.38×10^{-11} J compared to 2.09×10^{-10} and 4.78×10^{-11} J for 204 and 362 kHz, respectively) during the expansion phase, the large number of bubbles generated at this frequency at 613 kHz, that is, 1.81×10^{11}/L/s, increases the energy consumed for this case to 2.49×10^3 W/m^3 compared to that of 204 kHz (*i.e.,* 1.79×10^3 W/m^3, N = $8.55 \times 10^{+9}$/L/s) and 362 kHz (6.55×10^2 W/m^3, N = 1.37×10^{10}/L/s).

Secondly, during the collapse phase (Fig. 9.4), it can be seen that for all the used frequencies, an important amount of energy is received by bubbles population through the external pressure's forces of the surrounding liquid (*i.e.,* PV work).

On the other hand, it is found that the amount of energy dissipated at 204 kHz via mass transport (vapor condensation), heat exchange (outside the bubble) and reactions heat (endothermal character) is greater than that lost at 362 kHz for the same energy parameters (Fig. 9.4). Nevertheless, the global energy received by bubbles population over the collapse phase at 204 kHz, 1.22×10^4 W/m^3, is greater than that gained at 362 kHz (8.22×10^3 W/m^3) in spite of the increase of bubbles number from 8.55×10^9/L/s at 204 kHz to 1.37×10^{10}/L/s at 362 kHz. This result asserts again, as for the expansion regime, the fact that the single bubble system is the controlling key of power density either for bubbles population or for each of the energy parameters over the ultrasound frequency range from 204 to 362 kHz. The energy gained by a single bubble at 204 and 362 kHz during the compression phase is 1.42×10^{-9} and 6.00×10^{-10} J, respectively. It should be noted that the energy lost through mass transport, heat exchange and reactions heat at 204 kHz or 362 kHz are comparable. However, at 613 kHz (Fig. 9.4), it is observed that an important energy is dissipated through heat exchange (-2.70×10^4 W/m^3) compared to that lost via mass transport ($-4.91 \times 10^{+3}$ W/m^3), whereas the lowest amount of energy is consumed due to the overall endothermal character of chemical reactions ($-5.67 \times 10^{+1}$ W/m^3) taking place within the bubbles population. These results are in good agreement with those obtained of a single bubble energy analysis (data not shown). Moreover, a similar trend was obtained by Kerboua et al. (2021) through the study of the effect of dual frequency on the stable bubble energy balance. It should be noted that the energetic participation of chemical reactions is reduced proportionally with the increase of ultrasound frequency form 204 to 613kHz, where this is logically explained by the decrease of the bubble temperature as the wave frequency is increased (*i.e.*, sonoactivity of bubble goes down), as can be deduced from Figs 9.2 and 9.4. Similarly, to the previous expansion phase case, we found that above 362 kHz, the number of bubbles is the controlling parameter of power density either for bubbles population or for each of the energy parameters in multibubble system. This is because for a single bubble at 613 kHz, the energy gained during the compression mechanism is 2.69×10^{-10} J compared to 1.42×10^{-9} and 6.00×10^{-10} J at 204 and 362 kHz, respectively. However, the number of bubbles generated for this case (*i.e.*, 613 kHz, $N = 1.81 \times 10^{11}$/L/s) shows more consumption of energy (4.87×10^4 W/m^3) compared to the cases of 204 kHz (1.22×10^4 W/m^3, $N = 8.55 \times 10^9$/L/s) and 362 kHz (8.22×10^3 W/m^3, $N = 1.37 \times 10^{+10}$/L/s).

Finally, according to Fig. 9.5, it is found that approximately the same observations obtained through the compression phase are applied over the whole lifetime regime. The majority of energy input comes from the PV work mechanism. However, for the energetic mechanisms of reactions heat, mass transport and heat exchange, some competition is observed especially over the range of ultrasound frequency from 204 to 362 kHz. Accordingly, the power densities of these energy parameters are in the order:

- At 204 kHz: PV work > reactions heat > heat transfer > mass transport.
- At 362 kHz: PV work > heat transfer > reactions heat > mass transport.
- At 613 kHz: PV work > heat transfer > mass transport > reactions heat.

From Fig. 9.5, it can be concluded that for wave frequencies lower than 362 kHz, the majority of energy in multibubble system is dissipated through heat transfer and reactions heat, whereas, for higher frequencies (>362 kHz), heat exchange outside the bubble represents the main path of energy dissipation for the multibubble system. On the other hand, the lowest amounts of energy are lost via mass transport mechanism for all the used ultrasound frequencies. It should be noted that all these energetic analyses are based on the assumption of the direct fragmentation of bubbles at the first collapse.

9.5 Conclusion

In this chapter we attempted to reveal the impact of each of the energy parameters (PV work, heat exchange, mass transport and reaction heat) in a multibubble system over a range of ultrasound frequency (204, 362, and 613 kHz). Several interesting observations were obtained depending on bubbles lifetime phase and the adopted ultrasound frequency.

During the expansion, compression and the whole lifetime phases, it was observed that the impact of each of the energy parameters is not ultrasound frequency dependent conversely to the previous studies about the single bubble case. Additionally, it has been demonstrated that whatever the phase of bubbles lifetime, for ultrasound frequencies lower than 362 kHz, the controlling key of power density in multibubble system or for each of the energy parameters is the single bubble system. In contrast, above 362 kHz it seems that the number of acoustic cavities is the controlling parameter for the overall power density of the multibubble system and for each of the energy parameters.

During the expansion phase, it has been found that for a frequency range from 204 to 362 kHz, a comparable flow energy per unit volume is obtained through PV work (negative effect), heat exchange (positive effect) and mass transport (positive effect). At the opposite, at 613 kHz, energy densities due to the PV work, heat transfer are greater than that of mass transport.

During the collapse phase, it was observed that whatever the used wave frequency, an important amount of energy is gained by bubbles population via the external pressure forces of the surrounding liquid (PV work). Bellow 362 kHz, a

comparable energy flow is lost through mass transport (condensation at bubbles walls), heat exchange (outside bubbles) and reactions heat (endothermal character of reactions). Above 362 kHz, the majority of bubbles internal energy is dissipated via heat exchange compared to that lost by mass transport, whereas the lowest amount of energy is consumed due to the endothermal character of chemical reactions taking place within bubbles during the compression phase.

Finally, over the bubble's lifetime period, the majority of energy input per m^3 comes from the PV work. On the other hand, for wave frequencies lower than 362 kHz, energy is mainly dissipated through heat transfer and reactions heat, whereas, for higher frequencies, greater than 362 kHz, energy of bubbles population is lost principally via heat transfer outside the bubbles. The lowest amount of energy is dissipated through mass transport for all the used ultrasound frequencies.

Acknowledgments

This research. was funded by Algeria's Ministry of Education. and Science Research, as well as the General. Directorate for Scientific. Research and Technological. Development (GD-SRTD) (project No. A16N01UN250320220002).

References

Adewuyi, Y.G., 2001. Sonochemistry: environmental science and engineering applications. Ind. Eng. Chem. Res. 40 (22), 4681–4715. https://doi.org/10.1021/ie010096l.

Ashokkumar, M., 2011. The characterization of acoustic cavitation bubbles - an overview. Ultrasonics Sonochemistry, 18. Elsevier B.V., pp. 864–872, Issue 4.

Beckett, M.A., Hua, I., 2001. Impact of ultrasonic frequency on aqueous sonoluminescence and sonochemistry. J. Phys. Chem. A 105 (15), 3796–3802. https://doi.org/10.1021/jp003226x.

Brotchie, A., Grieser, F., Ashokkumar, M., 2009. Effect of power and frequency on bubble-size distributions in acoustic cavitation. Phys. Rev. Lett. 102 (8). https://doi.org/10.1103/PhysRevLett.102.084302.

Dehane, A., Merouani, S., Hamdaoui, O., 2021b. Carbon tetrachloride (CCl4) sonochemistry: a comprehensive mechanistic and kinetics analysis elucidating how CCl4 pyrolysis improves the sonolytic degradation of nonvolatile organic contaminants. Sep. Purif. Technol. 275, 118614. https://doi.org/10.1016/j.seppur.2021.118614.

Dehane, A., Merouani, S., Hamdaoui, O., 2021c. Theoretical investigation of the effect of ambient pressure on bubble sonochemistry: special focus on hydrogen and reactive radicals production. Chem. Phys. 547, 111171. https://doi.org/10.1016/j.chemphys.2021.111171.

Dehane, A., Merouani, S., Hamdaoui, O., Alghyamah, A., 2021a. A complete analysis of the effects of transfer phenomenons and reaction heats on sono-hydrogen production from reacting bubbles: impact of ambient bubble size. Int. J. Hydrogen Energy 46 (36), 18767–18779. https://doi.org/10.1016/j.ijhydene.2021.03.069.

Dehane, A., Merouani, S., Hamdaoui, O., Alghyamah, A., 2021d. A comprehensive numerical analysis of heat and mass transfer phenomenons during cavitation sono-process. Ultrason. Sonochem. 73, 105498. https://doi.org/10.1016/j.ultsonch.2021.105498.

Dehane, A., Merouani, S., Hamdaoui, O., Alghyamah, A., 2021e. Insight into the impact of excluding mass transport, heat exchange and chemical reactions heat on the sonochemical bubble yield: bubble size-dependency. Ultrason. Sonochem. 73, 105511. https://doi.org/10.1016/j.ultsonch.2021.105511.

Didenko, Y.T., McNamara, W.B., Suslick, K.S., 1999. Hot spot conditions during cavitation in water. J. Am. Chem. Soc. 121 (24), 5817–5818. https://doi.org/10.1021/ja9844635.

Gireesan, S., Pandit, A.B., 2017. Modeling the effect of carbon-dioxide gas on cavitation. Ultrason. Sonochem. 34, 721–728. https://doi.org/10.1016/j.ultsonch.2016.07.005.

Holzfuss, J., 2005. Unstable diffusion and chemical dissociation of a single sonoluminescing bubble. Physical Review E - Statistical, Nonlinear, and Soft Matter Physics 71 (2). https://doi.org/10.1103/PhysRevE.71.026304.

Jiang, Y., Petrier, C., Waite, T.D., 2006. Sonolysis of 4-chlorophenol in aqueous solution: effects of substrate concentration, aqueous temperature and ultrasonic frequency. Ultrason. Sonochem. 13 (5), 415–422. https://doi.org/10.1016/j.ultsonch.2005.07.003.

Kamath, V., Prosperetti, A., Egolfopoulos, F.N., 1993. A theoretical study of sonoluminescence. J. Acoust. Soc. Am. 94 (1), 248–260. https://doi.org/10.1121/1.407083.

Kang, J.W., Hung, H.M., Lin, A., Hoffmann, M.R., 1999. Sonolytic destruction of methyl tert-butyl ether by ultrasonic irradiation: the role of O_3, H_2O_2, frequency, and power density. Environ. Sci. Technol. 33 (18), 3199–3205. https://doi.org/10.1021/es9810383.

Kerboua, K., Hamdaoui, O., 2019. Void fraction, number density of acoustic cavitation bubbles, and acoustic frequency: a numerical investigation. J. Acoust. Soc. Am. 146 (4), 2240–2252. https://doi.org/10.1121/1.5126865.

Kerboua, Kaouther, Hamdaoui, O., Alghyamah, A, 2021. Energy balance of high-energy stable acoustic cavitation within dual-frequency sonochemical reactor. Ultrason. Sonochem. 73, 105471. https://doi.org/10.1016/j.ultsonch.2021.105471.

Koda, S., Kimura, T., Kondo, T., Mitome, H., 2003. A standard method to calibrate sonochemical efficiency of an individual reaction system. Ultrason. Sonochem. 10 (3), 149–156. https://doi.org/10.1016/S1350-4177(03)00084-1.

Kuijpers, M.W.A., Kemmere, M.F., Keurentjes, J.T.F., 2002. Calorimetric study of the energy efficiency for ultrasound-induced radical formation. In Ultrasonics 40 (1–8), 675–678. https://doi.org/10.1016/S0041-624X(02)00197-X.

Lu, X., Prosperetti, A., Toegel, R., Lohse, D., 2003. Harmonic enhancement of single-bubble sonoluminescence. Physical Review E - Statistical Physics, Plasmas, Fluids, and Related Interdisciplinary Topics 67 (5), 9. https://doi.org/10.1103/PhysRevE.67.056310.

Matyjaszewski, K., Greszta, D., Hrkach, J.S., Kim, H.K., 1995. Sonochemical synthesis of polysilylenes by reductive coupling of disubstituted dichlorosilanes with alkali metals. Macromolecules 28 (1), 59–72. https://doi.org/10.1021/ma00105a007.

Merouani, S., Ferkous, H., Hamdaoui, O., Rezgui, Y., Guemini, M., 2015a. A method for predicting the number of active bubbles in sonochemical reactors. Ultrason. Sonochem. 22, 51–58. https://doi.org/10.1016/j.ultsonch.2014.07.015.

Merouani, S., Hamdaoui, O., Boutamine, Z., Rezgui, Y., Guemini, M., 2016. Experimental and numerical investigation of the effect of liquid temperature on the sonolytic degradation of some organic dyes in water. Ultrason. Sonochem. 28, 382–392. https://doi.org/10.1016/j.ultsonch.2015.08.015.

Merouani, S., Hamdaoui, O., Rezgui, Y., Guemini, M., 2014a. Energy analysis during acoustic bubble oscillations: relationship between bubble energy and sonochemical parameters. Ultrasonics 54 (1), 227–232. https://doi.org/10.1016/j.ultras.2013.04.014.

Merouani, S., Hamdaoui, O., Rezgui, Y., Guemini, M., 2014b. Theoretical procedure for the characterization of acoustic cavitation bubbles. Acta Acustica United with Acustica 100 (5), 823–833. https://doi.org/10.3813/AAA.918762.

Merouani, S., Hamdaoui, O., Rezgui, Y., Guemini, M., 2015b. Sensitivity of free radicals production in acoustically driven bubble to the ultrasonic frequency and nature of dissolved gases. Ultrason. Sonochem. 22, 41–50. https://doi.org/10.1016/j.ultsonch.2014.07.011.

Moshaii, A., Faraji, M., Tajik-Nezhad, S., 2011. Study of single bubble sonoluminescence in phosphoric acid. Ultrason. Sonochem. 18 (5), 1148–1152. https://doi.org/10.1016/j.ultsonch.2010.12.001.

Nazari-Mahroo, H., Pasandideh, K., Navid, H.A., Sadighi-Bonabi, R., 2018. Influence of liquid compressibility on the dynamics of single bubble sonoluminescence. Physics Letters, Section A: General, Atomic and Solid State Physics, 382 (30), 1962–1967. https://doi.org/10.1016/j.physleta.2018.04.058.

Petrier, C., Francony, A., 1997. Incidence of wave-frequency on the reaction rates during ultrasonic wastewater treatment. Water Sci. Technol. 35, 175–180. https://doi.org/10.1016/S0273-1223(97)00023-1.

Pflieger, R., Chave, T., Vite, G., Jouve, L., Nikitenko, S.I., 2015. Effect of operational conditions on sonoluminescence and kinetics of H_2O_2 formation during the sonolysis of water in the presence of ar/o2 gas mixture. Ultrason. Sonochem. 26, 169–175. https://doi.org/10.1016/j.ultsonch.2015.02.005.

Sadighi-Bonabi, R., Alijan Farzad Lahiji, F., Razeghi, F., 2016. The effect of viscosity, applied frequency and driven pressure on the laser induced bubble luminescence in water–sulfuric acid mixtures. Physics Letters, Section A: General, Atomic and Solid State Physics, 380 (27–28), 2219–2226. https://doi.org/10.1016/j.physleta.2016.02.050.

Son, Y., Lim, M., Ashokkumar, M., Khim, J., 2011. Geometric optimization of sonoreactors for the enhancement of sonochemical activity. J. Phys. Chem. C 115 (10), 4096–4103. https://doi.org/10.1021/jp110319y.

Son, Y., Lim, M., Khim, J., 2009. Investigation of acoustic cavitation energy in a large-scale sonoreactor. Ultrason. Sonochem. 16 (4), 552–556. https://doi.org/10.1016/j.ultsonch.2008.12.004.

Son, Y., Lim, M., Park, I.B., Khim, J., 2008. Analysis of the ultrasonic cavitation energy in a pilot-scale sonoreactor. Japan. J. Appl. Phys. 47 (5), 4119–4122. https://doi.org/10.1143/JJAP.47.4119.

Storey, B.D., Szeri, A.J., 1999. Mixture segregation within sonoluminescence bubbles. J. Fluid Mech. 396, 203–221. https://doi.org/10.1017/S0022112099005984.

Toegel, R., Lohse, D., 2003. Phase diagrams for sonoluminescing bubbles: a comparison between experiment and theory. J. Chem. Phys. 118 (4), 1863–1875. https://doi.org/10.1063/1.1531610.

Torres, R.A., Pétrier, C., Combet, E., Carrier, M., Pulgarin, C., 2008. Ultrasonic cavitation applied to the treatment of bisphenol A. effect of sonochemical parameters and analysis of bpa by-products. Ultrason. Sonochem. 15 (4), 605–611. https://doi.org/10.1016/j.ultsonch.2007.07.003.

Vichare, N.P., Senthilkumar, P., Moholkar, V.S., Gogate, P.R., Pandit, A.B., 2000. Energy analysis in acoustic cavitation. Ind. Eng. Chem. Res. 39 (5), 1480–1486. https://doi.org/10.1021/ie9906159.

Wall, M., Ashokkumar, M., Tronson, R., Grieser, F., 1999. Multibubble sonoluminescence in aqueous salt solutions. Ultrason. Sonochem. 47 (5), 7–14. https://doi.org/10.1016/s1350-4177(98)00037-6.

Wang, X.K., Wei, Y.C., Wang, C., Guo, W.L., Wang, J.G., Jiang, J.X., 2011. Ultrasonic degradation of reactive brilliant red K-2BP in water with CCl_4 enhancement: performance optimization and degradation mechanism. Sep. Purif. Technol. 81 (1), 69–76. https://doi.org/10.1016/j.seppur.2011.07.003.

Yang, L., Sostaric, J.Z., Rathman, J.F., Weavers, L.K., 2008. Effect of ultrasound frequency on pulsed sonolytic degradation of octylbenzene sulfonic acid. J. Phys. Chem. B 112 (3), 852–858. https://doi.org/10.1021/jp077482m.

Yasui, K., 1995. Effects of thermal conduction on bubble dynamics near the sonoluminescence threshold. J. Acoust. Soc. Am. 98 (5), 2772–2782. https://doi.org/10.1121/1.413242.

Yasui, K., 2001. Temperature in multibubble sonoluminescence. J. Chem. Phys. 115 (7), 2893–2896. https://doi.org/10.1063/1.1395056.

Yasui, K., 2011. Fundamentals of acoustic cavitation and sonochemistry. Theoretical and Experimental Sonochemistry Involving Inorganic Systems. Springer, Netherlands, pp. 1–29.

Yasui, K., Tuziuti, T., Iida, Y., 2004. Optimum bubble temperature for the sonochemical production of oxidants. In Ultrasonics 42 (1–9), 579–584. https://doi.org/10.1016/j.ultras.2003.12.005.

Yasui, K., Tuziuti, T., Kanematsu, W., 2016. Extreme conditions in a dissolving air nanobubble. Phys. Rev. E 94 (1). https://doi.org/10.1103/PhysRevE.94.013106.

Zhu, J.J., Xu, S., Wang, H., Zhu, J.M., Chen, H.Y., 2003. Sonochemical synthesis of cdse hollow spherical assemblies via an in-situ template route. Adv. Mater. 15 (2), 156–159. https://doi.org/10.1002/adma.200390033.

Part III

Ultrasound assisted processes, sonochemical reactors and energy efficiency

10. Efficiency assessment and mapping of cavitational activities in sonochemical reactors 157
11. Sources of dissipation: an outlook into the effects of operational conditions 183
12. Mechanistic issues of energy efficiency of an ultrasonic process: Role of free and dissolved gas 193
13. Simulation of sonoreators accounting for dissipated power 219
14. Technological designs and energy efficiency: the optimal paths 249

Chapter 10

Efficiency assessment and mapping of cavitational activities in sonochemical reactors

Vinayak S. Sutkar, Amit V. Mahulkar and Aniruddha B. Pandit
Department of Chemical Engineering, Institute of Chemical Technology, Mumbai, India

10.1 Introduction

Cavitation is a phenomenon of nucleation, growth, and subsequent collapse (quasiadiabatic) of millions of microbubbles at millions of locations in a liquid medium at ambient operating conditions. Subsequent collapse of these microbubbles results in the generation of conditions of very high temperatures and pressures (a few hundred atmospheres pressure and a few thousand Kelvin temperature), known as pulse. Apart from the formation of hot spots, cavitation also results in strong acoustic streaming (liquid circulation), high shear stress near the microbubble wall, formation of micro-jets near the solid surface (due to the asymmetric collapse of microbubbles), generation of highly reactive free radicals and turbulence resulting in enhanced transport properties of the species. Thus, cavitation-based processes offer a viable, promising, and energy-efficient alternative to the conventional processes. Due to the above-mentioned effects, the cavitation phenomenon has been widely used in a variety of chemical transformations as chemical synthesis (Gogate et al., 2006) (in homogenous and heterogeneous reaction systems, to accelerate the rate of reaction, reduction in reaction time, increase in the reaction yield, possible switching of the reaction pathways resulting in increased selectivity, increase the effectiveness of the catalyst, reduction in induction time, and initiate the chemical reaction due to the generation of highly reactive free radicals.), water and wastewater treatment (oxidation or degradation of complex chemicals such as p-nitrophenol, Rhodamine B, phenol, dichloromethane, parathion, pentachlorophenate, CFC 11, and CFC 113, o-dichlorobenzene and dichloromethane, potassium iodide, sodium cyanide and carbon tetrachloride etc.), textile processing (enhancing the efficacy of dyeing technique), biotechnology (homogenization, water disinfection, and cell disruption for release of intracellular enzymes and foam control in bioreactors), crystallization (to initiate the nucleation and reduce agglomeration), atomization, polymer chemistry, extraction, emulsification and petrochemical industries, etc. So far, acoustic cavitation has proven promising and is widely used in producing the desired chemical and/or physical changes in processing applications, in which cavitation is generated by passing an ultrasound wave through the liquid medium.

However, in spite of extensive research and the vital potential that has proven on the laboratory scale, there are a limited number of applications being carried out on an industrial scale of operations owing to the lack of expertise in the fields of material science, acoustics, reactor design, and scale-up strategies etc. The possible challenges during the design and operation of cavitational reactors are:

- Exact quantification of the cavitational activities with respect to operating conditions, geometric configurations, and energy input,
- Lack of design strategies,
- Stochastic and localized behavior of the cavitation phenomena.

In this chapter, we will discuss energy efficiency assessment methods, and the distribution of cavitational activities in various types of sonochemical or cavitational reactors. We will also discuss various mapping techniques used to quantify the distribution of the cavitational activities, current reactor design trends, and the selection and optimization of operating parameters based on energy assessment and spatial and temporal distribution of cavitational activity.

Energy Aspects of Acoustic Cavitation and Sonochemistry: Fundamentals and Engineering. DOI: https://doi.org/10.1016/B978-0-323-91937-1.00015-3
Copyright © 2022 Elsevier Inc. All rights reserved.

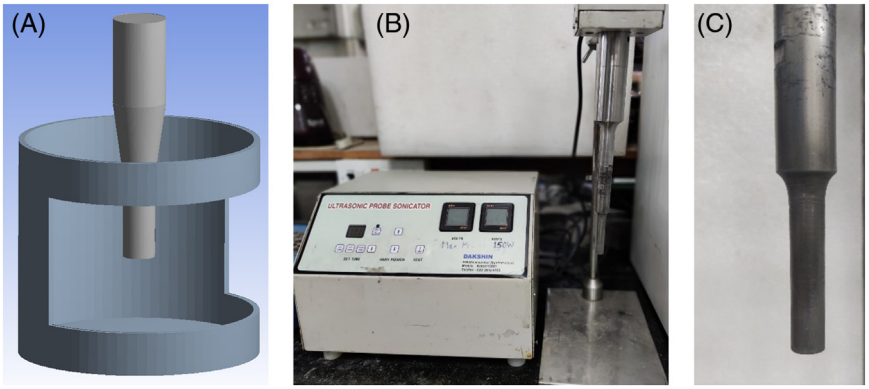

FIGURE 10.1 Ultrasonic horn. (A) 3D Exploded view of cylindrical vessel with ultrasonic horn. Actual image of ultrasonic horn (tip diameter of 13 mm, Dakshin Pvt. Ltd., India) with 250 W maximum power and 20 kHz frequency., (B) Ultrasound generator, and (C) close up view of ultrasonic horn without reaction vessel.

10.2 Types, classification and working principle of the sonochemical reactors

Ultrasonic horns: Horns type of sonochemical reactors are most commonly used for laboratory scale of operations because of its versatility over the range of operating volume and power. These reactors mainly consist of a reaction vessel of either cylindrical, rectangular, or square shape, ultrasound generator, power amplifier, and a temperature indicator, and/or controller. An ultrasound generator is connected to the transducer, which converts electrical energy into mechanical energy based on the piezoelectric effect. Generally, cavitation is induced by immersing the transducer tip (diameter in the range of 0.1-3 cm) at a certain distance from the free liquid surface. A schematic diagram of ultrasonic horns type of sonochemical reactors is shown in Fig. 10.1.

This arrangement allows flexibility to quickly adjust immersion transducer height, and input power. As the sound wave propagates through the liquid medium, cavitational intensity decreases exponentially with an increase in the distance from the transducer tip (that is, moving away from the transducer tip). In ultrasonic horn types of sonochemical reactors, pronounced distribution of cavitational effects is observed in a zone very close to the vibrating surface. Based on the frequency of irradiation and input power, it is generally assumed that the cavitational intensity becomes weak after 2–5 cm. The maximum operating capacity of the reactor generally ranges from 10 to 2000 mL. Horn type of sonochemical reactors usually have a single source of ultrasound generator. Typically, ultrasonic horns are suitable in laboratory scale of operations for characterization studies or checking the efficacy of the cavitation for the desired operation. Ultrasonic horn type of sonochemical reactors often experience low energy efficiency. This is mainly due to the fact that most of the energy dissipation is observed in a close vicinity to the horn tip. Hence, the cavitational activity is also limited to the proximity of the horn tip. Furthermore, ultrasonic horn type sonochemical reactors suffer from erosion due to high intensity.

Ultrasonic baths: Bath type of sonochemical reactors is used on both laboratory and pilot scale of operations. For laboratory operations reactor volume is lower compared with pilot scale, in the range of few liters. Ultrasonic bath is generally used after successful checking of the efficacy of the cavitation phenomena in ultrasonic horn. These reactors mainly consist of a reaction vessel of cylindrical, rectangular, square, pentagonal, hexagonal etc. shapes, ultrasound generator, power amplifier and temperature indicator and/or controller. Based on the application and the scale of operation, ultrasonic bath types of sonochemical reactors possess multiple transducers of identical or different frequencies. Multiple transducers significantly increase the cavitationally active volume. Multiple transducers are either located at the bottom or the side. Bottom transducers are arranged in triangular or square pitch whereas side transducers are arranged at an equal distance in vertical or peripheral directions. Actual images of ultrasonic bath reactors with two transduces located at the bottom is shown in Fig. 10.2.

Provision of multiple transducers allows to distribution of energy over a large volume. This improves the energy utilization efficiency by reducing the sound wave attenuation, erosion, and particle shedding close to the transducer/irradiating surface. Furthermore, the number of transducers and the position of each transducer can be easily modified to maintain a uniform and coherent distribution of cavitational activities. The ultrasonic bath type of reactor is operated in a batch or continuous manner, or in a series (where multiple units are connected to each other in flow through arrangement). Also, based on the batch size or operating volume, electric energy is supplied to the transducer in a continuous or a pulsed manner

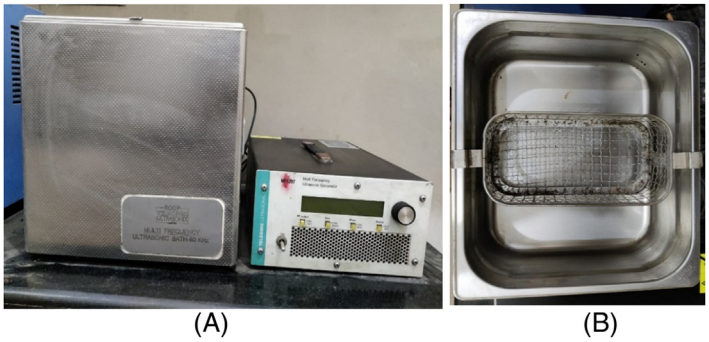

FIGURE 10.2 Ultrasonic bath. (A) Front view of dual frequency (209 and 694 kHz) ultrasonic bath with ultrasound generator (Roop Telesonics, India), (B) Top view of ultrasonic bath.

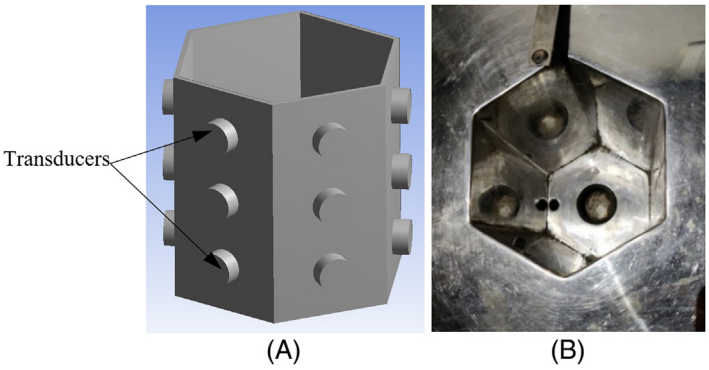

FIGURE 10.3 Hexagonal flow cell. (A) 3D view of hexagonal triple frequency flow cell with total 18 transducers (3 on each side, and with power of 50 W per transducer). (B) Actual image of the hexagonal flow cell, with capacity of 8 L, Transducers on the opposite sides have the same frequency, three operating frequencies 25, 30, and 41.5 kHz.

to avoid excessive heating of the transducer surfaces. Based on requirements, either two or more sets of transducers can be mounted on the ultrasonic bath. The transducers can operate independently or simultaneously at different frequencies.

For sonochemical reactors with multiple transducers, an appropriate selection of a number of transducers, frequency irradiation (identical or different), and the position of the transducers on the surface the reactors play an important role in maximizing energy utilization and uniform distribution of the cavitational activities. The combination of triple frequencies illustrates the maximum bubble size and highest lifetime as compared to the dual and single frequency operations. Gogate et al. performed experiments with single, dual, and triple frequency on the degradation of formic acid using triple-frequency hexagonal flow cell (f1 = 41.5 kHz, f2 = 30 kHz, and f3 = 25 kHz, operating capacity of 8 L), which is shown in Fig. 10.3. They reported that the combination of three frequencies gives maximum cavitational yields as compared to dual and single frequency operations (Gogate et al., 2003).

The hexagonal flow cell consists of eighteen transducers (three on each face of the hexagon) and seven combinations of operating frequencies. The distribution of cavitational activities was investigated using KI dosimetry and degradation of a reactive dye, Rhodamine B (Gogate et al., 2003). They reported uniform distribution of cavitational activities and higher energy efficiencies as compared with the conventional reactor configurations. The distribution of cavitational activities was obtained by measuring local pressure distribution by using a hydrophone and was reported to be uniform (Kumar et al., 2007). A similar type of result was reported in aluminum foil erosion (Avvaru & Pandit, 2008a). Uniform and intense erosion patterns were reported during triple frequency operation as compared to single frequency operation. Hodnett & Zeqiri used a cylindrical reactor (of diameter 312 mm and height 330 mm of operating capacity ~25 liters) with thirty transducers (of 25 kHz and a maximum power of 600 W) on the outer periphery placed in 10 columns with three in each row (Hodnett & Zeqiri, 2008). A 3D representation of the cylindrical reactor is shown in Fig. 10.4.

Ulltrasonic bath with Radial horn: In an ultrasonic bath with a longitudinal vibrating transducer, sound waves are generated from the curved surface of the cylindrical transducer. Sometimes these horns are also referred to as radial horns, because its shape is very similar to a horn type transducer-but the sound waves are emitted radially outwards from the curved

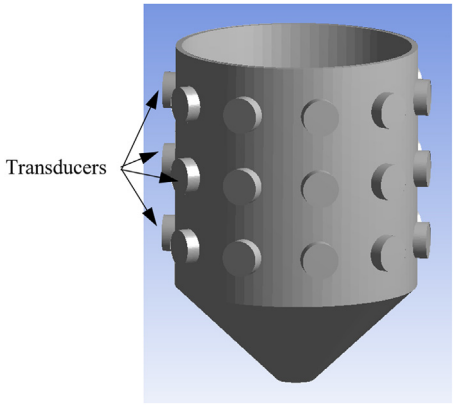

FIGURE 10.4 Multi transducer cylindrical sonochemical *reactor based on Hodnett, M. and Zeqiri, B. (2008). Toward a reference ultrasonic cavitation vessel: Part 2 - Investigating the spatial variation and acoustic pressure threshold of inertial cavitation in a 25 kHz ultrasound field. IEEE Transactions on Ultrasonics, Ferroelectrics, and Frequency Control, 55(8), 1809–1822. https://doi.org/10.1109/TUFFC.2008.864* Recreated 3D view of cylindrical sonochemical reactor with thirty transducers on side wall.

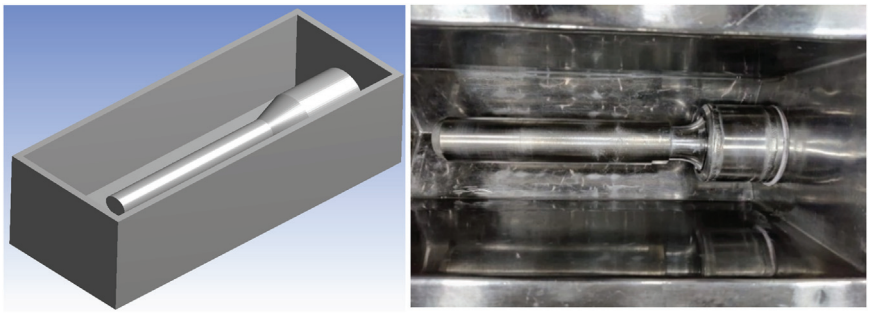

FIGURE 10.5 Ultrasonic bath with longitudinal vibrations. (A) 3D view and (B) actual image of ultrasonic bath with longitudinal (radial) horn. Manufacturer Roop Telesonics, India, 8 L capacity, 25 kHz, and 150 kW of power.

surface. One of the distinguishing features of a longitudinally vibrating transducer configuration is the large area of the irradiating surface, which is able to generate higher cavitational activity in the liquid medium. Bhirud et., (2010) performed calorimetric measurements in the ultrasound bath (frequency = 26 kHz and power =s 150 W) with longitudinally vibrating transducer (diameter = 3 cm and length = 24 cm). The 3D view of an Ultrasonic bath with the longitudinal transducer is shown in Fig. 10.5. The operating capacity of this sonochemical reactor (L x W x H = 15 × 33 × 20 cm^3) is 8 liters with the transducer. Maximum energy efficiencies were obtained at 65.9% of the capacity, which is much higher as compared with the conventional ultrasonic horn (Bhirud et al., 2004).

Mode of operation: All the sonochemical reactors can be operated in batch, semi-batch, and continuous mode. In the batch type of reactor, a specific amount of liquid is irradiated for a specified time, whereas in semi-batch reactor one of the reactant streams is kept continuous. Ultrasonic irradiation is usually accompanied with by the rise in temperature of the system. For heat sensitive materials, active external temperature control is usually provided (chiller or water bath). Passive mode of temperature control involves controlling the energy input to the system by operating in a pulsating manner (on and off mode). (Mitome & Hatanaka, 2002) studied and optimized the performance of the pulsating sonochemical reactors via sonoluminescence and observed that pulsing with a constant input power level enhanced sonoluminescence. Also, reported pulsing is more effective at a higher frequency as compared with lower frequency.

It should be noted that the transducer operation mode is independent of the reactor operation mode. Based on process requirements, the transducer and the reactor modes can be adjusted independently. For instance, in continuous operation of a reactor and transducer, the reactants are fed and products are removed continuously. Fig. 10.6 shows one of the tubular flow cell reactors. The tubular flow cell reactor consists of a vertical pipe with six transducers (of 33 kHz frequency and 300 W maximum power). This modular design also makes it possible to design sonochemical reactors for large scale & harsh operating conditions (corrosive, high pressure, abrasive slurries etc.).

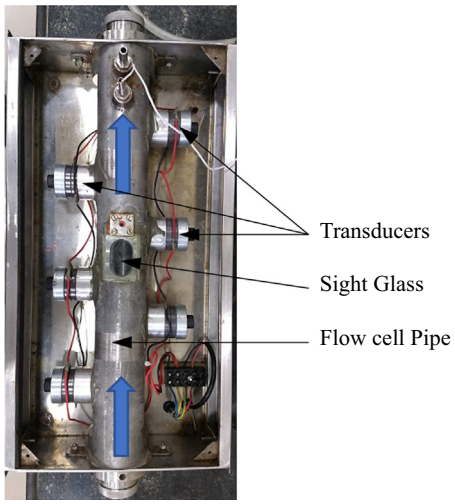

FIGURE 10.6 Tubular ultrasonic flow cell. Laboratory scale tube sonicator of length 450 mm and diameter 50 mm with maximum operating capacity of 850 ml, Sonicator possess six transduces with 33 kHz frequency and 50 W each.

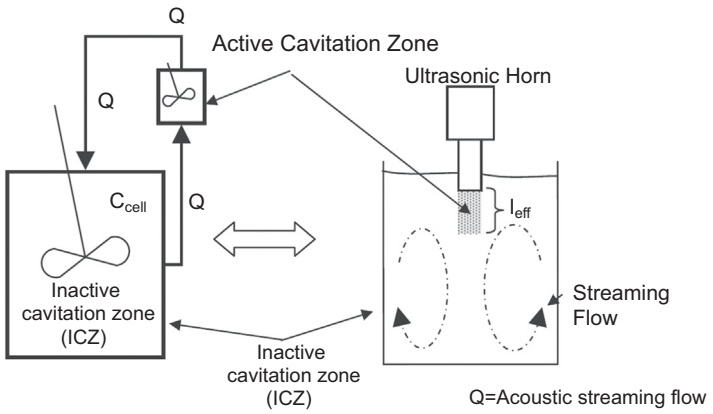

FIGURE 10.7 Active and Passive zone in cavitation reactor. *Modified from Mahulkar, A. V., Riedel, C., Gogate, P.R., Neis, U. & Pandit, A. B. (2009). Effect of dissolved gas on efficacy of sonochemical reactors for microbial cell disruption: Experimental and numerical analysis. Ultrasonics Sonochemistry, 16(5), 635–643.* https://doi.org/10.1016/j.ultsonch.2008.11.005 Schematic representation of active and passive (also known as inactive) cavitation zone in ultrasonic horn type sonochemical reactor. The modeling approach hypothesizing horn type reactor to he represented by two ideal continuous stirred tank reactors (CSTRs).

10.3 Overview of cavitational activities in the sonochemical reactors

10.3.1 Spatial and temporal distribution (mapping activities and bubble dynamics studies)

As briefly mentioned in the previous section, the cavitational activity in various sonochemical reactors significantly varies both in space and time, depending on the configuration of the transducer and mode of operation. The design and operating parameters determine the spatial distribution of cavitational activity; the temporal variation in cavitational activity significantly depends on variation in nucleation source and temperature with time.

10.3.2 Active and passive cavitational zones

In cavitation reactors, zones with high cavitational activity are called "active zones." Usually, active zones are located in the closed vicinity to the ultrasound source. (Mahulkar et al., 2009) modeled the sonochemical reactor by categorizing it as "Active" and "Passive" (Inactive) zone (Fig. 10.7). For systems operating at atmospheric conditions, the active cavitation zone is the volume where the pressure amplitude can go below the vapor pressure of liquid at the temperature. However, it

is also possible that nucleation can also happen at lower pressure amplitude, because of contaminants and discontinuity, but this criterion ensures generation of cavitation even in relatively cleaner liquids.

Zones with negligible cavitation activity are called passive or inactive zones. In these zones, the pressure amplitude is too low to create any substantial cavitational growth. Initially, it might seem that minimizing the distribution of passive or increasing active cavitation zone may improve the performance of the sonochemical reactor. However, by appropriate sizing distribution of the active and passive zones, the energy efficiency can be significantly improved. The positive cavitation zone increases the overall mass of the system, which can dampen the temperature rise and impart passive cooling to the system. By appropriately maintaining exchange of reactants between these zones at intervals, the temporal variation in the cavitational activity can be controlled/eliminated. For an efficient sonochemical reactor design, it is paramount to distribute the passive (or inactive) cavitation zone inside as well as outside the sonochemical reactor.

The modeling approach represented above is also very useful for designing large scale sonochemical reactors, for example, flow cells. This approach allows the chemical reaction engineering principles (e.g., ideal reactors, residence time distributions in active and inactive cavitation zones) to be used for designing sonochemical reactors.

10.3.3 Effect of operating parameters on distribution of cavitational activities

Apart from design parameters, operating conditions (parameters) also significantly affect the distribution of cavitational activity in the sonochemical reactor. Operating conditions like multiple frequencies, significant flow dynamics (acoustic streaming or forced flow patterns), and seeded nucleation are some of the most dominant operating conditions which could improve the distribution of cavitational activities. Implementing multiple frequencies creates nodes and antinodes over a larger volume of reactor along with significant interference of frequencies as compared to single frequency systems. While the active flow pattern moves the reactor content through the active and passive zones, thus exposing the entire reactor content intermittently to active cavitation zones. In the later part of this chapter, we discuss in detail the way in which these operating conditions affect the cavitational intensity and distribution.

10.3.4 Challenges in efficient design and operation of sonochemical reactors

Major challenges identified during efficient design, development, operation, and scale-up of the sonochemical reactor reported by (Sutkar & Gogate, 2009) are:

Estimation of spatial and temporal variation in cavitation activity: Cavitation is a dynamic phenomenon. The overall efficacy of the cavitation and its associated effects strongly depends on the operating parameters (for example, liquid bulk temperature, dissolved gases, intensity and frequency of irradiation, and static pressure, etc.), the geometrical configuration of the reactor and transducer(s) (Krefting et al., 2004). Some of the operating parameters, for example, dissolved gases, can also change with time, leading to temporal variation in cavitational activity. A small variation in these parameters significantly alters the intensity of the cavitation and hence the sonochemical reactor performance, yield, and selectivity of the chemical reactions. Due to these nonlinear and stochastic behaviors, it is very challenging to effectively design, operate and scale up a sonochemical reactor. For a given chemical transformation, a possible approach to address this challenge is the quantitative determination of the distribution of cavitational activities both in space and time. Also, it is important to understand its dependency on the operating and design parameters. Such accurate assessment of cavitational activities helps in optimizing reactor performance and operating conditions. One of the representative results related to the distribution of cavitational activities in sonochemical reactor is shown in Fig. 10.8 (Servant et al., 2001).

Identification of active and passive cavitation zones, and flow dynamics: Cavitational activities are usually concentrated in close proximity to the irradiating surface (as shown in Fig. 10.9). For low frequency (in a few kHz range) operation, the maximum energy gets dissipated near to the irradiating surface in a cone-like structure. Due to this, wider distribution in cavitational activities is observed in the sonochemical reactor. The exchange of reactor content between such active and passive cavitation zones depends on acoustic streaming (as shown in Fig. 10.10) and externally forced flow dynamics in the reactor. The periodic exposure of reactor content to the active cavitation zone is a significantly ignored aspect in sonochemical reactor design.

Reliable estimation of attenuation coefficient of sound waves: The intensity of sound waves inside the liquid medium decreases with an increase in the distance from transducers. This phenomenon is generally described as attenuation of the sound waves, which occurs due to reflection, refraction, and absorption of incident sound waves. The attenuation of sound waves is mainly responsible for the spatial variation of the cavitational activities in the reactor. The attenuation coefficient is a nonlinear function of several parameters the physical properties of the medium (compressibility, viscosity, speed of sound) and the presence of bubbles/ particles and their size distribution, shape factors, compressibility etc.

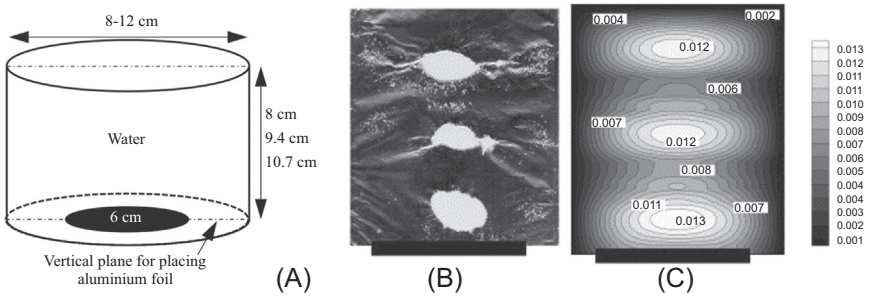

FIGURE 10.8 Pressure amplitude and cavitational activity. *From Servant, G., Laborde, J.-L., Hita, A., Caltagirone, J.-P. and Gérard, A. (2001). Spatio-temporal dynamics of cavitation bubble clouds in a low frequency reactor: Comparison between theoretical and experimental results. Ultrasonics Sonochemistry, 8(3), 163–174. https://doi.org/10.1016/S1350-4177(01)00074-8* (A) Schematic of ultrasonic bath with transducer placed in vessel bottom, (B) Erosion of aluminium foil placed in a vertical plane, (C) computed volume fraction of fragmentary transient cavitation bubble

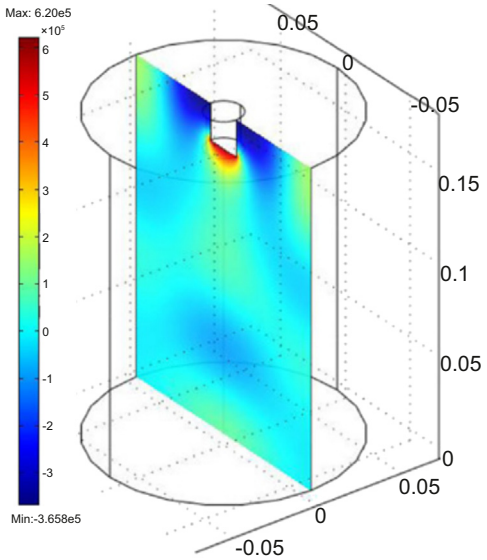

FIGURE 10.9 Pressure field predictions. *Modified from Sutkar, V. S., Gogate, P. R. and Csoka, L. (2010). Theoretical prediction of cavitational activity distribution in sonochemical reactors. Chemical Engineering Journal, 158(2), 290–295. https://doi.org/10.1016/j.cej.2010.01.049* Distribution of pressure field computed via numerical simulation with a similar geometrical configuration.

Estimation of tunable and nontunable parameters: Distribution of cavitational activities in a sonochemical reactor depends on the frequency of ultrasound, power density, and physiochemical properties of the solid, surface area of irradiation, number, and location of transducers in the reactor/reaction medium, reactor dimensions, and energy density (W/m^3). Apart from these parameters, cavitational activities depend on density, viscosity, and composition of new components formed during the chemical transformations, amount of the dissolved gases, formation of free radicals, the liquid level in the reactor, and generation of transient cavitation (bubbles mainly consist of vapor) or stable cavitation (bubbles mainly consist of gas or a small fraction of vapor). During cavitation events, the majority of the above-mentioned parameters change. During the efficient design, scale-up, and operation of a sonochemical reactor, it is paramount to consider both tunable and nontunable parameters. Nontunable parameters often need more attention and are challenging to control. For instance, a few of the no-tunable includes, composition of new components formed during the chemical transformations, and amount of the dissolved gases (via desorption and re-dissolution).

The distribution and characterization of the cavitational activities in the sonochemical reactors are described through mapping techniques. In these techniques, cavitational activities are quantified by estimating primary effects (temperature or pressure) and/or secondary effects (chemical or physical effects in terms of measurable quantities) to identify the active and passive zones. These techniques mainly determine the behavior of sonochemical reactors over the entire range of operations. This chapter provides an overview of basic aspects, applicability, and merits/demerits of various mapping techniques used

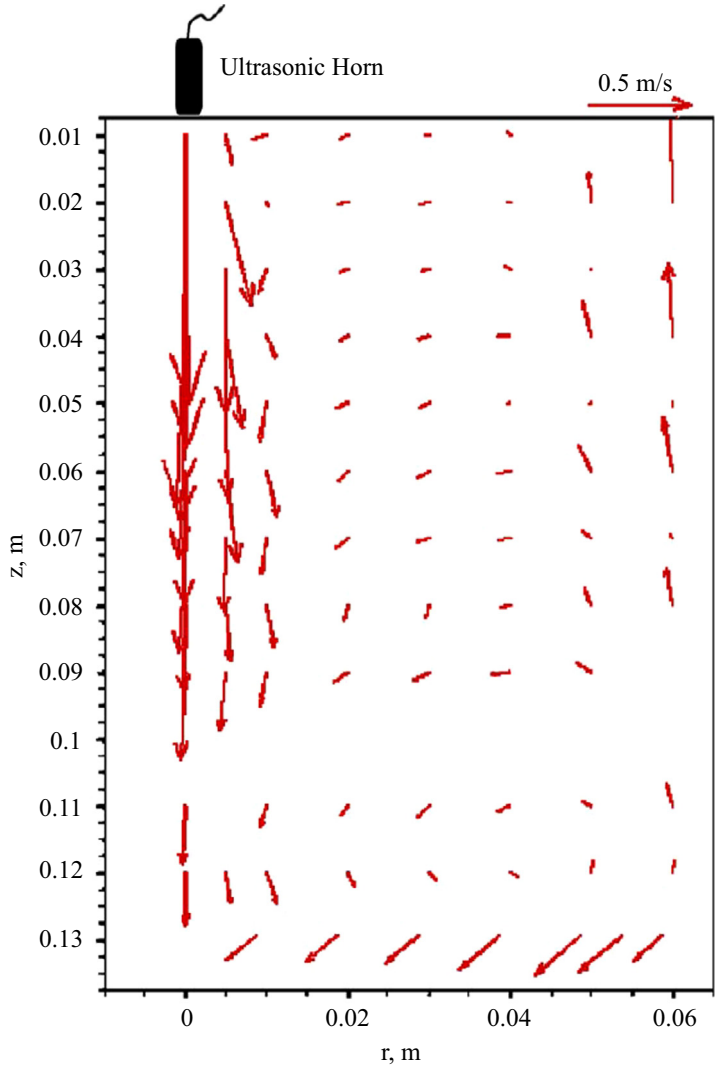

FIGURE 10.10 Velocity field measurements. *From Kumar, A., Kumaresan, T., Pandit, A. B. and Joshi, J. B. (2006). Characterization of flow phenomena induced by ultrasonic horn. Chemical Engineering Science, 61(22), 7410–7420. https://doi.org/10.1016/j.ces.2006.08.038* 2D vector plot for the mean velocity obtained from LDA (Laser Doppler anemometer) measurement for ultrasonic horn dipped 2 cm below the free water level in cylindrical vessel of 0.135 m diameter at 35 kW/m ^{3} at 20 kHz.

to estimate the distribution of cavitational activities in sonochemical reactors. Furthermore, it is important to perform an energy assessment. These assessments provide preliminary information related to the amount of energy dissipated in the bulk of the liquid medium, temperature rise and overall heat transfer.

10.4 Efficiency assessment and mapping of cavitational activities in sonochemical reactors

10.4.1 Efficiency assessment

In sonochemical reactors, transduces are used for the generation of ultrasound waves. The amount of energy transferred in the bulk of the liquid depends on the frequency and amplitude of the sound waves. Additionally, an appropriate selection of transducers including the number, dimensions, type, and location of transducers is one of the important factors affecting the distribution of cavitational activity. As indicated by bubble dynamics studies, generation, size, maximum lifetime, and collapse pressure of bubbles are complex functions of the amount of energy entering in the bulk of the liquid. Additionally, the extent of temperature rise depends on energy input, which results in altering physiochemical properties of the liquid

such as viscosity, density, thermal conductivity, gas solubility, vapor pressure, and molecular interactions. These changes in the liquid properties ultimately enhance the generation of cavitational events and alter the final collapse intensities. Further, during design, operation, and scale up of the sonochemical it is paramount to know hydrodynamic behavior (that is formation of macro and micro mixing zones via active and passive acoustic streaming and forced flow pattern), which critically depends on the extent of the energy dissipation rate. Sometimes, an appropriate calculation of the rate of energy input is important during processing and optimizing operating parameters for heat sensitive materials, especially observed in the biochemical, pharmaceutical, and material industries. In sonochemical reactors, the amount of energy entering/dissipated into the liquid is used to estimate the energy efficiency, also called efficiency assessment, which is the ratio of energy dissipated in the system to the supplied electrical energy. Generally, the energy dissipated in the sonochemical reactor is calculated by measuring the change in liquid temperature with time in either a discrete or continuous manner. During the discrete measurements, the change in the liquid temperature is measured at a frequent time interval. Whereas, during the continuous measurement, liquid temperature is measured continuously. Sometimes, acoustic impedance (Z) measurement, which is the function of density (ρ) and speed of sound (C), is also used to estimate the reactor energy efficiency. Margulis & Margulis described various techniques to estimate reactor energy efficiency, such as transducers amplitude measurement through vibrometer, use of piezoelectric or magneto restrictive sensitive elements, thermoelectric method, and optical measurements (interference and semi-shady methods) which measures the refraction index (Margulis and Margulis, 2003). The use of these methods is limited due to operational complications. Further, during cavitation events, the sonochemical reactor possesses a nonhomogeneous liquid medium due to uneven distribution of the bubbles at millions of locations in the bulk of the liquid. This alters the physicochemical properties of liquid media, especially density, speed of sound, and refraction index. This changes the acoustic resistance or impedance ($Z = \rho\ .C$). These limitations in the measurement method are overcome by the calorimetric method, which involves the measurement of the liquid temperature over a certain time. Further, the calorimetric method is based on the thermodynamic principle of conservation of energy and mass, which is the input energy supplied to the transducers is conserved in the form of heat via several routes (e.g., sound waves, acoustic streaming, and cavitational bubbles). This ignores the heat of reaction, which is in most cases a very small amount in single component medium for example, water in most cases. Here, the electrical form of the energy is converted to heat, which brings a temperature change in the liquid medium, reactor walls and the surfaces of the transducers.

Based on reactor geometry and transducer configurations, neglecting the temperature variation of the reactor walls and transducer surfaces can introduce significant errors in the estimations. Additionally, for more accurate results, it is a good idea to take into account energy loss to ambient air due to convective heat transfer. Also, the proportion of conductive and convective heat transfer losses with the ambience to the energy supplied to the system is significantly high at laboratory and pilot scale as compared to large scale sonochemical reactors. This changes the energy efficiency of sonochemical reactors as we scale it up.

A modified equation for the calorimetric method is (Gogate et al., 2011):

$$\text{Power dissipation} = \begin{pmatrix}\text{Energy utilized to raise the}\\ \text{bulk liquid temperature}\end{pmatrix} + \begin{pmatrix}\text{Energy absorbed}\\ \text{by reactor wall}\end{pmatrix} + \begin{pmatrix}\text{Energy absorbed}\\ \text{by transducer}\end{pmatrix} + \begin{pmatrix}\text{Energy lost to}\\ \text{the surrounding}\end{pmatrix} + \begin{pmatrix}\text{Energy conversion}\\ \text{losses in transducer}\end{pmatrix} \tag{10.1}$$

Mathematically it is expressed as:

$$P_{cal} = \left(m_L\, C_{P,L}\, dT\right) + \left(m_R\, C_{P,R}\, dT\right) + \left(m_T\, C_{P,T}\, dT\right) + \left(hAdT\right) + \text{Losses} \tag{10.2}$$

Where m_L is a liquid mass, m_R is the reactor mass, m_T is the mass of the transducers, $C_{P,L}$ is the specific heat of liquid at constant pressure, $C_{P,R}$ is the specific heat of reactor material, $C_{P,T}$ is the specific heat of transducers material, dT is the change in temperature, h is convective heat transfer coefficient and A is the area of heat transfer. For a sonochemical reactor constructed with low thermal conductivity materials such as plastic, Teflon, polyurethane, PTFE, etc. the energy absorbed by the wall can be neglected due to the measurement complexities for of a short time of operation.

After successful measurement of the power input via calorimetry, it is important to understand the parametric dependency of the power dissipation on the frequency of irradiation, physicochemical properties of bulk liquid, and reaction volume or, the height of liquid medium in the reactor, location, and surface area of the irradiating element. For instance, (Koda et al., 2003) analyzed the distribution of the cavitational activities as a function of power dissipation in various laboratory scale sonochemical reactors (with a capacity of 50 cm^3 and power of 35–220 W and frequency of 25–1200 kHz). The distribution of cavitational activities (in terms of chemical dosimetry) linearly depends on the power dissipation. Further, the extent of distribution depends on the reactor configuration and frequency of irradiation. Rochebrochard d'Auzay et al. performed an efficiency assessment of sonochemical reactor using various chemical dosimetry techniques such as iodine, nitrite, and

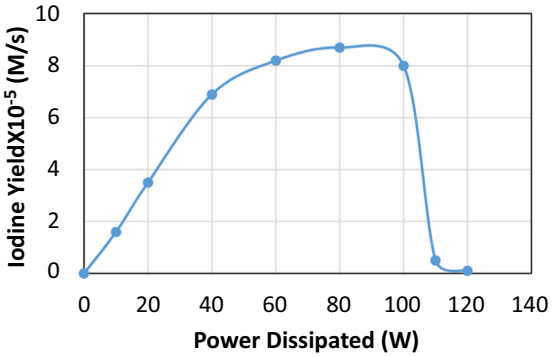

FIGURE 10.11 Iodine dosimetry. *Data from Henglein, A. and Gutierrez, M. (1993). Sonochemistry and sonoluminescence: effects of external pressure. J. Phys. Chem., 97(1), 158–162. https://doi.org/10.1021/j100103a027* Effect of power dissipation on Iodine yield.

nitrate (Rochebrochard d'Auzay et al., 2010). They also analyzed the effects of temperature, power density, and reactor configuration on reactor efficiency assessment. Reactor efficiency increases with power, irrespective of the dosimetry. In a few instances, distribution of cavitational activities increase with power and reaches to the optimum level. Based on the reactor configurations and applications beyond optimum power, the cavitational activities change marginally or remain unchanged or in some cases decrease significantly. This optimum power dissipation is mainly observed due to the enhanced shielding effect and acoustic decoupling losses. With increases in power number and rate of bubble formation increases, which helps in cavity cloud formation due to bubble coalescence. These bubble clouds significantly absorb and/or scatter the incident sound waves, resulting in lowering the transfer of energy transfer efficiency. Also, the decoupling losses due to changes in acoustic impedance significantly lowers the energy transfer efficiency from the transducer to the liquid medium. Henglein & Gutierrez studied the power dissipation effect on the KI oxidation in a sonochemical reactor at 20 kHz. As shown in Fig. 10.11, the amount of iodine formation increases linearly up to 50 W. After 50 W, iodine formation marginally increases to 100W and then decreases sharply. Further, they reported that optimum power strongly depends on reacting volume and operating pressure (Henglein & Gutierrez, 1993).

Contamine et al. reported that the power dissipation rate in a sonochemical reactor with a horn (diameter of 1.3 cm) depends on the physicochemical properties of the liquid media, area of the transducer, and the irradiation frequency (Contamine et al., 1995). Whillock & Harvey observed a linear and nonlinear increase in the distribution of the cavitational activities in terms of erosion rate for high and low frequencies with optimum power (Whillock & Harvey, 1997). Nonhomogeneity in the liquid media due to the presence of solids or immiscible liquids also play a role in deciding the optimum levels, and can negatively affect the distribution of cavitational activities owing to pronounced reflection, refraction, and attenuation of the sound waves. For a system with immiscible liquids like during biodiesel production or emulsification operations etc., the amount of energy dissipated in the system is the sum of energy dissipated in the individual phases, and at the interface. Also, for a system with exothermic and endothermic reactions, an appropriate amount of heat generated or absorbed during the reaction needs to be considered during the calculation of actual power. For an industrial scale of operations, it is established practice to quantify power density (W/m^3) which gives a good idea about the energy requirement per unit volume for a given physicochemical transformation.

10.4.2 Overview of techniques for quantifying cavitational activity distribution

Techniques used to determine the distribution of the cavitational activities in the sonochemical reactors are known as mapping techniques. Sutkar & Gogate presented an overview of the various techniques available for understanding the cavitational activity distribution by highlighting the basic aspects of each technique, their applicability and merits/demerits (Sutkar & Gogate, 2009). This section presents a condensed summary of various mapping techniques. Based on quantification methodology, these techniques are mainly classified into two groups; namely experimental and numerical techniques. Fig. 10.12 shows an overview of various mapping techniques. In experimental techniques, experiments are carried out to quantify the intensity of the cavitational activities during bubble collapse and/or after bubble collapse. The cavitational activities/effects generated during or just after the bubble collapse are called primary effects, which include temperature pulse, pressure pulse, generation of free radicals (inside or on the outer periphery of the bubble), and microcirculation. The effects generated after the bubble collapse are called secondary effects, such as degradation and oxidation reactions, intensification of mass transfer coefficients, enhanced electrochemical effects etc. The primary effects

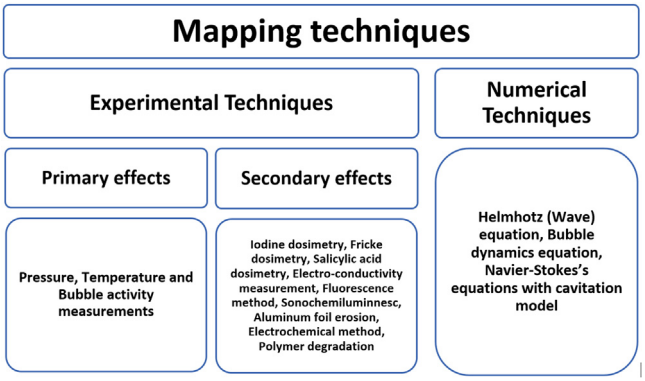

FIGURE 10.12 Mapping techniques *based on Sutkar, V. S. and Gogate, P. R. (2009). Design aspects of sonochemical reactors: Techniques for understanding cavitational activity distribution and effect of operating parameters. Chemical Engineering Journal, 155(1), 26–36. https://doi.org/10.1016/j.cej.2009.07.021* Classification of the mapping techniques.

are directly associated with the cavitation phenomena, whereas secondary effects are related to the cavitation phenomena via other measurable effects. Even though the generation of free radicals is considered as a primary effect, however, they are utilized in the chemical reactions after bubble collapse. In numerical techniques, cavitation effects, either primary or secondary, are carried out by solving wave equations, bubble dynamics equations, and Navier–Stokes's equations with coupled cavitation models etc.

10.4.3 Experimental techniques

10.4.3.1 Primary effects quantification

10.4.3.1.1 Pressure measurement

Cavitation phenomena result in the generation of high-pressure pulses locally at millions of locations in the liquid medium. The intensity of pressure generated during the bubble collapse is quantified using a hydrophone. Hydrophones are electronic devices used to measure the acoustic pressure intensity in the liquid medium with good spatial resolution, bandwidth, excellent directional characteristics (omnidirectional in an axial and radial plane), and sensitivity. Kanthale et al. used Bruel and Kjaer 8103, hydrophone (length of 50 mm and diameter of 9.5 mm) in a sonochemical reactor with 20 kHz frequency and the obtained signals were analyzed via Fast Fourier transform (FFT) (Kanthale et al., 2003). Similarly, Kumar et al. investigated distribution in cavitational activities in sound pressure levels (dB) (Kumar et al., 2007). Hydrophone measurement is an intrusive technique. The presence of hydrophones disturbs the liquid medium, which sometimes affects the distribution of cavitational activities. Calibration of the hydrophone is complex and is very sensitive to the calibration factor provided by manufacturers. Also, the calibration factor provided by manufacturers is constant/ fixed, which does not take into account the sluggishness of the hydrophone signal over a certain time. The accuracy of the measurement signal depends on data acquisition software. The hydrophone measures total pressure intensity, including noise. Sometimes it is challenging to distinguish effective pressure signals (responsible for the cavitation) from the noise.

Avvaru & Pandit measured acoustic spectra using small hydrophones (Bruel & Kjaer Ltd., Type 8103) with a charge amplifier (Bruel & Kjear Ltd., Type 2635) (Avvaru & Pandit, 2008a). The output of the amplifier is captured in a data acquisition system (N.I. Ltd., PCI 6251). Online FFT generated power spectrum with the LabView software (N.I. Ltd. Version 7.1). The inverse FFT analysis helped decipher the energy (acoustic pressure) spectrum for various frequencies. This analysis allowed segregation and quantification of intensity of ultrasound (of multiple frequencies), and cavitational intensity (of multiple frequencies). Further, the measured cavitational activities (both spatial and temporal) were well correlated with Iodide dosimetry for combination of frequencies (Fig. 10.13). These measurements can be conducted to quantify spatial and temporal variation in cavitational activity in sonochemical reactors. These measurements significantly give real time quantification of cavitational activity and is a very powerful tool for monitoring the performance of a large scale sonochemical reactor. As can be seen in Fig. 10.13 there exists a minimal (threshold) cavitation intensity above which Sonochemical transformation gets initiated. This way, the cavitational intensity measured by hydrophones can be used for identifying active and passive cavitational zones. Such co-relations between cavitation intensity and sonochemical yield should be obtained for respective systems. Additionally, correlating filtered pressure spectra operating parameters using

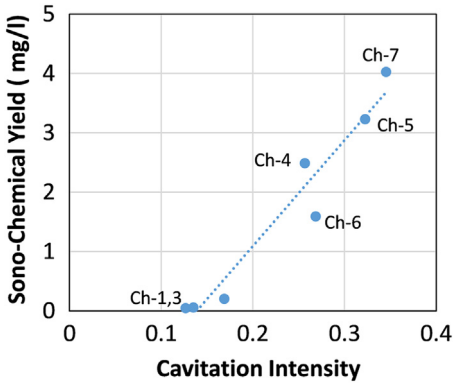

FIGURE 10.13 Cavitation yield and measured intensity. *Data from Avvaru, B. and Pandit, A. B. (2008). Experimental investigation of cavitational bubble dynamics under multi-frequency system. Ultrasonics Sonochemistry, 15(4), 578–589. https://doi.org/10.1016/j.ultsonch.2007.06.012* Co-relation (based on Iodide dosimetry) sonochemical yield of iodine (mg of Iodine liberation per litre) and cavitational intensity as measured by hydrophones (au.) in hexagonal reactor with combination of frequencies. Ch-1 is 41 kHz, Ch-2 is 30 kHz, Ch-3 is 25 kHz, Ch-4 is 30 and 41.5 kHz, Ch-5 is 25 and 41.5 kHz, Ch-6 is 25 and 30 kHz, and Ch-7 is with 25 kHz, 30 kHz and 41.5 kHz simultaneously.

machine learning (ML) algorithms or artificial intelligence, and control systems provide more accurate monitoring and improvement, and prognosis tools for large scale cavitational reactors.

10.4.3.1.2 Temperature measurement

As discussed, earlier cavitation phenomena resulted in the generation of high temperature pulses locally at millions of locations (bubbles) in the liquid medium. During this process, a significant amount of energy is transferred into the bulk of the liquid medium, which changes thermal conductivity, bulk viscosity and molecular interactions etc. These changes further modify the attenuation coefficient. In a homogenous liquid medium medium, absorption effects are dominant as compared to the scattering effects, whereas in a nonhomogenous liquid medium, both effects play a significant role. In homogenous and nonhomogeneous liquid media, the energy transfer results in an increase in the local temperature. This change in local temperature is measured either in a discrete or a continuous manner by inserting the temperature measurement devices such as a thermocouple or thermistor at various locations inside the liquid medium (Kuijpers et al., 2002). During the discrete measurement, a change in the liquid temperature is measured at a frequent time interval whereas, during the continuous measurement, temperature signals are captured continuously. Quantitative information obtained after post-processing of the measurement signals is used to quantify the distribution of cavitational activities in the reactor. Further, measured temperature signals are also used to quantify the efficacy of the sonochemical (or energy assessment) reactor by estimating the total energy dissipation rate in the sonochemical reactor. Temperature measurement is an intrusive technique. The inserted temperature measurement device disturbs the liquid media and witnesse's low reproducibility and sensitivity. Continuous and simultaneous measurement of temperature at various locations in the sonochemical reactor is very complex and cost intensive. Although the local temperature of the collapsing bubbles is higher than the liquid bulk temperature, it occurs over very small length scales (nanometers) and time scales (< microsecond). This makes it very challenging to directly measure the collapse temperature inside the bubble. The measured temperature is the bulk temperature, and it usually serves as a good measure of energy dissipated in the system for energy efficiency assessment.

10.4.3.2 Secondary effect quantification

Based on the maximum radius of the bubble reached during the lifetime of the cavity, and the lifetime of the bubble in the bulk of the liquid, the cavitational events are classified into two types, viz. transient and stable cavitation. The generation of transient or stable cavitation mainly depends on the operating parameters (frequency of irradiation, intensity, and input power etc.) and physicochemical properties of the liquid medium (chemical composition, density, viscosity, surface tension etc.). A small variation in the bubble sizes with a larger lifetime is observed during stable cavitation at low intensity of irradiation (in the range of 1–3 W/cm^3 Whereas a broader variation in the bubble size with a short lifetime is observed in transient cavitation at higher intensity of irradiation (in the range of 5–10 W/cm^3). Further, during both cavitation types, water vapor inside the bubbles dissociates and generates highly reactive free radicals such as OH$^\bullet$ radicals, O$^\bullet$ radicals, and H$^\bullet$ radicals. These formed free radicals are available for chemical reaction within the bubble during a collapsing phase or diffuse out of the bubbles into the surrounding liquid. Furthermore, a sudden collapsing bubble also results in the quick

displacement of the liquid, producing high shear forces. Also, at lower frequencies of irradiation, intense physical effects are observed, such as strong macro and micro-liquid circulation, high turbulence, micro-jet formation during asymmetrical bubble collapse etc.

As reported by Sutkar & Gogate, based on effective utilization of these effects, mapping techniques are further classified in two subgroups as chemical methods and physical methods (Sutkar & Gogate, 2009). During these methods, representative model chemical reactions or physical phenomena are selected, which proceed only by the action of cavitational effects, such as decomposition of KI, Fricke solution, salicylic acid, sonoluminescence, aluminum foil erosion etc. and are successfully used to investigate the distribution of cavitational activities in the sonochemical reactor.

10.4.3.2.1 Chemical methods

KI dosimetry or Iodine release method

Under ultrasonic irradiation, aqueous solution of potassium iodide (KI) is oxidized to form iodine molecules. During oxidation, I^- ions react with generated free radicals to form I^-_2. The excess I^- ions available in the solution further react with formed I^-_2 to form I^-_3. The amount of I^-_3 ions formed during the reaction is easily quantified using a UV spectrophotometer at 350 to 360 nm wavelength. The distribution or intensity of the cavitational activity is investigated by estimating the amount of I^-_3 ions measured in small cuvettes at various locations in the ultrasonic bath. Major chemical reactions during oxidation of potassium iodide solution include (Entezari & Kruus, 1994; Feng et al., 2002):

$$H_2O_2 + 2I^- + 2H^+ \rightarrow I_2 + 2H_2O$$

$$OH + I^- \rightarrow OH^- + I$$

$$I + I^- \rightarrow I_2^-$$

$$2I_2^- \rightarrow I_2 + 2I^-$$

$$I_2 + I^- \rightarrow I_3^-$$

$$H_2O \rightarrow H\cdot + OH\cdot$$

The distribution in cavitational activity (for mapping) is usually represented in terms of mg of Iodine liberated per unit time. The overall energy assessment is obtained by integrating the mg of Iodine liberated into the entire volume and energy delivered to the system. It is usually represented in terms of mg of Iodine liberated per Joule of electrical energy delivered to the system. Fig. 10.14 shows the distribution of cavitational activity estimated using Iodine dosimetry (Gogate et al., 2002). These results clearly shows the effects of harmonics on cavitational actviity. In this case frequency was 20 kHz and the wavelength was 7.5 cm, as used for analysis.

Fricke dosimetry

Ferrous ions/sulfate dosimetry is also known as Fricke dosimetry. Under ultrasonic irradiation of aqueous solution of Ferrous ions/sulfate, the generation of free radicals and hydrogen peroxide converts the ferrous ions to Ferric ions (Fe^{3+}) as (Feng et al., 2002):

$$Fe^{+2} + OH\cdot + H^+ \rightarrow H_2O + Fe^{+3}$$

$$Fe^{+2} + H_2O_2 + H^+ \rightarrow H_2O + Fe^{+3} + OH\cdot$$

$$Fe^{+2} + OH\cdot \rightarrow Fe^{+3} + OH\cdot$$

The extent of Fe^{3+} ions generation is proportional to the intensity of the cavitational activities and measured by UV spectrophotometer at 304 nm wavelengths. Fricke's dosimetry is very sensitive to impurities.

Salicylic acid dosimetry

In salicylic acid dosimetry an aqueous solution of salicylic acid is irradiated for a certain time, during which salicylic acid exclusively reacts with the hydroxyl radicals to form 2, 5- and 2, 3-dihydroxybenzoic acid along with very small quantities of catechol (Arrojo et al., 2007; Chakinala et al., 2007). An overview of the reaction scheme is schematically depicted in Fig. 10.15.

The intensity and/or distribution of cavitational activity is monitored by hydroxylation of salicylic acid. All the dosimetry measurements are based on the generation of free radicles after bubble collapse. The generation of free radicles is dominant

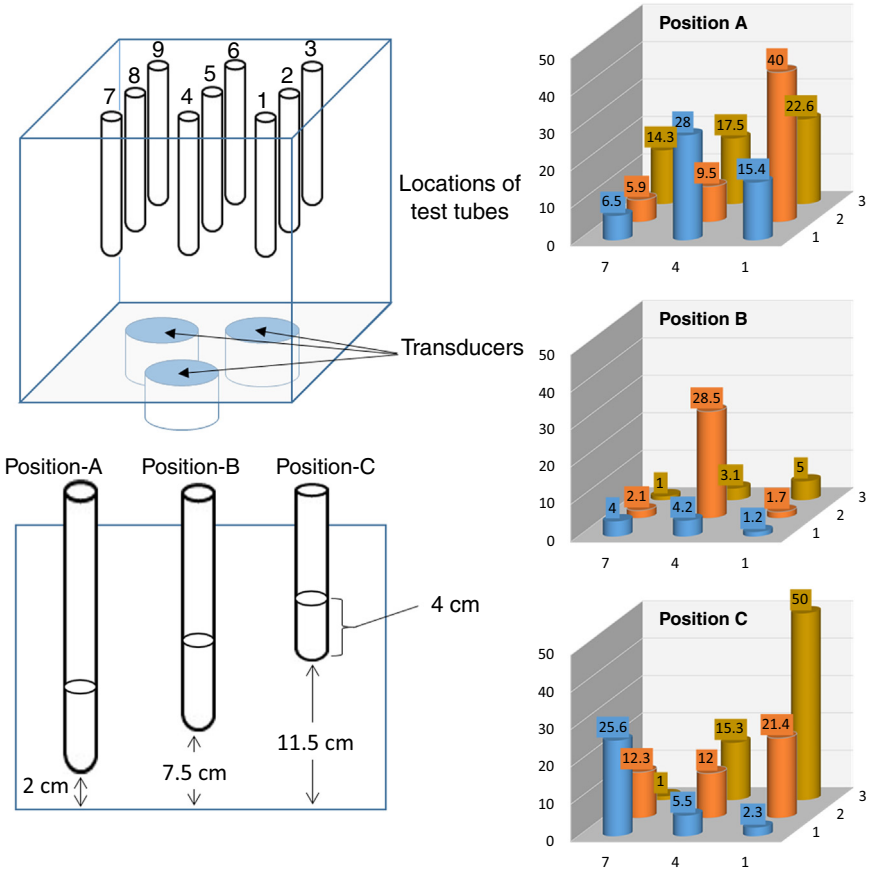

FIGURE 10.14 Distribution of cavitational activity in ultrasonic bath. *Based on Gogate, P. R., Tatake, P. A., Kanthale, P. M. and Pandit, A. B. (2002). Mapping of sonochemical reactors: Review, analysis, and experimental verification. AIChE Journal, 48(7), 1542–1560. https://doi.org/10.1002/aic.690480717*
Distribution of Iodine yield in the ultrasonic bath with triple transducers (20 kHz, 120 W total) mounted on the bottom wall. Iodine liberation was measured at 27 locations (9 locations in a plane, and at 3 planes at various distances from transducers).

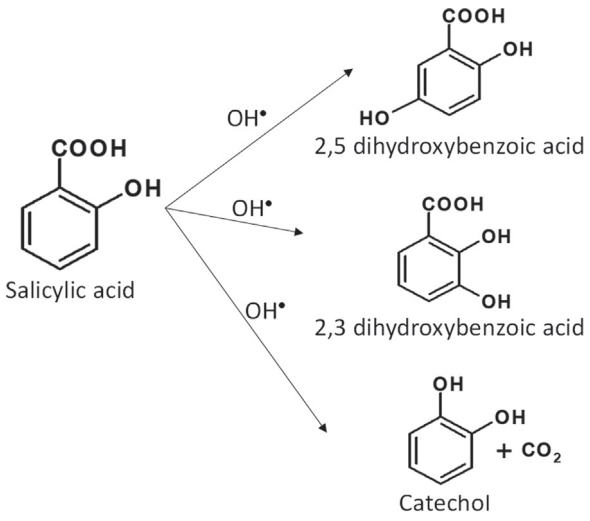

FIGURE 10.15 Salicylic acid dosimetry. Reactions in salicylic acid dosimetry.

during transient cavitation. However, the cavitational activity associated with oscillating bubbles (e.g., shear), is not considered in these measurements.

Electroconductivity measurement

Water contains a small amount of dissolved nitrogen (N_2) and oxygen (O_2), and other gases. Under normal/standard operating conditions, these gases do not react/interact with each other. However, during cavitation phenomena, that is, very high temperature and pressure, nitrogen and oxygen gases react with each other to form nitrogen oxide (NO). The formed nitrogen oxide is further oxidized to give nitrogen dioxide (NO_2) which combines with a water molecule to form Nitric (HNO_3) and Nitrous (HNO_2) acids. The formation of acids results in altering the electrical conductivity of the water. This peculiar phenomenon is used to estimate the distribution of the cavitational activity in the liquid medium (Feng et al., 2002). During this method, the intensity of cavitational activity mainly depends on the solubility of oxygen and nitrogen in the liquid medium, which is a function of temperature, pressure, and chemical composition.

The distribution of cavitational activity is quantified by changes in local conductivity of the solution measured in a cuvette. The overall energy efficiency can be obtained by integrating the change in conductivity per joule of electrical energy supplied to the system.

Fluorescence determination or Terephthatic acid (TA) dosimetry

Under ultrasonic irradiation, a nonfluorescent aqueous solution of Terephthalic acid (TA) reacts with hydroxyl radical ($OH^{\bullet}$) to form a highly fluorescent 2-hydroxyterephthalate ion or hydroxyl-terephthalic acid (HTA). Terephthalic acid dosimetry is based upon the hydroxylation of terephthalic acid (TA) by OH•. This reaction is very specific and sensitive to the generation of free radicals, hence represents the distribution of cavitational activity in liquid media. During the experiments, fluorescence intensities of the Terephthalic acid are measured within 2–4 hr. of irradiation (Feng et al., 2002; Little et al., 2007) under a dark environment, and fluorescence intensity is determined using Fluorescence Spectrophotometer at 310 to 426 nm wavelengths. Sometimes use of Aldrich ($IrC^{-}{}_6$) as a potent oxidant is also reported, which enhances the overall yield and intensity of HTA (Feng et al., 2002). Terephthalic dosimetry is time-consuming as compared to other methods. Further, experiments need to be done in a dark room.

10.4.3.2.2 Physical methods

Sonochemiluminescence

Sonoluminescence (SL) is the light emitted by cavitation bubbles due to propagation of the sound wave through liquid media, whereas Sonochemiluminescence (SCL) is the light emission when luminol reacts with OH radicals (Hu et al., 2008). SCL provides visualization of the distribution of cavitational activities in the sonochemical reactor. In this method, an aqueous solution of SCL reagent under alkaline conditions is irradiated by passing sound waves, where the intensity of luminescence is proportional to the cavitational activities. Generally, Luminol (3 aminophthalhydrazide) is used as the SCL reagent. Under alkaline conditions, the Luminol reagent gets oxidized by OH radicals, to produce 3-amino phthalate creating a blue light spectrum. SCL method is expensive and requires a dark environment. High precision equipment is required to capture SCL images.

Aluminum foil erosion

The erosion phenomena of aluminum foil are also used to estimate the distribution of cavitational activities in sonochemical reactors (Avvaru and Pandit, 2008a). During this technique, an aluminum foil (of a few micrometers thickness) is placed perpendicular to the irradiating surface. Distribution of the cavitational activities is qualitatively measured in terms of the erosion pattern on the aluminum foil. Horizontal insertion of the foil, perpendicular to the direction of transducers is not recommended due to the accumulation of the bubbles near the foil surface. The extent and distribution of cavitational activities are determined by capturing digital images. This method is generally employed for low frequency operations where physical effects are high. At low frequency, the wavelength of ultrasound is larger as compared to high frequency operation. Further bubble dynamics studies indicated that low frequency operations often produce bigger bubbles, which generate high intensity micro jets near the surface (in this case foil surface) during asymmetrical bubble collapse to produce intense physical effects. This method provides qualitative information related to the distribution of cavitational activities and is generally popular for low frequency operations. Also, the insertion of aluminum foil in the liquid media may disturb the propagation of sound wave and standing wave formation and erosion of the foil introduces impurities in the liquid media. Limited information is available to check the applicability of this method for heterogeneous and miscible systems. Fig. 10.16 shows representative results for Aluminium erosion in Hexagonal bath reactor for single, dual and triple frequency operation (Avvaru and Pandit, 2008a). These results show better distribution in cavitational activity when multiple frequency ultrasound is used.

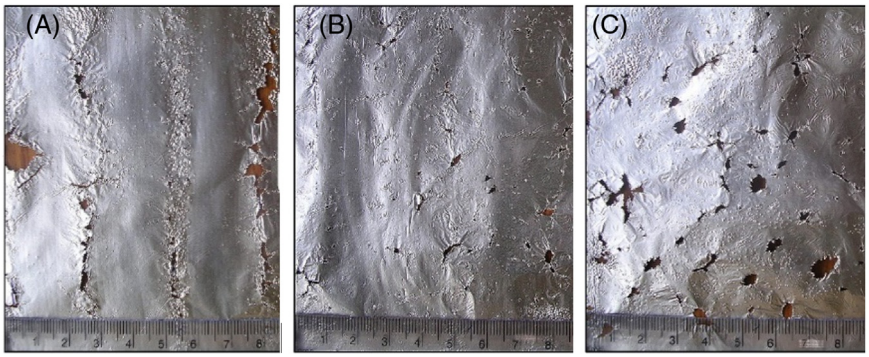

FIGURE 10.16 Aluminium foil erosion test. *From Avvaru, B. and Pandit, A. B. (2008). Experimental investigation of cavitational bubble dynamics under multi-frequency system. Ultrasonics Sonochemistry, 15(4), 578–589. https://doi.org/10.1016/j.ultsonch.2007.06.012* Aluminum erosion in Hexagonal flow reactor (A) single frequency—30 kHz, (B) dual frequency - 41.5 and 30 kHz), and (C) triple frequency 41.5, 30 and 25 kHz.

Polymer degradation

The molecular weight of a long chain polymer is reduced by passing sound waves through the polymer solution dissolved in a solvent (Harkal et al., 2006). Propagation of sound waves generally breaks the long chain polymer, due to the generation of high shear stress and the formation of microjets. The extent of chain breakage depends on the intensity of the cavitation event. The distribution of cavitational activities is determined by estimating reduction in polymer molecular weight by placing the polymer mixture at a different location in the sonochemical reactor.

Flow visualization and measurement techniques

Laser Doppler Anemometer (LDA) and Particle image velocimetry (PIV) are nonintrusive measurement techniques, employed to investigate average flow displacement or velocity. LDA is a point measurement method, while PIV obtains measurements over the entire plane. In these method, liquid media is seeded with tiny tracer particles and the average particle displacement of these particles is measured by capturing two subsequent images at a very short-time interval (in the range of a few micro-seconds) using a double-pulsed laser technique. The laser illuminates the liquid medium and the positions of the tracer particles is recorded using a digital camera. Based on the image resolution, captured images are subdivided into interrogation areas and cross-correlation is applied to determine average particle displacement (S_P). The particle velocity in each interrogation area is determined by:

$$v_{p(x,t)} = \frac{S_P}{M \triangle t} \tag{10.3}$$

Where M is the image magnification factor and is the time interval between the images, which is generally very short. Fig. 10.17 shows typical images of seeded particles (a), and vector plots (b and c).

In the sonochemical reactors, these techniques are used to determine acoustic streaming. Sometimes micro-bubbles generated during cavitation phenomena are used as tracer particles. However, the obtained results are nonreliable and nonreproducible. This is mainly due to the nonuniform distribution of the bubbles in the liquid medium. Further, terminal rise velocity depends on bubble size. The bubble of bigger size has higher buoyancy and slip velocity, and hence does not correctly represent the flow. Thus, it is not recommended to use cavitation bubbles as tracers (Nowak et al., 2015).

Boldo et al. investigated liquid circulation and extent of circulations in a reactor through the combination of PIV measurement and the time averaging holography method, and observed the maximum distribution of liquid velocity in the close vicinity to the irradiating surface. Further, the extent of liquid circulation is used to investigate the distribution of cavitational activity in the reactor (Boldo et al., 2004).

10.4.4 Numerical investigations

This section discusses various numerical tools available for predicting the cavitational activity in the sonochemical reactors. These are mostly used along with the experimental methods described in the previous section.

10.4.4.1 Acoustic wave amplitude prediction and pressure field

Acoustic wave amplitude is the driving force for the acoustic cavitation. Thus, correctly predicting the wave amplitude can help predict various primary and secondary effects of cavitation described earlier. There are several commercial

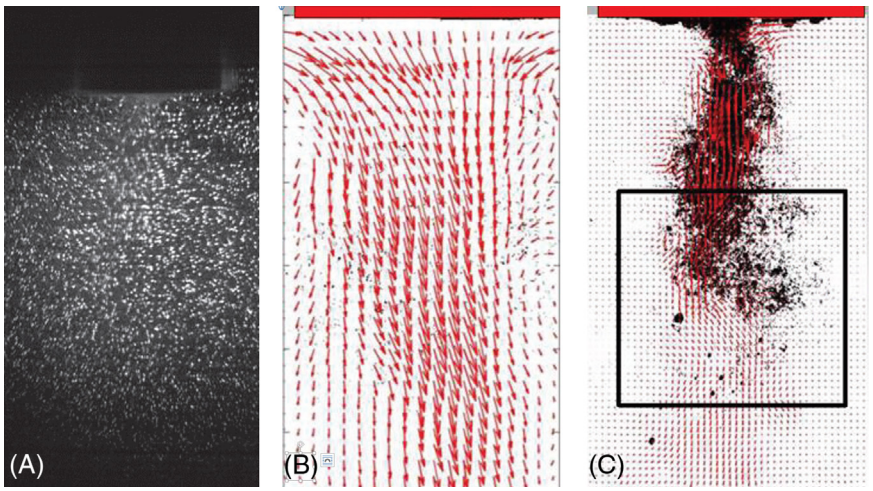

FIGURE 10.17 Flow pattern near the ultrasonic horn tip. *From Nowak, T., Cairós, C., Batyrshin, E. and Mettin, R. (2015). Acoustic streaming and bubble translation at a cavitating ultrasonic horn. AIP Conference Proceedings, 1685(1), 020002. https://doi.org/10.1063/1.4934382* (A) Images of fluorescent tracer particles (5000 fps, flash exposure bubbles: 2 μs, shutter exposure tracers: 166 μs; width of horn tip: 1 cm). Typical images of PIV evaluated streaming velocities (vector arrows) for the case of suppressed cavitation in (B) and for cavitating water (C). Bubbly regions and larger individual bubbles are grey (image width approx. 1.1 cm). Maximum velocities in (B) reach about 3 cm/s, while in (C) up to 1.8 m/s are observed.

simulation tools available for predicting the pressure field based on the time harmonic wave equation (inhomogeneous Helmholtz equation). COMSOL Multiphysics, is one of the most widely used simulation tools for this purpose. It allows simulating the wave equation for any geometry, and hence is a versatile tool for optimizing the pressure field in a sonochemical reactor. Several studies have been reported for predicting the pressure field using the same (Jiao et al., 2014; Jordens et al., 2013; Sutkar et al., 2010; Xu et al., 2013). Wei & Weavers used COMSOL for predicting pressure amplitudes in sonochemical reactors, and also validated the results with experimentally measured pressure amplitudes using hydrophones (Wei & Weavers, 2016). Klíma et al. conducted pressure filed simulation in FEMLab3.1 (now integrated in COMSOL) and also validated the model with experimental measurement (Klíma et al., 2007). Memoli et al. used PAFEC (Program for Automatic Finite Element Calculations) vibro-acoustics software for characterizing pressure field in cylindrical sonochemical reactor (Memoli et al., 2012). Overall, various modelling tools can very well predict the pressure amplitude in any complex geometry.

The biggest challenge in the prediction of pressure wave amplitude is correct estimation of the attenuation coefficient. The attenuation coefficient is not a constant value and is a function of ultrasonic frequency, physico-chemical properties of liquid medium, and most importantly the presence of cavitating bubbles or other phases. These make the attenuation coefficient vary both in space and time in sonochemical reactors. Thus, validation of pressure wave prediction with experimental data is very crucial for reliable predictions.

10.4.4.2 Acoustic streaming predictions

Flow field prediction corresponds to acoustic streaming or turbulence intensity or forced flow patterns. The ultrasonic horn type of reactor produces strong/ jet flow currents, while wall mounted or radial horn type sonicator produces weak flow currents. The jet-like flow currents are generated owing to the physical motion of the horn tip. Mahulkar & Pandit conducted single phase CFD simulations to predict the flow field using dynamic mesh in ANSYS Fluent (Mahulkar and Pandit, 2010).

The surface of the ultrasonic probe was simulated like a reciprocating piston, vibrating at the same frequency and amplitude as that of the horn. The predicted flow field (streaming velocities) matched well with the LDA measurements with reduced turbulence (Kumar et al., 2006). Fig. 10.18 shows a comparison of axial velocity predicted by CFD analysis and with measured velocities. The reduction in turbulence level was due to nonconsideration of the cavitation model. This indicates that secondary effects arise due to cavitating bubbles being very intense. For mass transferred controlled reaction, where mixing and/or homogenization play an important role. For such a system, it is necessary to correctly predict the turbulence and turbulent fluctuating pressure. Also, predication of acoustic streaming helps during estimation of movement/ exposure time (residence time distributions) of reactor content within active and passive zones. This also helps in determining the extent of conversion/transformation. Thus, during efficient design and scale-up of sonochemical reactors, acoustic streaming should be closely monitored.

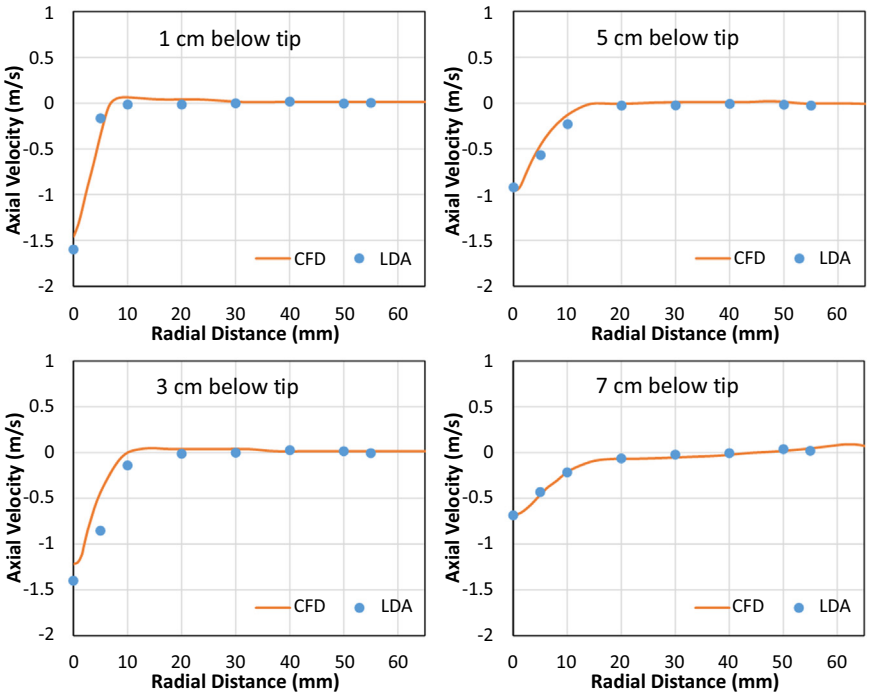

FIGURE 10.18 CFD based acoustic streaming predictions. *Data from Mahulkar, A. V. and Pandit, A. B. (Mahulkar and Pandit, 2010). Analysis of Hydrodynamic and Acoustic Cavitation Reactors.* Comparison of axial velocity profile predicted by CFD simulation from Mahulkar and Pandit, 2010 with axial velocities measured using LDA by Kumar et al. (2006).

10.4.4.3 Bubble dynamics across the volume of reactor

For a selected geometrical configuration and operating conditions, after correctly estimating the acoustic wave amplitude and acoustic streaming (or forced flow patterns), these parameters can be used as input parameters for predicting the bubble motions via bubble dynamics equations. Some of the important aspects of simulating the bubble dynamics are given below.

Choice of bubble dynamics equation: The most widely used bubble dynamics equations are the Rayleigh-Plesset equation (RPe)

$$R\ddot{R} + \frac{3}{2}\dot{R}^2 = \frac{1}{\rho_L}\left[P_i - \frac{4\mu}{R}\dot{R} - \frac{2\sigma}{R} - P_\infty\right] \tag{10.4}$$

Gilmore equation (Ge)

$$\left(1 - \frac{\dot{R}}{C}\right)R\ddot{R} + \frac{3}{2}\dot{R}^2\left(1 - \frac{1}{3}\frac{\dot{R}}{C}\right) = H\left(1 + \frac{\dot{R}}{C}\right) + \frac{R}{C}\dot{H}\left(1 - \frac{\dot{R}}{C}\right) \tag{10.5}$$

Where $H = {(P_i - P_\infty)}/{\rho_L}$

Keller-Miksis equation (KMe)

$$\left(1 - \frac{\dot{R}}{C}\right)R\ddot{R} + \frac{3}{2}\dot{R}^2\left(1 - \frac{1}{3}\frac{\dot{R}}{C}\right) = \frac{1}{\rho_l}\left(1 + \frac{\dot{R}}{C}\right)P_w + \frac{R}{\rho C}\cdot\frac{dP_w}{dt} \tag{10.6}$$

Tomita-Shima equation (TSe),

$$R\ddot{R}\left(1 - \frac{2\dot{R}}{C} + \frac{23\dot{R}^2}{10C^2}\right) + \frac{3}{2}\dot{R}^2\left(1 - \frac{4\dot{R}}{3C} + \frac{7\dot{R}^2}{5C^2}\right) + \frac{1}{\rho}\left[P_{\infty(t)} - P_{2(r=R)} + \frac{R}{C}\left(\dot{P}_{\infty(t)} - \dot{P}_{1(r=R)}\right) + \frac{1}{C^2}\left\langle -2R\dot{R}\left(\dot{P}_{\infty(t)} - \dot{P}_{1(r=R)}\right) + \frac{1}{2}\left(P_{\infty(t)} - P_{1(r=R)}\right)\left(\dot{R}^2 + \frac{3}{\rho}\left(P_{\infty(t)} - P_{1(r=R)}\right)\right)\right\rangle\right] = 0 \tag{10.7}$$

Where, $P_{1(r=R)} = P_B - \frac{2\sigma}{R} - \frac{4\mu\dot{R}}{R}$, and $P_{2(r=R)} = P_{1(r=R)} - \frac{4\mu}{3\rho C^2}\left(\dot{P}_{\infty(t)} - \dot{P}_{1(r=R)}\right)$

The significant difference between these equations is the treatment of compressibility of liquid medium. This aspect becomes important near the collapse stage of the bubble when bubble wall velocity increases close to the velocity of sound

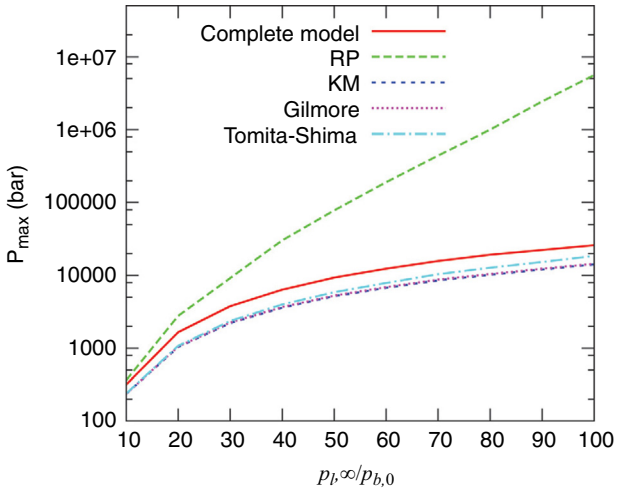

FIGURE 10.19 Comparison of cavity dynamics models. *From Fuster, D., Dopazo, C. and Hauke, G. (2011). Liquid compressibility effects during the collapse of a single cavitating bubble. The Journal of the Acoustical Society of America, 129(1), 122–131. https://doi.org/10.1121/1.3502464* Collapse pressure at the bubble centre for different models. RPe significantly over predicted the collapse pressure at higher amplitudes of driving pressures.

in liquid. Hence, for the rest of the growth and compression stages of the cavity, the bubble dynamics predicted by both equations almost stays the same. Overall, pressure and temperature at the time of collapse as predicted by these equations are different, but the radius time history of the cavity is almost similar. Fuster et al. compared the prediction of these equations with the complete model based on the 1D conservation equation for mass, momentum, and energy solved inside the bubble and in the surrounding liquid (Fuster et al., 2011). It was seen that RPe based models and detailed models were in tune for low amplitude pressure fluctuations. For peak pressure above 1000 atm, the RPe equations over predicted the collapse pressure by almost two orders of magnitude as compared to the other equations. With the Keller-Miksis, Gilmore and Tomita-Shima equations (as improved by (Lezzi & Prosperetti, 1987)) predictions significantly improved (see Fig. 10.19). Thus, depending on the end use, the appropriate choice of bubble dynamics model should be made. For physical transformation, where bubble radius history plays a key role (i.e., shear generated by stable cavitation) all the equations will predict, the similar results. Here, liquid compressibility is not very important. While for applications which rely on collapse pressure and temperature (i.e., chemical transformation by reaction in the cavity), TSe would predict more realistic results.

Cavity collapse criterion: The choice of the criterion for the collapse of a cavity significantly determines the collapse pressure and temperature inside the cavity. In literature, numerous criteria have been published for the same. Some of these are (1) assumption of a certain percentage of the initial radius of the bubble, (2) cavity content entering the critical phase of the liquid, and (3) critical material volume criterion. To correctly define the collapse criterion, it is crucial to correctly define the condition of collapse of the cavity. Some of the important aspects in the definition of 'collapse' stage are (1) when the cavity loses its identity as a "cavity" in the liquid medium, or (2 the cavity content reaches the physical limits. This criterion demarcates the pre and postcollapse events. This is also when the gas laws (ideal or real) become inapplicable to the content of cavity. This is also when the bubble dynamics equations would also be no longer valid, because the bubble interface can no longer be distinctly defined with respect to liquid medium. This clearly indicates that collapse criterion based on certain percentage of initial radius of cavity is unrealistic assumption. The one based on cavity contents entering the critical phase is also not valid because the identity of cavity can still exist in "critical phase" in terms of enhanced pressure and temperature as compared to surrounding liquid (which is still at ambient conditions). The third criterion is based on the material volume concept is based on volume of molecules. When the volume of the cavity equals the total minimum volume of molecules the cavity cannot shrink further. At this point, the physical limits of molecular volume have reached. During stable cavitation, the cavity would rebound even before reaching cavity collapse criterion. Overall, the criterion of material volume limit seems more realistic and is recommended for the bubble dynamics simulations.

Assumption of initial radius of cavity: Estimating the initial radius of a bubble needs correct characterization of the liquid medium either in terms of various nucleation sources or existing microbubbles, nanobubbles or larger bubbles present in the system. This is easy for cleaning liquid, but for many real-life applications for example, water treatment, it is very challenging. Also, it is possible that these parameters will change the treatment time. This aspect not only poses a significant challenge for predicting the bubble dynamics, but also to scale up the sonochemical reactor using the pilot trials data. Initial size of the bubble used for prediction should be representative of the liquid feed for real scaled-up version. In the absence of

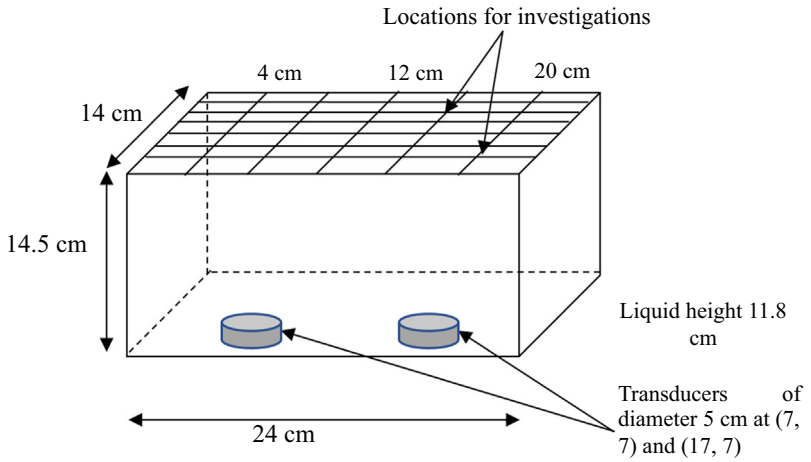

FIGURE 10.20 Locations to map the cavitational activity in ultrasonic bath. *Modified from Sutkar, V. S. and Gogate, P. R. (2010). Mapping of cavitational activity in high frequency sonochemical reactor. Chemical Engineering Journal, 158(2), 296–304. https://doi.org/10.1016/j.cej.2010.01.051* Schematic view of sonochemical reactor and different locations for measurements.

experimental input for initial size of the bubble, the only option is to conduct sensitivity analysis with initial size of bubble and validate the results with experimentally measured outcome. It is always possible that the initial bubble size will have a wide range and only a certain range of cavities can produce the desired outcome. Thus, the sensitivity of the outcome with respect to the initial size of the cavity should be performed.

Mass and heat exchange of cavity with the surrounding liquid: This significantly affects the bubble dynamics, as it can change the mass of the cavity content. Various mass exchange routes include diffusion of gas in and out of the cavity, evaporation, and condensation of vapor in and out of the cavity, or consumption/ generation of chemical species by reaction. Reaction can occur inside the bubble, at the interface, or in liquid bulk in the vicinity. The heat exchange with the surrounding liquid keeps the cavity isothermal for most of the time in expansion and part of the compression phase. The last phase of compression is always adiabatic, as compression is much more rapid than the rate of heat transfer.

10.5 Case study

Quantifying cavitational activity in ultrasonic bath (based on published work of (Sutkar & Gogate, 2010))

This case study serves as an example of using various experimental and numerical tools to quantify the cavitational activity in the cavitational reactor. Distribution of cavitational activity in a sonochemical reactor was carried out by investigating primary and secondary effects. Primary effects were quantified by solving the space dependent part of the wave equation in COMSOL Multiphysics and actual pressure field distribution was measured using a hydrophone (pressure sensor) coupled with a high-speed data acquisition system. Secondary effects were quantified in terms of decomposition of potassium iodide (KI). Lastly, bubble dynamics studies were performed by solving Rayleigh-Plesset Noltingk Neppiras equation to investigate collapse pressure, temperature and time. On the basis of obtained results at various locations in sonochemical reactor, best possible locations were suggested for maximizing physicochemical transformations.

10.5.1 Experimental setup

Experiments were performed in a sonochemical reactor (L x W x H = 24 × 14 × 14.5 cm^3, Roop Telesonic Ltd., Mumbai) as shown in Fig. 10.20 with 3.5 liters capacity. The reactor is fitted with two transducers (diameter = 5 cm) located at (7, 7) and (17, 7) with dual frequency of 694 kHz (wave length, $\lambda 1 = 0.216$ cm) and 204 kHz (wave length, $\lambda 2 = 0.735$ cm) and maximum power rating of 55 W and 224 W respectively. The reactor was divided into five planes (along z-direction) from the bottom of the reactor at heights corresponding to 10 $\lambda 1$, 20 $\lambda 1$, 30 $\lambda 1$, 40 $\lambda 1$, and 50 $\lambda 1$; where $\lambda 1$ is the wave length for the frequency 694 kHz.

10.5.2 Measurements of Iodine liberated in reactor

Decomposition of potassium iodide (KI) was carried out at different locations as depicted in Fig. 10.21. For this purpose, 5 ml of 2 % (w/w) KI solution was taken in a small test tube (of outer diameter of 1.5 cm and height of approximately 15 cm). Irradiation was carried for 3 minutes for each location. The results are shown below.

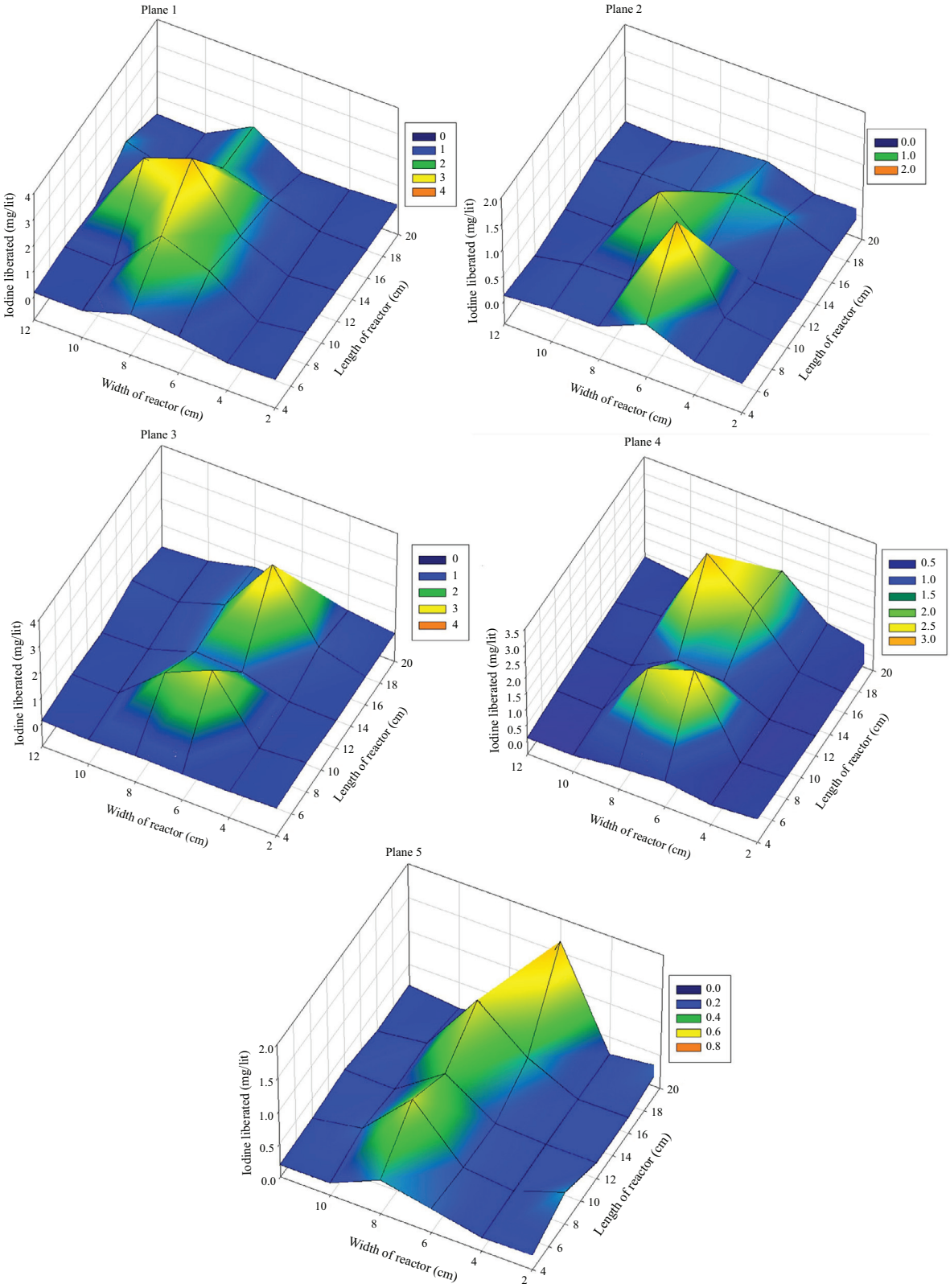

FIGURE 10.21 Iodine dosimetry mapping in ultrasonic bath *From Sutkar, V. S. and Gogate, P. R. (2010). Mapping of cavitational activity in high frequency sonochemical reactor. Chemical Engineering Journal, 158(2), 296–304. https://doi.org/10.1016/j.cej.2010.01.051* Amount of iodine liberated at 5 planes for 204 kHz frequency of irradiation. Maximum cavitational activity was observed in plane 1 (19.84 mg/lit, 2.16 cm from bottom) which is just above the irradiating surface. As we go away from irradiating surface (from plane 2–5) cavitational activity decreases up to plane 3 and a marginal increase was obtained at plane 4 (18.22 mg/lit, 3.14 cm from air-liquid interface) this is due formation of interference of waves at this location.

TABLE 10.1 Iodide dosimetry.
Quantitative comparison for amount of iodine liberation at various planes.

Frequency of Ultrasound	Plane-1 (mg/lit)	Plane-2 (mg/lit)	Plane-3 (mg/lit)	Plane-4 (mg/lit)	Plane-5 (mg/lit)	Plane-6 (mg/lit)	Power (W)	(Total iodine liberated)/Power
204 kHz	19.84	8.92	16.91	18.22	13.28	65.18	14.43	4.51
694 kHz	7.82	3	2.28	3.43	2.27	18.82	11.92	1.57

The amount of Iodine liberated on various planes is summarized in Table 10.1.

10.5.3 Quantification of local pressure field by wave equation

Quantification of pressure the amplitude on different planes was carried out by solving the space dependent part of the wave equation (Helmholtz equation) by considering the attenuation of the sound a wave in bulk liquid. The Helmholtz equation can be solved by applying suitable boundary conditions as:

1. At the tip of transducer $P = P_0$, the entire energy is entering into the system through the tip.
2. At the wall $P = 0$, the pressure amplitude vanishes near the wall

For solution, an Acoustic module from COMSOL Multiphysics version 3.3 was used, which considers finite element method as a numerical tool. As the sound wave propagates through the liquid medium, the intensity decreases as distance from the irradiating surface increases (see Fig. 10.22). Attenuation mainly occurs due to the conversion of kinetic energy associated with the waves into heat. Moholkar et al. have reported that the attenuation coefficient is a function of physicochemical properties as well as frequency and is given by the following equation (Moholkar et al., 2000):

$$\alpha_S = \frac{8\mu\pi^2 f^2}{3\rho C^3} \tag{10.8}$$

Where μ is viscosity (kg/m s^2), f is frequency of ultrasound (Hz), ρ is density of liquid (kg/m^3), and c is speed of sound (m/s). For the present system with a density of water of 997 kg/m^3, viscosity of 1 cP, the speed of sound is 1496.8 m/s attenuation coefficient is calculated as 3.196×10^{-4} /m and 3.69×10^{-3}/m for operating frequency 204 and 694 kHz respectively.

10.5.4 Bubble dynamics studies

The Rayleigh-Plesset equation describing the behavior of a single cavity in the fluctuating pressure field i vs considered. For single-frequency (f) operation, the local pressure field under the influence of an acoustic field can be given by:

$$P_\infty = P_O - P_A \sin(2\pi f t) \tag{10.9}$$

Where P_0 is the ambient pressure, P_A is the pressure amplitude due to the ultrasonic intensity of irradiation, given as:

$$P_A = \sqrt{2I\rho C} \tag{10.10}$$

Where, I is the intensity of ultrasound (W/m^2), ρ the density of the medium (kg/m^3) and C the velocity of sound in the medium (m/s). These parameters are used in the bubble dynamics equations presented earlier.

The variation in collapse pressure, temperature, cavity collapse time and maximum radius reached during cavitation have been investigated by assuming 1 atmospheric (ambient) pressure with initial cavity size of 2 μm, ambient temperature of 30 °C, dissolved gas fraction of 0.7. The obtained results are shown in Table 10.2.

10.5.5 Observations

Cavitational activity in terms of iodine liberation in reactors is nonuniform in nature. The obtained results show that as the distance from the transducer increases, cavitational activity decreases up to plane 3 and then a marginal increase is observed at plane 4 (at a distance of 8.64 from on the emitter's surface) for both the frequencies. However, a lower extent of iodine liberation was obtained at 694 kHz frequency compared to 204 kHz. So, the best location to carry chemical transformations is

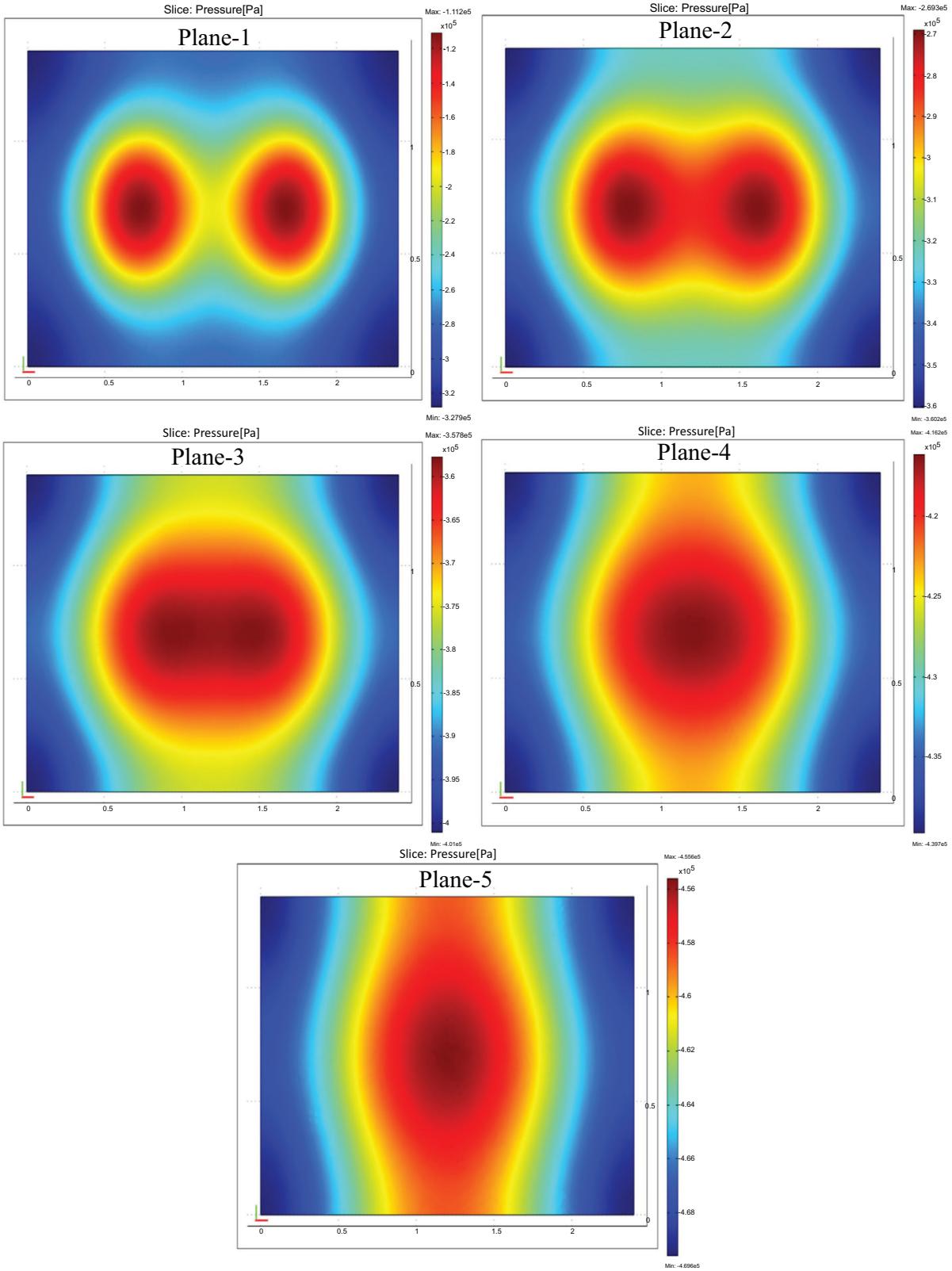

FIGURE 10.22 Predicted pressure amplitude in ultrasonic bath. *From Sutkar, V. S. and Gogate, P. R. (2010). Mapping of cavitational activity in high frequency sonochemical reactor. Chemical Engineering Journal, 158(2), 296–304. https://doi.org/10.1016/j.cej.2010.01.051* Variation of pressure amplitude in a reactor with 204 kHz frequency. A higher-pressure amplitude was observed in plane 1 very near to the wall of the reactor with the average pressure amplitude being 2.19 atm. As we go away from plane 1, the average pressure amplitude increases and the maximum was 4.62 atm obtained on plane 5.

TABLE 10.2 Bubble dynamics simulations.
Results of bubble dynamics simulations.

Sr. No	Frequency (kHz)	Collapse pressure $P_{c\ (atm)}$	Collapse temperature T_c (K)	Cavity collapse time (μs)	R_{max}/R
1	204	11480.73	6752.95	3.43	6.22
2	694	8699.17	5134.7	1.05	2.23

plane 4. The presence of NaCl results in enhanced cavitational activity attributed to a change in physicochemical properties, leading to lower attenuation of sound waves, high collapse pressure, and temperature and life time of the cavity.

10.6 Outlook and path forward

In this chapter we highlighted three crucial aspects in energy efficiency assessment and mapping of sonochemical reactors.

1. Experimental energy efficiency assessment using various dosimetry,
2. Experimental tools for mapping of cavitational activity in the sonochemical reactor, and
3. Modelling and simulation-based assessment of cavitational activity in on a sonochemical reactor.

Energy efficiency assessment and mapping is crucial not only to understand the correlation between the operating condition / design parameters and the extent of transformation, but also to develop rules for scaling up the sonochemical reactors. We outline the major challenges which we need to overcome to prepare well written rules for the scale up of sonochemical reactors. Incidentally, these are also the major gaps in the present understanding of the functioning of sonochemical reactor.

1. Realistic estimation of attenuation coefficient for the respective transfer medium,
2. characterization of nucleation sources and generation rate for real composition of liquid medium

While many of these dosimetry analyses are good representative of the efficiency and performance of sonochemical reactors, these are still results of the representative system and not the actual performance of the system with real reactants. Nucleation rates can be significantly different in dosimetry studies as compared to real life application with actual reactants in sonochemical reactors. As a result, there can be substantial deviation in efficiency of sonochemical reactors for dosimetry analysis and reactants. This necessitates the trial of a sonochemical reactor with actual reactants and drawing well defined cause and effect rules between the design parameters and operating conditions with the extent of transformation. Developing experimental tools/ protocols for quantifying nucleation rates would significantly help quantifying the cavitational activity in the sonochemical reactor. Once nucleation rates are quantified, it will also provide good estimate of attenuation coefficient.

It is also emphasized that nucleation rate is not a static parameter and will keep on changing with time and operating conditions. Hence, developing understanding/ co-relations with composition of reactants, and operating conditions is crucial. It would also help to analyze the performance of sonochemical systems with seeded nuclei. Seeded system can not only kept limited for exploratory purpose but also for real life applications. Mahulkar et al. has experimentally proven that when steam is introduced in presence of ultrasound the overall cavitational yield was significantly increased (Mahulkar et al., 2008). This was mainly because the steam bubble would provide ready nuclei for cavitation. While introducing steam might not be feasible for all the applications, it is suggested to explore alternate sources of ready nuclei for the respective applications.

References

Arrojo, S., Nerín, C., Benito, Y., 2007. Application of salicylic acid dosimetry to evaluate hydrodynamic cavitation as an advanced oxidation process. Ultrason. Sonochem. 14 (3), 343–349. https://doi.org/10.1016/j.ultsonch.2006.06.007.

Avvaru, B., Pandit, A.B., 2008a. Experimental investigation of cavitational bubble dynamics under multi-frequency system. Ultrason. Sonochem. 15 (4), 578–589. https://doi.org/10.1016/j.ultsonch.2007.06.012.

Bhirud, U.S., Gogate, P.R., Wilhelm, A.M., Pandit, A.B., 2004. Ultrasonic bath with longitudinal vibrations: a novel configuration for efficient wastewater treatment. Ultrasonics Sonochemistry 11 (3–4), 143–147. doi:https://doi.org/10.1016/j.ultsonch.2004.01.010.

Boldo, P., Renaudin, V., Gondrexon, N., Chouvellon, M., 2004. Enhancement of the knowledge on the ultrasonic reactor behaviour by an interdisciplinary approach. Ultrason. Sonochem. 11 (1), 27–32. https://doi.org/10.1016/S1350-4177(03)00112-3.

Chakinala, A.G., Gogate, P.R., Burgess, A.E., Bremner, D.H., 2007. Intensification of hydroxyl radical production in sonochemical reactors. Ultrason. Sonochem. 14 (5), 509–514. https://doi.org/10.1016/j.ultsonch.2006.09.001.

Contamine, R.F., Wilhelm, A.M., Berlan, J., Delmas, H., 1995. Power measurement in sonochemistry. Ultrason. Sonochem. 2 (1), S43–S47. https://doi.org/10.1016/1350-4177(94)00010-P.

Entezari, M.H., Kruus, P., 1994. Effect of frequency on sonochemical reactions. I: Oxidation of iodide. Ultrason. Sonochem. 1 (2), S75–S79. https://doi.org/10.1016/1350-4177(94)90001-9.

Feng, R., Zhao, Y., Zhu, C., Mason, T.J., 2002. Enhancement of ultrasonic cavitation yield by multi-frequency sonication. Ultrason. Sonochem. 9 (5), 231–236. https://doi.org/10.1016/S1350-4177(02)00083-4.

Fuster, D., Dopazo, C., Hauke, G., 2011. Liquid compressibility effects during the collapse of a single cavitating bubble. J. Acoust. Soc. Am. 129 (1), 122–131. https://doi.org/10.1121/1.3502464.

Gogate, P.R., Mujumdar, S., Pandit, A.B., 2003. Sonochemical reactors for waste water treatment: Comparison using formic acid degradation as a model reaction. Adv. Environ. Res. 7 (2), 283–299. https://doi.org/10.1016/S1093-0191(01)00133-2.

Gogate, P.R., Sutkar, V.S., Pandit, A.B., 2011. Sonochemical reactors: Important design and scale up considerations with a special emphasis on heterogeneous systems. Chem. Eng. J. 166 (3), 1066–1082. https://doi.org/10.1016/j.cej.2010.11.069.

Gogate, P.R., Tatake, P.A., Kanthale, P.M., Pandit, A.B., 2002. Mapping of sonochemical reactors: review, analysis, and experimental verification. AlChE J. 48 (7), 1542–1560. https://doi.org/10.1002/aic.690480717.

Gogate, P.R., Tayal, R.K., Pandit, A.B., 2006. Cavitation: a technology on the horizon. Current Science 91 (1), 35–46. https://www.currentscience.ac.in/show.issue.php?volume=91&issue=1.

Harkal, U.D., Gogate, P.R., Pandit, A.B., Shenoy, M.A., 2006. Ultrasonic degradation of poly(vinyl alcohol) in aqueous solution. Ultrason. Sonochem. 13 (5), 423–428. https://doi.org/10.1016/j.ultsonch.2005.07.002.

Henglein, A., Gutierrez, M., 1993. Sonochemistry and sonoluminescence: effects of external pressure. J. Phys. Chem. 97 (1), 158–162. https://doi.org/10.1021/j100103a027.

Hodnett, M., Zeqiri, B., 2008. Toward a reference ultrasonic cavitation vessel: Part 2 - investigating the spatial variation and acoustic pressure threshold of inertial cavitation in a 25 kHz ultrasound field. IEEE Trans. Ultrason. Ferroelectr. Freq. Control 55 (8), 1809–1822. https://doi.org/10.1109/TUFFC.2008.864.

Hu, Y., Zhang, Z., Yang, C., 2008. Measurement of hydroxyl radical production in ultrasonic aqueous solutions by a novel chemiluminescence method. Ultrason. Sonochem. 15 (5), 665–672. https://doi.org/10.1016/j.ultsonch.2008.01.001.

Jiao, Q., Bayanheshig, Tan, X., Zhu, J, 2014. Numerical simulation of ultrasonic enhancement on mass transfer in liquid-solid reaction by a new computational model. Ultrason. Sonochem. 21 (2), 535–541. https://doi.org/10.1016/j.ultsonch.2013.09.002.

Jordens, J., Honings, A., Degrève, J., Braeken, L., Gerven, T.V., 2013. Investigation of design parameters in ultrasound reactors with confined channels. Ultrason. Sonochem. 20 (6), 1345–1352. https://doi.org/10.1016/j.ultsonch.2013.03.012.

Kanthale, P.M., Gogate, P.R., Pandit, A.B., Wilhelm, A.M., 2003. Mapping of an ultrasonic horn: link primary and secondary effects of ultrasound. Ultrasonics Sonochemistry 10 (6), 331–335. doi:https://doi.org/10.1016/S1350-4177(03)00104-4.

Klíma, J., Frias-Ferrer, A., González-García, J., Ludvík, J., Sáez, V., Iniesta, J., 2007. Optimisation of 20 kHz sonoreactor geometry on the basis of numerical simulation of local ultrasonic intensity and qualitative comparison with experimental results. Ultrason. Sonochem. 14 (1), 19–28. https://doi.org/10.1016/j.ultsonch.2006.01.001.

Koda, S., Kimura, T., Kondo, T., Mitome, H., 2003. A standard method to calibrate sonochemical efficiency of an individual reaction system. Ultrason. Sonochem. 10 (3), 149–156. https://doi.org/10.1016/S1350-4177(03)00084-1.

Krefting, D., Mettin, R., Lauterborn, W., 2004. High-speed observation of acoustic cavitation erosion in multibubble systems. Ultrasonics Sonochemistry 11 (34), 119–123. doi:doi.org/10.1016/j.ultsonch.2004.01.006.

Kuijpers, M.W.A., Kemmere, M.F., Keurentjes, J.T.F., 2002. Calorimetric study of the energy efficiency for ultrasound-induced radical formation. Ultrasonics 40 (18), 675–678. doi:doi:https://doi.org/10.1016/S0041-624X(02)00197-X

Kumar, A., Gogate, P.R., Pandit, A.B., 2007. Mapping the efficacy of new designs for large scale sonochemical reactors. Ultrason. Sonochem. 14 (5), 538–544. https://doi.org/10.1016/j.ultsonch.2006.11.005.

Kumar, A., Kumaresan, T., Pandit, A.B., Joshi, J.B., 2006. Characterization of flow phenomena induced by ultrasonic horn. Chem. Eng. Sci. 61 (22), 7410–7420. https://doi.org/10.1016/j.ces.2006.08.038.

Lezzi, A., Prosperetti, A., 1987. Bubble dynamics in a compressible liquid. Part 2. Second-order theory. J. Fluid Mech. 185, 289–321. https://doi.org/10.1017/s0022112087003185.

Little, C., El-Sharif, M., Hepher, M.J., 2007. The effect of solution level on calorific and dosimetric results in a 70 kHz tower type sonochemical reactor. Ultrason. Sonochem. 14 (3), 375–379. https://doi.org/10.1016/j.ultsonch.2006.07.009.

Mahulkar, A.V., Bapat, P.S., Pandit, A.B., Lewis, F.M., 2008. Steam bubble cavitation. AlChE J. 54 (7), 1711–1724. https://doi.org/10.1002/aic.11509.

Mahulkar, A.V., Riedel, C., Gogate, P.R., Neis, U., Pandit, A.B., 2009. Effect of dissolved gas on efficacy of sonochemical reactors for microbial cell disruption: Experimental and numerical analysis. Ultrason. Sonochem. 16 (5), 635–643. https://doi.org/10.1016/j.ultsonch.2008.11.005.

Mahulkar, A.V., Pandit, A.B., 2010. Acoustic streaming: CFD Analysis. Analysis of hydrodynamic and acoustic cavitation reactors. VDM Verlag Dr. Müller.

Margulis, M.A., Margulis, I.M, 2003. Calorimetric method for measurement of acoustic power absorbed in a volume of a liquid. Ultrasonics Sonochemistry 10 (6), 343–345. doi:doi:https://doi.org/10.1016/S1350-4177(03)00100-7.

Memoli, G., Gélat, P.N., Hodnett, M., Zeqiri, B., 2012. Characterisation and improvement of a reference cylindrical sonoreactor Ultrason. Sonochem. 19, 939–952.

Mitome, H., Hatanaka, S., 2002. Optimization of a sonochemical reactor using a pulsing operation. Ultrasonics 40 (1), 683–687. https://doi.org/10.1016/S0041-624X(02)00258-5.

Moholkar, V.S., Sable, S.P., Pandit, A.B., 2000. Mapping the cavitation intensity in an ultrasonic bath using the acoustic emission. AIChE J. 46 (4), 684–694. https://doi.org/10.1002/aic.690460404.

Nowak, T., Cairós, C., Batyrshin, E., Mettin, R., 2015. Acoustic streaming and bubble translation at a cavitating ultrasonic horn. AIP Conf. Proc. 1685 (1), 020002. https://doi.org/10.1063/1.4934382.

Rochebrochard d'Auzay, S.d.L., Blais, J.F., Naffrechoux, E., 2010. Comparison of characterization methods in high frequency sonochemical reactors of differing configurations. Ultrason. Sonochem. 17 (3), 547–554. https://doi.org/10.1016/j.ultsonch.2009.10.024.

Servant, G., Laborde, J.-L., Hita, A., Caltagirone, J.-P., Gérard, A., 2001. Spatio-temporal dynamics of cavitation bubble clouds in a low frequency reactor: comparison between theoretical and experimental results. Ultrason. Sonochem. 8 (3), 163–174. https://doi.org/10.1016/S1350-4177(01)00074-8.

Sutkar, V.S., Gogate, P.R., 2009. Design aspects of sonochemical reactors: Techniques for understanding cavitational activity distribution and effect of operating parameters. Chem. Eng. J. 155 (1), 26–36. https://doi.org/10.1016/j.cej.2009.07.021.

Sutkar, V.S., Gogate, P.R., 2010. Mapping of cavitational activity in high frequency sonochemical reactor. Chem. Eng. J. 158 (2), 296–304. https://doi.org/10.1016/j.cej.2010.01.051.

Sutkar, V.S., Gogate, P.R., Csoka, L., 2010. Theoretical prediction of cavitational activity distribution in sonochemical reactors. Chem. Eng. J. 158 (2), 290–295. https://doi.org/10.1016/j.cej.2010.01.049.

Wei, Z., Weavers, L.K., 2016. Combining COMSOL modeling with acoustic pressure maps to design sono-reactors. Ultrason. Sonochem. 31, 490–498. https://doi.org/10.1016/j.ultsonch.2016.01.036.

Whillock, G.O.H., Harvey, B.F., 1997. Ultrasonically enhanced corrosion of 304L stainless steel II: the effect of frequency, acoustic power and horn to specimen distance. Ultrason. Sonochem. 4 (1), 33–38. https://doi.org/10.1016/S1350-4177(96)00015-6.

Xu, Z., Yasuda, K., Koda, S., 2013. Numerical simulation of liquid velocity distribution in a sonochemical reactor. Ultrason. Sonochem. 20 (1), 452–459. https://doi.org/10.1016/j.ultsonch.2012.04.011.

Chapter 11

Sources of dissipation: An outlook into the effects of operational conditions

Rana Kıdak
Cyprus International University, Nicosia, Turkey

11.1 Introduction

Ultrasound is sound wave with frequency higher than the upper audible limit of human hearing. This limit varies from person to person and is approximately 20 kilohertz (20,000 hertz) and it has many applications in several actively researched areas (Henglein, 1987). Sonochemistry is one of these areas and there is high interest due to the abundant availability of ultrasonic laboratory hardware, namely the sonicators and reactors.

The two main sonicators are disk type or a sonic probe (or horn) type. Both types have the same basic arrangement in that they contain an electrical generator and an ultrasonic transducer. The ultrasonic generator receives and converts energy to the sound waves with proper frequency. The generator provides high-voltage pulses of energy at the desired frequency to the transducer.

A transducer converts energy from one form to another or in other words, a signal in one form of energy to a signal in another. Piezoelectric transducers convert electrical energy to ultrasonic energy. Piezoelectric materials expand and contract when an electric field is applied. The transducer is the most important component in the system and all pieces of a modern ultrasonic equipment operates with the piezoelectric principle.

Ultrasonic irradiation of liquids produces excessive energy for chemical reactions. The chemical effects of ultrasound derive from acoustic cavitation, which is a nonlinear process that serves as a means of concentration of the diffuse energy of sound in liquids. This high-energy micro-environment is induced by the extreme conditions during the cavitation event by means of radicals and or extreme temperature and pressure (Griffing, 1952; Fitzgerald et al., 1956). The cavitation is composed of formation, growth and implosive collapse of bubbles in a liquid.

When ultrasound is exerted to a liquid, the expansion cycles forge negative pressure, leading to formation of cavities, if the negative pressure exceeds the local tensile strength of the liquid at its weaker spots. (Tensile strength is the maximum stress that a material can withstand from a stretching load without tearing). These cavities may be regarded as micro bubbles. Once formed, the micro bubbles irradiated with ultrasound will absorb energy from the sound waves and grow. The growth of cavity is intensity dependent. The intensity will be explained later in Section 11.6.1.1. Smaller cavities grow in a rapid way under higher intensities. The high rapidity of cavity expansion will result in smaller cavity in compression stage of acoustic cycle. Low intensities result in oscillation of the cavity bubble during multiple cycles and lead to diffusion of gases and water vapor into the bubble. The introduction gives rise to expansion of bubbles up to a critical size where it can absorb energy from the ultrasonic irradiation. This critical size is called the resonant size (Flint and Suslick, 1991). After the critical limit, the cavity implodes and results in aggressive conditions for chemical reactions (Ince et al., 2001; Suslick, 1990).

11.2 Theoretical approaches

Sonochemistry induced by ultrasonic irradiation of homogeneous fluids is a direct outcome of the extreme conditions generated in collapsing microbubbles. Such extremes are reported to produce unique catalytic effects, arising from inherent advantages of the system such as: (1) the ability to generate high-energy species and (2) the mimicry of autoclave reaction

Energy Aspects of Acoustic Cavitation and Sonochemistry: Fundamentals and Engineering. DOI: https://doi.org/10.1016/B978-0-323-91937-1.00016-5
Copyright © 2022 Elsevier Inc. All rights reserved.

conditions (i.e., high temperatures and pressures) on a microscopic scale (Suslick, 1990). These effects start in the cavities, which are made of microbubbles filled with vapor of the liquid medium and/or dissolved solutes and gases diffused into them. During the collapse of these cavities in pure aqueous systems, gaseous water molecules entrapped in expanded microbubbles are fragmented as in pyrolysis to generate highly reactive radical species such as hydroxyl radicals and hydrogen atoms.

There are some theories to describe sonochemistry. The mostly favored theory is the "Hot Spot Theory". Compression of a gas generates heat. The compression of cavities when they implode in irradiated liquids is so rapid that little heat can escape from the cavity during collapse. The surrounding liquid, however, is still cold and will quickly quench the heated cavity. Thus, one generates a short-lived, localized hot spot in an otherwise cold liquid. Such a hot spot is the source of sonochemistry; it has a temperature of roughly 5000°C, a pressure of about 1000 atmospheres, a lifetime considerably less than a microsecond, and heating and cooling rates above 10 billion°C per second (Suslick, 1990; Dahlem et al., 1998).

The second most accepted theory is "Electrical Theory" by Margulis (Margulis, 1995). This theory suggests that during bubble formation and collapse, enormous electrical field gradients are generated and these are sufficiently high to cause bond breakage and chemical activity.

The "Plasma Theory" by Lepoint and Muille also suggests the extreme conditions associated with the fragmentative collapse is due to intense electrical fields and seems not to involve a true implosion (Lepoint and Mullie, 1994). They compared the origin of cavitation chemistry to corona-like discharge caused by a fragmentation process and supported and indicated the formation of micro plasmas inside the bubble.

The "Supercritical Theory" proposed by Hoffmann suggests the existence of a layer in the bubble-solution interface where temperature and pressure may be beyond the critical conditions of water (647 K, 22.1 MPa) and showed that supercritical water is obtained during the collapse of cavitation bubbles generated sonolytically (Hua et al., 1995).

11.3 Formation of extreme conditions in reactions

Determination of the temperatures reached in a cavitation bubble has remained a difficult experimental problem. The transient nature of the cavitation event precludes direct measurement of the conditions generated during bubble collapse. Chemical reactions themselves, however, can be used to probe reaction conditions. The effective temperature of a system can be determined with the use of competing unimolecular reactions whose rate dependencies on temperature have already been measured. This technique of "comparative chemical thermometry" was used by Suslick et al., in 1986, to determine the effective temperature reached during cavity collapse (Suslick et al., 1986). For a series of organometallic reactions, the relative sonochemical rates were measured. In combination with the known temperature behavior of these reactions, the conditions present during cavity collapse could then be determined. The effective temperature of these hot spots was 5200 K. Of course, the comparative rate data represent only a composite temperature: during the collapse, the temperature has a highly dynamic profile, as well as a spatial gradient in the surrounding liquid.

When a liquid is subjected to ultrasound, not only does chemistry occur, but light is also produced. Such "sonoluminescence" provides an alternate measure of the temperature of the high-energy species produced during cavitation. From a comparison of synthetic to observed spectra, the effective cavitation temperature of the emitting species is 5100 K. The agreement between this spectroscopic determination of the cavitation temperature and that made by comparative rate thermometry of sonochemical reactions is surprisingly close.

The hydroxyl radicals generated by water sonolysis may either react in the gas phase or recombine at the cooler gas liquid interface and/or in the bulk during cavity collapse to produce hydrogen peroxide and water (Riesz and Mason, 1991; Fischer et al., 1986).

The reaction mechanism is shown below:

$$H_2O))) \rightarrow \cdot OH + \cdot H \text{ (pyrolysis)} \tag{11.1}$$

$$\cdot OH + \cdot H \rightarrow H_2O \tag{11.2}$$

$$2 \cdot OH \rightarrow H_2O + O \tag{11.3}$$

$$2 \cdot OH \rightarrow H_2O_2 \tag{11.4}$$

$$2 \cdot H \rightarrow H_2 \tag{11.5}$$

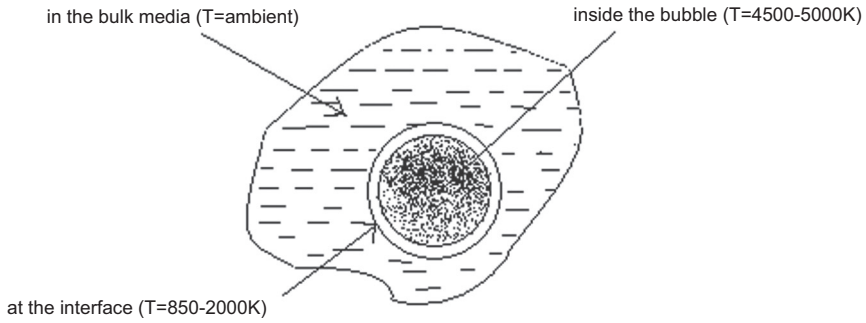

FIGURE 11.1 Possible sites of chemical reactions in homogeneous reaction media (Ince and Tezcanli, 1999).

11.3.1 Sonochemical reaction sites

Experiences in homogeneous sonochemistry have shown that there are three reaction sites in ultrasonically irradiated liquids as shown in Fig. 11.1 (Weavers et al., 1998):

*The cavitation bubble itself

*The interfacial sheath between the gaseous bubble and the surrounding liquid

*The solution bulk.

In water or effluent treatment practices, organic pollutants may be destroyed either at the first two sites upon combined effects of pyrolytic decomposition and hydroxylation, or in the solution bulk via oxidative degradation by hydroxyl radicals and hydrogen peroxide (Weavers et al., 1998). The intensity of oxidation reactions in the latter site is directly and exclusively related to the quantity of available uncombined hydroxyl radicals, as they migrate into the aqueous phase during collapse of cavity bubbles.

Assuming adiabatic bubble collapse, the maximum temperatures and pressures within the collapsed cavitation bubbles are predicted by Noltingk and Neppiras from approximate solutions of Rayleigh-Plesset Eqs. (11.6–11.7), as follows (Noltingk and Neppiras, 1950; Neppiras, 1980):

$$T_{max} = T_0 \left[\frac{P_a(\gamma - 1)}{P} \right] \tag{11.6}$$

$$P_{max} = P \left[\frac{P_a(\gamma - 1)}{P} \right]^{\left[\frac{\gamma}{\gamma - 1}\right]} \tag{11.7}$$

where T_o = ambient temperature in the solution bulk, P_a = pressure in the bubble at the moment of collapse (acoustic pressure), P = pressure in the bubble at its maximum size or the vapor pressure of the solution, γ= polytrophic ratio.

11.3.2 Definition of "cavitation treshold"

When very low power ultrasound is passed through a liquid and the power is gradually increased, a point is reached at which the intensity of sonication is sufficient to cause cavitation in the fluid. It is only at powers above the cavitation threshold that sonochemistry can occur because only then can the great energies associated with cavitational collapse be released into the liquid. In the medical profession, where the use of ultrasonic scanning techniques is widespread, keeping scanning intensities below the cavitation threshold is of vital importance, so as not cause chemical reactions in the body (Mason et al., 1990).

11.4 Transducers

The nature of cavitation at various frequencies and pressures depends on the type of transduce used. The active aggregation sites are formed either as standing waves for plate type transducers or at high energy density areas like around the tip for horn (or probe) type transducers (Ashokkumar et al., 2009).

A plate type transducer working at low frequencies may generate stable bubbles because of standing waves mainly at the antidotes of the waves (Ashokkumar et al., 2009). On the other hand, a plate type transducer working at high frequencies may attenuate and traveling waves may dominate the system.

This phenomenon may force the bubbles towards the liquid surface with the spreading waves, and they will be trapped in the standing waves, so the bubbles concentrate mostly on the surface (Ashokkumar et al., 2009; Lee et al., 2011). When mid to high frequencies are applied, a plate type transducer my produce transient cavitation through traveling waves (Leighton, 2012; Bussemaker and Zhang, 2014). Other researchers have observed that below 200 kHz, the bubbles tend to generate in form of high energy stable bubbles (Gielen et al., 2015), while Tronson et al. reported increased sonoluminescence by stable bubbles at 515 kHz (Tronson et al., 2002).

A horn type transducer operating at 20 kHz may produce both traveling and standing waves (Henglein, 1995). The horn tip is the most active zone because of the high energy density (Ashok kumar, 2011; Pflieger et al., 2015; Rooze et al., 2011). A thin layer of bubbles is formed at the horn surface which impedes the sound field's propagation and causes a reduction in pressure amplitude beyond its formation. This has been confirmed with measurements of pressure amplitude when the bubble layer is the size of an acoustic half wavelength, in this instance the impedance suddenly drops (Dubus et al., 2010). It has been suggested that traveling waves are more prevalent for the horn and that transient bubbles dominate (Tronson et al., 2002).

An ultrasound horn that operates at low frequency produces primarily traveling waves, and is beneficial in creating larger bubbles that collapse violently and are unstable in nature. This contributes to an increase in radical production and bubble instability. However, there can also be increased impedance due to bubble agglomeration at the tips surface and, as such, can be an inefficient method of achieving sonochemical reactions. Conversely, a plate transducer operating at high frequency may be advantageous with quasi acoustic streaming and radiation forces causing increased motion of the bubbles and active cavitation occurring in standing waves at the surface. Quasi acoustic streaming hinders coalescence, and increases the rate of growth and mass transfer that contributes to further instability and fragmentation.

11.5 Signals

When ultrasound is practiced in continuous signals, it becomes inefficient because of limited spatial distribution and loss of pressure amplitude (Tuziuti et al., 2008). For the above reasons, the signals are applied in pulsed, sweeping, or bimodel modes to increase the active cavitation (Henglein et al., 1989; Deojay et al., 2011; Lee et al., 2008; Hauptmann et al., 2013b; Flynn & Church, 1984; Casadonte et al., 2005). Especially, pulsed signals increase the active regions (Casadonte et al., 2005). The consecutive ON and OFF periods are optimized as they exert effects on sonoluminescence and sonochemical activity. The key point of optimization depends on the critical OFF period. If the ON period is short, the lifetime of active bubbles is short in the OFF period. On the other hand, if the ON period is long, the active bubbles may overgrow to coalesce and become degasified in the OFF period (Dekerckheer et al., 1998; Zhu et al., 2000; Hauptmann et al., 2013a).

11.6 Effects of operational parameters

11.6.1 The primary parameters

11.6.1.1 Power intensity

An ultrasonic system transforms electrical power to vibrational energy, which is then transmitted into the sonicated reaction medium. Part of it is lost to produce heat, and another part produces cavitation, but not all the cavitation energy produces chemical and physical effects. Some energy is reflected and some is consumed in sound re-emission. Hence, there can be significant differences between the power supplied from the generator and that delivered into the reactor. The intensity (I) in sonication is directly proportional to the square of the amplitude of vibration of the ultrasonic source. The direct measurement of the amplitude at the vibrating tip of a probe transducer may be a physical measurement, which is simply achieved by observing the vibration using a metallurgical microscope with a calibrated eyepiece. This measurement will give a parameter that should be directly proportional to the acoustic power, which is being transmitted into the reaction solution where the probe is immersed into. The intensity has the unit W/m^2 and is calculated by the Eq. 11.8 (Ince et al., 2001):

$$I = \frac{{P_a}^2}{2\rho c} \tag{11.8}$$

Where P_a = acoustic power (W), ρ = density of water (g/cm^3), c = speed of sound in water (1500 m/sec).

In general, an increase in intensity will provide an increase in the sonochemical effects, but there are limits to the ultrasonic energy input to the system (Roy, 1992).

A minimum intensity for sonication is required to reach the cavitation threshold. This minimum depends upon the frequency.

When a large amount of ultrasonic power enters a system, a great number of cavitation bubbles are generated in the solution. Many of these will coalesce forming larger, more long-lived bubbles. These will certainly act as a barrier to the transfer of acoustic energy through the liquid.

At high vibrational amplitude the source of ultrasound will not be able to maintain contact with the liquid throughout the complete cycle. Technically this is known as decoupling, and results in a great loss in efficiency of transfer of power from the source to the medium. Decoupling is more effective when large numbers of cavitation bubbles build up at or near the emitting surface of the transducer (Roy, 1992).

11.6.1.2 Pressure

The applied pressure has a critical effect on sonochemistry as it directly effects the power transferred to the liquid phase and yield of reactions (Suslick, 1997; Harada and Ono, 2015; Kanthale et al., 2008). The pressure also has optimal range as the other operational parameters. The lower limit determines when the nucleation and growth of cavitation bubbles will commerce and at the upper limit the coalescence and degassing will start to regress the active cavitation (Blake and Matula, 1999). High pressure with the optimal limits causes bubbles to fragment producing new bubbles to contribute to sonochemical activity (de Jong et al., 1992; de Jong et al., 1994; Wei et al., 1997; Yasui, 2011; Calvisi et al., 2007).

At high pressure, the primary and secondary Bjerknes' forces increase and bubbles are exposed to forces those which enhance to approach one another (Hatanaka et al., 2001). The rise in approach velocity is possible up to the point where the rate of film drainage between bubbles in contact starts to decrease, upon which there is rise in critical thickness for rupture to take place and rebound is more likely to occur (Kirkpatrick and Lockett, 1974).

The pressure also affects quasi acoustic and acoustic streaming and consequently bubble motion and coalescence (Mitome et al., 1997). Quasi acoustic streaming is created by attenuation of the sound field and it is affected by an energy gradient caused by the bubbles (Kumar et al., 2007). Quasi acoustic streaming results in distortion of standing waves (Henglein et al., 1989). Acoustic streaming generally occurs at the vicinity of individual bubbles (Mitome et al., 1997). Another concept related to pressure is the microjets. Microjects are high speed liquid jets that propagate from the proximal side of the bubble towards the nearby surface (Suslick and Price, 1999) and they occur from the bubble surface motions and the boundaries or solid surfaces due to asymmetry of flow between the bubble and the solid surface (Benjamin and Ellis, 1966). The pressure brings about negative yields in sonochemical reactions at high levels. This may be attributed not only to coalescence and degassing but also to the effects of increasing liquid agitation.

High pressure amplitudes increase the number of cavities available and these will experience high levels of structural instability due to increase in the force of collapse. Concurrently, due to bubble oscillation and surface instabilities, associated acoustic streaming can occur. The resulting translational and cavitational motion is further acted upon by the energy gradient of the sound field and facilitates quasi acoustic streaming which is increased with pressure amplitude. In summary, the effect of increasing pressure amplitude is to force bubbles into a structured positional and oscillatory regime which up to a point presents a mechanism for increased sonochemical activity (Wood et al., 2017).

11.6.1.3 Frequency

In sonochemistry the frequency ranges are roughly divided in three major regions; low frequency (20–100 kHz), medium frequency (100–1000 kHz) and high frequency (>1000 kHz). Most of the advanced oxidative effects have been observed within the low and/or medium range frequency regions, with very random studies in high frequency. The high frequency ultrasound has almost no chemical effects on any liquids, thus it is safely used in many medical applications with different purposes. Stable bubbles with resonance radius of ~170 micrometers are reported to be formed at low frequencies. Stable or long-lived bubbles undergo collapse only after a series of compression and rarefaction cycles, enabling sufficient time for vapor and gases dissolve in them. This delay in collapse time at low frequencies give way to radical scavenging, due to recombination reactions and inhibition of mass transfer of hydroxyl radicals to liquid (Mason and Lorimer, 1990). In low frequency applications, hydrophobic reactants diffuse into bubbles, and they are destructed by pyrolysis inside the cavitation bubble by the high temperature and pressure (Barbier and Petrier, 1996; Colarusso and Serpone, 1996; Petrier et al., 1994).

Application of higher frequencies within 300–1000 kHz range serve as creator of transient cavity bubbles, which have smaller resonance radii and short life times (Suslick, 1997). Before their collapse, such bubbles do not allow any gas to dissolve in their bodies and the radicals are abruptly released into the liquid phase without occurrence of any scavenging or recombination reactions. The abundance of radicals sprayed into the liquid effectuates the oxidative reactions on the non-volatile reactants (Barbier & Petrier, 1996; Lepoint & Mullie, 1994; Mason et al., 1990; Petrier et al., 2002).

11.6.1.4 Reactor design

The main concern of scientists and engineers working with ultrasonic systems is to accomplish maximum reaction yields and/or maximum pollutant destruction at optimal conditions. These features focus on the optimization of all operating parameters and mainly obtaining an efficient reactor as this feature has an important role in the effective power density delivered to the reaction liquid (Hua and Hoffmann, 1997; Mason and de Meulenaer, 1998).

It has been previously reported that the reaction yields can be optimized by adjusting the height of the liquid in the reactors. In a particular study, when the height was adjusted to H (which is an odd number multiple of the one fourth of the wavelength), the standing waves of great pressure amplitude occurred at low frequencies. Even though, the liquid height must be optimized at each and every reactor under different working condition, the maximum sonochemical activity is generally dependent on the effective absorption of the energy by the liquid. As shown in an example, appropriate liquid height provided high activity comparable at both low and high frequencies.

11.6.2 Secondary parameters

11.6.2.1 Liquid flow

Liquid flow which can be acquired through various methods such as mechanical stirring, circulation pumping or quasi or acoustic streaming, has impact on sonochemical activity. Flow enhances the release of limited number of cavitation bubbles from antinode regions, inducing less coalescence. Another role of flow is to enhance the mass transfer of gases into the bubbles. Liquid flow allows bubbles move into the liquid and travel to the active regions. Usually, these movements are nonlinear and bubbles are subjected to structural instability, asymmetric oscillation, and collapse, leading to an increase in activity. When liquid flow is provided via mechanical stirring or circulation pumping, other operating parameters such as applied power, frequency and reactor design, become influential on sonochemical activity. Low frequencies and high rpm applications (600,900,1300) provoked better chemical yields. On the contrary the yield was reduced at higher frequencies, supporting that coalescence is reduced at lower frequencies (Bussemaker and Zhang, 2014). Stirring also helps to give rise to peak sonoluminescence intensities at higher power applications.

Liquid flow is one of the causes of surface instabilization that induces acoustic streaming. When bubbles get trapped at antinode regions, flow will help them destabilize and even the bubbles left behind will be subjected to deformation and fragment (Wood et al., 2017).

11.6.2.2 Liquid temperature

Sonochemical reactions mechanisms and kinetics is strongly influenced by the liquid temperature just like the majority of all chemical reactions. The gas solubility decreases at higher temperatures and as a consequence the cavitation nuclei will be reduced, as the cavitation is formed at the weaker points in liquids. The cavitation threshold will be scaled up to higher power requirements, obstructing the sonochemical activity. Increased temperature acts as a barrier for the sonochemical reactions to occur. The main reason is that the vapor pressure increases and the surface tension and viscosity of the liquid decreases (Mason et al., 1990). Especially in case of volatile reactants, higher liquid temperatures will produce more vapor evoking cushion effect on bubble collapse (Suslick and Price, 1999).

11.6.2.3 Properties of solute

The physicochemical properties of reactants are the key factor for a scientist to decide about the operational parameters to be applied in sonochemistry. The concentration of reactants as well as the solubility, vapor pressure (or Henry's constant), Octanol-water partition coefficient (Log K_{ow}) play important roles for the selection of the right frequency, power, and reaction medium (Hua and Hoffmann, 1997; Suslick, 1990). As mentioned earlier, hydrophobic and nonvolatile reactants tend to diffuse into the stable bubbles where they are oxidized through pyrolytic paths or destructed at the bubble-liquid interface. On the contrary, hydrophilic reactants tend to stay in the liquid phase for various reasons. One of the reasons is that the cavitation bubbles have slight hydrophobic surfaces, and they exert repulsive forces if the reactant has low concentration. Such reactants at higher concentrations are subjected to other additional destructive pathways next to radical oxidation, such as hydroxylation at 300-500 kHz. The extent of decomposition depends on the solubility and concentration of the reactant.

11.6.2.4 Properties of solvent

Each solvent will have its own particular parameters so that the choice of solvent medium becomes very important when considering the reaction conditions to be used for sonochemistry. Consider the solvents water and pentane: The

intramolecular forces within these liquids are quite different, in that water has much stronger cohesion via hydrogen bonding than does pentane, which is held by van der Waals forces. Water also has a higher surface tension, giving water a much lower cavitation threshold than pentane (i.e., under otherwise identical conditions a greater intensity is required to cause cavitation in water than in pentane). The vapor pressure of water is considerably lower than that of pentane, so that it is a better choice of medium for sonochemical reactions than pentane (Mason et al., 1990).

11.6.2.5 Solid addition

As explained earlier, cavitation is a phenomenon in which the static pressure of the liquid reduces to below the liquid's vapor pressure, especially at weaker points in the liquids. Addition of solids in the liquids create cracks and weaker points in the liquid bulk and help to improve sonochemical activity when irradiated. It had been reported that glass beads, ceramic disks, SiO_2, Al_2O_3, and talc addition into the reaction medium enhanced cavitation effects. The presence of such material is reported to be especially useful for micronization of species (in ultrasonic cell disruption), and for the abrasion, activation, and alteration of the chemical properties of catalyst surfaces during ultrasonic irradiation of liquid media (Mason and de Meulenaer, 1998).

11.6.2.6 Gas addition

Presence of any gaseous or solid ingredient creates weak points in liquids and cavitation s favorably form at such liquid defect spots (Mason and de Meulenaer, 1998) . When liquid is fed or preferably saturated with a soluble gas, the cavitation is initiated via potential crevices that help to create nuclei (Petrier et al., 2002; Riesz and Mason, 1991). Gas introduction is almost essential in sonochemical activity because one of the effects of ultrasonic irradiation is degassing of liquids. So, researchers practically bubble up their reactors throughout the oxidation period to enhance the cavitation formation and help to increase the cavitational temperature and/or pressure as the dissolved gases absorbed in the bubbles will display catalytic effects.

The nature of saturating gas will affect the reaction depending on its chemical characteristic; such as thermal conductivity and the polytrophic ratio, which is the ratio of the specific heats of entrapped gases in the cavity (Hua and Hoffmann, 1997; Noltingk and Neppiras, 1950; Petrier et al., 2002; Riesz and Mason, 1991).

Noble gas introduction is a very common practice and depending on the decreasing order of the thermal conductivity, the heat loss to the liquid also decreases (Xe < Kr < Ar < Ne < He) (Hua and Hoffmann, 1997; Noltingk and Neppiras, 1950). Especially at higher frequencies, it becomes important to select gases with high polytrophic ratios and low thermal conductivity in order to increase the radical formation yields (Hua and Hoffmann, 1997). In a study by Colarusso and Serpone, despite equal polytrophic ratios of Argon and Helium in water, much higher yields of pyrolysis products were detected with the former, as attributed to its 10-fold lower thermal conductivity (Colarusso and Serpone, 1996).

11.7 Conclusion

Considering the facts that many scientists confirmed influence of the operating parameters in their studies, all the above-mentioned factors are important for their effects on the actual sonochemical applications. In a word, this section emphasizes that scientists/operators should learn deeply about the science behind these neglected factors in the application of sonochemistry.

References

Ashokkumar, M., 2011. The characterization of acoustic cavitation bubbles - an overview. Ultrasonics Sonochemistry, Vol. 18. Elsevier B.V., Amsterdam, pp. 864–872 Issue 4.

Ashokkumar, M., Lee, J., Iida, Y., Yasui, K., Kozuka, T., Tuziuti, T., Towata, A., 2009. The detection and control of stable and transient acoustic cavitation bubbles. PCCP 11 (43), 10118–10121. https://doi.org/10.1039/b915715h.

Barbier, P.F., Petrier, C., 1996. Study at 20 kHz and 500 kHz of the ultrasound-ozone advanced oxidation system : 4-Nitrophenol degradation. J Advanced Oxidation Technologies 1 (2). https://doi.org/10.1515/jaots-1996-0208.

Benjamin, T.B., Ellis, A.T., 1966. The collapse of cavitation bubbles and the pressures hereby produced against solid boundaries. Philos. Trans. R. Soc. A 260, 221–240.

Blake, J.R., Matula, T.J., 1999. Inertial cavitation and single–bubble sonoluminescence. Philosophical Transactions of the Royal Society of London. Series A: Mathematical, Physical and Engineering Sci 225–249. https://doi.org/10.1098/rsta.1999.0325.

Bussemaker, M.J., Zhang, D., 2014. A phenomenological investigation into the opposing effects of fluid flow on sonochemical activity at different frequency and power settings. 1. overhead stirring. Ultrason. Sonochem. 21 (1), 436–445. https://doi.org/10.1016/j.ultsonch.2013.07.002.

Calvisi, M.L., Lindau, O., Blake, J.R., Szeri, A.J., 2007. Shape stability and violent collapse of microbubbles in acoustic traveling waves. Phys. Fluids 19 (4), 047101. https://doi.org/10.1063/1.2716633.

Casadonte, D.J., Flores, M., Petrier, C., 2005. Enhancing sonochemical activity in aqueous media using power-modulated pulsed ultrasound: an initial study. Ultrason. Sonochem. 12 (3), 147–152. https://doi.org/10.1016/j.ultsonch.2003.12.004.

Colarusso, P., Serpone, N., 1996. Sonochemistry II.- effects of ultrasounds on homogeneous chemical reactions and in environmental detoxification. Res. Chem. Intermed. 22 (1), 61–89. https://doi.org/10.1163/156856796X00386.

Dahlem, O., Demaiffe, V., Halloin, V., Reisse, J., 1998. Direct sonication system suitable for medium-scale sohochemical reactors. AIChE J. 44 (12), 2724–2730. https://doi.org/10.1002/aic.690441213.

de Jong, N., Cornet, R., Lancée, C.T., 1994. Higher harmonics of vibrating gas-filled microspheres. Part one: simulations. Ultrasonics 32 (6), 447–453. https://doi.org/10.1016/0041-624X(94)90064-7.

de Jong, N., Hoff, L., Skotland, T., Bom, N., 1992. Absorption and scatter of encapsulated gas filled microspheres: theoretical considerations and some measurements. Ultrasonics 30 (2), 95–103. https://doi.org/10.1016/0041-624X(92)90041-J.

Dekerckheer, C., Bartik, K., Lecomte, J.P., Reisse, J., 1998. Pulsed sonochemistry. J. Phys. Chem. A 102 (46), 9177–9182. https://doi.org/10.1021/jp982489c.

Deojay, D.M., Sostaric, J.Z., Weavers, L.K., 2011. Exploring the effects of pulsed ultrasound at 205 and 616 kHz on the sonochemical degradation of octylbenzene sulfonate. Ultrason. Sonochem. 18 (3), 801–809. https://doi.org/10.1016/j.ultsonch.2010.10.005.

Dubus, B., Vanhille, C., Campos-Pozuelo, C., Granger, C., 2010. On the physical origin of conical bubble structure under an ultrasonic horn. Ultrason. Sonochem. 17 (5), 810–818. https://doi.org/10.1016/j.ultsonch.2010.03.003.

Fischer, C.H., Hart, E.J., Henglein, A., 1986. Ultrasonic irradiation of water in the presence of oxygen 18,18O2: isotope exchange and isotopic distribution of hydrogen peroxide. J. Phys. Chem. 90 (9), 1954–1956. https://doi.org/10.1021/j100400a043.

Fitzgerald, M.E., Griffing, V., Sullivan, J., 1956. Chemical effects of ultrasonics—"hot spot" chemistry. J. Chem. Phys. 25 (5), 926–933. https://doi.org/10.1063/1.1743145.

Flint, E.B., Suslick, K.S., 1991. The temperature of cavitation. Science 253 (5026), 1397–1399. https://doi.org/10.1126/science.253.5026.1397.

Flynn, H.G., Church, C.C., 1984. A mechanism for the generation of cavitation maxima by pulsed ultrasound. J. Acoust. Soc. Am. 76 (2), 505–512. https://doi.org/10.1121/1.391592.

Gielen, B., Jordens, J., Janssen, J., Pfeiffer, H., Wevers, M., Thomassen, L.C.J., Braeken, L., Van Gerven, T., 2015. Characterization of stable and transient cavitation bubbles in a milliflow reactor using a multibubble sonoluminescence quenching technique. Ultrason. Sonochem. 25 (1), 31–39. https://doi.org/10.1016/j.ultsonch.2014.08.013.

Griffing, V., 1952. The chemical effects of ultrasonics. J. Chem. Phys. 20 (6), 939–942. https://doi.org/10.1063/1.1700654.

Harada, H., Ono, Y., 2015. Improvement of the rate of sono-oxidation in the presence of CO2. Japan. J. Appl. Phys. 54 (7). https://doi.org/10.7567/JJAP.54.07HE10.

Hatanaka, S.I., Yasui, K., Tuziuti, T., Kozuka, T., Mitome, H., 2001. Quenching mechanism of multibubble sonoluminescence at excessive sound pressure. Japanese Journal of Applied Physics, Part 1: Regular Papers and Short Notes and Review Papers, 40 (5 B), 3856–3860. https://doi.org/10.1143/jjap.40.3856.

Hauptmann, M., Frederickx, F., Struyf, H., Mertens, P., Heyns, M., De Gendt, S., Glorieux, C., Brems, S., 2013a. Enhancement of cavitation activity and particle removal with pulsed high frequency ultrasound and supersaturation. Ultrason. Sonochem. 20 (1), 69–76. https://doi.org/10.1016/j.ultsonch.2012.04.015.

Hauptmann, M., Struyf, H., Gendt, S.D., Glorieux, C., Brems, S., 2013b. Evaluation and nterpretation of bubble size distributions in pulsed megasonic fields. J. Appl. Phys 113.

Henglein, A., 1987. Sonochemistry: historical developments and modern aspects. Ultrasonics 25 (1), 6–16. https://doi.org/10.1016/0041-624X(87)90003-5.

Henglein, A., 1995. Chemical effects of continuous and pulsed ultrasound in aqueous solutions. Ultrasonics - Sonochemistry 2 (2), S115–S121. https://doi.org/10.1016/1350-4177(95)00022-X.

Henglein, A., Ulrich, R., Lilie, J., 1989. Luminescence and chemical action by pulsed ultrasound. J. Am. Chem. Soc. 111 (6), 1974–1979. https://doi.org/10.1021/ja00188a004.

Hua, I., Hoechemer, R.H., Hoffmann, M.R., 1995. Sonolytic hydrolysis of p-nitrophenyl acetate. The role of supercritical water. J. Phys. Chem. 99 (8), 2335–2342. https://doi.org/10.1021/j100008a015.

Hua, I., Hoffmann, M.R., 1997. Optimization of ultrasonic irradiation as an advanced oxidation technology. Environ. Sci. Technol. 31 (8), 2237–2243. https://doi.org/10.1021/es960717f.

Ince, N.H., Tezcanli, G., Belen, R.K., Apikyan, G., 2001. Ultrasound as a catalyzer of aqueous reaction systems: the state of the art and environmental applications. Appl. Catal. B 29 (3), 167–176. https://doi.org/10.1016/S0926-3373(00)00224-1.

Ince and Tezcanli, 1999, Treatability of textile dye-bath effluents by advanced oxidation: Preparation for reuse, Wat. Sci. Technol., 40 (1), pp. 183–190.

Kanthale, P., Ashokkumar, M., Grieser, F., 2008. Sonoluminescence, sonochemistry (H2O2 yield) and bubble dynamics: frequency and power effects. Ultrason. Sonochem. 15 (2), 143–150. https://doi.org/10.1016/j.ultsonch.2007.03.003.

Kirkpatrick, R.D., Lockett, M.J., 1974. The influence of approach velocity on bubble coalescence. Chem. Eng. Sci. 29 (12), 2363–2373. https://doi.org/10.1016/0009-2509(74)80013-8.

Kumar, A., Gogate, P.R., Pandit, A.B., 2007. Mapping of acoustic streaming in sonochemical reactors. Ind. Eng. Chem. Res. 46 (13), 4368–4373. https://doi.org/10.1021/ie060575q.

Lee, J., Ashokkumar, M., Yasui, K., Tuziuti, T., Kozuka, T., Towata, A., Iida, Y., 2011. Development and optimization of acoustic bubble structures at high frequencies. Ultrason. Sonochem. 18 (1), 92–98. https://doi.org/10.1016/j.ultsonch.2010.03.004.

Lee, J., Yasui, K., Tuziuti, T., Kozuka, T., Towata, A., Iida, Y., 2008. Spatial distribution enhancement of sonoluminescence activity by altering sonication and solution conditions. J. Phys. Chem. B 112 (48), 15333–15341. https://doi.org/10.1021/jp8060224.

Leighton, T., 2012. The acoustic bubble.

Lepoint, T., Mullie, F., 1994. What exactly is cavitation chemistry? Ultrasonics - Sonochemistry 1 (1), S13–S22. https://doi.org/10.1016/1350-4177(94)90020-5.

Margulis, M., 1995. Sonochemistry and cavitation; opa (Amsterdam) B. V. gordon and breach science publ.

Mason, T.J., de Meulenaer E.C., 1998. Cordemans practical consideration for process optimization, 301–331.

Mason, T.J., Lorimer, J.P., Walton, D.J., 1990. Sonoelectrochemistry. Ultrasonics 28 (5), 333–337. https://doi.org/10.1016/0041-624X(90)90041-L.

Mitome, H., Kozuka, T., Tuziuti, T., Wang, L., 1997. Quasi acoustic streaming induced by generation of cavitation bubbles. In: Proceedings of the IEEE Ultrasonics Symposium, 1. IEEE, pp. 533–536.

Neppiras, E.A., 1980. Acoustic cavitation thresholds and cyclic processes. Ultrasonics 18 (5), 201–209. https://doi.org/10.1016/0041-624X(80)90120-1.

Noltingk, B.E., Neppiras, E.A., 1950. Cavitation induced by ultrasonics. Proceedings of Physical Society 63, 674–678.

Petrier, C., Lamy, M.-F., Francony, A., Benahcene, A., David, B., Renaudin, V., Gondrexon, N., 1994. Sonochemical degradation of phenol in dilute aqueous solutions: comparison of the reaction rates at 20 and 487 kHz. J. Phys. Chem. 98 (41), 10514–10520. https://doi.org/10.1021/j100092a021.

Petrier, C., Micolle, M., Merlin, G., Luche, J.L., Reverdy, G., 2002. Characteristics of pentachlorophenate degradation in aqueous solution by means of ultrasound. Environ. Sci. Technol. 26 (8), 1639–1642. https://doi.org/10.1021/es00032a023.

Pflieger, R., Chave, T., Vite, G., Jouve, L., Nikitenko, S.I., 2015. Effect of operational conditions on sonoluminescence and kinetics of H2O2 formation during the sonolysis of water in the presence of ar/o2 gas mixture. Ultrason. Sonochem. 26, 169–175. https://doi.org/10.1016/j.ultsonch.2015.02.005.

Riesz, P., Mason, T.J., 1991. Advances in Sonochemistry (Vol. 2).

Rooze, J., Rebrov, E.V., Schouten, J.C., Keurentjes, J.T.F., 2011. Effect of resonance frequency, power input, and saturation gas type on the oxidation efficiency of an ultrasound horn. Ultrason. Sonochem. 18 (1), 209–215. https://doi.org/10.1016/j.ultsonch.2010.05.007.

Roy, R.A., 1992. Cavitation Sonophysics, In: Crum, L.A., Mason, T.J., Reisse, J.L., Suslick, K.S. (eds). Sonochemistry and Sonoluminescence. NATO ASI Series, vol 524, Springer Publisher, Dordrecht, pp. 25-38. https://doi.org/10.1007/978-94-015-9215-4_2.

Suslick, K.S., 1990. Sonochemistry. Science 247 (4949), 1439–1445. https://doi.org/10.1126/science.247.4949.1439.

Suslick, K.S., 1997. Sonoluminescence and sonochemistry. In Proceedings of the IEEE Ultrasonics Symposium (Vol. 1, pp. 523–532). IEEE.

Suslick, K.S., Hammerton, D.A., Cline, R.E., 1986. The sonochemical hot spot. J. Am. Chem. Soc. 108 (18), 5641–5642. https://doi.org/10.1021/ja00278a055.

Suslick, K.S., Price, G.J., 1999. Applications of ultrasound to materials chemistry. Annual Review of Materials Science, 29, pp. 295–326 Annual Reviews Inc.

Tronson, R., Ashokkumar, M., Grieser, F., 2002. Comparison of the effects of water-soluble solutes on multibubble sonoluminescence generated in aqueous solutions by 20- and 515-kHz pulsed ultrasound. J. Phys. Chem. B 106 (42), 11064–11068. https://doi.org/10.1021/jp020363g.

Tuziuti, T., Yasui, K., Lee, J., Kozuka, T., Towata, A., Iida, Y., 2008. Mechanism of enhancement of sonochemical-reaction efficiency by pulsed ultrasound. J. Phys. Chem. A 112 (22), 4875–4878. https://doi.org/10.1021/jp802640x.

Weavers, L.K., Ling, F.H., Hoffmann, M.R., 1998. Aromatic compound degradation in water using a combination of sonolysis and ozonolysis. Environ. Sci. Technol. 32 (18), 2727–2733. https://doi.org/10.1021/es970675a.

Wei, K., Skyba, D.M., Firschke, C., Jayaweera, A.R., Lindner, J.R., Kaul, S., 1997. Interactions between microbubbles and ultrasound: in vitro and in vivo observations. J. Am. Coll. Cardiol. 29 (5), 1081–1088. https://doi.org/10.1016/S0735-1097(97)00029-6.

Wood, R.J., Lee, J., Bussemaker, M.J., 2017. A parametric review of sonochemistry: control and augmentation of sonochemical activity in aqueous solutions. Ultrason. Sonochem. 38, 351–370. https://doi.org/10.1016/j.ultsonch.2017.03.030.

Yasui, K., 2011. Fundamentals of acoustic cavitation and sonochemistry. Theoretical and Experimental Sonochemistry Involving Inorganic Systems. Springer, Netherlands, pp. 1–29.

Zhu, C., Feng, R., Zhao, Y., 2000. Sonochemical effect of a bifrequency irradiation. Chin. Sci. Bull. 45 (2), 142–145. https://doi.org/10.1007/bf02884660.

Chapter 12

Mechanistic issues of energy efficiency of an ultrasonic process: Role of free and dissolved gas

Vijayanand Suryakant Moholkar[a], **T. Sivasankar**[b], **Bhaskar Jyoti Choudhury**[a] and **Kuldeep Roy**[b]

[a] *Department of Chemical Engineering, Indian Institute of Technology Guwahati, Guwahati, Assam, India,* [b] *Department of Chemical Engineering, National Institute of Technology Trichy, Tiruchirapalli, India*

12.1 Introduction

In the last two decades, voluminous literature has been published that reports enhancement or intensification of numerous physical, chemical, or biological processes with application of ultrasound. It is well known that ultrasound manifests its physical and chemical effects mainly through the phenomenon of cavitation. Cavitation is essentially nucleation, growth, and implosive collapse of gas and vapor bubbles driven by bulk pressure variation induced by sonication (or propagation of ultrasound wave through the reaction or process medium). The main physical effect of ultrasound is oscillatory motion of fluid elements around their mean position. This low amplitude ($\sim$0.1 μm) and high frequency (20,000 cycles/s or higher) motion of liquid elements generates intense micromixing or microconvection in the medium. The cavitation bubble undergoes volume oscillations under influence of ultrasound, which also creates oscillatory motion of liquid in close vicinity of the bubble. In addition, transient cavitation also induces intense shock waves in the medium. These waves are generated due to reflection of the fluid elements from the bubble interface, as it comes to sudden halt during transient motion in compression phase. These shock waves, or more correctly acoustic waves, also induce spectacular effects in the liquid medium. These waves, if interrupted by the solid boundaries in the medium, such as particles or reactor wall, can cause mechanical damage to the solids. In case of particles, it can cause particle rupture and size reduction. For reactor walls (especially metal walls), it causes erosion. Typically for the catalytic reactions, these phenomena are beneficial, as they help in faster desorption of the product species, making catalytic sites more accessible. Acoustic waves also help in reduction of the poisoning of the catalyst. In biological processes, low intensity or intermittent sonication (with small duty cycles) helps in enhancing activity of the enzymes and microorganisms through spectacular phenomena of unfolding of the proteins. This process helps in exposure of inner hydrophobic residues with easier access to substrate binding sites. The efficiency of the biological processes shows marked enhancement with sonication as a consequence of faster kinetics and greater yields. In summary, ultrasound or sonication is a new technique of introducing energy into the medium on extremely small spatial and temporal scale, which results in remarkable outputs.

Despite these encouraging results, the commercial or industrial scale ultrasonic processes haven't been implemented yet. The main cause leading to this effect is low overall efficiencies of the ultrasound processors. Therefore, proper identification and establishment of the energy mechanism of the sonic processors is the key step in effective scale-up. In this chapter, we have presented an account of our research on energy conversion chain of an ultrasonic processor (Moholkar and Warmoeskereken, 2003). In addition, we have also presented two case studies, each of a physical and a chemical process, which are based on the theoretical structure of principles of energy conversion. In a sonic processor, the electrical energy supplied to the equipment undergoes several transformations before getting dissipated as cavitation energy, which brings about the required physical or chemical change. This energy conversion chain is shown in Fig. 12.1.

The three steps of energy conversion chain are: (1) conversion of electrical energy to mechanical energy in the form of shape oscillations of piezoelectric transducers. It may be noted that the electrical energy itself is initially transformed from

Energy Aspects of Acoustic Cavitation and Sonochemistry: Fundamentals and Engineering. DOI: https://doi.org/10.1016/B978-0-323-91937-1.00002-5
Copyright © 2022 Elsevier Inc. All rights reserved.

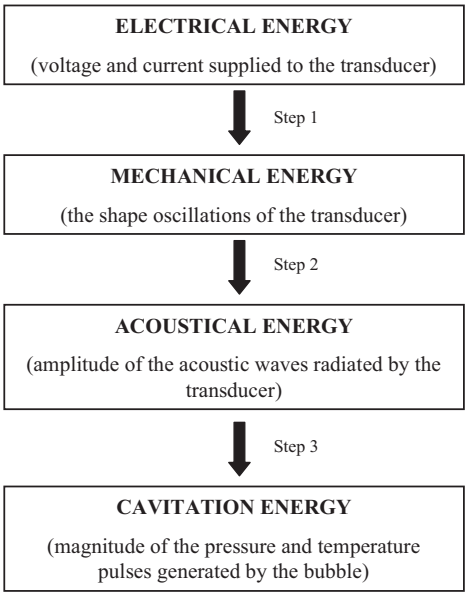

FIGURE 12.1 Chain of energy conversion in an ultrasonic processor. *(Reproduced from Moholkar and Warmoeskerken (2003) with permission of John Wiley and Sons).*

main supply (typically 50 / 60 Hz, 120 /220–240 V) to high frequency energy (20 kHz or higher) using a radio frequency amplifier. (2) The mechanical energy of the piezoelectric crystal is converted into acoustical energy in the form of ultrasound waves, once the shape oscillations of the electrical transducer are coupled to a liquid medium (usually water), (3) Final step of energy conversion is transformation of ultrasound energy into cavitation energy through gas or vapor bubbles present in the medium. The overall efficiency of the ultrasonic processor is a function of individual efficiencies of all steps in the energy transformation chain. Enhancing efficiency of the sonic processor would mean simultaneous maximization of the efficiencies of each of these steps. In other words, maximization of the energy conversion process requires an integrated approach. In this chapter, we have demonstrated as how the gas content (in both free and dissolved form) of the process medium (in liquid form) influences the energy conversion chain of the processor. The gas content of the medium is thus the key parameter in optimization and scale-up of the sonic processors. Our initial study comprises of simple experiments based on measurements of the acoustic emission and its spectral characteristics coupled to mathematical modelling of cavitation bubble dynamics. This is followed by two case studies within the theoretical framework, viz. (1) mass transfer intensification in textile with ultrasound (a physical or nonreactive process), and (2) enhancement of yield of a well-known sonochemical reaction.

12.2 Experimental summary

The initial experiments were carried out using a custom-built ultrasound horn and a glass cell. The schematic of the horn is shown in Fig. 12.2.

The resonance frequency of the horn was 25 kHz. The glass cell was mounted on a stainless-steel bottom, which could reflect the ultrasound waves incident on it. The tip of the ultrasound horn had a small groove, which helped in providing cavitation nuclei in the medium. The ultrasound horn was supplied high frequency electrical energy through a signal generator and radio frequency (RF) amplifier. The amplifier had maximum power output of 200 W for an input impedance of 50 Ω. The actual power consumed by the horn was monitored by measuring the voltage and current supplied to the horn. These measurements were carried out using a digital oscilloscope, which also provided measurement of the phase angle between voltage and current. This phase angle was maintained zero, so as to achieve maximum energy input to the horn at given conditions. The frequency of the RF voltage applied across the ultrasound horn was adjusted continuously. The acoustic emissions (or pressure signals) in the medium were measured using a 4-mm hydrophone. This hydrophone was not calibrated, and hence, provided only relative measurements of the acoustic emissions (or cavitation intensity) in the medium for different process conditions. These measurements were also carried out using an oscilloscope with sampling frequency of 2.5 MHz. The Fast Fourier Transform (FFT) of these signals was obtained.

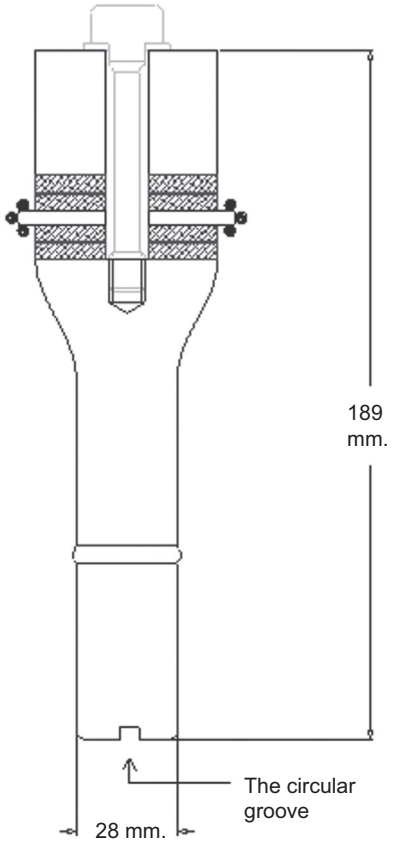

FIGURE 12.2 Schematic of the custom-built ultrasound probe or horn. *(Reproduced from Moholkar and Warmoeskerken (2003) with permission of John Wiley and Sons).*

Acoustic emission measurements were carried out using demineralized water of three qualities as medium: (1) saturated with dissolved gas (or dissolved air) with dissolved oxygen content of ~9 ppm, (2) undersaturated with dissolved air (dissolved oxygen content lowered to 2 ppm), and (3) undersaturated with dissolved air and pre-standing of 30 minutes. The ultrasound horn was driven at its resonance frequency of 25 kHz and the distance between the rigid bottom of the flow cell and the horn tip was adjusted to 6 cm, which is the wavelength of the ultrasound wave. The flow cell was driven below its cut-off frequency, and thus, the acoustic waves generated in the medium were of planar nature. The power consumption of the ultrasound horn can be calculated as: $\frac{(V_p I_p \cos\theta)}{4}$, where V_p is the peak-to-peak voltage, while I_p is peak-to-peak current input to the ultrasound horn, θ is the phase angle between them. The acoustic pressure amplitude generated by ultrasound horn is determined as $I = \frac{\eta P_A^2}{\rho \cdot c}$ where I = power input to horn per unit area, ρ = density of the medium, c = speed of sound in the medium. For lowering of the dissolved air content of water, a chemical method was used. By sparging CO_2 through demineralized water, dissolved air was stripped out, leaving behind water saturated with CO_2. Thereafter, the CO_2 was converted to HCO_3^- by addition of NaOH till pH of the solution reached 9. The rationale underlying using water of three conditions is as follows: Gas exists in the liquid medium in two forms—free gas and dissolved gas. The free gas in the medium is usually in the form of free-floating bubbles or the microbubbles trapped in the crevices of solid boundaries in the medium. If the dissolved gas content of the medium is below saturation, the free-floating bubbles can dissolve away, while gas pockets trapped in the crevices of the solid boundaries are relatively stable. These gas pockets can provide nuclei for cavitation phenomena in the medium. In present context, one potential location for the gas pockets is the groove and other crevices on the tip of the ultrasound horn. While introducing the horn into the liquid medium, the tip of the horn is held parallel to the water surface and not all air in the groove and crevices is replaced by water. This cases entrapment of some air, which becomes source of cavitation nucleation in the medium. As noted earlier, the distance between the horn tip and the stainless steel bottom (rigid boundary for reflection of acoustic waves) was adjusted as 6 cm, which is the wavelength (λ) of 25 kHz ultrasound wave with water as medium. The interference between the incident and reflected waves gives rise to formation of standing wave, with pressure antinode (or pressure maxima) located at the center point ($\lambda/2$) while two pressure

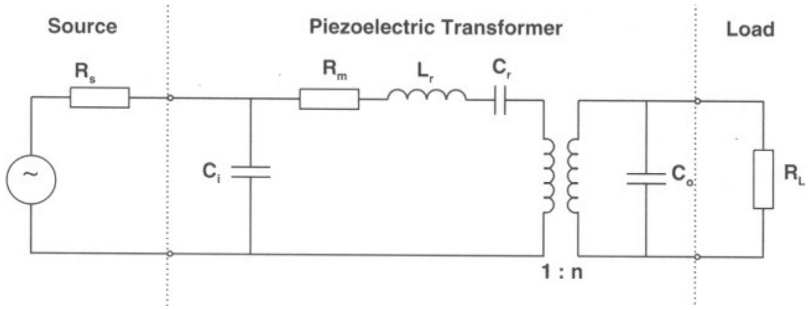

FIGURE 12.3 Equivalent electrical circuit of a piezoelectric transducer. *(Reproduced from Moholkar and Warmoeskerken (2003) with permission of John Wiley and Sons).*

nodes (velocity antinodes or maxima) located at distance of λ/4 and 3λ/4. The clouds of cavitation bubbles generated at the tip of ultrasound horn are expelled in water and move towards the pressure antinode due to Bjerknes forces. This phenomenon was confirmed with high speed photography (frame rate: 2000 fps). The rationale for water being left standing for 30 minutes after degassing to 2 ppm of dissolved O_2 was to cause denucleation of the medium. High undersaturation of liquid results in dissolution of all free gas in the liquid, including the free-floating bubbles and the gas pockets trapped in the crevices and grooves of the ultrasound horn. On the other hand, if water used immediately for experiments, it still has the microbubbles, which can form cavitation nuclei.

12.3 The mathematical model

In most ultrasonic processors, the piezoelectric transducers are used as source of ultrasound. The electrical characteristics of the transducers are affected by the type of mechanical loading to which they are subjected. The physical parameters affecting the mechanical loading can be represented by a circuit diagram, which also includes the electrical parameters of the transducers. The equivalent circuit of the transducer is shown in Fig. 12.3.

The converted mechanical impedance in the equivalent circuit has four components: (1) inductance, L_r, due to mass of the transducer, (2) capacitance, C_r, due to compliance of the transducer, (3) resistance, R_m, due to losses in the transducer, and (4) load resistance or radiation impedance (R_L) which is the product of the specific acoustic impedance of the medium in which the transducer vibrates (Z_R) and the area of the transducer. Out of these, R_m, L_r, and C_r, depend upon the material of construction and the dimensions of the transducer, and thus, cannot be manipulated or altered after fabrication of the transducer. The radiation impedance, R_L, depends on the conditions of the medium for ultrasound wave propagation. The maximum power transfer between the electrical power source and the piezoelectric transducer occurs at resonance conditions, when the internal impedance of the electrical power source (R_s) matches the value of ($R_m + R_L$), which is the total load impedance. At resonance conditions, the frequency-dependent component of impedance (i.e., reactance) is zero. In the present case, the transducer was made of piezoelectric material, which are good conductors. Thus, the value of R_m was just 4 Ω, while the internal impedance of the RF amplifier was 50 Ω. Thus, any rise in R_L (the acoustic impedance) would take the system closer to resonance leading to rise in power transfer between amplifier and the transducer.

12.3.1 Determining the acoustic impedance

The simplest model for determination of the acoustic impedance is sound radiation within a fluid-filled tube by a snuggly fitting piston on one end and a rigid reflector on the other end. This model resembles the experimental setup in our study. The oscillatory motion of the piston generates sound waves that travel in +ve and –ve directions in the tube (with the origin, $x = 0$, taken to be the mean position of piston face). Assuming that velocity of oscillatory motion of piston is written as: $V_o \cdot \cos(\omega t)$, the pressure and velocity of the waves are written as:

$$\frac{P}{\rho \cdot c} = \mathrm{Re}\left[e^{-i\omega t}\left(X \cdot e^{ikx} + Y \cdot e^{-ikx}\right)\right] \tag{12.1}$$

$$v = \mathrm{Re}\left[e^{-i\omega t}\left(X \cdot e^{ikx} - Y \cdot e^{-ikx}\right)\right] \tag{12.2}$$

The boundary conditions for determining X and Y are as follows: $x = 0$, $\hat{v} = v_o$, and $x = L$, $\hat{p}/\hat{v} = Z$. Substitution of these boundary conditions gives the relation between amplitudes of pressure and velocity in the tube as:

$$\hat{p} = \rho c v_o \left[\frac{Z \cos k(L-x) - i\rho c \sin k(L-x)}{\rho c \cos kL - iZ \sin kL} \right] \tag{12.3}$$

where, $k = 2\pi/\lambda$ is the wave number. The ratio $\hat{p}/v_o$ is the specific acoustic impedance and is basically an analogue of the Ohm's law, that is, ratio of driving force (i.e., acoustic pressure amplitude) to the velocity of particles or the fluid elements in the medium. In the present case, the boundary at $x = L$ is a solid rigid boundary, and thus, $\hat{v}(x = L) \approx 0$. Thus, value of Z is very high as compared to value of ρc (1500 m/s $\times$ 1000 kg/m^3 = 1.5E+06 kg/m^2·s). For the condition $Z \gg \rho c$, the above expression gets simplified as:

$$\frac{\hat{p}}{v_o} = i\rho c \cot(kL) = i\rho c \cot\left(\frac{2\pi L}{\lambda}\right) \tag{12.4}$$

However, as noted earlier, the distance between horn tip and solid boundary was equal to one wavelength, and thus, $L = \lambda$. This would mean $\hat{p}/v_o \to \infty$ (singularity); however, due to losses (such as viscous loss) and other nonidealities in the medium $\hat{p}/v_o = Z_R$, is not singular at $L = \lambda$, but is very high. Another important parameter that affects acoustic impedance is velocity of sound in the medium (c). Presence of gas bubbles in the liquid (even as dilute dispersion) results in reduction in the sound velocity in the liquid, and hence, the acoustic impedance as well. In this case, the acoustic impedance can be calculated using theory of acoustic wave propagation in bubbly liquids, as explained in the next section.

12.3.2 Acoustic wave propagation in bubbly liquids

Many authors in the past 5–6 decades have proposed models for acoustic wave propagation in bubbly liquids. However, the most rigorous model for the linear acoustic wave propagation in bubbly liquids was put forth by (Prosperetti and Commander 1989). This model was essentially a combination of the averaged equations for the bubbly mixtures given by Caflisch et al. (1985) and the nonlinear formulation for the internal dynamics of the bubble that includes viscous and thermal damping of bubbles (Prosperetti et al., 1986). For the complete development and formulation of the model, we refer the reader to original paper by (Prosperetti and Commander 1989). Given below is the summary of the main results of this paper. The complex sound speed in the bubbly liquid mixture is given as:

$$c_m = \frac{\omega}{k_m} = \frac{c}{\sqrt{1 + 4\pi c^2 \int_0^\infty \frac{R_o f(R_o) dR_o}{\omega_o^2 - \omega^2 + 2ib\omega}}} \tag{12.5}$$

Here, km is the complex wave number. A planar sound wave can be represented by general expression: $P = P_A \exp[i(\omega t - k_m x)]$. For finding phase velocity of sound wave and its attenuation, (Prosperetti and Commander 1989) substituted $\left(\frac{c}{c_m}\right) = u - iv$ in the above expression. With this substitution and simplification, it gives:

$$\exp[i(\omega t - k_m x)] = \exp\left(-\frac{\omega v}{c} x\right) \exp\left[i\omega\left(t - \frac{u}{c} x\right)\right] \tag{12.6}$$

From this expression, the phase velocity (v) and the attenuation coefficient (A) for the acoustic wave in the gas-liquid mixture are reduced as: $V = \frac{c}{u}$, and $A = \frac{\omega v}{c}$. With the assumption pf uniform number density of the bubbles (n_b) over working volume, and size uniformity of the bubbles (i.e. all the bubbles in the gas-liquid mixture have uniform initial mean radius, R_o), the expression for cm is simplified as:

$$c_m = \frac{\omega}{k_m} = \frac{c}{\sqrt{1 + \frac{4\pi c^2 n_b R_o}{\omega_o^2 - \omega^2 + 2ib\omega}}} \tag{12.7}$$

If the size of the bubbles is much smaller than the resonant bubble size corresponding to the frequency of the acoustic wave, or in other words, $\omega \ll \omega_o$, the natural oscillation frequency (ω_o) and the damping coefficient (b) are written as:

$$\omega_o = \frac{P_o}{\rho R_o^2}\left(3\gamma - \frac{2\sigma}{P_o R_o}\right) \tag{12.8}$$

$$b = \frac{\gamma - 1}{10\gamma}\frac{P_o}{\rho D} + \frac{2\mu}{\rho R_o^2} \tag{12.9}$$

It can be perceived that both V and A for the bubbly mixture are a function of the number population as well size distribution of the bubbles.

12.3.3 Cavitation nucleation and bubble dynamics

The bubbles in the liquids, which could either be in the form of tiny, free-floating bubbles or the gas pockets trapped in the crevices of solid boundaries in the processor or reactor. During propagation of the acoustic wave through the liquid, these bubbles undergo volume oscillations. The type of volumetric or radial motion that the bubbles or cavitation nuclei undergo is a function of the characteristics of the acoustic field, that is, frequency and the pressure amplitude. Two type of volumetric oscillations of the bubbles are characterized as: (1) stable motion (or stable cavitation) where bubble undergoes small-amplitude linear motion for several acoustic cycles, or (2) transient motion (or transient cavitation), where bubbles undergo explosive growth followed by transient collapse. Transient cavitation is a high energy event resulting in concentration of energy that has spectacular physical and chemical effects. The minimum acoustic pressure amplitude required to induce transient motion of the bubbles is known as the transient cavitation threshold (P_T) and is given as:

$$P_T = P_o + \frac{8\sigma}{9}\sqrt{\frac{3\sigma}{2R_o^3\left(P_o + \frac{2\sigma}{R_o}\right)}} \tag{12.10}$$

Apfel (1981) deduced a more general expression for the transient cavitation threshold which is a function of both frequency of the acoustic wave as well as initial size of the bubbles:

$$R_o = \frac{0.82}{\omega\sqrt{\frac{P_T}{P_o}}}\left[1 + \frac{2}{3}\frac{(P_T - P_o)}{P_o}\right]^{1/3} \tag{12.11}$$

For a typical bubble size distribution of 2–10 μm and acoustic frequency range of 20–100 kHz, the minimum value of P_T is $\approx$ 1 bar.

The radial motion of a bubble driven by ultrasound can be described by the bubble dynamics equation. One of the popular bubble dynamics equation is the Gilmore equation based on Kirkwood-Bethe hypothesis, which states that the shock waves generated during bubble motion propagate with a velocity equal to the sum of fluid velocity and the sound velocity. The equation of radial motion of the bubble is:

$$R\left(1 - \frac{U}{c}\right)\frac{d^2R}{dt^2} + \frac{3}{2}\left(1 - \frac{U}{3c}\right)\left(\frac{dR}{dt}\right)^2 = \left(1 + \frac{U}{c}\right)H + \frac{U}{c}\left(1 + \frac{U}{c}\right)\frac{dH}{dR} \tag{12.12}$$

H is the free enthalpy on the surface of the bubble, and can be derived using equation of state for water as: $P = A\left(\frac{\rho}{\rho_o}\right)^n - B$. The expression for H is:

$$H = \frac{n}{n-1}\frac{A^{\frac{1}{n}}}{\rho_o}\left\{\left[\left(P_o + \frac{2\sigma}{R_o}\right)\left(\frac{R_o}{R}\right)^{3\gamma} - \frac{2\sigma}{R} + B\right]^{\left(\frac{n-1}{n}\right)} - (P_\infty + B)^{\left(\frac{n-1}{n}\right)}\right\} \tag{12.13}$$

P_∞ is the bulk pressure in the liquid that drives the bubble motion. It is expressed as:

$$P_\infty = P_o - P_A \sin(\omega t) \tag{12.14}$$

The parameters A, B, and n in the equation of state for water have values 3001 atm, 3000 atm, and 7, respectively. c is the velocity of sound and is the function of the enthalpy as:

$$c^2 = c_o^2 + (n-1)H \tag{12.15}$$

where c_o is the sound velocity at STP conditions and is given as $\sqrt{\frac{An}{\rho_o}}$. During the radial motion, the bubble itself emits the acoustic waves. The pressure amplitude of these waves at a distance $r \gg R$ (far from bubble interface) is given as:

$$P_s(r,t) = \frac{\rho}{4\pi r}\frac{d^2V_b}{dt^2} = \rho\left(\frac{R}{r}\right)\left[2\left(\frac{dR}{dt}\right)^2 + R\frac{d^2R}{dt^2}\right] \tag{12.16}$$

P_s can also be interpreted as a measure of intensity of the bubble oscillations.

12.3.4 Rectified diffusion

During the radial motion of the cavitation bubble, there is exchange of mass between the bubble and the surrounding liquid. Both vapor of the bulk liquid and the dissolved gas diffuse across bubble interface (or bubble wall). As far as vapor transport across bubble wall is concerned, the evaporation and condensation processes are much faster than bubble dynamics. The bubble interior is, thus, mostly saturated with water vapor. The transport of gas, however, is a relatively slow process and occurs over a longer period of time. Depending on the saturation level of the liquid, a bubble may grow or dissolve during the radial motion driven by ultrasound. This process is called "rectified diffusion." The general mathematical expression for gas transport in a spherically symmetric system is described by equation:

$$\frac{DC}{Dt} \equiv \frac{\partial C}{\partial t} + v_r \frac{\partial C}{\partial r} = D_g \left(\frac{\partial^2 C}{\partial r^2} + \frac{2}{r} \frac{\partial C}{\partial r} \right) \tag{12.17}$$

For determining mass transfer of gas between the liquid and oscillating bubble, we need to solve above equation simultaneously with bubble dynamics equation. The two equations are coupled through the term v_r, and the boundary condition at the bubble wall, which is a function of gas pressure inside the bubble that changes continuously during radial bubble motion. For an oscillating bubble, the liquid velocity at a distance $r \gg R$ is:

$$v_r = \frac{R^2}{r^2} \left(\frac{dR}{dt} \right) \tag{12.18}$$

The boundary conditions at the bubble interface, and the infinity are: $C(R, t) = C_s \frac{P_i(R,t)}{P_o}$ and $C(\infty, \mathrm{t}) = C_o$. The net gas transport across bubble wall is:

$$\frac{dm_g}{dt} = 4\pi R^2 D_g \frac{\partial C}{\partial r}\bigg|_{r=R(t)} \tag{12.19}$$

A general solution of the problem of rectified diffusion was given by Lofstedt et al. (1995) and Fyrillas and Szeri (1994), which is applicable for both small (linear) and large (nonlinear) amplitude bubble motion. This method or solution essentially depicts the effect of dissolved gas in the medium on the bubble growth or shrinkage during radial motion. We give herewith a summary of the rectified diffusion model of Fyrillas and Szeri (1994). For greater details we refer the reader to the paper by Fyrillas and Szeri (1994).

The model of Fyrillas and Szeri (1994) is based on treating the rectified diffusion on two separate time scales. In this method, the total gas concentration field is split in two parts: (1) oscillatory part, $C_{osc}(r,t)$ that changes on a fast time scale T (the period of the acoustic wave), and (2) smooth part, $C_{smo}(r,t)$ that changes on slow diffusive time scale $\bar{t} = n\tau_D$ ($\gg T$), where τ_D is the diffusive time scale defined as $\tau_D = \frac{R_o^2}{D_g}$. Thus, the total gas concentration in space and time is:

$$C(r, t) = C_{osc}(r, t) + C_{smo}(r, t) \tag{12.20}$$

The smooth and oscillatory part of the diffusion problem was solved using singular perturbation analysis. The contribution of oscillatory part to mass transport across bubble was negligible. However, the smooth part contributes to the change in gas content of the bubble. In the asymptotic limit, the smooth profile $C_{smo}(r, \bar{t})$ is given as:

$$\bar{C}_{smo} = C_o + \left[C_s \frac{P_i(t)_{t,4}}{P_o} - C_o \right] \times \left\{ 1 - \frac{\int_0^h \frac{dh'}{\left(3h' + R^3(t)\right)^{\frac{4}{3}}{}_{t,0}}}{\int_0^\infty \frac{dh'}{\left(3h' + R^3(t)\right)^{\frac{4}{3}}{}_{t,0}}} \right\} \tag{12.21}$$

The variation in the mean radius of the bubble (R_o), which indicates growth or shrinkage of the bubble, is calculated as:

$$\frac{dm_g}{d\bar{t}} = 4\pi R_o^2 D_g \frac{\partial \bar{C}_{smo}}{\partial r}\bigg|_{r=R} = 4\pi R^2 \rho_g \frac{dR_o(\bar{t})}{d\bar{t}} \tag{12.22}$$

The variation in gas concentration (smooth part) at bubble interface is:

$$\frac{\partial \bar{C}_{smo}}{\partial r}\bigg|_{r=R} = \frac{C_s}{R_o^2(\bar{t})} \frac{\left[C_o - C_s \frac{P_i(t)_{t,4}(\bar{t})}{P_o} \right]}{\int_0^\infty \frac{dh'}{\left(3h' + R^3(t)\right)^{\frac{4}{3}}{}_{t,0}}} \tag{12.23}$$

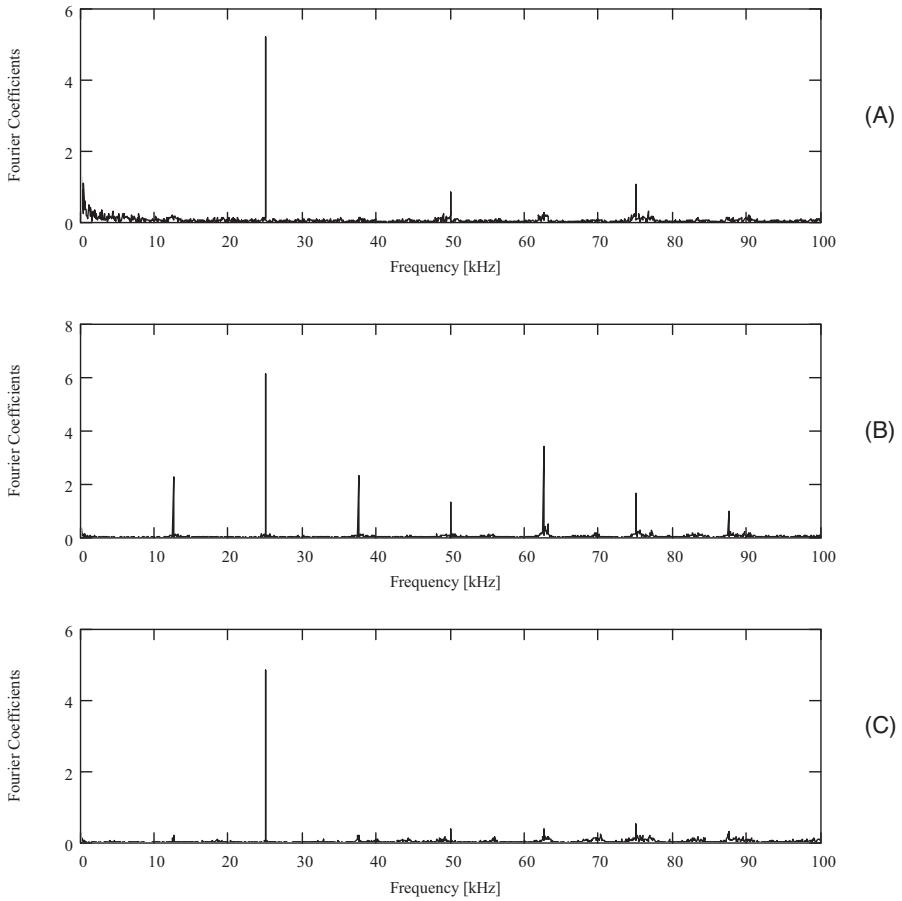

FIGURE 12.4 The FFT of pressure signals or the acoustic emission spectra at pressure antinode for water with different gas contents. (A) saturated water, (B) undersaturated water, (C) undersaturated and denucleated water. *(Reproduced from Moholkar and Warmoeskerken (2003) with permission of John Wiley and Sons).*

Combining above equations, we get an expression for the rate of change in mean bubble radius as:

$$\frac{d}{d\bar{t}}R_o(\bar{t}) = \frac{D_g C_s}{\rho_g R_o^2(\bar{t})} \frac{\left[C_o - C_s \frac{P_i(t)_{t,4}(\bar{t})}{P_o}\right]}{\int_0^\infty \frac{dh'}{\left(3h' + R^3(t)\right)^{\frac{4}{3}}_{t,0}}} \tag{12.24}$$

The time averages denoted by $\langle\rangle_{t,i}$ in above equations are defined as:

$$\left\langle f(t)_{t,i} = \frac{\int_0^T f(t)R^i(t)dt}{\int_0^T R^t(t)dt} \right\rangle \tag{12.25}$$

The time average of P_i (internal pressure of the bubble) can be calculated using bubble dynamics equation. The space integral in the denominator of equation for $\frac{dR_o(\bar{t})}{d\bar{t}}$ can be taken as $\approx 1/R_{max}$ as a saddle point approximation (Lohse and Hilgenfeldt, 1997; Lofstedt et al., 1995), where R_{max} = maximum bubble radius during oscillation over one acoustic period. The above set of equations can be solved using Runge-Kutta adaptive step size method.

12.4 Results and resasoning

The acoustic emission spectra, that is, FFT of the pressure signals measured at pressure antinode in the standing wave for water in three conditions of free and dissolved gas content are shown in Fig. 12.4. In the acoustic emission spectrum with saturated (or gassy) water as medium only one major peak is seen, corresponding to the fundamental (or ultrasound) frequency. A weak first harmonic ($2f$) of the fundamental frequency is also seen. In the second spectrum, with saturated water as the medium, a sharp subharmonic peak ($f/2$) and other ultraharmoncs (viz. $nf/2$, $n = 3, 5, 7\ldots$.) are visible. In addition,

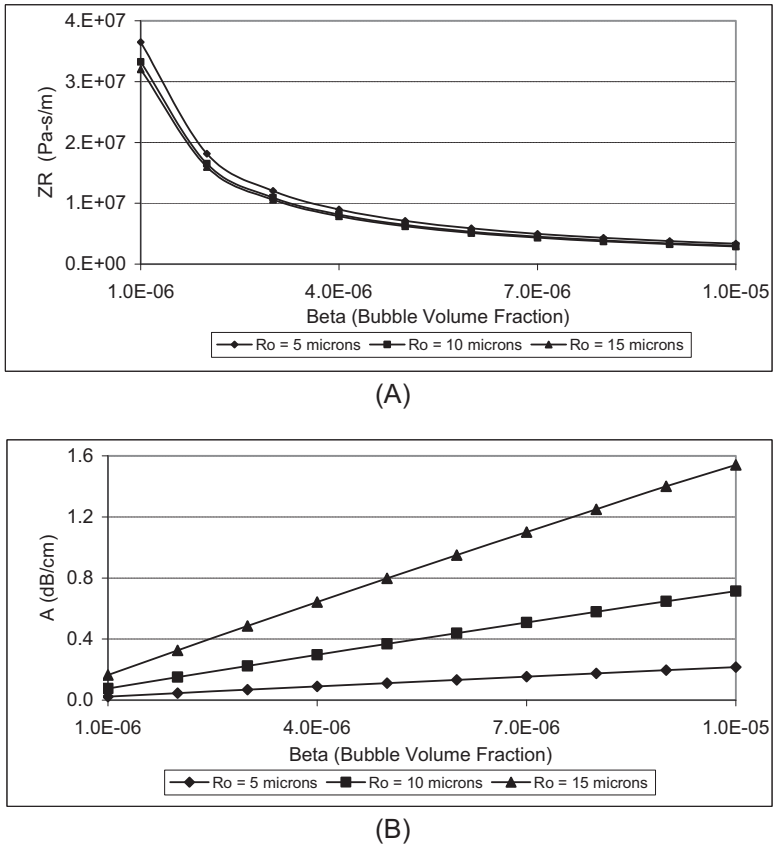

FIGURE 12.5 Trends in (A) specific acoustic impedance, and (B) attenuation coefficient with bubble volume fraction in the medium and the mean bubble radius. *(Reproduced from Moholkar and Warmoeskerken (2003) with permission of John Wiley and Sons).*

several harmonics (viz. *nf*, $f = 2, 3, 4\ldots..$) are also present. In the third set of experiments, where undersaturated water was used after 30 minutes of standing, all other frequency components except the fundamental frequency peak disappear. The power consumption of the ultrasound horn also showed 40% rise with undersaturation of the medium. The power consumption in third set of experiments, where undersaturated and denucleated medium was used, is almost similar as in the second set of experiments. The pressure amplitude of the ultrasound waves in the three experimental sets were: (1) 0.5 bar, (2) 0.8 bar, (3) 0.8 bar, as calculated using the formula previously stated.

12.4.1 Interpretation of the spectral characteristics

The spectral characteristics of the acoustic emission spectra, that is, the frequency components present in the spectrum, help in determining the kind of radial bubble motion—whether stable or transient, from which the acoustic emission originates. In other words, the spectral characteristics of the acoustic emission represent the cavitation intensity in the medium (Young, 1989; Leighton, 1994). The acoustic emission spectrum comprises of various frequencies related to the fundamental frequency (or driving frequency), that is, the subharmonics, ultraharmonics, and harmonics. The subharmonic component of the acoustic emission spectrum is of particular interest, as it originates from high energy transient bubble motion, and indicates high cavitation intensity in the medium.

Simulation results: The simulations of the mathematical model presented previously have been carried out using representative yet realistic values of physical parameters. The cavitation bubble population in the medium has a size distribution. We have assumed that this size distribution is represented by a single value of initial bubble radius $\approx 10\ \mu$m.

Specific acoustic impedance (Z_R) and attenuation coefficient (A): As evident from the analysis presented earlier, both Z_R and A are functions of total bubble volume fraction (β) and initial bubble radius (R_o). The trends in Z_R and A with β and R_o are shown in Fig. 12.5. These two parameters are related as: $\beta = 4\pi R_o^3 n_b/3$. It could be perceived from Fig. 12.5 that Z_R is a major function of β and relatively insensitive to R_o (for a fixed value of β). On the contrary, A is a major function of R_o for a given value of β. The major conclusion that can be drawn from results presented in Fig. 12.5(A) is that smaller

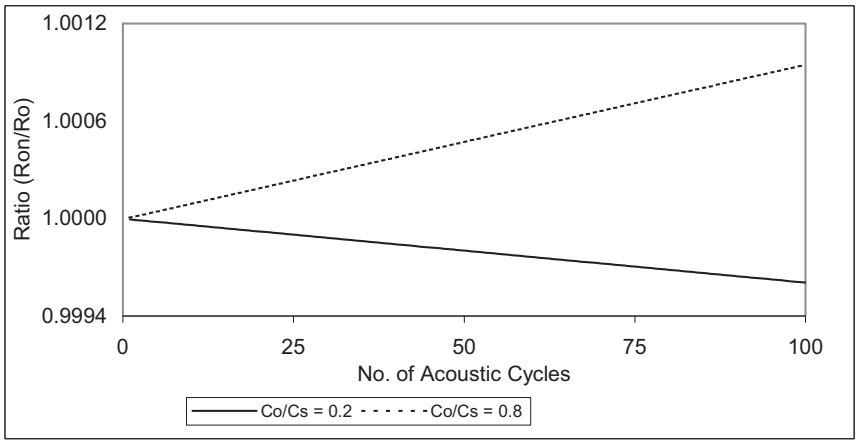

(A)

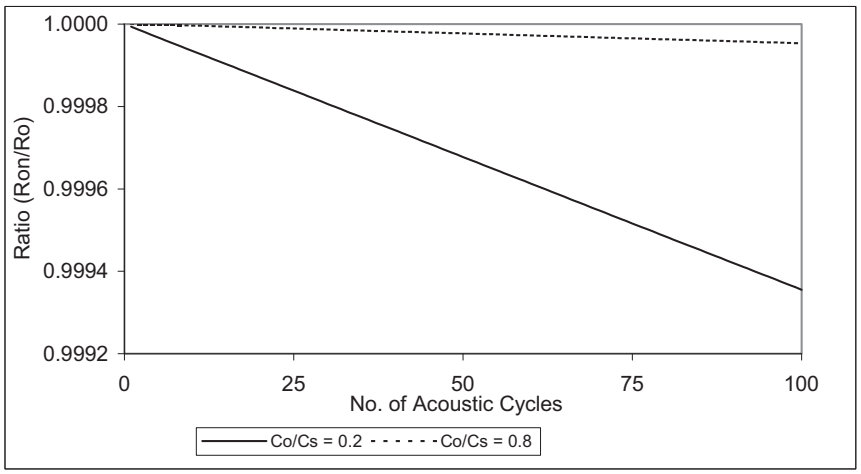

(B)

FIGURE 12.6 Simulations of growth or shrinkage of the cavitation bubbles due to rectified diffusion in water with different saturations of dissolved gas. (A) Ultrasound (or acoustic) pressure amplitude 1.3 bar (higher than transient cavitation threshold or $P_A > P_T$), (B) Ultrasound (or acoustic) pressure amplitude 0.8 bar (smaller than transient cavitation threshold $P_A < P_T$). Other parameters for simulations: $R_o = 10$ μm, $f = 25$ kHz. *(Reproduced from* Moholkar and Warmoeskerken (2003) *with permission of John Wiley and Sons).*

bubble volume fraction in the medium results in larger specific acoustic impedance. The theoretical model of the equivalent circuit of piezoelectric transducer presented earlier also helps perceive that rise in Z_R enhances power consumption of the ultrasound horn, as $R_m \gg R_s$. Concurrently the amplitude of the ultrasound wave in the medium reduces with smaller bubble fraction in the medium, for a given value of R_o. The overall consequence of making the medium undersaturated is marked rise in the acoustic pressure amplitude in the medium.

Influence of rectified diffusion (growth / shrinkage of the bubble): The simulations of variation in mean bubble radius during radial motion of a cavitation bubble in saturated and undersaturated medium are shown in Fig. 12.6. As noted earlier, the mean radius of a bubble varies (grows/shrinks) during radial motion as a result of rectified diffusion. Fig. 12.6(A) shows the rectified diffusion during radial bubble motion for acoustic pressure amplitude higher than transient cavitation threshold ($P_A > P_T$) in both (1) nearly saturated ($C_o/C_s = 0.8$), and (2) highly undersaturated medium ($C_o/C_s = 0.2$). It could be seen that cavitation bubbles grow in saturated medium, while they shrink in the undersaturated medium.

For $P_A < P_T$, the bubble undergoes stable cavitation, and in this case, the bubble shrinks during radial motion [as shown in Fig. 12.6(B)] irrespective of the saturation level of the medium. The total volume fraction of the bubbles in the medium varies due to rectified diffusion, as it is a function of both number density of the bubbles and the mean bubble radius. More importantly, the process of rectified diffusion also influence the parameters Z_R and A, as these parameters are a function of total volume fraction of the bubbles as well as mean radius of the bubble population. This, in turn, influence the power consumption of the ultrasound horn, and the amplitude of the acoustic waves generated in the medium.

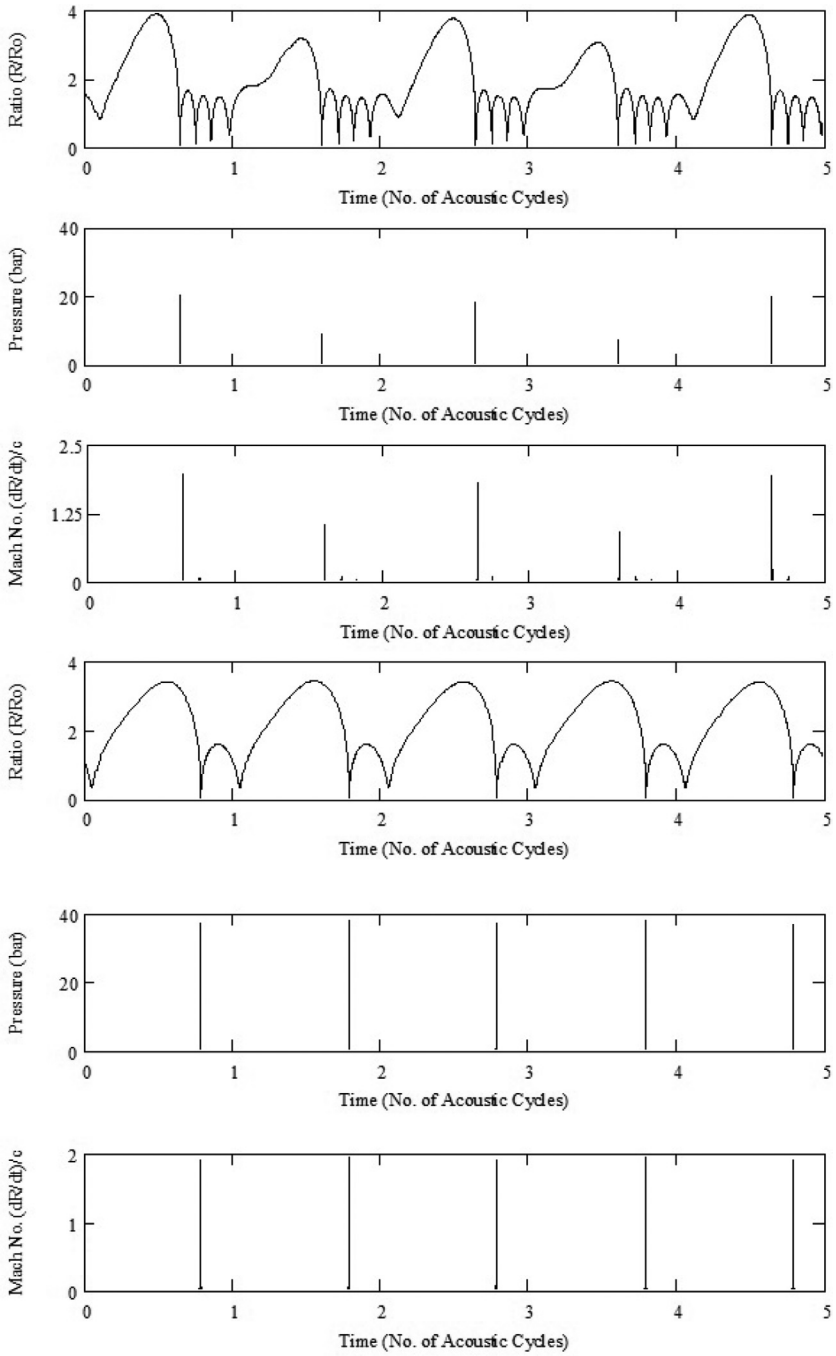

FIGURE 12.7 (continued…): Simulations of radial motion of cavitation bubbles for acoustic pressure amplitude higher than transient cavitation threshold. The initial bubble sizes are 5, 10, and 15 μm (in sequence of given figures). Each set of three figures represent radial motion of the bubble, acoustic wave emission, and bubble wall Mach number for a particular bubble size. Other parameters for simulations: $P_A = 1.3$ bar, $f = 25$ kHz. *(Reproduced from Moholkar and Warmoeskerken (2003) with permission of John Wiley and Sons).*

12.4.2 Radial motion of the bubbles

Figs. 12.7 and 12.8 depict the radial motion of the bubbles of different mean radii for acoustic pressure amplitudes above and below transient cavitation threshold ($P_A > P_T$, $P_A < P_T$). A mean bubble radius of 10 μm is taken as representative value. In addition we have also shown simulations of bubbles of two more sizes, viz. 5 μm and 15 μm. The former size corresponds to the undersaturated medium, where bubble shrinks, while the latter size corresponds to the saturated medium, where the bubble continuously grows during radial motion. The pressure amplitude of the acoustic waves emitted by the

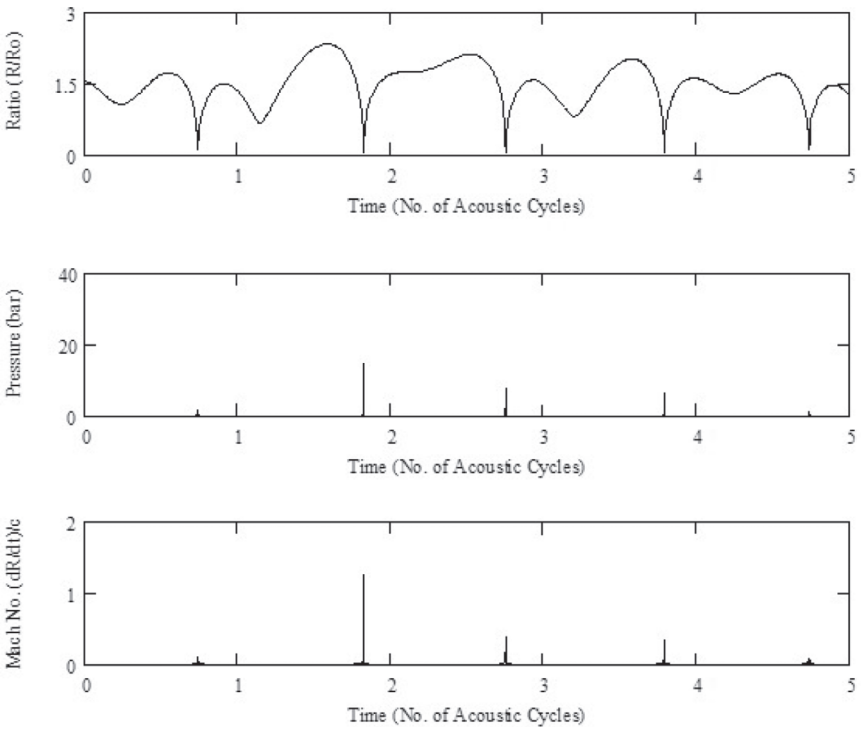

FIGURE 12.7, cont'd.

bubbles is also shown in Figs. 12.7 and 12.8, which represent the intensity of acoustic cavitation. It could be inferred that pressure amplitude of the acoustic waves radiated by the bubble decreases if the bubble grows from initial mean radius of 10 μm–15 μm. Same trend is also seen for shrinkage of the bubble from 10 μm to 5 μm. For acoustic pressure amplitudes less than transient cavitation threshold, the amplitudes of the waves emitted by the bubble are very small, and do not show significant variation with the saturation level of the medium. The major conclusion that can be drawn from simulations of radial motion is that cavitation intensity produced in the medium varies directly with the amplitude of the ultrasound wave. The distinction between radial motion of the bubble for the two cases, viz. $P_A > P_T$ and $P_A < P_T$, are also evident from Figs. 12.7 and 12.8.

In transient cavitation ($P_A > P_T$), the bubble expands several times of its initial size during growth, followed by an extremely rapid collapse that occurs in just few nanoseconds. As the bubble attains minimum radius during radial motion, the conditions inside the bubble reach extreme due to energy concentration. Any irregularity in the medium, such as bulk liquid motion or proximity to solid surfaces and boundaries in the medium may lead to fragmentation of the bubble. However, if the bubble is isolated in the medium, it rebounces after violent collapse and undergoes high energy transient motion for several acoustic cycles. Such radial motion also leads to spectacular phenomenon of single bubble sonoluminescence. Most of the mathematical models developed for radial bubble dynamics assume a single isolated bubble, and do not account for irregularities in the medium. Thus, the simulations presented in Fig. 12.7 indicate either stable cavitation or repetitive transient cavitation. It is worth mentioning at this stage that the simplest criteria for distinguishing between stable and transient motion of cavitation bubbles was proposed by Flynn (1975). Flynn (1975) stated that if a cavitation bubble expands to twice of its original size during the growth phase, the ensuing collapse is dominated by inertial forces. In this situation, spherical convergence of the surrounding liquid transfers increasing amount of kinetic energy to the bubble, resulting in high energy concentration. Another popular criteria for characterization of the transient cavitation is speed of the bubble wall (or bubble interface) during the compression phase. If the bubble wall velocity reaches or exceeds the sonic velocity in the medium, the motion of the bubble can be termed as transient.

12.4.3 Analysis of the spectral characteristics of acoustic emission

Analysis of the acoustic emission spectra for media with different saturation levels can be presented as follows:

(1) Gassy or saturated medium: In a saturated or gassy liquid medium, the cavitation nuclei are contributed by both sources, viz. the gas pockets trapped in the solid boundaries as well as free-floating bubbles. Thus, the total bubble volume

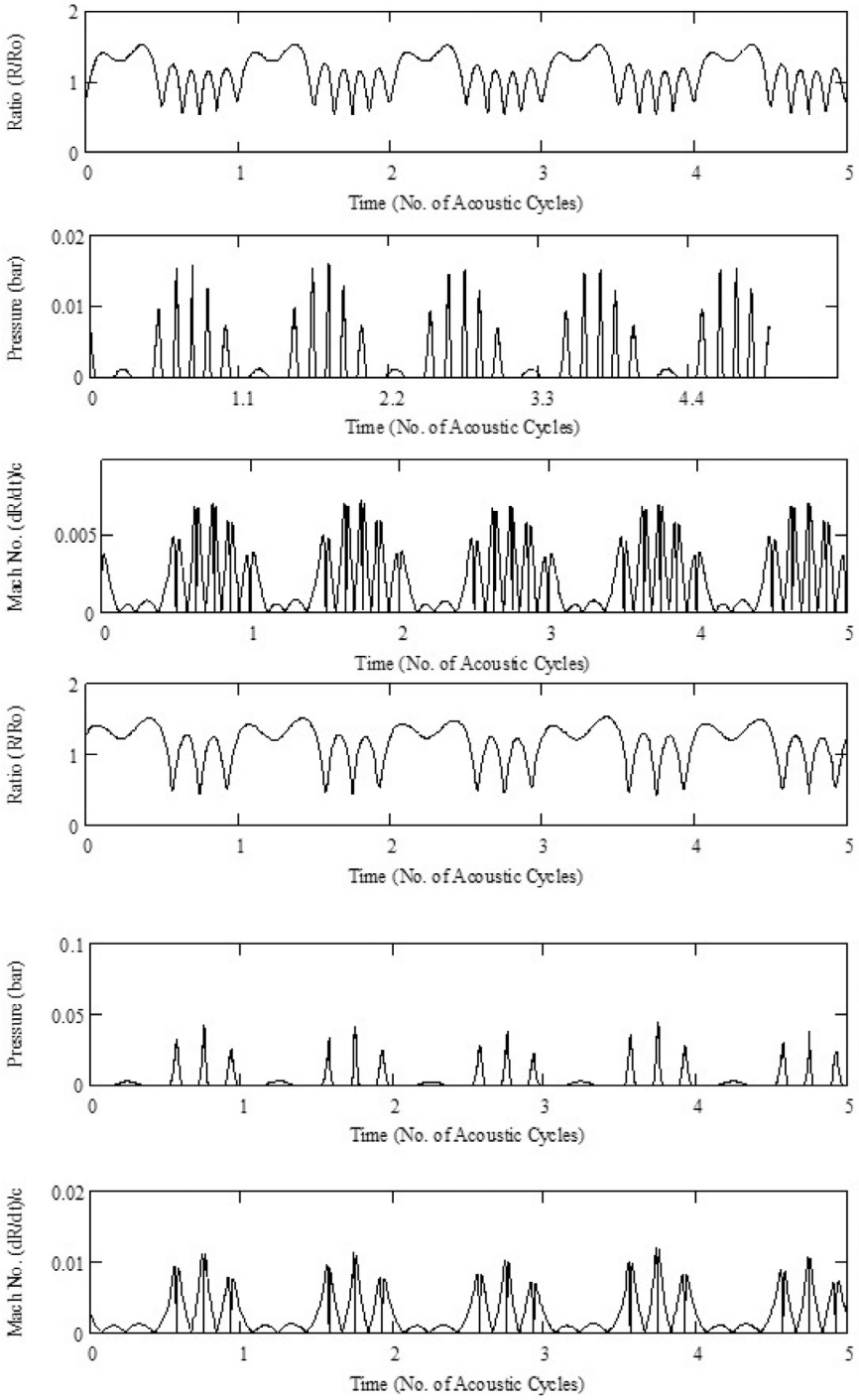

FIGURE 12.8 (continued…): Simulations of radial motion of cavitation bubbles for acoustic pressure amplitude higher than transient cavitation threshold. The initial bubble sizes are 5, 7.5, and 10 μm (in sequence of given figures). Each set of three figures represent radial motion of the bubble, acoustic wave emission, and bubble wall Mach number for a particular bubble size. Other parameters for simulations: $P_A = 0.8$ bar, $f = 25$ kHz. *(Reproduced from Moholkar and Warmoeskerken (2003) with permission of John Wiley and Sons).*

fraction in the medium is likely to be high. This reduces the specific acoustic impedance, which results in lower power consumption by the horn and smaller acoustic pressure amplitude. Another effect of large bubble volume fraction is rapid attenuation of the ultrasound wave. A combined consequence of this is lowering of the acoustic pressure amplitude throughout the reactor volume – even below the transient cavitation threshold ($P_A < P_T$). Therefore, the cavitation bubbles in the medium undergo small amplitude oscillatory motion, or in other words, stable cavitation. Moreover, as evident from simulations of rectified diffusion, the cavitation bubbles may also shrink and dissolve away during radial

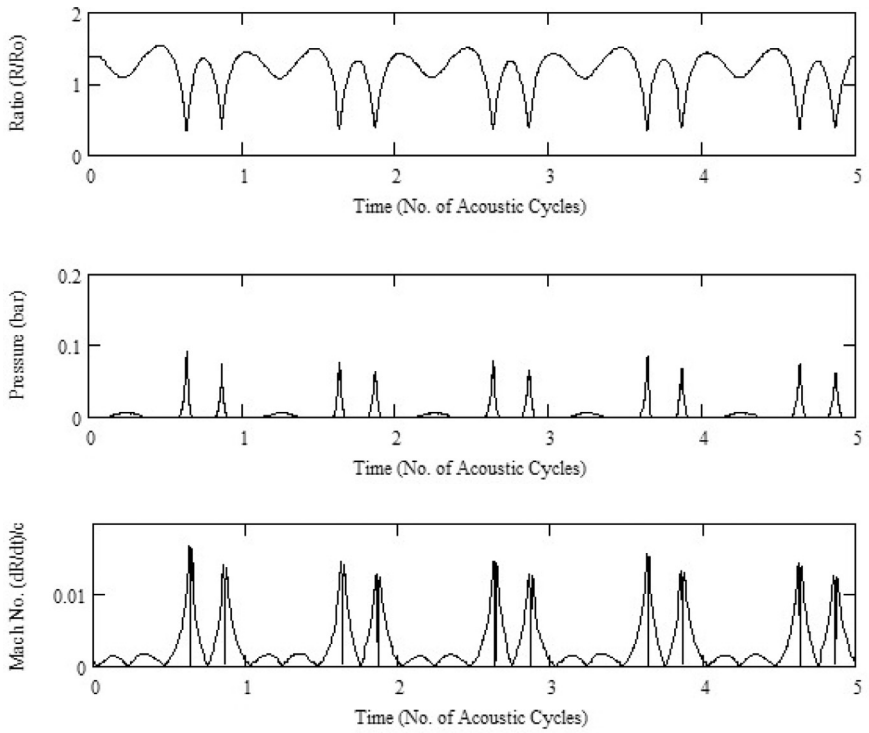

FIGURE 12.8, cont'd.

motion. Thus, the resultant cavitation intensity in the medium is small, which is reflected in acoustic emission spectrum, that is, absence of subharmonic and harmonic peaks. On a whole, it can be concluded that the energy transformation efficiency for gassy water is low.

(2) Undersaturated medium: Degassing or undersaturation of the medium causes reduction in both the free and dissolved gas content of the medium. The free-floating bubbles quickly dissolve away and the cavitation nuclei are only contributed by stabilized gas pockets in the crevices of solid boundaries. Small bubble population in the medium increases specific acoustic impedance, and the power consumption of the ultrasound horn. This increases the pressure amplitude of the ultrasound waves generated in the medium. Smaller bubble population also reduces the attenuation of the ultrasound waves. The collective consequence of this is relatively large ultrasound pressure amplitudes prevalent in the entire medium, probably higher than the transient cavitation threshold. The resultant radial motion of the bubble is of transient type that gives rise to strong acoustic emission comprising subharmonics, ultraharmonics, and the harmonics. These characteristics are present in the acoustic emission spectrum of undersaturated water. It may be noted that the cavitation bubbles in undersaturated medium will eventually dissolve away. Thus, an external supply of cavitation nuclei is essential (for example, through a gas sparger) to maintain cavitation intensity.

(3) Undersaturated and denucleated medium: In this situation, the free gas population in the medium was practically zero, which left no nuclei for cavitation events. For this case, the specific acoustic impedance is very high, as noted earlier. The power consumption of the horn and hence the amplitude of the ultrasound waves generated are also high. But despite this, no cavitation events take place in the medium, as the medium is completely devoid of the cavitation nuclei. Thus, the acoustic emission spectrum for the undersaturated and denucleated medium has only one peak corresponding to the ultrasound or fundamental frequency. One can conclude that overall efficiency of the energy transformation—from electrical energy to cavitation energy—is zero. Almost equal power consumption for undersaturated medium and undersaturated + denucleated medium essentially shows relatively smaller influence of free gas fraction on the specific acoustic impedance.

12.5 Overview

Concurrent analysis of experimental and simulations results presents an interesting account of the mechanistic facets of energy transformation chain in an ultrasonic processor. The energy transformation efficiency is the highest for undersaturated

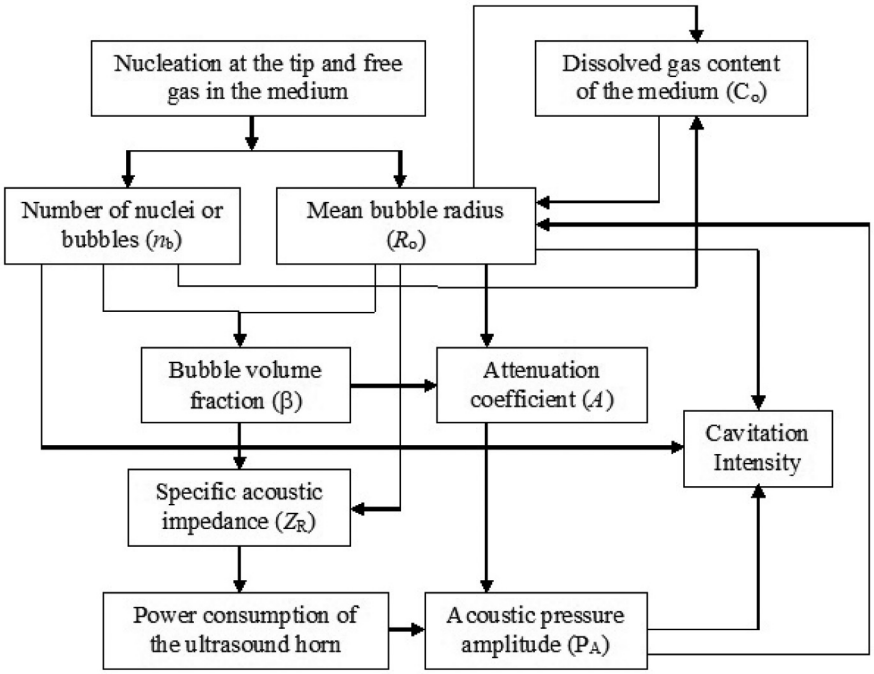

FIGURE 12.9 Interrelation between various physical parameters that affect the energy transformation chain in an ultrasonic processor. *(Reproduced from Moholkar and Warmoeskerken (2003) with permission of John Wiley and Sons).*

medium, and the lowest for undersaturated + denucleated medium. The gas content of the medium – in both free and dissolved form – have been revealed to be the critical parameters that influence different steps in energy transformation chain. The resultant cavitation intensity produced in the medium is determined by three parameters, viz. (1) specific acoustic impedance, (2) attenuation coefficient, and (3) acoustic pressure amplitude. The effect of free and dissolved gas content of the medium on the above parameters seems to be counterproductive. For a given saturation level of the medium, P_A affects R_o through rectified diffusion, while R_o affects P_A through specific acoustic impedance, as it is a function of total volume fraction of the bubbles in the medium.

The complete nature of interactions between the parameters n_b, R_o, P_A, C_o, A, and Z_R, and the resultant cavitation intensity in the medium, which can be deduced from the analysis of this work, is shown in Fig. 12.9.

12.6 Case studies of ultrasonic processes based on energy transformation analysis

We now present two case studies, each of a physical and chemical process, which is based on energy transformation analysis presented in previous sections. We essentially show as how the overall efficiency or the yield of processes can be enhanced with manipulation of the gas content of the medium. The physical process is that of enhancement of mass transfer in textiles and the chemical process is of enhancing the yield of oxidation of potassium iodide (popularly known as Weissler reaction).

12.7 Intensification of wet textile treatment

Wet textile processes such as washing, dyeing and rinsing are important components of textile processing chain. These processes involve mass transfer across textile materials, and intensification of this mass transfer forms the basis for improvement of these processes. Most textile, especially those made of natural fibers like cotton, are characterized by dual porosity, viz. interyarn porosity and intrayarn porosity. The interyarn and intrayarn regions form parallel paths for liquid flow during the wet textile processes. The internyarn region, being of much larger size, forms low resistance path for liquid flow. This renders the mass transfer in intrayarn region a diffusive process and also rate limiting step in overall mass transfer operation. It has been known since 1950s that ultrasound can intensify numerous wet textile processes. However, the exact mechanism of this enhancement was not clear. Several authors had proposed different hypotheses for the observed effects like reduction in boundary layer between textile surface and bulk liquid, reduction in size of dye (or dirt particles) that makes

their diffusion faster or enhanced swelling of fibers etc. Many results reported in literature were rather system specific and not reproducible. In other words, the literature in ultrasound-assisted wet textile processes was of "black box type" where main focus was on the results and not on underlying rationale.

Moholkar et al. (2004) have published a study which addressed the issue of identification and establishment of the mechanism of mass transfer enhancement in textiles with ultrasound. One of the strategies adopted by Moholkar et al. (2004) for this purpose was variation in gas content of the system. The system had two components, viz. washing medium (i.e., water) and the fabric. Another outcome of this study was identification of the optimum gas content of the medium, which yielded maximum mass transfer or maximum process efficiency. We give herewith a brief summary of the results of Moholkar et al. (2004) which clearly showed the influence of gas content on the efficiency of an ultrasonic process. For complete analysis with other details, the readers are referred to the original paper. The experimental approach of Moholkar et al. (2004) was based on basic principles of acoustics and cavitation. The experimental strategies and protocols helped in distinguishing between the contributions of acoustic phenomena (such as oscillatory velocity field induced by ultrasound or the acoustic streaming) and cavitation phenomena. Three of the strategies adopted by Moholkar et al. (2004) were:

(1) *Standing waves:* Formation of the standing waves results in generation of pressure antinodes (or velocity nodes), as noted earlier. Placing of the fabric at either of these locations can help distinguish between the effects of ultrasound wave and cavitation phenomena. At pressure antinode, cavitation phenomena will be maximum while at pressure node (or velocity antinode) ultrasound wave phenomena will be maximum.

(2) *Degassing of the washing medium:* The cavitation intensity in the medium increases with reduced gas content of the medium. However, denucleating of the medium along with undersaturation reduces cavitation intensity to zero, as demonstrated in previous section.

(3) *Denucleation of the textiles:* The air pockets located in the interyarn and intrayarn pores can provide nuclei for cavitation events within textile. The microconvection generated by cavitation bubbles can help enhance mass transfer within textiles. Comparison of the results with untreated and denucleated textile samples can reveal the contribution of cavitation events within textile itself to enhancement of mass transfer in textiles.

The experiments were planned using plain weave model fabric with dual porosity, which is a simple geomrty for transport of the monitor. The size of the monitor particles should be smaller than the intrayarn pores, which ensures their presence in these pores. The model fabric chosen was EMPA 101 fabric (ETH, Zurich). This was a plain-weave cotton fabric with density of 100 g/cm^2 and soiled with carbon soot and olive oil. The carbon particles in the soot are chemically neutral and their diffusion coefficient (as calculated from their size using Stokes-Einstein equation) was 10^{-12} m^2/s. Moreover, these particles did not form any strong bond of physical/chemical nature with cotton fibers, which may hinder their transport.

The experimental setup used in this study was similar to the previously described setup. Only change made in the setup was that the glass cell was divided in rings of length $\lambda/4$, which facilitated placing of the fabric at pressure antinode and node selectively. The experiments were divided in four categories: (1) Nondegassed fabric and nondegassed washing medium, (2) degassed fabric and nondegassed washing medium, (3) nondegassed fabric and degassed washing medium, (4) degassed fabric and degassed washing medium. In each of these categories, the experiments were carried out by placing the fabric at pressure antinode and node. In addition, the static pressure of the system was also varied using a pressure chamber. Experiments were conducted at elevated pressures of 2, 3, and 5 bar. The fabric was soaked for few minutes in detergent solution prior to experiments so as to loosen the carbon particles in the fabric. The saturation content of the washing medium was lowered using the same chemical method described earlier. The fabric samples were degassed by soaking them in highly undersaturated water (with dissolved oxygen content lowered to 2 ppm) and pressurizing the system for 7 bar. This process was expected to dissolve most of the air pockets trapped in the interyarn and intrayarn pores. In each case, fabric treatment was carried out for 3 minutes. In order to ensure uniform cavitation nucleation in the medium, external nuclei in the form of polystyrene suspension were added to the medium in the experimental categories with degassed medium. After the treatment, the fabric was dried in air. The washing effect was quantified using the reflectance measurement that gives an estimate of soil concentration in the fabric. The reflectometer used for these measurements had facility of converting the reflectance value into three parameters, viz. L (lightness), a (color shift between green-red) and b (color shift between blue-yellow). The washing efficiency was defined as percentage change in the lightness of the fabric after treatment.

Results and reasonings: Variations in washing efficiency with different process conditions are shown in Fig. 12.10.

The least washing efficiency was obtained for nondegassed water with nondegassed fabric at both pressure antinode and node. This result can be explained in terms of strong attenuation of the ultrasound waves due to large bubble population, which grows in mean size due to saturation of liquid medium with dissolved gas. As a consequence, both acoustic and cavitation intensity in the medium is small. Removal of gas in the fabric did not alter washing efficiency significantly,

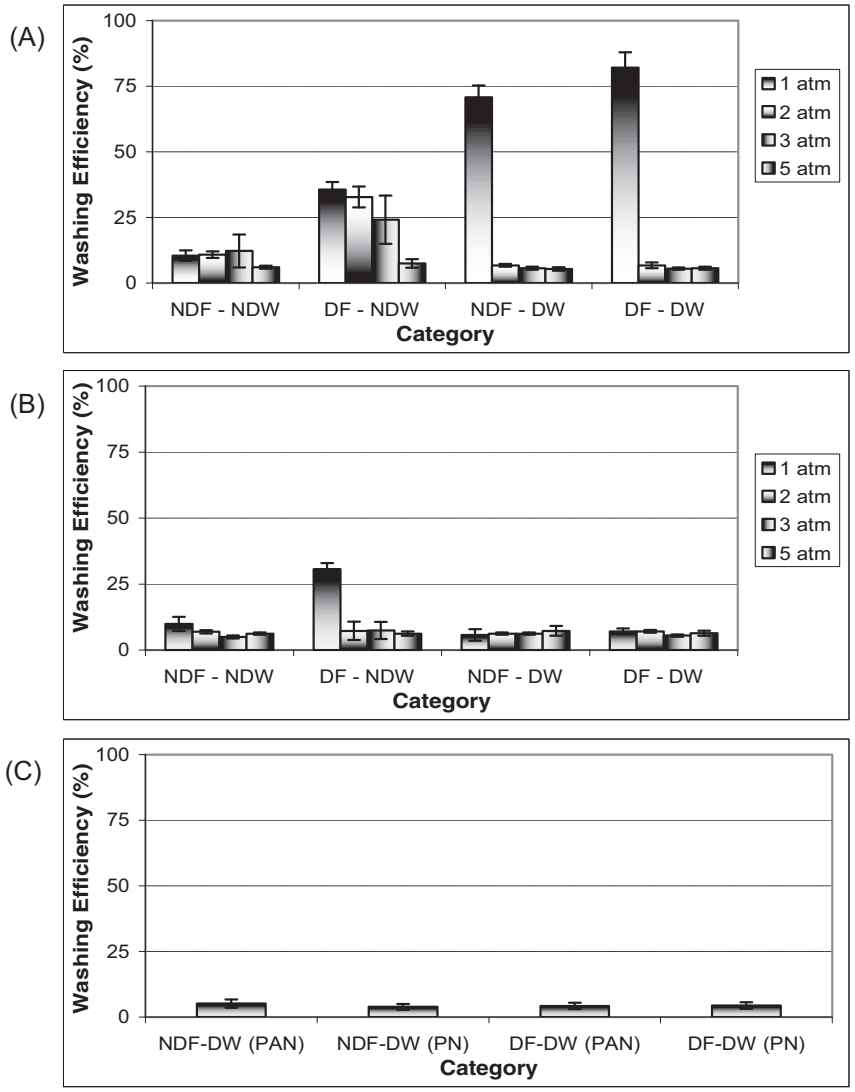

FIGURE 12.10 Variations in washing efficiency with gas content of washing medium and fabric, static pressure of the system, and the position of the fabric in standing wave. (A) washing efficiency at pressure antinode, (B) washing efficiency at pressure node, (C) washing efficiency with denucleation of the medium *(Reproduced from Moholkar et al. (2004) with permission of John Wiley and Sons).*

as very small fraction of the total cavitation nuclei in the medium are contributed by the fabric. However, a small rise in washing efficiency with degassing of fabric could be due to detachment of few carbon particles on the surface of fabric during degassing procedure. With degassing of the washing medium, the washing efficiency shows a marked rise at pressure antinode, but not at pressure node. This effect can be explain on basis of the analysis of variation in cavitation intensity with saturation level of the medium presented earlier. Finally, degassing (or denucleation) of the fabric along with washing medium also does not alter the washing efficiency for the reasons mentioned earlier. It is noteworthy that washing efficiency at pressure node for degassed or unsaturated washing medium is quite small. As noted earlier, the acoustic pressure amplitude at pressure node is quite small, while oscillatory velocity due to ultrasound is high. Negligible washing efficiency at pressure node clearly shows that oscillatory velocity due to ultrasound does not contribute towards washing of textile, or in general, the mass transfer in textile. This conclusion is also supported by the results of ultrasonic washing of textiles at elevated static pressure. As discussed in previous section, for the conditions of PA $<$ PT, the cavitation bubbles undergo stable oscillatory motion. The acoustic pressure amplitude in the present case was 1.6 bar (as noted in previous section), and thus, with rise in static pressure to 2 atm and higher, the bubble motion in the medium is converted to stable, oscillatory type. The cavitation intensity in the medium is reduced sharply, which is manifested in terms of least washing efficiency. Denucleation

of washing medium (using the same procedure as mentioned in previous section) in addition to degassing also results in negligible washing efficiency, as evident from Fig. 12.10.

In essence, the results of ultrasonic textile washing with variation in gas content of the medium are a vivid proof of the role of gas content on energy conversion efficiency of the physical processes.

12.8 Case study 2: Weissler reaction

In another study, Sivasankar et al. (2007) have examined the influence of variation in gas content in the medium on the yield of a well-known sonochemical reaction, that is, Weissler reaction. This reaction involves the ultrasound-mediated oxidation of potassium iodide to release iodine. This reaction is a standard dosimeter for sonochemical processes. The rate of a sonochemical reaction induced by sonication ($M + R^{\bullet} \rightarrow$ products) can be represented as: $r_M = k_R[M][R^{\bullet}]$, where [M] is the concentration reactants, [R*] is the concentration of radicals and kR is the kinetic constant. The kinetics and yield of a sonochemical reaction can be enhanced by using higher initial concentration of reactants or increasing radical production from cavitation bubbles. Another factor that influences the yield of sonochemical reaction is the probability of interaction between a reactant molecule and radicals produced out of bubble collapse. The cavitation events are, however, rather sporadic in nature and do not occur uniformly throughout reaction volume. Moreover, the radicals produced by the bubbles are highly unstable, and do not diffuse into the medium from the point of transient bubble collapse. Thus, only the reactant molecules present close to bubble interface have probability of interaction with radicals and undergo chemical change. If the concentration of reactant molecules in the vicinity of bubble interface is small, the radicals may recombine. This study was carried out to assess the effect of degassing of the medium on the yield of a sonochemical reaction.

Experimental: The experimental setup used in this study was of a different kind. A commercial, microprocessor controlled ultrasonic processor (Sonics & Materials, VCX 500) was used with frequency of 20 kHz and maximum theoretical power of 500 W (adjustable). The processor had facility of automatic amplitude compensation, which ensured delivery of constant electrical power to ultrasound probe. The processor was run at 20% of maximum theoretical power, that is, 100 W. For these operating conditions, the probe produced a sound wave of pressure amplitude 1.5 bar. In order to provide cavitation nuclei in the medium, a gas sparger fitted with porous silica filter was used. Experiments using either saturated or undersaturated (or degassed) medium were conducted with three initial concentrations of KI, viz. 2, 5, and 10% w/v. In this case, the chemical method for degassing used in previous studies was not useful, and hence, the gas content of the medium was lowered to 4 ppm of dissolved O_2, while for the saturated medium, DO content was ~8 ppm. The iodine liberated during sonication was analyzed on a UV-visible spectrophotometer. It may be noted that liberated iodine forms a complex I_3^- with iodide ions which has absorbance at 354 nm.

Mathematical model: The mathematical model for cavitation bubble dynamics used in this study was the diffusion limited model proposed by Toegel et al. (2000). This model essentially is an approximation of the full PDF model Storey and Szeri (2000), who showed that vapor entrapment in cavitation bubbles leading to formation of radicals is essentially a diffusion limited process. Large amount of evaporation occurs at the bubble interface during expansion phase of bubble motion. Vapor molecules enter the bubble and diffuse towards the bubble core. In the subsequent compression phase, the same vapor diffuses back and condenses at bubble wall (or gas-liquid interface). However, in the final moments of bubble compression, the velocity of the bubble interface becomes extremely fast (which reaches or exceeds the sonic velocity, as noted earlier). At this stage, the time scale of bubble motion becomes smaller than the time scale of vapor diffusion towards the bubble wall as well as the time scale of condensation or phase change at bubble wall. As a result, not all of the vapor that has entered the bubble during expansion can escape during compression. The entrapped vapor is subjected to conditions of extreme temperature and pressure generated during bubble collapse. Dissociation of vapor molecules occurs at these conditions resulting in generation of radicals. The model comprises of 4 simultaneous differential equations. These equations and the thermodynamic data are given in Tables 12.1(A) and (B).

The main components or the ordinary differential equations of this model are:

(1) Keller-Miksis equation for the radial motion of cavitation bubble.
(2) Equation for diffusive flux across the bubble interface.
(3) Equation for heat conduction through bubble interface.
(4) Overall energy balance treating the cavitation bubble as an open system.

The transport parameters for the heat and mass transfer (viz. thermal conductivity and diffusion coefficient) are determined based on the kinetic theory of gases (Chapman-Enskog theory using Lennard-Jones 12–6 potential) at the bulk temperature of the liquid medium. Thermal and diffusive penetration depths were estimated using dimensional analysis. This model accounts only for the vapor transport across bubble interface, and not gas transport, as the time scale for diffusion of

TABLE 12.1 (A) Model equation for cavitation bubble dynamics.

Model component	Equation	Initial value
1. Radial motion of the cavitation bubble	$\left(1-\frac{dR/dt}{c}\right)R\frac{d^2R}{dt^2}+\frac{3}{2}\left(1-\frac{dR/dt}{3c}\right)\left(\frac{dR}{dt}\right)^2=\frac{1}{\rho_L}\left(1+\frac{dR/dt}{c}\right)(P_i-P_t)+\frac{R}{\rho_L c}\frac{dP_i}{dt}-4\nu\frac{dR/dt}{R}-\frac{2\sigma}{\rho_L R}$ Internal pressure in the bubble: $P_i=\frac{N_{tot}(t)kT}{\left[4\pi\left(R^3(t)-h^3\right)/3\right]}$ Pressure in bulk liquid medium: $P_t=P_0-P_A\sin(2\pi ft)$	At $t=0$, $R=R_o$ $dR/dt=0$
2. Diffusive flux of water molecules	$\frac{dN_W}{dt}=4\pi R^2 D_W\left.\frac{\partial C_W}{\partial r}\right\|_{r=R}\approx 4\pi R^2 D_W\left(\frac{C_{W,R}-C_W}{l_{diff}}\right)$ Instantaneous diffusive penetration depth: $l_{diff}=\min\left(\sqrt{\frac{RD_w}{\lvert dR/dt\rvert}},\frac{R}{\pi}\right)$	At $t=0$, $N_w=0$
3. Heat conduction across bubble wall	$\frac{dQ}{dt}=4\pi R^2\lambda\left.\frac{\partial T}{\partial r}\right\|_{r=R}\approx 4\pi R^2\lambda\left(\frac{T_0-T}{l_{th}}\right)$ Thermal diffusion length: $l_{th}=\min\left(\sqrt{\frac{R\kappa}{\lvert dR/dt\rvert}},\frac{R}{\pi}\right)$	At $t=0$, $Q=0$
4. Overall energy balance	$C_{V,mix}\,dT/dt=dQ/dt-P_i dV/dt+(h_W-U_W)dN_W/dt$ Mixture heat capacity: $C_{V,mix}=\Sigma C_{V,i}N_i$ ($i=N_2/O_2/H_2O$) Molecular properties of water: Enthalpy: $h_w=4kT_o$ Internal energy: $U_W=N_W kT\left(3+\sum_{i=1}^{3}\frac{\theta_i/T}{\exp(\theta_i/T)-1}\right)$ Heat capacity of various species ($i=N_2/O_2/H_2O$): $C_{V,i}=N_i k\left(f_i/2+\sum\left((\theta_i/T)^2\exp(\theta_i/T)/\left(\exp(\theta_i/T)-1\right)^2\right)\right)$	At $t=0$, $T=T_0$

Notations for Table 12.1(A): R – radius of the bubble; dR/dt – bubble wall velocity; c – velocity of sound in bulk liquid medium; ρ_L – density of the liquid; ν – kinematic viscosity of liquid; σ – surface tension of liquid; λ – thermal conductivity of bubble contents; κ – thermal diffusivity of bubble contents; θ – characteristic vibrational temperature(s) of the species; N_w – number of water molecules in the bubble; N_{N2} – number of nitrogen molecules in the bubble; N_{O2} – number of oxygen molecules in the bubble; t – time, D_w – diffusion coefficient of water vapor; C_w – concentration of water molecules in the bubble; $C_{w,R}$ – concentration of water molecules at the bubble wall or gas–liquid interface; Q – heat conducted across bubble wall; T – temperature of the bubble contents; T_o – ambient (or bulk liquid medium) temperature; k – Bolzmann constant; h_w – molecular enthalpy of water; U_w – internal energy of water molecules; f_i – translational and rotational degrees of freedom; $C_{V,i}$ – heat capacity at constant volume for species i; N_{tot} – total number of molecules (gas + vapor) in the bubble; h – van der Waal's hard core radius; P_o – ambient (bulk) pressure in liquid; P_A – pressure amplitude of ultrasound wave; f – frequency of ultrasound wave.

TABLE 12.1 (B) Thermodynamic data for the model.

Species	Degrees of freedom (translational + rotational) (f_i)	Lennard–Jones force constants		Characteristic vibrational temperatures θ (K)
		σ (10^{-10} m)	ε/k (K)	
N_2	5	3.68	92	3350
O_2	5	3.43	113	2273
H_2O	6	2.65	380	2295, 5255, 5400

(Reproduced from Chakma and Moholkar (2013) with permission of John Wiley and Sons).
(Reproduced from Chakma and Moholkar (2013) with permission of John Wiley and Sons).

gases is much higher than the time scale for radial motion of the bubble. The set of simultaneous ODEs in Table 12.1(A) can be solved using Runge-Kutta adaptive step size method. An air bubble can be considered as a cavitation nuclei for simulations. The physical parameters and properties in the mathematical model can either be experimentally measured or taken from literature. Four important parameters required for the simulations of cavitation bubble dynamics are: (1) frequency and (2) pressure amplitude of ultrasound, (3) initial (or equilibrium) bubble radius, and (4) vapor pressure of water. The frequency of sonic processor was 20 kHz and the pressure amplitude was determined as 1.5 bar. A representative initial bubble size of 10 μm was selected for the unsaturated medium, while size of 20 μm was chosen for the gassy or

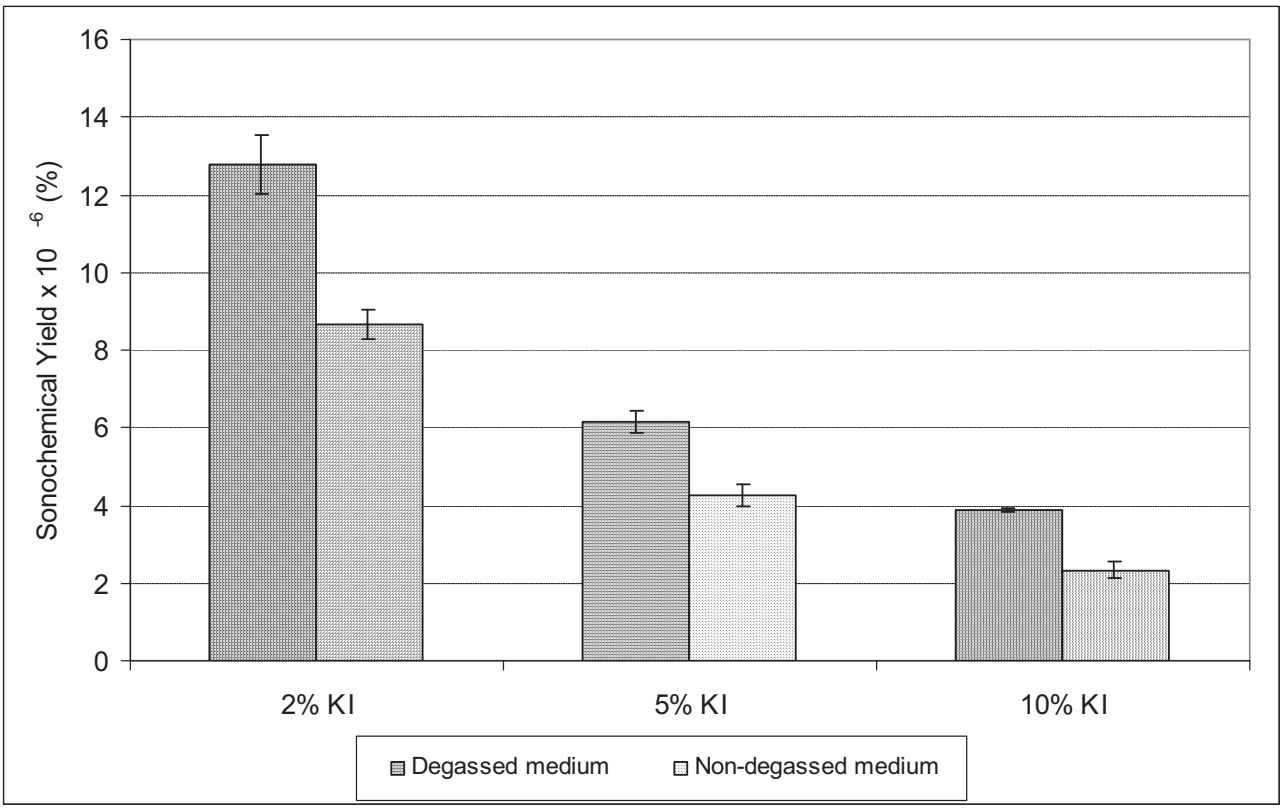

FIGURE 12.11 Trends in sonochemical yield with initial KI concentration and the saturation level of the medium *(Reproduced from Sivasankar et al. (2007) with permission of John Wiley and Sons).*

saturated medium. The smaller bubble size essentially shrinkage of the bubble due to undersaturation of the medium. The vapor pressure of water can be calculated using Antoine's equationa. However, presence of an electrolyte KI in the solution lowers the vapor pressure. Therefore a correction factor was applied to the vapor pressure on the basis of the concentration of KI in the solution. For determining the composition of the cavitation bubble (or concentrations of different species generated due to dissociation of vapor and gas molecules) during bubble collapse, an assumption of thermodynamic equilibrium was made. This assumption is based on the relative magnitudes of bubble collapse time scale and time scales of various radical reactions. The time scale of bubble collapse is of the order of few tens of nanoseconds ($\sim 10^{-8}$ s) while time scale of radical reactions is at least two orders of magnitude smaller ($\sim 10^{-10}$ s). Thus, thermodynamic equilibrium should prevail at the point of minimum radius during collapse. The equilibrium mole fractions of different molecular and radical species in the bubble (viz. H_2O, H_2, O_2, H^*, $^*OH$, O^*, H_2O_2, $HO_2{}^*$, and O_3) at the conditions of temperature and pressure at first compression of bubble was determined using Gibbs energy minimization.

Results and reasoning: The iodine liberation during sonication is a function of radical species produced by cavitation bubbles and depends on two factors: (1) the extent of water vapor entrapped in the bubble at the time of collapse, and (2) temperature and pressure peaks attained during collapse, which decides the equilibrium composition of the species produced from dissociation of gas and vapor molecules including the radical species responsible for KI oxidation. The simulations of cavitation bubble dynamics help determine these factors. The trends in sonochemical yield for different experimental conditions are shown in Fig. 12.11. The highest yield is obtained for 2% w/v KI solution with degassed reaction medium, while the lowest yield is seen for 10% w/v KI solution with nondegassed reaction medium. The yield of the reaction, defined as percentage of KI oxidized, reduced with initial KI concentration for both saturated and undersaturated medium. Nonetheless, the absolute amount of iodine liberated during sonication increased with KI concentration in the medium.

For all initial concentrations of KI (2, 5 and 10% w/v), the yield increased by ~50% with degassing of the reaction medium. Simulations of radial motion of air bubbles with initial radii (R_o) of 10 and 20 μm in 10% w/v KI solution are shown in Figs. 12.12 and 12.13, respectively.

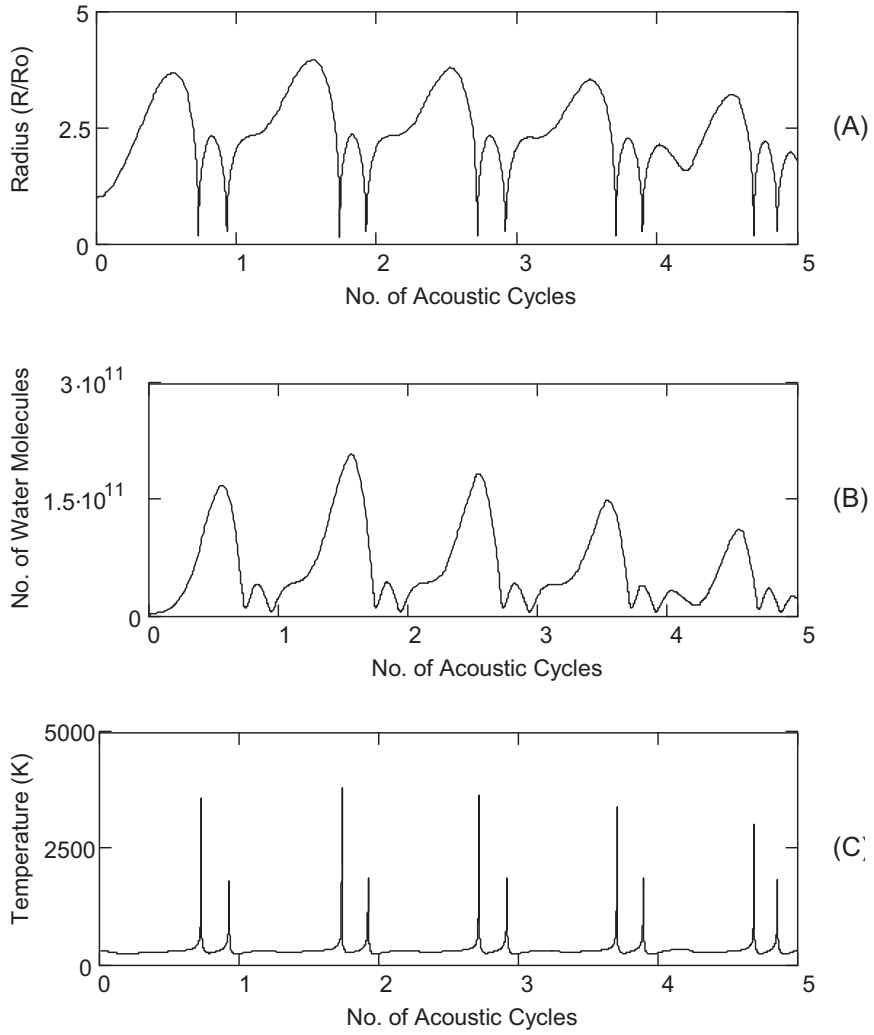

FIGURE 12.12 Cavitation bubble dynamics of 10 μm air bubble, which represents undersaturated medium. Other parameters: Initial KI concentration = 10% w/v, frequency = 20 kHz, acoustic pressure amplitude = 1.5 bar. Time variation of (A) radius of cavitation bubble (ratio R/R_o); (B) number of water vapor molecules evaporated in the bubble; (C) temperature of the bubble contents *(Reproduced from Sivasankar et al. (2007) with permission of John Wiley and Sons).*

The smaller bubble size represents degassed or undersaturated medium, while the larger bubble size indicates saturated or gassy medium. The summary of entire simulations results for KI solution of 2, 5, and 10% w/v concentration is given in Table 12.2.

This table lists the conditions of the cavitation bubble at transient collapse, viz. the number of water molecules entrapped in the bubble, and the temperature and pressure peaks reached in the bubble. The equilibrium composition of the bubble contents at the peak conditions of temperature and pressure determined using Gibbs energy minimization is also shown in this table. Among different radical species produced in the bubble, *OH is the dominant radical species. The total number of *OH radicals produced per individual bubble can be calculated by the product of the number of water molecules entrapped in the bubble and the equilibrium mole fraction of the *OH radicals at bubble collapse. The *OH radical is essentially the oxidant of KI to release iodine as: $2\,KI + 2^{\bullet}OH \rightarrow 2\,KOH + I_2$. Definite trends in extent of OH radical production per bubble can be observed from the simulations results with gas content of the medium and initial KI concentration as main governing factors.

(1) The highest yield of *OH radicals per bubble is seen for 2% w/v KI solution and initial bubble size of 10 μm (representing unsaturated medium). For higher concentrations of KI, the temperature peak reached in the bubble shows minor variation, but significant reduction is seen in extent of water vapor entrapment. For larger bubble of 20 μm

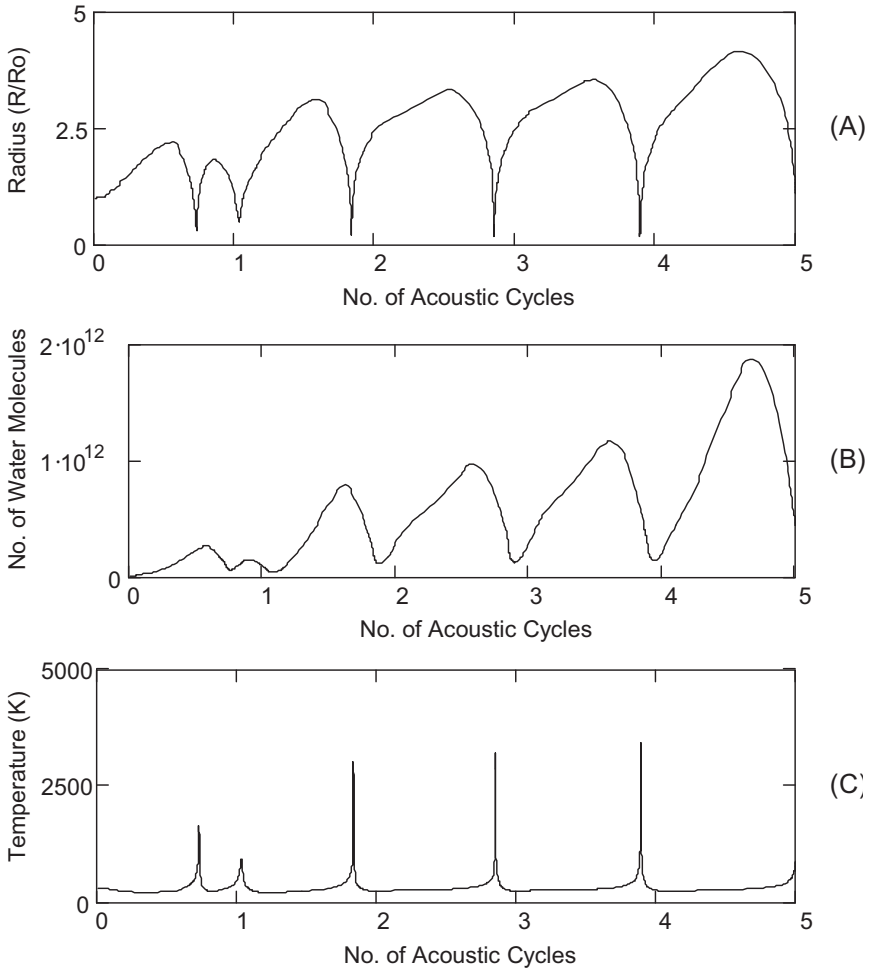

FIGURE 12.13 Cavitation bubble dynamics of 10 μm air bubble, which represents undersaturated medium. Other parameters: Initial KI concentration = 10% w/v, frequency = 20 kHz, acoustic pressure amplitude = 1.5 bar. Time variation of (A) radius of cavitation bubble (ratio R/R_o); (B) number of water vapor molecules evaporated in the bubble; (C) temperature of the bubble contents *(Reproduced from Sivasankar et al. (2007) with permission of John Wiley and Sons).*

initial size, similar trends are observed. An explanation for these results can be given as follows: the vapor pressure of water reduces with increasing KI concentration in the medium, which in turn, reduces the diffusive flux of water vapor molecules at the bubble interface. This essentially is manifested in terms of reduced entrapment of vapor molecules at the instance of bubble collapse. Secondly, the rise in *OH radical production with degassing of the medium can be explained as follows: in an undersaturated medium, the cavitation bubble shrinks in equilibrium size due to process of rectified diffusion. The extent of compression of a cavitation bubble during collapse phase is higher, and hence, the temperature peak attained at collapse as well. The attenuation of ultrasound wave in the medium is also smaller due to smaller bubble population. Thus, the actual pressure amplitude of the ultrasound wave experienced by the bubble is larger, which contributes towards the intensity of bubble collapse. A consequence of these two phenomena is larger equilibrium composition of *****OH radicals generated from dissociation of gas and vapor molecules entrapped in the bubble. Opposite effects are seen in a gassy or saturated medium. In this case, rectified diffusion makes the bubble grow during oscillation and the ultrasound wave as well undergoes large attenuation due to large density of the bubbles. As a result, relatively smaller temperature peak is attained during transient bubble collapse, which in turn, yields smaller equilibrium fraction of the *****OH radicals. Concurrent analysis of the experimental results and the results of simulations of cavitation bubble dynamics shows that sonochemical yield with saturation level of the medium and initial KI concentration essentially go hand-in-hand. This analysis also brings out an important conclusion that physical technique of reducing saturation level of the medium is far more efficient than the chemical technique of enhancing initial KI concentration. An interesting result is that the absolute amount of iodine liberation in the reaction shows

TABLE 12.2 Simulation results for air bubble.

Species	Parameters for simulations					
	$R_o = 10\ \mu m$ 2% w/v KI soln.	$R_o = 20\ \mu m$ 2% w/v KI soln.	$R_o = 10\ \mu m$ 5% w/v KI soln.	$R_o = 20\ \mu m$ 5% w/v KI soln.	$R_o = 10\ \mu m$ 10% w/v KI soln.	$R_o = 20\ \mu m$ 10% w/v KI soln.
	Conditions at the first compression of the bubble					
	$T_{max} = 3607$ K $N_{WT} = 2.2 \times 10^{+10}$	$T_{max} = 1745$ K $N_{WT} = 1.8 \times 10^{+11}$	$T_{max} = 3620$ K $N_{WT} = 2.1 \times 10^{+10}$	$T_{max} = 1832$ K $N_{WT} = 1.1 \times 10^{+11}$	$T_{max} = 3587$ K $N_{WT} = 1.9 \times 10^{+10}$	$T_{max} = 1639$ K $N_{WT} = 9.4 \times 10^{+10}$
Equilibrium composition of different radical species in the bubble at collapse (mol fraction)						
O_2	4.963×10^{-1}	6.222×10^{-1}	5.129×10^{-1}	6.251×10^{-1}	5.377×10^{-1}	6.624×10^{-1}
H_2O	4.390×10^{-1}	3.775×10^{-1}	4.218×10^{-1}	3.744×10^{-1}	4.006×10^{-2}	3.374×10^{-1}
$OH^{\bullet}$	4.945×10^{-2}	3.076×10^{-4}	4.968×10^{-2}	4.997×10^{-4}	4.698×10^{-2}	1.520×10^{-4}
$O^{\bullet}$	6.255×10^{-3}	3.299×10^{-6}	6.520×10^{-3}	6.982×10^{-6}	6.294×10^{-3}	1.233×10^{-6}
$HOO^{\bullet}$	5.893×10^{-3}	3.327×10^{-5}	6.015×10^{-3}	5.205×10^{-5}	5.716×10^{-3}	1.786×10^{-5}
H_2	1.808×10^{-3}	8.359×10^{-7}	1.761×10^{-3}	1.721×10^{-6}	1.561×10^{-3}	2.690×10^{-7}
H_2O_2	8.346×10^{-4}	3.632×10^{-6}	8.278×10^{-4}	5.638×10^{-6}	7.543×10^{-4}	1.817×10^{-6}
$H^{\bullet}$	4.263×10^{-4}	1.200×10^{-8}	4.297×10^{-4}	3.306×10^{-8}	3.849×10^{-4}	2.804×10^{-9}
O_3	5.075×10^{-5}	1.178×10^{-7}	5.434×10^{-5}	2.071×10^{-7}	5.492×10^{-5}	6.026×10^{-8}
Net amount of hydroxyl radicals produced per bubble						
N_{OH}	$1.103 \times 10^{+9}$	$5.599 \times 10^{+7}$	$1.033 \times 10^{+9}$	$5.497 \times 10^{+7}$	$8.879 \times 10^{+8}$	$1.421 \times 10^{+7}$

Note: Various notations used are as follows: T_{max} – temperature peak reached in the bubble at the time of first collapse; N_{WT} – number of water molecules trapped in the bubble at the instance of first collapse. (Reproduced from Sivasankar et al. (2007) with permission of John Wiley and Sons).

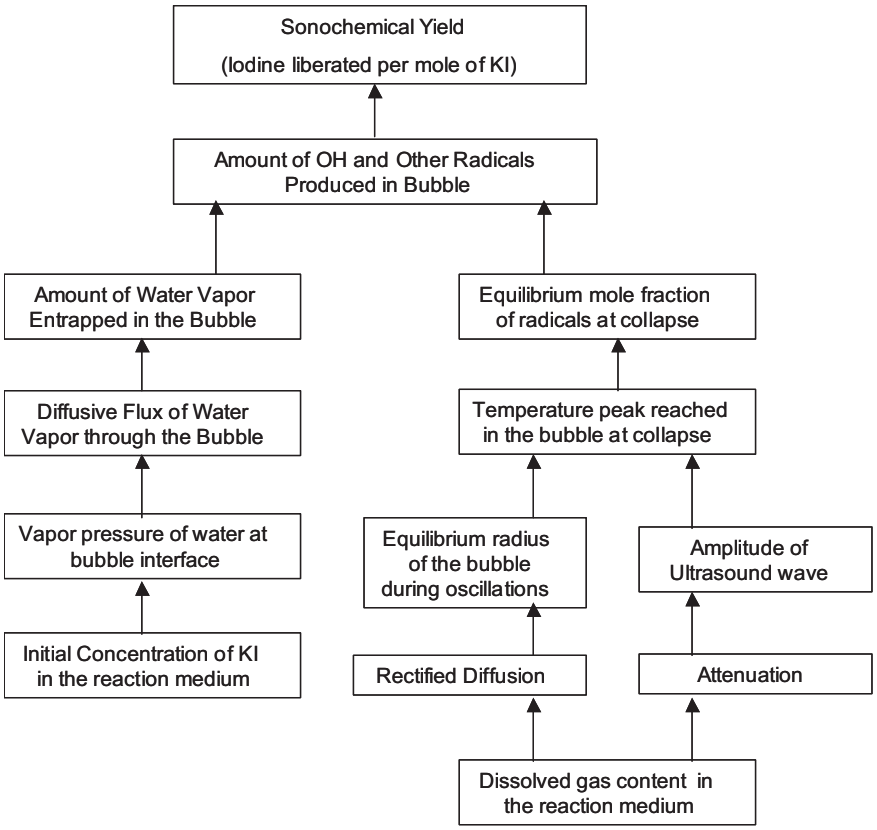

FIGURE 12.14 The physical mechanism of sonochemical yield: role of saturation level of the medium and initial KI concentration, and interdependence of physical factors *(Reproduced from Sivasankar et al. (2007) with permission of John Wiley and Sons).*

proportionate rise with initial KI concentration. This effect can be explained in terms of probability of interaction between radicals generated by cavitation bubbles and the KI molecules. Obviously, this probability varies directly with initial concentration of KI. Therefore, in 10% w/v KI solution, the net utilization of *OH radicals for the reaction is higher, although their production per cavitation bubble is smaller. For 2% w/v KI solution, it is expected that due to smaller probability of interaction with KI molecules, sizeable fraction of *OH radicals may undergo recombination.

In summary, the study of Sivasankar et al. (2007) is another vivid proof of influence of gas content of the medium on the overall efficiency of an ultrasound-assisted chemical process. However, in this case study, the initial reactant (i.e., KI) concentration has been revealed to be a counterproductive parameter. As the vapor pressure of water reduces with initial KI concentration, the phenomena of water vapor entrapment—which subsequently leads to formation of radicals—is adversely affected. The exact interdependent mechanism of the influence of two physical parameters, viz. saturation level of the medium and the initial KI concentration, on the sonochemical yield that can be deduced from the results of this study is shown in Fig. 12.14.

References

Apfel, R.E., 1981. Methods in Experimental Physics. Academic Press, New York, p. 355 Vol. 19, P. D. Edmonds.
Caflisch, R.E., Miksis, M.J., Papanicolaou, G.C., Ting, L., 1985. Effective equations for wave propagation in bubbly liquids. J. Fluid Mech. 153, 259–273.
Chakma, S., Moholkar, V.S., 2013. Physical mechanism of sono-Fenton process. AIChE J 59 (11), 4303–4313.
Flynn, H.G., 1975. Cavitation dynamics II. Free pulsations and models for cavitation bubbles. J. Acoust. Soc. Am. 58, 1160–1170.
Fyrillas, M.M., Szeri, A.J., 1994. Dissolution or growth of soluble spherical oscillating gas bubbles. J. Fluid Mech. 277, 381–407.
Leighton, T.G., 1994. The Acoustic Bubble. Academic Press, London.
Löfstedt, R., Weninger, K., Putterman, S.J., Barber, B.P., 1995. Sonoluminescing bubbles and mass diffusion. Phys. Rev. E 51, 4400–4410.
Lohse, D., Hilgenfeldt, S., 1997. Inert gas accumulation in sonoluminescing bubbles. J. Chem. Phys. 107, 6986–6997.
Moholkar, V.S., Warmoeskerken, M.M.C.G., 2003. Integrated approach to optimization of an ultrasonic processor. AIChE J 49 (11), 2918–2932.

Moholkar, V.S., Warmoeskerken, M.M.C.G., Ohl, C.D., Prosperetti, A., 2004. Mechanism of mass transfer enhancement in textiles by ultrasound. AIChE J 50 (1), 58–64.

Prosperetti, A., Commander, K.W., Crum, L.A., 1986. Nonlinear bubble dynamics. J. Acoust. Soc. Am. 83, 502–514.

Prospreretti, A., Commander, K.W., 1989. Linear pressure waves in bubbly liquids: comparison between theory and experiment. J. Acoust. Soc. Am. 85 (2), 732–746.

Sivasankar, T., Paunikar, A.W., Moholkar, V.S., 2007. Mechanistic approach to enhancement of the yield of sonochemical reaction. AIChE J 53 (5), 1132–1143.

Storey, B.D., Szeri, A.J., 2000. Water vapor, sonoluminescence and sonochemistry. Proc. R. Soc. London A 456, 1685–1709.

Toegel, R., Gompf, B., Pecha, R., Lohse, D., 2000. Does water vapor prevent upscaling sonoluminescence. Phys. Rev. Lett. 85, 3165–3168.

Young, F.R., 1989. Cavitation. McGraw-Hill, London.

CHAPTER 13

Simulation of sonoreators accounting for dissipated power

Olivier Louisnard [a] **and Igor Garcia-Vargas** [a,b,c]

[a] *Centre RAPSODEE, IMT Mines-Albi, UMR CNRS 5302, Université de Toulouse, Albi CT, France,* [b] *SinapTec, Lezennes, France,* [c] *Laboratoire de Génie Chimique, Université de Toulouse, CNRS, INP, UPS, Toulouse, France*

13.1 Introduction

Acoustic cavitation has proved its practical interest over the last decades in various physical and chemical processes: cleaning, sonochemistry, extraction, emulsification, crystallization, desagglomeration, and so on. The experimental configuration used, termed as sonoreactor, depicts an assembly of a liquid enclosed by the solid boundaries of a vessel and possibly a free surface, insonified by one or several ultrasonic transducers.

Examples of scale-up from laboratory to industrial scale exists, and manufacturers have made great efforts to be able to provide dedicated transducer technologies. Nevertheless, it should be recognized that more than two decades after the initiation of what could be called "sono-process engineering," conceptual and numerical tools to design sonoreactors rationally are still missing. Even at the laboratory scale, the simple questions "what is the ideal shape of our beaker?" or "how deep should we immerse our transducer in the beaker?" has no simple answer yet and only experimental parametric studies can give some hints in a given configuration (Wood et al., 2017). The main reason for that is the high complexity of acoustic cavitation physics. For example, the large variety of spatial and temporal scales involved prohibits the efficient use of dimensional analysis. But one of the highest difficulties, and probably of the most important physics ingredient of sonoreactor science. Studying sonoreactors by resorting to commercial finite element methods (FEM) codes to solve linear acoustics equation, which reduces to an Helmholtz equation $\nabla^2 P + k^2 P = 0$ under harmonic motion, appears therefore as a natural way, and has motivated a large number of studies (Nomura and Nakagawa, 2001; Gachagan et al., 2003; Sáez et al., 2005; Klíma et al., 2007; Yasui et al., 2007; Louisnard et al., 2009; Sutkar et al., 2010; Tudela et al., 2011; Wang and Yao, 2013; Xu et al., 2013; Niazi et al., 2014; Wei and Weavers, 2016; Zhang et al., 2018; Rashwan et al., 2020) [see also reference (Tudela et al., 2014) for a review].

However, the presence of cavitation bubbles drastically influences ultrasound propagation, which renders linear acoustics invalid. The history of bubbly fluids acoustics dates back to the pioneering work of Foldy (Foldy, 1944; Carstensen and Foldy, 1947; Morse and Feshbach, 1953), restricted to weak-amplitude waves. Later works, based on volume average methods, considered nonlinear and dispersive aspects of waves in bubbly liquids (Iordansky, 1960; van Wijngaarden, 1966; van Wijngaarden, 1968), coupling fluid mechanics conservation equations to Rayleigh nonlinear bubble dynamics equation, known as Iordansky-Kogarko-van Wijngaarden (IKvW) model. A decisive step was made by Caflisch and co-workers (Caflisch et al., 1985), who derived rigorously a simplified, but still nonlinear form of the IKvW model. The linearized form of Caflisch model, valid for weak bubbles oscillations, was considered by Commander & Prosperetti (Commander and Prosperetti, 1989). The resulting equation reads also as a Helmholtz equation with a complex sound velocity accounting for attenuation by bubbles. Owing to its simplicity, this model has been widely used in the context of sonoreactors (Dähnke et al., 1999; Dähnke et al., 1999; Dahlem et al., 1999; Servant et al., 2000–Servant et al., 2003; Mettin et al., 2006; Jordens et al., 2013).

It is easy to understand why the Commander & Prosperetti model should fail in the case of inertial cavitation, which is involved in nearly all sonoprocesses: the linear assumption restricts bubble expansions R_{max}/R_0 to values much smaller than 1, whereas inertial bubbles increase 10-fold or more their ambient radius before collapsing. As a consequence, wave attenuation predicted by this model is far too low to account for observed field in presence of cavitation, as was confirmed

Energy Aspects of Acoustic Cavitation and Sonochemistry: Fundamentals and Engineering. DOI: https://doi.org/10.1016/B978-0-323-91937-1.00021-9
Copyright © 2022 Elsevier Inc. All rights reserved.

by Campos-Pozuelo and co-workers (Campos-Pozuelo et al., 2005). Some dose of nonlinearity is therefore required for any model claiming to predict acoustic fields in cavitating liquids.

Acoustic waves attenuation occurs because part of the mechanical energy they transport is dissipated as the wave propagates, as was early recognized by Rozenberg (Rozenberg, 1971). In cavitating liquids, the main dissipators are the bubbles, and that energy dissipated is converted into heat, which founds the basis of the calorimetric method (Ratoarinoro et al., 1992; Romdhane et al., 1995; Margulis and Margulis, 2003). Thus, to account for attenuation in cavitating liquids, one must examine the energy dissipated by a single bubble. This simple reasoning led us to develop a model deriving from Caflisch equations, but avoiding its full linearization (Louisnard, 2012; Louisnard, 2012). Its reasonable success in predicting realistic acoustic fields in cavitating liquids lies in the rigorous pre-computation of bubbles energy dissipation from a nonlinear bubble-dynamics equation, which yields an attenuation coefficient dependent on the local field: large dissipation occurs in those zones were bubbles oscillate inertially (above the Blake threshold), whereas other regions dissipate virtually no energy. As attenuation increases with the field amplitude, the wave can be said to be self-attenuated.

This chapter is organized as follows. In Section 13.2, we recall the main features of linear acoustics, from which we deduce an equation of mechanical energy conservation, in the non-dissipative and dissipative cases. We recall the concepts of acoustic intensity, active power and acoustic impedance and show how the complex squared wavenumber is related to energy dissipation. Section 13.3 recalls the Caflisch model and its linear form, as expressed by Commander & Prosperetti. We show that this model cannot account for the strong attenuation of waves observed in sonoreactors. Its associate energy conservation equation is in strongly cavitating liquids (Louisnard, 2012). In Section 13.4, we recall the equations of vibration of elastic solids and piezo-electrics. Here again, we deduce the energy conservation equations and detail the global energy balance of a complete sonoreactor. Finally, Section 13.5 presents some new simulation examples. In the first one, the full transducer/reactor set is simulated and we detail how the frequency control strategy used in modern ultrasound generators can be reproduced in simulations. A comparison of the results with experimental electrical measurements is also presented. The second example examines to what extent experiments reported in the literature can be reproduced by simulation, using calorimetric results. A last example presents predictions for a transducer of complex shape, allowing energy flow through the lateral boundaries of the immersed part.

13.2 Linear acoustics

13.2.1 Energetics of nondissipative linear acoustics

Even if linear acoustics is by far a too rough assumption to describe sonoreactors, it is instructive to briefly recall the physics involved and the associate energetics. Acoustic waves result from the combination of inertia and compressibility of the medium. Under the assumption of small velocities, small pressure/density variations, isentropic motion and neglecting viscous forces, the Navier-Stokes equations can be linearized into:

$$\frac{1}{\rho_l c_l^2}\frac{\partial p}{\partial t} + \nabla \cdot \mathbf{v} = 0 \tag{13.1}$$

$$\rho_l \frac{\partial \mathbf{v}}{\partial t} + \nabla p = 0 \tag{13.2}$$

with $p(\mathbf{r}, t)$ is the acoustic pressure field, that is the pressure variations around the static pressure p_0,$\mathbf{v}(\mathbf{r}, t)$ the velocity field, $c_l = 1/(\kappa\rho_l)^{1/2}$ is the sound velocity, where κ is the isentropic compressibility of the fluid. Eliminating $\mathbf{v}$ between the two equations yields the standard propagation equation:

$$\nabla^2 p - \frac{1}{c_l^2}\frac{\partial^2 p}{\partial t^2} = 0$$

Eqs. (13.1)–(13.2) can be recast into an energy conservation, multiplying the first by p and taking the scalar product of the second with:

$$\frac{\partial}{\partial t}\underbrace{\left(\frac{1}{2}\frac{p^2}{\rho_l c_l^2} + \frac{1}{2}\rho_l v^2\right)}_{\text{Acoustic energy density } \mathscr{E}} + \nabla \cdot \underbrace{(p\mathbf{v})}_{\substack{\text{Energy}\\ \text{density}\\ \text{flux } \mathfrak{F}}} = 0. \tag{13.3}$$

The quantity $\mathscr{E}$, called acoustic energy density, is nothing else than a mechanical energy per unit volume, sum of kinetic energy involved in the fluid motion and elastic potential energy stored by the fluid. The vectorial quantity $\mathfrak{F} = p\mathbf{v}$, termed

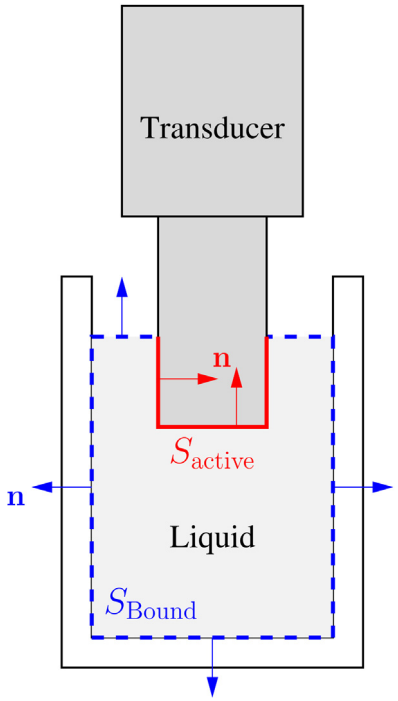

FIGURE 13.1 Sketch of a classical sonoreactor configuration. The liquid is in contact with the transducer through boundary S_{active} (solid line, red online) and otherwise bounded by boundaries S_{Bound} (dashed line, blue online). The arrows indicate the normal unit $\mathbf{n}$ vector pointing outward from the liquid.

as acoustic intensity, is an energy flux density and its streamlines materializes the acoustic energy paths in the fluid. Note that this quantity has unit W m^{-2}.

Eq. (13.3) describes how energy is stored in the medium and flows through it. A more understandable form can be obtained in global form. We assume that the fluid is enclosed between an active surface (typically the surface of a transducer) S_{active} and some passive surfaces S_{Bound} (typically the reactor external walls, or a free surface in contact with air, see Fig. 13.1). Integrating (13.3) over the whole volume of fluid and using divergence theorem (in what follows, $\mathbf{n}$ represents normal vector pointing outward the liquid):

$$\frac{d}{dt}\underbrace{\int_V \iiint \mathcal{E}dV}_{\substack{\text{Energy stored in}\\ \text{the liquid}}} = \underbrace{\iint_{\text{active}} p\mathbf{v}\cdot(-\mathbf{n})dS}_{\substack{\text{Acoustic power entering}\\ \text{liquid through}\\ \text{transducer}}} - \underbrace{\iint_{S_{\text{Bound}}} p\mathbf{v}\cdot\mathbf{n}dS}_{\substack{\text{Acoustic power leaving}\\ \text{liquid through}\\ \text{boundaries}}} \tag{13.4}$$

which expresses that the variations of acoustic energy stored in the fluid results from the difference between the mechanical energy fluxes entering and leaving this volume.

More eloquent results can be gained by assuming harmonic motion at angular frequency $\omega = 2\pi f$. Both pressure and velocity fields can be expressed in function of complex amplitudes (the star symbol represents complex conjugate):

$$p(\mathbf{r},t) = \frac{1}{2}\left(P(\mathbf{r})e^{i\omega t} + P^*(\mathbf{r})e^{-i\omega t}\right) \tag{13.5}$$

$$\mathbf{v}(\mathbf{r},t) = \frac{1}{2}\left(V(\mathbf{r})e^{i\omega t} + V^*(\mathbf{r})e^{-i\omega t}\right) \tag{13.6}$$

Under this assumption, the energy conservation Eq. (13.3) can be averaged over one cycle, so that the time derivative cancels out, which means that no acoustic energy is stored or lost on average. The average intensity vector fulfills:

$$\nabla\cdot\langle\Im\rangle = \frac{1}{4}\nabla\cdot\left(P\mathbf{V}^* + P^*\mathbf{V}\right) = \frac{1}{2}\nabla\cdot\mathrm{Re}\left(P\mathbf{V}^*\right) = 0 \tag{13.7}$$

The integral form is again more illustrative:

$$\underbrace{\iint_{S_{\text{active}}} \frac{1}{2}\text{Re}\left(P\mathbf{V}^*\right)\cdot(-\mathbf{n})dS}_{\substack{\mathcal{P}_{\text{active}}=\text{mean power}\\ \text{entering liquid through}\\ \text{immersed part of}\\ \text{transducer}}} = \underbrace{\iint_{S_{\text{Bound}}} \frac{1}{2}\text{Re}\left(P\mathbf{V}^*\right)\cdot\mathbf{n}dS}_{\substack{\text{Mean power leaving}\\ \text{liquid through}\\ \text{boundaries}}} \tag{13.8}$$

The first integral is referred to as active power in the context of sonoreactors and once divided by the transducer area S_{active}, it yields the mean input intensity, commonly used to quantify the energy transferred to the liquid. The above result states that in absence of dissipative phenomena, all the energy entering the sonoreactor could only escape through reactor boundaries. If the latter are infinitely rigid ($\mathbf{V}=0$, a good approximation for thick solid boundaries), or infinitely soft ($P=0$, adequate for a free surface between liquid and air), the second integral in Eq. (13.8) vanishes, and the latter states that no energy can be transferred by the transducer to the liquid: $\mathcal{P}_{\text{active}}$ should be zero! In such a situation, pressure and velocities are in phase quadrature everywhere ($\text{Re}(P\mathbf{V}^*)=0$), which means that a perfect standing wave establishes in the liquid, the boundaries (whatever their type provided that they do not dissipate or radiate energy outside) reflecting all the incident energy. Average acoustic intensity $\langle\mathfrak{I}\rangle = \langle p\mathbf{v}\rangle$ is null everywhere, and no energy can flow within the liquid.

It is thus clearly seen that the picture of non-dissipative linear acoustics is incompatible with the one of an energy transfer from a transducer to a liquid, and any simulation based on non-dissipative acoustics in the liquid can definitely not account for $\mathcal{P}_{\text{active}}$. The acoustic impedance relates the normal inward velocity on the boundary of a system, to the inward driving pressure force exerted on this boundary. On a point of the transducer, the local impedance of the reactor would thus be defined by:

$$Z_{\text{Trans,loc}} = \frac{P}{(\mathbf{V}\cdot(-\mathbf{n}))} \text{ on } S_{\text{active}} \tag{13.9}$$

In presence of pure standing waves, the latter would be therefore purely imaginary. The mean impedance seen by the transducer (or by a subset of the transducer area) is defined by

$$Z_{\text{Trans}} = \frac{\iint_{S_{\text{active}}} PdS}{\iint_{S_{\text{active}}} \mathbf{V}\cdot(-\mathbf{n})dS} \tag{13.10}$$

and is also purely imaginary in the case of perfect standing waves. An interesting particular case is when the normal velocity is constant on the transducer surface $\mathbf{V}.\mathbf{n}=V_0$, which yield the active power as:

$$\mathcal{P}_{\text{active}} = \frac{1}{2}\text{Re}(Z_{\text{Trans}})V_0^2 S_{\text{active}}, \tag{13.11}$$

which is the analog of Joule effect in conductors, and confirms that in presence of perfect standing waves, one would have $\mathcal{P}_{\text{active}}=0$.

Let's now assume that the sonoreactor has boundaries either fully transparent for waves, or fully dissipative (this is the case of anechoic chambers, but is a by far unrealistic assumption for sonoreactors). A traveling wave would set in, and all the energy transferred by the transducer would flow unaffected through the liquid down to the boundaries, where it would either dissipate or radiate outside. Eq. (13.8) would yield $\mathcal{P}_{\text{active}} = \mathcal{P}_{\text{bound}}$. Assuming further a plane wave, it can be shown that $P = \rho_l c_l \mathbf{V}$ everywhere (pressure and velocities are now in phase). In this case the transducer impedance would read $Z_{\text{Trans}} = \rho_l c_l$. The latter quantity is called liquid specific impedance. The active power reads in this case $\mathcal{P}_{\text{active}} = |P|^2/(2\rho_l c_l)S_{\text{active}}$, which is often used abusively to estimate the amplitude of the acoustic field in a sonoreactor from the power transferred by the transducer (measured by calorimetry). As will be shown below from simulations, this relation does not hold in general.

We note in conclusion of this reminder that following a common misbelief, ultrasonic bath would develop standing waves while immersed transducers would rather produce traveling waves. Both are wrong since both configurations obey to the same physics described above. In both cases, a dose of standing waves must develop because the liquid is enclosed by (at least partially) reflecting boundaries, and a dose of traveling waves is necessary to transfer some energy to the fluid. Mathematically, pressure and velocities are neither in phase quadrature nor in phase, and the impedance seen by the

transducer has nonzero real and imaginary parts. The co-existence of both type of waves is well-known (Mettin, 2005; Lee et al., 2008; Kauer et al., 2017) and is responsible of some bubble structures commonly observed in sonoreactors (Louisnard, 2012; Mettin, 2005). The key feature to explain this co-existence is dissipation, on which we focus in the next section.

13.2.2 Energetics of dissipative linear acoustics

Real acoustic waves in fluids, albeit potentially linear, are subject to irreversible processes, so that mechanical energy is dissipated into heat. The main dissipative processes are viscous friction, heat conduction, and relaxation (in gases). In this case, Eqs. (13.1) (13.2) are no longer valid. They must be supplemented by a viscous term, the energy conservation equation, and an equation of state, to account for the latter phenomena. The resulting equation is still a Helmholtz equation, but the wavenumber is now a complex quantity:

$$k = k_r - i\alpha, \tag{13.12}$$

where α is a positive coefficient representing an attenuation coefficient and has the same dimension (m^{-1}) as k_r. This can be easily understood by considering a plane wave travelling towards increasing:

$$p(x,t) = p_0 e^{i\omega t - ikx} = p_0 e^{-\alpha x} e^{i\omega t - ik_r x}.$$

Attenuation α is often defined in dB per unit length, with the following equivalence:

$$\alpha_{(\mathrm{dBm}^{-1})} = 20\log_{10} e \quad \alpha_{(\mathrm{m}^{-1})} \simeq 8.68589 \quad \alpha_{(\mathrm{m}^{-1})}.$$

To gain more insight into the practical meaning of α, one can notice that $\alpha/k_r = \alpha\lambda/2\pi$ where λ is the wavelength, so that the attenuation factor over one wavelength is $\exp(-2\pi\alpha/k_r)$. For example, a wave amplitude reduced by a two-fold factor over one wavelength would correspond to $\alpha/k_r = \ln 2/2\pi \simeq 0.110$.

The precise expression of α when accounting for the above-mentioned dissipative processes in homogeneous fluids can be found in classical acoustic textbooks (Morse and Ingard, 1968) and an interesting overview can be found in reference (Lighthill, 1978). Attenuation increases with ω^2 but remains small in water: in ambient conditions, α varies from 3.1×10^{-6} m^{-1} at 20 kHz to 7.8×10^{-3} m^{-1} at 1 MHz. This is way too low to account for the strong attenuation encountered in cavitating liquids.

One can obtain an interesting general relation between the squared complex wavenumber k^2, and therefore α, and the power dissipated in the liquid. Indeed, multiplying the Helmholtz equation by P^*, we obtain:

$$P^*\nabla^2 P + \left[\mathrm{Re}\left(k^2\right) + i\mathrm{Im}\left(k^2\right)\right]|P|^2 = 0.$$

Then, subtracting the complex conjugate of this equation to itself yields:

$$P^*\nabla^2 P - P\nabla^2 P^* = -2i\mathrm{Im}\left(k^2\right)|P|^2,$$

which, using the identity $\nabla\cdot(a\mathbf{u}) = a\nabla\mathbf{u} + \nabla a.\mathbf{u}$, can be recast as :

$$\nabla\cdot\left(P^*\nabla P - P\nabla P^*\right) = -2i\mathrm{Im}\left(k^2\right)|P|^2. \tag{13.13}$$

If we further assume for simplicity that the linearized momentum Eq. (13.2) is still valid (this will be true for the nonlinear model presented later in this paper), it reads for harmonic motion:

$$i\rho\omega\mathbf{V} = -\nabla P, \tag{13.14}$$

so that Eq. (13.13) can be re-interpreted as:

$$\nabla\cdot\langle\mathfrak{I}\rangle = \frac{1}{4}\nabla\cdot\left(P^*\mathbf{V} + P\mathbf{V}^*\right) = \frac{1}{2}\nabla\cdot\mathrm{Re}\left(P\mathbf{V}^*\right) = \frac{\mathrm{Im}\left(k^2\right)|P|^2}{2\rho\omega} \tag{13.15}$$

to be compared to the non-dissipative case Eq. (13.7). The left-hand side can be recognized as the divergence of the average acoustic intensity, and this equation generalizes the conservation Eq. (13.7) in presence of dissipative processes. In the configuration sketched in Fig. 13.1, integrating this equation over the whole liquid volume and using divergence theorem,

Eq. (13.8) can be generalized to a clear interpretation:

$$\underbrace{\iint_{S_{\text{active}}} \frac{1}{2}\text{Re}\left(P\mathbf{V}^*\right)\cdot(-\mathbf{n})dS}_{\substack{\mathcal{P}_{\text{active}}=\text{mean power entering liquid through immersed part of transducer}}} = \underbrace{\iint_{S_{\text{Bound}}} \frac{1}{2}\text{Re}\left(P\mathbf{V}^*\right)\cdot\mathbf{n}\,dS}_{\text{Mean power leaving liquid through boundaries}} + \underbrace{\iiint_{V} \frac{-\text{Im}\left(k^2\right)|P|^2}{2\rho\omega}dV}_{\text{Mean dissipated power in the liquid}} . \tag{13.16}$$

Assuming non-dissipative, non-transparent boundaries, the second integral would vanish, and the above result states that the average acoustic power transmitted to the liquid must equal the power dissipated in the liquid, whatever the physical origin of dissipation. Clearly the dissipated power in Eq. (13.16) must be positive, which implies that $-\text{Im}(k^2)$ must be positive. This justifies the minus sign in the definition (13.12) of the attenuation factor with $\alpha > 0$ since from definition (13.12), $\text{Im}(k^2) = -2k_r\alpha$. Eqs. (13.15) and (13.16) both account for this energy dissipation as the wave propagates.

The conclusion that must be retained from the above considerations is that whenever a sound wave can be described by a Helmholtz equation, the imaginary part of k^2, whatever its expression, is necessarily connected to the energy dissipated in the medium, and from (13.16), it contributes the active power transferred by the transducer to the liquid.

We can also note that Eq. (13.16) clearly shows that pressure and velocity can no longer be in phase quadrature on the whole the transducer surface, or, in terms of impedance (see Eq. 13.11), that $\text{Re}(Z_{\text{Trans}}) > 0$, which states that the transducer sees a dissipative acoustic load[1].

13.3 Sound propagation accounting for cavitation

The presence of cavitation bubbles invalidates classical linear acoustics, first because the acoustic pressure can reach or even exceed ambient pressure, and second because of the radial oscillations of bubbles scatter waves. The analysis is complicated by the self-organization of bubbles under the acoustic field which involves some complex physics: Bjerknes forces translating the bubbles and/or maintaining them in specific zones, growth-dissolution on average over one cycle, fragmentation, coalescence, nucleation. Clearly, a full model accounting for this bidirectional interaction between the acoustic fields and the bubble field is yet not at hand, although some interesting analysis exists (Kobelev and Ostrovskii, 1989; Akhatov et al., 1994; Parlitz et al., 1999; Mettin et al., 2002; Appel et al., 2004; Mettin, 2007; Gumerov and Akhatov, 2017).

13.3.1 The Caflisch model

We addressed the problem of the bubbles influence on wave propagation by reverting to classical nonlinear models of bubble liquids acoustics which once simplified, yields a reasonably simple model, albeit nonlinear, extending the Helmholtz formulation discussed above (Louisnard, 2012; Louisnard, 2012). Caflisch and co-workers extended acoustics to bubbly fluids by the following equations:

$$\frac{1}{\rho_l c_l^2}\frac{\partial p}{\partial t} + \nabla\cdot\mathbf{v} = N\frac{\partial}{\partial t}\left(\frac{4}{3}\pi R^3\right), \tag{13.17}$$

$$\rho_l\frac{\partial \mathbf{v}}{\partial t} + \nabla p = 0, \tag{13.18}$$

$$\rho_l\left[R\frac{\partial^2 R}{\partial t^2} + \frac{3}{2}\left(\frac{\partial R}{\partial t}\right)^2\right] = p_l - (p_0 + p), \tag{13.19}$$

where $R(\mathbf{r}, t)$ is the instantaneous radius of bubbles located near position $\mathbf{r}$, $p_g(\mathbf{r},t)$ the pressure inside these bubbles, N is the number of bubbles per unit volume, $p(\mathbf{r}, t)$ and $\mathbf{v}(\mathbf{r}, t)$ the acoustic pressure and velocity fields, respectively. The liquid pressure at the bubble interface p_l is related to gas pressure by:

$$p_l = p_g - \frac{2\sigma}{R} - 4\mu_l\frac{1}{R}\frac{\partial R}{\partial t}, \tag{13.20}$$

1. The integral must be positive but nothing impedes the integrand to change sign in some locations, which means that the transducer can receive energy from the liquid in those points. An example of occurrence of such behavior will be shown in Section 13.5.3.

where μ_l is the liquid viscosity and σ the surface tension. The expression of p_g depends on the model used for the thermal behavior of the bubble content. We defer this definition.

The subtlety of the model appears in the right-hand side of Eq. (13.17), and expresses how the compressibility of a bubbly liquid is affected by the radial dynamics of the bubbles. The presence of compressible bubbles increases the compressibility of the equivalent medium and thus affects the mass conservation equation. One must understand here however that this compressibility change may be of very complex nature: it depends on how bubbles expand or contract in response to the local pressure field, which is described by the nonlinear bubble dynamic Eq. (13.19) (a Rayleigh-Plesset equation in this case). The subtlety in the latter, credited to van Wijngaarden (van Wijngaarden, 1968) is to replace the usual driving term $p_\infty(t) = p_0 - p_a \sin\omega t$ by $p_0 + p(\mathbf{r}, t)$, where $p(\mathbf{r}, t)$ is the local acoustic pressure. As the latter is influenced by the other bubbles, this model accounts partially for the bubble-bubble interaction through their effect on the acoustic field. As noted by Prosperetti (Prosperetti, 1998), "*this feature of the model makes the whole machinery work*".

13.3.2 Linear case

The linearization of this models allows to draw some interesting analytical conclusions (Commander and Prosperetti, 1989). It yields a linear Helmholtz equation for the pressure field

$$\nabla^2 P + k^2 P = 0,$$

where the complex wave number is given by the linear dispersion relation (Foldy, 1944; van Wijngaarden, 1966; Caflisch et al., 1985; Commander and Prosperetti, 1989; Prosperetti, 1991; Doc et al., 2016):

$$k^2 = \frac{\omega^2}{c_l^2} + \frac{4\pi R_0 \omega^2 N}{\omega_0^2 - \omega^2 + 2ib\omega}, \tag{13.21}$$

where ω_0 is the bubble resonance frequency and b the damping factor of the linearized bubble oscillations, arising from viscous, thermal, and acoustic effects (Prosperetti, 1991; Devin, 1959; Prosperetti, 1977). This squared wavenumber differs from the one of linear acoustics by the fact that k^2 is now complex. The wavenumber k is thus complex too, and its imaginary part theoretically predicts the wave attenuation.

To justify the next section, it is instructive to examine the values of α that can be predicted from Eq. (13.21). As can be deduced from the latter, α can vary over a large range, especially near resonance since $\omega \simeq \omega_0$ yields an almost null denominator in (13.21). This near-resonance behavior displays interesting features, revisited recently (Doc et al., 2016), but here we focus on the case $\omega \ll \omega_0$ since bubbles encountered in high-amplitude low-frequency fields are mainly sub-resonant (Mettin, 2005; Burdin et al., 1999; Mettin et al., 1999). Since $b\omega/\omega_0^2 \ll 1$ always hold (Prosperetti, 1977), k^2 simplifies to:

$$k^2 \simeq \frac{\omega^2}{c_l^2} + 4\pi R_0 N \left(\frac{\omega}{\omega_0}\right)^2 \left(1 - i\frac{2b\omega}{\omega_0^2}\right),$$

and using again $2\omega/\omega_0^2 \ll 1$, we get $|\mathrm{Im}(k^2)| \ll |\mathrm{Re}(k^2)|$. It can be easily checked that this implies $\alpha \ll k_r$ and more precisely that $\alpha/k_r < b\omega/\omega_0^2 \ll 1$. We can conclude therefore from Section 13.2.2 that linear theory for sub-resonant bubbles will always predict a very small attenuation per wavelength, unable to account for the strong attenuation observed in inertially cavitating liquids. Clearly, this is due to the assumption of linear bubble oscillations and this stresses the important conclusion that Caflisch model must be kept in its nonlinear form, at least approximately. This justifies the model derived in reference (Louisnard, 2012) whose main lines are recalled in Section 13.3.5.

13.3.3 Energy formulation

The Caflisch model can be recast into an energy form, which allows the correct identification of the energy dissipated by the bubbles. We first proceed as for the linear acoustics equations and combining the first two equations of Caflisch model Eqs. (13.17), (13.18), we get:

$$\frac{\partial}{\partial t}\left(\frac{1}{2}\frac{p^2}{\rho_l c_l^2} + \frac{1}{2}\rho_l v^2\right) + \nabla \cdot (p\mathbf{v}) = Np\frac{\partial V}{\partial t}, \tag{13.22}$$

It has the same structure as Eq. (13.3) except for the right-hand-side which represents the consumption of acoustic energy by the bubbles. It involves the local acoustic pressure p and the volume of the bubbles responding to this field. We

will examine this term later. Here we do not make assume mono-harmonic motion, but only that all quantities are periodic, either at the transducer frequency, or possibly some sub-harmonic frequency, if any. Averaging over the largest period of the motion yields:

$$\nabla \cdot \langle \mathfrak{F} \rangle = Np\frac{\partial V}{\partial t} \tag{13.23}$$

which once again can be integrated over the full sonoreactor:

$$\underbrace{\iint_{S_{\text{active}}} \frac{1}{2}\text{Re}\left(P\mathbf{V}^*\right)\cdot(-\mathbf{n})dS}_{\substack{\text{Mean power entering}\\ \text{liquid through}\\ \text{transducer } \mathcal{P}_{\text{active}}}} = \underbrace{\iint_{S_{\text{Bound}}} \frac{1}{2}\text{Re}\left(P\mathbf{V}^*\right)\cdot\mathbf{n}\,dS}_{\substack{\text{Mean power leaving}\\ \text{liquid through}\\ \text{boundaries}}} + \underbrace{\iiint_{V} -N\left\langle p\frac{\partial V}{\partial t}\right\rangle}_{\substack{\text{Mean dissipated power}\\ \text{in the liquid by}\\ \text{thebubbles}}}. \tag{13.24}$$

This conservation equation clearly exhibits the fact that $\langle p\partial V/\partial t\rangle$ must be negative. This average is conditioned by the phase between the bubble oscillation and the pressure field driving this oscillation, whose origin will be made clear hereinafter.

We now show that the third equation of Caflisch model, which describes the bubble dynamics responding to the local acoustic field, can also be recast in an energetic form, once multiplied by $\partial V/\partial t = 4\pi R^2 \partial R/\partial t$. Noting that $\rho_l\left[R\partial^2 R/\partial t^2 + \frac{3}{2}(\partial R/\partial t)^2\right] \times \partial V/\partial t$ is the time-derivative of the radial kinetic energy of the liquid $K_l = 2\pi\rho_l R^3(\partial R/\partial t)^2$, RayleighPlesset equation becomes:

$$-p\frac{\partial V}{\partial t} = \frac{\partial}{\partial t}\left(K_l + 4\pi R^2\sigma + p_0 V\right) + 16\pi\mu_l R\left(\frac{\partial R}{\partial t}\right)^2 - p_g\frac{\partial V}{\partial t}, \tag{13.25}$$

This energetic form of Rayleigh equation represents the energy conservation of the liquid in radial motion around the bubble [2]. This equation states that the work done by the local acoustic pressure on the bubble may increase either the liquid kinetic energy, or the interfacial energy, dissipate into heat because of viscous friction in the liquid radial motion, or exert work on the gas content of the bubble. It may become more useful once averaged over one acoustic cycle. Assuming periodic motion of the bubble, the time derivatives give zero-averages and we get:

$$\left\langle -p\frac{\partial V}{\partial t}\right\rangle = \Pi_{\text{v}} + \Pi_{\text{th}}, \tag{13.26}$$

where

$$\Pi_{\text{th}} = \frac{1}{T}\int_0^T -p_g\frac{\partial V}{\partial t}dt, \tag{13.27}$$

$$\Pi_{\text{v}} = \frac{1}{T}\int_0^T 16\pi\mu_l R\left(\frac{\partial R}{\partial t}\right)^2 dt. \tag{13.28}$$

Eq. (13.26) is the key feature of the model described in reference (Louisnard, 2012): it just states that on average over one period (or over the smallest oscillation period in case of sub-harmonic oscillations), the work done by the local acoustic field is consumed by a bubble. The first reason is the viscous friction in the bubble radial motion (note that Π_{v} is trivially positive). To get a better understanding of the second contribution, we note that from first principle of thermodynamics, we have:

$$\frac{d\left(U_g + K_g\right)}{dt} = \dot{Q} - p_g\frac{dV}{dt}, \tag{13.29}$$

2. It should be noted the presence of the extra term $p_0 V$ appearing in (13.25), compared to reference (Louisnard, 2012). This term comes from the presence of p_0 in the RHS of (13.19), which is necessary for p to be understood as the acoustic pressure, not the total pressure. This in turn must be the if we want to write the acoustic intensity as $p\mathbf{v}$. This term is also absent in the original equation proposed by Caflisch et al. (Caflisch et al., 1985), which we think is a mistake. Fortunately, as this term cancels out after averaging, there are no consequences on our model and past results.

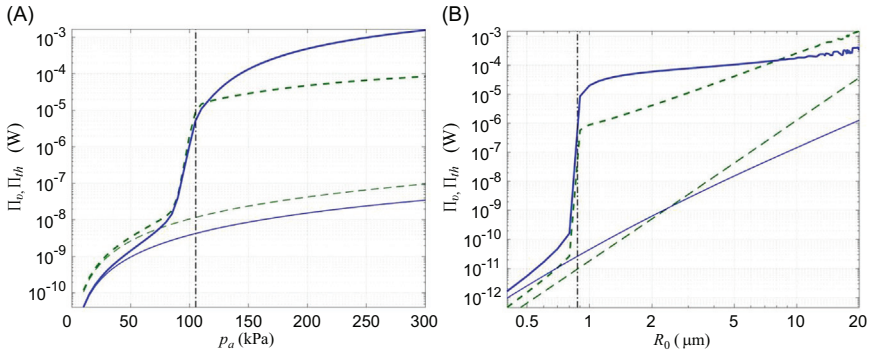

FIGURE 13.2 Power dissipated by an air bubble in water at $f = 20$kHz; by viscosity Π_v [thick solid line (blue online), from Eq. (13.28)]; by thermal diffusion, Π_{th} [thick dashed line (green online), from Eq. (13.27)]. The thin lines are the corresponding values obtained from linear theory and the vertical dash-dotted line represents the Blake threshold. (A) Bubble ambient radius $R_0 = 5\mu$m for different acoustic pressure levels p_a (B) Driving pressure $p_a = 150$kPa for different ambient radii R_0.

where U_g and K_g are the bubble gas content internal energy and kinetic energy, respectively, and $\dot{Q}$ is the heat flux from the surrounding liquid toward the bubble. Averaging over one period yields:

$$\Pi_{\text{th}} = -\langle \dot{Q} \rangle$$

which shows clearly that Π_{th} represents the mean thermal power lost by the bubble over one oscillation cycle. From second principle of thermodynamics, $\langle \dot{Q} \rangle$ must be negative so that Π_{th} must be positive.

The next step towards the model described in reference (Louisnard, 2012) can be easily understood by injecting Eq. (13.26) into the energy conservation equation, either Eq. (13.23) (local form) or (13.24) (global form). In the former case we obtain:

$$\nabla \cdot \langle \Im \rangle = N \left\langle p \frac{\partial V}{\partial t} \right\rangle = -N \left(\Pi_{\text{v}} + \Pi_{\text{th}} \right), \tag{13.30}$$

whose negative right-hand side represents the acoustic power dissipated per unit-volume by the bubbles. The denser the bubble cloud, the more energy is dissipated. It should be noted that this equation results directly from recasting Caflisch model in energetic form, assuming only that all quantities are periodic in time, and has therefore the same range of validity.

13.3.4 Energy dissipation functions

Before going further, we show typical orders of magnitude of Π_{v} and Π_{th}. Both quantities can be evaluated once the bubble dynamics $R(t)$ is known. To do so, we use the Keller-Miksis equation (which will be commented further hereinafter) with a classical sinusoidal driving term. Of course, as the Caflisch model is nonlinear, its exact resolution would yield a distorted, non-sinusoidal acoustic field, and one might question the validity of what follows. This is in fact the main (clearly unjustified) assumption of our model, as will be exposed in next section.

The thermal behavior of the gas content and water evaporation/condensation are accounted for by the reduced model of Toegel et al. (Toegel et al., 2000), assuming a uniform temperature and water content in the bubble core, with gradients localized near the bubble wall. This allows a reasonable estimation of the heat flow between the bubble and surrounding water, and therefore of Π_{th}. A van der Waals equation is assumed for the gas content. The driving pressure is assumed in the form $p(t) = p_0 - p_a \sin 2\pi f t$. We assume air bubbles in water at ambient conditions driven at $f = 20$kHz. The results are displayed in Figs. 13.2A (p_a varied for a 5μm bubble) and 13.2B (R_0 varied for a 1.5 bar field), where the values obtained from linear theory are also recalled for comparison. The first, and most important conclusion drawn from these graphs are that the estimations of Π_{th} and Π_v from the fully nonlinear dythreshold. The second result is that Π_v is near one order of magnitude larger than Π_{th}, except for ambient radii larger than 5μm. This allows to neglect Π_{th} in computations, so that cept for ambient radii larger than 5μm. This allows to neglect Π_{th} in computations, so that bubbles may be assumed to dissipate energy mainly by viscous friction. Assuming bubbles smaller than 5μm can be justified at 20kHz because it is consistent with the fragmentation thresholds either computed (Hilgenfeldt et al., 1996; Storey, 2001; Holzfuss, 2008; Lin et al., 2002), measured in single-bubble sonoluminescence (SBSL) experiments (Gaitan and Holt, 1999), or in multibubble fields (Mettin et al., 1999; Reuter et al., 2019), so that assuming $\Pi_{\text{th}} \ll \Pi_{\text{v}}$ in 20kHz fields sounds reasonable in a first approach.

It should be noted that the latter assumption seems to be in contradiction with more recent computations (Jamshidi and Brenner, 2013; Trujillo, 2020) who found a predominance of thermal effects above Blake threshold. On the other hand, the choice of Keller equation for our numerical simulations might sound irrelevant, since we started from a Rayleigh equation in Caflisch model and expressed the energy conservation equation from the latter. Keller equation

$$R\frac{\partial^2 R}{\partial t^2}\left(1-\frac{1}{c_l}\frac{\partial R}{\partial t}\right)+\frac{3}{2}\left(\frac{\partial R}{\partial t}\right)^2\left(1-\frac{1}{3c_l}\frac{\partial R}{\partial t}\right)=\frac{1}{\rho_l}\left[\left(1+\frac{1}{c_l}\frac{\partial R}{\partial t}\right)(p_L-p)+\frac{R}{c_l}\frac{\partial (p_L-p)}{\partial t}\right] \tag{13.31}$$

contain $O(1/c_l)$ corrections to the Rayleigh equation, accounting for the outward radiation of sound due to finite liquid compressibility. Therefore, its energetic counterpart also contains additional terms of order $O(1/c_l)$. It can be shown that once multiplied by $\partial V/\partial t$ and period-averaged, the Keller equation can be recast as:

$$\left\langle -p\frac{\partial V}{\partial t}\right\rangle = \Pi_{\mathrm{v}}+\Pi_{\mathrm{th}}+\Pi_{\mathrm{rad}}, \tag{13.32}$$

where

$$\Pi_{\mathrm{rad}}=-\left\langle \frac{\partial V}{\partial t}\left[\frac{\rho_l}{c_l}\left(\frac{\partial R}{\partial t}\right)^3+\frac{\partial}{\partial t}\left(\frac{R}{c_l}(p_l-p)\right)\right]+\frac{\dot{R}}{c_l}\frac{\partial K_l}{\partial t}\right\rangle. \tag{13.33}$$

This term is clearly linked to the compressibility of the liquid, and accounts for energy loss by radiation around the bubble. We did not evaluate these terms in our early studies (Louisnard, 2012; Louisnard, 2010) and subsequent computations. These terms were found to be significant in various studies (Jamshidi and Brenner, 2013; Trujillo, 2020; Dogan and Popov, 2016; Sojahrood et al., 2020). Moreover, some terms in (13.33) also involve additional viscous and thermal effects (through the p_l term), and there is a debate concerning the attribution of the latters to Π_{th},Π_{v} or Π_{rad} (Trujillo, 2020). We will reconsider these aspects in future work, and in absence of a clear consensus for now, we carry on considering only Π_{v} in our computations.

Finally, for further comments, we note that the original energy conservation Eqs. (13.22), (13.25) and (13.29) can be combined into a single one, yielding:

$$\frac{\partial}{\partial t}\left(\frac{1}{2}\frac{p^2}{\rho_l c_l^2}+\frac{1}{2}\rho_l v^2+K_l+4\pi R^2\sigma+p_0V+U_g+K_g\right)+\nabla\cdot(p\mathbf{v}) = -N16\pi\mu_l R\left(\frac{\partial R}{\partial t}\right)^2+N\dot{Q} \tag{13.34}$$

It has a clear structure of a conservation equation with an energy accumulation term (first term in LHS), an energy flux term (second term in LHS) and a source/sink term in the RHS. It can be noted that the instantaneous value of $\dot{Q}$ may have either a positive or negative sign, but is necessarily negative on average over one period, which is a consequence of second principle of thermodynamics. It can be easily checked than once averaged, the above equation yields again Eq. (13.30).

13.3.5 A reduced model (Louisnard, 2012)

The precedent considerations show how Caflisch equations can be re-interpreted in terms of energy conservation/dissipation but do not simplify its resolution. Knowing the bubble density N, Eqs. (13.17)–(13.20) should be solved numerically in time to get the acoustic field in the liquid. Solving such equations or similar ones is feasible but because they are hyperbolic, this requires elaborate numerical techniques and large computer resources and a small number of bubbles (Ando et al., 2011; Fuster and Colonius, 2011; Maeda and Colonius, 2019; Fuster, 2019), which we think unadapted for now at the scale of sonoreactors. Time-resolved simulation for weak amplitudes can also reasonably be considered (Louisnard, 1998; Vanhille and Campos-Pozuelo, 2008; Vanhille and Campos-Pozuelo, 2013; Vanhille and Campos-Pozuelo, 2009) but raises the problem of reaching a periodic steady-state for standing waves (Louisnard, 1998).

On the other hand, the simplicity of the linearized form proposed by Commander & Prosperetti (Commander and Prosperetti, 1989) remains attractive because the acoustic field is assumed mono-harmonic, which allows to eliminate the time variable and solve a Helmholtz equation. However, as shown in Section 13.3.2, this approach condemns a realistic evaluation of the field attenuation.

A trade-off should therefore be found. We showed in reference (Louisnard, 2012) that an intermediate approximate solution consists in keeping the assumption of mono-harmonicity, while using at the same time a realistic estimate of the power dissipated by bubbles from nonlinear bubble dynamics. As seen above, the latter point warrants a correct estimation

of the bubble field. More precisely, assuming that the acoustic field can be decomposed as:

$$p(\mathbf{r},t)=\frac{1}{2}\left(P(\mathbf{r})e^{i\omega t}+P^{*}(\mathbf{r})e^{-i\omega t}\right)+p_{\mathrm{osc}},$$

where ω is the driving angular frequency and p_{osc} denotes that part of the acoustic field oscillating at $n\omega$, $n\geq 2$, and under the (yet unjustified) assumption $p_{\mathrm{osc}}\partial V/\partial t\simeq 0$, it was proved that the complex amplitude P of the field obeys a nonlinear Helmholtz equation:

$$\nabla^2 P+\underbrace{\left(\mathrm{Re}\left(k^2\right)-2i\rho_l\omega N\frac{\Pi_{\mathrm{th}}(|P|)+\Pi_{\mathrm{v}}(|P|)}{|P|^2}\right)}_{k^2(|P|)}P=0. \tag{13.35}$$

The imaginary part of the squared effective wavenumber is logically linked to the power dissipated by each bubble, as seen in Section 13.2.2. In our original derivation of the above equation, we did not give an explicit form of $\mathrm{Re}(k^2)$ and proposed to replace it by its expression from the linear dispersion (Eq. (13.21) with $b=0$). The precise choice of $\mathrm{Re}(k^2)$ has no influence on calculations due to the fact that $\mathrm{Im}(k^2)$ takes huge values above Blake threshold. This was further discussed in (Trujillo, 2020; Trujillo, 2018).

13.3.6 Summary of the cavitating liquid model

The equation used in our model are:

$$\begin{array}{l}\nabla^2 P+k_l^2 P=0 \quad \text{where}|P|<P_B \quad \text{(no bubbles)}\\ \nabla^2 P+k_{\mathrm{NL}}^2 P=0 \quad \text{where } |P|\geq P_B \quad \text{(bubbles)}\end{array} \tag{13.36}$$

where $k_l=\omega/c_l$ and P_B is the Blake threshold (Akhatov et al., 1997; Hilgenfeldt et al., 1998; Louisnard and Gomez, 2003)

$$P_B=p_0\left(1+\left(\frac{4}{27}\frac{S^3}{1+S}\right)^{1/2}\right), \tag{13.37}$$

where $S=2\sigma/(p_0R_0)$ is the dimensionless Laplace tension and R_0 the bubble ambient radius. The nonlinear wavenumber k_{NL} is defined by:

$$\mathrm{Re}\left(k_{\mathrm{NL}}^2\right)=\frac{\omega^2}{c_l^2}+\frac{4\pi NR_0\omega^2}{\omega_0^2-\omega^2},\qquad \mathrm{Im}\left(k_{\mathrm{NL}}^2\right)=-2N\rho_l\omega\frac{\Pi_{\mathrm{v}}(|P|)}{|P|^2}.$$

The dissipation function $\Pi_{\mathrm{v}}(|P|)$ is pre-computed by a Keller bubble dynamics solver for a given ambient radius R_0 and the ratio $\Pi_{\mathrm{v}}/|P|^2$ can be easily fitted by:

$$\frac{\Pi_{\mathrm{v}}(|P|)/p_0V_0\omega}{(|P|/p_0)^2}=\exp\left[K_1+\frac{2}{\pi}K_2\tan^{-1}\left(K_3\frac{|P|}{p_0}-K_4\right)\right],$$

to be used in COMSOL as an analytic function. For a 5μm air bubble in water at ambient temperature in a 20 kHz field, the K_n are:

$$K_1=-2.2073,\quad K_2=5.3365,\quad K_3=4.4988,\quad K_4=0.96279$$

In all the simulations presented hereinafter, the dissipation function Π_{v} will be computed from these values, and the bubble density N in zones where $|P|$ is above the Blake threshold will be set to 50 bubbles/mm^3.

Finally, the acoustic velocity field can be computed from:

$$i\rho\omega\mathbf{V}=-\nabla P, \tag{13.38}$$

from which the period-average acoustic intensity vector can be obtained as:

$$\langle\mathfrak{I}\rangle=\frac{1}{2}\mathrm{Re}\left(P\mathbf{V}^{*}\right)$$

13.4 Acoustics of solid parts and piezo-electrics

13.4.1 Elastic materials

The cavitating liquid is generally in contact with active solid parts, namely the ultrasonic transducer(s) (the term "active" means a net mechanical energy transfer towards the liquid), and passive solid parts, typically the vessel walls or immersed objects. Representing the transducer, at least partially, is often necessary to avoid imposing a boundary condition directly to the liquid on the one hand, and to represent correctly the effects of the transducer deformation, a will be seen below.

Solid parts can be assumed elastic and therefore represented by Hooke's law, which states that the stress tensor $\bar{\bar{\mathcal{J}}}$ and strain tensor $\bar{\bar{\mathcal{S}}} = \frac{1}{2}\left(\bar{\bar{\nabla}}\mathbf{u}_S + {}^T\bar{\bar{\nabla}}\mathbf{u}_S\right)$ are linearly related ($\bar{\bar{\nabla}}$ denotes the gradient tensor). The unknown is the displacement field $\mathbf{u}_S$. For an isotropic material, Hooke's law writes:

$$\bar{\bar{\mathcal{J}}} = \lambda \mathrm{Tr}\bar{\bar{\mathcal{S}}}\,\bar{\bar{I}} + 2\mu\bar{\bar{\mathcal{S}}}, \tag{13.39}$$

where λ and μ are the Lamé constants, and Tr denotes the trace operator of a tensor. As $\bar{\bar{\mathcal{S}}}$ and $\bar{\bar{\mathcal{J}}}$ are symmetrical, they can be replaced by six -terms vectors, and the above equation can be rewritten in a more readable form, as (the null terms are materialized by dots):

$$\underbrace{\begin{bmatrix}\mathcal{T}_{xx}\\ \mathcal{T}_{yy}\\ \mathcal{T}_{zz}\\ \mathcal{T}_{yz}\\ \mathcal{T}_{xz}\\ \mathcal{T}_{xy}\end{bmatrix}}_{\bar{\mathcal{T}}} = \underbrace{\begin{bmatrix}\lambda+2\mu & \lambda & \lambda & . & . & .\\ \lambda & \lambda+2\mu & \lambda & . & . & .\\ . & . & \lambda+2\mu & . & . & .\\ . & . & . & \mu & . & .\\ . & . & . & . & \mu & .\\ . & . & . & . & . & \mu\end{bmatrix}}_{\mathbf{c}} \underbrace{\begin{bmatrix}\mathcal{S}_{xx}\\ \mathcal{S}_{yy}\\ \mathcal{S}_{zz}\\ 2\mathcal{S}_{yz}\\ 2\mathcal{S}_{xz}\\ 2\mathcal{S}_{xy}\end{bmatrix}}_{\bar{\mathcal{S}}}, \tag{13.40}$$

the elasticity tensor $\boldsymbol{c}$ being reduced to a 6×6 matrix. Elastic materials are more commonly defined by the Young modulus Y and the Poisson number v, with the following relations to the Lamé constants:

$$Y = \frac{\mu(3\lambda + 2\mu)}{\lambda + \mu},\ v = \frac{\lambda}{2(\lambda + \mu)},$$

From the knowledge of the stress tensor, the equation of motion is given by Newton's law, which writes, in absence of body forces:

$$\rho_S \frac{\partial^2 \mathbf{u}_S}{\partial t^2} = \nabla \cdot \bar{\bar{\mathcal{T}}} \tag{13.41}$$

where ρ_S is the solid material density, and the divergence of tensor $\nabla\cdot\bar{\bar{\mathcal{T}}}$ must be understood as $\partial\mathcal{T}_{ij}/\partial x_j$ in Einstein notations. The combination of Eqs. (13.39) and (13.41) constitutes the partial differential equation governing the motion of the solid.

If harmonic motion is assumed, setting

$$\begin{matrix}\mathbf{u}_S(\mathbf{r},t)\\ \bar{\bar{\mathcal{T}}}(\mathbf{r},t)\\ \bar{\bar{\mathcal{S}}}(\mathbf{r},t)\end{matrix} = \frac{1}{2}\begin{pmatrix}\mathbf{U}_S(\mathbf{r})\\ \bar{\bar{\mathrm{T}}}(\mathbf{r})\, e^{i\omega t} + \mathrm{c.c.}\\ \bar{\bar{\mathrm{S}}}(\mathbf{r})\end{pmatrix},$$

(c.c. denotes complex conjugate), Eq. (13.41) becomes $-\rho_S\omega^2\mathbf{U}_S = \nabla\cdot\bar{\bar{\mathbf{T}}}$, with $\bar{\bar{\mathbf{T}}}$ and $\bar{\bar{\mathbf{S}}}$ related by Hooke's law (13.39), and $\bar{\bar{S}} = \frac{1}{2}\left(\bar{\bar{\nabla}}\mathbf{U_S} + {}^T\bar{\bar{\nabla}}\mathbf{U_S}\right)$. The combination of the two equations allows linear propagation of waves in solids, which are much more involved than their linear counterpart in fluids, owing to the fact that two basic waves can coexist: longitudinal waves for which the material displacement $\mathbf{u}_S$ and the direction of propagation are parallel, and transverse waves for which they are orthogonal. The latter exist in solids because a shear deformation produces a restoring elastic force. Both waves have different propagation velocities and can superpose, which yields a large variety of wave phenomena.

13.4.2 Boundary conditions

The associated boundary conditions may take different forms. In sonoreactor problems, the simplest one is a free condition $\bar{\bar{\mathcal{T}}}\mathbf{n_S} = 0$ where $\mathbf{n_S}$ is the normal unit vector pointing outward from solid. This is used for example for free external boundaries of the vessel or of the transducer.

When the transducer is not fully modelled, it is often interesting to model its bottom part to account for its radial deformation (for example the bottom grey rectangle on Fig. 13.1). This will be clarified in the following sections, but enough to say for now that the normal displacement is known on some boundary of the modelled transducer part. In this case one just imposes $\mathbf{u}_S = U_0 e^{i\omega t}\mathbf{n}_S$ on such a boundary.

Finally, for those solid boundaries that are in contact with the fluid, two continuity equations relating the elasticity physics to the acoustics in the fluid are classically used:

$$\frac{\partial \mathbf{u}_S}{\partial t}\cdot\mathbf{n}_S = \mathbf{v}\cdot\mathbf{n}_S,\ \bar{\bar{\mathcal{T}}}\mathbf{n}_S = -p\mathbf{n}_S \tag{13.42}$$

The first expresses continuity of the normal velocity and the second ensures continuity of the normal force exerted on the solid. For harmonic motion these conditions become:

$$\rho_l\omega^2\mathbf{U}_S\cdot\mathbf{n}_S = \nabla P\cdot\mathbf{n}_S,\ \bar{\bar{\boldsymbol{T}}}\mathbf{n}_S = -P\mathbf{n}_S \tag{13.43}$$

where we have made use of (13.14) to derive the first equation. These interface equations are implemented by default in COMSOL when coupling solid vibrations to linear acoustics and the fact that Eq. (13.2) remains valid in Caflisch model allows us to use the same formulation for our cavitation model.

13.4.3 Energy conservation for solids

As for fluids, the equations of waves can be recast into an energetic form. Taking the scalar product of Eq. (13.41) by velocity $\mathbf{v}_S = \partial\mathbf{u}_S/\partial t$ and after some straightforward manipulations, we obtain:

$$\frac{\partial}{\partial t}\left(\frac{1}{2}\rho_S v_S^2 + \frac{1}{2}\bar{\bar{\mathcal{T}}} : \bar{\bar{\mathcal{S}}}\right) + \nabla\left(-\bar{\bar{\mathcal{T}}}\mathbf{v}_S\right) = 0 \tag{13.44}$$

which is the counterpart of Eq. (13.3) for waves in solids. The first and second terms in the time derivative are the kinetic energy and the elastic potential energy, respectively (the notation $\bar{\bar{\mathcal{T}}} : \bar{\bar{\mathcal{S}}}$ denotes the scalar $\mathcal{T}_{ij}\mathcal{S}_{ij}$ in Einstein notation). The term in the divergence is the acoustic intensity $\mathfrak{I}_S = -\bar{\bar{\mathcal{T}}}\mathbf{v}_S$ for solids, which is the counterpart of $\mathfrak{I} = p\mathbf{v}$ appearing in Eq. (13.3) for fluids. It is interesting to note that for boundaries separating the liquid and the solid, the interface conditions (13.42) imply that:

$$\mathfrak{I}_S\cdot\mathbf{n}_S = \mathfrak{I}\cdot\mathbf{n}_S,$$

which states, as expected, that the mechanical energy flux is continuous across such a boundary.

As for waves in fluid, more insight can be gained if we assume harmonic motion. Averaging Eq. (13.44) over one cycle, we get:

$$\nabla\cdot\mathfrak{I}_S = \frac{1}{4}\nabla\cdot\left(-\bar{\bar{\boldsymbol{T}}}\mathbf{V}_S^* - \bar{\bar{\boldsymbol{T}}}^*\mathbf{V}_S\right) = \frac{1}{2}\nabla\cdot\mathrm{Re}\left(-\bar{\bar{\boldsymbol{T}}}\mathbf{V}_S^*\right) = 0 \tag{13.45}$$

Integrating over the whole material volume and making use of divergence theorem:

$$\iint_S \frac{1}{2}\mathrm{Re}\left(-\bar{\bar{\boldsymbol{T}}}\mathbf{V}_S^*\right)\cdot\mathbf{n}_S dS = 0 \tag{13.46}$$

where S is the surface enclosing the material.

As an illustrative example of this result, let's consider the schematic sonoreactor of Fig. 13.3: the liquid, enclosed by a free surface in contact with air and a solid vessel S_{vessel}, is assumed to cavitate, following the model described in Section 13.3.5. A solid slab representing the bottom part of a transducer is in contact with the liquid through boundary S_{active}, its upper boundary S_{in} being vibrated by some (not represented) active system. All other boundaries of the solid parts are assumed free $\left(\bar{\bar{\boldsymbol{T}}}\mathbf{n}_S = 0\right)$. Note that $\mathbf{n}_S = -\mathbf{n}$ on boundaries between solid parts and the liquid.

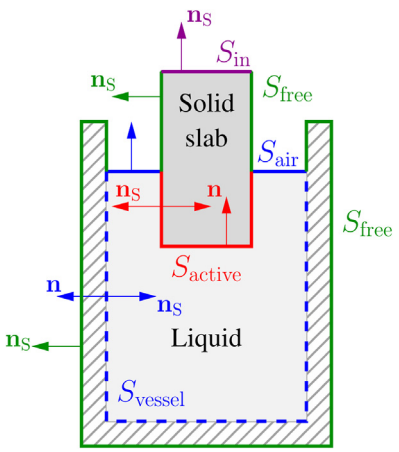

FIGURE 13.3 Sonoreactor configuration with an oscillating solid slab in contact with the liquid through boundary S_{active} (red online). On boundary S_{in} (violet online) the displacement is imposed. External boundaries of the solid are free so that $\bar{\bar{T}}\mathbf{n}_S = 0$ (green online). The liquid is bounded by the vessel by S_{vessel} (dashed, blue online) and by a free surface S_{air} (blue online).

Applying Eq. (13.16) to the liquid, and (13.46) once for the vibrating slab and once for the vessel, we get:

$$\text{Slab: } \underbrace{\iint_{S_{in}} \frac{1}{2}\mathrm{Re}\left(-\bar{\bar{T}}\mathbf{V}_S^*\right)\cdot(-\mathbf{n}_S)dS}_{\substack{\mathcal{P}_{in}\text{ mean power}\\ \text{entering slab from upper}\\ \text{boundary}}} = \underbrace{\iint_{S_{active}} \frac{1}{2}\mathrm{Re}\left(-\bar{\bar{T}}\mathbf{V}_S^*\right)\cdot\mathbf{n}_S dS}_{\substack{\mathcal{P}_{active}\text{ mean}\\ \text{power leaving solid slab}\\ \text{through immersed part}\\ \text{of transducer}}},$$

$$\text{Water: } \underbrace{\iint_{S_{active}} \frac{1}{2}\mathrm{Re}\left(P\mathbf{V}^*\right)\cdot(-\mathbf{n})dS}_{\substack{\mathcal{P}_{active}\text{ = mean power}\\ \text{entering liquid through}\\ \text{immersed part of}\\ \text{transducer}}} = \underbrace{\iint_{S_{vessel}} \frac{1}{2}\mathrm{Re}\left(P\mathbf{V}^*\right)\cdot\mathbf{n}_S dS}_{\substack{\mathcal{P}_{out}\text{ mean power}\\ \text{leaving liquid through}\\ \text{surface in contact}\\ \text{with vessel}}} + \underbrace{\iiint_{V} \frac{-\mathrm{Im}(k^2)|P|^2}{2\rho\omega}dV}_{\substack{\mathcal{P}_{diss}\text{ = mean dissipated}\\ \text{power in the liquid}}},$$

$$\text{Vessel: } \underbrace{\iint_{S_{vessel}} \frac{1}{2}\mathrm{Re}\left(-\bar{\bar{T}}\mathbf{V}_S^*\right)\cdot(-\mathbf{n}_S)dS}_{\substack{\mathcal{P}_{out}\text{ mean power}\\ \text{entering vessel walls}\\ \text{from liquid}}} . = 0$$

It can be clearly seen from the last equation that $\mathcal{P}_{out} = 0$, so that no acoustic energy can escape through the vessel. This is because the outer boundary of the latter is free and acts as a perfect reflector and because the solid does not dissipate energy. From there, the two other equations yield $\mathcal{P}_{in} = \mathcal{P}_{active} = \mathcal{P}_{diss}$. This summarizes the energy path from the upper surface slab S_{in}, which then flows into the liquid through S_{active} and ultimately fully dissipate within the liquid. This energy flow will be illustrated on simulations hereinafter.

This conclusion might seem trivial at first sight. However, it draws several interesting remarks:

- The net average energy flowing through transducer slab must equal the energy consumed by cavitation in the liquid. If for some reason the liquid were prevented to cavitate (for example by a previous degassing or by working at high static pressure), no energy could flow from the transducer, and this will be true whatever the nominal power displayed by the manufacturer. Contrarily to some common misinterpretation, the power transmitted by the transducer into the liquid is not a controllable parameter, whatever the complexity of the generator.
- All terms appearing in time-derivatives in the energy conservation equations [Eq. (13.34) for the liquid, and (13.44) for the solid] have disappeared from the final formulation. This does not mean that these energy terms are zero, but that they balance each other on average over one cycle. This is of course linked with the assumption of harmonic motion, which in

turn is conditioned by steady state oscillations. In the first instants after switching on the driving system, all these terms progressively build up from one cycle to the next and their sum is not constant, but once the standing waves have fully built up, only zero-average interchanges between all forms of energy occur (kinetic, potential, superficial and so on).

- Numerical estimation of the above integrals, and therefore of $\mathcal{P}_{\text{in}}, \mathcal{P}_{\text{active}}, \mathcal{P}_{\text{out}}, \mathcal{P}_{\text{diss}}$ is easy once the fields $P, \mathbf{V}, \mathbf{V}_S, \bar{\bar{\mathbf{T}}}$ have been computed. Such equations constitute therefore a useful validation tool of a FEM computation. Were the relation $\mathcal{P}_{\text{in}} = \mathcal{P}_{\text{active}} = \mathcal{P}_{\text{diss}}$ not be fulfilled by the fields computed numerically (up to some given tolerance) would reveal either errors in the modelling, or the need for mesh refinement.
- $\mathcal{P}_{\text{diss}}$ is the quantity measured by calorimetric experiment, and constitutes therefore the ideal candidate for comparison between numerical results and experiments. We will illustrate in the examples presented further on.

13.4.4 Piezo-electric materials

Piezo-electric materials are commonly used in most of modern ultrasonic transducers and convert stress/deformation into electric field/charges. They behave mechanically as elastic materials, and electrically as dielectric materials. Their constitutive equations can be written as linear relation between tensors $\bar{\bar{\boldsymbol{\mathcal{S}}}}$ and $\bar{\bar{\boldsymbol{\mathcal{T}}}}$ and vectors electric field $\mathcal{E}$ and electric displacement $\mathcal{D}$. Among the four possibilities, the so-called stress-charge formulation writes:

$$\bar{\bar{\boldsymbol{\mathcal{T}}}} = \mathbf{c}E\bar{\bar{\boldsymbol{\mathcal{S}}}} - e^t\mathcal{E} \tag{13.47}$$

$$\mathcal{D} = e\bar{\bar{\boldsymbol{\mathcal{S}}}} + \epsilon^S\mathcal{E} \tag{13.48}$$

where e is a 3×6 matrix, appearing in both equations, represents the bi-directional conversion between electrical and mechanical energy: when submitted to an electric field, stress appears in the material (first equation), and the deformation of the material produces charges on its boundaries (second equation). Eq. (13.47) can be seen as a generalization of Hooke's law, which is retrieved for $\mathcal{E} = 0$, that is, for a short-circuited piezo-electrics. Similarly, Eq. (13.48) is a generalization of the dielectrics equation $\mathcal{D} = \epsilon\mathcal{E}$ which is retrieved for $\bar{\bar{\boldsymbol{\mathcal{S}}}} = \bar{\bar{\mathbf{0}}}$. The 3×3 matrix ε^S is thus the permittivity at null strain, that is, when the material is blocked.

The mechanical equation governing the motion is the same as for passive solids Eq. (13.41). On the electrical side, Gauss law applies, which in absence of free charges within the piezoelectrics just writes $\nabla.\mathcal{D} = 0$. The unknown field can be advantageously taken as the scalar potential defined by $\mathcal{E} = \nabla\mathcal{V}$.

Mechanical boundary conditions are the same as for passive solids. Electrical boundary conditions of interest in transducer can be one of the following:

- Electrical potential $\mathcal{V} = \mathcal{V}_0(t)$ can be imposed on the face of a piezo-electrics if the generator imposes voltage. A null voltage should be imposed on the other face.
- On free boundaries (typically the lateral sides of piezo disks/rings), charge displacement must be zero, which writes $\mathcal{D} \cdot \mathbf{n}_S = 0$.
- Some generators impose the total current entering the piezo-electrics by one face rather than the voltage on this face. This input current writes:

$$\mathcal{I}_{\text{in}} = \iint_S \frac{\partial \mathcal{D}}{\partial t} \cdot (-\mathbf{n}_S) dS \tag{13.49}$$

where n_S is the outward normal unit vector. Care must be taken when the current divides into two piezoelectric disks/rings in the (common) case of sandwich transducers. In this case there is a discontinuity of $\mathcal{D}$ at the interface and the input current reads:

$$\mathcal{J}_{\text{in}} = \iint_S \frac{\partial(\mathcal{D}_2 - \mathcal{D}_1)}{\partial t} \cdot (\mathbf{n}_{12}) dS \tag{13.50}$$

where $\boldsymbol{n}_{12}$ is the normal unit vector pointing from piezo-electrics 1 toward piezoelectrics 2.

13.4.5 Energy conservation for piezo-electrics

The method is similar as for passive solids, taking scalar product of Eq. (13.41) by velocity $\mathbf{v}_S = \partial\mathbf{u}_S/\partial t$, but the stress in generalized Hooke's law (13.47) contains the additional electromechanical coupling term. Differentiating the second

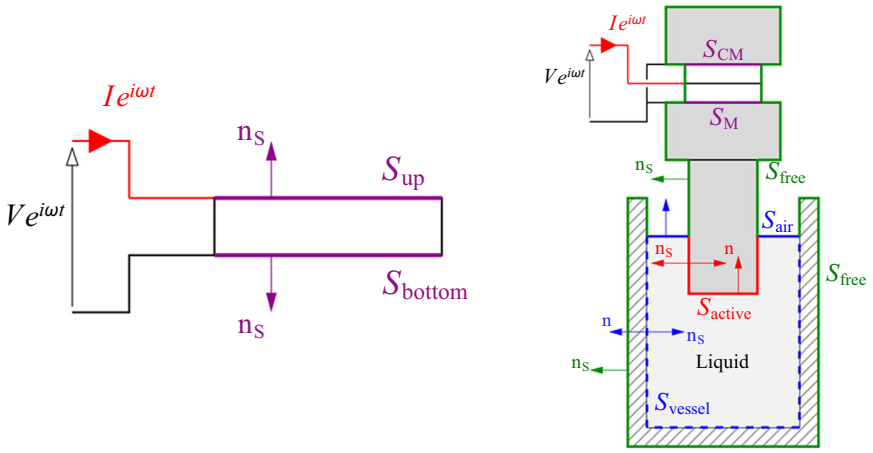

FIGURE 13.4 (A) Single piezoelectric disk. An imposed potential $Ve^{i\omega t}$ is imposed on upper face with a corresponding input current $Ie^{i\omega t}$. (B) Schematic sonoreactor configuration with representation of the full transducer, including piezo-electrics disks. The interface between the two piezoelectric disks has imposed voltage $Ve^{i\omega t}$. Mechanical energy $\mathcal{P}_M$ flows from piezo-electrics through S_M toward the bottom part of bottom of transducer, and further toward the liquid through S_{active}. All external solid boundaries are assumed free (green lines).

piezoelectric constitutive law Eq. (13.48) with time, and making use of $\nabla.\mathscr{D} = 0$ and $\mathscr{E} = -\nabla\mathscr{V}$, the conservation equation can be obtained after some straightforward calculations as:

$$\frac{\partial}{\partial t}\left(\frac{1}{2}\rho_S \upsilon_S^2 + \frac{1}{2}c^E\bar{\bar{\boldsymbol{\mathcal{S}}}} : \bar{\bar{\boldsymbol{\mathcal{S}}}} + \frac{1}{2}\epsilon^S\mathscr{E}\cdot\mathscr{E}\right) + \nabla\cdot\left(-\bar{\bar{\boldsymbol{\mathcal{T}}}}\mathrm{v}_S + \mathscr{V}\frac{\partial\mathscr{D}}{\partial t}\right) = 0 \tag{13.51}$$

The first two terms in the time derivative are the same as for passive solids, and the additional one represents the electrical potential energy. The new term in the divergence corresponds to a flux of electrical energy (since $\partial\mathcal{D}/\partial t$ is a current density corresponding to charges displacement within the piezo-electrics).

For harmonic motion, setting:

$$\begin{matrix}\mathcal{D}(\mathbf{r},t)\\ \mathcal{V}(\mathbf{r},t)\end{matrix} = \frac{1}{2}\left(\begin{matrix}\mathbf{D}(\mathbf{r})\\ V(\mathbf{r})\end{matrix}\ e^{i\omega t} + \text{ c.c. }\right),$$

averaging and integrating over the volume of the piezo-electrics yields:

$$\iint_S \frac{1}{2}\mathrm{Re}\left(-\bar{\bar{\boldsymbol{T}}}\mathbf{V}_S^*\right)\cdot\mathbf{n}_S dS + \iint_S \frac{1}{2}\mathrm{Re}\left(V^*\frac{\partial\mathbf{D}}{\partial t}\right)\cdot\mathbf{n}_S dS = 0$$

Let's consider for illustration a single piezo-electrics with one face maintained at uniform potential V and the other grounded (Fig. 13.4A), with free lateral sides ($\left(\bar{\bar{\boldsymbol{T}}}\cdot\mathbf{n}_S = 0, \mathbf{D}\cdot\mathbf{n}_S = 0\right)$. Using input current definition (13.49), the latter equation becomes:

$$\underbrace{\iint_{S_{up}} \frac{1}{2}\mathrm{Re}\left(-\bar{\bar{\boldsymbol{T}}}\mathbf{V}_S^*\right)\cdot\mathbf{n}_S dS}_{\substack{\text{Mechanical energy}\\ \text{leaving piezo by upper}\\ \text{face}}} + \underbrace{\iint_{S_{bottom}} \frac{1}{2}\mathrm{Re}\left(-\bar{\bar{\boldsymbol{T}}}\mathbf{V}_S^*\right)\cdot\mathbf{n}_S dS}_{\substack{\text{Mechanical energy}\\ \text{leaving piezo by bottom}\\ \text{face}}} = \underbrace{\frac{1}{2}\mathrm{Re}(V*I)}_{\substack{\mathcal{P}_{elec}\text{ active}\\ \text{electrical power}}}$$

where I is the current entering the piezo by the face at potential V. The RHS represents the active electric power consumed on the generator feeding the piezo-electrics, and the above equation states that the electrical power consumed by the piezo-electrics must balance the mechanical power flowing outwards through its mechanically loaded faces.

If we define the electrical (complex) impedance $Z_{elec} = V/I$ seen by the generator, the active electrical power reads:

$$\mathcal{P}_{elec} = \frac{1}{2}\mathrm{Re}(Z_{elec})|I|^2$$

This has the strong consequence that the real part of the transducer electrical impedance is positive and is nonzero only if some mechanical energy flows from the piezo-electrics towards the mechanical parts in contact with it.

Let's now take the more general configuration depicted in Fig. 13.4B, which represents a common sonoreactor with the full representation of the transducer, here with two piezoelectrics mounted top-to-tail, in contact through S_{CM} with a countermass above and through S_M with the mass/mechanical amplifier below, in turn in contact with the liquid. All external solid boundaries are free (green lines). Combining all integral energy conservation equations, it can be easily shown that:

$$\mathcal{P}_{CM} = 0\ \mathcal{P}_{elec} = \mathcal{P}_M = \mathcal{P}_{active} = \mathcal{P}_{diss}\ \mathcal{P}_{out} = 0$$

where $\mathcal{P}_{active}$, $\mathcal{P}_{diss}$ and $\mathcal{P}_{out}$ have the same meaning as before, $\mathcal{P}_{CM}$ is the power transmitted towards the countermass through the upper face of upper piezo, and $\mathcal{P}_M$ toward the bottom part of the transducer through the bottom face of bottom piezo. In addition to its interesting physical sense, the above relation constitutes a good numerical test for simulations. Energy flow in the whole system transducer/reactor will be illustrated in the next sections.

13.4.6 Dissipation in solids

We have assumed so far that neither passive solid parts nor piezo-electrics material dissipated mechanical energy, which resulted in a zero right-hand side in conservation Eqs. (13.44) and (13.51). It is well-known that industrial transducers heat after some operating time, and we give a brief account of this phenomena here.

Materials rheologic behavior depart from Hooke's law in various ways. The most common is viscoelasticity, whereby the material behaves simultaneously as an elastic material and as a fluid (Lakes, 2017). As seen above, the stress exerted on a deformed purely elastic material only depends on the strain. In fact, all materials flow like viscous fluids and part of the stress depends also on the strain rate, that is the rate at which the material is deformed. Clearly, everyday life shows that for most materials this behavior is insignificant but it becomes important as vibrations are considered, especially because viscous effects produce energy dissipation. Among the numerous existing models that can be used, the Kelvin-Voigt model assumes that an additional stress component is proportional to shear-rate. In the context of vibrations, this can be modelled by the definition of a complex Young modulus:

$$E = E'(\omega) + iE''(\omega)$$

where the real part $E'(\omega)$ is the standard part associated to elastic behavior and the imaginary part $E''(\omega)$ represents the viscous part. Both may depend on frequency. The ratio $E''/E' = \tan\delta$ is called loss tangent. Typical values of $\tan\delta$ are about 5×10^{-4} for steel and in the range $1 \times 10^{-4} - 1 \times 10^{-3}$ for titanium alloys (Lakes, 2017; Zhang et al., 1993). Values for glass at ambient temperature range typically between 1×10^{-4} and 1×10^{-3}. Plastic polymers are much more dissipative, and typical values for PMMA ranges between 0.03 and 0.1, with a marked dependence on the frequency (Lakes, 2017). This might be important when choosing the material of a vessel: a PMMA beaker may suck much more acoustic energy than a glass beaker would. This will be examined in the future.

When dissipation is accounted for in materials, clearly Eqs. (13.44), (13.46) do no longer hold and must be supplemented with an extra negative dissipation term on their right-hand side, which form will not be detailed here for brevity. COMSOL allows the definition of complex Young moduli and is able to compute the corresponding energy sink term, which can be further integrated to compute the power dissipated in solid dissipative parts.

Piezo-electrics also dissipate energy, on the mechanical side as passive solid parts, by Joule effect on the electrical side, and also in the electromechanical conversion. These effects can also be accounted for by assigning complex values to some components of the piezoelectric tensors in Eqs. (13.47), (13.48). Such refinements will not be considered here since the main dissipation occurs in the deformation of the bottom part of transducers.

13.5 Simulation examples

Several application examples can be found in precedent papers (Louisnard, 2012b; Louisnard, 2012a; Salinas et al., 2015; Louisnard et al., 2015). We present here new examples illustrating the possible use of our model in various configurations, keeping in mind that the active power can be extracted from our simulations and compared to experimental results of calorimetric method.

13.5.1 Known transducer

The equations proposed above allow the simulation of the full chain piezoelectric transducer/cavitating liquid/vessel. In this case the only inputs of the model are the frequency and current provided by the generator (Fig. 13.4B). If the latter are experimentally known, comparison between simulation and experiments becomes unambiguous and easy. This type of full

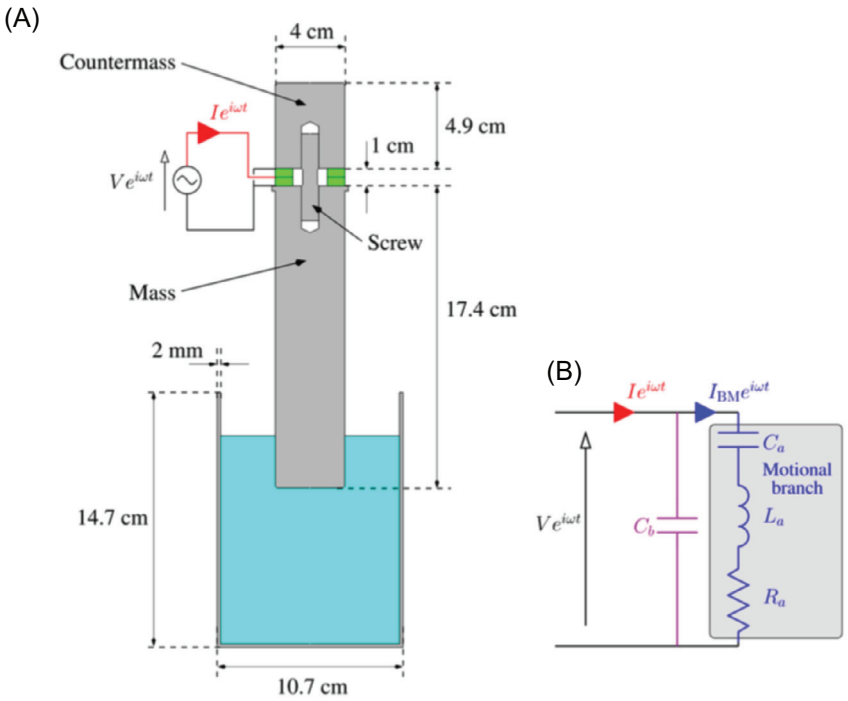

FIGURE 13.5 (A) Sketch of the experiment and geometry used in the simulation. Both the immersion depth and liquid height can be varied. (B) Equivalent circuit for the transducer.

simulation is however conditioned by the precise knowledge of the transducer design (geometry, materials data, piezoelectric data). We focus here on this case.

A dedicated transducer was provided by SINAPTEC and a standard commercial beaker was used (Fig. 13.5A). The transducer is a standard Langevin sandwich with two piezoelectric rings (green rectangles) mounted top-to-tail, pre-stressed between titanium allow mass and countermass by a steel prestress screw. The exact resonance frequency of the unloaded transducer was found to be $f_0 = 20253$ Hz with an impedance-bridge measurement.

The transducer and the vessel were modelled under COMSOL, with the models described in the precedent sections. The exact value of mass and countermass Young modulus was computed to fit the experimental resonance frequency. Damping was considered in the mass with $\tan\delta = 9 \times 10^{-4}$. This value was fitted from the measured impedance of the unloaded transducer at resonance. The screw was also assumed dissipative with $\tan\delta = 5 \times 10^{-4}$ (Lakes, 2017). The current $I = I_{0,\mathrm{RMS}}\sqrt{2}e^{j\omega t}$ was imposed using condition (13.50).

As the latter is nonlocal (an integral rather than a local value is imposed) and not implemented by default in COMSOL, we imposed an unknown potential V at the piezo interface, whose value is automatically computed by COMSOL to fulfill (13.50), which is implemented as a global equation.

There remains to define the frequency to be imposed. One could naively think that commercial generators set the frequency to the unloaded resonance frequency, so that all our simulations could be performed at $f_0 = 20253$ Hz. Unfortunately, this is not true. When the transducer is immersed in the liquid, it becomes loaded by a nonzero mechanical impedance, so that the resonance is slightly shifted. To circumvent that, ultrasonic generators use their own strategy of command to adjust the frequency to the system loading the transducer. Near resonance, a transducer can be approximately represented by the equivalent circuit displayed Fig. 13.5B: the C_b capacitive branch represents the dielectric behavior of the piezo-ceramic rings (2.94nF in the present case) whereas the blue RLC series circuit, called "motional branch," represents the mechanical behavior of the transducer impose a given input current amplitude in the transducer and adjust the frequency to cancel the reactive part of the motional branch impedance ($\mathrm{Im}Z_{\mathrm{BM}} = 0$). This ensures that all the available input power is transferred to the load.

To perform simulations as close as possible to the experimental conditions, we must therefore reproduce this behavior in the model. For every value of $I_{0,\,\mathrm{RMS}}$, we perform several simulations of the system at different frequencies close to and slightly below the resonance frequency. As the simulation provides the transducer voltage, we can compute the electrical impedance, and knowing C_b, we can compute the motional impedance Z_{BM} in function of f. The results are displayed

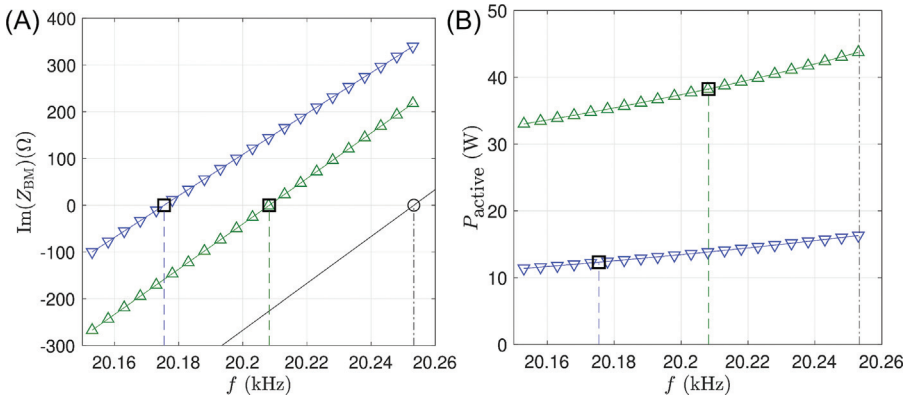

FIGURE 13.6 Simulation results in function of frequency, for input current $I_{0,\mathrm{RMS}} = 0.2$ A (∇ symbols, blue online) and $I_{0,\mathrm{RMS}} = 0.5$ A (Δ symbols, green online). Each point represents a single simulation of the full system. (A) Imaginary part of motional impedance. The black squares indicate the frequency at which $\mathrm{Im}Z_{\mathrm{BM}} = 0$. The generator will choose this frequency. The black thin line indicates the motional impedance of the unloaded transducer and the circle symbol is the unloaded resonance frequency. (B) Active power. The black square symbols reproduce the working frequencies and mark the predicted values of the active power for the two currents. The black dash-dotted line recalls the resonance frequency of the unloaded transducer.

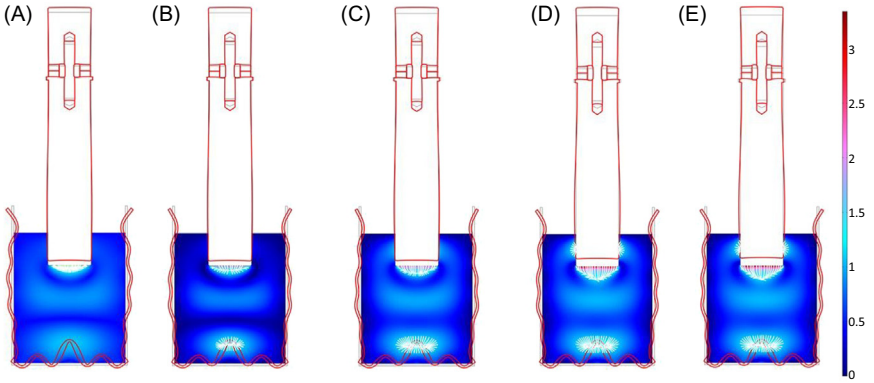

FIGURE 13.7 Computed acoustic field for (from left to right). $I_{0,\mathrm{RMS}} = 0.15, 0.25, 0.4, 0.6, 0.8$ A. The corresponding computed frequencies are 20155, 20191, 20208, 20214, 20217 Hz, respectively. The color plot represents the acoustic field in bar (the colorbar is the same for all plots). The white lines are the lines tangent to the primary Bjerknes force field and materialize the possible paths of the bubble in the liquid. The red lines materializes deformed solid boundaries.

Fig. 13.6A, for two different currents $I_{0,\mathrm{RMS}} = 0.2$ A and 0.5 A. Each curve $\mathrm{Im}Z_{\mathrm{BM}}$ intersects the f-axis at a given frequency, which is one elected by the generator. This frequency is clearly seen to depend on the input current and is several tenth of Hz lower than the unloaded resonance frequency.

Computed acoustic fields are displayed on Fig. 13.7 for a sample of input currents. The potential locations and paths of the bubbles are materialized by drawing the streamlines of the primary Bjerknes force (Louisnard, 2012) (white lines). As the input current is increased, new cavitation zones appears, either as streamers in the fluid, or as lateral structures on the side of the transducer. It must also be noted that the vessel undergoes complex flexural vibrations, which has a known effect on the acoustic field (Louisnard et al., 2009).

Fig. 13.8A displays all the computed power in function of current. The computed values are not only realistic, but it can be seen that the relation $\mathcal{P}_{\mathrm{active}} = \mathcal{P}_{\mathrm{diss}} = \mathcal{P}_{\mathrm{elec}} - \mathcal{P}_{\mathrm{solid}}$ is fulfilled (to a slight error for $\mathcal{P}_{\mathrm{active}}$), which proves that our simulations conserve energy. The zoom on Fig. 13.8B displays an interesting feature: for a current lower than 0.06 A, the dissipated power is zero. This is due to the fact that for such low excitation, the acoustic pressure is everywhere lower than the Blake threshold, and there is no cavitation in the liquid. The takeoff of the curve corresponds therefore to the cavitation threshold of the sonoreactor. Even below the latter however, the electrical power is not exactly zero due to the dissipation in the transducer. This is also evidenced on Fig. 13.9A, which shows the ratio $\mathcal{P}_{\mathrm{active}}/\mathcal{P}_{\mathrm{elec}}$, that is the fraction of the electrical power consumed that is effectively dedicated to cavitation. Starting from zero below the reactor cavitation threshold, the curve jumps abruptly to reach an almost constant value near 80%.

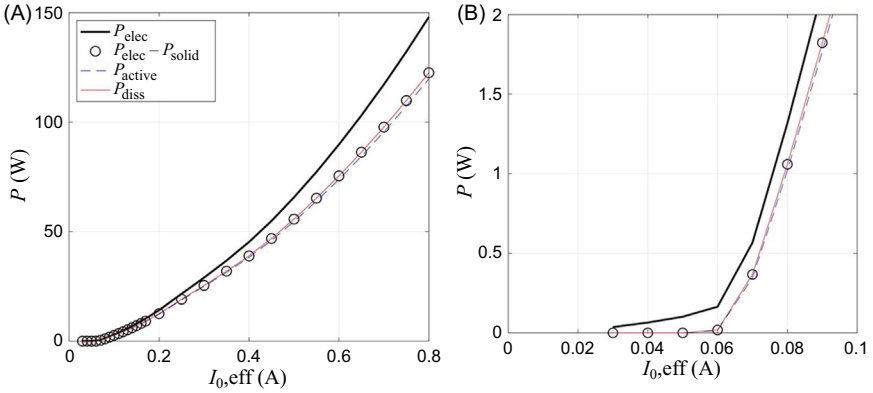

FIGURE 13.8 Illustration of energy conservation. Thick line: $\mathcal{P}_{elec}$, electrical power consumed; circle symbols: $\mathcal{P}_{elec} - \mathcal{P}_{solid}$; thin solid line (red online): $\mathcal{P}_{diss}$, power dissipated by cavitation; thin dashed line (blue online): $\mathcal{P}_{active}$, mechanical power entering liquid by transducer wet boundaries. Fig. (B) is a zoom on (A).

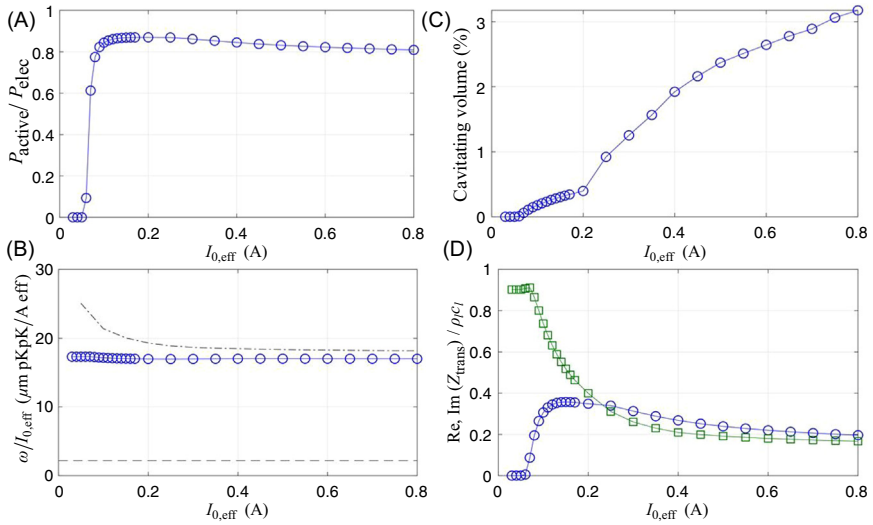

FIGURE 13.9 Various quantities extracted from simulations. (A) Ratio of active power to consumed electric power, owing to losses in the transducer. (B) Electromechanical conversion = ratio of transducer tip displacement (peak to peak) to the injected current. The horizontal dashed line indicates the conversion of the unloaded transducer at resonance frequency and the dash-dotted line the conversion one would obtain exciting the loaded sonoreactor at the latter. (C) Fraction of the liquid volume undergoing cavitation (on the criteria $|P| \geq p_{Blake}$ (D) Real part (circle symbols, blue online) and imaginary parts (square symbols, green online) of the mechanical impedance seen by the tip of the transducer, non-dimensionalized by the liquid specific impedance $Z_l = \rho_l c_l$.

Other interesting quantities can be extracted from simulations. Fig. 13.9B displays the electromechanical conversion factor, which is the peak displacement of the transducer tip per ampere injected. It can be seen that the factor is constant (about 17μm A^{-1}) over the whole range of input currents simulated. This is a consequence of the strategy of command explained above. If the sonoreactor were excited at its unloaded resonance frequency, this would no longer hold (see dash-dotted line on Fig. 13.9B). This shows that the strategy of ensuring a null reactive impedance of the motional branch while imposing at the same time the input current, allows to strictly control the displacement of the transducer tip. Our simulations therefore justify the claim of the manufacturer.

Another indicator of the sonoreactor efficiency is the volume fraction of fluid undergoing cavitation (Fig. 13.9C). Above the cavitation threshold the volume increases slowly up to a second threshold (near 0.2 A) where a noticeable increase appears. The latter is correlated with the appearance of new cavitation zones in the reactor, here a streamer appearing and growing above the bottom of the vessel, as evidenced on Fig. 13.7.

Fig. 13.9D displays the acoustic impedance seen by the sonotrode tip nondimensionalized by the liquid specific impedance $Z_{Trans}/\rho_l c_l$. We recall that the real part of this impedance represents the dissipative phenomena in the load [see Eq. (13.11)], that is, cavitation in the liquid (vessel walls have been assumed lossless), Thus, as expected, Re (Z_{Trans}) = 0

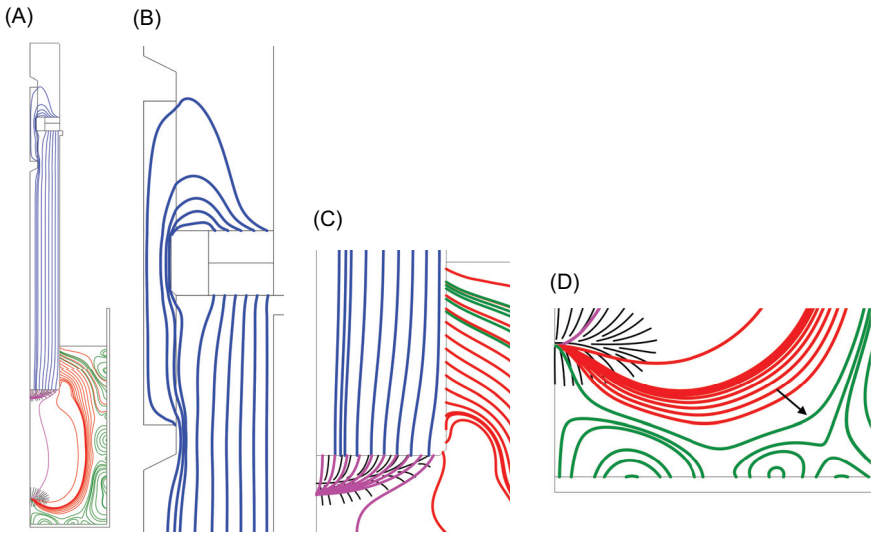

FIGURE 13.10 Streamlines of acoustic intensity ($I_{0,\mathrm{RMS}} = 0.25$ A). Blue lines: streamlines in the solid originating from the piezoelectric rings. Pink lines: streamlines in the liquid from transducer tip. Red lines: streamlines in the liquid from transducer lateral boundaries. Green lines: streamlines in the liquid from or to the internal vessel boundaries. (A) Whole sonoreactor; (B), (C), (D) are zooms on piezoelectric rings, transducer tip, and streamer, respectively.

below the cavitation threshold. When cavitation appears (near $I_{0,\mathrm{RMS}} = 0.06$ A), $\mathrm{Re}(Z_{\mathrm{Trans}})$ jumps to higher values and then slowly decreases near 0.2 $\rho_l c_l$ as excitation is increased. The fact that $\mathrm{Re}(Z_{\mathrm{Trans}}/\rho_l c_l)$ is not 1 demonstrates that the wave emitted by the transducer is not a pure plane traveling wave and $\mathrm{Im}(Z_{\mathrm{Trans}}) \neq 0$ reveals the presence of some standing wave in the medium. We take this opportunity to emphasize that this result definitely condemns the assumption $Z_{\mathrm{Trans}} = 1$ (which implies $P = \rho_l c_l V$ and an intensity equal to $\frac{1}{2}|P|^2/\rho_l c_l\big)$, which is commonly used to deduce the acoustic pressure in the sonoreactor from the calorimetric method. Finally, Fig. 13.9D shows that above some excitation threshold, $\mathrm{Re}(Z_{\mathrm{Trans}}) \simeq \mathrm{Im}(Z_{\mathrm{Trans}})$. This result in fact deeply related to our cavitation model and the fact that $\mathrm{Im}(k^2)$ is large. This will be discussed further elsewhere.

It is instructive to illustrate the precedent discussion on the energy flow and acoustic intensity on the present results. Fig. 13.10A shows the streamlines of the acoustic intensity vector ($-\bar{\bar{T}}\mathbf{u}_S$ in the solid and $p\mathbf{v}$ in the liquid) in the whole sonoreactor, and illustrates how acoustic energy flows from piezoelectric rings down to cavitation zones. Colors have been used to make the figure more readable: all lines are streamlines except the black ones which represent the primary Bjerknes force field and materialize the potential paths of bubbles. Energy lines originate from the outer faces of piezoelectric disks (Fig. 13.10B, blue lines) and end mainly on the transducer tip. A few lines end on the transducer lateral sides, which is not visible because energy transfer through the latter is weak (but not zero) in this configuration. The lines originating from the upper piezo ring cannot end on the countermass boundaries since the latter are free. They have therefore no other choice than turning around the piezo rings and flow downwards through the pre-stress screw. Almost all the lines starting from the transducer tip (Fig. 13.10C, pink lines) end up in the cavitation zone close to the transducer, where energy is dissipated. The most off-axis lines however, flow towards and end up in the streamer located near the bottom of the vessel (Fig. 13.10D). The same holds for the streamlines originating from the lateral side of the transducer (red lines Figs 13.10A,C,D). Interestingly, some streamlines (green lines) enter or leave the internal boundary of the vessel. This means that energy can flow inside the vessel but of course, the whole boundary must be zero. This suggest that a passive boundary in contact with the liquid can mediate the transport of acoustic energy from transducer to cavitation zones. This can be seen on Figs. 13.10A,C where some green lines flow from the lateral side of the transducer towards the vessel internal wall, and another line flows from the wall towards the streamer (arrow on Fig. 13.10D). In the present example, this feature is of little interest owing to the weak energy transported by this route, but might be worth investigating in order to design reflectors controlling the location of cavitation zones.

Finally we show a comparison with experimental results. For each current imposed, the liquid was insonified for only 30 seconds to avoid heating. The generator monitors several electrical quantities every 50 microseconds along each experiment. As the command loop takes about 1 second to adjust frequency, the first 2 seconds of each experiment were deleted. Then, for each experiment, all quantities of interest were averaged, the standard deviation of the fluctuations was computed, which yields an error bar for each point.

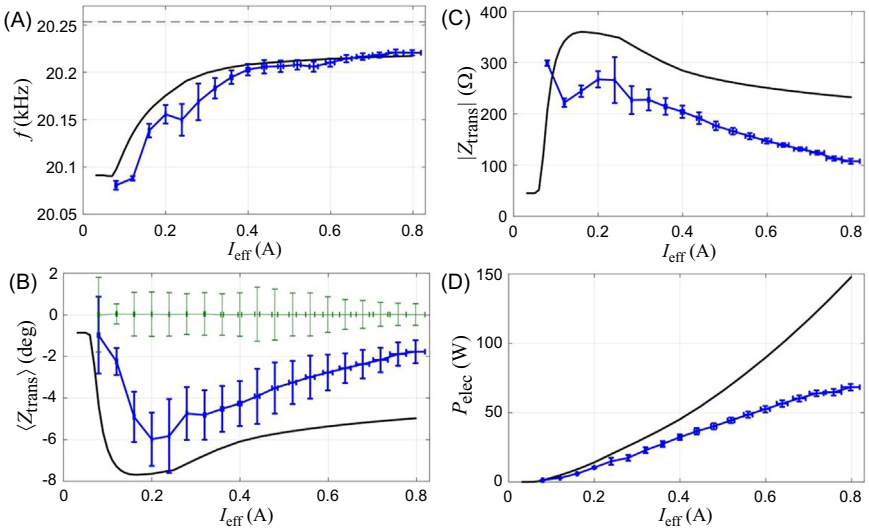

FIGURE 13.11 Comparison between simulations and experiments for sonoreactor of Fig. 13.5A. Continuous (black online) curves represent numerical results, curves with error bars (blue on line) represent experimental results. (A) Operating frequency. (B) Phase of transducer electrical impedance. The thin line (green online) is the measured phase of the motional impedance. (C) Module of transducer electrical impedance. (D) Electrical power consumed.

Fig. 13.11 compares four of the electrical quantities available to the simulation results. First, the frequency elected by the generator is displayed Fig. 13.11A. Our simulation catches correctly the evolution of frequency with current, which asymptotes to a value about 30 Hz below the unloaded resonance frequency, which suggests that our model of cavitating liquid yields a reasonable estimation of the load seen by the transducer. Fig. 13.11B shows the phase of the transducer impedance. The shapes of the experimental and numerical curves match, exhibiting a minimum near 0.2 A. The decreasing part corresponds to a transition between a fixed phase (horizontal part of the numerical curve) when there is no cavitation, so that linear acoustics applies in the liquid, and the progressive onset of cavitation near the transducer tip. As the streamer appears and grows up near $I_{0,\,\text{RMS}} = 0.2$ A (see Fig. 13.7) the load impedance changes and evolves slowly with input current. The experimental impedance phase of the motional branch is superposed on Fig. 13.11B for comparison (thin solid line) and demonstrates that the strategy of control of the frequency works correctly.

Fig. 13.11C displays the transducer impedance module. As for the phase, the shape of the curves match, except for very low drivings. We have no clear explanation for this mismatch for now, but in this region, the cavitation zone is restricted to a very small area, so that the acoustic impedance seen by the transducer undergoes large variations (see left part of graph Fig. 13.9D) which renders the frequency control more difficult. The generator did not allow to explore very low input currents, so that further comparison in this region remains difficult.

Finally, and most important, the numerical and experimental electrical power consumed are compared Fig. 13.11D. As can be seen, our numerical simulation overestimates the electrical power by a factor which is roughly 2. Changing the cavitation model parameters, R_0 in the range 3 μm to 5 μm and N_0 in 20 bubbles /mm^3 to 200 bubbles /mm^3 yields the same conclusion, with some very slight changes in the other variables. Moreover, the experimental curve slightly bends downwards for increasing currents, whereas the numerical curve does the opposite.

This means that our model overestimates the energy dissipated in the liquid, despite the latter was estimated on the basis of a real nonlinear bubble dynamics. The opposite curvatures of the curves Fig. 13.11D suggest that some additional saturating phenomenon is not caught by our model. This will be discussed further in the conclusion.

13.5.2 A nondocumented tip-transducer

The precise design of the transducer in generally not reported in the literature on acoustic cavitation, except for a manufacturer commercial reference. This prohibits the precise modelling of the full chain from transducer to liquid. One solution classically encountered in the literature consists in modelling only the liquid with some imposed acoustic pressure (Gachagan et al., 2003; Klíma et al., 2007; Sutkar et al., 2010; Xu et al., 2013; Niazi et al., 2014; Rashwan et al., 2020) or displacement (Louisnard et al., 2009) as the boundary condition on the transducer/liquid contact surface (denoted as S_{active} in Fig. 13.1). However the pressure/displacement on such a surface is probably non uniform and moreover, this condemns the prediction of the possible effects produced by the transducer deformation.

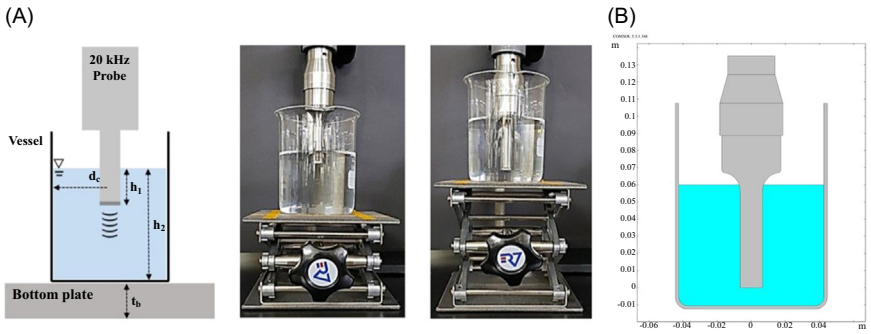

FIGURE 13.12 (A) Experimental setup of ref (Son et al., 2020). Both the transducer immersion depth (h_1) and liquid depth (h_2) can be varied. The transducer is only known through these pictures and the manufacturer reference. (B) Geometry of the transducer bottom part and filled vessel modelled in COMSOL.

We illustrate a possible simulation trade-off on the results of Son et al. (Son et al., 2020), who studied a standard sonoreactor configuration with variations of several geometric parameter (Fig. 13.12A). Among others, the liquid depth and the transducer immersion depth could be varied at constant input power level (50% of the maximum power, as indicated on the generator). The transducer used was a 20–kHz horn-type sonicator (VCX-750, Sonics & Materials Inc.) and the vessel was a 500 mL a commercial glass beaker.

We focus here on the reported results for a variable immersion depth. Results of luminol experiments reported in reference (Son et al., 2020) evidence the appearance of cavitation structures on the lateral boundaries of the transducer (similarly to the rightmost graphs of Fig. 13.7). This means that some acoustic energy flows through these boundaries and that the transducer must be modelled, at least partially for its bottom part. The best solution is to model that part of the transducer called booster (visible in Fig. 13.12A), which is half-wavelength long and plays the role of a mechanical amplifier, with a section reduction near its middle plane. We therefore reversed engineered this part from the picture available on the manufacturer site and the beaker was sketched from Fig. 13.12A. The final dimensions were finely tuned to set the resonance frequency of the booster at 20 kHz.

Proceeding this way, the excitation of the sonoreactor can be performed by applying a displacement peak amplitude $U_0 e^{i\omega t}$ on the upper boundary of the booster. To determine the adequate value of U_0 able to match the experiments, we rely on the calorimetric powers reported by the authors in function of transducer immersion (square symbols in Figs 13.13A,B) and adjust U_0 so that our computed $\mathcal{P}_{\text{active}}$ matches the calorimetric power reported for $H_1 = 35$ mm, ($\mathcal{P}_{\text{calo}} = 37.5$W). We obtain $U_0 = 2.125$ μm and use this same displacement for all immersion depth, computing each time $\mathcal{P}_{\text{active}}$.

Fig. 13.13 displays the comparison between experimental and computed powers. At the scale used by the authors (Fig. 13.13A), the agreement is reasonable. The power increase above $H_1 = 3$ cm (see zoom on Fig. 13.13B) was correlated by the authors to the appearance of a cavitation zone on the lateral transducer area. We also observed this feature by simulation even if a close match with the luminol figures of reference (Son et al., 2020) and our computed acoustic field could not be obtained. This is also confirmed by computing the fraction of energy feeding the liquid by lateral boundaries (Fig. 13.13C): for $H_1 > 3$ cm, it increases from almost 0 up to more 12 % for the largest immersion depths. We have observed this feature ubiquitously in all configurations where the immersion depth of a transducer was varied. Specific transducer designs can enhance this feature (see Section 13.5.3 below).

For decreasing immersion depths, one can observe an increasing overestimation of the active power by our simulations. An examination of the corresponding computed acoustic fields reveals that simulation predicts a streamer slightly above the vessel bottom, whereas luminol experiments do not reveal its existence. Thus, where we expected the experimental and numerical power curves to match reasonable well for all the geometric configurations, by adjusting the imposed displacement on only one point, no better result could be obtained. Varying the beaker thickness did not bring any further enhancement. However replacing the beaker internal walls by infinitely rigid boundaries, the power was found to fields revealed the suppression of the lateral cavitation structures. This underlines the potentially important role of the vessel boundaries to the distribution of energy inside the reactor.

Our attempt to match at best reported results of the literature stresses the difficulty to correctly design the simulation strategy when the transducer is not known. It is probable that the experimental frequency is not exactly 20 kHz, and that furthermore its value selfadapts in function of the geometric configuration, as described above for the SINAPTEC transducer. Another sources of discrepancy might be the precise geometry of the beaker and its mechanical properties.

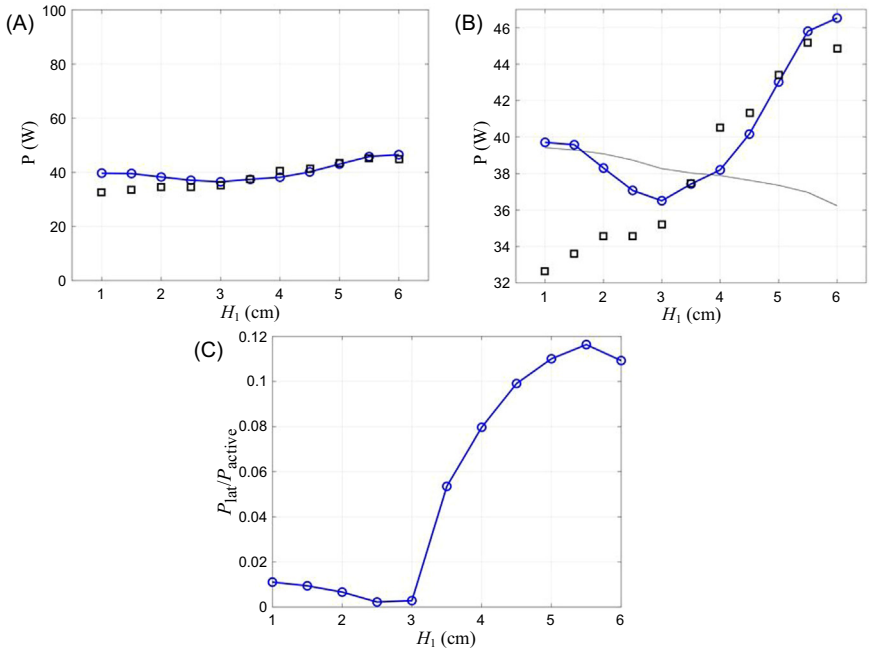

FIGURE 13.13 (A) Comparison of calorimetric power reported in reference [(Son et al., 2020), Fig. 13.2] (square symbols), and active power obtained by simulation (continuous line, blue online). Same scale as in original paper. (B) Zoom on (A). The thin line indicates the computed active power when vessel walls are replaced by infinitely rigid boundaries (C) Fraction of $\mathcal{P}_{\text{active}}$ entering the liquid by the lateral transducer area. Experimental points are reproduced from reference (Son et al., 2020) (courtesy of Elsevier).

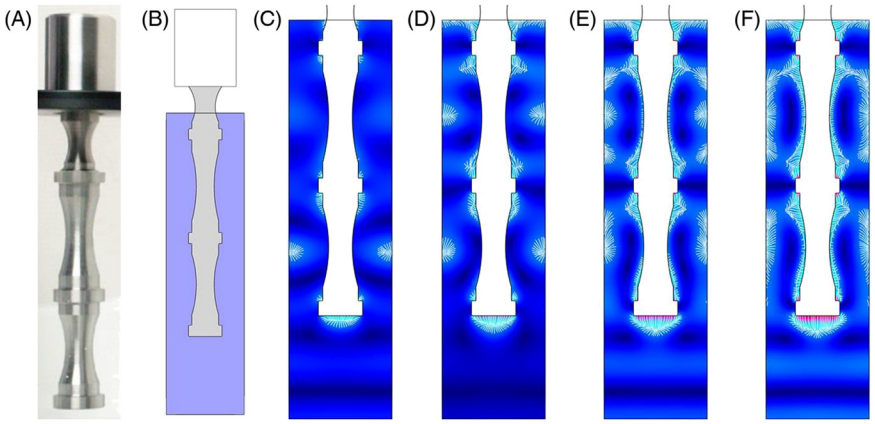

FIGURE 13.14 (A) Transducer SINAPTEC "radial probe" (B) Transducer and vessel modelled in COMSOL. The liquid boundaries are assumed infinitely rigid. The internal design of the transducer is not shown for confidentiality reasons. (C)–(F) Acoustic field for input current $I_{0,\text{RMS}} = 0.2$, 0.4, 0.6, 0.9 A. All the color plots represents the acoustic pressure amplitude $|P|$ with the same color scale, ranging between 0 and 2.75 bar.

13.5.3 A radial probe transducer

More complex shapes of transducers have been developed by manufacturers. The example on which we focus here is a so-called "radial probe" of SINAPTEC, constituted of concave curved parts separating periodic disk-shaped wings (Fig. 13.14A). This design allows a longitudinal motion of two successive wings in phase opposition.

We assume the transducer immersed in water at ambient temperature enclosed by infinitely rigid boundaries (Fig. 13.14B). The transducer is fully modelled, up to the piezoelectric disks. We examine the effect of the amplitude of current injected and, as in Section 13.5.1, the frequency locking strategy used by the generator is modelled. The resulting working frequency varies between 19917 Hz and 20186 Hz for the input currents simulated.

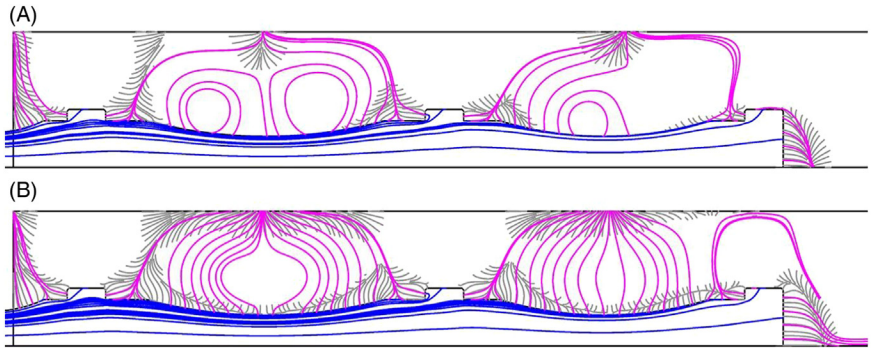

FIGURE 13.15 Streamlines of acoustic intensity. Blue lines: streamlines in the solid originating from the transducer active part (not represented, on the left). Pink lines: streamlines in the liquid originating from transducer surface. (A) $I_{0,\mathrm{RMS}} = 0.4$ A; (B) $I_{0,\mathrm{RMS}} = 0.9$ A.

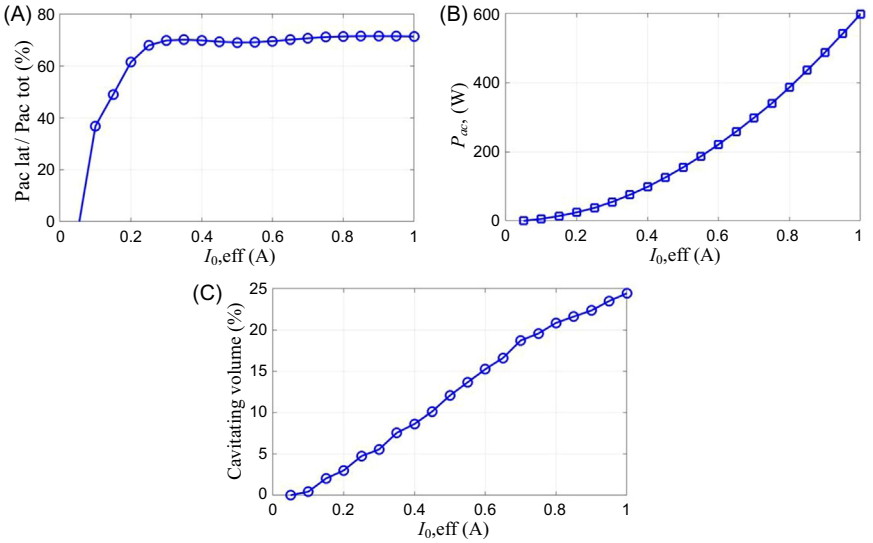

FIGURE 13.16 (A) Fraction of energy entering the liquid through transducer lateral surface. (B) Active power. (C) Volume fraction of fluid undergoing cavitation.

Figs. 13.14C–F display the computed acoustic field and the bubble locations. As current is increased, the cavitation zone near the transducer tip varies little, whereas increasing cavitation zones progressively invade the transducer lateral surface, starting from the wing neighborhood. Secondary cavitation zones also appear on the vessel rigid wall. This suggests that the lateral part of the transducer plays here a preponderant role, in contrast with tip sonotrodes studied above.

It is instructive here again to sketch the energy flow lines in the transducer and in the liquid, for two currents $I_{0,\mathrm{RMS}} = 0.4$ and 0.9 A (Fig. 13.15). Most of the energy lines flowing from the transducer active part (blue lines) are attracted by the lateral transducer surface, from where they further flow in the liquid down to cavitation zones (pink lines). Only a few near-axe lines reach the tip. For the lowest current (Fig. 13.15A), some lines can be observed to leave and further re-enter the transducer surface after a loop excursion in the liquid. This means that some parts of the transducer are active ($\langle p\mathbf{v}\cdot\mathbf{n}\rangle > 0$) whereas other are passive ($\langle p\mathbf{v}\cdot\mathbf{n}\rangle < 0$) even if of course the net energy flux leaving the transducer is positive. These loops tend to disappear for increasing currents (Fig. 13.15B).

The increasing importance of the energy flux through the lateral transducer for increasing drivings is confirmed by Fig. 13.16A : its fraction increases quickly with $I_{0,\,\mathrm{RMS}}$ and stabilizes near 70% for $I_{0,\,\mathrm{RMS}} > 0.25$ A. Fig. 13.16B shows that the active power increases up to 600 W for $I_{0,\mathrm{RMS}} = 1$ A. These large values suggest that this transducer can be used to dissipate large powers in the liquid. Owing to the large transducer emitting area however, the mean intensity remains lower than 4 W cm^{-3}.

Finally, it can be seen on Fig. 13.16C that within the range of currents simulated here, the cavitating volume increases almost linearly with the input current, with only a slight bending of the curve above 0.7 A. This suggests that the volume

of the cavitation zone could be further increased for larger currents, and therefore larger active power could be reached (of course provided that the generator remains able to drive the transducer in such conditions).

The above results show that this transducer design could be promising compared to classical tip transducers and is the subject of ongoing work. More results will be proposed in a future paper.

13.6 Conclusion

In this chapter, we have tried to formulate rigorously the equations of transport of acoustic energy through a sonoreactor, from the transducer down to the cavitation zones, from standard linear equations in solids and piezo-electrics and from a reduced nonlinear model of propagation in cavitating liquids (Louisnard, 2012). The latter, being based on a correct evaluation of the energy dissipated by individual bubbles, allows to compute realistic estimation of the power dissipated in the liquid, contrarily to the commonly used assumptions of nondissipative linear acoustics or dissipative linear acoustics in bubbly-liquids. By construction, our model conserves energy in the sense that the power feeding the liquid through the transducer boundaries matches exactly the power dissipated in the liquid by cavitation (plus the power dissipated in the vessel wall, if any). This allows in particular to rationally define the boundary conditions driving the system from calorimetric power experiments, and avoid the commonly used acoustic pressure boundary condition derived from an approximation of plane traveling wave, which in invalidated by our results.

Our formulation allows the full simulation of the transducer, thanks to the piezo-electrics and solid elasticity physics available in COMSOL. In this case the only inputs required for the model are the frequency and amplitude of the input current. However, modern ultrasound generators allow frequency to vary in a small range during experiments in order to ensure a maximal power transfer from the electronics to the acoustic load, which evolves with the operating conditions. We have shown how to mimic this strategy of frequency control in simulations and our results show for example that this method allows an exact linear relation between the transducer tip displacement and the injected current. Full simulations give us access to data difficult to measure, tip displacement, mechanical impedance, cavitating volume, fraction of power feeding the liquid through transducer lateral boundaries, and to others commonly reported by the ultrasonic generator: electrical impedance (module and phase), electrical power consumed, operating frequency. The latter were put to the test against experimental data in the case of a fully known sonoreactor configuration. Our results reproduce well the frequency shift of the generator in function which was found more than two-fold overestimated by our model.

To our knowledge, this is the first frontal comparison of electrical power computed by simulation and data reported by the driving generator, so that the fact that we obtain the correct orders of magnitude is encouraging. However, the discrepancy observed demonstrates that our cavitating model requires some enhancements. We give a brief overview on some ongoing work:

- The hypothesis of constant bubble density N and constant ambient radius R_0 is clearly too restrictive. Measurements are scarce in the literature (Burdin et al., 1999; Mettin et al., 1999; Reuter et al., 2019; Tsochatzidis et al., 2001; Kuroyama et al., 2014), and moreover these parameters vary in space. Theory on bubble fragmentation thresholds may help however to determine the bubble habitat on the R_0-axis (Koch et al., 2011) in function of the driving pressure. A semi-heuristic reasonable bubble size distribution function (in the range of a few m) could probably be computed in function of driving pressure.
- Our model assumes bubbles wherever the acoustic pressure exceeds the Blake threshold. This is known to be wrong where standing waves dominate, and pressure antinodes larger than 1.75 bar repel bubbles owing to an inversion of the primary Bjerknes force (Louisnard, 2012; Koch et al., 2011; Akhatov et al., 1997; Matula, 1999; Krefting et al., 2004). This yields bubble-free regions near such antinodes bounded by surfaces where the field is close to 1.75 bar, on which bubbles accumulate. These structures commonly observed have been termed as "Jellyfish structures" (Mettin, 2005; Mettin et al., 2002; Louisnard, 2008). By construction, our model cannot account for such configurations, which probably results in errors not only on the predicted bubbles location, but also on the dissipated power. The surgery to apply to our model is not trivial because this effect occurs only in standing waves zones, but not where traveling waves dominate (typically below the transducer) (Louisnard, 2012; Koch et al., 2004; Koch et al., 2004). However since our model correctly estimates the Bjerknes forces, reasonable corrections may be found. Work is in progress.
- As commented briefly in Section 13.3.4, the controversy on the value of dissipation functions Π_v, Π_{th} and Π_{rad} should be solved.

Sonoreactors engineering is a multi-disciplinary field mixing different specialties, each one relying on its own concepts: load impedance for transducers specialists, dissipated power for chemical engineers, acoustic pressure for cavitation physicists. We expect that our approach, albeit largely perfectible, may help to reconcile all these fields by reverting to common physics.

Acknowledgment

The authors wish to thank SinapTec for support through an industrial PhD grant awarded to of us (I.G.V.) by the French Association Nationale de la Recherche et de la Technologie (ANRT), Pascal Tierce for providing details on SinapTec transducers and for clarifying technical issues, Laurie Barthe for her help in experiments and designing future experimental work. We would also like to thank the French Centre National de la Recherche Scientifique (CNRS) for support via the cavitation research group (GDR CAVITATION) that stimulated fruitful discussions with all our colleagues involved in the field.

References

Akhatov, I., Gumerov, N., Ohl, C.D., Parlitz, U., Lauterborn, W., 1997. The role of surface tension in stable single bubble sonoluminescence. Phys. Rev. Lett. 78 (2), 227–230.

Akhatov, I., Mettin, R., Ohl, C.D., Parlitz, U., Lauterborn, W., 1997. Bjerknes force threshold for stable single bubble sonoluminescence. Phys. Rev. E 55 (3), 3747–3750.

Akhatov, I., Parlitz, U., Lauterborn, W., 1994. Pattern formation in acoustic cavitation. J. Acoust. Soc. Am. 96 (6), 3627–3635.

Ando, K., Colonius, T., Brennen, C.E., 2011. Numerical simulation of shock propagation in a polydisperse bubbly liquid. Int. J. Multiphase Flow 37 (6), 596–608.

Appel, J., Koch, P., Mettin, R., Lauterborn, W., 2004. Stereoscopic high-speed recording of bubble filaments. Ultrason. Sonochem. 11, 39–42.

Burdin, F., Tsochatzidis, N.A., Guiraud, P., Wilhelm, A.M., Delmas, H., 1999. Characterisation of the acoustic cavitation cloud by two laser techniques. Ultrason. Sonochem. 6, 43–51.

Caflisch, R.E., Miksis, M.J., Papanicolaou, G.C., Ting, L., 1985. Effective equations for wave propagation in bubbly liquids. J. Fluid Mech. 153, 259–273.

Campos-Pozuelo, C., Granger, C., Vanhille, C., Moussatov, A., Dubus, B., 2005. Experimental and theoretical investigation of the mean acoustic pressure in the cavitation field. Ultrason. Sonochem. 12, 79–84.

Carstensen, E.L., Foldy, L.L., 1947. Propagation of sound through a liquid containing bubbles. J. Acoust. Soc. Am. 19 (3), 481–501.

Commander, K.W., Prosperetti, A., 1989. Linear pressure waves in bubbly liquids: comparison between theory and experiments. J. Acoust. Soc. Am. 85 (2), 732–746.

Dahlem, O., Reisse, J., Halloin, V., 1999. The radially vibrating horn: a scaling-up possibility for sonochemical reactions. Chem. Eng. Sci. 54 (13), 2829–2838.

Dähnke, S., Swamy, K.M., Keil, F.J., 1999. A comparative study on the modeling of sound pressure field distributions in a sonoreactor with experimental investigation. Ultrason. Sonochem. 6 (4), 221–226.

Dähnke, S., Swamy, K.M., Keil, F.J., 1999. Modeling of three-dimensional pressure fields in sonochemical reactors with an inhomogeneous density distribution of cavitation bubbles. Comparison of theoretical and experimental results. Ultrason. Sonochem. 6, 31–41.

Devin, C., 1959. Survey of thermal, radiation and viscous damping of pulsating air bubbles in water. J. Acoust. Soc. Am. 31 (12), 1654–1667.

Doc, J.B., Conoir, J.M., Marchiano, R., Fuster, D., 2016. Nonlinear acoustic propagation in bubbly liquids: Multiple scattering, softening and hardening phenomena. J. Acoust. Soc. Am. 139 (4), 1703–1712.

Dogan, H., Popov, V., 2016. Numerical simulation of the nonlinear ultrasonic pressure wave propagation in a cavitating bubbly liquid inside a sonochemical reactor. Ultrason. Sonochem. 30, 87–97.

Foldy, L.L., 1944. The multiple scattering of waves. Phys. Rev. 67 (3-4), 107–119.

Fuster, D., 2019. A review of models for bubble clusters in cavitating flows. Flow Turbul. Combust. 102 (3), 497–536.

Fuster, D., Colonius, T., 2011. Modelling bubble clusters in compressible liquids. J. Fluid Mech. 688, 352–389.

Gachagan, A., Speirs, D., McNab, A., 2003. The design of a high power ultrasonic test cell using finite element modelling techniques. Ultrasonics 41 (4), 283–288.

Gaitan, D.F., Holt, R.G., 1999. Experimental observations of bubble response and light intensity near the threshold for single bubble sonoluminescence in an air-water system. Phys. Rev. E 59, 5495–5502.

Gumerov, N.A., Akhatov, I.S., 2017. Modes of self-organization of diluted bubbly liquids in acoustic fields: One-dimensional theory. J. Acoust. Soc. Am. 141 (2), 1190–1202.

Hilgenfeldt, S., Brenner, M.P., Grossman, S., Lohse, D., 1998. Analysis of Rayleigh-Plesset dynamics for sonoluminescing bubbles. J. Fluid Mech. 365, 171–204.

Hilgenfeldt, S., Lohse, D., Brenner, M.P., 1996. Phase diagrams for sonoluminescing bubbles. Phys. Fluids 8 (11), 2808–2826.

Holzfuss, J., 2008. Surface-wave instabilities, period doubling, and an approximate universal boundary of bubble stability at the upper threshold of sonoluminescence. Phys. Rev. E 77, 066309.

Iordansky, S., 1960. On the equations of motion for liquids containing gas bubbles. J. Appl. Mech. Tech. Phys. 3, 102–110.

Jamshidi, R., Brenner, G., 2013. Dissipation of ultrasonic wave propagation in bubbly liquids considering the effect of compressibility to the first order of acoustical Mach number. Ultrasonics 53 (4), 842–848.

Jordens, J., Honings, A., Degrève, J., Braeken, L., Van Gerven, T., 2013. Investigation of design parameters in ultrasound reactors with confined channels. Ultrason. Sonochem. 20 (6), 1345–1352.

Kauer, M., Belova-Magri, V., Cairós, C., Schreier, H.-J., Mettin, R., 2017. Visualization and optimization of cavitation activity at a solid surface in high frequency ultrasound fields. Ultrason. Sonochem. 34, 474–483.

Klíma, J., Frías-Ferrer, A., González-García, J., Ludvík, J., Sáez, V., Iniesta, J., 2007. Optimisation of 20kHz sonoreactor geometry on the basis of numerical simulation of local ultrasonic intensity and qualitative comparison with experimental results. Ultrason. Sonochem. 14, 19–28.

Kobelev, Y.A., Ostrovskii, L.A., 1989. Nonlinear acoustic phenomena due to bubble drift in a gas-liquid mixture. J. Acoust. Soc. Am. 85 (2), 621–629.

Koch, P., Krefting, D., Tervo, T., Mettin, R., Lauterborn, W., 2004. Bubble path simulations in standing and traveling acoustic waves. Proc. ICA 2004, Kyoto (Japan) Fr3.A.2, V3571–V3572.

Koch, P., Kurz, T., Parlitz, U., Lauterborn, W., 2011. Bubble dynamics in a standing sound field: The bubble habitat. J. Acoust. Soc. Am. 130 (5), 3370–3378.

Koch, P., Mettin, R., Lauterborn, W., 2004. Simulation of cavitation bubbles in travelling acoustic waves, D. Cassereau (ed.). In: Proceedings CFA/DAGA'04 Strasbourg, DEGA Oldenburg, pp. 919–920.

Krefting, D., Mettin, R., Lauterborn, W., 2004. High-speed observation of acoustic cavitation erosion in multibubble systems. Ultrason. Sonochem. 11, 119–123.

Kuroyama, T., Mizutani, K., Wakatsuki, N., Ohbuchi, T., 2014. Measurement of convergence ultrasound in cone-like bubble structure using light deflection method. In: 2014 IEEE International Ultrasonics Symposium. IEEE, pp. 1448–1451.

Lakes, R.S., 2017. Viscoelastic Solids, first edition edition CRC Press Revivals, CRC Press.

Lee, J., Yasui, K., Tuziuti, T., Kozuka, T., Towata, A., Iida, Y., 2008. Spatial distribution enhancement of sonoluminescence activity by altering sonication and solution conditions. J. Phys. Chem. B 112 (48), 15333–15341.

Lighthill, J., 1978. Acoustic streaming. J. Sound Vib. 61 (3), 391–418.

Lin, H., Storey, B.D., Szeri, A.J., 2002. Rayleigh-Taylor instability of violently collapsing bubbles. Phys. Fluids 14 (8), 2925–2928.

Louisnard, O., 1998. Contribution à l'étude de la propagation des ultrasons en milieu cavitant, PhD dissertation. Ecole des Mines de Paris, Paris.

Louisnard, O., 2008. Analytical expressions for primary Bjerknes force on inertial cavitation bubbles. Phys. Rev. E 78 (3), 036322.

Louisnard, O., 2010. Nonlinear attenuation of sound waves by inertial cavitation bubbles. Phys. Procedia 3, 735–742 international Congress on Ultrasonics, Santiago de Chile, January 2009.

Louisnard, O., 2012. A simple model of ultrasound propagation in a cavitating liquid. Part II: primary Bjerknes force and bubble structures. Ultrason. Sonochem. 19, 66–76.

Louisnard, O., 2012. A simple model of ultrasound propagation in a cavitating liquid. Part I: theory, nonlinear attenuation and traveling wave generation. Ultrason. Sonochem. 19, 56–65.

Louisnard, O., Cogné, C., Labouret, S., Montes-Quiroz, W., Peczalski, R., Baillon, F., Espitalier, F., 2015. Prediction of the acoustic and bubble fields in insonified freeze-drying vials. Ultrason. Sonochem. 26, 186–192.

Louisnard, O., Gomez, F., 2003. Growth by rectified diffusion of strongly acoustically forced gas bubbles in nearly saturated liquids. Phys. Rev. E 67 (3), 036610.

Louisnard, O., González-García, J.J., Tudela, I., Klima, J., Saez, V., Vargas-Hernandez, Y., 2009. FEM simulation of a sono-reactor accounting for vibrations of the boundaries. Ultrason. Sonochem. 16, 250–259.

Maeda, K., Colonius, T., 2019. Bubble cloud dynamics in an ultrasound field. J. Fluid Mech. 862, 1105–1134.

Margulis, M., Margulis, I., 2003. Calorimetric method for measurement of acoustic power absorbed in a volume of a liquid. Ultrason. Sonochem. 10 (6), 343–345.

Matula, T.J., 1999. Inertial cavitation and single-bubble sonoluminescence. Philos. Trans. R. Soc. London, Ser. A 357, 225–249.

Mettin, R., 2005. Bubble structures in acoustic cavitation. In: Doinikov, A.A. (Ed.), Bubble and Particle Dynamics in Acoustic Fields: Modern Trends and Applications. Research Signpost, Kerala (India), pp. 1–36.

Mettin, R., 2007. From a single bubble to bubble structures in acoustic cavitation. In: Kurz, T., Parlitz, U., Kaatze, U. (Eds.), Oscillations, Waves and Interactions. Universitätsverlag Göttingen, Göttingen, Germany, pp. 171–198.

Mettin R., Appel J., Krefting D., Geisler R., Koch P., Lauterborn W., Bubble structures in acoustic cavitation: observation and modelling of a "jellyfish"-streamer, Special Issue of the Revista de Acustica, Forum Acusticum Sevilla, Spain, 16-20 Sept. 2002, Sevilla, Spain, volume XXXIII, 2002 pp. 1–4

Mettin, R., Koch, P., Lauterborn, W., Krefting, D., 2006. Modeling acoustic cavitation with bubble redistribution. In: Sixth International Symposium on Cavitation - CAV2006 (paper 75), Wageningen (The Netherlands), pp. 125–129.

Mettin, R., Luther, S., Lauterborn, W., 1999. Bubble size distribution and structures in acoustic cavitation. In: Proc. 2nd Conf. on Applications of Power Ultrasound in Physical and Chemical Processing, Toulouse, France, pp. 125–129.

Morse, P.M., Feshbach, H., 1953. Methods of theoretical physics. McGraw-Hill, New-York.

Morse, P.M., Ingard, K.U., 1968. Theoretical acoustics. McGraw-Hill, New-York.

Niazi, S., Hashemabadi, S.H., Razi, M.M., 2014. CFD simulation of acoustic cavitation in a crude oil upgrading sonoreactor and prediction of collapse temperature and pressure of a cavitation bubble. Chem. Eng. Res. Des. 92 (1), 166–173.

Nomura, S., Nakagawa, M., 2001. Analysis of an ultrasonic field attenuated by oscillating cavitation bubbles. Acoustical Science and Technology 22 (4), 283–292.

Parlitz, U., Mettin, R., Luther, S., Akhatov, I., Voss, M., Lauterborn, W., 1999. Spatio temporal dynamics of acoustic cavitation bubble clouds. Phil. Trans. R. Soc. Lond. A 357, 313–334.

Prosperetti, A., 1977. Thermal effects and damping mechanisms in the forced radial oscillations of gas bubbles in liquids. J. Acoust. Soc. Am. 61 (1), 17–27.

Prosperetti, A., 1991. The thermal behaviour of oscillating gas bubbles. J. Fluid. Mech. 222, 587–616.

Prosperetti, A., 1998. A brief summary of L. van Wijngaarden's work up till his retirement. Appl. Sci. Res. 58, 13–32.

Rashwan, S.S., Dincer, I., Mohany, A., 2020. Investigation of acoustic and geometric effects on the sonoreactor performance. Ultrason. Sonochem. 68, 105174.

Ratoarinoro, N., Wilhelm, A.M., Berlan, J., Delmas, H., 1992. Effects of ultrasound emitter type and power on a heterogeneous reaction. Chem. Eng. J. 50 (1), 27–31.

Reuter, F., Lesnik, S., Ayaz-Bustami, K., Brenner, G., Mettin, R., 2019. Bubble size measurements in different acoustic cavitation structures: filaments, clusters, and the acoustically cavitated jet. Ultrason. Sonochem. 55, 383–394.

Romdhane, M., Gourdon, C., Casamatta, G., 1995. Thermoelectric sensor for ultrasonic intensity measurement. Ultrasonics 33 (2), 139–146.

Rozenberg, L.D., 1971. The cavitation zone. In: Rozenberg, L.D. (Ed.), High-intensity ultrasonic fields. Plenum Press, New-York.

Sáez, V., Frías-Ferrer, A., Iniesta, J., González-García, J., Aldaz, A., Riera, E., 2005. Characterization of a 20 kHz sonoreactor. Part I: analysis of mechanical effects by classical and numerical methods. Ultrason. Sonochem. 12, 59–65.

Salinas, V., Vargas, Y., Louisnard, O., Gaete, L., 2015. Influence of the liquid viscosity on the formation of bubble structures in a 20 kHz field. Ultrason. Sonochem. 22, 227–234.

Servant, G., Caltagirone, J.P., Gérard, A., Laborde, J.L., Hita, A., 2000. Numerical simulation of cavitation bubble dynamics induced by ultrasound waves in a high frequency reactor. Ultrason. Sonochem. 7, 217–227.

Servant, G., Laborde, J.L., Hita, A., Caltagirone, J.P., Gérard, A., 2001. Spatio-temporal dynamics of cavitation bubble clouds in a low frequency reactor: comparison between theoretical and experimental results. Ultrason. Sonochem. 8 (3), 163–174.

Servant, G., Laborde, J.L., Hita, A., Caltagirone, J.P., Gérard, A., 2003. On the interaction between ultrasound waves and bubble clouds in mono- and dual-frequency sonoreactors. Ultrason. Sonochem. 10 (6), 347–355.

Sojahrood, A.J., Haghi, H., Karshafian, R., Kolios, M.C., 2020. Critical corrections to models of nonlinear power dissipation of ultrasonically excited bubbles. Ultrason. Sonochem. 66, 105089.

Son, Y., No, Y., Kim, J., 2020. Geometric and operational optimization of 20–kHz probetype sonoreactor for enhancing sonochemical activity. Ultrason. Sonochem. 65, 105065.

Storey, B.D., 2001. Shape stability of sonoluminescence bubbles: comparison of theory to experiments. Phys. Rev. E 64, 017301.

Sutkar, V.S., Gogate, P.R., Csoka, L., 2010. Theoretical prediction of cavitational activity distribution in sonochemical reactors. Chem. Eng. J. 158 (2), 290–295.

Toegel, R., Gompf, B., Pecha, R., Lohse, D., 2000. Does water vapor prevent upscaling sonoluminescence ? Phys. Rev. Lett. 85 (15), 3165–3168.

Trujillo, F.J., 2018. A strict formulation of a nonlinear Helmholtz equation for the propagation of sound in bubbly liquids. Part I: theory and validation at low acoustic pressure amplitudes. Ultrason. Sonochem. 47, 75–98.

Trujillo, F.J., 2020. A strict formulation of a nonlinear Helmholtz equation for the propagation of sound in bubbly liquids. Part II: application to ultrasonic cavitation. Ultrason. Sonochem. 65, 105056.

Tsochatzidis, N., Guiraud, P., Wilhelm, A., Delmas, H., 2001. Determination of velocity, size and concentration of ultrasonic cavitation bubbles by the phase-Doppler technique. Chem. Eng. Sci. 56 (5), 1831–1840.

Tudela, I., Sáez, V., Esclapez, M.D., Bonete, P., Harzali, H., Baillon, F., González-García, J., Louisnard, O., 2011. Study of the influence of transducer-electrode and electrode-wall gaps on the acoustic field inside a sonoelectrochemical reactor by FEM simulations. Chem. Eng. J. 171 (1), 81–91.

Tudela, I., Sáez, V., Esclapez, M.D., Díez-García, M.I., Bonete, P., González-García, J., 2014. Simulation of the spatial distribution of the acoustic pressure in sonochemical reactors with numerical methods: a review. Ultrason. Sonochem. 21 (3), 909–919.

Vanhille, C., Campos-Pozuelo, C., 2008. Nonlinear ultrasonic propagation in bubbly liquids: a numerical model. Ultrasound Med. Biol. 34 (5), 792–808.

Vanhille, C., Campos-Pozuelo, C., 2009. Nonlinear ultrasonic waves in bubbly liquids with nonhomogeneous bubble distribution: Numerical experiments. Ultrason. Sonochem. 16, 669–685.

Vanhille, C., Campos-Pozuelo, C., 2013. Numerical simulations of three-dimensional nonlinear acoustic waves in bubbly liquids. Ultrason. Sonochem. 20 (3), 963–969.

van Wijngaarden, L., 1966. Linear and nonlinear dispersion of pressure pulses in liquidbubble mixtures. In: 6th Symposium on Naval Hydrodynamics, Washington DC. Office of Naval Research, pp. 115–128.

van Wijngaarden, L., 1968. On the equations of motion for mixtures of liquid and gas bubbles. J. Fluid Mech. 33 (3), 465–474.

Wang, Y.-C., Yao, M.-C., 2013. Realization of cavitation fields based on the acoustic resonance modes in an immersion-type sonochemical reactor. Ultrason. Sonochem. 20 (1), 565–570.

Wei, Z., Weavers, L.K., 2016. Combining COMSOL modeling with acoustic pressure maps to design sono-reactors. Ultrason. Sonochem. 31, 490–498.

Wood, R.J., Lee, J., Bussemaker, M.J., 2017. A parametric review of sonochemistry: control and augmentation of sonochemical activity in aqueous solutions. Ultrason. Sonochem. 38, 351–370.

Xu, Z., Yasuda, K., Koda, S., 2013. Numerical simulation of liquid velocity distribution in a sonochemical reactor. Ultrason. Sonochem. 20 (1), 452–459.

Yasui, K., Kozuka, T., Tuziuti, T., Towata, A., Iida, Y., King, J., Macey, P., 2007. FEM calculation of an acoustic field in a sonochemical reactor. Ultrason. Sonochem. 14 (5), 605–614.

Zhang, J., Perez, R., Lavernia, E., 1993. Documentation of damping capacity of metallic, ceramic and metal-matrix composite materials. J. Mater. Sci. 28 (9), 2395–2404.

Zhang, Z., Gao, T., Liu, X., Li, D., Zhao, J., Lei, Y., Wang, Y., 2018. Influence of sound directions on acoustic field characteristics within a rectangle-shaped sonoreactor: numerical simulation and experimental study. Ultrason. Sonochem. 42, 787–794.

Chapter 14

Technological designs and energy efficiency: The optimal paths

Kaouther Kerboua[a] and Oualid Hamdaoui[b]

[a] *Higher School of Industrial Technologies, Department of Engineering, Annaba, Algeria,* [b] *Chemical Engineering Department, College of Engineering, King Saud University, Riyadh, Saudi Arabia*

14.1 Introduction

The high-power ultrasound systems are mainly composed of two parts, the power driver and the piezoelectric transducers. These systems are widely used nowadays in surface cleaning applications, but have also other specific applications in the area of sonochemistry, ultrasound welding, ultrasound homogenization, and ultrasound assisted processes in general. The scaling up of these techniques requires an efficient and economical energy conversion. The piezoelectric transducer in the part of the high-power ultrasound system which is responsible of converting the electrical energy into an acoustic wave.

Although the piezoelectric transducers are the most commercially available devices for the creation of ultrasonic waves, they are not the only type of transducers that create power ultrasound. In fact, mechanical or electrical energy can be converted to acoustic energy through three main types of ultrasonic transducers, namely Gas driven transducers, liquid driven transducers, and electromechanical transducers (Mason and Cintas, 2002). The piezoelectric transducers belong to the last category, which counts also the magnetostrictive transducers.

As a transmitter, When the piezoelectric transducer is excited by electrical energy, piezoelectric material starts to vibrate and generates mechanical energy in the form of a wave oscillating with a frequency comprised between 16 kHz and several gigahertz. This range is known as "ultrasound" since it occurs above the limit of the audible sound by human (Lowe, 2001). In the commonly used high-power ultrasound systems, the piezoelectric transducer constitutes the first point of energy conversion, and hence significantly contributes to the determination of the energy efficiency of the overall system.

The quality of the energy conversion in an ultrasound system is also highly related to the excitation signal, thus, applying a high-quality excitation signal can notably enhance the performance of the system and limit the power dissipation.

The high-power ultrasound systems, composed of the electrical driver and the piezoelectric transducers, are integrated in specific devices intended for ultrasound assisted applications and sonochemistry. The disposition of the transducers, the geometry of the vessel receiving ultrasound, the sonication mode, the nature of the sonicated fluid, and its flow play a major role in the concentration of the acoustic energy emitted by the transducers into effective energy in the form of acoustic cavitation. Indeed, most of the applications of high-power ultrasound rely on the occurrence of the acoustic cavitation phenomenon, defined as the formation, expansion, and abrupt collapse of cavitation bubbles, inducing the microscopic concentration of acoustic energy into potential and mechanical energies manifesting in the form of chemical and physical effects. The energy engaged in such effects is ultimately converted into heat. Consequently, the energy conversion is generally probed through the calorimetric measurements (Margulis and Margulis, 2003; Son et al., 2012; Contamine t et al., 1995; Toma et al., 2011), while some innovative methods have been suggested to assess the percentage of acoustic energy dedicated to the formation of acoustic cavitation and its associated effects such as the measurement of cavitational energy (Son et al., 2012) and the disequilibrium calorimetry (Plattes et al., 2017).

The overall energy efficiency of any ultrasound assisted process depends then on the ultrasound system itself and its integration within the ultrasonic device. The present chapter discusses the various configurations related to both the ultrasound system, specifically the transducer part, and the integrated ultrasonic device according to its intended application. The chapter presents as well the theoretical bases of energy conversion at the different points, and the conventional and innovative techniques employed in the assessment of energy efficiency. Finally, the chapter underlines the major

Energy Aspects of Acoustic Cavitation and Sonochemistry: Fundamentals and Engineering. DOI: https://doi.org/10.1016/B978-0-323-91937-1.00014-1
Copyright © 2022 Elsevier Inc. All rights reserved.

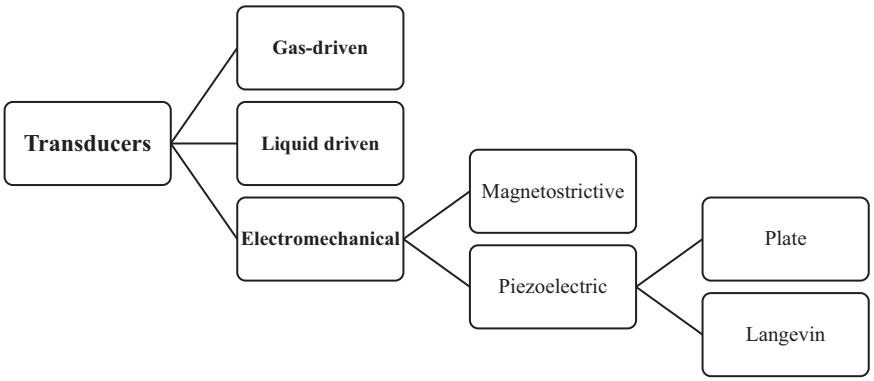

FIGURE 14.1 Classification of ultrasonic transducers.

requitements for the scaling up of the sonochemical and ultrasound assisted processes, especially for continuous flow operation, with respect to the decent energy conversion.

14.2 Ultrasound source

The generation of ultrasound is based on the creation of oscillatory acoustic vibration of specific materials, with a frequency above the limit of audible range for human. This process generally relies on the conversion of electric energy into acoustic energy using electromechanical (or electroacoustic) transducers. These transducers convert acoustic energy (sound) into electrical energy (voltage or current) or vice versa. When the transducers are used to generate ultrasound, they are called projector, transmitter, or source of ultrasound (Mattiat and Mason, 1972; Hamonic and Decarpigny, 1988).

Nevertheless, other technologies for the generation of ultrasound exist, they are classified into three categories, namely, gas-driven transducers, liquid-driven transducers, and electromechanical transducers as described in Fig. 14.1. The present section discusses these different technologies technically and in terms of efficiency.

14.2.1 Gas-driven transducers

The gas-driven transducers are composed of a gas jet, which is forced into an orifice where it expands and produces a shock wave. This creates an intense field of acoustic energy in the range of ultrasound focused between the nozzle body and the resonator chamber as shown in Fig. 14.2 (A). Such ultrasonic transducers are mainly used in the atomization application, the liquid is introduced into the region of focused ultrasound (between the nozzle and the resonant gap) and is energetically sheared into droplets by the acoustic field as illustrated in Fig. 14.2 (B). The atomized droplets of liquid are carried by the gas traveling outward in a fine soft plume shaped spray. The atomization is widely applied in industry for dust removal and humidification.

14.2.2 Liquid-driven transducers

The liquid-driven transducers are based on the forced circulation of a liquid at high velocity using a homogeniser pump (Soni et al., 2020). The liquid passes through a small orifice, then it expands to a larger volume (Venturi effect) as shown in Fig. 14.3, and a violent jet is formed toward a metal blade. The metal blade is caused to vibrate and the acoustic wave is created inducing acoustic cavitation.

The design of the liquid driven transducers relies on the disposition of the metal blade and the dimension and shape of the orifice. The velocity of the liquid flow controls the acoustic power transmitted by the vibrating blade to the liquid. The liquid-driven transducers are generally used as liquid whistle to create cavitation for applications in the area of mixing, emulsification, deagglomeration and disinfection.

14.2.3 Electromechanical transducers

14.2.3.1 Magnetostrictive transducers

The magnetostrictive transducers harness the magnetostriction property of some metals, defined as the ability of the material to reduce in size when exposed to a magnetic field, and return to the original size once the magnetic field is off (Vinogradov, Cobb, and Light, 2017). When the magnetic field is applied as a series of short pulses to the magnetostrictive material, it

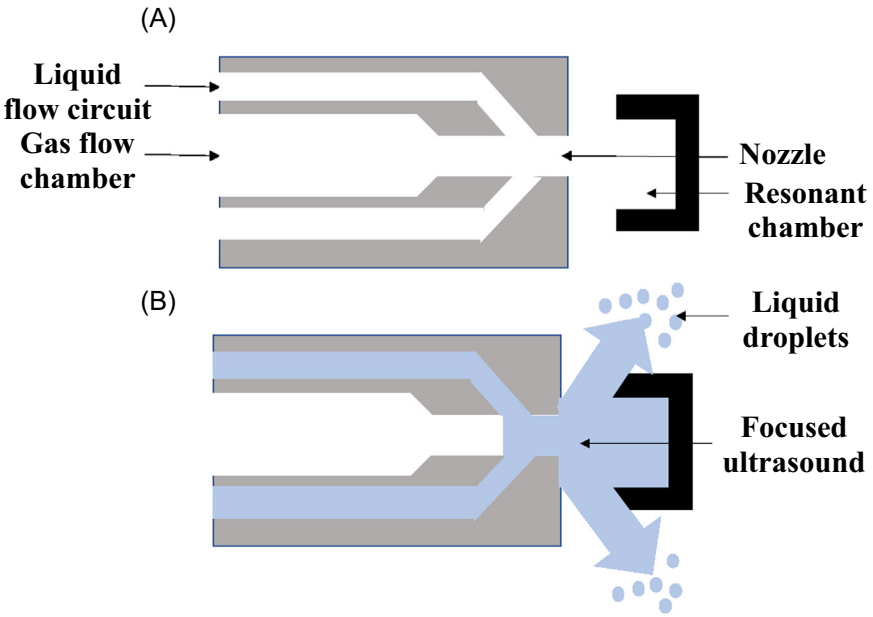

FIGURE 14.2 Schematic view of a gas driven transducer (A) and its application in atomization (B).

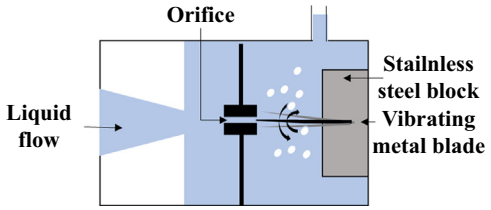

FIGURE 14.3 Schematic view of a liquid-driven transducer.

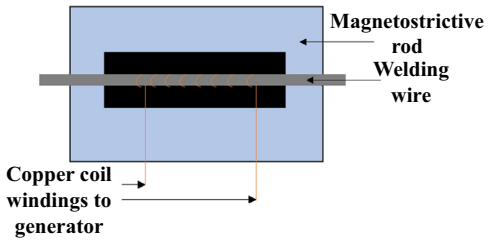

FIGURE 14.4 Schematic view of a magnetostrictive transducer.

vibrates at the same frequency. This property is verified with laminated metal or alloy, for instance with nickel (Lee and Asgar, 1971) as shown in Fig. 14.4.

However, the magnetostrictive transducers operate within a frequency range below an upper limit of 100 kHz. Beyond this limit, the metal cannot respond fast enough to the magnetostrictive effect. This limitation is the principal disadvantage of the magnetostrictive transducers and has not yet been overcame in spite of the recent development in the magnetostrictive materials. Besides, in terms of energy conversion, the electrical to mechanical energy efficiency is about 60% with the conventional metals, the resting 40% are converted into heat. This thermal dissipation requires a liquid cooling of the magnetostrictive transducers, particularly at long operation times. New materials have been developed to replace the conventional magnetostrictive metals in order to increase the electrical efficiency. To cite some, cobalt/iron combinations, aluminium/iron with a small amount of chromium, and Terfenol-D (Moffett et al., 1990; Olabi and Grunwald, 2008), which is a single cystal alloy of the rare earths terbium and dysprosium with iron, are suggested as alternative magnetostrictive

materials allowing the increase of the electrical efficiency to significant levels, in addition to an important gain in compactness and lightness.

From an industrial perspective, the use of magnetostrictive transducers with the novel materials offers a robust and powerful solution for sonication applications requiring low acoustic frequency operation (generally below 70 kHz). Thus, the magnetostrictive transducers, though significantly overcame by the piezoelectric transducers, can be proposed as an efficient technology for particular large-scale applications in the near future.

14.2.3.2 Piezoelectric transducers

Literally, "piezoelectricity" refers to electricity caused by pressure. Piezoelectric transducers are a type of electroacoustic transducer relying on the ability of some solid materials to convert the alternative current into an acoustic wave and vice versa (Safari and Akdoğan, 2008). The piezoelectric transducers were first used in sonars, one century ago, which used echoes to detect the presence of ships (Ahmad et al., 2019).

The direct piezoelectric effect, also called generator or sensor effect, consists of the change in the polarization in a material, induced by an applied mechanical stress, which results in an electrical discharge. This effect is used in the ultrasonic reception stage. The reverse piezoelectric effect consists of the dimensional change in a material induced by an applied electric field and known as mechanical strain. This effect is used in the ultrasonic emission stage and is harnessed in sonochemistry and ultrasound assisted processes.

The mechanical stress and electrical charge are related in direct or indirect piezoelectric effects by a proportional relationship, characterized by the piezoelectric charge constant *d*. This constant expresses the polarisation charge generated per unit of mechanical stress with direct piezoelectric effect, or inversely, the mechanical strain experienced per unit of electric field for reverse piezoelectric effect (Soin et al., 2016). The electric displacement D, the electric field E, the resulting mechanical stress T, and the elastic strain S are all related by the linear piezoelectric constitutive equations. The complexity of these equations depends on both the symmetry of the piezoelectric material and the particular geometry of the transducer element, which results in particular mechanical and electrical boundary conditions.

The piezoelectric transducers are made of monocrystalline materials and polycrystalline ferroelectric ceramics. The single crystal in these materials is characterized by an asymmetry in the structure of the unit cell of the crystal lattice, that is, a polar axis that forms below the Curie temperature, which constitutes a sufficient prerequisite for the effect to occur. In addition, piezoelectric materials have a spontaneous polarization, the positive and negative charge concentration of the unit cells are separate from each other. At the same time, the axis of the unit cell extends in the direction of the spontaneous polarization and a spontaneous strain occurs. Some materials such as the barium titanate adopt piezoelectric characteristics on a useful scale when an electric field is applied, which allows the application of the indirect piezoelectric effect at industrial scale.

The oscillation of piezoelectric elements starts when alternative current is applied. The incredibly fast response of piezoelectric materials when an alternative current is applied, being in the range of microseconds and lower, allows them to be of use in a wide range of applications, particularly in the generation of ultrasound, with frequencies up to 20 MHz. The actual use of piezoelectric transducers in power ultrasound applications such as bonding, cleaning and welding, covers the frequency range from 20 to 800 kHz.

The piezoelectric transducers, which are more efficient and operate over a wider frequency range, are generally considered to be the better choice in sonochemical and ultrasound assisted processes. According to the scale, plate and Langevin piezoelectric transducers can be used.

14.2.3.2.1 Plate piezoelectric transducers

Plate piezoelectric transducers, also known as ceramic transducers, can be easily adapted to a wide range of specific uses in industrial applications, owing to the facility of producing ceramic transducers in various sizes and shapes. In addition to the main piezoelectric active element, the commercial models of the piezoelectric transducers are composed of the electrodes, the front layer, that is, the matching layer and the lens, the rear layer, that is, the backing, and the casing. Fig. 14.5 illustrates a constructive schema of the plate piezoelectric transducer.

Plate transducers made of lead zirconate titanate, originating from the 1960s, are the most used nowadays (Wright, 2022). Emerging plate transducers made of polymers such as polyvinylidene fluoride (Khalifeh, 2020) and composite materials consisting of pillars of piezoceramic embedded in an epoxy resin matrix (Uchino, 2010) are currently gaining acceptance and may compete with the commercial lead zirconate titanate transducers.

It is worthy to note that the most powerful piezoelectric transducer known so far remains the Rochelle salt, which is a synthetic crystal. However, it cannot come into contact with any moisture, and it must be used at temperatures below 46°C (Shigeyuki, 2003; An et al., 2014; Fulay and Lee, 2021).

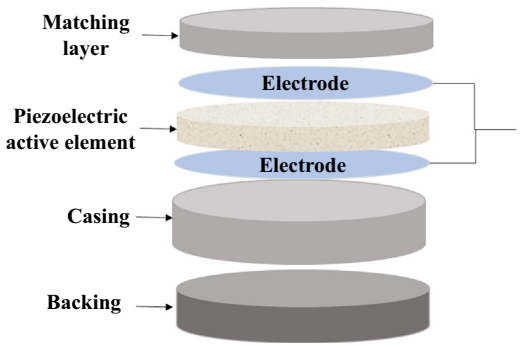

FIGURE 14.5 Schematic view of a plate piezoelectric transducer.

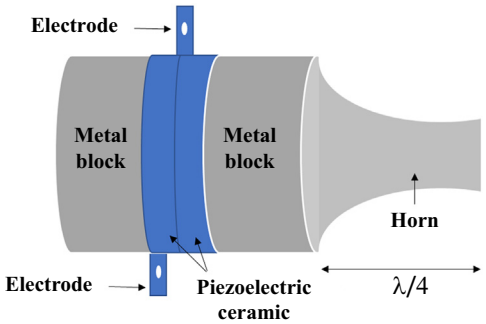

FIGURE 14.6 Schematic view of a Langevin transducer.

Fig. 14.5 shows the constituents of a typical plate piezoelectric transducer. The piezoelectric active element is the main component of the device; however, many other components are important for a proper operation of the transducer. For instance, a backing is used to remove unwanted resonances and radial vibrational modes. Moreover, due to the usually large differences in specific acoustic impedance between the transducer element and most irradiated media, significant energy losses occur. A matching layer is generally used to limit those losses.

When liquid medium is sonicated, an intermediate impedance matching layer is incorporated into the front face of the transducer, ideally one-quarter of a wavelength in thickness at the operating frequency. The matching layer is made of a material with an ideal specific acoustic impedance Z_L calculated based on the acoustic impedances of both the transducer element and the irradiated liquid, Z_1 and Z_2 respectively, as indicated in Eq. (14.1).

$$Z_L = \sqrt{{Z_1}^2 + {Z_2}^2} \tag{14.1}$$

When the plate piezoelectric transducer is attached to a solid such as a tank, the piezoelectric active element is generally covered with a hard ware-resistant face. An intermediate layer of liquid couplant is required between the transducer face and the surface of the solid. The liquid couplant is supposed to fill all the microscopic voids and surface imperfections and eliminate the trapped air that would interfere with the effective transmission of the ultrasonic field (Wright, 2022).

14.2.3.2.2 Langevin piezoelectric transducers

The Langevin transducer is a common piezoelectric transducer widely used in ultrasound applications such as ultrasonic cleaning, welding, machining, sonochemistry, underwater communication, and ultrasonic surgery. It is designed for converting high power electrical energy to high power ultrasound. The Langevin transducer is composed of a stack of piezoelectric elements, usually made of ceramic. The piezoelectric elements are disposed in a sandwich type arrangement and clamped by two metal blocks and a needle attached at each side of the structure as shown in Fig. 14.6. The Langevin transducer acts as an electrical-mechanical resonant circuit, when an alternative current is applied, the stack vibrates, that is, expands and contracts, inducing the vibration of the tail mass and the needle (Pérez-Sánchez et al., 2020; Lu et al., 2017; Lin, 2006; Guyomar et al., 2011).

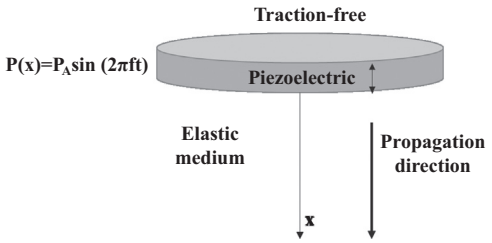

FIGURE 14.7 A piezoelectric plate transducer irradiating an elastic half space.

The Langevin piezoelectric transducer is also sometimes connected to a horn, which is a mechanical device that increases the amplitude of the mechanical vibration produced by the piezoelectric ceramics. These devices are fabricated as one-piece acoustic amplifier, as illustrated in Fig. 14.6, where the amplification factor A of the mechanical strain is a function of the maximum and minimum diameters of the horn, $D_1$and D_2 respectively, as indicated in Eq. (14.2).

$$A = \frac{{D_1}^2}{{D_2}^2} \tag{14.2}$$

The connection of the Langevin transducer to a horn induces a reduction of the area, which causes a decrease of the acoustic impedance, resulting in an increase in the magnitude of displacement. The length of the acoustic amplifier is generally taken as quarter of the wavelength at the considered acoustic frequency.

Finally, in order to distribute the vibration in a large area; a device called sonotrode can also be connected to the tip of the horn. Its role is to reduce the acoustic impedance of the irradiated medium by imposing an intermediate impedance.

From a theoretical point of view, various linear and nonlinear (Guyomar et al., 2011; Ghenna et al., 2016) models of Langevin transducer have been developed and proposed in the literature (Hayward and Gillies, 1989). For a large scale operation, the nonlinear equations should be adopted since the piezoelectric properties of the materials differ from linear behavior when driven at large levels.

14.3 Electric-acoustic energy conversion

Power transducers such as nebulizers, heaters, High Intensity Focalised Ultrasounds devices HIFU, de-scalers, mixing or homogenizing devices, cleaners, welders, motors, and transformers are used to project significant amounts of power into an irradiated media. Power ultrasound transducers are used to project acoustic energy in the range of ultrasound into a medium. The energy can be used to create acoustic cavitation bubbles with all their associated effects, or to promote mass transfer. Power ultrasound transducers differ from contact or immersion transducers in that they are designed to project power rather than a signal.

The key element of most commercial power ultrasound devices is the piezoelectric transducer, which converts electrical energy to mechanical energy. Ultrasound power transducer performance is strongly related to the applied electrical excitation. To have a suitable excitation for maximum energy conversion, it is required to analyze the effects of input signal waveform, medium and distortion on the characteristic and response of the high-power ultrasound system, including ultrasound transducer.

Let's consider a piezoelectric plate transducer made of ceramic, driven by an alternative current and emitting antiplane acoustic waves in an elastic half space, as shown in Fig. 14.7.

By applying the appropriate voltage to the transducer, the piezoelectric material generates a pulse, usually a sine wave, square wave, or spike, according to the excitation field. The electric field creates a physical expansion or contraction of the ceramic corresponding to the voltage. This is explained at the microscopic scale by the shift of the charge carriers in piezoelectric materials under the influence of an electric field as shown in Fig. 14.8, which leads to a macroscopic change in length, known as the inverse piezoelectric effect. The resonant frequency is the critical parameter governing the behavior of a piezoelectric material. It is then required to analyze the impedance frequency response of the piezoelectric material in order to determine the critical piezoelectric specifications, including its resonant frequency.

The expansion and contraction of the piezoelectric element under an alternative current creates a vibration of the particles of the irradiated medium, inducing pressure fluctuations. Rarefaction of the particles leads to lower pressure, and compression to increased pressure. The wavelength of the sound defines the distance between two rarefaction or compression

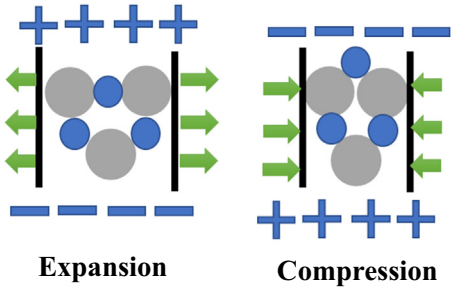

FIGURE 14.8 Shift in the charge carriers of a piezoelectric material under an electric field.

areas. The speed of the sound varies according to the density and the elastic properties of the medium. The created sound waves which are projected out from the ceramic propagate in all directions.

The design of the backing, housing, and front matching layers determines how the sound will propagate out into the surrounding medium. The different transducer parts are engineered to efficiently pass the sound in the desired direction and absorb or reflect the sound wave in all other directions.

To prevent the ultrasound wave from going out the back of a transducer, a "backing" layer is usually used. The backing layer consists of a material which absorbs most of the sound passing through and allows very little to pass back out. The backing is also carefully shaped to create multiple reflections within the backing to allow more opportunity to absorb the sound field. The backing is generally made of a soft material loaded with very heavy particles, like Tungsten, which can vibrate freely and dissipate the sound energy. Other materials are sometimes added to scatter the sound waves.

In order to keep on a good quality of wave transmission, it is necessary to analyze the acoustic impedances of the piezoelectric material and the irradiated medium. The difference between the acoustic impedances of both media determines whether and how well the sound waves can be transferred from one medium to another. If this difference is too large, the sound is reflected and transmission is inhibited. In practice, to efficiently propagate the sound out into the irradiated medium, an adaptation layer called the matching layer (or even the transformation layer) is used. The matching layer (or layers) is inserted between the piezo element and the surrounding medium, and is ideally quarter of the wavelength thick and made of a material which has an acoustic impedance midway between that of the piezoelectric material and the medium. It then ensures the smallest possible difference in sound impedance and therefore increases the transmission quality.

The matching layer acts like an antireflection coating on glass, allowing the sound to pass freely in both directions. The sound waves move forward and eventually strike something which reflects them back toward the transducer. This echo enters through the matching layer and strikes the ceramic element.

14.4 Performance of power transducers

In order to assess the performance of a piezoelectric transducer (Redwood, 1961; Shuyu, 2004), functional tests which consist of driving the transducer with a sine wave, square wave, pulse, or spike are conducted, depending on the intended use. These tests are usually carried out with an industry standard pulser-receiver, sometimes through an amplifier. The pulse and return signals are viewed on an oscilloscope, and numerical measurements are made in order to assess the cleanliness and the quality of the waveform.

Jimenez (2018) exposed a detailed experimental setup aiming to test an ultrasonic piezoelectric device intended to operate at cryogenic temperatures. The described procedure consisted first of selecting the material and shape of the piezoelectric element, the transducer-rod system build-up including the wear plate, the backing, and the matching layer, and finally the material and shape of the propagation medium. Once the assembly was set up, tests were carried out by sending a rectangular pulse of a certain width and amplitude to the source transducer. The pulse is transmitted by the source transducer through the material medium and sensed at the receiver transducer. The tests aimed to determine the characteristics of the piezoelectric transducer such as the resonance frequency of the ceramic material and the sound velocity of the propagating medium as a function of temperature. The resonance frequency of the piezoelectric element is first determined using the impedance analyzer. The pulse response, amplitude and arrival time of the piezoelectric transducer are assessed by sensing the received signal at the receiver transducer. The received signal is analyzed and the cross-correlation function is employed to determine the arrival time as a function of temperature. The tests allowed as well the characterization of the irradiated medium, by following the variation of the sound velocity and the acoustic impedance as functions of the temperature.

The effective electromechanical coupling coefficient k (Chen and Wang, 2005; Toftekær et al., 2020), which represents the efficiency of conversion of the electrical energy into acoustic energy, is also assessed to characterize the performance of the piezoelectric transducer. It is related to the energy converted per input energy R as shown in Eq. (14.3).

$$k = \sqrt{R} \tag{14.3}$$

Traditionally, the optimal combination of the components of the piezoelectric transducer is defined either based on trials and error calculations, or using simple analytical models. These procedures make it difficult or even impossible to find the cause of poor performance or deficiencies. Rafienezhad-Masouleh and Honarvar (2021) proposed a finite element modelling to assess the performance of a piezoelectric ultrasonic transducer, and overcome the limitation of one-dimensional analytical models. The authors elaborated a mathematical model for the complete transducer structure, including the piezoelectric disk, backing material, and matching layer, in both transmit and receive modes. The input of the model is an electrical pulse, and the output is an electrical voltage. The results proved that undesired echoes can be eliminated by increasing the attenuation of the backing material. It was also demonstrated that according to the impedance of the matching layer, variations of both the transducer bandwidth and the echo amplitude are noticed, and starting from a certain value of the impedance of the matching layer, the frequency spectrum can be double-humped.

14.5 Mapping acoustic wave propagation

Once the ultrasound source connected to the receiving medium, either liquid or solid, the acoustic wave undergoes considerable change due to the attenuation effect of the irradiated medium. The presence of acoustic cavitation bubbles accentuates dramatically this effect. A proper estimation of the wave attenuation in bubbly medium requires a realistic estimation of the power dissipation due to the oscillation of each bubble through (1) the thermal diffusion in the gas and (2) the viscous friction in the liquid (Louisnard, 2012; Zhang et al., 2018). The acoustic dissipation within a bubbly liquid is well described by the nonlinear model, and the results demonstrate a significant deviation in this case from the linear prediction.

The acoustic cavitation bubbles involved in sonochemistry and ultrasound assisted processes oscillate inertially. The propagation of an acoustic wave of arbitrary amplitude in such bubbly liquids is described by Caflisch model (Caflisch et al., 1985). In this model, the radial oscillation of all the bubbles is described by a continuous spatio-temporal radius function, while the number density of bubbles is considered as a time-independent function. The model is based on the principles of mass and momentum conservation, which result in the energy balance below:

$$\frac{\partial}{\partial t}\left(\frac{1}{2}\frac{p^2}{\rho_L {c_L}^2} + \frac{1}{2}\rho_L \vartheta^2\right) + \nabla.(pv) = Np\frac{\partial V(r,t)}{\partial t} \tag{14.4}$$

In Eq. (14.4), $V(r, t)$ refers to the volume of the acoustic cavitation bubble located at r at the instant t. The term $\frac{1}{2}\frac{p^2}{\rho_L {c_L}^2} + \frac{1}{2}\rho_L \vartheta^2$ represents the acoustic energy, which is the sum of the kinetic and potential compressional energy of the pure liquid. The term pv represents the acoustic intensity, where p is the acoustic pressure field, and v is the velocity field. The term $Np\frac{\partial V(r,t)}{\partial t}$ constitutes the mechanical power exchanged between the acoustic wave and the bubbles, from which a part is irreversibly dissipated as a heat and represents the physical origin of the wave attenuation.

Louisnard (2012) combined the Caflisch model with the bubble dynamics based on the Keller-Miksis equation. An energetic interpretation of the single bubble motion was then obtained as shown in Eq. (14.5):

$$\frac{\partial}{\partial t}\left(2\pi\rho_L \dot{R}^2 R^3 + 4\pi R^2 \sigma\right) = -16\pi\mu_L R\dot{R}^2 - p\frac{\partial V}{\partial t} + p_g\frac{\partial V}{\partial t} \tag{14.5}$$

Eq. (14.5) is equivalent to the Rayleigh equation. The term $2\pi\rho_L \dot{R}^2 R^3$ represents the kinetic energy of the radially moving liquid, while the term $4\pi R^2\sigma$ constitutes the interfacial potential energy. The term $-16\pi\mu_L R\dot{R}^2$ represents the power irreversibly lost by internal viscous friction within the liquid as it moves radially. The term $-p\frac{\partial V}{\partial t}$ is the power transferred from the acoustic field to the liquid surrounding the bubble, and is equivalent to the energy source available to drive the bubble oscillations and the radial motion of the liquid around. The term $p_g\frac{\partial V}{\partial t}$ is the mechanical power done by the gas on the liquid, and could be expressed as the time- derivative of a compressional energy. Eq. (14.5) has been multiplied by the number density of bubbles N, and combined with Eq. (14.4), to obtain a global energy conservation equation of the bubbly liquid.

$$\frac{\partial}{\partial t}\left(\frac{1}{2}\frac{p^2}{\rho_L {c_L}^2} + \frac{1}{2}\rho_L \vartheta^2 + N2\pi\rho_L \dot{R}^2 R^3 + N4\pi R^2\sigma\right) + \nabla.(pv) = -N16\pi\mu_L R\dot{R}^2 + Np_g\frac{\partial V(r,t)}{\partial t} \tag{14.6}$$

Louisnard (2012) averaged Eqs. (14.5) and (14.6) over one acoustic cycle, assuming periodic oscillations of all the fields, and performed numerical simulations of the dissipated energies, to determine the source of attenuation in a bubbly liquid. The author concluded that inertial bubbles dissipate much more energy than a linearly oscillating bubble, both by thermal diffusion in the gas and viscous dissipation in the liquid. Overall, the wave attenuation in an inertial cavitation field was demonstrated to be 4 orders of magnitude much larger than the value predicted by the classical linear dispersion relation. It was also proved that the relative predominance of thermal diffusion versus viscous dissipation depends on the ambient size of the bubble.

14.6 Overall energy efficiency

The overall energy efficiency of sonication in the case of a sonochemical reactor or ultrasound assisted process is classically characterized using the calorimetric measurements (Toma et al., 2011; Mhetre and Gogate, 2014; Dion, 2009). The procedure consists of measuring the temperature rise in the vessel during sonication starting at thermal equilibrium with the surroundings. The heat reconvered by the liquid is then simply expressed by the energy balance shown in Eq. (14.7).

$$\varphi = mC_p \frac{dT}{dt} \tag{14.7}$$

The validity of the aforementioned balance relies on neglecting the energy dissipation throughout the vessel wall, and remains acceptable as long as the vessel is thermally isolated. However, the rise of temperature within the liquid may result from the direct absorption of the ultrasonic wave by the liquid, and the release of the cavitational energy at the bubble collapse. In order to distinguish both origins of heat, Son et al. (Son et al., 2012) suggested an indirect technique to assess the cavitation energy by measuring the calorimetric energy in both cavitating and noncavitating liquid as shown in Eq. (14.8).

$$\varphi_{cavitation} = \varphi_{cavitating} - \varphi_{non-cavitating} \tag{14.8}$$

Where $\phi_{cavitation}$ is the cavitation power, $\phi_{,\,cavitating}$ is the calorimetric power in cavitating liquid obtained using a gas-saturated medium, and $\phi_{non\,-\,cavitating}$ is the calorimetric energy in noncavitating liquid obtained using degassed medium.

According to Plattes et al. (2017), the classic ultrasonic calorimetry presents a particular difficulty to evaluate the temperature rise at thermal equilibrium, because the relevant initial time and temperature intervals are small and measurement errors in the temperature readings become large. The same authors suggest to start the calorimetric measurement with a lower temperature in the reaction vessel than in the surroundings, that is, at thermal desequilibrium. The temperature rise is then measured in the reaction vessel and the surroundings during sonication. Finally, the temperature rise is determined at intercept by interpolation, the calorimetric power is then calculated in the reaction vessel.

14.7 Designs and energy efficiency

In order to enhance the effectiveness of energy conversion from acoustic to cavitational form, the design of the sonochemical and ultrasound-assisted processes has to be elaborated in a way that fits the desired effect (either physical or chemical) and limits the thermal and viscous dissipations of energy accompanying the oscillation of bubbles. The research teams of Gogate and Pandit have intensively investigated the relationship between the design of the sonochemical and ultrasound-assisted devices and their efficiencies (Gogate and Pandit, 2015; Gogate and Pandit, 2000a,b; Gogate et al., 2011; Mhetre and Gogate, 2014; Gogate et al., 2003a,b; Sutkar and Gogate, 2009; Gogate and Pandit, 2004).

In an early study, Gogate and Pandit (2000a) considered the physico-chemical conditions of the fluid, and the acoustic conditions of the irradiating wave to define a criterion for critical ultrasound intensity to avoid to overdesign or underdesign. A sound heuristic correlation has been developed based on the results of the study. According to the authors, it allows for a high confidence prediction of the pressure pulse generated as a function of initial nuclei sizes, frequency, and intensity of ultrasound, for the design of sonochemical reactors. A few years later, the same research group (Gogate et al., 2003a) designed A novel reactor in the form of triple frequency hexagonal flow cell operating at a capacity of 7 dm^3 and tested with the liberation of iodine from aqueous potassium iodide and the degradation of formic acid. The energy efficiency of the developed reactor, referring to electrical to mechanical energy transfer was estimated using a calorimetric technique, and has been calculated and compared with the conventional sonochemical reactors. The energy efficiency of the of the novel sonochemical reactor was found in the range of 75–78%, which is by far higher than the energy efficiency of the ultrasonic horn, lower than 10%, and that of the ultrasonic bath or the dual frequency flow cell, estimated at 35%. According to this

study, the triple frequency hexagonal flow cell reactor proved to be extremely efficient in transferring the supplied electrical energy to energy used for generation of cavities, which can be explained by the higher transducer surface area.

In another study dealing with the single bubble scale, Gogate et al. (2003b) performed numerical simulations to study the effects of intensity and frequency of irradiation along with the geometrical arrangement of the transducers and the liquid phase physicochemical properties on the collapse pressure generated and the maximum radius attained by the acoustic cavitation bubble. The increase of the vapor pressure of the liquid proved to rise the vapor content of the cavity and consequently lower the energy released during the collapse. In the other hand, in high viscous liquids, severe attenuation of the sound intensity occurs and the active cavitating zone gets reduced substantially, because the cohesive force would increase, inducing the increase of the threshold pressure and hence the energy required to generate cavitation.

Another design correlation has been elaborated by Gogate and Pandit (2004) to describe the relationship between the collapse pressure and the cavitational yield and assist the designers in selecting the operating parameters for a desired cavitational effect. In terms of energy efficiency, it was demonstrated that the triple frequency hexagonal flow cell with three transducers on each of the six sides is the most energy efficient with an order of 75%. This was explained by the uniform energy dissipation over a wider area and through multiple transducers as compared to the concentrated energy dissipation in the horn (energy efficiency less than 10%) and the ultrasonic bath with three transducers (energy efficiency of 18%).

Sutkar and Gogate (Sutkar and Gogate, 2009) established a number of recommendations for optimum operating parameters and design of large scale sonochemical reactors based on the experimental and theoretical results. The authors demonstrated that for a low frequency operation, maximum energy gets dissipated near to the irradiating surface in a cone like structure, which results in a maximum cavitational activity very near to the irradiating surface and wide variation in the energy dissipation rates in the remaining bulk of liquid. They also affirmed that in order to optimise energy transfer to the irradiated medium, it is imperative to distinguish active and passive zones in the sonochemical reactor and map the attenuation of the wave which occurs due to reflection, refraction and absorption (predominant in homogeneous liquid), and contributes to spatial variation of the cavitational activity. A special focus was given to the horn type systems, the authors revealed that the scale up prospects related to this type of transducers are very poor and cannot effectively transmit the acoustic energy into large process volume.

The heterogeneous case was treated by Gogate et al. (2011) in another paper, which aimed to develop a unified approach for the selection of different operating and geometric parameters for large heterogeneous sonochemical reactors.

The authors highlighted the importance of the mixing and hydrodynamic characteristics when dealing with heterogeneous systems. In terms of geometrical design, they demonstrated that an increase in the diameter of immersion transducer relatively to the reactor diameter results in the increase of cavitational activity till an optimum ratio, usually dependent on the application. The ratio of source to vessel diameters mainly affects the level of turbulent dissipation of energy and the intensity of the acoustic streaming, consequently this parameter would be more important when seeking for the physical effects of sonication in ultrasound assisted processes.

Mhetre and Gogate (2014) developed and studied experimentally a large scale sonochemical reactor operating at 40 kHz with a capacity of 72 L, constituted of multiple transducers rectangular flow cell type reactor, with a maximum power of 2400 W.

The ultrasonic flow cell design based on multiple transducers showed higher energy transfer efficiency of almost 50% as compared to conventional horn design. This enhancement was attributed to the significant suppression of the nonuniform distribution of cavitational activity.

Gogate and Pandit (2015) presented a detailed review of several works that dealt with design and configuration of sonochemical and ultrasound assisted processes. For instance, Seymour et al. (Seymour and Gupta 1997) developed an innovative design accounting for reflection and focusing of sound wave in the vessel of the receiving medium. Faid et al. (1998) characterized a resonant tube, known as "sonitube" chemically, electrochemically, and energetically. Gondrexon et al. (1999) presented a novel continuous three stages sonochemical reactor. Cravotto et al. (2005) proposed a novel design for a sonochemical reactor, including mechanical rotation. Dion (2009) described a new continuous reactor design based on the high-power converging acoustic waves in a tube to produce a relatively large volume confined acoustic cavitation zone in flowing liquid reagents under pressure. Liu et al. (2008) presented an ultrasound-assisted air loop reactor, whilst Nickel and Neis (2007) suggested another configuration of a continuous flow system based on horns.

Continuous flow and intensified sonochemical and ultrasound assisted processes gained wide interest in the last period (Kerboua and Hamdaoui, 2021). Novel designs have been developed and studied in order to improve the energy efficiency of the systems and enhance their performances for the intended use. Combinations of modelling and experiments have also brought answers for the extrapolation of small-scale results. In this context, Jordens et al. (2013) carried out a parametric analysis in order to determine the effect of design parameters on the performance of ultrasound reactors with confined

channels. Hussain and Janajreh (2016) and Hussain et al. (2016) proposed to study numerically a cylindrical reactor design for continuous flow reactant mixture circulation, and sonication by a sonotrode type ultrasound equipment. Wei and Weavers (2016) Combined COMSOL modelling with acoustic pressure maps to design sonoreactors, the simulated acoustic field was verified by acoustic pressure contour maps generated from hydrophone measurements in a plexiglass box filled with water. Johansson et al. (2017) Designed a flow type high-intensity ultrasound reactor, driven with three transducers mounted radially in the reactor wall with 120° spacing. This reactor was excited with nine dual frequency sonotrodes. John et al. (2017) developed a hybrid contact reactor for ultrasound assisted liquid–liquid extraction that incorporates both direct and indirect approaches of ultrasound transfer, with two possible open and closed interval connection configurations. More recently, Pradhan et al. (2019) reviewed the designs of microflowreactors for ultrasound assited photocatalysis. Giannakoudakis et al. (2020) presented also an interesting study on the design of a sonophotoreactor, with the perspective to achieve a sustainable selective oxidation with proper use of the energy emanating from both sources: light and ultrasound.

14.8 Conclusion

In the present chapter, the sonication pathway has been tracked from the ultrasound source to the vessel of the receiving medium, whether in sonochemical or ultrasound assisted processes. The ultrasound source has been detailed in terms of available technologies and their relative energy efficiency of conversion of energy forms into the intended acoustic wave. Piezoelectric transducers have been identified as the most energy and cost-efficient devices available in the market, especially for mid to high frequency use, generally required for sonochemistry. However, magnetostrictive transducers technology may know a comeback, particularly with the emergence of novel materials that show appropriateness and effectiveness for large scale industrial use at low frequency (below 70 kHz). The propagation of the acoustic wave in the vessel has been discussed from a theoretical point of view, starting from Caflisch theory, and several design aspects aiming to improve the energy transfer and limit dissipation have been presented. According to the intended application, several geometries, transducers' dispositions, specific operating conditions and eventual hybridation are retrieved in the literature. A quasi-agreement on the promising role of intensification and use of microflow reactor has been noticed, with energy efficiencies generally exceeding 50%. Among all the technologies, most of the researchers affirmed that the horn type systems remain the less promising, and are not at all appropriate for large scale use, particularly owing to their low energy efficiency.

References

Ahmad, K.A., M.K. Osman, Z. Hussain, M.F. Abdullah, A.A. Manaf, and N. Abdullah. 2019. "Design and characterization piezoelectric acoustic transducer for sonar application." Proceedings - 8th IEEE International Conference on Control System, Computing and Engineering, ICCSCE 2018, 233–237. https://doi.org/10.1109/ICCSCE.2018.8685014.

An, Y.-K., Kim, M.K., Sohn, H., 2014. Piezoelectric transducers for assessing and monitoring civil infrastructures, in: M.L. Wang, J.P. Lynch, H.B.T.-S.T. for C.I. Sohn (Eds.), Woodhead Publ. Ser. Electron. Opt. Mater., Woodhead Publishing, 2014: pp. 86–120. https://doi.org/10.1533/9780857099136.86.

Caflisch, RE., Miksis, MJ., Papanicolaou, GC., 1985, LuT., 1985. Effective equations for wave propagation in bubbly liquids. J. Fluid Mech. 153 (April), 259–273. https://doi.org/10.1017/S0022112085001252.

Chen, Q., Wang, Q.M., 2005. The effective electromechanical coupling coefficient of piezoelectric thin-film resonators. Appl. Phys. Lett. 86 (2), 1–4. https://doi.org/10.1063/1.1850615.

Contamine, RF., Wilhelm, A.M., Berlan, J., Delmas, H., 1995. Power measurement in sonochemistry. Ultrason. Sonochem. 2 (1), S43–S47. https://doi.org/10.1016/1350-4177(94)00010-P.

Cravotto, G., Omiccioli, G., Stevanato, L., 2005. An improved sonochemical reactor. Ultrason. Sonochem. 12 (3), 213–217. https://doi.org/10.1016/j.ultsonch.2004.01.002.

Dion, J.L., 2009. Contamination-Free high capacity converging waves sonoreactors for the chemical industry. Ultrason. Sonochem. 16 (2), 212–220. https://doi.org/10.1016/j.ultsonch.2008.07.009.

Faïd, F., Romdhane, M., Gourdon, C., Wilhelm, A.M., Delmas, H., 1998. A comparative study of local sensors of power ultrasound effects: electrochemical, thermoelectrical and chemical probes. Ultrason. Sonochem. 5 (2), 63–68. https://doi.org/10.1016/S1350-4177(98)00008-X.

Fulay, P., and J.-.K. Lee. 2021. "Ferroelectrics, piezoelectrics, and pyroelectrics." Electronic, Magnetic, and Optical Materials, 317–380. https://doi.org/10.1201/9781439882603-11.

Ghenna, S., F. Giraud, C. Giraud-audine, M. Amberg, B. Lemaire-semail, S. Ghenna, F. Giraud, et al. 2016. "Modelling, identification and control of a langevin transducer to cite this version : hal id : hal-01364291 modelling, identification and control of a langevin transducer."

Giannakoudakis, DA., Łomot, D., Colmenares, J.C., 2020. When sonochemistry meets heterogeneous photocatalysis: designing a sonophotoreactor towards sustainable selective oxidation. Green Chem. 22 (15), 4896–4905. https://doi.org/10.1039/d0gc00329h.

Gogate, P.R., Pandit, A.B., 2015. Design and scale-up of sonochemical reactors for food processing and other applications. Power Ultrasonics: Applications of High-Intensity Ultrasound. Elsevier Ltd, Cambridge, pp. 725–755. https://doi.org/10.1016/B978-1-78242-028-6.00024-7.

Gogate, P.R., Mujumdar, S., Pandit, A.B., 2003a. Large-Scale sonochemical reactors for process intensification: design and experimental validation. J. Chem. Technol. Biotechnol. 78 (6), 685–693. https://doi.org/10.1002/jctb.697.

Gogate, P.R., Pandit, A.B., 2000a. Engineering design method for cavitational reactors: I. sonochemical reactors. AIChE J. 46 (2), 372–379. https://doi.org/10.1002/aic.690460215.

Gogate, P.R., Pandit, A.B., 2000b. Engineering design methods for cavitation reactors II: hydrodynamic cavitation. AIChE J. 46 (8), 1641–1649. https://doi.org/10.1002/aic.690460815.

Gogate, P.R., Pandit, A.B., 2004. Sonochemical reactors: scale up aspects. Ultrason. Sonochem. 11 (3–4), 105–117. https://doi.org/10.1016/j.ultsonch.2004.01.005.

Gogate, P.R., Wilhelm, A.M., Pandit, A.B., 2003b. Some aspects of the design of sonochemical reactors. Ultrason. Sonochem. 10 (6), 325–330. https://doi.org/10.1016/S1350-4177(03)00103-2.

Gogate, PR., Sutkar, V.S., Pandit, A.B., 2011. Sonochemical reactors: important design and scale up considerations with a special emphasis on heterogeneous systems. Chem. Eng. J. 166 (3), 1066–1082. https://doi.org/10.1016/j.cej.2010.11.069.

Gondrexon, N., Renaudin, V., Petrier, C., Boldo, P., Bernis, A., Gonthier, Y., 1999. Degradation of pentachlorophenol aqueous solutions using a continuous flow ultrasonic reactor: experimental performance and modelling. Ultrason. Sonochem. 5 (4), 125–131. https://doi.org/10.1016/S1350-4177(98)00041-8.

Guyomar, D., Ducharne, B., Sebald, G., 2011. High nonlinearities in langevin transducer: a comprehensive model. Ultrasonics 51 (8), 1006–1013. https://doi.org/10.1016/j.ultras.2011.05.017.

Hamonic, B., Decarpigny, J.N., 1988. Power sonic and ultrasonic transducers design. Power Sonic and Ultrasonic Transducers Design. https://doi.org/10.1007/978-3-642-73263-8.

Hayward, G., Gillies, D., 1989. Block diagram modeling of tall, thin parallelepiped piezoelectric structures. Acoustical Soc Am 86 (5), 1643–1653.

Hussain, M.N., Janajreh, I., 2016. Sono-Chemical Reactor Design for Biodiesel Production via Transesterification, in: LIFE12 ENV/CY/544 Sustain. Manag. Livest. Waste Removal/Recovery Nutr. 1–14.

Hussain, M.N., Samad, T., Daqaq, M., Janajreh, I., 2016. Numerical modelling of sonicated, continuous transesterification and evaluation of reaction kinetics for optimizing biodiesel reactor design. Int. J. of Thermal &Environmental Engineering 11 (1), 79–86. https://doi.org/10.5383/ijtee.11.01.012.

Jimenez, MG. 2018. "Ultrasonic pulse generation by a piezoelectric transducer at cryogenic temperatures."

Johansson, O., Lofqvist, T., Pamidi, T.R.K., 2017. Design of high-intensity ultrasound reactor. IEEE Int Ultrasonics Symposium, IUS. https://doi.org/10.1109/ULTSYM.2017.8092948.

John, J.J., Kuhn, S., Braeken, L., Gerven, T.V., 2017. Temperature controlled interval contact design for ultrasound assisted liquid–liquid extraction. Chem. Eng. Res. Des. 125, 146–155. https://doi.org/10.1016/j.cherd.2017.06.025.

Jordens, J., Honings, A., Degrève, J., Braeken, L., Van Gerven, T., 2013. Investigation of design parameters in ultrasound reactors with confined channels. Ultrason. Sonochem. 20 (6), 1345–1352. https://doi.org/10.1016/j.ultsonch.2013.03.012.

Kerboua, K., Hamdaoui, O., 2021. Sonochemistry for water remediation: toward an up-scaled continuous technology. Applied Water Science Volume 2: Remediation Technologies, 2, pp. 437–468.

Khalifeh, S., 2020. Polymeric structures optimized for organic passive electronic components. Polymers in Organic Electronics, pp. 341–391. https://doi.org/10.1016/b978-1-927885-67-3.50012-2.

Lee, E.W., Asgar, M.A., 1971. The magnetostriction of nickel. Proceedings of the Royal Society of London. A. Mathematical and Physical Sciences 326 (1564), 73–85. https://doi.org/10.1098/rspa.1971.0192.

Lin, S., 2006. Study on the langevin piezoelectric ceramic ultrasonic transducer of longitudinal-flexural composite vibrational mode. Ultrasonics 44 (1), 109–114. https://doi.org/10.1016/j.ultras.2005.09.002.

Liu, Y.N., Jin, D., Lu, X.P., Han, P.F., 2008. Study on degradation of dimethoate solution in ultrasonic airlift loop reactor. Ultrason. Sonochem. 15 (5), 755–760. https://doi.org/10.1016/j.ultsonch.2007.12.004.

Louisnard, O., 2012. A simple model of ultrasound propagation in a cavitating liquid. part I: theory, nonlinear attenuation and traveling wave generation. Ultrason. Sonochem. 19 (1), 66–76. https://doi.org/10.1016/j.ultsonch.2011.06.008.

Lowe, M.J.S., 2001. Ultrasonics. Ultrasonics, Nondestructive Testing. Academic Press, Bucuresti, Romania, pp. 1437–1441. https://doi.org/10.1006/rwvb.2001.0143.

Lu, X., Hu, J., Peng, H., Wang, Y., 2017. A new topological structure for the langevin-type ultrasonic transducer. Ultrasonics 75, 1–8. https://doi.org/10.1016/j.ultras.2016.11.008.

Margulis, M.A., Margulis, I.M., 2003. Calorimetric method for measurement of acoustic power absorbed in a volume of a liquid. Ultrason. Sonochem. 10 (6), 343–345. https://doi.org/10.1016/S1350-4177(03)00100-7.

Mason, T.J., Cintas, P., 2002. Sonochemistry. Handbook of Green Chemistry and Technology. Wiley, Hoboken, New Jersey, pp. 372–396.

Mattiat, O.E., Mason, W.P., 1972. Ultrasonic transducer materials. Phys. Today 25. https://doi.org/10.1063/1.3070895.

Mhetre, A.S., Gogate, P.R., 2014. New design and mapping of sonochemical reactor operating at capacity of 72L. Chem. Eng. J. 258, 69–76. https://doi.org/10.1016/j.cej.2014.07.075.

Moffett, M.B., Clark, A.E., Wun-Fogle, M., Lindberg, J.F., Teter, J.P., McLaughlin, E.A., 1990. Characterization of terfenol-d for magnetostrictive transducers. J. Acoust. Soc. Am. 87 (S1). S95–S95 https://doi.org/10.1121/1.2028440 .

Nickel, K., Neis, U., 2007. Ultrasonic disintegration of biosolids for improved biodegradation. Ultrason. Sonochem. 14 (4), 450–455. https://doi.org/10.1016/j.ultsonch.2006.10.012.

Olabi, A.G., Grunwald, A., 2008. Design and application of magnetostrictive materials. Mater. Des. 29 (2), 469–483. https://doi.org/10.1016/j.matdes.2006.12.016.

Pérez-Sánchez, A., Segura, J.A., Rubio-Gonzalez, C., Baldenegro-Pérez, LA., Soto-Cajiga, J.A., 2020. Numerical design and analysis of a langevin power ultrasonic transducer for acoustic cavitation generation. Sens. Actuators A 311. https://doi.org/10.1016/j.sna.2020.112035.

Plattes, M., Köhler, C., Gallé, T., 2017. Disequilibrium calorimetry for determination of ultrasonic power in sonochemistry. MethodsX 4, 274–278. https://doi.org/10.1016/j.mex.2017.08.003.

Pradhan, S.R., Colmenares-Quintero, R.F., Quintero, J.C.C., 2019. Designing microflowreactors for photocatalysis using sonochemistry: a systematic review article. Molecules 24 (18). https://doi.org/10.3390/molecules24183315.

Rafienezhad-Masouleh, M., Honarvar, F., 2021. Investigation of the performance of a piezoelectric ultrasonic transducer by finite element modeling. Russ. J. Nondestr. Test. 57 (4), 269–280. https://doi.org/10.1134/S1061830921040094.

Redwood, M., 1961. Transient performance of a piezoelectric transducer. J. Acoust. Soc. Am. 33 (4), 527–536.

Safari, A., Akdoğan, E.K., 2008. Piezoelectric and acoustic materials for transducer applications. Springer US, New York https://doi.org/10.1007/978-0-387-76540-2.

Seymour, JD., Gupta, RB., 1997. Oxidation of aqueous pollutants using ultrasound: salt-induced enhancement. Ind. Eng. Chem. Res. 36 (9), 3453–3457. https://doi.org/10.1021/ie970069o.

Shigeyuki, S., 2003. Ceramics. Encyclopedia of Physical Science and Technology, (Third Edition). Elsevier, California, pp. 596–619.

Shuyu, L., 2004. Optimization of the performance of the sandwich piezoelectric ultrasonic transducer. J. Acoust. Soc. Am. 115 (1), 182–186. https://doi.org/10.1121/1.1635836.

Soin, N., Anand, S.C., Shah, T.H., 2016. *Energy Harvesting and Storage Textiles. Handbook of Technical Textiles*, Second Edi Elsevier Ltd https://doi.org/10.1016/b978-1-78242-465-9.00012-4.

Son, Y., Lim, M., Khim, J., Kim, L.H., Ashokkumar, M., 2012. Comparison of calorimetric energy and cavitation energy for the removal of bisphenol-a: the effects of frequency and liquid height. Chem. Eng. J. 183, 39–45. https://doi.org/10.1016/j.cej.2011.12.016.

Soni, P., Vaidya, D., Kaushal, M., Gupta, A., Gautam, A., Sharma, C., Arya, P., 2020. A review on high pressure processing and ultrasound processing in food industry. Chemical Science Review and Letters i (34) 552–564. https://doi.org/10.37273/chesci.CS205101115.

Sutkar, VS., Gogate, PR., 2009. Design aspects of sonochemical reactors: techniques for understanding cavitational activity distribution and effect of operating parameters. Chem. Eng. J. 155 (1–2), 26–36. https://doi.org/10.1016/j.cej.2009.07.021.

Toftekær, J.F., Benjeddou, A., Høgsberg, J., 2020. General numerical implementation of a new piezoelectric shunt tuning method based on the effective electromechanical coupling coefficient. Mech. Adv. Mater. Struct. 27 (22), 1908–1922. https://doi.org/10.1080/15376494.2018.1549297.

Toma, M., Fukutomi, S., Asakura, Y., Koda, S., 2011. A calorimetric study of energy conversion efficiency of a sonochemical reactor at 500kHz for organic solvents. Ultrason. Sonochem. 18 (1), 197–208. https://doi.org/10.1016/j.ultsonch.2010.05.005.

Uchino, K., 2010. Piezoelectric composite materials. Advanced Piezoelectric Materials: Science and Technology. Woodhead Publishing Limited, Cambridge, pp. 318–346. https://doi.org/10.1533/9781845699758.1.318.

Vinogradov, S., A. Cobb, and G. Light. 2017. "Review of magnetostrictive transducers (MsT) utilizing reversed wiedemann effect." *AIP Conference Proceedings* 1806 (February 2017). https://doi.org/10.1063/1.4974549.

Wei, Z., Weavers, LK., 2016. Combining comsol modeling with acoustic pressure maps to design sono-reactors. Ultrason. Sonochem. 31 (January), 490–498. https://doi.org/10.1016/j.ultsonch.2016.01.036.

Wright, W.M.D., 2022. *Ultrasonic Techniques*. Encyclopedia of Dairy Sciences. Elsevier, USA. https://doi.org/10.1016/b978-0-12-818766-1.00349-4.

Zhang, Y., Gao, Y., Guo, Z., Du, X., 2018. Effects of mass transfer on damping mechanisms of vapor bubbles oscillating in liquids. Ultrason. Sonochem. 40, 120–127. https://doi.org/10.1016/j.ultsonch.2017.07.004.

Part IV

Green, sustainable and benign by design process? The place and perspective of ultrasound assisted processes and sonochemistry in industrial applications based on energy efficiency

15. Acoustic cavitation and sonochemistry in industry: State of the art 265
16. Crystallization of pharmaceutical compounds: Process Intensification using ultrasonic irradiations - Experimental approach 279
17. Sonochemical degradation of fluoroquinolone and β-lactam antibiotics – A view on transformations, degradation efficiency and consumed energy 287
18. The use of ultrasonic treatment in technological processes of complex processing of industrial waste: energetic insights 299
19. The sonochemical and ultrasound-assisted production of hydrogen: Energy efficiency for the generation of an energy carrier 313
20. Future trends and promising applications of industrial sonochemical processes 329
21. Raising challenges of ultrasound assisted processes and sonochemistry in industrial applications based on energy efficiency 349

Chapter 15

Acoustic cavitation and sonochemistry in industry: State of the art

Md Hujjatul Islam[a] **and Bruno G. Pollet**[b]

[a] *Department of Chemical Engineering and Applied Chemistry, University of Toronto, Toronto, Canada,* [b] *Hydrogen Research Institute (HRI), Université du Québec à Trois-Rivières (UQTR), Trois-Rivières, Canada.*

15.1 Introduction

Power ultrasound is an emerging technology that is gaining interest in various industrial applications for both existing process intensification and new process development (Astráin-Redín et al., 2020). The first commercial application of ultrasound dates back to 1917 developed by Langevin for the estimation of water depth. Since then, ultrasound with frequencies in the megahertz (MHz) range has developed as a new technique for nondestructive applications such as testing and medical imaging where it doesn't affect the chemical and physical properties of the medium. On the other hand, low-frequency ultrasound which is also called power ultrasound has attracted immense interest to chemists and engineers since the propagation of power ultrasound in the medium can change its physicochemical properties through acoustic cavitation. This acoustic cavitation produced by power ultrasound is the basis of sonochemistry and its application in chemical processes (Mason, 1999).

Power ultrasound helps to produce safer and higher quality products than the conventional approach (Astráin-Redín et al., 2020). A broad range of industrial applications of power ultrasound has been in use for over 60 years. Although power ultrasound has seen a wide range of applications in the industry ranging from automotive to textiles, in this chapter we focus on the more widespread use of acoustic cavitation and sonochemistry in different industrial applications.

15.2 Power ultrasound and acoustic cavitation

Ultrasound is the acoustic longitudinal wave with frequencies higher than the human hearing range. This range varies from person to person. However, it is approximately above 20 kHz. High-frequency ultrasound that has a frequency above 1 MHz is called *low power ultrasound*. The delivered acoustic power is usually less than 10 W. These low-power ultrasounds do not influence the medium where it propagates. Due to this feature, high frequency and low power ultrasound are used for medical diagnosis. Low-frequency ultrasound that has a frequency between 20 kHz and 2000 kHz, is defined as "power ultrasound." It is transferred at a high-power level which can alter the medium where it propagates through. It can disrupt a liquid to generate cavitation or acoustic streaming (Legay et al., 2011; Pollet, 2012). In terms of transmission of power ultrasound in the material, it can be divided into direct transmission and indirect transmission. In the direct transmission, vibration from the ultrasound transducer occurs on a solid. Indirect transmission is happened via cavitation into a liquid by the transmission of acoustic vibrations (Islam et al., 2019; Pollet, 2012).

Among the several effects induced by ultrasound propagation into a liquid medium, the two major effects are acoustic cavitation and acoustic streaming. Acoustic streaming is caused by the dissipation of acoustic energy (Legay et al., 2011). Many tiny gas bubbles are formed when ultrasonic waves propagate through a liquid media such as water Fig. 15.1 (Pollet, 2012). When the acoustic pressure is higher than the atmospheric pressure, the instantaneous local pressure becomes negative during the rarefaction phase of the ultrasonic wave. Thus, the dissolved gases in the liquid cannot prevail as dissolved under negative pressure and escape as gas bubbles from the liquid. The tiny gas bubbles expand at the rarefaction phase due to

Energy Aspects of Acoustic Cavitation and Sonochemistry: Fundamentals and Engineering. DOI: https://doi.org/10.1016/B978-0-323-91937-1.00001-3
Copyright © 2022 Elsevier Inc. All rights reserved.

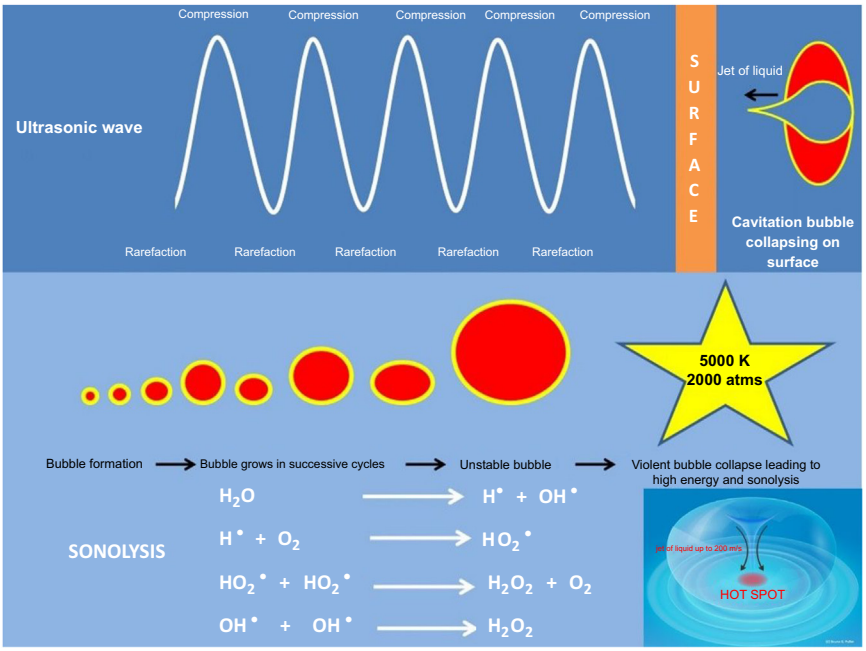

FIGURE 15.1 Sinusoidal waveform, bubble collapse, and sonolysis (Pollet, 2012).

the higher pressure at the bubble wall rather than the liquid pressure. Some of these bubbles violently collapse during the compression phase causing shock waves (Kyuichi Yasui, 2018).

The formation of bubbles by ultrasonication and their subsequent violent collapse is known as *acoustic cavitation* (Legay et al., 2011). Each cavitation bubble acts as a local "hotspot" in the aqueous media which generates temperatures of ca. 5000 C and pressures of ca. 2000 ATMs (Suslick, 1990). The collapsing of bubbles provides both chemical and mechanical effects into the aqueous media. The chemical effect occurs inside the bubble, which can be considered as a high-pressure and high-temperature micro-reactor (Pollet, 2012).

Acoustic cavitation bubbles can be classified as "transient" and "stable" that can cause sonoluminescence and sonochemistry. The transient cavitation bubbles live for a few acoustic cycles and undergo violent collapse which leads to the fragmentation of the bubble for further cavitation to occur. The stable cavitation bubble lives for hundreds of oscillation cycles which causes rapid sequential growth followed by near collapse. This collapse generates high energy resulting in Single Bubble Sonoluminescence (SBSL) (Ashokkumar & Mason, 2007).

15.3 Sonochemistry

Sonochemistry is the field of chemistry where chemical reactions take place by ultrasound driven by acoustic cavitation (Mason, 1990). These reactions can occur under single or multi-bubble cavitation. The multibubble cavitation is the dominant one as sonochemical reactions are almost always multibubble phenomena. As stated earlier, cavitation bubble collapse generates very high temperatures and pressures. When the cavitation bubbles form, they contain dissolved gas molecules and vapor from the solvent. In the extreme condition generated by bubble collapse, the solvent vapor and gas molecules produce various highly reactive radicals and other species such as OH radicals, O_3, H_2O_2, and O atoms (Mason, 1990; Yasui, 2018). These radical species react with solutes present in the aqueous solution (Yasui, 2018). The hydroxyl radical (OH) is the most dominant species that is produced during acoustic cavitation. The production of O_3 is insignificant compared to OH radicals. Generally, O atoms react with H_2O to produce H_2O_2 (Yasui, 2016). The oxidation-reduction potential of $OH^\bullet$ (+2.06 V) is much higher than that of H_2O_2 (+1.776 V). Therefore $OH^\bullet$ plays a more crucial role than H_2O_2 in sonochemistry (Lide and Frederikse, 1994).

Several factors affect the sonochemical reactions in which ultrasonic frequency (f) is the dominant factor. The mechanical forces yielded by sonication directly depend on the ultrasonic frequency. The maximum amount of mechanical effect can be obtained at a lower frequency. Acoustic power (P_w) or intensity () is another major factor that dominates the sonochemical reactions. The amount of transmitted acoustic power can be determined using a standard calorimetric method presented in

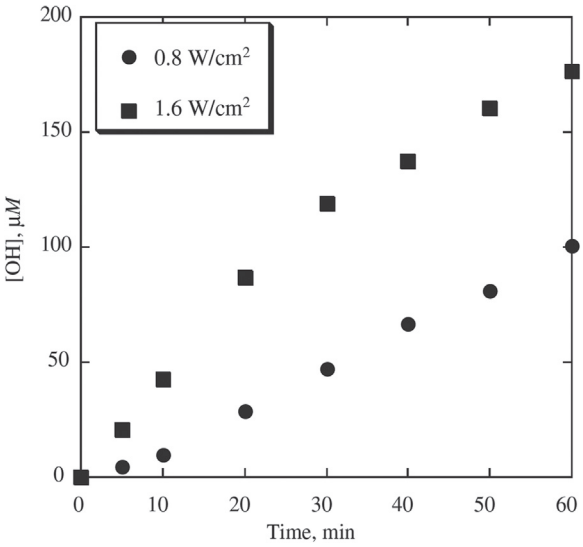

FIGURE 15.2 The production of OH radicals as a function of time at different acoustic intensity (Islam et al., 2019).

Eq. (15.1).

$$q = m\,C_p \Delta T \tag{15.1}$$

where q is the heat generated in J, m is the mass of the solution in kg, C_p is the specific heat capacity of the solution (e.g., for water, 4185.5 J/kg/K at 25°C and 101.325 kPa) and T is the temperature gradient in K. The production of radicals increases with increasing acoustic power. It is observed that with increasing acoustic power, the production of OH radicals increases Fig. 15.2 (Mason, 1990). Moreover, the bubble size and the number of active bubbles increase with increasing acoustic power at a given frequency (Islam et al., 2019).

Another important factor that affects the formation of radicals is the type of dissolved gases in the reaction media. The number of radicals generated by cavitation is the same as any of the noble gases. However, since the thermal conductivity of those gases decreases with increasing atomic weight, the maximum bubble temperature can be achieved by using the higher atomic number of gases. For example, helium (He) has the lowest atomic weight. Therefore, during bubble collapse, more heat will be dispersed to the surrounding from the bubble leading to a lower maximum bubble temperature. Lower bubble temperature will lead to the lower formation of primary radicals. Moreover, the presence of oxygen is critical for sonochemical reactions. Reactions involving O_2 and N_2 may occur also occur when air-saturated water is sonicated (Mason, 1990).

The solution temperature affects the sonochemical reactions in many different ways. At a higher solution temperature, the vapor pressure, as well as the internal pressure of the collapsing bubble, is higher. When the vapor pressure is higher, the maximum bubble collapse temperature will be lower yielding a lower number of primary radicals (Mason, 1990).

15.4 Physical and chemical effect of power ultrasound

There are several physical and chemical effects imparted by power ultrasound. These are mainly ultrasonic cutting, viscosity modification, emulsification, sonocrystallization and freezing, surface cleaning, foaming, and defoaming. In this section, a brief introduction of the major impacts is presented.

Ultrasonic Cutting: Ultrasound-assisted cutting is a unit operation where size reduction of the particle occurs utilizing the vibrational energy of ultrasound. It is coupled with conventional blade movement to improve cutting quality. A regular ultrasonic cutting machine is consisting of an ultrasonic transducer, horn, cutting knife, and power supply. The high-frequency vibration of the cutting blade helps to obtain small deformation, reduced total cutting force, avoidance of transversal cracks and crumbling, and reduction of cutting surface roughness (Kentish and Feng, 2014). Since ultrasonic cutting doesn't require high pressure, it minimizes broken edges and material damages. The vibration of the cutter helps reduce the friction which avoids sticking of material to the blade. This feature is particularly helpful when cutting viscoelastic and viscoplastic material. The quality of ultrasonic cutting largely depends on the geometry of the blade, the direction of

vibration of the knife, relative to the movement of the material, and the frequency and amplitude of the ultrasound (Arnold et al., 2011).

Viscosity modification: Acoustic cavitation produces an intense shear force which is highly effective in reducing the viscosity of the material. The reduction of viscosity occurs either through the disruption of aggregates and hydrophobic interactions or the reduction of polymer chain length. For instance, reduction of polymer chain length of polysaccharides such as dextran and pectin, dissolution of starch granules is facilitated by the ultrasonic viscosity modification. Moreover, the viscosity of diary fluids can be reduced through the disruption of the whey protein aggregates by shear forces (Kentish and Feng, 2014).

Emulsification: Two phenomena are affecting the emulsification process by power ultrasound. The first phenomenon is the acoustic field which produces interfacial waves between the oil and the liquid phase. This interfacial wave enables the formation of large oil droplets in the aqueous phase. The second phenomenon is the shear force which helps disintegrate these large oil droplets into smaller droplets. The droplet size largely depends on the surfactant used and the surfactant to oil ratio because of the interfacial energy between the two phases. Moreover, the homogenization and microfludization process can be intensified using ultrasound with minimal energy input. It was observed that by using ultrasound, droplet size can be reduced to below 50 nm. Smaller droplet size improves the mouthfeel and product texture and improves the stability of the emulsion. On the other hand, ultrasound can break down emulsions and improve the separation of oil and aqueous phases (Kentish and Feng, 2014).

Sonocrystallization: Power ultrasound is known to intensify the nucleation of crystals from a solution. It reduces the metastable zone where nucleation can occur faster at lower concentrations of solid and higher temperatures. Cavitation bubble provides a heterogeneous surface for nucleation to occur. The nucleation is induced by the rapid local cooling rates due to the cavitation event and the high local pressure exerted during bubble implosion. Moreover, ultrasound enhances the crystal size reduction and agglomeration of the newly formed crystals (Astráin-Redín et al., 2020).

15.5 Industrial applications

Power ultrasound has application in a wide range of industries with diverse fields. The widely used industries where power ultrasound is successfully employed are the food industry, biofuel production, petroleum industry, welding, and waste treatment. In this section, a state-of-the-art application of power ultrasound in the different industries is discussed.

15.5.1 Cavitation in the food industry

Ultrasound in the food industry can be considered as a green and nonchemical technology which enhances the quality and the safety of the final food products (Mumtaz, 2019). In the food industry, ultrasonication is performed primarily through liquid media. Thus, cavitation becomes the main mechanism of action in these processes (Astráin-Redín et al., 2020). Generally, ultrasonic applications in the food industry can be divided into low and high-intensity approaches. In low-intensity approaches, small amplitude ultrasonic waves at high frequency (>1 MHz) are used. This type of ultrasound doesn't damage the material through which they propagate. On the other hand, high-intensity ultrasound uses lower frequency and larger amplitude waves. High-intensity ultrasound can alter the physicochemical properties or structure of the material. The frequency of these types of ultrasounds is in the range of 20–100 kHz (Kentish and Feng, 2014).

The application of ultrasound in the food industry has three main perspectives; preservation, extraction, and modification. Recently, this nonthermal food processing technology has attracted immense interest (Mumtaz, 2019).

Dairy processing: Ultrasound has a wide range of applications such as butter separation, milk fat, whey protein powder, cheese, membrane cleaning for ultrafiltration, and spray drying of milk solution in the dairy industry (Mumtaz, 2019). It has a dual effect in the dairy industry where both activation and inactivation of microorganisms can be performed using power ultrasound. In microorganism activation, it can enhance the fermentation process which is the most time and resource-consuming stage in the production of fermented dairy products. Therefore, ultrasonic intensification of the fermentation process without any adverse effects is important. It was found that ultrasound can improve the quality of the fermented milk gels such as texture, syneresis, and water holding capacity. For dairy fermentation, most of the beneficial effects of ultrasonication lie over a short time of irradiation at low frequencies (in the range of 20–40 kHz) (Akdeniz and Akalın, 2020).

On the other hand, ultrasound can be used for the inactivation of microorganisms. This largely depends on ultrasonic power, frequency, sonication time, types of microorganism, pH, and temperature. Microbial inactivation mainly results from the strong shear forces and mechanical forces generated by acoustic cavitation. From several studies, it was found that acoustic cavitation by low frequency (20 kHz) power ultrasound can cause lethal damage to the *Enterobacter aerogenes,*

Bacillus while high-frequency ultrasound (850 kHz) doesn't have any effect on these microorganisms in milk (Akdeniz and Akalın, 2020).

Moreover, ultrasound was successfully employed in the dairy industry for COD (Chemical Oxygen Demand) removal from the dairy industry waste water. Ultrasound (20 kHz) was coupled with H_2O_2, Fenton, and Photo-Fenton process. It was found that the combined process is more efficient than the individual process. The percentage of COD removal depends on the sonication power, duty cycle, and solution pH. A total of 10.11% of COD removal was obtained when ultrasound was used alone at 800 W. When ultrasound was coupled with H_2O_2, the removal efficiency increases to 40.02%. In combination with the Fenton process, the COD removal was found to be 66.22% using ultrasound. The maximum COD removal of 88.78% was obtained when ultrasound was coupled with the Photo-Fenton process (Thakare and Wani, 2018).

Meat and poultry pasteurization: Sonication can be used to inhibit microbial growth in meat. In addition, sonication helps in retaining the color, texture, water retention, curing, marinating, cooking yield, thawing, and freezing. In addition, meat bacterial load can be minimized by using ultrasound in the production line for safe human consumption. It was found that gram-negative bacteria such as Bacillus *Pseudomonas fluorescens, Eschersia coli, Salmonella enterica ssp., Proteus sp*., and *Pseudomonas fluorescens* are sensitive to sonication. Moreover, the Lactic acid, Psychrophilic and mesophilic, psychrophilic, coliforms bacterial load of chicken meat decreases by sonication (Alarcon-Rojo et al., 2015).

Fruit and vegetable industry: Traditionally, decontamination techniques of fresh fruits and vegetables include one or a combination of methods such as washing with chlorine, chlorine dioxide, acidified sodium chloride, organic acid formulations, alkaline-based sanitizers, hydrogen peroxide, ozonated water, electrolyzed water, peroxyacetic acid, and mild heat treatment. In addition, other physical methods such as ultraviolet radiation, pulsed electric field, oscillating magnetic fields, and high pressure. Recently, power ultrasound has been successfully employed in fruit and vegetable industries for decontamination of lettuce, spinach, shredded carrots, truffles, cherry tomatoes, and strawberries. The high power and low-frequency ultrasound (20–45 kHz) and short processing time (1–10 minutes) are mainly used in the fruits and vegetables decontamination process. Although it was found that, for a given acoustic power, different ultrasonic frequency doesn't have a significant effect on the decontamination process. Simple water washing of vegetables can reduce the microbial log by around 1.43 ± 0.04 CFU/g. However, ultrasonic washing can reduce the microbial log of 1.98 ± 0.21 CFU/g. Some studies reported the use of ultrasonication combined with other chemicals such as organic acids, acidified sodium chloride, ethanol, chlorine dioxide for microbial inactivation and found that the combined effect is more beneficial than ultrasonication alone for decontamination of fruits and vegetables (Bilek and Turantaş, 2013).

15.5.2 Cavitation in the biofuel industry

Biofuels are biomass-derived fuels that consist of mainly esters of simple alkyl fatty acid. Because of the high viscosity of vegetable oil, they can't be used directly as fuel in the engine. Therefore, it is necessary to convert vegetable oil into biofuel. Currently, the two most familiar types of biofuels derived by the first-generation biofuel technology are bioethanol and biodiesel (Zore et al., 2021). Ultrasound plays a crucial role in the production of biodiesel and bioethanol from biomass. In this section, the role of power ultrasound in different unit processes of biofuel production is discussed.

15.5.2.1 Lignocellulosic biomass pretreatment

Lignocellulosic materials are the major source of carbon on earth. Therefore, biomass can be considered as a promising alternative source for producing liquid and gaseous fuel, building blocks, and fine chemicals with negligible environmental effects. The major biomass valorization processes include catalytic and biological conversion, pyrolysis, hydrothermal treatment. All these processes require a pretreatment step to ensure selectivity, conversion efficiency, and yield (Badiei et al., 2014; Flores et al., 2021; Silveira et al., 2015). The biomass pretreatment process includes physical, chemical, biological steps aiming at the separation of the biomass constituent such as lignin, cellulose, hemicellulose, and inorganic compounds for further processing. Usually, cellulose and hemicellulose fractions are used as feedstocks in the biorefinery for fermentation. Lignin on the other hand has been used as low energy fuel in industrial processes although researchers are studying extensively valorizing lignin. A considerable amount of lignin valorization industries is in operation around the world (Cherubini, 2010; Cherubini and Strømman, 2011).

The current pretreatment processes are generally based on alkaline/acid hydrolysis, biological treatment, and biomass extrusion. Most of these processes have satisfactory efficiency in biomass treatment. However, the major drawbacks are the excessive use of reagents, long pretreatment time, and extreme conditions such as high temperature and pressure. In this aspect, power ultrasound was widely investigated as an alternative and green pretreatment process. The physical effect caused by power ultrasound such as turbulence, microjets, microlevel mixing, shockwaves were found to be highly efficient

TABLE 15.1 Summary of ultrasonic pre-treatment of different biomass feedstock (Flores et al., 2021).

Biomass feedstock	Ultrasonication	Experimental parameters	Principle outcomes	Ref.
Bagasse	Frequency: 20 kHz,	Sonication time: 20 minutes	Decrease in cellulose dissolution time	(Lan et al., 2011)
	Power: 50 W	Temperature: 110°C		
	Sonicator type: Horn	Solvent: 1-butyl-3-methylimidazolium		
		chloride		
Corn stover	Frequency: 20 kHz,	Sonication time: 180 minutes	Glucose yield of 3 mg/mL of hydrolysate	(Nakashima et al., 2016)
	Power: 50 W	Temperature: 50°C		
	Sonicator type: Horn	Solvent: 0.8 M Na_2CO_3 + 1.2 M H_2O_2		
Grass	Frequency: 25 kHz,	Sonication time: 30 minutes	Increase of sugar production	(Yang and Wang, 2019)
	Power: 260 W	Temperature: 35°C		
	Sonicator type: Horn	Solvent: 1% HCl (wt%)		
Newspaper waste	Frequency: 20 kHz,	Sonication time: 70 minutes	80% of lignin removal	(Subhedar and Gogate, 2014)
	Power: 100 W	Temperature: 80°C		
	Sonicator type: Horn	Solvent: 1 M NaOH		
Rice straw	Frequency: 22 kHz,	Sonication time: 180 minutes	sugars yield of 7 g L-1 of hydrolysate	(Xiong et al., 2017)
	Power: 200 W	Temperature: 25°C		
	Sonicator type: Horn	Solvent: 0.88M H_2O_2+0.2 M $FeSO_4$		
Wheat straw	Frequency: 20 kHz,	Sonication time: 30 minutes	92% of theoretical sugar yield	(Zhong et al., 2017)
	Power: 650 W	Temperature: 50°C		
	Sonicator type: Horn	Solvent: 15% NH_4OH (wt%)		
Wood waste	Frequency: 40 kHz,	Sonication time: -	68% of lignin removal	(Wang et al., 2017)
	Power: 200 W	Temperature: 30°C		
	Sonicator type: bath	Solvent: filamentous fungi		

Modified from (Flores et al., 2021).

in biomass pretreatment (Flores et al., 2021). Power ultrasound used in the pretreatment process is mainly horn-based low-frequency ultrasound with a frequency lower than 50 kHz. It was found that the solubility of biomass increases significantly when sonicated compared to the silent condition. Ultrasound helps to reduce the particle size which increases the contact with the solvent and accelerates the conversion process (Bussemaker and Zhang, 2013; Flores et al., 2021). The main aspect of ultrasonic biomass pretreatment can be attributed to the time reduction, lower process temperature, ability to operate at atmospheric pressure, avoid using excessive chemicals. A hybrid system where ultrasound is combined with a conventional system can be used to achieve higher efficiency. Ultrasonic pretreatment of selected biomass feedstock is summarized in Table 15.1.

15.5.2.2 Biodiesel production from microalgae

The production of biodiesel from microalgae has been extensively studied in the past decade. Certain species of microalgae produce lipids that are potential feedstock for biodiesel substituting vegetable oil. However, one important step in the success of biodiesel production from microalgae is the efficient extraction of these lipids. The lipid is converted into biodiesel through a process called transesterification. In this process, three moles of methanol are required for each mole of triglyceride oil/lipid. Carbohydrates and proteins after the lipid extraction process can be converted into bioethanol through fermentation or biogas by anaerobic digestion. The overall biofuel production routes from microalgae are presented in Fig. 15.3.

Lipid extraction: The lipid composition in microalgae is largely dependent on environmental factors such as temperature, pH, salinity. Extraction of the lipid cells generally requires either disruption of the cell wall to release the cellular contents or the use of a suitable solvent. Microalgae have strong cell walls consisting of different components such as polysaccharides,

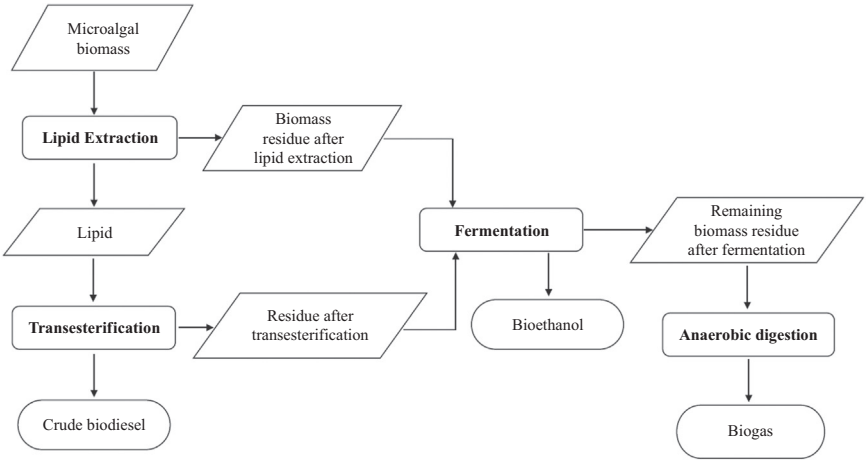

FIGURE 15.3 Biofuel production routes from microalgae.

uronic acid, mannose, xylan algaenan, glycoproteins. To extract the lipid from inside the cell, the cell wall needs to be broken. Ultrasonication has been efficiently used to break down living cells. For lipid extraction from microalgae, it is used in combination with a solvent. Several studies have shown that ultrasound increases the yield of lipid extraction when compared to solvent extraction methods such as Soxhlet, Bligh, dyer, or Folch alone in the absence of ultrasound. Ultrasonic frequency in the range of 20–40 kHz is usually used for lipid extraction. It was found that frequency doesn't play a crucial role in the total lipid yield. One of the most important parameters that affect lipid extraction is the sonication time. The lipid yield increases linearly with the increase in sonication time. However, the lipid yield increases up to an optimum point from where it starts to decrease possibly due to the degradation of the lipids. Moreover, the choice of a solvent also influences the efficiency of ultrasonic extraction (Natarajan et al., 2015).

Transesterification: The use of ultrasonic energy for the transesterification process for biodiesel production was pioneered by Maeda and coworkers (Stavarache et al., 2003). Low-frequency ultrasound (28–40 kHz) was found to decrease the reaction time compared to the mechanical stirring. In addition, the catalyst requirement is also 2–3 times lower. In the presence of ultrasound, the simple chain alcohols react faster whereas the secondary and tertiary alcohols show minor or no conversion effect even for longer sonication time (60 minutes). On the other hand, reaction time (10–20 minutes) is reduced significantly when 40 kHz ultrasound is used. However, the biodiesel production yield (98%–99%) is slightly better when a 28 kHz transducer was used with a longer sonication time. A bench-scale continuous system was also used to study the effect of power ultrasound in transesterification for biodiesel production. In this continuous system, the transesterification reaction highly depends on the residence time in the reactor and alcohol-oil molar ratio (Pulidindi & Gedanken, 2015). Transesterification is a mass transfer limited reaction considering the immiscible nature of the reactants such as lipid and alcohol. Using ultrasound, the mass transfer limitation can be significantly overcome yielding higher conversion efficiency (Kelkar et al., 2008). The mechanism of ultrasound-assisted transesterification reaction was studied by Kalva et al. (2009). It was suggested that the influence of ultrasound in the transesterification reaction is solely physical in nature than chemical. Ultrasonication accelerates the formation of a fine emulsion between the lipid and alcohol due to the microturbulence formed by cavitation activity. Stavarache et al. (2007) have concluded that ultrasonic transesterification for the production of biodiesel can be used for almost all vegetable oil.

15.5.2.3 Bio-ethanol, bio-methane, and bio-hydrogen production

Bioethanol is produced from a variety of lignocellulosic materials through processes consisting of substrate preparation, hydrolysis, fermentation, and purification. A pretreatment can be used also to increase the bioethanol yield. The pretreatment of lignocellulosic biomass helps in the degradation of the lignocellulosic structure which increases the availability of cellulose for enhanced hydrolysis and fermentation for bioethanol production. Several studies have revealed that the yield of bioethanol from sugarcane bagasse, sweet sorghum bagasse, oil palm fronds, rice straw has been significantly improved by using ultrasonication. Low-frequency ultrasound in between 20 and 40 kHz is used in this type of application where the physical effect is more dominant than chemical effects. It was found that increasing sonication time (Methrath Liyakathali et al., 2016) and sonication temperature (Pejin et al., 2012) of 40–60°C increase the yield of bioethanol from sugarcane (Bundhoo and Mohee, 2018).

Biomethane is produced through anaerobic digestion of biomass in an environment deprived of oxygen by a consortium of microorganisms. This technology is matured however due to the low yield from some of the substrates, biomass pretreatment is still necessary. Ultrasonication has been widely studied in the pretreatment of lignocellulosic biomass for delignification, degradations of cellulose crystalline lattice structure, cell degradation, floc disintegration, dissolution of organic matter for enhanced biogas production (Bundhoo & Mohee, 2018; Erden & Filibeli, 2010; Saini et al., 2015). By ultrasonic sludge pretreatment, an increase of methane yield from 5% to 30% has been reported (Akgul et al., 2017; Ruiz-Hernando et al., 2014; Tian et al., 2016; Yeneneh et al., 2013).

Bio-hydrogen can be produced through the dark fermentation of organic compounds in the absence of light and oxygen. Dark fermentation for bio-hydrogen production can occur without pretreatment. However, ultrasonic pretreatment of the substrate for disrupting of lignocellulosic structure, cell degradation, floc disintegration was found to be advantageous for bio-hydrogen production (Bundhoo et al., 2015; Bundhoo & Mohee, 2018). A maximum increase of 17.8% in bio-hydrogen yield was obtained for the sonicated sludge (Guo et al., 2011)

Although most of the studies presented in the literature reported a higher yield of bio-methane and bio-hydrogen from the ultrasonically treated sludge, however, the energy efficiency was found to be negative. Thus, it is concluded that the excess bio-methane or bio-hydrogen production cannot be compensated for the energy penalty required in the ultrasonic pretreatment process (Bundhoo & Mohee, 2018).

15.5.3 Cavitation in the petroleum industry

Power ultrasound has attracted increasing attention in the petroleum industry. The physicochemical effect caused by the periodic oscillation and implosion of acoustic bubbles can be utilized to perform various functions such as enhanced oil recovery, oil sand extraction, demulsification, desulfurization, viscosity reduction, oily wastewater treatment, and oily sludge treatment. In this section, a short overview of the use of ultrasound in these processes is presented.

Enhanced oil recovery: Due to the decrease in oil production, the development of technologies for enhanced oil recovery (EOR) is essential. In enhanced oil recovery, the viscosity and the absorbability of the crude oil are decreased by physical (electromagnetic waves, hydraulic fracturing, and direct current heating) and chemical methods which increases its fluidity (Luo et al., 2021; Yao et al., 2020). Chemical methods which include adding surfactants and acids have the disadvantages of high input cost and contamination of the reservoir. The physical methods are somewhat inefficient and environmentally unfriendly due to the use of potentially hazardous fracking fluid. Power ultrasound is a green and efficient technology that is used for EOR which minimize operating cost and environmental contamination. Ultrasound helps in the reduction of oil viscosity, inhibition of wax crystallization, and permeability of oil reservoir. Ultrasonic cavitation was found to be effective in inhibiting the growth of wax on the reservoir well which may block the oil flow. The long-chain hydrocarbons are broken down to short-chain hydrocarbons due to the cavitation effect which enhances the solubility of the wax. The first use of ultrasonic EOR technology was found in the United States. Oil production is increased by 50% using ultrasound for wells that have the permeability of 20 mD and 15% porosity (Avvaru et al., 2018). Usually, low-frequency (10–35 kHz) and high-power ultrasound (100 kW) are used in the EOR technology (Avvaru et al., 2018; Wang et al., 2017).

Demulsification and desulfurization: In the oil production process, water and surfactant are injected into the well which forms a stable water-oil emulsion. The water has to be removed before transporting and refining the oil since the emulsified water increase the oil viscosity. Moreover, the ions such as Na^{+}, Mg^{2+}, Ca^{2+}, Cl^{-} from the surfactants can corrode the refinery equipment and deactivate the catalyst (Hippmann et al., 2018; Luo et al., 2021; Xu et al., 2019). For crude oil demulsification, demulsifiers and electrostatic methods are widely used. However, the demulsifiers cause environmental pollution and the electrostatic method is found to be inefficient when the high-water content is present in the crude oil. Power ultrasound has been used in numerous lab-scale studies for demulsification due to its low cost, green process, and high adaptability. It was found that standing wave generated by power ultrasound helps in aggregating water droplets into bandings which can subsequently be separated. The optimum frequency for crude oil demulsification was found to be 45 kHz (Antes et al., 2015).

In addition to demulsification, desulfurization is another important step in crude oil processing. Although sulfur is not a harmful impurity in cracking, however, it contributes to the process of coke formation. The most common techniques for desulfurization are hydrotreating, adsorptions, alkaline cleaning, and Merox. All these techniques have the drawbacks of being high energy-intensive, selective of methods, loss of expensive catalyst, and complexity. Power ultrasound is found to be an environmentally friendly and efficient method for desulfurization which increases the degree of desulfurization up to four times (Kuimov et al., 2021).

Oil sand extraction: Oil sands are called bitumen sands that have 3%–20% bitumen, 80%-87% sands and clay, and 3%–6% water. Based on the recent data, Canada has the world's largest (85%) reserve of oil sand. Water washing is the most

widely used method in the petroleum industry for oil sand extraction (La & Guigard, 2015). However, the main drawback of this process is the high-water consumption and contamination of water. Ultrasonic oil sand extraction process is considered to be promising. The oscillating pressure waves can penetrate the bitumen and influence the oil-solid interface. Due to the physicochemical effect and enhanced mass transfer effect attributed by the acoustic cavitation, the bitumen content disintegrates. Microjets formed by cavitation are found to be effective in eroding the bitumen surface causing micro-holes. The micro-holes are responsible for removing the bitumen layer from the sand. On the other hand, highly active radicals formed by cavitation can degrade bitumen into small organic compounds such as resins and oil. It was also found that adding alkali can increase the efficiency of oil sad extraction (Feng & Aldrich, 2000). Sonication enhances the reaction between alkali and carboxylic acid in the bitumen resulting in the formation of in-situ surfactant. This anionic surfactant can reduce the bitumen/water interfacial tension as well as increase the zeta potential resulting in efficient separation of the bitumen from sand (Zhang et al., 2015). Ultrasonic frequency in the range of 20–40 kHz is used for studying different ultrasonic parameters such as acoustic power, sonication time, alkali concentration, and temperature for bitumen recovery from sands (Luo et al., 2021).

Viscosity reduction: Extraction and transportation of heavy oil is challenging due to its very high viscosity (higher than 1000 cP). The heavy oil contains a high amount of asphaltenes which are highly dense, polar, and insoluble in straight-chain alkanes. They tend to precipitate from the crude oil and agglomerate. In addition, the heavy oil viscosity increases exponentially with increasing asphaltene content. Therefore, it is crucial to prevent the agglomeration of asphaltenes for crude oil to reduce it's viscosity. Usually, a light oil or viscosity reducer is mixed with crude oil to reduce its viscosity. In addition, certain heating method is also used for viscosity reduction. However, this method increases the production cost significantly. Ultrasound has been proven to be promising in breaking down large oil molecules into smaller ones reducing crude oil's viscosity (Razavifar & Qajar, 2020). In addition, the dissipation of acoustic energy as heat into the oil reduces viscosity by increasing the temperature. It was observed that the treatment time is the dominant factor affecting viscosity reduction. Ultrasonic frequency in the range of 20 to 40 kHz was found to be effective in the viscosity reduction of crude oil (Luo et al., 2021).

Oily wastewater and sludge treatment: To improve oil production, numerous tertiary methods are used such as alkaline flooding, polymer flooding, and alkaline-surfactant-polymer flooding (ASP). ASP is responsible for producing a large amount of oily wastewater which is more difficult to treat than general wastewater. Several oily wastewater treatment methods such as flotation, membrane filtration, electrochemical methods, and chemical oxidation are being developed in the petroleum industry. Power ultrasound was found to be promising when it was combined with the traditional method for oily wastewater treatment. It was found that ultrasonic degradation of water-soluble polymers is effective in the frequency ranging from 200 to 600 kHz. Ultrasound was also combined with Fenton reagent to increase the oxidation effect on oily wastewater treatment than a standalone method (Yi et al., 2019). In addition, ultrasound can induce the polymerization of flocculants with hydrophobic groups accelerating the removal efficiency of oil from the wastewater. Membrane filtration efficiency for oily wastewater treatment can be improved by using ultrasound. The membrane fouling is one limiting factor in membrane filtration which can be caused overcome by the shockwave and microjets generated by acoustic cavitation (Luo et al., 2021; Zhang et al., 2019).

On the other hand, aqueous ultrasound treatment can be used to treat oily sludge with low energy consumption which produces no harmful gases. Due to the deep penetration of ultrasound, it can reach to the blind holes and gaps, yielding deep cleaning. It was found that the pulse pressure wave of ultrasound forces the water droplets and solid particles to vibrate which destabilizes the oily sludge. These water droplets then collide with each other and coalesce which facilitates the oil-water separation. The mechanism of oily sludge treatment for disintegrating the sludge particle is presented in Fig. 15.4. It can be seen that the mechanical effect is dominant in the treatment process where the shock wave and microjets degrade the hydrogen bonds between oil and solid particle resulting in oil desorption. Low-frequency power ultrasound in the range of 20 to 100 kHz was found to be effective in the oily sludge treatment (Luo et al., 2021).

15.5.4 Cavitation in the metal industry

Power ultrasound has been proven to be a front runner for many nonconventional techniques in the industry because of its environmentally friendly applications and efficiency in many physicochemical processes. As discussed in the earlier section, power ultrasound is already investigated and applied in many industries and several of them have the opportunity to be applied in large-scale operations (Abramov et al., 2019). In this section, application of ultrasound in the metal industry is discussed briefly.

Molten and solidifying metals: The application of ultrasound in molten and solidifying metals is one of the most promising and advanced technologies in the industry. The ultrasonic vibration in liquid metal helps in removing the

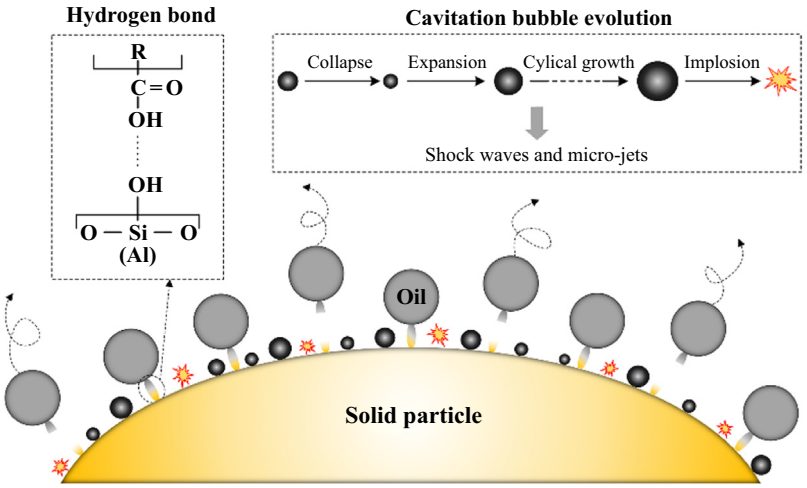

FIGURE 15.4 Mechanism of ultrasound-assisted oily sludge treatment (Luo et al., 2021).

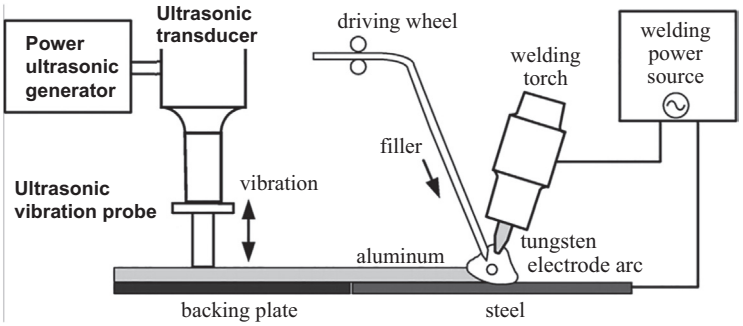

FIGURE 15.5 Schematic representation of ultrasound-assisted gas tungsten arc welding technique (Dong et al., 2012).

solid nonmetallic and gaseous impurities. Ultrasound helps in the reduction of the grain size, formation of equiaxed grains, variation of phase distribution, structure refinement, improvement in material homogeneity, and uniformity in alloy production. These improve the mechanical properties such as the strength and plasticity of the metals. Ultrasound has been used in the metal industry for aluminum and magnesium production where material defects due to solid and gaseous impurities must be minimized. It was observed that the efficiency of ultrasonic degassing is more efficient than conventional melt treatment using chlorine salts and evacuation. Ultrasonication helps in the reduction of hydrogen concentration in the aluminum alloy by the factor of 2–3 compare to untreated metals. In addition, ultrasonic vibration in solidifying metals results in refining its structure and homogeneity of the produced ingot or casting yielding a nondendritic structure (Abramov et al., 2019).

Welding: Ultrasound-assisted welding is found to be promising in improving the weld mechanical properties and microstructure due to the cavitation and acoustic flow created in the molten pool. The acoustic waves produce tensile stresses during the rarefaction phase causing cavitation in the molten pool. Moreover, the nonlinear effect caused by ultrasonication in the molten pool yields local high temperature and pressure regions affecting the solidification process significantly (Cui et al., 2006). Wang & Hong (2011) have developed a new method of twin-arc TIG welding using ultrasonic vibration. This welding method adopted combined ultrasonic arc and conventional DC arc technology. Here ultrasonic arc was used for improving the weld quality and DC arc was used as the main heat source to increase deposition efficiency. This method was proven to be efficient in thinning the micro-structure and improving the tensile properties of the weld. Ultrasonic vibration was also used in the welding of the high-strength aluminum alloy during the gas-tungsten arc welding (GTAW) process. An ultrasonic probe of 28 mm diameter and 20 kHz was placed 30 mm away from the weld pool Fig. 15.5 (Dong et al., 2012). It was found that the grain refinement, decreased Fe-Al intermetallics, microhardness in both the heat-affected zone and the weld were attained due to the ultrasonication. It also increases the weld strength by 27% in GTAW process.

15.6 Conclusion

Ultrasound can be effectively used in intensifying many industrial processes. During ultrasonication of liquid, an enormous amount of localized temperature and pressure is generated through the growth, radial motion, and collapse of bubbles. The intensity of this released energy can break down chemical bonds including plasma and photons. In many practical applications, the secondary effects caused by the cavitation become primary and direct causes for process intensification. The intensity of the secondary effects largely depends on the behavior of bubbles and sonication medium. The optimization of processes under sonication can be achieved through combined techniques of the regularities in cavitation energy, ultrasonic parameters, and reaction requirements. Acoustic cavitation varies greatly between rector types and ultrasonic systems. Proper ultrasonic frequency, power, sonication time, and temperature must be taken into consideration when applying ultrasound in different processes.

A diverse set of applications of acoustic cavitation and sonochemistry in the industry has been explored with important applications in the food, biofuel, and petroleum industry. The main application of ultrasound in food industry lies in the area of microorganism and enzyme activation and deactivation in dairy processing, meat and poultry pasteurization and decontamination of fruits and vegetables. On the other hand, acoustic cavitation and sonochemistry have a wide range of applications in the biofuel industry. These include biomass pretreatment, fermentation, and biodiesel production. Both physical and chemical effects induced by power ultrasound are responsible for the enhancement in the biofuel production processes. Acoustic frequency and power play a dominant role here. Moreover, power ultrasound possesses great aspects in both the upstream and downstream processing in the petroleum industry. In many oil fields, power ultrasound has been employed successfully increasing oil production. It is foreseen that the low frequency and high-power ultrasound are likely to remain the trend of industrial development of ultrasound where both the physical and chemical effect is dominant. However, the factors that appear to hinder the large-scale application of power ultrasound are the competition between the other less expensive processes, scaling up, general lack of information for proper application. For promoting the future application of ultrasonic technology in the industry, it is crucial to have adequate knowledge of the specific industrial problems.

References

Abramov, V., Abramova, A., Cravotto, G., Nikonov, R., Sister, V., Mazurkiewicz, A., Piatkiewicz, W., Smolik, J., Majcher, A., 2019. Industrial applications of high-intensity ultrasound. DEStech Transactions on Computer Science and Engineering. https://doi.org/10.12783/dtcse/fe2019/30700.

Akdeniz, V., Akalın, A.S., 2020. Recent advances in dual effect of power ultrasound to microorganisms in dairy industry: activation or inactivation. Crit. Rev. Food Sci. Nutr. https://doi.org/10.1080/10408398.2020.1830027.

Deniz, A., Monica, A.C., Cigdem, E., 2017. Influences of low-energy input microwave and ultrasonic pretreatments on single-stage and temperature-phased anaerobic digestion (TPAD) of municipal wastewater sludge. Energy 123, 271–282.

Alarcon-Rojo, A.D., Janacua, H., Rodriguez, J.C., Paniwnyk, L., Mason, T.J., 2015. Power ultrasound in meat processing. Meat Sci. 107, 86–93. https://doi.org/10.1016/j.meatsci.2015.04.015.

Antes, F.G., Diehl, L.O., Pereira, J.S.F., Guimarães, R.C.L., Guarnieri, R.A., Ferreira, B.M.S., Dressler, V.L., Flores, E.M.M., 2015. Feasibility of low frequency ultrasound for water removal from crude oil emulsions. Ultrason. Sonochem. 25 (1), 70–75. https://doi.org/10.1016/j.ultsonch.2015.01.003.

Arnold, G., Zahn, S., Legler, A., Rohm, H., 2011. Ultrasonic cutting of foods with inclined moving blades. J. Food Eng. 103 (4), 394–400. https://doi.org/10.1016/j.jfoodeng.2010.11.009.

Ashokkumar, M., Mason, T.J., 2007. Sonochemistry," in kirk-othmer encyclopedia of chemical technology.

Astráin-Redín, L., Ciudad-Hidalgo, S., Raso, J., Condón, S., Cebrián, G., Álvarez, I., 2020. Application of high-power ultrasound in the food industry. IntechOpen. https://doi.org/10.5772/intechopen.90444.

Avvaru, B., Venkateswaran, N., Uppara, P., Iyengar, S.B., Katti, S.S., 2018. Current knowledge and potential applications of cavitation technologies for the petroleum industry. Ultrason. Sonochem. 42, 493–507. https://doi.org/10.1016/j.ultsonch.2017.12.010.

Badiei, M., Asim, N., Jahim, J.M., Sopian, K., 2014. Comparison of chemical pretreatment methods for cellulosic biomass. APCBEE Procedia, 170–174. https://doi.org/10.1016/j.apcbee.2014.01.030.

Bilek, S.E., Turantaş, F., 2013. Decontamination efficiency of high power ultrasound in the fruit and vegetable industry, a review. Int. J. Food Microbiol. 166 (1), 155–162. https://doi.org/10.1016/j.ijfoodmicro.2013.06.028.

Bundhoo, M.A.Z., Mohee, R., Hassan, M.A., 2015. Effects of pre-treatment technologies on dark fermentative biohydrogen production: a review. J. Environ. Manage. 157, 20–48. https://doi.org/10.1016/j.jenvman.2015.04.006.

Bundhoo, Z.M.A., Mohee, R., 2018. Ultrasound-assisted biological conversion of biomass and waste materials to biofuels: a review. Ultrason. Sonochem. 40, 298–313. https://doi.org/10.1016/j.ultsonch.2017.07.025.

Bussemaker, M.J., Zhang, D., 2013. Effect of ultrasound on lignocellulosic biomass as a pretreatment for biorefinery and biofuel applications. Ind. Eng. Chem. Res. 52 (10), 3563–3580. https://doi.org/10.1021/ie3022785.

Cherubini, F., 2010. The biorefinery concept: using biomass instead of oil for producing energy and chemicals. Energy Convers. Manage. 51 (7), 1412–1421. https://doi.org/10.1016/j.enconman.2010.01.015.

Cherubini, F., Strømman, A.H., 2011. Chemicals from lignocellulosic biomass: opportunities, perspectives, and potential of biorefinery systems. Biofuels, Bioproducts and Biorefining, 5 (5), 548–561. https://doi.org/10.1002/bbb.297.

Cui, Y., Xu, C.L., Han, Q., 2006. Effect of ultrasonic vibration on unmixed zone formation. Scr. Mater. 55 (11), 975–978. https://doi.org/10.1016/j.scriptamat.2006.08.035.

Dong, H., Yang, L., Dong, C., Kou, S., 2012. Improving arc joining of al to steel and al to stainless steel. Mater. Sci. Eng. A 534, 424–435. https://doi.org/10.1016/j.msea.2011.11.090.

Erden, G., Filibeli, A., 2010. Ultrasonic pre-treatment of biological sludge: consequences for disintegration, anaerobic biodegradability, and filterability. J. Chem. Technol. Biotechnol. 85 (1), 145–150. https://doi.org/10.1002/jctb.2298.

Feng, D., Aldrich, C., 2000. Sonochemical treatment of simulated soil contaminated with diesel. Adv. Environ. Res. 4 (2), 103–112. https://doi.org/10.1016/S1093-0191(00)00008-3.

Flores, E.M.M., Cravotto, G., Bizzi, C.A., Santos, D., Iop, G.D., 2021. Ultrasound-assisted biomass valorization to industrial interesting products: state-of-the-art, perspectives and challenges. Ultrason. Sonochem. 72. https://doi.org/10.1016/j.ultsonch.2020.105455.

Guo, W.Q., Ding, J., Cao, G.L., Ren, N.Q., Cui, F.Y., 2011. Treatability study of using low frequency ultrasonic pretreatment to augment continuous biohydrogen production. Int. J. Hydrogen Energy 36 (21), 14180–14185. https://doi.org/10.1016/j.ijhydene.2011.04.057.

Hippmann, S., Ahmed, S.S., Fröhlich, P., Bertau, M., 2018. Demulsification of water/crude oil emulsion using natural rock alginite. Colloids Surf. A 553, 71–79. https://doi.org/10.1016/j.colsurfa.2018.05.031.

Islam, M.H., Burheim, O.S., Pollet, B.G., 2019. Sonochemical and sonoelectrochemical production of hydrogen. Ultrason. Sonochem. 51, 533–555. https://doi.org/10.1016/j.ultsonch.2018.08.024.

Kalva, A., Sivasankar, T., Moholkar, V.S., 2009. Physical mechanism of ultrasound-assisted synthesis of biodiesel. Ind. Eng. Chem. Res. 48 (1), 534–544. https://doi.org/10.1021/ie800269g.

Kelkar, M.A., Gogate, P.R., Pandit, A.B., 2008. Intensification of esterification of acids for synthesis of biodiesel using acoustic and hydrodynamic cavitation. Ultrason. Sonochem. 15 (3), 188–194. https://doi.org/10.1016/j.ultsonch.2007.04.003.

Kentish, S., Feng, H., 2014. Applications of power ultrasound in food processing. Annual Rev of Food Sci and Technol 5 (1), 263–284. https://doi.org/10.1146/annurev-food-030212-182537.

Kuimov, D., Minkin, M., Lukyanov, A., Abderrazzak, E.H., Tung, P.D., Mladenovic, V., Petkovic, M., Antipov, S., 2021. Cavitation as a method of improving the energy efficiency of oil industry enterprises. E3S Web of Conferences, 279, 01015. https://doi.org/10.1051/e3sconf/202127901015.

La, H., Guigard, S.E., 2015. Extraction of hydrocarbons from athabasca oil sand slurry using supercritical carbon dioxide. J. Supercrit. Fluids 100, 146–154. https://doi.org/10.1016/j.supflu.2015.01.020.

Lan, Wu, Liu, Chuan-Fu, Yue, Feng-Xia, Sun, Run-Cang, Kennedy, John F., 2011. Ultrasound-assisted dissolution of cellulose in ionic liquid. Carbohydrate Polymers 86 (2).

Legay, M., Gondrexon, N., Le Person, S., Boldo, P., Bontemps, A., 2011. Enhancement of heat transfer by ultrasound: review and recent advances. Int J Chem Eng 1–17. https://doi.org/10.1155/2011/670108.

Lide, D.R., Frederikse, H.P.R., 1994. Handbook of chemistry and physics.

Luo, X., Gong, H., He, Z., Zhang, P., He, L., 2021. Recent advances in applications of power ultrasound for petroleum industry. Ultrason. Sonochem. 70. https://doi.org/10.1016/j.ultsonch.2020.105337.

Mason, T., 1990. Sonochemistry: The Uses of Ultrasound in Chemistry. Royal Society of Chemistry, London, pp. 25–54.

Mason, T.J., 1999. Sonochemistry: current uses and future prospects in the chemical and processing industries. Philosophical Transactions of the Royal Soc A: Mathematical, Physical and Eng Sci, 357 (1751), 355–369. https://doi.org/10.1098/rsta.1999.0331.

Methrath Liyakathali, N.A., Muley, P.D., Aita, G., Boldor, D., 2016. Effect of frequency and reaction time in focused ultrasonic pretreatment of energy cane bagasse for bioethanol production. Bioresour. Technol. 200, 262–271. https://doi.org/10.1016/j.biortech.2015.10.028.

Mumtaz, A., 2019. Ultrasounds: a recent perspective in food industry. Pakistan J. Agric. Res 32, 334–342.

Nakashima, K., Ebi, Y., Kubo, M., Shibaski-Kitakawa, N., Yonemoto, T., 2016. Pretreatment combining ultrasound and sodium percarbonate under mild conditions for efficient degradation of corn stover Ultrason. Sonochem. 29, 455–460.

Natarajan, Chen, Lau, R., 2015. Ultrasound applications in lipid extractions from microalgae. Production of Biofuels and Chemicals with Ultrasound, 4. Springer, Dordrecht, pp. 117–139.

Pejin, D.J., Mojović, L.V., Pejin, J.D., Grujić, O.S., Markov, S.L., Nikolić, S.B., Marković, M.N., 2012. Increase in bioethanol production yield from triticale by simultaneous saccharification and fermentation with application of ultrasound. J. Chem. Technol. Biotechnol. 87 (2), 170–176. https://doi.org/10.1002/jctb.2675.

Pollet, B.G., 2012. Power ultrasound in electrochemistry: from versatile laboratory tool to engineering solution. Power Ultrasound in Electrochemistry: From Versatile Laboratory Tool to Engineering Solution. John Wiley and Sons, West Sussex, pp. 1–344. https://doi.org/10.1002/9781119967392.

Pulidindi, I., Gedanken, A., 2015. Employing novel techniques (Microwave and sonochemistry) in the synthesis of biodiesel and bioethanol. In Springer book series-production of biofuels and chemicals: ultrasound (Vol. 4, pp. 159–185). https://doi.org/10.1007/978-94-017-9624-8_6.

Razavifar, M., Qajar, J., 2020. Experimental investigation of the ultrasonic wave effects on the viscosity and thermal behaviour of an asphaltenic crude oil. Chem Eng and Processing - Process Intensification 153. https://doi.org/10.1016/j.cep.2020.107964.

Ruiz-Hernando, M., Martín-Díaz, J., Labanda, J., Mata-Alvarez, J., Llorens, J., Lucena, F., Astals, S., 2014. Effect of ultrasound, low-temperature thermal and alkali pre-treatments on waste activated sludge rheology, hygienization and methane potential. Water Res. 61, 119–129. https://doi.org/10.1016/j.watres.2014.05.012.

Saini, A., Aggarwal, N.K., Sharma, A., Yadav, A., 2015. Prospects for irradiation in cellulosic ethanol production. Biotechnology Res Int 1–13. https://doi.org/10.1155/2015/157139.

Silveira, M.H.L., Morais, A.R.C., Da Costa Lopes, A.M., Olekszyszen, D.N., Bogel-Łukasik, R., Andreaus, J., Pereira Ramos, L., 2015. Current pretreatment technologies for the development of cellulosic ethanol and biorefineries. ChemSusChem 8 (20), 3366–3390. https://doi.org/10.1002/cssc.201500282.

Stavarache, C., Vinatoru, M., Nishimura, R., Maeda, Y., 2003. Conversion of vegetable oil to biodiesel using ultrasonic irradiation. Chem. Lett. 32 (8), 716–717. https://doi.org/10.1246/cl.2003.716.

Stavarache, C., Vinatoru, M., Maeda, Y., 2007. Aspects of ultrasonically assisted transesterification of various vegetable oils with methanol. Ultrason. Sonochem. 14 (3), 380–386. https://doi.org/10.1016/j.ultsonch.2006.08.004.

Subhedar, Preeti B., Gogate, Parag R., 2014. Alkaline and ultrasound assisted alkaline pretreatment for intensification of delignification process from sustainable raw-material. Ultrason. Sonochem. 21 (1), 216–225.

Suslick, K.S., 1990. Sonochemistry. Science 247 (4949), 1439–1445. https://doi.org/10.1126/science.247.4949.1439.

Thakare, Y.D., Wani, K.S., 2018. Acoustic cavitation coupled with advance oxidation process for treatment of dairy industry wastewater. Int. J. Creat. Res. Thoughts-IJCRT 6, 79–90.

Tian, X., Trzcinski, A.P., Lin, L.L., Ng, W.J., 2016. Enhancing sewage sludge anaerobic \re-digestion\ with combinations of ultrasonic, ozone and alkaline treatments. J Environmental Chem Eng. 4 (4), 4801–4807. https://doi.org/10.1016/j.jece.2016.10.032.

Wang, J.J., Hong, X.O., 2011. Research on twin-arc tig welding with ultrasonic excitation and its effect to weld. Key Engineering Materials, 450. Trans Tech Publications Ltd, pp. 300–303.

Wang, Q.-F., Niu, L.-l., Jiao, J., Guo, N., Zang, Y.-P., Gai, Q.-Y., Fu, Y.-J., 2017. Degradation of lignin in birch sawdust treated by a novel Myrothecium verrucaria coupled with ultrasound assistance. Bioresour. Technol. 244 (1), 969–974.

Wang, Z., Zeng, J., Song, H., Li, F., 2017. Research on ultrasonic excitation for the removal of drilling fluid plug, paraffin deposition plug, polymer plug and inorganic scale plug for near-well ultrasonic processing technology. Ultrason. Sonochem. 36, 162–167. https://doi.org/10.1016/j.ultsonch.2016.11.026.

Xiong, Z.-Y., Qin, Y.-H., Ma, J.-Y., Yang, L., Wu, Z.-K., Wang, T.-L., Wang, W.-G., Wang, C.-W., 2017. Pretreatment of rice straw by ultrasound-assisted Fenton process. Bioresour. Technol. 277, 408–411.

Xu, X., Cao, D., Liu, J., Gao, J., Wang, X., 2019. Research on ultrasound-assisted demulsification/dehydration for crude oil. Ultrason. Sonochem. 57, 185–192. https://doi.org/10.1016/j.ultsonch.2019.05.024.

Yang, G., Wang, J., 2019. Ultrasound combined with dilute acid pretreatment of grass for improvement of fermentative hydrogen production. Bioresour. Technol. 275, 10–18. doi:10.1016/j.biortech.2018.12.013.

Yao, Y., Pan, Y., Liu, S., 2020. Power ultrasound and its applications: a state-of-the-art review. Ultrason. Sonochem. 62. https://doi.org/10.1016/j.ultsonch.2019.104722.

Yasui, K., 2016. Unsolved problems in acoustic cavitation #9. Handbook of Ultrasonics and Sonochemistry. Springer, Singapore, pp. 259–292.

Yasui, Kyuichi., 2018. Acoustic cavitation. SpringerBriefs in Molecular Science. Springer Nature, Cham, pp. 1–35 https://doi.org/10.1007/978-3-319-68237-2.

Yeneneh, A.M., Chong, S., Sen, T.K., Ang, H.M., Kayaalp, A., 2013. Effect of ultrasonic, microwave and combined microwave-ultrasonic pretreatment of municipal sludge on anaerobic digester performance. Water Air Soil Pollut. 224 (5). https://doi.org/10.1007/s11270-013-1559-4.

Yi, Z., Ma, X., Song, J., Yang, X., Tang, Q., 2019. Investigations in enhancement biodesulfurization of model compounds by ultrasound pre-oxidation. Ultrason. Sonochem. 54, 110–120. https://doi.org/10.1016/j.ultsonch.2019.02.009.

Zhang, R., Huang, Y., Sun, C., Xiaozhen, L., Bentian, X., Wang, Z., 2019. Study on ultrasonic techniques for enhancing the separation process of membrane. Ultrason. Sonochem. 55, 341–347. https://doi.org/10.1016/j.ultsonch.2018.12.041.

Zhang, Y., Ding, M., Liu, J., Jia, W., Ren, S., 2015. Studies on bitumen-silica interaction in surfactants and divalent cations solutions by atomic force microscopy. Colloids Surf. A 482, 241–247. https://doi.org/10.1016/j.colsurfa.2015.05.012.

Zhong, Chao, Jia, Honghua, Wei, Ping, 2017. Enhanced saccharification of wheat straw with the application of ultrasonic-assisted quaternary ammonium hydroxide pretreatment. Process Biochemistry 53, 180–187.

Zore, U.K., Yedire, S.G., Pandi, N., Manickam, S., Sonawane, S.H., 2021. A review on recent advances in hydrogen energy, fuel cell, biofuel and fuel refining via ultrasound process intensification https://doi.org/10.1016/j.ultsonch.2021.105536.

Chapter 16

Crystallization of pharmaceutical compounds: Process Intensification using ultrasonic irradiations - Experimental approach

Hamza Ferkous[a] **and Oualid Hamdaoui**[b]

[a] *Department of Process Engineering, Faculty of Tehnology, Badji Mokhtar - Annaba University, Algeria,* [b] *Chemical Engineering Department, College of Engineering, King Saud University, Riyadh, Saudi Arabia*

16.1 Introduction

Pharmaceutical industries use often crystallization as a unit operation for purification and separation processes (Lee and Yang, 2018). It is one of the best cheaper methods available for purification, recovery of solid, or production of pure materials from impure solutions (Duroudier, 2016). Food, chemicals, and pharmaceutical are the principal examples where the control of crystal size, distribution, crystalline form, and crystal polymorphism is important due to their impact on the purity and quality of crystalline particles (Takiyama, 2012). The first step in a process is to generate supersaturation to carry out the crystallization. These two categories of crystallization: (1) from a solution and (2) from a melt. The first involves the formation and growth of solid crystals of a solute in a supersaturated liquid solution. The second occurs when the temperature of a liquid is lowered below its freezing point and solid crystals of the substance are allowed to form (Ensminger and Bond, 2011). The use of ultrasonic waves increases the supersaturation, reduces the nucleation time, and inhibits the particle agglomeration, which in turn affects the size, shape and particle size distribution (Miyasaka et al., 2006). The application of ultrasound reduces the nucleation time and improves the distribution size by increasing the rate of crystallization (Yasui and Ashokkumar, 2011). There are two effects of ultrasound on the crystallization process: (1) physical effect which improves the solubility, and (2) chemical where the hydroxyl radicals are produced through cavitation. The effects of ultrasound on crystallization influence the induction period, supersaturation concentration, and metastable zone width (Luque de Castro and Priego-Capote, 2007).

16.2 Theorical approach

The acoustic wave is defined as the propagation of pressure oscillation with sound velocity in a medium such as liquid, gas or solid (Pierce, 2019). Cavitation is defined as a dynamic phenomenon involving nonlinear dynamics acoustics and various physical parameters due to change of liquid pressure, and it is mainly characterized by continuous formation and strong collapse of cavitation bubbles (Ye and Zhu, 2017). Cavitation can be separated into ultrasonic cavitation and hydrodynamic cavitation, and both change liquid environment pressure respectively by applying acoustic pressure load and special flow system geometric structure, leading to the cavitation phenomenon (Ye and Zhu, 2017).

Chemical and physical effects are the results of acoustic cavitation and do not take place by direct interactions between ultrasound and chemical spices (Kim and Suslick, 2018). The collapse of bubbles produces hot spots, which have intense local temperatures (∼5000 K) and pressure (∼1000 atm) and a rapid heating and cooling rate ($>10^{10}$ K/s) (McNamara et al., 1999) (McNamara et al., 2003). Cavitational collapse liberates shockwaves that have velocities as high as ∼4000 m/s and high-pressure amplitudes of 10^6 kPa (Sander et al., 2014). Unaccustomed sonochemical effects are produced by these

Energy Aspects of Acoustic Cavitation and Sonochemistry: Fundamentals and Engineering. DOI: https://doi.org/10.1016/B978-0-323-91937-1.00011-6
Copyright © 2022 Elsevier Inc. All rights reserved.

shockwaves, most importantly, high velocity collisions among solid particles suspended in such liquids. These collisions result in extreme heating at the point of impact, which can lead to effective local melting and dramatic increases in the rates of many solid–liquid reactions (Prozorov et al., 2004).

The physical effects may vary from the mechanical turbulence created due to the passage of ultrasound through water, namely vibration and acoustic streaming, to the physical consequences of acoustic cavitation, namely cavitation microstreaming, microjets and shockwaves (Yasui and Ashokkumar, 2011).

Crystallization from a solution is a core technology in major sectors of the chemical process and allied industries. Crystals are produced in varying sizes ranging from as small as a few a nanometer to several millimeters or more, both as discrete particles and structured agglomerates. Well-established examples include bulk and fine chemicals and their intermediates, such as common salt, sodium carbonate, zeolite catalysts and absorbents, ceramic and polyester precursor, detergents, fertilizers, foodstuffs, pharmaceuticals, and pigments. Particulate crystallization processes often require subsequent solid-liquid separation (Jones, 2003).

The application of ultrasound to crystallizations has offered significantly improved access to a large variety of crystalline materials (Sander et al., 2014). The first examination of the effect of ultrasound on crystallization (i.e., sonocrystallization) was reported in 1927 by Richards and Loomis (Richards and Loomis, 1927). The application of ultrasound in crystallization has been shown several positive effects on crystal nucleation rate, metastable zone width, crystal size distribution and crystal growth (Lee et al., 2018).

To create a solid phase, all industrial crystallizers employ various methods to give birth supersaturation by cooling and/or evaporation (Jones, 2003). Crystallization from a melt takes place when the temperature of the liquid is decreased below its freezing point and solid crystals of the substance are allowed to form (Ensminger and Bond, 2011). The steps in a process of forming single crystals from solution include: supersaturation, nucleation, diffusion of the solute from the solution to the solid surface and separating the crystals from the remaining liquid. The benefits obtained by sonocrystallization have been widely studied since the beginning of the 20th century and so far, it is clear that ultrasound can be a very useful tool for enhancing crystallization and controlling the properties of the final product. Crystal size, polymorphs, purity, process reproductivity and lower induction time are only some of the advantages of sonocrystallization (Nalesso et al., 2019). The employment of ultrasound to crystallization in the pharmaceutical and fine chemicals sectors of industry has received further impetus in recent years with the improved concentration on the specificity of effect, and the corresponding exigency to produce and purify complex chemical entities to very exigent standards (Ruecroft et al., 2005).

16.3 Physical effect of cavitation bubble on crystallization

16.3.1 Supersaturation

Supersaturation can be easily understood by a solution in which the solute concentration exceeds the equilibrium (saturation) solution concentration at a given temperature is known as a supersaturated solution. Supersaturated solutions are metastable. A metastable solution is represented as an inflection point where a small change is needed to change the state of the system, but one which is finite (Xu et al., 2017).

We can define the supersaturation by the fundamental driving force for crystallization and can be expressed dimensionless form as:

$$\frac{\mu - \mu^*}{RT} = \ln \frac{a}{a^*} = \ln \frac{\gamma c}{\gamma^* c^*} \tag{16.1}$$

Where μ is the chemical potential, c is the concentration, a is the activity γ is the activity coefficient and * represents the property at saturation. The activity coefficients are not known and the dimensionless chemical potential difference is approximated by the dimensionless concentration difference

$$\sigma = c - \frac{c^*}{c^*} \tag{16.2}$$

This substitution is only accurate when $\frac{\gamma}{\gamma^*} = 1$ or $\sigma \ll 1$ so that $\ln(\sigma + 1) = \sigma$. It has been shown that is generally a poor approximation at $\sigma > 0.1$ (Kim and Myerson, 1996), but it is still normally used because the needed thermodynamic data are usually unavailable. Supersaturation is also often expressed as a concentration difference

$$\Delta c = c - c^* \tag{16.3}$$

And as a ratio of concentrations

$$S = \frac{c}{c^*} \tag{16.4}$$

It is important to note that these definitions of supersaturation assume an ideal solution with an activity coefficient of 1. It is common practice to ignore activity coefficients in most cases and employ concentrations in expressions of supersaturation, however, in very nonideal solutions and precise studies of crystal growth and nucleation, activity coefficients are often used (Xu et al., 2017).

Another practice is to refer to supersaturation in terms of degrees. This refers to the difference between the temperature of the solution and the saturation temperature of the solution at the existing concentration. A simpler way to explain this is that the degrees of supersaturation is simply the number of degrees a saturated solution of the appropriate concentration was cooled to reach its current temperature. This is generally not a good unit to use, however, it is often mentioned in many studies (Xu et al., 2017).

The induction time is the passed time between supersaturation and the appearance of crystals. The use of ultrasonic irradiation decreases induction time due to the improved micro-scale mixing and turbulence caused by acoustic cavitation (H. N. Kim and Suslick, 2018). The effect of ultrasound on the induction time for the operation of crystallization was reported in many studies. When the sonocrystallization was performed the induction time was decreased (Guo et al., 2005). When the supersaturated ratio of the solution was reduced the difference in induction time between sonocrystallization and classic crystallization was enhanced (Guo et al., 2005).

The effects of ultrasound irradiations on the induction time of saturated roxithromycin solutions were inspected by Guo et al. (2005). When the supersaturation increases, the induction time decreases with and without ultrasound irradiations. On the other hand, ultrasound waves reduce significantly the induction time. At low absolute supersaturations, this effect is much more significant than the effect of high supersaturations levels.

M. Kurotani et al. studied the effect of ultrasound irradiation on the behavior of primary nucleation of amino acids in supersaturated solutions (Kurotani et al., 2009). In the presence of ultrasonic irradiation, the induction periods for three different supersaturations S (where S is the supersaturation ratio) are enhanced with increasing amounts of ultrasonic energy up to a certain level (Kurotani et al., 2009).

However, it was reported by Miyasaka et al. that the medium number of crystals increased from 13 to 9700 with increases in ultrasonic irradiation time at 4.5 W. Also, at 2.5 W, the increasing of ultrasonic irradiation time engenders a lowering of the medium number of crystals (Miyasaka et al., 2006).

16.3.2 Nucleation

The process of crystallization takes place across complex processes, evolving from the nucleation in the supersaturated system, followed by aggregation and growthbian (Guo et al., 2022). To describe homogeneous phase transitions and to provide a qualitative understanding of nucleation, classical nucleation theory (CNT) is one of the most commonly used theorical frameworks due to its simplicity and is still used to clarify experiments and simulations (Fitzner et al., 2017). The cluster size is the only pertinent parameter to the nucleation barrier and when the nucleus attains critical size, it can rise within a novel phase (Guo et al., 2022). It was reported that the cavitation bubbles resulting from ultrasound increase the nucleation rate during sonocrystallization (Bund and Pandit, 2007). The use of the CNT of crystallization to inspect the effects of acoustic waves is limited (Lee and Yang, 2018). It can be said that every cavity takes up a little part of solvent causing prompt local supersaturation. Every cavity generated represents a nucleation site for crystallization. The bubble collapse near a wall will generate a strong micro-jet in a liquid environment under an ultrasonic field and these nuclei are embarked toward the crystallization slurry resulting in additional cavitational opportunities (Bund and Pandit, 2007). The application of ultrasound to enhance the crystallization recovery was examined in several works. The high local temperatures and pressures combined with the microstreaming participate to boost mass and heat transfer (Khaire and Gogate, 2021). Khaire et al. was reported that the diffusion capacity of molecules expands with ultrasound power intensity and hence increases the nucleation rate in sonocrystallization (Khaire and Gogate, 2021). It was mentioned by Virone et al. that to provoke nucleation with a small sensitivity for the initial supersaturation and additionally the pressure pulse generated during the collapse of the cavitating bubbles, an acoustic cavitation is a performant tool (Virone et al., 2006). Lyczko et al exanimated the cooling mode of the crystallization of potassium sulphate in a batch reactor and mentioned that in presence of ultrasound, the induction time decreases from 9000 s to 1000 s (Vishwakarma and Gogate, 2017). The use of ultrasound in crystallization can also speed up the rate of nucleation of sucrose, D-fructose and sorbitol, and similarly generate nucleation in the crystallization system (Srinivasan et al., 1995).

16.3.3 Crystal growth

The speed of formation of a new crystallized solid principally depends on two mechanisms: crystal nucleation and growth (Uccheddu et al., 2011). The speed of crystal growth can be displayed as the rate of movement of a given crystal surface in the direction perpendicular to the face. Various faces of a crystal, nevertheless, usually have different linear growth rates. Variation occurs in the shape of crystals when individual faces grow at different rates, the overall crystal habit being determined by the slowest growing face (Jones, 2003).

Ultrasound can affect crystallization through the mechanisms of cavitation and acoustic streaming. Cavitation appears to be particularly effective as a means of inducing nucleation, and there is evidence of dramatic improvements in reproducibility obtained through sononucleation. These permits focus on controlling the crystal growth via the residence time in the crystallizer (Ruecroft et al., 2005). Several studies were published relating to increasing the crystallization process. The application of ultrasound to a liquid generates the phenomenon of cavitation in the process fluid. This cavitation effect produces bubbles during consecutive cycles of compression and rarefaction to a point of transient bubble collapse, maybe after only two acoustic cycles. This bubble collapse generates highly spatially resolved regions of extreme excitation, temperature (5000 K) and pressure (2000 atm), as well as concomitant release of shock waves (Ruecroft et al., 2005). The crystallization process increases with ultrasonic irradiations and it is generally due to the physical effects of cavitation associated with ultrasonic treatment, which intensify the crystal growth and subsequently the rate of crystallization (Khaire and Gogate, 2021).

16.4 Sonocrystallization of pharmaceutical compounds: Effect of operating parameters

16.4.1 Effect of US frequency

Many studies have mentioned the contribution of ultrasound in enhancing crystallization, additionally establishing the importance of frequency, and power of ultrasound (Jordens et al., 2019). The use of ultrasound in crystallization processes serves to reach control over nucleation, crystal growth, and fragmentation and therefore affect the particle size distribution, crystal, and polymorphic form (Dhumal et al., 2009). The utilization of lower frequencies between 20 kHz and 5 MHz can be created a large amount of acoustic energy to provoke cavitation bubbles in liquid (Jordens et al., 2019). The range of low frequency (particularly 15, 20, 25, and 30 were used too in the fast sonocrystallization (Li et al., 2003). Therefore, the application of these wavelengths has no evident differences in the form, the mean size, and the size distribution of resulting crystals, this signifies that these different frequencies have a similar impact on the nucleation and growth of crystals (Li et al., 2003). Low ultrasonic frequencies are optimal to enhance nucleation and fragmentation rates. This optimal frequency range can be supposed to be generally valid as the same frequency range between 20 and 100 kHz is commonly reported as the optimal one for enhancement of nucleation and fragmentation in bibliography (Jordens et al., 2019). Jordens et al. investigated the effect of frequencies of 16, 41, 98, 165, 570, 850, and 1140 kHz on the metastable zone width in one single reactor geometry and at the same calorimetric power of Acetaminophen. It was mentioned the highest reduction in MZW, and hence the fastest nucleation at a frequency of 41 kHz (Jordens et al., 2019). Bhangu et al. examined the effect of ultrasonic frequencies at 22, 44, 98, and 139 kHz but in various crystallization vessels and in a mixture of ethanol–water instead of pure water. The lowest induction times were noted at 98 kHz instead of 44 kHz (Kaur Bhangu et al., 2016a). The author supposed that, at 98 kHz, there was an optimum between the number of cavitation bubbles and the size of bubbles. Therefore, it is possible that the number of crystal nuclei formed would rise with increasing frequency and power (Jordens et al., 2019). At very high frequencies, the cavitational effect is decreased because either: (1) the rarefaction cycle of the sound wave creates a negative pressure which is insufficient in its duration and/or intensity to initiate cavitation or (2) the compression cycle occurs faster than the time for the microbubble to collapse. Lower frequency ultrasound generates more brutal cavitation, driving to higher localized temperatures and pressures (Adewuyi, 2001).

To inspect the effect of frequency on the sonocrystallization of sodium chloride, experiments were realized using two different frequencies: 45 kHz and 1700 kHz. The schematic of ultrasonic reactors is shown in Fig. 16.1. Fig. 16.2 represents the effect of US frequency on the change of sodium chloride crystals. Larger crystals size was obtained at low frequency which was attributed to enhanced crystal growth. Low frequencies generate principally bubbles of a transient type which grow to a large size and collapse more violently. High frequencies generate bubbles predominantly of stable cavitation type. Furthermore, as the number of cavitation bubbles increases, the intensity of the bubble collapse reduces with enhancing the US frequency. Similarly, to these results, Sánchez-García et al. (2019), Kaur Bhangu et al. (2016b) and Jordens et al. (2019) reported a reduction in the crystal size distribution with improving the US frequency.

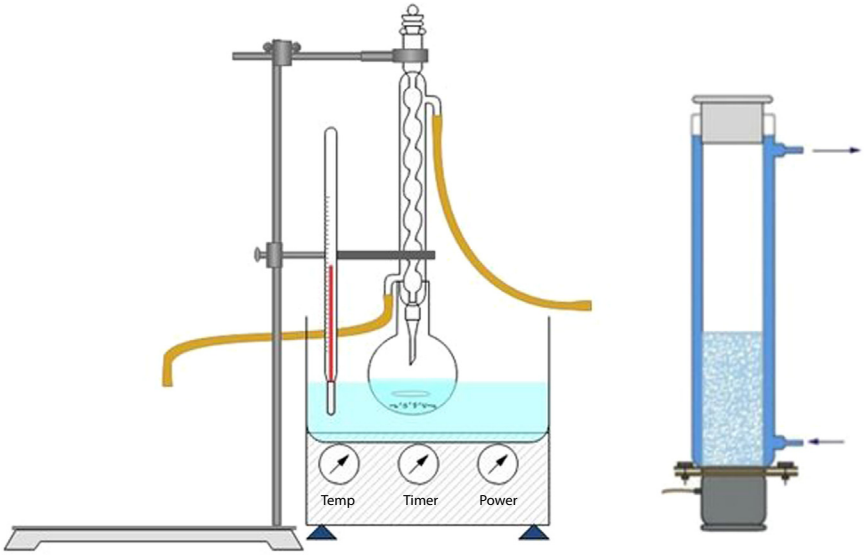

FIGURE 16.1 Schematic diagram of ultrasonic reactors.

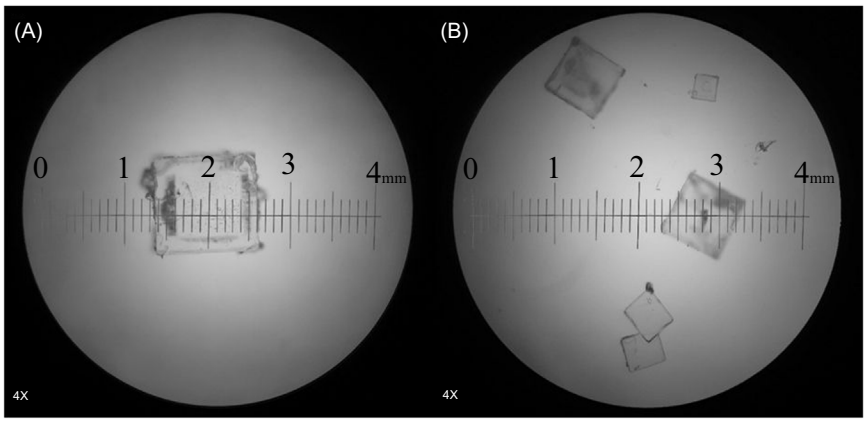

FIGURE 16.2 Effect of US frequency on crystal size of Sodium Chloride. (A) frequency = 45 kHz; Acoustic power = 4.1 W; volume = 50 mL; T = 25°C (B) frequency = 1700 kHz; Acoustic power = 4.1 W; volume = 50 mL; T = 25°C.

16.4.2 Effect of acoustic power

The sonocrystallization process is affected by US variables such as frequency, power intensity, but also by physical variables namely temperature, pressure, time, volume of cell, size of probe, and chemical variables such as substance concentration and pH (Castillo-Peinado and Luque de Castro, 2016). An increase in ultrasonic power enhances the cavitational effects, which drives to the reduction in the metastable zone width and the induction time based on the higher measures of nucleation. Additionally, the production of an enhanced number of nuclei leads to a diminution in the average particle size (Vishwakarma and Gogate, 2017). Conductivity measurements demonstrated that there was no dissolution or crystallization, but electron scanning microscopy demonstrated that the shape of crystals changed due to erosion. Also, crystal size is reduced with increasing US power (Luque de Castro and Priego-Capote, 2007). Amara et al. reported that, at high power, ultrasound has, in addition, an effect of abrasion on the crystals of potash alum. This result shows the potential of using low ultrasonic power to improve the control of the crystallization process (Amara et al., 2001). Park et al. examined the effect of power outputs within the range of 5–15 W at a constant frequency of 22.5 kHz. The paperwork demonstrates the reduction of particle size with the increase of power output from 5 to 15 W. In addition, it was confirmed that the particle size significantly decreased with an increased power output of the applied ultrasound (Park and Yeo, 2010). When the power outputs increase from 5 to 10 and 15 W, the average sizes of particles produced were 27.7, 19.3, and 14.6 μm, respectively, while the average size of particles obtained without ultrasound was 58.4 μm (Park and Yeo, 2010). Iyer et al. inspected the effect of power

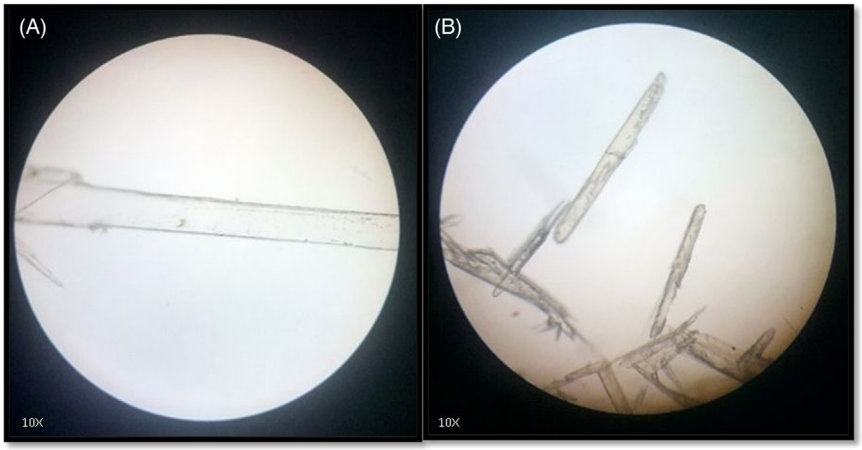

FIGURE 16.3 Effect of US power on salicylic acid crystallization. (A) Power input = 250 W; frequency = 20 kHz; T = 25°C. (B) Power input = 250 W; frequency = 20 kHz; T = 35°C.

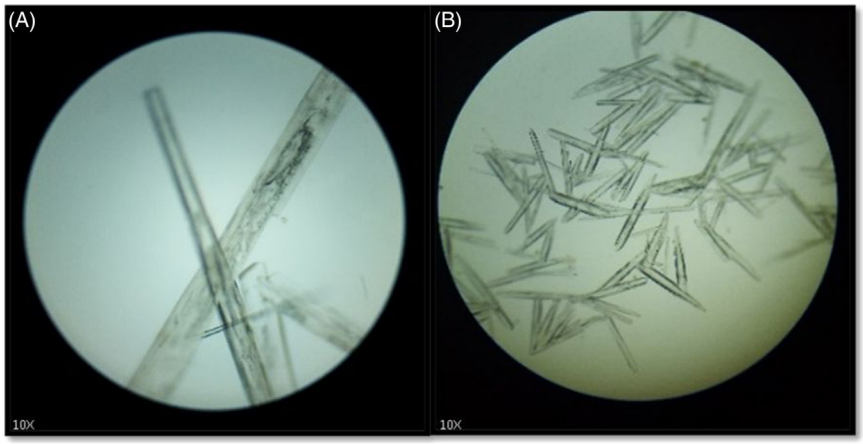

FIGURE 16.4 Effect of US power on salicylic acid crystallization. (A) Power input = 125 W; frequency = 20 kHz; T = 25°C. (B) Power input = 125 W; frequency = 20 kHz; T = 35°C. Fig. 16.3.

dissipation on the particle size distribution and yield of the samples obtained with and without ultrasound. It was reported that the conventionally crystallized sample resulted in a yield of 35.53% with mean length and breadth of 132.19 and 53.4 μm respectively. It was found that higher yields were obtained for the case of ultrasound assisted crystallization (Iyer and Gogate, 2017). Amara et al. (2001) have examined the abrasive effect in the aim to understand the mechanisms of the ultrasound action. The crystal's size, obtained at various ultrasonic powers (10 and 100 W), decreases with an increase of ultrasonic power. The quantity of smaller crystals is less at low power (10 W) and enhances significantly with an increase of ultrasonic power (Amara et al., 2001). Hatkar et al. studied the effect of operating parameters such as irradiation time, power, frequency of ultrasound, and type of reactor on the particle size distribution. It was reported that the abrasive effect of ultrasound was found to be more intense at higher power and the average particle size of salicylic acid crystals decreased considerably with an increase in acoustic power (Hatkar and Gogate, 2012). By increasing the US power, the number of cavitational events happen in the system improve assisted by an increased degree of acoustic streaming driving to an enhance in the physical effects which control the crystallization process in terms of prevention agglomeration and also particle breakage (Hatkar and Gogate, 2012). Sánchez-García et al. examined the influence of power ultrasound on lactose nucleation at 10, 20, and 30 W (Sánchez-García et al., 2019). At 20 W, the sonication of lactose solutions increased the formation of nuclei and minimized the induction time of nucleation. The results obtained in the presence of ultrasound showed that the coefficient k (the "birth" frequency) is also doubled in comparison with the nonsonicated treatment (Sánchez-García et al., 2019). An augmentation of the acoustic power at 30 W diminished the number of nuclei and boosted the induction time (Sánchez-García et al., 2019). Luque de Castro et al. examined the influence of US power (100, 200, and 300 W) on the crystallization

of hydroxyapatite (HAp)(Luque de Castro and Priego-Capote, 2007). An increasing of acoustic power reduces the particle size and no HAp crystals formed above 300 W (Luque de Castro and Priego-Capote, 2007). Below this threshold the particle size of the crystals formed enhanced with reducing US power. With other inorganic crystals, and as well as with organic ones, enhancing the acoustic power produces shorter, thicker crystals.

The influence of power input on the sonocrystallization of salicylic acid at 20 kHz was investigated. Figs. 16.3 and 16.4 illustrate the effect of two power inputs (125 and 250 W) on the sonocrystallization of salicylic acid. As can be seen in Fig. 16.3, the quantity of smaller crystals obtained at 250 W is less than at low power output (125 W). Similar results were reported in the literature (Luque de Castro and Priego-Capote, 2007; Sánchez-García et al., 2019).

16.5 Conclusion

This chapter demonstrates that the scale-up of sonocrystallization is undoubtedly one of the major defiance for its application in industry. The employment of ultrasound to initiate and control crystallization processes will seduce industrials to improve the control during the nucleation regime and may allow the nucleation and crystal growth balance to be regulated in order to optimize the product and particle properties. It also has been demonstrated that sonocrystallization reduces the induction time, generates the primary nucleation at lower supersaturation levels and boosts the rate of nucleation. The ultrasound can control the rate of nucleation and crystal growth and consequently the resulting size of each particle. It has been established that improving the US frequency increases the number of cavitation bubbles but the intensity of the bubble collapse decreases. The induction time decreases with increasing the US power which in turn raised the energy provided to the solution. Also, transient bubbles created relative more abrasion than stable bubbles which mainly caused particle breakage via fracturing. For transient cavitation bubbles, in contrast, relatively more abrasion was detected at higher power levels.

References

Adewuyi, Y.G., 2001. Sonochemistry: environmental science and engineering applications. Ind. Eng. Chem. Res. 40 (22), 4681–4715. https://doi.org/10.1021/ie010096l.

Amara, N., Ratsimba, B., Wilhelm, A.M., Delmas, H., 2001. Crystallization of potash alum: effect of power ultrasound. Ultrason. Sonochem. 8 (3), 265–270. https://doi.org/10.1016/S1350-4177(01)00087-6.

Bund, R.K., Pandit, A.B., 2007. Sonocrystallization: effect on lactose recovery and crystal habit. Ultrason. Sonochem. 14 (2), 143–152. https://doi.org/10.1016/j.ultsonch.2006.06.003.

Castillo-Peinado, L.d.L.S., Luque de Castro, M.D., 2016. The role of ultrasound in pharmaceutical production: sonocrystallization. J. Pharm. Pharmacol. 1249–1267. https://doi.org/10.1111/jphp.12614.

Iyer, S.R., Gogate, P.R., 2017. Ultrasound assisted crystallization of mefenamic acid: effect of operating parameters and comparison with conventional approach. Ultrason. Sonochem. 34, 896–903. https://doi.org/10.1016/j.ultsonch.2016.08.001.

Dhumal, R.S., Biradar, S.V., Paradkar, A.R., York, P., 2009. Particle engineering using sonocrystallization: salbutamol sulphate for pulmonary delivery. Int. J. Pharm. 368 (1–2), 129–137. https://doi.org/10.1016/j.ijpharm.2008.10.006.

Duroudier, J.P., 2016. Crystallization and Crystallizers. Elsevier Inc, Netherland, pp. 1–193. http://www.sciencedirect.com/science/book/9781785481864. (Accessed November 2021).

Ensminger, D., Bond, L.J., 2011. Ultrasonics: Fundamentals, Technology and Applications, 3rd Edition CRC Press, New York https://doi.org/10.1201/b11173.

Fitzner, M., Sosso, G.C., Pietrucci, F., Pipolo, S., Michaelides, A., 2017. Pre-critical fluctuations and what they disclose about heterogeneous crystal nucleation. Nat. Commun. 8 (1). https://doi.org/10.1038/s41467-017-02300-x.

Guo, D., Cao, X., Ding, G., Zhang, P., Liu, Y., Bian, J., 2022. Crystallization and nucleation mechanism of heavy hydrocarbons in natural gas. Energy 239, 122071. https://doi.org/10.1016/j.energy.2021.122071.

Guo, Z., Zhang, M., Li, H., Wang, J., Kougoulos, E., 2005. Effect of ultrasound on anti-solvent crystallization process. J. Cryst. Growth 273 (3–4), 555–563. https://doi.org/10.1016/j.jcrysgro.2004.09.049.

Hatkar, U.N., Gogate, P.R., 2012. Process intensification of anti-solvent crystallization of salicylic acid using ultrasonic irradiations. Chem. Eng. Process. 57–58, 16–24. https://doi.org/10.1016/j.cep.2012.04.005.

Jones, A.G., 2003. Crystallization Process Systems, 1st ed. Elsevier, Netherland, pp. 1–334.

Jordens, J., Gielen, B., Xiouras, C., Hussain, M.N., Stefanidis, G.D., Thomassen, L.C.J., Braeken, L., Van Gerven, T., 2019. Sonocrystallisation: observations, theories and guidelines. Chem Eng and Processing – Process Intensification 139, 130–154. https://doi.org/10.1016/j.cep.2019.03.017.

Kaur Bhangu, S., Ashokkumar, M., Lee, J., 2016a. Ultrasound assisted crystallization of paracetamol: crystal size distribution and polymorph control. Cryst. Growth Des. 16 (4), 1934–1941. https://doi.org/10.1021/acs.cgd.5b01470.

Kaur Bhangu, S., Ashokkumar, M., Lee, J., 2016b. Ultrasound assisted crystallization of paracetamol: crystal size distribution and polymorph control. Cryst. Growth Des. 16 (4), 1934–1941. https://doi.org/10.1021/acs.cgd.5b01470.

Kerboua, K., Hamdaoui, O., 2021. Sonochemistry for water remediation: toward an up-scaled continuous technology. Remediat. Technol 2, 437–468.

Khaire, R.A., Gogate, P.R., 2021. Understanding the role of different operating modes and ultrasonic reactor configurations for improved sonocrystallization of lactose. Chem Eng and Processing – Process Intensification 159. https://doi.org/10.1016/j.cep.2020.108212.

Kim, Y.C., Myerson, A.S., 1996. Diffusivity of protein in aqueous solutions. Korean J. Chem. Eng. 13 (3), 288–293. https://doi.org/10.1007/BF02705952.

Kim, H.N., Suslick, K.S., 2018. The effects of ultrasound on crystals: sonocrystallization and sonofragmentation. Cryst. 8 (7). https://doi.org/10.3390/cryst8070280.

Kurotani, M., Miyasaka, E., Ebihara, S., Hirasawa, I., 2009. Effect of ultrasonic irradiation on the behavior of primary nucleation of amino acids in supersaturated solutions. J. Cryst. Growth 311 (9), 2714–2721. https://doi.org/10.1016/j.jcrysgro.2009.03.009.

Lee, J., Yang, S., 2018. Antisolvent sonocrystallisation of sodium chloride and the evaluation of the ultrasound energy using modified classical nucleation theory. cryst. 8 (8). https://doi.org/10.3390/cryst8080320.

Lee, J., Yasui, K., Ashokkumar, M., Kentish, S.E., 2018. Quantification of cavitation activity by sonoluminescence to study the sonocrystallization process under different ultrasound parameters. Cryst. Growth Des. 18 (9), 5108–5115. https://doi.org/10.1021/acs.cgd.8b00547.

Li, H., Wang, J., Bao, Y., Guo, Z., Zhang, M., 2003. Rapid sonocrystallization in the salting-out process. J. Cryst. Growth 247 (1–2), 192–198. https://doi.org/10.1016/S0022-0248(02)01941-3.

Luque de Castro, M.D., Priego-Capote, F., 2007. Ultrasound-assisted crystallization (sonocrystallization). Ultrason. Sonochem. 14 (6), 717–724. https://doi.org/10.1016/j.ultsonch.2006.12.004.

McNamara, W.B., Didenko, Y.T., Suslick, K.S., 1999. Sonoluminescence temperatures during multi-bubble cavitation. Nature 401 (6755), 772–775. https://doi.org/10.1038/44536.

McNamara, W.B., Didenko, Y.T., Suslick, K.S., 2003. Pressure during sonoluminescence. J. Phys. Chem. B 107 (30), 7303–7306. https://doi.org/10.1021/jp034236b.

Miyasaka, E., Kato, Y., Hagisawa, M., Hirasawa, I., 2006. Effect of ultrasonic irradiation on the number of acetylsalicylic acid crystals produced under the supersaturated condition and the ability of controlling the final crystal size via primary nucleation. J. Cryst. Growth 289 (1), 324–330. https://doi.org/10.1016/j.jcrysgro.2005.11.084.

Nalesso, S., Bussemaker, M.J., Sear, R.P., Hodnett, M., Lee, J., 2019. A review on possible mechanisms of sonocrystallisation in solution. Ultrason. Sonochem. 57, 125–138. https://doi.org/10.1016/j.ultsonch.2019.04.020.

Park, M.W., Yeo, S.D., 2010. Antisolvent crystallization of roxithromycin and the effect of ultrasound. Sep. Sci. Technol. 45 (10), 1402–1410. https://doi.org/10.1080/01496391003689538.

Pierce, A.D., 2019. Acoustics: An Introduction to Its Physical Principales and Applications (Springer). Springer-Nature, New York.

Prozorov, T., Prozorov, R., Suslick, K.S., 2004. High velocity interparticle collisions driven by ultrasound. J. Am. Chem. Soc. 126 (43), 13890–13891. https://doi.org/10.1021/ja049493o.

Richards, W.T., Loomis, A.L., 1927. The chemical effects of high frequency sound waves I. a preliminary survey. J. Am. Chem. Soc. 49 (12), 3086–3100. https://doi.org/10.1021/ja01411a015.

Ruecroft, G., Hipkiss, D., Ly, T., Maxted, N., Cains, P.W., 2005. Sonocrystallization: the use of ultrasound for improved industrial crystallization. Org. Process Res. Dev. 9 (6), 923–932. https://doi.org/10.1021/op050109x.

Sánchez-García, Y.I., Ashokkumar, M., Mason, T.J., Gutiérrez-Méndez, N., 2019. Influence of ultrasound frequency and power on lactose nucleation. J. Food Eng. 249, 34–39. https://doi.org/10.1016/j.jfoodeng.2019.01.007.

Sander, J.R.G., Zeiger, B.W., Suslick, K.S., 2014. Sonocrystallization and sonofragmentation. In: Ultrasonics Sonochemistry, 21. Elsevier B.V., Netherland, pp. 1908–1915 Issue 6 https://doi.org/10.1016/j.ultsonch.2014.02.005.

Srinivasan, R., Shirgaonkar, I.Z., Pandit, A.B., 1995. Effect of sonication on crystal properties. Separation Sci. Tech. 30 (10), 2239–2243. https://doi.org/10.1080/01496399508013904.

Takiyama, H., 2012. Supersaturation operation for quality control of crystalline particles in solution crystallization. Adv. Powder Technol. 23 (3), 273–278. https://doi.org/10.1016/j.apt.2012.04.009.

Uccheddu, B., Kun, Z., Hammouri, H., Fevotte, G., 2011. Design of a csd observer during batch cooling crystallization dealing with uncertain nucleation parameters. In: In IFAC Proceedings Volumes (IFAC-PapersOnline) (Vol. 44, Issue 1, pp. 10460–10465). IFAC Secretariat.

Virone, C., Kramer, H.J.M., van Rosmalen, G.M., Stoop, A.H., Bakker, T.W., 2006. Primary nucleation induced by ultrasonic cavitation. J. Cryst. Growth 294 (1), 9–15. https://doi.org/10.1016/j.jcrysgro.2006.05.025.

Vishwakarma, R.S., Gogate, P.R., 2017. Intensified oxalic acid crystallization using ultrasonic reactors: understanding effect of operating parameters and type of ultrasonic reactor. Ultrason. Sonochem. 39, 111–119. https://doi.org/10.1016/j.ultsonch.2017.04.015.

Xu, W.R., Chen, J., Huang, Z.L., 2017. Preparation of aragonite whiskers by dolomite. In: MATEC Web of Conferences (Vol. 114). EDP Sciences.

Yasui, M.A.K., Ashokkumar, M., 2011. Fundamentals of Acoustic Cavitation and Sonochemistry. Theoretical and Experimental Sonochemistry Involving Inorganic Systems, 1st ed. Springer, New York, pp. 1–404. 2010. https://doi.org/10.1007/978-90-481-3887-6.

Ye, L., Zhu, X., 2017. Analysis of the effect of impact of near-wall acoustic bubble collapse micro-jet on al 1060 Ultrason. Sonochem. 36, 507–516.

Chapter 17

Sonochemical degradation of fluoroquinolone and β-lactam antibiotics – A view on transformations, degradation efficiency, and consumed energy

Efraím A. Serna-Galvis[a,b], **Jazmín Porras**[a] **and Ricardo A. Torres-Palma**[b]

[a] *Grupo de Investigaciones Biomédicas Uniremington, Facultad de Ciencias de la Salud, Corporación Universitaria Remington (Uniremington), Medellín, Colombia,* [b] *Grupo de Investigación en Remediación Ambiental y Biocatálisis (GIRAB), Instituto de Química, Facultad de Ciencias Exactas y Naturales, Universidad de Antioquia UdeA, Medellín, Colombia*

17.1 Principles of sonochemical treatment of organic pollutants in water

Hydrophilic and non-volatile organic pollutants (such as antibiotics) in water are eliminated by the sonochemical process through the degrading action of radicals (e.g., hydroxyl radical, $HO^{\bullet}$) generated *in situ*. Sonochemical degradation of organic pollutants is driven by the acoustic cavitation phenomenon, which consists of the growth and collapse of microbubbles in liquids under the influence of ultrasonic waves (Ashokkumar, 2011; Liu et al., 2021). The violent collapse of microbubbles generates hotspots, that is, small regions with singular temperature (up to 5000 K) and pressure (up to 1000 atm) conditions, promoting the cleavage of dissolved oxygen and water molecule to produce $HO^{\bullet}$ (Eqs. 17.1–17.4) (Calcio Gaudino et al., 2021). Also, hydrogen peroxide is produced from the recombination of radicals (Eq. 17.5) (Serna-Galvis et al., 2018). For sonochemical applications, ultrasound waves ranged from 20 kHz to 3000 kHz (3 MHz) are the most used, and two configurations of the reactors are very common: low frequency (< 100 kHz)/high power and high frequency (200–2000 kHz)/low power. Moreover, it is recognized that the maximum rate of production of radicals from the water cleavage occurs between 200 and 600 kHz (Li and Ashokkumar, 2018).

$$H_2O +))) \rightarrow H^{\bullet} + HO^{\bullet} \quad (17.1)$$

$$O_2 +))) \rightarrow 2\,O^{\bullet} \quad (17.2)$$

$$H_2O + O^{\bullet} \rightarrow 2\,HO^{\bullet} \quad (17.3)$$

$$O_2 + H^{\bullet} \rightarrow HO^{\bullet} + O^{\bullet} \quad (17.4)$$

$$2\,HO^{\bullet} \rightarrow H_2O_2 \quad (17.5)$$

Hydroxyl radical is one of the most powerful oxidants (E°: 2.73 V). $HO^{\bullet}$ mainly reacts with organic molecules by abstracting hydrogen from C-H, N-H, or O-H bonds, and addition to pi-systems (e.g., C=C bonds and aromatic rings). Also, $HO^{\bullet}$ can promote electron transfer (but this mechanism is seldom) with some compounds such as thioethers (Pignatello et al., 2006).

Energy Aspects of Acoustic Cavitation and Sonochemistry: Fundamentals and Engineering. DOI: https://doi.org/10.1016/B978-0-323-91937-1.00005-0
Copyright © 2022 Elsevier Inc. All rights reserved.

TABLE 17.1 Examples of the effect of operational conditions on sonochemical degradation of β-lactam antibiotics.

β-lactam antibiotic	Operational parameter	Best degradation	Reference
Amoxicillin	Frequency: 575, 861, and 1141 kHz	575 kHz	Kıdak and Doğan (2018)
Ampicillin	Frequency: 375 and 990 kHz	375 kHz	Montoya-Rodríguez et al. (2020b)
	Power: 4.0, 11.2, and 24.4 W	24.4 W	
Cephalexin	Power: 100, 200, 300, 400 and 500W	200W	Guo et al. (2010b)
	pH: 4.5, 6.5, 7.5, 8.5 and 10	6.5	
Dicloxacillin	Power: 20, 40, 60 W	60 W	Villegas-Guzman et al. (2015)
	pH: 3.0, 5.7 and 9.0	3.0	
Penicillin G	pH: 3.0, 5.0, 7.0, and 10.0	3.0	Saghafinia et al. (2011)
Oxacillin	Frequency: 375, 990, and 1175 kHz	375 kHz	Estrada-Flórez et al. (2020)

In the sonochemical system, three zones are recognized: (1) the cavitation bubble, (2) the bubble-solution interface, and (3) the bulk of solution (Camargo-Perea et al., 2021). The maximum $HO^{\bullet}$ concentration occurs at the bubble-solution interface, and ~10% of the produced radicals reach the bulk of the solution. Hence, the rate of degradation is strongly dependent on the closeness of pollutants to the cavitation bubble; and the distance between pollutant and bubble is determined by the hydrophobicity of the pollutant (Serna-Galvis et al., 2018; Liu et al., 2021). Indeed, very hydrophobic compounds are fastly degraded by the sonochemical action (Serna-Galvis et al., 2018).

Most β-lactam and fluoroquinolone antibiotics are non-volatile compounds, and they have hydrophobic/hydrophilic properties that condition their sonochemical degradation as presented below.

17.2 Sonochemical degradation of β-lactam antibiotics

β-lactams belong to the top consumed antibiotics worldwide. They are frequently found in hospital wastewater and effluents of the municipal wastewater treatment plants, ending up in the aquatic environment (Sta Ana et al., 2021). In the environmental water, β-lactams can induce toxicity and promote the development/proliferation of antibiotic-resistant bacteria (Chen et al., 2017).

Several works have studied the effect of operational parameters (frequency, power, and pH) on the degradation of β-lactam antibiotics by ultrasound. Table 17.1 summarizes the main results about the effect of operational parameters for some illustrative cases. As above-mentioned, the best β-lactam antibiotics degradation occurs between 200 and 600 kHz. Indeed, it is reported that if the frequency increases above 350 kHz, the production of $HO^{\bullet}$ decreases (Estrada-Flórez et al., 2020). The sonochemical frequency controls the cavitation process by modifying the number and size of the bubbles, the cavitation threshold, and the temperatures reached during the collapse (Montoya-Rodríguez et al., 2020b). Consequently, the generation of hydroxyl radicals is changed, which determines the degradation of the β-lactam antibiotics.

The increase in the power (or power density) typically enhances the degradation of organic pollutants. As power (or power density) is augmented, more violent cavitation events occur, accelerating the sonochemical production of free radicals involved in the elimination of β-lactam antibiotics. For instance, it is informed that a greater degradation of ampicillin occurs when the power is increased from 4.0 to 24.4 (Montoya-Rodríguez et al., 2020b). Similar results are reported for β-lactams such as amoxicillin, cephalexin, dicloxacillin, and penicillin G (Table 17.1). However, an excessive power does not lead to improving the sonochemical degradation of antibiotics because, at very high power, a large number of gas bubbles exist in the solution, which scatters the waves to the walls of the vessel or back to the transducer, resulting in attenuation of the sonochemical effects (Guo et al., 2010b).

Another parameter that determines the efficiency of sonochemical degradation of β-lactam antibiotics that have acidic and or basic functional groups is the change in the solution pH. Modifications to the pH result in a change in the hydrophobic properties of these antibiotics. In the case of dicloxacillin, its sonochemical degradation is more favored at pH below 3.0, when compared to the treatment at pH 5.7 or 9.0. The dicloxacillin (DXC) is a non-volatile organic compound with a carboxylic group having a pKa value of 2.8 (Villegas-Guzman et al., 2015).

At pH 3.0, a high fraction of dicloxacillin is in its hydrophobic molecular form and trends to accumulate at the bubble-solution interface, where can more easily react with the sonogenerated $HO^{\bullet}$; thereby, resulting in a higher degradation rate. In turn, higher pH values (e.g., 5.7 or 9.0) lead to ionization of the carboxylic group on this antibiotic, enhancing its hydrophilic

TABLE 17.2 Effect of structure of β-lactam antibiotic on the sonodegradation.

Antibiotic	Kinetic parameter*	Reference
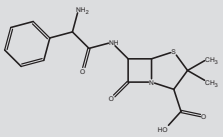	k: 0.032/min	Montoya-Rodríguez et al. (2020a)
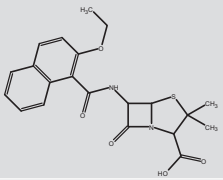	k: 0.055/min	
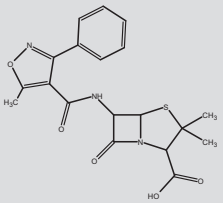	Rd: 0.78 μM/ min	Serna-Galvis et al. (2018)
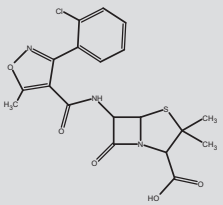	Rd: 0.86 μM/min	
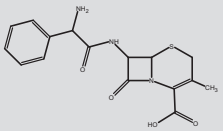	Rd: 0.73 μM/min	
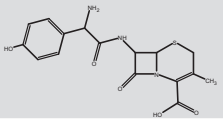	Rd: 0.42 μM/min	

nature, and the degradation takes place in the bulk of the solution mainly. In general, those pH conditions that favor the hydrophobic structures of the antibiotics increase their sonochemical degradation. Nonetheless, it must be mentioned that high basic conditions (e.g., pH > 11) can enhance the degradation of β-lactam antibiotics but this is associated with base-catalyzed hydrolysis more than sonochemical effects (Mitchell et al., 2014).

Despite all β-lactam antibiotics have the same structural nucleus, the presence of some functional groups determines their hydrophobicity. A comparison of the sonochemical treatment of nafcillin (NAF) and ampicillin (AMP) indicates that the NAF degradation is faster than AMP [Table 17.2 (Montoya-Rodríguez et al., 2020a)]. NAF contains an ethoxy-naphthyl moiety, which makes this β-lactam antibiotic more hydrophobic than AMP. Indeed, the Log *P* value (which is an indicator of hydrophobicity) for NAF (3.30) is higher than that for AMP (1.35), explaining the faster degradation of NAF under the sonochemical action.

Analogously, the treatment of cloxacillin (CLX) and oxacillin (OXA) by ultrasound reveals that CLX has an initial degradation rate higher than OXA [Table 17.2, (Serna-Galvis et al., 2018)]. This is related to the structural differences between the two antibiotics, which determine their hydrophobicity. Due to the chlorine presence, CLX is more hydrophobic than OXA. Similarly, cephalexin (CPX) is degraded faster than cefadroxil (CDX) by sonochemistry, and estimations using

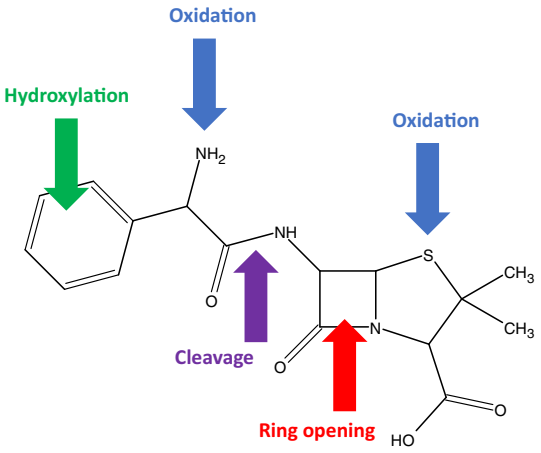

FIGURE 17.1 Main primary transformations of β-lactam antibiotics under ultrasound action.

the constitutional approach indicate that CDX is less hydrophobic because of the presence of an extra hydroxyl group compared with CPX (Serna-Galvis et al., 2018).

In addition to the effects of operational parameters and structural differences, the primary transformations of β-lactam antibiotics under sonochemical action have been reported (Serna-Galvis et al., 2016, 2018). Sonogenerated hydroxyl radicals promote the opening of the β-lactam nucleus (Fig. 17.1). This four-member ring is very strained and the carbonyl-nitrogen bond is weak, which makes the β-lactam ring highly reactive. The $HO^{\bullet}$ is also able to oxidize the primary amine or the thioether group adjacent to the β-lactam ring. Additionally, hydroxylation of the aromatic moieties and cleavage of the central amide on these antibiotics can be found during the sonochemical process.

It is important to remark that as the β-lactam nucleus is strongly modified by the action of the sonochemical process, the antimicrobial activity associated with this class of antibiotics is removed after sonication (Villegas-Guzman et al., 2015; Serna-Galvis et al., 2016, 2018). Moreover, the sonication of β-lactam antibiotics increases the biodegradability of the treated water, which indicates that the sonochemical process can be used as a treatment previous to biological systems (Naddeo et al., 2009; Villegas-Guzman et al., 2015).

Concerning the matrix composition of the solution containing the antibiotic, ultrasound has a particular behavior. In some cases, in more complex matrices than distilled water, the degradation of β-lactam antibiotics is low affected by the matrix components. The treatments by ultrasound of ampicillin, oxacillin, cloxacillin, and cefadroxil in matrices rich in hydrophilic components (e.g., simulated matrices of fresh urine, seawater, or hospital wastewater) have shown that the degradation of these β-lactam antibiotics is very close to the observed in distilled water because the few competition of the hydrophilic components by the sonogenerated $HO^{\bullet}$ (Serna-Galvis et al., 2016, 2018; Estrada-Flórez et al., 2020; Montoya-Rodríguez et al., 2020b).

Interestingly, in bicarbonate-rich matrices such as mineral water, and at low concentrations of the pollutants, their degradations are accelerated regarding their elimination in distilled water (Estrada-Flórez et al., 2020; Camargo-Perea et al., 2021). Under these conditions, the interaction of the sonogenerated $HO^{\bullet}$ with bicarbonate leads to the formation of carbonate radical ($CO_3^{\bullet -}$), which contributes to the degradation of the antibiotics. The carbonate radical is also an oxidizing agent (E°: 1.78 V) and has a lower recombination rate (1.2×10^7/M/s) than $HO^{\bullet}$ (5.5×10^9/M/s), then $CO_3^{\bullet -}$ can easily migrate to the solution bulk and react with the diluted pollutants (Camargo-Perea et al., 2021).

The sonochemical treatment is also applied to the degradation of β-lactam antibiotics in municipal wastewater effluents. For example, amoxicillin has been successfully degraded alone and in mixture with other pharmaceuticals in the secondary effluent of an urban wastewater treatment plant, decreasing both total organic carbon and toxicity of treated effluent (Naddeo et al., 2009).

On the other hand, as above mentioned, in addition to the generation of $HO^{\bullet}$, the sonochemical process in high frequency/low power systems can induce the formation of hydrogen peroxide (Eq. 17.5). The sonogenerated H_2O_2 is a byproduct that can be positively used in the combination of ultrasound with other processes. In this sense, the sonochemical degradations of AMP and NAF have been improved by the addition of UVC irradiation and ferrous ions to the ultrasound system, generating a sonophoto-Fenton process (Montoya-Rodríguez et al., 2020a). The reaction of iron with hydrogen peroxide produces extra $HO^{\bullet}$ in the solution bulk (Eq. 17.6, Fenton reaction). In turn, the UVC light promotes the homolysis

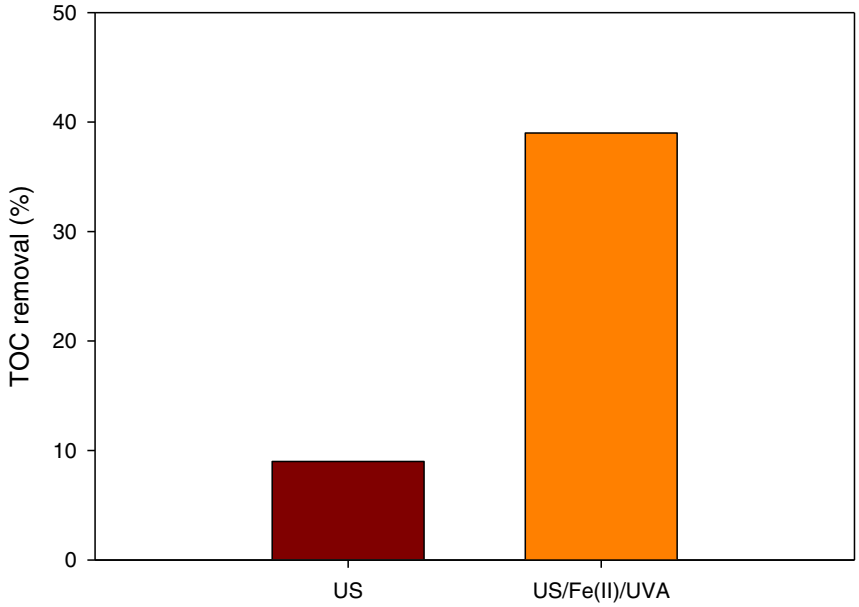

FIGURE 17.2 Comparison of TOC removal for the treatment of AMP by ultrasound alone (US) and sonophoto-Fenton (US/Fe(II)/UVA). Experimental conditions: [AMP]: 30 μM, [Fe(II)]: 90 μM, UVA: 4W, frequency 375 kHz, power 24.4 W, $pH_{initial}$: 6.5, volume: 250 mL, water matrix: distilled water.

of H_2O_2 (Eq. 17.7), and the photo-regeneration of ferric ions toward ferrous ions (Eq. 17.8). UVA light can also be used in the sonophoto-Fenton process. UVA light is not able to cleavage H_2O_2, but it effectively induces photo-regeneration of iron (Eq. 17.8). In fact, the combination of ultrasound with Fe^{2+} and UVA significantly increases the mineralization of AMP after 3 hours of treatment [Fig. 17.2, (Montoya-Rodríguez et al., 2020b)].

$$Fe^{2+} + H_2O_2 \rightarrow Fe^{3+} + HO^{\bullet} + HO^{-} \tag{17.6}$$

$$H_2O_2 + UVC \rightarrow 2HO^{\bullet} \tag{17.7}$$

$$Fe^{3+} + H_2O + UVC/UVA \rightarrow Fe^{2+} + HO^{\bullet} + H^{+} \tag{17.8}$$

Sono-Fenton process (from the combination of low-frequency ultrasound, H_2O_2, and Fe^{2+}) has been applied for the elimination of cephalexin, leading to 90% of the antibiotic elimination at 60 minutes, utilizing 60 mg/L of hydrogen peroxide and 8 mg/L of ferrous ions at pH 3.0 (Al-Musawi et al., 2019). In the sono-Fenton system, in addition to the Fenton reaction, the rupture of H_2O_2 toward $HO^{\bullet}$ is plausible by the ultrasound action.

For the elimination of β-lactam antibiotics, ultrasound has also been combined with OXONE ($KHSO_4$, K_2SO_4, $KHSO_5$; which is a source of peroxymonosulfate) and cobalt (II). This combination has been applied to degrade amoxicillin, achieving up to 90% of its chemical oxygen demand removal in 60 minutes of treatment (Su et al., 2012). The reaction of cobalt (II) or cobalt (III) with peroxymonosulfate produces radical species (Eqs. 17.9 and 17.10). Additionally, ultrasound can break peroxymonosulfate generating more radicals (Eq. 17.11) available for the elimination of pollutants.

$$Co^{2+} + HSO_{5^-} \rightarrow Co^{3+} + SO_4^{\bullet -} + HO^{-} \tag{17.9}$$

$$Co^{3+} + HSO_5^{-} \rightarrow Co^{2+} + SO_5^{\bullet -} + H^{+} \tag{17.10}$$

$$HSO_5^{-} +))) \rightarrow SO_4^{\bullet -} + HO^{\bullet} \tag{17.11}$$

The simultaneous presence of ultrasound waves and ozone (O_3) is another technique utilized for the degradation of amoxicillin (Kıdak and Doğan, 2018). Under this combination two main effects are recognized: (1) the increase in the mass transfer of O_3 from the gas phase to the bulk solution, favoring the reaction with the pollutants, by mechanical effects of ultrasound; (2) the decomposition of O_3 in the cavitation bubbles toward $HO^{\bullet}$ (Eq. 17.12) (Pang et al., 2011).

$$O_3 + H_2O +))) \rightarrow O_2 + 2HO^{\bullet} \tag{17.12}$$

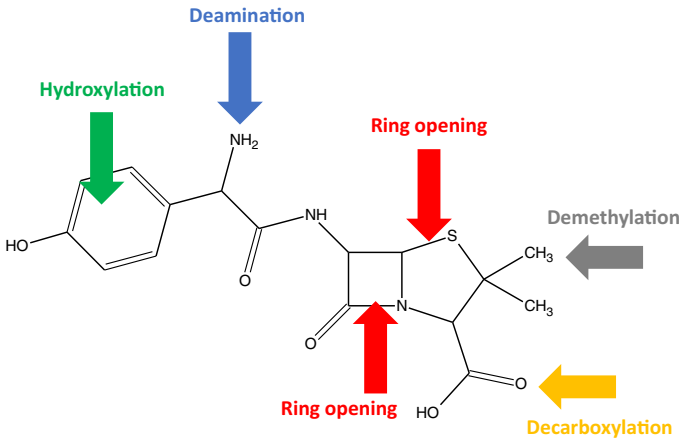

FIGURE 17.3 Primary transformation pathways induced by the ultrasound/O_3 system on amoxicillin.

The treatment of amoxicillin by the ultrasound/O_3 system promotes hydroxylation of the aromatic ring, demethylation, decarboxylation, opening of β-lactam and thiazole ring, and deamination (Fig. 17.3), with the subsequent sulfur loss with rearrangements. Furthermore, this combined system can induce the mineralization of the antibiotic (Kıdak and Doğan, 2018).

17.3 Degradation of fluoroquinolone antibiotics using ultrasound

Fluoroquinolone antibiotics are widely employed in human (since the 1980s) and veterinarian (since the 1990s) medicine, due to their fast-bactericidal action against several microorganisms. These antibiotics are not completely removed at municipal wastewater treatment plants, and consequently, their continuous introduction into the environment makes fluoroquinolones contaminants of emerging concern. Due to the high potential to promote antibiotic resistance, and toxic properties on vertebrate and invertebrate species, fluoroquinolones have an unfavorable environmental impact (Frade et al., 2014; Janecko et al., 2016). Thereby, diverse processes including ultrasound-based have been used to degrade fluoroquinolone antibiotics in aqueous matrices (De Bel et al., 2009; Guo et al., 2010a; Wei et al., 2018).

The effects of operational parameters such as frequency and power on the sonochemical degradation of fluoroquinolone antibiotics are similar to the observed for β-lactams. For instance, the sonochemical treatment of ciprofloxacin has been carried out at 544, 801, and 1081 kHz, finding that the fastest elimination of this fluoroquinolone occurred at the lowest tested frequency (De Bel et al., 2009). In the case of ciprofloxacin, the effect of temperature of solution bulk on the sonochemical degradation is also reported. The removal rate of this fluoroquinolone increased as the temperature augmented from 15 to 45°C.

The temperature of the solution bulk modifies factors such as vapor pressure, viscosity, gas solubility, and surface tension. As the temperature of solution bulk increases, the viscosity and surface tension diminish, lowering the threshold intensity required to produce cavitation. Hence, an increase in the number of cavitation bubbles is expected, promoting the production of radicals. At the same time, reactions with the hydroxyl radical in the solution bulk are facilitated by the increased temperature due to the higher mass transfer of different species, which leads to an enhancement of the reaction rate with nonvolatile pollutants, such as fluoroquinolone antibiotics (De Bel et al., 2009).

A strategy to enhance the degradation of fluoroquinolones is the addition of carbon tetrachloride (CCl_4) to low frequency/high power ultrasound systems (e.g., 20 kHz/200 W) (Guo et al., 2010a; Wei et al., 2018). The presence of CCl_4 in this sonochemical system induces the formation of chlorine radicals ($Cl^{\bullet}$), chlorine (Cl_2), and hypochlorous acid (HOCl) (Eqs. 17.13–17.16), which act as degrading agents of the antibiotics. When levofloxacin at 20 mg/L is treated in the presence of 0.01 mL of carbon tetrachloride, the removal of this fluoroquinolone achieves $\sim$ 50% in 30 minutes of sonication (which is five-folds the degradation obtained in the absence of CCl_4) (Guo et al., 2010a).

Likewise, the sonochemical degradation of ciprofloxacin is strongly accelerated by the addition of CCl_4 between 20.7 and 41.1 mmol/L. Under the ultrasound/CCl_4 process, ciprofloxacin experimented oxidative decarboxylation, piperazyl rupture, hydroxylation of the aromatic ring, and chlorination as primary transformations. Indeed, the treatment led to the elimination of the antibacterial activity against *E. coli* and *S. aureus*. This was associated with the modifications on quinolone and

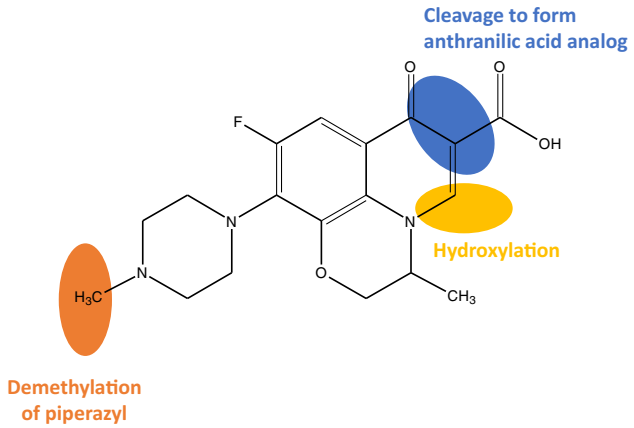

FIGURE 17.4 Primary transformations of levofloxacin under a sono-Fenton system (US/H_2O_2/Fe_3O_4).

piperazine moieties, whose transformations significantly reduce the antibacterial activity (Wei et al. 2018).

$$CCl_4 +))) \rightarrow Cl^{\bullet} + {}^{\bullet}CCl_3 \quad (17.13)$$

$$^{\bullet}CCl_3 +))) \rightarrow Cl^{\bullet} + CCl_2 \quad (17.14)$$

$$2\,Cl^{\bullet} \rightarrow Cl_2 \quad (17.15)$$

$$Cl_2 + H_2O \rightarrow HOCl + HCl \quad (17.16)$$

Although the presence of carbon tetrachloride has accelerating effects, an excess of CCl_4 can affect the sonodegradation because the adiabatic index of the gas mixture inside the cavitation bubble decreases. This diminishes the temperature reached in the compression of the bubble, which affects the intensity of cavitation, attenuating the dissociation of CCl_4; thereby, decreasing the concentration of the oxidizing species. Furthermore, at very high concentrations, carbon tetrachloride acts as a scavenger of oxidizing agents, obstructing the reaction between them and the target antibiotics (Guo et al., 2010a).

The addition of hydrogen peroxide has also beneficial effects on the sonochemical degradation of fluoroquinolones, using a low-frequency reactor (20 kHz). Indeed, the elimination of ofloxacin increases from 28% to 50% in the presence of 100 mmol/L of hydrogen peroxide. This is attributed to the generation of extra hydroxyl radicals (Eqs. 17.17–17.19) (Hapeshi et al., 2010).

$$H_2O_2 +))) \rightarrow 2\,HO^{\bullet} \quad (17.17)$$

$$H_2O_2 + H^{\bullet} \rightarrow H_2O + HO^{\bullet} \quad (17.18)$$

$$H_2O_2 + O^{\bullet} \rightarrow HO_2^{\bullet} + HO^{\bullet} \quad (17.19)$$

The combination of ultrasound with the Fenton reaction (hydrogen peroxide with ferrous ions) induces the acceleration of both degradation and mineralization of ciprofloxacin concerning the ultrasonic system alone. Moreover, the treatment of this fluoroquinolone in real wastewater by sono-Fenton guarantees the complete elimination of the antibiotic, the removals of chemical oxygen demand, and total organic carbon elimination higher than 50%, plus an increment in the biodegradability index from 0.21 to 0.36 (González Labrada et al., 2018).

In the same way, the treatment of levofloxacin is significantly enhanced by a heterogenous sono-Fenton system (i.e., ultrasound/H_2O_2/Fe_3O_4-nanoparticles). The enhancement in the degradation of the fluoroquinolone obeys two simultaneous mechanisms to increase the generation of degrading radicals: (1) the Fe_3O_4 particles provide more nucleation sites to form cavitation bubbles, and (2) Fe_3O_4 catalyzes the decomposition of H_2O_2 through Fenton-like reactions. Indeed, this sono-Fenton system induces, on levofloxacin, the formation of an anthranilic acid analog, the hydroxylation at the quinolone structure, and demethylation of the piperazyl ring as primary transformations (Fig. 17.4) (Wei et al., 2015).

Sonophoto-Fenton process (high-frequency ultrasound/Fe^{2+}/UVC light) has been applied for the degradation of ciprofloxacin and norfloxacin in presence of other pharmaceuticals in a biotreated hospital wastewater. After 90 minutes

TABLE 17.3 Energy conversion efficiency (Ne) at different ultrasound frequencies.

Frequency (kHz)	Ne (%)	Reference
20	27	Toma et al. (2011)
500	82	
544	32	De Bel et al. (2011)
801	26	
1081	4	

of treatment, the sonophoto-Fenton system degraded 70 and 89% of ciprofloxacin and norfloxacin, respectively. In the biotreated hospital wastewater the presence of organic matter having carboxylic groups is common. These carboxylic groups may complex iron (III), and the UVC irradiation can photolyze the complexes (Eq. 17.20), enhancing the catalytic cycle of iron, and consequently, favoring the degradation of organic pollutants such as ciprofloxacin and levofloxacin by the action of the sonophoto-Fenton process (Serna-Galvis et al., 2019b).

$$\mathrm{Fe(R-COO)^{2+} + UVC \rightarrow Fe^{2+} + R^{*} + CO_2} \tag{17.20}$$

The sonophoto-catalysis using ultrasound, UVA light, and TiO_2 is another possibility to enhance the elimination of fluoroquinolones by ultrasound. This combination for the degradation of ofloxacin leads to synergistic effects (~13%). Several reasons are presented to explain the synergy for the sonophoto-catalysis utilizing UVA light and TiO_2. Sonophoto-catalysis increases the production of $HO^{\bullet}$ in the reaction mixture due to the ultrasound waves enhance the mass transfer of the fluoroquinolone toward the catalyst surface. The photocatalytic activity is also increased because the ultrasound disaggregates the catalyst particles, augmenting the superficial area. Furthermore, the TiO_2 particles offer more nucleation sites for the cavitation bubbles. It should be highlighted that under the sonophoto-catalytic process, defluorination, piperazyl dealkylation, hydroxylation, decarboxylation, oxidation of hydroxyl groups, and cleavage of ofloxacin are the major transformation pathways. Interestingly, at short treatment times (e.g., 15–60 minutes) the toxicity of solution against *D. magna* is increased but at prolonged action of the process (e.g., 240 minutes) occurs the removal of the toxic compounds (Hapeshi et al., 2013).

17.4 Relationship between degradation efficiency and consumed power/energy

In the sonochemical processes, the generator of ultrasound waves utilizes electric power. However, only part of the input electric power is transformed into acoustic power (through the piezoelectric effect), due to this, energy conversion is transducer/reactor-dependent (Kimura et al., 1996; De Bel et al., 2011). For the interpretation of the fundamental aspects, it is relevant to determine the actual acoustic power. Calorimetry is the most common method to measure acoustic power. This involves the measurement of the initial rate of the temperature rise produced when a system is irradiated by ultrasound waves. It is assumed that almost all the mechanical energy produces heat, and thus the acoustic power entering the systems can be obtained via calorimetry (Kimura et al., 1996).

The temperature (T) is recorded against time (t) for a short period (e.g., 60–300 seconds), using a thermocouple placed into the reactor, and the acoustic power (P_{ac}, in J/s: W) is obtained according to Eq. 17.21, where Cp is the specific heat capacity of water (4.187 J/g/°C), m represents mass (in g) of water used, and dT/dt is the slope of T versus t plot (Kimura et al., 1996; Dükkanc et al., 2012).

$$P_{ac} = Cp \times m \times \left(\frac{dT}{dt}\right) \tag{17.21}$$

The ratio between the acoustic power and electric power (P_{el}) allows calculating the energy conversion efficiency ($N_e = P_{ac}/P_{el}$, or $N_e = 100(P_{ac}/P_{el})$) (Toma et al. 2011). This efficiency depends on the ultrasound frequency (Table 17.3). The frequency determines the compression cycle for the collapse of the cavitation bubble, and this also has an effect on the energy conversion efficiency. For instance, the increase in frequency from 544 to 1081 kHz makes shorter the compression cycle (0.92, 0.62, and 0.46 μs for 544, 801, and 1081 kHz, respectively), and consequently, the Ne is decreased from 32% at 544 kHz to 4% at 1081 kHz (De Bel et al., 2011).

For practical purposes, we must take into account both the electric power consumption and the degrading capability of the sonochemical process. A figure of merit to link the electric energy and degradation efficiency is the electrical energy

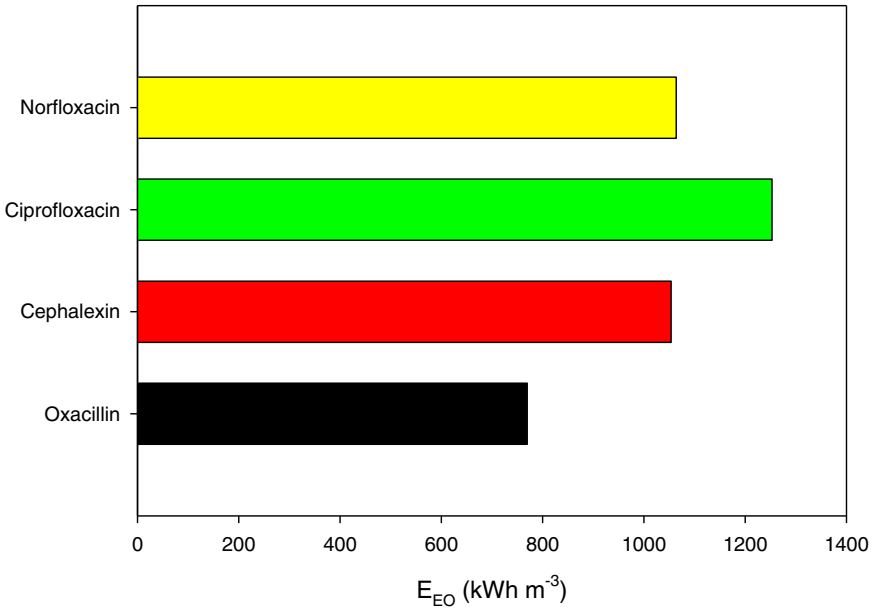

FIGURE 17.5 Estimated values of E_{EO} for the sonochemical treatment of some representative β-lactam and fluoroquinolone antibiotics. Conditions: P_{el}: 200W, frequency: 375 kHz, V: 300 mL, [antibiotic]: 40 μM in distilled water, $pH_{initial}$: 6.5.

consumption per order (E_{EO}). E_{EO} is defined as the electric energy (in kWh) required to degrade a pollutant by one order of magnitude (i.e., 90%) in one m^3 of contaminated water (Miklos et al., 2018). E_{EO} can be calculated using Eq. 17.22, where P_{el} means the electric power input to the sonochemical reactor (in kW), t is the time required to degrade 90% of the target pollutant (in h), and V represents the volume of treated water (in m^3).

$$E_{EO} = \frac{P_{el} \times t}{V} \tag{17.22}$$

Although E_{EO} values should only be determined for a process that is optimized with respect to water matrix, reagents consumption, reactor geometry, and other process-specific parameters, this figure of merit has been used as a first approach to compare processes. Thus, based on E_{EO} calculations from several works in the literature, it is concluded that sonochemistry is an electric energy-intensive process, which has a median E_{EO} value of 10^3 kWh m^{-3} magnitude order (Miklos et al., 2018). Fig. 17.5 shows the estimated values of E_{EO} for the sonochemical treatment of two β-lactam antibiotics (oxacillin and cephalexin), and two fluoroquinolones (ciprofloxacin and norfloxacin) antibiotics.

Another way to relate the electric power consumption with the degrading capability of the sonochemical process (i.e., an alternative to E_{EO}) is the specific electric energy consumption (SEC, in kWh/g). SEC denotes the electric energy consumption per mass removed of pollutant, and this indicator is calculated using Eq. 17.23 [where P_{el} is the electric power in kW, t represents the time in h, V is the treated volume in L, and C_o is the initial concentration of the pollutant, and C_t is the concentration at a selected time in g/L, (Gonzaga et al., 2021)].

$$SEC = \frac{P_{el} \times t}{V \times (C_o - C_t)} \tag{17.23}$$

As above-mentioned, the sonolysis of organic pollutants (such as antibiotics) requires high amounts of electric energy. Then, to increase the degradation efficiency and decrease the electric energy consumption, ultrasonic action is combined with other processes (such as ozonation or Fenton reaction), oxidizing agents (e.g., H_2O_2, and HSO_5^-), and/or light (e.g., UVA or UVC) (Anandan et al., 2020; Liu et al., 2021).

Table 17.4 compares the SEC values for the treatment of AMP during 1 hour by ultrasound, sono-Fenton, and sonophoto-Fenton processes. It can be highlighted that sono-Fenton and sonophoto-Fenton systems have SEC ~18 and 32% lower than ultrasound alone. Similar results have been reported for the treatment of fifteen pharmaceuticals (including ciprofloxacin and norfloxacin) in hospital wastewater by the coupling of a biological process (BP) with ultrasound-based systems. Indeed, the coupling BP/sonophoto-Fenton has a specific electric energy consumption ~7% lower than the coupling BP/ultrasound (Serna-Galvis et al., 2019b).

TABLE 17.4 Comparison of SEC values for the treatment of AMP by ultrasound, sono-Fenton, and sonophoto-Fenton.

Process	Ultrasound alone	Sono-Fenton [ultrasound + Fe(II)]	Sonophoto-Fenton [ultrasound + Fe(II) + UVA]
SEC (kWh/g)[a]	113.23	93.15	77.94

[a]Values calculated for the treatment of AMP (10.5 mg/L) using an ultrasound reactor operated at P_{el}: 200 W, frequency: 375 kHz, and V: 250 mL. For the combined processes: [Fe(II)]: 5 mg/L, and UVA: 4W. Treatment time: 1 hour. *Calculations were done by the authors using own data.*

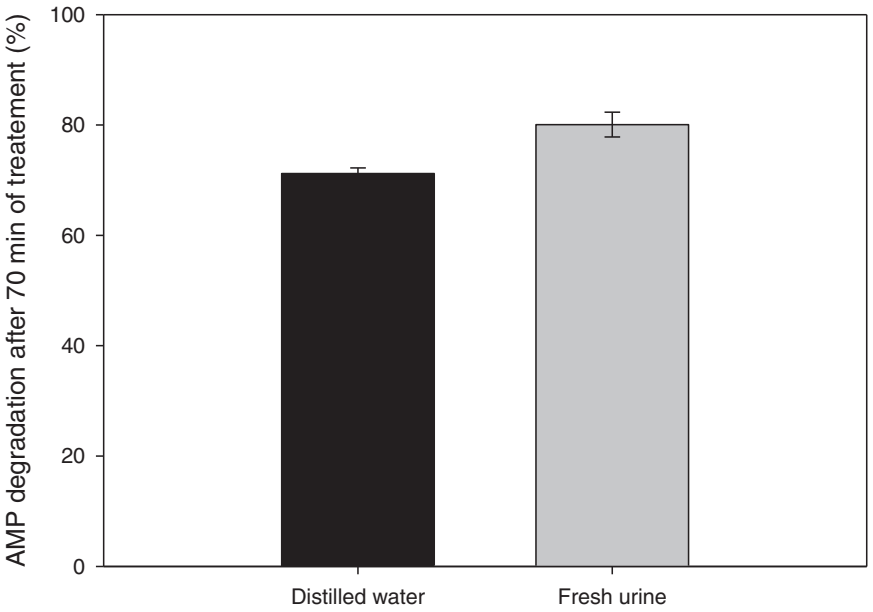

FIGURE 17.6 Comparison of sonochemical degradation of AMP in distilled water and simulated fresh urine. Experimental conditions: [AMP]: 30 μM, frequency: 375 kHz, P_{ac}: 24.4 W, $pH_{initial}$: 6.5, volume: 250 mL.

On the other hand, it should be mentioned that the ultrasound technique has still limitations to be performed at industrial levels. Energy conversion and high-volume processes (geometry of sonoreactor and transduces distribution) are considerable challenges toward further development of this technique. Indeed, transducers arrays and a larger exposed surface for ultrasound source, continuous flow reactor designs, and stirring during sonication should be investigated toward the industrial-scale application (Wu et al., 2013).

Despite current limitations to perform the sonochemical process at the industrial scale, some niche applications at small volumes are good opportunities for this technique. The treatment of antibiotics in urine is an example of these niche applications. In fact, ampicillin is efficiently degraded in simulated fresh urine by ultrasound (even achieving a removal rate higher than in distilled water, Fig. 17.6), having values of E_{EO} and SEC of 1360 kWh m^{-3} and 111 kWh/g, respectively.

Finally, it is very important to note that some part of the fundamental knowledge obtained from the sonochemical processes (e.g., the interaction of pollutants with the cavitation bubble, or the effect of addition of oxidants such as H_2O_2, OXONE, or O_3) could be transferred to other systems based on cavitation, such as hydrodynamic cavitation with Venturi pipes (Serna-Galvis et al., 2019a), which can be developed at industrial-scale with lower electric energy consumption (Carpenter et al., 2017).

17.5 Concluding remarks

At the end of this chapter, we can remark the following aspects:

- Sonochemical degradation of β-lactam and fluoroquinolone antibiotics is strongly influenced by the frequency and power of the ultrasound reactor and the pH of the water sample.
- Functional groups on the β-lactam and fluoroquinolone antibiotics determines their hydrophobicity, and consequently their degradation under ultrasound action.

- Primary structural transformations such as hydroxylations, oxidations, ring openings, and fragmentations are caused by the sonogenerated $HO^{\bullet}$ on the β-lactam and fluoroquinolone antibiotics. Additionally, the action of the sonochemical process is able to eliminate antimicrobial activity and decrease toxicity associated with these antibiotics.
- Combination of ultrasound with other processes, or the addition of radical precursors are good strategies to improve the degradation of antibiotics and reduce electric energy consumption.
- Currently, the ultrasound process is not applicable for the treatment of antibiotics in wastewater at a large scale. However, this could be an interesting technique for niche applications at small volumes such as the degradation of antibiotics in urine, which is a primary source of water pollution by these pharmaceuticals.

Acknowledgments

E. A. Serna-Galvis thanks MINCIENCIAS COLOMBIA for his postdoctoral fellowship during November 2020–October 2021 (Convocatoria 848 de 2019). R. A. Torres-Palma thanks the financial support provided by the Royal Society (UK) through the project: "Sound" methods of remediating emerging contaminants in hospital wastewater (ICA\R1\191053); as well as to Universidad de Antioquia (UdeA), for the support provided through "PROGRAMA DE SOSTENIBILIDAD" and the financing from MINCIENCIAS COLOMBIA through the projects No. 111577757323 and 111585269594.

References

Al-Musawi, T.J., Kamani, H., Bazrafshan, E., et al., 2019. Optimization the effects of physicochemical parameters on the degradation of cephalexin in sono-fenton reactor by using box-behnken response surface methodology. Catal Letters. 149, 1186–1196. https://doi.org/10.1007/s10562-019-02713-x.

Anandan, S., Kumar Ponnusamy, V., Ashokkumar, M., 2020. A review on hybrid techniques for the degradation of organic pollutants in aqueous environment. Ultrason. Sonochem. 67, 105130. https://doi.org/10.1016/j.ultsonch.2020.105130.

Ashokkumar, M., 2011. The characterization of acoustic cavitation bubbles - an overview. Ultrason. Sonochem. 18, 864–872. https://doi.org/10.1016/j.ultsonch.2010.11.016.

Calcio Gaudino, E., Canova, E., Liu, P., et al., 2021. Degradation of antibiotics in wastewater: new advances in cavitational treatments. Molecules 26. https://doi.org/10.3390/molecules26030617.

Camargo-Perea, A.L., Serna-Galvis, E.A., Lee, J., Torres-Palma, R.A., 2021. Understanding the effects of mineral water matrix on degradation of several pharmaceuticals by ultrasound: influence of chemical structure and concentration of the pollutants. Ultrason. Sonochem. 73, 105500. https://doi.org/10.1016/j.ultsonch.2021.105500.

Carpenter, J., Badve, M., Rajoriya, S., et al., 2017. Hydrodynamic cavitation: an emerging technology for the intensification of various chemical and physical processes in a chemical process industry. Rev. Chem. Eng. 33, 433–468. https://doi.org/10.1515/revce-2016-0032.

Chen, J., Wang, Y., Qian, Y., Huang, T., 2017. Fe(III)-promoted transformation of B-lactam antibiotics: hydrolysis vs oxidation. J. Hazard. Mater. 335, 117–124. https://doi.org/10.1016/j.jhazmat.2017.03.067.

De Bel, E., Dewulf, J., Witte, B.D., et al., 2009. Influence of pH on the sonolysis of ciprofloxacin: biodegradability, ecotoxicity and antibiotic activity of its degradation products. Chemosphere 77, 291–295. https://doi.org/10.1016/j.chemosphere.2009.07.033.

De Bel, E., Janssen, C., De Smet, S., et al., 2011. Sonolysis of ciprofloxacin in aqueous solution: influence of operational parameters. Ultrason. Sonochem. 18, 184–189. https://doi.org/10.1016/j.ultsonch.2010.05.003.

Dükkanc, M., Vinatoru, M., Mason, T.J., 2012. Sonochemical treatment of orange ii using ultrasound at a range of frequencies and powers. J Adv Oxid Technol 15 (2), 277–283. https://doi.org/10.1515/jaots-2012-0205.

Estrada-Flórez, S.E., Serna-Galvis, E.A., Torres-Palma, R.A., 2020. Photocatalytic vs. sonochemical removal of antibiotics in water: structure-degradability relationship, mineralization, antimicrobial activity, and matrix effects. J Environ Chem Eng 8, 104359. https://doi.org/10.1016/j.jece.2020.104359.

Frade, V.M.F., Dias, M., Teixeira, A., Palma, M.S.A., 2014. Environmental contamination by fluoroquinolones. Brazilian J Pharm Sci 50, 41–54. https://doi.org/10.1590/s1984-82502011000100004.

Gonzaga, I.M.D., Moratalla, A., Eguiluz, K.I.B., et al., 2021. Outstanding performance of the microwave-made MMO-Ti/RuO2IrO2 anode on the removal of antimicrobial activity of penicilling by photoelectrolysis. Chem. Eng. J. 420, 129999. https://doi.org/10.1016/j.cej.2021.129999.

González Labrada, K., Alcorta Cuello, D.R., Saborit Sánchez, I., et al., 2018. Optimization of ciprofloxacin degradation in wastewater by homogeneous sono-Fenton process at high frequency. J Environ Sci Heal - Part A Toxic/Hazardous Subst Environ Eng 53, 1139–1148. https://doi.org/10.1080/10934529.2018.1530177.

Guo, W., Shi, Y., Wang, H., et al., 2010a. Intensification of sonochemical degradation of antibiotics levofloxacin using carbon tetrachloride. Ultrason. Sonochem. 17, 680–684. https://doi.org/10.1016/j.ultsonch.2010.01.004.

Guo, W., Wang, H., Shi, Y., Zhang, G., 2010b. Sonochemical degradation of the antibiotic cephalexin in aqueous solution. Water SA 36, 651–654. https://doi.org/10.4314/wsa.v36i5.61998.

Hapeshi, E., Achilleos, A., Papaioannou, A., et al., 2010. Sonochemical degradation of ofloxacin in aqueous solutions. Water Sci. Technol. 61, 3141–3146. https://doi.org/10.2166/wst.2010.921.

Hapeshi, E., Fotiou, I., Fatta-Kassinos, D., 2013. Sonophotocatalytic treatment of ofloxacin in secondary treated effluent and elucidation of its transformation products. Chem. Eng. J. 224, 96–105. https://doi.org/10.1016/j.cej.2012.11.048.

Janecko, N., Pokludova, L., Blahova, J., et al., 2016. Implications of fluoroquinolone contamination for the aquatic environment—a review. Environ. Toxicol. Chem. 35, 2647–2656. https://doi.org/10.1002/etc.3552.

Kıdak, R., Doğan, Ş., 2018. Medium-high frequency ultrasound and ozone based advanced oxidation for amoxicillin removal in water. Ultrason. Sonochem. 40, 131–139. https://doi.org/10.1016/j.ultsonch.2017.01.033.

Kimura, T., Sakamoto, T., Leveque, J.M., et al., 1996. Standardization of ultrasonic power for sonochemical reaction. Ultrason. Sonochem. 3, S157–S161. https://doi.org/10.1016/S1350-4177(96)00021-1.

Li, W., Ashokkumar, M., 2018. Introduction to ultrasound and sonochemistry. Electrochem. Soc. Interface 27, 43–46. https://doi.org/10.1149/2.F04183if.

Liu, P., Wu, Z., Abramova, AV., Cravotto, G., 2021. Sonochemical processes for the degradation of antibiotics in aqueous solutions: a review. Ultrason. Sonochem. 74, 105566. https://doi.org/10.1016/j.ultsonch.2021.105566.

Miklos, D.B., Remy, C., Jekel, M., et al., 2018. Evaluation of advanced oxidation processes for water and wastewater treatment- a critical review. Water Res. 139, 118–131. https://doi.org/10.1016/j.watres.2018.03.042.

Mitchell, S.M., Ullman, J.L., Teel, A.L., Watts, R.J., 2014. pH and temperature effects on the hydrolysis of three β-lactam antibiotics: ampicillin, cefalotin and cefoxitin. Sci. Total Environ. 466–467, 547–555. https://doi.org/10.1016/j.scitotenv.2013.06.027.

Montoya-Rodríguez, D.M., Ávila-Torres, Y., Serna-Galvis, E.A., Torres-Palma, R.A., 2020a. Data on treatment of nafcillin and ampicillin antibiotics in water by sonochemistry. Data Br 29, 105361. https://doi.org/10.1016/j.dib.2020.105361.

Montoya-Rodríguez, D.M., Serna-Galvis, E.A., Ferraro, F., Torres-Palma, R.A., 2020b. Degradation of the emerging concern pollutant ampicillin in aqueous media by sonochemical advanced oxidation processes - parameters effect, removal of antimicrobial activity and pollutant treatment in hydrolyzed urine. J. Environ. Manage. 261, 110224. https://doi.org/10.1016/j.jenvman.2020.110224.

Naddeo, V., Meriç, S., Kassinos, D., et al., 2009. Fate of pharmaceuticals in contaminated urban wastewater effluent under ultrasonic irradiation. Water Res. 43, 4019–4027. https://doi.org/10.1016/j.watres.2009.05.027.

Pang, Y.L., Abdullah, A.Z., Bhatia, S., 2011. Review on sonochemical methods in the presence of catalysts and chemical additives for treatment of organic pollutants in wastewater. Desalination 277, 1–14. https://doi.org/10.1016/j.desal.2011.04.049.

Pignatello, J.J., Oliveros, E., Mackay, A., 2006. Advanced oxidation processes for organic contaminant destruction based on the fenton reaction and related chemistry. Crit. Rev. Environ. Sci. Technol. 36, 1–84. https://doi.org/10.1080/10643380500326564.

Saghafinia, M.S., Emadian, S.M., Vossoughi, M., 2011. Performances evaluation of photo-fenton process and sonolysis for the treatment of penicillin g formulation effluent. Procedia Environ Sci 8, 202–208. https://doi.org/10.1016/j.proenv.2011.10.033.

Serna-Galvis, E.A., Botero-Coy, A.M., Martínez-Pachón, D., et al., 2019a. Degradation of seventeen contaminants of emerging concern in municipal wastewater effluents by sonochemical advanced oxidation processes. Water Res. 154, 349–360. https://doi.org/10.1016/j.watres.2019.01.045.

Serna-Galvis, E.A., Montoya-Rodríguez, D., Isaza-Pineda, L., et al., 2018. Sonochemical degradation of antibiotics from representative classes-Considerations on structural effects, initial transformation products, antimicrobial activity and matrix. Ultrason. Sonochem. 50, 157–165. https://doi.org/10.1016/j.ultsonch.2018.09.012.

Serna-Galvis, E.A., Silva-Agredo, J., Botero-Coy, A.M., et al., 2019b. Effective elimination of fifteen relevant pharmaceuticals in hospital wastewater from colombia by combination of a biological system with a sonochemical process. Sci. Total Environ. 670, 623–632. https://doi.org/10.1016/j.scitotenv.2019.03.153.

Serna-Galvis, E.A., Silva-Agredo, J., Giraldo-Aguirre, A.L., et al., 2016. High frequency ultrasound as a selective advanced oxidation process to remove penicillinic antibiotics and eliminate its antimicrobial activity from water. Ultrason. Sonochem. 31, 276–283. https://doi.org/10.1016/j.ultsonch.2016.01.007.

Sta Ana, K.M., Madriaga, J., Espino, M.P., 2021. β-Lactam antibiotics and antibiotic resistance in asian lakes and rivers: an overview of contamination, sources and detection methods. Environ. Pollut. 275, 116624. https://doi.org/10.1016/j.envpol.2021.116624.

Su, S., Guo, W., Yi, C., et al., 2012. Degradation of amoxicillin in aqueous solution using sulphate radicals under ultrasound irradiation. Ultrason. Sonochem. 19, 469–474. https://doi.org/10.1016/j.ultsonch.2011.10.005.

Toma, M., Fukutomi, S., Asakura, Y., Koda, S., 2011. A calorimetric study of energy conversion efficiency of a sonochemical reactor at 500 kHz for organic solvents. Ultrason - Sonochemistry 18, 197–208. https://doi.org/10.1016/j.ultsonch.2010.05.005.

Villegas-Guzman, P., Silva-Agredo, J., Giraldo-Aguirre, A., et al., 2015. Enhancement and inhibition effects of water matrices during the sonochemical degradation of the antibiotic dicloxacillin. Ultrason. Sonochem. 22, 211–219. https://doi.org/10.1016/j.ultsonch.2014.07.006.

Wei, H., Hu, D., Su, J., Li, K., 2015. Intensification of levofloxacin sono-degradation in a US/H2O2 system with Fe3O4 magnetic nanoparticles. Chinese J Chem Eng 23, 296–302. https://doi.org/10.1016/j.cjche.2014.11.011.

Wei, H., Shi, J., Yang, X., et al., 2018. CCl4-Enhanced ultrasonic irradiation for ciprofloxacin degradation and antibiotic activity. Water Environ. Res. 90, 579–588. https://doi.org/10.2175/106143017X15131012153077.

Wu, T.Y., Guo, N., Teh, C.Y., Hay, J.X.W., 2013. Advances in ultrasound technology for environmental remediation. In: Wu, TY, Guo, N, Teh, CY, Hay, JXW (Eds.), Challenges and Recent Developments of Sonochemical Processes. Springer, Netherlands, Dordrecht, pp. 109–120.

Chapter 18

The use of ultrasonic treatment in technological processes of complex processing of industrial waste: Energetic insights

Yarusova S.B., Gordienko P.S., Buravlev I.Yu., Bulanova S.B. and Sushkov Yu.V.
Institute of Chemistry, Far Eastern Branch of Russian Academy of Sciences, Vladivostok, Russia

18.1 Introduction

The results presented indicate the prospects of ultrasonic treatment (UST) application in the process of calcium silicates synthesis from waste products of technogenic origin and expands new possibilities for the realization of directed synthesis of the compounds. Also, the proposed approach is promising for the industrial technology of complex processing of waste boric acid production.

The use of the ultrasonic method expands the possibilities of the directed synthesis of various inorganic materials. The use of the sonochemical approach makes it possible not only to significantly increase the rate of chemical transformations, primarily in heterogeneous systems, but also in many cases to obtain highly dispersed phases with controlled micromorphology (Baranchikov et al., 2007; Khmelev et al., 2010).

The intensification of heterophase synthesis is due to the fact that during ultrasonic processing of suspensions, when ultrasonic waves are applied, cavities (bubbles) are formed in the liquid, which generate shock waves when collapsing. These waves significantly reduce the thickness of the laminar boundary layer; a local temperature rise is possible. The result of these phenomena can be an increase in solubility, as well as an intensification of other heterophase processes (Gordina et al., 2019; Vaičiukyniene et al., 2015).

High-power ultrasonic vibrations activate reagents during solid-phase processes. By the example of studying a number of oxide systems, it was shown that the generation of structural defects caused by the passage of acoustic vibrations through reaction mixtures could have a significant effect on the kinetics of diffusion-limited solid-phase reactions. The use of UST makes it possible in many cases to reduce the temperature threshold of the onset of the solid-phase reaction (Yaroslavtsev, 2009).

Ultrasonic action is also actively used for the synthesis of silicates of various compositions and structures, while various man-made wastes are used as initial components (Belviso et al., 2013; Gordina et al., 2019; Ojumu et al., 2016; Pal et al., 2013; Vaičiukyniene et al., 2015; Wang et al., 2008a).

Indian scientists synthesized NaP zeolite at room temperature by means of preliminary UST of the reaction mixture. It is shown that the sonation energy promotes the formation of active radicals, which are responsible for the rapid crystallization of the zeolite phase. It was concluded that the sonochemical synthesis of NaP zeolite was advantageous in terms of reducing the cost of equipment and electricity (no heating unit is required to carry out the synthesis process) and reducing its duration (Pal et al., 2013).

Italian scientists proposed to obtain zeolites from fly ash of various compositions (SiO_2 content up to 53.4 wt%) in seawater using the traditional hydrothermal method and the hydrothermal process in seawater, which was preceded by sonication. The results showed that UST lowered the crystallization temperature of the zeolite (Belviso et al., 2013).

Lithuanian scientists (Vaičiukyniene et al., 2015)] synthesized NaA zeolite by the sonochemical method (5–30 min, 20 kHz, 200–250 W) at room temperature and short crystallization time. Amorphous silica, which is a by-product of the

Energy Aspects of Acoustic Cavitation and Sonochemistry: Fundamentals and Engineering. DOI: https://doi.org/10.1016/B978-0-323-91937-1.00008-6
Copyright © 2022 Elsevier Inc. All rights reserved.

production of aluminum fluoride (composition: 63.85% SiO_2, 18.38% H_2SiF_6, 9.27% AlF_3, 8.98% H_2O), was used as the initial component for obtaining NaA zeolite. It has been established that the NaA zeolite can be synthesized from a suspension prepared from by-product silica under normal conditions by treating the suspension with 200 W ultrasonic waves. The highest degree of zeolite crystallinity (25.81%) was obtained in the synthesis of suspensions held for 24 hours. With an increase in the ultrasonic wave power from 210 to 250 W, the time required to obtain NaA zeolite with similar crystallinity decreased from 15 to 10 minutes. Therefore, it is advisable to use the maximum ultrasound power. From a comparison of hydrothermal and sonochemical synthesis of NaA zeolite, it can be argued that with the same reaction time, sonochemical synthesis is more efficient.

In (Ojumu et al., 2016), the possibility of replacing high-temperature melting with sonochemical treatment during the synthesis of zeolite A from South African coal ash was substantiated. The results obtained showed that 10 minutes of high-intensity ultrasonic irradiation successfully replaced the traditional 90-minute energy-intensive melting stage. The use of ultrasound has also significantly lowered the crystallization temperature of zeolite A, thereby further increasing the energy efficiency of the entire process.

Chinese scientists have described the synthesis of highly crystalline zeolite MCM-22 using hexamethyleneimine as an organic template using ultrasonic aging (frequency and power of ultrasonic waves 40 KHz and 50 W, time 30–60 minutes). It was found that ultrasonic aging promoted the formation of MCM-22 by shortening the crystallization time, decreasing the amount of template used, expanding the SiO_2/Al_2O_3 ratio in the synthesis gel, and decreasing the average crystal size in the products. It is believed that acoustic cavitation is responsible for the above results due to the cracking of crystal grains and an increase in the concentration of soluble silicates for the growth of MCM-22 zeolite (Wang et al., 2008b).

There are known works on the synthesis of calcium silicates $nCaO{\cdot}mSiO_2$ and hydrosilicates $nCaO{\cdot}mSiO_2{\cdot}pH_2O$ using ultrasonic action (Liu et al., 2012; Zhang and Chang, 2010) Interest in these compounds is due to their unique physicochemical and technological properties, which provides a wide range of their use in construction, paint and varnish, polymer, and other industries (Gladun et al., 2011).

In (Liu et al., 2012)], for the hydrothermal synthesis of xonotlite $Ca_6[Si_6O_{17}](OH)_2$, it is proposed to use a carbide slag modified using ultrasonic technology. The results show that the activity of the carbide slag is improved as a result of ultrasonic exposure at 160 W for 3 hours, and the carbide slag, after appropriate modification, can be used to obtain pure xonotlite.

The authors of (Zhang and Chang, 2010) successfully obtained spheres of calcium silicate hydrate by the sonochemical method (40 kHz, 175 W) in the presence of cetyltrimethylammonium bromide. It was found that both ultrasound and surfactant played an important role in the formation of hollow spheres. Ultrasound guided the formation of micelle templates, followed by the growth of CSH precipitates on the micelle surface. The possibility of using the obtained hollow spheres for medical purposes (preparation of bioactive bone implants with drug delivery properties) is shown.

This section shows the use of UST in the processing of industrial waste. As a specific example, the process of synthesis of calcium silicates from the industrial waste of boron production is considered. The effect of ultrasonic action on the kinetics of the formation of these compounds from technogenic raw materials in an alkaline medium has been studied, and some of their functional properties have been considered.

18.2. Characteristics of technogenic waste

Research related to the development of physical and chemical foundations for the integrated processing of boric acid production waste (borogypsum) has been actively carried out since 2007 by the Institute of Chemistry of the Far Eastern Branch of the Russian Academy of Sciences in conjunction with other scientific and educational organizations.

Waste from boric acid production, or borogypsum, is waste obtained during the sulfuric acid processing of datolite concentrate enriched in the basic substance—datolite mineral ($2CaO{\cdot}B_2O_3{\cdot}2SiO_2{\cdot}H_2O$) – up to 72%–76% and containing impurities in the form of calcite ($CaCO_3$), wollastonite ($CaO{\cdot}SiO_2$), garnet ($3CaO{\cdot}Fe_2O_3{\cdot}3SiO_2$), hedenbergite ($CaO{\cdot}FeO{\cdot}2SiO_2$), giesengerite ($Fe_2O_3{\cdot}xSiO_2{\cdot}yH_2O$), and quartz ($SiO_2$).

When the datolite concentrate interacts with sulfuric acid, boric acid, calcium sulfate, hydrated silicon dioxide, and iron (III) sulfate are formed. As a result of sulfuric acid decomposition of datolite concentrate with sulfuric acid, a solid residue is obtained—borogypsum, containing simultaneously different phases of calcium sulfate: $CaSO_4{\cdot}2H_2O$ dihydrate, $CaSO_4 \cdot 0.5H_2O$ hemihydrate, and $CaSO_4$ anhydrite. Long-term storage of wet sludge in the sludge collector leads to the hydration of metastable calcium sulfates, and after 2–3 months of storage at positive temperatures, the dump borogypsum contains only dihydrate and impurities Fig. 18.1. Borogypsum sludge contains 0.9–2.2 wt% of B_2O_3, as a result of which it is called borogypsum. The volume of accumulated borogypsum on the territory of Russia is more than 50 million tons.

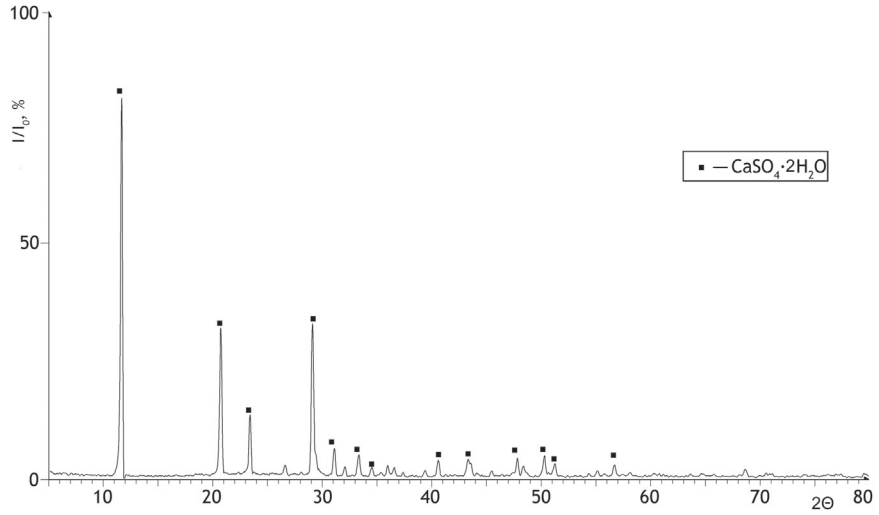

FIGURE 18.1 Diffraction pattern of boric acid production waste (borogypsum).

Borogypsum is characterized by the following content of the main components, wt%: SiO_2 – 26–28; CaO – 26–28; SO_4^{2-} – 38–40; Fe_2O_3 – 1.8–2; Al_2O_3 – 0.6–0.8; B_2O_3 – 0.7–1.2; MnO – 0.2; MgO – 0.1–0.2. The main components of borogypsum are calcium sulfate dihydrate and amorphous silica. Thus, wastes from boric acid production are a unique raw material for the production of calcium silicates, since they are characterized by an optimal chemical composition and ratio of components, while additional charging of the initial reaction mixture from other sources is not required.

The authors of (Gordienko, et al., 2011b) for the first time showed the possibility of complex processing of borogypsum with the production of calcium hydrosilicates $nCaO{\cdot}mSiO_2{\cdot}pH_2O$, wollastonite $Ca_6Si_6O_{18}$ and potassium fertilizers.

The process of obtaining hydrosilicates of calcium and wollastonite from boric acid production waste (borogypsum) in the presence of an alkaline agent (potassium or sodium hydroxide) is described by the general equation:

$$n(CaSO_4 \cdot 2H_2O) + m(SiO_2 \cdot q\,H_2O) + 2n\,KOH + (k - 3n - mq)\,H_2O = nCaO \cdot mSiO_2\,k\,H_2O + n\,K_2SO_4$$

In order to optimize the synthesis process, studies were carried out on the effect of ultrasonic, microwave, and autoclave treatment of the reacting mixture (Gordienko et al., 2015, 2012; Yarusova et al., 2017).

18.3 Experimental part

18.3.1 Ultrasonic synthesis of calcium hydrosilicate

Weighed portions of borogypsum were mixed with a solution of potassium or sodium hydroxide (analytical grade) in a stoichiometric ratio. The synthesis was carried out at 20°C in tightly closed plastic vessels with a capacity of 100 mL, placed in a UNITRA-UNIMA washing bath of the UM-1 type manufactured by LABIMEX (Poland) (25 kHz, 25 W) with the UST of the reaction mixture for the following time intervals: 10 minutes, 15 minutes, 30 minutes, 1 hour, 3 hour, 5, hour, 7 hour, 9 hour, 12 hour, 24 hour, 48 hour, 72 hour, 96 hour.

Simultaneously, the synthesis was carried out at similar ratios, temperature, and time intervals, but without UST, with stirring on a laboratory shaker type 358 S (Poland) (shaking frequency 200 cycles/min). After the end of the specified time interval, the precipitates were separated from the solution by filtration, washed with distilled water, and dried at a temperature of 85–90°C for several hours. The reaction rate was monitored by the residual concentration of potassium hydroxide or sodium hydroxide in the solution, which was determined by acid-base titration using 0.1 n HCl solution prepared from fixanal as a titrant.

18.3.2 Methods of analysis

X-ray diffraction patterns of the precipitation were taken on an automatic diffractometer D8 ADVANCE (Germany) with sample rotation in Cu *Kα*—radiation. X-ray phase analysis was performed using the EVA search program with a PDF-2 powder data bank.

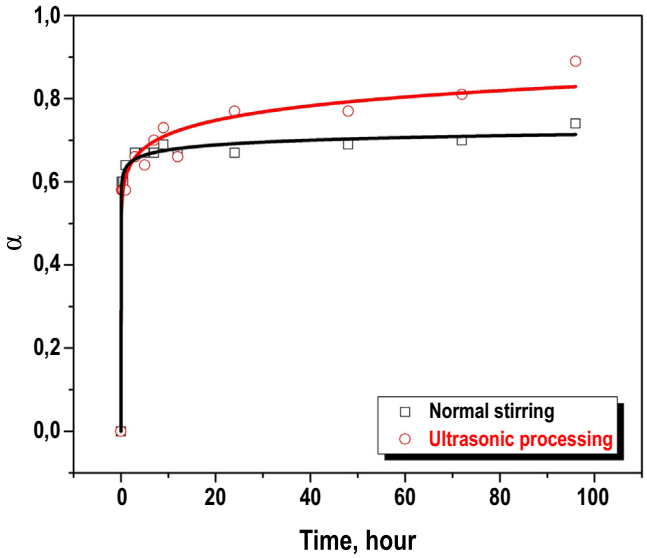

FIGURE 18.2 Dependencies of the degree of the passage of the reaction on time at 20°C (potassium hydroxide) under normal conditions and with the ultrasonic treatment of the reacting mixture.

To determine the elemental composition of the obtained samples, the energy-dispersive X-ray fluorescence method was used using an EDX-800HS spectrometer (Shimadzu, Japan). The analysis was carried out without taking into account light elements using the spectrometer software. The relative measurement error did not exceed ± 2%.

The thermal behavior of precipitation was studied on a Q-1500 D derivatograph of the F. Paulik, P. Paulik, L. Erdei system of the MOM company (Hungary) (the temperature determination accuracy is ± 5°C).

IR absorption spectra of the samples were recorded in the range of 400–4000/cm in vaseline oil using a Shimadzu FTIR Prestige-21 Fourier spectrometer (Japan) at room temperature.

The specific surface of the samples was determined by the method of low-temperature adsorption of nitrogen using a Sorbtometer-M device (Russia).

The content of Co^{2+} ions in solutions was determined by atomic absorption spectrometry on a two-beam SOLAAR M6 spectrometer (Thermo, United States) using an analytical line at 240.7 nm.

18.4 Analysis of the kinetics of the reaction of alkaline treatment of borogypsum under conditions of ultrasonic exposure

The time dependencies of the degree of reaction progress during the formation of calcium hydrosilicate from boroпypsum using the UST and conventional stirring in the synthesis process using potassium and sodium hydroxides as an alkaline reagent are shown in Fig. 18.2 and Fig. 18.3, respectively.

From the obtained dependencies, it can be seen that the UST of the reacting mixture affects the reaction rate and the yield of the target product. After 96 hours of interaction at the same temperature under conditions of UST, the degree of reaction when using potassium hydroxide as an alkaline agent reaches 89%, and sodium hydroxide—80%. Under normal stirring for potassium and sodium hydroxides, the reaction rates are 74% and 71%, respectively. At the initial time intervals of synthesis (from 10 minute to 1 hour), no significant differences in the kinetics of the reaction under normal stirring and UST are observed. After 1 hour of interaction with both potassium hydroxide and sodium hydroxide, the yield of the target product with ordinary stirring and with UST does not exceed 60%–64%.

It should be noted that when studying the kinetics in the $CaSO_4 \cdot 2H_2O - Na_2SiO_3 - H_2O$ model system under ultrasonic action, the degree of reaction progress reaches 62–69% only after 7 h of synthesis Fig. 18.4 (Gordienko, et al., 2009).

On the basis of the obtained experimental data, constants were calculated that characterize the rate of reactions proceeding under conditions of UST and with ordinary stirring. Since practically the same kinetic regularities were obtained for potassium and sodium hydroxides, the analysis of the results obtained was carried out using potassium hydroxide as an example.

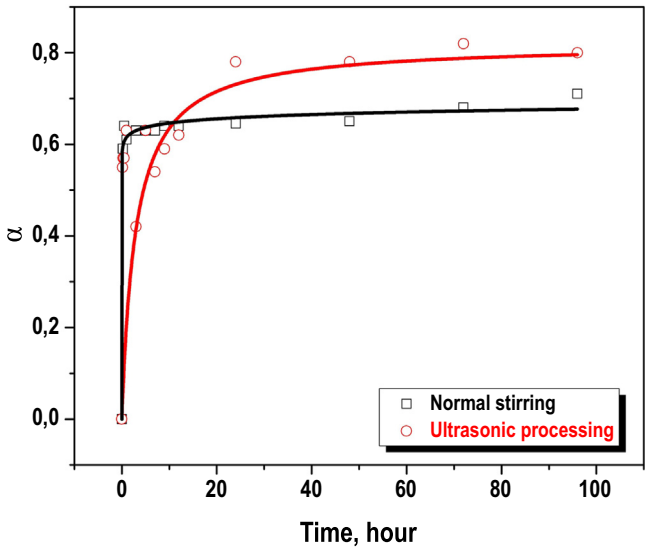

FIGURE 18.3 Dependencies of the degree of the passage of the reaction on time at 20°C (sodium hydroxide) under normal conditions and with the ultrasonic treatment of the reacting mixture.

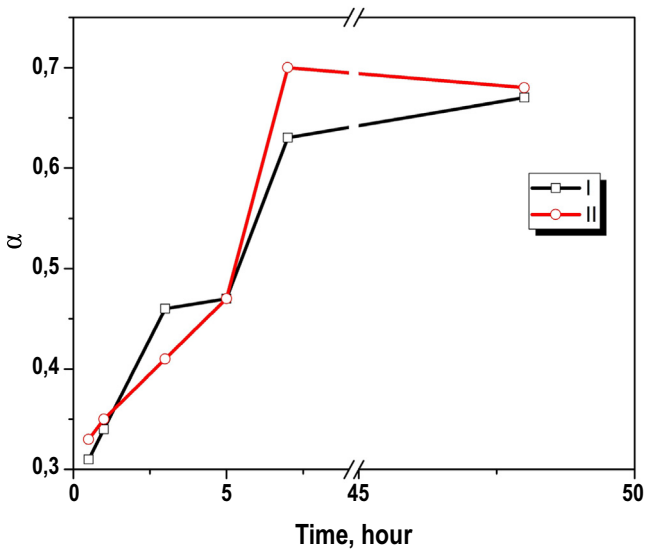

FIGURE 18.4 Dependence of the degree of product formation α on time τ (h) during the formation of calcium hydrosilicate in the model system $CaSO_4 \cdot 2H_2O$–Na_2SiO_3–H_2O: I—gravimetric method, II—atomic absorption method.

For the calculation, the generalized topochemical equation of Kolmogorov-Erofeev was used (Boldyrev, n.d.):

$$\alpha = 1 - e^{-kt^n}$$

where α is the fraction of the reacted substance at the time t; n and k are constants determined graphically and characterizing the order of the reaction and the reaction rate constant.

Fig. 18.5 shows the logarithmic dependencies of the degree of the passage of the reaction from time to time under conditions of UST and with normal stirring.

Linear dependencies in logarithmic coordinates indicate the constancy of n in the given time intervals. The kinetic data processed according to the generalized topochemical equation are shown in Table 18.1.

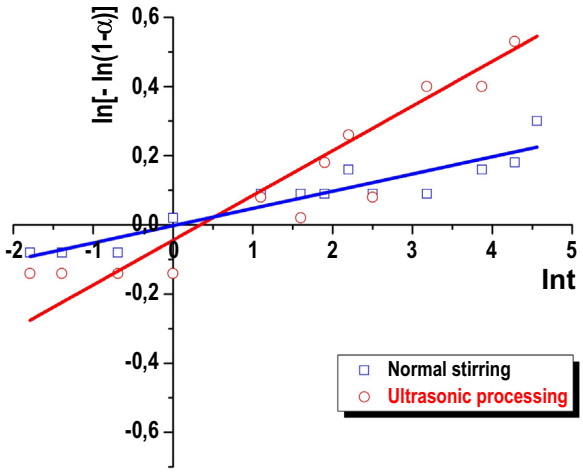

FIGURE 18.5 Logarithmic dependencies of the degree of the the passage of the reaction ln[-ln(1-α)] on the time ln t during the formation of calcium hydrosilicate under ultrasonic treatment and with ordinary stirring (potassium hydroxide).

TABLE 18.1 The order of the reaction (n) and the rate constant (k) of the reaction of the interaction of borogypsum with potassium hydroxide.

Synthesis conditions	n	k	R^2
Ultrasonic treatment	0,1292	0,9569 $h^{-0,1292}$	0,8475
Ordinary stirring	0,0498	0,997 $h^{-0,0498}$	0,8694

It should be noted that, formally, the rate constant of the reaction of the interaction of borogypsum with potassium hydroxide is determined from the dependence:

$$k = \frac{1}{K^n}$$

where K is the reaction rate constant, which, based on Eq. (18.1), has the dimension h, n is the order of the reaction, and k is a constant determined graphically from the logarithmic dependence. Thus, for the reaction of interaction of borogypsum with potassium hydroxide during UST $K^n = 1.408^{0.1292}$ $[h^{0.1292}]$, with ordinary stirring without ultrasonic action $K^n = 0.047^{0.0498}$ $[h^{0.0498}]$.

From the data presented in the table, it can be seen that the order of the reaction in both cases is <1, which indicates the occurrence of the reaction in the diffusion region.

Experimental data on the kinetics of ultrasonic interaction of borogypsum and potassium hydroxide were analyzed using the equation proposed by P.S. Gordienko and by the authors of (Gordienko et al., 2019):

$$\alpha_t = \alpha_m \cdot K \cdot t \cdot \left[\frac{1}{(1+Kt)}\right]$$

where K is a constant (time^{-1}), $\alpha\ t$ is the degree of passage of the reaction at time t, $\alpha\ m$ is the maximum value of the degree of passage of the reaction, t is the reaction time.

From Eq. (18.3), it follows that the constant K can be determined both from the experimental dependencies of the values of $\alpha\ t$ on t by calculation, according to the equation:

$$K = \sum \frac{\frac{\alpha_t}{t} \cdot \left(\frac{1}{\alpha_m - \alpha_t}\right)}{N}$$

TABLE 18.2 Parameters of the kinetics equation for the formation of calcium hydrosilicate from boron production wastes under ultrasonic treatment and with ordinary stirring.

Processing mode, temperature (°C)	Equation parameters		
	α_{max}	K/h	R^2
Ordinary stirring, 20°C, KOH (NaOH)	0.69 (0.64)	13.7 (62.0)	0.9695 (0.8356)
Ultrasonic treatment, 20°C, KOH (NaOH)	0.71 (0.69)	7.4 (19.4)	0.6911 (0.6441)

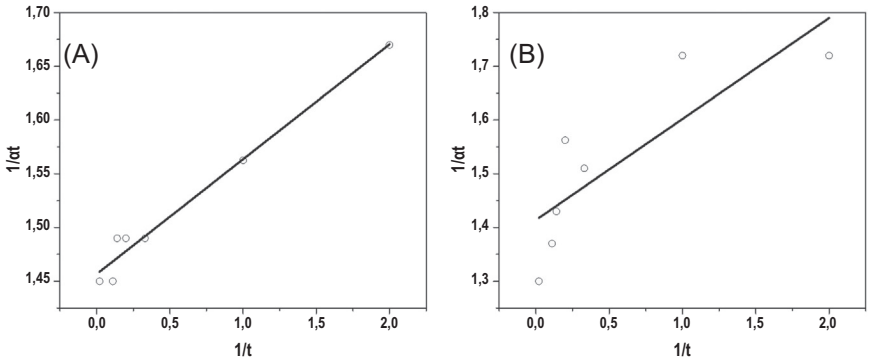

FIGURE 18.6 Dependencies of the reciprocal of the degree of passage of the reaction α_t on: (A) ordinary stirring; (B) ultrasonic treatment.

where N is the number of α t values at the corresponding reaction times, and graphically when presenting experimental data on kinetics in the form of a linear dependence $\frac{1}{\alpha_t}$ on $\frac{1}{t}$:

$$\frac{1}{\alpha_t} = \frac{1}{\alpha_m} + \frac{1}{K \cdot t \cdot \alpha_m}$$

where is $^1/_{\alpha_m}$ the value of the ordinate at $t \to \infty$; K is determined from the angle of inclination of a straight line or from the equation obtained by processing experimental results using the least-squares method:

$$y = a + bx$$

where $a = {}^1/_{\alpha_m}$, $b = {}^1/_{\alpha_m}\,{}^1/_K$ and $K = {}^a/_b$.

In this work, the proposed equation was applied to analyze the kinetics of the topochemical reaction of boric acid production waste (borogypsum) with potassium and sodium hydroxides under ultrasonic action.

Table 18.2 shows the parameters obtained graphically when presenting experimental data on kinetics in the form of the dependence of the reciprocal of the degree of the passage of the reaction of formation of calcium hydrosilicate on the reciprocal of the processing time (Fig. 18.6) (Gordienko et al., 2021).

The investigated system "borogypsum – alkali – water" is multicomponent ($CaSO_4$–SiO_2–KOH (NaOH)–H_2O); therefore, the Gibbs free energy values $\Delta G^\circ_{ch.r}$ of the corresponding reactions proceeding in the system under consideration were calculated (Table 18.3).

As calculations of ΔG°_{298} in the systems under consideration show, in the reaction of waste with potassium or sodium hydroxides, both sequential and parallel reactions with the participation of both calcium sulfate and silicon dioxide, which are components of the waste, are possible:

$$CaSO_4\,2H_2O + 2KOH \rightarrow K_2SO_4 + Ca(OH)_2 + 2H_2O \quad (18.1)$$

$$Ca(OH)_2 + SiO_2 \rightarrow CaSiO_3 + H_2O \quad (18.2)$$

or

$$SiO_2 + 2KOH \rightarrow K_2SiO_3 + H_2O \quad (18.3)$$

$$K_2SiO_3 + CaSO_4 \rightarrow CaSiO_3 + K_2SO_4 \quad (18.4)$$

TABLE 18.3 Gibbs free energy ΔG°ch.r in multicomponent systems based on boroпypsum and alkalis (KOH, NaOH) at a temperature of 298 K.

No.	Reaction	ΔG°_{298}, kJ
KOH		
1. 2. 3. 4.	$CaSO_4+2KOH \rightarrow Ca(OH)_2 + K_2SO_4$ $SiO_2+2KOH \rightarrow K_2SiO_3+H_2O$ $K_2SiO_3+ CaSO_4 \rightarrow K_2SO_4+$ $CaSiO_3K_2SiO_3+Ca(OH)_2 \rightarrow CaSiO_3+ 2KOH$	-118,0 -123,1 -58,4 +87,8
NaOH		
5. 6. 7. 8.	$CaSO_4+2NaOH \rightarrow Ca(OH)_2 + Na_2SO_4$ $SiO_2+2NaOH \rightarrow Na_2SiO_3+H_2O$ Na_2SiO_3+ $CaSO_4 \rightarrow Na_2SO_4+ CaSiO_3Na_2SiO_3+$ $Ca(OH)_2 \rightarrow CaSiO_3+2NaOH$	-78,0 -93,6 -27,4 +58,4
9. 10. 11.	$Ca(OH)_2+SiO_2 \rightarrow CaSiO_3+H_2O$ $Ca(OH)_2+CO_2 \rightarrow$ $CaCO_3+H_2O$ $CaSiO_3+CO_2 \rightarrow CaCO_3+SiO_2$	-35,4 -73,01 -37,6

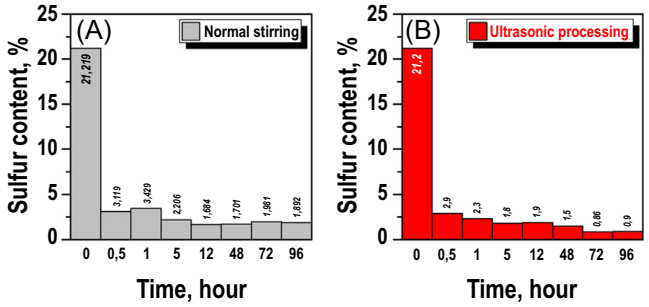

FIGURE 18.7 Sulfur content in samples after synthesis with ultrasonic treatment and normal stirring (potassium hydroxide).

The total value of free energy (in absolute value) for reactions I and II is lower than for reactions III and IV, that is, reactions III and IV are more thermodynamically probable reactions. Similar patterns are characteristic of the corresponding reactions, but with sodium hydroxide.

According to X-ray phase analysis, all samples obtained as a result of synthesis under conditions of UST and conventional stirring contain an amorphous phase and impurities of calcium carbonate $CaCO_3$ and silicon dioxide SiO_2. The presence of calcium carbonate may be due to the fact that during the synthesis, calcium sulfate interacts with potassium hydroxide to form calcium hydroxide $Ca(OH)_2$, which, in turn, intensively interacts with CO_2 in the air to form $CaCO_3$. In addition, as a result of interaction with water vapor and absorption of CO_2 from the air, the formed calcium hydrosilicate partially decomposes with the formation of $CaCO_3$ and amorphous silica, which is confirmed by previous studies and corresponding calculations (Daval et al., 2009; Di Lorenzo et al., 2018; Gordienko et al., 2014).

In the case of using potassium hydroxide as an alkaline agent, it should be noted that the phase of calcium sulfate dihydrate $CaSO_4 \cdot 2H_2O$ is present in all samples (from 10 minutes to 96 hour) synthesized under normal stirring conditions. During UST, the $CaSO_4 \cdot 2H_2O$ phase is present only in the samples synthesized in time intervals from 10 minutes to 12 hours. On the diffractograms of the samples obtained in time intervals from 24 to 96 hours, the calcium sulfate phase is absent.

When sodium hydroxide is used, the $CaSO_4 \cdot 2H_2O$ phase is present only in samples synthesized in time intervals from 10 minutes to 48 hours (under normal stirring conditions) and from 10 minutes to 24 hours under UST.

The quantitative determination of the elemental composition showed that the sulfur content in the samples decreased with an increase in the duration of the synthesis (Fig. 18.7 and Fig. 18.8). After ultrasonic synthesis, depending on the time, the sulfur content varies with the use of potassium hydroxide from 0.9 to 3.2 wt%, sodium hydroxide—from 0.7 to 5.2 wt%.

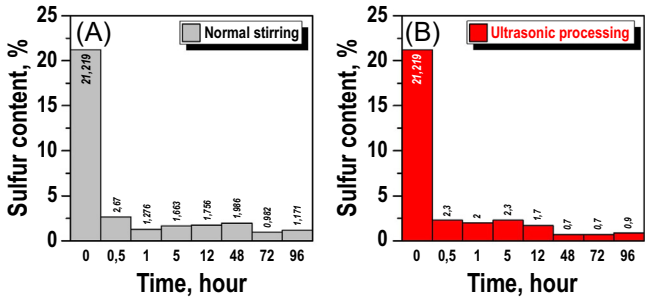

FIGURE 18.8 Sulfur content in samples after synthesis with ultrasonic treatment and normal stirring (sodium hydroxide).

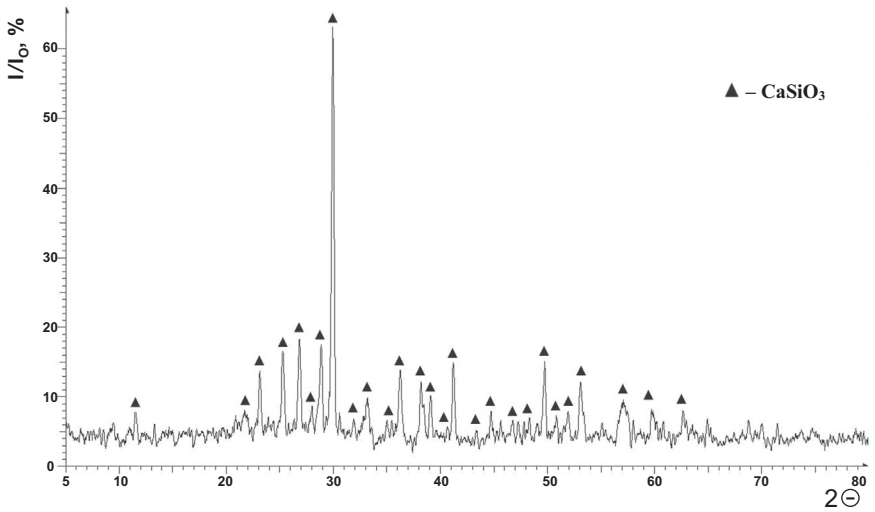

FIGURE 18.9 Diffraction pattern of a sample obtained under ultrasonic treatment for 9 hours (potassium hydroxide) after firing at 1000°C for 40 minutes.

With normal stirring, the sulfur content in the sediments is 1.5%–5.3% when potassium hydroxide is used, and 1.0–3.1 wt% of sodium hydroxide.

After firing at 1000°C for 40 minutes, the phase composition of the samples synthesized both under the conditions of UST and under conditions of ordinary stirring for 9 hours is characterized by the presence of triclinic wollastonite (Fig. 18.9).

A thermogravimetric study is presented for a sample obtained under conditions of ultrasonic synthesis for 5 h. It has been established that the sample under study loses mass in two stages upon heating in the temperature ranges of 60–180 and 180–700°C, 41.5 and 47.9% of the initial sample mass, respectively (Fig. 18.10). Based on the data of X-ray phase analysis and IR spectra of nonvolatile residues at these temperatures, it was found that the endothermic effect in the temperature range 60–180°C was associated with the removal of washing, adsorption, and crystallization water, while the endothermic effect in the temperature range of 180–700°C was associated with removal of bound water during dehydration of calcium hydrosilicates in the process of polycondensation of silanol groups. The endothermic effect at 760°C refers to the decomposition reaction of calcium carbonate. On the thermogravigrams of calcium carbonate of the "CP (chemically pure)" brand, the endothermic effect is recorded in the temperature range of 700–900°C. Decomposition of calcium carbonate is also confirmed by diffraction patterns and IR spectra of nonvolatile residues at 760°C.

X-ray phase analysis and IR spectrum of the non-volatile residue at a temperature of 820°C showed that the exothermic effect on the DTA curve at about 820°C is associated with the rearrangement of the crystal lattice and the transition of calcium hydrosilicate to β-wollastonite. This exo effect is not accompanied by a loss of sample mass.

The data of IR spectroscopic analysis of the initial borogypsum and synthesized samples, both before and after firing, are shown in Fig. 18.11 and Fig. 18.12.

As can be seen from the presented figures, the IR spectra of the synthesis products obtained with ordinary stirring and with the UST of borogypsum are identical. It can be seen from the given IR spectra that the reaction products (Fig. 18.11

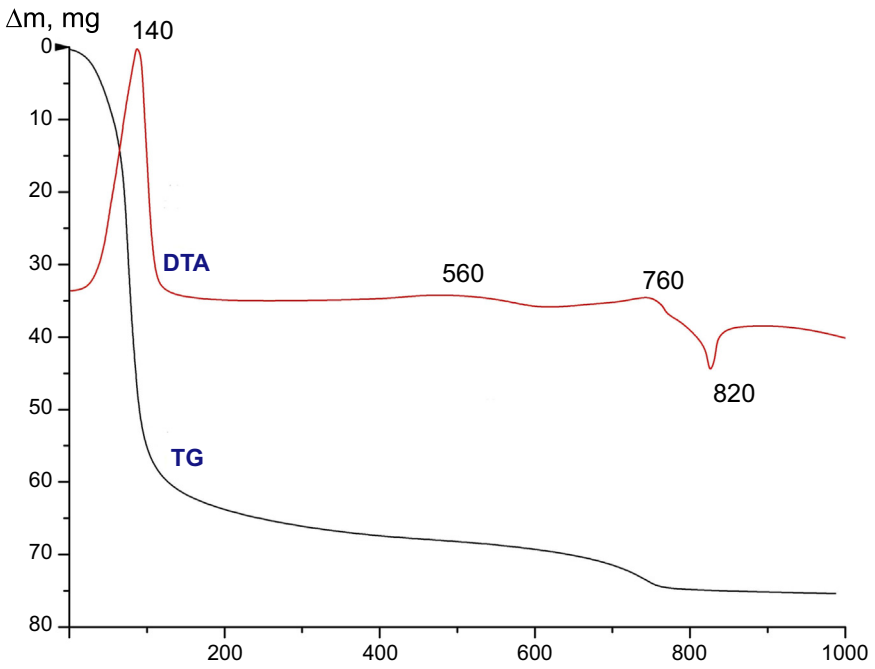

FIGURE 18.10 Thermogravigram of a sample obtained under ultrasonic treatment from borogypsum for 5 hours (potassium hydroxide) (the mass of the initial sample m = 0.142 g).

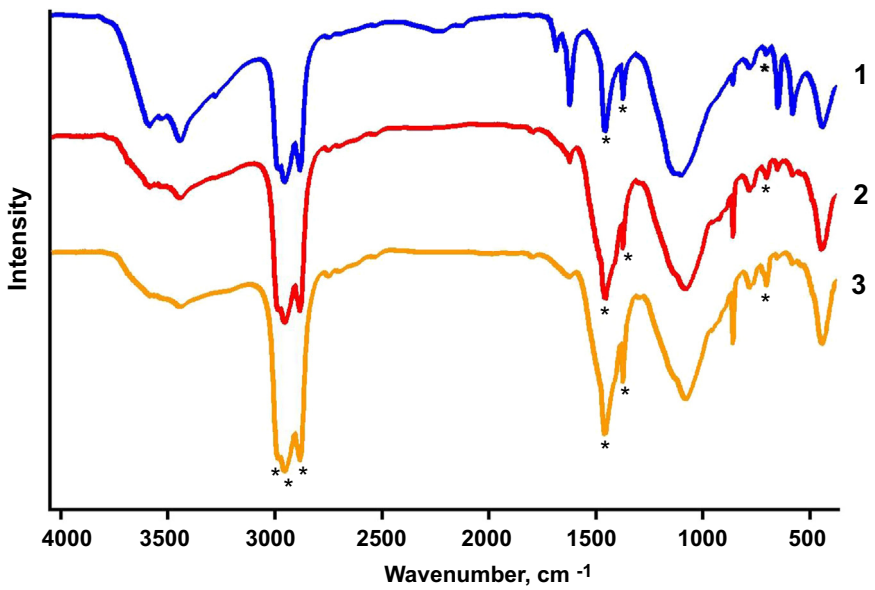

FIGURE 18.11 IR spectra of samples: 1 – borogypsum (control sample); 2, 3 – the reaction product of borogypsum and potassium hydroxide after drying at 85°C (synthesis time 9 hours): 2 – usual stirring, 3 – ultrasonic treatment; * – peaks of Vaseline.

and Fig. 18.12) are characterized by an intense absorption band in the 850–1100/cm region associated with asymmetric vibrations of Si–O–Si bridging bonds, as well as with asymmetric and symmetric vibrations of terminal Si–O bonds. With an increase in the firing temperature to 900°C (Fig. 18.12), a transition of amorphous hydrated calcium silicate to the crystalline phase of wollastonite is observed. The group of bands in the range of 550–750/cm is attributed to symmetric vibrations of Si–O–Si bridging bonds in [SiO_4] tetrahedra. The absorption bands in the low-frequency region 400–550/cm are associated with bending vibrations of terminal O–Si–O bonds and vibrations of calcium—oxygen bonds in [CaO_6]

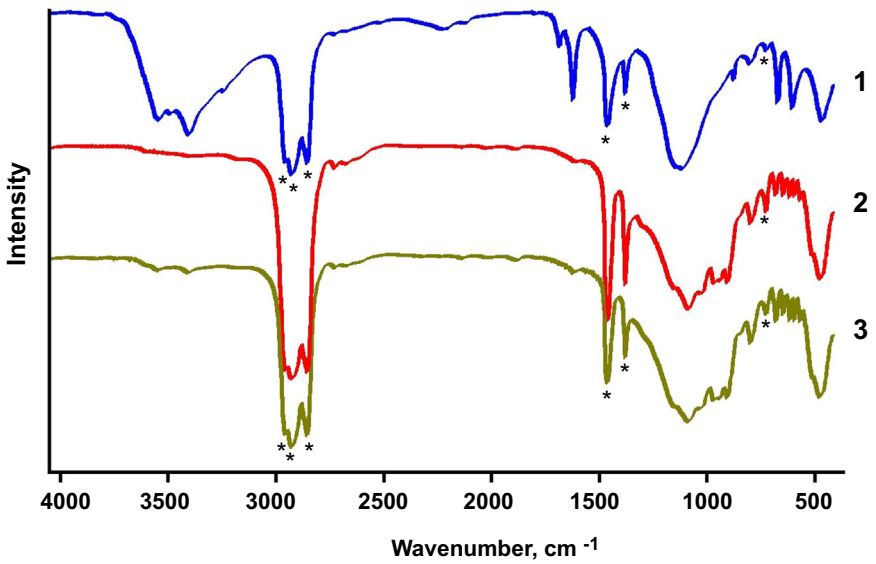

FIGURE 18.12 IR spectra of samples: 1 – borogypsum (control sample); 2, 3 – the reaction product of borogypsum and potassium hydroxide after firing at 900°C for 1 hour: 2 – usual stirring, 3 – ultrasonic treatment; * – peaks of Vaseline.

octahedra (Ismail et al., 2016; Kalinkina et al., 2001; Ribas et al., 2020; Sitarz et al., 1999). In addition, in the IR spectra of the initial reaction products (before firing) in Fig. 18.11, absorption bands are identified in the region of 1430 and 880/cm, which, according to (Bellamy, 1963; Nakamoto, 1966), are attributed to calcium carbonate and disappear during firing (Fig. 18.12). For borogypsum containing up to 70% calcium sulfate dihydrate (Fig. 18.11 and Fig. 18.12, spectrum 1), absorption bands are characteristic in the region of 1190–1020 and 650–470/cm, caused by stretching and bending vibrations of SO_4^{2-}. The absorption bands in the region of 1600 and 3400/cm are caused by bending and stretching vibrations of crystallization water (Nakamoto, 1966).

Similar absorption bands are observed in the IR spectra of the reaction products of borogypsum and sodium hydroxide.

18.5. Application of the product of UST of borogypsum as a sorbent

The scientific literature contains data on the use of calcium silicates as sorbents of heavy metals, organic dyes, and microorganisms (Coleman, 2006; Coleman et al., 2006; Maeda and Ishida, 2011; S.B. Yarusova et al., 2016; Yarusova et al., 2021).

The authors investigated the sorption properties of the product of alkaline treatment of borogypsum with potassium hydroxide using ultrasonic action at room temperature for 6 hours (Gordienko, et al., 2011a) in relation to Co^{2+} ions.

As a result of UST, a sample with a specific surface of 50 m^2/g was obtained, containing, along with an X-ray amorphous phase, crystalline phases of calcite $CaCO_3$ and quartz SiO_2. After annealing the sample at 1000°C, the X-ray diffraction pattern contains characteristic diffraction peaks, which indicate the formation of a triclinic wollastonite structure (Gordienko, et al., 2009). Data on the sorption characteristics of the material under static conditions were obtained, isotherms of sorption of cobalt ions at 20°C from aqueous solutions of cobalt (II) chloride $CoCl_2 \cdot 6H_2O$ were analyzed at the ratio of solid and liquid phases S:L = 1:40 in the range of concentrations of Co^{2+} ions from $4 \cdot 10^{-3}$ to 1.02/10 mol/l.

From the given sorption isotherms (Fig. 18.13), it can be seen that the sorption characteristics of the material obtained from borogypsum during UST are not inferior to the model calcium silicate sample obtained from the reagents, and are approximately the same in magnitude within the error of measuring the concentrations of cobalt ions. The limiting value of the sorption capacity is ~ 4.1 mmol/g.

To explain the mechanism of cobalt sorption, the Gibbs free energy ΔG°_{298} was calculated for the reactions of the interaction of an aqueous solution of cobalt chloride with calcium silicate, which are possible in the system under consideration:

$$2CaSiO_3 + 2CoCl_2 = Co_2SiO_4 + 2CaCl_2 + SiO_2 \quad (18.5)$$

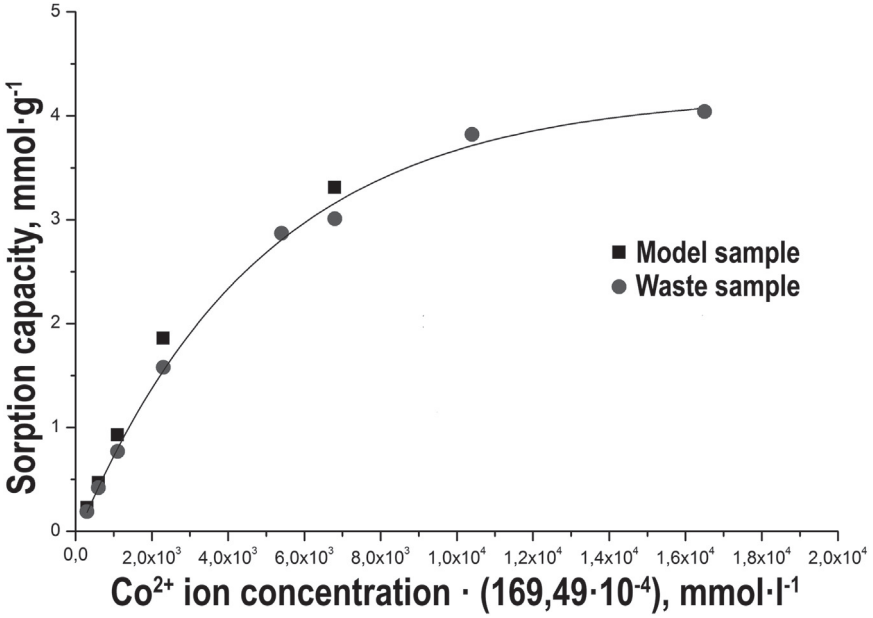

FIGURE 18.13 Isotherms of sorption of cobalt ions by model calcium silicate and obtained from borogypsum under conditions of ultrasonic exposure.

Taking into account the solubility of CO_2 in air, it is also necessary to take into account the interaction of carbonic acid, which is much stronger than polysilicic acids (acidity index for H_2CO_3 is 6.4) with calcium silicate, which actually leads to the decomposition of silicate with the formation of calcium carbonate and amorphous forms of silicon dioxide (Daval et al., 2009; Di Lorenzo et al., 2018; Gordienko et al., 2014). Both the initial calcium silicates and the products of their interaction with carbonic acid, due to their chemical nature, interact with all salts of heavy metals, stronger than polysilicon and carbonic acids, by the type of cation exchange. In this regard, one should take into account the reactions (VI–VIII):

$$CaSiO_3 + CaCO_3 + 2CoCl_2 = Co_2SiO_4 + 2CaCl_2 + CO_2 \tag{18.6}$$

$$CaSiO_3 + CaCO_3 + 2CoCl_2 + 2H_2O = 2Co(OH)_2 + 2CaCl_2 + SiO_2 + CO_2 \uparrow \tag{18.7}$$

$$CaCO_3 + 2CoCl_2 = CoCO_3 + CaCl_2 \tag{18.8}$$

The formation of metal metasilicates or orthosilicates depends on the thermodynamic properties of the substances involved in the reaction. According to the calculated values of ΔG°_{298} in the system under consideration, the most probable reactions are V, VII, and VIII with the calculated values of Gibbs free energy, respectively – 31.6; – 1057.4, and – 7.9 kJ.

It was found that one of the mechanisms of sorption in the systems under study was cation exchange between the components of the sorbent and a solution containing cobalt (II) ions. A material based on amorphous calcium silicate obtained under conditions of UST from industrial waste is of interest as a potential sorbent for purifying aqueous media from cobalt ions.

18.6 Conclusions

1. The paper shows the use of UST in the processing of industrial waste. As an example, the process of synthesis of calcium silicates from the man-made waste of boron production (borogypsum) is considered. The effect of ultrasonic action on the kinetics of the formation of these compounds from technogenic raw materials in an alkaline medium has been studied.
2. It was found that the UST of the reacting mixture allows one to increase the reaction rate and the yield of the target product. After 96 hours of interaction at the same temperature under conditions of UST, the degree of reaction when using potassium hydroxide as an alkaline agent reaches 89%, and sodium hydroxide—80%. Under normal stirring for potassium and sodium hydroxides, the reaction rates are 74% and 71%, respectively. At the initial time intervals of synthesis (from 10 minutes to 1 hour), no significant differences in the kinetics of the reaction under normal stirring and UST are observed.

3. An analysis of the kinetics of the topochemical reaction of the formation of calcium hydrosilicates from waste products of boric acid production in an aqueous alkaline medium under ultrasonic action has been carried out. The time constants of the formation of calcium hydrosilicate have been determined. It was found that the order of the reaction in the cases under consideration was <1, which indicates the occurrence of the reaction in the diffusion region.
4. For the investigated multi-component system "borogypsum–alkali–water'' ($CaSO_4$–SiO_2–KOH (NaOH)–H_2O), the calculation of the Gibbs free energy $\Delta G^{\circ}_{ch.r}$ of the corresponding reactions was carried out. It has been established that in the reaction of waste with potassium or sodium hydroxides, both sequential and parallel reactions with the participation of both calcium sulfate and silicon dioxide, which are components of the waste, are possible. Thermodynamically more probable are the reactions of the interaction of amorphous silica with alkali, followed by the interaction of the resulting silicate of the corresponding alkali metal with gypsum dihydrate to form calcium silicate.
5. The sorption properties of the product of alkaline treatment of borogypsum with potassium hydroxide, obtained by ultrasonic action at room temperature for 6 hours, with respect to Co^{2+} ions, have been investigated. It is shown that the maximum sorption capacity of the test material reaches ~ 4.1 mmol/g.
6. The conducted research will optimize the process of complex processing of borogypsum with the production of calcium hydrosilicates, wollastonite, potassium fertilizers, silicate sorbents, additives for the production of building materials.

Acknowledgments

This work was supported by a grant from the Government of the Primorye Territory (Russia) (2020–2021). This work was performed as part of a State Task for the Institute of Chemistry, Far Eastern Branch, Russian Academy of Sciences, topic no. FWFN(0205)-2022-0002, sections 3, 4.

References

Baranchikov, A.Y., Ivanov, V.K., Tretyakov, Y.D., 2007. Sonochemical synthesis of inorganic materials. Russ. Chem. Rev. 76 (2), 133–151. https://doi.org/10.1070/RC2007v076n02ABEH003644.

Bellamy, L., 1963. Infrared spectra of complex molecules. Foreign Literature Publishers, p. 590.

Belviso, C., Cavalcante, F., Fiore, S., 2013. Ultrasonic waves induce rapid zeolite synthesis in a seawater solution. Ultrason. Sonochem. 20 (1), 32–36. https://doi.org/10.1016/j.ultsonch.2012.06.004.

Boldyrev, V.V. (n.d.). Methods for studying the kinetics of thermal decomposition of solids.

Coleman, N.J., 2006. Interactions of cd(ii) with waste-derived 11 Å tobermorites. Sep. Purif. Technol. 48 (1), 62–70. https://doi.org/10.1016/j.seppur.2005.07.021.

Coleman, N.J., Brassington, D.S., Raza, A., Mendham, A.P., 2006. Sorption of Co^{2+} and Sr^{2+} by waste-derived 11 Å tobermorite. Waste Manage. (Oxford) 26 (3), 260–267. https://doi.org/10.1016/j.wasman.2005.01.019.

Daval, D., Martinez, I., Corvisier, J., Findling, N., Goffé, B., Guyot, F., 2009. Carbonation of ca-bearing silicates, the case of wollastonite: experimental investigations and kinetic modeling. Chem. Geol. 262 (3–4), 63–78. https://doi.org/10.1016/j.chemgeo.2009.01.022.

Di Lorenzo, F., Ruiz-Agudo, C., Ibañez-Velasco, A., Gil-San Millán, R., Navarro, J.A.R., Ruiz-Agudo, E., Rodriguez-Navarro, C., 2018. The carbonation of wollastonite: a model reaction to test natural and biomimetic catalysts for enhanced CO_2 sequestration. Minerals 8 (5). https://doi.org/10.3390/min8050209.

Gladun, V.D., Akatieva, L.V., & Holkin, A. (2011). Synthetic calcium silicates. Moscow: irisbook, 232.

Gordienko, P.S., Bagramyan, V.V., Yarusova, S.B., Sarkisyan, A.A., Krysenko, G.F., Polyakova, N.V., Sushkov, Y.V., 2012. Effect of microwave treatment on the kinetics of formation and morphology of calcium hydrosilicates. Russ. J. Appl. Chem. 85 (10), 1519–1523. https://doi.org/10.1134/S1070427212100059.

Gordienko, P.S., Shabalin, I.A., Yarusova, S.B., Zhevtun, I.G., Vasilenko, O.S., 2019. Equation for the kinetics of sorption of heavy-metal ions on synthetic aluminosilicates. Russ. J. Phys. Chem. A 93 (11), 2284–2290. https://doi.org/10.1134/S0036024419110116.

Gordienko, P.S., Suponina, A.P., Yarusova, S.B., Bulanova, S.B., Krysenko, G.F., Kolzunov, V.A., 2009. Study of the kinetic aspects of formation of calcium monosilicate in the model system $CaSO_4 \cdot 2H_2O$–$Na_2O \cdot SiO_2$. Russ. J. Appl. Chem. 82 (9), 1505–1509. https://doi.org/10.1134/S1070427209090018.

Gordienko, P.S., Yarusova, S.B., Bulanova, S.B., Suponina, A.P., Zarubina, N.V., Mayorov, V.Y., 2011. Sorption properties of materials based on calcium silicates in relation to Co^{2+} ions. Chem Technol. 282–290.

Gordienko, P.S., Yarusova, S.B., Buravlev, I.Yu., Zhevtun, I.G., 2021. Studying the Kinetics of the Alkaline Processing of Boron Production Wastes under Different Conditions. Russ. J. Phys. Chem. A 95 (1), 38–42. doi:10.1134/S003602442101009X.

Gordienko, P.S., Yarusova, S.B., Kolzunov, V.A., Sushkov, Y.V., Cherednichenko, A.I., Krysenko, G.F., Barinov, N., 2011. Preparation of calcium silicates from waste processing of boron-bearing minerals. Chem Technol. 142–147.

Gordienko, P.S., Yarusova, S.B., Suponina, A.P., Krysenko, G.F., Bulanova, S.B., Kolzunov, V.A., Barinov, N., 2009. Hydrochemical synthesis of calcium silicates in the systems $CaCl^{2-}$ $CaCl_2$–Na_2SiO_3–H_2O,$CaSO_4 \cdot 2H_2O$–Na_2SiO_3–H_2O, $CaSO_4 \cdot 2H_2O$–SiO_2–nH_2O–KOH. Composition, structure, properties //Vestnik of FEB RAS 30–33.

Gordienko, P.S., Yarusova, S.B., Suponina, A.P., Sushkov, Yu.V., Stepanova, V.A., 2015. Effect of ultrasonic treatment on the kinetics of the formation of calcium hydrosilicate from boron-containing technogenic wastes. Theor. Found. Chem. Eng. 49 (5), 726–730. https://doi.org/10.1134/s0040579515050061.

Gordienko, P.S., Yarusova, S.B., Suponina, A.P., Yudakov, A.A., Zhevtun, I.G., 2014. Effect of hydration and air exposure on sorption properties and phase composition of calcium silicate hydrate. Russ. J. Gen. Chem. 84 (13), 2596–2602. https://doi.org/10.1134/S1070363214130179.

Gordina, N.E., Prokof'ev, V.Yu., Borisova, T.N., Elizarova, A.M, 2019. Synthesis of granular low-modulus zeolites from metakaolin using mechanochemical activation and ultrasonic treatment. IZVESTIYA VYSSHIKH UCHEBNYKH ZAVEDENII KHIMIYA KHIMICHESKAYA TEKHNOLOGIYA 62 (7). https://doi.org/10.6060/ivkkt201962fp.5725.

Ismail, H., Shamsudin, R., Hamid, A., M., A., 2016. Effect of autoclaving and sintering on the formation of β-wollastonite. Mater. Sci. Eng. C 58, 1077–1081. https://doi.org/10.1016/j.msec.2015.09.030.

Kalinkina, E.V., Kalinkin, A.M., Forsling, W., Makarov, V.N., 2001. Sorption of atmospheric carbon dioxide and structural changeof ca and mg silicate minerals during grinding II. enstatite, åkermanite and wollastonite. Int. J. Miner. Process. 61 (4), 289–299. https://doi.org/10.1016/S0301-7516(00)00038-7.

Khmelev, V.N., Slivin, A.N., Barsukov, R.V., Tsyganok, S.N., Shalunov, A.V., 2010. Application of high intensity ultrasound in industry. - Biysk: i.i. Polzunov Altai State Technical University, p. 176.

Liu, F., Wang, X., Cao, J., 2012. Effect of ultrasonic process on carbide slag activity and synthesized xonotlite. Phys. Procedia 56–62. https://doi.org/10.1016/j.phpro.2012.03.049.

Maeda, H., Ishida, E.H., 2011. Hydrothermal preparation of diatomaceous earth combined with calcium silicate hydrate gels. J. Hazard. Mater. 185 (2–3), 858–861. https://doi.org/10.1016/j.jhazmat.2010.09.099.

Nakamoto, K. (1966). Infrared spectra of inorganic and coordination compounds, 411.

Ojumu, T.V., Du Plessis, P.W., Petrik, L.F., 2016. Synthesis of zeolite a from coal fly ash using ultrasonic treatment - a replacement for fusion step. Ultrason. Sonochem. 31, 342–349. https://doi.org/10.1016/j.ultsonch.2016.01.016.

Pal, P., Das, J.K., Das, N., Bandyopadhyay, S., 2013. Synthesis of nap zeolite at room temperature and short crystallization time by sonochemical method. Ultrason. Sonochem. 20 (1), 314–321. https://doi.org/10.1016/j.ultsonch.2012.07.012.

Ribas, R.G., Campos, T.M.B., Schatkoski, V.M., de Menezes, B.R.C., Montanheiro, T.L.d.A., Thim, G.P., 2020. α-wollastonite crystallization at low temperature. Ceram. Int. 46 (5), 6575–6580. https://doi.org/10.1016/j.ceramint.2019.11.143.

Sitarz, M., Handke, M., Mozgawa, W., 1999. Calculations of silicooxygen ring vibration frequencies. Spectrochimica Acta – Part A: Molecular and Biomolecular Spectroscopy 55 (14), 2831–2837. https://doi.org/10.1016/S1386-1425(99)00101-8.

Vaičiukyniene, D., Kantautas, A., Vaitkevičius, V., Jakevičius, L., Rudžionis, Ž., Paškevičius, M., 2015. Effects of ultrasonic treatment on zeolite naa synthesized from by-product silica. Ultrason. Sonochem. 27, 515–521. https://doi.org/10.1016/j.ultsonch.2015.06.001.

Wang, B., Wu, J., Yuan, Z.-Y., Li, N., Xiang, S., 2008a. Synthesis of MCM-22 zeolite by an ultrasonic-assisted aging procedure. Ultrason. Sonochem. 15 (4), 334–338. https://doi.org/10.1016/j.ultsonch.2007.07.007.

Wang, B., Wu, J., Yuan, Z.-Y., Li, N., Xiang, S., 2008b. Synthesis of MCM-22 zeolite by an ultrasonic-assisted aging procedure. Ultrason. Sonochem. 15 (4), 334–338. https://doi.org/10.1016/j.ultsonch.2007.07.007.

Yaroslavtsev, A.B. (2009). Solid state chemistry. Moscow: nauchniy mir, 328.

Yarusova, S.B., Gordienko, P.S., Yudakov, A.A., Azarova, Y.A., Yashchuk, R.D., 2016. Kinetics of the sorption of heavy-metal ions by a sorbent obtained from boric acid production waste. Theor. Found. Chem. Eng. 50 (5), 841–845. https://doi.org/10.1134/S0040579516050250.

Yarusova, S.B., Somova, S.N., Kharchenko, U.V., Gordienko, P.S., & Beleneva, I.A. (2021). Effect of the conditions of the synthesis of calcium silicates on the kinetics of microbiological treatment of aqueous media. Russian j inorganic chemistry. 66,1135–1140. https://doi.org/10.1134/S0036023621080313

Yarusova, SB., Gordienko, P.S., Sharma, Y.C., Perfilev, A.V., Kozin, A.V., 2017. Industrial waste as raw material for producing synthetic wollastonite in Russia. Int J Environ Sci and Develop 1–5. https://doi.org/10.18178/ijesd.2017.8.1.910.

Zhang, M., Chang, J., 2010. Surfactant-assisted sonochemical synthesis of hollow calcium silicate hydrate (CSH) microspheres for drug delivery. Ultrason. Sonochem. 17 (5), 789–792. https://doi.org/10.1016/j.ultsonch.2010.01.012.

Chapter 19

The sonochemical and ultrasound-assisted production of hydrogen: energy efficiency for the generation of an energy carrier

Nour Hane Merabet and Kaouther Kerboua
Higher School of Industrial Technologies, Department of Engineering, Annaba, Algeria

19.1 Introduction: hydrogen and ultrasound

19.1.1 State of the art

Hydrogen has attracted worldwide attention as the alternative fuel of the near future, aiming to replace hydrocarbons by a clean energy (Jain, 2009). Hydrogen is the most abundant element in the universe with high specific energy combustion of 140 MJ/kg, a value that makes of hydrogen a valuable energy carrier (Islam et al., 2019; Kerboua and Hamdaoui, 2019a).

Hydrocarbon's reforming is the most widely used and efficient technique to generate hydrogen, due to the low costs of production. However, this method of H_2 synthesis is considered as a polluting technique due to the high emissions of greenhouse gases (Islam et al., 2019, 2020). On the other hand, hydrogen production from water as a feedstock (considered as a green process to generate hydrogen) is based on various techniques such as electrolysis, photolysis, and photocatalysis. Nevertheless, unlike the first technique, water splitting technology is considered as a low efficient process (Kerboua and Hamdaoui, 2019a).

Lately, the application of ultrasound in chemistry, which is known as sonochemistry, has gained considerable interest due to the positive effects it brings to the conventional process (Torres-Palma and Serna-Galvis, 2018). Richard and Loomis (Richards and Loomis, 1927) were the first to experiment the chemical effects induced by high-frequency acoustic waves.

When subjected to ultrasonic waves, water knows the formation of microscopic chemical sites where water molecules are cleaved, the process is known as sonolysis. Sonolysis can then be a promising technology for dissociating water molecules (Theerthagiri et al., 2020). During the sonolysis of water, acoustic cavitation defined as the formation, growth, and violent collapse of bubbles is generated as a result of the propagation of ultrasound waves across the aqueous solution (Kerboua and Hamdaoui, 2019b; Merouani et al., 2015a,b). The sonloysis mainly results in the formation of free radicals such as $H^{\bullet}$ and $OH^{\bullet}$ (Penconi et al., 2015). Hence, hydrogen is produced by the recombination of these free radicals.

Parke and Taylor (Parke and Taylor, 1956) were the first to verify the formation of hydrogen and hydroxyl radicals during water sonication. Furthermore, Henglein (Hart and Henglein, 1985) conducted an experimental study where solutions of potassium iodide and sodium formate were exposed to an ultrasonic wave of 300 kHz under atmospheres of argon, oxygen, and argon–oxygen mixtures, the study was carried out in order to quantify the products of sonolysis. Hydrogen and hydrogen peroxide were the main products according to the same study.

Recently, tens ofstudies have focused on modeling and simulation of sonochemical processes. Merouani et al. through considerable works (Merouani et al., 2013; Merouani et al., 2015a,b; Merouani et al., 2016) developed a numerical model to describe the mechanism of the sonochemical hydrogen production (Merouani et al., 2015a,b). The same research group

Energy Aspects of Acoustic Cavitation and Sonochemistry: Fundamentals and Engineering. DOI: https://doi.org/10.1016/B978-0-323-91937-1.00004-9
Copyright © 2022 Elsevier Inc. All rights reserved.

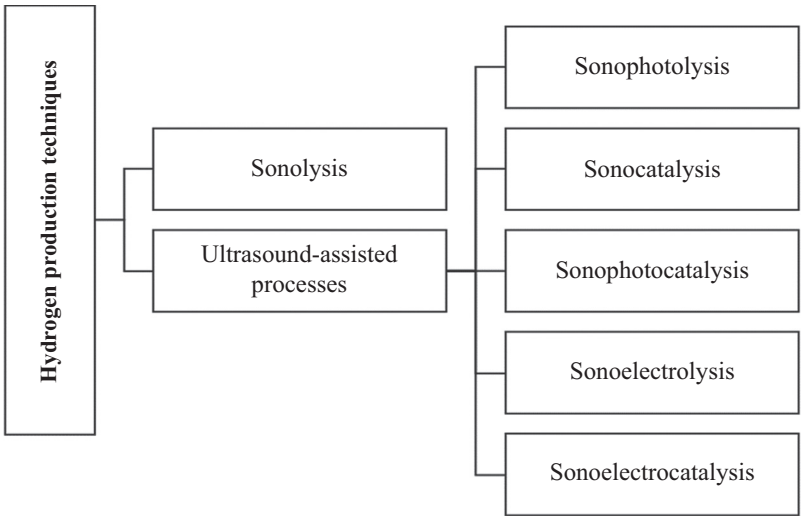

FIGURE 19.1 Hydrogen production techniques using ultrasounds.

carried out several parametric studies based on numerical simulation of the sonochemical production of H_2 (Merouani et al., 2015a,b) including the effects of ambient size of the bubble and maximum temperature and pressure attained at the harsh collapse (Merouani and Hamdaoui, 2016, 2018). Lately, Dehane et al. (Dehane et al., 2021) studied numerically the effect of statistic pressure on the size and the temperature of the bubble in the sonochemical process. In a recent paper, Kerboua et al. (Kerboua et al., 2021a) investigated theoretical and experimental approaches of the sonolytic production of hydrogen at single bubble and multibubble scales, under different atmospheres. Both experimental and theoretical approaches showed a perfect agreement.

On the other hand, water dissociation through ultrasound-assisted pathways is also a possible clean method for hydrogen production. It consists in combining sonication to catalysis, electrolysis and photolysis which results in sonocatalysis, sonophotolysis, sonoelectrolysis, sonoelectrocatalysis, and sonophotocatalysis, as illustrated in Fig. 19.1.

Indeed, it was demonstrated that ultrasound-aided processes induce synergetic effects in terms of pollutants degradation efficiency as compared to each isolated method (Kerboua and Hamdaoui, 2020; Merouani et al., 2016), indicating a higher production of free radicals and supposing possible higher emergence of hydrogen.

Kerboua et al. (Kerboua and Hamdaoui, 2019a) presented in 2019 a detailed review of ultrasound pathways for hydrogen generation including sonolysis, sonophotolysis, sonocatalysis, and sonophotocatalysis.

Through an experimental investigation, Penconi et al. (Penconi et al., 2015) investigated the hydrogen production by photolysis, sonolysis, and photosonolysis of water in different synthesized solid solutions. This latter consists in the combination of light irradiation with ultrasound sources. It was found that coupling ultrasounds to photolysis process enhances significantly H_2 production.

Cotana et al. (Cotana et al., 2007) coupled sonolysis and photolysis in order to investigate the effect of ultrasounds and sunlight radiation on water under different pressure conditions. It was observed that coupling ultrasounds to electromagnetic waves enhanced the hydrogen production process by 5.1% (Kerboua and Hamdaoui, 2019a). Moreover, the amount of hydrogen production was higher for lower pressure.

In a similar study of Rossi et al. (Rossi et al., 2009), which deals with the hydrogen production from water by the combined action of ultrasounds and catalyzed photolysis known as sonophotocatalysis, it was demonstrated that sonophotocatalysis enhances hydrogen production by 14.6%. Sonophotocatalytic pathway refers to the simultaneous irradiation of ultrasound and light where usually nanostructured materials or semiconductors are used as electrodes (Harada, 2001).

At the opposite, Harada (Harada, 2001) affirmed in another experimental study that coupling sonolysis to photocatalysis process resulted in a drop in hydrogen production (Kerboua and Hamdaoui, 2020; Kerboua and Hamdaoui, 2019a).

Electrolysis is another synthesis process consisting of splitting water into hydrogen and oxygen by applying an electrical power. Yet, 4% of the total production of hydrogen is obtained via water electrolysis worldwide (Islam et al., 2020). Water dissociation via electrolysis can be improved by applying acoustic power (Theerthagiri et al., 2020; Zore et al., 2021). The research group of Pollet presented pioneering works in this field. They demonstrated that water electrolysis could be

enhanced when integrating the sonication into the process (Theerthagiri et al., 2020). Tens of studies investigated the sonoelectrolysis process for hydrogen production and reported the positive effect of ultrasound on increasing the amount of hydrogen production. For instance, in a study conducted by Li et al. (Li et al., 2009), sonoelectrolysis promoted the yield of hydrogen production by 5% to 25%. Furthermore, Zadeh (Zadeh, 2014) and Symes (Symes, 2011) investigated the effect of ultrasound on weak acidic and alkaline electrolysis of water for hydrogen production. The observations showed that ultrasound increased the rate of H_2 production by lowering the overpotential (Islam et al., 2020).

Coupling the electrocatalytic pathway to ultrasound could be a promising pathway for hydrogen production in terms of energy efficiency. It is the method where catalysts are used as electrodes in water splitting via a sonoelectrochemical process. Pollet et al. (Pollet et al., 2020) assumed that ultrasound improves the hydrogen evolution reaction activity HER on platinium electrode and decreases the overpotential compared to the silent technique.

It must be pointed out that in contrast to sonolysis, in ultrasound-aided pathways, more experimental studies have been investigated while very few theoretical works, or not at all, could be found in the literature.

19.1.2 Role of ultrasound

19.1.2.1 Role of ultrasound in water sonolysis

Ultrasound consists of a sound wave of a frequency that is higher than the frequency of human's audible hearing range and varies from 20 kHz to 10 MHz. The direct or indirect application of ultrasounds in a variety of fields has proven its efficiency due to the enhancement in reaction rates in chemical or electrochemical systems (Thompson and Doraiswamy, 1999).

In water sonolysis, the propagation of ultrasound waves in a liquid medium produces two major phenomena, namely acoustic streaming and acoustic cavitation bubbles. The most important effect is acoustic cavitation that is defined as the nucleation, growth, and violent implosion of microbubbles. The formation of bubbles is due to the drop of the pressure of the liquid to negative values in the presence of dissolved gases in the liquid medium (Torres-Palma and Serna-Galvis, 2018). Bubble growth may occur either by rectified diffusion or due to the coalescence of these bubbles (Kerboua and Hamdaoui, 2020). Several effects occur at the oscillation and collapse of these microbubbles. Some are of physical nature, namely the microstreaming, microjets, and shockwaves, inducing agitation and mass transfer, some others are of chemical nature, namely sonochemistry which mainly consists in the production of reactive radicals as a result of the apparition of a hot spot (Merouani, et al., 2015a,b; Zore et al., 2021). Indeed, each cavitation bubble acts as a hotspot that generates extreme temperature and pressure in the range of 5000 K and 1000 atm (Torres-Palma and Serna-Galvis, 2018). In the literature, it was proved that this increase in temperature and pressure conducts to the creation of combustion conditions inside the bubble, which generates highly reactive species such as $H^{\bullet}$, $OH^{\bullet}$, and H_2O_2 (Theerthagiri et al., 2020). It is generally assumed that in the case of pure sonolysis, chemical effects associated with sonication, namely sonochemistry, are responsible for the production of hydrogen. The physical effects of sonication are rarely invoked in the case of sonication.

Hart and Henglein (Hart and Henglein, 1985) and Guttiérez et al. (Gutiérrez et al., 1987) affirmed that hydrogen peroxide is formed via the combination of $HO^{\bullet}$ radicals while hydrogen is produced through the combination of $H^{\bullet}$ radicals as indicated in the following reaction.

$$H^{\bullet} + H^{\bullet} \leftrightarrow H_2 \tag{19.1}$$

The evolution of the sonochemical mechanism and consequently the sonochemical hydrogen production depends on several sonochemical parameters such as ultrasonic frequency, acoustic power, dissolved gases, composition of the liquid, liquid temperature, and pH of the solution (Torres-Palma and Serna-Galvis, 2018). Various studies found in the literature invoke the impact of these operational parameters on the sonochemical activity of the acoustic cavitation bubble.

When it comes to the effect of ultrasonic frequency, Lim et al. (Lim et al., 2011) affirmed that the raise of ultrasonic frequency leads to the increase in the cavitation collapse per time unit (Torres-Palma and Serna-Galvis, 2018). An early study was conducted by Kang et al. (Kang et al., 1999) and reported that at frequencies in the range of 200–350 kHz, the generation of free radicals was the highest. This has been also demonstrated numerically by Kerboua et al. using an upscaled model (Kerboua, Hamdaoui, and Alghyamah, 2021). In order to explain the mechanism of hydrogen production during sonication of water, Merouani et al. (Merouani et al., 2015a,b) elaborated a numerical model of cavitation in a single argon bubble. It was reported that at respective frequencies of 20 and 355 kHz, the reaction time reduced to the half when passing from the former to the latter. This was explained by the fact that at high frequencies time for bubble collapse is shorter, hence, the reaction inside a bubble is rapid and has not sufficient time to evolve and then converts free radicals into H_2. Very recently, Kerboua et al. (Kerboua et al., 2021a) investigated numerically and experimentally the sonochemical production of hydrogen as a function of acoustic frequency over the range from 20 to 488 kHz. It was demonstrated that

at single bubble scale and for similar sonication duration, the highest hydrogen production is attained at 210 kHz, while the modeling and simulation at multibubble scale revealed an optimum at 20 kHz. This was in perfect accordance with the experimental variation of the yield of sonochemical hydrogen as a function of frequency for similar acoustic intensities.

It was also observed in the study of Merouani et al. (Merouani et al., 2015a,b) that the major amount of hydrogen was formed in the bubble through recombination of $H^{\bullet}$ and $HO^{\bullet}$ radicals via reaction 19.2.

$$H^{\bullet} + HO^{\bullet} \leftrightarrow H_2 + O^{\bullet} \tag{19.2}$$

While a minor fraction of hydrogen was generated at the liquid phase of the bubble via reaction (19.1).

In another work, Merouani et al. (Merouani and Hamdaoui, 2016) investigated numerically the size of a single bubble for the production of hydrogen. Several parameters such as ultrasonic frequency (from 140 to 1100 kHz), acoustic intensity (0.75 and 1 W/cm^2), and liquid temperature (from 20 to 50°C) have been examined for their effects on the optimal ambient radius for the sonochemical hydrogen production from a single acoustic cavitation bubble. It was found that the optimum radius of the bubble for hydrogen production increased with the raise of ultrasonic intensity, in parallel, the evolution of the optimum radius was inversely proportional to the ultrasonic frequency and liquid temperature for one acoustic cycle. More recently, in an opinion paper published by Kerboua et al. (Kerboua et al., 2021b), the effect of the ambient size of the bubble has been inspected in terms of the generated "hot spot" conditions and consequently hydrogen production. The nature of the bubble has been particularly highlighted and the yields of produced hydrogen were compared to the conventional sonochemical activity limit.

Properties of dissolved gas generate also a specific impact on the sonochemical process for H_2 production. Several studies could be found in the bibliography to explain the impact of dissolved gas on the cavitation events, thus, on the H_2 production. For example, Hart and Henglein (Hart and Henglein, 1985) analyzed the products of water and iodide solution sonolysis under argon, oxygen, and argon–oxygen atmospheres. It was observed that the amount of hydrogen production under the argon atmosphere was higher than H_2O_2 and O_2 species. In a recent research, Kerboua et al. (Kerboua et al., 2021b) investigated numerically the effect of dissolved gases on the kinetic of the sonochemical hydrogen production. The study was conducted under four atmospheres, namely N_2, O_2, Ar, and air at 20 kHz. The study demonstrated that argon provides the optimal conditions for the sonochemical activity, particularly in terms of hydrogen production at the single bubble scale. In another study conducted by Gielen et al. (Gielen et al., 2016), hydrogen production was the highest under argon saturated atmosphere while the lowest yield was retrieved under CO_2 . This observation was explained by the thermal properties of each saturating gas, namely the thermal conductivity and the polytropic index. The gases with higher polytropic index induce more important increase in the temperature inside the bubble during the collapsing stage. On the other hand, low-thermal conductivity favors high hot spot temperature at implosion stage by reducing the heat dissipation, which may improve the sonochemical reactions producing hydrogen (Merouani et al., 2015c; Rooze et al., 2013). In general, at the implosion of the bubble, energy is higher with monoatomic gases such as helium and argon than with diatomic gases due to the larger ratio of specific heat (Thompson and Doraiswamy, 1999). Additionally, Rooze et al. (Rooze et al., 2013) reported that the increase of the amount of dissolved gases in aqueous solution yields in the increase in bubble nucleation (Lubetkin, 2003), this was explained by the decrease in surface tension when the gas is more soluble. However, the impact of dissolved gases on the cavitation phenomenon is still under discussion. It is important to retain that argon has the highest polytropic index and the lowest thermal conductivity, which leads to the highest heat accumulation in the bubble volume. In contrast, carbon dioxide is characterized by the lowest polytropic index and the highest thermal conductivity.

The effect of several other parameters was also the subject of numerous researches. For example, it was demonstrated by Kerboua et al. (Kerboua and Hamdaoui, 2018) that the increase of the acoustic amplitude at a single bubble scale results in the enhancement of hydrogen production. However, experiments revealed that at bubble population scale, the increase of the acoustic intensity does not indefinitely promote the sonochemical production of hydrogen. For instance, it was proven that increasing the acoustic power induces an increase in the rate of reaction until attaining a maximum before decreasing again with the increase of the acoustic intensity (Thompson and Doraiswamy, 1999). The decrease in the reaction rate is due to the cloud of cavitation bubbles formed at high powers near the probe surface that slows the energy transferred from the probe to the fluid (Contamine et al., 1995). The sonochemical production of hydrogen is then expected to show an optimum in function of the acoustic frequency. Literature also reports the effect of liquid medium composition on the sonochemical activity, and some works have particularly focused on hydrogen production. For instance, Penconi et al. (Penconi et al., 2015) demonstrated that adding ethanol to water solution in 20% vol in the sonolysis process yields to the increase in hydrogen production of about 1.4%. In an early study by Buttner et al. (Büttner et al., 1991) dealing with the sonolysis of a water–methanol mixture, it was reported that the sonochemical production of hydrogen attains an optimum within a 10% v/v solution of methanol. In the same context, Kerboua et al. (Kerboua et al., 2021d) elaborated a numerical study to inspect the effect of methanol concentration in an aqueous solution on the sonochemical hydrogen production under a frequency of

200 kHz and an amplitude of 1.5 atm. This was attributed to the additional decomposition reactions affecting the methanol molecule which is rich in hydrogen atom. The generated free radicals increases then the probability of recombination leading to the formation of hydrogen. This is mostly applicable to all the other molecules containing a high fraction of the hydrogen element.

It is worthy to note that modeling of ultrasound effect is usually associated with the single acoustic cavitation bubble. Atcheley et al. (Atchley et al., 1988) explained in an experimental work dealing with the cavitation thresholds that ultrasound effects are due not only to a single cavitation bubble but to the cloud of bubbles. Furthermore, Leighton et al. (Leighton, 1995) affirmed that bubbles are not expected to behave according to the single bubble theory, and it is not sufficient to take into consideration the bubble population and the mutual effects of the bubbles. Leighton et al. (Leighton, 1995) remarked that bubble population disperse, focus, and channel the sound waves as they propagate through the medium and localize the cavitational activity to discrete "hot spots." Hence, portions of the liquid solution may experience intense sonochemical activity, while some other portions may be submitted to silent conditions.

19.1.2.2 Role of ultrasound in assisted pathways

Ultrasound-assisted processes, as reported in the literature, promise to be an effective pathway for enhancing H_2 production. The ultrasound-assisted processes rely mainly on the physical effects induced by acoustic cavitation, particularly at its collapse. However, it is not excluded that physical and chemical effects related to acoustic cavitation bubble may be combined and act simultaneously in the hybrid process.

In photosonolysis, the superposition of light and ultrasound results simply in an addition of their respective characteristics (Toma et al., 2001). Dharmarathne et al. (Dharmarathne et al., 2012) used photons generated from cavitation which is called sonoluminescence to examine the use of sonoluminescence and sonochemiluminescence as photon sources in photocatalytic process.

When solid in solution is irradiated by ultrasound it is called sonocatalysis. Ultrasound can affect the catalyst surface by altering the desorption of radicals on the solid surface (Thompson and Doraiswamy, 1999) allowing better contact of reactants with the catalyst and hence higher production rate of hydrogen.

In the case of sonophotocatalysis, it was reported by Penconi et al. (Penconi et al., 2015) that ultrasound and thus acoustic cavitation contributes in the enhancement of synergy effect due to particle decomposition, with a consequent size reduction and surface area evolution of the catalyst. The acoustic waves are also believed to promote mass transport in the liquid media by provoking an agitation effect (Kerboua and Hamdaoui, 2019a). In addition, in sonocatalysis and sonophotocatalysis, it is thought that active sites are higher in electrodes with an amorphous structure than a crystalline one because of unsaturated vacancies on its surface (Yadav et al., 2021).

In the case of sonoelectrolysis, splitting water to H_2 and O_2 by applying electrical energy via electrolysis is basically most used water-based method for hydrogen production. Coupling this technique to ultrasound has shown noticeable improvements in hydrogen production. It is thought that the action of ultrasound waves removes bubbles from electrode surfaces and liberates the nucleation sites, thus new electrochemical reactions appear as a result of cavitation activity, which then conducts to hydrogen production. Furthermore, Walton et al. (Walton et al., 1996) studied the effect of ultrasound in water, NaCl, and HCl electrolysis, they observed an enhancement in hydrogen and chlorine evolution at the electrodes.

Cataldo (Cataldo, 1992) who was the first to investigate the effect of ultrasound during the electrolysis of aqueous solutions of NaCl and HCl, reported that the application of ultrasound results in the increase of hydrogen production on the cathode and chlorine on the anode. In the same paper, Cataldo (Cataldo, 1992) assumed that the main phenomenon resulting during sonication is the degassing activity on the electrode which decreases the accumulation of bubbles in the solution and at the electrode surface. According to Pollet (Pollet, 2012), these crucial effects of ultrasound activity contribute to the limitation of the overpotential. Additionally, ultrasound waves and acoustic cavitation bubbles produce depolarization effects, increase the mass transfer rate, decrease the double layer thickness (Walton et al., 1996) and also facilitate the passage of ions through the electrode double layer. Hence, ultrasonic waves encourage species that are adsorbed at the electrode to desorb from the electrode surface; which is the case with graphite electrodes. Thus, the overpotential may be lowered due to the aforementioned effects, resulting in an enhancement in the rate of H_2 generation.

The role of ultrasound was also studied by Li et al. (Li et al., 2009) for water electrolysis in alkaline solution and different concentrations of NaOH under 60 KHz and 50 W. It was observed that applying ultrasound results in an enhancement in the range of 10%–25% in terms of energy-saving and mass transfer and thus an improvement in H_2 production efficiency within the range of 5% to 18% at high current density exceeding 80 $mA.cm^{-2}$.

McMurray et al. (McMurray et al., 1998) investigated the effect of ultrasound on hydrogen evolution and oxygen reduction by using a titanium sonotrode and graphite electrodes and reported that hydrogen and oxygen evolution increased as a result of the rise of mass transfer and the decrease of activation overpotential.

Zadeh (Zadeh, 2014) investigated the effect of added ultrasound on a conventional alkaline water electrolysis, where it was determined that ultrasound improved the production efficiency by 4.5% and energy efficiency by 1.3%. The introduction of the ultrasound resulted in bubble removal from the surface of the electrode and the electrolyte solution, which prepared the electrode surface for the electrochemical reactions and thus enhanced the hydrogen generation.

When acoustic cavitation bubble oscillates and collapses on the electrode surface, microstreaming, and microjets, which are physical effects accompanying the bubble oscillation and collapse, respectively, are believed to contribute significantly to the increase of mass transfer to the electrode surface, electrode surface cleaning and activation (Islam et al., 2020).

Finally, in sonoelectrocatalysis, Li et al. (Li et al., 2021) explained in their study that in electrocatalysis, ultrasounds affect the crystalline structure, enlarge the interlayer resulting in expanded electrochemical active surface area, and enhancing oxygen evolution reaction. In addition, Pollet et al. (Pollet et al., 2020) studied the effect of power ultrasound on hydrogen evolution production in sonoelectrocatalysis process. According to these authors, under sonication and due to the secondary Bjerknes effect (Zhang et al., 2016), micro bubbles coalesce to macro bubbles, which increases the bubble size and enhances consequently the bubbles' buoyancy, augmenting electrolyte hydrogen degassing. Thus, it was concluded that ultrasound helps the detachment of hydrogen bubbles from the platinium electrode surface and does not change the mechanism of Hydrogen evolution reaction. The action of sonication, and acoustic cavitation bubble is deemed as purely physical in this case.

19.2 The ultrasound-assisted pathway for hydrogen production: theoretical approach and outcomes

19.2.1 Proposed mechanisms and comprehensive findings

Ultrasound-assisted pathways are based on several theories that explain the application of ultrasounds in the aforementioned techniques. These theories relate to either sonochemical or sonophysical mechanisms or their combination.

Sonochemical mechanisms describing the plausible reactions occurring in the reactional sites of the acoustic bubble were explored by several researchers. In the present section, mechanisms proposed to explain hydrogen production within the cavitation bubble during the collapse phase will be presented.

Merouani et al. (Merouani et al., 2015a,b), as reported in a previous section, proposed a series of numerical simulations of chemical reactions within an argon bubble during water sonolysis. The numerical pathway is based on several assumptions and equations. It was reported that radicals start to form via H_2O splitting as the bubble temperature increases during the adiabatic phase. It was observed that when applying an acoustic pressure, the bubble initially expands during the rarefaction phase of the acoustic wave, then during the compression phase, the bubble violently implodes to a minimum size. Bubbles undergo successive collapses accompanied by an increase of pressure and temperature inside the bubble to the range of thousands of bars and Kelvin, respectively. At the final stage of the collapse and in the presence of water vapor, chemical reactions are generated inside the bubble under these enormous conditions giving rise to chemical products such as: O, H_2, H_2O_2, $H^\bullet$, $OH^\bullet$, $HO_2^\bullet$. It was concluded that hydrogen was principally produced within the gas phase of the bubble through the reaction 19.2.

In an attempt to understand the mechanism of the sonochemical production of hydrogen, Kerboua et al. (Kerboua et al., 2021a) proposed a numerical model to quantify the hydrogen production at single acoustic cavitation bubble and multibubble scale. The dosage of hydrogen was also performed experimentally using gas chromatography technique GC coupled to a thermal conductivity detector TCD. The experiments were carried out under four saturating gases, namely Ar, N_2, O_2, and air. Kerboua et al. (Kerboua et al., 2021a) reported the following common elementary reactions possible for hydrogen production inside a single bubble during collapse.

$$H^\bullet + H^\bullet + M \rightarrow H_2 + M \tag{19.3}$$

$$H^\bullet + HO_2^\bullet \leftrightarrow H_2 + O_2 \tag{19.4}$$

$$H^\bullet + H_2O \leftrightarrow H_2 + OH^\bullet \tag{19.5}$$

$$H^\bullet + H_2O_2 \leftrightarrow H_2 + HO_2^\bullet \tag{19.6}$$

In another study, Kerboua et al. (Kerboua et al., 2021b) clarified that the nature of the dissolved gas could change the kinetics of the aforementioned reactions of hydrogen production within the acoustic cavitation bubble by activating supplementary reactions. The possible reactions are reported in Tables 19.1–19.3 under Ar, N_2, O_2, and air, respectively.

TABLE 19.1 Chemical scheme containing the possible elementary reactions resulting of the cleavage of water under Ar atmosphere inside a single acoustic cavitation bubble.

i	Reaction i	Third body coefficient	A_i	b_i	E_i/R_g (K)	ΔH_i (kJ/mol)
1	$H_2O + M \rightarrow H^\bullet + {}^\bullet OH + M$	H_2O: 12, H_2:0.73, Ar: 0.38	1.91×10^{17}	-1.83	5.96×10^{04}	508.220
2	${}^\bullet OH + M \rightarrow H^\bullet + O + M$	H_2O: 12, H_2: 2.5, Ar: 0.75	9.88×10^{11}	-0.74	5.09×10^{04}	436.230
3	$O + O + M \rightarrow O_2 + M$	H_2O: 12, H_2: 2.5, Ar: 0.75	6.17×10^{05}	-0.50	0.00×10^{00}	-505.400
4	$H^\bullet + O_2 \rightarrow O + {}^\bullet OH$	–	1.92×10^{08}	0.00	8.27×10^{03}	69.150
5	$H^\bullet + O_2 + M \rightarrow HO2^\bullet + M$	H_2O: 14, H_2: 1.3, Ar: 0.67	1.48×10^{00}	0.60	0.00×10^{00}	20.480
6	$O + H_2O \rightarrow {}^\bullet OH + {}^\bullet OH$		2.97×10^{00}	2.02	6.74×10^{03}	72.590
7	$HO_2{}^\bullet + H \rightarrow O_2 + H_2$		1.66×10^{07}	0.00	4.14×10^{02}	-239.670
8	$HO_2{}^\bullet + O \rightarrow {}^\bullet OH + O_2$		7.08×10^{07}	0.00	1.48×10^{02}	-162.210
9	$HO_2{}^\bullet + {}^\bullet OH \rightarrow H_2O + O_2$		3.25×10^{07}	0.00	0.00×10^{00}	-231.850
10	$H_2 + M \rightarrow H + H + M$;	H_2O: 12, H_2: 2.5	2.89×10^{07}	0.00	-2.50×10^{02}	-304.440
11	$O + H_2 \rightarrow {}^\bullet OH + H^\bullet$	–	4.58×10^{13}	-1.40	5.25×10^{04}	444.470
12	${}^\bullet OH + H_2 \rightarrow H^\bullet + H_2O$	–	3.82×10^{06}	0.00	4.00×10^{03}	8.230
13	$H_2O_2 + O_2 \rightarrow HO_2{}^\bullet + HO_2{}^\bullet$	–	2.16×10^{02}	1.52	1.74×10^{03}	-64.330
14	$H_2O_2 + M \rightarrow {}^\bullet OH + {}^\bullet OH + M$	H_2O: 12, H_2: 2.5, Ar: 0.64	4.63×10^{10}	-0.35	2.55×10^{04}	175.350
15	$H_2O_2 + H^\bullet \rightarrow H_2O + {}^\bullet OH$		2.95×10^{08}	0.00	2.44×10^{04}	-217.890
16	$H_2O_2 + H^\bullet \rightarrow H_2 + HO_2{}^\bullet$	–	2.41×10^{07}	0.00	2.00×10^{03}	-290.930
17	$H_2O_2 + O \rightarrow {}^\bullet OH + HO_2{}^\bullet$	–	6.03×10^{07}	0.00	4.00×10^{03}	-64.320
18	$H_2O_2 + {}^\bullet OH \rightarrow H_2O + HO_2{}^\bullet$	–	9.55×10^{00}	2.00	2.00×10^{03}	-56.080
19	$H^\bullet + {}^\bullet OH + M \rightarrow H_2O + M$	H_2O: 12, H_2: 0.73, Ar:0.38	2.20×10^{10}	-2.00	0.00×10^{00}	-508.220
20	$H^\bullet + O + M \rightarrow {}^\bullet OH + M$	H_2O: 12, H_2: 2.5, Ar:0.75	4.71×10^{06}	-1.00	0.00×10^{00}	-436.230
21	$O_2 + M \rightarrow O + O + M$	H_2O: 12, H_2: 2.5, Ar:0.75	4.52×10^{11}	-0.64	5.98×10^{04}	505.400
22	$O + {}^\bullet OH \rightarrow H^\bullet + O_2$		5.48×10^{05}	0.39	-1.47×10^{02}	-69.150
23	$HO_2{}^\bullet + M \rightarrow H^\bullet + O_2 + M$	H_2O: 14, H_2: 1.3, Ar: 0.67	3.09×10^{06}	0.53	2.46×10^{04}	-20.480
24	${}^\bullet OH + {}^\bullet OH \rightarrow O + H_2O$	–	1.47×10^{-01}	2.11	-1.46×10^{03}	-72.590
25	$O_2 + H_2 \rightarrow HO_2{}^\bullet + H^\bullet$	–	3.16×10^{06}	0.35	2.79×10^{04}	239.670
26	${}^\bullet OH + O_2 \rightarrow HO_2{}^\bullet + O$	–	2.03×10^{04}	0.72	1.85×10^{04}	162.210
27	$H_2O + O_2 \rightarrow HO_2{}^\bullet + {}^\bullet OH$	–	3.25×10^{06}	0.33	2.68×10^{04}	231.850
28	$H^\bullet + H^\bullet + M \rightarrow H_2 + M$	H_2O: 12, H_2: 2.5	5.86×10^{07}	0.24	3.47×10^{04}	304.440
29	${}^\bullet OH + H^\bullet \rightarrow O + H_2$	–	1.15×10^{08}	-1.68	4.12×10^{02}	-444.470
30	$H^\bullet + H_2O \rightarrow {}^\bullet OH + H_2$	–	2.67×10^{-02}	2.65	2.45×10^{03}	-8.230
31	$HO_2{}^\bullet + HO_2{}^\bullet \rightarrow H_2O_2 + O_2$	–	2.30×10^{03}	1.40	9.22×10^{03}	64.330
32	${}^\bullet OH + {}^\bullet OH + M \rightarrow H_2O_2 + M$	H_2O: 12, H_2: 2.5, Ar: 0.64	4.20×10^{08}	0.00	6.03×10^{03}	-175.350
33	$H_2O + {}^\bullet OH \rightarrow H_2O_2 + H^\bullet$	–	1.00×10^{02}	-0.37	0.00×10^{00}	217.890
34	$H_2 + HO_2{}^\bullet \rightarrow H_2O_2 + H^\bullet$	–	1.27×10^{02}	1.31	3.59×10^{04}	290.930
35	${}^\bullet OH + HO_2{}^\bullet \rightarrow H_2O_2 + O$	–	1.04×10^{05}	0.70	1.20×10^{04}	64.320
36	$H_2O + HO_2{}^\bullet \rightarrow H_2O_2 + {}^\bullet OH$	–	8.66×10^{-03}	2.68	9.34×10^{03}	56.080
37	$O_2 + H_2 \rightarrow H^\bullet + HO_2{}^\bullet$	–	1.84×10^{04}	0.59	1.55×10^{04}	128.670

Wang et al. (Wang et al., 2010) proposed a mechanism for the sonochemical hydrogen production in the presence of Au/TiO_2 as a catalyst in methanol/water solutions. The investigation was carried out using a modified gas chromatograph to analyze the hydrogen-isotope composition of the evolved hydrogen gas. it was observed that hydrogen was formed by three pathways.

(i) According to the first pathway, after propagation of acoustic waves in water, hotspots phenomena occur and bubbles undergo enormous conditions of temperature and pressure. Hence, $H^\bullet$ and $OH^\bullet$ radicals form. These radicals recombine

TABLE 19.2 Chemical scheme containing the possible elementary reactions resulting of the cleavage of water under O_2 atmosphere inside a single acoustic cavitation bubble.

i	Reaction i	Third body coefficient	A_i	b_i	E_i/R_g (K)	ΔH_i (kJ/mol)
1	$H + O_2 \rightarrow O + {}^{\bullet}OH$	–	1.92×10^{8}	0	8270	69.17
2	$O + H_2 \rightarrow H^{\bullet} + {}^{\bullet}OH$	–	5.08×10^{-2}	2.67	3166	8.23
3	${}^{\bullet}OH + H_2 \rightarrow H^{\bullet} + H_2O$	–	2.18×10^{2}	1.51	1726	−64.35
4	${}^{\bullet}OH + {}^{\bullet}OH \rightarrow H_2O + O$	–	2.1×10^{2}	1.4	200	−72.59
5	$H_2 + M \rightarrow H^{\bullet} + H^{\bullet} + M$	H_2: 2.5, H_2O: 16.0	4.58×10^{13}	−1.4	52500	444.47
6	$O + O + M \rightarrow O_2 + M$	H_2: 2.5, H_2O: 16.0	6.17×10^{3}	−0.5	0	−505.4
7	$O + H^{\bullet} + M \rightarrow {}^{\bullet}OH + M$	H_2O: 5.0	4.72×10^{5}	−1.0	0	−436.23
8	$H^{\bullet} + {}^{\bullet}OH + M \rightarrow H_2O + M$	H_2: 2.5, H_2O: 16.0	2.25×10^{10}	−2.0	0	−508.82
9	$H^{\bullet} + O_2 + M \rightarrow HO_2{}^{\bullet} + M$	H_2: 2.5, H_2O: 16.0	2.00×10^{3}	0	−500	−204.8
10	$H^{\bullet} + HO_2{}^{\bullet} \rightarrow O_2 + H_2$	–	6.63×10^{7}	0	1070	−239.67
11	$H^{\bullet} + HO_2{}^{\bullet} \rightarrow {}^{\bullet}OH + {}^{\bullet}OH$	–	1.69×10^{8}	0	440	−162.26
12	$O + HO_2{}^{\bullet} \rightarrow O_2 + {}^{\bullet}OH$	–	1.81×10^{7}	0	−200	−231.85
13	${}^{\bullet}OH + HO_2{}^{\bullet} \rightarrow O_2 + H_2O$	–	1.45×10^{10}	−1.0	0	−304.44
14	$HO_2{}^{\bullet} + HO_2{}^{\bullet} \rightarrow O_2 + H_2O_2$	–	3.0×10^{6}	0	700	−175.35
15	$H_2O_2 + M \rightarrow {}^{\bullet}OH + {}^{\bullet}OH + M$	H_2: 2.5, H_2O: 16.0	1.2×10^{11}	0	22900	217.89
16	$H_2O_2 + H^{\bullet} \rightarrow H_2O + {}^{\bullet}OH$	–	3.2×10^{8}	0	4510	−290.93
17	$H_2O_2 + H^{\bullet} \rightarrow H_2 + HO_2{}^{\bullet}$	–	4.82×10^{7}	0	4000	−64.32
18	$H_2O_2 + O \rightarrow {}^{\bullet}OH + HO_2{}^{\bullet}$	–	9.55	2	2000	−56.08
19	$H_2O_2 + {}^{\bullet}OH \rightarrow H_2O + HO_2{}^{\bullet}$	–	1.00×10^{7}	0	900	−128.67
20	$O_3 + M_1 \rightarrow O_2 + O + M_2$	M_1 O_2: 1.64; M_2 O_2: 1.63, H_2O: 15	2.48×10^{8}	0	11430	109.27
21	$O_3 + O \rightarrow O_2 + O_2$	–	5.2×10^{6}	0	2090	−396.14
22	$O_3 + {}^{\bullet}OH \rightarrow O_2 + HO_2{}^{\bullet}$	–	7.8×10^{5}	0	960	−164.92
23	$O_3 + HO_2{}^{\bullet} \rightarrow O_2 + O_2 + {}^{\bullet}OH$	–	1×10^{5}	0	1410	−121.92
24	$O_3 + H^{\bullet} \rightarrow HO_2{}^{\bullet} + O$	–	9×10^{6}	0.5	2010	−135.65
25	$O_3 + H^{\bullet} \rightarrow O_2 + {}^{\bullet}OH$	–	1.6×10^{7}	0	0	−96.2
26	$O + {}^{\bullet}OH \rightarrow H + O_2$	–	7.18×10^{5}	0.36	−342	-69.17
27	$H^{\bullet} + {}^{\bullet}OH \rightarrow O + H_2$	–	2.64×10^{-2}	2.65	2245	-8.23
28	$H^{\bullet} + H_2O \rightarrow {}^{\bullet}OH + H_2$	–	1.02×10^{3}	1.51	9370	64.35
29	$H_2O + O \rightarrow {}^{\bullet}OH + {}^{\bullet}OH$	–	2.21×10^{3}	1.4	8368	72.59
30	$H^{\bullet} + H^{\bullet}$ 2 $H^{\bullet} + M \rightarrow H_2 + M$	H_2: 2.5, H_2O: 16.0	2.45×10^{8}	−1.78	480	-444.47
31	$O_2 + M \rightarrow O + O + M$	H_2: 2.5, H_2O: 16.0	1.58×10^{11}	−0.5	59472	505.4
32	${}^{\bullet}OH + M \rightarrow O + H^{\bullet} + M$	H_2O: 5.0	4.66×10^{11}	−0.65	51200	436.23
33	$H_2O + M \rightarrow H^{\bullet} + {}^{\bullet}OH + M$	H_2: 2.5, H_2O: 16.0	1.96×10^{16}	−1.62	59700	508.82
34	$HO_2{}^{\bullet} + M \rightarrow H^{\bullet} + O_2 + M$	H_2: 2.5, H_2O: 16.0	2.46×10^{9}	0	24300	204.8
35	$O_2 + H_2 \rightarrow H^{\bullet} + HO_2{}^{\bullet}$	–	2.19×10^{7}	0.28	28390	239.67
36	${}^{\bullet}OH + {}^{\bullet}OH \rightarrow H^{\bullet} + HO_2{}^{\bullet}$	–	1.08×10^{5}	0.61	18230	162.26
37	$O_2 + {}^{\bullet}OH \rightarrow O + HO_2{}^{\bullet}$	–	3.1×10^{6}	0.26	26083	231.85
38	$O_2 + H_2O \rightarrow {}^{\bullet}OH + HO_2{}^{\bullet}$	–	2.18×10^{10}	−0.72	34813	304.44
39	$O_2 + H_2O_2 \rightarrow HO_2{}^{\bullet} + HO_2{}^{\bullet}$	–	4.53×10^{8}	−0.39	19700	175.35
40	${}^{\bullet}OH + {}^{\bullet}OH + M \rightarrow H_2O_2 + M$;	H_2: 2.5, H_2O: 16.0	9.0×10^{-1}	0.90	−3050	-217.89
41	$H_2O + {}^{\bullet}OH \rightarrow H_2O_2 + H^{\bullet}$	–	1.14×10^{3}	1.36	38180	290.93
42	$H_2 + HO_2{}^{\bullet} \rightarrow H_2O_2 + H^{\bullet}$	–	1.41×10^{5}	0.66	12320	64.32
43	${}^{\bullet}OH + HO_2{}^{\bullet} \rightarrow H_2O_2 + O$	–	4.62×10^{-3}	2.75	9277	56.08
44	$H_2O + HO_2{}^{\bullet} \rightarrow H_2O_2 + {}^{\bullet}OH$	–	2.8×10^{7}	0	16500	128.67
45	$O_2 + O + M \rightarrow O_3 + M$;	M_1 O_2: 1.64; M_2 O_2: 1.63, H_2O: 15	4.1	0	−1057	-109.27

TABLE 19.3 Chemical scheme containing the possible elementary reactions resulting of the cleavage of water under N_2 or air atmosphere inside a single acoustic cavitation bubble.

i	Reaction i	Third body coefficient	A_i	b_i	E_i/R_g (K)	ΔH_i (kJ/mol)
1	$H + O_2 \rightarrow O + {}^{\bullet}OH$	–	1.92×10^{8}	0	8270	69.17
2	$O + H_2 \rightarrow H^{\bullet} + {}^{\bullet}OH$	–	5.08×10^{-2}	2.67	3166	8.23
3	${}^{\bullet}OH + H_2 \rightarrow H^{\bullet} + H_2O$	–	2.18×10^{2}	1.51	1726	−64.35
4	${}^{\bullet}OH + {}^{\bullet}OH \rightarrow H_2O + O$	–	2.1×10^{2}	1.4	200	−72.59
5	$H_2 + M \rightarrow H^{\bullet} + H^{\bullet} + M$	H_2: 2.5, H_2O: 16.0	4.58×10^{13}	−1.4	52500	444.47
6	$O + O + M \rightarrow O_2 + M$	H_2: 2.5, H_2O: 16.0	6.17×10^{3}	−0.5	0	−505.4
7	$O + H^{\bullet} + M \rightarrow {}^{\bullet}OH + M$	H_2O: 5.0	4.72×10^{5}	−1.0	0	−436.23
8	$H^{\bullet} + {}^{\bullet}OH + M \rightarrow H_2O + M$	H_2: 2.5, H_2O: 16.0	2.25×10^{10}	−2.0	0	−508.82
9	$H^{\bullet} + O_2 + M \rightarrow HO_2{}^{\bullet} + M$	H_2: 2.5, H_2O: 16.0	2.00×10^{3}	0	−500	−204.8
10	$H^{\bullet} + HO_2{}^{\bullet} \rightarrow O_2 + H_2$	–	6.63×10^{7}	0	1070	−239.67
11	$H^{\bullet} + HO_2{}^{\bullet} \rightarrow {}^{\bullet}OH + {}^{\bullet}OH$	–	1.69×10^{8}	0	440	−162.26
12	$O + HO_2{}^{\bullet} \rightarrow O_2 + {}^{\bullet}OH$	–	1.81×10^{7}	0	−200	−231.85
13	${}^{\bullet}OH + HO_2{}^{\bullet} \rightarrow O_2 + H_2O$	–	1.45×10^{10}	−1.0	0	−304.44
14	$HO_2{}^{\bullet} + HO_2{}^{\bullet} \rightarrow O_2 + H_2O_2$	–	3.0×10^{6}	0	700	−175.35
15	$H_2O_2 + M \rightarrow {}^{\bullet}OH + {}^{\bullet}OH + M$	H_2: 2.5, H_2O: 16.0	1.2×10^{11}	0	22900	217.89
16	$H_2O_2 + H^{\bullet} \rightarrow H_2O + {}^{\bullet}OH$	–	3.2×10^{8}	0	4510	−290.93
17	$H_2O_2 + H^{\bullet} \rightarrow H_2 + HO_2{}^{\bullet}$	–	4.82×10^{7}	0	4000	−64.32
18	$H_2O_2 + O \rightarrow {}^{\bullet}OH + HO_2{}^{\bullet}$	–	9.55	2	2000	−56.08
19	$H_2O_2 + {}^{\bullet}OH \rightarrow H_2O + HO_2{}^{\bullet}$	–	1.00×10^{7}	0	900	−128.67
20	$O_3 + M_1 \rightarrow O_2 + O + M_2$	M_1 O_2: 1.64; M_2 O_2: 1.63, H_2O: 15	2.48×10^{8}	0	11430	109.27
21	$O_3 + O \rightarrow O_2 + O_2$	–	5.2×10^{6}	0	2090	−396.14
22	$O_3 + {}^{\bullet}OH \rightarrow O_2 + HO_2{}^{\bullet}$	–	7.8×10^{5}	0	960	−164.92
23	$O_3 + HO_2{}^{\bullet} \rightarrow O_2 + O_2 + {}^{\bullet}OH$	–	1×10^{5}	0	1410	−121.92
24	$O_3 + H^{\bullet} \rightarrow HO_2{}^{\bullet} + O$	–	9×10^{6}	0.5	2010	−135.65
25	$O_3 + H^{\bullet} \rightarrow O_2 + {}^{\bullet}OH$	–	1.6×10^{7}	0	0	−96.2
26	$O + {}^{\bullet}OH \rightarrow H + O_2$	–	7.18×10^{5}	0.36	−342	-69.17
27	$H^{\bullet} + {}^{\bullet}OH \rightarrow O + H_2$	–	2.64×10^{-2}	2.65	2245	-8.23
28	$H^{\bullet} + H_2O \rightarrow {}^{\bullet}OH + H_2$	–	1.02×10^{3}	1.51	9370	64.35
29	$H_2O + O \rightarrow {}^{\bullet}OH + {}^{\bullet}OH$	–	2.21×10^{3}	1.4	8368	72.59
30	$H^{\bullet} + H^{\bullet} + M \rightarrow H_2 + M$	H_2: 2.5, H_2O: 16.0	2.45×10^{8}	−1.78	480	-444.47
31	$O_2 + M \rightarrow O + O + M$	H_2: 2.5, H_2O: 16.0	1.58×10^{11}	−0.5	59472	505.4
32	${}^{\bullet}OH + M \rightarrow O + H^{\bullet} + M$	H_2O: 5.0	4.66×10^{11}	−0.65	51200	436.23
33	$H_2O + M \rightarrow H^{\bullet} + {}^{\bullet}OH + M$	H_2: 2.5, H_2O: 16.0	1.96×10^{16}	−1.62	59700	508.82
34	$HO_2{}^{\bullet} + M \rightarrow H^{\bullet} + O_2 + M$	H_2: 2.5, H_2O: 16.0	2.46×10^{9}	0	24300	204.8
35	$O_2 + H_2 \rightarrow H^{\bullet} + HO_2{}^{\bullet}$	–	2.19×10^{7}	0.28	28390	239.67
36	${}^{\bullet}OH + {}^{\bullet}OH \rightarrow H^{\bullet} + HO_2{}^{\bullet}$	–	1.08×10^{5}	0.61	18230	162.26
37	$O_2 + {}^{\bullet}OH \rightarrow O + HO_2{}^{\bullet}$	–	3.1×10^{6}	0.26	26083	231.85
38	$O_2 + H_2O \rightarrow {}^{\bullet}OH + HO_2{}^{\bullet}$	–	2.18×10^{10}	−0.72	34813	304.44
39	$O_2 + H_2O_2 \rightarrow HO_2{}^{\bullet} + HO_2{}^{\bullet}$	–	4.53×10^{8}	−0.39	19700	175.35
40	${}^{\bullet}OH + {}^{\bullet}OH + M \rightarrow H_2O_2 + M$	H_2: 2.5, H_2O: 16.0	9.0×10^{-1}	0.90	−3050	-217.89
41	$H_2O + {}^{\bullet}OH \rightarrow H_2O_2 + H^{\bullet}$	–	1.14×10^{3}	1.36	38180	290.93

(*continued on next page*)

TABLE 19.3 Chemical scheme containing the possible elementary reactions resulting of the cleavage of water under N_2 or air atmosphere inside a single acoustic cavitation bubble—cont'd

i	Reaction i	Third body coefficient	A_i	b_i	E_i/R_g (K)	ΔH_i (kJ/mol)
42	$H_2 + HO_2^\bullet \rightarrow H_2O_2 + H^\bullet$	–	1.41×10^5	0.66	12320	64.32
43	$^\bullet OH + HO_2^\bullet \rightarrow H_2O_2 + O$	–	4.62×10^{-3}	2.75	9277	56.08
44	$H_2O + HO_2^\bullet \rightarrow H_2O_2 + {}^\bullet OH$	–	2.8×10^7	0	16500	128.67
45	$O_2 + O + M_1 \rightarrow O_3 + M_2$	M_1 O_2: 1.64; M_2 O_2: 1.63, H_2O: 15	4.1	0	−1057	-109.27
46	$N_2+O_2 \rightarrow N_2O + O$	–	6.3×10^7	0	55200	336.05
47	$O_2+N \rightarrow O + NO$	–	6.4×10^3	1	3150	133.37
48	$O+NO+ M_1 \rightarrow O + NO_2 + M_2$	M_1 NO: 20; M_2 O: 20, N_2: 20	1.1×10^3	0	-940	-311.14
49	$O+ N_2 \rightarrow N + NO$	–	7.6×10^{10}	0	38000	314.24
50	$HO^\bullet + N \rightarrow H^\bullet + NO$	–	4.5×10^7	0	0	202.53
51	$HO^\bullet + NO + M \rightarrow HNO_2 + M$	H_2: 2.3	8×10^3	0	-1000	-208.02
52	$HO^\bullet + NO_2 + M \rightarrow HNO_3 + M$	N_2: 2	5×10^5	0	0	-206.25
53	$HO^\bullet + N_2 \rightarrow N_2O + H^\bullet$	–	2.5×10^6	0	39000	267.32
54	$N_2O + O \rightarrow N_2+O_2$	–	1×10^8	0	14100	-336.05
55	$O + NO \rightarrow O_2+N$	–	1.5×10^3	1	19500	-133.37
56	$O + NO_2 + M_1 \rightarrow O+NO+ M_2$	M_1 NO: 20; M_2 O: 20, N_2: 20	1.1×10^{10}	0	33000	311.14
57	$N + NO \rightarrow O+ N_2$	–	1.6×10^7	0	0	-314.24
58	$H^\bullet + NO \rightarrow HO^\bullet + N$	–	1.7×10^8	0	24500	-202.53
59	$HNO_2 + M \rightarrow HO^\bullet + NO + M$	H_2: 2.3	5.1×10^{11}	-1	25000	208.02
60	$HNO_3 + M \rightarrow HO^\bullet + NO_2 + M$	N_2: 2	1.6×10^9	0	15400	206.25
61	$N_2O + H^\bullet \rightarrow HO^\bullet + N_2$	–	7.6×10^7	0	7600	-267.32

and give rise to H_2 and H_2O_2. For capturing radicals, a spin trap 5,5-Dimethyl-1-pyrroline-N-oxide DMPO was used, which in turn gives rise to a long-lived spin adducts through the following reactions:

$$H_2O \xrightarrow{\text{heat}} H^\bullet + HO^\bullet \tag{19.7}$$

$$H^\bullet + HO^\bullet \rightarrow H_2O \tag{19.8}$$

$$H^\bullet + H^\bullet \rightarrow H_2 \tag{19.9}$$

$$2\,HO^\bullet \rightarrow H_2O_2 \tag{19.10}$$

$$HO^\bullet + DMPO \rightarrow DMPO - OH \tag{19.11}$$

$$H^\bullet + DMPO \rightarrow DMPO - H \tag{19.12}$$

(ii) In the second pathway, H-abstraction from methanol by H• generated by water cleavage occurs when methanol is added with a concentration of ~5% (v/v). Enhancement in H_2 yield is explained in this case by the fact that methanol captures H• and HO• radicals which leads to the effective inhibition of recombination between H• and HO•.

(iii) Finally, the third and last pathway is about the thermal reforming of methanol which also generates H_2. Furthermore, it was observed that thermal sonochemical reactions within the cavitation bubbles were improved by Au/TiO_2. H_2 generated during water sonolysis in the presence of Au/TiO_2 was higher than in the presence of TiO_2, which is at its turn higher than in the absence of the catalyst (Wang et al., 2010).

19.2.2 Experimental findings

In addition to the aforementioned theoretical studies, the literature counts some works that have experimented the ultrasound-assisted pathways for hydrogen production. Sasikala et al., (Sasikala et al., 2007), investigated a novel effect of enhancement of hydrogen yield from water. The experiment was carried out in the presence of dispersed metallic particles, semiconductor photocatalyst, transition metal oxide, mixed oxide, or insulator material. The effect of methanol on hydrogen yield production was also studied. It was observed that hydrogen yield was enhanced when adding methanol and using both methanol and suspended particles during water sonolysis. This enhancement was attributed to the fact that in the presence of these suspended particles, the number of cavitation bubble increases, in addition to the efficient scavenging of $HO^{\bullet}$ radicals by methanol. The experimental study of Sasikala et al. (Sasikala et al., 2007) relied on the sonochemical pathway promoted by the creation of nucleation sites for acoustic cavitation bubbles by the addition of particles (heterogenous nucleation), and the scavenging of hydroxyl radical, providing more free hydrogen radicals for the formation of hydrogen molecule.

Lin et al. (Lin and Hourng, 2014) reported that under the ultrasonic field, the bubbles covering the nucleation sites on the electrode are rapidly removed from the electrode and then, the nucleation sites are refilled by the bulk electrolyte to form a new gas bubble. Hence, in sonoelectrolysis, the pathway of the ultrasonic enhancement of hydrogen production is rather physical, relying on the degassing effect of ultrasounds.

In an experimental investigation performed by Penconi et al. (Penconi et al., 2015), the authors investigated the hydrogen production by photolysis, sonolysis, and photosonolysis of water with different solid solutions. It was found that the hybrid action of light and ultrasound waves in the presence of S: $Y_{0.8}$ $Ga_{0.2}$ InO_3 favors an appreciable synergistic effect for H_2 production. According to the author, this enhancement of the synergetic effect was explained by the fact that acoustic cavitation bubbes enhance the photocatalytic activity by improving the surface area of catalytic. In addition, the presence of ethanol in water generates more nuclei for bubble formation. Finally, it also relies on the improvement of mass transport due to the stirring effect provoked by the acoustic streaming and turbulence created from cavitation.

Dharmarathne et al. (Dharmarathne et al., 2012) examined the use of sonoluminescence and sonochemiluminescence as in situ photon sources to photocatalytically generate molecular hydrogen in aqueous solutions under 355 kHz ultrasound. Sonochemically produced radicals were found to interfere with the photocatalytic processes; nevertheless, significant amounts of H_2 could be produced from SL or SCL activation of the photosensitizer. The predominant pathway of the ultrasonic effect is rather optical in this study, the sonoluminescent bubble appears to act as a photon source to activate the photosensitizer. However, optimization of the overall process by reducing undesirable side reactions remains to be tackled according to the authors.

The study of Rossi et al. (Rossi et al., 2009) dealt with the hydrogen production from water by the combined action of sonolysis and catalyzed photolysis. Hydrogen production from the aqueous solution was evaluated using gas chromatography. Gas sampling was made using a gastight syringe inserted into the reactor through the duct with porous septa in butilic rubber and Teflon. The study affirmed that sonophotocatalysis enhances hydrogen production by 14.6%. According to the authors, the ultrasounds' action passes mainly by the photosonolysis pathway.

19.3 Analysis and orientations on the future of the sonochemical hydrogen: insights into the main challenges

19.3.1 Energy-yields balance

It could be remarked that most of the published literature in the field of hydrogen generation using sonochemistry and ultrasound aided-pathways has focused only on determining the most effective atmosphere to improve hydrogen yield (Gielen et al., 2016; Merouani et al., 2015a,b; Merouani et al., 2016; Merouani and Hamdaoui, 2016), investigating the effect of different parameters on hydrogen yield (Cataldo, 1992; Dehane et al., 2021; Kohno et al., 2011; Li et al., 2009; Pollet et al., 2020) or studying sonochemical reactions inside the bubble (Leighton, 1995; Merouani et al., 2015a,b; Wang et al., 2010). Although most scientists agreed on the positive effect of ultrasound on chemical reactions in hydrogen production as a green process, the energy efficiency was often ignored as a key for the scaling-up of the technology.

In a recent study, Kerboua et al.(Kerboua et al., 2021a) investigated the efficiency of sonochemical hydrogen production as a green process based upon operational efficiency metrics related to mass and energy yields at both microscopic and macroscopic scales. The energy efficiency was estimated through the ratio of acoustic to electric powers, as shown in Eq. (19.13).

$$E_e = \frac{P}{P_e} \tag{19.13}$$

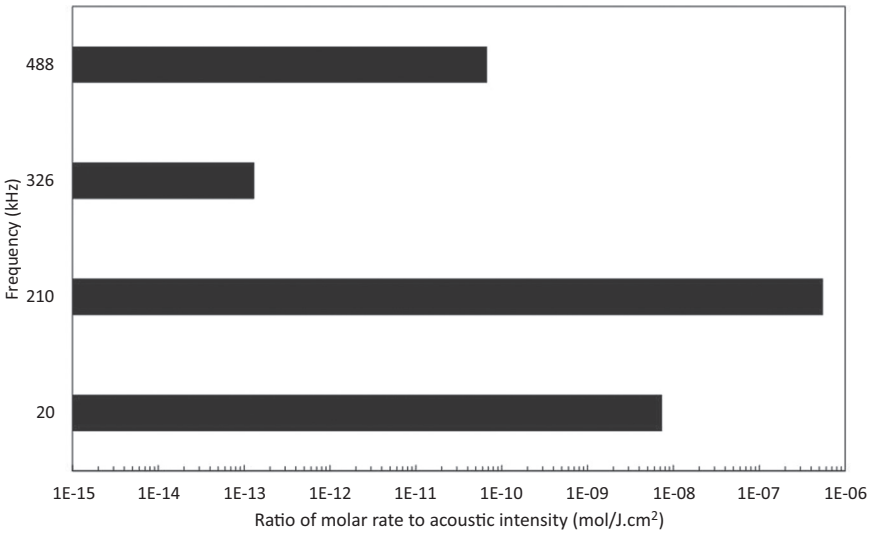

FIGURE 19.2 Mass to acoustic energy ratio at reactor scale in function of frequency. Simulated hydrogen yield to acoustic energy ratio at reactor scale in function of frequency for a common acoustic intensity of 0.48 W/cm^2.

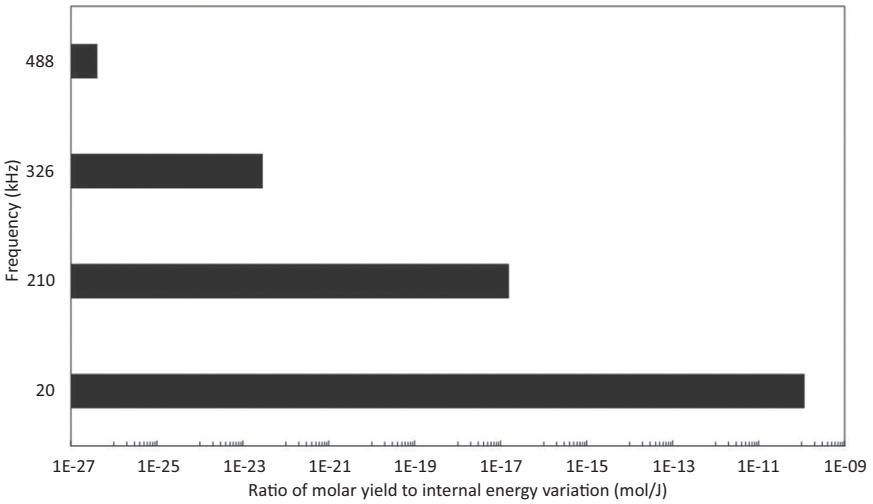

FIGURE 19.3 Mass to internal energy ratio at single bubble scale in function of frequency. Simulated hydrogen yield to internal energy ratio at single bubble scale in function of frequency for a common acoustic intensity of 0.48 W/cm^2.

While the mass to energy efficiency was evaluated via the yield of produced hydrogen to acoustic energy and internal energy. Results are shown in Figs. 19.2 and 19.3 for both reactor and single bubble scale, respectively.

Owing to the fact that the sonochemical activity and consequently the sonochemical production of hydrogen harnesses a fraction of the effective acoustic energy transmitted to the liquid medium, the study of Kerboua et al. (Kerboua et al., 2021a) also estimated the efficiency of electric to acoustic energy conversion in function of the acoustic frequency. The results showed that the highest percentage of conversion of electric energy to acoustic energy was achieved at 20 KHz with 61.25%.

When investigating the synergistic effects in hydrogen production through water sonophotocatalysis, Gentili et al. (Gentili et al., 2009) have highlighted the importance of minimizing energy consumption and getting hydrogen with a net energy balance. However, due to the complexity of regulating energy balance, alternative enhancement was proposed such as improving the acoustical matching between the source and liquid, optimizing the durability of catalysts, water/ethanol ratio, and surface/volume ratio of the solution.

Concerning sonoelectrolysis, Kirchoff et al. (Kirchoff et al., 2010) focused on energy efficiency for hydrogen production. They invented a device with catalytic enhancements to raise the volume and mass of generated H_2 and lower the

amount of energy required as much as possible. Similarly, Burjanadze (Burjanadze, 2014) developed a device for hydrogen generation via cavitation-electrolysis. Plasma chemical technique was combined to electrochemical process for hydrogen production in order to increase the energy efficiency of sonoelectrolysis process and minimize hydrogen generation cost.

According to Islam et al. (Islam et al., 2019) energy consumption may be reduced using ultrasound by reducing the decomposition voltage. Hence, they demonstrated through numerical investigation that sonoelectrochemical energy efficiency could be increased by 10% as compared to electrochemical process. Lin et al. (Lin and Hourng, 2014) referred to the importance of reducing electrical power and economical power efficiency in sonoelectrolysis hydrogen production. Therefore, the difference in electrical power and economical power efficiency are essential reference values when using ultrasonic water electrolysis according to the same authors.

Finally, it is worthy to note that literature suffers from a lack of works treating the energy-yield balance which needs to be taken into consideration for the scaling-up of sonolysis and ultrasound-aided techniques of hydrogen production.

19.3.2 Adapting the technology

The application of ultrasounds at large scales to promote electrochemical and sonoelectrochemical processes has been known since 1960, for the degradation of organic compounds and the treatment of sewage sludge (Mason, 2000). However, the use of sonochemical and ultrasound-assisted pathways for hydrogen production is currently under investigation only at laboratory and pilot scales. When moving to large scale processes, the problem becomes more complex. Larger volume is needed, which requires more power and hence higher energy consumption and cost. Practically, two issues will occur when bigger volumes are adopted, more transducers are needed and homogeneity of acoustic amplitude inside the reactor volume is disturbed (Kerboua and Hamdaoui, 2021). Some researchers made serious attempts to partially resolve the problematic of scaling up sonochemistry and ultrasound assisted processes. For instance, Tudela (Tudela et al., 2014) reviewed the simulation works concerning the acoustic field inside the reactor at large scale and highlighted the problems that arise in sonochemical reactors, namely the vibration of the reactor walls and the nonlinear phenomena inherent to the presence of ultrasonic cavitation. The author reported that vibration of the solid boundaries should be taken into consideration since these later affect the acoustic field and cause the deformation of the reactor's wall. Pollet (Pollet, 2012) reported that there is probably an enhancement in the mass transfer in sonoelectrochemical process via bubble motion. On the other hand, the design of sonochemical reactors and the integration of ultrasound emitters in conventional devices needs additional focus to scale-up hydrogen production. Mason (Mason, 2003) investigated the possibilities for the scale up process in sonochemistry. Mason reported that understanding the physical and chemical effects of the acoustic cavitation process is a crucial phase for optimizing sonochemical process at pilot scale and moving to industrial scale. Minimization of energy consumption may be the major challenge at techno-economic perspective that needs deeper inspection for large scale process. Mason (Mason, 2003) assumed that reducing energy consumption could be achieved through the improvement of reactor geometry which according to Sancheti and Gogate (Sancheti and Gogate, 2017) should affect the kinetic and operational parameters such as the ultrasonic frequency, the acoustic power, the temperature and the pressure, the sonication time, the liquid physiochemical properties (dissolved gases), and the mixing parameters in stirred reactors (Kerboua and Hamdaoui, 2020).

Mason (Mason, 2000) reported that transducers are essential components to consider when studying sonochemical processes. In addition, efficient transducers that ensure uniform cavitational activity at large scale are a major challenge (Gogate et al., 2011). Piezoelectric transducers are the most utilized for generating ultrasonic waves in cutting, welding, and sonochemistry application. Langevin piezoelectric transducers are also widely used due to their adaption in high volume and high acoustic powers; however, these transducers are designed for low frequencies (Kerboua and Hamdaoui, 2021), Langevin transducers are then not effective for an ultrasound application in water splitting. Another technology that may solve the problem of homogeneity in acoustic fields at large volume is the use of microflow sonochemical reactors, with a specific design that may adapt the size range of the ultrasound waves with the size range of the channels composing the microfluid device (Kerboua and Hamdaoui, 2021). Dong et al. (Dong et al., 2015) combined directly the Langevin ultrasound transducer to a microreactor to achieve a high power ultrasonic microreactor and enhance the overall mass transfer, the designed ultrasonic microreactor was adapted to high power, large volume and higher throughput with relatively low cost. However, the direct integration of microreactors induces a high dissipation of heat and input energy and requires a control of temperature and cooling system which can be insufficient at high acoustic frequencies (Kerboua and Hamdaoui, 2021). For this reason, another configuration in microreactors can be adopted, which is the indirect combination of microreactors. Hübner et al. (Hübner et al., 2012) designed an indirect combined microreactor with Langevin ultrasonic transducer to solve the energy dissipation problem.

Sonochemical and ultrasound-assisted pathways have gained attention as green processes, however, there are several criteria to identify hydrogen production via ultrasound as a green process. Mason (Mason, 2003) underlined the green

characters of ultrasound in chemical processes, namely reduced energy consumption, faster reactions, use of environmental friendly chemical products (solvents) and the adoption of alternative and renewable feedstocks.

Furthermore, using renewable feedstocks in sonochemical hydrogen production processes have gained interest of researchers. The exploitation of renewable sources for generating electricity in sonoelectrolysis and as a source of irradiation in photosonolysis and sonophotocatalysis processes is a possible way to be assessed.

Cotana (Cotana et al., 2007) studied the effect of combining sunlight and sonolysis for hydrogen generation, where sunlight irradiations were simulated using a xenon lamp whose spectrum is very close to that of sunlight. Nevertheless, to the best of our knowledge, no work has been conducted using sunlight radiation directly in sonophotolysis process for H_2 generation.

That's said, the use of ultrasound in sonochemical and sonoelectrochemical processes for hydrogen production is currently gaining more and more interest, and researchers are already on the right track and promising results at the laboratory scale have been demonstrated. However, the transition to an up-scaled technology becomes a timely need in order to adapt the promising hybrid process to industrial scale in the near future.

19.4 Conclusion

During the last decades, several research studies have been carried out toward hydrogen production using sonochemistry and ultrasound-assisted techniques. The main objective of this chapter was to present the ultrasound hydrogen production's pathways from a multiscale point of view.

Currently, the mechanism behind the improvement of reactions in the presence of ultrasound for hydrogen production is still under discussion and scientists are making efforts to explain it. It is generally assumed that in the case of pure sonolysis, chemical effects associated with sonication, namely sonochemistry, are responsible of the production of hydrogen. The physical effects of sonication are rarely invoked in the case of sonolysis. However, in the case of ultrasound-coupled techniques, namely, sonophotolysis, sonocatalysis, sonophotocatalysis, sonoelectrolysis, and sonoelectrocatalysis, the pathway of the ultrasonic enhancement of hydrogen production is rather physical, relying on the degassing effect of ultrasounds, microstreaming, microjets and shockwaves, and the shearing and turbulent effects ultrasound can cause in the medium.

Hydrogen production using sonochemistry and ultrasound aided techniques depends on several parameters that need to be considered such as the ultrasonic frequency, the ambient size of the single bubble, the acoustic power, the liquid medium composition and the dissolved gases.

From a techno-economic perspective, it is clear that in the area of hydrogen production using ultrasound, engineering data of ultrasonic reactor design and scaling-up are lacking, which requires more efforts for the transition to up-scaled technologies for sonohydrogen production.

References

Atchley, A.A., Frizzell, L.A., Apfel, R.E., Holland, C.K., Madanshetty, S., Roy, R.A., 1988. Thresholds for cavitation produced in water by pulsed ultrasound. Ultrasonics 26 (5), 280–285. https://doi.org/10.1016/0041-624X(88)90018-2.

Burjanadze, S. (2014). Device for hydrogen generation by cavitation electrolysis. In Int Patent. US patent.

Büttner, J., Gutiérrez, M., Henglein, A., 1991. Sonolysis of water-methanol mixtures. J. Phys. Chem. 95 (4), 1528–1530. https://doi.org/10.1021/j100157a004.

Cataldo, F., 1992. Effects of ultrasound on the yield of hydrogen and chlorine during electrolysis of aqueous solutions of NaCl or HCl. J. Electroanal. Chem. 332 (1–2), 325–331. https://doi.org/10.1016/0022-0728(92)80362-8.

Contamine, R.F., Wilhelm, A.M., Berlan, J., Delmas, H., 1995. Power measurement in sonochemistry. Ultrason. Sonochem. 2 (1), S43–S47. https://doi.org/10.1016/1350-4177(94)00010-P.

Cotana, F., Rossi, F., Urbani, M., 2007. Study of water photosonolysis for hydrogen production. In: 3rd International Green Energy Conference, pp. 3–8.

Dehane, A., Merouani, S., Hamdaoui, O., 2021. Theoretical investigation of the effect of ambient pressure on bubble sonochemistry: Special focus on hydrogen and reactive radicals production. Chem. Phys. 547, 111171. https://doi.org/10.1016/j.chemphys.2021.111171.

Dharmarathne, L., Ashokkumar, M., Grieser, F., 2012. Photocatalytic generation of hydrogen using sonoluminescence and sonochemiluminescence. J. Phys. Chem. C 116 (1), 1056–1060. https://doi.org/10.1021/jp209946s.

Dong, Z., Yao, C., Zhang, X., Xu, J., Chen, G., Zhao, Y., Yuan, Q., 2015. A high-power ultrasonic microreactor and its application in gas-liquid mass transfer intensification. Lab Chip 15 (4), 1145–1152. https://doi.org/10.1039/c4lc01431f.

Gentili, P.L., Penconi, M., Ortica, F., Cotana, F., Rossi, F., Elisei, F., 2009. Synergistic effects in hydrogen production through water sonophotolysis catalyzed by new La2xGa2yIn2(1-x-y)O3 solid solutions. Int. J. Hydrog. Energy 34 (22), 9042–9049. https://doi.org/10.1016/j.ijhydene.2009.09.027.

Gielen, B., Marchal, S., Jordens, J., Thomassen, L.C.J., Braeken, L., Van Gerven, T., 2016. Influence of dissolved gases on sonochemistry and sonoluminescence in a flow reactor. Ultrason. Sonochem. 31, 463–472. https://doi.org/10.1016/j.ultsonch.2016.02.001.

Gogate, P.R., Sutkar, V.S., Pandit, A.B., 2011. Sonochemical reactors: important design and scale up considerations with a special emphasis on heterogeneous systems. Chem. Eng. J. 166 (3), 1066–1082. https://doi.org/10.1016/j.cej.2010.11.069.

Gutiérrez, M., Henglein, A., Dohrmann, J.K., 1987. H atom reactions in the sonolysis of aqueous solutions. J. Phys. Chem. 91 (27), 6687–6690. https://doi.org/10.1021/j100311a026.

Harada, H., 2001. Sonophotocatalytic decomposition of water using TiO2 photocatalyst. Ultrason. Sonochem. 8 (1), 55–58. https://doi.org/10.1016/S1350-4177(99)00050-4.

Hart, E.J., Henglein, A., 1985. Free radical and free atom reactions in the sonolysis of aqueous iodide and formate solutions. J. Phys. Chem. 89 (20), 4342–4347. https://doi.org/10.1021/j100266a038.

Hübner, S., Kressirer, S., Kralisch, D., Bludszuweit-Philipp, C., Lukow, K., Jänich, I., Schilling, A., Hieronymus, H., Liebner, C., Jähnisch, K., 2012. Ultrasound and microstructures—a promising combination? Chem. Sus. Chem. 5 (2), 279–288. https://doi.org/10.1002/cssc.201100369.

Islam, M.H., Burheim, O.S., Pollet, B.G., 2019. Sonochemical and sonoelectrochemical production of hydrogen. Ultrason. Sonochem. 51, 533–555. https://doi.org/10.1016/j.ultsonch.2018.08.024.

Islam, M.H., Lamb, J.J., Burheim, O.S., Pollet, B.G., 2020. Ultrasound-assisted electrolytic hydrogen production. Micro-Optics and Energy: Sensors for Energy Devices. Springer International Publishing, Denmark, pp. 73–84. https://doi.org/10.1007/978-3-030-43676-6_7.

Jain, I.P., 2009. Hydrogen the fuel for 21st century. Int. J. Hydrog. Energy 34 (17), 7368–7378. https://doi.org/10.1016/j.ijhydene.2009.05.093.

Kang, J.W., Hung, H.M., Lin, A., Hoffmann, M.R., 1999. Sonolytic destruction of methyl tert-butyl ether by ultrasonic irradiation: the role of O3, H2O2, frequency, and power density. Environ. Sci. Technol. 33 (18), 3199–3205. https://doi.org/10.1021/es9810383.

Kerboua, K., Hamdaoui, O., 2018. Numerical estimation of ultrasonic production of hydrogen: effect of ideal and real gas based models. Ultrason. Sonochem. 40, 194–200. https://doi.org/10.1016/j.ultsonch.2017.07.005.

Kerboua, K., Hamdaoui, O., 2019a. Energetic challenges and sonochemistry: a new alternative for hydrogen production? Curr. Opin. Green Sustain. Chem. 18, 84–89. https://doi.org/10.1016/j.cogsc.2019.03.005.

Kerboua, K., Hamdaoui, O., 2019b. Sonochemical production of hydrogen: enhancement by summed harmonics excitation. Chem. Phys. 519, 27–37. https://doi.org/10.1016/j.chemphys.2018.11.019.

Kerboua, K, Hamdaoui, O., 2020. Sonochemistry in green processes: modeling, experiments, and technology. Sustainable Green Chemical Processes and their Allied Applications. Springer Cham, pp. 409–460.

Kerboua, K., Hamdaoui, O., 2021. Sonochemistry for Water Remediation: Toward an Up-Scaled Continuous Technology. Appl. Water Sci, 2. Remediat. Technol., pp. 437–468.

Kerboua, K., Hamdaoui, O., Islam, M.H., Alghyamah, A., Hansen, H.E., Pollet, B.G., 2021a. Low carbon ultrasonic production of alternate fuel: operational and mechanistic concerns of the sonochemical process of hydrogen generation under various scenarios. Int. J. Hydrog. Energy doi:10.1016/j.ijhydene.2021.05.191.

Kerboua, K., Merouani, S., Hamdaoui, O., 2021b. Ultrasonics sonochemistry how do dissolved gases affect the sonochemical process of hydrogen production ? an overview of thermodynamic and mechanistic effects – On the “hot spot theory”. Ultrason. Sonochem. 72.

Kerboua, K., Hamdaoui, O., Alghyamah, A, 2021c. Acoustic frequency and optimum sonochemical production at single and multi-bubble scales: a modeling answer to the scaling dilemma. Ultrason. Sonochem. 70, 105341. https://doi.org/10.1016/j.ultsonch.2020.105341.

Kerboua, K., Hamdaoui, O., Al-Zahrani, S, 2021d. Sonochemical production of hydrogen: a numerical model applied to the recovery of aqueous methanol waste under o xygen-argon atmosphere. Environ. Prog. Sustain. Energy 40 (2). doi:10.1002/ep.13511.

Kirchoff J.A., Marques, J., Nottke, F., Seligmann, R. J., Vasquez, P., & Koeneman, R. (2010). Cavitation assisted sonochemical hydrogen production system. US Patent.

Kohno, M., Mokudai, T., Ozawa, T., Niwano, Y., 2011. Free radical formation from sonolysis of water in the presence of different gases. J. Clin. Biochem. Nutr. 49 (2), 96–101. https://doi.org/10.3164/jcbn.10-130.

Leighton, T.G., 1995. Bubble population phenomena in acoustic cavitation. Ultrason.—Sonoche. 2 (2), S123–S136. https://doi.org/10.1016/1350-4177(95)00021-W.

Li, S.D., Wang, C.C., Chen, C.Y., 2009. Water electrolysis in the presence of an ultrasonic field. Electrochim. Acta 54 (15), 3877–3883. https://doi.org/10.1016/j.electacta.2009.01.087.

Li, X., Hu, Q., Xu, Y., Liang, X., Feng, J., Zhao, K., Guan, G., Jiang, Y., Hao, X., Tang, K., 2021. Generation of oxygen vacancies in NiFe LDH electrocatalysts by ultrasound for enhancing the activity toward oxygen evolution reaction. Carbon Resour. Convers. 4, 76–83. https://doi.org/10.1016/j.crcon.2020.12.007.

Lim, M., Son, Y., Khim, J., 2011. Frequency effects on the sonochemical degradation of chlorinated compounds. Ultrason. Sonochem. 18 (1), 460–465. https://doi.org/10.1016/j.ultsonch.2010.07.021.

Lin, M.-Y., Hourng, L.-W., 2014. Ultrasonic wave field effects on hydrogen production by water electrolysis. Null 37 (8), 1080–1089. https://doi.org/10.1080/02533839.2014.912787.

Lubetkin, S.D., 2003. Why is it much easier to nucleate gas bubbles than theory predicts? Langmuir 19 (7), 2575–2587. https://doi.org/10.1021/la0266381.

Mason, T.J., 2000. Large scale sonochemical processing: Aspiration and actuality. Ultrason. Sonochem. 7 (4), 145–149. https://doi.org/10.1016/S1350-4177(99)00041-3.

Mason, T.J., 2003. Sonochemistry and sonoprocessing: the link, the trends and (probably) the future. Ultrason. Sonochem. 10 (4–5), 175–179. Issues https://doi.org/10.1016/S1350-4177(03)00086-5.

McMurray, H.N., Worsley, D.A., Wilson, B.P., 1998. Hydrogen evolution and oxygen reduction at a titanium sonotrode. Chem. Commun. 8, 887–888. https://doi.org/10.1039/a800801i.

Merouani, S., Ferkous, H., Hamdaoui, O., Rezgui, Y., Guemini, M., 2015c. New interpretation of the effects of argon-saturating gas toward sonochemical reactions. Ultrason. Sonochem. 23, 37–45. https://doi.org/10.1016/j.ultsonch.2014.09.009.

Merouani, S., Hamdaoui, O., 2018. Correlations between the sonochemical production rate of hydrogen and the maximum temperature and pressure reached in acoustic bubbles. Arab. J. Sci. Eng. 43 (11), 6109–6117. https://doi.org/10.1007/s13369-018-3266-3.

Merouani, S., Hamdaoui, O., 2016. The size of active bubbles for the production of hydrogen in sonochemical reaction field. Ultrason. Sonochem. 32, 320–327. https://doi.org/10.1016/j.ultsonch.2016.03.026.

Merouani, S., Hamdaoui, O., Rezgui, Y., Guemini, M., 2016. Computational engineering study of hydrogen production via ultrasonic cavitation in water. Int. J. Hydrog. Energy 41 (2), 832–844. https://doi.org/10.1016/j.ijhydene.2015.11.058.

Merouani, S., Hamdaoui, O., Rezgui, Y., Guemini, M., 2013. Effects of ultrasound frequency and acoustic amplitude on the size of sonochemically active bubbles-Theoretical study. Ultrason. Sonochem. 20 (3), 815–819. https://doi.org/10.1016/j.ultsonch.2012.10.015.

Merouani, S., Hamdaoui, O., Rezgui, Y., Guemini, M., 2015a. Mechanism of the sonochemical production of hydrogen. Int. J. Hydrog. Energy 40 (11), 4056–4064. https://doi.org/10.1016/j.ijhydene.2015.01.150.

Merouani, S., Hamdaoui, O., Rezgui, Y., Guemini, M., 2015b. Sensitivity of free radicals production in acoustically driven bubble to the ultrasonic frequency and nature of dissolved gases. Ultrason. Sonochem. 22, 41–50. https://doi.org/10.1016/j.ultsonch.2014.07.011.

Parke, A.V.M., Taylor, D., 1956. 855. The chemical action of ultrasonic waves. J. Chem. Soc. 4442–4450. doi:10.1039/JR9560004442.

Penconi, M., Rossi, F., Ortica, F., Elisei, F., Gentili, P., 2015. Hydrogen production from water by photolysis, sonolysis and sonophotolysis with solid solutions of rare earth, gallium and indium oxides as heterogeneous catalysts. Sustainability 7 (7), 9310–9325. https://doi.org/10.3390/su7079310.

Pollet, B., Foroughi, F., Faid, A., 2020. Does power ultrasound (26 kHz) affect the hydrogen evolution reaction (HER) on Pt polycrystalline electrode in a mild acidic electrolyte ? Ultrason. Sonochem. 69 (105238), 1–9. doi:10.1016/j.ultsonch.2020.105238.

Pollet, B. G., 2012. Power ultrasound in electrochemistry: From versatile laboratory tool to engineering solution. Wiley.

Richards, W.T., Loomis, A.L., 1927. The chemical effects of high frequency sound waves I. A preliminary survey. J. Am. Chem. Soc. 49 (12), 3086–3100. https://doi.org/10.1021/ja01411a015.

Rooze, J., Rebrov, E.V., Schouten, J.C., Keurentjes, J.T.F., 2013. Dissolved gas and ultrasonic cavitation—a review. Ultrason. Sonochem. 20 (1), 1–11. https://doi.org/10.1016/j.ultsonch.2012.04.013.

Rossi F, Nicolini A, Filipponi M, Corsi, N. (2009) Study of Catalysts for Water Photosonolysis to Increase the Hydrogen Production Photosonolysis process. *HYPOTHESIS VIII Lisbon*. 1–6.

Sancheti, S.V., Gogate, P.R., 2017. A review of engineering aspects of intensification of chemical synthesis using ultrasound. Ultrason. Sonochem. 36, 527–543. https://doi.org/10.1016/j.ultsonch.2016.08.009.

Sasikala, R., Jayakumar, O.D., Kulshreshtha, S.K., 2007. Enhanced hydrogen generation by particles during sonochemical decomposition of water. Ultrason. Sonochem. 14 (2), 153–156. https://doi.org/10.1016/j.ultsonch.2006.06.005.

Symes, D. (2011). Sonoelectrochemical (20 kHz) Production of Hydrogen from Aqueous Solutions; University of Birmingham: Birmingham, UK.

Theerthagiri, J., Madhavan, J., Lee, S.J., Choi, M.Y., Ashokkumar, M., Pollet, B.G., 2020. Sonoelectrochemistry for energy and environmental applications. Ultrason. Sonochem. 63, 104960. https://doi.org/10.1016/j.ultsonch.2020.104960.

Thompson, L.H., Doraiswamy, L.K., 1999. Sonochemistry: science and engineering. Ind. Eng. Chem. Res. 38 (4), 1215–1249. https://doi.org/10.1021/ie9804172.

Toma, S., Gaplovsky, A., Luche, J.L., 2001. The effect of ultrasound on photochemical reactions. Ultrason. Sonochem. 8 (3), 201–207. https://doi.org/10.1016/S1350-4177(00)00073-0.

Torres-Palma, R.A., Serna-Galvis, E.A., 2018. Sonolysis. Advanced Oxidation Processes for Waste Water Treatment. Academic Press, Cambridge, Massachusetts, USA, pp. 177–213. https://doi.org/10.1016/B978-0-12-810499-6.00007-3.

Tudela, I., Sáez, V., Esclapez, M.D., Díez-García, M.I., Bonete, P., González-García, J., 2014. Simulation of the spatial distribution of the acoustic pressure in sonochemical reactors with numerical methods: a review. Ultrason. Sonochem. 21 (3), 909–919. https://doi.org/10.1016/j.ultsonch.2013.11.012.

Walton, D.J., Burke, L.D., Murphy, M.M., 1996. Sonoelectrochemistry: chlorine, hydrogen and oxygen evolution at platinised platinum. Electrochim. Acta 41 (17), 2747–2751. https://doi.org/10.1016/0013-4686(96)00133-8.

Wang, Y., Zhao, D., Ji, H., Liu, G., Chen, C., Ma, W., Zhu, H., Zhao, J., 2010. Sonochemical hydrogen production efficiently catalyzed by Au/TiO 2. J. Phys. Chem. C 114 (41), 17728–17733. https://doi.org/10.1021/jp105691v.

Yadav, A., Hunge, Y., Kang, S., 2021. Ultrasound assisted synthesis of highly active nanoflower-like CoMoS 4 electrocatalyst for oxygen and hydrogen evolution reactions. Ultrason. Sonochem. 72 (105454), 1–9. doi:10.1016/j.ultsonch.2020.105454.

Zadeh, S.H., 2014. Hydrogen production via ultrasound-aided alkaline water electrolysis. J. Autom. Control Eng. 103–109. doi:10.12720/joace.2.1.103-109.

Zhang, Y., Zhang, Y., Li, S., 2016. The secondary Bjerknes force between two gas bubbles under dual-frequency acoustic excitation. Ultrason. Sonochem. 29, 129–145. https://doi.org/10.1016/j.ultsonch.2015.08.022.

Zore, U.K., Yedire, S.G., Pandi, N., Manickam, S., Sonawane, S.H., 2021. A review on recent advances in hydrogen energy, fuel cell, biofuel and fuel refining via ultrasound process intensification. Ultrason. Sonochem. 73, 105536. https://doi.org/10.1016/j.ultsonch.2021.105536.

Chapter 20

Future trends and promising applications of industrial sonochemical processes

Gaurav G. Dastane, Vinayak S. Sutkar, Amit V. Mahulkar and Aniruddha B. Pandit
Department of Chemical Engineering, Institute of Chemical Technology, Mumbai, India

20.1 Intensification of chemical process via cavitation

Process intensification can in general be brought about by delivering energy at the right place, in right form, of appropriate intensity and over correct timescale. In cavitation, the energy is present in multiple forms, for example, pressure pulse, temperature spike, intense turbulence, chemical energy (free radicals), etc. Also, the location of this energy delivery is usually restricted to in and around the oscillating cavity, where the secondary reactant is mostly present. The time scales of energy delivery is also much shorter (∼microseconds) at the cavity collapse event. Such combination of form, timescale and length scales of delivered energy, makes cavitation potentially capable of replacing several current unit operations and processes. However, many of the end effects either in terms of pressure pulse/spike in temperature are impossible to measure experimentally hence, one needs to rely on secondary effects. This makes it difficult for professionals from industry, who does not have functional knowledge about cavitation, to accept the potential benefits of cavitation. Hence for wider acceptability process engineers and designers usually demand demonstrated proofs with the explanation of mechanism of improvement. In this chapter, we discuss some of the demonstrated applications of acoustic cavitation, also we highlight the gaps in demonstration and understanding in these to explore the field further.

20.2 Demonstrated applications in various fields

20.2.1 Water/wastewater treatment and biotechnology applications

Water/waste water processes (or other similar processes which do not yield a high value product) operate with lower operating cost margins. This significantly limits the choice of adaptable technologies. Thus it is crucial to make the acoustic cavitation based methods to fit the cost constraints. While acoustic cavitation can deliver higher energy density per unit volume as compared to Hydrodynamic cavitation, it has lower energy conversion efficiency (electrical to cavitational yield). As a result, hydrodynamic cavitation is a preferred choice when it comes to low energy cost and large volume applications like water treatment. For biotechnology applications like recovering high-value products/enzymes from microbial cell could be well-suited application for acoustic cavitation.

Advanced oxidation processes (AOP): Cavitation accompanied with other oxidation processes (photocatalytic oxidation, wet air oxidation, ozone, hydrogen peroxide) have been widely reported to be effective for effluent treatment processes (Ferkous et al., 2015; Gogate and Pandit, 2004). In most of these processes, the hydroxyl radical is generated which oxidizes the majority of pollutants. While cavitation can generate hydroxyl radicals upon cavity collapse, it is also seen to synergistically work with other oxidation processes to improve the oxidation potential. Some of the latest review articles presented on this topic are mentioned here for reference (Abbas-Shiroodi et al., 2021; Abdurahman et al., 2021; Bhat and Gogate, 2021; Korpe and Rao, 2021; Wang et al., 2021; Yasuda, 2021). *The overall trend gathered from these studies indicate that while more and more model pollutants have been demonstrated to be treated by combination of cavitation and AOPs, the demonstration with real effluent data with detailed analysis of raw and treated effluent is still scarce.*

Energy Aspects of Acoustic Cavitation and Sonochemistry: Fundamentals and Engineering. DOI: https://doi.org/10.1016/B978-0-323-91937-1.00009-8
Copyright © 2022 Elsevier Inc. All rights reserved.

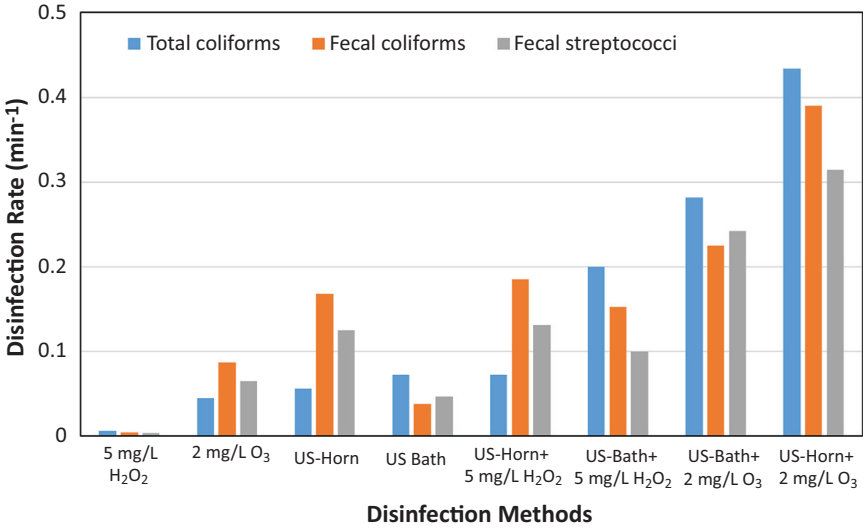

FIGURE 20.1 Hybrid (cavitation + chemicals) microbial disinfection methods. Data from Jyoti, K. K. & Pandit, A. B. (2003). Hybrid cavitation methods for water disinfection. *Biochemical Eng. J.*, 14(1), 9–17. https://doi.org/10.1016/S1369-703X(02)00102-X Disinfection rate constant for various combinations of Ultrasound and Ozone/ Hydrogen peroxide.

Microbial disinfection: It is widely reported that cavitation can disrupt cell wall of microbes. Few of these are listed here (Antoniadis et al., 2007; Gao et al., 2016; Greenly and Tester, 2015; Hunter et al., 2008; Ince and Belen, 2001; Save et al., 1994). This aspect is widely used for disinfecting water, and extracting valuable intracellular contents from microbes. Degradation of phycocyanin using high-frequency ultrasound by direct oxidation using free radicals is reported (Liu et al., 2018). Simultaneous use of ultrasound and sodium hypochlorite showed 4 log reduction in fecal coliforms (Zhou et al., 2016). Osman et al., used multiple orifice based ultrasonic resonator for treating ballast water from ships (Osman et al., 2016). Also there are several reports which indicate that pretreatment/cotreatment of microbial cells with chemicals (e.g., ozone, H_2O_2) or processes which reduce the cell wall strength can significantly enhance the extent of disruption with cavitation (Fig. 20.1) (Jyoti and Pandit, 2003; Jyoti and Pandit, 2004). *The main challenge in using only cavitation for water disinfection is that probability of interaction of cavity and microbial cell significantly reduces as the microbial concentration decreases. Hence the combination of cavitation with chemicals or light based treatment (volumetric treatment) method is needed.*

Enzyme recovery: For application like intracellular enzyme recovery, it is possible to concentrate the microbial density to much higher values for treatment in cavitation apparatus. This significantly increases the interaction between cavities and cells. Thus energy requirements for cell disruption (J/ m^3 of treated volume) can be significantly reduced (Agrawal and Pandit, 2003). Similar to microbial disinfection methods, even for recovering intracellular materials the hybrid approach of combining cavitation with pH treatment, heat, was found to be more effective (Farkade et al., 2006; Vogels and Kula, 1992). *One of the challenges in using chemicals and/or cavitation is that the extracted/ released intracellular content should not get degraded due to action of chemicals/ cavitation and not contaminating the final product.*

Activity improvement: Zhang et al. (2008) reported bioactivity improvement of sludge (Zhang et al., 2008). This application involves concentrating the sludge and subjecting it to ultrasound. A high concentration of sludge ensures high energy utilization. The activity is improved in several ways like increasing the number of approachable sites/microbes, increasing the void of sludge to reduce density, and increase dispersion in water.

Protein modification: Ultrasound has also been reported to modify the protein structure which makes it possible for improving the protein solubility, bioavailability, texture, taste, and appearance. Umego et al. presented recent review on ultrasound-assisted enzymolysis. In general, protein unfolding is expected to increase the protein solubility, availability so that solvation of the protein increases (Umego et al., 2021). *Similar to intracellular material recovery, the protein damage due to cavitation is one of the major challenges to overcome in this application.*

20.2.2 Nanomaterials

Nanoparticles, nanocomposites, and nanostructured materials are gaining huge attention due to modified chemical and physical properties and characteristics such as size, shape, chemical composition, physical and chemical stability, crystalline

structure, surface area, surface roughness, melting point, wettability, thermal conductivity, catalytic activity, and light absorption and scattering etc. In majority of the cases, modified material properties are more attractive than the properties of the corresponding raw materials. Based on its origin the nanostructured materials are mainly classified as (1) Incidental nanomaterials, which are produced incidentally as a byproduct of industrial processes. (2) Engineered nanomaterials, which are manufactured based on requirements for a given application, and (3) Natural nanomaterials, which are generally found in the bodies of organisms, insects, plants, animals and human bodies (Jeevanandam et al., 2018).

For engineered nanostructured materials, developing a new manufacturing technique which is clean and sustainable, reliable, and cost-effective is challenging. Ultrasound-assisted methods offer a viable alternative for preparation of wide range of nanostructured materials. These methods provide unique reaction conditions and which are a facile and effective way to readjust properties of nanostructured materials due to the cavitation effect, which are unavailable by conventional methods. Cavitation phenomena results in generation of high temperatures and pressure pulses locally, strong acoustic streaming, high shear stress near the bubble wall, formation of microjets near the solid surface, generation of highly reactive free radicals, and turbulence resulting in enhanced transport properties of the specie at ambient operating conditions. These distinguishing features often result in a rapid reaction rate conditions, better flexibility during tuning of morphology by altering the operating parameters, and efficacy to produce nanoparticles with uniform shape, narrow size distribution, better stability, and phase purity.

Ultrasound-assisted methods are successfully utilized for the preparation of various nanostructured materials, including single metallic (Wani et al., 2011), bimemetallic/alloy (Mizukoshi et al., 1997), single metal oxides (Dhas et al., 1997), mixed metal oxides (Dutta et al., 2009), carbides (Hyeon et al., 1996), nitrides (Li et al., 1999), sulfides (Mahajan et al., 2004), tellurides (Li et al., 2001), selenides (Zhu et al., 1999), nanoparticles deposited on supports (Yang et al., 2006), nanoparticles inserted into mesoporous supports (Perkas et al., 2007), inorganic nanocomposites (Jiang et al., 2010), inorganic-organic nanocomposites (Vinodgopal et al., 2010), etc.

Wani et al. synthesized silver nanoparticles in ultrasonic bath (20 kHz, 2.5 W/cm^2, 12 h) from aqueous solution of $AgNO_3$ and sodium borohydrate/sodium citrate. It was found that the size and morphology were dependent on the strength of reducing agent. Spherical, uniform, and mono-dispersed Ag nanoparticles with (ca. 10 nm size, 2.6 m^2/g surface area and 89 nm pore size) and (ca. 3 nm, 13.1 m^2/g, and 137 nm) were produced using sodium borohydrate (strong reducing agent) and sodium citrate (weak reducing agent), respectively (Wani et al., 2011).

The key advantage of using sonication for nanomaterial synthesis is its ability to react miniscule quantities of reactants present in the cavity. A tight control over the reactant quantities are possible by tuning the cavity dynamics and the size and by controlling the mass transfer of species in it. This depends on nucleation sites and ultrasound intensity. The nature of nucleation also plays an important role. Homogenous nucleation occurs when cavities are generated purely by overcoming the tension created by low pressure in the liquid. Heterogeneous nucleation occurs when cavities are generated at the discontinuity in the liquid continuum. Discontinuity could be due to the presence of dispersed/dissolved species in liquid or surface structures. Homogenous nucleation usually results in uncontrolled nucleation and the energy requirement for such nucleation is also higher as compared to heterogeneous nucleation. Mahulkar et al. showed that providing readily available nuclei (in form of steam or gaseous bubble) can significantly improve the overall efficiency of sonication (Mahulkar et al., 2008). *Based on similar method, by providing vaporizable/gaseous reactants required for developing nanomaterials mixed with the water vapor (steam) to condense as dispersed microbubble. These microbubbles when subjected to controlled ultrasonic intensity can generate nanomaterials in a well-controlled size distribution and with low energy requirement.*

20.2.3 Food and beverage

Food processing and preservation has become extremely important in order to cater to the ever-growing demands of the world population. Processed food items with a longer shelf life are available around the year, are compact for storage and reduce the wastage of food. Conventional food processing methods employ direct heating to kill the microorganisms present in food items to make them more long lasting. Such processes require large amount of energy and are time consuming, yet their productivity is low compared to the amount of energy consumed. Also, such methods are ineffective for food items that are heat sensitive. Acoustic cavitation offers a green and innovative alternative for food processing operations such as extraction, pasteurization, drying, etc. In this section, some of the key applications in food processing, which can be further improved using acoustic cavitation have been discussed briefly.

20.2.3.1 Extraction of valuable components

Extraction of bioactive compounds from food materials has been carried out for several years. The efficiency of the extraction process is mainly dependent on the method used for extraction. However, these processes have their limitations in terms of

TABLE 20.1 Ultrasonic extraction of bioactive compounds from food materials.

Source	Key Findings	References
Grape Pomace	• Bioactive compounds were extracted using ultrasound • Ultrasound power and sonication time were optimized • 45% more extraction yield of anthocyanin was obtained	Rocha and Noreña (2020)
Jaboticaba Peels	• Phenolics and anthocyanin were extracted • Sonication power and time were optimized	Fernandes et al. (2020)
Purple Yam	• Anthocyanin was extracted using ultrasound • Upto 22.6% extraction yield was obtained	Ochoa et al. (2020)
Bitter Gourd	• Polyphenols and proteins were extracted • Antioxidant activity of 69.9% was observed for the extracted compounds	Chakraborty et al. (2020)
Piper betle L.	• Essential oils were extracted from the leaves • Ultrasound assisted extraction resulted in greater yield compared to conventional hydro-distillation	Jadhav et al. (2020)
Date seeds	• Date Seed oil was extracted using ultrasound and solvents • Higher extraction yield was obtained compared to maceration and Soxhlet extraction method	Jadhav et al. (2016)

the yield and efficiency. Also, they need long processing time, consume a large amount of chemicals and usually are not environment friendly. Application of ultrasound for the extraction of natural compounds from food materials significantly reduces the time required for extraction. The microjets produced due to collapse of cavities, rupture the cell walls of the organic matter, and the compounds in the media (Mason et al., 2011; Tiwari, 2015). The microturbulence produced due to cavitation as well as acoustic streaming ensures that the solvent penetrates deeply & completely in the substrate matrix, thus increasing the diffusive mass transfer rates and reducing the solvent quantity required for extraction (Chemat et al., 2017). The selectivity of the extraction process is also significantly more in case of ultrasound-assisted extraction, thus reducing the purification steps required downstream of the extraction process (Mevada et al., 2019). Overall, ultrasound-assisted extraction is usually more energy-efficient and requires lower operating cost compared to conventional techniques (Bhargava et al., 2021; Chemat et al., 2017). Such ultrasound-assisted extraction process can also be effectively utilized in extracting bio active compounds from the "waste" food material. Several studies on extraction using ultrasound have been reported in literature (Dolatowski et al., 2007; Gallo et al., 2018). Some recent examples of application of ultrasound in extraction of bioactive compounds from food material are listed in Table 20.1.

Additionally, ultrasound can also be used to extract undesired impurities from food items. Ultrasound has been found to be effective in removal of organic phosphorous and pesticide molecules from wine using ultrasound-assisted solvent extraction (Cinelli et al., 2014). Similarly, ultrasound-assisted extraction was found to be effective in removal of phthalates from baby food (Russo et al., 2016).

20.2.3.2 Emulsification

Emulsions and suspensions are common forms of food items that are in dispersed state. Having uniform and small droplet size is beneficial for homogenizing of the dispersed phase, as well as to enhance the heat and mass transfer between the continuous and dispersed phase (Hongyu et al., 2000). Additionally, smaller droplet sizes also result in greater stability of the emulsions. Ultrasound can be a very effective tool for the preparation of stable emulsions with small droplet sizes and narrow size distribution (Canselier et al., 2002; Taha et al., 2020). There have been numerous studies reported in the literature that demonstrate the effectiveness of ultrasound in preparing stable emulsions. The effect of ultrasound conditions on the quality of emulsions is also well reported (Canselier et al., 2002). Some of the recent studies on application of ultrasound for emulsification include preparation of chicken myofibrillar protein emulsion (Li et al., 2020), preparation of water-in-oil-in-water emulsions of sunflower oil and skimmed milk (Leong et al., 2017), and many more (Parthasarathy et al., 2013).

In addition to emulsification, ultrasound can sometimes also be used for the separation of dispersed phase from the continuous phase. It has been reported that ultrasound irradiation of frequencies lower than 30 kHz can be used for the separation of oil and water phases from an emulsion due to formation of standing waves and Bjerken's forces (see Fig. 20.2) (Luján-Facundo et al., 2016; Mettu et al., 2020). However, more research is needed in this field as variation in the ultrasound frequency may cause opposite effect of stabilizing the emulsions.

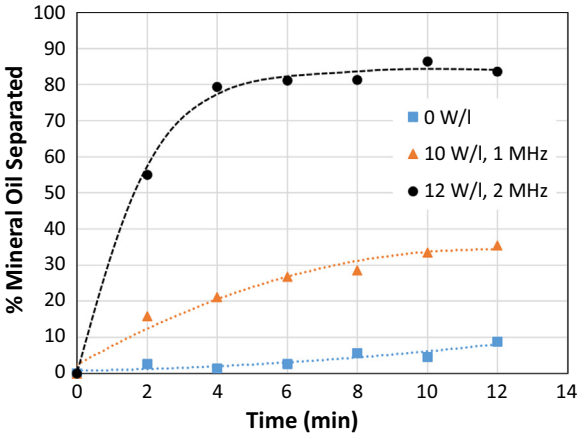

FIGURE 20.2 Mineral oil separation from its emulsion using ultrasound. Data from Mettu, S., Yao, S., Sun, Q., Lawson, S. R., Scales, P. J., Martin, G. J. O. & Ashokkumar, M. (2020). Effect of bulk viscosity and emulsion droplet size on the separation efficiency of model mineral oil-in-water (O/W) emulsions under ultrasonic standing wave fields: a theoretical and experimental investigation. Industrial Eng. Chem. Res., 59(16), 7901–7912. https://doi.org/10.1021/acs.iecr.0c00616 Extent of mineral oil separated from its emulsion using ultrasound over time for different power inputs.

20.2.3.3 Drying and rehydration

The application of ultrasound can accelerate drying rates of food items such as fruits, vegetables, meat, and fish, thus reducing the drying time, increasing mass transfer rates while still maintaining the key characteristics of the food item (Kowalski et al., 2017). Ultrasound-assisted drying has been reported to be an exceptional alternative to conventional methods of drying. During ultrasonic cavitation, the liquid evaporates due to the "sponge effect," which enhances the rate of diffusion of water inside the product to its surface (de la Fuente-Blanco et al., 2006). Microchannels are generated inside the food item due to cavitation of water at intracellular as well as extracellular levels. Sometimes the flow currents generated due to surface vibrations caused by ultrasound, can also assist in the removal of moisture from the surface (Bhargava et al., 2021; Yao, 2016). Ultrasound pretreatment can result in loss or gain of moisture in food samples, depending on the ultrasound conditions. Ultrasound-assisted drying is benefited by increasing the ultrasound power. The ultrasound also affects the physical and chemical properties of the food. Generally ultrasound results in faster mass transfer rates, better color retention, and lower reduction in nutrients (Huang et al., 2020). Some recent studies on the application of ultrasound in drying of food items are listed in Table 20.2.

The dried food items are rehydrated by immersing them in warm water before use. The rehydrated product may show some differences in its structure and composition as compared to the original product. To reduce these differences, a pretreatment is used before rehydration to maintain the product properties and reduce any shrinkage. Ultrasound can be used as a pretreatment for drying as well as rehydration of food items. The use of ultrasound can lead to pore formation in the sample that facilitates better absorption of water as well as better retention of the absorbed water (Tao et al., 2019; Zhao et al., 2019). Studies have been carried out to evaluate ultrasound as a pretreatment for rehydration process for shitake mushrooms (Tian et al., 2016; Zhao et al., 2019), minced meat (Aksoy et al., 2019), cabbage (Tao et al., 2019), carrots (Ricce et al., 2016), apple (Rojas et al., 2020), kiwis (Wang et al., 2019), and many more (Bhargava et al., 2021; de la Fuente-Blanco et al., 2006; Kumar et al., 2020). Ultrasound pretreatment is also effective in rehydration of dried grains. The rehydrated grains require significantly lower rehydration time while retaining the original starch properties (see Fig. 20.3). Moreover, the grains can also germinate successfully and are ideal for sprouting (Miano et al., 2016; Patero and Augusto, 2015). Hence, the ultrasound treatment can help in long-term storage of grains without any compromise in its quality.

20.2.3.4 Crystallization

In the case of food items, freezing and crystallization are interrelated and involve nucleation followed by formation of ice crystals (Qiu et al., 2020). The application of ultrasound during the cooling process reduces the time required for crystallization and provides enhanced nucleation rate. The crystals formed during ultrasound-assisted crystallization are exceptionally fine in size and do not cause damage to the cells in the food items (Sun and Hu, 2003). The micromixing achieved due to ultrasound also improves heat transfer rates, thus reducing the cooling time (Li and Sun, 2002). Ultrasound-assisted freezing is thus widely used in cold storage for food items as well as pharmaceuticals (Dalvi-Isfahan et al., 2017; Fu et al., 2020; Kiani and Sun, 2018; Li and Sun, 2002; Qiu et al., 2020). Additionally, ultrasound is also used in the

TABLE 20.2 Application of ultrasound in drying of food items.

Food item	Key findings	References
Red Pepper	Ultrasound was found to be effective only at low drying temperatures and low air velocity. At high temperatures, ultrasound increased the drying time.	Cárcel et al. (2019); Vega-Gálvez et al. (2009)
Green Beans	Dried using ultrasound assisted vacuum drying Drying time reduced by up to 1 hour.	Tekin et al. (2017)
Strawberry	Strawberries were freeze dried in presence of ultrasound. The nucleation rate of ice was enhanced, and characteristic freezing time was reduced due to application of power ultrasound.	Cheng et al. (2014)
Apple	Drying time was reduced due to enhanced heat and mass transfer rates. Power ultrasound resulted in formation of microchannels inside the apple, damaging the tissue due to the stress generated by ultrasound.	Kowalski et al. (2017); Rodríguez et al. (2014)
Grape Skin	Air borne power ultrasound with convective drying was used. Ultrasound lowered the antioxidant potential. Activation of oxidase and cell degradation were reported to be the reason. Predrying with ultrasound followed by convective drying improves the drying kinetics and enhances the food quality.	Cruz et al. (2016)
Kiwifruit	Ultrasound was used as pretreatment before osmotic dehydration. Ultrasound enhances the mass transfer rates during drying due to formation of microchannels.	Nowacka et al. (2014)
Seaweeds	Ultrasound pretreatment was followed by hot air drying. Reduction in energy and drying time while the color quality improved.	Kadam et al. (2015)
Ginger Slices	Osmosonication pretreatment showed improvement in preserving the contents of the sample. Only ultrasound treatment was more effective in retaining the color of the sample.	Osae et al. (2019)

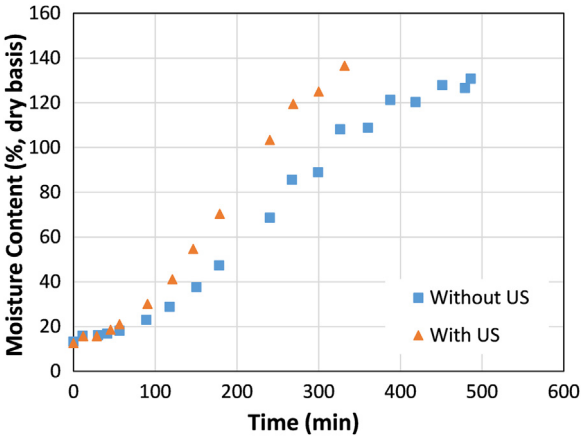

FIGURE 20.3 Mung bean re-hydration with ultrasound. Data from Miano, A. C., Pereira, J. da C., Castanha, N., Júnior, M. D. da M. & Augusto, P. E. D. (2016). Enhancing mung bean hydration using the ultrasound technology: Description of mechanisms and impact on its germination and main components. Scientific Reports, 6(1), 1–14. https://doi.org/10.1038/srep38996 Mung bean re-hydration rate comparison with and without ultrasound (US).

crystallization of milk fats (Martini et al., 2008), triglycerides (Kiani and Sun, 2018), and ice cream (Tabatabaie and Mortazavi, 2008). Furthermore, ultrasound can also prevent crystal encrustation on the cooling surfaces (Zhu et al., 2020).

20.2.3.5 Preservation

Microorganisms and enzymes are the main reasons for deterioration of food quality. The growth of microbes in food can cause serious health issues, while the enzymes in food can breakdown lipids and proteins and reduce the quality of food (Chemat et al., 2011). Ultrasound is effective in killing the micro-organisms and inactivating the enzymes in various food products such as milk, juices, meat, etc. (Pagnossa et al., 2020). The effectiveness of ultrasound against microbes varies depending on the type of microorganism present. Spores have higher resistance as compared to other microbial forms, Gram-positive bacteria are more resilient than the Gram-negative bacteria, and viruses have a higher level of tolerance (Kentish and Feng, 2014; Mason et al., 2003; Ojha et al., 2017). Similarly, extent of inactivation of enzymes also varies depending on the molecular structure of the enzyme (Mason et al., 2003).

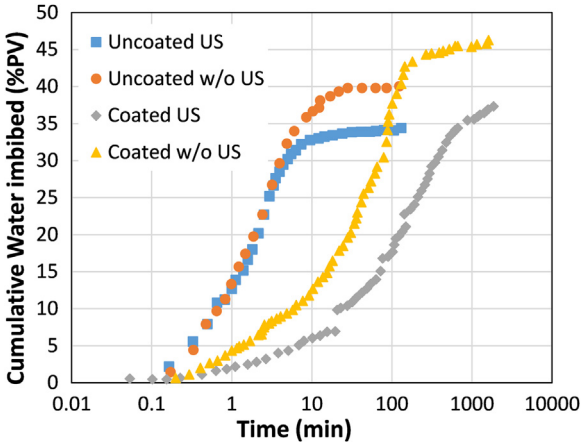

FIGURE 20.4 Air–water imbibition into Berea sandstone using ultrasound. Data from Hamida, T. & Babadagli, T. (2007). Analysis of capillary interaction and oil recovery under ultrasonic waves. Transport Porous Media 2007 70:2, 70(2), 231–255. https://doi.org/10.1007/S11242-006-9097-9 Air–water imbibition into Berea sandstone under influent of ultrasound.

Ultrasound has been reported to non-thermally pasteurize milk and juices at room temperature (Aghajanzadeh and Ziaiifar, 2021; Bhattacharjee et al., 2019; Monteiro et al., 2018, 2020; Oliveira et al., 2018; Silva et al., 2020). Ultrasound is also combined with other methods such as use of heat and ultrasound or high pressure and ultrasound (Adal, 2019; Demirdöven and Baysal, 2009; Jiranek et al., 2008).

20.2.3.6 Path forward for food processing

It is evident that ultrasound has a wide range of applications in food and beverage industry. The technology can play a crucial role in extending the shelf life of the food items and reducing the food wastage, and thus helping in sustainable use of our resources. However, to achieve this, the technology needs to be scaled up effectively.

Researchers worldwide are working on innovative ways to scale up the technology. One of the promising ways to scale up is to use hydrodynamic cavitation instead of ultrasound. Hydrodynamic cavitation utilizes pressure variations in flow to induce cavitating conditions instead of the sound waves used in ultrasound cavitation. Hydrodynamic cavitation has been successfully tested for various applications in food processing industry (Arya et al., 2020). This technology is easier to scale up as compared to ultrasound and there is a scope for research in application-specific designing of hydrodynamic cavitation reactors.

20.2.4 Petroleum industry

Applying cavitation-based technologies in refineries and petroleum industries is even more challenging as compared to other industries. Because refineries and petroleum industries usually operate on slimmer cost margins per unit ton of processed material. Lately, several industries have started looking into possible benefits of cavitation. Applications of ultrasound in various processes observed in the petroleum industry such as enhanced oil recovery, extraction of oil from unconventional sources (from oil shale and tar-sands), pipeline transport (such as Asphaltene suspension), and downstream refinery process (such as demulsification, oxidative desulfurization, demetallization, cracking or upgrading of heavy oil) have been reported (Avvaru et al., 2018).

Enhanced oil recovery: During enhanced oil recovery ultrasound-assisted processes enhances surfactant solubility, capillary imbibition recovery of oil (see Fig. 20.4) (Hamida and Babadagli, 2007), removal of mud particles from well opening, and increase the permeability (Venkitaraman et al., 1995). Ultrasound-assisted CO_2 flooding is reported to be more effective as compared to conventional CO_2 flooding (Hamidi et al., 2017). Ultrasound-assisted process provides synergistic effects however in the near future development of more efficient/robust ultrasonic transducers plays an important role during enhanced oil recovery.

Extraction of oil from unconventional sources: Ultrasound-assisted processes enhance kerogen recovery via intense acoustic steam agitation and the formation of microjets results in breaking the covalent interactions and intensify the penetration of solvents into different regions of multiphase systems. Ultrasonic extraction of kerogen from Jordan oil shale with tetrahydrofuran solvent with 90% extraction yield and reduced extraction time is reported (Matouq et al., 2009).

Ultrasonic extraction of kerogen from Huadian oil shale with 15.6% extraction yield using a solvent (with CHCl3 (60 wt. %) and CS2 (40 wt.%)) is also demonstrated (P. Zhao et al., 2013). Despite of the good extraction results, ultrasound-assisted processes are used on a laboratory scale of operations. *This might be due to the high cost associated with the grinding of whole-rock to the target size and solvent regeneration during the process*.

Downstream refinery process (such as demulsification, desulfurization, cracking or upgrading of heavy oil):

Ultrasound-assisted demulsification of water-crude oil emulsions: Dissolved metal salts (such as NaCl, CaCl2, and MgCl2) available in the Crude oil gets hydrolyzed in presence of water, which deactivates the refinery catalysts and induces metal corrosion. In order to dissolve the chloride salts via the desalting process, known amount of water is mixed with the crude oil. This results in the generation of water-in-oil (w/o) emulsions due to the presence of polar substances such as resins and asphaltene. At a higher concentration of metal concentration overall separation via conventional methods such as electrostatic, multistage desalting processes, cross-flow membrane, and microwave-assisted demulsification techniques become challenging (Diehl et al., 2011). While ultrasonic cavitation-based methods work better at higher concentrations. Ultrasound-based methods proposes the formation of standing sound waves breaks the emulsion through a combination of coagulation and coalescence which increases the demulsification efficiencies due to breaking of the interfacial films.

Ultrasonic assisted oxidative desulfurization: oxidative desulfurization is one of the promising technologies to remove high molecular weight Sulphur containing compounds from petroleum crude at relatively low temperatures (50–60°C) and pressure. In this technology, heavier sulfur compounds are oxidized using an oxidant without breaking the C–S bond to their respective sulphoxide and sulphone. Ultrasound-assisted oxidative desulfurization can improve the overall reaction between the oil phase and aqueous phase oxidant. Further, the reaction can be carried out at a relatively lower temperature and pressure (Avvaru et al., 2018).

Overall, in refinery/petrochemical industrial complexes the quantum of process/waste streams is quite large. Thus, designing cavitation-based processes specific to treating specific process/waste stream can be targeted. Efforts made to develop these niche solutions offered for these specific stream could lead to significant savings for refining/petrochemicals complexes.

20.2.5 Textile processing

In recent years, ultrasonic cavitation has been explored as an efficient and green technology for intensification of physical and chemical processes in textile processing industry. The conventional textile processing techniques are not considered environment friendly due to use of several biorefractory chemicals and harmful solvents. Cavitation has been considered as a green technology that can reduce the environmental impact of such processes while also increasing the efficiency of the process.

As cavitation by its definition requires a liquid medium for its occurrence, its applications in textile industry are limited to the wet processing of the textiles. During wet processing, dyes and finishes are transferred to the textile substrate via liquid medium. This process is primarily dependent on operating temperature as well as time. The conventional approach is complex and energy intensive (Harifi and Montazer, 2015). These processes also use large amount of chemicals for controlling the mass transfer rates from the liquid to the textile surface. Cavitation offers advantages in terms of reduction in energy consumption, lower chemical consumption, lower process time as well as enhancement in product quality.

Ultrasound finds applications in the preparation, dyeing as well as finishing stages of textile processing. Some of the examples of applications of ultrasound cavitation in these processes are discussed here.

20.2.5.1 Textile preparation

In textile preparation, it is important to clean the textile fibers before any further processing can be carried out. Cleaning of the fibers removes any grease or dirt on the fibers and makes it ready for subsequent dyeing and finishing. The conventional approach of washing the fibers requires large amount of water, chemicals, energy as well as longer operation time (Warmoeskerken et al., 2002). The use of ultrasound for cleaning different types of fibers has been explored by several researchers. The microjets generated during cavity collapse along with the microstreaming effect of ultrasound is responsible for the removal of any material deposited on the fibers (Li et al., 2014). The studies in the literature report that ultrasound can clear dirt and grease from all types of fibers without damaging the fibers. Additionally, use of ultrasound for cleaning resulted in reduced felting while maintaining the strength and color, increased tensile strength and water absorption with improved thermal properties of wool (Hurren et al., 2008; Li et al., 2014; McNeil and McCall, 2011). It is also reported that ultrasound-assisted cleaning led to lower loss of tenacity in polyester fabrics, as compared to conventional methods. However, little

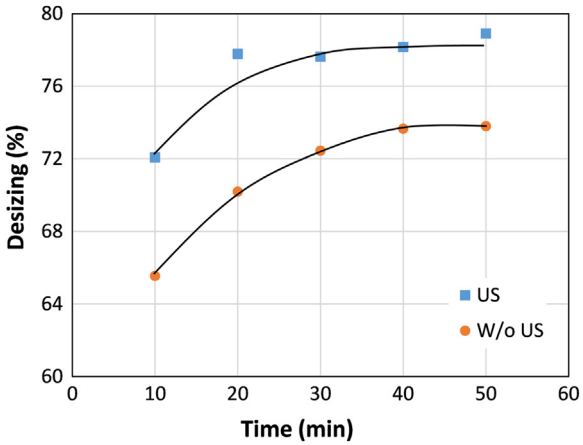

FIGURE 20.5 Ultrasonic desizing of fabric. Data from Wang, W. M., Yu, B. & Zhong, C. J. (2012). Use of ultrasonic energy in the enzymatic desizing of cotton fabric. J. Cleaner Production, 33, 179–182. https://doi.org/10.1016/j.jclepro.2012.04.010 The saved treatment time showed that the overall reaction rate between enzyme and starch was accelerated by ultrasonic energy resulting in better desizing.

damage to the fabric and some soil re-deposition was also reported (Canoğlu et al., 2004; Gotoh and Harayama, 2013). Another study also reported effectiveness of ultrasound in removing stains from silk with lower shrinkage, less wrinkling, and lower loss of tensile strength (Ma et al., 2014).

Additionally, ultrasound used along with enzymes has also been reported to be effective in removal of size and starch applied during sizing of fabric. The ultrasound enhances the mixing during the desizing process, damages the substrate layer on the fabric surface, and also provides activation energy for the catalyzed reaction carried out by the enzymes, thus increasing the rate of removal of substances from the fabric (Hao et al., 2013; Mahmoodi et al., 2010; Szabó and Csiszár, 2013; Thakore and Abate, 2017; Wang et al., 2012). Fig. 20.5 shows that the saved treatment time showed that the overall reaction rate between enzyme and starch was accelerated by ultrasonic energy (Wang et al., 2012).

Another important application of ultrasound in textile preparation is in bleaching of the fabric. Bleaching is carried out using hydrogen peroxide and ultrasound (Mistik and Yükseloğlu, 2005; Moses and Jagannathan, 1996; Thakore et al., 1990). Application of laccase as a greener alternative to peroxide has also been explored (Abou-Okeil et al., 2010; Basto et al., 2007; Gonçalves et al., 2014b). The ultrasound intensifies the effect of the bleaching agent and results in reduced bleaching time along with enhanced whiteness. The ultrasound is also reported to lower the energy, time, and chemical requirement of the process (Gonçalves et al., 2014b).

20.2.5.2 Textile dyeing

Dyeing is one of the most important step in textile processing. Applications of ultrasound in dyeing have been explored by researchers for several years. The use of ultrasound in textile dyeing has been reported to reduce the time required for dyeing (Kamel et al., 2007; Khatri et al., 2011); lower the required dyeing temperature, and hence reduce the energy requirement (Ferrero and Periolatto, 2012; Kamel et al., 2005); reduce the requirement of auxiliary agents such as salt and alkalis (Khatri et al., 2011; Udrescu et al., 2014); and also enhance the uptake of the dye (Abou-Okeil et al., 2010; Kamel et al., 2010). Several mechanisms for ultrasound enhancement of the dyeability of the textiles have been proposed, as shown in Fig. 20.6. Several studies have been reported on ultrasound-assisted dyeing of various types of fabrics. Few recent studies for each fabric type have been listed in Table 20.3.

Furthermore, ultrasound is found to be especially effective in dyeing of the textile fibers with natural dyes, as ultrasound can play a role in enhancement of dye extraction from the organic source while also assisting in the dyeing process. Traditionally, the extraction of the natural pigments from plants or fruits is carried out using chemical processes at high temperature, which may result in deterioration of the dye properties (Jajpura and Nayak, 2020). However, ultrasound offers an greener and more efficient approach to the extraction process (Kamel et al., 2010; Sheikh et al., 2016; Sivakumar et al., 2009; Vankar and Shanker, 2008).

20.2.5.3 Textile finishing

Textile finishing is nothing but finishing the textile surface with coating of different materials for functional and/or visual purposes. Earliest applications of ultrasound in textile finishing have been reported in application of cross-linking resins like

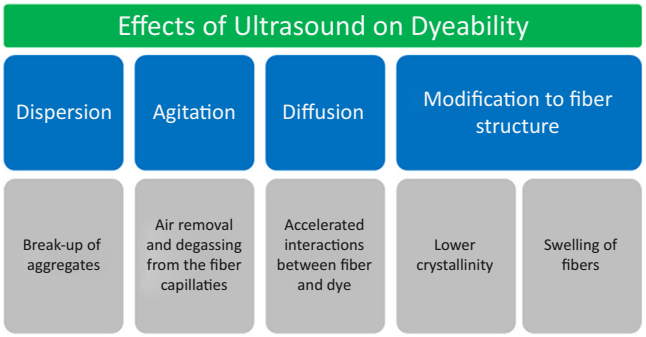

FIGURE 20.6 Effects of ultrasound responsible for accelerated dyeing. Data from Harifi, T. & Montazer, M. (2015). A review on textile sonoprocessing: a special focus on sonosynthesis of nanomaterials on textile substrates. In Ultrasonics Sonochemistry (Vol. 23, pp. 1–10). https://doi.org/10.1016/j.ultsonch.2014.08.022. Mechanism and effects of ultrasound responsible for accelerated dyeing.

TABLE 20.3 Application of ultrasound in dyeing of different textiles.

Fabric type	Key findings	References
Wool	Dye absorption rate increased by at least 50%. Conventional dyeing needs temperature around 98°C, which results in damage of fabric. To prevent this, additional protective agents are required, which are toxic. By using ultrasound, dyeing temperatures were lowered to 60°C, reducing energy requirement as well as additional chemical requirement	Eren (2012), Ferrero and Periolatto (2012), McNeil and McCall (2011)
Cotton	Dyeing was carried out at room temperature. Dye particles were deagglomerated by ultrasound resulting in enhanced color strength compared to conventional dyeing. Ultrasound as well as its combined treatment with enzymes was effective in extraction and dyeing with natural dye. Intermittent sonication was found to be more effective as compared to continuous sonication	Guesmi et al. (2013), Sun et al. (2010), Tissera et al. (2016), Vankar et al. (2007)
Leather	Diffusion rate of dyes were enhanced resulting in improved dye exhaustion and fastness properties in shorter time.	Sivakumar et al. (2008), Sivakumar and Rao (2003), Sivakumar and Rao (2001)
Polyester	Dyeing polyester is carried out at high temperature in high pressure vessel due to its high glass transition temperature and crystalline structure. The process can be carried out at ambient pressure by using carrier chemicals, which are not eco-friendly. Ultrasound enables dyeing of polyester at lower temperature and ambient pressure without using additional chemicals. Energy requirement is reduced while improving dyeing uniformity.	Altay et al. (2018), Osman and Khairy (2013), Rehman et al. (2020)
Jute	Ultrasound improved the color strength of dyed samples without compromising the color fastness.	Hassan and Saifullah (2018)
Cellulose Acetate	Ultrasound eliminated need for using any additional chemicals for dyeing. Color yield and fastness of the samples was similar to the conventional dyeing method. The dyeing time was reduced significantly.	Udrescu et al. (2014)
Polylactic Acid (PLA)	Ultrasound resulted in increase in color strength for some selective disperse dyes, due to deagglomeration of the dye particles, resulting in improved dye dispersion. In case of some other disperse dyes, ultrasound was not found to be effective with lower color strength and pale dyeing. The ineffectiveness was attributed to breakage of the dye dispersions at the operating conditions. It is recommended that the operating conditions like pH, temperature and ultrasound power need to be optimized to get favorable results.	Burkinshaw and Jeong (2012a), Burkinshaw and Jeong (2012b), Lee and Kim (2001), Wang et al. (2010)

urea–formaldehyde on cotton, coating of fluoro-chemical repellents on military fabrics, coating cotton fiber with softener, etc. (Harifi and Montazer, 2015).

Recently with the development of nanotechnology, application of ultrasound in textile finishing with nanomaterials has caught interest of the researchers. Ultrasound cavitation has been known as an effective method of producing nanoparticles. Hence using ultrasound provides a single-step, energy-efficient process for synthesis as well as coating of textile fibers with

TABLE 20.4 Functional nanoparticle coated on fabrics.

Nanomaterial	Key applications
Silver (Ag) nanoparticles	Silver nanoparticles on wool resulted in antimicrobial properties with satisfactory stability over multiple washing cycles (Hadad et al., 2007). Single step process for coating of Ag nanoparticles using US on cotton, nylon, and polyester was reported (Perelshtein et al., 2008). Method for loading of Ag nanoparticles on silk as well as polyethylene was developed (Abbasi et al., 2012; Abbasi and Morsali, 2011)
TiO_2 nanoparticles	TiO_2 particles on cotton fabric provide antifungal and anti-microbial protection. It also provides UV protection and self-cleaning property to cotton. One-step process for synthesis and coating of TiO_2 nanoparticles using US has been reported (Akhavan Sadr and Montazer, 2014; Perelshtein et al., 2012). TiO_2 or N-doped TiO_2 loading on wool gives it enhanced properties such as antibacterial/antifungal, self-cleaning, hydrophilicity, low cytotoxicity, increased tensile strength, and lower photo-yellowing and lower alkaline solubility (Behzadnia et al., 2014a; Behzadnia et al., 2014b).
ZnO nanoparticles	Deposition of ZnO nanoparticles on fabric provides antimicrobial properties. Methods for coating of ZnO nanoparticles on cotton (Perelshtein et al., 2013; Perelshtein et al., 2009a; Petkova et al., 2014), silk (Khanjani et al., 2013) as well as wool (Behzadnia et al., 2015) have been reported.
CuO nanoparticles	CuO also provides antibacterial properties to the fabric. Method for coating CuO nanoparticles on cotton bandages has been reported in literature (Perelshtein et al., 2009b).
Mn_3O_4 nanoparticles	Coating silk with sphere like Mn_3O_4 Nanoparticles has been reported to provide antibacterial resistance (Khanjani and Morsali, 2013a).
$Mg(OH)_2$ nanoparticles	$Mg(OH)_2$ nanoparticles coated on silk make it flame-retardant (Khanjani and Morsali, 2013b).

nanomaterials (Abbasi et al., 2012; Behzadnia et al., 2015; Perelshtein et al., 2012). Some of the studies involving coating fabrics with nanoparticles have been listed in Table 20.4.

Additionally, ultrasound cavitation also finds application in the treatment of the effluents generated from the textile industries. These effluent streams contain several bio-refractory pollutants including the dyes and other chemicals used in textile processing. US cavitation can be an effective advanced oxidation process to break these compounds into biodegradable materials. The application of ultrasonic cavitation in effluent treatment include advanced processes, and microbial disinfection in combination with other treatment methods (see Section 20.4.1 of this chapter).

20.2.5.4 Learnings for textile process

Ultrasonic cavitation finds several applications at various stages of textile processing industry. However, the technology faces challenges in terms of scale-up. Several studies have been carried out to model the effects of ultrasound in the sonochemical reactors. Few researchers have also been able to scale-up the processes to pilot scales (Abramova et al., 2013; Gonçalves et al., 2014a; Perincek et al., 2009; Vouters et al., 2004). However, more research needs to be carried out in this area to make the technology viable at large scale.

20.2.6 Azeotropic distillation

Selective ethanol separation from ethanol–water solution was demonstrated using ultrasonic atomization. Even for dilute ethanol concentration in liquid bulk, higher concentration of ethanol in mist was demonstrated (Sato et al., 2001) (see Fig. 20.7). It was hypothesized that Ethanol molecules got concentrated on the interface. Ultrasonic atomization shreds the surface layer as droplets. Capillary waves were suggested to be responsible for ethanol mist (Sato et al., 2001). The capillary wave theory was supported by the jet breakup and resulting atomization above the liquid surface was as an alternative explanation for selective ethanol separation provided (Kirpalani and Toll, 2002). Ultrasound creates microbubbles in the liquid jet. Sonoluminescence experiments in alcohol-water solution indicated accumulation of ethanol in the bubble (Ashokkumar et al., 1997). Microbubble cloud travels within the liquid jet and collapses in regions of accumulated acoustic energy. Thus releasing ethanol-rich mist.

Recent studies have shown that ultrasound cavitation can affect the vapor liquid equilibrium (VLE) of a mixture (Liang et al., 2017). Suzuki et al. had reported similar behavior in ethanol/water mixture, where cavities collapsed at the surface releasing the alcohol vapor in the bubble to the vapor phase (Suzuki et al., 2012). This has a significant effect on shifting the vapor–liquid equilibrium. The ultrasonic wave also creates vacuum conditions at micro scale, which alter the azeotropic concentration of the vapor components inside the cavity and results in a shift in the VLE. The enhancement in heat and

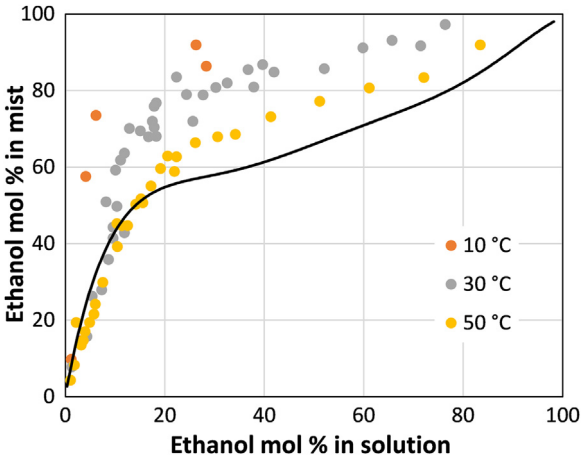

FIGURE 20.7 Ultrasonic purification of ethanol. Data from Sato, M., Matsuura, K. & Fujii, T. (2001). Ethanol separation from ethanol-water solution by ultrasonic atomization and its proposed mechanism based on parametric decay instability of capillary wave. J. Chemical Phys., 114(5), 2382–2382. https://doi.org/10.1063/1.1336842 Selective ethanol separation from ethanol–water solution, using ultrasonic atomization.

mass transfer due to the micro turbulence generated during cavitation also alters the thermodynamics of the process and may change the VLE of the system.

Cavitation is a transient process that occurs in microseconds and at a micro scale, that is, it causes physico-chemical effects locally but doesn't significantly affect the global operating conditions of the distillation process. Unlike other conventional processes such as extractive distillation, Ultrasound-assisted distillation doesn't need any separating agent and separation can be achieved in a single column. This can help in reducing the equipment size and safety issues related to the addition, recovery and recycling of separating agents through multiple equipment.

The ultrasound intensity and frequency have an effect on the Ultrasound-assisted azeotropic distillation process. An increase in the intensity causes an increase in the number of cavities which ultimately results in more local vacuum points and hence affects the thermodynamics of the VLE of the system. The ultrasonic frequency has the opposite effect on the performance of ultrasonic-assisted distillation. At lower US frequency, the larger cavity size is obtained which increases the mass transfer of vapor phase into the bubble. Also, larger cavities are likely to move toward the liquid surface due to buoyancy, where they collapse and release the vapor, which is required for the vapor–liquid separation process. Some of the reported studies on US-assisted azeotropic distillation are summarized in Table 20.5.

It should be noted here that the micropoint vacuum conditions generated during sonication help create a low pressure operating condition, which is preferred for separation of low boiling point azeotrope. However, for high boiling azeotropes (e.g., nitric acid-water and sulfuric acid-water mixtures), high-pressure conditions are required to shift the azeotropic point, which is difficult to achieve with ultrasound. This is one of the limitations of using ultrasound for the distillation of azeotropic mixtures (Mahdi and Al-Kawaz, 2018).

The ultrasound-assisted azeotropic distillation provides numerous advantages over conventional distillation. However, it also requires additional energy for operating ultrasonic transducers and a thorough cost comparison considering the additional energy cost of the ultrasound system against the cost savings due to a reduction in the number of distillation columns and its operating cost and cost of separating material management system is necessary. Further studies are required to make the system efficient, economically attractive, simple in operation, and environmentally friendly.

20.3 Outlook and path forward

Numerous applications of acoustic cavitation have been demonstrated. To make these more acceptable for industrial implementation the largest challenge is consistency/reproducibility and reduction in energy consumption. These key challenges and possible path for overcoming the same are described below

Improving energy conversion efficiency*:* The two major energy conversion losses (from electricity to sound energy) in ultrasonic devices are (1) piezoelectric crystals and resonator design, and (2) boundary layer separation at the irradiation surface. The efficiency of piezo electric crystals together with resonator material and design significantly decides the energy conversion. The energy losses at the irradiation surface due to boundary layer separation is increased at low frequency and higher intensity. The way to reduce this loss is to operate at high frequency and low intensity. For applications which need

TABLE 20.5 Ultrasound for separation of azeotropic mixtures.

System	Process conditions	Result Summary
Ethanol/Ethyl acetate (ETAC) (Mahdi et al., 2015)	**Feed**: 65 mol% of ETAC added at the bottom of the column at 100 kmol/h. **Azeotropic Concentration:** 55 mol% ETAC at minimum boiling point of 71.8°C. **US intensity**: 500 W/cm^2 **US frequency**: 25 kHz.	Number of stages for the desired separation: 2799 mol% . ETAC was separated with the ultrasonic intensity of 500 W/cm2 and 25 kHz frequency. Good separation (99 mol% purity of the top product) is also reported for other azeotropic mixture (ethanol–water, n-butanol-water and methyl acetate-methanol)
Methyl tert-butyl ether (MTBE) and methanol (MeOH) mixture (Anschuetz et al., 2012)	**Feed:** 70 mol% MTBE **System I**: US Horn **Amplitude:** 22 W/cm^2 **Frequency:** 24 kHz **System II**: US bath **Amplitude:** 22 W/cm^2 **Frequency:** 35 kHz	Number of theoretical stages decreased from three to two. Marginal change in the azeotropic point
Ethyl acetate andethanol mixture (Mahdi and Al-Kawaz, 2018)	**Feed**: 65% Ethyl acetate at 333.15 K and 1 bar **Azeotropic Concentration:** 55 mol% ETAC at minimum boiling point of 71.8°C **Ultrasound Conditions:** Ultrasonic transducer added in the equilibrium stages. Sonication stages start from the feed stage to the top column (rectifying section), **Ultrasound intensity:** 500 W/cm^2 **Ultrasound frequency:** 25 kHz **Reflux ratio:** 8 **Number of stages:** 35	A top product with 99% purity of ETAC was obtained. Effect of operating parameters was observed for purity of the top product and heat duty 14.6%. Reduction in operating cost compared to extractive distillation. System is limited to minimum boiling point azeotropic mixtures

higher intensity, alternate methods of concentrating/focusing sound toward a smaller volume from larger irradiating surface can be used. While the above-mentioned aspects can be improved, it also calls for searching for alternate methods to generate ultrasound. Fluidic oscillator/resonators are some options reported in the literature and should be improved further (Osman et al., 2016).

Reducing the energy for nucleation & improving the consistency of nucleation*:* Nucleation needs the most energy among various stages of cavitation (nucleation, cavity growth, and collapse). The energy efficiency can be significantly improved by eliminating the nucleation stage (Mahulkar et al., 2008). Preseeding the medium with potential nuclei is one such alternative. Preseeding will not only reduce the energy requirement for the overall process, but it will also improve the spatial and temporal consistency of cavitation intensity in the sonochemical reactor. Preseeding can be done by various options like controlling/improving the quantity of dissolved gases, using injected vaporous bubbles as nuclei, encapsulating the dispersed phase in the vapor bubble at the time of injection. Reactor wall/surface roughness can also act as nucleation sites. Improving fluid turbulence over the rough surface can also induce nucleation.

References

Abbasi, A.R., Kalantary, H., Yousefi, M., Ramazani, A., Morsali, A., 2012. Synthesis and characterization of ag nanoparticles@polyethylene fibers under ultrasound irradiation. Ultrason. Sonochem. 19, 853–857. https://doi.org/10.1016/j.ultsonch.2011.11.011.

Abbasi, A.R., Morsali, A., 2011. Synthesis and properties of silk yarn containing ag nanoparticles under ultrasound irradiation. Ultrason. Sonochem. 18, 282–287. https://doi.org/10.1016/J.ULTSONCH.2010.06.002.

Abdurahman, M.H., Abdullah, A.Z., Shoparwe, N.F., 2021. A comprehensive review on sonocatalytic, photocatalytic, and sonophotocatalytic processes for the degradation of antibiotics in water: synergistic mechanism and degradation pathway. Chem. Eng. J. 413, 127412. https://doi.org/10.1016/J.CEJ.2020.127412.

Abou-Okeil, A., El-Shafie, A., El Zawahry, M.M., 2010. Ecofriendly laccase-hydrogen peroxide/ultrasound-assisted bleaching of linen fabrics and its influence on dyeing efficiency. Ultrason. Sonochem. 17, 383–390. https://doi.org/10.1016/j.ultsonch.2009.08.007.

Abramova, A., Gedanken, A., Popov, V., Ooi, E.H., Mason, T.J., Joyce, E.M., Beddow, J., Perelshtein, I., Bayazitov, V., 2013. A sonochemical technology for coating of textiles with antibacterial nanoparticles and equipment for its implementation. Mater. Lett. 96, 121–124. https://doi.org/10.1016/j.matlet.2013.01.041.

Adal, Eda, 2019. Microbial inactivation by ultrasound in the food industry. Technological Developments in Food Preservation, Processing, and Storage. IGI Global, pp. 86–96. https://doi.org/10.4018/978-1-7998-1924-0.ch005.

Aghajanzadeh, S., Ziaiifar, A.M., 2021. Pasteurization of juices with non-thermal technologies. Sustainable Food Processing and Engineering Challenges. Academic Press, Cambridge, USA, pp. 25–73. https://doi.org/10.1016/b978-0-12-822714-5.00002-4.

Agrawal, P.B., Pandit, A.B., 2003. Isolation of α-glucosidase from saccharomyces cerevisiae: cell disruption and adsorption. Biochem. Eng. J. 15, 37–45. https://doi.org/10.1016/S1369-703X(02)00178-X.

Aksoy, A., Karasu, S., Akcicek, A., Kayacan, S., 2019. Effects of different drying methods on drying kinetics, microstructure, color, and the rehydration ratio of minced meat. Foods 8, 216. https://doi.org/10.3390/foods8060216

Akhavan Sadr, F., Montazer, M., 2014. In situ sonosynthesis of nano TiO_2 on cotton fabric. Ultrasonics Sonochemistry 21, 681–691. doi:https://doi.org/10.1016/j.ultsonch.2013.09.018.

Altay, P., Özcan, G., Tekçin, M., Şahin, G., Çelik, S., 2018. Comparison of conventional and ultrasonic method for dyeing of spunbond polyester nonwoven fabric. Ultrason. Sonochem. 42, 768–775. https://doi.org/10.1016/j.ultsonch.2017.12.040.

Antoniadis, A., Poulios, I., Nikolakaki, E., Mantzavinos, D., 2007. Sonochemical disinfection of municipal wastewater. J. Hazard. Mater. 146, 492–495. https://doi.org/10.1016/J.JHAZMAT.2007.04.065.

Arya, S.S., Sawant, O., Sonawane, S.K., Show, P.L., Waghamare, A., Hilares, R., Santos, J.C.Dos, 2020. Novel, nonthermal, energy efficient, industrially scalable hydrodynamic cavitation–applications in food processing. Food Rev. Int. doi:10.1080/87559129.2019.1669163.

Ashokkumar, M., Hall, R., Mulvaney, P., Grieser, F., 1997. Sonoluminescence from aqueous alcohol and surfactant solutions. J. Phys. Chem. B 101, 10845–10850. https://doi.org/10.1021/JP972477B.

Avvaru, B., Venkateswaran, N., Uppara, P., Iyengar, S.B., Katti, S.S., 2018. Current knowledge and potential applications of cavitation technologies for the petroleum industry. Ultrason. Sonochem. doi:10.1016/j.ultsonch.2017.12.010.

Basto, C., Tzanov, T., Cavaco-Paulo, A., 2007. Combined ultrasound-laccase assisted bleaching of cotton. Ultrason. Sonochem. 14, 350–354. https://doi.org/10.1016/j.ultsonch.2006.07.006.

Behzadnia, A., Montazer, M., Rad, M.M., 2015. In-situ sonosynthesis of nano N-doped zno on wool producing fabric with photo and bio activities, cell viability and enhanced mechanical properties. J. Photochem. Photobiol. B Biol. 149, 103–115. https://doi.org/10.1016/j.jphotobiol.2015.05.006.

Behzadnia, A., Montazer, M., Rashidi, A., Rad, M.M., 2014a. Sonosynthesis of nano tio2 on wool using titanium isopropoxide or butoxide in acidic media producing multifunctional fabric. Ultrason. Sonochem. 21, 1815–1826. https://doi.org/10.1016/j.ultsonch.2014.03.009.

Behzadnia, A., Montazer, M., Rashidi, A., Rad, M.M., 2014b. Rapid sonosynthesis of N-doped nano tio2 on wool fabric at low temperature: introducing self-cleaning, hydrophilicity, antibacterial/antifungal properties with low alkali solubility, yellowness and cytotoxicity. Photochem. Photobiol. 90, 1224–1233. https://doi.org/10.1111/php.12324.

Bhargava, N., Mor, R.S., Kumar, K., Sharanagat, V.S., 2021. Advances in application of ultrasound in food processing: a review. Ultrason. Sonochem. doi:10.1016/j.ultsonch.2020.105293.

Bhat, A.P., Gogate, P.R., 2021. Cavitation-based pre-Treatment of wastewater and waste sludge for improvement in the performance of biological processes: a review. J. Environ. Chem. Eng. 9, 104743.

Bhattacharjee, C., Saxena, V.K., Dutta, S., 2019. Novel thermal and non-thermal processing of watermelon juice. Trends Food Sci. Technol. 10.1016/j.tifs.2019.09.015.

Burkinshaw, S.M., Jeong, D.S., 2012a. The dyeing of poly(lactic acid) fibres with disperse dyes using ultrasound: part 1—initial studies. Dye. Pigment. 92, 1025–1030. https://doi.org/10.1016/j.dyepig.2011.06.020.

Burkinshaw, S.M., Jeong, D.S., 2012b. The dyeing of poly(lactic acid) fibres with disperse dyes using ultrasound: part 2—fastness. Dye. Pigment. 92, 988–994. https://doi.org/10.1016/j.dyepig.2011.07.005.

Anschuetz, F., Franke, M., Braeutigam, P., Ondruschka, B., 2012. The separation of azeotropic mixtures by ultrasound-assisted distillation. 13th Meeting of the European Society of Sonochemistry, July 01–05, 2012, Lviv – Ukraine

Canoğlu, S., Gültekin, B.C., Yükseloğlu, S.M., 2004. Effect of ultrasonic energy in washing of medical surgery gowns. Ultrasonics 42 (1–9), 113–119. https://doi.org/10.1016/j.ultras.2004.02.012.

Canselier, J.P., Delmas, H., Wilhelm, A.M., Abismaïl, B., 2002. Ultrasound emulsification—an overview. J. Dispers. Sci. Technol. 23, 333–349. https://doi.org/10.1080/01932690208984209.

Cárcel, J.A., Castillo, D., Simal, S., Mulet, A., 2019. Influence of temperature and ultrasound on drying kinetics and antioxidant properties of red pepper. Dry. Technol. 37, 486–493. https://doi.org/10.1080/07373937.2018.1473417.

Chakraborty, S., Uppaluri, R., Das, C., 2020. Optimization of ultrasound-assisted extraction (UAE) process for the recovery of bioactive compounds from bitter gourd using response surface methodology (RSM). Food Bioprod. Process. 120, 114–122. https://doi.org/10.1016/j.fbp.2020.01.003.

Chemat, F., Rombaut, N., Sicaire, A.G., Meullemiestre, A., Fabiano-Tixier, A.S., Abert-Vian, M., 2017. Ultrasound assisted extraction of food and natural products. mechanisms, techniques, combinations, protocols and applications. A review. Ultrason. Sonochem. doi:10.1016/j.ultsonch.2016.06.035.

Chemat, F., Zill-e-Huma, Khan, Muhammed Kamran, 2011. Applications of ultrasound in food technology: Processing, preservation and extraction. Ultrasonics Sonochemistry 18 (4), 813–835. doi:https://doi.org/10.1016/j.ultsonch.2010.11.023.

Cheng, X.F., Zhang, M., Adhikari, B., 2014. Effect of ultrasonically induced nucleation on the drying kinetics and physical properties of freeze-dried strawberry. Dry. Technol. 32, 1857–1864. https://doi.org/10.1080/07373937.2014.952741.

Cinelli, G., Avino, P., Notardonato, I., Russo, M.V., 2014. Ultrasound-vortex-assisted dispersive liquid-liquid microextraction coupled with gas chromatography with a nitrogen-phosphorus detector for simultaneous and rapid determination of organophosphorus pesticides and triazines in wine. Anal. Methods 6, 782–790. https://doi.org/10.1039/c3ay41641k.

Cruz, L., Clemente, G., Mulet, A., Ahmad-Qasem, M.H., Barrajón-Catalán, E., García-Pérez, J.V., 2016. Air-borne ultrasonic application in the drying of grape skin: kinetic and quality considerations. J. Food Eng. 168, 251–258. https://doi.org/10.1016/j.jfoodeng.2015.08.001.

Dalvi-Isfahan, M., Hamdami, N., Xanthakis, E., Le-Bail, A., 2017. Review on the control of ice nucleation by ultrasound waves, electric and magnetic fields. J. Food Eng. doi:10.1016/j.jfoodeng.2016.10.001.

de la Fuente-Blanco, S., Riera-Franco de Sarabia, E., Acosta-Aparicio, V.M., Blanco-Blanco, A., Gallego-Juárez, J.A., 2006. Food drying process by power ultrasound. Ultrasonics 44, e523–e527. https://doi.org/10.1016/j.ultras.2006.05.181.

Demirdöven, A., Baysal, T., 2009. The use of ultrasound and combined technologies in food preservation. Food Rev. Int. 25, 1–11. https://doi.org/10.1080/87559120802306157.

Dhas, A., Koltypin, Y., Gedanken, A., 1997. Sonochemical preparation and characterization of ultrafine chromium oxide and manganese oxide powders. Chem. Mater. 9, 3159–3163. https://doi.org/10.1021/CM9704645.

Diehl, L.O., Moraes, D.P., Antes, F.G., Pereira, J.S.F., de Fátima, M.P.S., Guimarães, R.C.L., Paniz, J.N.G., Flores, É.M.M., 2011. Separation of heavy crude oil emulsions using microwave radiation for further crude oil analysis. Sep. Sci. Technol. 46, 1358–1364. https://doi.org/10.1080/01496395.2011.560590.

Dolatowski, Z.J., Stadnik, J., Stasiak, D., 2007. Applications of ultrasound in food technology. ACTA Sci. Pol. 63, 89–99.

Dutta, D.P., Ghildiyal, R., Tyagi, A.K., 2009. Luminescent properties of doped zinc aluminate and zinc gallate white light emitting nanophosphors prepared via sonochemical method. J. Phys. Chem. C 113, 16954–16961. https://doi.org/10.1021/JP905631G.

Eren, Z., 2012. Ultrasound as a basic and auxiliary process for dye remediation: a review. J. Environ. Manage. doi:10.1016/j.jenvman.2012.03.028.

Farkade, V.D., Harrison, S.T.L., Pandit, A.B., 2006. Improved cavitational cell disruption following pH pretreatment for the extraction of β-galactosidase from kluveromyces lactis. Biochem. Eng. J. 31, 25–30. https://doi.org/10.1016/J.BEJ.2006.05.015.

Ferkous, H., Hamdaoui, O., Merouani, S., 2015. Sonochemical degradation of naphthol blue black in water: effect of operating parameters. Ultrason. Sonochem. 26, 40–47. https://doi.org/10.1016/J.ULTSONCH.2015.03.013.

Fernandes, F.A.N., Fonteles, T.V., Rodrigues, S., Brito, E.S.de, Tiwari, B.K., 2020. Ultrasound-assisted extraction of anthocyanins and phenolics from jabuticaba (Myrciaria cauliflora) peel: kinetics and mathematical modeling. J. Food Sci. Technol. 57, 2321–2328. https://doi.org/10.1007/s13197-020-04270-3.

Ferrero, F., Periolatto, M., 2012. Ultrasound for low temperature dyeing of wool with acid dye. Ultrason. Sonochem. 19, 601–606. https://doi.org/10.1016/j.ultsonch.2011.10.006.

Fu, X., Belwal, T., Cravotto, G., Luo, Z., 2020. Sono-physical and sono-chemical effects of ultrasound: primary applications in extraction and freezing operations and influence on food components. Ultrason. Sonochem. doi:10.1016/j.ultsonch.2019.104726.

Gallo, M., Ferrara, L., Naviglio, D., 2018. Application of ultrasound in food science and technology: a perspective. Foods doi:10.3390/foods7100164.

Gao, S., Lewis, G., Hemar, Y., 2016. Ultrasonic inactivation of microorganisms. Handbook of Ultrasonics and Sonochemistry 1355–1381. https://doi.org/10.1007/978-981-287-278-4_69.

Gogate, P.R., Pandit, A.B., 2004. A review of imperative technologies for wastewater treatment I: oxidation technologies at ambient conditions. Adv. Environ. Res. 8, 501–551. https://doi.org/10.1016/S1093-0191(03)00032-7.

Gonçalves, I., Herrero-Yniesta, V., Perales Arce, I., Escrigas Castañeda, M., Cavaco-Paulo, A., Silva, C., 2014a. Ultrasonic pilot-scale reactor for enzymatic bleaching of cotton fabrics. Ultrason. Sonochem. 21, 1535–1543. https://doi.org/10.1016/j.ultsonch.2014.02.009.

Gonçalves, I., Martins, M., Loureiro, A., Gomes, A., Cavaco-Paulo, A., Silva, C., 2014b. Sonochemical and hydrodynamic cavitation reactors for laccase/hydrogen peroxide cotton bleaching. Ultrason. Sonochem. 21, 774–781. https://doi.org/10.1016/j.ultsonch.2013.08.006.

Gotoh, K., Harayama, K., 2013. Application of ultrasound to textiles washing in aqueous solutions. Ultrason. Sonochem. 20, 747–753. https://doi.org/10.1016/j.ultsonch.2012.10.001.

Greenly, J.M., Tester, J.W., 2015. Ultrasonic cavitation for disruption of microalgae. Bioresour. Technol. 184, 276–279. https://doi.org/10.1016/J.BIORTECH.2014.11.036.

Guesmi, A., Ladhari, N., Sakli, F., 2013. Ultrasonic preparation of cationic cotton and its application in ultrasonic natural dyeing. Ultrason. Sonochem. 20, 571–579. https://doi.org/10.1016/j.ultsonch.2012.04.012.

Hadad, L., Perkas, N., Gofer, Y., Calderon-Moreno, J., Ghule, A., Gedanken, A., 2007. Sonochemical deposition of silver nanoparticles on wool fibers. J. Appl. Polym. Sci. 104, 1732–1737. https://doi.org/10.1002/APP.25813.

Hamida, T., Babadagli, T., 2007. Analysis of capillary interaction and oil recovery under ultrasonic waves. Transp. Porous Media 70, 231–255. https://doi.org/10.1007/S11242-006-9097-9.

Hamidi, H., Sharifi Haddad, A., Mohammadian, E., Rafati, R., Azdarpour, A., Ghahri, P., Ombewa, P., Neuert, T., Zink, A., 2017. Ultrasound-assisted CO2 flooding to improve oil recovery. Ultrason. Sonochem. 35, 243–250. https://doi.org/10.1016/J.ULTSONCH.2016.09.026.

Hao, L., Wang, R., Fang, K., Liu, J., 2013. Ultrasonic effect on the desizing efficiency of amylase on starch-sized cotton fabrics. Carbohydr. Polym. 96, 474–480. https://doi.org/10.1016/j.carbpol.2013.04.003.

Harifi, T., Montazer, M., 2015. A review on textile sonoprocessing: a special focus on sonosynthesis of nanomaterials on textile substrates. Ultrason. Sonochem. https://doi.org/10.1016/j.ultsonch.2014.08.022.

Hassan, M.M., Saifullah, K., 2018. Ultrasound-assisted pre-treatment and dyeing of jute fabrics with reactive and basic dyes. Ultrason. Sonochem. 40, 488–496. https://doi.org/10.1016/j.ultsonch.2017.07.037.

Hongyu, W., Hulbert, G.J., Mount, J.R., 2000. Effects of ultrasound on milk homogenization and fermentation with yogurt starter. Innov. Food Sci. Emerg. Technol. 1, 211–218. https://doi.org/10.1016/S1466-8564(00)00020-5.

Huang, D., Men, K., Li, D., Wen, T., Gong, Z., Sunden, B., Wu, Z., 2020. Application of ultrasound technology in the drying of food products. Ultrason. Sonochem. doi:10.1016/j.ultsonch.2019.104950.

Hunter, G., Lucas, M., Watson, I., Parton, R., 2008. A radial mode ultrasonic horn for the inactivation of escherichia coli K12. Ultrason. Sonochem. 15, 101–109. https://doi.org/10.1016/J.ULTSONCH.2006.12.017.

Hurren, C., Cookson, P., Wang, X., 2008. The effects of ultrasonic agitation in laundering on the properties of wool fabrics. Ultrason. Sonochem. 15, 1069–1074. https://doi.org/10.1016/j.ultsonch.2008.04.002.

Hyeon, T., Fang, M., Suslick, K., 1996. Nanostructured molybdenum carbide: sonochemical synthesis and catalytic properties. J. Am. Chem. Soc. 118, 5492–5493. https://doi.org/10.1021/JA9538187.

Ince, N.H., Belen, R., 2001. Aqueous phase disinfection with power ultrasound: process kinetics and effect of solid catalysts. Environ. Sci. Technol. 35, 1885–1888. https://doi.org/10.1021/ES000157R.

Jadhav, A.J., Holkar, C.R., Goswami, A.D., Pandit, A.B., Pinjari, D.V., 2016. Acoustic cavitation as a novel approach for extraction of oil from waste date seeds. ACS Sustain. Chem. Eng. 4, 4256–4263. https://doi.org/10.1021/acssuschemeng.6b00753.

Jadhav, N.L., Garule, P.A., Pinjari, D.V., 2020. Comparative study of ultrasound pretreatment method with conventional hydrodistillation method for extraction of essential oil from piper betle L. (Paan). Indian Chem. Eng. doi:10.1080/00194506.2020.1828193.

Jajpura, L., Nayak, R., 2020. Ultrasound applications in textiles and apparels. Sustainable Technologies for Fashion and Textiles 143–161. doi:https://doi.org/10.1016/B978-0-08-102867-4.00007-4.

Jeevanandam, J., Barhoum, A., Chan, Y.S., Dufresne, A., Danquah, M.K., 2018. Review on nanoparticles and nanostructured materials: history, sources, toxicity and regulations. Beilstein J. Nanotechnol. 998 (9), 1050–1074. https://doi.org/10.3762/BJNANO.9.98.

Jiang, W., Zhang, X., Gong, X., Yan, F., 2010. Sonochemical synthesis and characterization of magnetic separable Fe3O4–TiO2 nanocomposites and their catalytic properties. Zhang, Z., 1, 278–287. https://doi.org/10.1080/19475411.2010.528873.

Jiranek, V., Grbin, P., Yap, A., Barnes, M., Bates, D., 2008. High power ultrasonics as a novel tool offering new opportunities for managing wine microbiology. Biotechnol. Lett. doi:10.1007/s10529-007-9518-z.

Jyoti, K.K., Pandit, A.B., 2003. Hybrid cavitation methods for water disinfection. Biochem. Eng. J. 14, 9–17. https://doi.org/10.1016/S1369-703X(02)00102-X.

Jyoti, K.K., Pandit, A.B., 2004. Ozone and cavitation for water disinfection. Biochem. Eng. J. 18, 9–19. https://doi.org/10.1016/S1369-703X(03)00116-5.

Kadam, S.U., Tiwari, B.K., O'Donnell, C.P., 2015. Effect of ultrasound pre-treatment on the drying kinetics of brown seaweed ascophyllum nodosum. Ultrason. Sonochem. 23, 302–307. https://doi.org/10.1016/j.ultsonch.2014.10.001.

Kamel, M.M., El-Shishtawy, R.M., Youssef, B.M., Mashaly, H., 2007. Ultrasonic assisted dyeing. IV. dyeing of cationised cotton with lac natural dye. Dye. Pigment. 73, 279–284. https://doi.org/10.1016/j.dyepig.2005.12.010.

Kamel, M.M., El-Shishtawy, R.M., Yussef, B.M., Mashaly, H., 2005. Ultrasonic assisted dyeing III. dyeing of wool with lac as a natural dye. Dye. Pigment. 65, 103–110. https://doi.org/10.1016/j.dyepig.2004.06.003.

Kamel, M.M., Helmy, H.M., Mashaly, H.M., Kafafy, H.H., 2010. Ultrasonic assisted dyeing: dyeing of acrylic fabrics C.I. astrazon basic red 5BL 200%. Ultrason. Sonochem. 17, 92–97. https://doi.org/10.1016/j.ultsonch.2009.06.001.

Kentish, S., Feng, H., 2014. Applications of power ultrasound in food processing. Annu. Rev. Food Sci. Technol. 5, 263–284. https://doi.org/10.1146/annurev-food-030212-182537.

Khanjani, S., Morsali, A., 2013a. Ultrasound-assisted coating of silk yarn with sphere-like mn 3O4 nanoparticles. Ultrason. Sonochem. 20, 413–417. https://doi.org/10.1016/j.ultsonch.2012.07.022.

Khanjani, S., Morsali, A., 2013b. Ultrasound-promoted coating of silk yarn with different morphology of magnesium hydroxide nanostructures. Ultrason. Sonochem. 20, 729–733. https://doi.org/10.1016/j.ultsonch.2012.09.001.

Khanjani, S., Morsali, A., Joo, S.W., 2013. In situ formation deposited zno nanoparticles on silk fabrics under ultrasound irradiation. Ultrason. Sonochem. 20, 734–739. https://doi.org/10.1016/j.ultsonch.2012.09.013.

Khatri, Z., Memon, M.H., Khatri, A., Tanwari, A., 2011. Cold pad-batch dyeing method for cotton fabric dyeing with reactive dyes using ultrasonic energy. Ultrason. Sonochem. 18, 1301–1307. https://doi.org/10.1016/j.ultsonch.2011.04.001.

Kiani, H., Sun, D.W., 2018. Numerical simulation of heat transfer and phase change during freezing of potatoes with different shapes at the presence or absence of ultrasound irradiation. Heat Mass Transf. und Stoffuebertragung 54, 885–894. https://doi.org/10.1007/s00231-017-2190-5.

Kirpalani, D.M., Toll, F., 2002. Revealing the physicochemical mechanism for ultrasonic separation of alcohol–water mixtures. J. Chem. Phys. 117, 3874. https://doi.org/10.1063/1.1495849.

Korpe, S., Rao, P.V., 2021. Application of advanced oxidation processes and cavitation techniques for treatment of tannery wastewater—a review. J. Environ. Chem. Eng. 9, 105234. https://doi.org/10.1016/J.JECE.2021.105234.

Kowalski, S.J., Mierzwa, D., Stasiak, M., 2017. Ultrasound-assisted convective drying of apples at different process conditions. Dry. Technol. 35, 939–947. https://doi.org/10.1080/07373937.2016.1239631.

Kumar, Y., Sharanagat, V.S., Singh, L., Nema, P.K., 2020. Convective drying of spine gourd (Momordica dioica): effect of ultrasound pre-treatment on drying characteristics, color, and texture attributes. J. Food Process. Preserv. 44, e14639. https://doi.org/10.1111/jfpp.14639.

Lee, K.W., Kim, J.P., 2001. Effect of ultrasound on disperse dye particle size. Text. Res. J. 71, 395–398. https://doi.org/10.1177/004051750107100505.

Leong, T.S.H., Zhou, M., Kukan, N., Ashokkumar, M., Martin, G.J.O., 2017. Preparation of water-in-oil-in-water emulsions by low frequency ultrasound using skim milk and sunflower oil. Food Hydrocoll 63, 685–695. https://doi.org/10.1016/j.foodhyd.2016.10.017.

Li, B., Sun, D.W., 2002. Novel methods for rapid freezing and thawing of foods—a review. J. Food Eng. https://doi.org/10.1016/S0260-8774(01)00209-6.

Li, B., Xie, Y., Liu, Y., Huang, J., Qian, Y., 2001. Sonochemical synthesis of nanocrystalline silver tellurides Ag2Te and Ag7Te4. J. Solid State Chem. 158, 260–263. https://doi.org/10.1006/JSSC.2001.9103.

Li, K., Fu, L., Zhao, Y.Y., Xue, S.W., Wang, P., Xu, X.L., Bai, Y.H., 2020. Use of high-intensity ultrasound to improve emulsifying properties of chicken myofibrillar protein and enhance the rheological properties and stability of the emulsion. Food Hydrocoll. 98, 105275. https://doi.org/10.1016/j.foodhyd.2019.105275

Li, Q., Ding, C., Yu, H., Hurren, C.J., Wang, X., 2014. Adapting ultrasonic assisted wool scouring for industrial application. Text. Res. J. 84, 1183–1190. https://doi.org/10.1177/0040517512474365.

Li, S., Lee, J.S., Hyeon, T., Suslick, K.S., 1999. Catalytic hydrodenitrogenation of indole over molybdenum nitride and carbides with different structures. Appl. Catal. A Gen. 184, 1–9. https://doi.org/10.1016/S0926-860X(99)00044-7.

Liang, S., Cao, Y., Liu, X., Li, X., Zhao, Y., Wang, Yongkun, Wang, Yinglong, 2017. Insight into pressure-swing distillation from azeotropic phenomenon to dynamic control. Chem. Eng. Res. Des. 117, 318–335.

Liu, C., Cao, Z., He, S., Sun, Z., Chen, W., 2018. The effects and mechanism of phycocyanin removal from water by high-frequency ultrasound treatment. Ultrason. Sonochem. 41, 303–309. https://doi.org/10.1016/J.ULTSONCH.2017.09.051.

Luján-Facundo, M.J., Mendoza-Roca, J.A., Cuartas-Uribe, B., Álvarez-Blanco, S., 2016. Cleaning efficiency enhancement by ultrasounds for membranes used in dairy industries. Ultrason. Sonochem. 33, 18–25. https://doi.org/10.1016/j.ultsonch.2016.04.018.

Ma, M., You, L., Chen, L., Zhou, W., 2014. Effects of ultrasonic laundering on the properties of silk fabrics. Text. Res. J. 84, 2166–2174. https://doi.org/10.1177/0040517514537370.

Mahajan, D., Marshall, C.L., Castagnola, N., Hanson, J.C., 2004. Sono synthesis and characterization of nano-phase molybdenum-based materials for catalytic hydrodesulfurization. Appl. Catal. A Gen. 258, 83–91. https://doi.org/10.1016/J.APCATA.2003.08.014.

Mahdi, T., Ahmad, A., Ripin, A., Nasef, M.M., 2015. Separation of azeotropic mixture using multi-stage ultrasound-assisted flash distillation. Chem. Prod. Process Model. 10, 237–242. https://doi.org/10.1515/cppm-2015-0003.

Mahdi, T., Al-Kawaz, A.E., 2018. A simulation study of enhanced distillation using ultrasound waves for the separation of azeotropic mixtures. Am. J. Eng. Appl. Sci. 11, 97–107. https://doi.org/10.3844/ajeassp.2018.97.107.

Mahmoodi, N.M., Arami, M., Mazaheri, F., Rahimi, S., 2010. Degradation of sericin (degumming) of persian silk by ultrasound and enzymes as a cleaner and environmentally friendly process. J. Clean. Prod. 18, 146–151. https://doi.org/10.1016/j.jclepro.2009.10.003.

Mahulkar, A.V., Bapat, P.S., Pandit, A.B., Lewis, F.M., 2008. Steam bubble cavitation. AIChE J. 54, 1711–1724. https://doi.org/ https://doi.org/10.1002/aic.11509 .

Martini, S., Suzuki, A.H., Hartel, R.W., 2008. Effect of high intensity ultrasound on crystallization behavior of anhydrous milk fat. J. Am. Oil Chem. Soc. 85, 621–628. https://doi.org/10.1007/s11746-008-1247-5.

Mason, T. J., Paniwnyk, L., Chemat, F., 2003. Ultrasound as a preservation technology. Food Preservation Techniques. Woodhead Publishing, California, USA, pp. 303–337. https://doi.org/10.1533/9781855737143.3.303.

Mason, T.J., Paniwnyk, L., Chemat, F., Vian, M.A., 2011. Ultrasonic food processing. RSC Green Chem. 53, 388–414.

Matouq, M., Koda, S., Maricela, T., Omar, A., Tagawa, T., 2009. Solvent extraction of bitumen from jordan oil shale assisted by low frequency ultrasound. J. Japan Pet. Inst. 52, 265–269. https://doi.org/10.1627/JPI.52.265.

McNeil, S.J., McCall, R.A., 2011. Ultrasound for wool dyeing and finishing. Ultrason. Sonochem. 18, 401–406. https://doi.org/10.1016/j.ultsonch.2010.07.007.

Mettu, S., Yao, S., Sun, Q., Lawson, S.R., Scales, P.J., Martin, G.J.O., Ashokkumar, M., 2020. Effect of bulk viscosity and emulsion droplet size on the separation efficiency of model mineral oil-in-water (O/W) emulsions under ultrasonic standing wave fields: a theoretical and experimental investigation. Ind. Eng. Chem. Res. 59, 7901–7912. https://doi.org/10.1021/acs.iecr.0c00616.

Mevada, J., Devi, S., Pandit, A., 2019. Large scale microbial cell disruption using hydrodynamic cavitation: energy saving options. Biochem. Eng. J. 143, 151–160. https://doi.org/10.1016/j.bej.2018.12.010.

Miano, A.C., Pereira, J.da C., Castanha, N., Júnior, M.D.da M., Augusto, P.E.D., 2016. Enhancing mung bean hydration using the ultrasound technology: description of mechanisms and impact on its germination and main components. Sci. Rep. 6, 1–14. https://doi.org/10.1038/srep38996.

Mistik, S.I., Yükseloğlu, S.M., 2005. Hydrogen peroxide bleaching of cotton in ultrasonic energy. Ultrasonics 43, 811–814. https://doi.org/10.1016/j.ultras.2005.06.002.

Mizukoshi, Y., Okitsu, K., Maeda, Y., Yamamoto, T.A., Oshima, R., Nagata, Y., 1997. Sonochemical preparation of bimetallic nanoparticles of gold/palladium in aqueous solution. J. Phys. Chem. B 101, 7033–7037. https://doi.org/10.1021/JP9638090.

Monteiro, S.H.M.C., Silva, E.K., Alvarenga, V.O., Moraes, J., Freitas, M.Q., Silva, M.C., Raices, R.S.L., Sant'Ana, A.S., Meireles, M.A.A., Cruz, A.G., 2018. Effects of ultrasound energy density on the non-thermal pasteurization of chocolate milk beverage. Ultrason. Sonochem. 42, 1–10. https://doi.org/10.1016/j.ultsonch.2017.11.015.

Monteiro, S.H.M.C., Silva, E.K., Guimarães, J.T., Freitas, M.Q., Meireles, M.A.A., Cruz, A.G., 2020. High-intensity ultrasound energy density: how different modes of application influence the quality parameters of a dairy beverage. Ultrason. Sonochem. 63, 104928. https://doi.org/10.1016/j.ultsonch.2019.104928.

Moses, J.J., Jagannathan, K., 1996. Bleaching of cotton using hydrogen peroxide in ultrasonic energy and dyeing. Colourage 43, 19–24.

Nowacka, M., Tylewicz, U., Laghi, L., Dalla Rosa, M., Witrowa-Rajchert, D., 2014. Effect of ultrasound treatment on the water state in kiwifruit during osmotic dehydration. Food Chem. 144, 18–25. https://doi.org/10.1016/j.foodchem.2013.05.129.

Ochoa, S., Durango-Zuleta, M.M., Felipe Osorio-Tobón, J., 2020. Techno-economic evaluation of the extraction of anthocyanins from purple yam (Dioscorea alata) using ultrasound-assisted extraction and conventional extraction processes. Food Bioprod. Process. 122, 111–123. https://doi.org/10.1016/j.fbp.2020.04.007.

Ojha, K.S., Mason, T.J., O'Donnell, C.P., Kerry, J.P., Tiwari, B.K., 2017. Ultrasound technology for food fermentation applications. Ultrason. Sonochem. doi:10.1016/j.ultsonch.2016.06.001.

Oliveira, A.F.A., Mar, J.M., Santos, S.F., da Silva Júnior, J.L., Kluczkovski, A.M., Bakry, A.M., Bezerra, J.de A., Nunomura, R.de C.S., Sanches, E.A., Campelo, P.H., 2018. Non-thermal combined treatments in the processing of açai (Euterpe oleracea) juice. Food Chem. 265, 57–63. https://doi.org/10.1016/j.foodchem.2018.05.081.

Osae, R., Zhou, C., Xu, B., Tchabo, W., Tahir, H.E., Mustapha, A.T., Ma, H., 2019. Effects of ultrasound, osmotic dehydration, and osmosonication pretreatments on bioactive compounds, chemical characterization, enzyme inactivation, color, and antioxidant activity of dried ginger slices. J. Food Biochem. 43, e12832. https://doi.org/10.1111/jfbc.12832.

Osman, H., Khairy, M., 2013. Optimization of polyester printing with disperse dye nanoparticles. Indian J. Fibre Text. Res. 38, 202–206.

Osman, H., Lim, F., Lucas, M., Balasubramaniam, P., 2016. Development of an ultrasonic resonator for ballast water disinfection. Phys. Procedia 87, 99–104. https://doi.org/10.1016/J.PHPRO.2016.12.016.

Pagnossa, J.P., Rocchetti, G., Ribeiro, A.C., Piccoli, R.H., Lucini, L., 2020. Ultrasound: beneficial biotechnological aspects on microorganisms-mediated processes: ultrasound: beneficial aspects on microorganisms processes. Curr. Opin. Food Sci. doi:10.1016/j.cofs.2019.10.006.

Parthasarathy, S., Siah Ying, T., Manickam, S., 2013. Generation and optimization of palm oil-based oil-in-water (O/W) submicron-emulsions and encapsulation of curcumin using a liquid whistle hydrodynamic cavitation reactor (LWHCR). Ind. Eng. Chem. Res. 52, 11829–11837. https://doi.org/10.1021/ie4008858.

Patero, T., Augusto, P.E.D., 2015. Ultrasound (US) enhances the hydration of sorghum (Sorghum bicolor) grains. Ultrason. Sonochem. 23, 11–15. https://doi.org/10.1016/j.ultsonch.2014.10.021.

Perelshtein, I., Applerot, G., Perkas, N., Grinblat, J., Gedanken, A., 2012. A one-step process for the antimicrobial finishing of textiles with crystalline tio 2 nanoparticles. Chem. - A Eur. J. 18, 4575–4582. https://doi.org/10.1002/chem.201101683.

Perelshtein, I., Applerot, G., Perkas, N., Guibert, G., Mikhailov, S., Gedanken, A., 2008. Sonochemical coating of silver nanoparticles on textile fabrics (nylon, polyester and cotton) and their antibacterial activity. Nanotechnology 19, 245705. https://doi.org/10.1088/0957-4484/19/24/245705.

Perelshtein, I., Applerot, G., Perkas, N., Wehrschetz-Sigl, E., Hasmann, A., Guebitz, G.M., Gedanken, A., 2009a. Antibacterial properties of an in situ generated and simultaneously deposited nanocrystalline Zno on fabrics. ACS Appl. Mater. Interfaces 1, 361–366. https://doi.org/10.1021/am8000743.

Perelshtein, I., Applerot, G., Perkas, N., Wehrschuetz-Sigl, E., Hasmann, A., Guebitz, G., Gedanken, A., 2009b. CuO–cotton nanocomposite: formation, morphology, and antibacterial activity. Surf. Coatings Technol. 204, 54–57. https://doi.org/10.1016/J.SURFCOAT.2009.06.028.

Perelshtein, I., Ruderman, E., Perkas, N., Tzanov, T., Beddow, J., Joyce, E., Mason, T.J., Blanes, M., Mollá, K., Patlolla, A., Frenkel, A.I., Gedanken, A., 2013. Chitosan and chitosan-ZnO-based complex nanoparticles: formation, characterization, and antibacterial activity. J. Mater. Chem. B 1, 1968–1976. https://doi.org/10.1039/c3tb00555k.

Perincek, S., Uzgur, A.E., Duran, K., Dogan, A., Korlu, A.E., Bahtiyari, I.M., 2009. Design parameter investigation of industrial size ultrasound textile treatment bath. Ultrason. Sonochem. 16, 184–189. https://doi.org/10.1016/j.ultsonch.2008.06.003.

Perkas, N., Zhong, Z., Grinblat, J., Gedanken, A., 2007. Deposition of gold particles on mesoporous catalyst supports by sonochemical method, and their catalytic performance for co oxidation. Catal. Lett. (120) 19–24. https://doi.org/10.1007/S10562-007-9257-8.

Petkova, P., Francesko, A., Fernandes, M.M., Mendoza, E., Perelshtein, I., Gedanken, A., Tzanov, T., 2014. Sonochemical coating of textiles with hybrid zno/chitosan antimicrobial nanoparticles. ACS Appl. Mater. Interfaces 6, 1164–1172. https://doi.org/10.1021/am404852d.

Qiu, L., Zhang, M., Chitrakar, B., Bhandari, B., 2020. Application of power ultrasound in freezing and thawing processes: effect on process efficiency and product quality. Ultrason. Sonochem. doi:10.1016/j.ultsonch.2020.105230.

Rehman, F., Adeel, S., Saif, M., Khosa, M.K., Anjum, M., Kamran, M., Zuber, M., Asif, M., 2020. Ultrasonic assisted improvement in dyeing behaviour of polyester fabric using disperse red 343. Polish J. Environ. Stud. 29, 261–265. https://doi.org/10.15244/pjoes/75957.

Ricce, C., Rojas, M.L., Miano, A.C., Siche, R., Augusto, P.E.D., 2016. Ultrasound pre-treatment enhances the carrot drying and rehydration. Food Res. Int. 89, 701–708. https://doi.org/10.1016/j.foodres.2016.09.030.

Rocha, C.B.da, Noreña, C.P.Z., 2020. Microwave-Assisted extraction and ultrasound-assisted extraction of bioactive compounds from grape pomace. Int. J. Food Eng. 16. doi:10.1515/ijfe-2019-0191.

Rodríguez, Ó., Santacatalina, J.V., Simal, S., Garcia-Perez, J.V., Femenia, A., Rosselló, C., 2014. Influence of power ultrasound application on drying kinetics of apple and its antioxidant and microstructural properties. J. Food Eng. 129, 21–29. https://doi.org/10.1016/j.jfoodeng.2014.01.001.

Rojas, M.L., Augusto, P.E.D., Cárcel, J.A., 2020. Ethanol pre-treatment to ultrasound-assisted convective drying of apple. Innov. Food Sci. Emerg. Technol. 61, 102328. https://doi.org/10.1016/j.ifset.2020.102328.

Russo, M.V., Avino, P., Notardonato, I., 2016. Fast analysis of phthalates in freeze-dried baby foods by ultrasound-vortex-assisted liquid-liquid microextraction coupled with gas chromatography-ion trap/mass spectrometry. J. Chromatogr. A 1474, 1–7. https://doi.org/10.1016/j.chroma.2016.10.058.

Sato, M., Matsuura, K., Fujii, T., 2001. Ethanol separation from ethanol-water solution by ultrasonic atomization and its proposed mechanism based on parametric decay instability of capillary wave. J. Chem. Phys. 114, 2382. https://doi.org/10.1063/1.1336842.

Save, S.S., Pandit, A.B., Joshi, J.B., 1994. Microbial cell disruption: role of cavitation. Chem. Eng. J. Biochem. Eng. J. 55, B67–B72. https://doi.org/10.1016/0923-0467(94)06062-2.

Sheikh, J., Jagtap, P.S., Teli, M.D., 2016. Ultrasound assisted extraction of natural dyes and natural mordants vis a vis dyeing. Fibers Polym. 17, 738–743. https://doi.org/10.1007/s12221-016-5031-0.

Silva, E.K., Arruda, H.S., Pastore, G.M., Meireles, M.A.A., Saldaña, M.D.A., 2020. Xylooligosaccharides chemical stability after high-intensity ultrasound processing of prebiotic orange juice. Ultrason. Sonochem. 63, 104942. https://doi.org/10.1016/j.ultsonch.2019.104942.

Sivakumar, V., Anna, J.L., Vijayeeswarri, J., Swaminathan, G., 2009. Ultrasound assisted enhancement in natural dye extraction from beetroot for industrial applications and natural dyeing of leather. Ultrason. Sonochem. 16, 782–789. https://doi.org/10.1016/j.ultsonch.2009.03.009.

Sivakumar, V., Rao, P.G., 2001. Application of power ultrasound in leather processing: an eco-friendly approach. J. Clean. Prod. 9, 25–33. https://doi.org/10.1016/S0959-6526(00)00028-7.

Sivakumar, V., Rao, P.G., 2003. Studies on the use of power ultrasound in leather dyeing. Ultrason. Sonochem. 10, 85–94. https://doi.org/10.1016/S1350-4177(02)00148-7.

Sivakumar, V., Swaminathan, G., Rao, P.G., Ramasami, T., 2008. Influence of ultrasound on diffusion through skin/leather matrix. Chem. Eng. Process. Process Intensif. 47, 2076–2083. https://doi.org/10.1016/j.cep.2007.10.020.

Sun, D., Guo, Q., Liu, X., 2010. Investigation into dyeing acceleration efficiency of ultrasound energy. Ultrasonics 50, 441–446. https://doi.org/10.1016/j.ultras.2009.07.002.

Sun, D.W., Hu, Z., 2003. CFD simulation of coupled heat and mass transfer through porous foods during vacuum cooling process. Int. J. Refrig. 26, 19–27. https://doi.org/10.1016/S0140-7007(02)00038-5.

Suzuki, K., Arashi, K., Nii, S., 2012. Determination of droplet and vapor ratio of ultrasonically-atomized aqueous ethanol solution. J. Chem. Eng. Japan 45, 337–342.

Szabó, O.E., Csiszár, E., 2013. The effect of low-frequency ultrasound on the activity and efficiency of a commercial cellulase enzyme. Carbohydr. Polym. 98, 1483–1489. https://doi.org/10.1016/j.carbpol.2013.08.017.

Tabatabaie, F., Mortazavi, A., 2008. Study of ice cream freezing process after treatment with Ultrasound. World Appl. Sci. J. 4, 188–190.

Taha, A., Ahmed, E., Ismaiel, A., Ashokkumar, M., Xu, X., Pan, S., Hu, H., 2020. Ultrasonic emulsification: an overview on the preparation of different emulsifiers-stabilized emulsions. Trends Food Sci. Technol. doi:10.1016/j.tifs.2020.09.024.

Tao, Y., Han, M., Gao, X., Han, Y., Show, P.L., Liu, C., Ye, X., Xie, G., 2019. Applications of water blanching, surface contacting ultrasound-assisted air drying, and their combination for dehydration of white cabbage: drying mechanism, bioactive profile, color and rehydration property. Ultrason. Sonochem. 53, 192–201. https://doi.org/10.1016/j.ultsonch.2019.01.003.

Tekin, Z.H., Başlar, M., Karasu, S., Kilicli, M., 2017. Dehydration of green beans using ultrasound-assisted vacuum drying as a novel technique: drying kinetics and quality parameters. J. Food Process. Preserv. 41, e13227. https://doi.org/10.1111/jfpp.13227.

Thakore, K.A., Abate, B., 2017. Application of ultrasound in the pretreatment of cotton fabric. Cellul. Chem. Technol. 51, 983–992.

Thakore, K.A., Smith, C.B., Clapp, T.G., 1990. Application of ultrasound to textile wet processing. Am. Dyest. Report. 79, 30–44.

Tian, Y., Zhao, Y., Huang, J., Zeng, H., Zheng, B., 2016. Effects of different drying methods on the product quality and volatile compounds of whole shiitake mushrooms. Food Chem. 197, 714–722. https://doi.org/10.1016/j.foodchem.2015.11.029.

Tissera, N.D., Wijesena, R.N., de Silva, K.M.N, 2016. Ultrasound energy to accelerate dye uptake and dye-fiber interaction of reactive dye on knitted cotton fabric at low temperatures. Ultrason. Sonochem. 29, 270–278. https://doi.org/10.1016/j.ultsonch.2015.10.002.

Tiwari, B.K., 2015. Ultrasound: a clean, green extraction technology. TrAC - Trends Anal. Chem. doi:10.1016/j.trac.2015.04.013.

Udrescu, C., Ferrero, F., Periolatto, M., 2014. Ultrasound-assisted dyeing of cellulose acetate. Ultrason. Sonochem. 21, 1477–1481. https://doi.org/10.1016/j.ultsonch.2013.12.026.

Umego, E.C., He, R., Ren, W., Xu, H., Ma, H., 2021. Ultrasonic-assisted enzymolysis: principle and applications. Process Biochem. 100, 59–68. https://doi.org/10.1016/J.PROCBIO.2020.09.033.

Vankar, P.S., Shanker, R., 2008. Ecofriendly ultrasonic natural dyeing of cotton fabric with enzyme pretreatments. Desalination 230, 62–69. https://doi.org/10.1016/j.desal.2007.11.016.

Vankar, P.S., Shanker, R., Verma, A., 2007. Enzymatic natural dyeing of cotton and silk fabrics without metal mordants. J. Clean. Prod. 15, 1441–1450. https://doi.org/10.1016/j.jclepro.2006.05.004.

Vega-Gálvez, A., Di Scala, K., Rodríguez, K., Lemus-Mondaca, R., Miranda, M., López, J., Perez-Won, M., 2009. Effect of air-drying temperature on physico-chemical properties, antioxidant capacity, colour and total phenolic content of red pepper (Capsicum annuum, L. var. hungarian). Food Chem. 117, 647–653. https://doi.org/10.1016/j.foodchem.2009.04.066.

Venkitaraman, A., Roberts, P.M., Sharma, M.M., 1995. Ultrasonic removal of near-wellbore damage caused by fines and mud solids. SPE Drill. Complet. 10, 193–197. https://doi.org/10.2118/27388-PA.

Vinodgopal, K., Neppolian, B., Lightcap, I.V., Grieser, F., Ashokkumar, M., Kamat, P.V., 2010. Sonolytic design of graphene-Au nanocomposites. simultaneous and sequential reduction of graphene oxide and au(iii). J. Phys. Chem. Lett. 1, 1987–1993. https://doi.org/10.1021/jz1006093.

Vogels, G., Kula, M.R., 1992. Combination of enzymatic and/or thermal pretreatment with mechanical cell disintegration. Chem. Eng. Sci. 47, 123–131. https://doi.org/10.1016/0009-2509(92)80206-R.

Vouters, M., Rumeau, P., Tierce, P., Costes, S., 2004. Ultrasounds: an industrial solution to optimise costs, environmental requests and quality for textile finishing. Ultrasonics Sonochemistry 11 (1), 33–38. https://doi.org/10.1016/S1350-4177(03)00113-5.

Wang, B., Su, H., Zhang, B., 2021. Hydrodynamic cavitation as a promising route for wastewater treatment—a review. Chem. Eng. J. 412, 128685. https://doi.org/10.1016/J.CEJ.2021.128685.

Wang, Jun, Xiao, H.W., Ye, J.H., Wang, Jin, Raghavan, V., 2019. Ultrasound pretreatment to enhance drying kinetics of kiwifruit (Actinidia deliciosa) slices: pros and cons. Food Bioprocess Technol. 12, 865–876. https://doi.org/10.1007/s11947-019-02256-4.

Wang, L., Zhao, H.F., Lin, J.X., 2010. Studies on the ultrasonic-assisted dyeing of poly(trimethylene terephthalate) fabric. Color. Technol. 126, 243–248. https://doi.org/10.1111/j.1478-4408.2010.00253.x.

Wang, W.M., Yu, B., Zhong, C.J., 2012. Use of ultrasonic energy in the enzymatic desizing of cotton fabric. J. Clean. Prod. 33, 179–182. https://doi.org/10.1016/j.jclepro.2012.04.010.

Wani, I.A., Ganguly, A., Ahmed, J., Ahmad, T., 2011. Silver nanoparticles: ultrasonic wave assisted synthesis, optical characterization and surface area studies. Mater. Lett. 65, 520–522. https://doi.org/10.1016/J.MATLET.2010.11.003.

Warmoeskerken, M.M.C.G., Van Der Vlist, P., Moholkar, V.S., Nierstrasz, V.A., 2002. Laundry process intensification by ultrasound. Colloids Surfaces A Physicochem. Eng. Asp. 210, 277–285. https://doi.org/10.1016/S0927-7757(02)00372-2.

Yang, C., Hu, X., Wang, D., Dai, C., Zhang, L., Jin, H., Agathopoulos, S., 2006. Ultrasonically treated multi-walled carbon nanotubes (MWCNTs) as ptru catalyst supports for methanol electrooxidation. J. Power Sources 160, 187–193. https://doi.org/10.1016/J.JPOWSOUR.2006.05.015.

Yao, Y., 2016. Enhancement of mass transfer by ultrasound: application to adsorbent regeneration and food drying/dehydration. Ultrason. Sonochem. doi:10.1016/j.ultsonch.2016.01.039.

Yasuda, K., 2021. Sonochemical green technology using active bubbles: degradation of organic substances in water. Curr. Opin. Green Sustain. Chem. 27, 100411. https://doi.org/10.1016/J.COGSC.2020.100411.

Zhang, G., Zhang, P., Gao, J., Chen, Y., 2008. Using acoustic cavitation to improve the bio-activity of activated sludge. Bioresour. Technol. 99, 1497–1502. https://doi.org/10.1016/J.BIORTECH.2007.01.050.

Zhao, P., Zhao, Y., Zou, C., Gu, T., 2013. Study on ultrasonic extraction of kerogen from huadian oil shale by solvents. Oil Shale 30, 491–500. https://doi.org/10.3176/oil.2013.4.03.

Zhao, Y.Y., Yi, J.Y., Bi, J.F., Chen, Q.Q., Zhou, M., Zhang, B., 2019. Improving of texture and rehydration properties by ultrasound pretreatment for infrared-dried shiitake mushroom slices. Dry. Technol. 37, 352–362. https://doi.org/10.1080/07373937.2018.1456449.

Zhou, X., Zhao, J., Li, Z., Song, J., Li, X., Yang, X., Wang, D., 2016. Enhancement effects of ultrasound on secondary wastewater effluent disinfection by sodium hypochlorite and disinfection by-products analysis. Ultrason. Sonochem. 29, 60–66. https://doi.org/10.1016/J.ULTSONCH.2015.09.001.

Zhu, J., Koltypin, Y., Gedanken, A., 1999. General sonochemical method for the preparation of nanophasic selenides: synthesis of znse nanoparticles. Chem. Mater. 12, 73–78. https://doi.org/10.1021/CM990380R.

Zhu, Z., Zhang, P., Sun, D.W., 2020. Effects of multi-frequency ultrasound on freezing rates and quality attributes of potatoes. Ultrason. Sonochem. 60, 104733. https://doi.org/10.1016/j.ultsonch.2019.104733.

Chapter 21

Raising challenges of ultrasound-assisted processes and sonochemistry in industrial applications based on energy efficiency

Mohit Singla and Nandan Sit

Department of Food Engineering and Technology, Tezpur University, Tezpur, Assam, India

21.1 Introduction

Cavitation is the driving force behind sonochemistry and ultrasonic processing. It was originally recognized and classified in 1895 by Thornicroft, who discovered that it was the reason of inefficient propeller drive on the high-speed torpedo boat HMS Daring (Mason, 2012). The sort of cavitation created by propellers driving through water, that is, hydrodynamic cavitation, was the focus of this and subsequent early investigations.

Ultrasonics is the study of application of sound wave energy vibrating at frequencies greater than 20,000 Hz which is beyond the audible range for humans (Al-Juboori et al., 2015a, b). Sound is transmitted from one place to another by means of waves. The general method involved in the generation of ultrasonic waves is the rapid vibration of a dense material, which causes the surrounding air of the material to vibrate with the same frequency and spread out in the form of ultrasonic waves (Pokhrel et al., 2016).

In the industrial, medicinal, and other areas, ultrasonics has become a valuable instrument. It has widespread applications in materials science, industrial processes, oceanology, marine navigation, petroleum and mineral prospecting, medicine, dentistry, and noise cancellation (Al-Juboori et al., 2015a). The first widespread use was in underwater exploration for determining the depth of water. Ultrasonics has further industrial and diagnostic applications (Mason, 1992).

Since ultrasonic waves can vibrate the particles through which they pass, they are often used to shake, or even destroy, certain materials (Eskin and Tzanakis, 2018). An example of this procedure is ultrasonic emulsification. It can also be used for breaking up the kidney stones and gallstones, thus avoiding invasive surgery (Tripathi et al., 2019).

Ultrasonic energy has been used in industry since the middle of the 20th century, although only a few applications have been commercially commercialized thus far (Tripathi et al., 2019). However, in the last 10 or 15 years, there has been a resurgence of interest in ultrasonic processing, particularly in industries where ultrasonic energy may be used to enhance or create effects in a clean and efficient manner. Power ultrasound appears to be becoming an emerging technology for process development in key areas such as the food industry, environment, pharmaceuticals and chemicals manufacturing, equipment, and so on (Mason, 2012).

The design and development of efficient power ultrasonic systems (generators and reactors) capable of large-scale successful operation particularly suited to each particular process might be a key challenge in the use of high-intensity ultrasound to industrial processes.

This chapter examines some recent challenges in ultrasonic processing in order to demonstrate the current state and future promise of high-power ultrasonics as an innovative technology in a variety of industries.

Energy Aspects of Acoustic Cavitation and Sonochemistry: Fundamentals and Engineering. DOI: https://doi.org/10.1016/B978-0-323-91937-1.00017-7
Copyright © 2022 Elsevier Inc. All rights reserved.

21.2 Theoretical aspects of ultrasound energy

Ultrasonic waves (frequencies greater than 20 kHz) are a type of sound wave that shows all of the qualities of sound waves. They are divided into four groups depending upon the type of vibration of the particle in the media with regard to the inclination of the propagation of initial waves (longitudinal/compressional waves, transverse/shear waves, surface/Rayleigh waves, and plate/Lamb waves) (Raj et al., 2004). On the basis of their frequency, ultrasound is classified into three groups: power ultrasound (20–100 kHz), high-frequency ultrasound (100 kHz–1 MHz), and diagnostic ultrasound (1–500 MHz). Ultrasound is employed in chemically critical systems, using a frequency range of 20–100 kHz where physicochemical changes are sought because it can generate bubble cavitation (Pilli et al., 2011; Rastogi, 2011). In frequency ranges of 1–10 megahertz, ultrasound is utilized for navigation and communication by animals, and also for identification of fractures or faults in substances, underwater echo locating, and diagnostic reasons (Pilli et al., 2011). Ultrasound waves are composed of a cyclic sequence of expansion (low density or rarefaction) and compression phases imparted by mechanical vibration when applied to liquids (Tang, 2003). Positive pressure is applied through compression cycles to the liquid molecules pushing them together, whereas rarefaction or expansion cycles apply negative pressure to the molecules and tear them apart (Vajnhandl and Majcen Le Marechal, 2005). When the amplitude of pressure in the rarefaction areas becomes excess to the tensile forces of the liquid, tiny spaces emerge which are vapor-filled and called as cavitation bubbles (Chen, 2012). Ultrasonic generators are unable to produce high enough negative pressures to create cavitation as pure liquids have large tensile strengths. Most liquids are impure, and their tensile strength is diminished because of the existence of numerous microscopic entities, pre-existing dissolved solids, and other pollutants. Impurities in liquids signify weak places in the liquid where cavitation bubbles might form (Vajnhandl and Majcen Le Marechal, 2005). For example, greater than 1000 atmosphere of negative pressure is required for cavitation when using pure water; yet bubbles may be formed with only a few atmospheres of pressure while using tap water (Chowdhury and Viraraghavan, 2009).

Upon generation of a bubble, there are two types of cavitation that can take place inside liquids: stable and transient. In stable cavitation, the bubble wall combines with the acoustical field and oscillates for numerous cycles about the equilibrium radius in the stable type of cavitation. The size of the bubble oscillates in phases with expansion and compression cycles at low acoustic intensities, and the bubbles expand slowly across many acoustic cycles (Thangavadivel et al., 2012). In terms of chemical impacts, this process has limited relevance due to the modest difference in bubble size variations (Destaillats et al., 2003). Water vapor, dissolved gases, and organic vapor will enter the bubble due to influence of the surface area of bubble during expansion and depart during contraction; the process is also known as corrected diffusion (Thangavadivel et al., 2012).

Transient cavitation is common when a high-intensity acoustic field is applied. After a number of cycles, the expanding cavitation bubble becomes unstable and collapses in the compression phase of the ultrasonic wave. Bubble size increases dramatically up to hundreds from tens of times its equilibrium radii before rapidly collapsing under a millionth of a second in this cavitation phenomenon (Destaillats et al., 2003; Vajnhandl and Majcen Le Marechal, 2005). Nonetheless, cavitation categorization is ambiguous, since stable cavitation can lead to transient cavitation, or transient cavitation can result in extremely minute bubbles which afterward experience stable cavitation (Vajnhandl and Marechal, 2005). In concise words, cavitation is the result of the recurrence of three separate steps: creation or nucleation, expansion or fast growth through the rounds till reaching a critical size, and abrupt slump in the liquid (Pang et al., 2011).

The scattered sound energy is created and concentrated by means of cavitation. When a cavity bubble is in a low- or high-intensity acoustic field and has experienced fast expansion and can no longer absorb energy efficiently, the liquid rushes in, and the bubble cavity implodes (Suslick, 1990). Every bubble would operate as a hotspot when it collapsed, providing enough energy to raise the temperature and pressure to 5000 K and 500 atm, respectively, with a cooling rate of 109 K/s (Suslick, 1990). These collapsing bubbles generate a novel technique for high-energy chemical reactions due to high localized temperatures and pressure (Suslick, 1990).

There are a number of factors that influence cavitation and bubble collapse, which are mentioned below.

(a) Frequency of the acoustic wave: a high-frequency sound wave will limit cavitation due to (1) the negative pressure created by the rarefaction cycle is inadequate in length and/or intensity to commence cavitation or (2) the compression cycle occurs faster than the time for microbubbles to collapse (Adewuyi, 2001). More violent cavitations will be generated at lower frequencies, resulting in higher localized temperatures and pressure (Vajnhandl and Majcen Le Marechal, 2005)

(b) Intensity: as the strength of the acoustic wave rises, so does its amplitude, giving rise to a more dramatic slump of cavitation bubbles (Adewuyi, 2001).

(c) Solvent properties: high vapor-pressure solvents with low viscosity and low surface tension are more likely to produce cavities (Adewuyi, 2001). As a high amount of vapors gets into the bubbles, the vapor pressure gets lowered and less violent bubbles burst (Peters, 1996).

TABLE 21.1 Some industrial uses for ultrasound.

Field	Application
Welding	Fabrication of thermoplastic items and metal welding using specialized heating at the material's intersection
Cutting	Cutting of various types of materials, from fragile ceramics to food items, with precision
Atomization	Low-velocity spray coating, spray drying nozzles, and water sprays for dust control and humidifiers
Cleaning and decontamination	Cleaning and disinfection of medical instruments and food processing equipment with aqueous-based solvents; cleaning of engineering goods, tiny electronic items, and jewelry
Medicine	Imaging, muscular strain therapy, blood clot elimination, tumor detection, and diagnosis
Geology	Pulse/echo methods are used to find minerals, oil reserves, and ocean depth gauges. At sea, ranging echoes (SONAR)
Food processing	Emulsification and dispersion of pigments and powders in liquid media; extraction, impregnation, crystallization, and filtering

(d) Gas characteristics: due to the availability of soluble gases, a greater number of cavitation nuclei tend to develop. Higher solubility of the gas, on the other hand, would allow greater permeation of gas molecules into the cavitational bubble, resulting in a less dramatic cave-in (Vajnhandl and Majcen Le Marechal, 2005). The heat capacity ratio (Cp/Cv) or polytropic ratio(c) affects the quantity of heat released during the collapse, as well as the thermal conductivity of the gas (Adewuyi, 2001; Peters, 1996).

(e) External pressure: a lowering of liquid's vapor pressure and increase in the force required to create cavitation takes place due to higher external pressure (Vajnhandl and Majcen Le Marechal, 2005).

(f) Temperature: lowering the reaction temperature boosts sonochemical reaction speeds in the case of nonvolatile substrates (that react by radical reaction in solution). An increase in cavitation intensity is caused by the reduction in the volume of vapor diffusing into the bubbles to bolster the cavitational cave-in (Adewuyi, 2001; Destaillats et al., 2003).

21.3 Industrial uses of ultrasound power

The various industrial applications of ultrasound are summarized in Table 21.1.

21.3.1 Cleaning and decontamination

Cleaning by ultrasound is now a widely used general technology that laboratories and some industries are using for certain applications. Although the laboratory ultrasonic cleaning bath is well-known, industrial applications of ultrasonic cleaning are possibly less so. Ultrasonic cleaning can be used to carefully clean micro-components in clean rooms or for very massive things like engine blocks in manufacturers. As cleaning by ultrasound occurs through streams caused by cavitational fall-in on and near surfaces, it is very efficient in removing biological pollution. These jets are capable of readily dislodging microorganisms that have adhered to surfaces. In this case, ultrasonic cleaning has the benefit of being able to access crevices that are difficult to reach with traditional cleaning methods. As a result, everything from large crates utilized to pack foods to endoscope-type exquisite surgical instruments are cleaned in this manner (Mason, 2000).

Power ultrasound is now being researched for application in biological water remediation (Phull and Mason, 1999). Biocide, which is often chlorine, chlorine dioxide, or ozone in the large-scale water business, is used in traditional disinfection procedures. Current trends suggest that the amount of biocide used in sterilization should be reduced; nonetheless, some bacteria can develop resistant strains, necessitating a greater concentration. Power ultrasonography has two key impacts that allow it to improve the efficiency of conventional biocides. To begin with, cavitation's mechanical impacts can crash bacterial cluster or material aggregates that carry bacteria onto themselves. The protection offered to living bacteria in the center of agglomerates will be removed as a result. Second, ultrasonic can improve the permeation capability of biological cell walls, enhancing the bacterial absorption of biocide.

A cooling tower water treatment system that uses a mixture of ultrasound and electromagnetic radiation has been created. The Sonoxide system addresses two primary limitations of cooling circuits: algae accumulation and limescale (Mason, 2000). It can destroy algae when exposed to ultrasound at a flow rate of 2 m^3/h with just 450 W of acoustic power. As it produces a type of crystal of calcium carbonate that does not settle as scale, the same low energy need is adequate to solve the problem of limescale formation. The water in the cooling circuit carries the crystals away, and a hydrocyclone

separates them. The main benefits of this treatment are its less consumption of energy, the removal of the water dependency for softening or biocidal chemicals, and a significant lowering of the cooling circuit's water demand.

Treatment of sewage slurry is another use of sonochemistry in the environment. The most popular method for stabilizing sewage sludge is anaerobic fermentation, which gives a bulk reduction, methane generation, and better dewatering qualities. The fermentation approach has the drawback of being sluggish, with typical residence durations in anaerobic digesters of around 20 days.

Utilizing ultrasound to speed up the breakdown of sewage sludge in absence of air has been reported (Tiehm et al., 1997). Treating the sample using ultrasound at 31 kHz of frequency and powerful acoustic potency at 50% technical level lowered the residence duration to 192 h, resulting in 2.2 times the biogas output of a control fermenter. This sort of procedure is likely to be utilized on an industrial scale after it has been optimized.

Water has also been treated using ultrasonic irradiation for chemical cleanup. The physical and chemical characteristics of organic molecules in aqueous solution determine the method of sonochemical breakdown. This is due to the fact that the cavitation bubble can work in two different ways. When volatile compounds enter the bubble, they are destroyed by the severe circumstances created when it collapses.

The bubble functions as a supplier of radicals (H•, HO•, and HOO•) that reach to most of the solution and interact with contaminants when chemicals stay in the aqueous phase. This is well demonstrated in a research comparing the breakdown of carbolic-acid (to carboxylic acids) and tetrachloride of carbon (to CO_2 and Cl) in oxygen-soaked water at various frequencies (Pétrier and Francony, 1997). The data plainly reveal that the chemical pollutants behave differently, with phenol degradation mimicking peroxide production, suggesting that the reaction occurs at the interface of the bubble or outwards of the bubble. The volatile CCl_4, on the other hand, decomposes in the periphery of the bubble, and increase in frequency speeds up the operation significantly.

On offshore rigs drilling oil, there is an ecological issue with the disposal of drilling mud. This substance is a complicated blend of ingredients that is flushed inside the drill hole in helping for lubrication and flotation purposes. The mud, along with the dirt from the drill hole, gets polluted from oil after usage, and need to be properly cleaned before throwing the solids into the sea. Cleanliness protocols exist, however, the cleaned commodity is obtained as minute agglomerates that sink to the sea and gather around the platform legs when deposited in the water. This creates problems for marine animals and a stumbling block for maintaining the rig. An ultrasonic device was created on-site to deagglomerate the cleansed mud. Each module is rated at a capacity of 2-kilowatt and made up of stainless steel and 1 m long and 12 cm in across with a long arrangement of piezoelectric transducers attached to the exterior, all of which are encased in a casing (Avern and Copercini, 1997). The apparatus decreases the particle size of the drilling mud by providing a flow treatment. As a consequence, the expelling of mud from the oil rig disperses throughout the sea bed rather than getting collected near the platform legs.

21.3.2 Extraction and impregnation

Upon caving-in of a cavitation bubble in the vicinity of a porous medium, the resulting jet can propel liquid into the bulk material. Procedures consisting of the separation or impregnation of a liquid in or from a solid could prove beneficial from this effect.

The precise selection of solvent and blending parameters such as thermal treatment and turbulence are the foundations of traditional solvent extraction procedures for chemical compounds from vegetable material. Solvent extraction is increasingly used to make a variety of economically significant medicines, flavors, and colorants from vegetable sources (Singla and Sit, 2021). The application of power ultrasound has been demonstrated to improve the extraction of natural items from and within the bodies of plants and their seeds (Mason, 1999).

To enhance dying, the same sonochemically driven impregnation procedure might be applied. The conventional method for dyeing leather includes immersing the item in a liquid dye mixture for a length of time while agitating it, usually by tumbling.

Ultrasound has proven to enhance the rate of dye permeation inside leather, which provides the economically appealing option of achieving a faster turnaround by lowering immersion periods (Xie et al., 1999). Because the majority of leather technology procedures include treating the material with liquids and superficial perforation, a variety of tanning procedures are being studied to see whether sonication might improve their efficiency.

21.3.3 Crystallization and precipitation

A solution containing the components to be crystallized is supersaturated either by cooling or evaporation, and then seeded in conventional crystallization processes. Seeding has the disadvantage of being nonuniformly begun, resulting in crystal growth occurring at varying speeds at distinct nucleus locations. The crystals that arise may have a highly wide and irregular

crystal size distribution. Controlling the beginning of crystal formation in a big assembling process is equally crucial. It frequently happens uncontrollably as a result of a little shift in environmental conditions, such as varying the temperature or pressure.

Because ultrasound may commence seeding and regulate continuous crystal development in a saturated or super cooled media, it has shown to be particularly beneficial in crystallization procedures. The reason behind this is thought to be through the formation of cavitation bubbles functioning as starting point for crystal formation and the rupture of seeds/nuclei already present in the media, giving rise to enhancement in the quantity of nuclei sent out. It is feasible to generate crystals of a consistent and specified size using the precise sonication settings, which is critical in manufacturing of pharmaceutical products (Mason, 2000).

There's another feature of power ultrasound that is very useful in crystallization operations: the cavitation's cleaning action successfully prevents crystal encrustation on cooling devices in the crystallization vat, ensuring continual efficient heat transmission.

21.3.4 Filtration and separation

There are sectors that specialize in a broader variety of ultrasound-related operations, such as phase separation (Mason, 2003). As a result, the segregation of minute particles from gases or liquids is an ongoing industrial concern (Riera-Franco De Sarabia et al., 2000). Furthermore, using of ultrasound for the food component separation has recently been examined (Feng et al., 2008). Ultrasound standing waves, on the other hand, have the potential to transfer cells in suspension into strips separated by a half-wave acoustic wavelength in a standing wave field (Riera-Franco De Sarabia et al., 2000; Stack et al., 2005). To test the applicability of ultrasound for coagulating grease from wastewater, a small-scale technique was constructed. Ultrasound was used with a transducer surface area of 0.15 Wcm^2 and a treatment liquid of 4.3 mW per milliliter (Stack et al., 2005). Sonoelectrocoagulation was shown to possess ability to remove up to 100% of soap and grease from wool cleansing discharge, in accordance with regulatory restrictions of 250 mg per liter for discharges that were previously treated to get grease-plus-soap levels in the normal range of 2000–3000 mg per liter.

Many sectors need the segregation of particles from liquids or the isolating the genuine liquor. This stage is usually carried out with different membranes, which have been utilized in procedures varying from basic filter pads to semipermeable membranes to those that purify polymeric compounds using a size-exclusion principle. However, one of the most common difficulties encountered in filtration through membrane is fouling, and as a result, filters need to be replaced after sometime or shut down and hence need to be cleaned regularly. This procedure consumes lot of time and money in industrial applications (Mason and Lorimer, 2002). Fouling of the membranes is influenced by parameters of feed suspension (particle-size and concentration, pH, and ionic strength), membrane characteristics (hydrophobicity, charge, and pore-size), and hydrodynamics (cross-flow velocity transmembrane pressure) (Kyllönen et al., 2006). Due to the requirement for efficient cleanliness of filter for enhanced filtration, employment of add-on forces like ultrasound has garnered increasing attention in recent years, as it is linked to an increase in flux, mainly by breaking the cake layer and decreasing the concentration of solute at the surface of the membrane (Kobayashi et al., 1999; Lamminen et al., 2004; Muthukumaran et al., 2004).

The use of ultrasound piezoceramic transducers operating at frequencies of 20, 40, or 200 kHz was investigated by using real industrial wastewaters from the paper industry for increasing the filtration in the cross-flow membrane (Kyllönen et al., 2006). With mean pore sizes of 0.12, 0.19, 0.25, and 0.75 m, alumina-based ceramic membranes were utilized in the cross-flow studies. The filtration power intensity was so great that the membranes gradually deteriorated in some areas on the membrane surface. In pressured settings, it was revealed that the ultrasonic field produced by the utilized transducers was uneven. Ultrasound treatments at one bar pressure at intermission breaks in filtration, on the other hand, proved effective and gentle in the cleaning of membrane. 120 W (power intensity of 1.1 Wcm^2) used as input power for a fraction of a minute was sufficient in cleaning, and when 5 s of ultrasonic treatment was administered to the filters during a short break in filtering, the flow improvement was substantial. The ultrasound irradiation was performed at 27 or 200 kHz of frequency and a 200 W input power (1.8 Wcm^2 or 4.1 Wcm^2), and the effect of this ultrasonic treatment was stronger when frequency of 27 kHz was used.

Commercially available ultrasonic processing systems have projected capital and operational costs that are equivalent to wet high-intensity magnetic separation. Sonication can give additional mechanism for mineral processing, as well as surface cleaning in general, because the equipment present or needed adjustments will operate as intended. It would also be more eco-friendly as compared with the existing procedure for reducing iron contamination on silica grains through acid leaching.

21.3.5 Textile industry

In the textiles industry, the conventional procedure for textile dyeing is agitating the stuff in an aqueous mix containing the colorant for a length of time, with the goal of transporting or diffusing into the fiber different colors or chemicals

(Moore and Ausley, 2004; Vouters et al., 2004). Impregnation through forcing sonochemical energy can help with imparting color through dyeing in this method. Ultrasound (20 kHz, 5 W cm^2) can accelerate the rate of dye penetration into the fabric, providing a commercially appealing option for lowering immersion periods and conserving dye amounts (Mason and Lorimer, 1998; Xie et al., 1999). Apart from accelerating the process and similar or better outcomes than traditional procedures, ultrasonography enables for accelerating the process at low profile of temperature and chemical concentration. By this approach, ultrasound-assisted coloring of textiles has been created for the textile manufacturing units, including coloring/dyeing and associated processing such as preparing the size, preparing the emulsions, dye dispersions, and thickeners for use in preparing print-paste, as well as treatment of the process residue (Vajnhandl and Majcen Le Marechal, 2005).

Using natural and synthetic fibers, the impacts on quality of dye dispersion, solubility of the dye in water, and absorption of the dye by textile materials were explored at various frequencies. For example, a localized case of temperature rise and effect of swelling caused by ultrasound may increase dye/leather diffusion (Sivakumar and Rao, 2003). Despite the fact that ultrasound-aided wet process of textile development has progressed in the lab from its initial report in 1941, it has yet to be utilized on a massive scale (Sivakumar et al., 2009). In conclusion, cavitation occurrences are widely linked to advancements in the ultrasound-assisted dyeing process, and efforts are ongoing to bring it to a massive scale (Vajnhandl and Majcen Le Marechal, 2005; Vouters et al., 2004)

The use of a low-frequency ultrasonic field (26 kHz) was to lower the size of the dispersion type dye particles and C.I. Dispersive Red 60 was examined (Lee and Kim, 2001). The conclusion was that the volume of microscopic particles rose while the volume of large particles decreased. After 1 h of ultrasound, the particle size in the region of 65–72 m fell from 14% to 0% of total volume of particles, and this lowering down in particle size improved fixation ability of the dye. Under 20 kHz ultrasound, the diffusion and permeability of C.I. Direct Red 81 through a cellophane film were enhanced (Thakore et al., 1990). Dyeing/coloring silk with cationic dyes, acidic dyes, or metal-complex dyes at lower temperatures, aided by 26 kHz ultrasonic (600 W), was investigated, and the results of the absorbance of dye were compared with the ones prepared by the traditional procedure. In compared to the conventional methods (85°C for 60 min), dyeing under ultrasound revealed an enhancement in the dye absorption for all the dye classes at lower temperatures of 45°C and 50°C and a lowering in duration of dyeing 15 min. In addition, there was no evidence of cavitation-induced fiber damage (Shukla and Mathur, 1995). Using C.I. Astrazon Basic Red 5BL 200 percent for the dyeing of acrylic fibers was carefully explored in a 5.75 L ultrasonic bath at 38.5 kHz and 100–500 W. The sonic cavitation phenomena, which may cause dispersion, degassing, and diffusion, was attributed to improving the ultrasonic dyeing process (Kamel et al., 2010).

Washing procedures are carried out in addition to the dyeing process for eliminating natural elements or contaminants from the surface of the fiber. It has been suggested that ultrasonic might be useful in this procedure as well (Sivakumar et al., 2009; Vouters et al., 2004). Gallego-Juarez et al. (Gallego-Juarez et al., 2010) recently described a method for washing the textile semi-automatically by applying ultrasonic energy and utilizing specific shaking plates, which was derived from a previously patented technology for washing the textiles continuously (Juarez et al., 2001). In total, 1.75 g L1 sodium-dodecyl-benzene-sulphonate (SDBS) and 3.5 g L1 sodium-triphosphate were used in the washing solution. Textiles were submerged in a few millimeters of liquid layer and transported in a flat format via the radiator using a roller-type device. The core area of the plate between two of its node lines was eliminated of bulkiness, a grooved shape was constructed on the backside of the plate radiator. The grooved-plate radiator is built of titanium alloy and has a radiating surface of 110 cm^2. It has a power capacity of 600 W and can attain acoustic intensities of 4.5 Wcm^2 at 21 kHz. It was discovered that cleaning rendition at 2 cm/s rises practically linearly with ultrasonic power intensity up to a point when saturation occurs. Even at very low acoustic intensities, the washing performance was significantly better than that of a conventional washing machine. The ultrasonic washing procedure used extremely little energy, at around 0.1 kWh per kilogram of material (Gallego-Juarez et al., 2010).

Ultrasound was also examined in the finishing process for deoiling polyamide and desizing cotton(Vouters et al., 2004). The concept of a jigger machine was used to create a dynamic apparatus. For sonication, a plunge sonotrode with a diameter of 6 cm and a frequency of 24 kHz, and a power of up to 600 W was adapted. From 20 to 25 m long and 10 cm wide textile pieces were used at a fabric speed of 10 m/min. The power of the ultrasonic was 40 W/L. The deoiling technique for polyamide was tested using a nonionic detergent and sodium hydroxide. Temperatures in the range of 60°C–70°C produced better outcomes. The residual grease level was usually lower than with ultrasound, and the chemical, water, and energy savings were roughly 30%, 20%, and 40%, respectively. Cotton desizing was done with -amylase at 80°C for 30 min. The production time for desizing was reduced by 30% when ultrasonic was used. The final fiber quality was improved, and ultrasound had a favorable influence on size removal while causing no harm to the fibers. An additional cost analysis revealed a 10% cost increase for ultrasound-assisted finishing over the traditional procedure, although finishers were willing to accept it provided the final quality was enhanced.

21.3.6 Electrochemistry

There are a few examples of large-scale electrochemical applications in industry, most notably in electroplating; however, the most of them are inefficient in terms of electrical power usage. Researchers have been interested by the idea of using ultrasonic sonoelectrochemistry to improve such processes for some years (Mason et al., 1990). Electrochemical processes might be complex, but they always simply come down to ion transport to and from the electrode surface. When an electrode is submerged in an aqueous solution, a thin diffusion layer forms at the surface, and because electrochemistry necessitates ions passing through this layer, any disturbance will interrupt the process. The cavitational collapse jet effect will assist diffusion to and from the electrode surface, which is often the rate-controlling step, by reducing the thickness of this diffusion layer. This has a number of advantageous sonoelectrochemical effects, including decreased electrode fouling, increased mass transport, manipulation of reaction mechanisms, altered adsorption phenomena, and surface effects, production of altered product distributions, increased yields and current efficiencies, improved synthetic routes, increased limiting current in analytical applications, and so on. Electroplating, synthesis, analysis, environmental research, biotechnology, catalysis, sensor science, and polymer synthesis are only a few of the applications for sonoelectrochemical approaches (Compton et al., 1997). Although the majority of this research is done in laboratories, industrial applications are likely to develop in the near future.

21.4 Energy efficiency of ultrasound-assisted processes

21.4.1 Acoustic cavitation based methods

Sonoluminescence approaches, sonochemical techniques, or erosive and dispersive effects measures can all be used to assess the sonic cavitation effects that occur inside or around collapsing bubbles (Al-Juboori et al., 2015a). For collecting spatial and temporal resolution of cavitation sites, sonoluminescence techniques are applied. These approaches have a number of drawbacks, including the need for specialized experimental circumstances (i.e., transparent medium under blackout), uncertain light emission processes, and a limitation to events that occur during the gas phase of collapsing bubbles (Leighton, 1997).

Chemical probes such as oxidation of potassium iodide (KI) and Fricke solution, as well as the breakdown of macromolecules, are commonly used to test the chemical efficiency of ultrasonic reactors (Rae et al., 2005). Because sonochemical approaches are solely concerned with the power involved in chemical reactions, they may produce an underestimation of the overall ultrasonic energy lost (Gogate et al., 2001). Another drawback of these methods is the recombination of free radicals (González-García et al., 2010).

As a result, power measurements based on dispersive and erosive effects are solely connected to the strong mechanical effects of ultrasonic propagation, and their measurement accuracy is harmed by free radical corrosive effects. Because of these drawbacks, they are unsuitable for ultrasonic power measurements (Al-Juboori et al., 2015a).

21.4.2 Energy or flow velocity method

Radiation force, sound pressure measures, and calorimetric techniques are among the techniques used. Radiation force measurement works on the principle that when an item is subjected to ultrasonic energy, it receives a constant force (radiation pressure force) (Silva, 2010). This force is proportional to the amount of ultrasonic power used. Only ultrasonic power in medical imaging equipment below the cavitation threshold may be measured using this methodology (Jaksukam and Umchid, 2011; Karaböce et al., 2011).

Hydrophones are used to measure sound pressure in order to determine the spatial distribution of ultrasonic pressure intensity. Hydrophones fragile nature and sensitivity to conflicting pressure signals from oscillating bubbles might restrict their use in high-power measurements (Banerjee and Dasgupta, 2010; Kim et al., 2014).

The concept behind calorimetric ultrasonic power measurement is that practically all ultrasonic power is transformed to heat (Toma et al., 2011; Zeng and McGough, 2009). Because of their simplicity and cost-effectiveness, calorimetric methods are the best way for measuring high ultrasonic power. However, due to convective heat losses, calorimetric measurements at high power densities might be erroneous (Banerjee and Dasgupta, 2010).

21.4.3 Physical properties measurement methods

The propagation of ultrasonic waves changes the pressure in the irradiated material, which changes several characteristics including the optical index of refraction (Stewart, 1982). Measurement of diffraction in an optical beam

TABLE 21.2 Influences of factors affecting acoustic cavitation.

Factors	Influence
Intensity	The acoustic amplitude and collapse pressure will increase as the intensity increases.
Frequency	Inversely related to cavitation intensity.
Viscosity	For optimum cavitation impact, it must be kept to a minimum.
Temperature	When the temperature rises, the chemical activity rises as well.
Presence of gas	Cavitation is made more difficult by removing gas from a liquid.
Vapor pressure	Cavitation is difficult to achieve in a low-vapor-pressure solution. As the vapor pressure drops, the cavitation effects increase dramatically.
External pressure	The severity of cavitational collapse will rise as the external pressure is increased.

(Shaw and Hodnett, 2008), schlieren visualization (Szabo, 2004), and interferometric method (Stewart, 1982) may all be used to identify this change. These measures are unsatisfactory for high-power quantification and need complex setups.

21.5 Factors affecting the application of ultrasound

Table 21.2 shows the various factors affecting ultrasound processing.

21.5.1 Effect of solution

Precursors, solvents, additives, and chemical agents, dissolved gas, and other sonochemical components are all present in a solution (Cui et al., 2012; Jung et al., 2008; Vabbina et al., 2014). Changing just one of them can have a significant impact on the process. The influence of solvent, in particular, is critical among these applied solution parameters. It conveys the combined influence of viscosity, vapor pressure, and surface tension, which may be linked to each of the sonochemical stages: pressure building, diffusion, and bubble development (Leong et al., 2010; Lorimer and Mason, 1987). The influence of viscosity on process yield is reflected in vapor pressure, which may be used to separate primary and secondary sonochemistry. Even though it includes a drop in cavitation intensity due to greater growth and growth density, low surface tension solvents assist the bubble achieve an appropriate size and stable. The addition of a solute lowers the surface tension, which can be further reduced with the addition of surfactants (Leong et al., 2010; Leong et al., 2014). These compounds can also be utilized to initiate novel chemical processes in order to acquire novel materials, as a stabilizing or growth-directing agent, or just to investigate their influence on cavitation (Lee et al., 2005; Leong et al., 2014).

Electrolytes have been observed to reduce bubble coalition while increasing single bubble sonoluminescence. The electrolyte at the bubble interface causes an electrical repulsion between bubbles, which aids in their sole growth while also increasing their compression resistance. As a result of the unique structure and crystallinity of nanomaterials, better physical and chemical properties have been attained (Mohandes and Salavati-Niasari, 2013; Nemamcha et al., 2006). Inside the bubble, atomic-level mixing provides an alternative, perhaps low-energy path for chemicals to make new materials or improve existing ones in terms of stability, reactivity, and other properties.

In terms of bubble coalition and single bubble sonoluminescence, increasing precursor concentration produces comparable results (Price et al., 2004). As a result of the change in precursor concentration, the shape of nanoparticles changes throughout growth (Vabbina et al., 2014). The capacity of liquid to cavitate is hindered by low gas concentration, degassing, and the use of old solution, which affects sonochemical output.

21.5.2 Effect of frequency

The pressure cycle is influenced by frequency. The pressure changes abruptly as the frequency rises, generating a lot of turbulence inside the liquid. At high frequency and amplitude, this produced phenomenon, known as acoustic streaming, dominates acoustic cavitation (Leighton, 2012). Bubbles are continually pushed and hurried as a result of streaming, and they die immaturely, resulting in poor cavitation and material development. The growth of a cavitating bubble is hampered by the shortened diffusion time during the high-frequency experiment, in addition to the influence of streaming. Increased frequency results in smaller bubbles with a more uniform size distribution (Brotchie et al., 2009a; Merouani et al., 2014). The energy accumulating inside the bubble, on the other hand, does not reciprocate the increase in frequency as linearly

as the change in size. The temperature within the bubble was determined in the range of 3400 K at 20 kHz, 3700 K at 1056 kHz, and 4300 K at 355 kHz when analyzing the creation of various hydrocarbon compounds during sonication of aqueous tert-butyl (Ciawi et al., 2006). As a result, the rate and type of radical generation vary with frequency, resulting in primary radicals and ions being formed only within a particular frequency range; in other words, it is impracticable to assume extreme scenarios like O_2 ionization at any frequency and power (Merouani et al., 2013). The influence of frequency on cavitation is intensified within a frequency range that relies on the kind of solution employed, according to theoretical calculations, simulations, and sonoluminescence studies (Ciawi et al., 2006).

As a result of the influence of frequency on cavitation, the material synthesis process is affected. By measuring the rate and size of gold nanoparticles formed at various ultrasonic frequencies, Okitsu et al. (Okitsu et al., 2005) analyzed the creation of gold nanoparticles. The rate of creation of gold nanoparticles grows linearly from 0 to 213 kHz, peaks at 213 kHz, then drops gradually, according to a study done by sonicating an aqueous auric chloride and 1-propanol solution at constant power and temperature. The size of nanoparticles decreases with frequency, with the smallest gold being 10 nm at the highest frequency, according to TEM data. Koda et al. (Koda et al., 2003) investigated the Fricke reaction, KI oxidation, and breakdown of porphyrin derivatives in the frequency range of 19.5–1200 kHz to assess sonochemical efficiency with regard to frequency. The generation of free radicals in each system was studied using an individual reaction system and a calorimeter and UV spectrometer. At frequencies of 100–500 kHz, the rate of reaction and production of Fe^{3+} (Fricke), I_3 (KI oxidation), and H_2TPPS^{4-} (porphyrin breakdown) radicals were substantial in all cases, with ~300 kHz being the highest.

21.5.3 Effect of power

The applied power, or power density, has an impact on the pressure amplitude and should be able to meet the cavitation pressure requirements. However, dramatically increasing power can alter bubble dynamics by allowing bubbles to form abnormally during expansion, which can lead to poor cavitation and material growth (Brotchie et al., 2009b; Merouani et al., 2013). As a result, in order to regulate bubble growth, the applied power and frequency must constantly be in sync. With a distance of 30 mm below the transducer, at an input power of 179 W, the average bubble size measured at a distance of 30 mm below the transducer was determined to be ~10 μm. At frequencies of 500 kHz or less, the size of the bubble appears to rise with applied power (Brotchie et al., 2009a). However, at high frequencies, raising power above a certain threshold has a nonlinear influence on bubble formation. Raising the power from 0 to 5 W resulted in an increase in bubble size from ~1.8 μm to ~4 μm in a typical scenario (1056 kHz), whereas increasing the power further (5–30 W) resulted in a wavering growth pattern with a change of ~0.8 μm. The impact of increasing power with altering frequency reciprocates similarly—bubble growth was found to be linear between 200 and 300 kHz, while a quasi-linear relationship was detected between 500–1000 kHz, and increasing power decreased bubble size at 1000 kHz and above (Merouani et al., 2013). High frequency and power induce acoustic streaming, which has a negative effect at 1000 kHz.

As in the case of frequency, the type of radicals generated varies with applied power and causes significant changes in the morphology and crystallinity of nanomaterials (Kandjani et al., 2008; Merouani et al., 2013). The size of nanoparticles appears to shrink as power increases, yet the sonochemical output rises. Maintaining a low temperature was shown to be beneficial in synthesizing smaller nanoparticles and reducing the creation of byproducts (Kandjani et al., 2008).

21.5.4 Effect of sonication time

The influence of experiment time and cycle number on nanomaterial production causes morphological diversity (Vabbina et al., 2014; Wahab et al., 2007). The main growth that serves as seed makes the creation of additional structures simpler as the duration and cycle of sonication increases. New heterostructures are built on top of old ones, depending on the surface energy. The shape of ZnO nanomaterial generated through sonication of aqueous zinc acetate dihydrate, zinc nitrate hexahydrate, and hexamethylene tetramine indicated apparent variations in the period of sonication (Vabbina et al., 2014). MoS_2 is produced by sonication of molybdenum hexacarbonyl, sulfur, and o-xylene converted from 2D nanoflakes to 3D nanospheres, similar to organic fullerenes, after being sonicated for a long period (Singh et al., 2007). Increased sonication can potentially influence the product's crystalline structure. After prolonged sonication, stibnite nanoparticles generated sonochemically altered from amorphous nano-spheres to crystalline nano-rods and nano-whiskers (Wang et al., 2003).

21.5.5 Effect of substrate

The substrate on which nanomaterials are produced undergoes dramatic morphological changes, as well as alterations in their electrical, chemical, and other characteristics (Vabbina et al., 2014; Xiao et al., 2009). The produced Au–Pt nano composite

on chitosan surface grows more smaller and denser than those formed on bare ITO, as evidenced by a chitosan modified ITO glass substrate. Similarly, ZnO grown on graphene-coated substrates grew at a faster pace and had a greater density than ZnO grown on bare SiO_2 or PET substrates (Vabbina et al., 2014). In contrast to the production of 2D nanoflakes on bare SiO_2, ZnO on graphene generated 3D nanostructures appropriate for applications requiring continuous transport medium (Cau and Nikitenko, 2012) after prolonged sonication. In addition, the photoconductivity of ZnO grown on top of graphene rose significantly when compared to Si. In the case of noble metals, substrate selection is critical for improving their sensing and catalytic properties (Xiao et al., 2009). The size, orientation, density, and other properties of such nanometals are influenced by the surface on which they are produced, and using substrates with large surface area, such as graphene, carbon nanotubes, and chitosan, has been shown to increase their growth and characteristics.

21.5.6 Physical effect of ultrasound

The effect of shock waves and microjets, as well as applications developed from them because sonochemistry is primarily concerned with the chemical effect of ultrasound. Shockwave has a stronger effect than microjets and can cause brittle materials to break down into pieces, ductile materials to deform, and layered materials to exfoliate (Doktycz and Suslick, 1990; Kass, 2000; Prozorov et al., 2004; Viculis et al., 2003). After sonication of their respective slurry, zinc, iron, tin, chromium, and other transition metal microparticles (~50 μm) form dumbbell-like formations (Doktycz and Suslick, 1990). Due to their huge size, sonicating a slurry of nickel micro particles (~160 μm) revealed remarkably little interparticle coalition. The kinetic energy generated by shock wave acceleration diminishes as particle size rises. The temperature at the location of impact can reach 2890 K, as demonstrated by molybdenum particle coalition. Low-melting-point metals consolidate, whereas high-melting-point metals shatter. When tungsten microparticles were sonicated, they showed no substantial physical change (Doktycz and Suslick, 1990). Because of its potential application in the production of graphene and other modern materials, the exfoliating effect of ultrasound has grown in popularity among sonochemists. Sonochemically produced graphene has significantly improved physical and chemical properties as compared to traditional approaches (Lotya et al., 2009; Xu and Suslick, 2010; Zhang et al., 2010). According to Xu and Suslick (Doktycz and Suslick, 1990), the bulk of graphene exfoliated from graphite flakes has less than 5 layers and has extremely low surface roughness and damage (Xu and Suslick, 2010). Similarly, Lisa et al. describe a unique approach for manufacturing carbon nanoscrolls using alkali metals and ultrasonic to exfoliate graphite (Viculis et al., 2003). Ultrasonic exfoliation has also eased the production of single to few layers of molybdenum disulfide (MoS_2), tungsten disulfide (WS_2), and boron nitride (BN) (Wang et al., 2013). Shockwave can interact directly with a particle of adequate size and cause fragmentation in addition to interparticle collision (Zeiger and Suslick, 2011). Zeiger et al. (Zeiger and Suslick, 2011) report the impact of coupling between aspirin crystal and shock wave that leads to fragmentation, after excluding alternative causes of impact. The action of microjet, in contrast to shockwave, is perplexing to sonochemists since the rushing jet causes undesirable effects such as surface erosion, pitting, and deformation. Microjets effect, on the other hand, may be regulated and used for a variety of purposes, including cleaning, metal activation, catalysis, drug synthesis, and so on (Suslick, 1989). Microjets remove oxide and other surface coatings easily and completely, making them a preferable alternative to heating and traditional techniques for activating metal and reactive chemicals. Microjets have also been used in engineering, according to Barton et al., who disclose the production of a microelectrode array sensor using controlled pitting (Barton et al., 2004).

21.5.7 Bulk liquid temperature

Cavitation is a dynamic phenomena that is influenced greatly by operational factors such as bulk liquid temperature, static pressure, and sonoreactor geometry. According to Sutkar and Gogate (Sutkar and Gogate, 2009), the bulk temperature influences the reaction mechanism of the sonochemical process. Any little changes in temperature will modify the liquid medium's pressure and acoustic intensity, resulting in a significantly altered cavitational impact (Krefting et al., 2004). As a result, understanding the properties of the flow and acoustic fields inside the sonoreactor requires investigating the temperature change caused by ultrasound irradiation. Marangopoulos et al. (Marangopoulos et al., 1995) and Zeqiri et al.(Zeqiri et al., 2003) are two of the few studies that have investigated the quantitative measurement of factors such as temperature and pressure field throughout an entire range of operation as a function of different operating parameters. The effects of ultrasonic irradiation on the temperature and pressure distribution inside a sonoreactor were investigated by Kim et al. (Kim et al., 2009). For forecasting energy density, four (4) different solvents were studied at varying ultrasonic powers. Temperature change as a function of sonication duration at different ultrasonic powers (300–450 W). The temperature of all liquid medium rises with time. Differences in the physical and thermodynamic characteristics of all liquid media, on the other hand, are the cause of temperature trends that vary over time. The literature on the influence of liquid bulk temperature

is limited, and the specific mechanism of this impact is unknown. The temperature of the liquid bulk has a substantial impact on the temperature of the bubbles and, in turn, the rate of hydrogen generation. The temperature of the liquid bulk is critical since it serves as the surrounding medium for the acoustic cavitation bubbles. In fact, when the temperature of the bulk liquid rises, the temperature of the bubble rises as well, causing the liquid-vapor pressure to rise and more vapors to be trapped inside the bubble (Rashwan et al., 2019). Increasing the bulk temperature, on the other hand, will make the bubbles collapse less violently, impacting the breakdown of water molecules and resulting in less active radicals. The combination of these two critical elements should therefore result in an ideal liquid bulk temperature at which the highest rate of hydrogen generation may be attained.

21.6 Energy efficiency and scale up issue for industrial application of ultrasound

Electrical power is converted into vibrational or ultrasonic energy, which is mechanical energy, via the ultrasonic system (Mason, 1992; Pestman et al., 1994; Rawson, 1987). This mechanical energy is subsequently transferred to the reaction media, which has been sonicated. The efficiency of the energy conversion is determined by both the equipment and the ultrasonication settings. As a result, measuring the quantity of electrical energy required to create the mechanical vibration is insufficient to determine the quantity of acoustic energy transmitted into the liquid medium. In terms of total input energy, sonolysis is somewhat inefficient. This is due to the fact that a portion of the entire energy input is wasted as heat and another portion is used to create cavitation. However, not all cavitational energy has chemical or physical consequences. Sound re-emission consumes some energy (i.e., harmonics and subharmonics) (Ley and Low, 2012; Mason, 1992). The poor efficiency of the electrical energy—acoustic energy—chemical effects conversion sequence may limit this technology from being used as a main therapy. The limitation of sonolysis for the management of H_2S and other trace pollutants in water, as shown by Kotronarou et al. (Kotronarou et al., 1992), is that it is somewhat inefficient in terms of energy input. Only a small part of the overall energy provided to the system resulted in "productive" free-radical reactions, according to their predictions. There is inefficiency in the transfer of power at each level, when the sonochemical advantage is lost to heat or sound. As a result, it is clear that determining an energy balance is difficult.

The effect/input power of the sonochemical yield is measured in moles of products created per second. Despite the difficulties of determining a precise energy balance, "sonochemical yield" is defined in a similar manner to "photochemical yield" in general (Berlan and Mason, 1992; Mason, 1992). As a result, the overall power input into the power generators is less than the acoustic power supplied to the reaction mixture. The problem is to put these energy losses to good use, such as pollution control.

In addition to understanding the characteristics of reaction mixtures and reaction kinetics, a successful scale-up method is required, which necessitates thorough investigation, quantification, and optimization of all aspects impacting cavitation efficiency.

Much further, the bulk of documented investigations for ultrasonic pollution degradation have used laboratory-scale piezoelectric probe (0.25–0.5 in.) batch reactors with modest volumes (20–200 mL) (Mason and Lorimer, 1998; Pestman et al., 1994). Because of its capacity to produce high power output and ease of operation, the probe-type reactor is extensively utilized to provide optimal performance at various amplitudes. However, Kotronarou and Hoffmann (Kotronarou and Hoffmann, 1995) observed that dispersing the same energy input across a larger area increased response rate and energy use efficiency significantly. Sonolysis reactors with larger radiating surfaces were also shown to be more energy-efficient than the direct immersion probe reactor, which has a low (1 cm^2) radiating surface. The probe-type reactor system is not an optimum reactor configuration for the efficient creation of transient cavitation for two reasons in addition to its low energy usage efficiency. First, the blanketing effect generated by the high formation of cavitation bubbles at the tip reduces sonication efficiency. Second, the titanium tip on probe-type transducer tips has a relatively short life before it has to be replaced. Because of these factors, direct probe sonolysis is not economically viable for specialized applications. Kotronarou and Hoffmann (Kotronarou and Hoffmann, 1995) observed a direct linear relationship between the applied power at a fixed frequency and the observed rate of loss of S(-II) in their studies of H_2S ultrasonic oxidation, indicating that a continuous-flow stirred-tank probe reactor could achieve significant conversion efficiencies. The utilization of huge high-powered sonicators in the CSTR mode might result in feasible degradation efficiencies, according to their preliminary studies. For the degradation of p-nitrophenol, Hua et al. (Hua et al., 1995) reported that a near field acoustical processor, or NAP (where liquid flows between two high intensity vibrating plates), was more efficient than a probe reactor. They found that NAP supplied 1.5 times the power per unit volume of the probe reactor, but 19 times more p-nitrophenol destruction per kilojoule energy applied to the system. The probe reactor's G value was similarly found to be around 1 order of magnitude lower than the NAP's, despite the fact that the degradation rate constants were of the same magnitude. The G value is a radiation chemistry efficiency metric that is defined as the number of molecules undergoing reaction per 100 eV of electrical

energy delivered for each species in neutral water (Bielski et al., 1985). The NAP parallel-plate reactor produces lower sound intensity but more acoustic power per unit volume than conventional probe reactors. However, there has been little study done on the NAP and tank reactors, and there isn't much data comparing their performance to that of the probe reactor.

21.6.1 Challenges in ultrasound in food processing

The nonstandardized reporting of technique and control parameters remains a barrier prior to widespread use of the technology. Standardized reporting in terms of energy density, probe type, and sample quantities would make techno-economic evaluation easier before commencing operations. Nonetheless, much study and development are necessary to fully comprehend, optimize, and implement this complicated process. The technology must be thoroughly evaluated and demonstrated to be both safe and economically viable (Awad et al., 2012).

The majority of the investigations are based on the commercially accessible ultrasonic frequency (20 or 40 kHz). The use of various ultrasonic frequencies, as well as modifying factors such as temperature, treatment time, and acoustic power, should be explored (Rastogi, 2011).

The ultrasonic technique is used in a various applications, including monitoring aqueous solution and suspension concentrations, determining droplet size and concentration in emulsions, monitoring crystallization in fats, and checking creaming profiles in emulsions and suspensions; in particular, for on-line determination of these properties during processing. It is a quick, accurate, nondestructive, and noninvasive approach that may be used on a concentrated or opaque system (Singla and Sit, 2021). Furthermore, it is simple to modify for on-line measurements, which would be beneficial for monitoring food processing activities.

The presence of tiny gas bubbles in a sample can cause ultrasound to be attenuated to the point where it is unable to propagate through the material. Even though the signal from the bubbles may interfere with other components, this problem may be solved by taking reflection rather than transmission measurements. To make theoretical predictions of a material's ultrasonic characteristics, a lot of information regarding its thermo-physical attributes, such as densities, compressibilities, heat capacities, and thermal conductivities, are required. As a result, theoretical evaluations of data from systems with multiple components with unknown attributes are few (Leadley and Williams, 2005).

Low-intensity ultrasound is used in the food industry since it is relatively low-cost. For many years, scientists have known that high-intensity ultrasound may be used to change the physical and chemical characteristics of products. Despite this, manufacturers have only lately begun to adapt laboratory-scale equipment for large-scale processing operations. The availability of low-cost apparatus that has been shown to offer considerable benefits over competing technologies is a major factor in the growing adoption of high-intensity ultrasound.

Many foods have a high amount of attenuation, such as plant tissues, aerated meals, and certain semicrystalline lipids (chocolates), making measuring difficult. Cleaning, fouling, and other practical constraints may make the use of a reduced route length impractical in a real-world process. The spatial resolution is reduced when lower frequencies are used. In certain circumstances, a number of sample factors are changing at the same time, affecting the ultrasonic characteristics. The basic sensor may not be enough, in this case, resulting in wide and difficult-to-resolve peaks. Additional difficulties in further measuring the property based on temperature may be introduced if it is impossible to achieve highly accurate and consistent temperature control throughout the sample. Due to the presence of air in the sample, there is a significant impedance mismatch between gas bubbles and other food ingredients, resulting in air bubble reflection and severe scattering. Ultrasound can thus be used to identify included air that isn't visible otherwise (Soltani Firouz et al., 2019).

21.6.2 Challenges in sonochemical processes for pollutant degradation

Energy efficiency and scaling up processes are the two key issues addressed by researchers in the field of sonochemistry for industrial applications (Chen et al., 2012). Despite several investigations, complete mineralization of organic pollutants by ultrasonic irradiation alone remains a tough task due to sluggish degradation rates, especially for nonvolatile chemicals (Grčić et al., 2010; Wang et al., 2011). When the pollutant concentration is very high, the rise in fluid viscosity creates a barrier to nucleation that must be overcome. During rectified diffusion processes, the existence of viscous bubbles might obstruct the movement of water vapor, dissolved gases, and volatile organics into bubbles. The rate of OH^- generation and pollutant degradation will both be reduced as a result of this event. As a result, supplying energy to achieve the nucleation threshold, particularly at high frequencies, is a significant difficulty (Thangavadivel et al., 2012).

If employed alone, ultrasonic irradiation has the potential to produce damaging by-products in addition to the slow rate of oxidative potential. If ultrasound is employed, the objective should be to achieve rapid mineralization of the organic chemical in order to reduce the amount of time harmful intermediates are present (Adewuyi, 2005). As a result, researchers

focused on combining different technologies with ultrasonic systems in order to obtain the necessary substrate efficiency, total mineralization, and decrease the reaction time necessary to remove pollutants (Grčić et al., 2010).

Choosing processes that complement each other and result in a synergistic impact is typically crucial in the design of such hybrid systems. Because of the ultrasonic system's economic, physical, and technological constraints, it might be combined with other treatment procedures to successfully treat resistant wastes and decrease treatment costs significantly compared to a single-step method (Adewuyi, 2005). The use of different additives to improve mineralization processes is a popular topic of discussion (Madhavan et al., 2010; Naddeo et al., 2010).

Despite the numerous intriguing uses of sonochemical reactors, there have only been a few successful industrial-scale uses (Katekhaye and Gogate, 2011). Ultrasonic transducers are built of a restricted number of materials, and their selection must be compatible with the pH of the working environment. The transducer tips or cone will need to be changed regularly due to pitting difficulties (Thangavadivel et al., 2012). Aside from resolving physical equipment limitations, tests on various scales of operation are required to properly understand and resolve challenges associated with scaling up, such as changes in the flow field and turbulence characteristics (Gogate, 2007). Gogate and Pandit (Gogate and Pandit, 2004) suggested several valuable design equations as a starting point for developing design/scale-up techniques. However, translating the design equations into generalized forms that are applicable for many reactions and sonochemical reactor designs remains a difficulty. They proposed some future efforts that should be focused on the development of sonoreactors:

1. Testing comparable design equations across a broader range of operational parameters.
2. Accurate measurement of the amount of free radicals produced during the collapse, as well as the actual number of radicals involved in the reaction.
3. Determining the nuclei/cavity size.
4. Determining total and transitory bubble activity under different levels of violence.
5. The impact of the collapse pressure created and the maximum bubble size obtained are combined.

Furthermore, ultrasonic treatment has challenges in terms of volumetric flow rate, reaction energy rates, and total cost in order to suit industrial demands (Adewuyi, 2005). According to Mahamuni and Adewuyi (Mahamuni and Adewuyi, 2010), the cost of employing ultrasound to cure different contaminants is greater than alternative treatments that use sophisticated oxidation processes (AOPs). This remark was corroborated by Chen and Huang (W. S. Chen and Huang, 2011), who discovered in their investigation that ultrasonic treatment alone was not a cost-effective procedure in terms of energy usage. The overall energy transfer efficiency of this technique was found to be below 10% since electrical energy must be transformed to mechanical vibration, then to cavitation energy before pollutant degradation can occur (Thangavadivel et al., 2012).

21.6.3 Challenges for sonohydrogen reactor design

In fact, acoustic frequency, acoustic intensity, dissolved gas, and water bulk temperature all affect the rate of hydrogen generation (Merouani et al., 2016). However, a method to estimate the hydrogen generation rate has yet to be fully established, and numerous computational and experimental experiments are still required.

21.6.3.1 Ultrasonic frequency

As the most critical characteristic in sonohydrogen creation, the amount of hydrogen created from such a process is very frequency dependent. The rate of hydrogen creation rises as the applied frequency rises (Brotchie et al., 2009a). The maximum bubble core temperature and pressure, the amount of trapped water vapors, and the collapse duration are all dynamic parameters that influence the hydrogen generation rate with frequency. The bubble will have more time to develop and increase at low frequencies, which will allow more water vapor to be trapped inside the bubble core.

As a result, the bubble will collapse rapidly, resulting in increased pressure and temperature, which will encourage the chemical process to produce additional radicals. The collapse period will be very short at higher frequencies, and the bubbles will not have enough time to create radicals since the reaction inside the bubbles will be very quick. We can explain why the applied ultrasonic frequency has a considerable influence on the hydrogen generation rate by combining all of these parameters. Brotchie et al. (Brotchie et al., 2009a) observed that the H_2O_2 production rate increases as the frequency increases until it reaches an optimal point, after which it decreases. This may be explained by the generation of bubble clouds, which attenuate the acoustic intensity, lowering the H_2O_2 production rate.

21.6.3.2 Dissolved gas

The impact of dissolved gas on hydrogen generation is determined by two key physical properties: (1) specific heat capacity ratio (g 14 Cp/Cv) and (2) thermal conductivity (k). The larger heat capacity dissolved gas might accumulate a greater temperature. Dissolved gases with low thermal conductivity, on the other hand, have limited heat dissipation, allowing more heat to be held inside the bubble. As a result, choosing a dissolved gas with a high heat capacity and low thermal conductivity will be the best choice for improving the dissociation process of water vapor and, as a result, generating more hydrogen.

21.6.3.3 Acoustic power

The rate of hydrogen generation is greatly influenced by the acoustic intensity. This is due to the fact that the acoustic bubble acts as a microcombustor during the collapse, producing high-temperature chemical reactions and extremely reactive radicals as a result of these chemical reactions. Three parameters control the chemical reaction: bubble temperature, collapse time, and bubble size, which correspond to the quantity of water vapor trapped in the bubble. The expansion ratio of the bubbles will grow as the acoustic intensity rises, allowing more water vapor to be trapped in each bubble. In the same way, when the compression ratio rises, the temperature of the bubble rises.

As a result of the increased expansion and compression ratios of the bubbles, an unusual chemical reaction will occur, resulting in the production of more free radicals as the water molecules inside the bubbles dissociate. Additionally, raising the acoustic intensity will lengthen the collapse time, giving the chemical process more opportunity to make additional reactive-radicals. Combining all of these elements results in increased H_2 production.

21.6.3.4 Bubble temperature

The bubble temperature is one of the key factors that influence the mole percentage of hydrogen generated. Two operating conditions, such as frequency and acoustic amplitude, are linked to the maximum bubble temperature. Merouani et al. (Merouani et al., 2014) used multiple gas-based models to calculate the quantity of H_2 produced as a function of bubble temperature. It can be shown that an ideal hydrogen rate is found between 5000 and 7000 K. The amount of hydrogen produced increases as the bubble temperature rises. The results demonstrated that the amount of hydrogen produced is larger at a low acoustic amplitude and high frequency, whereas it is lower at a high acoustic amplitude and low frequency.

On the other hand, increased acoustic amplitude and low frequency should be used to achieve the highest bubble temperature at the conclusion of bubble collapse Merouani et al. (Merouani et al., 2014). Merouani et al. (Merouani et al., 2016) conducted a detailed numerical analysis of hydrogen generation in water utilizing sonic cavitation bubbles. In the case of air as a dissolved gas, the influence of ultrasonic frequency on the rate of hydrogen formation. While the rate of hydrogen generation in relation to ultrasonic frequencies at various acoustic intensities [W/cm^2]. To summarize this section, the amount of water vapors trapped inside the bubbles controls the total generation of H_2. A number of preliminary computational and experimental tests are required to determine this quantity of water vapors. To gain an adequate knowledge of the events, a wide number of characteristics, including frequency and intensity, must be investigated. Furthermore, optimization and regression/statistical analysis must be carried out in order to determine the optimal point and the most important parameter that will result in the highest H_2 production rate.

21.7 Recent developments in design and scale-up of sonoreactors for industrial processes

Several research have shown that sonochemical treatments have the potential to be employed as one of the strategies for environmental cleanup (Adewuyi, 2005). On a laboratory scale, the effects of sonic cavitation phenomena have been successful in a variety of applications, but a well-defined design and scale-up process are still absent (Gogate et al., 2011). Existing data based on laboratory scales may result in extremely high scale-up ratios and, as a result, a considerable degree of uncertainty (Gogate, 2007). The lack of knowledge necessary in multiple domains such as material science, acoustics, chemical engineering, and others impacted the effectiveness of scaling up laboratory ultrasonic processes (Sutkar and Gogate, 2009).

It is critical to remember that efficiency is the primary concern when scaling up sonochemical operations. Because not all of the cavitational energy causes chemical or physical consequences when ultrasound is utilized as a sole treatment method, it is a very energy-intensive procedure (Adewuyi, 2005). Cavitational activity in a sonochemical reactor is influenced not only by reactor configurations such as transducer position, irradiative element surface area, and reactor dimension, but also by operational factors such as power density, liquid medium height, and others. The reaction process and total yield of a sonochemical reaction are also affected by bulk temperature, acoustic intensity, and static pressure in the fluid (Sutkar and Gogate, 2009). In addition to increasing energy conversion efficiency, more effort is needed to improve cavitation sites and

free radical production rates for a given energy input. To enhance the degradation process by ultrasonic irradiation, alternative energy sources or the inclusion of free radicals such as H_2O_2, O_3, air, and ferrous ions are usually required (Adewuyi, 2005).

Due to their low cavitationally active volume, the two most typical ultrasonic configurations, ultrasonic horn or ultrasonic bath with a single transducer, could not be employed for large-scale processing (Bhirud et al., 2004). Maximum cavitation events only occur near the irradiating surface, and energy dissipation rates in the bulk of the liquid will vary greatly (Sutkar and Gogate, 2009). As a result, there were designs that used multiple transducers operating at the same or various frequencies, or a single big transducer positioned at the bottom of the reactor that emits sound waves longitudinally out from the bottom perpendicular to the horn's axis (Bhirud et al., 2004; Kumar et al., 2007). Multiple transducers, on the other hand, have not been shown to be feasible or cost-effective in big industrial installations (Gallego-Juárez et al., 2010).

Gogate et al. (Gogate et al., 2011) illustrated some of the most significant factors to consider when choosing a reactor, scaling it up, and optimizing it. Mason (Mason, 1992) was one of the first to analyze the potential and practical usage of ultrasonic technology in industries when it came to reactor selection. It was determined that while selecting a sonoreactor, it is critical to determine the type of ultrasonic treatment needed for a certain chemical process . Ultrasonic applications can be divided into two categories: those based on chemical effects (sonochemistry) and those based on physical effects (sonoprocessing) (Toma et al., 2011). Cavitation must be provided throughout the transformation itself, either continuously or in a suitably pulsed operation, for sonochemistry (Gogate et al., 2011). The production of OH and H causes this effect, which in turn causes or influences a chemical process. Sonoprocessing, on the other hand, is associated with microstreaming and mixing, which helps to speed up cleaning, extraction, polymer breakdown, and other processes (Yasuda and Koda, 2012). Rather than acquiring improved acoustic characteristics, efforts in sonochemical equipment modeling have concentrated on facilitating the chemistry. Ultrasonic system production appears to be adapting to the growing use of ultrasound in many applications. However, the fundamental aim, which is a high-energy-efficiency sonoreactor, has yet to be industrialized (Toma et al., 2011).

In order to recreate the desired cavitation field on a larger scale, it is required to first identify and understand the mechanism of interaction from observable ultrasonic events. Then, in terms of operating/design factors that impact cavitation, the best circumstances for achieving the required transformation must be determined (Gogate et al., 2011). There have been several methods developed for examining cavitational activity in sonoreactors. The characterization of cavitational phenomena and their effects is typically accomplished through mapping, a stepwise procedure in which cavitational activity in a sonoreactor is quantified using primary effects (temperature or pressure measurements at the time of bubble collapse) and/or secondary effects (quantification of chemical or physical effects in terms of measurable quantities) (Sutkar and Gogate, 2009).

Mason and Cordemans (Mason and Cordemans De Meulenaer, 1998) proposed the following actions to enhance an ultrasonic process:

1. Adding solids or gas bubbles as nuclei to assist in cavitation.
2. Try out different gases or gas mixtures in the chamber.
3. Experiment with various solvents for various temperature ranges and cavitation energy.
4. Optimizing the needed power for the desired reaction.
5. When employing a solid–liquid system, do not charge all of the components in the reactor at the same time.
6. If at all feasible, make the two-phase system as homogeneous as viable.
7. Experiment with different reactor forms (diameter and volume).
8. Avoiding standing waves by performing sonochemical reactions at high power settings with mechanical agitation is preferable (but not always).
9. If at all feasible, convert a batch system to a continuous one.
10. Select conditions that allow you to compare various sonochemical reactions.

21.7.1 Reactor design

Sonochemistry equipment typically includes a sonochemical reactor, temperature control unit, ultrasonic generator, and power amplifier. The sonochemical reactors' cells can be built of acryl resin, glass, or stainless steel, with or without a stainless steel frame. As a sound source, a piezoelectric ceramics or magnetostrictive transducer is placed within the reactor. Horn-type and Langevine-type transducers are utilized for low frequency. PZT (lead zirconate titanate) is utilized for higher frequency by placing it at the bottom of the vessel or attaching the holder that includes PZT transducers. The form of the reactor vessel, the attachment of the transducer, and the irradiation technique are all factors to consider while designing a sonochemical reactor, in addition to these component pieces. Because its usual acoustic source is a circular disc, the former

provides a significant advantage for theoretical sound field analysis. A cylindrical sonochemical reactor consists of beaker-scale reactors. Rectangular sonochemical reactors, on the other hand, are beneficial for practical usage since they are simple to create on a big scale. The rectangular sonochemical reactor may also be used to see the liquid flow in the vessel. The hexagonal reactors were created to increase the cavitation effects (Gogate et al., 2003).

The vibrating plate is attached directly to the transducer in the transducer unit for higher frequency and is fixed at the bottom of sonochemical reactors. For successful sound wave transmission into liquid, a vibrating plate with a thickness of (n/2) or less than (/10) is recommended. Where n is an integer and this is the sound wavelength in a vibrating plate. The other kind of transducer unit comprises a transducer, vibration plate, holder, and rubber. This sort of transducer unit is easily interchangeable and makes reactor maintenance easier in industrial settings.

To increase cavitation effects, ultrasonic irradiation can be undertaken using several sound sources. The "Superposition of sonochemical fields" and "Large scale of sonoreactor" sections will cover the scenario of a sonochemical reactor with many transducers.

21.7.2 Frequency of sonication

Because cavitation behavior is greatly influenced by frequency, frequency is one of the most essential consideration elements in sonochemistry. Busnel et al. (Busnel et al., 1953) were the first to demonstrate that the frequency dependence of the yield of I_2 in KI solution at various input electric powers peaks at 300 kHz. The sonochemical impact generated by water sonolysis is most efficient around 300–500 kHz, according to these findings. Mark et al. (Mark et al., 1998) used fluorescence spectroscopy to investigate the frequency dependence of sonochemical effects in terephthalate solution. They also discovered that sonochemical reactions had a considerable frequency dependency.

Koda et al. (Koda et al., 2003) reassessed the frequency dependence of three common sonochemical processes (Fricke reaction, KI oxidation, and breakdown of porphyrin derivatives) and proposed the following sonochemical efficiency:

$$SE = m/E_{US} = C/P_{US}\ t/V$$

where

m is number of reacted molecules
C is concentration of I_3 or Fe^{3+} ions in solution
E_{US} is ultrasound energy
P_{US} is ultrasound power t is ultrasonic irradiation time
V is volume of solution, respectively

The sonochemical efficiency value has been utilized by Asakura et al. (Asakura et al., 2007, 2008) and Kojima et al. (Kojima et al., 2010) to assess the performance of large sonochemical reactors.

The ultrasonic power, which is determined by calorimetry and reflects ultrasonic power put into solution, is divided by all of the findings. The decomposition conversion of TPPS (1 RTPPS) is the value of (1 RTPPS). 1 RTPPS has a frequency dependency that differs somewhat from that of KI oxidation and Fricke reaction. Around 300 kHz, TPPS decomposition ratios are about four times higher than those in the lower frequency domain, while Fe3+ and I_3 product yields are around ten times higher than those below 100 kHz, where they appear to be frequency independent. The sonochemical effects drop sharply at 500 kHz. The sonochemical effects reported at 1.2 MHz are of the same order as those observed below 100 kHz. These findings suggest that the mechanisms underlying TPPS breakdown differ from those behind KI oxidation and the Fricke reaction produced by H_2O sonolysis. In the case of TPPS breakdown, direct sonolysis of TPPS at the cavity interface may occur in addition to H_2O sonolysis.

The observed dependency of chemical effects on frequency can be attributable to a number of parameters, including bubble temperature, cavitation threshold, bubble population, bubble lifespan, and so on. According to bubble dynamics, as the sonication frequency increases, the maximum temperature reached in the collapse of a bubble falls (Hung and Hoffmann, 1999). The cavitation threshold rises with frequency, resulting in a narrower active zone in which bubbles can be generated in a nonuniform sound field (Kojima et al., 2001). The chemical effects are reduced by these circumstances. In a standing-wave field, on the other hand, the bubble population grows due to a shorter interval of active zones corresponding to a drop in wavelength at a higher frequency. With increased frequency, the duration of bubbles shortens (Leighton, 1995). This implies that additional radicals generated in a bubble can escape and react with whatever else is present in the medium. All of these variables contribute to enhanced chemical impacts. Other factors include bubble cloud and the quantity of vaporized molecules inside a bubble (Lauterborn and Holzfuss, 1986; Pétrier and Francony, 1997; Yasui, 2002) might be to blame.

Experimentally, the frequency dependency of physical effects is not yet known. Because the bubble size fluctuates with frequency, the physical consequences are predicted to be frequency dependent. The shear force created by the relative motion of the solvent along the polymer chains during bubble collapse, that is, mechanical or physical impacts, is the principal source of acoustic degradation of polymers in solution. The rate of polymer degradation under sonication varies depending on the sonication frequency. Without a radical scavenger, ultrasonic degradation of a water-soluble polymer in an aqueous solution is more efficient at 500 kHz frequency, according to Koda et al. (Koda et al., 2011). According to Grönroos et al. (Grönroos et al., 2001), the most widespread degradation of polyvinyl alcohol in aqueous solutions occurs at frequencies of 23, 40, and 900 kHz. Latest research had shown that as the frequency is raised, the deterioration rate lowers. Although it is legitimate to acknowledge that physical effects are frequency dependent, the frequency-dependent behavior of physical effects requires further exploration.

21.7.3 Large-size sonochemical reactor

An effective scale-up of the sonochemical reactors is necessary to broaden the industrial use of sonochemistry. The influence of liquid height or irradiation volume on sonochemical reactions is a significant problem in the scale-up of sonochemical reactors.

21.7.3.1 Effect of liquid height

Recently, Asakura et al. (Asakura et al., 2008) have used cylindrical reactor 70 mm in diameter. The sonochemical efficiency of the cylindrical sonochemical reactor has been investigated as a function of frequency and liquid height when the irradiation frequencies were 45, 129, 231, and 490 kHz. The liquid height varied from 10 to 700 mm. The sonochemical efficiency of the cylindrical reactor was evaluated by KI dosimetry and calorimetry. The value of sonochemical efficiency for each frequency was discovered to be dependent on the liquid height. The fluctuation in sonochemical efficiency with frequency at liquid heights of 30, 100, and 500 mm, as well as comparative data from Koda et al. (Koda et al., 2003). Although the experimental parameters, such as reactor types and irradiation techniques, differ in these both investigations, the frequency dependence of the sonochemical efficiency value for a liquid height of 100 mm is relatively comparable. The sonochemical efficiency value at 45 kHz is quite low for a liquid height of 30 mm, and the peak occurs at a high frequency. With an increase in frequency to around 200 kHz, the sonochemical efficiency value drops for a liquid height of 500 mm; above 200 kHz, it tends to grow. It should be noted that the sonochemical efficiency value at a liquid height of 500 mm at a frequency of 45 kHz is roughly eight times the sonochemical efficiency value assessed at the laboratory scale by Koda et al. (Koda et al., 2003).

21.7.3.2 Large-scale sonochemical reactor

Chemical impacts research has primarily been carried out in laboratory-scale sonochemical reactors with volumes of less than 1 dm^3. To put sonochemical wastewater treatment and material processing into practice, a large sonochemical reactor on a pilot size (greater than 100 dm^3) or an industrial size must be designed and developed (more than 1 m^3). Large sonochemical reactors have been studied by a number of researchers.

Large-scale sonochemical reactors with a low frequency of 20–50 kHz have been created. Mason (Mason, 1992) discussed the many forms of large-scale sonochemical reactors (cleaning bath, submersible transducer assembly, probe system, and flow system). Hexagonal column sonochemical reactor was created by Gogate et al. (Gogate et al., 2003). Each sidewall of the reactor included three types of transducers operating at 20, 30, and 50 kHz, and the sample volume was 7.5 dm^3. Asakura et al. (Asakura et al., 2007) employed a large-scale sonochemical reactor operating at 44.3 kHz and measuring 350 mm × 350 mm × 850 mm on the inside (height). Thirteen transducers in the device were fastened to the reactor bottom with a stainless steel plate. They investigated examined the impact of liquid height on the sonochemical reaction in the range of 87 to 592 mm, which corresponded to a sample volume of roughly 18–80 dm^3. The sonochemical efficiency was nearly six times that of a laboratory-scale sonochemical reactor with a volume of less than 0.2 dm^3.

There have been reports of large-scale sonochemical reactors operating at high frequencies of 200–600 kHz. Gonze et al. (1998) built a 500 kHz cylindrical reactor with a diameter of 300 mm. The reactor, which has a capacity of 28 dm^3, has three transducers at the bottom. They also created a variety of 500 kHz sonochemical reactors and compared the performance of the sonochemical reactions. Destaillats et al. (2001) designed a sonochemical reactor with a capacity of 6 dm^3 using four 612 kHz transducers. They found that the degradation reaction rate of dichloromethane in water was 3 to 7 times faster than in small-scale reactors.

Asakura et al. (Asakura et al., 2008) built a 500 kHz large-scale sonochemical reactor with interior dimensions of 508 mm × 508 mm × 672 mm (height) with 12 transducers at the bottom. They used this reactor to study the influence of liquid height on the sonochemical reaction in the range of 300 to 500 mm for sample volumes ranging from 77 to 131 dm^3. Both findings are comparable, with a maximum value of sonochemical efficiency of roughly 400 mm in both cases. This is due to the great directivity of ultrasonic propagation at 500 kHz, and the sonochemical reaction fields only extend a little in a direction perpendicular to ultrasonic propagation.

21.8 Future prospects for the scale-up of sonochemistry

Although changes in the field of sonochemistry have been occurring gradually, but advances in the ultrasonic technology will certainly help to advance sonochemistry itself. There are numerous fields that will see great advances in sonochemistry in coming years but many of these will be on a small scale or at an academic level. It will make a major impact in larger-scale projects once it will trigger the interest of industry and establish the topic in mainstream chemistry.

In the past, using power ultrasound in a process was accepted if it proved to be simply a better method than the existing technology. However, the sonochemical process was not optimized. A much greater input from chemical engineering and computer modeling can be evidenced in the design of the next generation of sonochemical reactors (Mason, 1999). This advancement will certainly scale-up of sonochemistry itself and this drive will be a move toward benign synthesis. The application of sonochemistry in electrochemistry and environmental protection are two study fields that will probably develop in the near future.

The use of sonochemistry in electrochemical reaction can enhance a number of beneficial sonoelectrochemical effects follow from this, including enhanced mass transport; altered adsorption phenomena and surface effects; diminishing of electrode fouling; manipulation of reaction mechanisms; production of altered product distributions; increased yields and current efficiencies; improved synthetic routes, increased limiting current in analytical applications, and lessened cell power requirements.

The environmental sonochemistry has also been a major growth area. However, the amount of energy required to remove chemical contaminants from water is large so it is not likely that sonochemistry will and immediate industrial use in that particular field. Research into the sonolysis of aqueous solutions of chemicals will, however, continue to be in the mainstream of academic research since it is a valuable probe for the chemical effects of cavitation. A few groups have investigated the uses of ultrasound for microbiological decontamination. Although bacteria are difficult to kill with ultrasound in the absence of a bactericide, larger biological contaminants such as plankton and algae can be destroyed using low-power ultrasound without the need for additional chemicals. This does provide a real possibility for future development with several technologies approaching realization.

There is still much to be done, but the outlook for sonochemistry is optimistic, and with the combined efforts of chemists, physicists, and engineers, power ultrasound will be regarded a feasible alternative for future chemical facilities.

21.9 Conclusion

The focus of this chapter has been on a limited number of sonoprocesses in which we have been actively engaged and which are currently in the industrial or semi-industrial stages. It is worth noting that certain methods have already been scaled up to industrial grade. Ultrasound is an energy-intensive technology, therefore additional innovations are expected to bring significant value. Ultrasound operations are economically viable due to cheap maintenance and competitive energy prices. This criterion can be met by a wide range of applications that are well-established or have great future potential. Despite this, the innovative technology's potential remains relatively unexplored. This study seeks to emphasize the characteristics and routes where sonochemistry meets other nonconventional approaches, as well as comparative factors and solutions for overcoming obstacles, where possible. The scientific method emphasizes a multidisciplinary approach to better knowledge and the potential to predict future behavior. In other words, it is in our best interests to take a comprehensive approach to process intensification and technology innovation.

References

Adewuyi, Y.G., 2001. Sonochemistry: environmental science and engineering applications. Ind. Eng. Chem. Res. 40 (22), 4681–4715. https://doi.org/10.1021/ie010096l.

Adewuyi, Y.G., 2005. Sonochemistry in environmental remediation. 1. Combinative and hybrid sonophotochemical oxidation processes for the treatment of pollutants in water. Environ. Sci. Technol. 39 (10), 3409–3420. https://doi.org/10.1021/es049138y.

Al-Juboori, R.A., Yusaf, T., Bowtell, L., 2015a. Energy conversion efficiency of pulsed ultrasound. Energy Procedia 75, 1560–1568. https://doi.org/10.1016/j.egypro.2015.07.340.

Al-Juboori, R.A., Yusaf, T., Bowtell, L., Aravinthan, V., 2015b. Energy characterisation of ultrasonic systems for industrial processes. Ultrasonics 57 (C), 18–30. https://doi.org/10.1016/j.ultras.2014.10.003.

Asakura, Y., Ishio, K., Kojima, Y., Kato, D., Fukutomi, S., Yasuda, K., Koda, S., 2007. Effect of liquid height on sonochemical reaction in a large-scale reactor of a rectangular parallelepiped using low frequency ultrasound. J. Chem. Eng. Jpn. 40 (12), 1088–1092. https://doi.org/10.1252/jcej.07WE087.

Asakura, Y., Nishida, T., Matsuoka, T., Koda, S., 2008. Effects of ultrasonic frequency and liquid height on sonochemical efficiency of large-scale sonochemical reactors. Ultrason. Sonochem. 15 (3), 244–250. https://doi.org/10.1016/j.ultsonch.2007.03.012.

Avern, N., Copercini, P.A., 1997. Ultrasonic technology improves drill cuttings disposal. World Oil 218 (7), 75–78.

Awad, T.S., Moharram, H.A., Shaltout, O.E., Asker, D., Youssef, M.M., 2012. Applications of ultrasound in analysis, processing and quality control of food: a review. Food Res. Int. 48 (2), 410–427. https://doi.org/10.1016/j.foodres.2012.05.004.

Banerjee, R.K., Dasgupta, S., 2010. Characterization methods of high-intensity focused ultrasound-induced thermal field. Adv. Heat Transfer 42 (C), 137–177. https://doi.org/10.1016/S0065-2717(10)42002-X.

Barton, A.C., Collyer, S.D., Davis, F., Gornall, D.D., Law, K.A., Lawrence, E.C.D., Mills, D.W., Myler, S., Pritchard, J.A., Thompson, M., Higson, S.P.J., 2004. Sonochemically fabricated microelectrode arrays for biosensors offering widespread applicability: part i. Biosens. Bioelectron. 20 (2), 328–337. https://doi.org/10.1016/j.bios.2004.02.002.

Berlan, J., Mason, T.J., 1992. Sonochemistry: from research laboratories to industrial plants. Ultrasonics 30 (4), 203–212. https://doi.org/10.1016/0041-624X(92)90078-Z.

Bhirud, U.S., Gogate, P.R., Wilhelm, A.M., Pandit, A.B., 2004. Ultrasonic bath with longitudinal vibrations: a novel configuration for efficient wastewater treatment. Ultrasonics Sonochem. 11 (Issues 3–4), 143–147. https://doi.org/10.1016/j.ultsonch.2004.01.010.

Bielski, B.H.J., Cabelli, D.E., Arudi, R.L., Ross, A.B., 1985. Reactivity of HO2/O−2 radicals in aqueous solution. J. Phys. Chem. Ref. Data 14 (4), 1041–1100. https://doi.org/10.1063/1.555739.

Brotchie, A., Grieser, F., Ashokkumar, M., 2009a. Effect of power and frequency on bubble-size distributions in acoustic cavitation. Phys. Rev. Lett. 102 (8). doi:10.1103/PhysRevLett.102.084302.

Brotchie, A., Grieser, F., Ashokkumar, M., 2009b. Effect of power and frequency on bubble-size distributions in acoustic cavitation. Phys. Rev. Lett. 102 (8). doi:10.1103/PhysRevLett.102.084302.

Busnel, R.-G., Picard, D., Bouzigues, H., 1953. Rapports entre la longueur d'onde et l'oxydation de l'iodure de potassium par les ultrasons. J. de Chimie Physique 97–101. doi:10.1051/jcp/1953500097.

Cau, C., Nikitenko, S.I., 2012. Mechanism of W(CO)6 sonolysis in diphenylmethane. Ultrason. Sonochem. 19 (3), 498–502. https://doi.org/10.1016/j.ultsonch.2011.10.003.

Chen, D., 2012. Applications of Ultrasound in Water and Wastewater Treatment. In: Handbook on Applications of Ultrasound. CRC Press, Florida, USA, pp. 395–428.

Chen, D., Sharma, S.K., Mudhoo, A. (Eds.), 2012. Handbook on applications of ultrasound: sonochemistry for sustainability. CRC press. Florida, USA.

Chen, W.S., Huang, Y.L., 2011. Removal of dinitrotoluenes and trinitrotoluene from industrial wastewater by ultrasound enhanced with titanium dioxide. Ultrason. Sonochem. 18 (5), 1232–1240. https://doi.org/10.1016/j.ultsonch.2010.11.014.

Chowdhury, P., Viraraghavan, T., 2009. Sonochemical degradation of chlorinated organic compounds, phenolic compounds and organic dyes—a review. Sci. Total Environ. 407 (8), 2474–2492. https://doi.org/10.1016/j.scitotenv.2008.12.031.

Ciawi, E., Rae, J., Ashokkumar, M., Grieser, F., 2006. Determination of temperatures within acoustically generated bubbles in aqueous solutions at different ultrasound frequencies. J. Phys. Chem. B 110 (27), 13656–13660. https://doi.org/10.1021/jp061441t.

Compton, R.G., Eklund, J.C., Marken, F., 1997. Sonoelectrochemical processes: a review. Electroanalysis 9 (7), 509–522. https://doi.org/10.1002/elan.1140090702.

Cui, W., Qi, S., Chen, W., Zhou, C., Tu, J., 2012. Effect of alcohol on single-bubble sonoluminescence. Phys. Rev. E 85 (2). doi:10.1103/physreve.85.026304.

Destaillats, H., Hoffmann, M.R., Wallace, H.C., 2003. Sonochemical degradation of pollutants. In: Chemical Degradation Methods For Wastes and Pollutants, (Ed. M. A. Tarr). Marcel Dekker Inc., New York, USA, pp. 191–220.

Doktycz, S.J., Suslick, K.S., 1990. Interparticle collisions driven by ultrasound. Science 247 (4946), 1067–1069. https://doi.org/10.1126/science.2309118.

Eskin, D.G., Tzanakis, I., 2018. High-frequency vibration and ultrasonic processing. Springer Series in Materials Science, 273. Springer Verlag, Switzerland, pp. 153–193.

Feng, H., Yang, W., Hielscher, T., 2008. Power ultrasound. Food Sci. Technol. Int. 14 (5), 433–436. https://doi.org/10.1177/1082013208098814.

Gallego-Juarez, J.A., Riera, E., Acosta, V., Rodríguez, G., Blanco, A., 2010. Ultrasonic system for continuous washing of textiles in liquid layers. Ultrason. Sonochem. 17 (1), 234–238. https://doi.org/10.1016/j.ultsonch.2009.06.005.

Gallego-Juárez, J.A., Rodriguez, G., Acosta, V., Riera, E., 2010. Power ultrasonic transducers with extensive radiators for industrial processing. Ultrason. Sonochem. 17 (6), 953–964. https://doi.org/10.1016/j.ultsonch.2009.11.006.

Gogate, P.R., 2007. Application of cavitational reactors for water disinfection: current status and path forward. J. Environ. Manage. 85 (4), 801–815. https://doi.org/10.1016/j.jenvman.2007.07.001.

Gogate, P.R., Mujumdar, S., Pandit, A.B., 2003. Large-scale sonochemical reactors for process intensification: design and experimental validation. J. Chem. Technol. Biotechnol. 78 (6), 685–693. https://doi.org/10.1002/jctb.697.

Gogate, P.R., Pandit, A.B., 2004. Sonochemical reactors: scale up aspects. Ultrasonics Sonochemistry, 11. Elsevier, pp. 105–117.

Gogate, P.R., Sutkar, V.S., Pandit, A.B., 2011. Sonochemical reactors: important design and scale up considerations with a special emphasis on heterogeneous systems. Chem. Eng. J. 166 (3), 1066–1082. https://doi.org/10.1016/j.cej.2010.11.069.

González-García, J., Esclapez, M.D., Bonete, P., Hernández, Y.V., Garretón, L.G., Sáez, V., 2010. Current topics on sonoelectrochemistry. Ultrasonics, 50 (2), 318–322.

Grčić, I., Obradović, M., Vujević, D., Koprivanac, N., 2010. Sono-Fenton oxidation of formic acid/formate ions in an aqueous solution: from an experimental design to the mechanistic modeling. Chem. Eng. J. 164 (1), 196–207. https://doi.org/10.1016/j.cej.2010.08.059.

Grönroos, A., Pirkonen, P., Heikkinen, J., Ihalainen, J., Mursunen, H., Sekki, H., 2001. Ultrasonic depolymerization of aqueous polyvinyl alcohol. Ultrasonics Sonochemistry 8 (3), 259–264. https://doi.org/10.1016/S1350-4177(01)00086-4.

Hua, I., Hochemer, R.H., Hoffmann, M.R., 1995. Sonochemical degradation of p-nitrophenol in a parallel-plate near-field acoustical processor. Environ. Sci. Technol. 29 (11), 2790–2796. https://doi.org/10.1021/es00011a014.

Hung, H.M., Hoffmann, M.R., 1999. Kinetics and mechanism of the sonolytic degradation of chlorinated hydrocarbons: frequency effects. J. Phys. Chem. A 103 (15), 2734–2739. https://doi.org/10.1021/jp9845930.

Jaksukam, K., Umchid, S., 2011. A primary level ultrasonic power measurement system developed at National Institute of Metrology, Thailand. Int. J. Applied Biomed. Eng. 4 (1), 24–29.

Juarez, A.G., Corral, G.R., de Parga, G.N.V., Martinez, F.V., van der Vlist, P., 2001. Process and device for continuous ultrasonic washing of textile. U.S. Patent No. 6,266,836. U.S. Patent and Trademark Office, Washington DC, USA.

Jung, S.H., Oh, E., Lee, K.H., Yang, Y., Park, C.G., Park, W., Jeong, S.H., 2008. Sonochemical preparation of shape-selective zno nanostructures. Cryst. Growth Des. 8 (1), 265–269. https://doi.org/10.1021/cg070296l.

Kamel, M.M., Helmy, H.M., Mashaly, H.M., Kafafy, H.H., 2010. Ultrasonic assisted dyeing: dyeing of acrylic fabrics C.I. astrazon basic red 5BL 200%. Ultrason. Sonochem. 17 (1), 92–97. https://doi.org/10.1016/j.ultsonch.2009.06.001.

Kandjani, A.E., Tabriz, M.F., Pourabbas, B., 2008. Sonochemical synthesis of zno nanoparticles: the effect of temperature and sonication power. Mater. Res. Bull. 43 (3), 645–654. https://doi.org/10.1016/j.materresbull.2007.04.005.

Karaböce, B., Sadikoğlu, E., Bilgiç, E., 2011. Ultrasound power measurements of hitu transducer with a more stable radiation force balance. J. Phys. Conf. Ser. 279 (1), 012014. https://doi.org/10.1088/1742-6596/279/1/012014.

Kass, M.D., 2000. Ultrasonically induced fragmentation and strain in alumina particles. Mater. Lett. 42 (4), 246–250. https://doi.org/10.1016/S0167-577X(99)00192-5.

Katekhaye, S.N., Gogate, P.R., 2011. Intensification of cavitational activity in sonochemical reactors using different additives: efficacy assessment using a model reaction. Chem. Eng. Process. 50 (1), 95–103. https://doi.org/10.1016/j.cep.2010.12.002.

Kim, H.J., Chi, M.H., Hong, I.K., 2009. Effect of ultrasound irradiation on solvent extraction process. J. Ind. Eng. Chem. 15 (6), 919–928. https://doi.org/10.1016/j.jiec.2009.09.025.

Kim, K.S., Mizuno, Y., Nakamura, K., 2014. Fiber-optic ultrasonic hydrophone using short fabry-perot cavity with multilayer reflectors deposited on small stub. Ultrasonics 54 (4), 1047–1051. https://doi.org/10.1016/j.ultras.2013.12.009.

Kobayashi, T., Chai, X., Fujii, N., 1999. Ultrasound enhanced cross-flow membrane filtration. Sep. Purif. Technol. 17 (1), 31–40. https://doi.org/10.1016/S1383-5866(99)00023-4.

Koda, S., Kimura, T., Kondo, T., Mitome, H., 2003. A standard method to calibrate sonochemical efficiency of an individual reaction system. Ultrason. Sonochem. 10 (3), 149–156. https://doi.org/10.1016/S1350-4177(03)00084-1.

Koda, S., Taguchi, K., Futamura, K., 2011. Effects of frequency and a radical scavenger on ultrasonic degradation of water-soluble polymers. Ultrason. Sonochem. 18 (1), 276–281. https://doi.org/10.1016/j.ultsonch.2010.06.007.

Kojima, Y., Asakura, Y., Sugiyama, G., Koda, S., 2010. The effects of acoustic flow and mechanical flow on the sonochemical efficiency in a rectangular sonochemical reactor. Ultrason. Sonochem. 17 (6), 978–984. https://doi.org/10.1016/j.ultsonch.2009.11.020.

Kojima, Y., Koda, S., Nomura, H., 2001. Effect of ultrasonic frequency on polymerization of styrene under sonication. Ultrason. Sonochem. 8 (2), 75–79. https://doi.org/10.1016/S1350-4177(00)00064-X.

Kotronarou, A., Hoffmann, M.R., 1995. The chemical effects of collapsing cavitation bubbles. American Chemical Soc. 233–251. doi:10.1021/ba-1995-0244.ch012.

Kotronarou, A., Mills, G., Hoffmann, M.R., 1992. Oxidation of hydrogen sulfide in aqueous solution by ultrasonic irradiation. Environ. Sci. Technol. 26 (12), 2420–2428. https://doi.org/10.1021/es00036a013.

Krefting, D., Mettin, R., Lauterborn, W., 2004. High-speed observation of acoustic cavitation erosion in multibubble systems. Ultrasonics Sonochemistry, 11. Elsevier, pp. 119–123.

Kumar, A., Gogate, P.R., Pandit, A.B., 2007. Mapping the efficacy of new designs for large scale sonochemical reactors. Ultrason. Sonochem. 14 (5), 538–544. https://doi.org/10.1016/j.ultsonch.2006.11.005.

Kyllönen, H., Pirkonen, P., Nyström, M., Nuortila-Jokinen, J., Grönroos, A., 2006. Experimental aspects of ultrasonically enhanced cross-flow membrane filtration of industrial wastewater. Ultrason. Sonochem. 13 (4), 295–302. https://doi.org/10.1016/j.ultsonch.2005.04.006.

Lamminen, M.O., Walker, H.W., Weavers, L.K., 2004. Mechanisms and factors influencing the ultrasonic cleaning of particle-fouled ceramic membranes. J. Membr. Sci. 237 (1–2), 213–223. https://doi.org/10.1016/j.memsci.2004.02.031.

Lauterborn, W., Holzfuss, J., 1986. Evidence for a low-dimensional strange attractor in acoustic turbulence. Phys. Lett. A 115 (8), 369–372. https://doi.org/10.1016/0375-9601(86)90278-1.

Leadley, C.E., Williams, A., 2005. Pulsed electric field processing, power ultrasound and other emerging technologies. Food Processing Handbook https://doi.org/10.1002/3527607579.ch7.

Lee, J., Kentish, S., Ashokkumar, M., 2005. Effect of surfactants on the rate of growth of an air bubble by rectified diffusion. J. Phys. Chem. B 109 (30), 14595–14598. https://doi.org/10.1021/jp051758d.

Lee, K.W., Kim, J.P., 2001. Effect of ultrasound on disperse dye particle size. Text. Res. J. 71 (5), 395–398. https://doi.org/10.1177/004051750107100505.

Leighton, T., 2012. The acoustic bubble. Academic press. London, UK.

Leighton, T.G., 1997. A strategy for the development and standardisation of measurement methods for high power/cavitating ultrasonic fields: review of cavitation monitoring techniques. ISVR Technical Report No. 263, Inst. Sound and Vibrat. Res., Southampton, UK.

Leighton, T.G., 1995. Bubble population phenomena in acoustic cavitation. Ultrasonics—Sonochem. 2 (2), S123–S136. https://doi.org/10.1016/1350-4177(95)00021-W.

Leong, T., Wu, S., Kentish, S., Ashokkumar, M., 2010. Growth of bubbles by rectified diffusion in aqueous surfactant solutions. J. Phys. Chem. C 114 (47), 20141–20145. https://doi.org/10.1021/jp107731j.

Leong, Thomas, Yasui, K., Kato, K., Harvie, D., Ashokkumar, M., Kentish, S., 2014. Effect of surfactants on single bubble sonoluminescence behavior and bubble surface stability. Phys. Rev. E 89 (4). doi:10.1103/physreve.89.043007.

Ley, S.V., Low, C.M., 2012. Ultrasound in synthesis (Vol. 27). Spri. Sci. Bus. Med. Berlin, Germany.

Lorimer, J.P., Mason, T.J., 1987. Sonochemistry. part 1 - The physical aspects. Chem. Soc. Rev. 16, 239–274. https://doi.org/10.1039/CS9871600239.

Lotya, M., Hernandez, Y., King, P.J., Smith, R.J., Nicolosi, V., Karlsson, L.S., Blighe, F.M., De, S., Zhiming, W., McGovern, I.T., Duesberg, G.S., Coleman, J.N., 2009. Liquid phase production of graphene by exfoliation of graphite in surfactant/water solutions. J. Am. Chem. Soc. 131 (10), 3611–3620. https://doi.org/10.1021/ja807449u.

Madhavan, J., Grieser, F., Ashokkumar, M., 2010. Combined advanced oxidation processes for the synergistic degradation of ibuprofen in aqueous environments. J. Hazard. Mater. 178 (1–3), 202–208. https://doi.org/10.1016/j.jhazmat.2010.01.064.

Mahamuni, N.N., Adewuyi, Y.G., 2010. Advanced oxidation processes (AOPs) involving ultrasound for waste water treatment: a review with emphasis on cost estimation. Ultrason. Sonochem. 17 (6), 990–1003. https://doi.org/10.1016/j.ultsonch.2009.09.005.

Marangopoulos, I.P., Martin, C.J., Hutchison, J.M.S., 1995. Measurement of field distributions in ultrasonic cleaning baths: implications for cleaning efficiency. Phys. Med. Biol. 40 (11), 1897–1908. https://doi.org/10.1088/0031-9155/40/11/009.

Mark, G., Tauber, A., Laupert, R., Schuchmann, H.P., Schulz, D., Mues, A., Von Sonntag, C, 1998. OH-radical formation by ultrasound in aqueous solution—Part II: terephthalate and fricke dosimetry and the influence of various conditions on the sonolytic yield. Ultrason. Sonochem. 5 (2), 41–52. https://doi.org/10.1016/S1350-4177(98)00012-1.

Mason, T.J., 1999. Ultrasonically assisted extraction of bioactive principles from plants and their constituents. Adv. Sonochem. 5, 209–248.

Mason, T.J., Lorimer, J.P., 2002. Applied sonochemistry: the uses of power ultrasound in chemistry and processing (Vol. 10). Weinheim: Wiley-Vch., Germany.

Mason, T.J., Lorimer, J.P., 1998. Sonochemical theory, application and uses of ultrasound in chemistry. Ellis Horwood Publishers, Prentice Hall, New Jersey, USA.

Mason, T.J., de Meulenaer, E.C., 1998. Practical considerations for process optimisation. In: Synthetic Organic Sonochemistry, (Ed. J-L. Luche). Springer, Massachusetts, USA, pp. 301–329. https://doi.org/10.1007/978-1-4899-1910-6.

Mason, T.J., 1992. Industrial sonochemistry: potential and practicality. Ultrasonics 30 (3), 192–196. https://doi.org/10.1016/0041-624X(92)90072-T.

Mason, T.J., 2000. Large scale sonochemical processing: aspiration and actuality. Ultrason. Sonochem. 7 (4), 145–149. https://doi.org/10.1016/S1350-4177(99)00041-3.

Mason, T.J., 2003. Sonochemistry and sonoprocessing: the link, the trends and (probably) the future. Ultrasonics Sonochem. 10 (Issues 4–5), 175–179. https://doi.org/10.1016/S1350-4177(03)00086-5.

Mason, T.J., 2012. Trends in sonochemistry and ultrasonic processing. In: AIP Conference Proceedings, 1433, pp. 21–26.

Mason, T.J., Lorimer, J.P., Walton, D.J., 1990. Sonoelectrochemistry. Ultrasonics 28 (5), 333–337. https://doi.org/10.1016/0041-624X(90)90041-L.

Merouani, S., Hamdaoui, O., Rezgui, Y., Guemini, M., 2016. Computational engineering study of hydrogen production via ultrasonic cavitation in water. Int. J. Hydrogen Energy 41 (2), 832–844. https://doi.org/10.1016/j.ijhydene.2015.11.058.

Merouani, S., Hamdaoui, O., Rezgui, Y., Guemini, M., 2013. Effects of ultrasound frequency and acoustic amplitude on the size of sonochemically active bubbles-Theoretical study. Ultrason. Sonochem. 20 (3), 815–819. https://doi.org/10.1016/j.ultsonch.2012.10.015.

Merouani, S., Hamdaoui, O., Rezgui, Y., Guemini, M., 2014. Theoretical estimation of the temperature and pressure within collapsing acoustical bubbles. Ultrason. Sonochem. 21 (1), 53–59. https://doi.org/10.1016/j.ultsonch.2013.05.008.

Moore, S.B., Ausley, L.W., 2004. Systems thinking and green chemistry in the textile industry: concepts, technologies and benefits. J. Clean. Production 12 (6), 585–601. https://doi.org/10.1016/S0959-6526(03)00058-1.

Muthukumaran, S., Yang, K., Seuren, A., Kentish, S., Ashokkumar, M., Stevens, G.W., Grieser, F., 2004. The use of ultrasonic cleaning for ultrafiltration membranes in the dairy industry. Sep. Purif. Technol. 39 (1–2), 99–107. https://doi.org/10.1016/j.seppur.2003.12.013.

Naddeo, V., Belgiorno, V., Kassinos, D., Mantzavinos, D., Meric, S., 2010. Ultrasonic degradation, mineralization and detoxification of diclofenac in water: optimization of operating parameters. Ultrason. Sonochem. 17 (1), 179–185. https://doi.org/10.1016/j.ultsonch.2009.04.003.

Okitsu, K., Ashokkumar, M., Grieser, F., 2005. Sonochemical synthesis of gold nanoparticles: effects of ultrasound frequency. J. Phys. Chem. B 109 (44), 20673–20675. https://doi.org/10.1021/jp0549374.

Pang, Y.L., Abdullah, A.Z., Bhatia, S., 2011. Review on sonochemical methods in the presence of catalysts and chemical additives for treatment of organic pollutants in wastewater. Desalination 277 (1–3), 1–14. https://doi.org/10.1016/j.desal.2011.04.049.

Pestman, J.M., Engberts, J.B.F.N., de Jong, F., 1994. Sonochemistry: theory and applications. recueil des travaux chimiques des pays-bas, 113(12), 533–542. https://doi.org/10.1002/recl.19941131202

Peters, D., 1996. Ultrasound in materials chemistry. J. Mater. Chem. 6 (10), 1605–1618. https://doi.org/10.1039/jm9960601605.

Pétrier, C., Francony, A., 1997. Ultrasonic waste-water treatment: incidence of ultrasonic frequency on the rate of phenol and carbon tetrachloride degradation. Ultrason. Sonochem. 4 (4), 295–300. https://doi.org/10.1016/S1350-4177(97)00036-9.

Phull, S.S., Mason, T.J., 1999. The use of ultrasound in microbiology. Advances in Sonochemistry, 5. (Ed. T. J. Mason). JAI press, Elsevier, Connecticut, USA, pp. 176–208.

Pilli, S., Bhunia, P., Yan, S., LeBlanc, R.J., Tyagi, R.D., Surampalli, R.Y., 2011. Ultrasonic pretreatment of sludge: a review. Ultrason. Sonochem. 18 (1), 1–18. https://doi.org/10.1016/j.ultsonch.2010.02.014.

Pokhrel, N., Vabbina, P.K., Pala, N., 2016. Sonochemistry: science and engineering. Ultrasonics Sonochem. 29, 104–128. https://doi.org/10.1016/j.ultsonch.2015.07.023.

Price, G.J., Ashokkumar, M., Grieser, F., 2004. Sonoluminescence quenching of organic compounds in aqueous solution: frequency effects and implications for sonochemistry. J. Am. Chem. Soc. 126 (9), 2755–2762. https://doi.org/10.1021/ja0389624.

Prozorov, T., Prozorov, R., Suslick, K.S., 2004. High velocity interparticle collisions driven by ultrasound. J. Am. Chem. Soc. 126 (43), 13890–13891. https://doi.org/10.1021/ja049493o.

Rae, J., Ashokkumar, M., Eulaerts, O., Von Sonntag, C., Reisse, J., Grieser, F., 2005. Estimation of ultrasound induced cavitation bubble temperatures in aqueous solutions. Ultrason. Sonochem. 12 (5), 325–329. https://doi.org/10.1016/j.ultsonch.2004.06.007.

Raj, B., Rajendran, V., Palanichamy, P., 2004. Science and technology of ultrasonics. Alpha Science International Ltd. Oxford, UK.

Rashwan, S.S., Dincer, I., Mohany, A., Pollet, B.G., 2019. The sono-hydro-gen process (Ultrasound induced hydrogen production): challenges and opportunities. Int. J. Hydrogen Energy 44 (29), 14500–14526. https://doi.org/10.1016/j.ijhydene.2019.04.115.

Rastogi, N.K., 2011. Opportunities and challenges in application of ultrasound in food processing. Crit. Rev. Food Sci. Nutr. 51 (8), 705–722. https://doi.org/10.1080/10408391003770583.

Rawson, F.F., 1987. Ultrasonic technology in today's industry. Physics Bulletin 255–257. doi:10.1088/0031-9112/38/7/020.

Riera-Franco De Sarabia, E., Gallego-Juárez, J.A., Rodríguez-Corral, G., Elvira-Segura, L., González-Gómez, I., 2000. Application of high-power ultrasound to enhance fluid/solid particle separation processes. Ultrasonics 38 (1), 642–646. https://doi.org/10.1016/S0041-624X(99)00129-8.

Shaw, A., Hodnett, M., 2008. Calibration and measurement issues for therapeutic ultrasound. Ultrasonics 48 (4), 234–252. https://doi.org/10.1016/j.ultras.2007.10.010.

Shukla, S.R., Mathur, M.R., 1995. Low-temperature ultrasonic dyeing of silk. J. Soc. Dyers Colour. 111 (11), 342–345. https://doi.org/10.1111/j.1478-4408.1995.tb01681.x.

Silva, G.T., 2010. Dynamic radiation force of acoustic waves on absorbing spheres. Braz. J. Phys. 40 (2), 184–187. https://doi.org/10.1590/S0103-97332010000200010.

Singh, D.M.D.J., Pradeep, T., Bhattacharjee, J., Waghmare, U.V., 2007. Closed-Cage clusters in the gaseous and condensed phases derived from sonochemically synthesized mos2 nanoflakes. J. Am. Soc. Mass Spectrom. 18 (12), 2191–2197. https://doi.org/10.1016/j.jasms.2007.09.020.

Singla, M., Sit, N., 2021. Application of ultrasound in combination with other technologies in food processing: a review. Ultrason. Sonochem. 73, 105506. https://doi.org/10.1016/j.ultsonch.2021.105506.

Sivakumar, V., Rao, P.G., 2003. Studies on the use of power ultrasound in leather dyeing. Ultrason. Sonochem. 10 (2), 85–94. https://doi.org/10.1016/S1350-4177(02)00148-7.

Sivakumar, V., Swaminathan, G., Rao, P.G., Ramasami, T., 2009. Sono-leather technology with ultrasound: a boon for unit operations in leather processing - review of our research work at Central Leather Research Institute (CLRI), India. Ultrasonics Sonochem. 16 (1), 116–119. https://doi.org/10.1016/j.ultsonch.2008.06.002.

Soltani Firouz, M., Farahmandi, A., Hosseinpour, S., 2019. Recent advances in ultrasound application as a novel technique in analysis, processing and quality control of fruits, juices and dairy products industries: a review. Ultrason. Sonochem. 57, 73–88. https://doi.org/10.1016/j.ultsonch.2019.05.014.

Stack, L.J., Carney, P.A., Malone, H.B., Wessels, T.K., 2005. Factors influencing the ultrasonic separation of oil-in-water emulsions. Ultrason. Sonochem. 12 (3), 153–160. https://doi.org/10.1016/j.ultsonch.2003.10.008.

Stewart, H.F., 1982. Ultrasonic measurement techniques and equipment output levels. Springer Science and Business Media LLC. In: Essentials of medical ultrasound, (Eds. M. H. Repacholi and D. A. Benwell). Humana Press Inc. New Jersey, USA, pp. 77–116.

Suslick, Kenneth S., 1989. The chemical effects of ultrasound. Sci. Am. 260 (2), 80–86. https://doi.org/10.1038/scientificamerican0289-80.

Suslick, K.S., 1990. Sonochemistry. Science 247 (4949), 1439–1445. https://doi.org/10.1126/science.247.4949.1439.

Sutkar, V.S., Gogate, P.R., 2009. Design aspects of sonochemical reactors: techniques for understanding cavitational activity distribution and effect of operating parameters. Chem. Eng. J. 155 (1–2), 26–36. https://doi.org/10.1016/j.cej.2009.07.021.

Szabo, T.L., 2004. Diagnostic ultrasound imaging: inside out. Academic press, London, UK.

Tang, W.Z., 2003. Physicochemical treatment of hazardous wastes. CRC Press, Boca Raton, Florida, USA.

Thakore, K.A., Smith, C.B., Hite, D., Carlough, M., 1990. Short communication. the effects of ultrasound and the diffusion coefficient of C.I. direct red 81 in cellulose. Text. Chem. Color. 22 (11), 21–22.

Thangavadivel, K., Megharaj, M., Mudhoo, A., Naidu, R., 2012. 18 Degradation of organic pollutants using ultrasound. In: Handbook on applications of ultrasound: sonochemistry for sustainability (Eds. Chen, D., Sharma, S. K., Mudhoo, A.). CRC press, Florida, USA. pp. 447–474.

Tiehm, A., Nickel, K., Neis, U., 1997. The use of ultrasound to accelerate the anaerobic digestion of sewage sludge. Water Science and Technology, 36. Elsevier Science Ltd, pp. 121–128.

Toma, M., Fukutomi, S., Asakura, Y., Koda, S., 2011. A calorimetric study of energy conversion efficiency of a sonochemical reactor at 500kHz for organic solvents. Ultrason. Sonochem. 18 (1), 197–208. https://doi.org/10.1016/j.ultsonch.2010.05.005.

Tripathi, P., Shrivastava, S.K., Bhambhani, P., Verma, S.K., Khare, V.K., 2019. Ultrasonics: past, present & future. Int. J. Eng. Development Res. 7 (3), 611–615.

Vabbina, P.K., Karabiyik, M., Al-Amin, C., Pala, N., Das, S., Choi, W., Saxena, T., Shur, M., 2014. Controlled synthesis of single-crystalline zno nanoflakes on arbitrary substrates at ambient conditions. Particle Particle Syst. Characterization, 31(2), 190–194. https://doi.org/10.1002/ppsc.201300208

Vajnhandl, S., Majcen Le Marechal, A., 2005. Ultrasound in textile dyeing and the decolouration/mineralization of textile dyes. Dyes Pigm. 65 (2), 89–101. https://doi.org/10.1016/j.dyepig.2004.06.012.

Viculis, L.M., Mack, J.J., Kaner, R.B., 2003. A chemical route to carbon nanoscrolls.(Brevia). Science 5611, 1361–1362.

Vouters, M., Rumeau, P., Tierce, P., Costes, S., 2004. Ultrasounds: an industrial solution to optimise costs, environmental requests and quality for textile finishing. Ultrasonics Sonochemistry, 11. Elsevier, pp. 33–38.

Wahab, R., Ansari, S.G., Kim, Y.S., Seo, H.K., Shin, H.S., 2007. Room temperature synthesis of needle-shaped zno nanorods via sonochemical method. Appl. Surf. Sci. 253 (18), 7622–7626. https://doi.org/10.1016/j.apsusc.2007.03.060.

Wang, H., Lu, Y.N., Zhu, J.J., Chen, H.Y., 2003. Sonochemical fabrication and characterization of stibnite nanorods. Inorg. Chem. 42 (20), 6404–6411. https://doi.org/10.1021/ic0342604.

Wang, X.K., Wei, Y.C., Wang, C., Guo, W.L., Wang, J.G., Jiang, J.X., 2011. Ultrasonic degradation of reactive brilliant red K-2BP in water with CCl4 enhancement: performance optimization and degradation mechanism. Sep. Purif. Technol. 81 (1), 69–76. https://doi.org/10.1016/j.seppur.2011.07.003.

Wang, Y., Zhou, C., Wang, W., Zhao, Y., 2013. Preparation of two dimensional atomic crystals BN, WS2, and mos2 by supercritical CO2 assisted with ultrasound. Ind. Eng. Chem. Res. 52 (11), 4379–4382. https://doi.org/10.1021/ie303633c.

Xiao, F., Zhao, F., Zhang, Y., Guo, G., Zeng, B., 2009. Ultrasonic electrodeposition of gold−platinum alloy nanoparticles on ionic liquid−chitosan composite film and their application in fabricating nonenzyme hydrogen peroxide sensors. J. Phys. Chem. C 113 (3), 849–855. https://doi.org/10.1021/jp808162g.

Xie, J.P., Ding, J.F., Attenburrow, G.E., Mason, T.J., 1999. Influence of power ultrasound on leather processing. part I: dyeing. J. Am. Leather Chem. Assoc. 94 (4), 146–157.

Xu, H., Suslick, K.S., 2010. Sonochemical synthesis of highly fluorescent ag nanoclusters. ACS Nano 4 (6), 3209–3214. https://doi.org/10.1021/nn100987k.

Yasuda, K., Koda, S., 2012. 22 Development of sonochemical reactor. In: Handbook on applications of ultrasound: Sonochemistry for sustainability (Eds. Chen, D., Sharma, S. K., & Mudhoo, A.). CRC press. Florida, USA. 581–598.

Yasui, K., 2002. Effect of volatile solutes on sonoluminescence. J. Chem. Phys. 116 (7), 2945–2954. https://doi.org/10.1063/1.1436122.

Zeiger, B.W., Suslick, K.S., 2011. Sonofragmentation of molecular crystals. J. Am. Chem. Soc. 133 (37), 14530–14533. https://doi.org/10.1021/ja205867f.

Zeng, X., McGough, R.J., 2009. Optimal simulations of ultrasonic fields produced by large thermal therapy arrays using the angular spectrum approach. J. Acoust. Soc. Am. 125 (5), 2967–2977. https://doi.org/10.1121/1.3097499.

Zeqiri, B., Gelat, P.N., Hodnett, M., Lee, N.D., 2003. A novel sensor for monitoring acoustic cavitation. part I: concept, theory, and prototype development. IEEE Trans. Ultrasonics, Ferroelectrics Frequency Control, 50 (10), 1342–1350. https://doi.org/10.1109/TUFFC.2003.1244751.

Zhang, W., He, W., Jing, X., 2010. Preparation of a stable graphene dispersion with high concentration by ultrasound. J. Phys. Chem. B 114 (32), 10368–10373. https://doi.org/10.1021/jp1037443.

Index

Page numbers followed by "*f*" and "*t*" indicate, figures and tables respectively.

A

Acoustic cavitation, 3, 35, 89, 219, 265
  bubble growth, 41
  bubble inception, 38
  bubble nuclei and blake threshold, 40
  bubble oscillation, 38, 42
  cavitation types and expected effects, 41
  heterogeneous nucleation theory, 39
  homogeneous nucleation theory, 38
  microjet, 43
  microstreaming, 44
  noise, 145
  physical effects, 43
  shockwave, 44
Acoustic cavitation emission (ACE) signal, 84
Acoustic energy, 15
  density, 220
  macroscopic dissipation, 45
  parameters, 15
  propagation across liquid medium, 15
Acoustic radiation, 16
  from collapsing bubble, 16
  energy, 102
  force, 99
  interpretation, 103
  measurement, 103
  in near field, 103
  radiation force measurement, 102
  sonolator, 104, 105
Acoustic streaming, 36
  Eckart streaming, 37
  mechanism, 37
  numerical modeling, 37
  Rayleigh streaming, 37
Acoustic waves, 220
  amplitude prediction, 172
  attenuation, 220
  in liquid medium, 36
  mapping, 256
  propagation, 30
  ultrasonic wave, 36
Advanced oxidation processes (AOP), 329
Alkaline-surfactant-polymer flooding (ASP), 273
Aluminum foil erosion, 171
Arrhenius constants, 50
Azeotropic distillation, 339

B

Bifurcation structure, 119
Biofuel industry, 269
  biodiesel production, 270
  lignocellulosic biomass pretreatment, 269
Bjerknes force, 17, 100
  primary, 42, 100
  secondary, 42, 101
Blake nucleation threshold, 7
Blake's threshold pressure, 41, 229
Bubble dynamics equation, 174
Bubble model, 146
  complex bubble oscillations, 111
  damping constants, 114
  final construction, 118
  full ODE thermal model, 149
  linear thermal model, 151
  maxima method, 118
  nonlinear bubble behavior analysis, 118
  nonlinear dissipation terms, 118, 119
  nonlinear resonances, 116
  Poincaré section, 118
  scattered pressure, 152 155–152 155
  thermal effects, 148
Bubble nuclei, 40
Bubble oscillation, dynamics, 9, 42
Bubble theory, 85
Bubble wall motion equation, 131, 133
  Gilmore equation, 132
  Herring equation, 132
  Keller-Miksis equation, 132
  Prosperetti-Lezzi equation, 132
  Rayleigh-Plesset equation, 133

C

Caflisch equations, 220, 228
Caflisch model, 224, 225, 226, 227, 228
Cavitation phenomena, 41, 279, 340, 362
  based technologies, 335
  erosion, 41
  fatigue, 41
  pitting, 41
  sound propagation accounting, 224
  threshold, 3, 7, 43*t*, 185
Cavity collapse criterion, 175
Ceramic transducers, 252
Chaotic oscillations, 149
Chemical probes, 355
Coalescence, thermodynamics, 7
Collision efficiency factor, 52
Color Doppler ultrasound imaging, 84
Color flow image, 84
Computed acoustic fields, 237
Condensation, nonequilibrium, 13
Conduction, 14
Convection, 14
Cooling tower water treatment system, 351

D

Damping constants, 134
Damping mechanisms, 131
Demulsification, 272
Desulfurization, 272
Diffusion, 12
Dissipative linear acoustics, 220
Divergence theorem, 231
Duplicated reactions, 53,
see also Sonochemical reactions

E

Eckart streaming, 37
Elastic materials, 230
Electric-acoustic energy conversion, 254
Electrical microdischarge theory, 11
Electrical power, 355, 359
Electrocatalytic pathway, 80
Electroconductivity measurement, 171
Electrolysis process, 80
Emulsification, 268
Emulsions, 332
Energy concentration, 15
  acoustic energy, 15
  acoustic radiation, 16
  engineering outcomes, 20
  macroscopic energy conversion, 19
  propagation across liquid medium, 15
  volume energy concentration, 18
Energy conservation equation, 227, 228
Energy controlling mechanisms
  chemical activity, 148
  energy variation, 149
  model description, 146
Energy conversion
  acoustical conditions, 196
  energetic evolution, 196
  energy analysis, 197
  theoretical background, 194
Energy dissipation functions, 227
Energy efficiency, 360
Engineered nanostructured materials, 331
Enhanced oil recovery (EOR), 272
Enzyme recovery, 330
Evaporation, nonequilibrium, 13

F
Fast Fourier transform (FFT), 167
Finite element methods, 219
Fluoroquinolone antibiotics, 292
Food industry, 268
  processing and preservation, 331
Fourrier's law, 14
Fricke dosimetry, 169

G
Gas bubbles, linear oscillations, 133
  bubble wall motion equation, 133
  damping constants, 134
  linearization process, 133
Gas cavitation, 41
Gilmore equation, 132

H
Harmonic motion, 230, 234
Helmholtz equation, 219, 223, 225, 228
Henry's law constant, 6
Herring equation, 132
Hertz-Knudsen model, 147, 194
Heterogeneous nucleation theory, 4, 5, 39
Heterogenous system, 82,
see also Sonochemical reactions
High-power ultrasonic vibrations, 299
Homogeneous nucleation theory, 4, 38
Hot spot theory, 10
Hydrodynamic cavitation, 35
Hydrogen production techniques, 77, 78*f*
Hydrophones, 355

I
Inertial cavitation, 41
In–situ chemical oxidation (ISCO), 87
Iodine release method, 169,
see also Sonochemical reactors
Iordansky-Kogarko-van Wijngaarden (IKvW) model, 219

K
Keller equation, 228
Keller-Miksis equation, 132, 146, 194, 227

L
Langevin piezoelectric transducers, 253
Laser Doppler Anemometer (LDA), 172
Linear acoustics equations, 220, 225
Linear thermal model (LTM), 151
Liquid compressibility and acoustic damping, 136
Louisnard model, 119

M
Mach number, 44
Macroscopic dissipation, 45
Macroscopic energy conversion, 19
Microbial disinfection, 330
Microjet, 43
Microstreaming, 36, 43, 44
Muller-Platte needle hydrophones, 86
Multi-bubble cavitation, 266
Multibubble system, 146
Multiple bubble sonoluminescence (MBSL), 82
Multiple transducers, 158

N
Nanoparticles, 330
Navier-Stokes equations, 9, 220
Non-dissipative linear acoustics, 222
Nondocumented tip-transducer, 240
Nonlinear bubble behavior analysis, 118
  final construction, 118
  maxima method, 118
  Poincaré section, 118
Nonlinear dissipation, 118, 119,
see also Bubble model
Nonlinear oscillations, of bubbles, 141
  bubble wall motion equations, 143
  viscous and acoustic damping mechanisms, 141
Nucleation sites, 5, 39

O
Oil sand extraction, 272
Ordinary differential equations (ODE), 50
Oscillating bubble, 196

P
Partial differential equations (PDE), 146
Particle image velocimetry (PIV), 86, 172
Perfluorooctanesulfonic acid (PFOS), 79
Peroxydisulfate, 87
Peroxymonosulfate, 87
Pharmaceutical compounds
  acoustic power, 283
  crystal growth, 282
  nucleation, 281
  supersaturation, 280
  theorical approach, 279
  US frequency, 282
Piezo-electrics, 233, 235
Plasma chemical technique, 325
Plate piezoelectric transducers, 252
Polymer degradation, 172
Polytropic model, 12
Power transducers, 255
Power ultrasound, 265, 267
  biodiesel production, 270
  biofuel industry, 269
  bio-hydrogen production, 271
  food industry, 268
  industrial applications, 268
  lignocellulosic biomass pretreatment, 269
  metal industry, 273
  petroleum industry, 272
Pressure-dependent reactions, 52,
see also Sonochemical reactions
Process intensification, 329
Prosperetti-Lezzi equation, 132

R
Rankine-Hugoniot relations, 44
Rayleigh equation, 226, 228
Rayleigh-Plesset equation, 133, 225
Rayleigh streaming, 37
Rectified diffusion, 31 35–31 35,
see also Ultrasonic process
  threshold, 8
Repetitive transient cavitation, 41

S
Salicylic acid dosimetry, 169
Scaling up processes, 360
Schlieren image, 103
Sequential and parallel reactions, 305
Shockwave, 16, 44
Single acoustic cavitation bubble, 4
  Blake nucleation threshold, 7
  bubble inception, growth and dynamics of oscillation, 4
  bubble oscillation, 9
  conduction, 14
  convection, 14
  diffusion, 12
  evaporation and condensation, 13
  gaseous nucleus formation, 5
  heterogeneous nucleation theory, 5
  homogeneous nucleation theory, 4
  hot spot theory, 10
  polytropic model, 12
  rectified diffusion threshold, 8
  sonochemistry, energetics of, 12
  thermodynamics, 7, 11
  thresholds, 7
  transient cavitation threshold, 8
Single bubble sonoluminescence (SBSL), 82, 266
Sonocatalysis, 317
Sonochemical assisted pathways, 325
Sonochemical degradation, 288
Sonochemical mechanism, 82
Sonochemical reaction, 77
  acoustic bulk cavitation, 85
  application, 86
  bulk solution, 81
  color Doppler ultrasound imaging, 84
  complete bubble model, 54
  duplicated reactions, 53
  energy efficiency considerations, 68
  in gas phase of collapsing bubbles, 78
  governing equations, 50
  heterogenous system, 82
  homogeneous system, 81
  at interfacial region surrounding collapsing bubbles, 79
  micro-PIV measurements, 86
  numerical technique, 60
  pressure-dependent reactions, 52
  pure oxygen/water vapor bubble, 54
  single bubble, chemical yield, 61
  sites, 185
  sonoluminescence, 82
  state-of-the-art reaction mechanism, 50
  three-body reactions, 52
  tube arrest method, 83
  ultrasonic cavitation observation and measurement, 82
Sonochemical reactors
  acoustic streaming predictions, 173

acoustic wave amplitude prediction, 172
active and passive cavitational zones, 161
bubble dynamics, 174
bubble dynamics studies, 178
case study, 176
cavitational activities, 161, 162, 164, 166
challenges, 162
chemical methods, 169
efficiency assessment, 164
electroconductivity measurement, 171
experimental setup, 176
flow visualization and measurement techniques, 172
fluorescence determination, 171
iodine liberated, 176
iodine release method, 169
local pressure field, 178
numerical investigations, 172
observations, 178
physical methods, 171
polymer degradation, 172
pressure measurement, 167
primary effects quantification, 167
secondary effect quantification, 168
sonochemiluminescence, 171
spatial and temporal distribution, 161
temperature measurement, 168
Sonochemical treatment, 287
Sonochemiluminescence, 171
Sonochemistry, 49, 266
energetics, 12
equipment, 363
Sonocrystallization, 268
Sonohydrogen reactor design, 361
Sonolator, 104, 105,
see also Acoustic radiation energy
Sonoluminescence, 82, 171
Sonoluminescence approaches, 355
Sonolysis reactors, 359
Sonoreactor, 219
configuration, 221*f*, 232*f*
Standard propagation equation, 220
Streak photography, 86
Stress-charge formulation, 233
Supersaturation, 280
Suspensions, 332

T

Technogenic waste, 300
Terephthatic acid
dosimetry, 171
Textile finishing, 337
Textile industry, 353
Thermal damping, 134
basic equations, 134
nonuniform pressure inside bubble, 135
uniform pressure inside bubble, 136
Thermal layer width, 14
Three-body reactions, 52,
see also Sonochemical reactions
Total damping constants, 137
Transducers, 185
electromechanical, 250
gas-driven, 250
Langevin piezoelectric, 253
liquid-driven, 250
magnetostrictive, 250
piezoelectric, 252
plate piezoelectric, 252
Transesterification, 271
Transient cavitation, 8, 27, 350, 359
Tube arrest method, 83

U

Ultrasonic process, 158, 159*f*, 183, 353
acoustic emission, 204
acoustic impedance, 27
acoustic wave propagation, 30
frequency, 187, 357, 360, 361, 362
gas addition, 189
liquid flow, 188
liquid temperature, 188
mathematical model, 25
method, 299
power intensity, 186
pressure, 187
processing systems, 353
radial motion, 203
reactor design, 188
rectified diffusion, 31 35–31 35
resasoning, 200
secondary parameters, 188
signals, 186
solid addition, 189
solute properties, 188
solvent properties, 188
sonochemical reaction sites, 185
sonoelectrochemistry, 355
spectral characteristics, 201
synthesis, 301
theoretical approaches, 183
transducers, 185, 250*f*
treatment application, 299
waves, 350, 353
Weissler reaction, 210
wet textile treatment, 207
Ultrasound, 250, 330, 333, 350
assisted azeotropic distillation process, 340
assisted drying, 333
assisted methods, 331
assisted pathways, 325, 318
assisted processes, 317, 335
defined, 15
designs and energy efficiency, 257
electromechanical transducers, 250
gas-driven transducers, 250
Langevin piezoelectric transducers, 253
liquid-driven transducers, 250
magnetostrictive transducers, 250
overall energy efficiency, 257
piezoelectric transducers, 252
plate piezoelectric transducers, 252

V

Vapor, 137
basic equations, 137
cavitation, 41
linear oscillations, 138
mass transfer, 139
Viscosity modification, 268
Volume energy concentration, 18,
see also Energy concentration

W

Wave propagation, 139
basic equations, 139
wave speed and attenuation, 141
Wet textile treatment, 207

X

X-ray diffraction patterns, 301
X-ray phase analysis, 306, 307

Y

Young modulus, 236

ENERGY ASPECTS OF ACOUSTIC CAVITATION AND SONOCHEMISTRY

Fundamentals and Engineering

Oualid Hamdaoui
Chemical Engineering Department, College of Engineering, King Saud University, Riyadh, Saudi Arabia
Kaouther Kerboua
Higher School of Industrial Technologies, Department of Engineering, Annaba, Algeria

Relates fundamental modelling and up-scaled experiments to acoustic cavitation and its intrinsic energy balance.

Energy Aspects of Acoustic Cavitation and Sonochemistry: Fundamentals and Engineering covers topics ranging from fundamental modelling to up-scaled experiments. The book relates acoustic cavitation and its intrinsic energy balance to macroscopic physical and chemical events, which are analyzed from an energetic perspective. The outcomes are directly projected into practical applications and technological assessments covering energy consumption, thermal dissipation, and energy efficiency of a diverse set of applications in mixed-phase synthesis, environmental remediation, and materials chemistry. A special interest is dedicated to the sonochemical production of hydrogen and its energetic dimensions.

Key Features

- Provides a concise and detailed description of energy conversion and exchange within the single acoustic cavitation bubble and bubble population, accompanying physical and chemical effects.
- Features a comprehensive approach, supported by experiments and modelling, of energy concentration within the sonochemical reactor, jointly with energy dissipation and damping phenomenon.
- Gives a clear definition of energy efficiency metrics of industrial sono-processes, and their application to the main emergent industrial fields harnessing acoustic cavitation and sonochemistry, notably for the production of hydrogen.

ELSEVIER elsevier.com/books-and-journals

ISBN 978-0-323-91937-1
9 780323 919371